Spacecraft Thermal Control Handbook

Volume I: Fundamental Technologies

David G. Gilmore
Editor

Second Edition

Preface

In keeping with its goal of strengthening its relationship with customers and industry, The Aerospace Corporation has prepared this handbook, a compendium of corporate knowledge and heritage in the field of thermal control of uncrewed spacecraft. The objective of this effort was to develop a practical handbook that provides the reader with enough background and specific information to begin conducting thermal analysis and to participate in the thermal design of spacecraft systems. It is assumed that the reader has had at least one introductory heat-transfer class and understands the fundamental principles of conductive, radiative, and convective heat transfer.

The handbook is written in such a way as to be useful to thermal engineers of all experience levels. The first two chapters provide a general overview of uncrewed spacecraft systems and space flight thermal environments. Chapter 3 describes a number of actual spacecraft and component thermal designs to familiarize those new to the field with some historical design approaches. Subsequent chapters discuss, in detail, thermal control hardware and the thermal design and testing process. The final chapter provides an overview of emerging thermal technologies for the future.

This book is actually a revised and updated edition of *Satellite Thermal Control Handbook,* published by The Aerospace Corporation in 1994. The name change reflects the expanded scope of this work, which now includes thermal environments and design techniques for interplanetary spacecraft, in addition to the Earth-orbiting satellites that were the focus of the original handbook. The reader will now find an updated characterization of the thermal environment in Earth orbit, new material documenting the environments of interplanetary missions, more detailed information about each of the thermal control hardware elements found in the first edition, and presentation of some newer technologies such as heat switches and precision temperature control techniques.

Two additional volumes of this handbook are planned. Volume 2, devoted to cryogenics, is expected to be published late in 2003. Volume 3, covering heat pipes, loop heat pipes, and capillary pumped loops, is planned for a later date.

Acknowledgments

Contributing Authors

K. Aaron, Jet Propulsion Laboratory, California Institute of Technology, Pasadena, California
Chapter 17, Precision Temperature Control

J. Ambrose, Lockheed Martin, Sunnyvale, California
Chapter 17, Precision Temperature Control

B. J. Anderson, NASA/MSFC, Huntsville, Alabama
Chapter 2, Spacecraft Thermal Environments

W. Batts, Computer Sciences Corporation, Huntsville, Alabama
Chapter 2, Spacecraft Thermal Environments

V. Baturkin, National Technical University of Ukraine, formerly Kyiv Polytechnic Institute, Kyiv, Ukraine
Chapter 8, Mountings and Interfaces

R. Bettini, B.F. Goodrich Aerospace, Danbury, Connecticut
Chapter 3, Thermal Design Examples

P. Bhandari, Jet Propulsion Laboratory, California Institute of Technology, Pasadena, California
Chapter 12, Pumped Fluid Loops

G. C. Birur, Jet Propulsion Laboratory, California Institute of Technology, Pasadena, California
Chapter 12, Pumped Fluid Loops
Chapter 20, Technology Projections

L. Bledjian, The Aerospace Corporation, El Segundo, California
Chapter 11, Phase-Change Materials

D. A. Boyd, Smithsonian Astrophysical Observatory, Cambridge, Massachusetts
Chapter 17, Precision Temperature Control

A. Chuchra, Swales Aerospace, Beltsville, Maryland
Chapter 13, Thermoelectric Coolers

J. F. Clawson, Jet Propulsion Laboratory, California Institute of Technology, Pasadena, California
Chapter 2, Spacecraft Thermal Environments

G. Cluzet, Alcatel, Velizy, France
Chapter 3, Thermal Design Examples

R. L. Collins, The Aerospace Corporation, El Segundo, California
Chapter 15, Thermal Design Analysis

B. Cullimore, C&R Technologies, Littleton, Colorado
Chapter 14, Heat Pipes

G. M. DeVault, The Boeing Company, Houston, Texas
Chapter 18, Space Shuttle Integration

J. Doenecke, Astrium, Friedrichshaten, Germany
Chapter 3, Thermal Design Examples

M. Donabedian, The Aerospace Corporation, El Segundo, California
Chapter 5, Insulation

R. J. Eby, Orbital Sciences Corporation, Dulles, Virginia
Chapter 9, Louvers

D. Ferguson, Swales Aerospace, Beltsville, Maryland
Chapter 2, Spacecraft Thermal Environments

C. Finch, BAE Systems, Basildom, United Kingdom
Chapter 3, Thermal Design Examples

M. Fong, Lockheed Martin Corporation, Sunnyvale, California
Chapter 4, Thermal Surface Finishes

D. G. Gilmore, The Aerospace Corporation, El Segundo, California
Chapter 1, Spacecraft Systems Overview
Chapter 2, Spacecraft Thermal Environments
Chapter 3, Thermal Design Examples
Chapter 4, Thermal Surface Finishes
Chapter 5, Insulation
Chapter 6, Radiators
Chapter 7, Heaters
Chapter 15, Thermal Design Analysis

D. F. Gluck, DFG Engineering, Albuquerque, New Mexico
Chapter 8, Mountings and Interfaces

G. E. Gurevich, Microcosm Inc., El Segundo, California
Chapter 18, Space Shuttle Integration

D. V. Hale, Lockheed Martin, Huntsville, Alabama
Chapter 11, Phase-Change Materials

B. E. Hardt, The Aerospace Corporation, El Segundo, California
Chapter 9, Louvers
Chapter 20, Technology Projections

B. P. Harris, United Space Alliance, Houston, Texas
Chapter 18, Space Shuttle Integration

A. Hashemi, Lockheed Martin, Palo Alto, California
Chapter 17, Precision Temperature Control

M. J. Hoover, Lockheed Martin, Huntsville, Alabama
Chapter 11, Phase-Change Materials

C. G. Justus, Computer Sciences Corporation, Huntsville, Alabama
Chapter 2, Spacecraft Thermal Environments

R. D. Karam, Orbital Sciences Corporation, Dulles, Virginia
Chapter 9, Louvers

T. T. Lam, The Aerospace Corporation, El Segundo, California
  Chapter 12, Pumped Fluid Loops
  Chapter 20, Technology Projections

K. Lankford, Starsys Research Corporation, Boulder, Colorado
  Chapter 10, Heat Switches

E. I. Lin, Jet Propulsion Laboratory, California Institute of Technology, Pasadena, California
  Chapter 5, Insulation

J. C. Lyra, Jet Propulsion Laboratory, California Institute of Technology, Pasadena, California
  Chapter 7, Heaters

J. F. Maddox, Smithsonian Astrophysical Observatory, Cambridge, Massachusetts
  Chapter 17, Precision Temperature Control

M. B. H. Mantelli, Federal University of Santa Catarina, Florianopolis, Brazil
  Chapter 16, Thermal Contact Resistance

E. M. Mattison, Smithsonian Astrophysical Observatory, Cambridge, Massachusetts
  Chapter 17, Precision Temperature Control

C. R. Miller, NASA/JSC, Houston, Texas
  Chapter 18, Space Shuttle Integration

M. Nikitkin, Swales Aerospace, Beltsville, Maryland
  Chapter 14, Heat Pipes

T. P. O'Donnell, Jet Propulsion Laboratory, California Institute of Technology, Pasadena, California
  Chapter 20, Technology Projections

M. J. O'Neill, Lockheed Martin, Huntsville, Alabama
  Chapter 11, Phase-Change Materials

B. Patti, European Space Agency, Leiden, Netherlands
  Chapter 3, Thermal Design Examples

J. Pecson, Lockheed Martin, Palo Alto, California
  Chapter 17, Precision Temperature Control

R. C. Prager, The Aerospace Corporation, El Segundo, California
  Chapter 14, Heat Pipes

H. A. Rotter, NASA/JSC, Houston, Texas
  Chapter 18, Space Shuttle Integration

J. G. Santiago, Stanford University, Palo Alto, California
  Chapter 20, Technology Projections

R. Serna, NASA/JSC, Houston, Texas
  Chapter 18, Space Shuttle Integration

W. K. Smith, The Boeing Company, Houston, Texas
Chapter 18, Space Shuttle Integration

T. Stevenson, University of Leicester, Leicester, United Kingdom
Chapter 13, Thermoelectric Coolers

R. Stoll, B.F. Goodrich Aerospace, Danbury, Connecticut
Chapter 3, Thermal Design Examples

W. K. Stuckey, The Aerospace Corporation, El Segundo, California
Chapter 4, Thermal Surface Finishes

J. W. Stultz, Jet Propulsion Laboratory, California Institute of Technology, Pasadena, California
Chapter 5, Insulation
Chapter 7, Heaters

T. D. Swanson, NASA Goddard Space Flight Center, Greenbelt, Maryland
Chapter 20, Technology Projections

G. T. Tsuyuki, Jet Propulsion Laboratory, California Institute of Technology, Pasadena, California
Chapter 2, Spacecraft Thermal Environments
Chapter 5, Insulation

B. Turner, BAE Systems, Basildom, United Kingdom
Chapter 3, Thermal Design Examples

R. F. C. Vessot, Smithsonian Astrophysical Observatory, Cambridge, Massachusetts
Chapter 17, Precision Temperature Control

K. Vollmer, Astrium, Friedrichshaten, Germany
Chapter 3, Thermal Design Examples

J. W. Welch, The Aerospace Corporation, El Segundo, California
Chapter 19, Thermal Testing

Y. Yoshikawa, Lockheed Missiles and Space Company, Sunnyvale, California
Chapter 3, Thermal Design Examples

M. M. Yovanovich, University of Waterloo, Waterloo, Canada
Chapter 16, Thermal Contact Resistance

Contents

Contents

Contents

Contents

1 Spacecraft Systems Overview

D. G. Gilmore[*]

Introduction

During the past 40 years, hundreds of spacecraft have been built in support of scientific, military, and commercial missions. Most can be broadly categorized as either three-axis-stabilized spacecraft, spin-stabilized spacecraft, or pallets; these types are distinguished by their configurations, internal equipment, and thermal-control designs. This chapter is a brief overview of the characteristics of each of these different types of spacecraft and the missions they support. Representative thermal designs for each type are discussed in more detail in Chapter 3.

Spacecraft Configurations

The most common spacecraft configuration today is three-axis-stabilized. This type of spacecraft is characterized by a body that is roughly box-shaped and by deployable solar-array panels. Examples are the Defense Meteorological Satellite Program (DMSP), the Japanese Earth Resources Satellite (JERS), and the Russian communications satellite Gorizont, shown in Fig. 1.1. The bodies of these spacecraft are usually kept inertially stable except for a slow rotation induced about one axis to keep the payload antennas or sensors continuously pointed toward Earth as the satellite orbits. The solar-array panels are then counterrotated relative to the spacecraft body to keep them inertially fixed on the sun. Some three-axis spacecraft, such as the European Infrared Space Observatory (ISO, Fig. 1.1), have restrictions on attitude (the vehicle's orientation relative to an inertial coordinate system) or low power requirements that allow them to use fixed solar arrays that do not rotate to track the sun.

A typical internal equipment complement for a three-axis-stabilized spacecraft is shown in the exploded view of a Fleet Satellite Communications (FLTSAT-COM) satellite in Fig. 1.2. The spacecraft is commonly referred to in terms of a "payload" and a "bus," or "platform." The payload is the equipment that services the primary mission—for example, a cloud-cover camera for a weather satellite or an infrared (IR) sensor for a missile early-warning system. Since FLTSATCOM is a communication satellite, the payload is the communications subsystem, which consists of the antennas on the Earth-facing side of the vehicle and the communications electronics boxes mounted in the upper hexagonal compartment, as shown in Fig. 1.2. The bus consists of all other spacecraft subsystems that support the payload. These subsystems typically include

- Structures subsystem: the physical structure of the spacecraft, to which all electronics boxes, thrusters, sensors, propellant tanks, and other components are mounted

---

*The Aerospace Corporation, El Segundo, California.
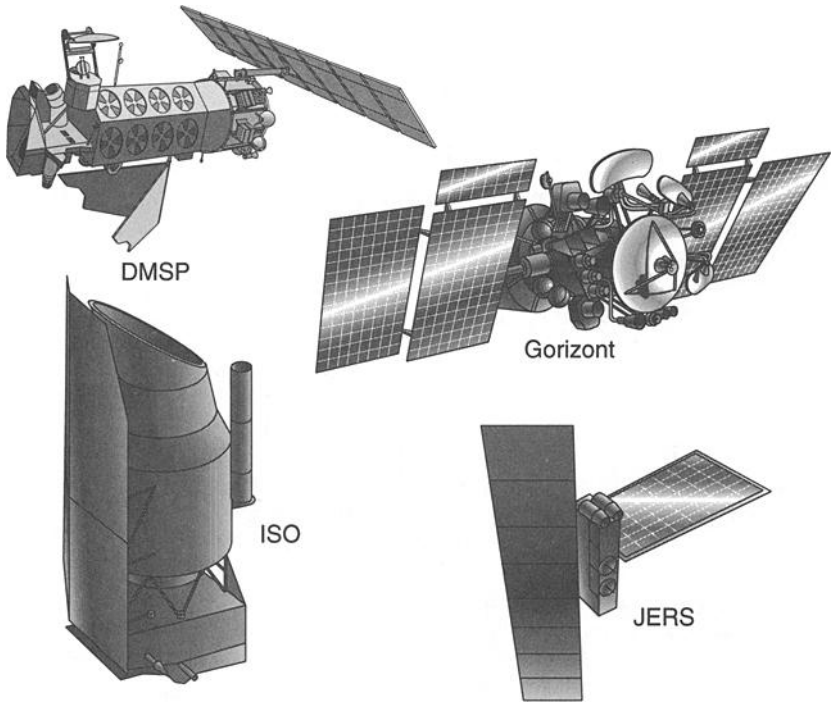
Fig. 1.1. Three-axis-stabilized satellites.

- Electrical power/distribution subsystem (EPS or EPDS): the equipment used to generate and distribute electrical power to the spacecraft, including solar arrays, batteries, solar-array controllers, power converters, electrical harnesses, battery-charge-control electronics, and other components
- Telemetry, tracking, and command subsystem (TT&C): The electronics used to track, monitor, and communicate with the spacecraft from the ground. TT&C equipment generally includes receivers, transmitters, antennas, tape recorders, and state-of-health sensors for parameters such as temperature, electrical current, voltage, propellant tank pressure, enable/disable status for various components, etc.
- Attitude/velocity control subsystem (ACS or AVCS): The devices used to sense and control the vehicle attitude and velocity. Typical components of the ACS system include sun and Earth sensors, star sensors (if high-precision pointing is required), reaction or momentum wheels, Inertial Measurement Units (IMUs), Inertial Reference Units (IRUs), and the electronics required to process signals from the above devices and control satellite attitude.

- Propulsion subsystem: Liquid and solid rockets or compressed-gas jets and associated hardware used for changing satellite attitude, velocity, or spin rate. Solid rockets are usually used for placing a satellite in its final orbit after separation from the launch vehicle. The liquid engines (along with associated plumbing lines, valves, and tanks) may be used for attitude control and orbit adjustments as well as final orbit insertion after launch.
- Thermal-control subsystem (TCS): The hardware used to control temperatures of all vehicle components. Typical TCS elements include surface finishes, insulation blankets, heaters, and refrigerators.

Many of these subsystem components are shown in the drawing of FLTSAT-COM in Fig. 1.2.

The second category of spacecraft is spin-stabilized. These are less common than the three-axis-stabilized type and have been used mostly for relatively high-altitude missions in geosynchronous or Molniya orbits (p. 9). Some spinning satellites, however, are used in low-altitude orbits. A typical "spinner," Intelsat VI, is shown in Fig. 1.3. As the category name implies, these satellites achieve attitude stability by spinning like a top. Each spins at approximately 15 rpm about the axis of a cylindrical solar array. In the case of Intelsat VI, the communications payload is mounted on a large shelf, which is despun relative to the rest of the spacecraft so that it points continuously at Earth.

A spinner has the same basic subsystems as a three-axis-stabilized spacecraft: structures, EPS, TT&C, ACS, propulsion, and TCS. Usually, the payload is contained entirely on the despun section, while most of the other subsystems are on the spinning side. Some types of spinners, however, such as the Defense Support Program satellites (DSP; Fig. 1.4), do not have a despun shelf. In the case of DSP, the payload, an IR telescope/sensor, spins with the rest of the satellite; the rotation of the vehicle provides a scanning motion for the sensor.

A pallet is technically a collection of one or more payloads plus some limited support services, such as power distribution, data recording, or telemetry sensors. Pallets may be anything from a small experiment mounted to the side of a host spacecraft to a large structure containing many instruments and mounted in the payload bay of the space shuttle. The principal difference between the pallet and other spacecraft is that the pallet is not able to function autonomously, but instead relies on the host vehicle for ACS, EPS, and TT&C support.

The Experiment Support System (Fig. 1.5) is a typical pallet system. It consists of a rather large structure that supports a half-dozen experiments and an equipment compartment containing power distribution, command processing, and data recording equipment. The pallet is mounted in the space-shuttle payload bay, and the shuttle provides ACS, EPS, and TT&C functions. In addition to the pallet itself, there is a command monitor panel mounted in the crew compartment to allow the astronauts to control the operation of the experiments on the pallet. Because of the support provided by the shuttle, the pallet does not have propulsion, ACS, EPS, or TT&C subsystems, and it is incapable of operating on its own in space.
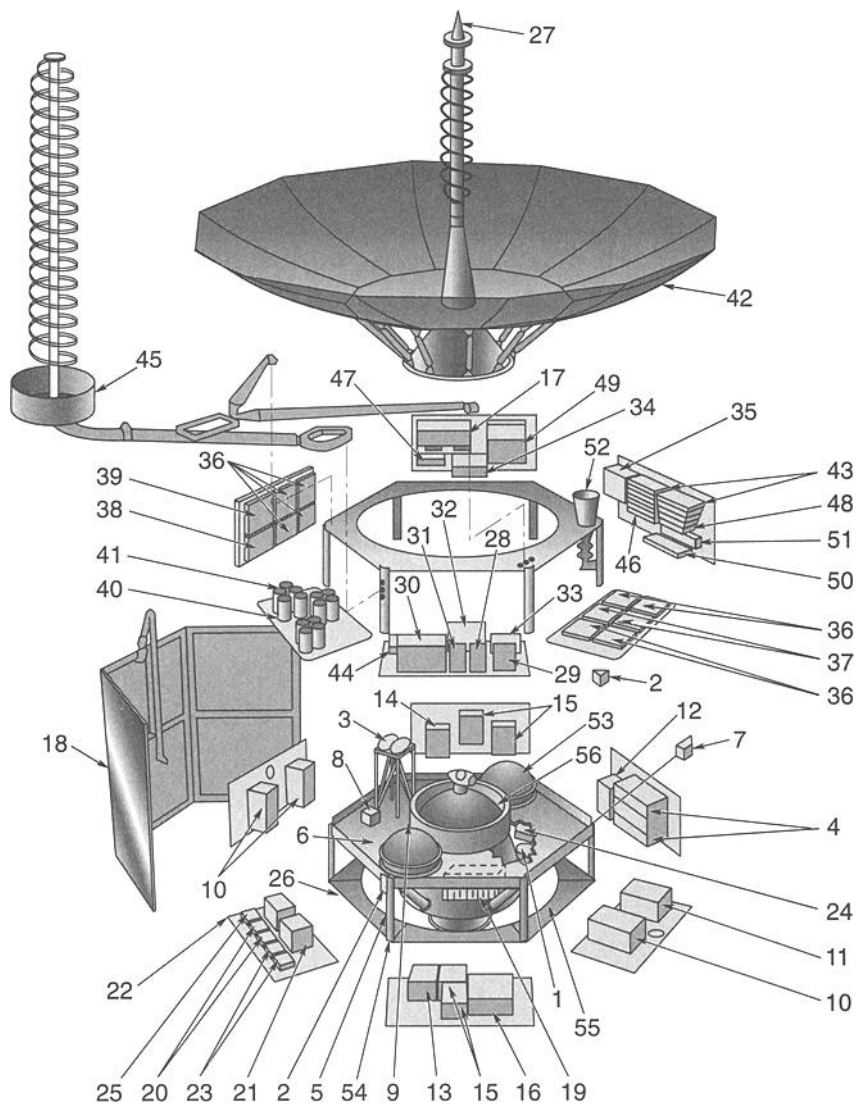
Fig. 1.2. Exploded view of FLTSATCOM. (Legend on facing page.)

Legend for Fig. 1.2.

Attitude and Velocity Control

1. Solar array drive assembly
2. Sun sensor assembly
3. Earth sensor assembly
4. Control and auxiliary electronics
5. Spinning Earth sensor assembly
6. Reaction wheel assembly
7. Coarse sun sensor assembly
8. Earth sensor electronics
9. Nutation damper assembly

Electrical Power/ Distribution System

10. Battery assembly
11. Power control unit
12. Converter, spacecraft equipment
13. Converter, communications no. 1
14. Converter, communications no. 2
15. Converter, transmitter
16. Payload switching unit no. 1
17. Payload switching unit no. 2
18. Solar panel assembly
19. Electrical integration assembly

Telemetry, Tracking, and Command System

S-Band Command Group

20. S-band receiver
21. Decrypter KIR23 (2 required)
22. Command unit

S-Band Telemetry Group

23. S-band telemetry transmitter
24. PCM encoder

S-Band Antenna Group

25. S-band diplexer
26. RF coaxial switch
27. S-band antenna

Communication System UHF Transponder

28. Preamp/downconverter/IF limiter no.1
29. IF filter limiter no. 2
30. Processor receiver/synthesizer
31. Repeater receiver
32. Command receiver/synthesizer
33. Oven-controlled crystal oscillator (2)
34. AF processor
35. UHF command decoder
36. UHF transmitter Navy low power
37. UHF transmitter Navy high power
38. UHF transmitter (DODWB)
39. UHF transmitter (AFNB)
40. UHF transmitter filter
41. UHF multicoupler filter assembly
42. Transmit antenna assembly
43. Frequency generator
44. Receiver filter
45. UHF receive antenna assembly
46. Signal distribution unit no. 1
47. Signal distribution unit no. 2
48. Passive hybrid

SHF Transponder

49. FB processor
50. SHF receiver
51. SHF transmitter
52. SHF antenna

Propulsion System

53. Propellant tank
54. Fill and drain valve
55. Thruster assembly
56. Apogee kick motor

Telemetry and command antenna

C-Band multiple beam antennas

K-Band spot beam antennas

Earth coverage antennas

Communications equipment

Traveling wave tube amplifiers

Nickel-hydrogen batteries

Thermal radiator

Spinning structure and electronics

Orbit and attitude control propulsion system

Solar cell arrays
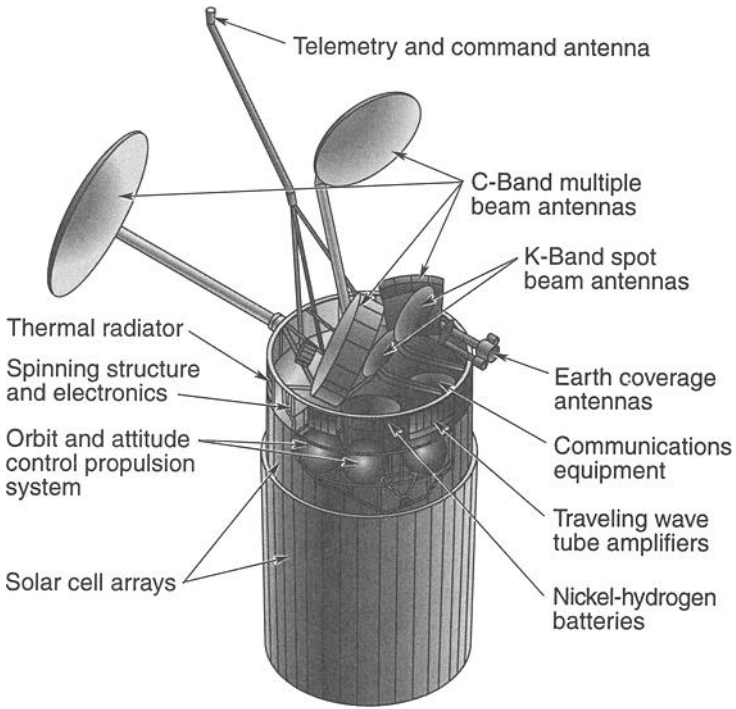
Fig. 1.3. Intelsat VI satellite.
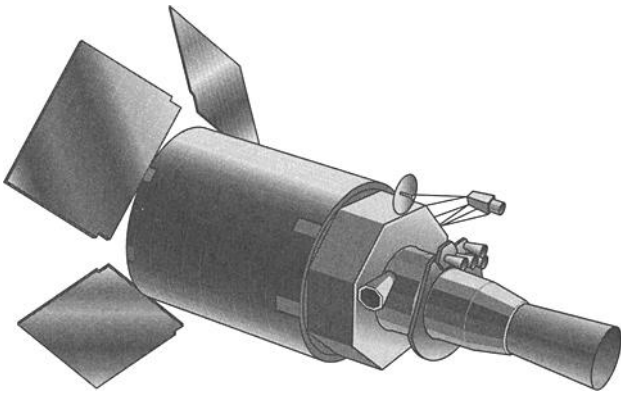
Fig. 1.4. DSP satellite.
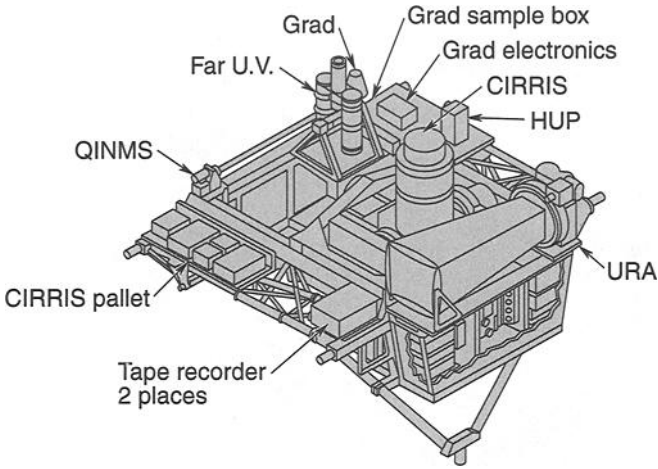
Fig. 1.5. Experiment Support System.

Another spacecraft configuration worth noting here is that of upper stages. Although they are not spacecraft per se, upper stages may be of a similar level of complexity, and they may contain some of the same subsystems. They are included in this handbook because upper-stage thermal control after separation from the booster is quite similar to the thermal control of spacecraft.

Upper stages are generally used to raise a spacecraft to a higher operational orbit from the relatively low orbit to which the booster delivers it. The duration of their missions varies from a few hours to several days. Upper stages can use solid, liquid, or cryogenic propellants. The Inertial Upper Stage (IUS, Fig. 1.6) is an example of a solid-propellant upper stage that can be used in conjunction with either the space shuttle or expendable boosters. The IUS itself has two stages; the first is generally used to put the spacecraft into a highly elliptical transfer orbit, and the second is fired at transfer-orbit apogee (the point in the orbit with the greatest altitude above the planet surface) to make the orbit circular at the higher altitudes. Like a satellite, the IUS has structures, EPS, TT&C, ACS, propulsion, and thermal-control subsystems.

Earth Orbits

A variety of orbits are used for different types of Earth-oriented missions. The most common orbits, in order of increasing altitude, are low Earth (LEO), Molniya, and geosynchronous (GEO). These are drawn to scale in Fig. 1.7. The following section briefly describes these orbits, and a more detailed discussion of orbit parameters can be found in Chapter 2.

Orbits whose maximum altitudes are less than approximately 2000 km are generally considered low Earth orbits. They have the shortest periods, on the order of an hour and a half. Some of these orbits are circular, while others may be somewhat elliptical. The degree of eccentricity is limited by the fact that the orbit is not much larger than Earth, whose diameter is approximately 12,760 km (Fig. 1.7). The inclination of these orbits, which is the angle between the plane of the equator

Spacecraft interface plane

Thrust vector control potentiometer

Equipment support section

Nozzle

Solid rocket motor

Interstage structure

Extendable exit cone

Solid rocket motor

Control system

Inertial measurement unit

Star scanner

STS antenna

Computer

Pyro switching unit

Transponder (optional)

Fuel tank

Reaction engine mode

Encrypter (optional)

Signal interface unit

Signal conditioning unit

Spacecraft connectors

T34D interface unit

DC-DC converter (optional)

Encrypter (optional)

STS antenna (optional)

Fuel tank

Reaction engine module

Diplexer (optional)

Reaction engine module

SRM-2 safe and ARM (2)

T34D medium-gain antenna

STS antenna (optional)

Battery (3)

Battery (3)

Thrust vector control

Computer

Transponder

Fuel tank (optional)

Reaction engine module

Thrust vector control A

Power distribution unit

Environmental measurement unit

Power transfer unit

Decrypter (optional)

Signal conditioning unit

STS antenna

Power amplifier

Power amplifier (optional)

Diplexer

Fig. 1.6. Inertial upper stage.

Fig. 1.7. Orbit types.

and the plane of the orbit, can vary from 0 deg to greater than 90 deg. Inclinations greater than 90 deg cause a satellite in LEO to orbit in a direction opposite to Earth's rotation. Low Earth orbits are very often given high inclinations so that the satellite can pass over the entire surface of Earth from pole to pole as it orbits. This coverage is important for weather and surveillance missions.

One particular type of low Earth orbit maintains the orbit plane at a nearly fixed angle relative to the sun (Fig. 1.8). The result of this is that, on every orbit, the satellite passes over points on Earth that have the same local time, that is, the same local sun-elevation angle. Because Earth rotates beneath the orbit, the satellite sees a different swatch of Earth's surface on each revolution and can cover the
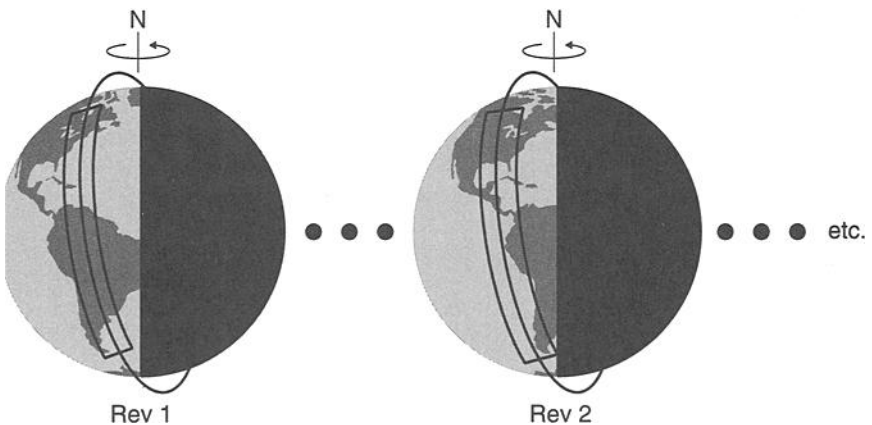
Fig. 1.8. Sun-synchronous orbit.

entire globe over the course of a day. The ability to see the entire surface of Earth at the same local sun angle is important for weather observation and for visual-surveillance missions. This type of orbit is known as sun-synchronous and is discussed in more detail in Chapter 2. Sun-synchronous orbits may be positioned so that satellites always see points on Earth at a specific time, anywhere from local sunrise/sunset to local noon. They are often known as "noon" or "morning" orbits.

The next higher type of common orbit is known as Molniya. These orbits are highly elliptical (apogee 38,900 km, perigee [the point in the orbit with the lowest altitude above the planet surface] 550 km) and highly inclined (62 deg). They provide good views of the north polar region for a large portion of the orbit (Fig. 1.9). Because the satellite travels very slowly near apogee, it has a good view of the polar region for up to eight hours out of its 12-hour period. A constellation of three satellites in Molniya orbits can provide continuous coverage of the northern hemisphere for missions such as communication with aircraft flying over the polar region.

The highest common orbit type is geosynchronous. These orbits are circular and have very low inclinations (< 10 deg). They have an altitude of 35,786 km. Their distinguishing characteristic is a period matching Earth's rotation, which allows a satellite to remain over the same spot on Earth at all times. This characteristic is valuable for a wide variety of missions, including weather observation, communication, and surveillance.

One final useful observation is that most Earth-orbiting satellites travel through their orbits in a counterclockwise motion as seen from above the north pole. They move in this direction to take advantage of the initial eastward velocity given to the the satellite as a result of Earth's rotation (approximately 1500 km/h at the Kennedy
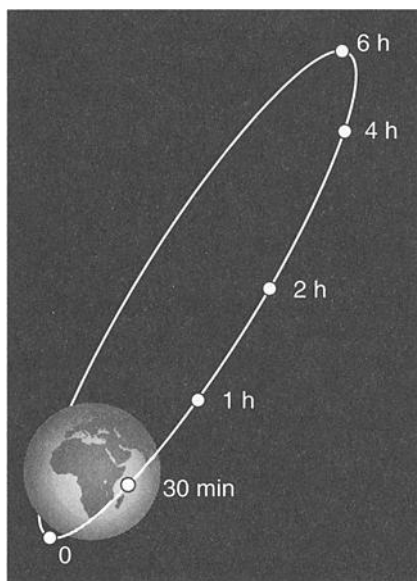
Fig. 1.9. Molniya orbit.

Space Center). To travel the orbit in the opposite direction would require the booster to overcome the initial 1500 km/h eastward velocity before starting to build up speed in a westerly direction. This requirement would significantly affect booster size and allowable payload weight.

Interplanetary Orbits

Orbits used in interplanetary missions range from simple, direct planet-to-planet transfer orbits to complicated trajectories involving close flybys past multiple planets on the way to a final destination. Lunar transfer orbits, such as those used on the Apollo program (Fig. 1.10), offer direct, minimum-energy transfer to the moon. Similar direct transfers are usually used for missions to Mars or Venus, as shown in Fig. 1.11. Spacecraft going to the outer planets often take advantage of gravity assists from flybys past other planets along the way. In a flyby, the spacecraft enters the gravitational field of a planet it is passing, and it achieves a net acceleration as a result of the planet's own velocity. This gravitational "slingshot" effect allows for either a smaller, lower-cost launch vehicle or the accommodation of more payload equipment mass. The Venus-Venus-Earth-Jupiter Gravity Assist trajectory (VVEJGA) of the Cassini mission to Saturn is shown in Fig. 1.12, and Table 1.1 summarizes the key orbital parameters for the planets of our solar system. The wide range of environments encountered in a Cassini-type trajectory can complicate the spacecraft thermal design process; this idea is discussed in subsequent chapters.
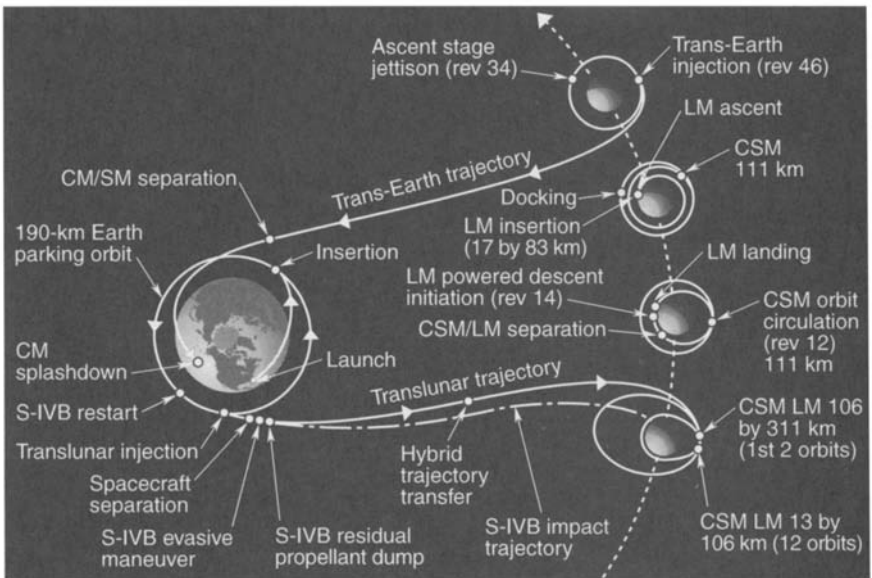
Fig. 1.10. Lunar transfer orbits (NASA). Spacecraft modules: CM, command module; CSM, command-service module; LM, lunar module; SM, service module; S-IVB, Saturn IVB.
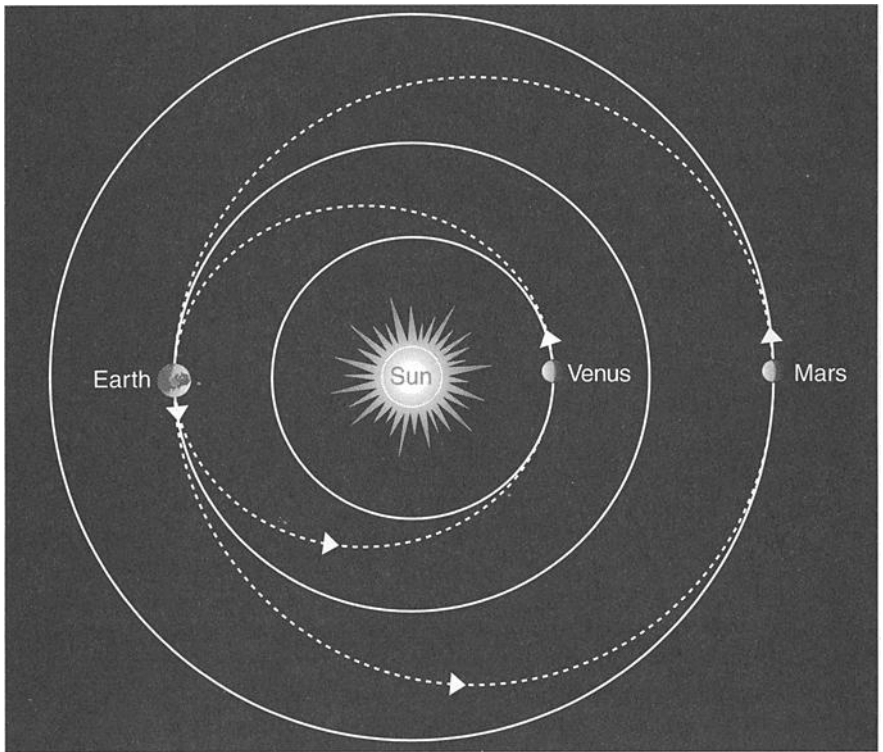
Fig. 1.11. Minimum-energy direct transfers used for missions to Mars or Venus.
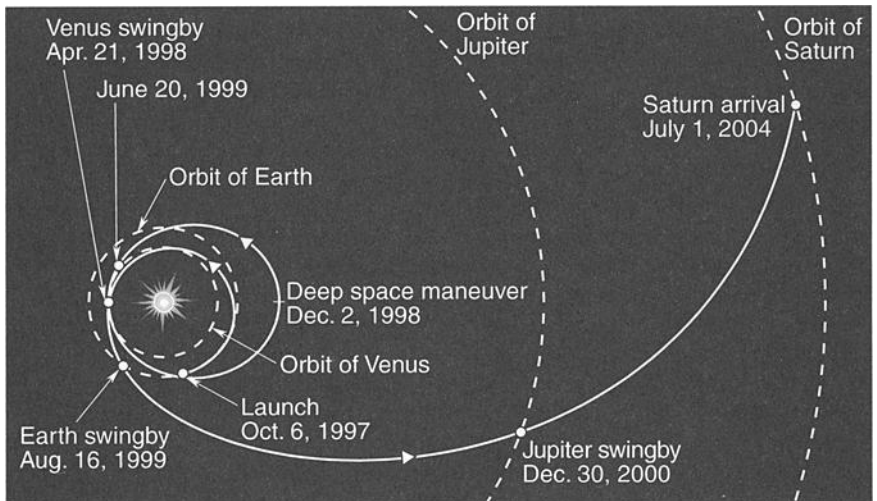
Fig. 1.12. VVEJGA trajectory. (Courtesy of NASA)

In some interplanetary missions, aerocapture maneuvers (Fig. 1.13) are used to slow the spacecraft and place it in orbit around a planet. This process involves sending the spacecraft close enough to the planet so that it actually passes through the upper reaches of the planet's atmosphere. Friction in the atmosphere slows the vehicle to a velocity that is below the planet's escape velocity. Injecting the spacecraft into orbit around the planet at just the right altitude and direction is critical to avoid its being either excessively heated or deflected back into interplanetary space. Several orbits around the planet may be required to gradually lower the orbit altitude.

Table 1.1. Planetary Orbit Parameters

	Orbit Semimajor Axis (AU)	Min. Distance from Sun (AU)	Max. Distance from Sun (AU)	Equatorial Radius (km)
Mercury	0.3871	0.3075	0.4667	2425
Venus	0.7233	0.7184	0.7282	6070
Earth	1.000	0.9833	1.0167	6378
Moon	1.000	0.9833	1.0167	1738
Mars	1.524	1.381	1.666	3397
Jupiter	5.20	4.95	5.45	71,300
Saturn	9.54	9.01	10.07	60,100
Uranus	19.18	18.28	20.09	24,500
Neptune	30.06	29.80	30.32	25,100
Pluto/Charon	39.44	29.58	49.30	3200 (Pluto)

Fig. 1.13. Aerocapture maneuvers.

In some cases, a similar process helps minimize the use of propellant when certain kinds of orbit changes are required during a spacecraft's orbital mission. Aerocapture maneuvers create significant heat loads that must be addressed in the thermal design process.

Some rather unique orbits rely on balances between centrifugal and gravitational forces among multiple bodies. The Italian-French mathematician Josef Lagrange discovered that in cases where one body orbits around a much larger one, such as the moon around Earth or Earth around the sun, the centrifugal force and the two gravitational forces balance each other at five points. A body located precisely at any of these points will therefore remain there unless perturbed. These points, known as the Lagrange points, are designated L1 through L5, as shown in Fig. 1.14. L1, L2, and L3 are so unstable that, for a body positioned at any of them, a slight perturbation can knock the body out of equilibrium and send it on its way. The other two points, L4 and L5, are stable enough for a body positioned at either one to return to equilibrium if perturbed. For the unstable Lagrange points, a spacecraft can be placed in a small, fairly stable orbit around the point that requires little in the way of corrective maintenance maneuvers. The Solar and Heliospheric Observatory (SOHO) is placed at the Earth-sun L1 point; the Microwave Anisotropy Probe (MAP) satellite and the Next Generation Space Telescope are considering the Earth-sun L2 point as a possible home.
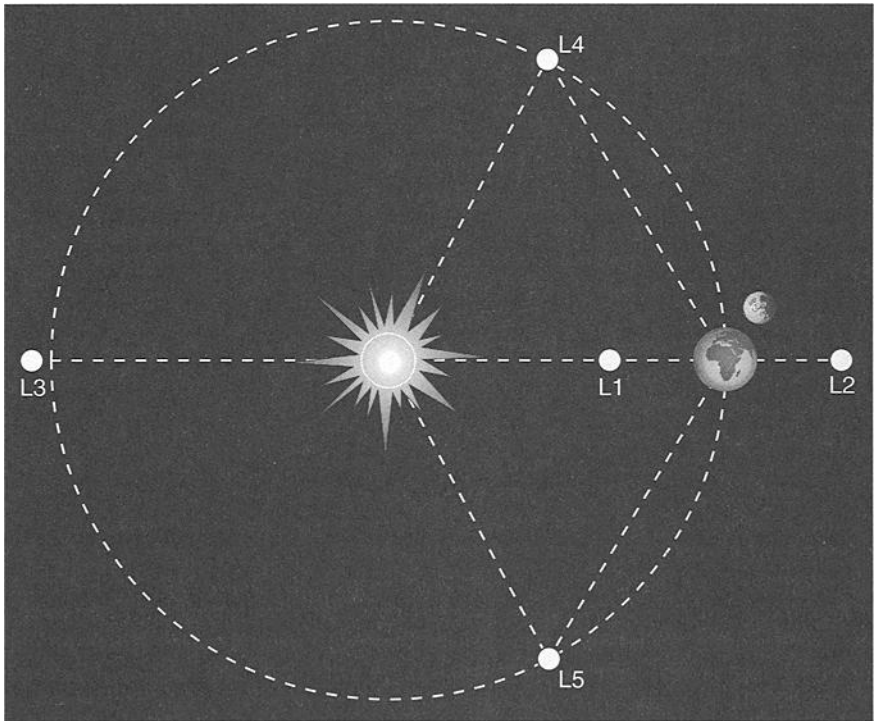
Fig. 1.14. Lagrange points.

Missions

A wide variety of missions are supported by the three general types of spacecraft platforms discussed earlier. The type of mission will dictate the orbit, the payload, and, in some cases, the platform. Typical missions include communication, scientific observation, weather monitoring, navigation, remote sensing, surveillance, and data relay. This section briefly describes each of these missions.

The most common mission for both commercial and military satellites is communication; there are currently 294 operating communication satellites in orbit. Thuraya and Singapore Telecom-1 (ST-1, Fig. 1.15) are commercial communication satellites. "Comsats" relay radio, telephone, television, or data signals from one point on Earth to another. These satellites are usually, but not always, in high-altitude geosynchronous orbits, where they remain over the same point on Earth at all times. Communication can be provided between any two points on the side of Earth to which the satellite has a direct view. Communication between two points
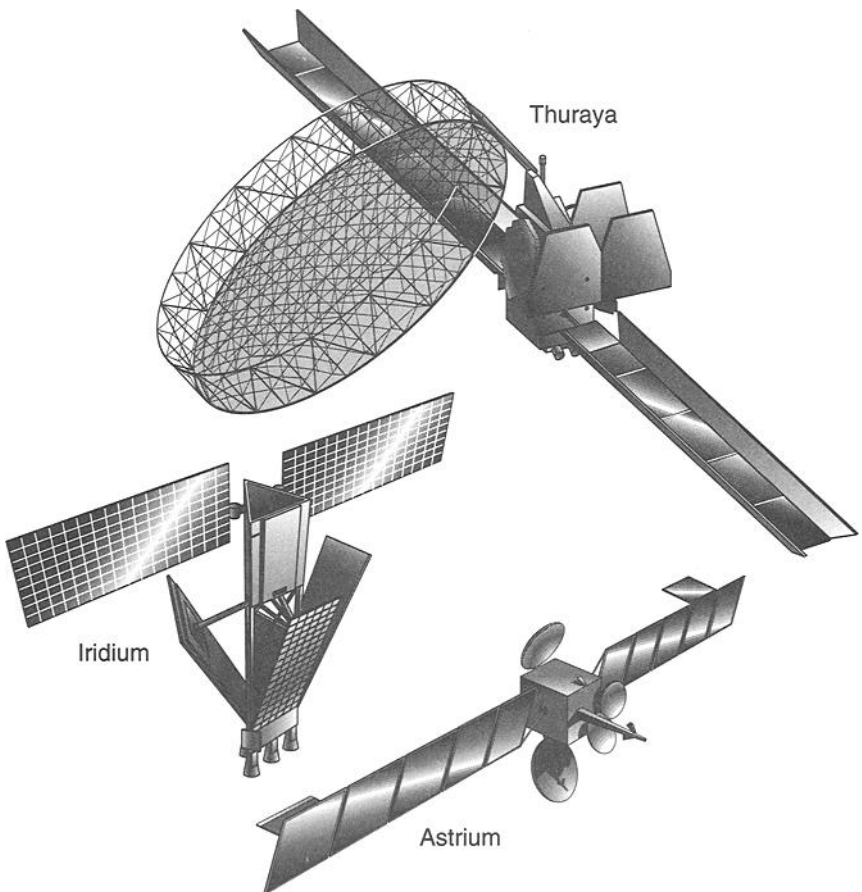
Fig. 1.15. Comsats.

on opposite sides of Earth, however, requires the use of multiple satellites with crosslinks between them. Both Thuraya and ST-1 are typical communication satellites that do not have crosslink capability. Iridium (Fig. 1.15) is a satellite constellation that has crosslinks and is able to provide communication between any two points on Earth.

Weather monitoring is another mission common to civilian and military space programs. The DMSP spacecraft (Fig. 1.16) is a typical low-altitude weather satellite. It carries visual and IR cameras that continuously photograph cloud patterns, as well as secondary sensors, such as Special Sensor Microwave Imager/Sounder (SSMIS), that can monitor phenomena such as surface wind speeds, soil moisture content, and precipitation rates. Low-altitude weather satellites are usually in sun-synchronous orbits. This allows them to scan the entire surface of Earth at the same local sun angle over the course of a day. High-altitude weather satellites, such as NASA's GOES (Geostationary Operational Environmental Satellite, Fig. 1.16), are usually in geosynchronous orbits that allow them to continuously photograph one entire hemisphere of Earth.

Navigation constitutes a third type of spacecraft mission. For the United States, this mission is currently fulfilled by one satellite program, NAVSTAR-GPS (Global Positioning System). The GPS system includes a constellation of 24 satellites in 12-hour circular orbits. Each GPS satellite (Fig. 1.17) continuously broadcasts a signal that can be picked up by small receivers on the ground, in aircraft, or even
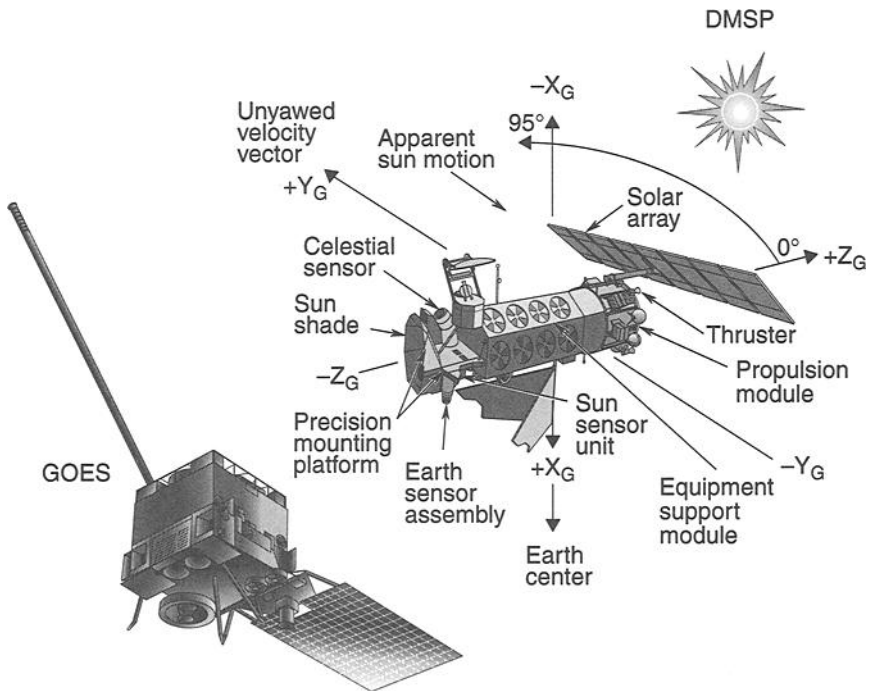
Fig. 1.16. Weather satellites.
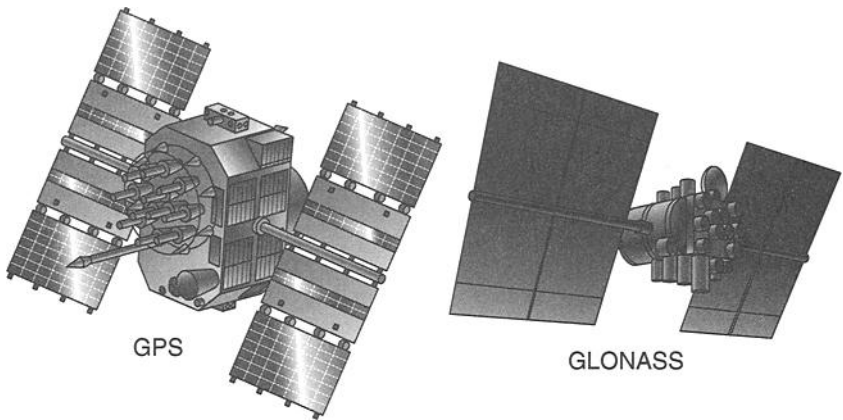
Fig. 1.17. Positioning satellites.

in another satellite. If three or more GPS satellites are visible at any one time, the receiver can determine its own position and velocity to within 1 m and 0.1 m/sec. Russia also operates a system of positioning satellites, known as GLONASS (Global Navigation Satellite System, Fig. 1.17), that are located in similar orbits. A next-generation navigation satellite program, aptly named Galileo, is also currently planned by the European Space Agency.

Surveillance is a general category for satellites whose mission is to monitor various activities on Earth. This surveillance can be in the form of IR sensors to detect missile launches, radar to track aircraft or ships, visual observation of ground activities, or intercept of radio transmissions. Satellites designed to support each of these different missions have markedly different configurations.

Space Imaging's Ikonos (Fig. 1.18) is a commercial optical-surveillance satellite. It provides 1-m panchromatic and 4-m color resolution digital imagery of Earth's
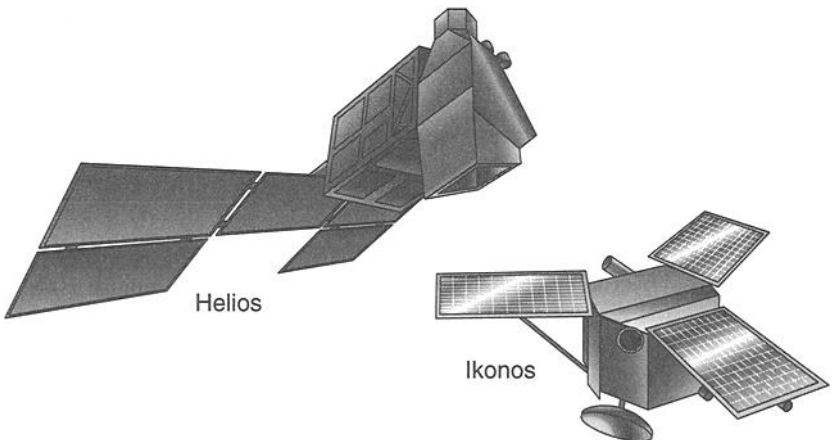
Fig. 1.18. Surveillance satellites.

surface. Its photos are used for mapping, urban planning, and environmental assessment. Helios (Fig. 1.18) is a national optical-surveillance satellite operated by France.

The DSP spacecraft shown in Fig. 1.4 is an example of an IR surveillance satellite. The payload is an IR telescope that detects and tracks missiles by the heat emitted from their rocket plumes. The detectors in the telescope are cooled to approximately 150 K by a cryogenic radiator with a helium-coolant loop. The entire satellite rotates at 6 rpm to provide a scanning motion that sweeps the linear detector array across Earth's surface. Ground software reconstructs the sweep into an Earth image with all heat sources displayed. DSP provides the United States with its first warning of missile launches.

Space Based Radar (SBR, Fig. 1.19) is an example of a radar-surveillance satellite. Spacecraft proposed for this program are quite large, with antenna dimensions on the order of 30 m. They would be developed to track aircraft and ships, with some designs being proposed to track missiles and individual warheads for defense applications. Radarsat, a remote-sensing satellite program led by the Canadian Space Agency, is also shown in Fig. 1.19.

Relay satellites support another type of mission similar to that of communication satellites except that the communication link is between the ground and a second satellite (Fig. 1.20). Such links eliminate the need for ground stations spaced throughout the world, and they provide continuous contact with satellites in any orbit. An example of a relay satellite is NASA's Tracking and Data Relay Satellite System (TDRSS), shown in Fig. 1.20. TDRSS is used to provide ground-to-ground and ground-to-satellite links and to communicate with shuttle astronauts.

Most Earth-orbiting scientific satellites need go no higher than low Earth orbit to accomplish their missions. Astronomical satellites, such as the Earth Observing
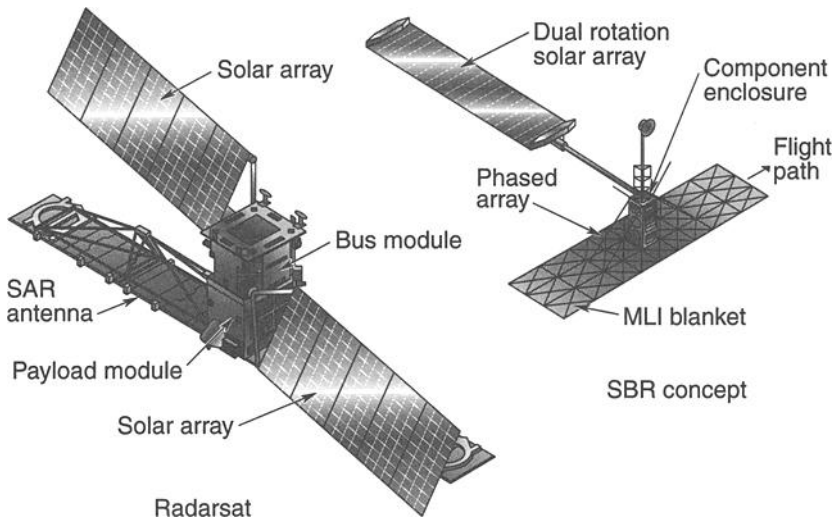
Fig. 1.19. Radar satellites.
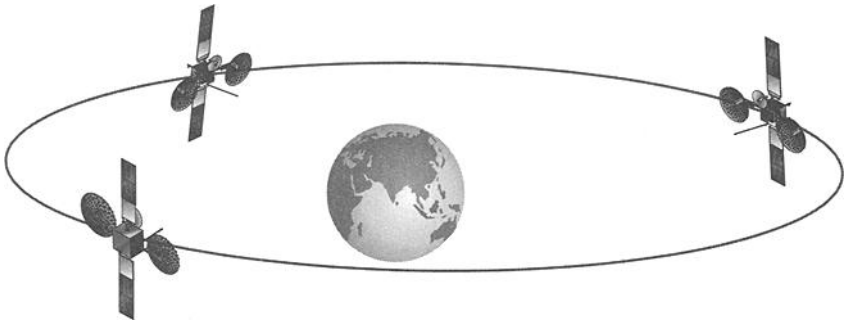
Fig. 1.20. TDRSS relay.

System (EOS) and the Hubble Space Telescope (Fig. 1.21), need only get above Earth's atmosphere to conduct their observations. A low-altitude orbit is an advantage for programs like EOS, whose mission is to study Earth. Some missions, like the Russian Granat X-ray and gamma-ray observatory (Fig. 1.21), do require high-altitude Earth orbits. There are also, of course, missions that require interplanetary scientific spacecraft to leave Earth's orbit entirely. These programs, such as Cassini (Fig. 1.21), sometimes must follow complicated trajectories through the solar system to get to their final destination.
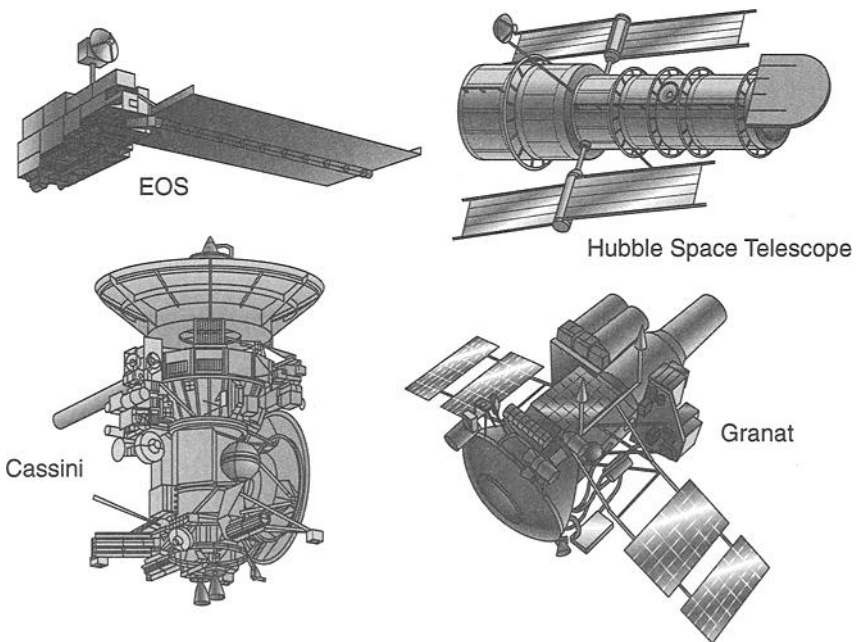
Fig. 1.21. Scientific satellites.

Remote-sensing missions are accomplished by satellites such as the U.S. Landsat, the French SPOT (*Systeme Pour l'Observation de la Terre*), and the European ERS (Earth Resources Satellite) (Fig. 1.22). These vehicles gather images in a variety of wavelengths. This information is used to manage crops and other Earth resources and to support environmental and global change research. For this kind of mission, the satellites are usually placed in sun-synchronous polar orbits at an altitude of approximately 830 km.
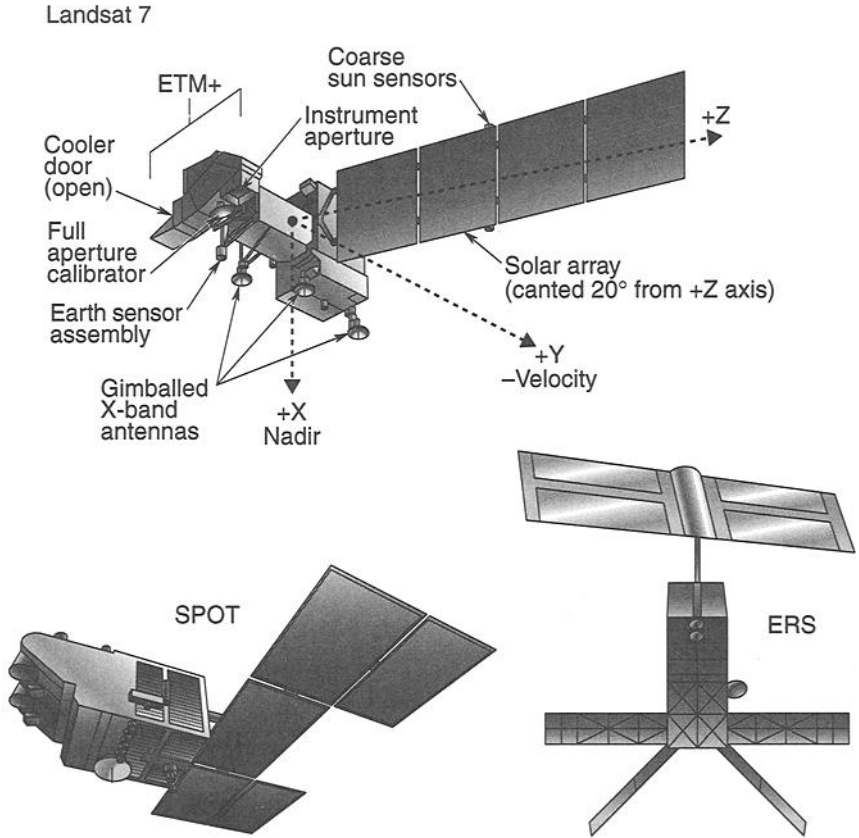
Fig. 1.22. Remote-sensing satellites.

2 Spacecraft Thermal Environments

J. F. Clawson,[*] G. T. Tsuyuki,* B. J. Anderson,[†] C. G. Justus,[‡]
W. Batts,[‡] D. Ferguson,[**] and D. G. Gilmore[††]

Environments of Earth Orbit

Spacecraft thermal control is a process of energy management in which environmental heating plays a major role. The principal forms of environmental heating on orbit are direct sunlight, sunlight reflected off Earth (albedo), and infrared (IR) energy emitted from Earth. During launch or in exceptionally low orbits, there is also a free molecular heating effect caused by friction in the rarefied upper atmosphere. This chapter gives an overview of these types of environmental heating.

The overall thermal control of a satellite on orbit is usually achieved by balancing the energy emitted by the spacecraft as IR radiation against the energy dissipated by its internal electrical components plus the energy absorbed from the environment; atmospheric convection is absent in space. Figure 2.1 illustrates this relationship.
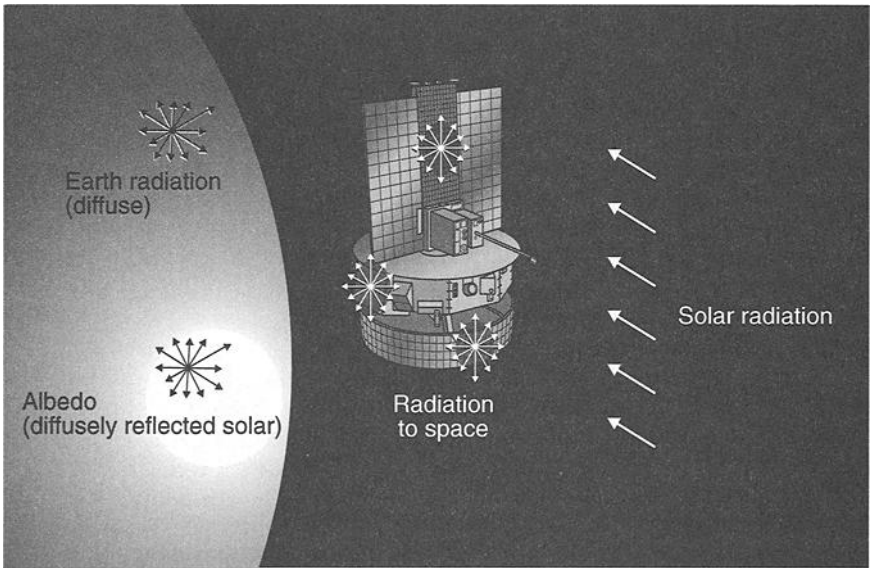
Fig. 2.1. Satellite thermal environment.

*Jet Propulsion Laboratory, California Institute of Technology, Pasadena, California.
†NASA/MSFC, Huntsville, Alabama.
‡Computer Sciences Corporation, Huntsville, Alabama.
**Swales Aerospace, Beltsville, Maryland.
††The Aerospace Corporation, El Segundo, California.

Like a spacecraft's temperature, Earth's temperature is the result of a balance between absorbed and emitted energy. If one considers Earth and its atmosphere as a whole and computes averages of absorbed and outgoing energy over long time periods, one finds that the absorbed solar energy and the IR radiant energy emitted by Earth are essentially in balance; Earth is therefore very nearly in radiative equilibrium with the sun and deep space. However, the forms of energy are not in balance everywhere on the globe at all times, and important variations are found with respect to local time, geography, and atmospheric conditions.

In low Earth orbit (LEO), a space vehicle's altitude is small compared to the diameter of Earth. This means that a satellite views only a small portion of the full globe at any given time. The satellite's motion as it orbits therefore exposes it to rapidly changing environmental conditions as it passes over regions having different combinations of land, ocean, snow, and cloud cover. These short-duration swings in environmental conditions are not of much concern to massive, well-insulated spacecraft components. Exposed lightweight components such as solar arrays and deployable radiators, however, will respond to the extreme environments that are encountered for short time periods, so one must consider those environments in the design process. As the following discussion shows, the shorter the thermal time constant a particular component has, the wider the range of environments that must be considered.

Direct Solar

Sunlight is the greatest source of environmental heating incident on most spacecraft in Earth orbit. Fortunately, the sun is a very stable energy source. Even the 11-year solar cycle has very little effect on the radiation emitted from the sun, which remains constant within a fraction of 1% at all times. However, because Earth's orbit is elliptical, the intensity of sunlight reaching Earth varies approximately ±3.5%, depending on Earth's distance from the sun. At summer solstice, Earth is farthest from the sun, and the intensity is at its minimum value of 1322 W/m^2; at winter solstice, the intensity is at its maximum of 1414 W/m^2. The intensity of sunlight at Earth's mean distance from the sun (1 AU) is known as the solar constant and is equal to 1367 W/m^2. The above values are recommended by the World Radiation Center in Davos, Switzerland,[2.1,2.2] and are believed accurate to within 0.4%.

Solar intensity also varies as a function of wavelength, as shown in Fig. 2.2. The energy distribution is approximately 7% ultraviolet, 46% visible, and 47% near (short-wavelength) IR, with the total integrated energy equal to the 1322 to 1414 W/m^2 values mentioned above. An important point, however, is that the IR energy emitted by the sun is of a much shorter wavelength than that emitted by a body near room temperature. This distinction allows for the selection of thermal-control finishes that are very reflective in the solar spectrum but whose emissivity is high in the room-temperature (long-wavelength) IR portion of the spectrum, as shown in Fig. 2.3. These finishes minimize solar loads while maximizing a spacecraft's ability to reject waste heat. They are discussed in more detail in Chapter 4.

Albedo

Sunlight reflected off a planet or moon is known as albedo. A planet's albedo is usually expressed as the fraction of incident sunlight that is reflected back to space,
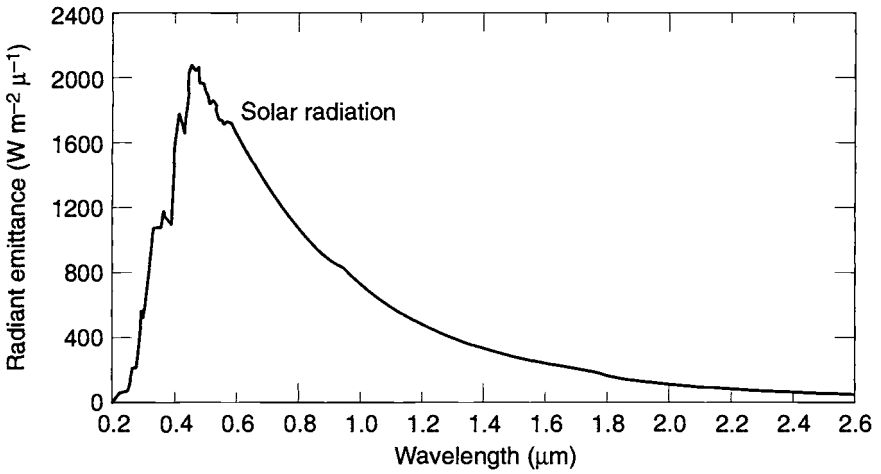
Fig. 2.2. Solar spectral distribution.
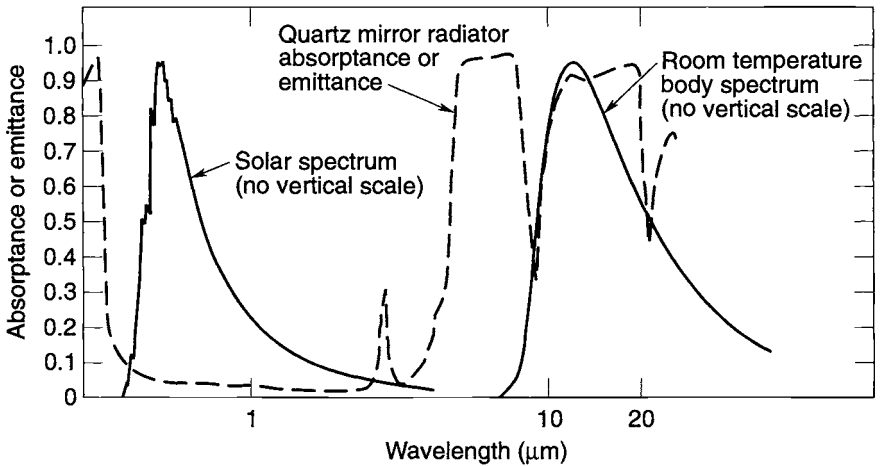
Fig. 2.3. Solar and room-temperature-body spectral distributions.

and it is highly variable. Usually, reflectivity is greater over continental regions than oceanic regions and generally increases with decreasing local solar-elevation angles and increasing cloud coverage. Because of greater snow and ice coverage, decreasing solar-elevation angle, and increasing cloud coverage, albedo also tends to increase with latitude. These variations make selection of the best albedo value for a particular thermal analysis rather uncertain, and variations throughout the industry are not unusual.

Another important point is that the albedo heat flux reaching a spacecraft will decrease as the spacecraft moves along its orbit and away from the subsolar point (the point on Earth or another planet where the sun is at the zenith, i.e., directly overhead), even if the albedo constant remains the same. This happens because the albedo factor is a reflectivity, not a flux. As the spacecraft moves away from the subsolar point it is over regions of Earth's surface where the local incident solar energy per square meter is decreasing with the cosine of the angle from the subsolar point. The albedo heat load on the spacecraft will therefore approach 0 near the terminator (the dividing line between the sunlit and dark sides of a planet), even if the albedo value (reflectivity) is 1.0. This geometric effect is accounted for by the analysis codes used to perform spacecraft thermal analysis. The analyst is just responsible for selecting the albedo (reflectivity) value itself.

Earth IR

All incident sunlight not reflected as albedo is absorbed by Earth and eventually reemitted as IR energy. While this balance is maintained fairly well on a global annual average basis, the intensity of IR energy emitted at any given time from a particular point on Earth can vary considerably depending on factors such as the local temperature of Earth's surface and the amount of cloud cover. A warmer surface region will emit more radiation than a colder area. Generally, highest values of Earth-emitted IR will occur in tropical and desert regions (as these are the regions of the globe receiving the maximum solar heating) and will decrease with latitude. Increasing cloud cover tends to lower Earth-emitted IR, because cloud tops are cold and clouds effectively block upwelling radiation from Earth's warmer surface below. These localized variations in Earth-emitted IR, while significant, are much less severe than the variations in albedo.

The IR energy emitted by Earth, which has an effective average temperature around $-18°C$, is of approximately the same wavelength as that emitted by spacecraft; that is, it is of much longer wavelength than the energy emitted by the sun at $5500°C$. Unlike short-wavelength solar energy, Earth IR loads incident on a spacecraft cannot be reflected away from radiator surfaces with special thermal-control coatings, since the same coatings would prevent the radiation of waste heat away from the spacecraft. Because of this, Earth-emitted IR energy can present a particularly heavy backload on spacecraft radiators in low-altitude orbits.

The concept of Earth-emitted IR can be confusing, since the spacecraft is usually warmer than the effective Earth temperature, and the net heat transfer is from spacecraft to Earth. However, for analysis, a convenient practice is to ignore Earth when calculating view factors from the spacecraft to space and to assume that Earth does not block the view to space. Then the difference in IR energy is added back in as an "incoming" heat rate called Earth-emitted IR.

Recommended Values for Earth IR and Albedo

References 2.3 through 2.13 document early studies of albedo and Earth IR and contain detailed data pertaining to their variations, as measured by satellite-based sensors. Most of these early studies recommended design values for Earth IR and albedo based on monthly averages of the satellite data. These recommendations were made because of the unreasonableness of recommending that all spacecraft

hardware be designed to accommodate the short-term, extreme values of albedo and Earth IR resulting from local surface and atmospheric conditions.

Unfortunately, most spacecraft hardware has a thermal time constant on the order of minutes to a few days, not months. In the early 1990s, the International Space Station (ISS) program recognized that the monthly average thermal environments generally used by the satellite design community were not sufficient for designing safety-critical, short thermal-time-constant components such as the station's deployable radiators. NASA therefore funded studies at the Marshall Space Flight Center (MSFC) to improve the understanding of the LEO thermal environment for ISS and other spacecraft programs.[2.14] This work was updated in 2001 by Anderson, Justus, and Batts.[2.15]

The albedo and Earth IR values recommended here are based on the NASA/MSFC study, which considered 28 data sets of 16-second-resolution satellite sensor data collected monthly from the Earth Radiation Budget Experiment (ERBE). ERBE is a multisatellite experiment that has as its primary objective the global data collection of such Earth radiation budget parameters as incident sunlight, albedo, and Earth-emitted IR. This experiment was selected as a data source because of its thorough coverage and high-quality data from active-cavity, flat-plate radiometers in a fixed (nonscanning) wide-field-of-view mode. This type of instrument directly measures the albedo and Earth IR as a spacecraft surface would receive them. The sensors flew on an ERBE satellite in a low-inclination, 610-km-altitude orbit and on the National Oceanic and Atmospheric Administration (NOAA) 9 and 10 satellites in high-inclination, 849- and 815-km-altitude orbits, respectively. The sensor measurements were adjusted for altitude to derive effective albedo and IR values at the top of the atmosphere, which was assumed to be 30 km above Earth's surface. Therefore, in conducting a thermal analysis, one would use the environmental constants reported here with the Earth radius modeled as 6408 km. (However, if the actual equatorial radius of 6378 km were used instead of the top-of-the-atmosphere radius, the error would be less than 1%, which is not very significant compared to other analysis uncertainties.)

The MSFC study performed a statistical analysis of the ERBE data to identify the maximum and minimum albedo and Earth IR heating rates a spacecraft might be exposed to on orbit over various time periods from 16 sec to 24 h. The time periods were selected to encompass the range of thermal time constants found in most spacecraft hardware. (The values do not change significantly for periods greater than 24 h.) Ideally, such a study would provide the analyst with both an environmental heating rate and the probability that the value would not be exceeded over the duration of the spacecraft's mission. Unfortunately, this would require a statistical data set covering a time period that is very long compared to a spacecraft's design life. Because of the limited data set available, results are reported here according to the percentage of the time that one can expect the value will be exceeded on orbit. That is, the values shown will probably be exceeded during the mission, but not very often. Tables 2.1 and 2.2 summarize a conservative (3.3-σ) set of recommended albedo and Earth IR values that will be exceeded only 0.04% of the time, while Tables 2.3 and 2.4 give less severe (2-σ) values that will be exceeded 5% of the time.

Table 2.1. Earth IR and Albedo[a], 3.3-σ Values[b]
Cold Case

Surface Sensitivity	Time Period	Inclination (deg)					
		0–30		30–60		60–90	
		Albedo	IR (W/m^2)	Albedo	IR (W/m^2)	Albedo	IR (W/m^2)
Albedo	16 sec	0.06	273	0.06	273	0.06	273
	128 sec	0.06	273	0.06	273	0.06	273
	896 sec	0.07	265	0.08	262	0.09	264
	30 min	0.08	261	0.12	246	0.13	246
	90 min	0.11	258	0.16	239	0.16	231
	6 h	0.14	245	0.18	238	0.18	231
	24 h	0.16	240	0.19	233	0.18	231
IR	16 sec	0.40	150	0.40	151	0.40	108
	128 sec	0.38	154	0.38	155	0.38	111
	896 sec	0.33	173	0.34	163	0.33	148
	30 min	0.30	188	0.27	176	0.31	175
	90 min	0.25	206	0.30	200	0.26	193
	6 h	0.19	224	0.31	207	0.27	202
	24 h	0.18	230	0.25	210	0.24	205
Both albedo and IR	16 sec	0.13	225	0.15	213	0.16	212
	128 sec	0.13	226	0.15	213	0.16	212
	896 sec	0.14	227	0.17	217	0.17	218
	30 min	0.14	228	0.18	217	0.18	218
	90 min	0.14	228	0.19	218	0.19	218
	6 h	0.16	232	0.19	221	0.20	224
	24 h	0.16	235	0.20	223	0.20	224

[a]Albedo values shown on the table must be corrected to account for non-Lambertian reflection near the terminator. If orbit-average albedo is used in the analysis, the above values must be corrected according to orbit β angle (use table below). If the analysis changes the albedo value as the spacecraft moves about its orbit, the correction must be applied according to angle from subsolar point. (Use one correction or the other, not both.) No correction is needed for Earth IR.

[b]Values exceeded 0.04% of the time.

Short-Term Albedo Correction		Orbit-Average Albedo Correction	
Position from Subsolar Point (deg)	Add Correction	Orbit β angle (deg)	Add Correction
0	none	0	0.04
20	0.02	20	0.05
40	0.04	40	0.07
50	0.05	50	0.09
60	0.08	60	0.12
70	0.13	70	0.16
80	0.20	80	0.22
90	0.31	90	0.31

Table 2.2. Earth IR and Albedo[a], 3.3-σ Values[b]
Hot Case

| Surface Sensitivity | Time Period | Inclination (deg) | | | | | |
| | | 0–30 | | 30–60 | | 60–90 | |
		Albedo	IR (W/m²)	Albedo	IR (W/m²)	Albedo	IR (W/m²)
Albedo	16 sec	0.43	182	0.48	180	0.50	180
	128 sec	0.42	181	0.47	180	0.49	184
	896 sec	0.37	219	0.36	192	0.35	202
	30 min	0.33	219	0.34	205	0.33	204
	90 min	0.28	237	0.31	204	0.28	214
	6 h	0.23	248	0.31	212	0.27	218
	24 h	0.22	251	0.28	224	0.24	224
IR	16 sec	0.22	331	0.21	332	0.22	332
	128 sec	0.22	326	0.22	331	0.22	331
	896 sec	0.22	318	0.22	297	0.20	294
	30 min	0.17	297	0.21	282	0.20	284
	90 min	0.20	285	0.22	274	0.22	250
	6 h	0.19	269	0.21	249	0.22	221[c]
	24 h	0.19	262	0.21	245	0.20	217[c]
Both albedo and IR	16 sec	0.30	298	0.31	267	0.32	263
	128 sec	0.29	295	0.30	265	0.31	262
	896 sec	0.28	291	0.28	258	0.28	259
	30 min	0.26	284	0.28	261	0.27	260
	90 min	0.24	275	0.26	257	0.26	244
	6 h	0.21	264	0.24	248	0.24	233
	24 h	0.20	260	0.24	247	0.23	232

[a]Albedo values shown on the table must be corrected to account for non-Lambertian reflection near the terminator. If orbit-average albedo is used in the analysis, the above values must be corrected according to orbit β angle (use table below). If the analysis changes the albedo value as the spacecraft moves about its orbit, the correction must be applied according to angle from subsolar point. (Use one correction or the other, not both.) No correction is needed for Earth IR.
[b]Values exceeded 0.04% of the time.
[c]For orbits with β angles greater than 80 deg, increase this value by approximately 15 W/m².

| Short-Term Albedo Correction | | Orbit-Average Albedo Correction | |
Position from Subsolar Point (deg)	Add Correction	Orbit β angle (deg)	Add Correction
0	none	0	0.04
20	0.02	20	0.05
40	0.04	40	0.07
50	0.05	50	0.09
60	0.08	60	0.12
70	0.13	70	0.16
80	0.20	80	0.22
90	0.31	90	0.31

Table 2.3. Earth IR and Albedo[a], 2-σ Values[b]
Cold Case

Surface Sensitivity	Time Period	Inclination (deg)					
		30		60		90	
		Albedo	IR (W/m^2)	Albedo	IR (W/m^2)	Albedo	IR (W/m^2)
Albedo	16 sec	0.09	270	0.10	267	0.10	267
	128 sec	0.09	267	0.10	265	0.10	265
	896 sec	0.10	261	0.13	252	0.14	252
	30 min	0.12	257	0.16	242	0.17	244
	90 min	0.13	249	0.18	238	0.18	230
	6 h	0.15	241	0.19	233	0.19	230
	24 h	0.16	240	0.19	235	0.19	230
IR	16 sec	0.30	195	0.33	183	0.35	164
	128 sec	0.29	198	0.33	184	0.34	164
	896 sec	0.26	209	0.28	189	0.27	172
	30 min	0.23	216	0.25	200	0.25	190
	90 min	0.20	225	0.23	209	0.24	202
	6 h	0.18	231	0.23	212	0.23	205
	24 h	0.17	233	0.23	212	0.23	207
Both albedo and IR	16 sec	0.15	236	0.19	227	0.20	225
	128 sec	0.16	237	0.19	227	0.20	225
	896 sec	0.16	237	0.20	226	0.20	227
	30 min	0.16	237	0.20	225	0.20	226
	90 min	0.16	237	0.20	225	0.21	224
	6 h	0.17	237	0.20	226	0.21	226
	24 h	0.17	236	0.20	226	0.20	225

[a]Albedo values shown on the table must be corrected to account for non-Lambertian reflection near the terminator. If orbit-average albedo is used in the analysis, the above values must be corrected according to orbit β angle (use table below). If the analysis changes the albedo value as the spacecraft moves about its orbit, the correction must be applied according to angle from subsolar point. (Use one correction or the other, not both.) No correction is needed for Earth IR.
[b]Values exceeded 5% of the time.

Short-Term Albedo Correction		Orbit-Average Albedo Correction	
Position from Subsolar Point (deg)	Add Correction	Orbit β angle (deg)	Add Correction
0	none	0	0.04
20	0.02	20	0.05
40	0.04	40	0.07
50	0.05	50	0.09
60	0.08	60	0.12
70	0.13	70	0.16
80	0.20	80	0.22
90	0.31	90	0.31

Table 2.4. Earth IR and Albedo[a], 2-σ Values[b]
Hot Case

Surface Sensitivity	Time Period	Inclination (deg)					
		30		60		90	
		Albedo	IR (W/m^2)	Albedo	IR (W/m^2)	Albedo	IR (W/m^2)
Albedo	16 sec	0.29	205	0.36	201	0.38	197
	128 sec	0.29	211	0.35	202	0.37	199
	896 sec	0.26	225	0.29	213	0.28	213
	30 min	0.24	234	0.27	223	0.26	223
	90 min	0.22	246	0.26	229	0.24	219
	6 h	0.20	252	0.25	231	0.23	224
	24 h	0.20	252	0.25	232	0.23	224
IR	16 sec	0.17	285	0.17	280	0.17	280
	128 sec	0.17	284	0.17	279	0.17	279
	896 sec	0.18	279	0.18	264	0.18	263
	30 min	0.18	274	0.20	258	0.20	258
	90 min	0.19	268	0.21	254	0.21	242
	6 h	0.19	261	0.21	242	0.21	216[c]
	24 h	0.18	258	0.21	241	0.21	215[c]
Both albedo and IR	16 sec	0.21	260	0.23	240	0.24	237
	128 sec	0.21	260	0.23	240	0.24	238
	896 sec	0.21	261	0.23	241	0.23	240
	30 min	0.21	258	0.23	240	0.23	242
	90 min	0.20	258	0.23	241	0.23	232
	6 h	0.19	255	0.23	242	0.22	230
	24 h	0.19	257	0.23	241	0.23	230

[a]Albedo values shown on the table must be corrected to account for non-Lambertian reflection near the terminator. If orbit-average albedo is used in the analysis, the above values must be corrected according to orbit β angle (use table below). If the analysis changes the albedo value as the spacecraft moves about its orbit, the correction must be applied according to angle from subsolar point. (Use one correction or the other, not both.) No correction is needed for Earth IR.
[b]Values exceeded 5% of the time.
[c]For orbits with β angles greater than 80 deg, increase this value by approximately 15 W/m^2.

Short-Term Albedo Correction		Orbit-Average Albedo Correction	
Position from Subsolar Point (deg)	Add Correction	Orbit β angle (deg)	Add Correction
0	none	0	0.04
20	0.02	20	0.05
40	0.04	40	0.07
50	0.05	50	0.09
60	0.08	60	0.12
70	0.13	70	0.16
80	0.20	80	0.22
90	0.31	90	0.31

The decision whether to use the 2-σ or 3.3-σ values for a given thermal design analysis should be based on the program's tolerance for risk, the consequences of a predicted temperature being occasionally exceeded, and the impact of conservatism on program cost and design complexity. Comparing the tables, however, reveals a difference that is not very large between the 2- and 3.3-σ values for components with time constants on the order of 90 min or more. As a further point of reference, a commonly used analysis-uncertainty margin of 10°C (see Chapter 15) corresponds to roughly a 2-σ protection against a predicted temperature being exceeded. For the rare instances in which a critical lightweight component (such as a tether) would break if exposed to an extreme environment even once, note that the worst measurements in the database exceeded the 3.3-σ values of Tables 2.1 and 2.2 by 17 W/m^2 for Earth IR and 0.06 for albedo for the 16-sec and 128-sec measurement periods.

During the study, it became apparent that the albedo and Earth IR values were dependent not only on the time period considered, but on the orbit inclination, orbit beta angle, and angle from the subsolar point as well (see pp. 36–43 for definition and discussion of these orbital parameters). Orbit-average Earth IR, for instance, is lower for high-inclination orbits because the satellite spends a significant amount of time over the cooler polar regions. Albedo, on the other hand, tends to increase at large angles from the subsolar point because sunlight is reflected off Earth with more forward scatter at the low angles of incidence that occur closer to the terminator. (The albedo is more Lambertian, or equal in all directions, closer to the subsolar point.) This latter effect causes the orbit-average albedo factor to increase for higher beta-angle orbits that keep the spacecraft closer to the terminator than the subsolar point during the sunlit portion of the orbit. An important point to note is that the correction factor shown in Tables 2.1 through 2.4 must be added to the tabulated albedo values to account for this effect.

Over the years some have questioned the appropriateness of using both the highest albedo and highest IR when performing a hot-case spacecraft thermal analysis, or both the lowest albedo and lowest IR when performing a cold-case analysis. The rationale is that if albedo is high, then the local Earth temperature, and therefore emitted planetary IR, must be low because so much sunlight is being reflected. The MSFC study shows that this reasoning is valid to some extent. As illustrated by the contour plots of 128-second data shown in Fig. 2.4, albedo and Earth IR are partially correlated. Low Earth IR values tend to be associated with high albedo while high Earth IR tends to be associated with low-to-moderate albedo. To address this issue, the MSFC study sorted the data in such a way that unrealistically severe combinations of the two parameters were avoided. To do this, the study used pairs of albedo and IR measurements taken at the same time on the same spacecraft. To select an appropriate albedo to use with a 3.3-σ hot Earth IR value, for example, analysts considered only those albedo measurements taken at the same time as the IR measurements that were at the 99.96 percentile (3.3-σ) level and above. Just the albedos associated with those hottest IR measurements were then averaged to come up with a reasonable combination of the two environmental parameters. This process was used to select the Earth IR-albedo pairs shown in Tables 2.1 through 2.4.
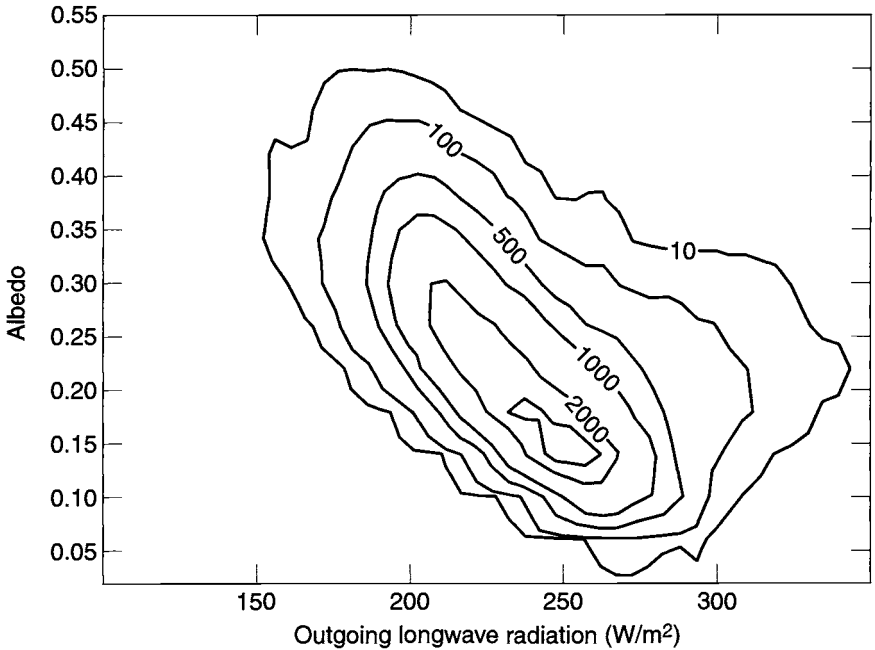
Fig. 2.4. Albedo-Earth IR pairs for medium-inclination orbits, 128-second data. (Contour intervals indicate relative frequency of occurrence.)

In selecting the appropriate hot- and cold-case albedo and Earth IR values for a particular thermal analysis, the analyst should also consider how sensitive the principal exposed surfaces are to IR versus solar energy. Most spacecraft radiator finishes, for example, have a low absorptance (say 0.2) and high emittance (around 0.8) and will therefore be much less sensitive to solar-wavelength albedo than to Earth-emitted IR. To enable better definition of the appropriate environmental constants for a particular analysis, Tables 2.1 through 2.4 contain recommended values for designs that are predominantly sensitive to either IR or albedo, or equally sensitive to both. In Tables 2.3 and 2.4, for instance, the values listed for IR-sensitive surfaces represent the 2-σ high and low Earth IR values along with the *average* albedos that occur during these extreme IR conditions.

Occasionally, one will come across a sensor or other component that requires extreme temperature stability over some period of time. In such situations, one must consider the rapid fluctuations in environmental heating that the device may see as it moves along its orbit. Figure 2.5 shows how Earth IR varied over one particular three-hour period. A low-mass device with a good radiative coupling to these environmental fluctuations might exceed a temperature-stability limit that is particularly tight. Such cases need to be evaluated on an individual basis considering the range of environments for various time periods shown in Tables 2.1 through 2.4.
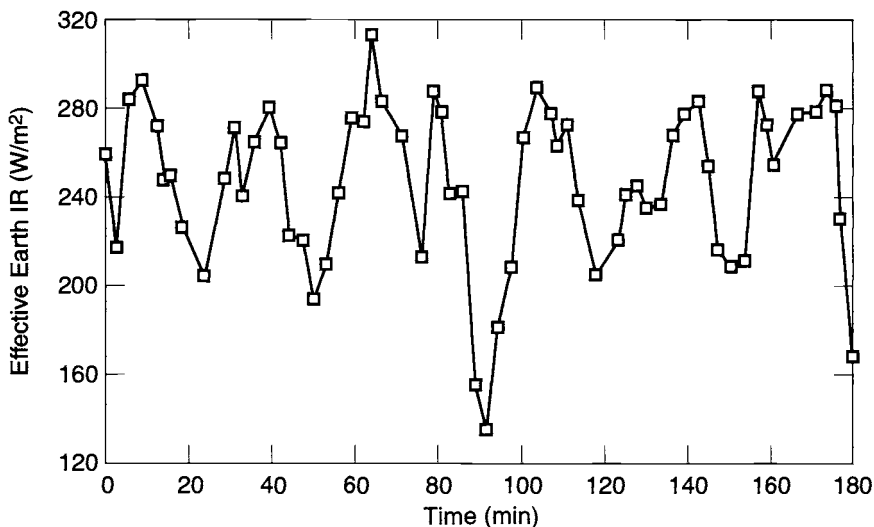
Fig. 2.5. Earth IR seen over a three-hour period by a spacecraft in LEO.

Free Molecular Heating

Another significant form of environmental heating is free molecular heating (FMH). This kind of heating is a result of bombardment of the vehicle by individual molecules in the outer reaches of the atmosphere. For most spacecraft, FMH is only encountered during launch ascent just after the booster's payload fairing is ejected. A desirable practice is to drop the fairing as soon as possible after launch to minimize the amount of dead weight the booster must deliver to orbit. The point at which the fairing is separated is often determined by a trade-off between the desire to save weight and the need to protect the payload spacecraft from excessive atmospheric heating.

Fairing separation always occurs at altitudes high enough for the resultant heating to be in the free or near-free molecular regime; that is, the heating is modeled as collisions of the body with individual molecules rather than as a gas-flow heating problem. The heating rate is given by:

$$Q_{FMH} = \alpha \left(\frac{1}{2}\right) \rho V^3 \tag{2.1}$$

where ρ is atmospheric density, V is vehicle velocity, and α is the accommodation coefficient (approximately 0.6 to 0.8, but a value of 1.0 is recommended for conservatism).

Atmospheric density is a highly variable parameter governed by a number of factors that cause the upper atmosphere to expand or contract. These factors include the level of solar electromagnetic activity ("F10.7," measured at a wavelength of 10.7 cm); the geomagnetic index (A_p); the longitude, latitude, and local

hour of the point in question; altitude; and day of the year. Atmospheric densities are calculated today using sophisticated atmospheric models with a dozen or more input parameters. The outputs of these models are atmospheric densities that will not be exceeded with a particular level of confidence (usually 97%). The output is expressed probabilistically because the level of solar activity, which is a major factor, is not predictable precisely.

The velocity of the vehicle relative to the atmosphere can be calculated in a rather straightforward manner for a satellite in orbit. The velocity during launch ascent, however, must be calculated using sophisticated booster-trajectory simulation programs that model and optimize the performance of the booster. Like atmospheric density, the trajectory and velocity of the booster are probabilistic, but to a lesser extent. The uncertainties are the result of variations in rocket-motor performance, guidance-system accuracies, high-altitude wind effects, and so on, and can result in the vehicle traveling at a different altitude or velocity than expected at any given time.

The atmospheric modeling and trajectory simulations are generally conducted by specialists in those areas, who then supply the thermal engineer with curves of worst-case heating versus time. With such a curve and a knowledge of the spacecraft attitude relative to the velocity vector, the thermal engineer may calculate the heat load on the spacecraft by simply multiplying the heating rate by the cross-sectional area of the surface in question and the cosine of the angle between the surface normal and velocity vector. A heating-rate curve for one particular mission during launch ascent is shown in Fig. 2.6.

As stated earlier, most spacecraft see FMH only during launch. Some spacecraft, however, have orbits with very low perigee altitudes and can therefore experience FMH in their operational orbits. In general, operational-orbit FMH rates should be assessed for any spacecraft with a perigee altitude below 180 km.
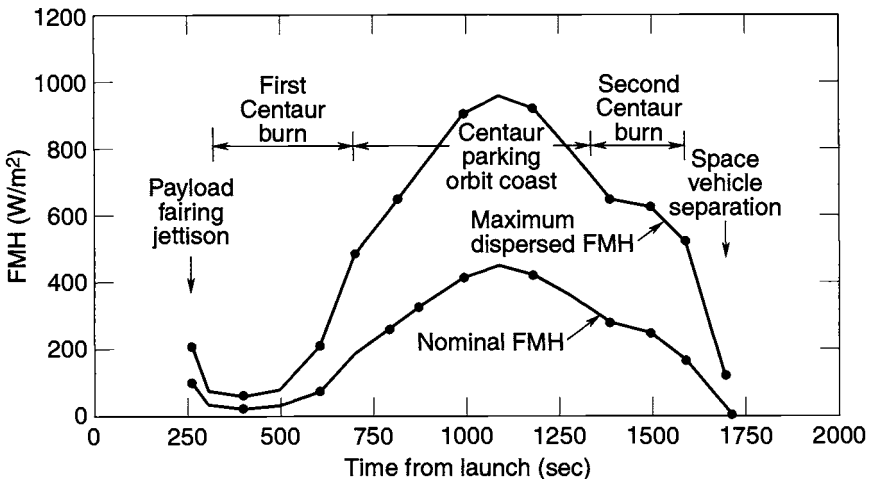
Fig. 2.6. Example of FMH profile.

Charged-Particle Heating

Charged particles constitute an additional heating source, although weak compared to the four principal environmental heating sources discussed above and generally not significant in the thermal design of room-temperature systems. At cryogenic temperatures, however, charged-particle heating can become a significant factor in thermal design because of the high sensitivity of such systems to environmental heat loads.

The near-Earth trapped charged particles, known as the Van Allen belts, lie about the plane of the geomagnetic equator and feature relativistic electrons and protons. The spatial characteristics of the Van Allen belts and the spectral properties of the trapped particles within them undergo both regular and irregular variations with time, accounted for by the solar-activity level. The bulk of the Van Allen belts is approximately bounded by altitudes of 6500 and 52,000 km. In 1958, Van Allen discovered the inner proton belt peaking in intensity at an approximate altitude of 9400 km, while Fan et al.,[2.16] O'Brien et al.,[2.17] and Dessier and Karplus[2.18] helped to establish the existence of other electron peaks. Vette[2.19] developed a complete mapping of the Van Allen belt radiations.

Standard trapped-particle environmental models include electron data for maximum and minimum solar-activity periods, an interim model for outer-zone electrons, and the maximum and minimum solar-activity model for energetic trapped protons. These data represent omnidirectional integral intensities averaged over periods in excess of 6 months in orbit. Over most regions of magnetospheric space, short-term excursions can vary from these values by factors of 100 to 1000, depending on particle energies and the type and intensity of the causative event.

Data on trapped proton and electron fluxes as functions of energy for circular, geomagnetic equatorial orbits ranging in altitude from 3200 to 35,800 km (synchronous) are presented in Fig. 2.7. As illustrated, the concentration of relativistic (> 5 MeV) protons is evident at lower altitudes (< 6400 km), while near synchronous altitude (35,800 km), proton energies are less than 2 MeV. Conversely, electrons feature high flux levels and energies less than approximately 5 MeV over a wide spectrum of altitudes.

The heating caused by these charged particles generally occurs in the first few hundredths of a centimeter of a material's thickness and is therefore essentially front-surface-absorbed, like solar, IR, or free molecular heating. Charged-particle heating rates, while not significant at room temperature, can significantly raise the equilibrium temperature of a cryogenic radiator, as shown in Fig. 2.8. A radiator designed for steady-state operation at 70 K in circular equatorial Earth orbit will warm to approximately 72.9 K for the charged-particle heating conditions at 3200 km altitude, while warming to 74.7 K and 70.4 K for the conditions at 6400 km and synchronous altitudes, respectively. In the theoretical limit where $T_{equiv} = 0$ K, the charged-particle heating effect will warm the radiator to approximately 27.3 K for the synchronous (35,800-km) circular equatorial Earth orbit condition. (The equilibrium temperature increase for the 19,100-km-altitude condition is nearly identical to the results for 3200 km, and therefore was not included in Fig. 2.8. For such systems, charged-particle heating must therefore be considered in the design and sizing of radiators. See Jimenez for a detailed discussion of this phenomenon.[2.20])

- Circular, equatorial orbit
- Solar minimum (AP8MIN) model
- Re = earth radius = 6371 km
- Omnidirectional flux data

- Circular, equatorial orbit
- Solar minimum (AE4 and AE6) model
- Re = earth radius = 6371 km
- Omnidirectional flux data
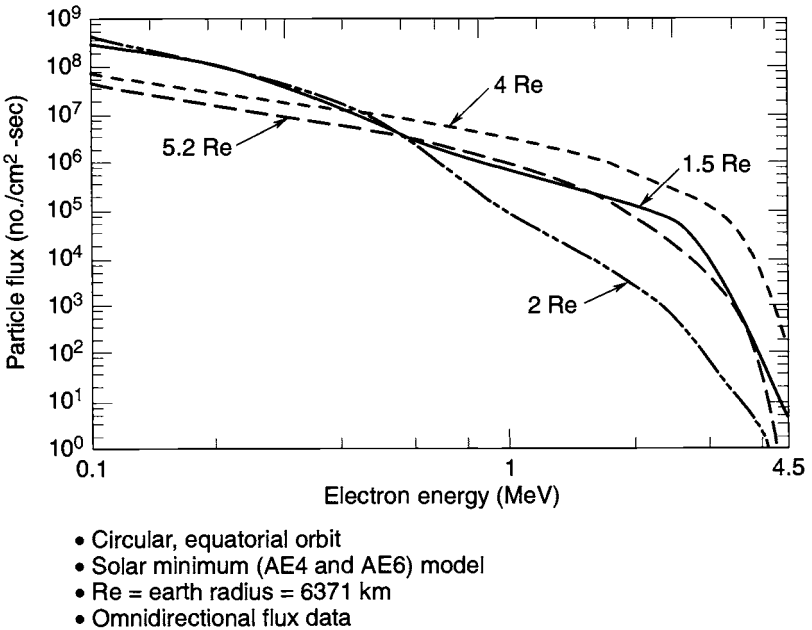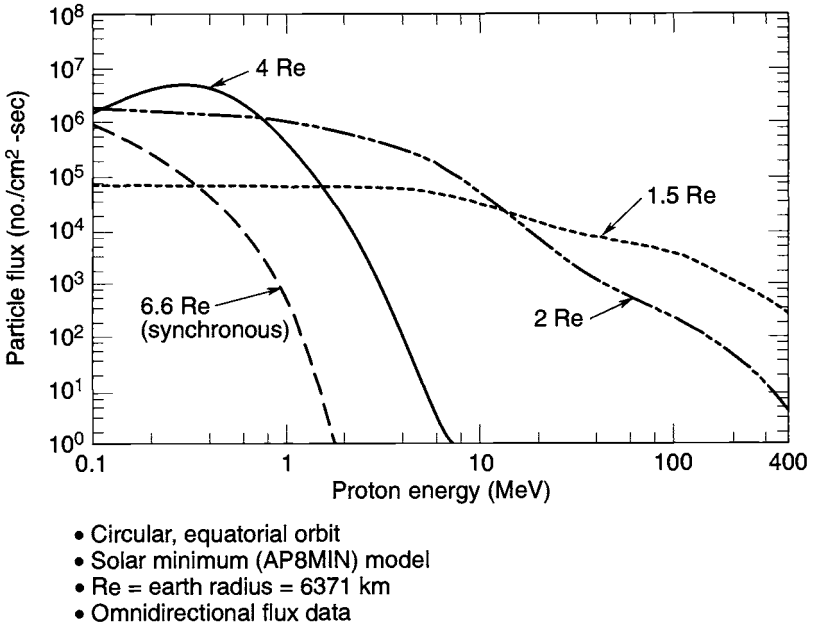
Fig. 2.7. Proton and electron flux for several Earth equatorial orbits.
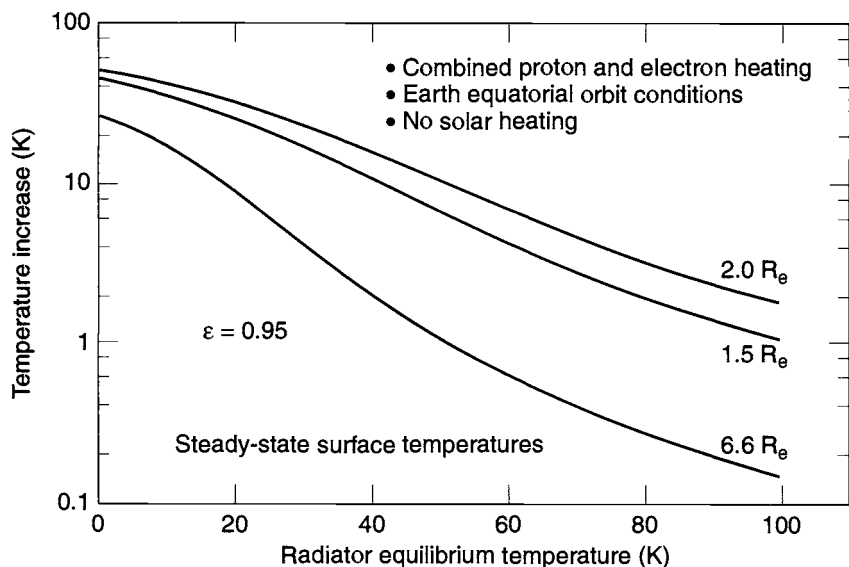
Fig. 2.8. Equilibrium temperature increase of an aluminum radiator as a result of natural environment charged-particle heating.

Standard Earth Orbits

In Chapter 1 the most common types of Earth orbits were described: LEO, geosynchronous (GEO), Molniya, and sun-synchronous. In this section, characteristics of the thermal environments encountered in each of these orbits will be discussed. Calculation of the actual heat loads that these environments impose on spacecraft surfaces will be addressed in Chapter 15.

Terminology

To begin this discussion, some terminology definition is required. Several orbital parameters are commonly used in analyses of environmental heating. These are generally the same parameters used by orbit analysts to describe the spacecraft orbit, and their use simplifies the process of getting the inputs necessary to conduct the thermal analysis for any given program. The most important parameters are defined here and illustrated in Figs. 2.9 and 2.10.

Equatorial plane: the plane of Earth's equator, which is perpendicular to Earth's spin axis.

Ecliptic plane: The plane of Earth's orbit around the sun. From the point of view of Earth, the sun always lies in the ecliptic plane. Over the course of a year, the sun appears to move continuously around Earth in this plane. Because of the tilt of Earth's spin axis, the equatorial plane is inclined 23.4 deg from the ecliptic plane, shown in Fig. 2.9 as the angle δ.

Sun day angle: The position angle of the sun in the ecliptic plane measured from vernal equinox. At vernal equinox this angle is 0 deg, at summer solstice 90
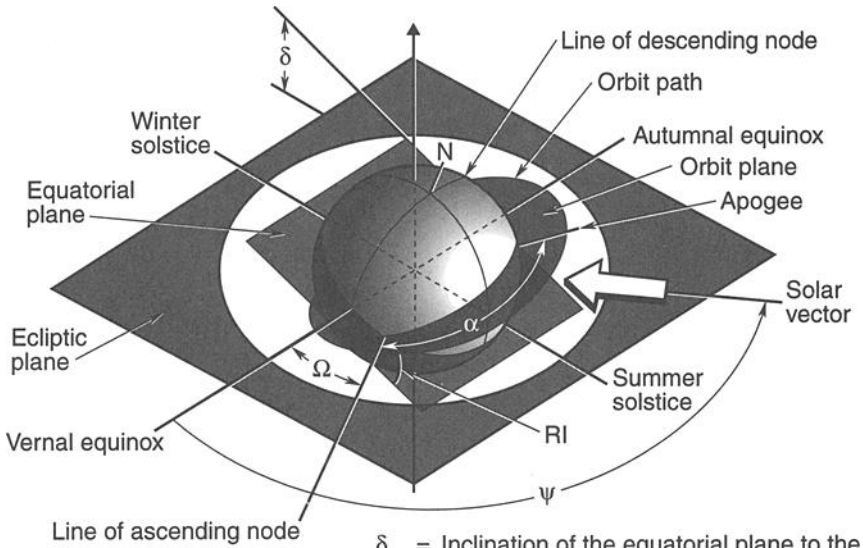
δ = Inclination of the equatorial plane to the
       ecliptic plane

Ω = Right ascension of the ascending node

α = Argument of apogee

ψ = Sun day angle

RI = Orbit inclination to the equatorial plane

$AA = (R_a + R_p)/2$

$EE = 1 - R/AA$
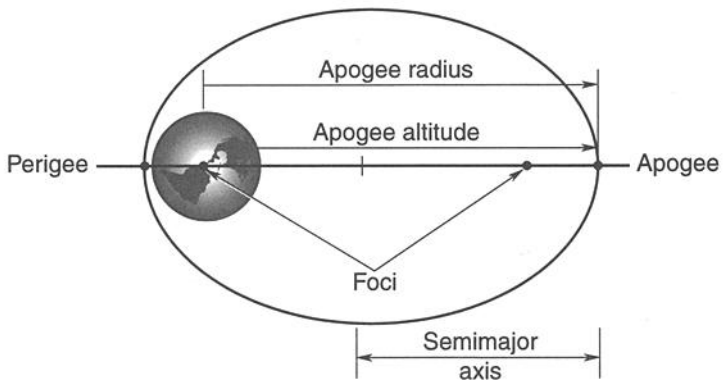
Fig. 2.9. Orbital parameters.

deg, at autumnal equinox 180 deg, and at winter solstice 270 deg. This angle is shown as ψ in Fig. 2.9 and should not be confused with the "right ascension" of the sun, which is measured in the equatorial plane and is slightly different on most days of the year.

Orbit inclination: The angle between the orbit plane and the equatorial plane, shown as RI in Fig. 2.9. Orbit inclinations typically vary from 0 to 98 deg, although inclinations greater than 98 deg are possible. For inclinations less than 90 deg, the satellite appears to be going around its orbit in the same direction as Earth's rotation. For inclinations greater than 90 deg, it appears to be going opposite Earth's rotation. In this case its orbit is known as a retrograde orbit.

Altitude: the distance of a satellite above Earth's surface.

Apogee/perigee: Apogee is the point of highest altitude in an orbit; perigee, the lowest.

Ascending node/descending node: The ascending node is the point in the orbit at which the spacecraft crosses Earth's equator while traveling from south to north (i.e., when it is "ascending"). The descending node is the point crossed during the southbound portion of the orbit.

Right ascension and declination: The position of an object in the celestial coordinate system (Fig. 2.10). Right ascension is the position angle in the equatorial plane measured from vernal equinox. Declination is the position angle above or below the equatorial plane.

Right ascension of the ascending node (RAAN): The position angle of the ascending node measured from vernal equinox in the equatorial plane (Ω in Fig. 2.9). Earth's equatorial bulge causes the ascending and descending nodes to drift slightly on each revolution about Earth. (Earth is not a true sphere.) This drifting is known as "nodal regression." For most orbits the RAAN drifts continuously with time and varies from 0 to 360 deg.
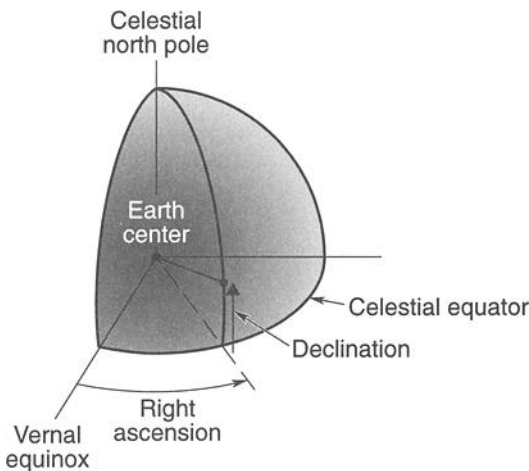
Fig. 2.10. Celestial coordinates.

Semimajor axis: the semimajor axis of the orbit ellipse.

$$a = \frac{r_a + r_p}{2}, \tag{2.2}$$

where a is the orbit semimajor axis, r_a is the orbit radius at apogee (Earth's radius + apogee altitude), and r_p is the orbit radius at perigee (Earth's radius + perigee altitude).

Period: The time required to make one revolution about the Earth. As orbit altitude increases, so does the period. The orbit period may be calculated using the relation

$$P = 2\pi \left(\frac{a^3}{\mu}\right)^{1/2}. \tag{2.3}$$

where P is the period, μ is the product of the universal gravitational constant and the mass of the planet (for Earth, $\mu = 3.98603 \times 10^{14}$ m^3/s^2), and a is the semimajor axis of the orbit (for a circular orbit, this is the orbit radius). The period of circular orbits versus orbit altitude is plotted in Fig. 2.11.

Eccentricity: The degree of oblateness of the orbit, defined as the ratio of one-half the interfocal distance to the semimajor axis. For a circular orbit, the eccentricity is 0. As the orbit becomes more elliptical, the eccentricity increases. Eccentricity is related to the apogee and perigee radii and the semimajor axis by the following relationships:

$$r_a = a(1+e), \text{ and} \tag{2.4}$$
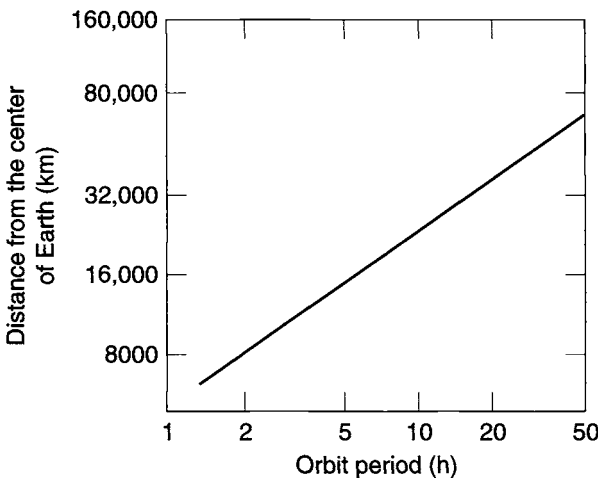
Fig. 2.11. Total amount of time per orbit.

$$r_p = a(1-e), \tag{2.5}$$

where r_a is the orbit radius at apogee, r_p is the orbit radius at perigee, a is the orbit semimajor axis, and e is the eccentricity.

Argument of apogee: For an elliptical orbit, the angle between the ascending node and apogee measured in the direction of satellite motion. This angle, shown as α in Fig. 2.9, can vary from 0 to 360 deg.

Orbit Beta Angle

Although the above parameters are used by orbit and thermal analysts to describe particular orbits, another parameter, known as the orbit beta angle (β), is more useful in visualizing the orbital thermal environment, particularly for low Earth orbits. The orbit beta angle is the minimum angle between the orbit plane and the solar vector, and it can vary from −90 to +90 deg, as illustrated in Fig. 2.12(a). The beta angle is defined mathematically as

$$\beta = \sin^{-1}(\cos\delta_s \sin RI \sin(\Omega - \Omega_s) + \sin\delta_s \cos RI), \tag{2.6}$$

where δ_s is the declination of the sun, RI is the orbit inclination, Ω is the right ascension of the ascending node, and Ω_s is the right ascension of the sun.

As viewed from the sun, an orbit with β equal to 0 deg appears edgewise, as shown in Fig. 2.12(b). A satellite in such an orbit passes over the subsolar point on Earth where albedo loads (sunlight reflected from Earth) are the highest, but it also has the longest eclipse time because of shadowing by the full diameter of Earth. As β increases, the satellite passes over areas of Earth further from the subsolar point, thereby reducing albedo loads; however, the satellite is also in the sun for a larger percentage of each orbit as a result of decreasing eclipse times. At some point, which varies depending on the altitude of the orbit, eclipse time drops to 0. With β equal to 90 deg, a circular orbit appears as a circle as seen from the sun; no eclipses exist, no matter what the altitude; and albedo loads are near 0. Fig. 2.12(b) shows how orbits of various beta angles appear as seen from the sun. Note
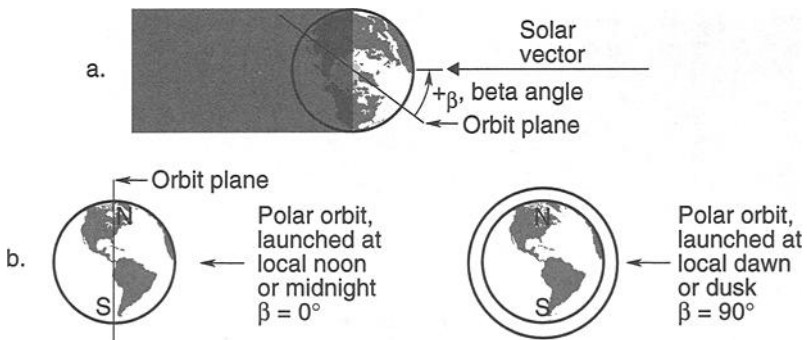
Fig. 2.12. Orbit beta angle.

that beta angles are often expressed as positive or negative; positive if the satellite appears to be going counterclockwise around the orbit as seen from the sun, negative if clockwise.

Figure 2.13 shows how eclipse times vary with β for circular orbits of different altitudes. The eclipse fraction of a circular orbit can be calculated from Eq. (2.7).

$$f_E = \frac{1}{180°}\cos^{-1}\left[\frac{(h^2 + 2Rh)^{1/2}}{(R + h)\cos\beta}\right] \quad \text{if } |\beta| < \beta^* \tag{2.7}$$

$$= \qquad\qquad 0 \quad \text{if } |\beta| \geq \beta^*,$$

where R is Earth's radius (6378 km), h is orbit altitude, β is orbit beta angle, and β^* is the beta angle at which eclipses begin.

β^* may be calculated using Eq. (2.8), as follows:

$$\beta^* = \sin^{-1}\left[\frac{R}{(R + h)}\right] 0° \leq \beta^* \leq 90°. \tag{2.8}$$

Both Eqs. (2.7) and (2.8) assume Earth's shadow is cylindrical, which is valid for low orbits where no appreciable difference exists between the umbral and penumbral regions of total and partial eclipsing, respectively. For 12-hour and geosynchronous orbits, these equations may be slightly in error.

For any given satellite, β will vary continuously with time because of the orbit nodal regression and the change in the sun's right ascension and declination over the year. The regression rates as a function of inclination for circular orbits of different altitudes are shown in Fig. 2.14. The sun's right ascension and declination throughout the year are shown in Fig. 2.15. The β history for a particular satellite
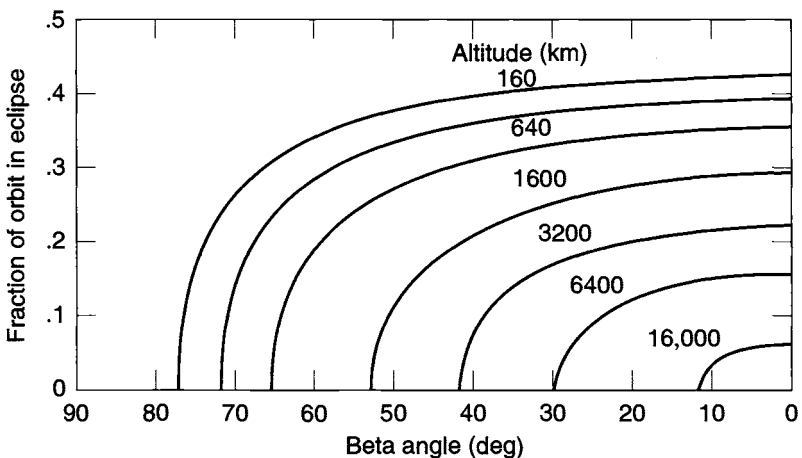
Fig. 2.13. Eclipse durations.

$$\bar{h} = \frac{h_{apogee} + h_{perigee}}{2}$$

Note:
For retrograde orbit use supplementary value of inclination and change sign of $\dot{\Omega}$ to plus.
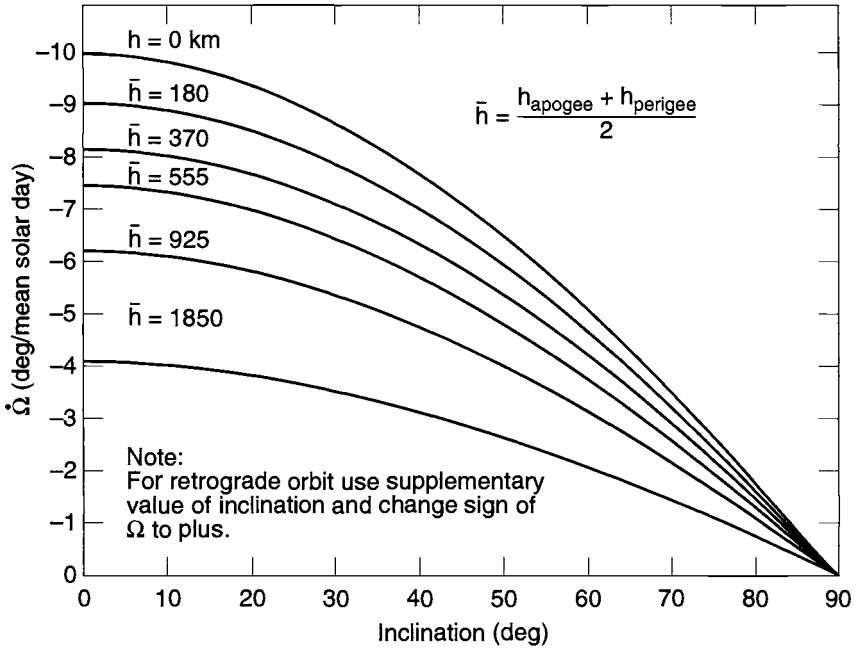
Fig. 2.14. Regression rate due to oblateness vs. inclination for various values of average altitude.

in a 500-km-altitude, circular orbit is shown in Fig. 2.16. The absolute value of β can vary from 0 to a maximum that equals the orbit inclination plus the maximum declination of the sun (i.e., inclination plus 23.4 deg).
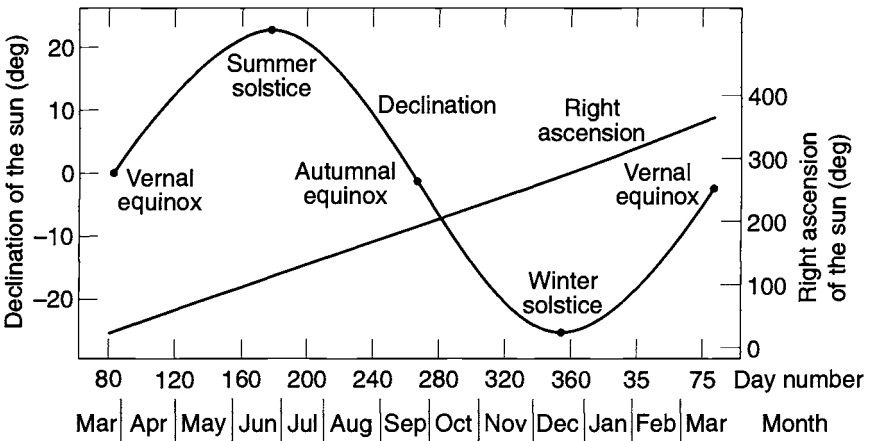
Fig. 2.15. Solar declination and right ascension vs. date.
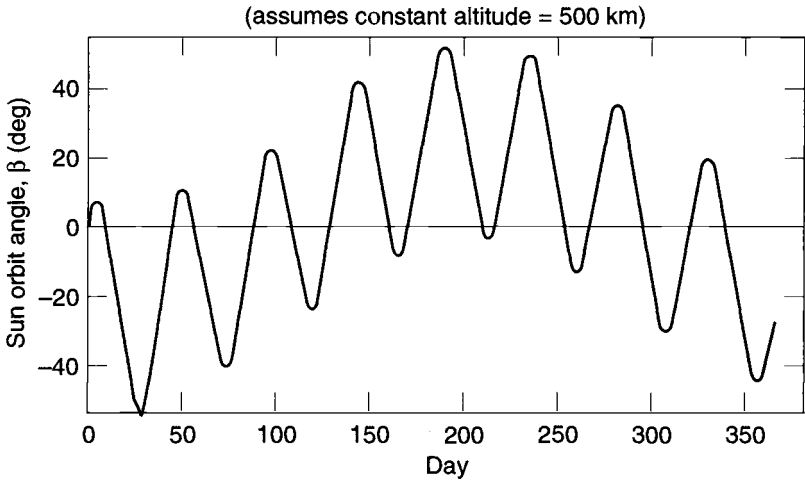
Fig. 2.16. Sample orbit-beta-angle drift (Lockheed Martin).

If the nodal regression of an orbit proceeds eastward at exactly the rate at which the sun's right ascension changes over the year, thereby "following" the sun, the orbit is called sun-synchronous. Because the sun moves uniformly eastward along the equator through 360 deg a year (about 365.242 mean solar days), the required rate of nodal regression is 360/365.242, or 0.985647 deg/day. For circular orbits, sun-synchronism is possible for retrograde orbits (i.e., inclination > 90 deg) up to an altitude of about 5975 km.

The orbit inclination required to achieve sun-synchronism in circular orbits is shown as a function of orbit altitude in Fig. 2.17. Note that, because of the change in the sun's declination over the year, β is not constant but varies over a small range. The β histories for 833-km sun-synchronous orbits with different initial values for RAAN are shown in Fig. 2.18.
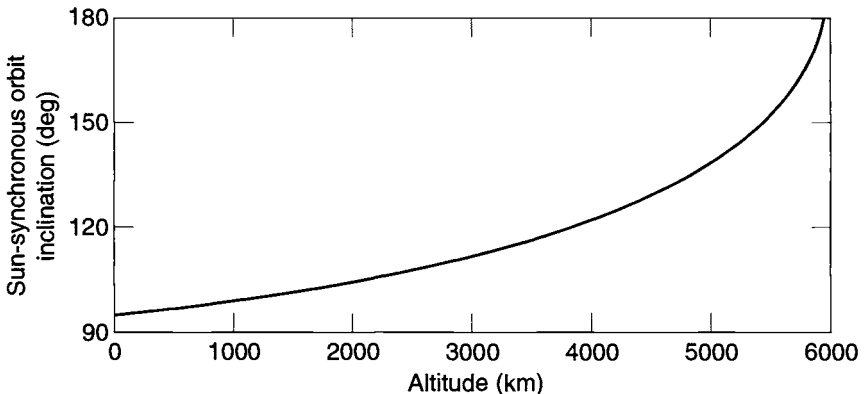
Fig. 2.17. Altitude vs. inclination for sun-synchronous orbits.
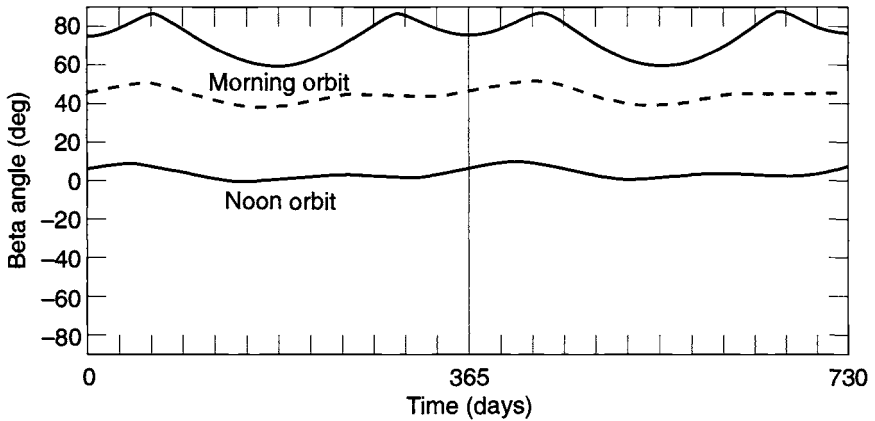
Fig. 2.18. Orbit-beta-angle histories for sun-synchronous, 833-km orbits.

Low Earth Orbits

The chief advantage in thinking in terms of β is that it simplifies the analysis of orbital thermal environments. By analyzing the environments at several discrete β values, one can be confident that all possible combinations of orbit RAAN and sun day angles have been covered. Figure 2.19 shows such an analysis for a spinning
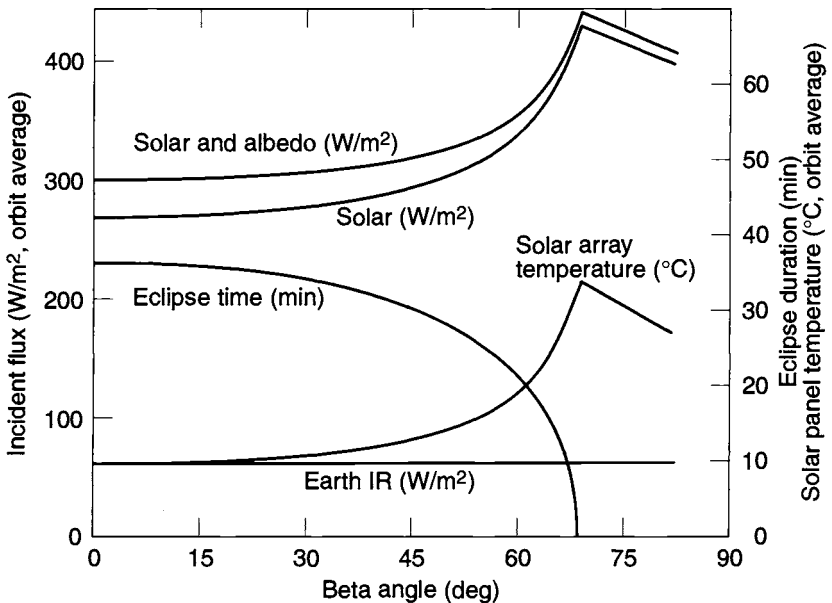
Fig. 2.19. Cylinder in low Earth orbit.

cylindrical satellite in a 555-km-altitude LEO. Earth-emitted IR was considered constant over Earth and therefore independent of orbit inclination, RAAN, or β. The IR load to the satellite therefore is constant with β. Since the eclipse time decreases with β, however, the satellite spends more time in the sun, thereby increasing the orbit-average solar load, as shown in Fig. 2.19. Also, as β increases, the albedo loads decrease, as can be seen by comparing the "solar" and "solar plus albedo" curves in Fig. 2.19. The net result for this particular satellite was that solar-panel orbit-average temperature (which provides a radiative heat sink for the internal components) was a minimum at $\beta = 0$ deg and a maximum at $\beta = 65$ deg.

Geosynchronous Orbits

As orbit altitude increases, environmental loads from Earth (IR and albedo) decrease rapidly. The graph in Fig. 2.20 shows these loads on a black plate over the subsolar point for various altitudes. By the time a spacecraft reaches GEO orbit, these loads are insignificant for most thermal-design analyses. The one exception to this rule is the case of cryogenic systems, which operate at such low temperatures that even small environmental heat loads from Earth are significant to the thermal design.

With such small Earth loads, the only significant environmental load for non-cryogenic systems in GEO orbit is solar. At this altitude the spacecraft is in the sun most of the time, and the maximum possible eclipse duration is only 72 minutes out of the 24-hour orbit. Since most GEO orbits have inclinations of less than 4 deg, eclipses occur only around vernal and autumnal equinox, in periods known as "eclipse seasons." During summer and winter the sun's declination causes Earth's shadow to be cast above or below the satellite orbit, making eclipses impossible, as shown in Fig. 2.21. For circular, 24-hour orbits inclined by more than a few degrees, eclipses could occur during seasons other than equinox, but such orbits are rather rare and the maximum eclipse duration would be the same.
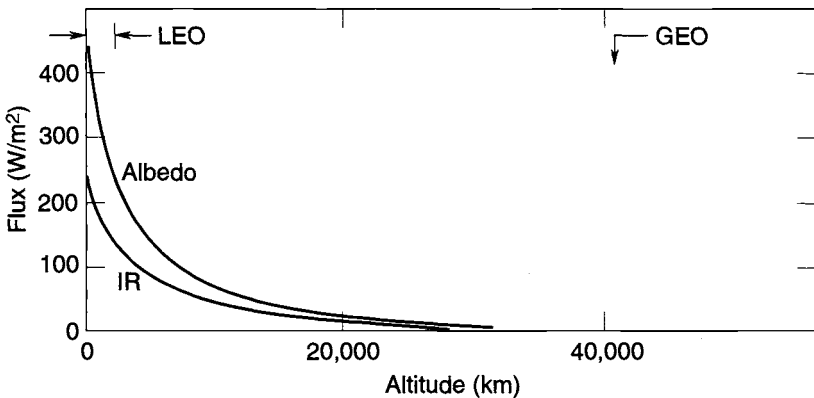
Fig. 2.20. Earth heat loads vs. altitude.
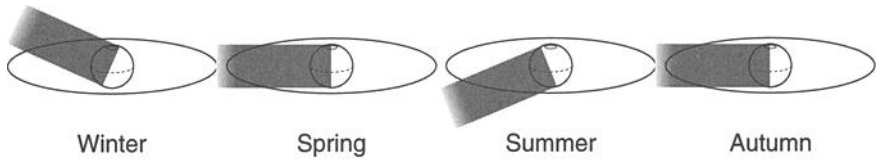
Fig. 2.21. GEO orbit eclipse, once per orbit, spring and autumn only (Northrop Grumman).

Many of the satellites in GEO orbit are the three-axis type, with one side of the vehicle constantly facing Earth, as shown in Fig. 2.22. For satellites such as this, the north and south faces receive the lowest peak solar flux, since the sun can only rise to a 23.4-deg angle above the surface (or maybe a little higher if the orbit has a slight inclination). As the spacecraft travels the orbit, the sun maintains a fixed elevation angle from these surfaces as the spacecraft rotates to always face Earth, as shown in Fig. 2.22. This elevation angle changes from +23.4 deg in summer (sun on the north surface) to –23.4 deg in winter (sun on the south surface). The other four surfaces will see the sun circle around them during the orbit, with the result of a cosine variation in intensity from no sun to a full sun normal to the surface. Because the sun can only rise to an angle of 23.4 deg "above" the north/south faces, the maximum solar load on these surfaces is (sin 23.4 deg) (1.0 normal sun) = 0.4 suns, while the maximum load on all the other faces is 1.0 sun. Therefore a common practice is to mount the highest-power dissipation components on the north and south faces, where the reduced solar loads make it easier to reject heat from the spacecraft.

The moon can also cause eclipses. These are far less frequent than Earth eclipses and are of shorter duration, so they are not thermal design drivers for most spacecraft. Furthermore, while Earth and the moon can physically cause consecutive eclipses, the probability of this actually occurring is extremely remote and is usually not considered in spacecraft thermal design. Nonetheless, an assessment of the impact of consecutive eclipses on vehicle survival is a good idea if the
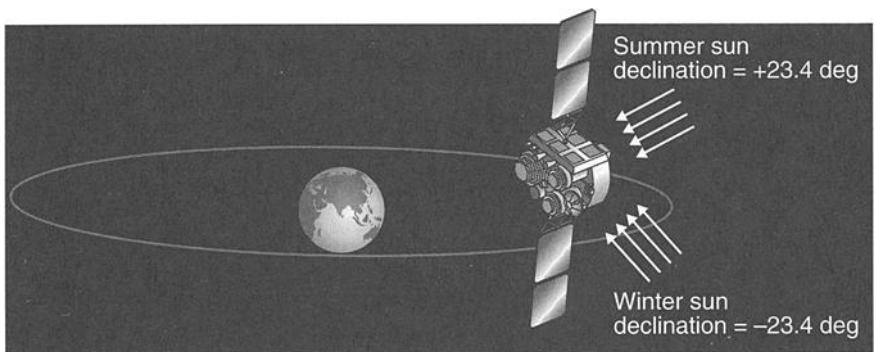
Fig. 2.22. Solar illumination of GEO satellite.

spacecraft orbit could result in such a condition. At least one spacecraft has unexpectedly encountered consecutive eclipses and, although the vehicle survived, its payload temperatures fell well below allowable limits.

Twelve-Hour Circular Orbits

The thermal environment in 12-hour circular orbits is much like that in GEO orbits. Earth loads (IR and albedo) are not significant unless cryogenic systems are involved, leaving solar loads as the only environmental loads. At this time, these orbits are being used primarily by the Global Positioning System (GPS) and its Russian counterpart, GLONASS (Global Navigation Satellite System). Both of these programs include a number of satellites in 12-hour circular orbits with many different inclinations.

The angles of solar illumination on spacecraft in 12-hour circular orbits, unlike the angles on GEO vehicles, can vary considerably with various orbit inclinations, but the maximum eclipse length is 56 minutes for all 12-hour circular orbits.

Molniya Orbits

Molniya orbits are unusual in that they have an extreme degree of eccentricity (i.e., they are very elliptical) and a high inclination (62 deg). With perigee altitudes in the LEO range of approximately 550 km and apogee altitudes of near GEO altitude (38,900 km), a spacecraft in such an orbit goes through a wide swing in thermal environments. Near perigee Earth loads are high, but at apogee only the solar loads are significant. Since its velocity is much higher near perigee, the spacecraft tends to spend most of the 12-hour orbit period at higher altitudes and relatively little time at low altitudes, where Earth loads are significant. Figure 2.23 shows the position of a spacecraft in a Molniya orbit at 1-hour intervals and a graph of Earth IR load versus time on a flat plate facing Earth to illustrate the environmental changes that occur around the orbit.
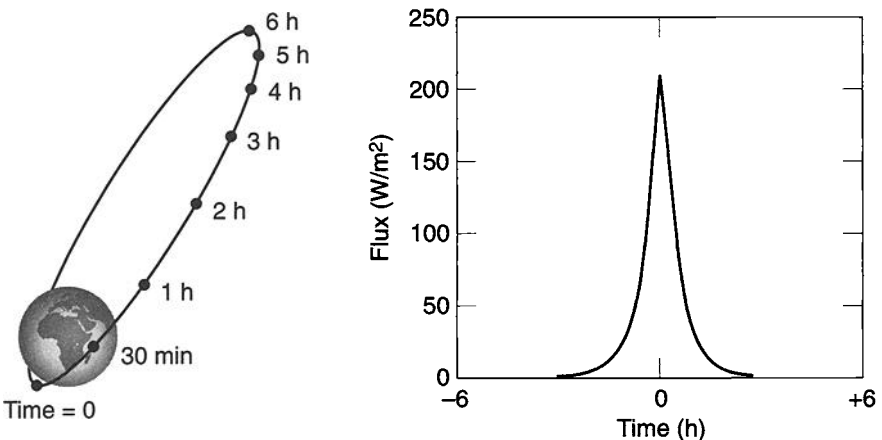
Fig. 2.23. Earth IR heating in Molniya orbit, flat black plate facing Earth.

Eclipse times for Molniya orbits vary considerably with season. During summer, spring, and fall, Earth's shadow is cast on the southern portion of the orbit, where the spacecraft is at low altitude and traveling very fast (see Fig. 2.24). This results in relatively short eclipse times. During the winter Earth's shadow is cast on more northerly portions of the orbit, where the spacecraft is at higher altitude and lower velocity; the result is longer eclipse times. The range of eclipse times for Molniya orbits is 0 (for high-β orbits) to 72 minutes for certain winter eclipses.

Environments of Interplanetary Missions

Environments of Interplanetary Cruises

Interplanetary cruise trajectories can expose spacecraft to a range of thermal environments much more severe than those encountered in Earth orbit. During most of an interplanetary cruise, the only environmental heating comes from direct sunlight. As noted in Chapter 1, some missions require close flybys past planets for a gravity-assisted change of velocity and direction. During a flyby, a spacecraft is exposed to IR and albedo loads from the planet. Table 2.5 provides the size and basic orbital characteristics of the planets and Earth's moon.

During an interplanetary cruise, a spacecraft's distance from the sun determines the thermal environment at all times except during planetary flybys. If the mean solar intensity near Earth is defined as 1 "sun," then a spacecraft would be exposed to 6.5 suns at the mean orbit of Mercury, but only 0.0006 suns at the mean orbit of Pluto/Charon. Equation 2.9 and Fig. 2.25 show solar flux as a function of distance from the sun in AU.

- No eclipse
- Winter
- High beta angles

- Short eclipse
- Summer
- High beta angles

- Maximum eclipse
- Winter
- Low beta angle
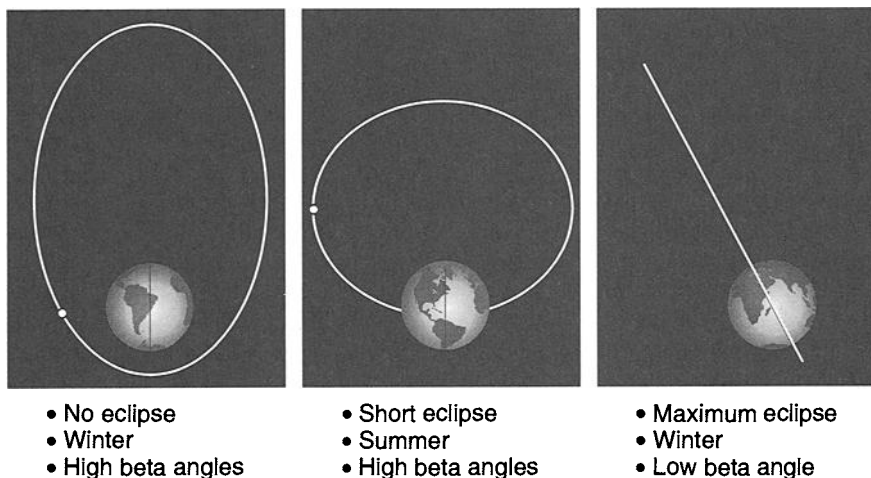
Fig. 2.24. Molniya eclipses.

Table 2.5. Planetary Size and Orbit Parameters

Planet	Orbit Semimajor Axis (AU)	Perihelion Distance (AU)	Aphelion Distance (AU)	Equatorial Radius (km)
Mercury	0.3871	0.3075	0.4667	2425
Venus	0.7233	0.7184	0.7282	6070
Earth	1.000	0.9833	1.0167	6378
Moon	1.000	0.9833	1.0167	1738
Mars	1.524	1.381	1.666	3397
Jupiter	5.20	4.95	5.45	71,300
Saturn	9.54	9.01	10.07	60,100
Uranus	19.18	18.28	20.09	24,500
Neptune	30.06	29.80	30.32	25,100
Pluto/Charon	39.44	29.58	49.30	3,200 (Pluto)

$$\text{Solar flux} = \frac{1367.5}{\text{AU}^2} \frac{\text{W}}{\text{m}^2} \tag{2.9}$$

To give a feel for the thermal environments encountered during interplanetary missions, we will use the concept of a "reference sphere." This reference will be an isothermal sphere with an absorptance and emittance of 1.0. The equilibrium temperature of the sphere will provide a rough indication of how "hot" or "cold" the local thermal environment is. Figure 2.26 shows the sphere's equilibrium
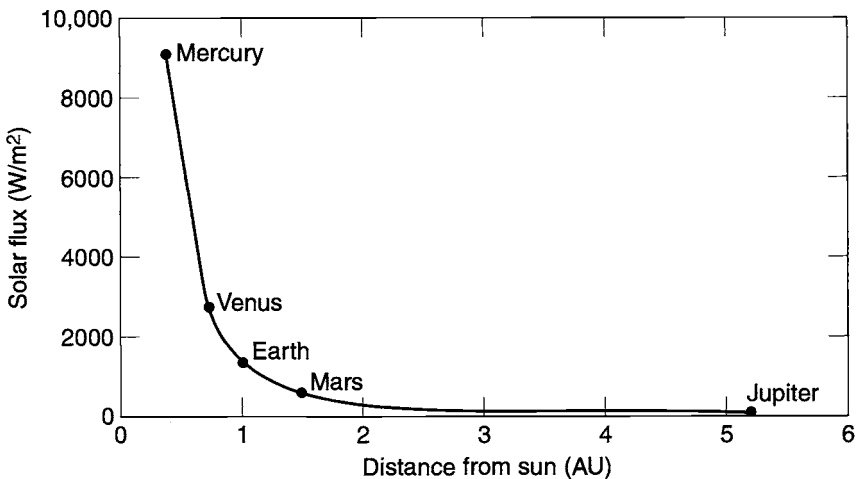
Fig. 2.25. Solar flux as a function of distance from the sun.
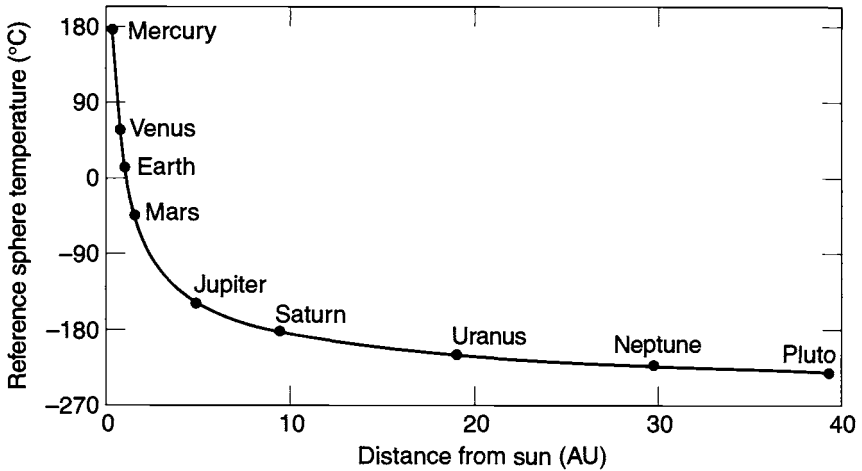
Fig. 2.26. Temperature as a function of distance from the sun.

temperature as a function of distance from the sun. At Earth's distance, the sphere's temperature is a relatively comfortable 6°C. At the average orbital distance of Mercury, the temperature is a scorching 174°C. At Mars, it falls to –47°C. For the outer planets, temperature drops sharply: –150°C for Jupiter, –183°C for Saturn, –209°C for Uranus, –222°C for Neptune, and –229°C for Pluto/Charon.

During planetary flybys, planet IR and albedo loads are added to the solar load for short periods of time. On most spacecraft, the thermal mass of the vehicle largely damps out the temperature rise of most components during flyby. Exposed lightweight components, however, may be significantly affected.

Environments of Mercury

Since Mercury is the closest planet to the sun, the thermal environment in its vicinity is, understandably, hot! Because Mercury's orbital period (its "year") is about 88 Earth days long and its period of rotation is approximately 58 Earth days, Mercury's "day" lasts for 176 Earth days. The rotation is so slow, in fact, that the surface temperature of the side of the planet facing the sun is essentially in equilibrium with the solar flux while the dark side is quite cold. Thus, the surface temperature, which drives the planetary IR emission, falls off as a cosine function from the subsolar region to the terminator. Mercury has no atmosphere to attenuate radiation from the surface to space. Hanson describes the surface temperature as a function of angle from the subsolar point as follows:[2.21]

$$T = T_{subsolar}(\cos\phi)^{1/4} + T_{terminator}\left(\frac{\phi}{90}\right)^3 \quad \text{for } \phi \le 90° \qquad (2.10)$$

$$T = T_{terminator} \qquad\qquad\qquad\qquad \text{for } \phi > 90° \qquad (2.11)$$

where

$$T_{subsolar} = 407 \pm \frac{8}{r^{0.5}} \text{ K,} \qquad (2.12)$$

$T_{terminator}$ is 110 K, ϕ is the angle from the subsolar point, and r is the Mercury-Sun distance in AUs.

The range of planetary emission corresponding to the above equations (see Table 2.6) is a remarkable 6 to 12,700 W/m^2! (To avoid confusion and potential analysis errors, note that this surface-temperature model assumes a surface emittance of 0.77±0.06. Most other discussions of a planet's effective surface temperature treat the surface as a blackbody with an emittance of 1.0. If the blackbody approach were used here, the calculated surface temperatures would be somewhat lower than what is shown above.)

The high surface temperatures on Mercury are driven by its proximity to the sun and generally low albedo. Depending on the geological features in the region being considered, specific albedo values can range from 0.08 to 0.25, as shown in Table 2.7 (from Murray *et al.*), meaning that most of the incident solar energy is absorbed and reradiated as planetary IR.[2.22]

If the black reference sphere introduced earlier were placed in a circular orbit around Mercury at an altitude of 0.1 planet radii, its instantaneous temperature would range from 336 to −197°C, as shown in Table 2.8. The exceptionally wide swing in temperature (336 to −197°C) in the β = 0° orbit is a reflection of the eclipse plus the big difference between the surface temperatures, and therefore planetary IR, on the dayside and nightside. The orbit-average temperatures of 27

Table 2.6. Mercury Orbital Environments

	Perihelion	Aphelion	Mean
Direct solar (W/m^2)	14,462	6278	9126
Albedo (subsolar peak)	0.12	0.12	0.12
Planetary IR (W/m^2)			
Maximum (subsolar peak)	12,700	5500	8000
Minimum (dark side)	6	6	6

Table 2.7. Normal Albedo of Mercury

Geological Features	Albedo Values
Bright craters and rays	0.19 to 0.25
Heavily cratered terrain and textured plains	0.11 to 0.19
Flat-floored plains	0.10 to 0.13
Smooth plains	0.08 to 0.12

Table 2.8. Reference Sphere in Orbit Around Mercury

	$\beta = 0°$		$\beta = 90°$	
	Perihelion (°C)	Aphelion (°C)	Perihelion (°C)	Aphelion (°C)
Maximum	336	222	245	147
Minimum	−197	−197	245	147
Average	89	27	245	147

to 245°C are quite high, as one would expect to find at distances so close to the sun. The eccentricity of Mercury's orbit also results in unusually large differences between perihelion and aphelion solar flux and planetary IR, which are reflected in the significantly different temperatures of our reference sphere under perihelion and aphelion conditions.

Environments of Venus

The thermal environment in orbit around Venus is not only considerably cooler than the environment around Mercury because of Venus's greater distance from the sun, but it is also considerably different in terms of the relative contribution of the solar and IR components. The fact that Mercury's albedo is very low means that most of the incident solar energy is absorbed by the planet's surface, then reradiated as IR energy. Venus, on the other hand, is entirely covered by clouds and therefore has a very high albedo of around 0.8, as shown in Table 2.9. This high albedo results in a low cloud-top temperature and a planetary IR emission (Table 2.10, from Tomasko *et al.*) that is even less than that of Earth.[2.23]

The cloud system of Venus also causes some solar backscattering effects at large angles from the subsolar point. These effects in turn create some limb-brightening near the terminator. For low-altitude orbits, modeling Venus's albedo as diffuse (Lambertian) with a cosine falloff from the subsolar point, as most analysis codes do, is fairly accurate. In fact, at the subsolar point, this approach is slightly conservative for altitudes up to about 1700 km (0.28 Venus radii). For higher altitudes, the limb-brightening effect becomes more prevalent, and consequently the assumption of diffuseness can underestimate albedo loads by about 10% for a spacecraft at an altitude of 6070 km (1 Venus radius) and by up to 41% at very large altitudes. However, because the albedo flux is fairly small at those altitudes, especially in comparison to the direct solar, this nonconservatism may not be particularly significant. Full evaluation of Venus's directional albedo characteristics is therefore recommended only for particularly sensitive components.

Table 2.9. Venus Orbital Environments

	Perihelion	Aphelion	Mean
Direct solar (W/m^2)	2759	2650	2614
Albedo	0.8 ± 0.02	0.8 ± 0.02	0.8 ± 0.02
Planetary IR (W/m^2)	153	153	153

Table 2.10. Planetary IR Emission of Venus

Latitude (deg)	Emission Flux (W/m^2)	T (°C)
0–10	146.3	–47.6
10–20	153.4	–44.9
20–30	156.7	–43.7
30–40	158.7	–43.0
40–50	155.5	–44.2
50–60	152.0	–45.5
60–70	138.5	–50.7
70–80	143.5	–48.7
80–90	178.4	–36.2

Placing our black reference sphere in a 607-km-altitude (0.1-radii-altitude) orbit around Venus produces the temperatures shown in Table 2.11. Although Venus is generally much cooler than Mercury, it does share with that planet a large temperature swing in the $\beta = 0°$ orbit. In the case of Mercury, the swing is driven by large planetary IR loads from the sunlit side of the planet. For Venus, the high temperatures are caused by the very large albedo loads. Temperatures during the eclipsed portion of the orbit are somewhat higher than is the case for Mercury, as a result of Venus's higher planetary IR on the dark side. Venus's orbit, like those of most of the planets, does not have as high an eccentricity as Mercury's, so the temperatures of the reference sphere are not greatly different for perihelion and aphelion conditions.

Lunar Environments

As a result of the lack of an atmosphere and the length of the lunar day, the thermal environment in orbit around the moon is similar to that around Mercury; it is dominated by planetary IR that diminishes as a cosine function of the angle from the subsolar point. The moon's equatorial surface-temperature distribution, which drives the emitted IR, is shown versus angle from the subsolar point in Fig. 2.27. It is derived from Apollo 11 data (by Cremers, Birkebak, and White) using a cosine

Table 2.11. Reference Sphere in Orbit Around Venus

	$\beta = 0°$		$\beta = 90°$	
	Perihelion (°C)	Aphelion (°C)	Perihelion (°C)	Aphelion (°C)
Maximum	122	119	67	64
Minimum	–105	–105	67	64
Average	14	12	67	64
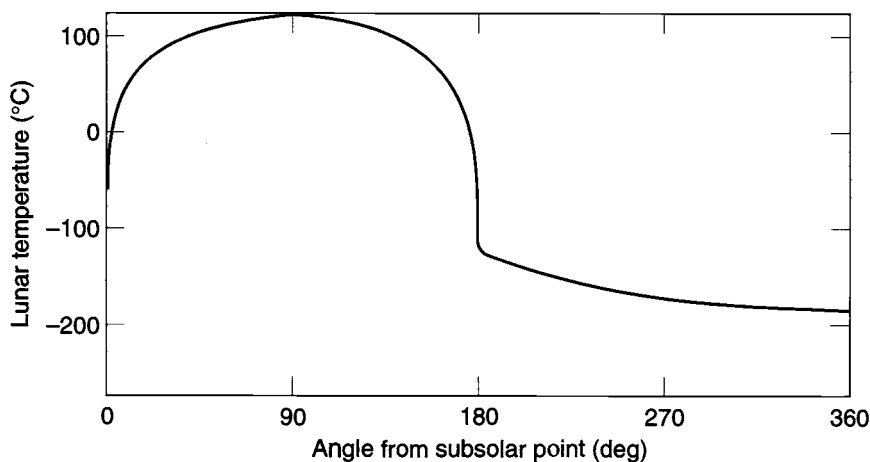
Fig. 2.27. Lunar surface temperature.

relationship for temperature to about 70 deg and assumes a surface emittance of 0.92.[2.24] A similar distribution is thought to apply in all directions from the subsolar point, not just in the equatorial plane. The temperature on the dark side of the moon is on the order of −170°C.

As bright as the moon may appear in the night sky, its average albedo is only 0.073, making it as absorptive as black paint! Even the most reflective lunar geological regions have albedo values less than 0.13, as shown in Table 2.12 (from Ref. 2.25). This low albedo (high absorptance) causes the high surface temperature on the sunlit side. A summary of the moon's thermal environmental parameters is shown in Table 2.13.

When our reference sphere is placed in orbit around the moon at an altitude of 0.1 lunar radii, we see a temperature response (Table 2.14) qualitatively like the response of Mercury, with high temperatures over the subsolar point and very low temperatures during eclipse. This pattern, again, is characteristic of the long day

Table 2.12. Albedo of Lunar Surface Features

Geological Regions	Normal Albedo[a]
Copernican-type craters	0.126
Apennine Mountains	0.123
Mare Serenitatis	0.093
Mare Tranquillitatis	0.092
Mare Fecunditatis	0.092
Langrenus Crater	0.129

[a]Approximate average values.

Table 2.13. Lunar Orbital Environments

	Perihelion	Aphelion	Mean
Direct solar (W/m^2)	1414 ± 7	1323 ± 7	1368 ± 7
Albedo (subsolar peak)	0.073	0.073	0.073
Planetary IR			
Maximum (W/m^2) (subsolar peak)	1314	1226	1268
Minimum (W/m^2) (dark side)	5.2	5.2	5.2

Table 2.14. Reference Sphere in Orbit Around the Moon

	$\beta = 0°$		$\beta = 90°$	
	Perihelion (°C)	Aphelion (°C)	Perihelion (°C)	Aphelion (°C)
Maximum	67	61	22	17
Minimum	−199	−199	22	17
Average	−56	−59	22	17

and the lack of an atmosphere to retain surface heat; these factors combine to produce very low dark-side surface temperatures and, consequently, minimal dark-side planetary IR.

The Apollo program missions have provided interesting lessons pertaining to spacecraft thermal balance, both in orbit around the moon and on its surface. The planetary IR is so large in lunar orbit that spacecraft radiator surfaces are affected to a much greater extent than they are in Earth orbit. In particular, the lesson here is to choose radiator locations and spacecraft attitude to minimize radiator views to the lunar surface, when possible. Since most radiators have a low solar absorptance and high IR emittance, pointing the radiator towards the sun to some extent, to minimize its view to the lunar surface, is frequently preferable.

A similar effect has occurred during lunar surface operations of Apollo missions. The proximity of relatively low mountains near Hadley Rille (Apollo 15) and Taurus Littrow (Apollo 17) affected the thermal performance of lunar surface equipment. Specifically, electronic equipment with zenith-pointing radiators actually had small view factors (a few percent) to the nearby mountains. The IR load from the hot mountains raised temperatures of the equipment by at least 10°C. Thus, the presence of mountains for lunar surface operations cannot be ignored.

Another important factor in lunar surface operations is dust, which can easily be thrown up by lunar rover operations or just by a person walking. Since lunar dust is very dark, a small amount settling on radiators can significantly raise their normally low solar absorptance. This effect was so strong that, by the last Apollo Lunar Rover mission, the crew brushed dust off radiator surfaces at almost every stop of the Rover vehicle.

The last lesson to note is the effect of the extremely low thermal conductivity of lunar soil. The low conductivity results in the surface temperature in shadowed areas almost reaching the −170°C nightside value very quickly. These shadowed "cold spots" in the proximity of surface equipment can substantially reduce the IR load on the equipment. These were of particular concern for the operators of the Apollo 14 Modular Equipment Transporter, which had rubber tires whose lower temperature limit was −57°C. The shadows created by the tires themselves required that the vehicle be parked such that one tire did not shadow the other, creating a tire undertemperature condition.

Environments of Mars

Mars is the last planet in our tour of the solar system near which a spacecraft will experience significant environmental heating. The average solar flux (see Table 2.15) is 589 W/m^2, or about 42% of what is experienced by an Earth-orbiting spacecraft. As a result of the eccentricity of Mars's orbit, however, the solar flux at Mars varies by ±19% over the Martian year, which is considerably more than the ±3.5% variation at Earth. Albedo fractions are similar to Earth's, being around 0.25 to 0.28 at the equator and generally increasing toward the poles, as shown in Table 2.16. Like Earth's poles, the reflective polar caps of Mars are responsible for the planet's high albedo at high latitudes. Befitting the "red planet," the spectral distribution of Martian albedo, compared to other planets' albedos, shows a shift to the red end of the spectrum, peaking at 0.7 μm (Earth albedo peaks at 0.47 μm).

Martian planetary IR values have been derived from Mariner and Viking Orbiter spacecraft data. The best description is a plot of equivalent blackbody (emittance = 1.0) surface temperature vs. latitude and longitude for both perihelion and aphelion conditions, as shown in Figs. 2.28 and 2.29. These data, derived from Pallucone and Kieffer,[2.26] are currently used in the design of Mars-orbiting spacecraft.

The data are based on an assumption that the environments described above experience no dust storms. The presence of a global dust storm would slightly increase the overall albedo, with dark-area albedos increasing more than bright-area ones. The increased atmospheric opacity would also damp the effective diurnal temperature range, making the planetary IR more benign.

Our reference sphere, in orbit around Mars at a 0.1-planet-radius altitude, experiences instantaneous temperatures from +11 to −163°C and orbit averages from −22 to −82°C, as shown in Table 2.17. Mars's thin, relatively cloudless atmosphere

Table 2.15. Mars Orbital Environments

	Perihelion	Aphelion	Mean
Direct solar (W/m^2)	717	493	589
Albedo (subsolar peak)	0.29	0.29	0.29
Planetary IR			
Maximum (W/m^2) (near subsolar)	470	315	390
Minimum (W/m^2) (polar caps)	30	30	30

Table 2.16. Mars Albedo Distribution

Latitude (deg)	Maximum Albedo	Minimum Albedo
80 to 90	0.5	0.3
70 to 80	0.5	0.2
60 to 70	0.5	0.2
50 to 60	0.5	0.17
40 to 50	0.28	0.17
30 to 40	0.28	0.18
20 to 30	0.28	0.22
10 to 20	0.28	0.25
0 to 10	0.28	0.25
−10 to 0	0.28	0.20
−20 to −10	0.25	0.18
−30 to −20	0.22	0.18
−40 to −30	0.22	0.18
−50 to −40	0.25	0.3
−60 to −50	0.25	0.4
−70 to −60	0.3	0.4
−80 to −70	0.4	0.4
−90 to −80	0.4	0.4

Table 2.17. Reference Sphere in Orbit Around Mars

	$\beta = 0°$		$\beta = 90°$	
	Perihelion (°C)	Aphelion (°C)	Perihelion (°C)	Aphelion (°C)
Maximum	11	−16	0	−26
Minimum	−162	−163	−32	−53
Average	−63	−82	−22	−43

is highly transmissive to IR. This condition contributes to the cold nighttime surface temperatures and causes nightside planetary IR to be much lower than that on the dayside. The low temperature of our sphere during the $\beta = 0°$ eclipse is a consequence of this surface cooling. This variation contrasts with the more uniform planetary IR of Earth and Venus, both of which have atmospheres that impede radiation from the surface to space, giving those planets more uniform day and night temperatures.
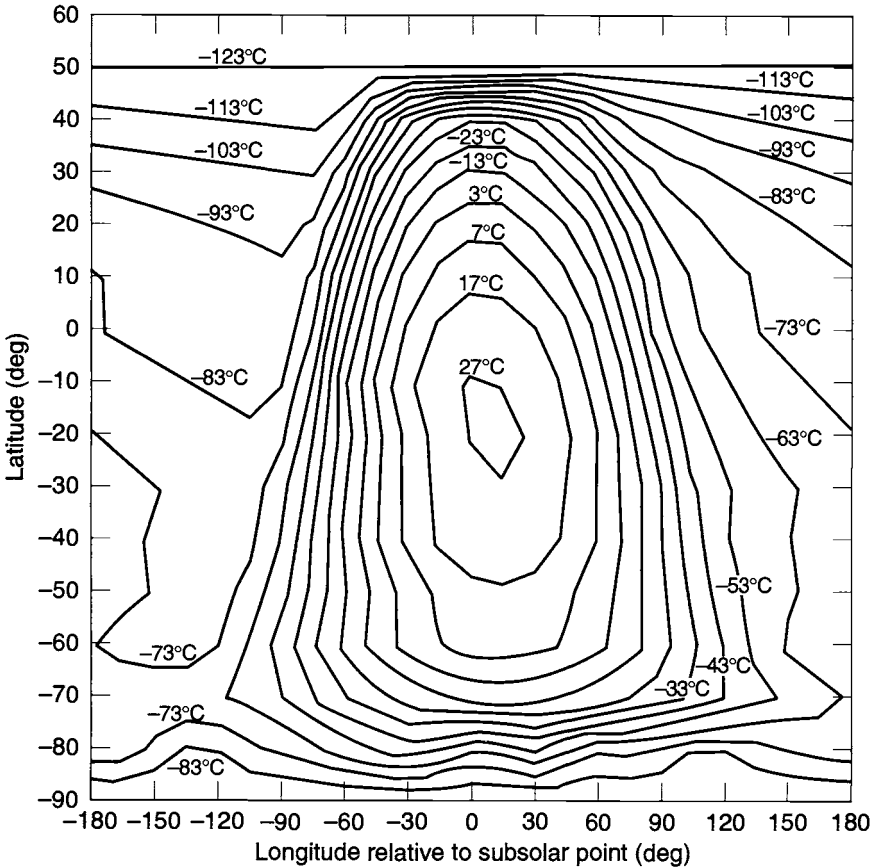
Fig. 2.28. Mars perihelion surface temperature.

Environments of the Outer Planets

The thermal environments of the outer planets, Jupiter through Pluto/Charon (Refs. 2.27 through 2.32), are very cold as a result of their large distances from the sun. Solar intensity drops by more than an order of magnitude between Mars and Jupiter. Substances that are gases on Earth become liquids and solids on these extremely cold worlds. Solar, albedo, and planetary IR fluxes in the vicinity of these planets are small compared to the IR emitted by room-temperature objects. Under these conditions, environmental loads can often be ignored in the thermal
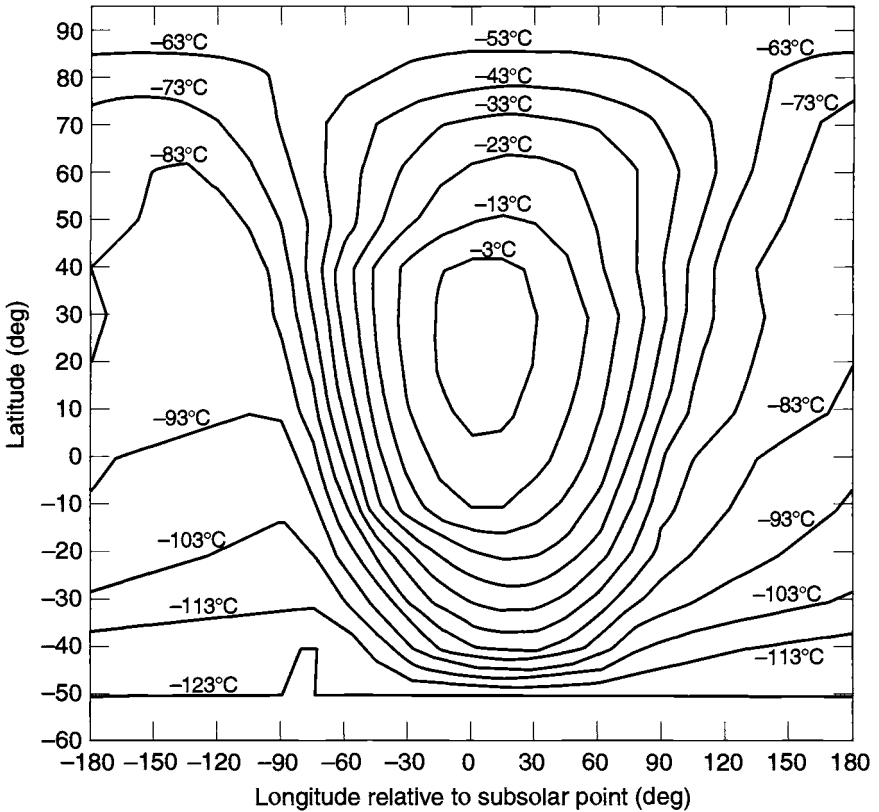
Fig. 2.29. Mars aphelion surface temperature.

design and analysis of spacecraft hardware that functions at room temperature, such as payload electronics. Only sensitive instruments, cryogenic radiators, and exposed, uninsulated components will register the feeble effects of environmental heat loads in the vicinity of these planets.

Table 2.18 summarizes the environmental parameters of the outer planets and identifies associated references. The temperature of our reference sphere in orbit around each planet is shown in Table 2.19. As these numbers indicate, thermal control of spacecraft in this part of the solar system is about keeping things warm. There is no "hot" environment!

Table 2.18. Outer-Planet Orbital Environments

Planet	Perihelion	Aphelion	Mean	Reference
Jupiter				
Direct solar (W/m^2)	56	46	51	
Albedo	0.343	0.343	0.343	24
Planetary IR (W/m^2)	13.7	13.4	13.6	24
Saturn				
Direct solar (W/m^2)	16.8	13.6	15.1	
Albedo	0.342	0.342	0.342	25
Planetary IR (W/m^2)	4.7	4.5	4.6	25
Uranus				
Direct solar (W/m^2)	4.09	3.39	3.71	
Albedo	0.343	0.343	0.343	26
Planetary IR (W/m^2)	0.72	0.55	0.63	27
Neptune				
Direct solar (W/m^2)	1.54	1.49	1.51	
Albedo	0.282	0.282	0.282	26
Planetary IR (W/m^2)	0.52	0.52	0.52	28
Pluto/Charon				
Direct solar (W/m^2)	1.56	0.56	0.88	
Albedo	0.47	0.47	0.47	29
Planetary IR (W/m^2)	0.8	0.3	0.5	29

Aerobraking Environments

Aerobraking maneuvers, as mentioned in Chapter 1, are sometimes used to make large changes in orbit altitude or inclination, and they are especially useful in slowing down a spacecraft on an interplanetary trajectory to the point where orbital capture by a planet is possible. Aerobraking occurs when a portion of the orbit enters a planet's atmosphere, creating aerodynamic drag on the spacecraft (Fig. 2.30). This drag slows the spacecraft, thereby gradually lowering the altitude or changing the orbital plane, and it can also rapidly warm the spacecraft because of friction in the atmosphere. The advantage aerobraking provides is placement

Table 2.19. Reference Sphere in Orbit Around the Outer Planets

	$\beta = 0°$		$\beta = 90°$	
	Perihelion (°C)	Aphelion (°C)	Perihelion (°C)	Aphelion (°C)
Jupiter				
Maximum	−130	−136	−139	−144
Minimum	−181	−182	−139	−144
Average	−154	−57	−139	−144
Saturn				
Maximum	−167	−171	−173	−177
Minimum	−203	−203	−173	−177
Average	−183	−186	−173	−177
Uranus				
Maximum	−200	−203	−204	−208
Minimum	−229	−232	−204	−208
Average	−213	−216	−204	−208
Neptune				
Maximum	−214	−215	−217	−218
Minimum	−232	−232	−217	−218
Average	−223	−223	−217	−218
Pluto/Charon				
Maximum	−211	−225	−215	−228
Minimum	−228	−238	−215	−228
Average	−219	−231	−215	−228

of the spacecraft into the desired orbit at reduced mass and cost. Without an aerobraking maneuver, a spacecraft would require additional fuel, and possibly additional thrusters, to adjust the orbit or achieve planetary orbit capture.

The heating rates that the spacecraft will be exposed to during an aerobraking maneuver are usually calculated by specialists in orbit dynamics and atmospheric sciences and are provided to the thermal engineer as a heating rate per unit area normal to the spacecraft velocity vector. Several parameters must be considered, however, to fully characterize the thermal effects of aerobraking on the spacecraft.

The duration and intensity of the aeroheating need to be identified for each successive pass through the atmosphere, with the effects of any potential navigation errors (e.g., velocity or altitude) conservatively included. Because aerobraking orbits decay primarily by decreases in the apogee, more severe orbit-average heating
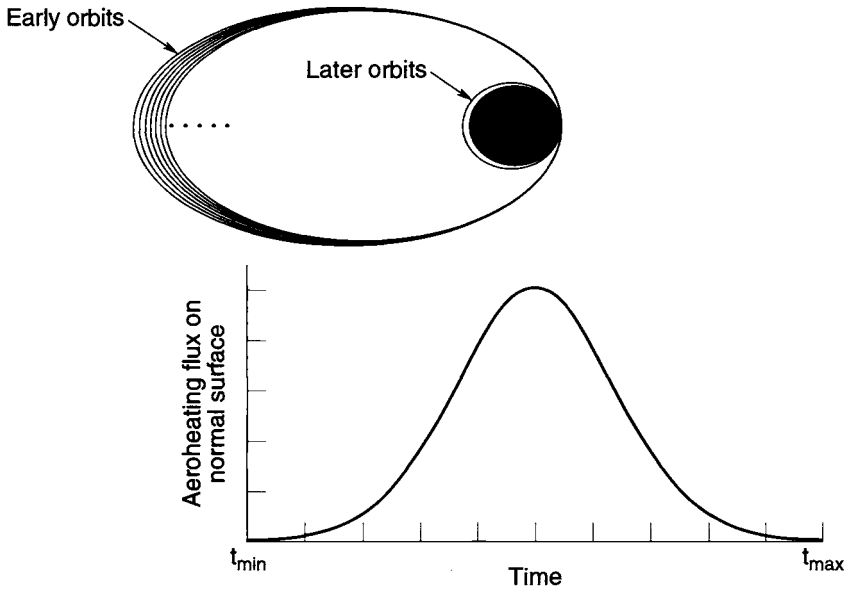
Fig. 2.30. Representative aerobraking maneuver and heating rates.

can result over successive orbits because the fraction of time during which aeroheating occurs increases as the orbit period decreases. Finally, the thermal engineer must analytically determine the heating rate for each spacecraft surface by multiplying the heating rate provided by the orbit analysts by the cosine of the angle between the velocity vector and the surface. The thermal analyst must then use the calculated heating rates to assess the impact of aeroheating on the entire spacecraft with a conservative, detailed transient analysis of the aerobraking maneuver.

Along with the mass advantages of aerobraking to the mission come numerous challenges to the thermal design. Aerobraking maneuvers can be the stressing hot-case condition that drives the design of some spacecraft components. Frequently, orbit analysts want to increase aerodynamic drag by positioning large deployable appendages, such as solar arrays, so that their surface area normal to the space-craft velocity vector is maximized. Unfortunately, such positioning results in maximum aeroheating as well. Therefore, spacecraft attitude and configuration compromises to mitigate the thermal impact of the aerobraking maneuver are common. Deployables, often with a low thermal mass per unit area, should receive special attention from the thermal analysis to ensure temperature require-ments are not exceeded. Also, if the spacecraft orientation vector has a known uncertainty, the thermal engineer should examine several possible orientation angles to make sure that the most severe aeroheating for each sensitive component is identified.

One component of most thermal designs that is vulnerable to aeroheating is the multilayer insulation (MLI) blanket. Since MLI is naturally insulating and the

outer layers possess a very low thermal mass per unit area, a blanket exposed to significant aeroheating will reach very high temperatures (possibly exceeding 300°C) in a negligible amount of time. Typical MLI materials, such as Mylar interior layers and Dacron scrim, may not survive the severity of the aerobraking maneuver. Alternate high-temperature MLI designs, such as those discussed in Chapter 5, can survive much higher temperatures and should provide adequate radiative insulation.

Launch and Ascent Environments

Spacecraft thermal-control systems are usually designed to the environment encountered on orbit. Vehicle temperatures during transportation, prelaunch, launch, and ascent must be predicted, however, to ensure temperature limits will not be exceeded during these initial phases of the mission. In some cases, thermal design changes or constraints on launch environments, such as maximum eclipse duration or FMH rates, are necessary to prevent excessively high or low temperatures from occurring on the spacecraft.

The transportation and prelaunch phases usually include shipping of the spacecraft, preparations and testing in the clean room at the launch site, and the final countdown period with the spacecraft on the booster at the launchpad. A typical transportation sequence is shown in Fig. 2.31. Thermal control during these phases is generally achieved by controlling the environment. For transportation, when the spacecraft is not powered, ambient temperature and humidity limits are specified to keep all components within nonoperating temperature limits and to prevent moisture condensation. During testing and storage at the launch site, room temperature conditions may be acceptable, or constraints may be required on how long the vehicle may be powered up to prevent reaching operating-temperature limits. If these "passive" approaches are not sufficient, special air-conditioning units may be required to blow cold air into or onto the spacecraft when it is powered on, although this is unusual.

Once the spacecraft is encapsulated in the booster fairing or placed in the space-shuttle cargo bay on the pad, thermal control is achieved by blowing conditioned air or nitrogen through the fairing enclosure. The inlet temperature of this conditioned gas is usually specifiable over some nominal range such as 10–27°C for the Titan IV or 7–32°C for the shuttle. The temperature of the gas may warm or cool significantly from heat gained or lost to the payload fairing or shuttle vehicle as the gas flows through the payload compartment. The electronic waste heat generated by most spacecraft, however, is usually not sufficient to cause a significant rise in purge-gas temperature.

With some spacecraft, thermal analysis of prelaunch conditions may show that purge gas alone may not be enough to provide adequate cooling for all components If this is the case, special air- or liquid-cooling ducts or loops may be required to provide extra cooling. However, since these cooling loops add significant cost and complexity to launch thermal control and may sometimes present reliability problems, the engineer should investigate other options, such as intermittently turning off components, before implementing special cooling provisions.

Launch Operations at Eastern Range
(Cape Canaveral)

Launch
Complex-41

(PHSF)

N

Skid strip
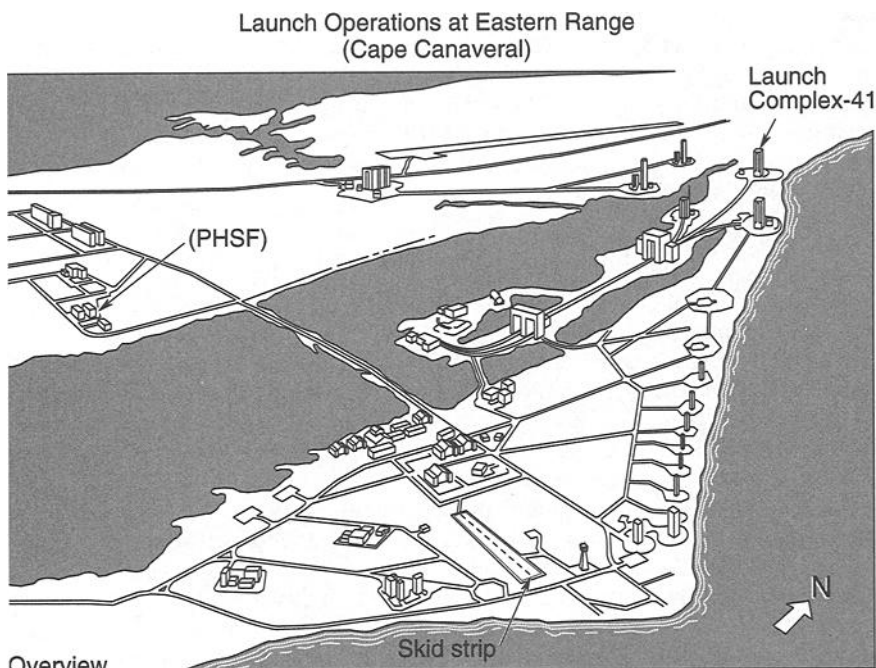
Overview
- C5-A arrives at skid strip
- Satellite shipping container convoys to Payload Hazardous Safe Facility (PHSF)
- Satellite processed to vertical in PHSF and convoys to LC-41
- Hoist satellite at LC-41 and mate to booster

Fig. 2.31. Launch site processing.

From liftoff through final orbit insertion, the thermal environment becomes more severe. The approach is to predict spacecraft temperatures for the worst hot and cold conditions and, where necessary, implement constraints on such values as maximum eclipse time and maximum FMH. Changes to the thermal design or severe constraints on launch are usually implemented only as a last resort.

A typical launch-and-ascent sequence for an expendable booster is shown in Fig. 2.32. For the first few minutes the environment surrounding the spacecraft is driven by the payload-fairing temperature, which rises rapidly to 90–200°C as a result of aerodynamic heating. Fairing temperatures for the Atlas II booster are shown in Fig. 2.33. During the same period, a very slight cooling effect results from the depressurization of the gas in the payload compartment. This cooling effect, however, is very feeble; it is noticeable for only a few minutes on very low-mass items such as the outer layer of an MLI blanket, and it is usually ignored in launch thermal analysis. The effects of the payload-fairing temperature rise are more significant, but they will still only cause a temperature rise on relatively low-mass, exposed components such as solar arrays, insulation blankets, antennas, and very lightweight structures. The effect is further mitigated on some boosters by acoustic blankets inside the fairing that also provide an insulating effect.
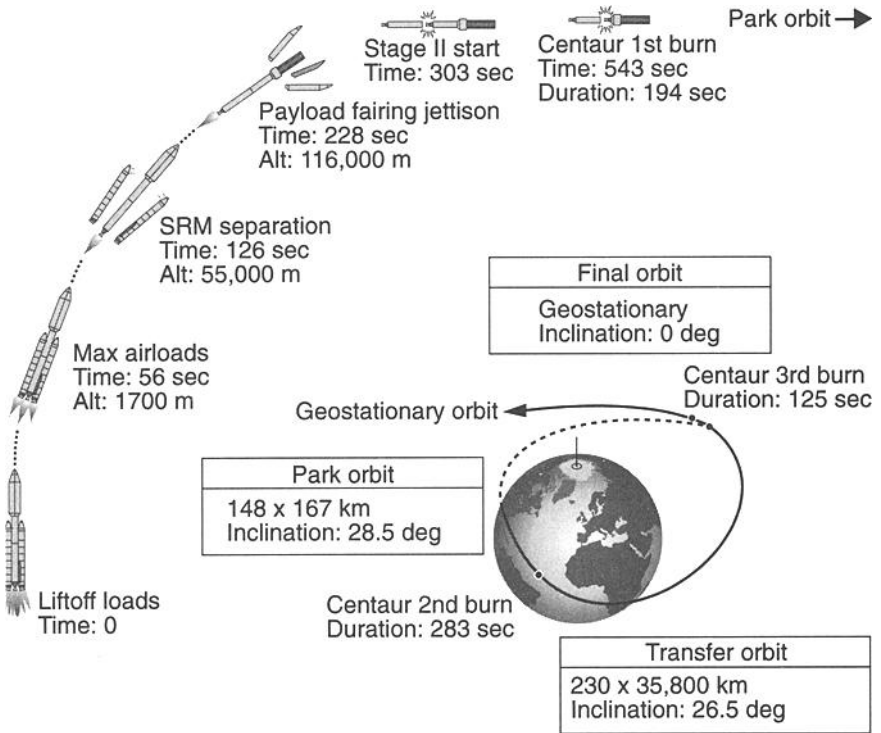
Fig. 2.32. Representative geosynchronous mission profile.
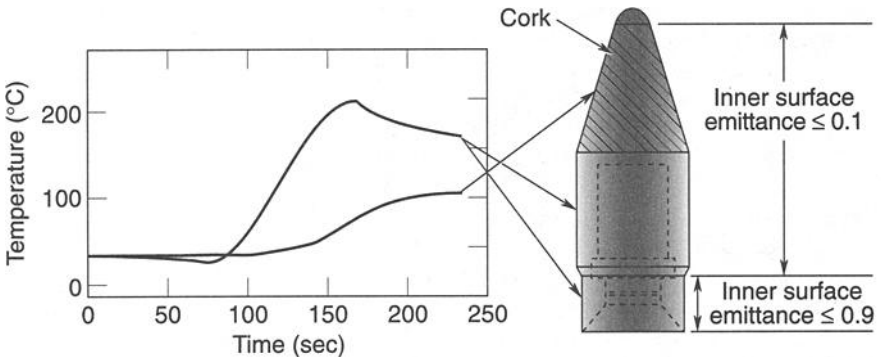
Fig. 2.33. Atlas fairing temperatures.

Within 2 to 5 min after liftoff, the vehicle is high enough that aerodynamic effects are gone and FMH drops low enough that the fairing may be jettisoned to save weight and thereby increase payload capacity. Because dropping the fairing

as soon as possible is desirable, FMH rates are usually still very significant for up to 30 min after fairing separation. Curves of FMH versus time are usually generated by the booster contractor using sophisticated atmospheric and trajectory simulation codes, and they are supplied to the spacecraft thermal engineers. These curves may be complex, rising and falling as the booster altitude and velocity change, as shown in the sample curve of Fig. 2.6.

From the time of fairing separation onward, the spacecraft is exposed to a combination of FMH, solar, Earth IR, and albedo loads, and sometimes plume heating effects from the main rocket engines and attitude-control thrusters. During rocket firing, the attitude is set by guidance considerations. Between burns, however, the attitude may be changed for thermal or other reasons. It is not uncommon for the upper stage/spacecraft to go into a "barbecue roll" during these coast periods to maintain a moderate thermal environment for the payload. A thermal analysis is required to verify that spacecraft temperatures remain within limits under the combination of conditions discussed above. If temperature limits are exceeded, constraints on FMH, eclipse time, vehicle attitudes, or prelaunch purge temperatures are negotiated with the booster contractor to moderate the thermal environment. If such constraints are impractical, thermal design changes may be required to resolve the problem.

The ascent phase typically lasts 30 to 45 min and results in insertion either into a temporary parking orbit, into a transfer orbit, or directly into the final mission orbit. Direct insertion into the final orbit may occur for low Earth or highly elliptical (e.g., Molniya) orbits. Higher-altitude circular orbits, such as GEO or 12-hour orbits, require an elliptical transfer orbit to move the spacecraft to the higher altitude. An apogee-kick-motor burn at the apogee of the transfer orbit makes the orbit circular at the desired altitude (see Fig. 2.32). During the parking or transfer orbits, the spacecraft will be exposed to the usual solar, IR, and albedo loads and is usually in a reduced power mode with appendages such as solar arrays stowed. Eclipses during transfer orbits to GEO altitudes can last as long as 3.5 hours. This is almost three times longer than the maximum eclipse in GEO orbits and can present thermal-control problems if eclipse times are not limited by launch constraints. Because of the reduced power dissipation and long eclipses, the most common concern during this period is unacceptably low temperatures on the spacecraft, although high temperatures can occur if the spacecraft is inertially stable with the sun shining continuously on a sensitive component.

Once the spacecraft reaches its final orbit, a period lasting anywhere from a few hours to several weeks occurs, during which the spacecraft attitude is stabilized, appendages such as solar arrays and antennas are deployed, and bus and payload electronics are powered up. The thermal-control system must maintain acceptable temperatures during this period, and survival heaters are sometimes required. The sequence of events—when certain attitudes are achieved, when payloads are turned on, and so on—is also sometimes driven by thermal considerations.

For launches on the space shuttle, the prelaunch, ascent, and transfer-orbit events are similar to those of the expendable booster. The shuttle, however, has a far more complex park-orbit condition during which the spacecraft may be exposed to a wide range of thermal conditions for periods ranging from six hours

to several days, with the longer duration typically a result of contingency operations or multiple payload deployments. Unlike an expendable booster, which jettisons its fairing a few minutes after liftoff, the shuttle doors may remain closed for up to three hours, limiting the payload spacecraft's ability to reject waste heat. Once the doors are open, the bay may be pointed toward Earth, which is fairly benign, or toward deep space or the sun, in which case the environments are more severe. Maneuvers are also required periodically for shuttle guidance-system alignments, communication, etc. Because the bay liner is insulated, a spacecraft sitting in the shuttle payload bay may be exposed to more extreme conditions than if it were on a conventional booster, where it would simultaneously see a combination of sun, Earth, and deep space. In addition to the complex on-orbit environment, abort reentry conditions must also be considered. This additional complexity, along with safety considerations, makes the thermal integration process an order of magnitude more difficult for a shuttle launch than for a launch on a conventional booster.

A more in-depth discussion of spacecraft-to-launch-vehicle thermal integration is contained in Refs. 2.33 and 2.34, which cover integration with the Titan IV and space-shuttle launch vehicles, respectively, and Chapter 18, which discusses the shuttle integration process in detail.

References

2.1. C. Fröhlich and R. W. Brusa, "Solar Radiation and Its Variation in Time," *Sol. Phys.* **74**, 209–215 (1981).

2.2. C. Fröhlich and C. Wehrli, "Spectral Distribution of Solar Irradiance from 25000 nm to 250 nm," World Radiation Center, Davos, Switzerland, 1981.

2.3. "Solar Electromagnetic Radiation," NASA SP-8005 (May 1971).

2.4. "Earth Albedo and Emitted Radiation," NASA SP-8067 (July 1971).

2.5. D. F. Gluck, "Space Vehicle Thermal Testing: Environments, Related Design and Analysis, Requirements, and Practice," The Aerospace Corporation, Report No. TOR-86A(2902-08)-1, 27 September 1987.

2.6. G. L. Stephens, G. G. Campbell, and T. H. Von der Haar, "Earth Radiation Budgets," *J. Geophys. Res.* **86** (20 October 1981).

2.7. G. L. Smith, D. Rutan, and T. D. Bess, "Atlas of Albedo and Absorbed Solar Radiation Derived from Nimbus 7 Earth Radiation Budget Data Set—November 1978 to October 1985," NASA Ref. Pub. 1231, 1990.

2.8. R. L. Collins, "Albedo and Earthshine," The Aerospace Corporation IOC 87.5462.4-25, 27 April 1987.

2.9. M. Donabedian, "Thermal Uncertainty Margins for Cryogenic Sensor Systems," The Aerospace Corporation, ATM 90(9975)-3, 21 November 1989.

2.10. D. S. Glaister, "Space Environment for Cryogenic Radiator," The Aerospace Corporation, ATM No. 90(9975)-35, 3 May 1990.

2.11. B. R. Barkstrom and G. L. Smith, "The Earth Radiation Budget Experiment: Science and Implementation," *Rev. Geophys.* **24**, 379–390 (1986).

2.12. B. R. Barkstrom, E. Harrison, G. Smith, R. Green, J. Kibler, R. Cess, and ERBE Science Team, "Earth Radiation Budget Experiment (ERBE Archival and April 1985 Results)." *Bull. Am. Meteorol. Soc.* **70** (10), 1254–1262 (1989).

2.13. T. D. Bess and G. L. Smith, "Earth Radiation Budget: Results of Outgoing Long-wave Radiation from Nimbus-7, NOAA-9, and ERBS Satellites," *J. Appl. Meteorol.* **32** (5), 813–824 (1993).

2.14. "Natural Orbital Environment Criteria Guidelines for Use in Space Vehicle Development," NASA Technical Memorandum 4527, June 1994.

2.15. B. J. Anderson, C. G. Justus, and W. Batts, "Guidelines for the Selection of Near-Earth Thermal Environment Parameters for Spacecraft Design," NASA Technical Memorandum TM-2001-211221 (October 2001).

2.16. C. Y. Fan *et al.*, "Dynamics and Structure of the Outer Radiation Belt," *J. Geophys. Res.* **66**, 2207 (1961).

2.17. B. J. O'Brian. *et al.*, "Absolute Electron Intensities in the Heart of the Earth's Outer Radiation Zone," *J. Geophys. Res.* **67**, 1 (1962).

2.18. A. J. Dessler and R. Karplus, "Some Properties of the Van Allen Radiation," *Phys. Rev. Letters* **4**, 271 (1960).

2.19. J. I. Vette, Models of the Trapped Radiation Environment, Vol. I and II, NASA Rept. SP-3024 (1966).

2.20. R. D. Jimenez, "Natural Environment Charged Particle Heating of Spacecraft Cryogenic Components," The Aerospace Corporation, Report No. TOR-0088(3062)-3, 19 September 1988.

2.21. O. L. Hanson, "Surface Temperature and Emissivity of Mercury," *Astrophys. J.* **190**, 715–717 (15 June 1974).

2.22. B. C. Murray *et al.*, "Mercury's Surface: Preliminary Description and Interpretation from Mariner 10 Pictures," *Science* **185** (4146), 164–179 (12 July 1974).

2.23. M. G. Tomasko *et al.*, "The Thermal Balance of Venus in Light of the Pioneer Venus Mission," *J. Geophys. Res.* **85** (A13), 8187–8199 (30 December 1980).

2.24. C. J. Cremers, R. C. Birkebak, and J. E. White, "Lunar Surface Temperature at Tranquility Base," AIAA paper 71-79, *AIAA 9th Aerospace Sciences Meeting* (New York, New York, 1971).

2.25. Apollo 15 Preliminary Science Report NASA SP-289, 1972.

2.26. F. D. Pallucone and H. H. Kieffer, "Thermal Inertia Mapping of Mars from 60°S to 60°N," *Icarus* **45**, 415–426 (1981).

2.27. R. A. Hanel *et al.*, "Albedo, Internal Heat, and Energy Balance of Jupiter: Preliminary Results of the Voyager Infrared Investigation," *J. Geophys. Res.* **86** (A10), 8705–8712 (30 September 1981).

2.28. R. A. Hanel *et al.*, "Albedo, Internal Heat Flux, and Energy Balance of Saturn," *Icarus* **53**, 262–285 (1983).

2.29. J. B. Pollack *et al.*, "Estimates of the Bolometric Albedos and Radiation Balance of Uranus and Neptune," *Icarus* **65**, 442–466.

2.30. G. S. Orton, "Thermal Spectrum of Uranus: Implications for Large Helium Abundance," *Science* **231**, 836–840 (February 1986).

2.31. Preliminary Science Data from Voyager 2 Neptune Encounter, 25 August 1989.

2.32. S. R. Sawyer *et al.*, "Spectrophotometry of Pluto-Charon Mutual Events: Individual Spectra of Pluto and Charon," *Science* **238**, 1560–1563 (December 1987).

2.33. R. Pleasant and W. Kelly, "Thermal Integration of Satellite Vehicles with Titan/ Centaur," AIAA 89-1723, *AIAA 24th Thermophysics Conference* (12–14 June, 1989).

2.34. "Shuttle/Payload Integration, Information Document for Thermal," NASA JSC-21000-INF, September 1986.

3   Thermal Design Examples

D. G. Gilmore,[*] Y. Yoshikawa,[†] R. Stoll,[‡] R. Bettini,[‡] B. Patti,[**]
G. Cluzet,[††] J. Doenecke,[‡‡] K. Vollmer,[‡‡] C. Finch,[***] and B. Turner[***]

Introduction

The purpose of a thermal-control system is to maintain all of a spacecraft's components within the allowable temperature limits for all operating modes of the vehicle, in all of the thermal environments it may be exposed to (i.e., those discussed in Chapter 2). To illustrate how thermal control is achieved, this chapter describes some typical thermal designs. While these designs are currently in wide use, they are not the only possible thermal designs for the spacecraft and components examined here, and creative alternative solutions to thermal design problems are always desirable. The designs described in the following discussions should therefore be considered examples only.

Establishing a thermal design for a spacecraft is usually a two-part process. The first step is to select a thermal design for the body, or basic enclosures, of the spacecraft that will serve as a thermal sink for all internal components. The second step is to select thermal designs for various components located both within and outside the spacecraft body. The following sections give a qualitative description of typical designs. For a more detailed discussion of the design-selection process and the thermal analysis required to verify a design, see Chapter 15, "Thermal Design Analysis."

Spin-Stabilized Satellites

Of all the thermal designs for spin-stabilized satellites ("spinners"), the most common is the one typified by Defense Satellite Communications System (DSCS) II, Satellite Data Systems, North Atlantic Treaty Organization (NATO) II, and a host of commercial communication satellites. The design approach is to use the spinning solar array as a heat sink for the internal components. A cylinder spinning with the sun normal to the spin axis will be close to room temperature if the ratio of solar absorption to infrared (IR) emittance (α/ε) is near 1.0, as is the approximate case with the solar cells that cover the cylinder. Because of its temperature, the spinning solar array makes a convenient heat sink for internal components.

Figure 3.1 illustrates the thermal balance in a typical spinning satellite. Electronics boxes, usually mounted on shelves, radiate their heat to the solar array and sometimes also to the forward or aft ends of the satellite if extra radiator area is required. The electronics boxes are typically painted black for high IR emittance

*The Aerospace Corporation, El Segundo, California.
†Lockheed Missiles and Space Company, Sunnyvale, California.
‡B.F. Goodrich Aerospace, Danbury, Connecticut.
**European Space Agency, Leiden, Netherlands.
††Alcatel, Velizy, France.
‡‡Astrium, Friedrichshaten, Germany.
***BAE Systems, Basildom, United Kingdom.
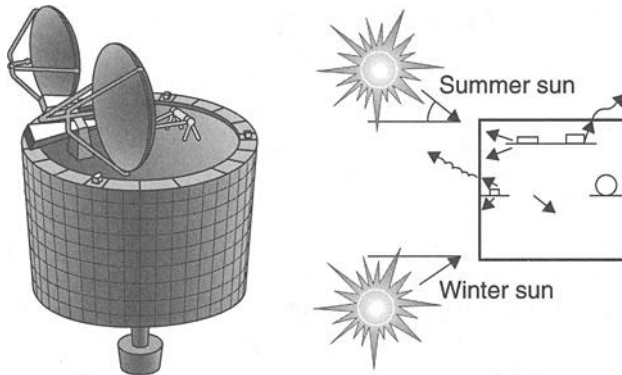
Fig. 3.1. "Spinner" thermal balance.

and are mounted so as to ensure good heat conduction to the shelves. For most boxes the combined surface area of the box itself and its shelf is sufficient to radiate the waste heat to the solar array without development of a large temperature difference between the box and the room-temperature array. If a box is small and has high heat dissipation, a thermal "doubler" (a sheet of high-conductivity material such as aluminum, beryllium, or copper) may be placed under the box to help spread the heat out on the shelf and increase the effective radiating area of the box.

Because most spinners are placed in high-altitude geosynchronous orbits, they experience no more than one eclipse per day, and those eclipses last a maximum of 72 min. During eclipse the solar-array temperature drops dramatically, typically from room temperature to a value on the order of −75°C. In this period, the temperature of the electronics boxes and other components also drops; however, because their thermal mass is high, they do not cool nearly as fast as the relatively lightweight solar array. The result is that the spacecraft can often coast through the eclipse without falling below the minimum allowable operating temperature of the electronics. If the thermal design analysis shows that some components get too cold, then either a lower-emittance finish on the cold units or a heater may be required to reduce their radiative coupling to the solar array or provide extra heat during eclipse. The use of heaters during eclipse should be minimized, however, since they drive up the size, and therefore the mass, of batteries.

Three-Axis-Stabilized Satellites

The most common type of satellite today is the three-axis-stabilized variety typified by the Tracking and Data Relay Satellite System (TDRSS), *Systeme Pour l'Observation de la Terre* (SPOT), FLTSATCOM, Defense Meteorological Satellite Program (DMSP), and many others. The designs of almost all these satellites take the same basic approach to thermal control of the satellite body: insulating the spacecraft from the space environment using multilayer insulation (MLI) blankets and providing radiator areas with low solar absorptance and high IR emittance to reject the satellite's waste heat. The overall thermal balance of such a satellite is illustrated in Fig. 3.2.

- Insulate main body with multilayer insulation (MLI) blanket

- Provide low solar absorptance (α), high infrared emittance (ε) radiators to reject waste heat

- Use heaters to protect equipment when satellite is in low power mode

- Use surface finishes and insulation to control appendage temperatures (antennas and solar arrays typically have very wide temperature ranges)
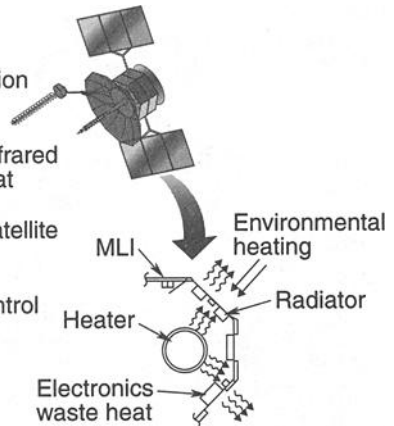
Fig. 3.2. Three-axis-satellite thermal control.

The high-power-dissipation boxes in a three-axis satellite are usually mounted on the walls of the satellite; this positioning provides them with a direct conduction path to the radiating areas on the outside surface. As with the spinner, some of the high-power boxes in the three-axis satellite may require a doubler or heat pipes to spread the heat out over a wider area of the wall to which they are mounted. Boxes mounted on shelves, panels, and other structures internal to the vehicle radiate their waste heat directly or indirectly to the outside walls of the spacecraft, where the heat is then rejected to space. Because this type of design is insulated and uses low-solar-absorptance radiators, it is less sensitive to sun position, albedo loads, and eclipses than designs for spinners are.

Propulsion Systems

Almost all satellites have onboard propulsion systems for attitude control and small orbit corrections. The propulsion system typically consists of small (less than 3 kg of thrust) compressed-gas or liquid-propellant thrusters and all the assorted tanks, lines, valves, and other components used to store propellants and feed the thrusters. Some satellites may also have a solid-rocket motor to provide the final boost from transfer orbit to operational orbit. Propulsion-system components must meet special thermal-control requirements to avoid the freezing of liquid propellants, to prevent temperature gradients within solid propellants, and to limit the temperature differences between fuel and oxidizer in liquid bipropellant systems.

The most common propellant now used for onboard propulsion systems is hydrazine. In a hydrazine monopropellant system, a catalyst in each thruster triggers a decomposition of the liquid hydrazine into a number of gases, including nitrogen, ammonia, and water, accompanied by the release of a large amount of heat. The schematic of a typical hydrazine propulsion system shown in Fig. 3.3 includes tanks, lines, valves, thrusters, and filters.
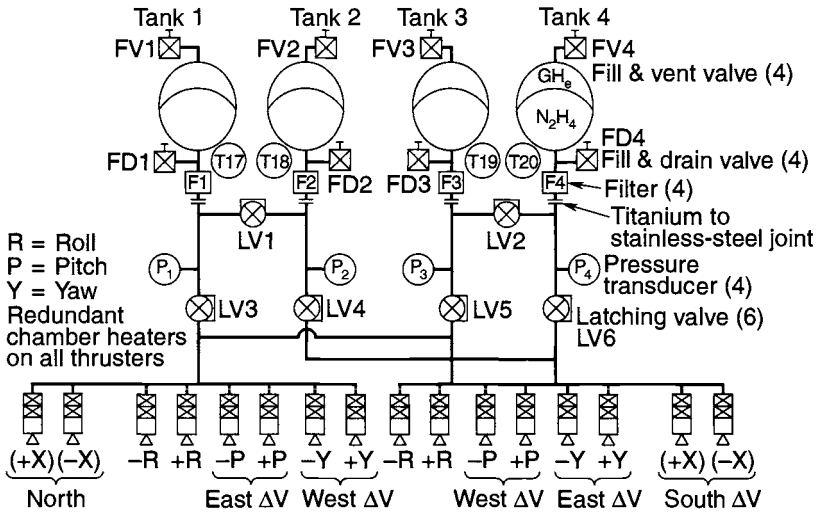
Fig. 3.3. DSCS propulsion-system schematic.

A typical thermal design for a propulsion system is shown in Fig. 3.4. The general approach is to conductively isolate all of the propulsion components from the vehicle structure using low-conductivity standoffs and attachment fittings, and to cover the components in a low-emittance finish or MLI to provide radiative isolation. Heaters are also often used, especially on low-mass items such as propellant
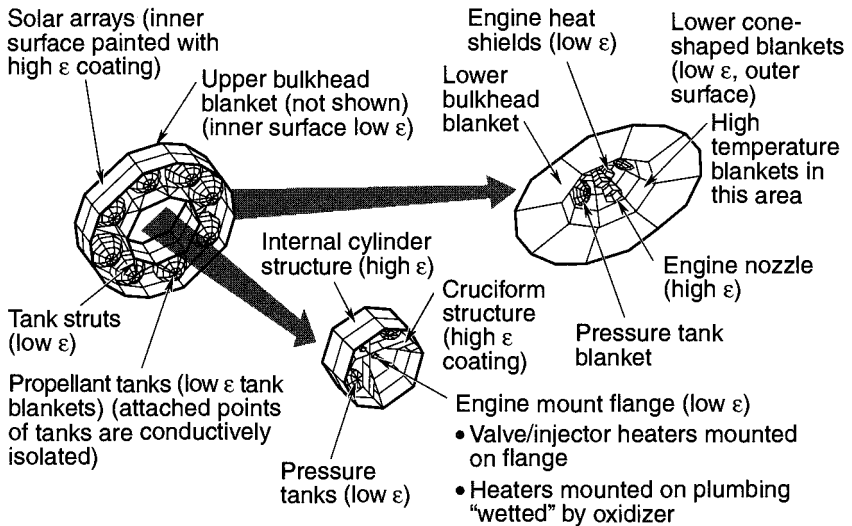
Fig. 3.4. Integrated apogee-boost-system thermal design.

lines, which may cool very quickly during eclipses or other short-term cold conditions. Heaters may be either hardwired (on all the time) or controlled to a fixed temperature using thermostats or solid-state controllers. In addition, the heater power density (W/cm of line) may sometimes have to be varied along the line to ensure that acceptable temperatures are maintained as the line runs through "hot" and "cold" areas of the spacecraft. Heaters must be used and propulsion components must be isolated, because the spacecraft may get quite cold during some launch or operational modes, and hydrazine freezes at 2°C.

Thermal control of a thruster is a bit more complicated than thermal control of propulsion-system components. Not only must the thruster be kept above the freezing point of the hydrazine (or other propellants), but also the vehicle must be protected against heating from the rocket plume and heat soakback from the rocket-engine body during and after the firing. Figure 3.5 shows the thermal design for a Milstar bipropellant thruster located on the exterior of the satellite.

The entire thruster assembly is thermally isolated from the spacecraft via low-conductivity titanium standoffs. The thruster valves and injector are covered with MLI to minimize heat losses when the thruster is not operating; however, a total of 52 sq cm of radiator area has been provided to help cool the thruster after firing.

To keep the thruster warm during nonoperating periods, thermostatically controlled heaters are provided on the injector plate. These heaters are sized to make up for heat lost by radiation from the exposed nozzle and the small radiator areas on the sides of the thruster enclosure. (The nozzle is not covered by insulation since it gets extremely hot during engine firing and must be able to radiate freely to space.) In addition, a single-layer low-emissivity heat shield protects the enclosed elements from radiant heating from the nozzle as well as heating from the rocket plume.
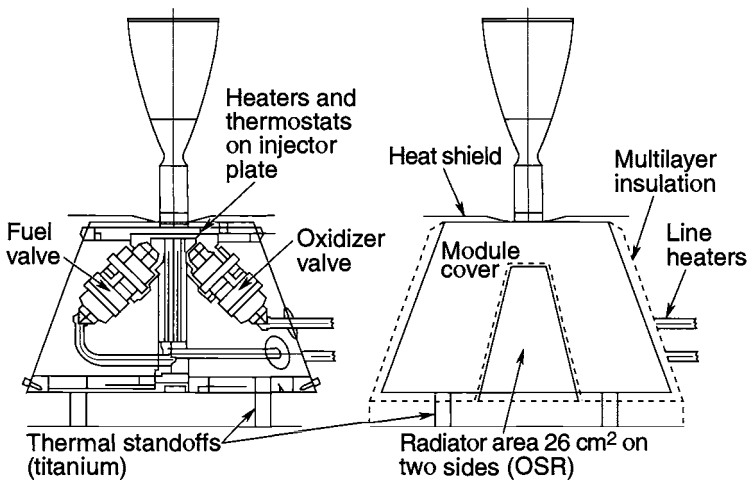
Fig. 3.5. Milstar thruster thermal design.

Most liquid thrusters are designed to limit the conduction path between the combustion chamber/nozzle and the valve bodies. This isolation is more evident in the hydrazine thruster shown in Fig. 3.6. Here isolation is achieved using a tubular support of low-conductivity stainless steel filled with holes. Fuel is fed to the thrust chamber through long, slender stainless-steel tubes. During and after a firing, the nozzle and combustion chamber become very hot, but the heat is primarily radiated to space rather than conducted back to the valves.

Plume shields, such as those on the Milstar thruster discussed above, are often used to protect spacecraft hardware physically near to thrusters or large rocket motors. These heat shields are typically made of thin sheets of high-temperature, low-emissivity metals such as stainless steel or titanium. The metal can withstand the high temperatures to which the shield is driven, and the low emissivity limits the heat reradiated from the shield back toward the spacecraft. (The space-facing sides of such shields often have high-emissivity finishes to help reduce shield temperature.) A large heat shield used to protect the back end of a spacecraft from the plume of a large solid-rocket motor is shown in Fig. 3.7. The plumes from solid
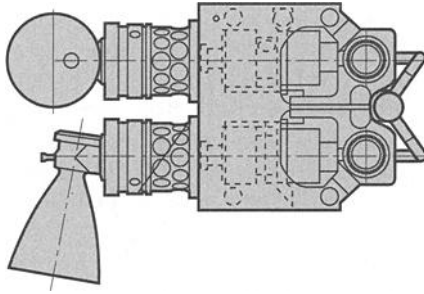
Fig. 3.6. Hydrazine thruster module.
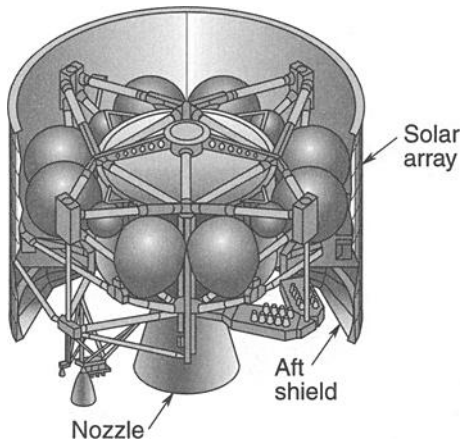
Fig. 3.7. Plume shield.

rockets produce much higher radiant heating rates than do the plumes from liquid motors because the solid-rocket-motor plumes are full of solid particles, which have a much higher emissivity than the gases in a liquid-motor plume.

Solid-rocket motors are often used to transfer a spacecraft from the transfer orbit in which the launch vehicle has placed it to the final operational orbit. Propellant in these solid motors usually must be kept within a certain temperature range, and temperature gradients in the propellant must be kept below a specified value. The most common approach to achieving these requirements is to wrap the motor in MLI and provide conduction isolators at the mounting points, as is shown in Fig. 3.8. Sometimes insulating shields or blankets on the nozzles and across the nozzle exit plane must be provided, since an exposed nozzle can cause a large heat leak and/ or temperature gradient in the propellant. (The blanket across the nozzle exit plane is, of course, blown off when the motor ignites.) If the motor is to be used immediately after launch, insulation alone may be satisfactory, since the motor is massive and will cool very slowly. If, however, several days will elapse before the motor is used, then heaters may be required on the motor case to keep the propellant from getting too cold.

Batteries

Two different types of batteries, nickel cadmium (NiCd) and nickel hydrogen (NiH$_2$), are commonly used on spacecraft. Their thermal-control requirements and thermal design differ somewhat.

The most common battery type in older spacecraft power systems is NiCd. These batteries usually need to be maintained at a temperature between 0 and 10°C to maximize their life. As their temperature rises above this range, their maximum useful life decreases significantly. Below this range, the electrolyte may freeze and damage the battery. Another requirement, common to many types of batteries, is that all batteries on the spacecraft and all cells within a battery be kept at the same temperature, plus or minus a specified value (for example, ±5°C). This isothermality requirement is necessary to ensure that all cells charge and discharge at the same rate.
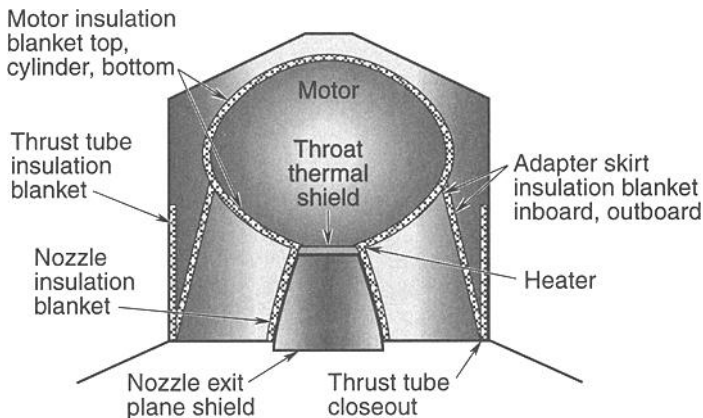
Fig. 3.8. Solid-rocket-motor thermal design.

Although some (usually small) NiCd batteries are mounted inside spacecraft and simply painted black to radiate the waste heat from charge and discharge inefficiencies to the spacecraft interior, the most common battery thermal designs use radiators and thermostatically controlled heaters, as shown in Fig. 3.9. Heat from individual rectangular battery cells is conducted down aluminum fins placed between cells to a baseplate, which in turn radiates off its other side directly to the space environment. The radiator is usually sized to keep the batteries somewhat below the maximum allowable temperature under worst hot-case conditions, and thermostatically controlled heaters are then used to maintain minimum allowable temperatures under cold-case conditions. This design ensures that battery temperatures will be precisely controlled at all times.

At the time of this writing, NiH_2 batteries have become common on most new spacecraft programs, especially those requiring long life and minimum battery weight. Like the NiCd battery, the NiH_2 battery requires a closely controlled isothermal operation around the 0-to-20°C range. Because NiH_2 batteries are high-pressure devices, however, they are manufactured as cylindrical pressure-vessel cells that are typically packaged together on "trays," as shown in Fig. 3.10.

For the purpose of discussion, the thermal designs that incorporate these batteries can be divided into four types. (See Fig. 3.10.) The simplest involves direct-conduction coupling between the cells and a baseplate/radiator with a heater used to control minimum temperature, as is used on Global Positioning System (GPS) II and APEX programs. The second category introduces fixed-conductance heat pipes to isothermalize the batteries and couple them to remote radiators, as in a configuration like the one on Milstar. The third type of design introduces variable-conductance heat pipes to minimize heater power and/or accommodate the wide variations in environmental back loads that can occur in some applications. The fourth group of designs, as typified by the Hubble Space Telescope, is similar to the third, except it makes use of louvers in place of variable-conductance heat pipes.
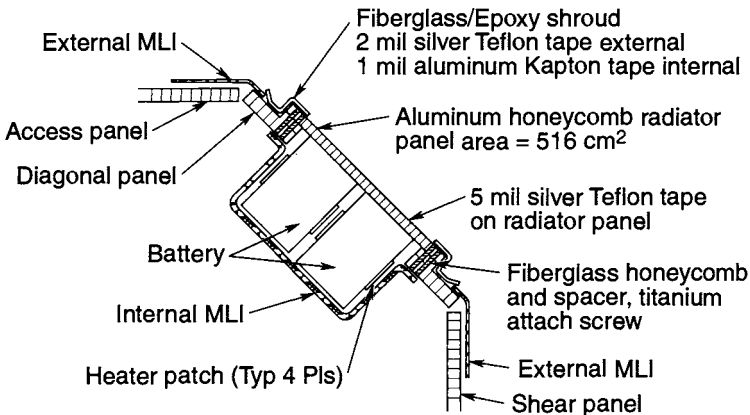
Fig. 3.9. Nickel-cadmium-battery thermal design.

Heat pipe
radiator   Milstar

Space telescope

VCHP radiator

GPS II

• Honeycomb radiator
  (far side)
• Heaters on cells
• MLI (near side)
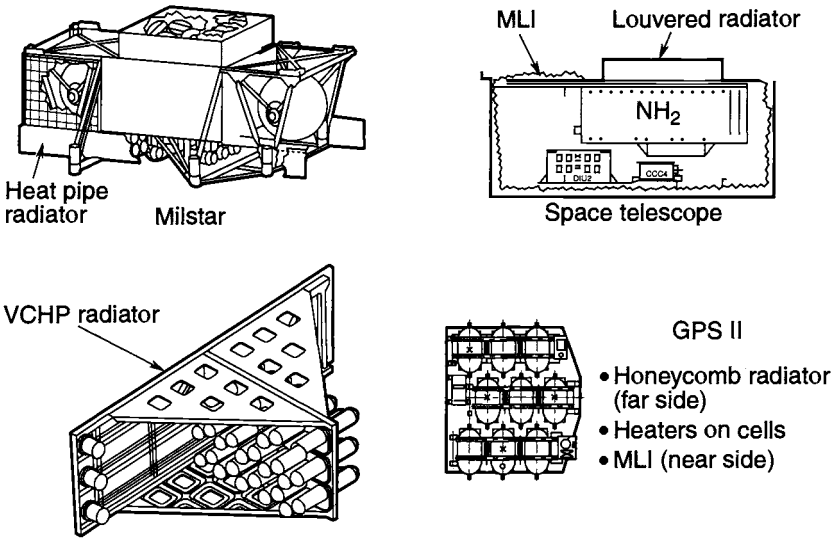
Fig. 3.10. Battery thermal designs.

The approach used in designing these systems is to size the radiator for a heat-load value between the orbit average and the peak heat load. Ideally, the radiator would be sized to the peak load occurring during discharge or overcharge (plus any environmental load) so that the battery could be kept around 0°C at all times. This kind of sizing, however, would result in a very large radiator and very high heater power during the charge and trickle-charge periods when the battery is generating little or no waste heat. To reduce the radiator size and heater power, a radiator size closer to that required for the orbit-average heat dissipation is usually chosen, and the cell temperatures are allowed to rise to around room temperature during discharge and overcharge. The minimum possible radiator size is the size required for the orbit-average power; however, the radiator is sized somewhat above orbit-average heat level so cell temperatures can be pulled back down below 5°C quickly after the discharge or overcharge heat pulses. This oversizing reduces the amount of time the battery is above the desired temperature range, but may result in the need for heaters during the charge phases, even for conditions of the hot design case.

Note that the waste-heat rates of batteries are sometimes difficult to quantify. Thermal dissipation varies with state of charge, temperature, and charge rate, and it may differ for batteries of the same general type. Complex power thermal models are sometimes constructed to deal with these variables; however, close coordination between thermal and power-system engineers usually suffices to ensure that conservative but reasonable heating rates are used in the thermal analysis.

Antennas

Many types of antennas are used on spacecraft, including helixes, solid reflectors, mesh reflectors, and horns, as shown in Fig. 3.11. The thermal-control requirements
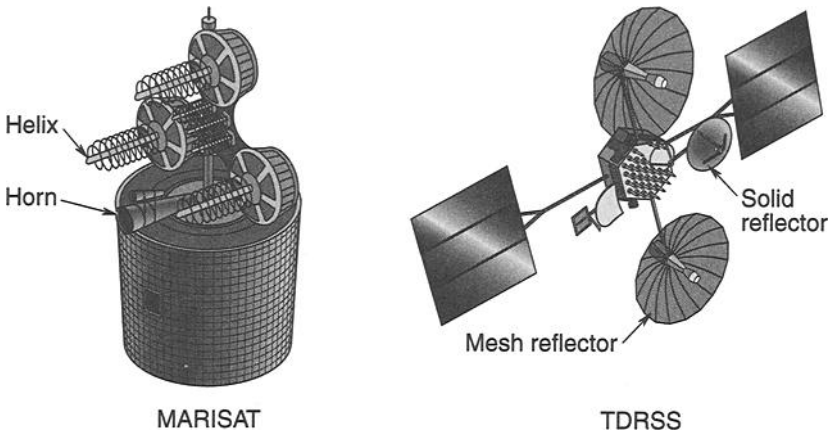
Fig. 3.11. Satellite antennas.

for antennas are usually to maintain temperatures within the allowable ranges for the materials they are made of and, especially for reflectors, to keep thermally induced distortions within acceptable limits. For most antennas, an acceptable design can be developed using paints, insulation blankets, and/or low coefficient-of-thermal-expansion structural materials.

Typical antenna thermal designs are shown in Fig. 3.12. Horns, whether transmitting directly to Earth or used in conjunction with a reflector, are often simply covered with MLI with an astroquartz or white-painted plastic film (such as Kapton) covering the aperture. Aluminized Kapton, which is often used on other parts of the spacecraft, cannot be used to cover an antenna aperture because the conductive aluminum layer is not transparent to radio-frequency (RF) energy. Any material used
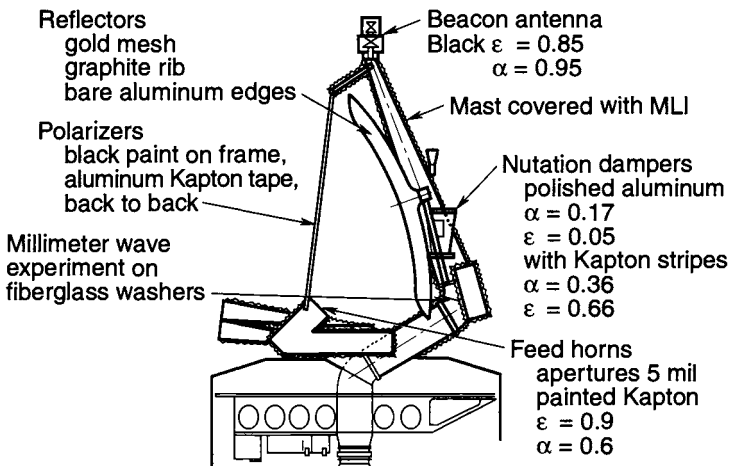
Fig. 3.12. Representative antenna thermal design.

in the path of an antenna beam must be close to 100% RF-transparent so as not to attenuate the signal.

Solid-dish antenna reflectors are generally painted white on the exposed (reflecting) side and covered with MLI on the back. The white paint limits the solar heating of the antenna and reduces temperature gradients in the dish that can be caused by shadowing. If support struts are present for a center reflector or center feed, the support structure is generally also painted white. Since uneven illumination of the dish or struts can cause thermal distortions that degrade RF-beam quality, a thermostructural analysis is generally required to verify the design. Some reflectors are made of very low coefficient-of-thermal-expansion composite materials that allow them to withstand very large temperature swings. Such antennas may have no thermal-control finishes applied to the reflector or support struts, although some insulation or heaters may be needed near locations where aluminum fittings are bonded to the composite material.

Mesh antennas are generally more difficult to analyze than solid reflectors, as a result of the complex shadowing and radiation interchange that occurs with a sparse open structure. As with other antennas, however, the main thermal-control requirements are to keep all materials within allowable temperature ranges and to limit thermal distortion to acceptable levels. These requirements can usually be met by painting the low-coefficient-of-thermal-expansion antenna structural ribs with a low-absorptance, low-emittance paint, or covering them with MLI, as shown in Fig. 3.12. Either approach tends to minimize temperature gradients across the diameter of the tubular ribs, thereby limiting thermal bending and dish distortion. The use of paints, if feasible, is preferable to the use of MLI, since the former provides a much "cleaner" design from a mechanical-packaging and antenna-deployment standpoint. The antenna mesh (usually gold- or silver-coated stainless steel) is generally left bare and allowed to cycle between very high (+150°C) and very low (−130°C) temperatures, since applying a thermal coating to the fine wire mesh would be difficult. As is the case with solid-dish antennas, some mesh antennas made from composite materials can withstand wide temperature swings and, therefore do not need any thermal-control coatings.

Helix antennas, like the other types, must maintain material temperature limits and minimize distortion; however, the distortion problem associated with helix antennas is usually much less severe than it is with dish or mesh reflectors. Temperatures of helix antennas can generally be maintained with paints and bare metal finishes. They do not present a challenging thermal design problem.

Sun, Earth, and Star Sensors

All spacecraft have sun, Earth, or star sensors to determine attitude. The smallest ones fit in the palm of the hand, while the largest are up to a meter across. They may be mounted internal or external to the spacecraft, and sun sensors are sometimes mounted on the solar-array structure (Fig. 3.13).

Attitude-sensor thermal designs vary depending on the installation or temperature sensitivity of the device. Figure 3.14 shows the thermal design of a sun sensor mounted internal to a spin-stabilized satellite. The sensor is conductively isolated from the solar array to limit temperature drops during eclipse. The inside face of
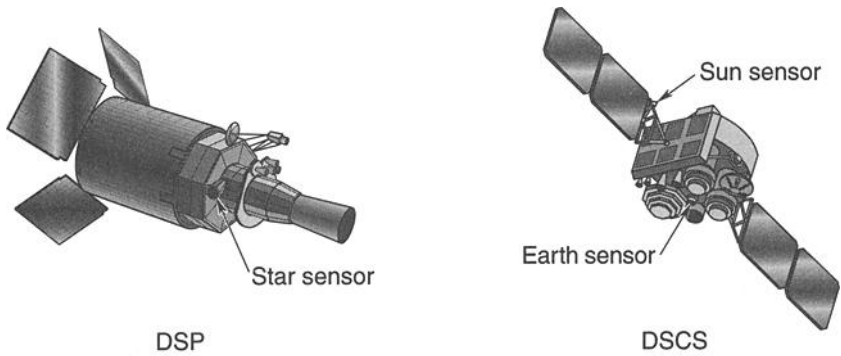
Fig. 3.13. Attitude-control sensors.

the unit is painted black to give good thermal coupling to the relatively stable temperature of the internal spacecraft hardware. The outside face is 80% polished aluminum and 20% black paint, which gives an α/ϵ ratio of .34/.22. This ratio was tailored to produce some warming when the satellite is in the sun while limiting heat loss during eclipse.

Figure 3.14 also shows an Earth sensor that has a very tight temperature-control requirement of ±0.6°C on the sensing element. The approach used in designing this application is to conductively isolate the sensor from the spacecraft structure to which it is mounted, radiatively isolate the sensor from the external environment using MLI blankets, and provide a small radiator area and a proportionally controlled heater to maintain precise temperature control of the sensor element.
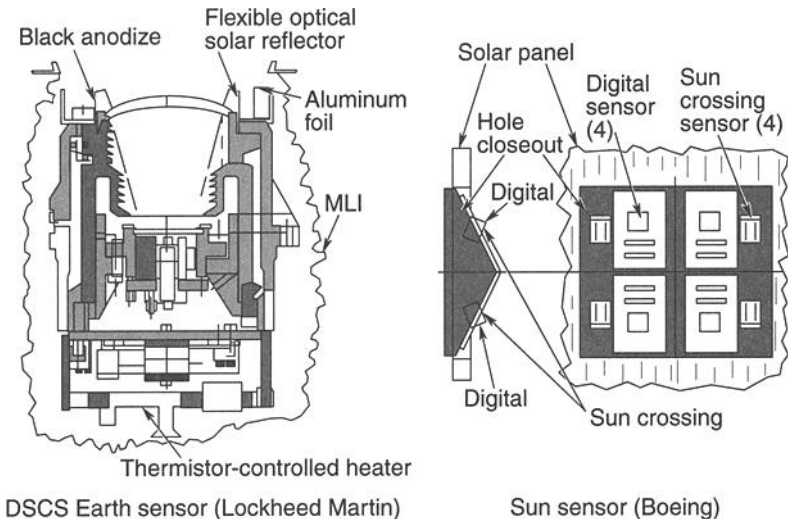
Fig. 3.14. Sun- and Earth-sensor thermal designs.

Figure 3.15 shows the thermal design used to develop a large star-sensor assembly for high-precision attitude control. Thermal-control requirements for this device include not only its minimum and maximum operating temperatures (+10 and +40°C), but also limitations on temperature gradients, which could misalign the optical elements.

The entire device is thermally isolated from the spacecraft with plastic mounting blocks to reduce sensitivity to spacecraft temperature changes. A shutter is provided to prevent sunlight from coming directly down the optical boresight. Thermal expansion of the "metering" structure slightly varies the separation of the optical elements to counteract temperature-induced changes in the mirror curvature and maintain focus over the range of operational temperatures. This structure, however, cannot have temperature gradients across its diameter, since they would cause the primary and secondary mirrors to rotate out of plane with one another. To prevent such temperature gradients, the metering structure is protected by thermal shields both inside and outside. These shields are made with high-thermal-conductivity aluminum that is thick enough to conduct heat from hot areas where the sun may be shining to cold areas in the shade. The inner and outer shields are also thermally coupled with high-conductivity "posts" that run through small holes cut in the metering structure. The shield surfaces facing the metering structure, and the metering structure itself, also have low-emissivity finishes to further reduce sensitivity to both temperature gradients and temperature fluctuations in the shields. Finally, the outer surface of the outer shield has a thermal finish that is tailored to reduce sensitivity to the asymmetric environments that the sensor will see on this particular spacecraft. All of these design features work together to ensure a highly isothermal optical-support structure.
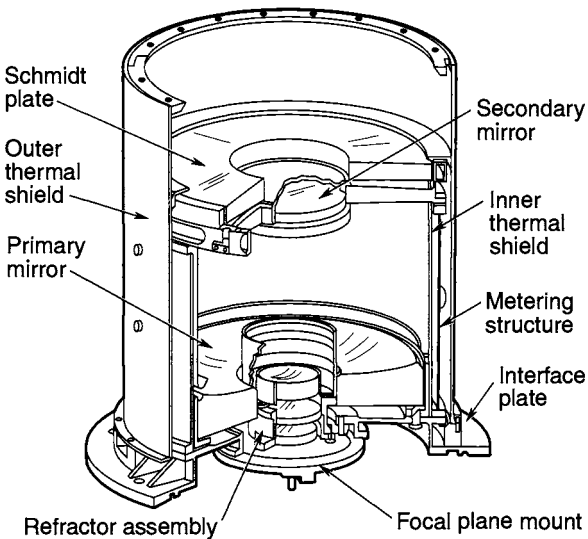
Fig. 3.15. Star-sensor thermal design.

Cooled Devices

Some spacecraft payloads require cooling to low temperatures. The most common types of cooled instruments include IR-sensor focal planes and optics, as well as low-noise amplifiers for RF receivers. Several devices are available for cooling such applications, including radiators, stored-cryogen cooling systems, and refrigerators. This section describes specific designs that make use of coolers; for a more complete discussion of these technologies, see Vol. 2 of this handbook.

The Defense Support Program (DSP) satellite uses a system of radiators to cool the optics and focal plane, as shown in Fig. 3.16. The optical elements (mirrors)
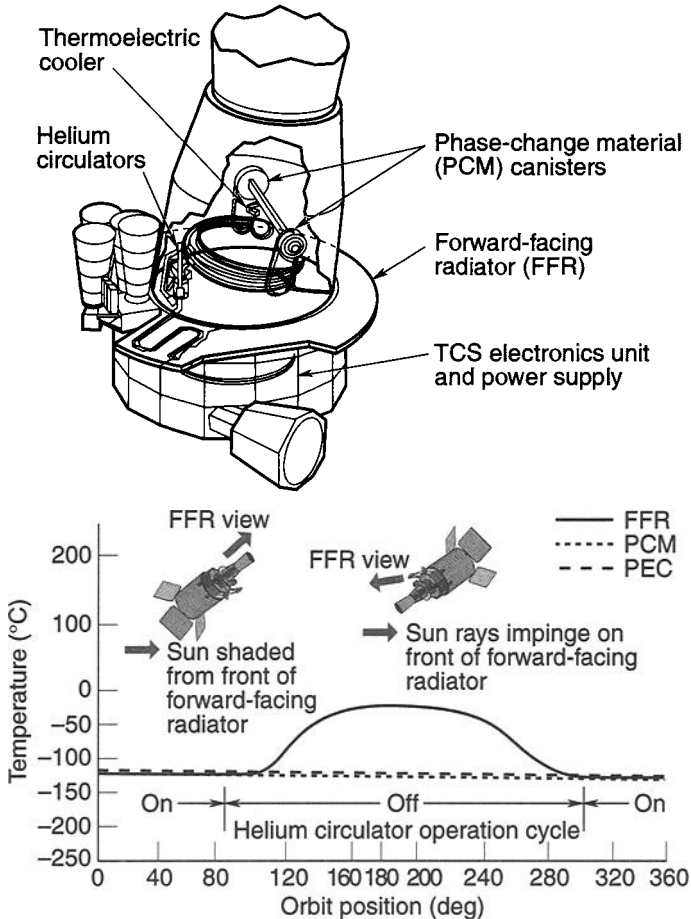
Concept
- Helium circulator transports focal plane/PCM heat to nonsolar illuminated forward-facing radiator (FFR)
- Circulator turned off when FFR solar illuminated–focal plane heat melts PCM
- PCM is refrozen when circulator resumed

Fig. 3.16. DSP sensor thermal control.

and the telescope enclosure and baffles are cooled passively by covering the telescope enclosure with low-absorptance, high-emittance quartz mirrors. Cooling the optics and enclosure reduces the amount of IR radiation emitted from those surfaces. Without this cooling, the sensors at the focal plane would not be able to see their targets over the IR "noise" created by the telescope itself. The focal-plane assembly is connected to a phase-change-material (PCM) heat sink and a passive radiator by a pumped-helium loop. The operating principle of this system (shown in Fig. 3.16) is the transporting of heat from the focal plane and PCM to the radiator by means of a pumped-helium loop during the half of the orbit when the sun does not shine on the radiator. During the other half-orbit, solar illumination heats the radiator to temperatures well above those of the focal plane. To avoid a focal-plane temperature rise, the helium circulation is shut off, effectively decoupling the radiators, and the heat loads from the focal plane are stored in the PCM. When the sun moves behind the vehicle, the circulator is turned back on to reject the focal-plane heat and the excess heat stored in the PCM. Minimizing heat leaks into the forward-facing radiator by the use of MLI and low-conductance supports on the back side is critical to achieving low-temperature performance. Even small heat leaks into the radiator during the shadowed half-orbit can raise its temperature considerably from 173 K. (Because of the T^4 nature of radiation-heat transfer, only one-fifth as much heat is needed to raise radiator equilibrium temperatures one degree at 173 K than at room temperature. For lower-temperature radiators the sensitivity is even greater; for example, the sensitivity is greater by a factor of 50 at 80 K than at room temperature. For this reason, low-temperature radiators are extremely sensitive to heat loads from the environment or heat leaks from the spacecraft.)

Devices requiring cooling to very low temperatures and having limited lifetime requirements (less than 1 or 2 years) usually employ stored-cryogen cooling systems. Designs for such devices use a cryogenic fluid or solid stored in a dewar as a heat sink to absorb waste heat from the device and maintain it at a low temperature. An example of such a system is the Infrared Astronomical Satellite (IRAS). The cryogen in this case is 70 kg of helium stored at 1.85 K in a tank that is wrapped around the satellite's telescope assembly, as in Fig. 3.17. As the telescope is operated, it generates heat, and this, along with the parasitic heat leaks through the tank insulation and supports, causes the helium to boil off. The vapor, rather than simply being directly vented to space, is routed through heat-exchange tubes mounted on thermal shields surrounding the tank in various stages. The thermal capacity of the vapor is thereby used to absorb some of the heat getting through the insulation, and the vapor is eventually vented back out to space. Performance of the MLI and the low-conductance tank-support struts is critical to reducing parasitic heat leaks and maintaining the lifetime of the system. Shielding of the instrument is also important. For this particular satellite, the dewar-and-telescope assembly is shadowed from the sun by the solar array and a sunshade-and-radiator system (shown in Fig. 3.18), which, along with spacecraft attitude constraints, are used to block solar and Earth heat loads from entering the telescope aperture.

Fig. 3.17. Infrared Astronomical Satellite (IRAS) thermal design.
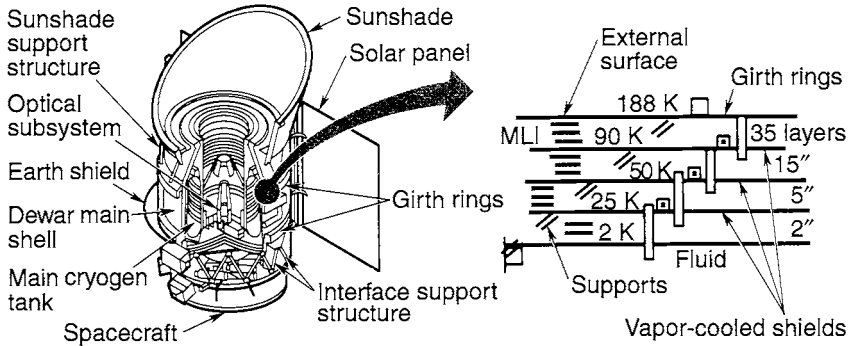
- •70 kg He stored at 1.85 K
- • 2.2 K focal plane
- • Design life = 1 year
- • Volume = 311 cm³
- • Dry weight (tankage) = 386 kg

- • Instrument heat load = 12.2 mW
- • Heat leak dominated by supports (55%)
- • MLI heat leak only 17 % total
- • Parasitic heat leak:
    - - Total = 33 mW
    - - Q/A = 0.013 W/m²

Applications with moderate-to-large cooling requirements and a lifetime in excess of 1 or 2 years normally employ refrigerators. However, refrigerators have drawbacks, which will be discussed in Vol. 2. A sample refrigerator design is the DSP Third Color Experiment cryocooler, shown in Fig. 3.19. Here a refrigerator is mounted in the telescope assembly to provide additional cooling to a set of sensors that are mounted on, but conductively isolated from, the primary focal plane. A heat pipe is used to transfer heat from the sensor (TCE Segment V in the figure) to the refrigerator-compressor cold heat pipe, to a radiator mounted on the side of the spacecraft. The temperature boost given by the refrigerator results in a much smaller radiator area because of the T^4 nature of radiation heat transfer. The reduced size and mass of the radiator more than compensate for the mass of the refrigerator and the extra electrical-power-system mass required to run it.

Solar Arrays

Thermal control of solar arrays is generally straightforward. The solar cells preclude the use of any thermal finishes on the sun-facing side of the array, so the array's thermal radiative properties are controlled by the high-absorptance, high-emittance solar cells themselves (see Fig. 3.20). To keep array temperatures as low as possible (a practice that increases electrical efficiency), designs usually call for the back of an array to be painted with high-emittance black or white paint. The white paint is used primarily in low-altitude orbits where albedo loads from Earth may illuminate the back side of the array. As a result of their high absorptance, high emittance, large area, and low mass, solar arrays typically cycle through wide

Inner radiator 3M velvet black paint 401-C10

Inner cone polished aluminum

Outer radiator Hughson A-276 white paint

Intermediate radiator

Vacuum-deposited gold Coilzak

MLI blanket outer service

• Second surface silvered Teflon

IRAS external thermal control finishes

- • Inner shield surface specularly reflects Earth Limb IR
- • Black painted radiators have high emissivity, no solar exposure
- • Inner cone self-emission less than 1×10^{-16} W at the detector
- • Twenty-four low heat leak fiberglass rods support sunshade outer stage off of outer-shell girth ring
- • Outer MLI blanket protects outer radiator from solar
- • Inner radiator isolated from other radiator by staged MLI blankets
- • Sunshade protects aperture from ram effect molecular contamination

Outer cone

Outer MLI blanket

MLI

Inner cone

Intermediate cone

Outer radiator (97 to 136 K)

Vacuum deposited gold on Coilzak

⇐ Worst case Earth limb IR

⇐ Worst case solar

Inner radiator (72 to 106 K)

Intermediate radiator (82 to 112 K)

Aperture

Sunshade support structure

Sunshade three-stage radiative cooler

Fig. 3.18. IRAS sunshade.

temperature ranges as they travel from sunlight to eclipse: +65 to −75°C in low Earth orbit, and +55 to −145°C in geosynchronous orbit.

The support structure for the solar array is sometimes thermally isolated from the array drive motor on the spacecraft by low-conductance spacers. This isolation is implemented primarily to prevent heat leaks out of the motor, since the structure temperatures themselves can usually be controlled to acceptable ranges with paint finishes. Occasionally, special thermal shields may also be required on the edges of arrays to protect them from rocket-motor plumes or free molecular heating during launch. However, these requirements are not very common.

The Huygens Probe

A spacecraft that can serve as a good example of the thermal design issues raised in this chapter is the Huygens probe, which is part of the Cassini mission. The Cassini/Huygens spacecraft is part of a joint project of the National Aeronautics and Space Administration (NASA) and the European Space Agency (ESA), dedicated to the exploration of Saturn and its moons. The spacecraft's two major hardware components are the Cassini orbiter, which will study Saturn, and the
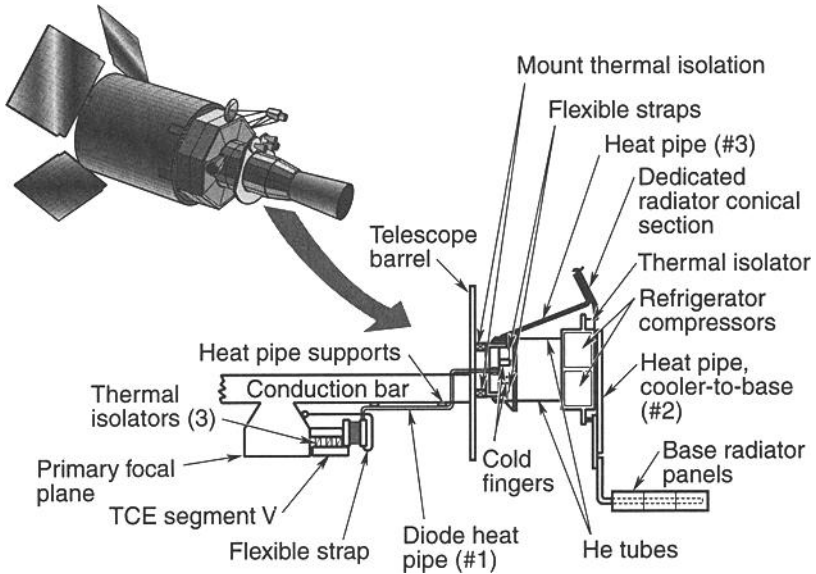
Fig. 3.19. DSP sensor detail.
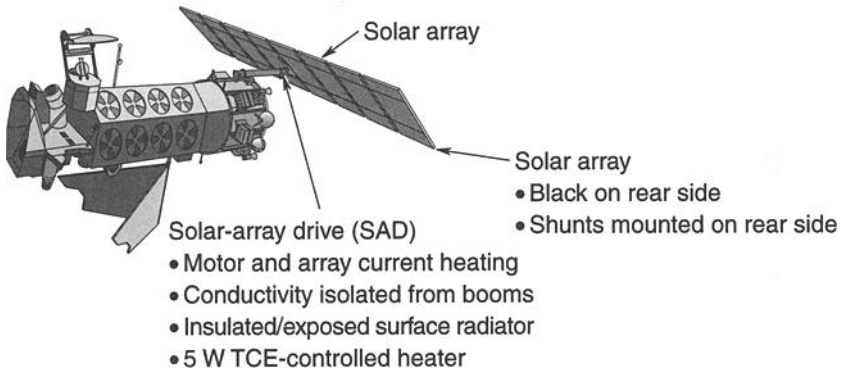
Fig. 3.20. DMSP solar array and drive.

Huygens probe, which will explore Titan, Saturn's largest moon (Fig. 3.21). Titan is the only moon in our solar system possessing a significant atmosphere that is denser than Earth's. The scientific objectives of the Huygens probe, which was developed by ESA, are to assess the composition and dynamics of Titan's atmosphere and to gather surface-property data.
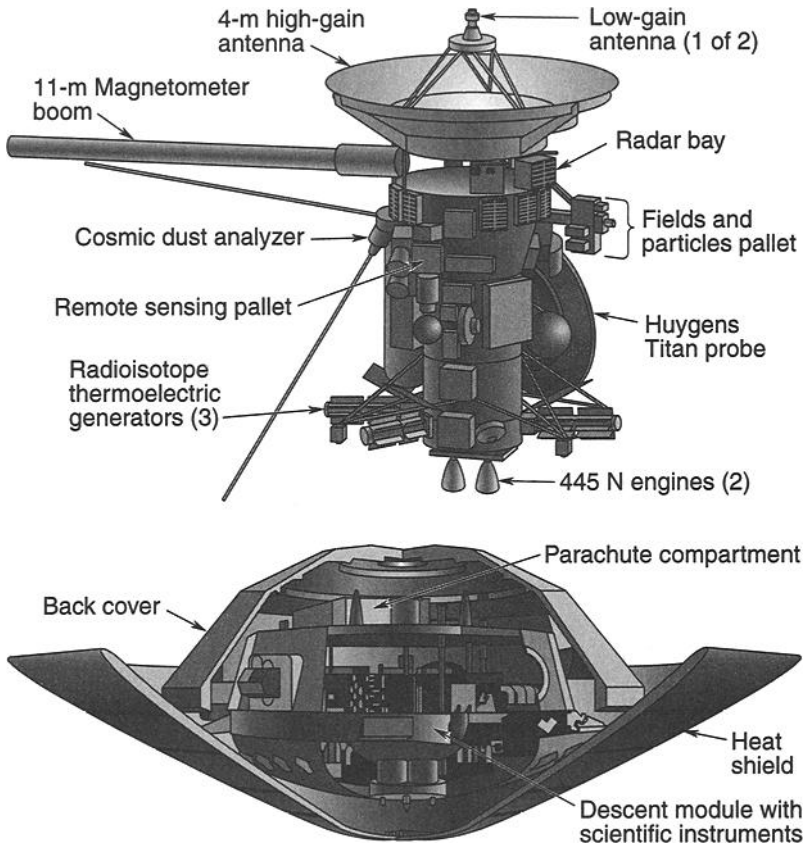
Fig. 3.21. The Huygens probe will explore Titan, Saturn's largest moon.

Since their launch in October 1997, these two spacecraft have flown as a single vehicle through a lengthy interplanetary trajectory that has included gravity assists from Venus, Earth, and Jupiter, as shown on p. 12. After they go into orbit around Saturn in 2004, Huygens will separate from Cassini on a trajectory to intercept the path of Titan. The probe will then coast for 22 days, remaining in a dormant state until its payload instruments are powered up shortly before entry into Titan's atmosphere. After aerobraking has reduced Huygens's velocity from 7000 m/s to 500 m/s, parachutes will be deployed and the protective aeroshell jettisoned at an altitude of approximately 170 km. Payload instruments will then collect atmospheric and surface data during the 2.5-hour parachute descent to Titan's surface (Fig. 3.22). The data will be relayed to Earth through the Cassini orbiter.

The Huygens probe bus carries six experiments and provides them with mechanical mounting, electrical power, and thermal control throughout the mission, from launch to surface impact. The bus consists of two functional subsystems: the entry assembly, which serves as a protective cocoon, and the descent module. The entry assembly surrounds the descent module and provides mechanical and electrical
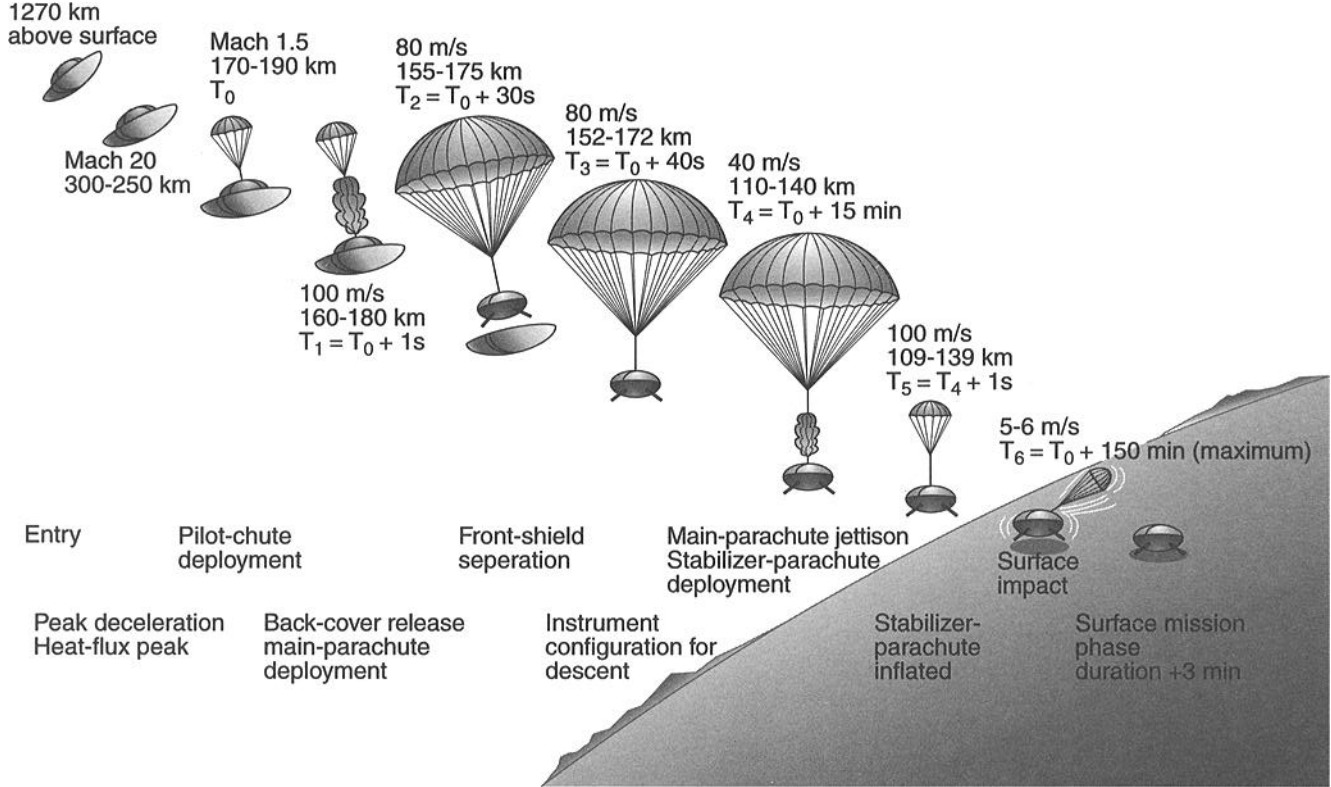
Fig. 3.22. Payload instruments collect data during descent to Titan's surface.

connections to the Cassini orbiter, as well as the heat shields necessary to protect the vehicle during aerobraking in Titan's atmosphere. It also provides some thermal control for the descent module during the cruise and postseparation coast phases.

After the aerobraking maneuver, the entry assembly is jettisoned, exposing the descent module, which coasts through Titan's atmosphere via the deployed parachutes. The descent module consists of an aluminum shell and two platforms supporting the six experiments and bus electronics (Fig. 3.23).

Thermal Design Drivers

Throughout the various phases of the mission, the Huygens probe encounters severe hot and cold environments from which it must be protected by its thermal-control subsystem. From a thermal viewpoint, the mission comprises five distinct phases: prelaunch and launch ascent, interplanetary cruise, coast after separation from Cassini, entry into the atmosphere of Titan, and descent. The probe's thermal design is driven primarily by the four flight phases of the mission, with ground air-conditioning equipment providing thermal control during the prelaunch phase. The hot design cases occur during the cruise phase, when Huygens is attached to Cassini and is exposed to solar intensities up to 3800 W/m^2 at its closest approach to the sun, as well as combined solar, IR, and albedo heating encountered during its two Venus flybys. The cold case occurs during the phase in which the probe coasts after separation from Cassini, when Huygens receives only 17 W/m^2 of sunlight and no other significant environmental or internal-electronics heating. During the atmospheric entry and descent phases, the thermal environment is complicated by the presence of an atmosphere. Aeroheating rates during aerobraking can reach 1,000,000 W/m^2 on the front shield. During descent, atmospheric gases that are very cold (−200°C at a 45-km altitude) introduce free and forced convection effects that the thermal design must account for. The principal requirement for the thermal-control subsystem is to keep the probe components within the temperature limits shown in Table 3.1 during all of these mission phases.

Table 3.1. Huygens Probe Temperature Limits[a]

Component	Op. Limits (°C)		Nonop. Limits (°C)	
	T_{min}	T_{max}	T_{min}	T_{max}
Experiments: ACP, DISR, TUSO, GCMS, HASI, SSP	−20	50	−20	60
Bus units: CDMU, PCDU, transm.	−20	50	−20	60
Batteries	−10	30	−10	50
Parachute deploy device	−50	15	−50	60
Spin eject device	−70	40	−70	60
Front shield- and back cover mechanisms	−70	40	−70	60

[a]Reprinted with permission from SAE Paper No. 981644 ©1998 Society of Automotive Engineers, Inc.

Huygens Thermal Design

As with most spacecraft thermal designs, the Huygens design (Fig 3.23) relies primarily on insulation, heaters, and surface finishes to achieve thermal control. However, the Huygens thermal design differs from others in a number of ways; for example, unlike most spacecraft, Huygens must have insulation suitable for vacuum, atmospheric, and high-flux aerobraking environments. Another unusual feature of Huygens's thermal design is that its heaters are radioisotope heater units (RHUs) rather than electrical-resistance heaters. RHUs consist of small canisters of plutonium that generate heat directly through radioactive decay. Also of interest is the design's inclusion of attitude constraints that allow Cassini's high-gain-antenna dish to be used as an umbrella to shadow both Cassini and Huygens during the early part of the interplanetary cruise phase, when solar intensity is very high.

MLI Blankets

To protect the probe from environmental extremes before it enters Titan's atmosphere, its entire outside surface, including the front aeroshield, is covered with MLI blankets, as shown in Fig. 3.23. Because of the probe's complicated geometry, achieving a good fit requires 43 separate blankets. These blankets are of two varieties, standard and high-temperature, as shown in Fig 3.24. Both types include netlike Dacron separators between individual blanket layers; however, the high-temperature variety only makes use of the separators between layers that are deep inside the blanket. The reason for this difference in the use of separators is that some blankets, such as those near Cassini's rocket engines, will experience external heating rates high enough to raise the temperature of the first several layers of the blanket above the 140°C limit for Dacron. Even in the standard blanket, the first three layers do not use the separators because even brief solar exposure at 0.6 AU could overheat the Dacron. Where separators are not used, the blanket layers themselves are wrinkled to minimize contact between layers and thereby improve insulation performance.
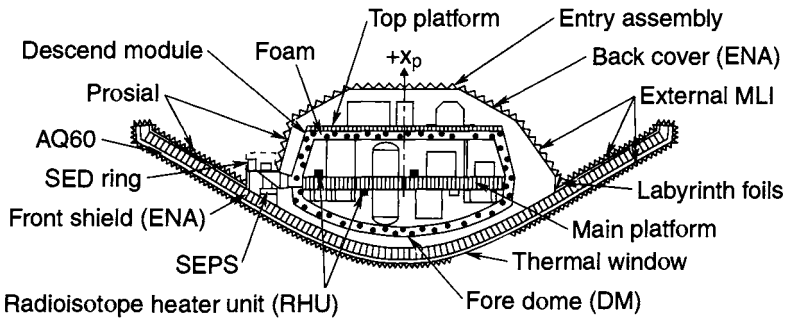
Fig. 3.23. The Huygens probe thermal design. (Reprinted with permission from SAE Paper No. 981644 © 1998 Society of Automotive Engineers, Inc.)
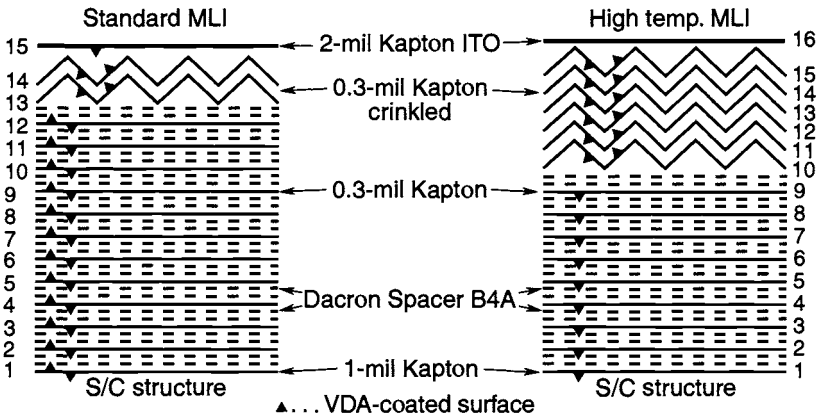
Fig. 3.24. MLI blankets protect the Huygens probe from environmental extremes. (Reprinted with permission from SAE Paper No. 981644 © 1998 Society of Automotive Engineers, Inc.)

Foam Insulation

Because MLI loses most of its insulating capability at pressures greater than 10^{-3} torr, it cannot be used as insulation in a planetary atmosphere. Foam insulation is therefore used on the internal side of all descent-module external surfaces to retain heat during the descent through Titan's cold atmosphere. Extensive analysis and a number of tests were required to characterize the ingestion of atmospheric gases and the resultant convection heat-transfer environment within the descent module and to devise an effective approach to packaging the foam insulation.

Heaters

All electrical power onboard Cassini is generated from radioisotope thermoelectric generators (RTGs) because Saturn's great distance from the sun makes the use of solar panels impractical. Instead of using electricity from the RTGs to power electric heaters, the Huygens thermal design uses RHUs to place the heat of plutonium decay directly where it is needed, thereby bypassing the inefficiencies of the thermoelectric conversion process. The RHU approach therefore saves spacecraft mass, although it does introduce a complication in that an RHU heater cannot be turned off.

To make up for the fact that the Huygens payload electronics are not operating for almost the entire mission, and therefore not generating waste heat, 35 RHUs are used to warm the descent module. Of the 35 RHUs, 13 are on the lower face of the main platform, 14 are on the top face of the main platform, and 8 are on the top platform (see Fig. 3.23). Each RHU dissipates around 1 W of heat, with the 35-W total sufficient to keep the equipment inside the descent module above minimum allowable temperatures.

Thermal Window

Because Huygens is entirely covered by MLI, and predicting MLI's effectiveness with any precision is difficult, a thermal "window" was placed in the insulation near the apex of the front shield, as shown in Fig. 3.23. The window provides a known heat leak, which ensures that the RHUs will not overheat internal components if the MLI insulation performs better than nominally expected. The window consists of a cut-out in the MLI that exposes a 0.165-m^2 area of the front shield that is covered by a thin aluminum plate. The plate is painted white to provide a high emittance while minimizing the effect of any solar illumination. The inside surface of the shield and the outside surface of the descent module are both painted black in this area to improve the radiative heat-transfer path from the descent module to the window.

Aeroshield

The purpose of the aeroshield is to provide an appropriately shaped structure to produce the desired deceleration forces during the probe's entry into Titan's atmosphere and to protect the probe from the very high heating rates encountered during this mission phase. The aeroshield structure is composed of a central aluminum nose cap surrounded by a conical aluminum honeycomb cone. Because Huygens's MLI covering is constructed of materials that cannot survive high temperatures, that covering will burn off shortly after the start of the entry phase. Thermal protection is therefore provided by an 18-mm-thick layer of AQ60 ablative material on the front surface of the aeroshield plus a 2-mm-thick layer of Prosial on the rear side of the aeroshield and the outside of the entry module back cover, as indicated in Fig. 3.23. Ablative materials are typically used on entry shields because the charring and vaporization process allows a tremendous amount of heat to be absorbed with minimal mass. In some cases, heating rates are so high that no material could survive, making the sacrifice of an ablative layer the only practical means of surviving atmospheric entry.

Gap Closeout

The front shield and back cover of the entry assembly must separate at the end of the entry phase. To avoid potential cold-welding, contact between the two is limited to discrete points where the separation devices are located. Around the rest of the separation ring, a 13-mm gap is provided to avoid metal-to-metal contact. Because this gap presents a path for heat loss by radiation, a closeout had to be devised that would block radiative heat transfer without introducing any possibility of snags or cold welding that might prevent clean separation of the two pieces of the enclosure. This was accomplished by using Kapton foils to create a "labyrinth gap," as shown in Fig. 3.25.

Surface Finishes

Various surface finishes either enhance or inhibit radiative heat transfer within the Huygens probe. Low-emittance finishes are used on all external surfaces of the descent module to minimize heat transfer between it and the surrounding entry module. As mentioned earlier, however, a small patch of black paint is placed on the descent module to provide a controlled radiant heat leak to the front shield to
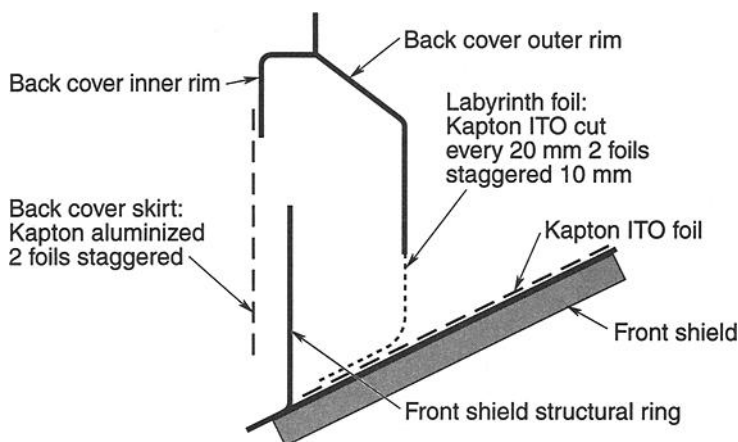
Fig. 3.25. Use of Kapton foils to create a "labyrinth gap." (Reprinted with permission from SAE Paper No. 981644 © 1998 Society of Automotive Engineers, Inc.)

guard against overheating. Most of the payload and bus electronics boxes inside the descent module, and the structural platforms that support them, are painted black to enhance radiative heat transfer and thereby help isothermalize the compartment. The internal surface of the foam insulation on the descent module walls is covered with a low-emittance aluminized Kapton film to reflect IR radiation from the internal equipment back into the compartment and thereby enhance the insulating effect of the foam. The batteries are given a low-emittance finish intended to retain heat generated during discharge and thereby raise the battery temperature for better electrical performance. A seal closes out the gap around the tubes that draw in samples of Titan's atmosphere.

Vent and Seal

A small (6-cm^2) vent in the descent module's top platform is just large enough to allow air trapped in the module to escape during launch and to allow Titan's atmospheric gases to enter during descent, without the development of an excessive pressure differential. If the pressure difference were too high, the module structure could be damaged.

Some of the payload instruments have tubes that protrude through the wall of the descent module to draw in samples of Titan's atmosphere during descent. To prevent an undesirable flow of cold gas into the module cavity, a seal was developed to close out the gap around the tubes. This seal, shown in Fig. 3.26, closes the gap while providing enough flexibility to accommodate displacements of the shell that will occur as a result of shaking during launch and atmospheric entry.

System Overview: The Hubble Space Telescope

The following top-level description of the thermal design of NASA's Hubble Space Telescope gives an appreciation for the extensive application of thermal control in the development of a typical satellite. The discussion illustrates the thermal engineer's need to consider the thermal control of all vehicle components. A
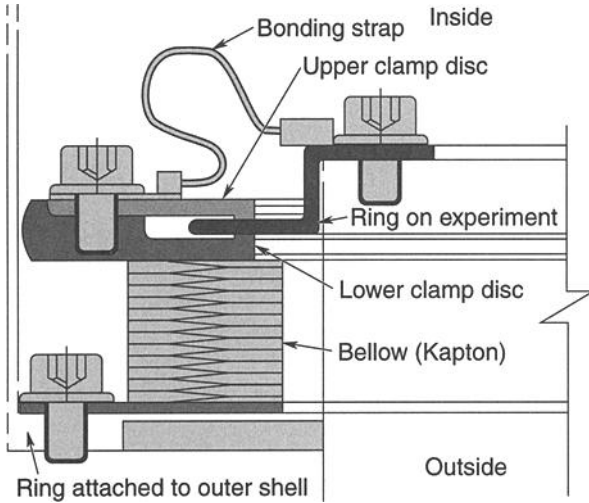
Fig. 3.26. Seal closing gap around tubes protruding through descent-module wall. (Reprinted with permission from SAE Paper No. 981644 © 1998 Society of Automotive Engineers, Inc.)

great deal of analysis, parametric study, design iteration, and testing is required to arrive at the final thermal design. The total thermal effort can exceed 20 person-years for some satellites.

The Hubble Space Telescope is a large optical-imaging satellite. Although it is sophisticated and its mission operations are complex, its thermal control has been achieved using common thermal-control hardware: thermal surface finishes, MLI, heaters, thermal isolators, and louvers. (Refer to Chapters 4 through 9 for detailed discussions of each of these elements.) The satellite was designed and built by Lockheed Missiles and Space Company and BF Goodrich Danbury Optical Systems (formerly Perkin-Elmer) under a NASA contract. For the purposes of discussion, the satellite has been broken down into the following sections, which are illustrated in Fig. 3.27: aperture door, light shield, forward shell, support-system-module equipment section, optical-telescope-assembly equipment section, aft shroud, optical telescope assembly, solar-array assembly, and external components (latches and drives, coarse sun sensors, low-gain antennas, magnetic sensing systems, magnetic torquer bars, and high-gain antennas).

The thermal-control system maintains all component and structure temperatures within allowable limits under all required mission conditions, including normal operation, orbit maintenance while the satellite is docked with the space shuttle, and safemode hold. The satellite is traveling a 28.5-deg-inclination circular orbit at altitudes that range from 398 to 593 km. The orbit beta angle varies between +52 and –52 deg, and eclipse time ranges from 26 to 36 min, as shown in Fig. 3.28. Certain attitude restrictions in effect prevent adverse solar-illumination conditions on the telescope.
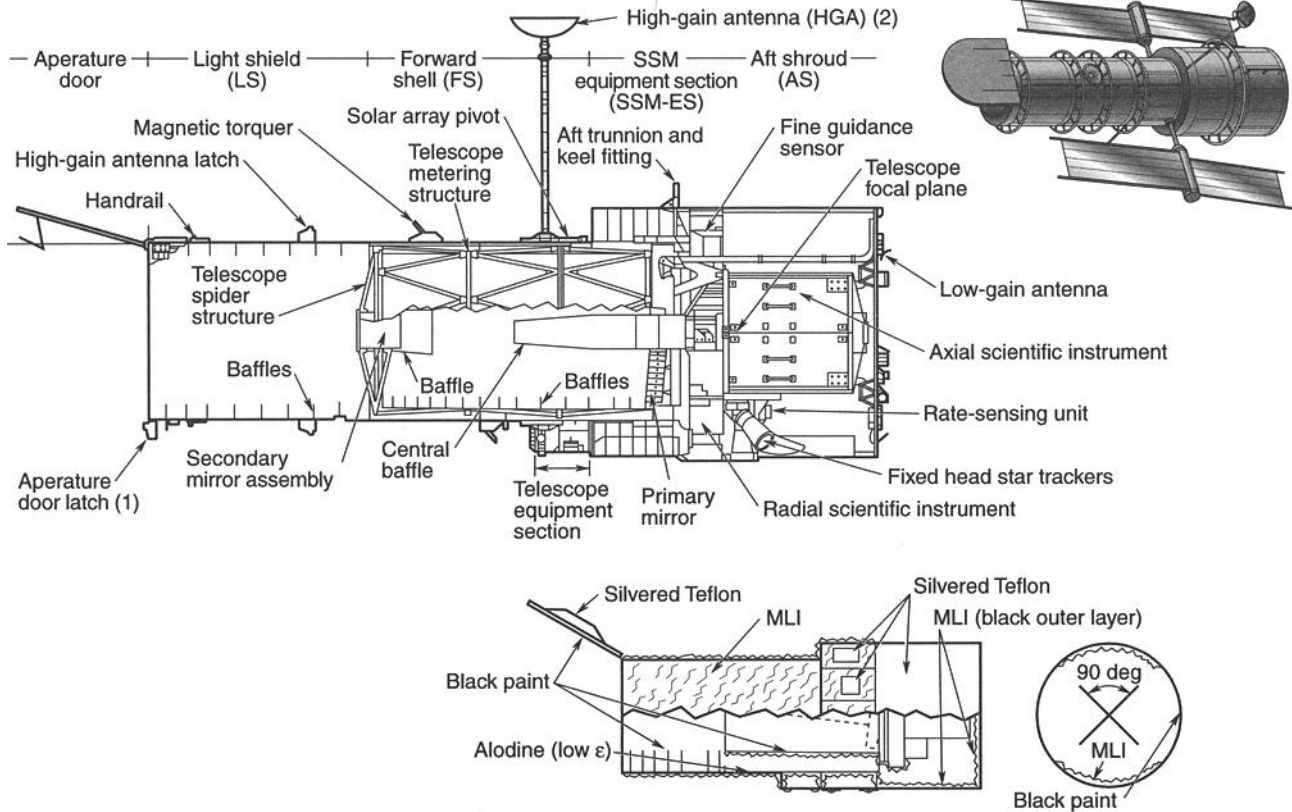
Fig. 3.27. The Hubble Space Telescope.
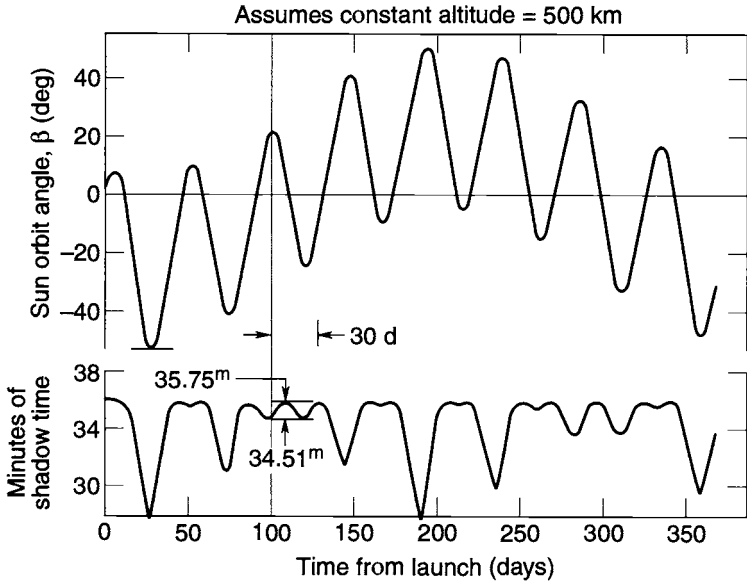
Fig. 3.28. Space telescope beta angle and eclipse time.

The general approach was to keep the thermal design as passive as possible. To minimize sensitivity to the wide range of sun angles, the vehicle's external surface was almost entirely covered with MLI with a low-α/ε-ratio silvered Teflon or aluminized Teflon outer layer. Low-contamination materials were used in constructing the vehicle, and venting paths were designed to prevent contamination of thermal and optical surfaces.

The Aperture Door

The aperture door is a 3.8-cm-thick honeycomb structure. The core is aluminum honeycomb (.95-cm cells, 25 kg/m^3, and .64-cm cells, 54 kg/m^3), and the facesheets are 0.3-mm-thick aluminum.

The surface finish of the side of the door that faces the optics and never sees the sun is a glossy black paint (glossy black Chemglaze Z302) as required by the telescope straylight analysis. The outer surface is covered with aluminized Teflon tape to minimize temperatures and gradients with full solar heating. The aperture door has one flight-temperature sensor, located at the center of the outer surface.

The aperture door has a radiative coupling with the telescope, and the orbit average temperature must be maintained below 33°C for the hot case and above –90°C for the cold case. The passive thermal design of the door has maintained its temperature within these limits.

The Light Shield

The light shield is the 3-m-diameter, 4-m-long forward portion of the barrel structure in front of the telescope. It has eight internal baffles for straylight control as well as a baffle at the forward end. The baffles and internal surface of the light

shield are coated with an optical black paint (flat black Chemglaze Z306) as required by the telescope straylight analysis. The α/ε ratio of the black paint is 0.95/0.92. The external surface of the light shield is covered with MLI blankets (an outer layer of aluminized Teflon, 15 layers of .008-mm embossed double-aluminized Kapton, and an inner layer of .025-mm single-aluminized Kapton). An effective emittance of 0.02 has been used for the MLI blankets. The MLI blankets are mounted on the structure to reduce the structural temperature variation, and they also function as part of the meteoroid protection system. There are eight flight-temperature sensors on the light-shield structures. This design meets the orbit-average temperature requirement of −33 to −59°C.

The Forward Shell

The forward shell is a 3-m-diameter, 3-m-long cylinder that encloses the telescope assembly. The forward-shell internal surface finish is alodine with an emittance of approximately 0.15. The external surfaces are covered with MLI blankets identical to the light-shield MLI blankets (an outer layer of aluminized Teflon, 15 layers of .008-mm embossed double-aluminized Kapton, and an inner layer of .025-mm single-aluminized Kapton). The MLI covers the external rings except for the structural ring at station 358, which is covered with aluminized Teflon. The forward shell has eight flight-temperature sensors. Temperature of the forward shell is maintained between −23 and −53°C on an orbit-average basis.

The Support-System-Module Equipment Section

The support-system-module equipment section (SSM-ES) consists of an annular ring of compartments surrounding part of the telescope, as shown in Fig. 3.27. Its outside and inside diameters are approximately 4.3 m and 3 m, and it is 1.53 m long. The ring is divided into 12 compartments that house various electronics boxes, as shown in Fig. 3.29.
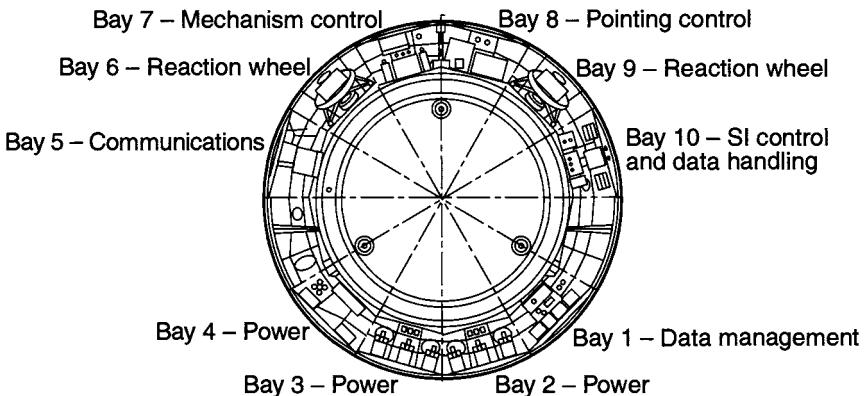
Fig. 3.29. Support-system-module equipment section.

The equipment section's thermal-control subsystem is designed to control the temperatures of all its internal components, to control the temperatures and gradients of the structure that interfaces with the telescope and scientific instruments, and to control conductive heat transfer through the telescope attachments. The thermal design is primarily passive, using MLI, low-α/ε-ratio surface properties, component locations, and mounting configurations. It is augmented with thermostatically controlled heaters. Additionally, louver assemblies are used on the two battery-bay doors to conserve heater power.

The design approach is to cover all surfaces of the equipment section with MLI except for some radiator areas on the "doors" of the equipment compartments, as in Fig. 3.30. These radiator areas are covered with silvered Teflon for high emittance and low solar absorptance. MLI also covers the equipment-section surfaces facing the telescope and the scientific instruments in the aft-shroud area to limit thermal interactions with those components. In addition, some of the equipment-section compartments are thermally isolated from one another with MLI.

The majority of the electronic components are mounted on the honeycomb doors of the bays, except Bays 6, 9, 11, and 12, which do not have honeycomb doors. The battery-bay doors (Bays 1 and 2) and the communications-bay door (Bay 5) have additional aluminum doubler plates (3 mm) bonded on the internal door surfaces under the components for better heat distribution. All of the other components are
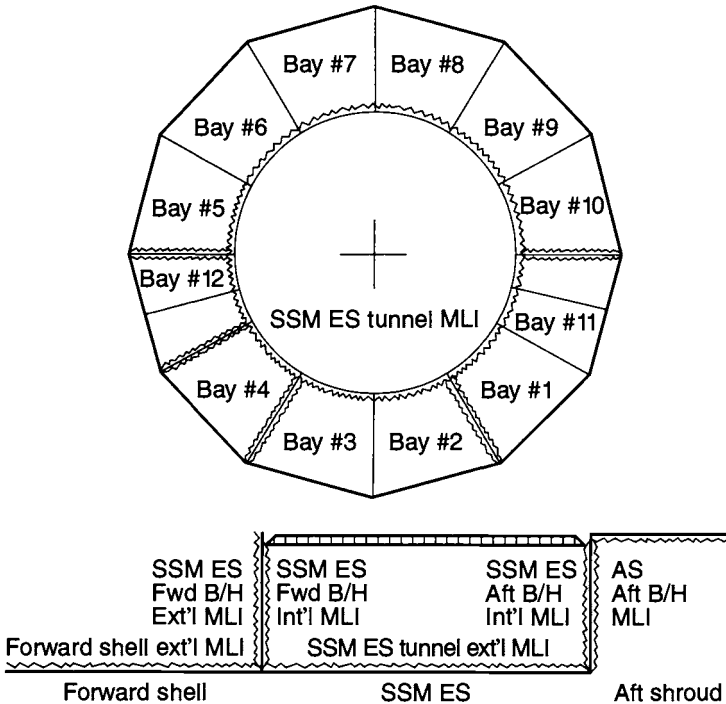
Fig. 3.30. SSM equipment-section MLI.

mounted directly on the door or mounted on the structure at the bottom of the bay called the "tunnel structure." Along the bottom of the bay are structural beams with additional members for mounting components. The reaction-wheel assemblies (RWA) have separate mounting structures to provide the correct orientation.

Thermostatically controlled heaters, if needed, maintain minimum temperatures during normal component operation, and they maintain survival temperatures during times when components are not operating. The batteries have integral internal heater systems. Heaters are mounted on the RWAs, and the remaining equipment-section heaters are mounted on the doors or component mounting structures. Sixteen primary heater circuits are used for the equipment section: one circuit for the computer in Bay 1; one circuit for each of the six batteries in Bays 2 and 3; one circuit for Bay 4; one circuit for the tape recorders in Bay 5; one circuit for the communication equipment in Bay 5; one circuit for each of the four RWAs in Bays 6 and 9; one circuit for the Bay 7 and Bay 8 door heaters, plus the tape recorder in Bay 8; and one circuit for the scientific-instrument electronics trays in Bay 10. Sixteen secondary heater circuits serve as backup. Several heater circuits control more than one heater system: the Bay 5 tape-recorder circuit has two tape-recorder heater systems; the communication circuit has two separate heater systems on the tray; each RWA circuit has separate heater systems for the inboard and outboard bearing; Bay 7 and Bay 8 are on one heater circuit, with heater systems on the Bay 7 door, Bay 8 door, and the tape-recorder mounting structure; and the scientific-instrument electronics circuit has two heater systems on the tray.

Each heater system, both primary and secondary, has two thermostats wired in series with its heater elements. The systems are thereby protected against open heaters, thermostats, or wires. The second thermostat wired in series will back up a failed closed thermostat in either the primary or the secondary system. Two independent failures are required to disable these heater systems. The primary and secondary heater elements can be on the same strip. If a second heater strip is present, the primary heaters are wired in parallel with the secondary heaters. Table 3.2 lists all Space Telescope heaters. These heaters were enabled prior to launch, and their status was verified with the first available telemetry data received during deployment operations from the space shuttle.

Many of the electronic components in the equipment section have no internal temperature sensors. To provide temperature data for these components, 20 temperature sensors have been placed near the interface of these components and their respective mounting structures.

The following sections describe the thermal designs of selected bays in the equipment section. Bay 1 is a typical electronics-box bay, with a fairly wide range of allowable temperatures, and its design uses radiator area on the door, MLI, and heaters to achieve thermal control. Bays 2 and 3 contain NiH_2 batteries, which must be controlled within a relatively narrow temperature range (-5 to $+20°C$). MLI, heaters, radiator areas, louvers, and aluminum doublers are used on these bays. Bays 7 and 8 have relatively low levels of electronic waste heat to dissipate and therefore have no radiators; these bays rely on MLI and heaters to keep components within temperature limits.

Table 3.2. Space Telescope Heaters

Location	Type	Size (cm)	Htrs. per Strip	Htr. Strips[a]	Htrs.	Nom.Resist. Ω@25°C ± 3%	Each Htr. W @ 28V	Total W @ 28V	Thermostats Close (°C)	Open (°C)	Close (°C)	Open (°C)	No. Req'd.
Bay 1 DF224,	Primary	1.3 × 20.3	1	2	2	50.7	15.46	30.9	−8 ± 1.1	−9 to −6	−23 ± 0.6	−23 to −21	2
computer	Secondary		1	2	2		15.46	30.9	−12 ± 1.1	−12 to −8	−24 ± 0.6	−24 to −23	2
Bay 4 door	Primary	2.5 × 25.4	2	4	4	152.0	5.16	20.6	−21 ± 2.8	−12 ± 2.8	−29 ± 1.7	−24 ± 1.7	2
(PDU/PCU)	Secondary				4		5.16	20.6	−26 ± 2.8	−18 ± 2.8	−32 ± 1.7	−28 ± 1.7	2
Bay 5 communi-	Primary	3.8 × 17.8	2	4	4	50.7	15.46	51.9	−7 ± 1.1	−7 to −3	−22 ± 0.6	−22 to −19	4
cation tray	Secondary	5.1 × 12.7			4	50.7	15.46	51.9	−9 ± 1.1	−9 to −6	−23 ±0.6	−23 to −21	4
Tape recorder	Primary	0.9 × 25.4	2	6	6	101.4	7.73	46.4	−4 ± 1.1	−4 to −1	−20 ± 0.6	−20 to −18	6
(1, 2, 3)	Secondary				6		7.73	46.4	−7 ± 1.1	−7 to −3	−22 ± 0.6	−22 to −19	6
Bays 6 and 9	Primary	1.3 × 43.7	2	8	8	50.7	15.46	123.7	−12 ± 1.1	−12 to −8	−24 ± 0.6	−24 to −22	20
RWA (1–4)	Secondary	1.3 × 67.1			8	50.7	15.46	123.7	−15 ± 1.1	−15 to −12	−26 ± 0.6	−26 to −24	20
Bay 7 door	Primary	2.5 × 25.4	2	2	2	76.0	10.32	20.6	−14 ± 1.1	−14 to −11	−26 ± 0.6	−26 to −24	2
	Secondary				2		10.32	20.6	−16 ± 1.1	−16 to −13	−27 ± 0.6	−27 to −25	2
Bay 8 door	Primary	2.5 × 25.4	2	2	2	76.0	10.32	20.5	−21 ± 2.8	−12 ± 2.8	−29 ± 1.7	−24 ± 1.7	2
	Secondary				2		10.32	20.5	−26 ± 2.8	−18 ± 2.8	−32 ± 1.7	−28 ± 1.7	2
Bay 10	Primary	3.3 × 19.1	2	4	4	27.6	28.41	113.5	−7 ± 1.1	−7 to −3	−22 ± 0.6	−22 to −19	8
Si and DH tray	Secondary				4		28.41	113.5					8
Magnetometer	Primary	2.5 × 10.2	2	2	4	209.1	3.75	15.0	−26 ± 2.8	−18 ± 2.8	−32 ± 1.7	−28 ± 1.7	4
(MSS 1, 2)	Secondary				4		3.75	15.0	−32 ± 2.8	−23 ± 2.8	−36 ± 1.7	−31 ± 1.7	4
Coarse sun	Primary	2.5 × 25.4	2	5	5	192.0	4.08	20.42	−32 ± 2.8	−23 ± 2.8	−36 ± 1.7	−31 ± 1.7	10
sensor (1–5)	Secondary				5		4.08	20.42	−34 ± 2.8	−26 ± 2.8	−37 ± 1.7	−32 ± 1.7	10
FHST Δ plate	Primary	4.4 × 5.1	2	9	9	94.1	8.33	75.0	−1 ± 1.1	−1 to 3	−18 ± 0.6	−18 ± 1.7	6
(1, 2, 3)	Secondary				9		8.33	75.0	−3 ± 1.1	−3 to 0	−19 ± 0.6	−19 ± 1.7	6
Mechanisms	Primary	2.2 × 30.7	2	1	1	78.4	10.0	10.0	−26 ± 2.8	−18 ± 2.8	−33 ± 1.7	−28 ± 1.7	2
AD hinge min	Secondary				1		10.0	10.0	−32 ± 2.8	−23 ± 2.8	−31 ± 1.7	−31 ± 1.7	2
AD passive hinge	Primary	2.2 × 27.9	2	1	1	52.5	14.93	14.9	−51 ± 2.8	−42 ± 2.8	−46 ± 1.7	−41 ± 1.7	2
	Secondary				1		14.93	14.9	−58 ± 2.8	−49 ± 3.3	−50 ± 1.7	−45 ± 1.7	2

Table 3.2. Space Telescope Heaters—*Continued*

Location	Type	Size (cm)	Htrs. per Strip	Htr. Strips[a]	Htrs.	Nom.Resist. Ω@25°C ±3%	Each Htr. W @ 28V	Total W @ 28V	Thermostats Close (°C)	Open (°C)	Close (°C)	Open (°C)	No. Req'd.
AD active hinge	Primary	2.2 × 30.7	2	1	1	78.4	10.0	10.0					
	Secondary				1		10.0	10.0					
AD latch motor	Primary	2.2 × 30.7	1	1	1	78.4	10.0	10.0	−32 ± 2.8	−23 ± 2.8	−36 ± 1.7	−31 ± 1.7	2
HGA hinge motor	Primary	2.2 × 30.7	1	2	2	78.4	10.0	20.0	−32 ± 2.8	−23 ± 2.8	−36 ± 1.7	−31 ± 1.7	4
HGA latch motor	Primary	2.2 × 30.7	1	2	2	78.4	10.0	20.0	−32 ± 3.3	−23 ± 2.8	−36 ± 1.7	−31 ± 1.7	4
HGA TAG	Primary	vendor-	1	4	4	114.0	5.88	27.5	13 ± 1.7	13 to 33	−7 ± 1.1	−7 to −6	8
(gimbals)	Secondary	supplied	1	4	4		5.88	27.5	16 ± 1.7	16 to 19	−9 ± 1.1	−9 to −7	8
S/A latch motor	Primary	2.2 × 30.7	1	4	4	78.4	10.0	40.0	−32 ± 2.8	−23 ± 2.8	−36 ± 1.7	−31 ± 1.7	8
					Miscellaneous								
SADM survival	Primary		1	2	2	118.0	6.64	13.3	−43	−29	−42.0	−34	2
(± wing)	Secondary		1	2	2		6.64	13.3					
PDM survival	Primary		1	4	4	240.0	3.27	13.1	−43	−29			2
(± wing)	Secondary		1	4	4		3.27	13.1			−42.0	−34	
SDM survival	Primary		1	2	2	88.7	8.84	17.7	−29	−15	−34.0	−26	4
(± wing)	Secondary		1	4	4	153.0	5.12	20.5					
Diode tray, 2 strings	Plus wing		1	10	10	14.9	2.10	21.0	−43	−29	−42.0	−34	4
of 5 per ± wing	Minus wing		1	10	10	14.9	21.0	21.0			−42.0	−34	4
Battery Bay 2	Primary				6		40.0	240.0	−2 to 1	−1 to 3	−19 to −17	−18 to −16	
Type 44	Secondary								−8 to 5	−7 to −3	−22 to −21	−22 to −19	
Battery Bay 3	Primary				6		40.0	240.0	−2 to 1	−1 to 3	−19 to −17	−19 to −16	
Type 44	Secondary								−8 to 5	−7 to −3	−22 to −21	−22 to −19	
Battery Bay 2	Primary				6		40.0	240.0	−2 to 0	−2 to 2	−19 to −18	−19 to −17	
NiH$_2$	Secondary								−5 to −3	−4 to −1	−21 to −19	−20 to −18	
Battery Bay 3	Primary				6		40.0	240.0	−2 to 0	−2 to 2	−19 to −18	−19 to −17	
NiH$_2$	Secondary								−5 to −3	−4 to −1	−21 to −19	−20 to −18	

[a]Heater strip has dual heaters (primary and secondary).

Bay 1

The DF 224 computer, data management unit (DMU), and one of the two gimbal-electronics assemblies (GEA) are located in Bay 1. The DMU is mounted on the door, and both the computer and GEA are mounted on the tunnel structure. Figure 3.31 shows the location of components and monitors in Bay 1. A summary of the thermal characteristics of Bay 1 follows in Table 3.3.

Bays 2 and 3

Nickel-hydrogen batteries, charge current controllers (CCC), one of the four data interface units (DIU), and two oscillators are located in Bays 2 and 3. One NiH_2 battery module, which contains three NiH_2 batteries, is located in Bay 2 and one module is in Bay 3. Each module is mounted on the inner door surface, which has an aluminum plate (3 mm) bonded to the surface. Three CCCs are mounted on the tunnel structure in both Bays 2 and 3. The two oscillators are mounted on the tunnel structure in Bay 2, and the DIU is mounted on the tunnel structure in Bay 3. Figure 3.32 presents the location of components and monitors in Bay 2. A summary of the thermal characteristics of the battery bays follows in Table 3.4.
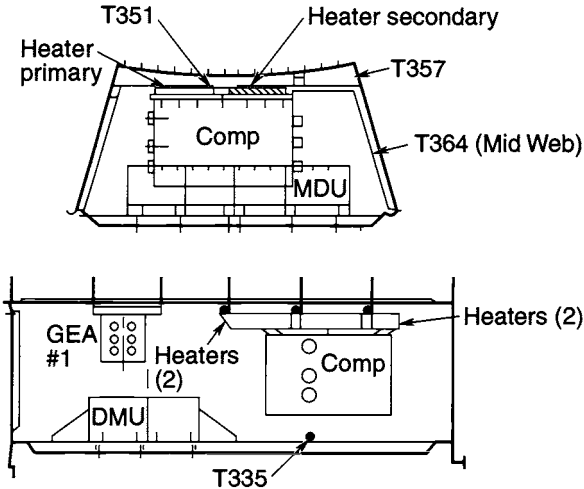
Fig. 3.31. SSM equipment section, Bay 1.

Table 3.3. Thermal Characteristics of the System-Support-Module Equipment Section (Bay 1)

Door: Silvered Teflon Radiator/Multilayer Insulation (MLI)	
Teflon (%)	MLI (%)
100	0

Thermostats

The two primary thermostats are wired in series, as are the two secondary.

Set points	Open (°C)	Close (°C)
Primary	−9 to −6	−9 ± 1
Secondary	−12 to −9	−12 ± −1

Heater System

The two primary heaters are wired in parallel, as are the two secondary heaters. There are four strips, each at 15.46 W at 28 V; therefore, primary heaters and secondary heaters can supply a total of 30.9 W. These heaters are located at the computer mounting structure.

	Temperature Limits	
	Operating (°C)	Nonoperating (°C)
DF 224 Computer	−18/49	−54/57
DMU	−40/35	−50/55
GEA	−29/60	−43/60
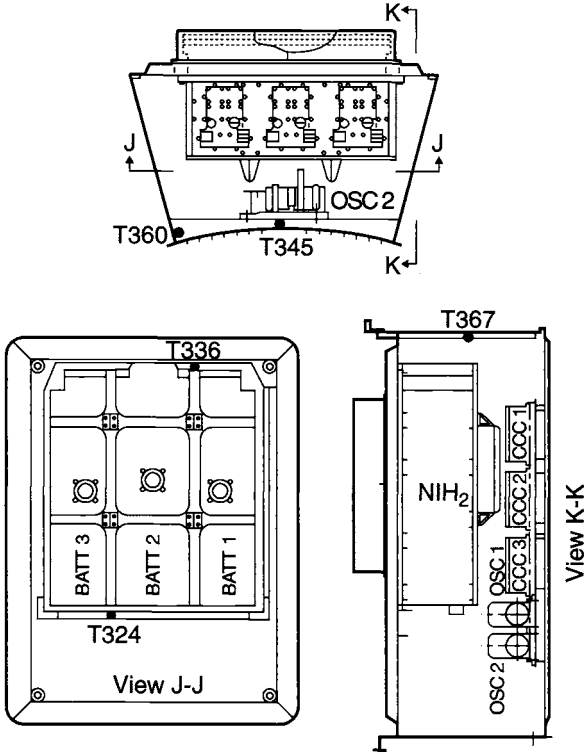
Fig. 3.32. SSM equipment section, Bay 2.

Table 3.4. Thermal Characteristics of the System-Support-Module Equipment Section (Bays 2 and 3)

Door: Silvered Teflon Radiator/Multilayer Insulation (MLI)

	Teflon (%)	MLI (%)
Bay 2	63	37
Bay 3	69	31

Thermostats

Each battery has primary and secondary thermostats located on cells 8 and 10.

Set points	Open (°C)	Close (°C)
Primary	−2 to 2	−2 to 0
Secondary	−4 to −1	−5 to −3

Heater System

Individual primary and secondary heater patches are located on each battery-cell sleeve, within each battery. Both heater sets are wired in parallel. Battery primary and secondary heaters are rated at 40 W each. Total power for six battery primary heaters is 240 W. Similarly, total power is 240 W for the six secondary heaters. A schematic for these heaters is shown in Fig.3.33.

| | Temperature Limits | |
	Operating (°C)	Nonoperating (°C)
Batteries (NiH_2)	−5/20	−20/38
Clk Osc Inner	62.5/67	−60/45
DIU #2	−40/60	−40/60
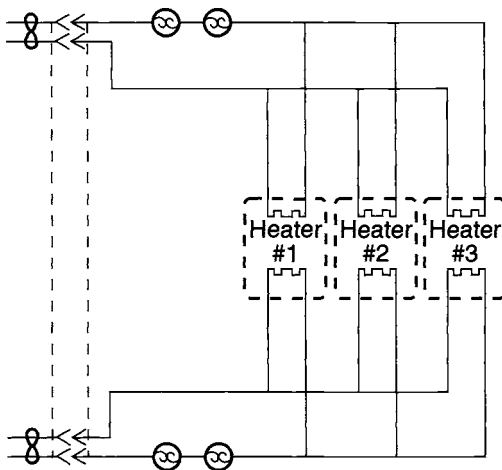
Fig. 3.33. Battery heaters.

Bays 7 and 8

Bay 7 contains the solar-array-drive electronics (SADE), deployment-control electronics (DCE), one of the four DIUs, one of the two gimbal-electronics assemblies (GEA), and the mechanism control unit (MCU). The two SADEs, DCE, and GEA are mounted on the inner door surface. The MCU and DIU are mounted on the tunnel structure. Bay 8 contains the instrument control unit (ICU), retrieval mode gyro assembly (RMGA), pointing and safemode electronics assembly (PSEA), magnet torque electronics (MTE), and one of the three tape recorders (T/R). The ICU is mounted on the inner door surface. The RMGA, PSEA, MTE (monitors located internally to the PSEA), and T/R are mounted on the tunnel structure. Figures 3.34 and 3.35 present the location of components and monitors in Bays 7 and 8. A summary of the thermal characteristics of Bays 7 and 8 follows in Table 3.5.
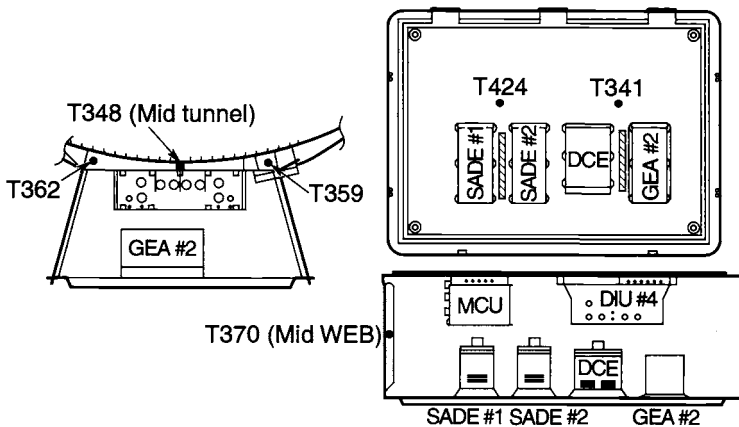
Fig. 3.34. SSM equipment section, Bay 7.
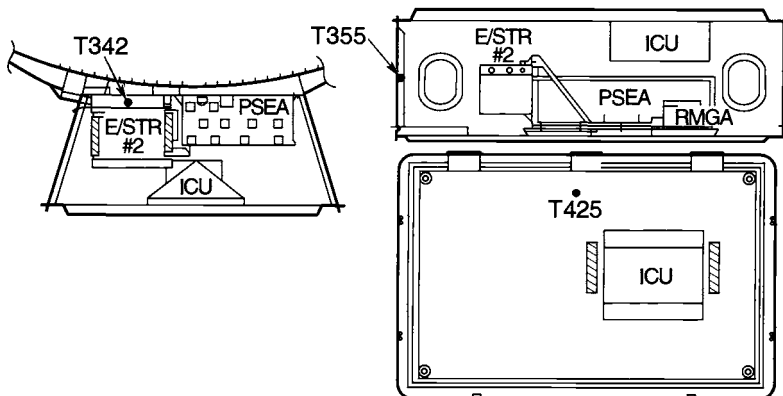

Fig. 3.35. SSM equipment section, Bay 8.

Table 3.5. Thermal Characteristics of the System-Support-Module Equipment Section (Bays 7 and 8)

	Door: Silvered Teflon Radiator/Multilayer Insulation (MLI)	
	Teflon (%)	MLI (%)
Bay 7	0	100
Bay 8	0	100

Thermostats		
The two primary thermostats are wired in series, as are the two secondary.		

Set points	Open (°C)	Close (°C)
Bay 7: Primary (door)	−14 to −11	−14 ±1
Secondary (door)	−16 to −13	−16 ± 1
Bay 8: Primary (door)	−12 ± 3	−21 ± 3
Secondary (door)	−18 ± 3	−26 ± 3
Primary (T/R)	−4 to −1	−4 ± 1
Secondary (T/R)	−7 to −3	−7 ± 1

Heater System	
Bay 7	The two primary heaters are wired in parallel, as are the two secondary. Primary and secondary heaters are bonded onto a single strip. One heater strip is placed on the door between the two SADEs and the other strip between the DCE and GEA. Primary and secondary heaters are rated at 10.32 W each. Total primary heater power is 20.6 W; the same for secondary.
Bay 8: Tray	The two primary heaters are wired in parallel, as are the two secondary. Primary and secondary heaters are bonded onto a single strip. The two heater strips are placed on the door on opposite sides (along the V1 axis) of the ICU. Primary and secondary heaters are rated at 10.32 W each. Total primary heater power is 20.56 W; the same is true for the secondary.
Tape recorder	Primary heaters are wired in parallel, as are the secondary. Primary and secondary heaters are bonded onto a single strip. Two strips are placed on the mounting bracket adjacent to the tape recorder. Primary and secondary heaters are rated at 7.73 W each. Total Bay 8 tape-recorder primary-heater power is 15.5 W; the same is true for the secondary.

Temperature Limits		
	Operating (°C)	Nonoperating (°C)
Bay 7: DIU #4	−40/60	−40/60
SADE	−34/60	−34/60
DCE	−34/60	−34/60
GEA	−29/60	−43/60
MCU	−40/60	−60/60
Bay 8: PSEA	−12/54	−12/54
Tape recorder	−12/43	−40/43
ICU	−30/60	−60/60

Tunnel Structure

The six temperature sensors on the tunnel structure are isolated from the bays by the internal MLI blankets and will not respond rapidly to local power-level changes. Each of the sensors is placed approximately in the center of its panel. Figure 3.36 presents the location of the six thermistors on the tunnel structure.

SSM Equipment Section Forward and Aft Bulkhead Structure

The equipment section forward bulkhead and aft bulkhead structures are covered with MLI on both forward and aft surfaces. The forward bulkhead external MLI is identical to the light-shield and forward-shell MLI, with an outer layer of aluminized Teflon. An exception is the area covered by the optical-telescope equipment section, which has an outer layer of double-aluminized Kapton (DAK). Both the forward and aft bulkhead MLI within the equipment section have outer layers of DAK. The aft bulkhead MLI outer surfaces facing the aft shroud components have an outer layer of black Kapton for straylight control. Figure 3.37 presents the locations of the six sensors on the forward bulkhead and the five sensors on the aft bulkhead. These are generally located close to the center of the bay. There are six additional sensors on the aft bulkhead to monitor the axial and tangential links to the equipment-section side of the telescope.

The Optical-Telescope-Assembly Equipment Section

The electronics of the optical-telescope assembly (OTA) are mounted in an equipment section. It consists of several compartments forming a section of a ring around

Fig. 3.36. SSM equipment section tunnel-structure thermistors.

the forward shell, just forward of the support-system-module equipment section, as shown in Fig. 3.27. This OTA equipment section, shown in Fig. 3.38, consists of nine bays. The following list identifies their contents.

- Bay A: Empty
- Bay B: Data interface unit 1 (DIU 1)
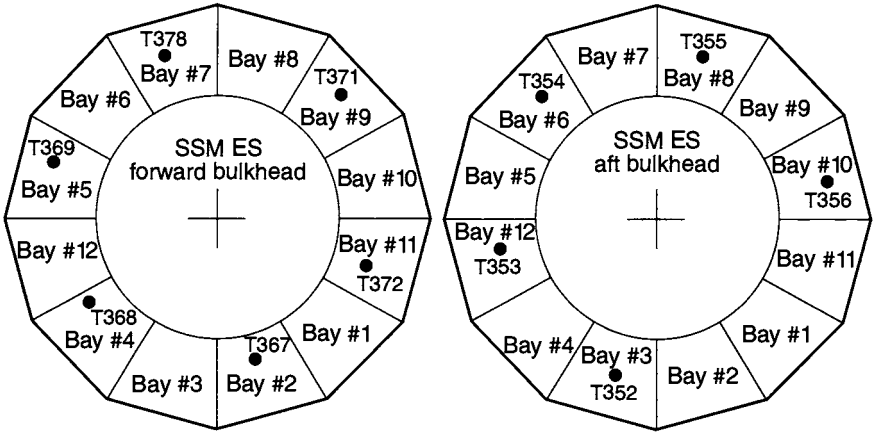
Fig. 3.37. SSM equipment-section bulkhead thermistors.
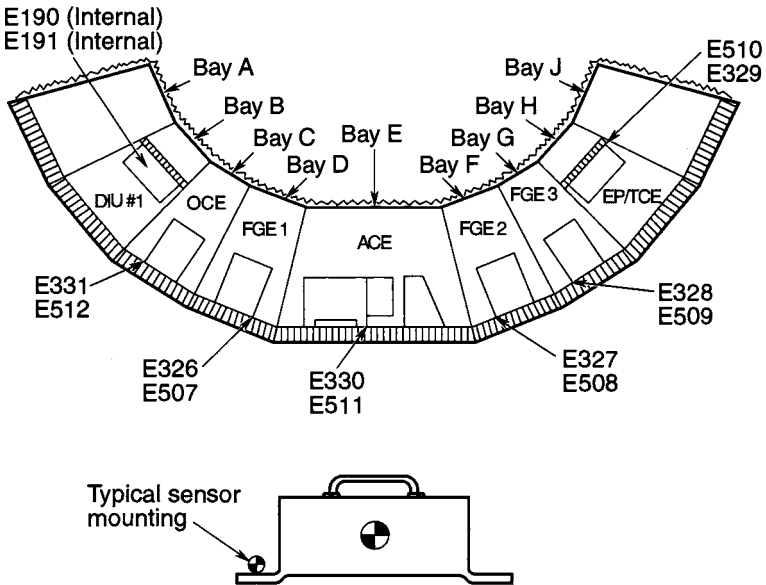
Fig. 3.38. OTA equipment section.

- Bay C: Optical control electronics (OCE)
- Bay D: Fine guidance electronics 1 (FGE 1)
- Bay E: Actuator control electronics (ACE)
- Bay F: Fine guidance electronics 2 (FGE 2)
- Bay G: Fine guidance electronics 3 (FGE 3)
- Bay H: Electrical power/thermal-control electronics (EP/TCE)
- Bay J: Empty

The environment of the OTA equipment section is cold because the section, located on the bottom of the vehicle, is shielded from direct solar in all normal vehicle orientations.

The OTA equipment section makes use of active thermal-control designs (heaters and thermostats) as well as passive ones (MLI and surface finishes). Figure 3.39 presents the MLI pattern for each of the bay doors. The three FGE bays and the OCE bay have heaters. The DIU and EP/TCE bays do not have heaters because they are always operating and do not drop below their minimum turn-on temperature of −40°C. The ACE bay also does not have heaters, since both the FGEs surrounding the ACE normally operate and also have their own heaters, to maintain the FGEs above their turn-on temperature. All heaters are located on the
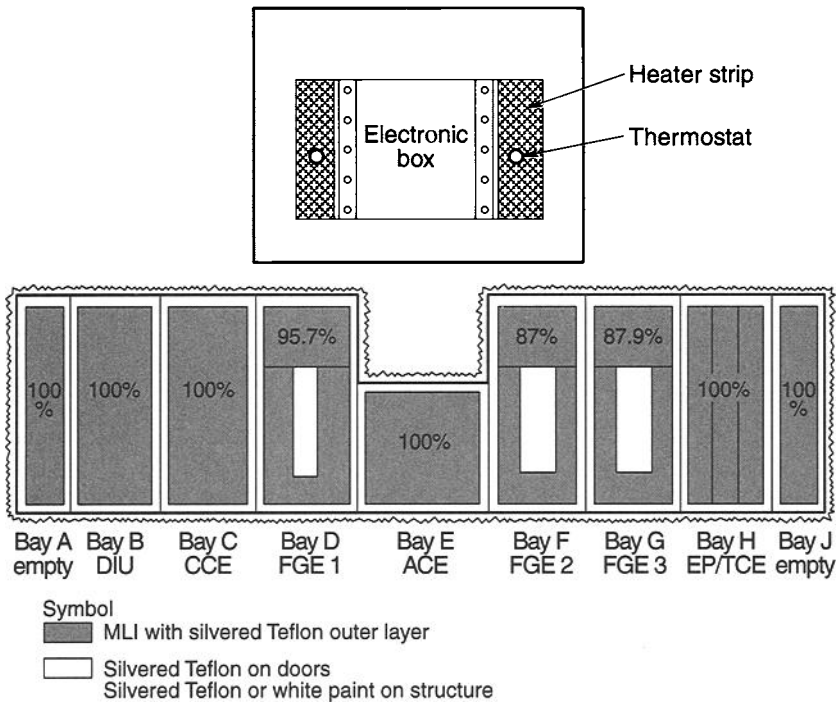
Fig. 3.39. OTA equipment-section thermal finishes.

supporting rail. Each of the boxes has two thermistors and is located internally. The heaters are required for safemode operation to maintain acceptable turn-on temperatures.

All OTA equipment-section electronics boxes are painted black except the EP/TCE, which is covered with MLI on three sides, to help retain heat. All boxes have the same temperature limits except for the DIU, which has limits as listed in Table 3.6.

The Aft Shroud

The SSM aft shroud is a 14-ft-diameter, 12-ft-long cylindrical section at the rear of the vehicle. It encloses the three fine-guidance sensors, the wide-field planetary camera, four axial scientific instruments (HSP, HRS, FOS, and FOC), the telescope focal-plane structure, and a shelf with three rate-sensing units (RSUs) and three fixed-head star trackers (FHSTs) mounted on it (see Figs. 3.27 and 3.40). The aft-shroud thermal design consists of the use of silvered Teflon on all external

Table 3.6. Thermal Characteristics of the Optical-Telescope-Assembly Equipment Section

| Surface Properties		
$\varepsilon > 0.85$, except EP/TCE has MLI on three sides.		
Minimum Turn-on (°C)		
−40		
Thermostats		
The two primary thermostats are wired in series, and the two heaters are wired in parallel.		
Set points	Open (°C)	Close (°C)
Primary	−28.9	−40
Secondary	−28.9	−40
Heater System		
Each of the two heater strips per box contains both a primary and a secondary heater.		
Heater Powers		
Box	Primary Heater @ 28V (W)	Secondary Heater @ 28V (W)
OCE	4.9	4.96
FGE 1	49.6	49.3
FGE 2	44.3	43.8
FGE 3	35.6	35.2
Temperature Limits		
	Operating (°C)	Nonoperating (°C)
DIU	−40/38	−40/60
All other	−23/35	−55/85
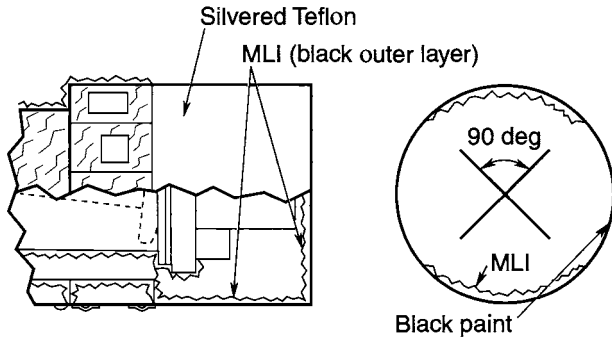
Fig. 3.40. Aft-shroud thermal finishes.

surfaces except for the FHST light shades and the astronaut handrails. All internal surfaces are black for straylight control. The internal top and bottom 90-deg cylindrical sections, as well as the entire internal aft bulkhead, are covered with black Kapton outer-layer MLI blankets. The side 90-deg surfaces are not covered with MLI and are used as radiators to reject heat from the internal instruments to space. These surfaces have black radiation shields on the inside face to control radiative couplings to the internal instruments.

The thermal interface between the aft shroud and the scientific instruments was difficult to establish and verify. Effective sink temperatures were established as the means by which this thermal interface could allow the instrument contractors to perform their analyses, develop their designs, and proceed with testing. These sink temperatures allowed the instrument to interface with the aft shroud by using only three temperatures instead of the actual radiation couplings to the hundreds of nodes in the shroud. The sink temperatures were calculated using the complete math-model radiation couplings and all the temperatures in the aft shroud. Unfortunately, flight-temperature monitors are not located on all the node points used for the sink-temperature calculations. Accordingly, an algorithm was constructed that weighted the node points that had flight sensors.

The Optical-Telescope Assembly

The optical-telescope assembly (OTA) is the primary payload and consists of a number of components, including the optics, their support structure, baffles, electronics, and the scientific instruments at the focal plane, as shown in Fig. 3.41. This entire assembly attaches to the SSM equipment section and is enclosed by the light shield, forward shell, aperture door, and aft shroud (Fig. 3.27), which act as a thermal "cocoon" to isolate the telescope assembly from the thermal variations of the external environment.

The dominant requirements that drove the thermal design of the telescope assembly were both the .003 arc-sec (rms) pointing stability over a 24-h period and the need to maintain optical wave-front performance better than $\lambda/20$ (rms). This optical requirement places strict limits on thermomechanical distortions of the
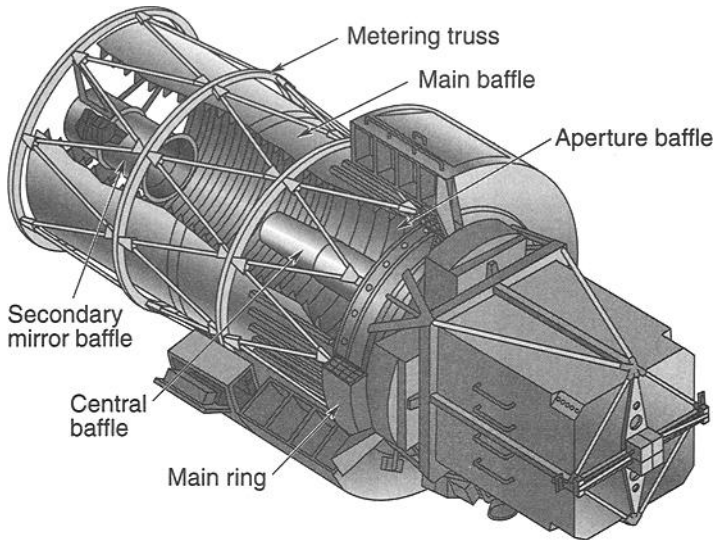
Fig. 3.41. Optical-telescope assembly.

optical mirrors and their supporting structure. These distortion limitations, in turn, call for very tight control of temperatures and temperature gradients.

The thermal design approach selected to meet these requirements was to insulate most structures with MLI or low-emittance surface finishes, provide conductive isolation at mechanical attachments, and use a large number of small heaters with very small deadbands to maintain temperatures at precisely 21.1°C. The following sections describe the thermal design of each of the telescope components shown in Fig. 3.41.

The Main Ring

The main ring is the OTA's primary structural member. All other telescope components are attached to it, and it, in turn, attaches the telescope assembly to the SSM at the SSM equipment section through three tangential and three axial links. Ring temperatures are controlled using 36 heaters with a set point of 21.1°C and a control band of only 0.1°C, as shown in Figs. 3.42 and 3.43. Heater powers and the effects of surrounding temperature variations are minimized by wrapping the entire ring and the ring-to-SSM attachment links in MLI with an $\varepsilon^* < .01$, and by limiting the conductance at all of the attach points shown in Fig. 3.42 to very small values, using low-conductivity materials where required. Also, a number of cables pass through or are attached to the ring. Thermal interactions with these cables are minimized by wrapping them in MLI or low-emittance gold tape and attaching them to the ring with low-conductance standoffs. A total of 23 flight-temperature sensors are on the ring.

O Metering truss
O Main baffle
☆ #16 baffle
☐ FPS bipods
△ Reaction plate
☉ SSM and PM axial
◇ SSM tangential
◑ PM tangential

Heater, typical 36 places
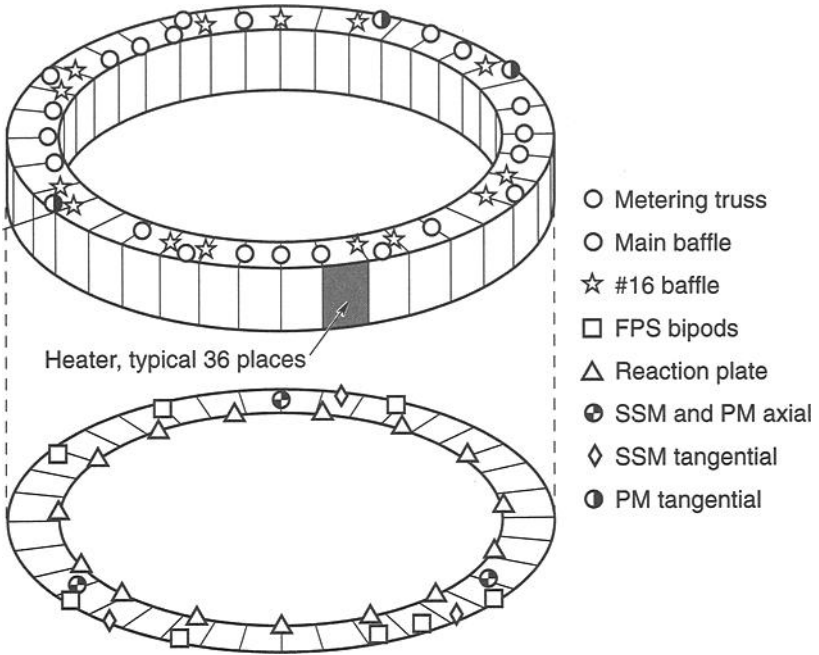
Fig. 3.42. OTA main-ring mounting points and heaters.

Controller

As close as possible

As close to heater zone centerline as possible

Sensor location

Sensor

<2.5 mm

Cut-out
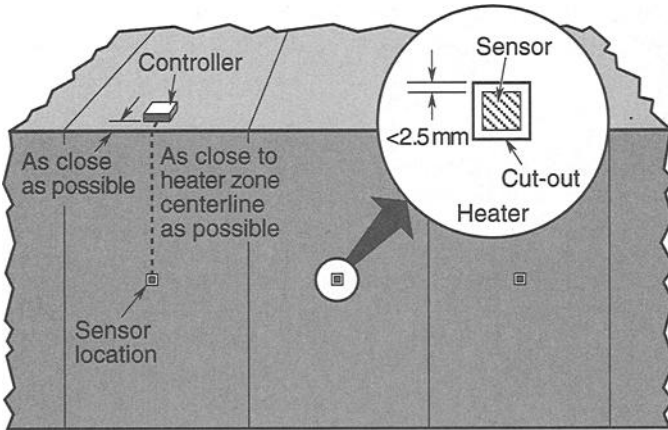
Heater

Fig. 3.43. OTA main-ring heater detail.

The Primary-Mirror Assembly

The primary-mirror assembly (see Fig. 3.44) consists of the primary mirror, the reaction plate, the mirror-to-reaction-plate mounts, and the mirror-figure control actuators. Mirror-figure distortion and mirror displacement relative to the main ring brought about by thermomechanical effects are the principal drivers in the thermal design. The design approach is to provide radiative isolation by wrapping the entire assembly in MLI ($\varepsilon^* < .01$) except for the front face of the mirror, which has a very low emittance of .01 to .03. (A value of .02 was used for design, .03 for heater sizing.) The assembly is radiatively isolated from the baffle that passes through the central hole (see Fig. 3.45) by gold tape or MLI and a guard heater.
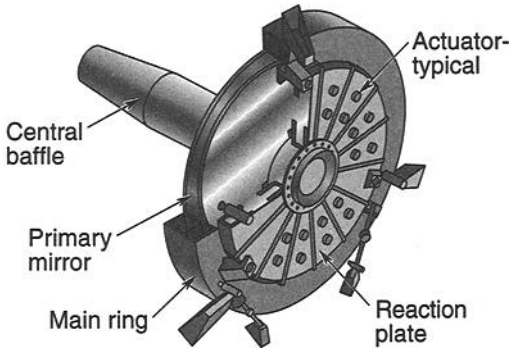
Fig. 3.44. Primary-mirror assembly.
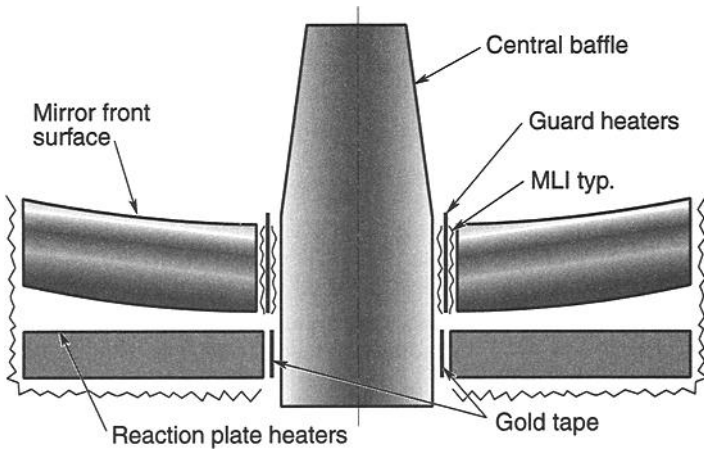
Fig. 3.45. Primary-mirror assembly central baffle.

The guard heater system, shown in detail in Fig. 3.46, reduces heat flow through the MLI by maintaining a very small ΔT between the mirror and the guard-heater plates. This effectively shields the mirror MLI from seeing the central baffle, which can get very cold as a result of its radiative view to space through the telescope aperture. MLI between the guard-heater plate and the control baffle reduces the heater power required to drive the guard-plate heaters. Conduction heat losses to the main ring and central baffle are controlled by designing low-conductance mountings between the reaction plate and the main ring, and between the reaction plate and the central baffle.

The front of the reaction plate and the rear of the mirror are both high-emittance, and they form a radiant-interchange cavity. Temperatures of both are maintained by 36 precision-controlled heaters (Table 3.7), with set points of 21.1°C and differentials of 0.1°C, mounted to the reaction plate, as shown in Fig. 3.47. Heat from the reaction plate is then radiated to the mirror. Because of the high emittance of the mirror's back face and very low emittance of its front face, its temperature follows that of the reaction plate and is not strongly influenced by the view to deep space or to the telescope enclosure. During extended nonoperating periods, the 36 precision heaters are turned off, and 18 backup heaters on thermostats (10 to 20°C dead band)
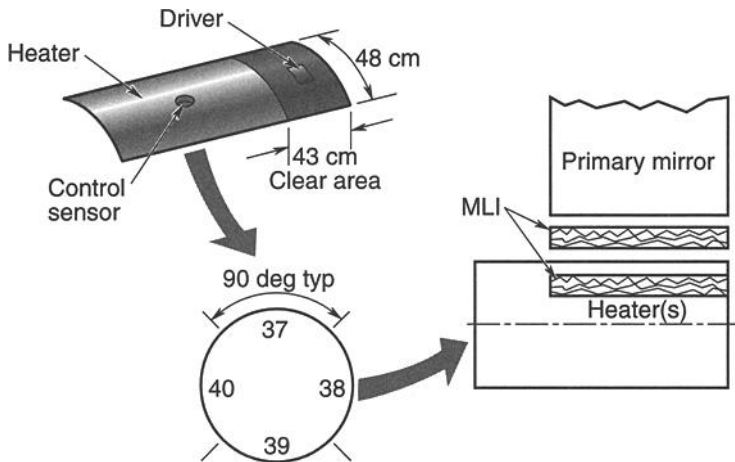
Fig. 3.46. Central baffle guard heater.

Table 3.7. OTA Primary-Mirror Assembly Heater-System Powers

	Heater Size	
Heater No.	Power (W)	Area (cm^2)
1–6	2.0 each	45 each
7–21	1.2 each	116 each
22–36	1.2 each	116 each

	Heating sizing power (W)	
Heater no.	Total	Clear area (cm^2)
1 – 6	2.0/heater	45/heater
7 – 21	1.2/heater	116/heater
22 – 36	1.2/heater	116/heater

Typical heater/driver/control
sensor relationship
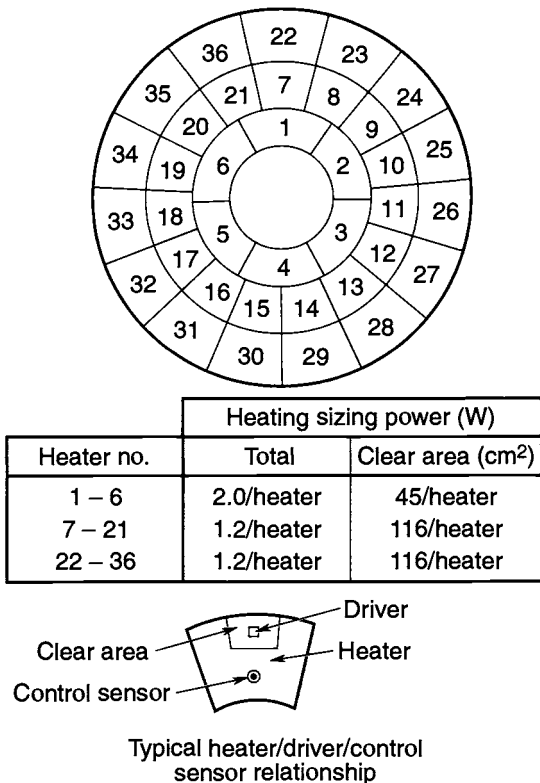
Fig. 3.47. Mirror reaction-plate heaters.

are turned on. To minimize the radiative effects of the 36 figure-control actuators and the three axial links, they are covered with MLI or low-emittance finishes. Contact conductances between the mirror and the actuators and axial links are minimized.

Baffle Assemblies

Three baffle assemblies are required for telescope straylight control, as shown in Fig. 3.41: the main baffle assembly, the central baffle assembly, and the secondary-mirror baffle assembly. The main baffle is the large cylinder extending forward from the main ring just inside the metering-truss assembly. The central baffle extends from the mirror reaction plate forward through the hole in the center of the mirror. The secondary-mirror baffle extends rearward from the secondary-mirror assembly in the front end of the telescope.

The thermal designs of all of the baffles are passive. The principal concern in these designs is to provide adequate conductive isolation between the baffles and the structure to which they are mounted, so that they will not act as fins, carrying energy away from a temperature-controlled structure. Also of concern is the need to prevent baffle excursion into the telescope optical path as a result of thermal

deformation and radiant-sink temperature requirements of critical components viewing the baffles.

The interior surface of the main baffle must be painted black for optical stray-light control. The exterior surface is covered with MLI to minimize the radiative influences of the surroundings. Conductive isolation is provided where the main baffle mounts to the main ring to avoid upsetting the thermal balance of the ring. The only significant thermal couplings for the main baffle are to the light shield and to the external environment by radiation out the telescope aperture. Main-baffle temperatures are therefore driven by the external environments.

Both the interior and exterior surfaces of the central baffle must be painted black for straylight control. Low-conductance mounts are provided where the central baffle attaches to the mirror plate to avoid upsetting the reaction-plate thermal balance. The temperature of the central baffle is therefore driven by its radiative couplings to the main baffle and forward shield, and to the external environment through the telescope aperture.

The secondary-mirror baffle also must be painted black on both inside and outside surfaces for optical reasons. This baffle is not, however, conductively isolated from the secondary-mirror housing. Its temperature, therefore, is the result of conductive coupling to the secondary-mirror housing and radiative couplings to the main baffle, forward shield, aperture door, and the external environment.

Metering-Truss Assembly

The metering truss must precisely maintain the position of the secondary-mirror assembly with respect to the primary mirror during telescope operations. The truss is constructed of graphite epoxy ring and strut members, with four spider legs to hold the secondary-mirror assembly, as shown in Fig. 3.48. Limits on truss temperatures
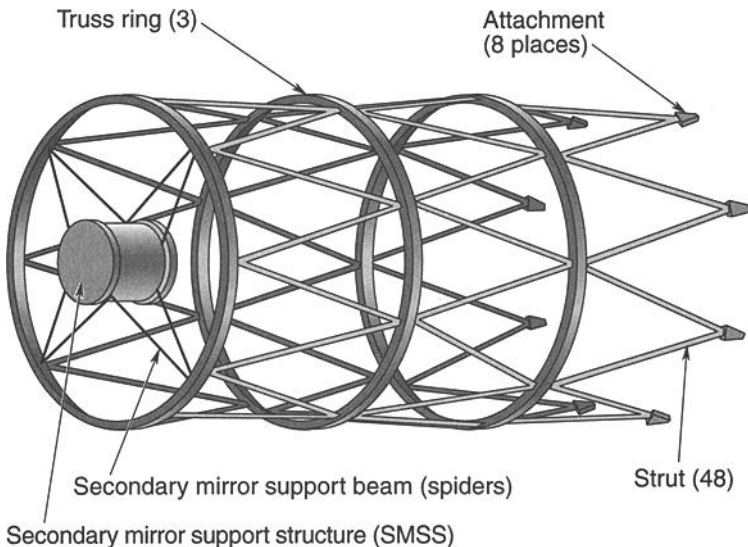
Fig. 3.48. OTA metering truss.

and temperature gradients are based on despace, decenter, and tilt as a result of thermostructural distortions.

The entire metering truss, except for the spider mounts, is covered with MLI blankets, as shown in Fig. 3.49. In addition, the entire truss assembly sits between the MLI blankets on the outside of the main baffle and the low-emittance internal surface of the forward shell, which provides further isolation. The truss is bolted to the main ring at eight places without any special thermal isolation. The spider mounts have a high absorptance for straylight control and a low emittance to minimize heat loss. All temperature and temperature-gradient requirements are met with this passive design.

Secondary-Mirror Assembly

Thermostructural deformation of the secondary mirror and displacement of the mirror relative to the metering truss drive the temperature and temperature-gradient limits for the secondary-mirror assembly. The thermal design approach is to surround the secondary mirror with three precision-heater-controlled plates (shown in Fig. 3.50) that act as a constant-temperature (21±0.1°C) enclosure for the
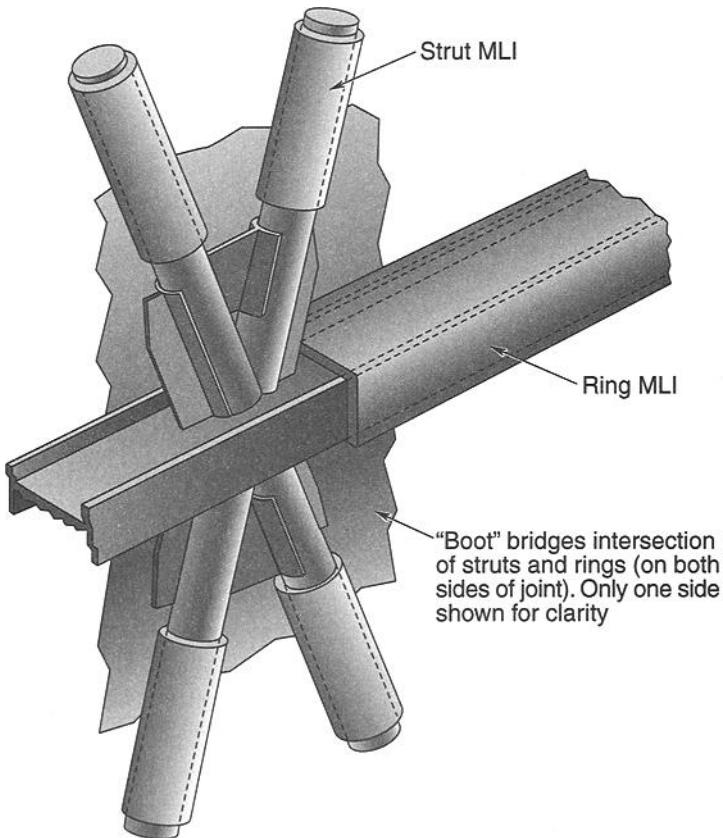
Fig. 3.49. Metering-truss detail.
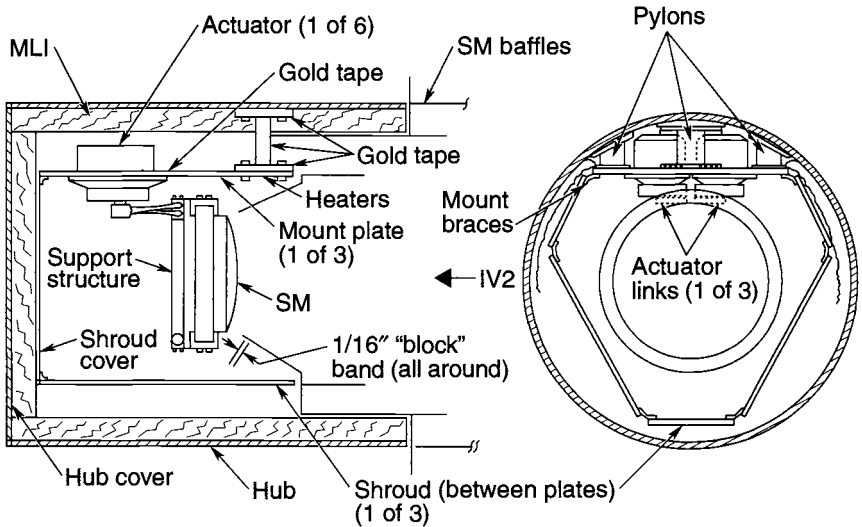
Fig. 3.50. Secondary-mirror assembly.

mirror and as a mounting surface for the actuators that control mirror position. The inside surfaces of these plates have a high emittance to ensure good radiation coupling to the back of the secondary mirror. The outside faces of these plates and the actuators mounted to them are covered with a low-emittance gold tape. Further isolation from the cylindrical hub is provided by MLI blankets and low-conductivity mounting pylons.

The secondary-mirror baffle—attached to the hub structure—extends down into the mirror cavity. The side of the baffle facing into the cavity is low-emittance to minimize the effects of its wide temperature swings on cavity temperatures. The side facing the optical path is painted black for straylight control and therefore is high-emittance. The low-emittance finish on the front of the secondary mirror, however, minimizes its radiative coupling to the baffle. The graphite epoxy/invar mirror support structure also has a low-emittance finish to decouple it somewhat from even the small temperature variation ($\pm0.1°C$) of the heater-controlled plates.

Focal-Plane Assembly

The focal-plane assembly, shown in Fig. 3.51, consists of the focal-plane structure, axial and radial scientific instruments, fine guidance-system sensors, and an equipment shelf to which the FHST and RSUs are mounted. This entire assembly is located behind the primary-mirror assembly and is attached to the telescope main ring.

The thermal design strategy of the focal-plane assembly structure, shown in Fig. 3.52, is the same as the strategies for the other telescope structural elements, that is: place precision-controlled heaters on all structural members to control their temperature and wrap them in MLI to minimize heater power and temperature gradients. Conductive isolators are provided to limit heat loss to the scientific instruments, the equipment shelf, and the telescope aft ring. All cables leaving the focal-plane assembly structure are wrapped in MLI, and guard heaters are installed a short distance from where the cable leaves the structure, as shown in
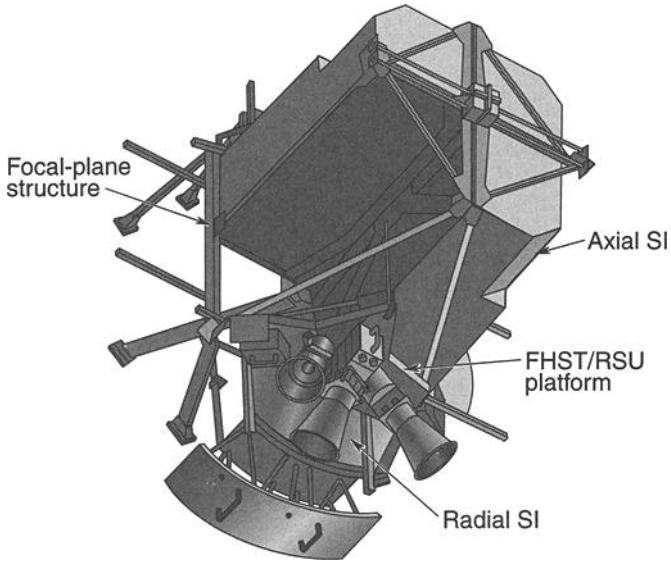
Fig. 3.51. Focal-plane assembly.
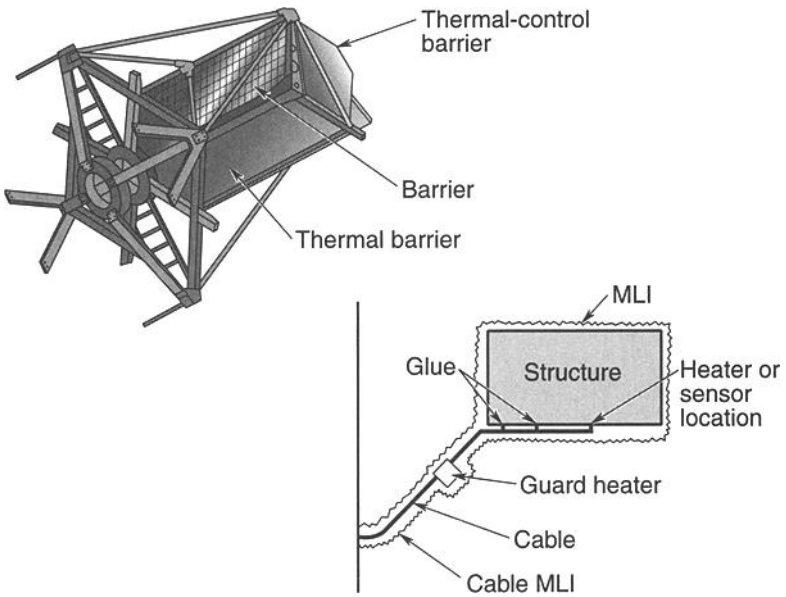
Fig. 3.52. Focal-plane assembly structure and cables.

Fig. 3.52, to ensure that the cable temperature is the same as that of the structure so that no heat transfer will occur down the cable.

The equipment shelf (shown in Fig. 3.53) is a dimensionally stable platform for mounting three FHSTs and three RSUs. The platform is attached to the focal-plane assembly structure and is thermally controlled by a passive design that can minimize changes in temperature gradients in order to meet a 3-arc-sec alignment stability for the sensors. The thermal design approach is to cover the shelf in MLI and conductively isolate it from the focal-plane assembly structure and the six sensors by the use of low-conductivity mounts. The thermal design of the shelf and sensors is shown in Fig. 3.54.

Rate-sensing unit (RSU)

Fixed-head star tracker (FHST)
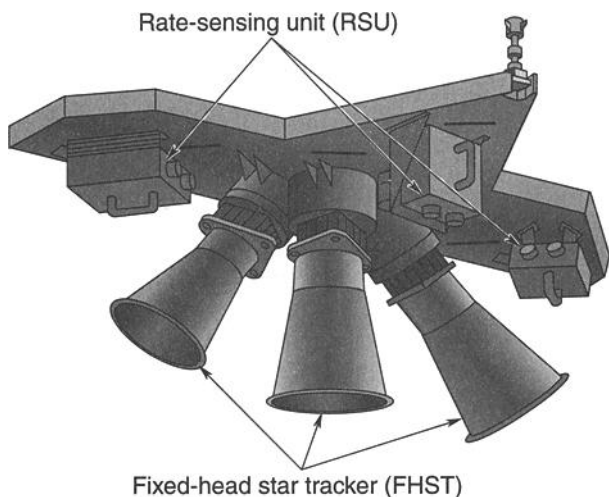
Fig. 3.53. Focal-plane assembly shelf.

FPS

Flexure (3 Plcs)

Shell

MLI

Aluminum plate

GFRP fixture

$\varepsilon^* \leq .01$ both sides and flexure (3 Plcs)

RSU

RSU 2&3

FHST

$\varepsilon \leq 0.05$

NAV base

2 units

$\varepsilon \leq 0.06$

Ti flexure

$\varepsilon \leq 0.05$

1 unit

3 units

Light shade

SSM wall
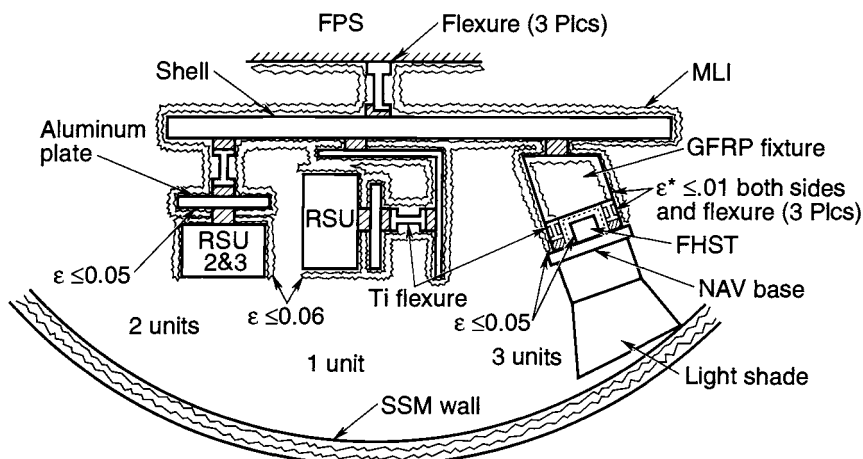
Fig. 3.54. Equipment-shelf thermal design.
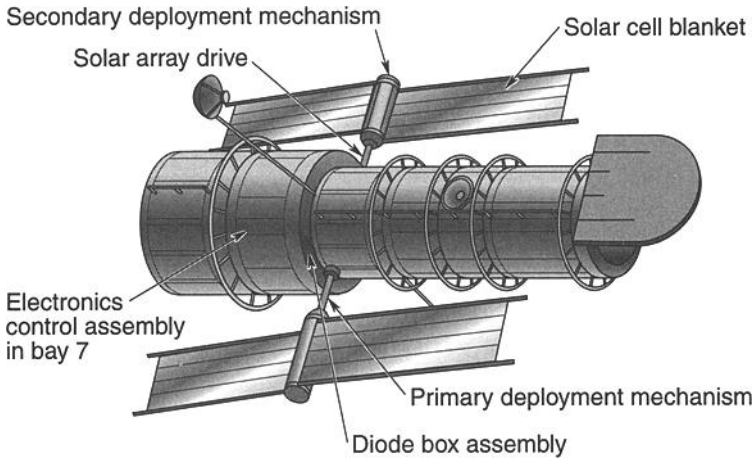
Fig. 3.55. Solar-array components.

The Solar-Array Assembly

The Hubble Space Telescope solar array (SA) was designed by British Aerospace for ESA. Six major parts make up the SA: the primary deployment mechanism (PDM), solar-array drive mechanism (SADM), secondary deployment mechanism (SDM), diode box assembly (DBA), the solar-array blanket, and the solar-array electronics (SADE and DCE) mounted in equipment section Bay 7. Figure 3.55 is a drawing of an SA assembly and its major external parts. The SA thermal design is passive after array deployment (SA heaters are used prior to SA deployment) and uses a combination of three thermal-control tapes. The SA heater systems are left enabled after deployment to protect SA components, even though the cold-case thermal analyses have shown that heaters are not required. The types and properties of the three surface-finish tapes are as follows:

- Aluminized Kapton ($\alpha/\varepsilon = .12/.04$)
- Aluminized Teflon ($\alpha/\varepsilon = .14/.62$)
- Silvered Teflon ($\alpha/\varepsilon = .07/.82$)

The general thermal design approach for the SA components has been to use the lowest emittance possible consistent with maintaining acceptable maximum temperatures, allowing for any temperature increase during motor operation. The combination of the low solar absorptance and emittance results in minimizing the effect of changes in the environment while maintaining acceptable gradients.

Primary Deployment Mechanism (PDM)

Both sides of the PDM are totally covered with aluminized Kapton. MLI is used on top of the mechanism and along the deployment arm, as shown in Fig. 3.56. The external surfaces of the MLI are 25% silvered Teflon and 75% aluminized Kapton. PDM thermal characteristics are listed in Table 3.8.
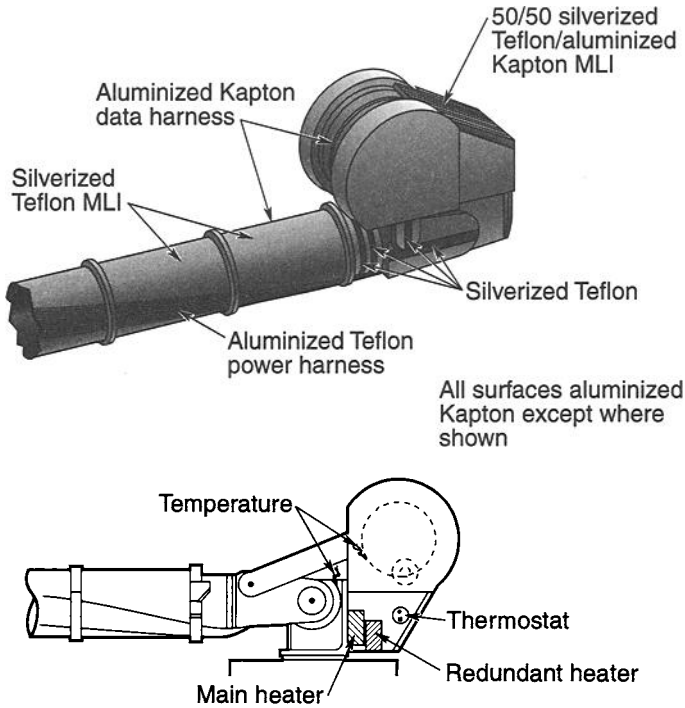
Fig. 3.56. Solar-array primary deployment mechanism.

Table 3.8. Thermal Characteristics of the Solar-Array-Assembly PDM

Surface Properties		
See Fig. 49.		

Thermostats

The two primary thermostats are wired in series, and the two heaters are wired in parallel.

Set points	Open (°C)	Close (°C)
Primary	–29	–42
Secondary	–29	–42

Heater System

Four heater strips are present per PDM, with each strip a primary and secondary heater at 3.27 W; therefore the primary heaters supply a total of 13.1 W, as do the secondary.

Temperature Limits	
Operating (°C)	Nonoperating (°C)
–43/55	–55/80

Secondary Deployment Mechanism

The thermal design of the SDM is shown in Fig. 3.57. Different combinations of aluminized Kapton, silvered Teflon, and aluminized Teflon control various elements of the SDM. The SDM heater system is configured to allow bypass of the thermostats to directly power the heaters. The heaters are bypassed prior to secondary deployment of the SAs.

During deployment, the SDMs were within their operating temperature limits of −10 to 25°C. After deployment, the SDM thermostatically controlled heaters were reinstated; the SDMs have remained within their nonoperational temperature limits of −55 to +80°C. Thermal characteristics of the SDMs are as listed in Table 3.9.

Solar-Array Drive Mechanism

The SADM function is to slew the SA assemblies so that the sun's rays are normal to the blankets. The SADMs are located on the external skin of the forward shell. MLI is used over the cover around the motor. The outer surfaces of both the MLI
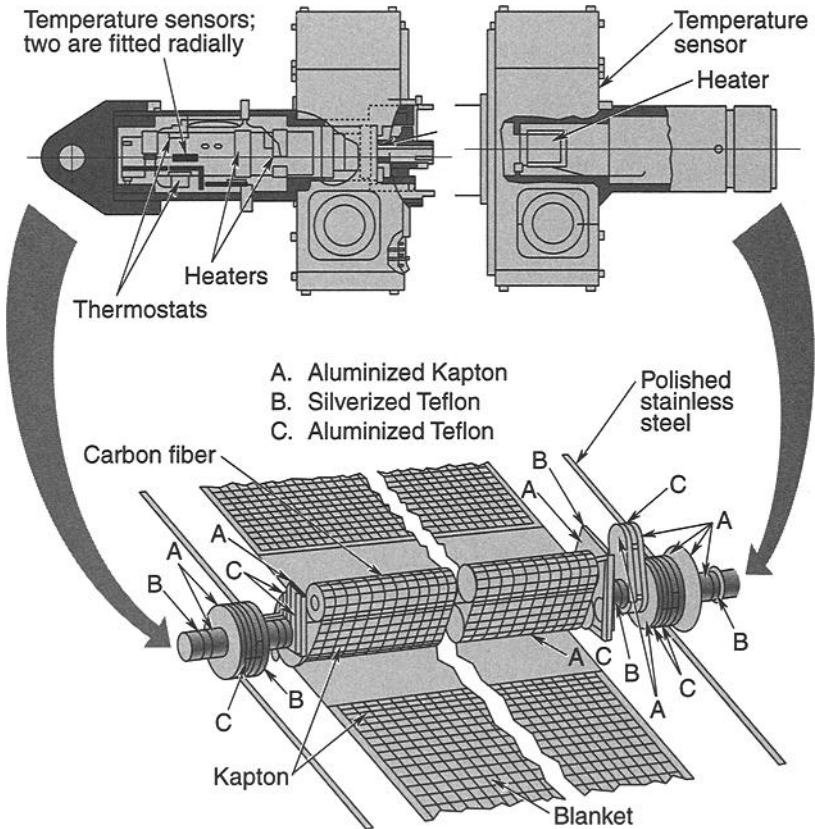

Fig. 3.57. Solar-array secondary deployment mechanism.

Table 3.9. Thermal Characteristics of the Solar-Array-Assembly SDM

Surface Properties		
See Fig. 50.		

Thermostats		
The two primary thermostats are wired in series, and the two heaters are wired in parallel.		
Set points	Open (°C)	Close (°C)
Primary	–15	–29
Secondary	–15	–29

Heater System
Six heater strips are present per SDM, two primary and four secondary, 8.84 W for each primary and 5.12 for each secondary. Therefore, the primary heaters supply a total of 17.7 W and the secondary supply 20.5 W.

Temperature Limits	
Operating (°C)	Nonoperating (°C)
SDM –10/25	–55/80

and uninsulated areas are 25% silvered Teflon and 75% aluminized Kapton. The SADM structure is thermally isolated from the support structure on the forward shell. Figure 3.58 is a drawing of the SADM. Thermal characteristics of the SADMs are listed in Table 3.10.

Solar-Array Blankets

Figure 3.58 presents a drawing of the back surface field reflector (BSFR) SA blanket. There are no heater systems on the SA blankets. The SA electrical-conversion efficiency is about 11%, which would effectively reduce the absorptance to 0.68 instead of the 0.76 shown below. Thermal characteristics of the SA blankets are given in Table 3.11.

Table 3.10. Thermal Characteristics of the Solar-Array-Assembly SADM

Thermostats		
The two primary thermostats are wired in series, and the two heaters are wired in parallel.		
Set points	Open (°C)	Close (°C)
Primary	–29	–43
Secondary	–29	–43

Heater System
Two heater strips are present per SADM and with each strip a primary and secondary heater at 6.64 W; therefore the primary heaters supply a total of 13.3 W, as do the secondary.

Temperature Limits	
Operating (°C)	Nonoperating (°C)
–43/55	–55/80

Fig. 3.58. Deployed solar array.

Solar-Array Diode Box Assembly

The two DBAs are mounted externally on the forward bulkhead of the SSM equipment section approximately 9 deg apart. The DBA brackets are conduction-isolated from the equipment-section structure. The diode plates and box-surface finishes are shown in Fig. 3.59. Thermostatically controlled heaters are mounted on the diode plates to maintain minimum temperatures prior to SA deployment. The predicted orbit-temperature range for the DBA is −20 to 93°C. No temperature monitors are on the DBA.

Table 3.11. Thermal Characteristics of the Solar-Array-Assembly Blanket

| | Surface Properties | |
	Solar cell α/ε	Rear substrate α/ε
	.76/.83 (BSFR)	.54/.90
	Temperature Limits	
	Operating (°C)	Nonoperating (°C)
SA blanket	−100/100	−105/105
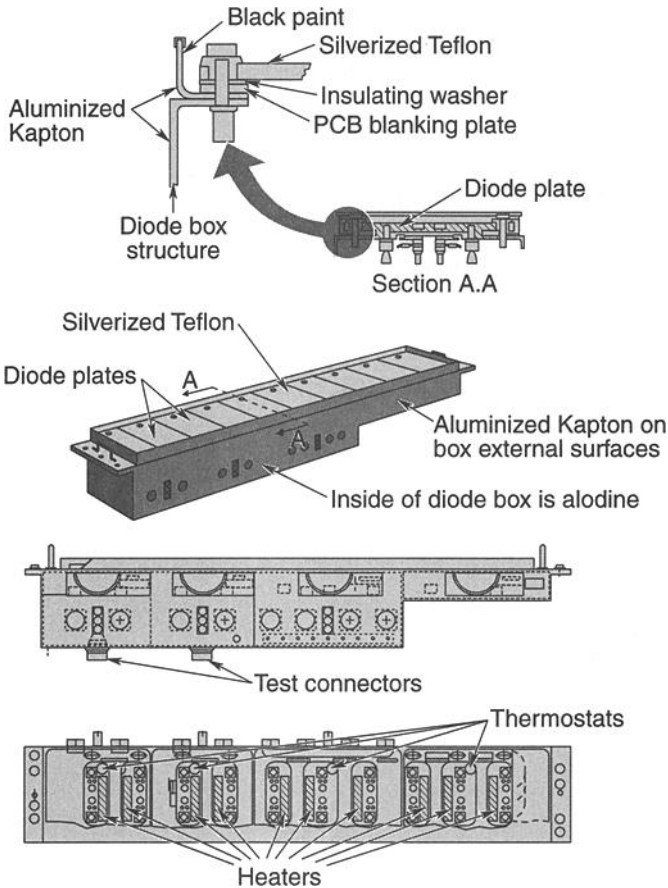
Fig. 3.59. Solar-array diode box assembly.

The External Components

The external components include the following:

- Latches and drives on the high-gain antennas, solar arrays, and aperture door (AD)
- Coarse sun sensors (CSS)
- Low-gain antennas (LGA)
- Magnetic sensing systems (MSS)
- Magnetic torquer (MT) bars
- High-gain antennas (HGA)

All of the external components have both active thermal design features (heaters and thermostats) as well as passive ones (MLI, isolators, and surface finishes), except for the MT bars, LGAs, and HGA dish, which have only passive thermal control. The solar-array mechanisms have heater systems, and the SA blankets and arm are passively controlled.

Several heater circuits control heaters for the external components. The retrieval/deployment heater circuit enables or disables all the heaters on the latches and drives (except for the AD hinge) that are used for deployment and retrieval from the space shuttle. The LS/FS heater circuit controls the AD hinge heater, the HGA two-axis-gimbal (TAG) heaters, and the MSS heaters. All the CSS heaters are on a separate circuit. The latches and drives used only for deployment and retrieval have only a single-heater system, and all the other external-component heater systems have completely redundant heater systems. The solar arrays have heater circuits for the diode boxes, SADM/PDM, SDM, and SDM retrieval/survival heaters.

Latches and Drives

Among the external components are two HGA drives, two HGA latches, two forward SA latches, two SA aft latches, one AD drive, two AD hinge systems (one passive and one active), and one AD latch located on the external shell of the vehicle. Figures 3.60 and 3.61 show the locations of these components and the associated thermistors. During deployment, all of the latches and drives were maintained above their lower operational temperature limits by heaters (a retrieval/deployment heater circuit). After deployment, this heater circuit was disabled and temperatures of the latches and drives (except for the AD drive and hinges, which are on a different heater circuit) were allowed to drop. Temperature plots indicated that each component dropped in temperature from ambient temperature just after launch and started cycling on its heater as expected.

The AD hinge heaters are always enabled, since the AD may be closed at any time. AD drive and hinge temperatures showed that the heaters are cycling properly. Thermal characteristics of the latches and drives are shown in Table 3.12.
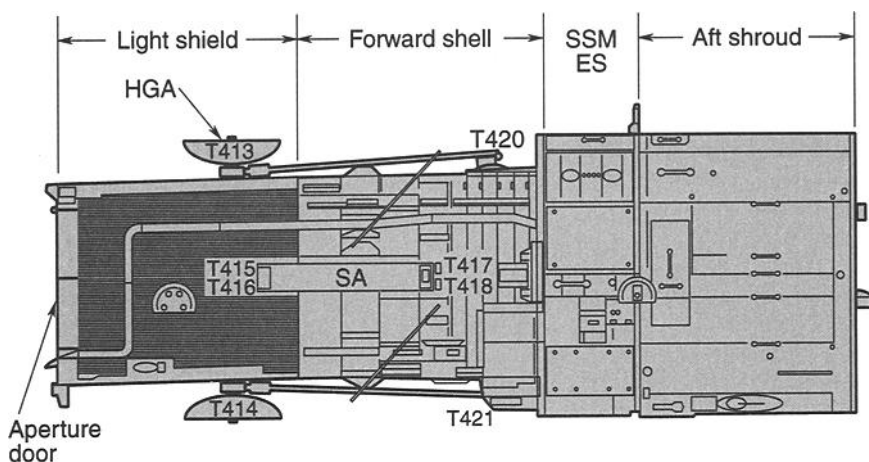
Flight Subsystem Thermistors

MSID No.	Mnemonic	Description
T413	T+HALCH	+HGA latch temp
T414	T−HGLCH	−HGA latch temp
T415	T+SAFLCH	+SA Fwd latch temp
T416	T−SAALCH	−SA Aft latch temp
T417	T−SAFLCH	−SA Fwd latch temp
T418	T−SAALCH	−SA Aft latch temp
T420	T+HGALDR	+HGA Hinge dry temp
T421	T−HGALDR	+HGA Hinge dry temp

Fig. 3.60. Latch and drive thermistors
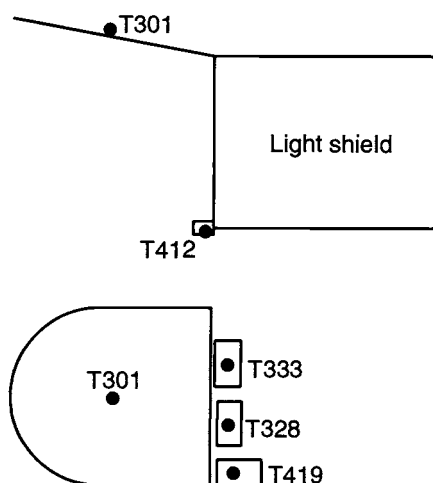
Fig. 3.61. Aperture door and coarse sun-sensor thermistors.

Table 3.12. Thermal Characteristics of Latches and Drives

	Surface Properties MLI $\alpha/\varepsilon = 0.12/0.80$	
	Thermostats The two primary thermostats are wired in series with the heater.	
	Open (°C)	Close (°C)
Set points (latch/drive)		
Primary	−23 ± 3	−32 ± 3
Set points (AD drive)		
Primary	−18 ± 3	−26 ± 3
Secondary	−23 ± 3	−32 ± 3
Set points (AD hinge)		
Primary	−42 ± 3	−51 ± 3
Secondary	−49 ± 3	−58 ± 3

Heater System
The AD drive and AD hinge system have both primary and secondary heater systems, whereas all latches and HGA drives have only primary heaters for retrieval and deployment.

Temperature Limits	
Operating (°C)	Nonoperating (°C)
−40/40	−73/40

Coarse Sun Sensors (CSS)

Five coarse sun-sensor assemblies are located on the vehicle; two at the forward end of the light shield and three on the aft bulkhead. Figure 3.62 presents a drawing

Flight subsystem monitors

MSID No.	Mnemonic	Description
G360	GCSS5T	CSS 5 Temp
G361	GSS1T	CSS 1 Temp
G362	GCSS2T	CSS 2 Temp
G363	GCSS3T	CSS 3 Temp
G364	GCSS4T	CSS 4 Temp
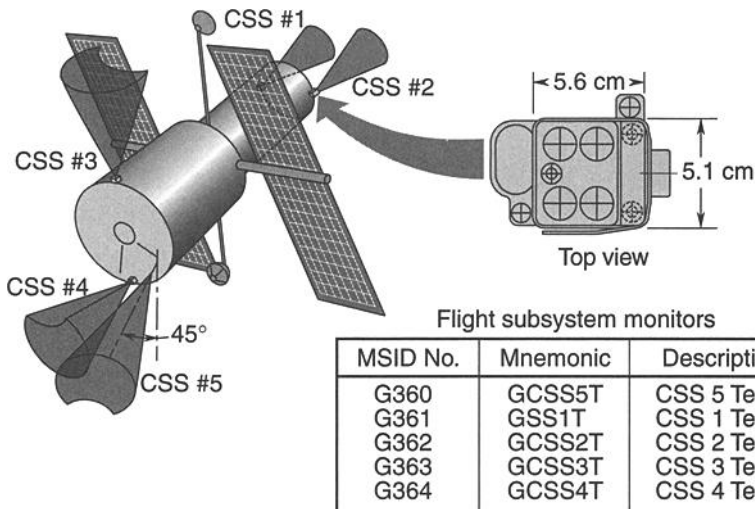
Fig. 3.62. Coarse sun-sensor locations and thermistors.

of a CSS along with the location and viewing directions of the CSSs. Thermal characteristics of the CSSs are specified in Table 3.13.

Low-Gain Antennas (LGA)

Two LGAs are located on the vehicle; one on the aft bulkhead, the other on the forward end of the light shield. Figure 3.63 is a drawing of an LGA. The predicted temperatures for the LGAs are −70.5°C for the cold case and 41.1°C for the hot

Table 3.13. Thermal Characteristics of the Coarse Sun-Sensor Assemblies

Surface Properties		
MLI $\alpha/\varepsilon = 0.12/0.80$		

Thermostats		
The two primary thermostats are wired in series with the heater.		
Set points	Open (°C)	Close (°C)
Primary	−23.3 ± 2.8	−31.7 ± 2.8
Secondary	−26.1 ± 2.8	−34.4 ± 2.8

Heater System

One heater strip is present per each CSS, with each strip containing both a primary and a secondary heater at 4.08 W. CSS 4 and CSS 5 are mounted on a common bracket and have only one heater system.

Temperature Limits	
Operating (°C)	Nonoperating (°C)
−40/38	−67/120
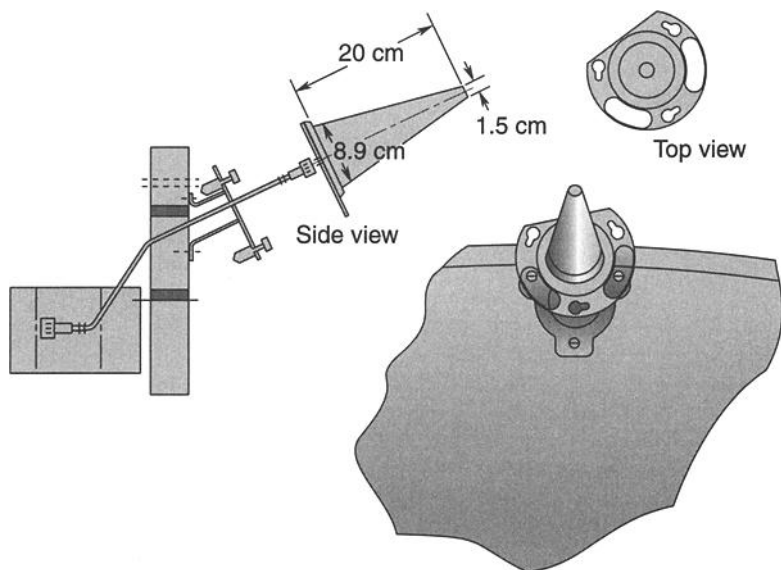
Fig. 3.63. Low-gain antenna

case. The temperature limits for the LGAs are −100 to +70°C. There are no flight thermistors located on the LGAs.

Magnetic Sensing Systems (MSS)

The two MSSs are located on the light shield near the forward end. Two small boxes make up each of the two MSSs: an electronics unit and a sensor unit, with the electronics unit containing the thermistor and heater systems. Figure 3.64 contains a drawing of an MSS and shows the location of the MSSs. Table 3.14 contains thermal characteristics of the MSSs.

Magnetic Torquer Bars

Four MT bars are mounted on the forward shell. Each bar is covered with MLI and is conduction-isolated from the forward shell by nonmetallic spacers. No heater systems for the MT bars are present. Figure 3.65 is a drawing of an MT bar, and it shows the locations of the bars relative to the vehicle. Bars 1 and 4 experience greater temperature fluctuations than bars 2 and 3. Bars 1 and 4 are located on the half of the vehicle that receives direct solar heating, whereas bars 2 and 3, located on the bottom of the vehicle, are shielded from the sun. Thermal characteristics of the MT bars are given in Table 3.15.

HGA Two-Axis Gimbals (TAG)

The HGA two-axis gimbals are located between the HGA mast and the HGA dish. The TAGs point and track the HGA dishes to the TDRSS relay satellites. There are four thermistors for each TAG. One thermistor is located near each of the TAG's bearings. Figure 3.66 depicts a TAG, and Table 3.16 contains thermal characteristics of the TAGs.
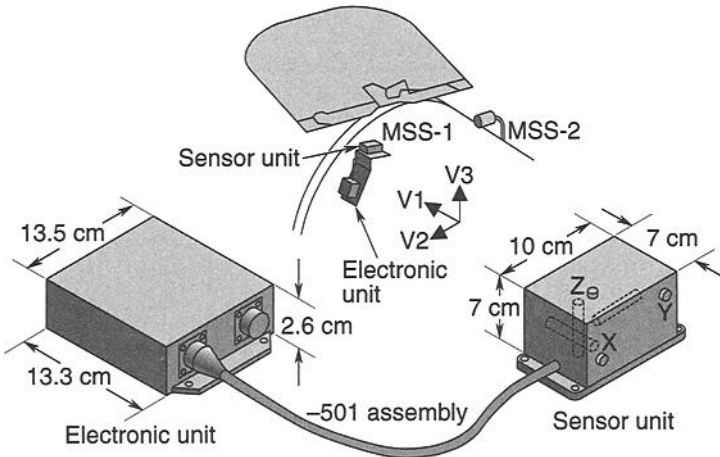
Flight subsystem monitors

MSID No.	Mnemonic	Description
G314	GMS1T	MSS-1 Temp
G318	GMS2T	MSS-2 Temp

Fig. 3.64. Magnetic sensing system.

Table 3.14. Thermal Characteristics of the Magnetic Sensing Systems

Surface Properties		
MLI α/ε = 0.12/0.80		

Thermostats

The two primary thermostats are wired in series, and the two heaters are wired in parallel.

Set points	Open (°C)	Close (°C)
Primary	−17.8 ± 2.8	−26.1 ± 2.8
Secondary	−23.3 ± 2.8	−31.7 ± 2.8

Heater System

Two heater strips are present per each MSS, with each strip containing both a primary and a secondary heater at 3.75 W. Therefore the primary heaters supply a total of 7.5 W, as do the secondary.

	Temperature Limits	
	Operating (°C)	Nonoperating (°C)
Electronics	−40/72	−55/125
Sensor	−73/72	−100/+100
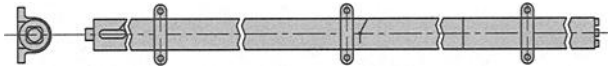
Flight Subsystem Monitors

MSID No.	Mnemonic	Description
G771	GMT1ABT	MTE 1A Bar TMP
G772	GMT1BBT	MTE 1B Bar TMP
G773	GMT2ABT	MTE 2A Bar TMP
G774	GMT2BBT	MTE 2B Bar TMP
G775	GMT3ABT	MTE 3A Bar TMP
G776	GMT3BBT	MTE 3B Bar TMP
G777	GMT4ABT	MTE 4A Bar TMP
G778	GMT4BBT	MTE 4B Bar TMP

#4   #1
#3   #2

Looking forward
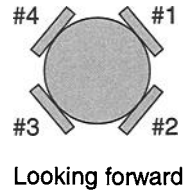
Fig. 3.65. Magnetic torquer bars.

Table 3.15. Thermal Characteristics of Magnetic Torquer Bars

Surface properties		
MLI α/ε = .12/.80		

	Temperature limits	
	Operating	Nonoperating
MT bars	-65/70°C	-65/70°C
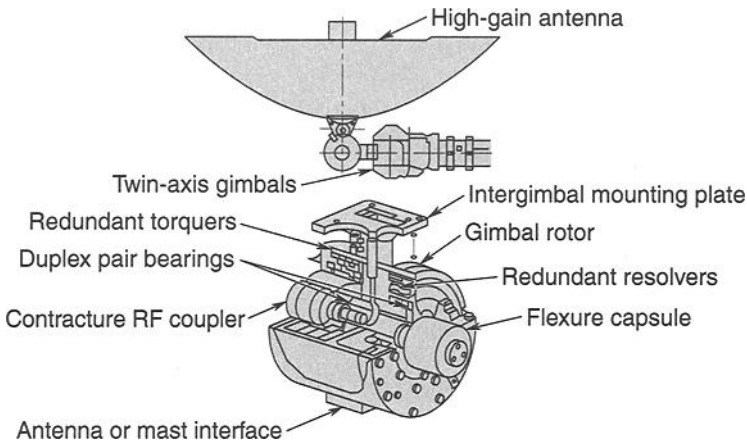
Flight subsystem monitors

MSID No.	Mnemonic	Description
H526	HG1+GXT	GEA1 + GMBL X TMP
H527	HG1+GYT	GEA1 + GMBL Y TMP
H528	HG1−GXT	GEA1 − GMBL X TMP
H529	HG1−GYT	GEA1 − GMBL Y TMP
H530	HG2+GXT	GEA2 + GMBL X TMP
H531	HG2+GYT	GEA2 + GMBL Y TMP
H532	HG2−GXT	GEA2 − GMBL X TMP
H533	HG2−GYT	GEA2 − GMBL Y TMP

Fig. 3.66. High-gain-antenna two-axis gimbal.

Table 3.16. Thermal Characteristics of the High-Gain-Antenna Two-Axis Gimbals

Surface Properties

Gold alodine $\alpha/\varepsilon = 0.23/0.05$

Thermostats

The two primary thermostats are wired in series, and the two heaters are wired in parallel.

Set points	Open (°C)	Close (°C)
Primary	18.9 to 21.7	18.9 ± 1.1
Secondary	16.1 to 18.9	16.1 ± 1.1

Heater System

Eight heater strips are present per each TAG, with each strip a primary or secondary heater at 6.88 W; therefore the primary heaters supply a total of 27.5 W, as do the secondary.

Temperature Limits

Operating (°C)	Nonoperating (°C)
−18/93	−18/93

4 Thermal Surface Finishes

D. G. Gilmore,[*] W. K. Stuckey,[*] and M. Fong[†]

Introduction

Spacecraft thermal designs employ wavelength-dependent thermal-control coatings for various purposes. Solar reflectors, such as second-surface mirrors, white paints, and silver- or aluminum-backed Teflon, are used to minimize absorbed solar energy, yet they emit energy almost as a blackbody would. To minimize both the absorbed solar energy and infrared (IR) emission, polished metal such as aluminum foil or gold plating is used. Black paint is commonly utilized on the interior of the vehicle, to facilitate radiant heat transfer among internal components. Thus the existing state of the art includes a rather wide variety of wavelength-dependent coatings. The problems of in-space stability, outgassing, and mechanical adhesion to the substrate have all been resolved for most coatings. Many fully qualified coatings are available, so development and qualification of a new coating is normally unnecessary.

The external surfaces of a spacecraft radiatively couple the spacecraft to space. Because these surfaces are also exposed to external sources of energy, such as sunlight and Earth-emitted IR, their radiative properties must be selected to achieve an energy balance at the desired temperature between spacecraft internal dissipation, external sources of heat, and reradiation to space, as illustrated in Fig. 4.1.

The two primary surface properties of importance are the IR emittance and the solar absorptance. Figure 4.2 indicates the range of properties available for different types of materials. Two or more coatings are sometimes combined in a checkerboard or stripe pattern to obtain the desired combination of average absorptance and emittance.

Thermal-control surfaces fall into four basic categories: solar reflector, solar absorber, flat reflector, and flat absorber (see Fig. 4.3). The solar reflector reflects incident solar energy while absorbing and emitting IR energy. Solar reflectors are characterized by a very low α/ε ratio. Solar absorbers absorb solar energy while emitting only a small percentage of the IR energy. Flat reflectors reflect energy throughout the spectral range (i.e., in both the solar and IR regions), while flat absorbers absorb throughout the spectral range.

Common Thermal Surface Finishes

Almost all visible surfaces on the inside and outside of uncrewed spacecraft are thermal-control finishes; this reflects the fact that all physical objects absorb and emit thermal energy in the form of radiation. The flow of heat resulting from absorption and emission by these surfaces must be controlled in order to achieve a thermal balance at the desired temperatures. The principal external surface finishes

*The Aerospace Corporation, El Segundo, California.
†Lockheed Martin Corporation, Sunnyvale, California.

139

Environmental loads $+\Sigma Q_{int}$ = Reradiated energy

(Steady state)
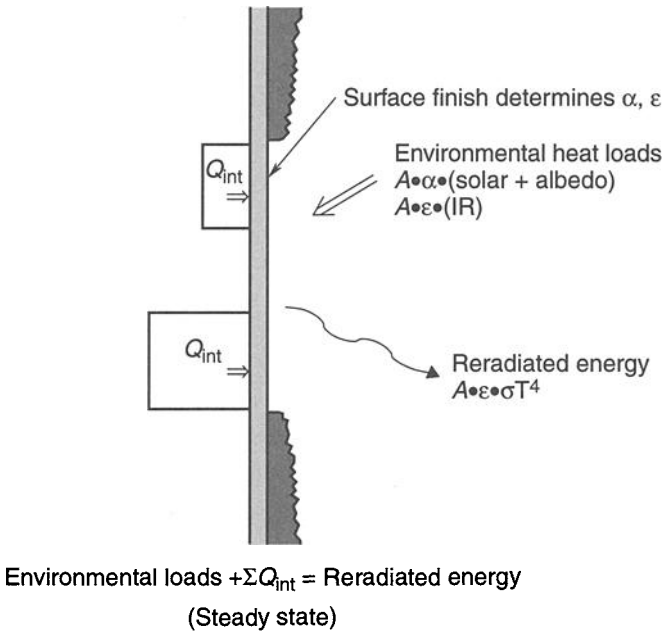
Fig. 4.1. Radiator energy balance (no external blockage).

seen on most spacecraft are the outer layer of insulation blankets, radiator coatings, and paints. Electronics boxes located inside the spacecraft, and the structural panels to which they are attached, are usually painted to achieve a high emittance. (While most paints have the required high emittance regardless of color, black paints have been the conventional choice for internal applications.) Internal temperature-sensitive components that do not dissipate much heat, such as propellant lines or tanks, often have a low-emittance finish of aluminum or gold. Common thermal finishes and their optical properties are shown in Table 4.1.

The outer-cover layer of insulation blankets is usually made of aluminized Kapton, black Kapton, or Beta cloth. Aluminized Kapton is a gold-colored material that has a moderate solar absorptance, a high IR emittance, and a typical thickness of 1 to 3 mils. Black Kapton has a high solar absorptance because it is loaded with carbon to improve electrical conductivity for blanket-grounding purposes. Beta cloth is a very tough Teflon-coated glass fabric that has a low solar absorptance and high emittance. As will be discussed in Chapter 5, the choice of which material to use as the outer-cover layer of the blanket is driven by design requirements such as thermal optical properties, glint prevention, electrical grounding, stress handling, and micrometeoroid protection.

Radiator coatings are typically second-surface mirrors or white paint. The principle behind the second-surface mirror (illustrated in Fig. 4.4) is the use of a visibly transparent material, such as quartz glass or Teflon, to achieve a high emittance, along with a reflective silver or aluminum coating on the back to minimize
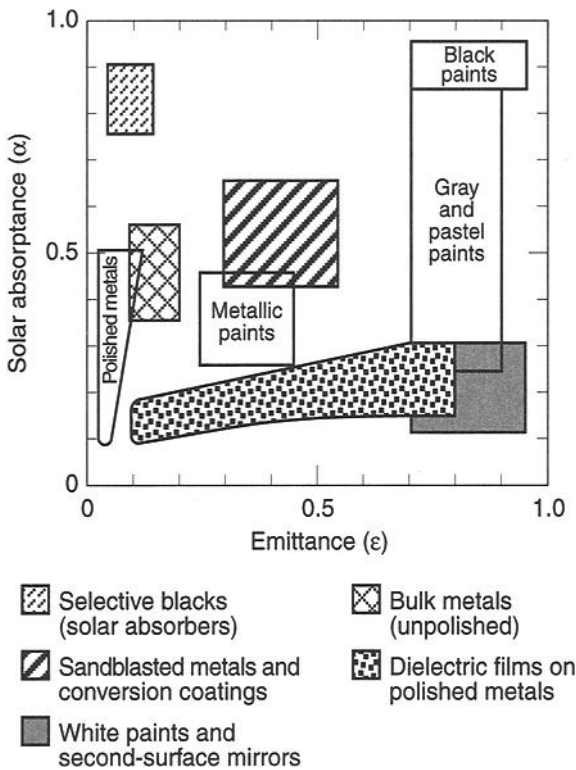
Fig. 4.2. Surface properties by type of finish.

solar absorptance. Quartz second-surface mirrors, often referred to as optical solar reflectors (OSRs), typically come in small tiles with dimensions on the order of a few cm and a thickness of up to 0.25 mm (10 mils). These tiles are bonded to the radiator surface with acrylic or silicone adhesives. (When bonding to a metal substrate, acrylic adhesive should not be used below –45°C because the mirrors may crack or delaminate.) Teflon second-surface mirror material, sometimes referred to as flexible OSR, comes in a variety of thicknesses (and therefore emittances) and is usually supplied as a tape or sheet with an acrylic adhesive backing for ease of installation. Standard quartz and Teflon OSRs are highly specular, but they also come in a diffuse variety that has a somewhat higher absorptance.

While space-qualified paints are available in a variety of colors, black and white are by far the most commonly used. Almost all paints have a high emittance, so the choice is really between solar absorptance (and its degradation in the space environment), ease of application, and electrical conductivity to meet grounding requirements. Most internal spacecraft surfaces are painted black for high emittance, while exterior surfaces, including radiators, are often painted white to minimize absorbed solar energy. In choosing a white paint, one must consider that some paints will experience a greater increase in absorptivity than others as a result
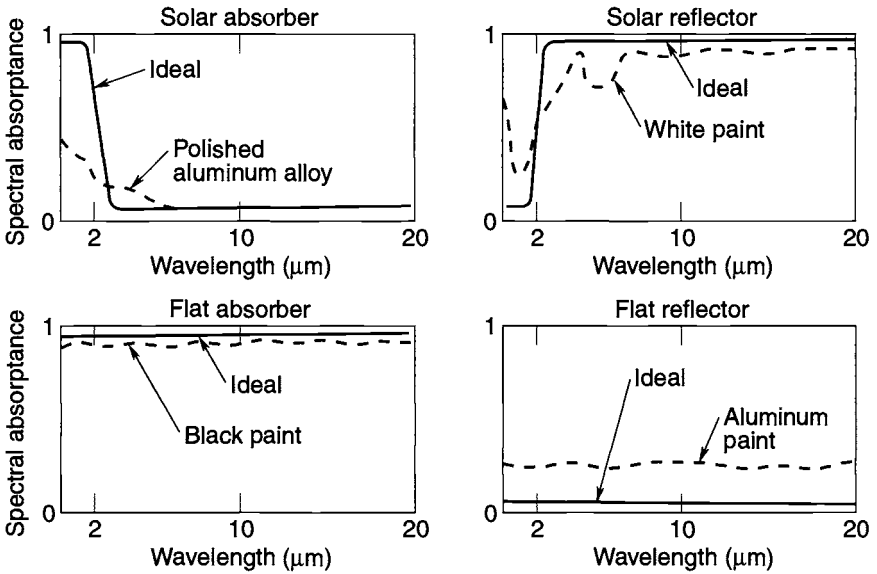
Fig. 4.3. Ideal representation of four basic passive-control surfaces.

of the effects of the space environment. Metallic paints, such as leafing aluminum paint, may have an emittance as low as 0.2, but these are rarely used on spacecraft. In situations where radiative heat transfer must be minimized, low-emittance metallic finishes are often used. These include bare or polished surfaces of aluminum components, Kapton tape with a vapor-deposited aluminum or gold coating (metal side exposed), or bare stainless steel. Typical applications are aluminized (or aluminum) tape on propellant lines and tanks to limit heat loss and stainless-steel radiation shields to block the radiative view from hot thruster nozzles to sensitive spacecraft components. In general, these metallic finishes are not used on large exterior surfaces because their high absorptance-to-emittance ratio would make them run very hot in direct sunlight. Small exterior components that are conductively coupled to spacecraft structure, however, may sometimes have a metallic finish.

A number of specialty finishes find occasional use in spacecraft thermal control. These include very high-absorptance, very low-emittance finishes, like Maxorb and TiNOX, that are used to raise the temperature of a surface exposed to the sun; very low-absorptance, overcoated silver for sun shields on cryogenic radiators; moderately low solar-absorptance and -emittance finishes like aluminum paints or silicon-oxide-coated aluminum for mitigating temperature swings of exposed spacecraft structure; and controlled anodize and alodine processes for aluminum surfaces on which other thermal-control coatings are not allowed. The thermal engineer should be very careful about using absorptance and emittance values that are reported in the literature for anodized or alodined surfaces because the surface optical properties are highly dependent on the specific process used. Properties obtained from these processes are very repeatable, though, if the process is tightly
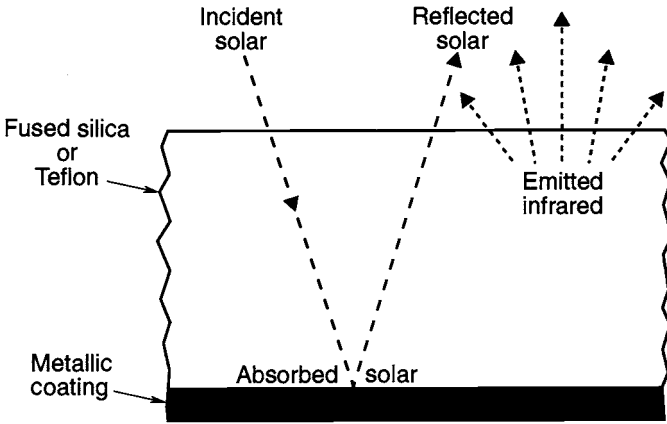
Fig. 4.4. Second-surface mirror thermal finish.

controlled, such as by a military specification. Duckett and Gilliland[4.1] describe a NASA/Langley-developed controlled chromic-acid-anodizing process for aluminum that allows the user to select any combination of emittance (within the range of 0.10 and 0.72) and absorptance (within the range of 0.2 to 0.4) and obtain both values to within ±0.02.

Appendix A and Touloukian[4.2] contain a much more extensive list of space-qualified finishes that have been used on actual satellites along with corresponding optical properties that have been obtained from a variety of sources. Most of the values given here are for "normal" temperature ranges, and substantial changes may occur at cryogenic or very high temperatures.[4.2, 4.3] While the reported properties have been obtained from what are believed to be reliable sources, differences in reported values are not uncommon. Therefore, in designs that are sensitive to surface properties, measuring the absorptance and emittance of samples of the actual flight finish is recommended.

Causes of Thermal Surface Degradation

Thermal-control finishes are affected in orbit by charged particles, ultraviolet (UV) radiation, high vacuum, and the contaminant films that deposit out on almost all spacecraft surfaces. The general result of these processes is an increase in solar absorptivity with little or no effect on IR emittance. This is normally undesirable from a thermal-control standpoint because spacecraft radiators must be sized to account for the substantial increase in absorbed solar energy that occurs because of degradation over the mission. These radiators, which are oversized to handle the high solar loads at end-of-life, cause the spacecraft to run much cooler in the early years of the mission, sometimes necessitating the use of heaters to avoid undertemperatures of electronic components. The degradation is, therefore, a problem not only because of the solar load, but also because of the change in load

Table 4.1. Properties of Common Thermal Surface Finishes

Surface Finish	α—Absorptance (beginning-of-life)	ε—Emittance
Optical Solar Reflectors		
8-mil quartz mirrors	0.05 to 0.08	0.80
Quartz mirrors (diffuse)	0.11	0.80
2-mil silvered Teflon	0.05 to 0.09	0.66
5-mil silvered Teflon	0.05 to 0.09	0.78
2-mil aluminized Teflon	0.10 to 0.16	0.66
5-mil aluminized Teflon	0.10 to 0.16	0.78
White Paints		
S13G-LO	0.20 to 0.25	0.85
PCBZ	0.16 to 0.24	0.87
Z93	0.17 to 0.20	0.92
ZOT	0.18 to 0.20	0.91
Chemglaze A276	0.22 to 0.28	0.88
Black Paints		
Chemglaze Z306	0.92 to 0.98	0.89
3M Black Velvet	~0.97	0.84
Aluminized Kapton		
1/2 mil	0.34	0.55
1 mil	0.38	0.67
2 mil	0.41	0.75
5 mil	0.46	0.86
Metallic		
Vapor-deposited aluminum (VDA)	0.08 to 0.17	0.04
Bare aluminum	0.09 to 0.17	0.03 to 0.10
Vapor-deposited gold	0.19 to 0.30	0.03
SiOx on VDA tape	0.14	0.12
FSS-99 (overcoated silver)	0.03	0.02
Miscellaneous		
1/4-mil aluminized Mylar, Mylar side	(Material degrades in sunlight)	0.34
Beta cloth	0.32	0.86
Astro Quartz	~0.22	0.80
TiNOX	0.95	0.05
Maxorb	0.90	0.10

over the course of the mission. The stability of coating properties is important in order to limit maximum temperatures and minimize heater-power requirements.

The following sections describe the effects of contaminants, UV radiation, atomic oxygen (AO), charged particles, and space debris on commonly used spacecraft thermal-control materials. This information should provide a basic understanding of the damage mechanisms and aid in the selection of materials to withstand these environments.

Contamination

In many instances, contamination effects are the major contributor to optical degradation of spacecraft surfaces. The degradation of optical surfaces with mission life appears as an increase in solar absorptance of thermal-control materials or a loss of transmission through or reflection from sensitive surfaces of telescopes and detectors. Contaminants are of two different varieties: particles and compounds outgassed from spacecraft materials like plastic films, adhesives, foams, lubricants, and paints.

Some particles are present within the launch vehicle fairing that encloses the spacecraft until a few minutes after liftoff, and more are generated as a result of rocket motor firings during liftoff, stage separation, and attitude control. These particles are deposited on spacecraft surfaces as a result of direct rocket motor plume impingement or turbulence inside the payload fairing that causes particles and other contaminants that are already present to circulate during launch ascent.

The other source of contamination is the low molecular weight fractions of polymeric materials that volatilize during mission life and generally condense on cooler surfaces such as radiators. This outgassing is strongest early in the mission (the first few months to one year) and tapers off with time. Since migration of volatile constituents through solids is a slow process at ordinary spacecraft temperatures, these low molecular weight fractions continue to outgas for several years. These volatile contaminants condense on surfaces at a much greater rate if the surface is illuminated by the sun because UV radiation enhances the chemical binding process. UV illumination will also cause a deposited contaminant layer to darken over time, thereby increasing the solar absorptance of the surface. Studies based on space-flight experience, laboratory experiments, and modeling suggest that on average, surface solar absorptance increases by about 0.01 for every 100 Å of contaminant film thickness, although reported values vary widely.

Significant effort has gone into the development of spacecraft materials over the past several decades to limit the amount of outgassing from polymeric materials in order to minimize spacecraft contamination effects. Outgassing data are obtained by a standard test that conforms to ASTM E 595-77/84. The test consists of heating small specimens to 125°C for 24 hours while accumulating the outgassing products on a surface maintained at 25°C. The data are reported as percent total mass loss (percent TML) and percent collected volatile condensable materials (percent CVCM). The NASA criteria on outgassing from candidate spacecraft materials limit percent TML to less than 1.0% and percent CVCM to less than 0.1%. Table 4.2 lists outgassing data from commonly used thermal-control surface materials, most of which were obtained from NASA/GSFC and Lockheed Martin

Table 4.2. Outgassing Data for Thermal-Control Surface Materials

Material	TML (%)	CVCM (%)
OSR	0.00	0.00
FEP Teflon	0.77	0.35
Kapton	0.78	0.03
Glass fabric/Kapton	0.42	0.05
Black Kapton	0.50	0.02
Glass fabric/Black Kapton	0.53	0.06
White polyurethane paint	0.99	0.08
Black polyurethane paint	1.91	0.28
White silicone paint	0.54	0.10
Black silicone paint	0.43	0.04
White inorganic paint	>1.00	0.00

Corporation. Clean metals and metal finishes are not a source of volatile material and therefore do not contribute to the contamination of spacecraft thermal-control or optical surfaces.

Examination of contamination deposits on the Long Duration Exposure Facility (LDEF), which was recovered in January 1990 by the space shuttle after nearly 6 years in low Earth orbit (LEO), has revealed that contamination mechanisms are still only partially understood. For example, a contamination or brown stain occurred in a number of places on the spacecraft's external surfaces and, as expected, the heavier contamination deposits appeared near vent holes. On an OSR sample, however, the solar absorptance was unchanged, which is contrary to expectation because the surface of the OSR was cool and should have been a site of contaminant deposition. Also not anticipated was the discovery of contamination deposits on locations not in the direct line-of-sight of a contamination source. While analytical techniques for simulating contamination processes have advanced substantially, predicting the amount of contamination that any particular thermal-control surface will experience remains challenging. Contamination can be minimized, however, by protection of surfaces from booster exhaust plumes, by optimum placement of spacecraft vent holes and attitude-control thrusters, and by selection of low outgassing materials.

UV Radiation

The UV portion of the electromagnetic spectrum is usually divided into two regions: the near UV, with wavelengths between 0.20 and 0.40 μm, and the more damaging "vacuum UV" (VUV), with wavelengths below 0.20 μm. The VUV is so named because its wavelengths are only transmitted in the vacuum of space; atmospheric gases absorb these shorter wavelengths. The principal solar UV radiation is at wavelengths between 0.25 and 0.40 μm. This portion of the solar UV remains relatively constant throughout a solar cycle. However, the VUV portion fluctuates with solar activity and can increase by up to a factor of 3, depending on wavelength, as peak solar activity occurs.

Damage mechanisms that explain the darkening of spacecraft thermal-control materials by solar UV are not fully understood. At least two mechanisms are thought to account for an increase in solar absorptance of materials. First, short-wavelength UV and X-ray photons are capable of causing charge separation or electron imbalance in ionic crystals, forming color centers. The color centers have optical absorption bands associated with their formation, which leads to an increase in solar absorptance. A more probable damage mechanism to explain an increase in solar absorptance in polymeric materials such as thermal-control films, paints, and contamination deposits is the capability that solar UV photons have of initiating chemical reactions in these kinds of materials. The process involves absorption of the UV photon and an accompanying electronic excitation of a polymeric molecule. The electronically excited polymeric molecule usually contains sufficient energy to break a chemical bond within the polymeric molecule, forming two free radicals. Free radicals are chemical species that have an unpaired electron in the valence shell and, as such, are very reactive. These free radicals react with neighboring molecules, forming larger molecular species that may be stable, thus ending the process, or the products themselves may also be free radicals so that the process continues until a stable species is formed. A stable product is formed by the recombination of two free radicals.

The larger molecules formed by the absorption of solar UV photons generally have optical absorption bands above 0.40 μm in the solar spectrum. The presence of the multiple absorption bands of these larger molecules throughout the solar spectrum shows up as an increase in solar absorptance. Some materials, such as Teflon, are relatively stable under solar UV illumination and exhibit only small increases in solar absorptance, although no explanation has been offered for this resistance to damage. On the other hand, polyurethane and silicone paint binders show large increases in solar absorptance as a result of UV irradiation.

Atomic Oxygen

A major damaging component of the LEO space environment is AO, which can severely erode externally applied hydrocarbon-type thermal-control materials. AO is formed by the UV photolysis and dissociation of molecular oxygen in the upper atmosphere. The concentration of AO varies inversely with altitudes between 100 and 1000 km and directly with solar activity as a result of the increased VUV component of solar irradiance. AO erosion of spacecraft materials in orbits above 1000 km is not a concern because there is neglible AO at these higher altitudes, but erosion may be a factor while the vehicle is in a parking orbit.

AO is a very reactive chemical species because its valence shell contains an unpaired electron. In addition, the reactivity of AO is enhanced in LEO because the high velocity of the spacecraft (about 8 km/s) relative to the surrounding atmosphere imparts an additional energy to AO equivalent to 5 eV in the ram direction. This energy is sufficient to break chemical bonds commonly found in polymeric materials or contamination deposits. In the case of hydrocarbon thermal-control materials, the products (CO, CO_2, and H_2O) formed by AO attack are volatile and evaporate from the surface, exposing additional material for further reaction. In the case of silicone materials (all of which contain some hydrocarbon), AO erosion effects are normally limited to the outer few atomic layers. The exposed

hydrocarbon components of the silicone polymer are eroded, producing a silicate-type (or glasslike) structure on the surface that resists further oxidations. As a result of the formation of this glasslike layer, silicones are considered to be stable to the AO environment.

AO erosion rates (reaction efficiency) of commonly used thermal-control materials are listed in Table 4.3. The erosion-rate data were generally obtained from space-shuttle testing of these materials for limited periods of exposure (2 weeks or less). Measurements of erosion rates from materials on LDEF basically confirm these rates. Recovered silverized Teflon specimens exhibited an enhanced erosion rate as a result of the high concentration of AO encountered by ram-facing surfaces at the lower altitudes (LDEF was recovered at 350 km) and during the peak in solar activity. If silverized or aluminized Teflon is being considered for use in an orbit similar to that of LDEF (in general, below 400 km), detailed AO flux and fluence calculations will be required to determine optical properties at end-of-life.

AO erosion effects have been known for several years. As a result, protective coatings that resist oxidation have been developed for Kapton and Teflon thermal-control materials, although the coating is delicate and easily rubbed off of Teflon during spacecraft manufacturing and ground handling. The erosion rates in Table 4.3 do not apply to materials with protective coatings.

A rough assessment of a material's susceptibility to AO attack can be made using the erosion rate data from Table 4.3 and the data from Fig. 4.5, which shows the concentration of AO in the neutral atmosphere for solar-activity extremes. The

Table 4.3. Atomic-Oxygen Reaction Efficiencies of Commonly Used Thermal-Control Materials

Material	AO Reaction Efficiency 10^{-24} cm^3/AO atom
Fused silica	Negligible
Clear FEP or TFE Teflon	0.05
Polyimide (Kapton)	2.6
Carbon-filled (black) polyimide	2.5
Gloss white polyurethane paint	0.9
Flat black polyurethane paint	0.9
Gloss black polyurethane paint	4.5
Silicone paints	Negligible
Z-93 white paint	Negligible
YB-71 white paint	Negligible
Aluminum, bare and anodized	Negligible
Beryllium	Negligible
Magnesium, DOW 17 coated	Negligible
Stainless steel	Negligible
Titanium, bare and anodized	Negligible
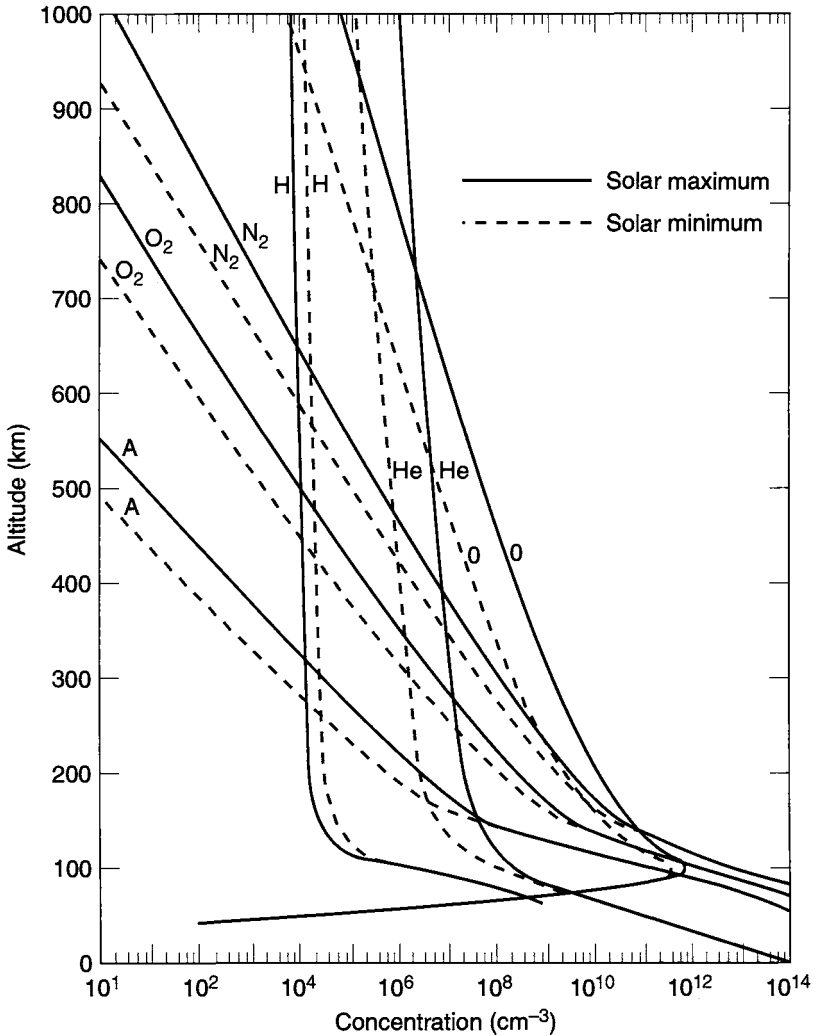
Fig. 4.5. AO concentration.

AO fluence in the ram direction is the product of AO concentration, spacecraft velocity, and mission time. For example, at 500 km altitude the maximum AO concentration is about 6×10^7 atoms/cm^3 and orbital velocity is about 8000 m/sec; the annual fluence is therefore $(6 \times 10^7$ atoms/cm$^3) \times (8 \times 10^5$ cm/sec) $\times$ (31.5 $\times$ 10^6 sec) = 1.5×10^{21} atoms/cm^2. Surface mass loss is the product of AO concentration and reaction efficiency. The approximate annual surface erosion of unprotected Kapton in the above environment is $(1.5 \times 10^{21}$ atoms/cm$^2) \times (2.6 \times 10^{-24}$ cm^3/atom) = 3.9×10^{-3}cm. More precise evaluations of material erosion rates are generally performed by materials-science specialists.

Protons, Electrons, and Neutrons

Protons and electrons are charged-particle components of the space environment that are capable of damaging most thermal-control materials and, together with solar UV, are responsible for spacecraft charging effects. Neutrons, as their name implies, are electrically neutral and have great penetrating power but do little or no damage to spacecraft thermal-control materials.

As illustrated by Fig. 4.6, highly energetic protons and electrons are concentrated in the inner and outer Van Allen radiation belts because of Earth's magnetic field. The Van Allen belts are two concentric doughnut-shaped rings situated above the equator. Geosynchronous orbit (GEO) is located in the outer Van Allen belt; consequently, external surfaces of spacecraft in GEO are subjected to large doses of ionizing radiation. The charged particles in the Van Allen belts are omnidirectional, so all external spacecraft surfaces are equally irradiated. Only the sun-facing surfaces are simultaneously irradiated with solar UV and charged particles. The lower boundary of the inner Van Allen belt is located at an altitude of about 1000 km, so spacecraft in LEO are not normally exposed to significant amounts of ionizing radiation. Increases in solar absorptance in LEO are mainly the result of solar UV radiation. Materials on spacecraft in polar orbits and in orbits that intercept the South Atlantic Anomaly are subjected to an ionizing radiation dose in these regions of space, but the dose is usually less than several Mrads, which generally induces insignificant changes in solar absorptance.

The most damaging of the energetic charged particles are the 30-keV plasma-sheet protons and the 7-keV plasma-sheet electrons, which can deposit a very large dose of about 10^{11} rads to spacecraft outer surfaces during a 5-year mission in GEO. The 30-keV protons are capable of penetrating FEP Teflon to a depth of
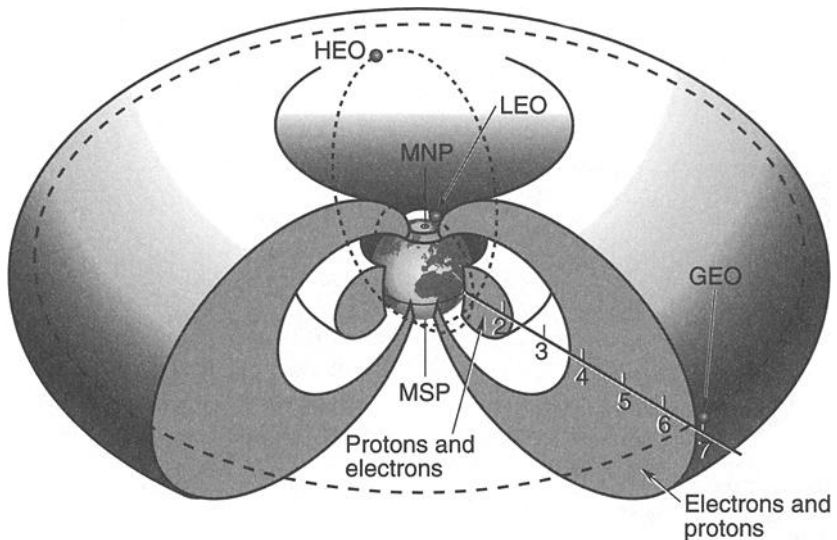

Fig. 4.6. Earth's radiation belts.

0.01 mil. The 7-keV plasma-sheet electrons and 200-keV electrons of the Van Allen belts can penetrate Teflon to a depth of 0.06 and 10 mil, respectively. When energetic protons and electrons of the space environment penetrate a polymeric material, collisions between the relatively fast-moving charged particle and molecules of the solid produce ionization. The ionized molecules chemically react with neighboring molecules, forming larger polymeric molecules. These larger polymeric molecules generally have optical-absorption bands in the solar portion of the spectrum, which results in an increase in solar absorptance. Kapton, for example, experiences large increases in solar absorptance when used in geosynchronous orbits or other high-radiation environments. However, there are some transparent materials, such as fused silica, that do not darken as a result of exposure to ionizing radiation, partially because of the purity of the material.

Micrometeoroids and Debris

According to estimates, a spacecraft in LEO is 10 times more likely to encounter a particle of space debris than a meteor. Recent surveys of LEO and GEO space environments conducted using ground-based optical telescopes and radars, along with data from returned LEO spacecraft, reveal a growing accumulation of space debris. Optical and radar techniques are capable of detecting debris fragments as small as 10 cm in diameter. The flux of particles smaller than 1 cm is inferred by counting craters on returned spacecraft. Particles with diameters of 1 to 10 cm have not been mapped and constitute a hazard to astronauts during extravehicular activity and to the integrity of spacecraft in LEO.

Approximately 16,000 debris objects have been tracked in LEO, with about 6000 objects still in orbit; the remainder have reentered Earth's atmosphere as a result of drag. The number of objects in LEO decreases slightly with peak solar activity.

Meteors, which are naturally occurring objects, are thought to be traceable to asteroids and comets with some retaining the orbit of the parent body. In general, meteors are considered omnidirectional relative to Earth.

Analysis of the exterior surfaces of LDEF indicated that hundreds of small particles struck the vehicle. Ten times as many craters were found on the leading edge as on the trailing edge, indicating the greater abundance of debris objects versus meteorites. The largest particle to impact LDEF was about 5 mm in diameter. From a thermal-control point of view, collisions with objects of this size and smaller are not a problem because the craters that are formed occupy a small percent of the vehicle's total surface area. Since the total amount of damage is small, little change in overall optical properties occurs. In the case of silvered Teflon, some darkening of the silver around the impact zones occurred where the particle penetrated to the metalized layer. AO was able to react with the exposed silver metal, forming a ring of dark silver oxide, but again, the net effect on optical properties was negligible. No OSRs were struck during the nearly 6 years in LEO. However, if a tile were struck by a relatively small meteorite or debris particle, the damage would be limited since the tiles are usually bonded to the substrate.

Degradation Rates for Common Thermal Finishes

Different thermal surface finishes are affected in different ways by exposure to the space environment. Some surfaces are sensitive to all of the degrading environments discussed above, while others are essentially immune to the effects of one or more of them. Because the environments can be very different in different orbits, the rate of degradation for a given material can also be quite different depending on the orbit in which the spacecraft resides.

Quartz mirrors experience essentially no damage from UV and charged particles, leaving only contamination as a source of increased absorptivity. Because contaminant outgassing is strongest early in the mission, a rather large increase in solar absorptance occurs in the first few years, followed by a small steady increase until end-of-life. Figure 4.7 shows the observed rate of contamination-induced absorptance increase for quartz-mirror radiators on several spacecraft. The spacecraft-to-spacecraft variations are not completely understood, but they are known to be strongly dependent upon such factors as the types of materials used in the spacecraft, the venting of outgassed materials across thermal surfaces as they leave the spacecraft, and the presence of sunlight, which enhances the deposition and darkening of contaminants on surfaces. Because of these effects on quartz-mirror radiators, many programs are switching to lower outgassing materials and redesigning vent paths to ensure that outgassed contaminants are directed out to space without impinging onto thermally sensitive surfaces.
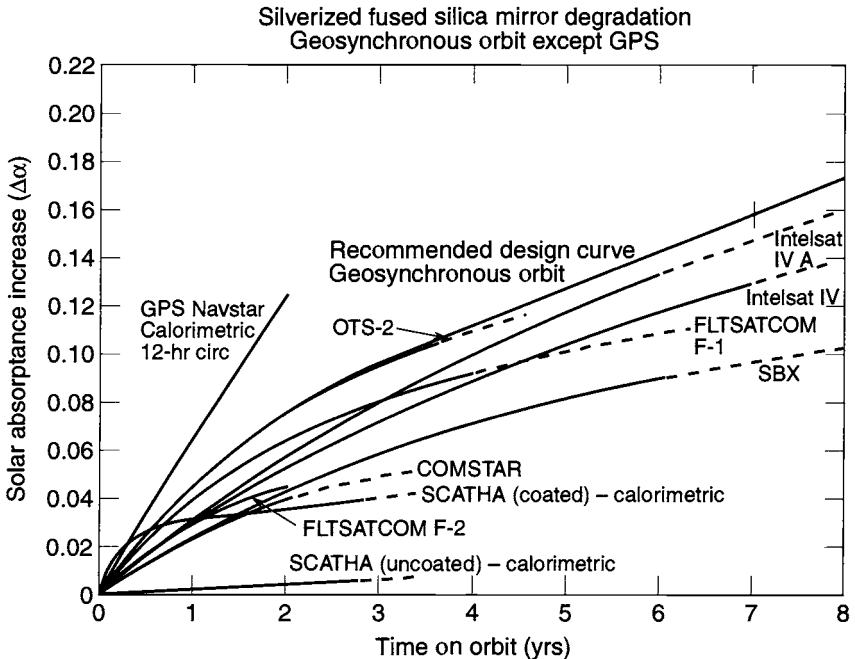
Fig. 4.7. Degradation of quartz mirrors in geosynchronous orbit.

Aluminized or silvered Teflon films show absorptance degradation as a result of both charged-particle damage to the Teflon and contaminant deposition, as illustrated in Fig. 4.8. Teflon film degradation rates observed on a number of flight spacecraft are summarized in Fig. 4.9. As these data show, the degradation strongly depends on orbit. LEO is the most benign because of the relative absence of charged-particle damage. Degradation in GEO is more severe because of the more intense radiation environment. Spacecraft placed in the 12-hour circular orbits typical of navigation satellites can experience extreme degradation because they
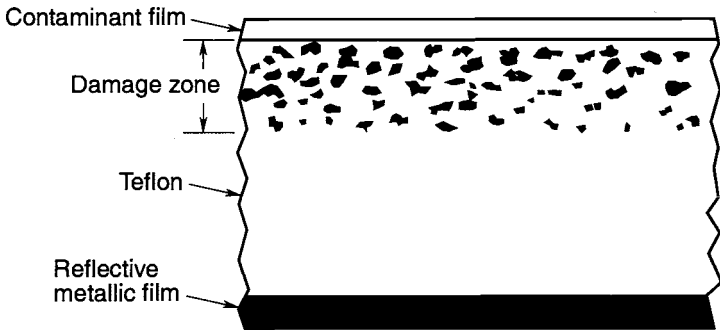
Fig. 4.8. Metalized Teflon degradation model.
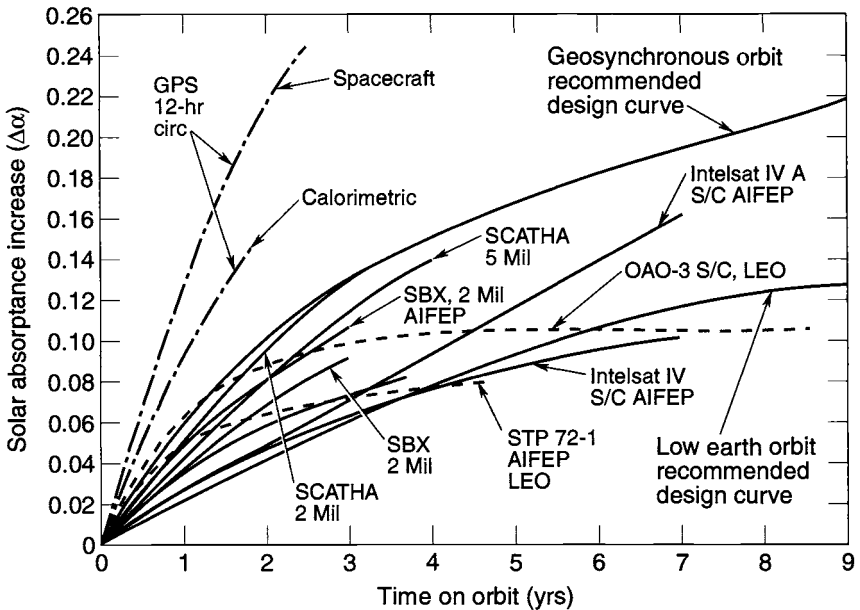
Fig. 4.9. Metalized Teflon degradation.

pass through very intense regions of the Van Allen belts. At the lower LEO altitudes, AO erosion may also result in degraded emittance, depending on total fluence levels. To evaluate emittance degradation, an estimate of the AO fluence is made based on the mission profile, and the total surface recession over the life of the mission is predicted. The emittance of the material at end-of-life is then determined based on the well-established values for emittance of Teflon as a function of thickness. Recommended absorptance degradation values for Teflon surfaces in LEO and GEO are shown in Fig. 4.9.

Surface finishes that are not affected by UV or charged particles, such as polished metals, will still suffer absorptance increases because of contamination. For such materials, degradation rates similar to those for quartz mirrors should be used (see Fig. 4.7) if the surface has a low beginning-of-life absorptance.

White paints, such as S13GLO, are affected most strongly by UV radiation and charged particles, and their absorptance may rise from around 0.20 to 0.70 in just a few years. Black paint and other high-absorptance surfaces generally do not degrade much from space-environment exposure. Any change in black paint is more likely to be a slight reduction in absorptivity of a few percentage points from UV bleaching over time. Absorptivity degradation as a function of time for several paints is shown in Fig. 4.10.

Materials used as the outer-cover layer of insulation blankets also suffer absorptance changes from space-environment effects. Kapton and Beta cloth show substantial degradation and can turn almost black after several years in GEO, as shown in Fig. 4.11. Degradation in the LEO environment is significantly less severe because of the relative absence of radiation. Black Kapton actually sees a reduction in absorptance as a result of UV bleaching. Fortunately, when these materials are used as the outer layer of a blanket, the impact of their absorptance increases on spacecraft temperatures is mitigated to a large extent by the small role that heat transfer through the blanket plays in overall spacecraft thermal balance.

The degradation rates discussed above are for Earth-orbiting spacecraft. With the exception of AO, interplanetary missions will experience the same degradation
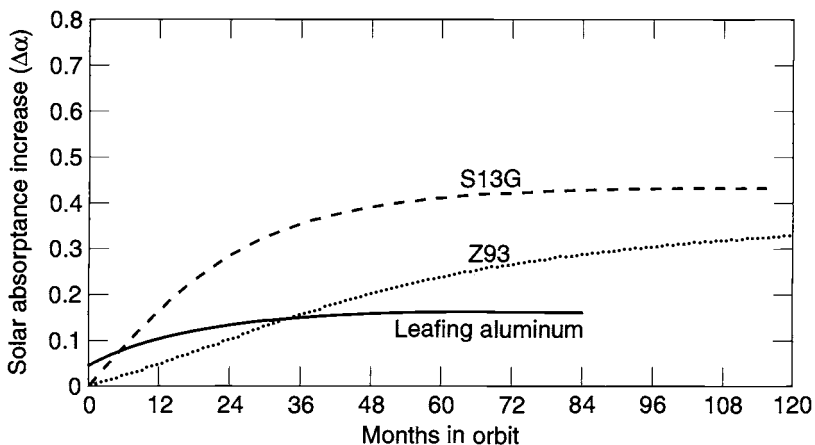

Fig. 4.10. Paint degradation.
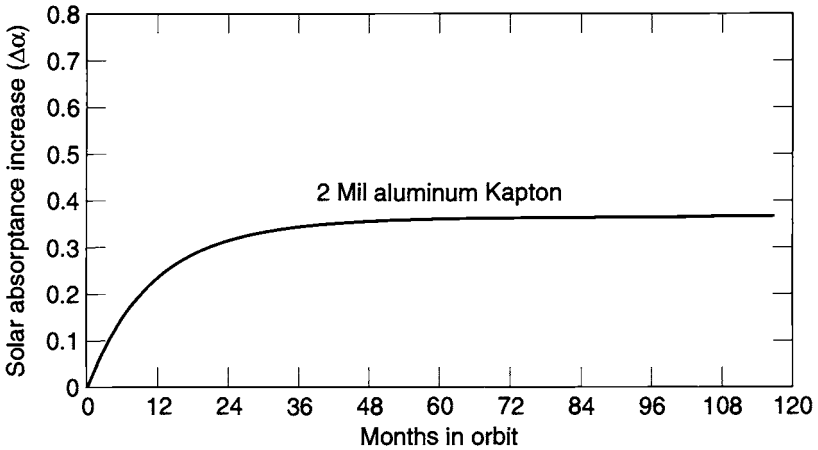
Fig. 4.11. Kapton absorptance degradation.

environments as those in Earth orbit, only at different intensities. Materials sensitive to UV will experience more rapid degradation during missions to Venus than they would in Earth orbit. Materials sensitive to charged particles, on the other hand, will degrade at a slower rate during interplanetary cruises than they would in GEO because they are not exposed to the trapped radiation of the Van Allen belts. By computing the charged-particle and UV dose that a material will receive during any particular mission, materials scientists can estimate the degradation the surface will suffer over time. Because of the very low intensity of sunlight at great distances from the sun, absorptance increases resulting from surface degradation will not cause a significant increase in temperatures once a spacecraft approaches the orbit of Jupiter or beyond.

LDEF Results

LDEF was launched by the space shuttle in April 1984 into a 465-km orbit at 28.5-deg inclination, and it was recovered in January 1990 at 325 km. On the mission were 57 experiments containing over 10,000 specimens to test the effects of the LEO space environment on materials, components, and systems. The principal environmental factors affecting thermal finishes are solar UV radiation; bombardment by AO atoms, which are present at very low densities in low orbits; electron and proton radiation; and micrometeoroids. Originally planned for one year, the exposure actually lasted almost six years. While many LDEF investigations are continuing, results to date have given valuable information on long-term performance in orbit.

The 69-month LDEF mission resulted in far longer space exposure of material surfaces than other hardware previously returned from orbit, such as from the short-duration shuttle experiments, or hardware returned from the Solar Maximum Repair Mission. LDEF was gravity-gradient stabilized, with one side of the vehicle continuously pointing down toward Earth's center, and another side always

facing the velocity vector, within 1 deg. The vehicle contained 86 experiment trays measuring 127 cm by 86 cm, which were oriented around the vehicle in 12 rows, with additional trays on the sides facing Earth and facing directly away from Earth. During the mission, the leading-edge materials (i.e., those facing into the velocity vector) were exposed to approximately 9×10^{21} oxygen atoms/cm^2, a level at which erosion of over 10 mils would be expected for many polymers. The trailing-edge exposure was only about 10^4 oxygen atoms/cm^2, making AO effects insignificant compared to solar UV and charged particles. Trailing-edge samples are, therefore, more representative of higher-altitude orbits where AO concentrations are insignificant. The solar exposure ranged from about 5000 to 14,500 equivalent sun-hours, depending on location on the LDEF, with 34,200 thermal cycles. The radiation environment on the surface was $\sim2.5 \times 10^5$ rads of electron radiation and 1.6×10^3 rads of proton radiation.

The LDEF observations on thermal-control materials are particularly significant for AO effects on the leading edge for low Earth orbits, while the trailing-edge samples show the effects of UV radiation. The Thermal Control Surfaces Experiment provided on-orbit leading-edge data on thermal properties of 25 materials during the first 18 months of the mission.[4.4] The inorganic binder paints, such as Z93 (zinc oxide in a potassium silicate binder) and YB-71 (zinc orthotitanate in a potassium silicate binder), were shown to be stable in the LEO environment. Some thermal-control materials degraded more, others less, than predicted from ground tests. The thermal-control properties (α/ε) of organic binder paints, commonly used for their ease of application, were observed to degrade by as much as a factor of 3 on the trailing edge, but they showed much smaller changes on the leading edge. Data from paints flown on the M0003 experiment on LDEF are shown in Table 4.4.[4.5]

The polyurethane paint A276 on LDEF is interesting because the multiple locations on hardware completely around the vehicle allowed the effects of orientation on performance of the paint to be clearly measured, as shown in Fig. 4.12.[4.6] The data from the trailing edge at or near 180 deg clearly show the degradation of the paint by the solar UV, while the degraded binder on the leading edge near 0 deg has been removed by the AO erosion to maintain properties near the initial values.

The Kapton and Mylar thermal blankets on LDEF were of particular interest because of the susceptibility of these materials to erosion from reaction with AO on leading-edge surfaces. In fact, one of the initial observations of damage to LDEF materials on-orbit was the observation of the severely eroded Mylar blankets

Table 4.4. Solar Absorptance of Thermal-Control Paints on LDEF M0003

Paint	Initial α	Leading-Edge α	Trailing-Edge α
YB-71	0.130	0.182	0.182
A276	0.282	0.228	0.552
S13GLO	0.147	0.232	0.458
D111	0.971	0.933	0.968
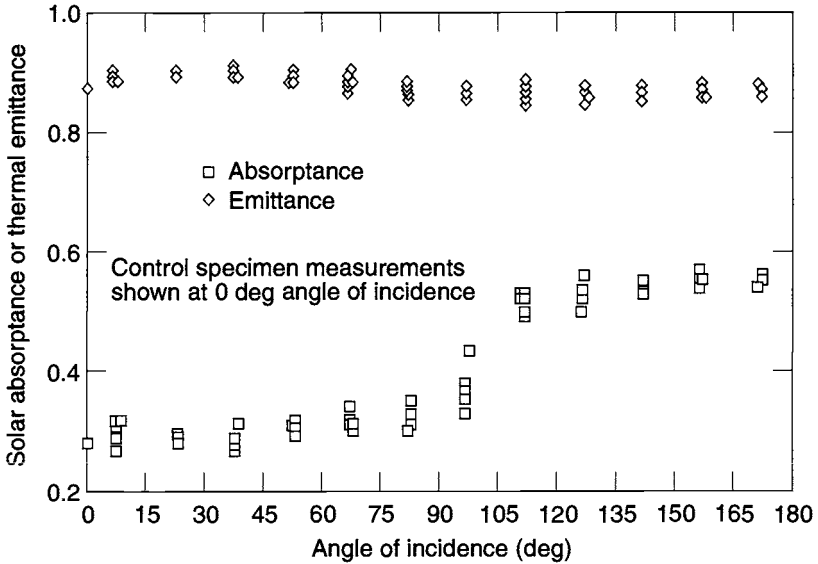
Fig. 4.12. Optical properties from A276 white thermal-control discs.[4.4]

on the space-facing end of the LDEF structure. There were 5-mil Kapton blankets on the leading edge of LDEF where the Kapton had been completely removed and only the few thousand Å of metalization remained. The AO fluence of ~9 × 10²¹ O atoms/cm² observed on LDEF leading-edge surfaces led to a predicted loss of over 10 mils of Kapton, based on the reaction efficiency from earlier shuttle flights of 3.0×10^{-24} cm³/O atom. The observed erosion for Kapton (and a number of other organic polymers) on LDEF was consistent with previously determined reaction efficiencies.

A variety of visible changes were observed on both the leading- and trailing-edge silvered FEP Teflon surfaces on LDEF. The 5-mil silvered Teflon blankets were visibly altered during the LDEF mission, but the thermal properties did not degrade significantly except in those areas that were contaminated. However, caution should be used in other applications depending on the thermal-blanket thickness and the planned orbit. The cloudy, diffuse appearance of the Teflon on the leading edge was caused by an unexpectedly high erosion of the Teflon layer. For short exposures in LEO, such as the prior shuttle experiment to study AO effects, very low erosion had been observed, consistent with a recession rate of $<0.1 \times 10^{-24}$ cm³/O atom. The LDEF has permitted the first orbital measurement of the erosion of the Teflon layer on the leading edge from AO; previous attempts could not measure the smaller thickness decrease of the Teflon. The ~1 mil of erosion observed on LDEF is apparently the result of synergistic effects of the VUV and AO environment.[4.7] Thermal measurements show the expected decrease in emissivity as the thickness is decreased. The diffuse reflectance increased for

those areas toward the leading edge roughened by exposure to both AO and solar UV, giving rise to the uniformly clouded appearance. LDEF data has shown that a value of $0.34 \times 10^{-24} cm^3/O$ atom is clearly more appropriate for longer exposures. In practice, the known reaction efficiency and expected oxygen fluence are used to predict the expected life of a film with a given initial thickness. Most blanket areas from the trailing-edge side, exposed only to solar UV, remained specular. The LDEF results for silvered Teflon indicate that the thermal performance shows minimal degradation from the solar UV exposures of up to 11,000 ESH. For the trailing-edge blankets, the UV exposure caused polymer-chain scission at the surface and resulted in decreases of percent elongation to failure and ultimate tensile strength.[4.8]

Another effect observed silvered FEP Teflon blankets on LDEF was the severe degradation associated with cracked silver-Inconel layers. Improper application, which produced cracking of the metalization, allowed migration of the Y966 adhesive through the metalization, and subsequent darkening by solar UV. This process led to increases in absorptance up to 0.25 in small areas. Lifetime predictions should also include consideration of the fraction of the blanket surface that will likely be darkened or destroyed by meteoroid and debris impacts, and potential absorptance increases caused by contaminant films over a fraction of the surface. These considerations were minor for LDEF. Impacts darkened 2% or less of the surface area of each LDEF blanket, and delaminated < 5% of the area on each blanket. Contaminant films caused absorptance changes as high as about 0.25, but only for relatively small surface areas.

Electrical Grounding

Spacecraft flying in regions where significant space plasmas exist must contend with electrical-charge buildup on external surfaces. If the charge becomes large enough, static-electricity discharges through the surface finish to the spacecraft structure occur. Such discharges can damage spacecraft electrical components or interfere with their operation. Missions that use midaltitude to geosynchronous-altitude Earth orbits or high-inclination low-Earth-orbits, as well as orbits around Jupiter and Saturn, are generally affected to some degree by this problem. Therefore, spacecraft programs using these orbits will often have requirements to ground thermal surface finishes. The degree of grounding specified will usually reflect how sensitive spacecraft components are to static discharges and how severe the charging environment is in the mission orbit.

A few thermal finishes, such as Z307 black paint, PCBZ white paint, and black Kapton, are electrically conductive enough so that surface charges can be readily bled off to the spacecraft structure. Other materials, however, are good electrical insulators and require special grounding techniques. Electrically insulating films such as gold Kapton, quartz mirrors, and Teflon can be grounded by applying a thin indium tin oxide (ITO) coating over the material and providing an electrical connection from the ITO to the spacecraft structure. However, the ITO is fragile and may be degraded with even minimal handling. Wiping for cleaning purposes can ruin the surface, as can bending during manufacture or storage. Thermal bake-out of the hardware may also contribute to loss of ITO surface conductivity.

Because of the difficulty of grounding Teflon, it has largely disappeared as an external thermal-control material on satellites in GEO.

In the case of metalized finishes like silvered Teflon, aluminized Kapton, and quartz mirrors, the metal layer may also have to be grounded. This may be accomplished through mechanical connections or the use of adhesives that have been made conductive by the addition of metal particles. Unfortunately, in some instances, grounding requirements may prevent the use of a finish that would have been best strictly from a thermal-control standpoint.

References

4.1. R. J. Duckett and C. S. Gilliland, "Variable Anodic Thermal Control Coating on Aluminum," AIAA-83-1492, *AIAA 18th Thermophysics Conference* (1–3 June 1983).

4.2. Y. S. Touloukian, *Thermophysical Properties of Matter* (IFI/Plenum, New York and Washington, 1972).

4.3. M. Donabedian, "Emittance of Selected Thermal Control Surfaces at Cryogenic Temperatures," The Aerospace Corporation, ATM 90(9975)-10 (15 December 1989).

4.4. D. L. Wilkes and L. H. Hummer, "Thermal Control Surfaces Experiment-Initial Flight Data Analysis-Final Report," AZ Technology Report No. 90-1-100-2 (1991).

4.5. M. J. Meshishnek, S. R. Gyetvay, and C. H. Jaggers, "Long Duration Exposure Facility Experiment Deintegration/Findings and Impacts," *LDEF-69 Months in Space First Post-Retrieval Symposium*, ed. Arlene S. Levine (NASA Conference Publication 3134, 1992) pp. 1073–1107.

4.6. J. L. Golden, "Results of Examination of the A276 White and Z306 Black Thermal Control Paint Discs Flown on LDEF," *LDEF-69 Months in Space First Post-Retrieval Symposium*, ed. Arlene S. Levine (NASA Conference Publication 3134, 1992) pp. 975–987.

4.7. C. S. Hemminger, W. K. Stuckey, and J. C. Uht, "Space Environmental Effects on Silvered Teflon Thermal Control Coatings," *LDEF-69 Months in Space First Post-Retrieval Symposium*, ed. Arlene S. Levine (NASA Conference Publication 3134, 1992) pp. 831–845.

4.8. G. Pippin, W. K. Stuckey, and C. S. Hemminger, "Performance of Silvered Teflon Thermal Control Blankets on Spacecraft," *LDEF Materials Results for Spacecraft Application Conference* (Huntsville, Ala., 27 October 1992).

5 Insulation

M. Donabedian,[*] D. G. Gilmore,[*] J. W. Stultz,[†]
G. T. Tsuyuki,[†] and E. I. Lin[†]

Introduction

Multilayer insulation (MLI) and single-layer radiation barriers are among the most common thermal-control elements on spacecraft. MLI blankets prevent both excessive heat loss from a component and excessive heating from environmental fluxes, rocket plumes, and other sources. Most spacecraft flown today are covered with MLI blankets, with cutouts provided for areas where radiators reject internally generated waste heat. MLI blankets are also typically used to protect internal propellant tanks, propellant lines, solid rocket motors, and cryogenic dewars. Single-layer radiation barriers are sometimes used in place of MLI where less thermal isolation is required, since they are lighter and cheaper to manufacture. Applications requiring insulation under atmospheric conditions generally use foam, batt, and aerogel materials because MLI is not very effective in the presence of a gas. See Chapter 3 for specific examples of how insulation is used in typical thermal designs.

MLI is composed of multiple layers of low-emittance films, as shown in Fig. 5.1. The simplest MLI construction is a layered blanket assembled from thin (1/4-mil thick) embossed Mylar sheets, each with a vacuum-deposited aluminum finish on one side. As a result of the embossing, the sheets touch at only a few points, and conductive heat paths between layers are thus minimized. The layers are aluminized on one side only so that the Mylar can act somewhat as a low-conductivity spacer. Higher-performance construction is composed of Mylar film metalized (with aluminum or gold) on both surfaces with silk or Dacron net as the low-conductance spacers. Testing done at JPL[5.1] showed that replacing flat, aluminized Mylar/Dacron spacers with embossed, aluminized Kapton and no spacers increased the effective emittance of blankets by 19%.

Blankets were originally used only for limiting the heat flow to and from a spacecraft. Today they may also protect against micrometeoroids, atomic oxygen (AO), electron charge accumulation, and rocket-engine plume impingement. In addition, blanket design must accommodate requirements for durability, flammability, contamination control, launch loads, pressure decay, spacecraft venting, glint minimization, and restrictions on magnetic materials. Because most launch sites are near beaches (or even in the middle of the ocean, as in the case of Sea-Launch), exposure to salt spray and other corrosive agents is possible, so blanket design must take that exposure into account. All of these functions and design requirements must be addressed by blanket developers, who are also striving to minimize mass, cost, risk, and development time.

---

*The Aerospace Corporation, El Segundo, California.
†Jet Propulsion Laboratory, California Institute of Technology, Pasadena, California.
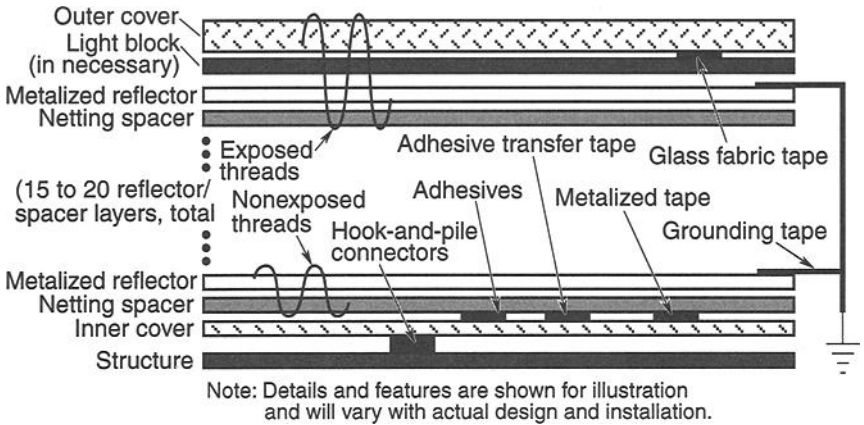
Fig. 5.1. Composition of a typical MLI blanket. (Courtesy NASA[5.2])

Blanket Performance

Heat transfer through MLI is a combination of radiation, solid conduction, and, under atmospheric conditions, gaseous conduction. These forms of heat transfer are minimized in different ways. Radiative heat transfer is minimized by interposing as many enclosing reflective surfaces (metalized sheets) as is practical between the object being insulated and its surroundings. Solid-conduction heat transfer is minimized by keeping the density of the low-conductance spacers between the reflective surfaces as low as possible and making the blanket "fluffy" to minimize contact between layers. Gaseous-conduction heat transfer is minimized by allowing the insulation to vent to space after the vehicle is launched or by using the insulation in an evacuated wall, such as the space between a cryogenic pressure vessel and the external vacuum-jacket shell.

Because these heat-transfer mechanisms operate simultaneously and interact with each other, the thermal conductivity of an insulation system is not strictly definable, analytically, in terms of variables such as temperature, density, or physical properties of the component materials. A useful technique is to refer to either an apparent thermal conductivity, K_{eff}, or an effective emittance, ε^* (informally known as "E-star"), through the blanket. Both values can be derived experimentally during steady-state heat transfer.

The low thermal conductivity of evacuated-insulation systems can largely be attributed to the removal of gas from the void spaces within the insulation. The degree of vacuum necessary to achieve the desired effectiveness can be established by considering the mechanism by which the heat flows. The gas conduction can be divided into two regions: the region ranging from atmospheric pressure down to a few torrs (1 torr = 1 mm of mercury) of pressure, in which gas conduction is independent of pressure, and the region at pressures below a few torrs, in which gas conduction depends on pressure. The transition from one type of gas-conduction region to the other depends upon the dimensions of the system with respect to the mean free path of the gas molecules. The effect of gas pressure on conductivity can be characterized by the curves in Fig. 5.2. The effective conductivity begins
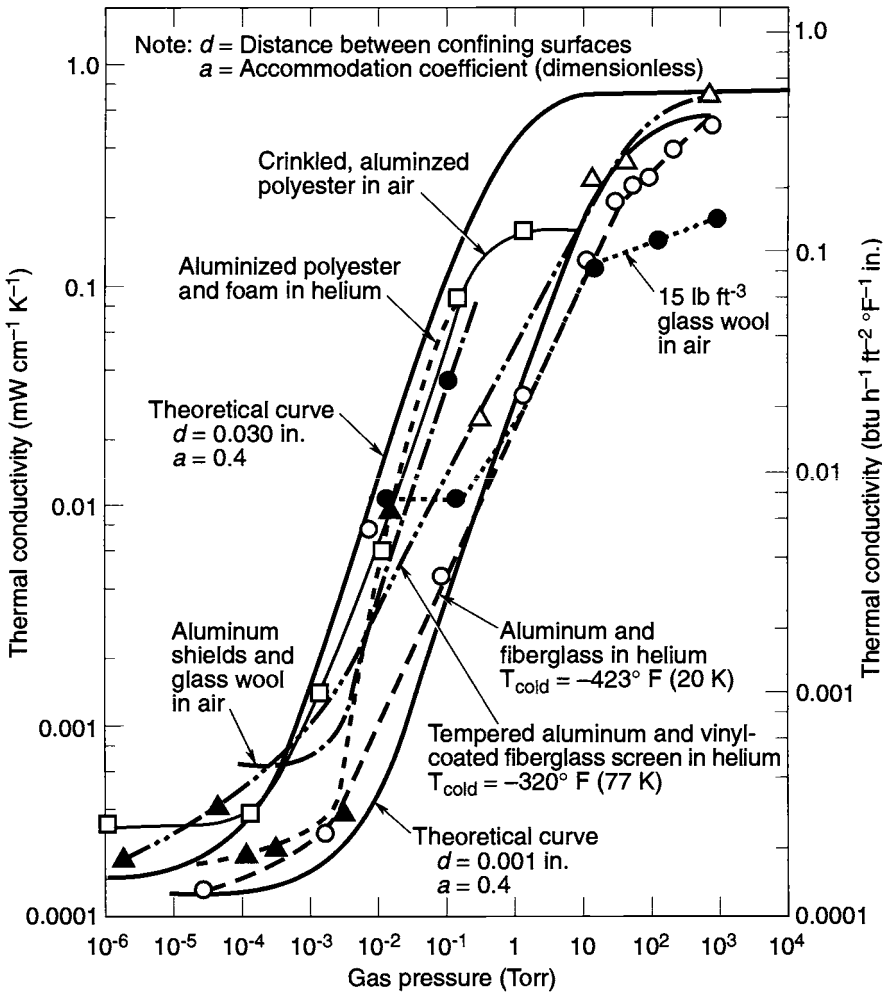
Fig. 5.2. Effect of gas pressure on thermal conductivity.

to decrease sharply between 1 and 10 torr until about 10^{-4} to 10^{-5} torr, where the heat conducted by the gas is only a small portion of the residual heat transfer. A finite value of effective thermal conductivity remains at lower pressures as a result of heat transfer by solid conduction and radiation between the elements of the insulation.

In theory, for highly evacuated MLI systems (i.e., systems with gas pressures of 10^{-5} torr or less), the emittance ε for a blanket of N noncontacting layers of emissivities ε_1 and ε_2 on opposite sides is computed as

$$\varepsilon = \frac{1}{\dfrac{1}{\varepsilon_1} + \dfrac{1}{\varepsilon_2} - 1}\left(\frac{1}{N+1}\right). \tag{5.1}$$

In practice, the effective emittance of an MLI blanket is generally derived from experimental tests at gas pressure of 10^{-5} torr or less calculated from

$$\varepsilon = \frac{Q}{A\sigma(T_H{}^4 - T_C{}^4)}, \tag{5.2}$$

where T_H and T_C are the hot and cold boundary temperatures in degrees Kelvin, A is the surface area of the blanket (m^2), Q is the net heat transferred in (W), and σ is the Stefan-Boltzmann constant in units of $W/m^2 \cdot K^4$.

Alternately, an effective thermal conductivity, K_{eff}, is also used. When K_{eff} is expressed in units of $W/m \cdot K$, ε^* is related to K_{eff} by the equation

$$\varepsilon^* = \frac{(K_{eff})(T_H - T_C)}{(l)(\sigma)(T_H{}^4 - T_C{}^4)}, \tag{5.3}$$

where l is the thickness of the MLI between the hot and cold boundaries.

In Fig. 5.3, theoretical and experimental data for embossed aluminized (one surface) Mylar insulation are plotted against number of insulation-blanket layers. As indicated by Eq. (5.1), the emittance for a multilayer blanket theoretically varies (directly) with one over one plus the number of layers. However, in practice, simply increasing the number of layers past a certain value will not improve performance. As the number of layers increases, radiative heat transfer becomes small compared with conductive "shorts" between layers and other losses. Thus, a point of
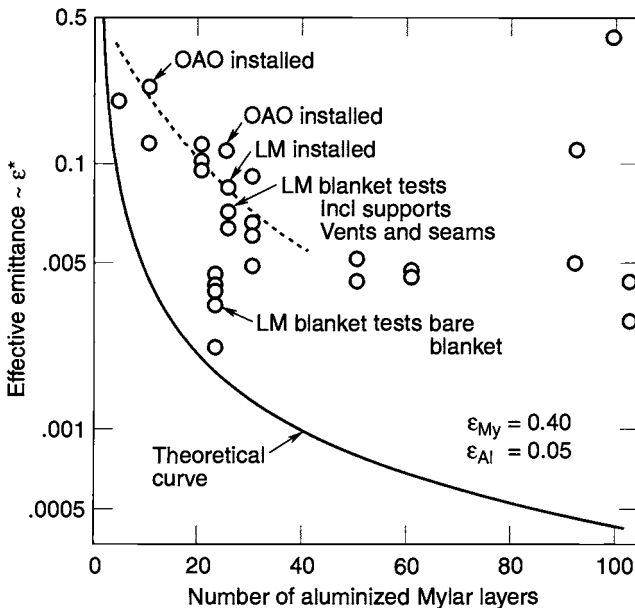

Fig. 5.3. Effective emittance vs. number of single aluminized layers.

diminishing returns is reached. Taking all of these factors into account, one finds that about 25 layers usually suffice to obtain a minimum overall conductance value.

In well-controlled laboratory tests, values of 0.005 or lower for ε^* can be achieved. However, experience has shown that when a blanket is configured for spacecraft application, an ε^* more like 0.015 to 0.030 is representative of current design, manufacturing, and installation methods for medium-area applications. As the size of the application increases, the relative performance generally increases, as indicated by the data in Fig. 5.4. This relationship results from the smaller relative influences of heat leaks that result from edge effects, seams, cable penetrations, etc. For very-large-area applications with minimal penetrations, like ones on the Spacelab, the laboratory performance approaches 0.005 at 30 layers, as shown by the test data in Fig. 5.5. Performance data from cryogenic tankage and controlled calorimeter tests typically also show better performance of ε^* down to 0.002, and K_{eff} down to 1×10^{-5} Btu/hr·ft·°R, as shown in Figs. 5.4 and 5.6. The data in Fig. 5.6, although given in terms of K_{eff}, can be found quite comparable to the data in Fig. 5.5 when the average temperatures are similar and Eq. (5.3) is used. The data of Fig. 5.4 show that the control of discontinuities through the design and fabrication of insulation joints and penetration is crucial to the problem of reducing the effective emittance of MLI blankets. Small-area blankets show high effective emittance along with considerable manufacturing variation. Very small blankets used to wrap propellant lines typically have effective emittances ranging from 0.05 to 0.30, making simple, low-emittance surface finishes a simpler and
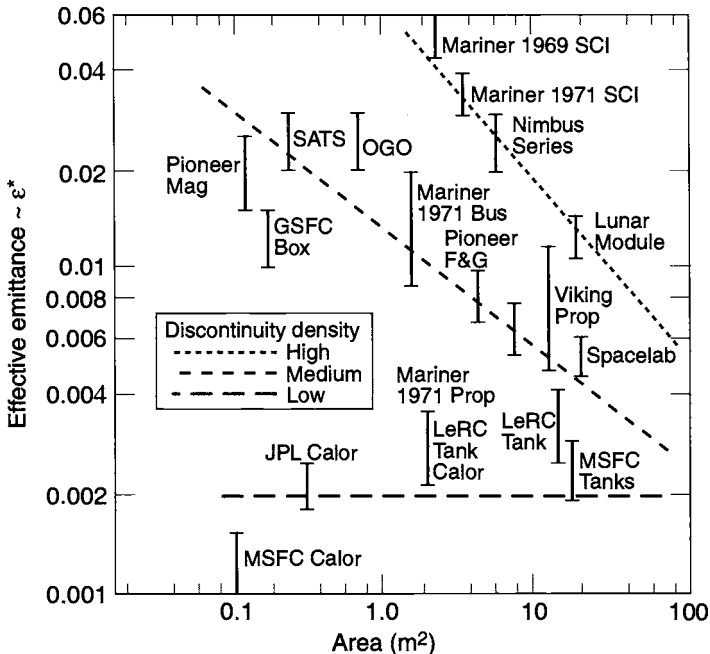
Fig. 5.4. Effective emittance vs. installed area.
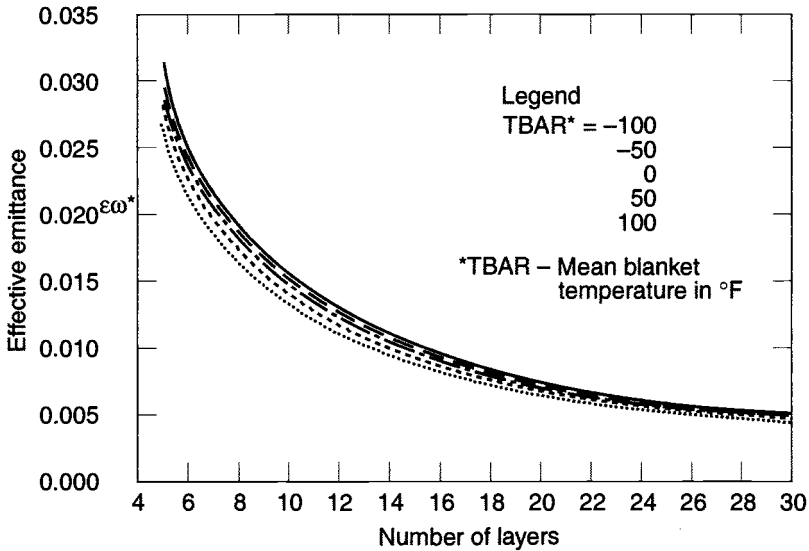
Fig. 5.5. MLI blanket effective emittance derived from the Spacelab thermal test data.

$$K_{\text{eff}} = \left[1.027\text{E--}7 \frac{T_H + T_C}{2} + 3.333\text{E--}16 \frac{T_H^{4.67} - T_C^{4.67}}{T_H - T_C} \right] \times 0.625$$

- Double aluminized Mylar with Tissueglass spacers
- 110 layers/in. (0.75 to 1.25 in.)
- Pressure = 10^{-6} Torr
- T_H = Hot boundry temperature (°R)
- T_H = Cold boundry temperature (°R)
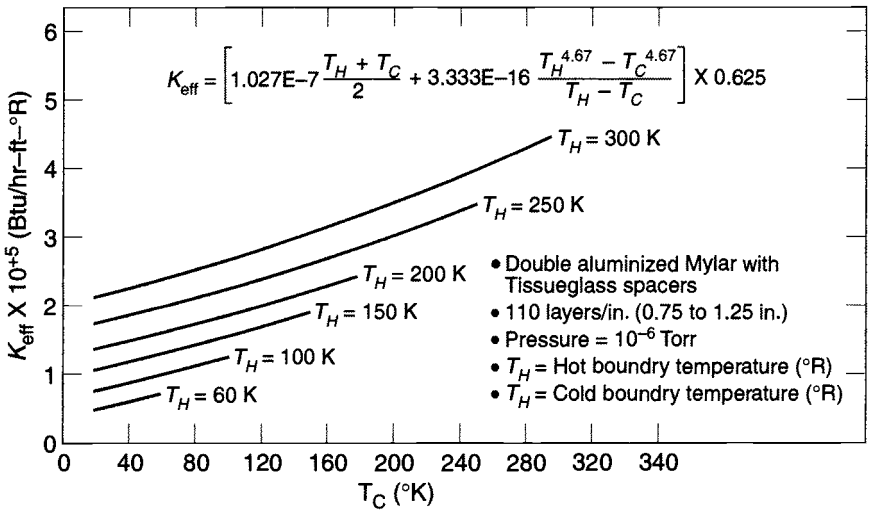
Fig. 5.6. Effective thermal conductivity of MLI blankets.

equally effective alternative for internal propellant lines. External lines exposed to sunlight may still require MLI blankets, however, to avoid overheating that might be caused by the high absorptance-to-emittance ratios typical of low-emittance surface finishes.

The effect of seams on blanket performance was dramatically illustrated in work done at JPL for the Cassini program. Twenty-layer test blankets with Dacron net

separators were instrumented to measure temperature drops through the blanket at various locations. Results, summarized in Fig. 5.7, show that blanket effective emittance varied from 0.006 near the center to almost 0.15 near the seam! The resulting local radiative heat loss from the room-temperature test article to the LN_2-cooled chamber wall varied by an order of magnitude, from less than 3 W/m^2 to almost 30 W/m^2, depending on distance from the seam. These data also show that seams can doom very small insulation blankets to poor performance, making low-emittance surface finishes a more attractive option in small-area applications where solar illumination is not an issue. The performance of an MLI system can be severely degraded by the pressure of even very modest amounts of gas. Data from General Dynamics (Fig. 5.8) show that an increase from 1×10^{-5} torr to 1×10^{-4} torr increased the system heat-leak by 33%. This demonstrates further the importance of reducing outgassing and the prevention of contamination of the blankets that may account for some cases of thermal performance degradation of MLI systems.

While a range of MLI blanket effective emittances should be considered in defining the hot and cold spacecraft thermal design analysis cases, a more nominal estimate of blanket performance can be made using an empirical relationship developed by J. Doenecke.[5.3] By analyzing measured blanket performance reported from a number of sources, the following equation was developed to relate effective
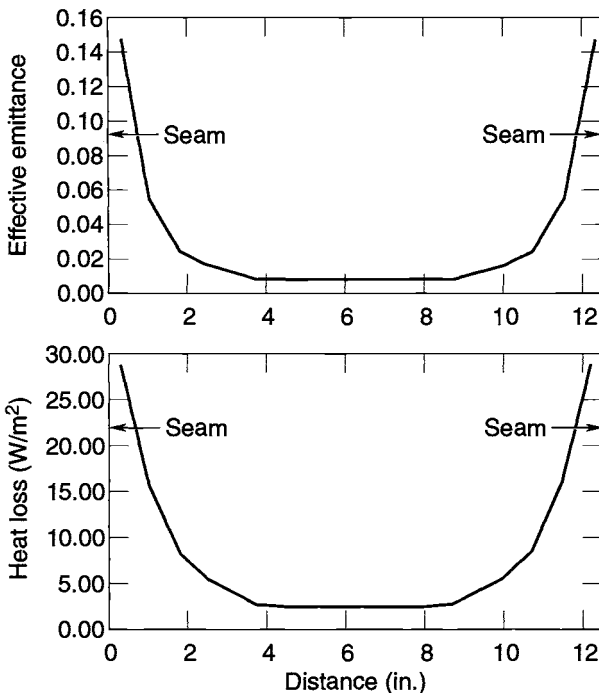
Fig. 5.7. Effect of a seam on MLI blanket performance.
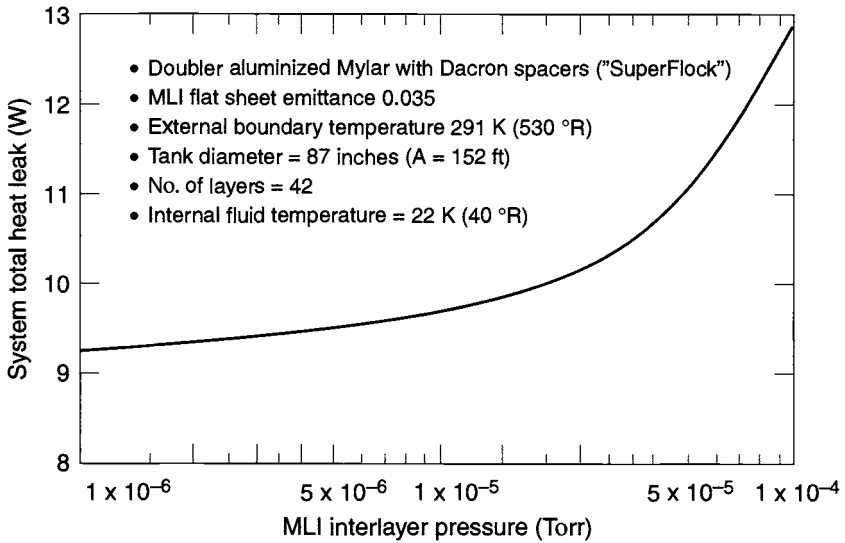
Fig. 5.8. Effect of gas pressure on MLI blanket performance of a cryogenic tank (from General Dynamics data).

emittance to the number of layers, the size of the blanket, the fraction of blanket area taken up by penetrations, and the average temperature of the blanket layers:

$$\varepsilon_{eff} = \left(0.000136 \cdot \frac{1}{4\sigma T_m^2} + 0.000121 \cdot T_m^{0.667} \right) \cdot f_N \cdot f_A \cdot f_P \quad ^* \quad (5.4)$$

This relationship is valid for values of T_m in the range of −140 to +140°C. Values of f_N and f_P can be found in Table 5.1, while f_A is determined by the following relationship:

$$f_A = 1/10^{(0.373 \cdot \log A)}, \quad ^* \quad (5.5)$$

where A is the area in square meters. (Equation [5.5] should be used only for blanket areas between 0.05 and 3 m^2. For areas outside this range, the values at 0.05 or 3 m^2 should be used.) The average temperature of the blanket layers, T_m, is defined as:

$$4T_m^3 = \frac{(T_h^4 - T_c^4)}{(T_h - T_c)} = (T_h^2 + T_c^2) \cdot (T_h + T_c), \quad ^* \quad (5.6)$$

where T_h and T_c are the temperatures of the external layers on the hot side and cold side of the blanket, respectively. Because ε_{eff} influences T_h and T_c, it may be necessary to perform a few iterations between Eqs. (5.4) and (5.6).

Table 5.1. Correction Factors to be Used in Eq. (5.4)[a]

Number of Layers	f_N	
5	2.048	
10	1.425	
15	1.164	
20	1.000	
25	0.905	
30	0.841	
Penetrations (%)	f_P[b] ($\varepsilon_i = 0.04$)	f_P[b] ($\varepsilon_i = 0.03$)
0.1	0.756	0.704
0.2	0.783	0.737
0.5	0.865	0.837
1.0	1.000	1.000
1.5	1.133	1.161
2.0	1.266	1.322

[a]Reprinted with permission from SAE Paper No. 932117 ©1993 Society of Automotive Engineers, Inc.
[b]Surface emittance of internal layers. Use 0.04 for layers with 1000 Å vapor-deposited alluminum and 0.03 for layers with 750 Å vapor-deposited gold (typical for Sheldahl).

Blanket Design Requirements

Figure 5.9 identifies the principal factors that the thermal engineer must consider when specifying blankets for a particular application. These factors include temperature, solar absorptance, IR (infrared) emittance, effective emittance, and specularity. The blanket design must also take into account requirements—such as grounding or glint suppression—that have been levied by the other subsystems.

Materials

The designer must ensure that all materials used in blanket fabrication meet all of the spacecraft-materials requirements discussed above. These requirements include, but are not limited to, specifications regarding operational and nonoperational temperature limits, mechanical loads, fluid exposure, charged particles, ultraviolet (UV) radiation, electrical grounding and bonding, contamination, and life expectancy. Ground transportation, storage, handling, and spacecraft on-orbit conditions must all be considered during materials selection.

All materials used in making an MLI blanket should be treated as flight-critical hardware from the time they are received. This requirement should extend to all vendors in the manufacturing chain. Materials should not be handled with bare hands or exposed to uncontrolled or corrosive environments. They should not be pulled or unnecessarily wrinkled, as these actions may stress blanket layers and lead to defects that do not appear until after launch.

Temperature: >250°C _____ <250°C _____

Glint (stray light) Prevention: _____yes _____no

Electrostatic Discharge Prevention: _____ yes _____no

Free Neutral (Atomic) Oxygen Prevention: _____ yes _____no

Venting: _____hardware side _____ space side

Solar Absorptance: _____exterior _____ interior

Infrared Emittance: _____exterior _____ interior

Effective Emittance: _____

Micro-meteoroid Protection: _____yes _____no

Grounding: _____all layers _____ exterior layers only

Contamination Prevention (Bakeout):   _____ yes _____no

Nonmagnetic Material: _____yes _____no

Attachment Method: _____Tie-cord _____Velcro _____Tape

Fig. 5.9. Checklist of factors thermal engineers must consider when specifying blankets.

Outer Cover

The set of properties required of the outer layer is one of the most important fac-
tors influencing the choice of blanket materials. Usually the thermal engineer is free
to choose an outer-layer material (such as aluminized Kapton or Beta cloth) with a
moderate α/ε ratio that will run at a comfortable temperature when exposed to
sunlight. In some cases, however, electrostatic discharge or glint-suppression
requirements will dictate the use of black Kapton, or micrometeoroid-protection
needs will require the use of the heavier Beta cloth material. Sometimes Tedlar or
painted Kapton is also used as an outer-cover material, but Mylar never is, because
it is incompatible with UV exposure. In any event, materials used for the outer-
cover layer (space side) of MLI blankets should be opaque to sunlight, generate a
minimal amount of particulate contaminants, and be compatible with the environ-
ments and temperatures to which they will be exposed over the duration of the
mission. Properties of principal outer-layer materials are summarized in Table 5.2.

In the rare instance where a very low α/ε ratio is needed to minimize the thermal
impact that solar exposure will have on internal components, a silvered Teflon sur-
face finish may be used on the outer blanket layer.

When Teflon is used, however, it should be bonded to a durable support material
such as Kapton because the Teflon will lose all mechanical strength over time as a
result of the effects of charged particles and thermal cycling. This lesson was
learned the hard way, first by the NATO II satellite that experienced failure of an
aluminized Teflon sun shield in the 1970s and again by the Hubble Space Telescope
when it experienced tears in the Teflon cover layer of its MLI blankets in the 1990s.

Table 5.2. MLI Outer-Cover Materials (Courtesy of NASA[5.2])

Material	Beta Cloth	Beta Cloth, Aluminized	Tedlar, Reinforced	Kapton, Coated & Backed	Teflon, Backed	Teflon, Coated & Backed
Description	Fiberglass woven cloth impregnated with PTFE Teflon (500F: no silicone)	Fiberglass woven cloth impregnated with PTFE Teflon with one side alumized	PVF reinforced with open weave Nomex bonded w/polyester adhesive, one side alumized	Kaplon, transparent indium tin oxide conductive coating and aluminum backing	FEP Teflon, vacuum deposited silver and Inconel backing layers	Teflon, transparent indium tin oxide conductive coating and silver/Inconel backing
Vendors	Chemfab	Chemfab, Dunmore	Sheldahl, Dunmore	Sheldahl, Dunmore	Sheldahl, Dunmore	Sheldahl, Dunmore
Weave Texture, wrap x fill, yams/cm Yarn fiber diam, mm	Plain 32x24 0.00004	Plain 32x24 0.00004	N/A	N/A	N/A	N/A
Fabric/film thickness, cm (in.)	0.020 (0.008)	0.020 (0.008)	0.01 (0.004) +20%	[1]	[1]	[1]
Weight, gm/cm^2	0.0237	0.0271	—	[1]	[2]	[3]
Tensile strength, min. Warp, kg/cm Fill, kg/cm	16 10.7	16 10.7	—	—	—	—
Elongation at break, % min. Warp Fill	6.5 2.0	6.5 2.0	—	70 70	300 300	300 300
Tearing strength, min.	0.82	0.82	—	—	—	—
Useful temp. range, °C Continuous, min/max Intermittent, min/max	<204	<204	−72/107 <175	−73/65	−184/150 −184/260	−73/65

Table 5.2. MLI Outer-Cover Materials (Courtesy of NASA[5.2]) —*Continued*

Material	Beta Cloth	Beta Cloth, Aluminized	Tedlar, Reinforced	Kapton, Coated & Backed	Teflon, Backed	Teflon, Coated & Backed
Teflon by weight, %	17–22	17–22	—	—	—	—
Aluminum thickness, Å	—	350	—	—	—	—
Surface resistivity, Ω/square	—	—	—	250,000	—	250,000
Solar absorptance (α), min.	0.45 (white side)	0.37 (VDA side)	0.30	[1]	0.10	0.14
IR emittance (ε), max.	0.80 (white side)	0.30 (VDA side)	0.80	[1]	[2]	[3]
Environmental compatibility	A0+UV	A0+UV	Short-term AO	Short-term AO Long-term UV	Short-term AO Long-term UV	Short-term AO Long-term UV

Weight, Solar Absorptance, and IR Emissivity for Covers of Varying Thickness

	[1] Kapton			[2] Teflon, backed		[3] Teflon, coated	
Thickness (cm)	Weight (gm/cm²)	α	ε	Weight (gm/cm²)	ε	Weight (gm/cm²)	ε
0.0013	0.0019	0.41	0.50	0.028	0.40		
0.025	0.0036	0.44	0.62	0.0055	0.48	—	
0.0051	0.0071	0.49	0.71	0.011	0.60	0.011	0.60
0.0076	0.011	0.51	0.77	—		—	
0.0127	0.019	0.54	0.81	0.027	0.75	0.027	0.75
0.0191				0.055	0.80	—	
0.0254				0.055	0.85	—	

Interior Layers

The general requirements for interior blanket layers are that they should have low emittance, generate a minimal amount of particulate contaminants, and be compatible with the environments and temperatures to which they will be exposed during the mission. The most commonly used material for the interior layers is Mylar that is aluminized on one or both sides. Because the outer layer protects them from the abuse of handling during the spacecraft-manufacturing process, the inner layers are usually made much thinner than the outer layer to save weight. the interior layers are also often perforated to aid in venting trapped air during launch ascent. Properties of reflector-layer materials are shown in Table 5.3.

Table 5.3. MLI Interior-Layer Materials (Courtesy of NASA[5.2])

Material	Aluminized Kapton	Goldized Kapton	Aluminized Mylar	Polyester	Teflon
Description	Single or double aluminized	Single or double goldized	Double aluminized	Single or double aluminized	Single or double aluminized
Vendors	Sheldahl, Dunmore	Sheldahl	Sheldahl, Dunmore	Sheldahl, Dunmore	Sheldahl, Dunmore
Thickness, mm (mil)	0.0076–0.127 (0.3–5.0)	0.0076–0.127 (0.3–5.0)	0.0051–0.127 (0.2–5)	0.00006–0.0013 (0.25–5)	0.00003–0.0013 (0.1–5)
metal, Å	1000	750	1000	300	300
Weight, gm/cm^2				—	—
0.0051 mm (0.2 mil)			0.0007		
0.0064 mm (0.25 mil)			0.00093		
0.0076 mm (0.3 mil)	0.0011	0.0011			
0.013 mm (0.5 mil)	0.0019	0.0019	0.0017		
0.025 mm (1.0 mil)	0.0036	0.0036	0.0033		
0.051 mm (2.0 mil)	0.071	0.071	0.0066		
0.076 mm (3.0 mil)	0.011	0.011	0.0104		
0.127 mm (5.0 mil)	0.019	0.019	0.0175		
Temperature, °C					
Continuous, max/min	–250/+288	–250/+288	–250/+93[a]	260	260
Intermittent, max/min	–250/+400	–250/+400	–250/+150		
Absorptance, α (max/typ)	0.14; 0.12	0.30; 0.28	0.14; 0.12	< 0.14	< 0.14
IR emittance, ε	0.05; 0.03[b]	0.04; 0.02[b]	0.05; 0.03[c]	< 0.04	< 0.04

[a]Temperature range for double-aluminized Mylar may be limited to 120°C (250°F) depending on sensitivity of blanket design to shrinkage. Shrinking the blanket before installation is advised.
[b]Typical emittance from noncoated side for Kapton, single goldized, see table in footnote c.
[c]Typical emittance from noncoated side for Mylar, single aluminized, see table.

Typical Emittance from Noncoated side

Kapton, single goldized			Mylar, single aluminized		
Thickness, cm (in.)	α	ε	Thickness, cm (in.)	α	ε
0.00076 (0.0003)	0.31	0.50	0.00064 (0.00025)	0.16	0.33
0.00013 (0.0005)	0.31	0.55	0.0013 (0.0005)	0.16	0.46
0.0025 (0.001)	0.33	0.65	0.0025 (0.001)	0.19	0.57
0.0051 (0.002)	0.34	0.75	0.0051 (0.002)	0.23	0.72
0.0076 (0.003)	0.27	0.81	0.0076 (0.003)	0.25	0.77
0.0127 (0.005)	0.41	0.86	0.0127 (0.005)	0.27	0.81

The temperature of the outer-layer material should be calculated for worst-case solar exposure or plume heating conditions to determine if it will impact the interior layers. A high outer-layer temperature may rule out the use of some interior-layer materials that cannot withstand high temperatures, such as aluminized Mylar that melts at 250°C. In such instances, a higher-temperature material, such as aluminized Kapton, must be used for at least the first several layers. (See page 193 for a description of the high-temperature blankets developed for the Cassini program.) For most applications in Earth orbit, however, this limitation does not apply.

Separators

The principal requirements for the separator material are that it have minimal contact area with the blanket layers, have low thermal conductivity, produce minimal particulate contamination, and be compatible with the temperatures to which it will be exposed during the mission. The most commonly used separator materials are Dacron and Nomex netting. Properties of these materials are shown in Table 5.4.

Inner Cover

The inner cover faces the underlying spacecraft hardware. Like the other blanket layers, it must generate a minimal amount of particulate contaminants and be compatible with the environments and temperatures to which it will be exposed over the duration of the mission. The main role of the inner cover is to protect the thin interior layers from the stress of handling. Often, the exposed surface of the inner-cover layer (the side facing the hardware) is not aluminized in order to reduce the chance of an electrical short. Mylar is not recommended for the inner cover because of flammability concerns. Properties of some inner-cover materials are shown in Table 5.5.

Table 5.4. MLI Separator-Layer Materials (Courtesy of NASA[5.2])

Material	Dacron Netting	Nomex Netting
Description	100% polyester fabric mesh[a]	100% Nomex aramid fabric mesh[b]
Vendors	Apex Mills	Stern & Stern Textiles, J.P. Stevens
Thickness, mm (in.)	0.16 ± 0.01 (0.0065 in. ± 0.0005)	0.16 ± 0.01 (0.0065 in. ± 0.0005)
Construction		
Meshes/cm^2	7.8 ± 1.2	7.9 ± 1.2
Denier filaments	40	40
Weight, gm/m^2	6.3 ± 0.85	6.3 ± 0.85
Burst strength, kg/cm	5.625	5.625
Temperature range, °C	−70 + 120 continuous	−70 + 120 continuous
	−70 + 177 intermittent	−70 + 177 intermittent

[a]Dacron netting may shrink and melt above 177°C.
[b]Nomex netting may contain a phthalate plasticizer added for flexibility. The plasticizer should be removed by chemical means or vacuum bakeout before assembly of the blanket.

Table 5.5. MLI Inner-Cover Materials (Courtesy of NASA[5.2])

Material	Aluminized	Double Goldized	Glass Reinforced
Description	Polyimide reinforced with aramid (Nomex or equivalent) open-weave fabric; 1- or 2-sided aluminum	Double-goldized polyimide reinforced with aramid (Nomex or equivalent) open-weave scrim fabric	Aluminized Polyimide with fiberglass backing
Vendors	Dunmore, Complex Plastics	Dunmore, Complex Plastics	Dunmore, Sheldahl
Available thicknesses, mm (in.)	0.013, 0.025, 0.0762 (0.0005, 0.001, 0.003) ± 20%	0.01 (0.00045) ± 56%	0.01 (0.00045) ± 56%
Metalized thicknesses, Å	1,000	750	300
Reinforcement	Leno weave, 6.3 x 5.9/ cm yarn count of 200 denier yarn	Leno weave, 6.3 x 5.9/ cm yarn count of 200 denier yarn	1070 or 108 fiberglass
Ply adhesion, kg/cm	0.054	0.054	0.18
Tear resistance, kg min avg	1.4	1.4	1
Tensile strength, kg/cm			
Warp	7.14	4.46	17.85
Fill	7.14	3.57	17.85
Elongation, % avg.			
Warp	50	9	50
Fill	50	5	50
Porolation, pinholes/m^2 (Light visible through 90% of holes)	145,300 ± 2152 Open area 3% of surface	145,300 ± 2152	N/A
Weight, gm/m^2	50	–	50
Infrared emittance (ε)	0.06 aluminized side	0.04 coated side	< 0.04
	0.4 reinforced side	0.2 coated, reinforced side	

In recent years, vendors have also started offering complex laminates of reflective surfaces on impact-resistant or structural materials. Properties for some of these potential cover layers are shown in Table 5.6.

Table 5.6. Laminated Inner-Cover Materials[a] (Courtesy of NASA[5.2])

Material	Double Nomex Laminate	Kevlar/Kapton Laminate	Lightweight Laminate
Description	Aluminum coated	Corrosion resistant, perforated	Aluminum coated, perforated
Vendors	Dunmore, Sheldahl	Dunmore, Sheldahl	Dunmore, Sheldahl
Layer sequence	Teflon, aluminum coated **Nomex** 0.3 mil Kapton, aluminum coated 0.5 mil FEP, aluminum coated **Nomex** 0.3 mil Kapton, aluminum coated DB-15 corrosion coating	FEP, aluminum coated Kevlar 0.5 mil Kapton, aluminum coated DB-15 corrosion coating	0.5 mil Kapton, aluminum coated Nomex, aluminum coated
Tensile strength, kg/cm	8.0	8.0	8.0
Tear strength, kg	4.5	4.5	4.5
Material yield, gm/m^2	74	74	74
Maximum temperature, °C	<121	<121	<121
Emittance (ε)	<0.04	<0.04	<0.04
Absorptance (α)	<0.14	<0.14	<0.14

[a]Aluminum coatings are 350 Å for Dunmore, 1000 Å for Sheldahl.

Tapes

Pressure-sensitive adhesive tapes are used to close blanket edges and cutouts, to protect seams stitched with organic thread from AO erosion, to provide reinforcement of interior or cover layers in local areas, and to aid in electrical grounding of the blanket. Tapes can be purchased from a manufacturer or "homemade" out of any blanket-layer material by simply applying a transfer adhesive and cutting strips of the desired length and width. Usually the tape should have the same optical properties as the surface to which it is applied, but different optical properties are acceptable if they do not significantly affect the performance of the entire blanket and do not cause temperatures in the vicinity of the tape to exceed allowable material or adhesive limits. (Gold-coated tape on the outer cover of a blanket, for instance, would run quite hot in the sun because of its high α/ε ratio.) Surfaces to be taped must be clean and free of oils to ensure a good bond. The tapes are usually applied with a hard roller and are sometimes tacked in place every few centimeters with thread to ensure that pieces cannot float away if the tape lifts.

Double-sided transfer adhesive tapes may be used to make tape from a blanket material, to laminate two thin films, or to bond a thin film (or a blanket) to an object. The properties of representative transfer adhesive tapes are shown in Table 5.7.

Tapes made from glass fabric or Teflon-impregnated glass fabric are durable and have surface properties similar to Beta cloth outer-cover-layer material. Properties of these tapes are shown in Table 5.8.

Tapes made from aluminized or gold-coated plastic films are appropriate for use where a low emittance is desired, such as on interior layers of a blanket. Properties of representative metalized tapes are listed in Table 5.9.

Electrically conductive adhesive tapes can be used in grounding the blanket layers. Properties of some conductive tapes are listed in Table 5.10.

Table 5.7. Plain Transfer Adhesive Tapes (Courtesy of NASA[5.2])

Material	Scotch Adhesive Tape, 3M Y966	Scotch Adhesive Tape, 3M 9460	Scotch Adhesive Tape, 3M Y9473	Tedlar Tape
Description	Polyimide w/ 966 PSA	Polyimide w/ 9460 PSA	Polyimide w/ 9473 PSA	Tedlar film w/ 3MY966 PSA
Vendors	3M, Dunmore	3M, Dunmore	3M, Dunmore	Complex Plastics, Dunmore
Substrate film thickness, mm (in.)	0.05 (0.002)	0.05 (0.002)	0.25 (0.01)	0.1 (0.004)
Maximum operation temp., °C	160		–	
Continuous		< 150		149
Intermittent		< 260		260
Peel adhesion, gm/ cm, 90° @ 1m/min				
Aluminum,	–	1340	–	547
Stainless steel	547	1407		
Acrylic plastic	–	1273		
Polycarbonate	–	1005		

Table 5.8. Glass Fabric Tapes (Courtesy of NASA[5.2])

| Material | Teflon (PTFE)-Impregnated Glass Cloth Tape | | | Polyimide |
	Plain	Aluminized	Goldized	Aluminized
Description	w/3M 5451 silicone PSA	Aluminized on one side, 3M Y966 acrylic PSA	Gold coated on one side, 3M Y966 acrylic PSA	w/108 fiberglass, 966 PSA, 1st or 2nd coating
Vendors	Sheldahl	3M, Sheldahl, Dunmore	Sheldahl	Dunmore, Sheldahl
Widths, cm (in.)	2.54, 5.08 (1,2)	2.54, 5.08 (1,2)	2.5, 5.1, 7.6, 10.2 (1, 2, 3, 4)	--
Substrate film thickness, mm (in.)	0.15 (0.006)	0.08 (0.0032) ±10%	0.08 (0.0032) ± 10%	0.18 (.007)
Weight, gm/m^2	9.15	--	--	--
Tensile strength, kg/cm	12.5	2.14	2.14	
Elongation, % max.	--	10	10	--
Unwind force, gm/cm	--	447	447	--
Panel adhesion, gm/cm	391	447	447	279
Temperature range, °C				
Continuous	−73 to +204	--	--	< 149
Intermittent	< 260			
IR emittance, ε, max	--	0.04	0.04	0.14 (1st) 0.39 (2nd)
Absorptance, α, max	--	--	--	0.04 (1st) 0.62 (2nd)
Resistance, Ω/square	--	--	--	≤ 250,000

Table 5.9. Metalized Tapes (Courtesy of NASA[5.2])

Material	Kapton, Aluminized	Kapton, Goldized	Mylar	Teflon
Description	Polyimide film, 3M 966 PSA, aluminum coating	Polyimide film, 3M 848 PSA, gold coating	Polyethylene teraphthalate film, PSA aluminum coating	PFTE w/ aluminum 2nd surface
Vendors	Dunmore, Sheldahl	3M, Sheldahl	Complex Plastics, Sheldahl, Dunmore	Dunmore, Sheldahl
Thickness, mm (in.)				
Substrate	0.013-0.025 (0.0005-0.001)	0.025 (0.001)	–	0.051 (0.002)
Total	0.064-0.076 (0.0025-0.003)	0.051 (0.002)	–	0.102 (0.004)
Tensile strength, kg/cm	4.64	4.64	–	–
Unwind force, gm/cm	–	447	–	–
Adhesion, gm/cm	279–447	145	–	279
Infrared emittance, ε	0.04[a]	0.04	0.05	< 0.04
Absorptance, α	0.14–0.39	–	–	< 0.14

[a]Type III Kapton tape has the same requirements except that there is no requirement for emissivity. Kapton tape is also available in 0.013-mm (0.0005-in.) thickness.

Table 5.10. Electrically Conductive Tapes (Courtesy of NASA[5.2])

Material	Aluminum Tape	DM-106, DM-140	MO06061
Description	PSA w/conductive particles[a]	Black E7 polyimide with 966OSA[b]	Black E7 polyimide with 966PSA[c]
Vendors	3M	Dunmore	Dunmore
Thickness, mm (in.)			
Substrate film	0.102 (0.004)	0.025 (0.001)	0.025 (0.001)
Total		0.076 (0.003)	0.076 (0.003)
Tensile strength, kg/cm	–	3022	3022
Adhesion, gm/cm	–	279	279
Resistance, Ω/square	$<10^9$	$<4 \times 10^9$	$<10^9$
Infrared emittance, ε	0.05 (max)	>0.81	>0.81
Absorptance, α		<0.95	<0.95

[a]Must be baked out before flight.
[b]Available with aluminum coating.
[c]Available with 9703 conductive PSA (MO06061).

Thread

Thread is usually used to stitch blanket seams, to attach Velcro, and to join blankets to one another. Seams that are not exposed to low-Earth-orbit AO can be sewn with polymeric thread that is free of wax, paraffin, and other volatile finishes (see Table 5.11). For blankets exposed to AO, erosion-resistant threads, such as those listed in Table 5.12, are usually required. During manufacture, the sewing-machine tension must be adjusted so as not to overly compress the layers along the seam and thus minimize thermal shorting.

Manufacturing blankets with glass or ceramic thread may be difficult as a result of sewing-needle wear and thread breakage. In cases where design requirements or manufacturing capabilities do not allow glass or ceramic thread to be used in an application involving AO exposure, polymeric thread may be used if it is covered by a protective material such as glass-fabric tape or Kapton tape with an indium tin oxide (ITO) protective coating. Metallic thread should not be used in most blanket seams because of its tendency to cause heat shorts, although proper blanket design can mitigate this problem. If metallic thread is required to meet electrical grounding requirements, the amount of thread used should be limited to what is required to achieve an adequate ground.

Table 5.11. Threads for Seams Not Exposed to Atomic Oxygen (Courtesy of NASA[5.2])

Material	Nomex Thread	Nylon Thread	Nylon Thread	Reinforced Kevlar Thread
Specification	MIL-T-43636, Type II, Size E	MIL-T-43636, Type I, Size E	MIL-T-43636, Type I, Size F	
Description	Aramid, nonmelting, low-volatile-content thread, no silicone finish	Aramid, nonmelting, low-volatile-content thread	Aramid, nonmelting, low-volatile-content thread	Polyimide thread w/stainless-steel wire reinforcement and Teflon coating
Vendors	Synthetic Thread Co.	Synthetic Thread Co.	Synthetic Thread Co.	Alpha Associates
Diameter, mm (in.)	0.41 (0.016)	0.41 (0.016)	0.46 (0.018)	0.43 (0.017)
Plies	3	3	4	3
Twist, turns/cm	3.3	3.3	3.1	3.3
Yield, m/kg, max, min	4167, 4560 2813, 3078	4288, 5980 2895, 4038	3226, 3407 2178, 2300	1988 1343
Breaking strength, kg	2.36	2.36	3.13	9.07
Elongation, maximum %	38	38	38	(not available)
Maximum operation temp.,°C	<329 25% fail @ 371	<329 25% fail @371	<329 25% fail @ 371	<371

Table 5.12. Threads for Seams Exposed to AO (Courtesy of NASA[5.2])

Material	Quartz Thread	Glass Thread Coated w/PTFE	Reinforced Glass Thread Coated w/ PTFE	Nextel 312, 440
Specification	MIL-C-20079, Type III, Class 3	MIL-C-20079, Type III, Classes 3 and 4	MIL-C-20079, Type III, Class 6	3M ceramic materials
Description	High-temperature quartz thread	Fiberglass coated with PTFE Teflon	Fiberglass reinforced with stainless steel wire and coated with PTFE teflon	Aluminum borosilicate ceramic thread combined with Rayon
Vendors	Alpha Associates, W.F. Lake Corp.	Alpha Associates, W.F. Lake Corp.	Alpha Associates, W.F. Lake Corp.	3M
% weight, other thread	16 to 24, PTFE	13 to 16, PTFE	13 to 16, PTFE	10, Rayon[a]
Temperature range, °C	–240 to 1093	–240 to +316	–240 to +316	< 300

Thread Properties					
Quartz thread	TFQ-12	TFQ-18	TFQ-24		
Diameter, mm (in.)	0.356 (0.014)	0.432 (0.017)	0.508 (0.020)		
Yield, m/kg	1982	1327	991		
Tensile strength, kg	5.44	9.07	10.89		
Glass thread					
Diameter, mm (in.)	0.356 (0.014)	0.432 (0.017)	0.533 (0.021)	0.686 (0.027)[b]	0.762 (0.030)[b]
Yield, m/kg	1982	1327	991	773	252
Tensile strength, kg	5.4	9	10.9	15.9	22.7
Reinforced glass thread	TFE-12	TFE-18	TFE-24		
Diameter, mm (in.)	0.36 (0.014)	0.43 (0.017)	0.53 (0.021)		
Yield, m/kg	2015	1343	1007		
Tensile strength, kg	5.4	9.1	10.9		
Nextel 312, 440	AT-21	AT-28	AT-32	BT-28	BT-32
Diameter, mm (in.)	0.533 (0.021)	0.711 (.028)	0.813 (.032)	0.711 (.028)	0.813 (.032)
Yield, m/kg	1007	672	504	585	430
Tensile strength, kg	4.5	6.4	7.3	6.4	6.4

[a]Rayon fibers improve sewability. Rayon is susceptible to AO; loss may affect abrasion resistance but not overall strength of the thread. Nextel 312 fibers can withstand temperatures up to 1204°C, Nextel 440 to 1370°C.

[b]May not be suitable for sewing.

Adhesives

Low-outgassing, silicone-based adhesives are commonly used to bond fasteners to structure in low-to-moderate-temperature applications. These silicone adhesives should not be used on surfaces directly exposed to the low Earth-orbit environment or on surfaces expected to reach temperatures of 200°C or more. The bond should be allowed to set for at least 24 hours. Heating up to 65°C may be used to improve adhesion.

Provisions for Venting

Vent paths must be provided to evacuate the air trapped between blanket layers before launch. For some blankets this requirement is satisfied by making all blanket layers from a material with small perforations (e.g., 0.8-mm holes every 6 mm). In other blankets it is satisfied by leaving one or more edges unsealed or by cutting small X-shaped openings at a regular interval. If a blanket is not adequately vented, it will billow out during the depressurization of launch ascent and may be severely damaged or torn loose from the vehicle. The vent paths must have sufficiently low gas-flow resistance to ensure that residual pressure between blanket layers drops below 10^{-4} torr within a few hours of launch so that the blankets will be fully effective. Pressure decay rates for the Titan IV are shown in Fig. 5.10. While the maximum pressure decay rate is on the order of 1.7 kPa/s, blankets are commonly designed to rates as high as 10 kPa/s. JPL, for instance, provides 0.11 cm^2 of vent area per L of trapped gas volume to meet a design-pressure decay rate of 8.6 kPa/s. Blankets designed to satisfy this criterion have shown no ballooning when tested at rates as high as 15 kPa/s. A typical edge-vent opening is shown in Fig. 5.11.

In designing the blanket layout, the engineer must consider the direction of the vent paths. Gases trapped within the blanket, between the blanket and spacecraft
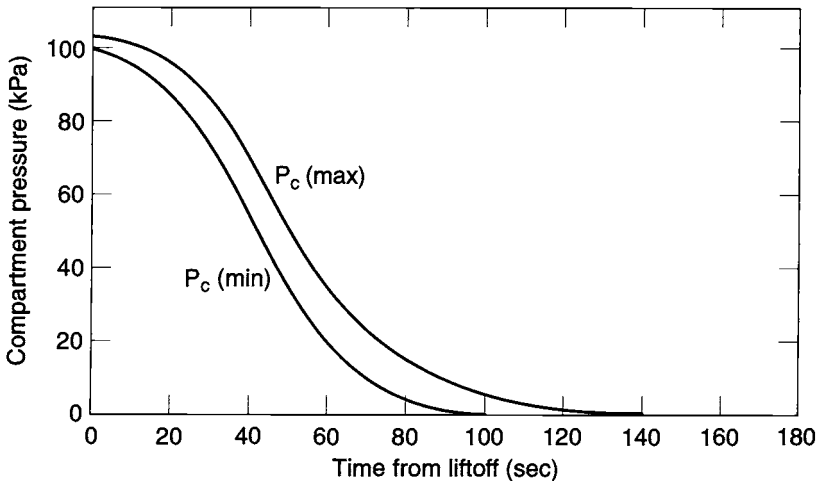
Fig. 5.10. Pressure decay rates during launch ascent.

Tape removed from edge of blanket (2.5 cm)

Filter (74 –μm mesh) folded around untaped edge of blanket

Edges of filter taped
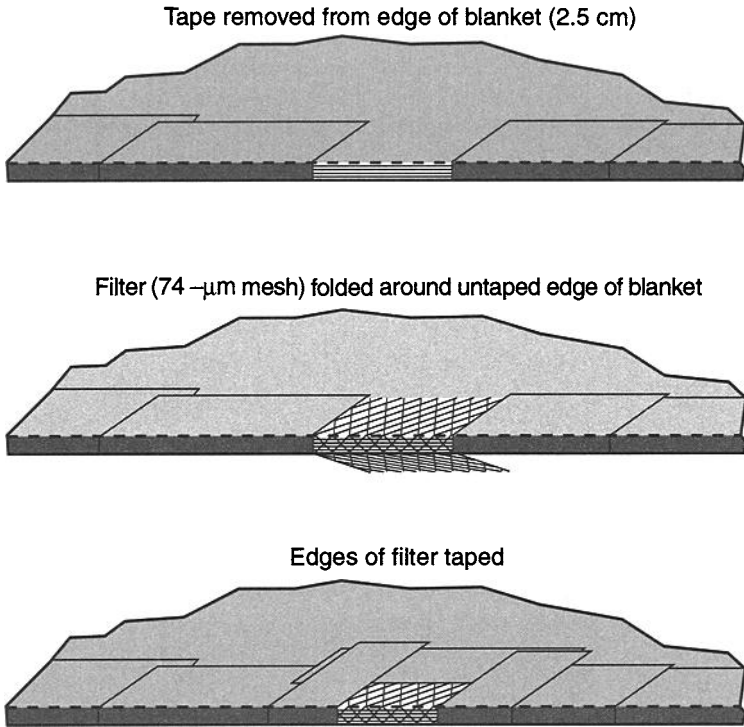
Fig. 5.11. Typical MLI blanket edge-vent hole.

structure, and within the spacecraft itself must all be directed away from contamination-sensitive surfaces such as radiators and optics. This requirement may, for instance, dictate that blanket edges adjacent to radiators be taped down to the structure to prevent gas from flowing out from under the blanket and across the radiator.

Attachments[*]

Hook-and-Pile Fasteners

The most common means of attaching blankets to a spacecraft or to each other is via a closure known as "hook-and-pile fasteners," or, more commonly, Velcro. This type of closure consists of a piece of fabric made of small hooks that stick to other small loops that make up a separate, corresponding piece of fabric. The hook piece may be attached to the spacecraft or to the blanket by an adhesive such as Eccobond 57C or EPON 815 applied to the fastener tape. A mechanical technique such as riveting may also be used to attach the hook side to the spacecraft, provided that structural stress and fatigue factors are considered. The pile side may be

---

[*]Many of the recommendations in this section are courtesy of NASA/MSFC.[5.2]

sewn to the blanket or attached by ultrasonic welding using an appropriate adhesive. Welds or stitching may pass through the entire blanket to provide a more durable attachment or to prevent inner-layer shifting, but they will degrade the performance of the blanket in a small local area. Space-shuttle flammability requirements limit the size of each hook-and-pile fastener to 77 cm^2 and require adjacent fasteners to be separated by at least 5 cm. Hook-and-pile fasteners make blanket installation and removal quick and easy, although they are not acceptable on some programs because they generate some particulate contaminants during blanket removal.

Most hook-and-pile fasteners used today, such as those shown in Table 5.13, are made from organic materials. These materials may only be used in locations where

Table 5.13. Organic Hook-and-Pile Fasteners[a] (Courtesy of NASA[5.2])

Material	Astro Velcro Fastener	Nomex Fasteners	Nylon Fasteners	Polyester Fasteners
Specification	MIL-F-21840	MIL-F-21840, Type I, Class 2	MIL-F-21840, Type II, Class 1	MIL-F-21840, Type II, Class 1
Description	Hook fastener tape of polyester hooks on Beta glass ground, pile fastener tape of Teflon loops on Beta glass ground	Hook fastener tape made of Nylon hooks on Nomex ground, pile fastener tape of 100% Nomex	Hook-and-pile fastener tapes made of nylon	Hook-and-pile fastener tapes made of polyester
Vendors	Velcro USA Inc.	Velcro USA Inc., Aplix	Velcro USA Inc., Aplix	Velcro USA Inc., Aplix
Hook and loop filament size, mm (in.)	0.2 (0.008)	0.17 (0.007)	0.2 (0.008)	0.2 (0.008)
Hooks/linear cm	110	112	100	75
Hook tape breaking strength, kg min	N/A	70.3	56.7	72.6, 100 pile
Loop tape breaking strength, kg min	N/A	65.3	45.4	54.4, 100 pile
Composite shear strength, kg min	6.8	6.8	6.8	10.8
Composite peel strength, kg min	0.40	N/A	N/A	N/A
Temperature range, °C	−57 to +93	−57 to +93	−57 to +93	−57 to +93
Comments		Recommended for high-temperature applications		OK for a few cycles of UV or chemical interaction

[a]Data for these materials are given for 2.5-cm-wide (1-in-wide) tapes. Hooks are generally placed every four picks on the ground fabric, loops are every three picks. Composite shear strength is tested with 7.6 cm (3 in.) overlap of hook-and-pile tapes.

they will not be directly exposed to AO for more than a few hours. When using these fasteners in a low-Earth-orbit environment, NASA/MSFC recommended allowing 6 to 12 mm overhang by the blanket to shield the fastener from either direct or scattered AO. (In some cases, flaps as large as 5 cm have been used.) Hook-and-pile fasteners are generally available in 2.5-cm widths, but they can sometimes be found in widths of 1.6, 1.9, 3.8, and 5 cm. To prevent unraveling, NASA/MSFC also recommended that one *not* slit the fastener tapes lengthwise or trim selvage edges. Fastener tapes may be slit widthwise for forming an arc or adjustment around a protrusion.

Metallic hook-and-pile fasteners are also available for use at high temperatures or in applications requiring extended exposure to AO. These fasteners should not be used in situations where more than 10 peel cycles will be encountered (i.e., situations where the fastener or blanket will be detached more than 10 times). Consideration must also be given to the possibility of electrically conductive particles being shed by the metallic pile every time the blanket is removed. Such particles could cause shorts if they were to find their way into cable connectors or electronics boxes. Properties of metallic hook-and-pile fasteners are given in Table 5.14.

Lacing/Tie Cord

In many cases blankets must be attached to each other or to a spacecraft by hand ties or laces. Flat and round braided lacing materials, either Teflon-coated or uncoated, are available and are described in Table 5.15. Laces should be taut, with no slack that would let the blanket shift and expose protected areas or break away. However, they should not be pulled so tight as to cause the blanket to bunch or pucker. At their ends, the laces should be tied off in a square knot that is snug with the fabric. A granny knot, which resembles a square knot, is unacceptable. The tips of the laces should be protected to ensure that they do not unravel.

The laces should attach to the blanket by loops made of fabric (or other material) attached to the outer-cover layer or by metal grommets that allow the laces to pass straight through the blanket. Grommets must have a firm grip on the material and prevent tears from propagating from the hole. A well-secured flap of material

Table 5.14. Metallic Hook-and-Pile Fasteners (Courtesy of NASA[5.2])

Material	Hi-Grade Stainless Steel Fastener
Specification	MIL-F-21840
Description	Hook-and-pile fastener tapes made of noncorrosive metal
Vendors	Velcro USA Inc.
Hook size, mm	0.1
Hooks/linear cm	98
Hook tape breaking strength, kg min	45.4
Loop tape breaking strength, kg min	45.4
Composite shear strength, kg min	6.8
Temperature range, °C	−40 to +427

Table 5.15. Lacing Tapes and Tie Cords[a] (Courtesy of NASA[5.2])

Material	Flat Braid	Round Braid
Specification	See below	See below
Description	PTFE coated before braiding	PTFE coated before braiding
Vendors	W.F. Lake	W.F. Lake
Yield, m/kg	446–872	730–2332
Thickness, mm	0.2–0.5	N/A
Width, mm	3.2–1.2	N/A
Diameter, mm	N/A	0.7–1.2
Break strength, kg	68.1–18.1	36.3–22.7
Elongation, %	< 5	< 5
Temperature, °C	–240 to 288	–240 to 288

[a]Applicable specifications: MIL-T-43435B; MIL-C-20079H; U.S. Navy 17773A1118A007X

should be placed over the laced joint to prevent sunlight from entering the gaps between the blankets or between the blanket and spacecraft structure.

Provisions for Electrical Grounding

Some missions fly through or in regions where space plasmas exist. Plasma can serve as a medium for surface charging that can result in considerable potential buildup on the external surface of the spacecraft, including the outer-cover layer of MLI blankets. This buildup can lead to static electric discharge between the spacecraft and the surrounding plasma or between parts of the spacecraft that are to some degree electrically isolated from one another. In addition to surface charging, electrons that have sufficient energy to penetrate the outer-cover layer of the blanket, but low enough energy to stop in interior layers, can charge the inner layers until a large electrostatic discharge occurs. Static discharges of any type can interfere with payload operation or damage key electrical or electronic components, possibly resulting in the loss of the spacecraft. Notable orbits in which charging is significant include midaltitude to geosynchronous-altitude Earth orbits and high-inclination low Earth orbits, as well as orbits around Jupiter and Saturn.

Spacecraft flying in orbits where charging is an issue will typically have requirements to ground insulation blankets. Sometimes only the metalized layers of large blankets must be grounded; in other situations the outer surface of the outer-cover layer must also be coated with a conductive material and grounded. The degree of grounding required will usually reflect how sensitive spacecraft components are to static discharges and how severe the charging environment is in the mission orbit. For spacecraft carrying scientific instruments that measure low-energy electrons, any electron charge accumulated on the blanket's outer layer may disrupt the measurements, even if no discharge event occurs.

The best way to eliminate charge buildup and resultant discharges from the blanket is to make all layers of the blanket conductive and ground them to the spacecraft structure. The aluminum or gold coatings used on most interior blanket layers provide a good conductive path. The scrim-reinforced aluminized Kapton

that is sometimes used as an outer cover, however, can present grounding challenges because the scrim layer has to be removed in a small area to expose the conductive aluminum sandwiched between the Kapton and scrim. The easiest way to get conductive outer-cover layers is to use carbon-loaded (black) Kapton, which is a conductive enough material even without special coatings. One possible problem with black Kapton, however, is that it has an absorptance-to-emittance ratio that is higher than the ratio of traditional (gold-colored) aluminized Kapton, and it will therefore run hotter in sunlight. For many missions, the thermal design can accommodate the higher outer-layer temperature, although achieving this capability may require additional effort by the thermal engineer. For other missions, thermal requirements demand the lower temperatures achievable with gold Kapton or even Teflon outer layers. ITO-coated (sputtered, rather than vapor-deposited) aluminized Kapton and Teflon may be used in these situations. The ITO serves as a transparent, electrically conductive layer that may be grounded to the spacecraft structure. An important point, however, is that the ITO is fragile and may be degraded with even minimal handling. Wiping for cleaning purposes can ruin the surface, as can bending during manufacture or storage. Thermal bakeout of the blankets may also contribute to the loss of ITO surface conductivity. Because of the difficulty of grounding Teflon, it has largely disappeared as a thermal-control material on satellites in geosynchronous orbits.

The conductive blanket layers are usually connected at discrete points and grounded to the spacecraft structure. A typical grounding assembly consists of a conductive metal strip interleaved between the blanket layers and secured by a small bolt, as shown in Fig. 5.12. This assembly is made by cutting away a small square of the separator layers and applying a grounding tape (such as aluminum tape with conductive adhesive) accordion-style between adjacent blanket layers, as shown in the figure. A hole is then punched through all layers for the bolt. The bolt passes through a flat washer, an eyelet terminal, the blanket, another flat washer, a lock washer, and a lock nut. Brass and corrosion-resistant steel (CRES) are the preferred materials for bolts, eyelets, and washers. A wire of the required length, such as 22-gauge Teflon-insulated wire, is crimped to the eyelet terminal. The electrical resistance of the assembly should be less than 1 Ω.

The number of grounding assemblies required depends on blanket size, the mission charging environment, and the spacecraft sensitivity to discharge. On some programs, blankets with an area less than one square meter are exempt from grounding requirements, while on others all blankets must be grounded. Blankets with areas greater than one square meter are almost always required to have at least two ground straps and often two ground straps per square meter.

Fabrication

Fabrication starts after the thermal engineer has defined the spacecraft or component blanket requirements and continues until delivery or installation of the blankets on the flight item. By the start of this phase, the cognizant hardware, thermal, and blanket engineers should have begun a dialogue in which blanketing requirements are discussed. These requirements include surface properties, grounding, micrometeoroid protection, and contamination, as outlined in Table 5.1. The method of attaching and supporting the blankets, including any blanket standoffs

These layers of netting get cut away

Aluminum foil

Aluminum Polyimide Tape
(as required to hold grounding
insert to reflector layer
during ground installation)

Outside

Screw

Grounding
jumper

2.54 cm (1in.)

Outer
cover

Reflector
layer

Grounding
insert

Separation
layer
(trimmed
back)

Inner
cover

Grommet

Aluminum Polyimide Tape
(install after grommet installation
on polyimide cover only)

Inside

Fig. 5.12. Typical MLI blanket electrical-grounding assembly. (Courtesy of NASA[5.2])

required for micrometeoroid protection, should be understood by this point, since these items drive the size of the blanket pattern.

Several vendors provide blanket patterning and fabrication services, including Swales Aerospace of Beltsville, Maryland, and Space Systems Loral of Palo Alto, California. Use of such support contractors may be an effective way to deal with large patterning tasks when the schedule lacks sufficient time for patterning.

The Work Area

Fabrication should take place in a workshop area that qualifies as a Class 100,000 clean room. Temperature and humidity should be controlled and a positive pressure maintained in the room to preserve the cleanliness and optical properties of the MLI material being used or stored in the shop. Temperature and humidity should be monitored 24 hours a day.

The fabrication area should have layout/sewing tables large enough to support the largest blankets being fabricated, sewing machines, a storage area for the rolls of film from which the blankets are fabricated, and cabinets to house tapes, thread, layout tools, punches, patterns, etc.

All tools, equipment, templates, holding fixtures, and other structures that may contact the blankets should be cleaned before use with a solvent having a nonvolatile residue not exceeding 0.02 g/L. Solvents must be compatible with the component materials so that the materials are not damaged by normal cleaning operations. Workshop tables should be protected with clean covers when they are not in use. Blankets and materials should be handled with clean white gloves or powder-free latex gloves suitable for clean-room use. Workers should wear clean laboratory smocks and practice good housekeeping in the work area. Any workers who may be above the blanket assembly area should wear foot coverings.

The Spacecraft Model

Because blankets are custom-tailored to each piece of hardware, access to a geometrical representation of the components to be insulated is required to aid in blanket development. The completed flight hardware itself would be ideal, but schedule often makes this impractical. Therefore, a model of the spacecraft or component to be insulated is usually required to aid in sizing and fitting the blanket. While this model should contain representations of all the items that the blankets must enclose, details like cables, purge lines, propellant/pressurant lines, and micrometeoroid standoffs for the blanket are sometimes missing.

Unfortunately, models that everyone swears are flyable often turn out to be anything but. Sometimes, blankets made on such models must be changed to fit the flight hardware even as the latter is en route to final spacecraft-level testing! Depending on the magnitude of these changes, completely new blankets may have to be fabricated, and that additional labor increases costs and affects schedule. Therefore, the blanket engineer should resist beginning the blanket-fabrication process unless the model is of sufficient fidelity to represent the final hardware design. Making sure all parties understand the potential costs and schedule impacts of not having a complete model before proceeding is the responsibility of the blanket engineer. How well the model represents flight hardware is the responsibility of the hardware engineer and, to a limited degree, the thermal engineer.

Patterning

Like the manufacture of clothing, blanket fabrication involves the use of patterns. Patterning is the biggest challenge in the blanket-development process. Any method that produces a pattern that fits the hardware is a good one and probably a variation of the right one. Sometimes a detailed pattern can be developed from the full-scale drawing of the hardware to be insulated. At other times the geometry is so complex that the pattern evolves from many pieces of paper taped together on the model (a process some refer to as "throwing paper at the hardware"). Variations between these extremes exist, but development of a pattern always tends to contain a little of each approach.

A pattern starts simple and grows in complexity as cutouts, interfaces to other blankets, hardware attachments, and additional details are incorporated. Eventually, the final pattern evolves and is placed on the hardware for comments from the thermal and hardware-cognizant engineers. This is the time to address open issues. Identify where the blanket ground location should be. Ensure that laced edges will not be in the sun. Consider issues related to blanket installation. Concave surfaces (corners, blanket-to-blanket intersections, etc.) that may be illuminated should also be avoided. Determine whether the blanket must be readily removable to reach the hardware for activities such as calibration checks, propellant loading, or pyro arming. Eliminate line-of-sight paths to apertures and optically sensitive surfaces relative to primary vent paths. Are micrometeoroid requirements being met? Is all hardware present? These are the types of questions and concerns that need to be addressed before proceeding to the detailing of the final pattern. No question is too "dumb."

The final pattern contains all the information needed to fabricate the blanket. Patterns are like engineering drawings; they may contain a title, part number, material list, centerlines, hidden lines, fold lines, fabrication notes, and other information. Flight patterns should be retained in the thermal blanket shop for up to one year following launch. Before destroying a pattern, check with the project to make sure another flight of the same spacecraft or instrument configuration will not be made. Hardware usually changes for a reflight, but the original flight pattern can serve as a good preliminary pattern for a subsequent flight. Do not dispose of any patterns until determining that no future use for them has been planned.

Construction Details

In most cases, blanket edges are bound with 1.5-to-2-cm tape and stitched, as shown in Fig. 5.13. The standard tapes are either glass (white), carbon-filled (black) Kapton, or aluminized Kapton, but tapes can be made from any outer-layer material by applying a double-sided transfer adhesive to cut strips of the material. If electrically conductive binding tape like black Kapton is used, the binding should be grounded to the conductive exterior layers by turning under a small (1-cm) tab of the binding every 15 to 30 cm before stitching the edge, as in Fig. 5.13. This is not done for the glass or ITO-coated tapes, because the glass tape is nonconductive and ITO cracks along the tab edge, breaking the conductive path.

Stitching the blanket edge prevents interior layers from shifting during the launch vibration environment and makes the blanket more durable. Some manufacturers
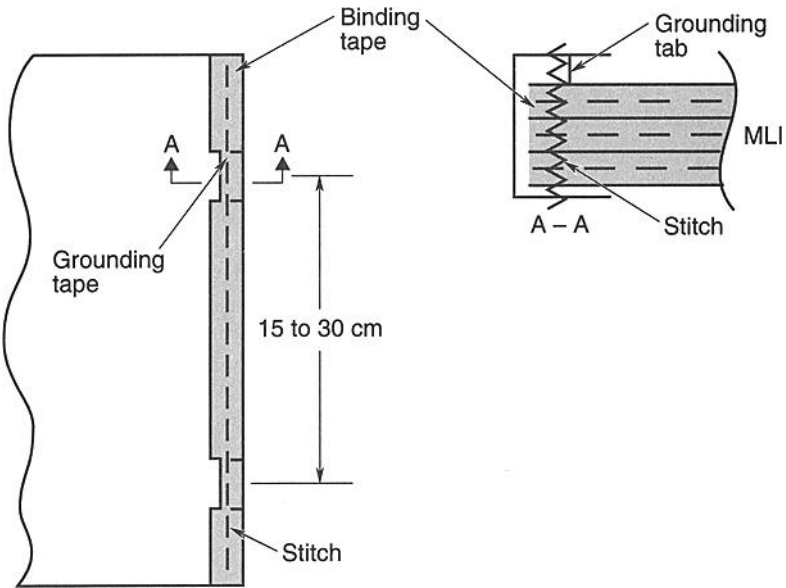
Fig. 5.13. Typical MLI blanket edge finish.

stitch around the entire periphery, while others limit the amount of stitching to improve blanket performance. NASA/MSFC[5.2] recommended stitch length is 3 to 6 mm. Use a 13-mm backstitch to secure each seam at the end. If the thread breaks or runs out in the middle of a stitch line, back up about 25 mm and restart the stitch in a previously made needle hole to reduce blanket perforations. Buttons on each side of the blanket, loosely held together with thread or cord, are also sometimes used toward the center of larger blankets to prevent billowing.

Although minimizing the number of seams or joints is important, a blanket must sometimes be assembled from several smaller ones. The blankets may be sewn together with the edges turned in or out, as Fig. 5.14 shows. The overlapped seam shown in the figure should be used only where performance is not critical, because a direct heat-leak path exists through the seam to the surroundings. The blanket-to-blanket grounding may be accomplished as shown in Fig. 5.15. Approximately 4 cm should separate the blanket-to-blanket grounds as shown, because sewing the seam becomes difficult to impossible (needles break, etc.) when the grounds overlap.

For blankets that are combined with lace or Velcro for installation on the spacecraft, an edge with overlap or underlap is recommended, as in Fig. 5.16. The lap minimizes heat leaks at the blanket joint and can be a good place to locate ground-strap assemblies. The amount of lap can vary, since it is a continuation of the blanket. The lacing tab is separately constructed, cut to length, and sewn on the blankets as indicated on the pattern. Sewing is along the tab edge opposite the holes, which enables lifting the tab for easy access to the holes for lacing (although a curved needle is often used to aid in the lacing process). Holes 3 mm in diameter
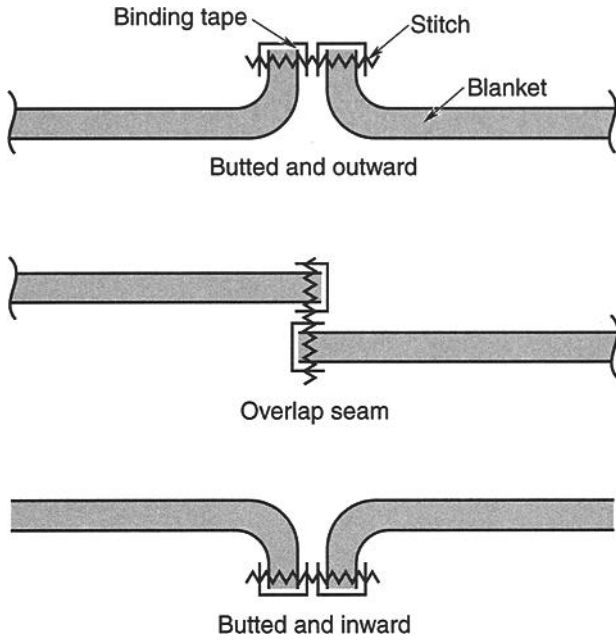
Fig. 5.14. Blanket-to-blanket seam arrangements.
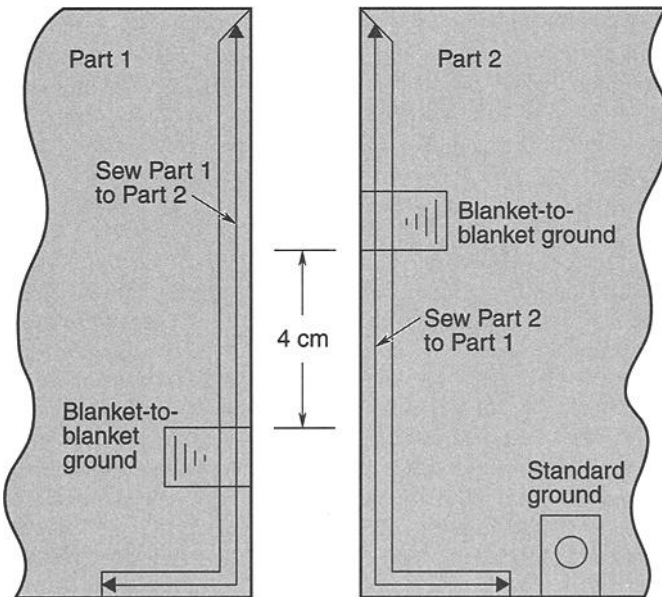
Fig. 5.15. Blanket-to-blanket electrical grounding.
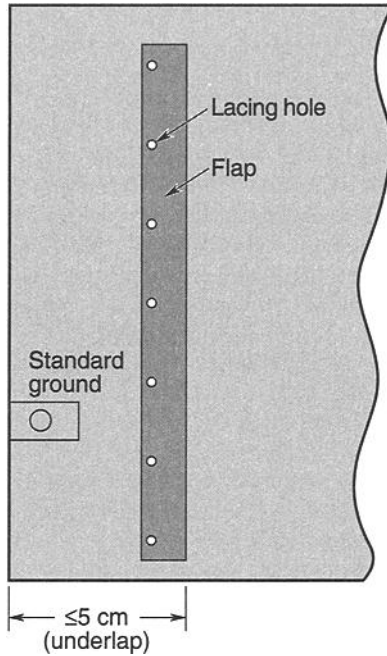
Fig. 5.16. Overlapped blanket-to-blanket joint.

are then punched approximately 3 cm apart. Matching holes in the interfacing blanket are punched during installation of the blankets on the hardware to match those already in the lacing tab.

Bakeout and Cleaning

All blankets should be baked out in a vacuum at high temperature to allow moisture and volatile materials to outgas prior to assembly on the flight spacecraft. Blankets should also be inspected for contamination before flight. Observed contaminants may be removed by drip-wiping with a clean-room wipe and vacuuming, as required. When using Beta cloth as a cover layer, vacuum it with a brush attachment in the direction of the fabric's warp. (Cloth warp is in the direction of the raised fibers. Sometimes it is indicated by an alignment thread placed by the manufacturer; otherwise it can be seen using a x30 microscope.) A clean-room wipe moistened with an appropriate solvent may also be used to clean blankets, but excessive wiping, cleaning, and solvent use should be avoided. Any blankets permanently degraded by contamination (such as oil spills) must be replaced.[5.2]

High-Temperature Blankets

For some applications, blankets may have to endure temperatures beyond the allowable limits of materials commonly used in blanket construction, such as aluminized Mylar films and Dacron nets (Table 5.16). In such circumstances, other

materials must be considered. This was the case in the Cassini program, where insulation blankets would be exposed to solar irradiances 2.7 times greater than that encountered in Earth orbit, plus the heating effects of engine plumes and radiation from radioisotope thermoelectric generators. To enable spacecraft to survive these environments, JPL developed two blanket lay-ups, one good to an outer-cover-layer temperature of 250°C and the other to 430°C.

In the moderate-temperature (250°C) design, the first 5 layers of Mylar and 5 layers of Dacron net commonly found in MLI blankets are replaced with 5 layers of embossed aluminized Kapton. The Kapton is good to 400°C, and the embossed pattern provides some separation between blanket layers. By the sixth layer, temperatures drop to the point where standard Mylar and Dacron materials can be safely used, as indicated by test data shown in Fig. 5.17. In the high-temperature (400°C) design, all Mylar and Dacron materials are removed. A black Kapton outer-cover layer is used, and all internal layers are constructed of embossed aluminized Kapton. The temperature profile through the high-temperature lay-up is also shown in Fig. 5.17.

Some development has been done on extremely-high-temperature blankets constructed of metals, such as molybdenum or tantalum, that have ceramic separators and are good to temperatures over 2000°C. Such blankets do not perform as well as conventional blankets, because of the higher emittance that all metals exhibit at very high temperatures and the greater local conductive shorting effects caused by the higher conductivity of metal layers as opposed to plastic ones.

Suggestions

MLI blanket design and construction is a craft that is perfected through experience and lessons learned. Unfortunately, these lessons are sometimes learned the hard way, through failure of blanket designs. What follows is a list of specific lessons

Table 5.16. Temperature Limits for MLI Blanket Materials

Constituent	Melting Point (°C)	Zero Strength Temp (°C)	Field Service Temp (°C)
Kapton film	None		−269 to +400
Mylar film	250	248	−60 to +150
Teflon film	327	310	
Dacron net	256	245	
Nomex scrim	427		
Glass scrim	> 400		
Adhesive			
3P			max 200–260
Acrylic			max 120
Silicone			max 150
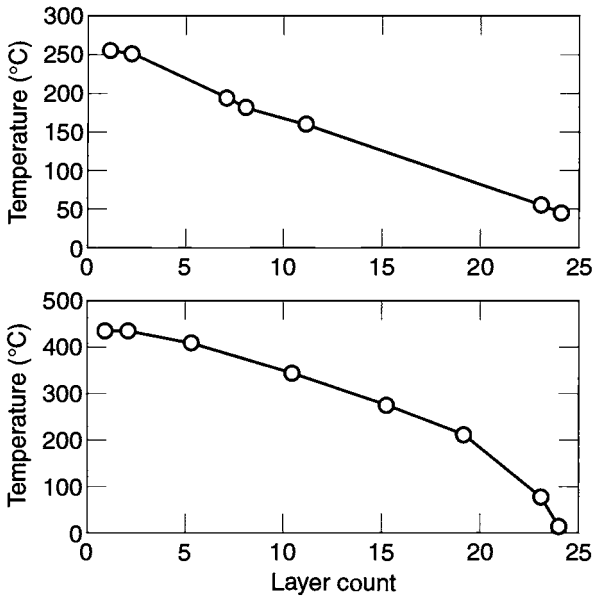
Fig. 5.17. Temperature drop through moderate- and high-temperature MLI blankets.

that have been learned and reported by engineers and technicians making blankets for spacecraft programs. These are offered as suggestions to help the reader avoid the numerous pitfalls encountered by others in past thermal-design development efforts.

Design Suggestions

- Avoid developing designs with excessive contouring of blankets to fit the shape of the hardware. Doing so increases the number of seams, leading to more heat loss and higher patterning and fabrication costs. Contouring may enhance the appearance of blankets, but that is about all that can be said in support of it. Note, however, that contouring may sometimes be needed to meet field-of-view requirements.
- Minimize seam length. Check the edge lengths of a box before deciding on a seam between the side and top versus seaming up the four corners. From a sewing standpoint, short seams (four corners) are preferred over long seams (side to the top).
- Make the material lay-up (especially the internal layers) the same for all blankets. Doing so is not always possible, but changing the number of layers is generally more costly than the savings in material costs. Pulling a new lay-up for a blanket (15 to 20 layers) takes two people 2 to 24 hours and ties up one of the blanket-shop tables. During busy periods, blanket lay-ups are pulled after hours (with staff working at overtime rates) to keep the table available for cutting, binding, seaming, etc.
- Design the blanket to fit loosely for good and repeatable thermal performance. A laced edge with an underlap enables adjustment to the desired loose fit.

Therefore, incorporating a laced edge with an underlap into a multiple-blanket design is good practice.

- Allow for blanket shrinkage during cooldown. The outer layer of an efficient thermal blanket can cool 200°C in the shade with a total view of space (150°C of cooling may be seen in an LN_2-cooled chamber test). The coefficient of expansion for Kapton, Dacron, and Mylar is approximately 0.00002 cm/cm/°C. Therefore, 200°C of cooling results in 0.004 cm/cm or 0.4 cm per 100 cm. The shrinkage can be significant for large blankets and must be considered in the blanket design. During thermal vacuum testing, looking through the chamber windows after cooldown to check for blankets that appear too taut is strongly encouraged, although there are never enough windows to see all the blankets. If a blanket appears to fit too tight in the test chamber, correct the fit after the test, because the blanket can cool another 50°C in flight and shrink an additional 25%.

- If a blanket requires significant improvement thermally, consider breaking it into two blankets with staggered seams. The seams of the inner blanket can be overlapped and taped, because the outer blanket will be sewn and laced (or attached via Velcro). Because of the overlapping the patterns for the two blankets will be different.

- Make a 15-layer blanket by winding a 5-layer blanket around the cylinder 3 times. This is another approach that has been used successfully. It eliminates the through-side seam but the top/bottom seam (attachment to the side) remains and blanket-to-blanket grounds must be added for flight blankets. Sometimes the top/bottom blankets can be a continuation of the side and folded and overlapped to create closure on the top/bottom.

- Do not allow several organizations to do the thermal blanketing. Whoever has responsibility for the spacecraft should have total control. Avoid dividing responsibility for shipping materials, defining blanket interfaces, and performing other tasks. Cost savings will not be gained, and questions may arise about who has final responsibility.

- Minimize the number of blanket lay-up configurations to save fabrication time.

- Be alert for particulate contamination problems caused by Velcro. Electrically conductive Velcro increases the concerns because the particles can cause electrical shorts.

- Avoid taped "blanket close-out" designs. They are not compatible with multi-installations. Grounding of the closure tape is also a problem, as is the possibility of blankets coming loose if the tape debonds.

- Bring the blanket designer into the early stages of the development process. Bringing the designer in late results in poor hardware attachment (if any) and insufficient appreciation for the spacecraft configuration, mission, field of view, etc.

Patterning Suggestions

- Realize that experience is the best teacher for patterning. Developers learn through experience to recognize when a geometry is complex enough to require the "throwing paper at the hardware" approach. Preliminary cubical, cylindrical, spherical, and conical patterns can be constructed from drawings

or measurements made on the hardware, but experience teaches how to merge these basic blanket shapes into one complex blanket system.

- Eliminate pattern approaches that increase fabrication time. Doing so saves costs and results in simpler designs that are generally more thermally efficient. For example, a blanket for a cylindrical geometry can be made in one piece rather than three separate pieces for the top, bottom, and side. A one-piece format eliminates blanket-to-blanket grounds that would be needed between the three pieces (saves fabrication costs), reduces the length of seams (is thermally more efficient), and requires documentation for one blanket pattern rather than three (saves patterning costs).
- Allow for blanket thickness. After completing the preliminary pattern, add 5 mm at each corner. Extend the edges of a pattern by 5 mm where a seam will be incorporated. Sometimes adding 3 mm of material to hardware surfaces may be appropriate to simulate the blanket thickness.
- Avoid patterning the flight spacecraft with nonflight hardware. Doing so often results in the blankets not fitting with the real hardware.
- Before submitting a pattern for fabrication, check the ground-to-ground spacing and ensure the mating seams are the same length.
- Ensure that the internal seams match up correctly. Sometimes the internal seams become numerous. Stenciling letters at the beginning and end of the seam can help make sure the seams match up. This technique helps prevent mistakes but does not replace discussing the details of the pattern with the blanket fabrication technician.

Fabrication Suggestions

- Do not solder lugs to ground braid, because lugs tend to break off after a minimum of flexing (working).
- Do not vacuum-deposit aluminum over the scrim backing. If the scrim is sufficiently coarse, little electrically conductive islands are created because the deposited aluminum does not bridge over the scrim.
- Periodically check in on the blanket-fabrication progress.
- If cutouts are required for cables, apertures, radiators, struts, etc., as they often are, make sure that their edges are bound. Binding takes longer on curved edges, so the use of square cutouts in place of circles is encouraged. Also, replacing multiple, closely packed circles with a single rectangular cutout will save fabrication time and probably is insignificant thermally because less seam area balances more exposed area. On the pattern near the cutout, provide a note as to the cutout's purpose (e.g., "cable pass-through," "probe-strut exit"). Such a note may help others to understand the pattern for a later reflight application.
- Determine whether X-shaped crossing openings constitute a better thermal approach than a hole for a cable or strut pass-through. After passing the strut or cable through the openings, use ties to snug the blanket around the tube/cable.
- Stamp the part number and serial number on the finished blanket and make sure that the location of the stamp can be seen on the pattern. Position the stamp along the edge, and, because it can be difficult to find on large blankets, locate it near one of the blanket ground points.

Insulation for In-Atmosphere Applications

Missions involving planetary landers, rovers, or atmospheric probes usually require insulation that performs well in the presence of an atmosphere. MLI may still be required to protect the hardware during an interplanetary cruise, but foam, batt, or aerogel materials are generally added to provide insulation after atmospheric entry and landing in situations where ambient pressure is expected to be high enough to substantially degrade MLI performance (Fig. 5.2). If atmospheric pressure and gravity are low enough, simple trapped-gas spaces alone may be sufficient to limit heat loss to the surroundings. The underlying principle behind all of these types of insulation is to trap gas within volumes small enough to eliminate convection effects. Total heat transfer is thereby limited to what can conduct through the low-conductivity insulation material and gas and radiate across the insulation through a process of multiple absorptions and emissions within the insulation-material structure.

Batt Insulation

Fiberglass batt insulation, such as Microlite AA, is similar to building insulation and has been used successfully on planetary landers. Shaped batt insulation (Fig. 5.18) can be fabricated on a mold and furnace-fired to the desired shape. An MLI blanket may also be attached to the exterior surface for ease of handling and for improving thermal performance in a vacuum. Performance of this insulation is a function of temperature, the type of gas, and, to some degree, pressure. Figure 5.19 shows the conductivity of Microlite AA fiberglass batt insulation as a function of temperature in an 8-torr CO_2 atmosphere representative of Martian surface conditions. Fiberglass batt densities are typically in the range of 5–25 kg/m^3, with the lower-density versions having the best thermal performance per kilogram.
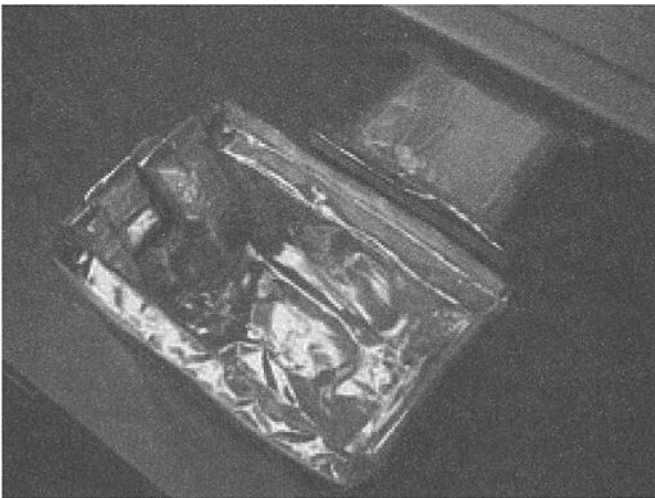
Fig. 5.18. Shaped batt insulation.
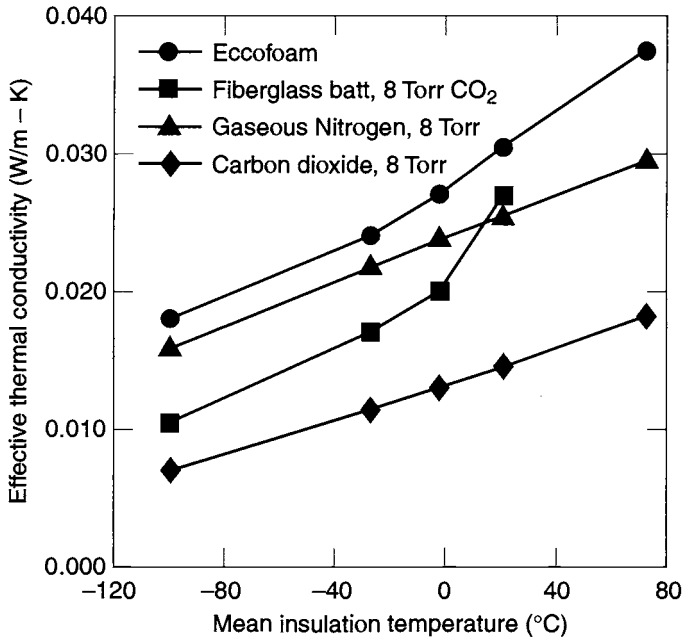
Fig. 5.19. Conductivity of Microlite batt insulation at 8 torr CO_2.

Foam Insulation

Foams, such as Eccofoam and Basotect, are also used as insulation under atmospheric conditions. Foam densities are on the order of 8–11 kg/m^3, while their conductivity is a function of pressure, type of gas, and whether the foam is of the open- or closed-cell variety. In general, closed-cell foams do not perform as well at low pressures because a higher residual gas pressure is maintained in the closed cells. Analysis and testing performed by MBB Deutsche Aerospace for the Huygens probe program characterized the contributions of gas conduction, radiation, and solid conduction to the overall conductivity of Basotect open-cell foam at one Earth atmosphere pressure, as shown in Fig. 5.20. This analysis indicates that gas conduction is the largest contributor to heat transfer through the insulation at one atmosphere. As expected, foam conductivity fell substantially as gas pressure decreased (Fig. 5.21).

The development process for the foam insulation used on the Huygens probe (Fig. 5.22a) also showed that convection effects around and within the foam can dramatically affect insulation performance. The onset of convection within a porous medium occurs when the product of the Rayleigh and Darcy numbers exceeds 39.5 for a foam volume with impermeable side walls and 3.0 if the warm side of the foam is permeable.[5.4] The product is obtained with Eq. (5.7).
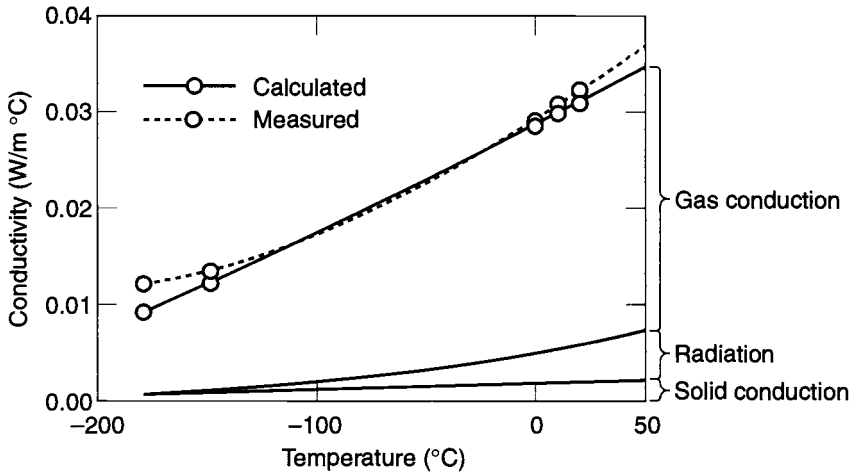
Fig. 5.20. Conductivity of Basotect foam at one Earth atmosphere.
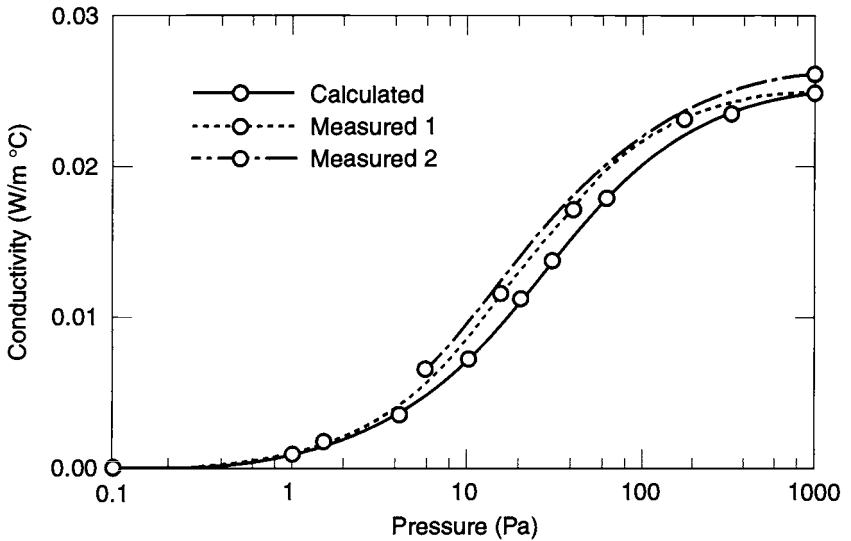
Fig. 5.21. Conductivity of Basotect foam versus pressure.

$$Ra \cdot Da = \frac{g\beta p^2 c_p L^3 \Delta T}{R^2 \overline{T}^2 \mu K} \cdot \frac{P}{L^2} \sim \frac{g p^2 c_p L \Delta T P}{R^2 \overline{T}^{4.7}} \tag{5.7}$$

where g is the gravitational constant, β is the thermal expansion coefficient (and $=$ $1/T$, with T being temperature), p is pressure, P is permeability, c_p is specific heat, L is length, R is the gas constant, μ is dynamic viscosity, and K is conductivity. Since the Rayleigh number is proportional to the square of the pressure and inversely proportional to the temperature to the 4.7 power, convection effects are much more likely to occur at low temperature and high pressure. The initial Huygens design called for Basotect foam enclosed in Kapton bags that would be attached to the inner surface of the descent module walls via Velcro, as shown in Fig. 5.22(b). However, the Huygens probe was to operate in a low-temperature regime where convection would be expected to occur around and within its foam insulation, greatly reducing the insulation's effectiveness. To overcome this problem, a number of corrective design changes were implemented, including:

- Elimination of the Velcro and bonding of the foam-filled Kapton bags directly to the descent module wall, as shown in Fig. 5.22(c).
- Use of fewer, but larger, foam bags to minimize the number of joints between bags.
- Making the foam bags about 2% larger than needed to account for the shrinkage that occurs as water outgases from the foam in a vacuum. Also, pressing small foam bags in the joints ensured that no gaps would open up between adjacent bags.
- Insertion of Kapton webs inside the foam, as shown in Fig. 5.22(c), to prevent convection within the foam. The angle of these internal webs was varied, as shown in Fig. 5.22(d), because the direction of the natural convection flow would be different at different locations.
- Perforation of the Kapton sheet facing the inside of the probe, to allow the bag to vent with pressure changes. Two perforated sheets, instead of one, were placed on this side of the bag, with holes staggered, to block any direct path for convection in and out of the bag.
- Use of buttons held in place with thread to prevent billowing of the Kapton bag that would allow convection to occur between the bag and the foam (Fig. 22[c]).
- Use of additional small bags to close all gaps around the experiment inlet/outlet tubes that pass through the foam insulation.

Aerogels

With a density only three times the density of air, aerogel is the lightest solid material known. It is sometimes called "frozen smoke" because of its appearance (Fig. 5.23). While it functions in essentially the same way as foam or batt insulation—that is, by trapping gas and thereby preventing convection—its mass is much lighter, and it has tremendous insulating capability.

A typical silica aerogel has a conductivity of around 0.017 W/m·K at Earth atmospheric conditions, much of which is a result of gas conduction within the material. The Lawrence Berkeley Laboratory data shown in Fig. 5.24 indicates
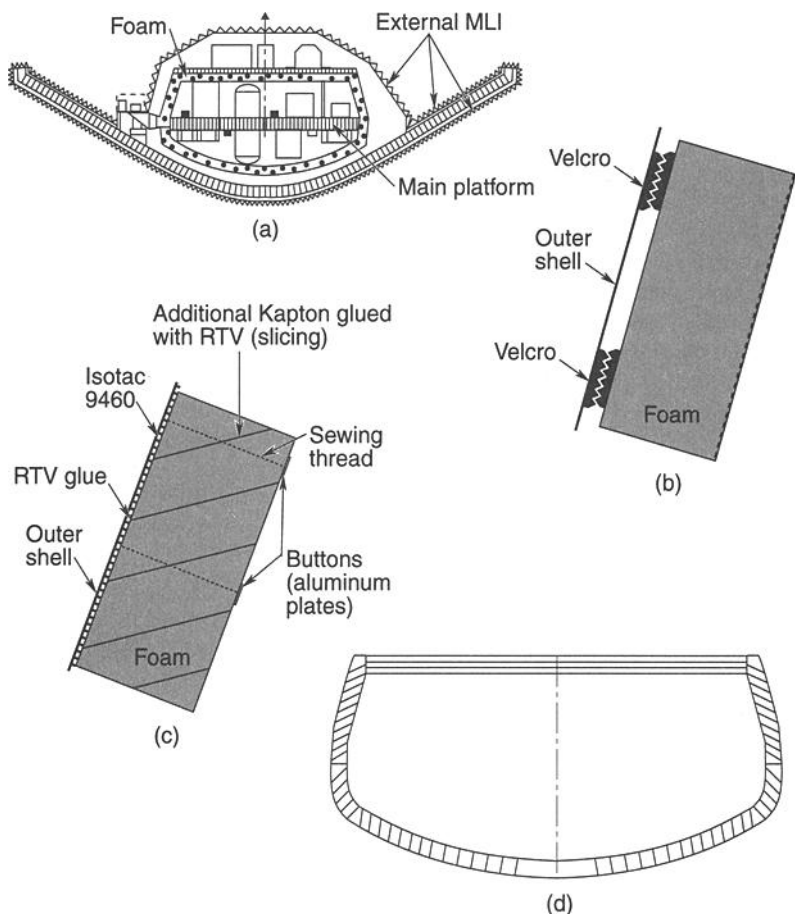
Fig. 5.22. Huygens probe foam insulation. (Reprinted with permission from SAE Paper No. 981644 ©1998 Society of Automotive Engineers, Inc.)

that conductivity drops rapidly with decreasing pressure until radiation becomes the dominant heat-transport mechanism at around 50 torr. Because silica is somewhat transparent to long-wavelength IR, radiation transport through the material can be reduced by adding carbon black to the silica. Figure 5.24 shows that adding 9% carbon black (by mass) cuts the overall conductivity of the material in half at low pressure by impeding the radiative heat transport process. An important note is that the conductivity values shown in Fig. 5.24 will differ for atmospheres of other gases. One disadvantage of aerogels is that they are extremely delicate and can therefore pose packaging challenges that may increase the weight of the insulation system. JPL's Rover Sojourner (Fig. 5.25) used a silica aerogel packaged in a low-conductivity composite box structure to insulate the rover's electronics during the cold Martian night. The Sojourner aerogel had an effective conductivity of 0.0163 W/m·K at 10 torr CO_2 and 24°C and a density of only 20 mg/cm^3.
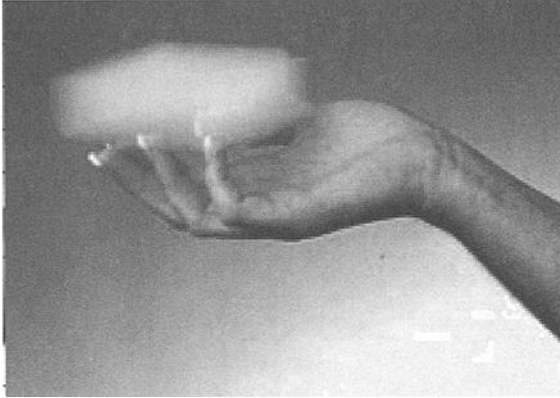
Fig. 5.23. Aerogel
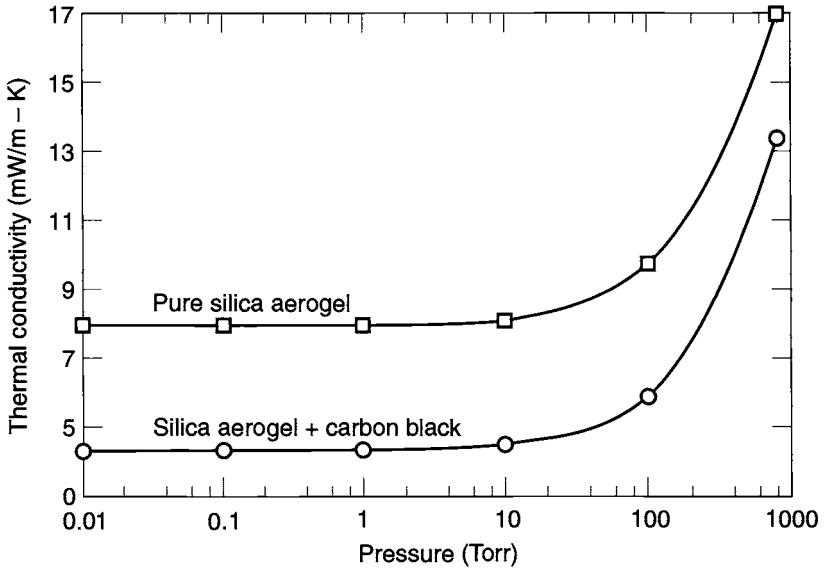
Fig. 5.24. Aerogel thermal conductivity versus pressure. (Courtesy Lawrence Berkeley Laboratory)
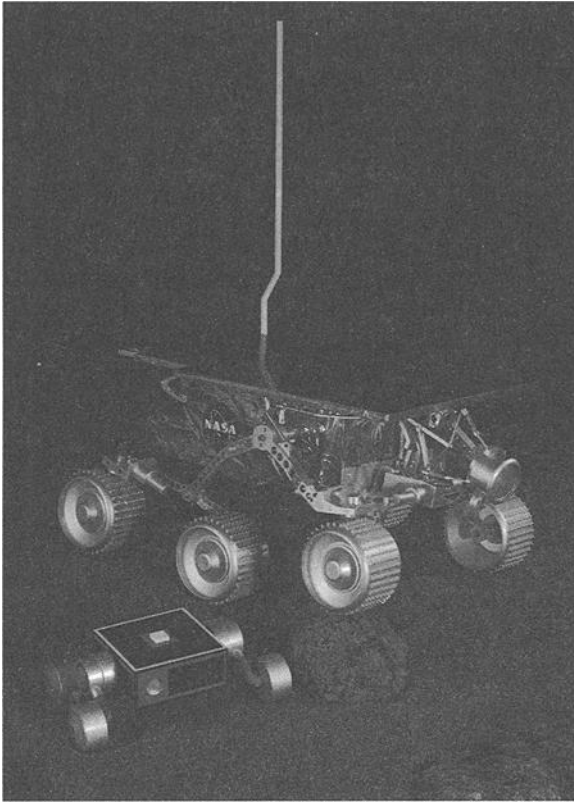
Fig. 5.25. Rover Sojourner.

Gas Void Method

In situations where ambient gases are of low density and conductivity, and where gravity is sufficiently low, simply trapping gas within a closed volume may provide very good insulation performance. Studies performed by JPL for the Mars Surveyor 2001 Program have shown that free convection should not occur between two parallel plates of dimensions 25.4 cm × 25.4 cm on the Martian surface if they are spaced apart by less than 2.3 cm and that convection would be negligible for gaps up to 6 cm.[5.5] To exploit this discovery, a design approach was developed in which a "dead air" zone was achieved around electronic units by attaching formed Mylar "bumpers" that hold an MLI blanket several cm off the surface, as shown in Fig. 5.26. The conductive path through the bumpers is negligible, and radiative heat transfer is minimized by applying a low-emittance finish to the unit and the inner cover of the MLI blanket. This arrangement provides both MLI for insulation during the interplanetary cruise and a trapped CO_2 insulator during surface operations. In a comparison with traditional foam and batt insulation, this design reduced heat losses by 38% while reducing mass by 60%, cost by 33%, and fabrication time by 75%.
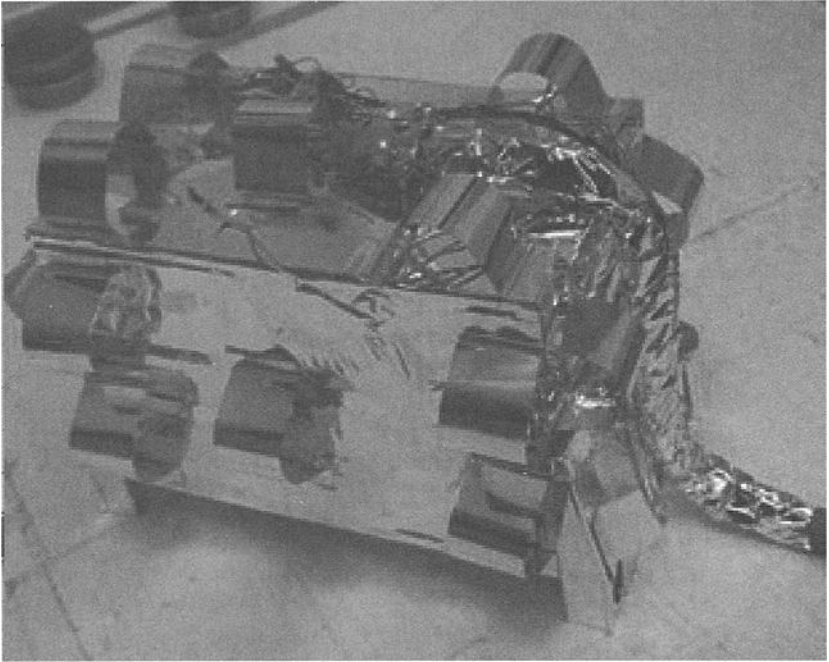
Fig. 5.26. Gas void insulation.

References

5.1. E. I. Lin, J. W. Stultz, and R. T. Reeve, "Test-Derived Effective Emittance for Cassini MLI Blankets and Heat Loss Characteristics in the Vicinity of Seams," AIAA paper 95-2015 (June 1995).

5.2. M. M. Finckenor and D. D. Dooling, "Multilayer Insulation Material Guidelines," NASA/TP-1999-209263 (April 1998).

5.3. J. Doenecke, "Survey and Evaluation of Multilayer Insulation Heat Transfer Measurements," SAE paper 932117 (1993).

5.4. K. E. Wilkes, "Onset of Natural Convection in a Horizontal Porous Medium with Mixed Thermal Boundary Conditions," *Journal of Heat Transfer* **117**, 543–547 (May 1995).

5.5. G. Tsuyuki, G. Birur, K. Novak, and J. Stoltz, "Lightweight Thermal Insulation for Mars Surface Applications," AIAA paper 2001-0210 (June 2001).

6 Radiators

D. G. Gilmore[*]

Introduction

Spacecraft waste heat is ultimately rejected to space by radiator surfaces. Radiators occur in several different forms, such as spacecraft structural panels, flat-plate radiators mounted to the side of the spacecraft, and panels deployed after the spacecraft is on orbit. Whatever the configuration, all radiators reject heat by infrared (IR) radiation from their surfaces. The radiating power depends on the surface's emittance and temperature. The radiator must reject both the spacecraft waste heat plus any radiant-heat loads from the environment or other spacecraft surfaces that are absorbed by the radiator, as shown in Fig. 6.1. Most radiators are therefore given surface finishes with high IR emittance ($\varepsilon > 0.8$) to maximize heat rejection and low solar absorptance ($\alpha < 0.2$) to limit heat loads from the sun. Typical finishes, discussed in more detail in Chapter 4, include quartz mirrors, silvered or aluminized Teflon, and white paint.

Environmental loads $+\Sigma Q_{int}$ = Reradiated energy
(Steady state)
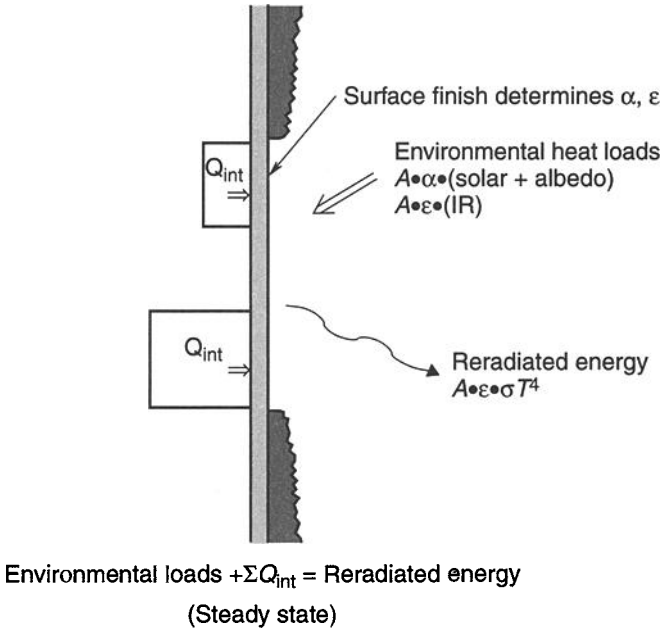
Fig. 6.1. (*Fig. 4.1, reproduced here for your convenience.*) **Radiator energy balance. Environmental loads + ΣQ_{int} = reradiated energy (steady state, no external blockage).**

---

*The Aerospace Corporation, El Segundo, California.

The radiating power of a radiator is a strong function of temperature. The total heat leaving a radiator surface is given by the simple expression

$$\dot{Q} = A\varepsilon\sigma T^4 \tag{6.1}$$

where A is surface area, ε is emittance, and σ is the Stefan-Boltzmann constant $(5.669 \times 10^{-8}\ W/m^2 \cdot K^4)$, and T is absolute temperature (K).

The T^4 term results in a large increase in radiating capability with temperature, as shown in Fig. 6.2. The radiating power at 50°C is about twice that at 0°C. At cryogenic temperatures the effect is even more pronounced, with a 70 K radiator having only 1/300th the heat-rejection capability of a room-temperature radiator. This characteristic makes cryogenic radiators extremely sensitive to environmental heating and heat leaks through insulation and supports, and it leads to special design considerations.

Most spacecraft radiators reject between 100 and 350 W of internally generated electronics waste heat per square meter. The upper end of this range is typical of a radiator that runs at a fairly high temperature (say 40°C) and experiences a relatively modest heat backload from the environment or other spacecraft surfaces. The lower end of the range might represent a radiator running below room temperature in low Earth orbit, where environmental backloads can be substantial. The actual sizing is determined by a thermal analysis that considers the desired operating temperature, worst-case satellite waste heat, environmental heating, and radiative and conductive interactions with other spacecraft surfaces. Weights for radiators typically vary from almost nothing, if an existing structural panel is used as a radiator, to around 12 kg/m² for a heavy deployable radiator and its support/ deployment structure.
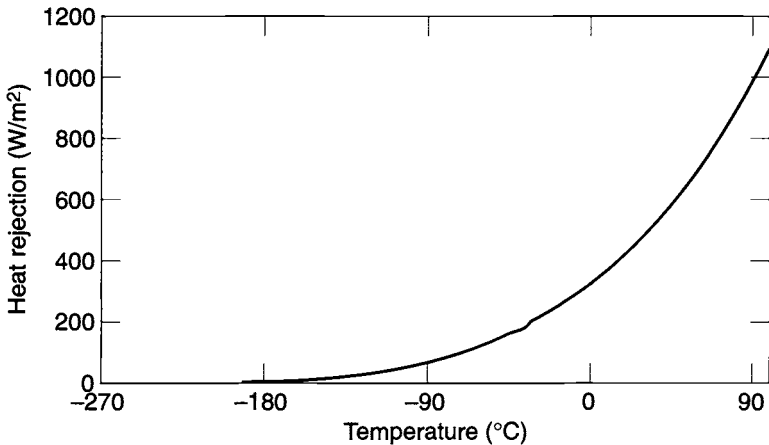
Fig. 6.2. Blackbody radiator heat rejection.

Passive Structure Radiators

The most common and simplest radiator is illustrated in Fig. 6.1. An existing aluminum honeycomb-panel wall of the spacecraft serves both as part of the structure and as a radiator, with its weight normally charged to the structures subsystem. The panel face-sheets spread heat out from the electronics boxes with an area on the outside face acting as the radiating surface. Heat is conducted fairly well from the inner to outer face sheets through the aluminum honeycomb core. Lateral heat conduction, however, occurs mainly in the face sheets. Appendix B includes equations for calculating the conductance of honeycomb cores in different directions.

Sometimes the face sheets are made thicker than required for structural reasons to help spread the heat out from the boxes and give a greater "fin efficiency." Separate plates of aluminum or other material may also be placed under high-power boxes to help spread the heat out on the panel. These plates are called "doublers" (see Chapter 8). Weights that result from increased face-sheet thickness or the use of doublers are generally charged to the thermal-control subsystem.

Structural Panels with Heat Pipes

If a honeycomb-panel radiator has mounted to it some electronics boxes that have high heat dissipation, then the lateral conduction in the face sheets may not be sufficient to spread the heat out over an area large enough to radiate it to space. This situation would result in very large temperature gradients in the panel and cause the high-power boxes to exceed their upper temperature limits. Doublers or increased face-sheet thickness may be used to overcome this problem; however, at a certain point these techniques will result in an unacceptably large weight increase.

To avoid this weight penalty, designers often use heat pipes to spread the heat. The results of one trade study comparing heat pipes to doublers on a communication satellite are shown in Fig. 6.3.

For an application with fairly constant heat loads, such as a panel of TWT amplifiers on a communication satellite, constant-conductance heat pipes may be used, as shown in Fig. 6.4. Variable-conductance heat pipes may be used in a situation with a wide variation in equipment or environmental heat loads, or a requirement to minimize cold-case heater power or to tightly control the temperature range of a component. A variable-conductance heat-pipe radiator panel is shown in Fig. 6.5. References 6.1, 6.2, and 6.3 discuss applications of fixed- and variable-conductance heat-pipe radiator panels on satellites.

Body-Mounted Radiators

Some applications require a radiator that is not part of the vehicle structure. The radiator may need to run at a temperature different from that of the rest of the spacecraft, or no vehicle structural panels may be convenient candidates for use as a radiator. In such situations a "body-mounted" radiator may be used. The radiator itself may be a honeycomb panel or a stiffened aluminum plate. Heat is transported from the heat-dissipating components to the radiator using fixed- or variable-conductance heat pipes, loop heat pipes, or capillary pumped loops, and additional heat pipes may be used to spread the heat out in the radiator panel itself.
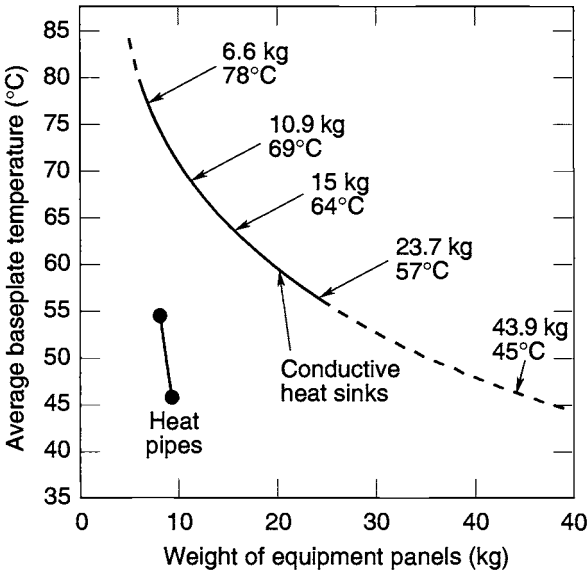
Fig. 6.3. Weight of conductive doublers versus heat pipes.
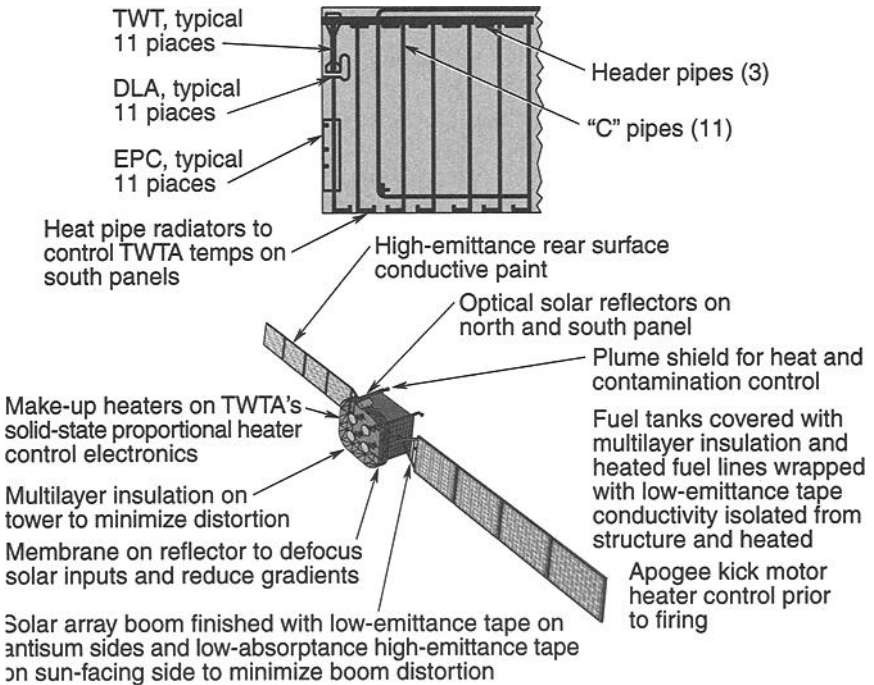

Fig. 6.4. Heat-pipe radiator panel.
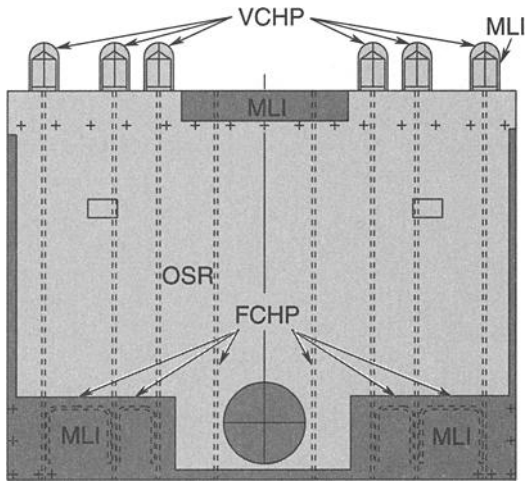
Fig. 6.5. Variable-conductance heat-pipe radiator.

Low-conductance mountings and multilayer insulation may be used to thermally isolate the radiator panel from the spacecraft. The body-mounted radiator used to reject waste heat from a cold plate on NASA's Earth Observing System AM spacecraft is shown in Fig. 6.6.

Deployable Radiators

At this time, most uncrewed spacecraft can reject internal waste heat using structural-panel or body-mounted radiators. However, as satellite power levels (and therefore waste heat) increase or as satellite size is reduced through the use of high-density electronics packaging, the satellite bus at some point simply lacks enough area to reject the internally generated waste heat. In such a situation, deployable radiators are sometimes required to increase the available radiating area.

An example of a deployable radiator is the Alpha Deployable Radiator manufactured by Swales Aerospace. As shown in Fig. 6.7, Alpha uses redundant-loop heat pipes (considered passive pumping devices) to transport heat across flexible joints to a two-sided, four-square-meter radiator panel. Alpha is designed to be attached to a spacecraft through spherical-bearing hinges, pyrotechnic or paraffin release actuators, and snubbers. It has a stated capacity of 1250 W at an evaporator temperature of 36°C. Design and performance details are shown in Table 6.1. Deployable radiators that replace the flexible joint used by Swales with condenser lines coiled around (or near) the deployment axis of rotation have been developed by other companies. These designs, however, are patent protected and therefore not freely available for use by others.

Lockheed Martin/Vought Systems has developed several deployable radiator systems for crewed spacecraft that use active, mechanically pumped fluid loops to transport heat. The largest of these radiators (Fig. 6.8) is for the International Space Station; it uses a pumped liquid ammonia loop to transport 16 kw out to each radiator assembly. A smaller version of this radiator is used to cool the Space Station

Radiator details

Spreader heat pipes

CPL reservoir

E E

C

D

CPL fill and drain valves

C

D

CPL pressure switches

CPL noncondensable gas traps

CPL to heat pipe heat exchangers

Cold plate/radiator assembly

Cold plate with CPL evaporators

Vapor lines

Liquid lines
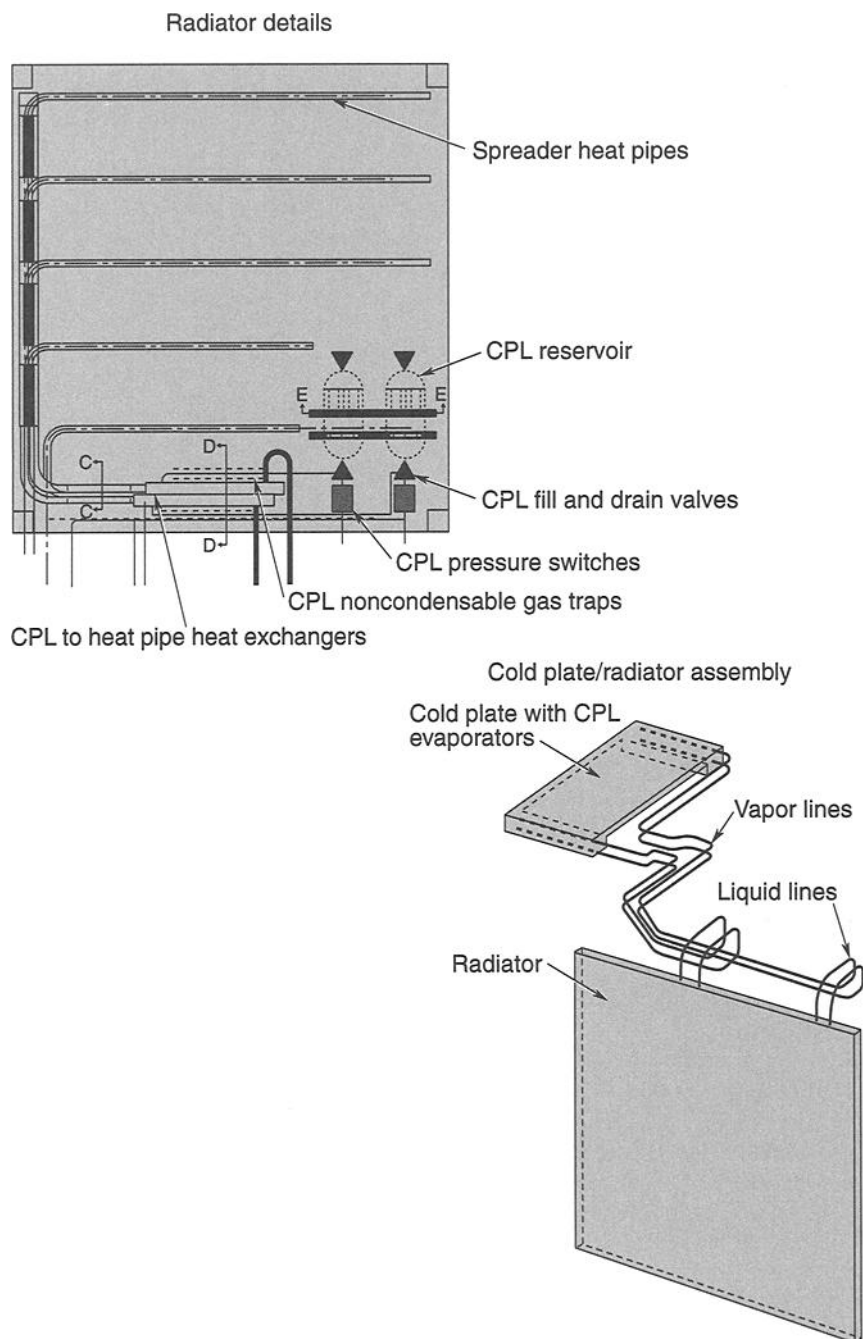
Radiator

Fig. 6.6. Body-mounted radiator for Earth Observing System. (Courtesy of NASA)
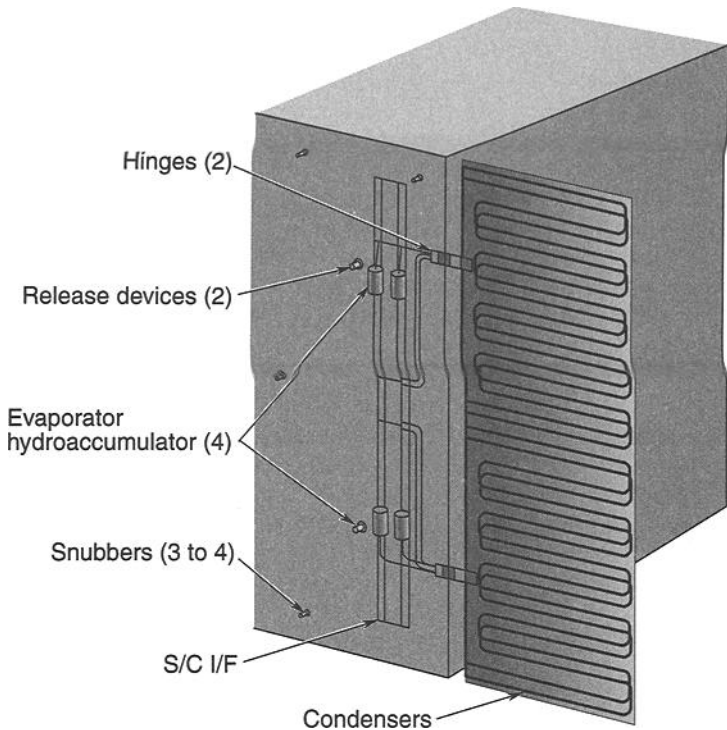
Fig. 6.7. Alpha Deployable Radiator. (Courtesy of Swales Aerospace)
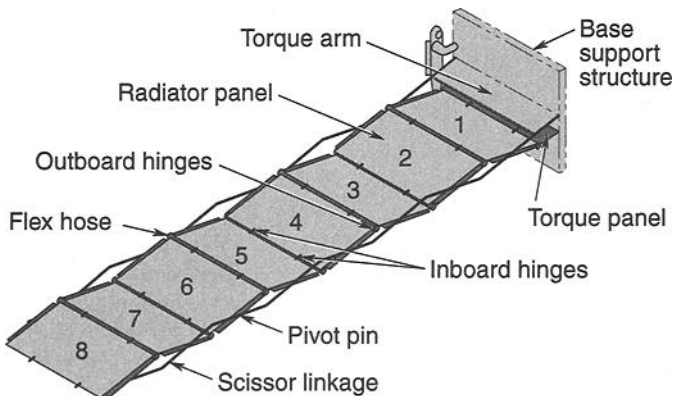
Fig. 6.8. Space Station deployable radiator.

electrical-power subsystem. The space shuttle uses Vought deployable radiators with a mechanically pumped freon heat-transport loop, as shown in Fig. 6.9. Further information on mechanically pumped fluid-loop cooling systems can be found in Chapter 12.

Table 6.1. Alpha Radiator Characteristics

Characteristic	Description
Radiator	
Heat-rejection capacity	1250 W
Size	1.27 m × 3.18 m
Coating	Silver Teflon or quartz mirrors
Loop heat pipes	
Number of LHPs	4
Single pipe capacity at 65°C	>600 W @ 1 m adverse tilt
Evaporator length	457 mm
Condenser type	Direct condensation serial
Ground test elevation	>1 m with 1 failed LHP
Mechanisms	
Flex lines	Flex hose, 6.4 mm ID
Release device	G&H NEA
Hinge	Spherical bearing, torsion spring
Mass	
LHPs	9.5 kg
Radiator	10.2 kg w/silver Teflon, 11.3 kg w/quartz mirrors
Mechanisms	2.0 kg
Total	21.7 to 22.8 kg
Specific heat rejection	57.6 to 54.8 W/kg

Almost all radiators using mechanically pumped fluid loops to date were developed for crewed systems that either have short mission durations (e.g., the space shuttle) or are massively redundant and serviceable by astronauts (e.g., the Space Station; it has six main radiator assemblies). Uncrewed spacecraft, however, are usually designed for long-duration missions with no servicing. Pumped fluid loops have generally been a concern for such missions because of the potential for failure of mechanical pumps. This situation has recently begun to change with the use of pumped loops on the JPL Mars Pathfinder and Mars Exploration Rover programs. As the power levels of uncrewed spacecraft continue to rise, mechanically pumped loop cooling systems may at some point demonstrate a significant weight advantage over competing passive (heat-pipe) systems. Therefore, if the

Typical radiation panel
physical characteristics

15.1 ft.

10.5 ft.

Outlet
manifold

Facesheet (.80")

1.90"

68 parallel flow tubes
0.131 in. I.D.
Silver/Teflon coating both sides
$\alpha = .11$, $\varepsilon = .76$

Space shuttle active
thermal-control subsystem

"Radiator kit" panel   Aft coldplates

Aft radiator panel

Forward
deployment
radiator panels

NH$_3$ boiler

GSE H-X

Hydraulics H-X

Flash
evaporator

Fuel cell H-X

O$_2$ restrictor

To radiators

Interchanger

From
radiators

Radiators flow
control assembly

Midbody coldplates

Flow proportioning module

Freon 21 pump package   Payload H-X

(One loop shown)

Fig. 6.9. Space shuttle active cooling system.

mechanical pumps can demonstrate sufficient reliability, pumped-loop radiator systems may become more common on uncrewed spacecraft in the future.

Radiator Freezing

Every spacecraft that uses radiators with passively or actively pumped fluid loops must address the issue of potential damage resulting from the freezing, and subsequent thawing, of fluids during cold-case operating or safe-mode conditions. Unlike water, most fluids expand when they melt. If a section of frozen coolant line melts, the liquid may be trapped between two frozen sections, resulting in a large local pressure buildup that can burst the line. This failure mechanism has caused the rupture of coolant loops during ground testing and propellant lines on orbiting spacecraft and therefore must be seriously considered in the design of radiators.

Because deployable radiators have a large area and low mass, and they are completely exposed to the environment, they are particularly susceptible to freezing

under cold-case conditions. Analysis of the deployable Space Station radiators shown in Fig. 6.8 and described in Table 6.2 indicated that the ammonia coolant lines in the radiator panels could drop to –94°C, well below the –77°C freezing point of ammonia. Further testing showed that local thawing of a line produced internal pressures as high as 2.96×10^8 N/m^2, which was beyond the yield stress of the stainless-steel radiator tubes.

The Space Station program investigated several options to prevent freezing, including preheating the radiators before eclipses, using beryllium or lithium instead of aluminum or packing the radiator with phase-change material to increase thermal capacitance, and using heaters or radiator retraction during cold conditions. After reviewing these and other options, NASA decided that the most reliable and cost-effective solution was to design the radiator to freeze without damage or operational impacts. This alternative eliminated the need for active monitoring of the environment and other costly schemes to avoid freezing. Damage resulting from local thawing of a frozen line was prevented by changing the tube material from 321 stainless steel, with a yield stress of 2.06×10^8 N/m^2, to inconel, with a yield stress of 1.20×10^9 N/m^2. Varying the spacing of the tubes in each radiator panel, as shown in Fig. 6.10, allows tubes with larger radiating area

Table 6.2. Heat Rejection System (HRS)

HRS Fact Sheet	
Purpose	
• Cools Space Station crew, subsystems, and experiment heat loads	
Programmatics	
• Customer: McDonnell Douglas Space Systems Company/NASA-JSC	
• Contract duration: 5/91–1/98	
Deliverables	
• 3 dev. panels	• 1 qual. unit
• 1 qual. burst panel	• 6 flight units
• 1 full-scale engr. proto	• 9 shipping containers
Characteristics	
• Each unit consists of 8 panels, 9' × 11'	
• Deployed by scissors mechanism	
• 75' deployed length	
• 2200 lbs per unit	
• Two cooling temperatures:	
-2°C units: 11 kW cooling each	
+11°C units: 16 kW cooling each	
• Condensing ammonia two-phase cooling fluid	
• Bonded honeycomb panel construction	
•White ceramic thermal paint	
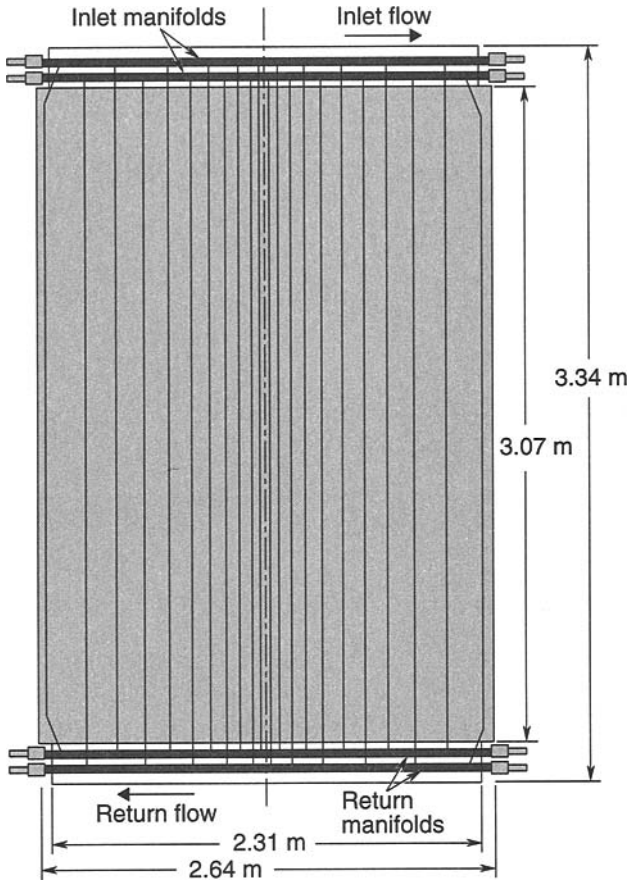
Fig. 6.10. Freeze-tolerant radiator design.

to freeze first, forcing more warm ammonia to flow through the more closely spaced tubes that have less radiating area. This scheme prevents complete freezing of the radiator even under worst cold-case conditions.

Radiator Effectiveness

In the design of a radiator employing parallel heat pipes or coolant tubes, the engineer must determine the spacing of the pipes or tubes and the thickness of the fins. The smallest radiator area would be achieved if one were to use very thick fins and close pipe spacing for maximum fin efficiency. Despite its small size, however, such a radiator would be very heavy because of the large number of pipes and the thick fins. Since weight is usually the critical driver for satellite development, a somewhat less-efficient, but lighter, radiator may be preferred.

For any radiator, one may determine an optimum combination of heat-pipe spacing and fin thickness, to find the minimum total radiator weight. The generalized heat-balance equation for a fin radiating to an effective sink temperature T_s is:

$$\frac{d^2T}{dx^2} - \frac{(t_B - t_T)}{Lt_T + (t_B - t_T)(L - x)} \frac{d_T}{d_x} \frac{\sigma\left(\frac{\varepsilon_1}{\cos\beta_1} + \frac{\varepsilon_2}{\cos\beta_2}\right)L}{2K[Lt_T + (t_B - t_T)(L - x)]}(T^4 - T_s^4) = 0 \qquad (6.2)$$

and the boundary conditions to be satisfied are:

$$T|_{x=0} = T_B \qquad (6.3)$$

$$\frac{dT}{d_x}\bigg|_{x=L} = 0 \qquad (6.4)$$

(see Fig. 6.11 for an illustration of the parameters). This equation was solved numerically by Chang (Ref. 6.4) to derive the following expression for fin effectiveness for a fin of uniform thickness:

$$\eta_e = (1 - 1.125\zeta + 1.60\zeta^2)(1 - \theta^{*4}) \quad 0.01 \le \zeta \le 0.2 \qquad (6.5)$$

$$= (-0.405\log\zeta + 0.532)(1 - \theta^{*4}) \quad 0.2 \le \zeta \le 2.0 \qquad (6.6)$$

$$\zeta = \frac{\sigma L^2 T^3 B(\varepsilon_1 + \varepsilon_2)}{kt} \qquad (6.7)$$

$$\theta^* = \frac{T_s}{T_B} \qquad (6.8)$$
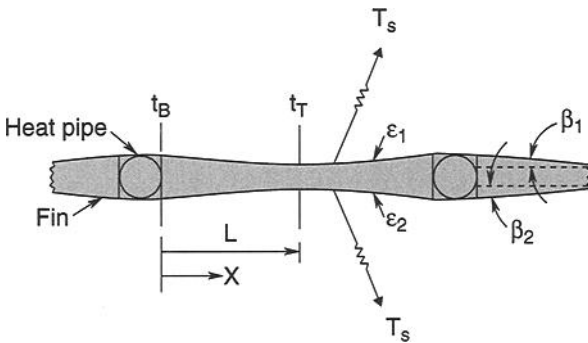
Fig. 6.11. Radiator analysis terminology and variables.

where ε_1 and ε_2 are the radiator emittance of side 1 and side 2, L is heat-pipe spacing divided by 2, T_B is temperature at fin base, T_S is radiative sink temperature, σ is the Stefan-Boltzmann constant, k is fin conductivity, and t is fin thickness.

It is important to note that this expression for fin effectiveness is not the same as the usual definition of fin efficiency. Here it is the ratio of the net heat rejected by the fin to the heat that would be rejected by an isothermal fin to a 0 K sink. This definition of effectiveness therefore accounts for the thermal backload to the fin from the sink as well as the efficiency of the fin itself. The heat rejected from the radiator is therefore calculated as $Q = A\varepsilon\eta_e\sigma T_B^4$ instead of the usual $Q = A\varepsilon\eta_e\sigma(T_B^4 - T_s^4)$.

Equation (6.5) or (6.6) can be used to calculate the effectiveness of the radiator for various combinations of heat-pipe spacing (L) and fin thickness (t). Once the effectiveness is known, the total area required to radiate the satellite waste heat, and the resultant weights of heat pipe, fin material, and radiator optical coating, can be easily calculated. Figure 6.12 shows the results of such an analysis for a two-sided flat-aluminum-heat-pipe radiator rejecting 1000 W at 21°C to an effective sink temperature of -87°C. (The effective sink temperature accounts for the backloads on the radiator caused by environmental heating and radiative interchange with other spacecraft surfaces.) The heat pipes were assumed to weigh 0.11 kg per linear meter.

The minimum radiator weight occurs for a fin thickness of approximately 0.18 mm, a heat-pipe spacing of approximately 20 cm, and an overall fin effectiveness of only 0.5. If thicker fins and closer pipe-spacing is used, the fin effectiveness increases and the size goes down, but the total weight is much greater. If 0.51 mm fins and 10 cm pipe-spacing is used, the fin effectiveness increases to 0.78 and the
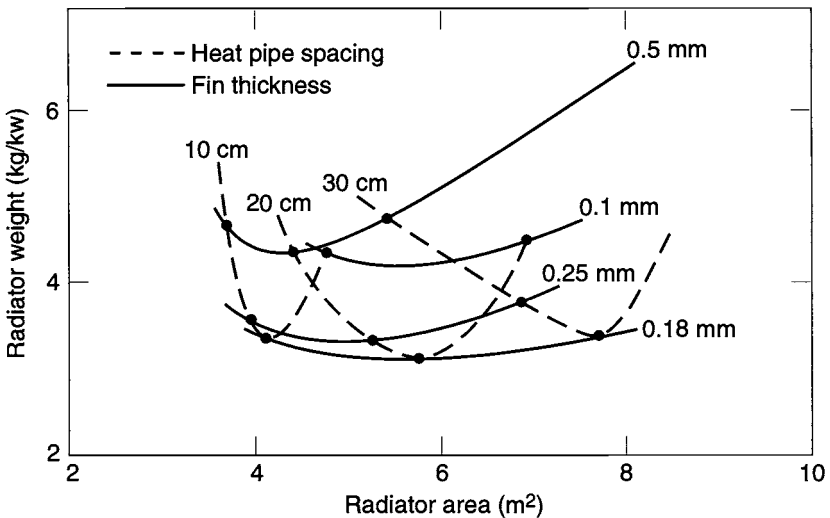
Fig. 6.12. Radiator analysis results.

size is reduced by 36%, but the weight increases by 50%. The actual total weight of the radiator must, of course, include any support structure and, for a deployable radiator, deployment-mechanism weight. The minimum fin thickness may also, in some designs, be driven by structural considerations. The above calculation does, however, illustrate the fact that maximum fin efficiency does not give a minimum radiator weight.

Experimental Radiators

A number of more exotic radiator technologies have been studied, including flexible, moving-belt, and liquid-droplet radiators. The flexible radiator shown in Fig. 6.13 can be conveniently stowed in a small volume. The moving-belt radiator in Fig. 6.14 transports heat by moving the radiator surface and thereby eliminates the need for heat pipes or fluid loops in the radiator itself. Liquid-droplet or liquid-sheet radiators, shown in Fig. 6.15, eliminate the radiator fin and tubes entirely, and radiate heat directly from a low-vapor-pressure fluid that is sprayed out into space and then collected and recirculated. The use of heat pumps to boost the radiating temperature of any radiator and thereby reduce its size has also been studied. More information on each of these experimental technologies can be found in Refs. 5 through 12.
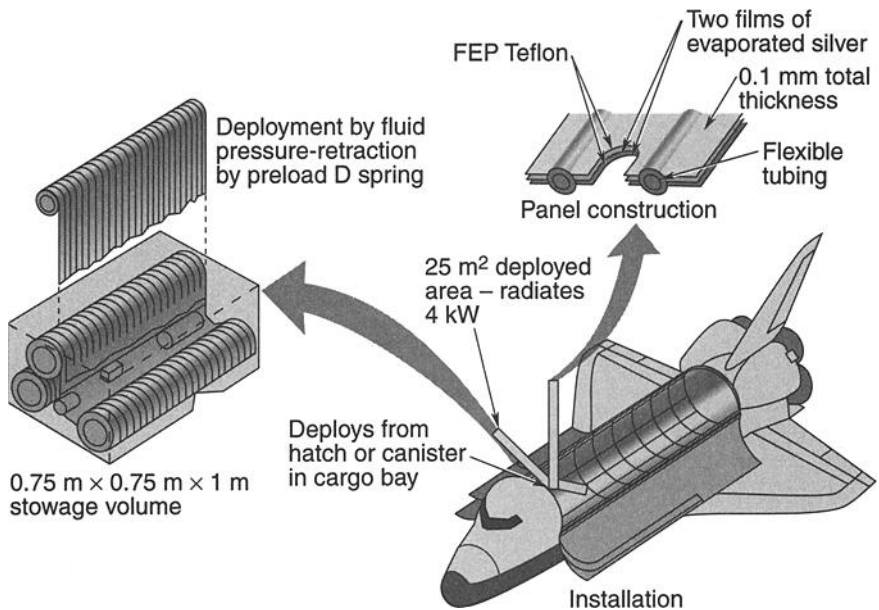
Fig. 6.13. Flexible radiator system.
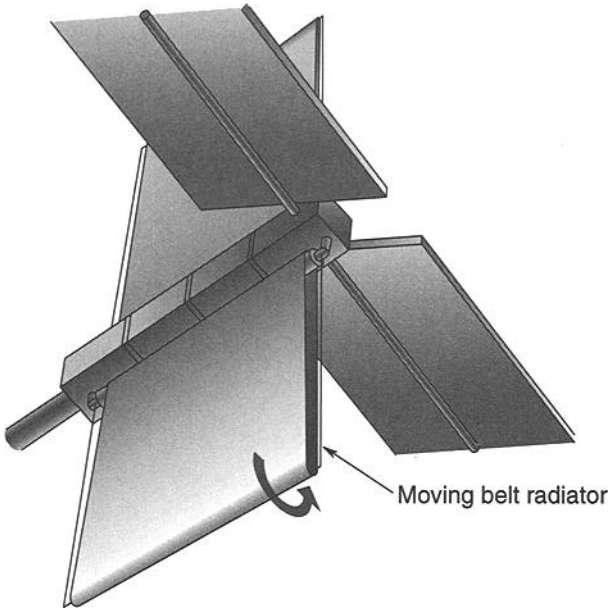
Fig. 6.14. Moving-belt radiator.

Radiative "fins" and "heat pipes" of conventional radiators
replaced by multiple steams of liquid droplets
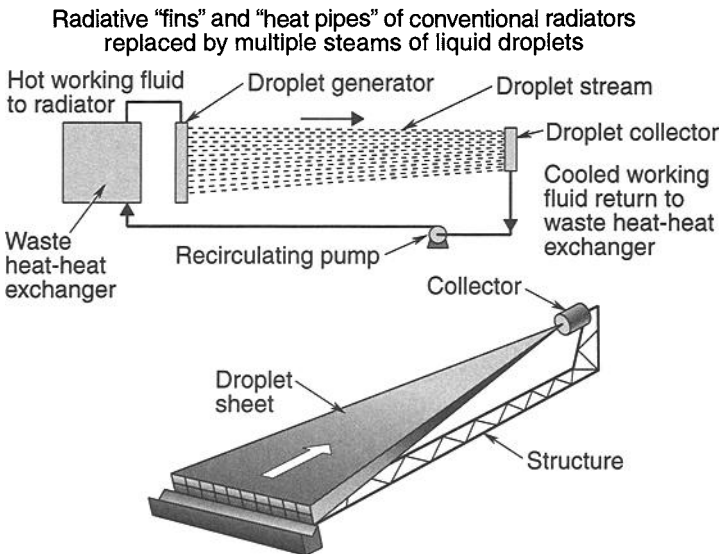
Fig. 6.15. Liquid-droplet radiator.

References

6.1. P. C. Wise, J. Raisch, W. Kelly, and S. P. Sharma, "Thermal Design Verification of a High Power Direct Broadcast Satellite," AIAA-86-1339, June 1986.

6.2. P. Joy and L. Goliaszewski, "Advanced Thermal and Power Systems for the Satcom-Ku Satellites," AIAA-86-0618, June 1986.

6.3. H. Masumoto *et al.*, "Development of a VCHP/FCHP Radiator System for 3-Axis Stabilized Geostationary Satellite Application," AIAA-85-1012, June 1985.

6.4. H. V. Chang, "Optimization of a Heat Pipe Radiator Design," AIAA-84-1718, June 1984.

6.5. R. L. Cox and J. W. Leach, "Flexible Deployable - Retractable Space Radiators," AIAA-77-764 June 1977.

6.6. P. F. Dexter and W. L. Haskin, "Analysis of Heat Pump Augmented Systems for Spacecraft Thermal Control," AIAA-84-1757, June 1984.

6.7. B. Drolen, "Heat-Pump Augmented Radiator for High Power Spacecraft Thermal Control," AIAA-89, January 1989.

6.8. K. A. White, R. Ponnappan, J. E. Beam, and E. T. Mahefkey, "Conceptual Design of a 1 m Long 'Roll Out Fin' Type Expandable Space Radiator," AIAA-86-1323, June 1986.

6.9. K. A. White, "Liquid Droplet Radiator Development Status," AIAA-87-1537, June 1987.

6.10. D. L. Chubb and K. A. White, "Liquid Sheet Radiator," AIAA-87-1525, June 1987.

6.11. A. F. Presler *et al.*, "Liquid Droplet Radiator Program at the NASA Lewis Research Center," ASME 86-HT-15, June 1986.

6.12. Lt. J. Feig, "Radiator Concepts for High Power Systems in Space," AIAA-84-0055, January 1984.

7 Heaters

D. G. Gilmore,[*] J. C. Lyra,[†] and J. W. Stultz[†]

Introduction

Under ideal circumstances, thermal control of a satellite or component would be achieved only through passive techniques, such as the use of surface finishes. Unfortunately, though, variations in environment and component heat-generation rates, along with the degradation of surface finishes over time, can drive temperature variations in a passive design to ranges larger than some components can withstand. Heaters therefore are sometimes required in a thermal design—to protect components under cold-case environmental conditions or to make up for heat that is not dissipated when an electronics box is turned off. Heaters may also be used with thermostats or solid-state controllers to provide precise temperature control of a particular component. Another common use for heaters is to warm up components to their minimum operating temperatures before the components are turned on. Each of these three applications is described in this chapter.

Heater Types

The most common type of heater used on spacecraft is the patch heater, several of which appear in Fig. 7.1. It consists of an electrical-resistance element sandwiched between two sheets of flexible electrically insulating material, such as Kapton. The patch heater may contain either a single circuit or multiple circuits, depending on whether or not redundancy is required within it. Redundancy is generally required on spacecraft systems, because heater circuits can fail. Sometimes
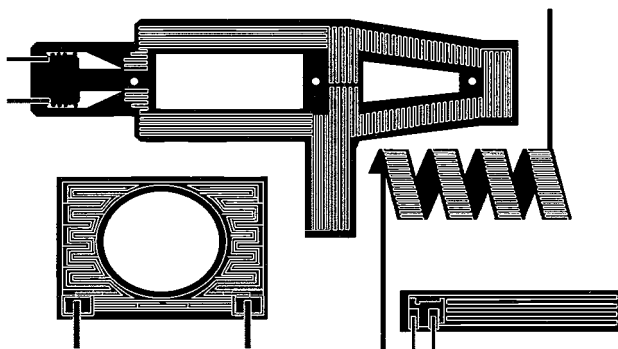
Fig. 7.1. Patch heaters made in custom shapes.

---

*The Aerospace Corporation, El Segundo, California.
†Jet Propulsion Laboratory, California Institute of Technology, Pasadena, California.

223

the redundancy is provided within the patch heater, and sometimes it is provided externally, through the use of two separate patches. The patch heaters in Fig. 7.1 illustrate custom shapes in which these heaters may be made. In most instances, however, the patch is a simple rectangle of standard dimensions.

Another type of heater, the cartridge heater, is often used to heat blocks of material or high-temperature components such as hydrazine-thruster catalyst beds. Such a heater, shown in Fig. 7.2, consists of a wound resistor enclosed in a cylindrical metallic case. Typically a hole is drilled in the component to be heated and the cartridge is potted into the hole. Another attachment technique involves the use of a clamp or small bracket to hold the heater. Cartridge heaters are usually a quarter-inch or less in diameter and up to a few inches long.

Control

Almost all heaters allow some sort of control over their operation. This capability typically involves a relay that is commandable from the ground to enable or disable power being supplied to the heater, a fuse to protect the spacecraft from a short circuit, and, usually, a thermostat or solid-state controller to turn the heater on and off at predetermined temperatures. In more sophisticated satellites, onboard computers sometimes monitor temperatures and turn heaters on and off at appropriate times using relays.

The simplest control arrangement involves only the heater itself, a fuse, and a ground-commandable relay to turn the heater on and off. This arrangement is generally used for heaters activated only for special events, or for heaters that can be left on all the time. A common application is heating up the catalyst beds on hydrazine thrusters to around 100°C before thrusters are fired. (Firing with a low initial catalyst-bed temperature decreases the catalyst life.) The heater is commanded on, the catalyst-bed is heated, the thruster is fired, and the heater is turned off until the next maneuver, all under ground control. A heater used with a hydrazine thruster is illustrated in Fig. 7.3.

Most applications of heaters on spacecraft require some automatic heater control to keep a component at a desired temperature and to minimize the amount of time the heater is on so as to reduce power consumption. Historically, the most common control device has been a mechanical thermostat, such as the Elmwood thermostat shown in Fig. 7.4. These usually consist of a small, hermetically sealed can containing a switch driven by a snap-action bimetal actuator. The temperature at which the thermostat clicks on, known as its set point, is fixed for any given thermostat. The engineer can either order a custom device or select one from an array of standard thermostats available from the manufacturer to get a set point close to what is desired.
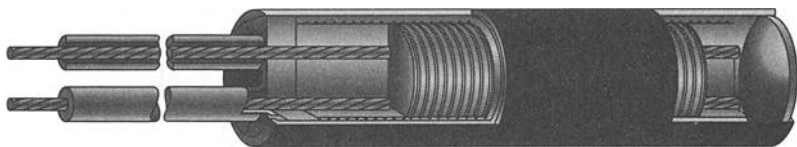

Fig. 7.2. Cartridge heater.
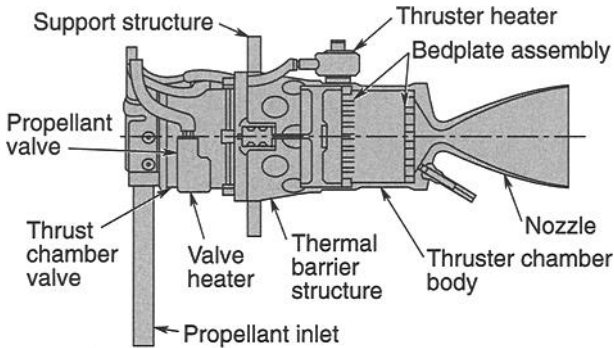
Fig. 7.3. Hydrazine thruster with heater.

In addition to the set point, the dead band, the difference between the temperatures at which the thermostat turns on and turns off, is important. A small dead band reduces the temperature swing of the device being heated and reduces power consumption a little (since the average temperature is lower). On the other hand, a small dead band also increases the number of cycles on the thermostat itself and decreases its reliability. Dead bands less than 4°C are not recommended, because of past problems. Small dead bands have been known to increase the chance of "dithering," a state in which the thermostat rapidly cycles on and off. This is a failure condition that can cause the set point to drift lower, resulting in an excessively low temperature of the component being controlled.

Even though thermostats are fairly reliable, a large number may be present on a typical satellite (up to several hundred), so occasional on-orbit failures may occur. Because of this risk, and the increasing life requirements of satellites, solid-state controllers are becoming more common. Such a controller (Fig. 7.5, Table 7.1) replaces the mechanical switch with an electronic device that has a higher reliability and life expectancy. Solid-state controllers are used extensively on the Defense
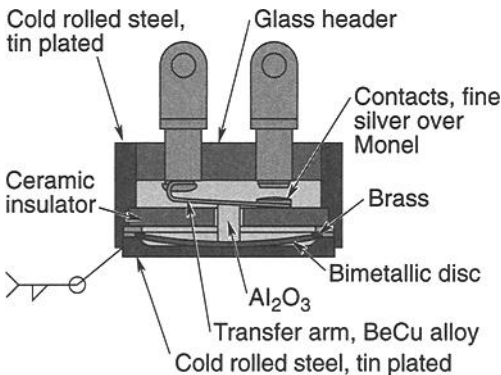
Fig. 7.4. Elmwood thermostat.
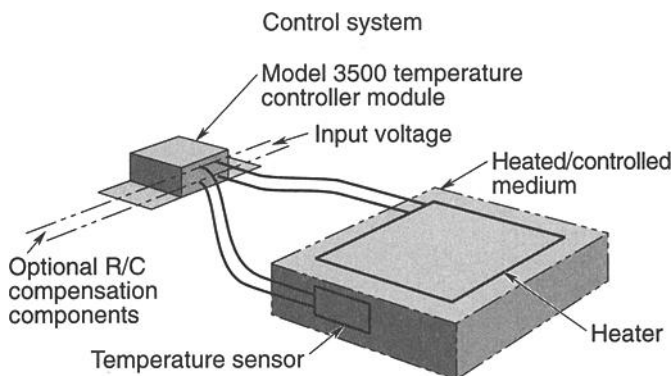
Fig. 7.5. Tayco solid-state controller.

Table 7.1. Tayco Solid-State Controller Specifications

Characteristic	Value
Package	Hermetically sealed can, $16.5 \times 21.6 \times 24.1$ mm
Control power (heater)	0 to 100 W, higher power available
Quiescent power (standby)	30 mW
Input power	28 Vdc nominal, 15 Vdc to 45 Vdc range
Efficiency	98% minimum
Set-point accuracy	.25°C, closer tolerances available
Weight	Less than 30 g
Loop gain	Provisions for external adjustment of control-loop gain
Compensation	Provisions for addition of loop compensation
MTBF	4.7 million hours minimum @ 25°C controller ambient
Electronic components	Meet requirements of JAN TXV, MIL-8838, MIL-R-55182, and MIL-C39014 (commercial model also available)
Module ambient (heat-sink temp)	−55 to +75°C

Meteorological Satellite Program, the Hubble Space Telescope, and the International Space Station. They employ a temperature sensor that can be located either internally or at remote locations. Another advantage of solid-state controllers is that extremely tight dead bands (< 0.1°C) are possible for very precise temperature control, such as is required by the Hubble Space Telescope. Optical systems, some sensors, and electronic-frequency standards often require precise temperature control, which cannot be achieved with a thermostat.

Recently, a number of military and scientific satellites have started to use onboard computers to control heaters. Such systems read the temperatures from telemetry sensors placed throughout the vehicle and send signals to turn relay-controlled heaters on and off as required. This process allows enormous flexibility, because it enables the control set points and dead bands to be adjusted on orbit by uplinking new tables and/or logic to the spacecraft computer. In one instance, the loss of an entire satellite was averted because of the flexibility of its computer-controlled heaters.

Failure Modes of Mechanical Thermostats

While mechanical thermostats have generally proven very reliable, they may occasionally fail closed (i.e., with the heater on), fail open (with the heater off), or dither (resulting in reduced heater output). The primary causes of failure are internal contamination, manufacturing defects, excessive narrowness of the dead band, inadequate screening, improper installation, excessive current, and pitted contacts. Thermostats may fail closed as a result of welding of the contacts under high current. Failures in the open position may result from the intrusion of a contaminant between the contacts that prevents them from closing. Dithering may occur if the dead band is less than 4°C or if a contaminant-induced increase in electrical resistance between the contacts results in internal thermostat heating and early trip-off. The Hubble Space Telescope and several other programs had a number of thermostats fail open during ground testing. Analysis of the failed units showed that they contained water and ambient air. When the temperature dropped below freezing, ice formed on the contacts, preventing electrical contact when the thermostats reached their set points, which were all below 0°C.

An analysis performed at The Aerospace Corporation showed how increases in the internal electrical resistance of a thermostat can cause internal self-heating and thermostat dithering. The analysis was performed after examination of a number of dithering thermostats from a military satellite program showed that internal contamination by carbon, silicon, and silver had caused the thermostats' resistance to increase from 25 to 300 mOhm. A 40-node analytical model of the thermostats in question, attached to an electronics box, showed that only 100 mW of internal heating were needed to cause dithering. As shown in the analysis results summarized in Fig. 7.6, even small increases in resistance in larger heaters (greater than 2 amps) can cause enough internal heating to induce dithering, and smaller heaters (0.7 amp) could be problematic with large resistance increases. The predicted temperatures, shown in Fig. 7.7, illustrate how the dithering thermostat kept itself warm while allowing the electronics-box temperature to fall.

While process improvements have been instituted by thermostat manufacturers to address these issues, problems still occasionally occur. Therefore, for design robustness, the power of individual heater circuits should be kept below 20 W to minimize sensitivity to contact electrical-resistance increases. In applications below 0°C, solid-state controllers or computer-controlled heaters are recommended to eliminate the possibility that the heater will be disabled as a result of ice forming on the contacts. In all cases, because failures like those discussed above may only show up after hundreds of cycles, an adequate test program should be implemented to ensure that failures occur on the ground, where they can be corrected.
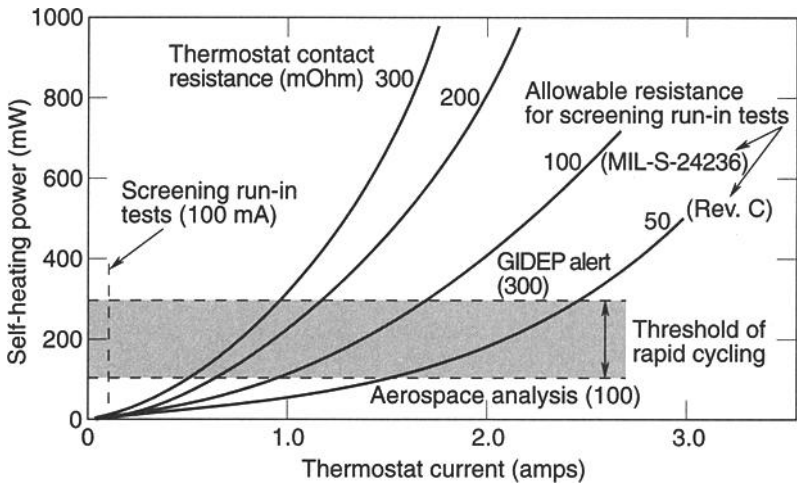
Fig. 7.6. Thermostat self-heating resulting from contact electrical resistance.
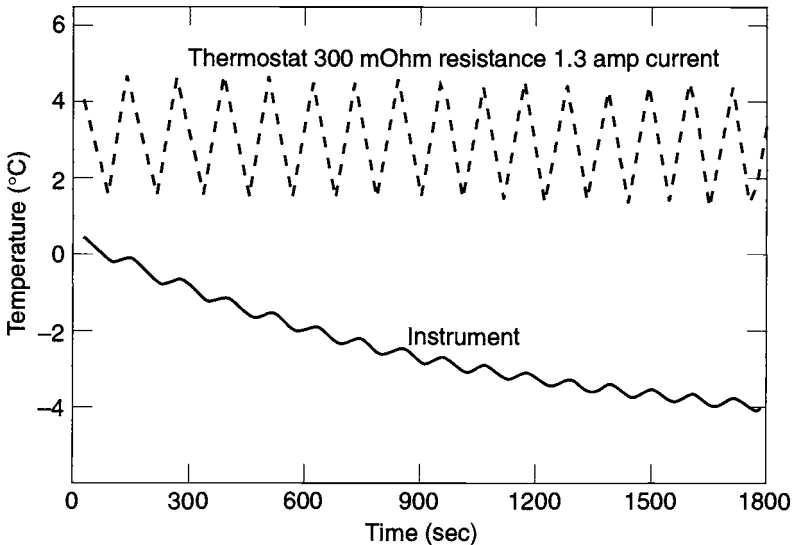

Fig. 7.7. Effect of thermostat dithering on component temperature control.

Circuits

A typical satellite has dozens of heaters and may use different thermostats, relays, solid-state controllers, and computers to control them. Many different types of redundancy schemes may be employed, even on the same satellite, depending on the criticality of a given heater.

The representative heater in Fig. 7.8 consists of redundant resistance elements in a single-patch heater. Each element is powered by a separate spacecraft power bus
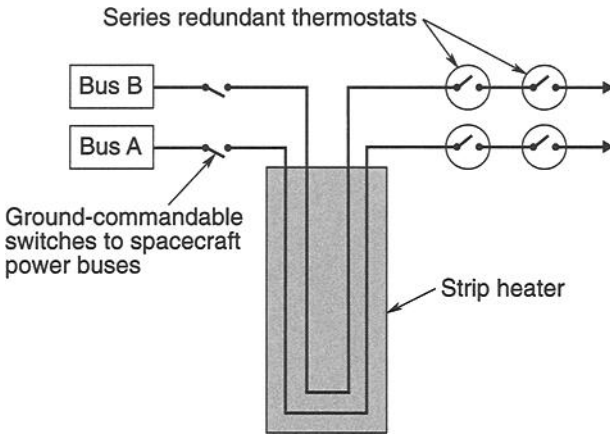
Fig. 7.8. Heater circuit example.

(satellite power systems are normally redundant), and each element has its own enable/disable relay, which is commandable from the ground. Series-redundant thermostats provide single-fault tolerance on each element for a thermostat that fails closed. If one of these thermostats fails open, however, the circuit is dead. A number of these heaters are used on the satellite. A typical panel of equipment with heater and thermostat locations is shown in Fig. 7.9. The heaters are the dark rectangular patches, and the thermostats are the black dots. The branch of the bus that supplies power to these heaters is fused, although this is not shown in Fig. 7.8.
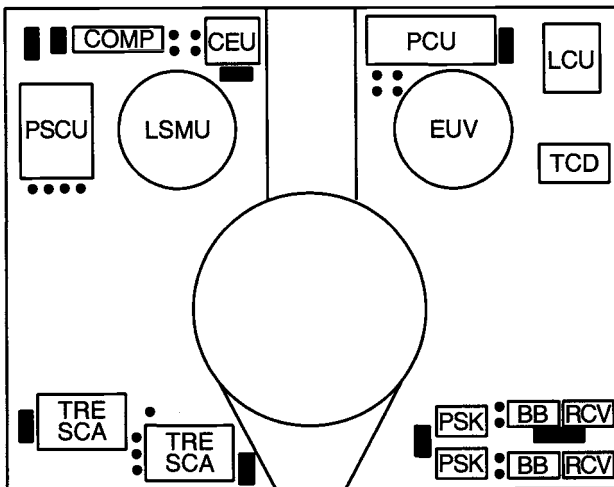
Fig. 7.9. Heater and thermostat layout.

There are many ways to lay out heaters and thermostats, depending on the level of reliability required. Figure 7.10 shows four different schemes used on one satellite. The most reliable (Type I in the figure) consists of redundant resistance elements working off of different power buses, each element employing "quad-redundant" thermostats. A quad-redundant arrangement requires at least two failures to disable thermostatic control. The other arrangements represent designs that have lower reliability but require fewer thermostats.

A schematic for the heater system used on one equipment panel on the Defense Satellite Communication System (DSCS) spacecraft, shown in Fig. 7.11, illustrates a typical application. Two sets of heaters are used: a set of survival heaters, with a set point of −18°C, which are used during launch before the spacecraft is fully powered up in its operational orbit, and a set of control heaters, with a set point of 13°C, which are used during normal on-orbit operations. The survival heaters have a lower set point to reduce their power draw (less heat is radiated away from the spacecraft at the lower temperature). The operational heaters, however, need a higher set point, since the satellite's electronics boxes will not function properly at the survival temperature. Two sets of heaters would not be required if the satellite used a computer-controlled heater system in which software could access different groups of set points during survival-mode and normal on-orbit operations.

The survival heaters are not redundant because they are not normally used and because the failure of a single heater would not result in a loss of the mission. They are, however, always connected to the power bus, without relays, to protect the spacecraft at all times. The control heaters, on the other hand, are completely redundant in circuitry, with one control thermostat on each circuit. Each circuit also has an overtemperature thermostat that switches off the heater at 20°C if the primary thermostat fails closed. Some of the "A-side" heaters are grouped together
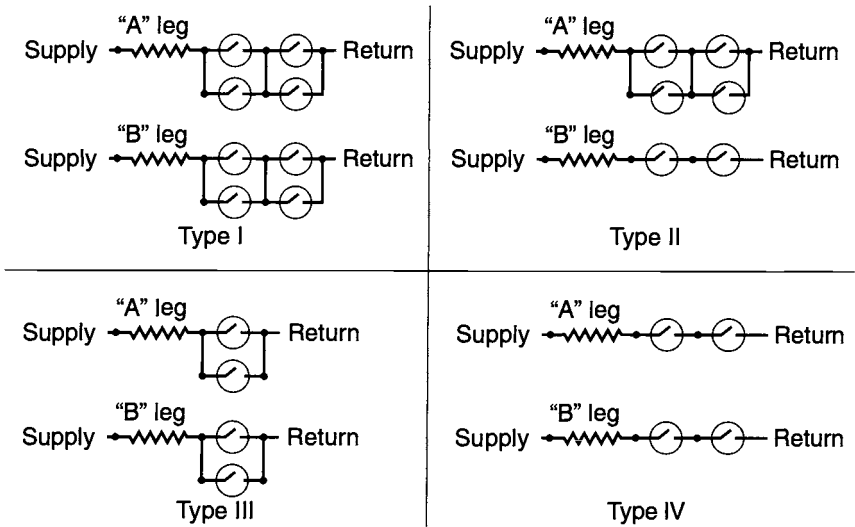

Fig. 7.10. Some heater wiring schemes.

| | | NPC
+28 V
bus | | | | NPC
+28 V
bus |

Heater	Name	Load Shed Relay	Heater CMDs CT	Control heaters	OT	Survival heaters	ST
TDAL	CH 1	A	13.3°C	4.2W	20.0°C	4.2W	−17.8°C
TDAL	CH 1	B	13.3°C	4.2W	20.0°C	4.2W	−17.8°C
TDAL	CH 2	A	13.3°C	4.2W	20.0°C	4.2W	−17.8°C
TDAL	CH 2	B	13.3°C	4.2W	20.0°C	4.2W	−17.8°C
TDAL	CH 3/4	A	13.3°C	4.2W	20.0°C	4.2W	−17.8°C
TDAL	CH 3/4	B	13.3°C	4.2W	20.0°C	4.2W	−17.8°C
TDAL	CH 5/6	A	13.3°C	4.2W	20.0°C	4.2W	−17.8°C
TDAL	CH 5/6	B	13.3°C	4.2W	20.0°C	4.2W	−17.8°C
Freq. std.		A	−11.1°C	4.2W	−5.6°C	2.0W	−17.8°C
Freq. std.		B	−11.1°C	2.0W	−5.6°C	2.0W	−17.8°C
LNA oven		A	22.0W ET	25.0°C	OT −17.8°C OT −17.8°C	22.0W	
LNA oven		B	22.0W ET	25.0°C	−17.8°C −17.8°C	22.0W	

CT: Control thermostat
OT: Overtemperature thermostat
ST: Survival thermostat
ET: Electronic thermostat
Temperature shown is thermostat set point

Fig. 7.11. DSCS satellite north panel heater schematic.

on a single commandable enable/disable relay, as are some of the "B-side" heaters. Two of the heaters are controlled by electronic thermostats used on the low-noise amplifier oven to precisely control the temperature of an oscillator crystal. This DSCS heater schematic is offered only as an example; wide variations in heater-circuit layouts are found on different satellites.

Computer-Controlled Heater System Example

Milstar (Fig. 7.12) is a large geosynchronous military communication satellite that uses a computer-controlled heater system. In addition to keeping components
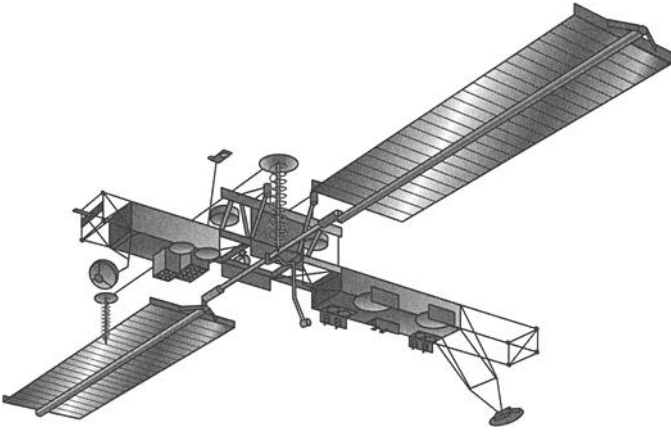
Fig. 7.12. Milstar satellite.

warm, computer control allows temperature set points to be changed during the mission, allows multiple propellant tanks to be kept at precisely the same temperature, and allows attitude-control gyros to be kept at a very constant temperature, all while enhancing spacecraft peak-power management capability.

Heater System Architecture

The overall architecture of the heater system (Fig. 7.13) consists of several layers of increasingly distributed control electronics, starting with the central spacecraft computer (the Milstar satellite processor) and ending with the actual heater elements used to warm 143 separate thermal zones scattered throughout the spacecraft. While management of the heater system occurs through the spacecraft computer, most of the actual heater-control logic resides in several lower-level distributed processor units located in different parts of this rather large vehicle. As shown in Fig. 7.13, each distributed processor contains three data files that store the current status of all heaters and telemetry temperature-sensor readings, the specified temperature set points for each heater, and addressing information that allows the processor to control multiple heaters over a single digital-signal bus. Processor software compares the temperature of each component being heated to the stored set points and turns the appropriate heaters on or off, as needed, to keep all temperatures within the desired control range.

Each distributed processor unit drives a number of controller units that convert the digital commands from the processor into the analog signals needed to drive the heater switch units (HSUs) that actually turn the individual heaters on and off. Each controller drives several heater-circuit zones. The distributed processor units also convert analog telemetry-sensor signals (temperature, heater on/off status, etc.) to digital form for heater control-loop feedback and periodic downlinking to the ground station for monitoring the vehicle's state of health.

As is the case with most spacecraft components, the heater system incorporates redundancy for high reliability. The central Milstar satellite processor, the distributed
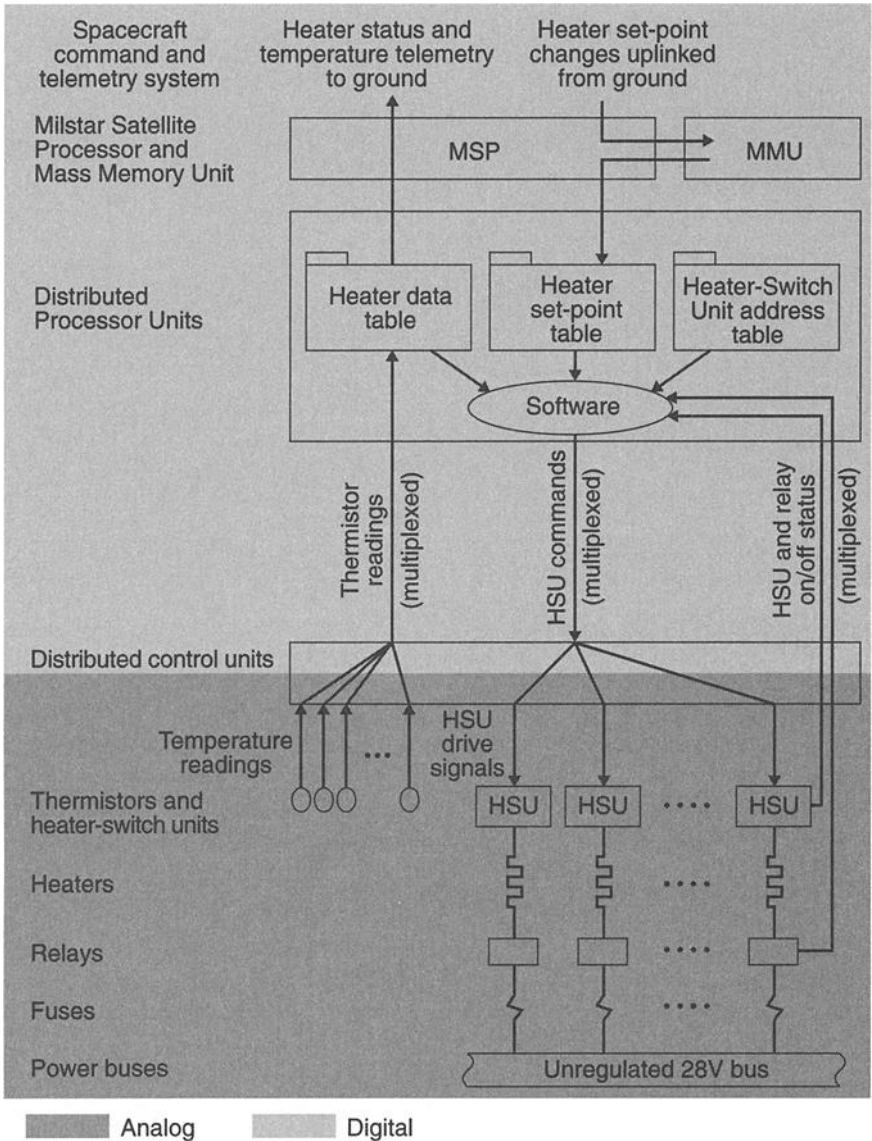
Fig. 7.13. Heater system architecture.

processor units, the controller units, the heaters and thermistors all have redundant A and B sides that are fully cross-strapped, as shown in Fig. 7.14. In such an arrangement, no single failure can disable a heater, and some multiple-failure scenarios can be accommodated. While most of the figures and discussion that follow describe a single side of the heater-control system, the reader should bear in mind that an essentially identical backup side also exists.
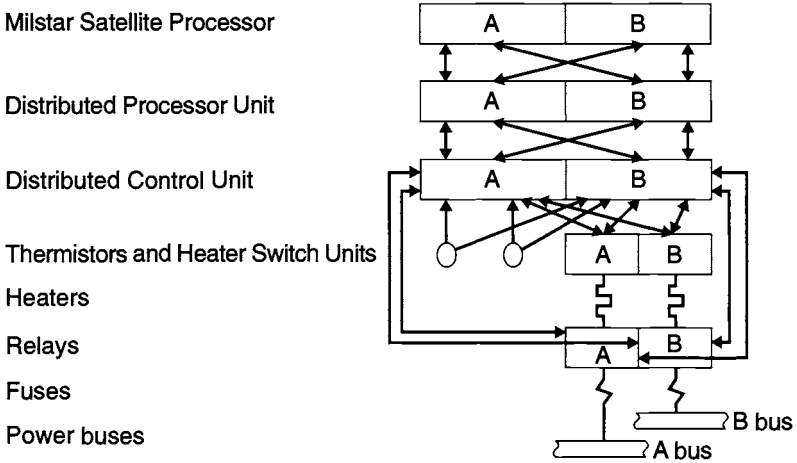
Fig. 7.14. Heater-system redundancy.

Hardware

Heater Switch Units

There are 156 heater switch units (HSUs) located throughout the spacecraft, each capable of switching on and off a heater of up to 225 W while dissipating no more than 9.6 W of internal waste heat. A typical HSU (Fig. 7.15) consists of a copper-cased microcircuit hybrid unit mounted on a circuit board and enclosed in a rectangular case measuring 3.5 by 3.3 by 1.0 cm. The hybrid microcircuit consists of a transistor switch and associated SGEMP (system-generated electromagnetic pulse) suppression components required to survive in hostile military environments. A + or – 15 Vdc drive signal from the controller unit maintains the HSU in either an on or off state, respectively. If the drive signal is interrupted, a bank of capacitors in the controller unit power supply provides a sustained –15 Vdc drive to place all HSUs in an off state. This is done to prevent all of the HSUs driven by that controller from turning on if the supply of power to the controller is momentarily interrupted.

Thermistors

Four different types of thermistor are used to sense temperatures on the spacecraft. In most thermal zones, a Yellow Springs thermistor with a calibration range of –40 to 85°C is used. For components or structural elements that experience a wider range of temperatures, Rosemount thermistors with a range of –157 to +121°C are used. (Sketches of these two sensors appear in Fig. 7.16.) The attitude-control thruster manufacturer also supplies two kinds of Tayco wire-type resistor temperature sensors with their hardware; the sensors on the valves, which have a useful range of –18 to +260°C, and the sensors on the injectors, which have a useful range of –18 to +677°C.
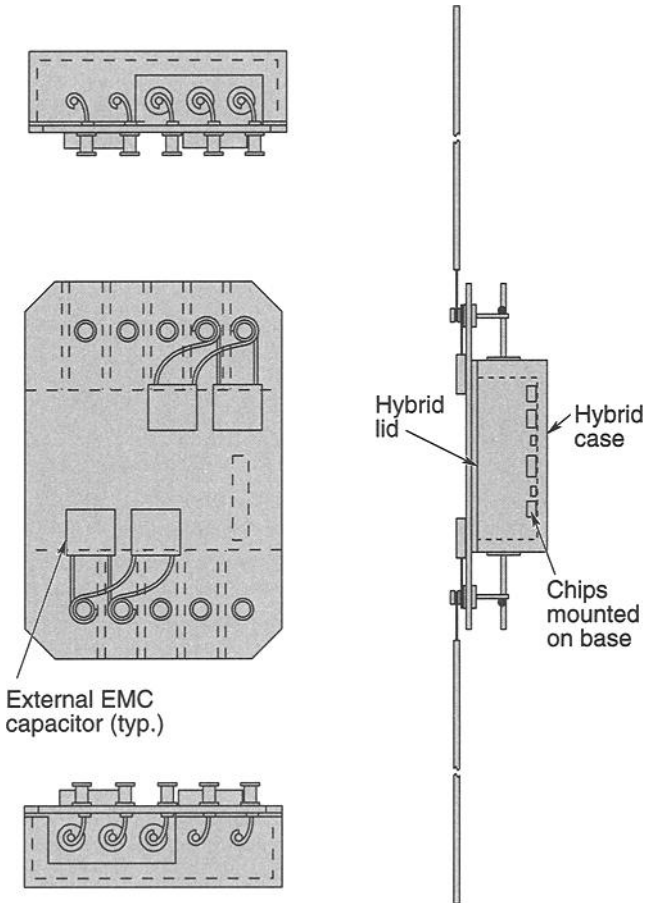
Fig. 7.15. Heater Switch Unit (HSU).

For sensors installed inside the spacecraft, where they are protected from extraneous signal noise, the thermistor assembly consists basically of a temperature-sensitive resistor, as shown in Fig. 7.17(a). For externally mounted sensors, SGEMP protection is provided by diodes installed in the thermistor-diode assembly module, as shown in Fig. 7.17(b). Each assembly can have either one or two thermistors; the one-thermistor version is used for health and status monitoring, while the two-thermistor unit is used for heater control.

Heaters

Milstar uses several different Tayco heaters. Except for those used by the propellant lines and thrusters, all spacecraft surface heaters are flat single- or dual-element patch heaters, as shown in Fig. 7.18. The propellant lines use dual-element spiral or circular patch heaters shaped to fit around the propellant lines, as shown
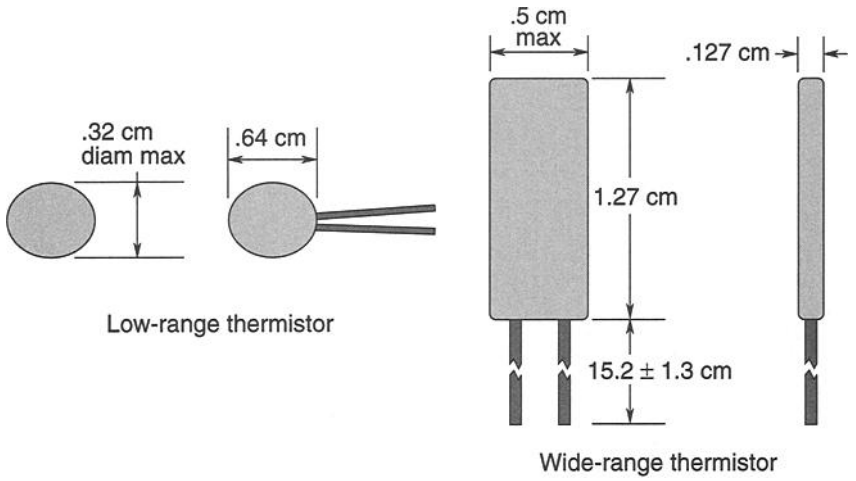
Fig. 7.16. Temperature sensors.

(a) Internal thermistor assembly

(b) External thermistor assembly
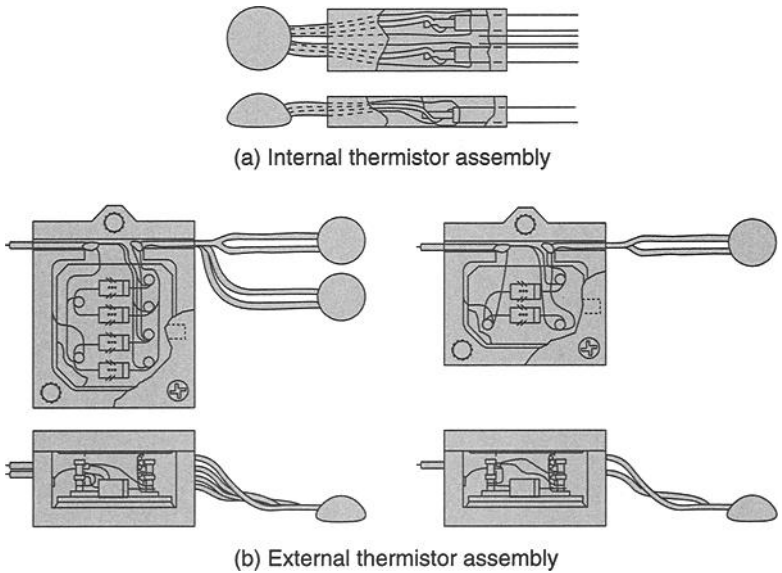
Fig. 7.17. (a) & (b) Temperature-sensor assemblies.
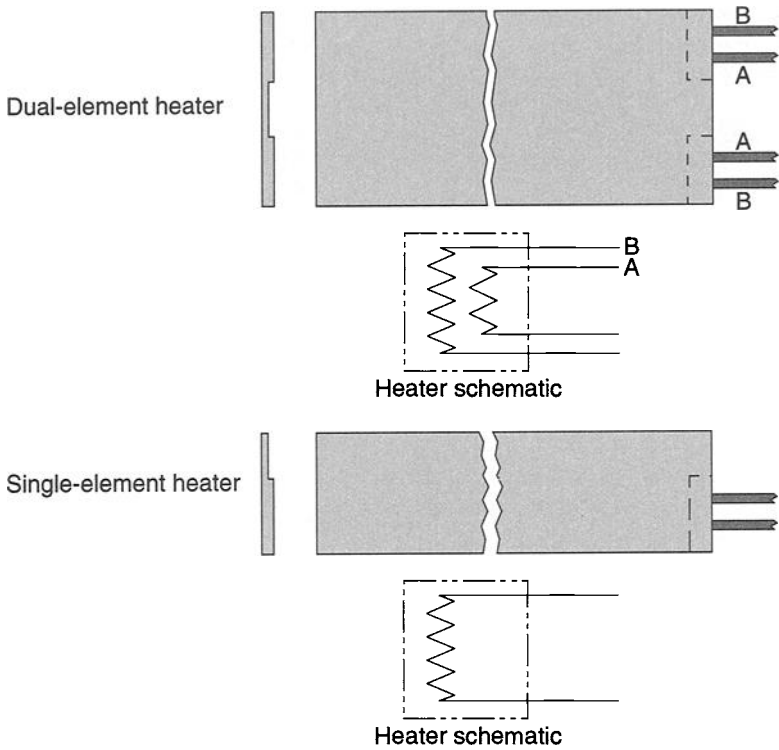
Fig. 7.18. Flat patch heaters.

in Fig. 7.19. All of the patch heaters consist of a wire heating element embedded in a Kapton laminate. Thruster heaters consist of a wire heating element embedded in magnesium oxide and encased in stainless steel.

Relays

As is the case on most spacecraft, relays are provided to enable or disable the power supplied to the heaters. Commands from the ground can be sent through the Milstar satellite processor and the appropriate processor unit and control unit to disable any heater that has failed on or developed a soft short.

Fuses

Each heater circuit has a fuse, as shown in Fig. 7.13, to ensure that a hard short in the circuit does not immediately drag down the entire power bus before a command can be sent from the ground to disable the shorted heater.

Spiral

Circular
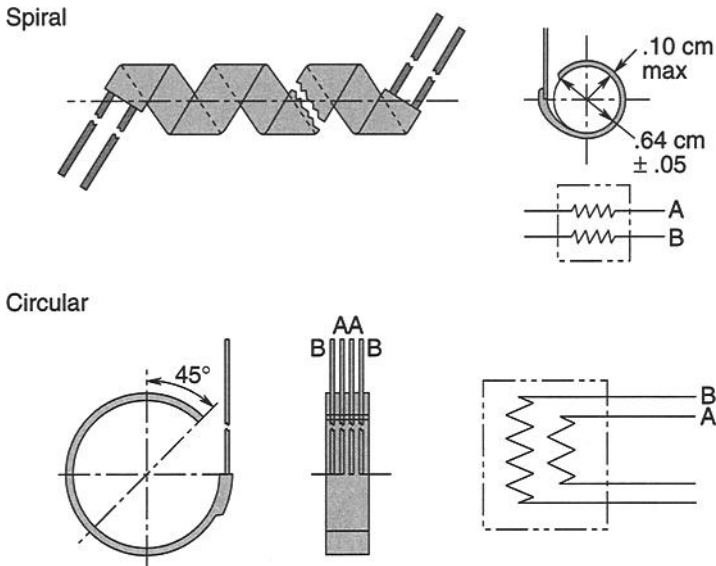
Fig. 7.19. Propellant-line heaters.

Software Control Algorithm

As was mentioned earlier, heater system operation is controlled in the distributed processor units, which contain software that monitors component temperatures and turns heaters on and off, as appropriate, to maintain the desired temperature.

Reading and Calibrating Temperatures

The first step in the control process is for the processor units to read and calibrate the temperature-sensor data sent to them by the controller units. Temperature is actually measured indirectly by measuring the resistance of the sensing thermistor. Table 7.2 shows the relationship between resistance and temperature for one particular thermistor. After reading the thermistor, however, the control unit does not output the resistance, R_t, as a decimal number, but quantizes it in "counts" according to the following equation:

$$\text{Counts} = \frac{(9.9875)(R_t) - 5.6355}{0.1079 + (0.009766)(R_t)} \tag{7.1}$$

Figure 7.20 shows the resulting relation between telemetry counts and temperature for the thermistor described in Table 7.2.

Because component tolerance, temperature, aging, and radiation affect the measurement process, each controller unit has several high- and low-resistance precision-reference resistors that the distributed processor unit uses to calibrate the measurements reported by that controller. The processor reads the resistances of all of the thermistors and reference resistors, compares the measured values for the reference resistors to their known values to derive a correction term, adjusts all
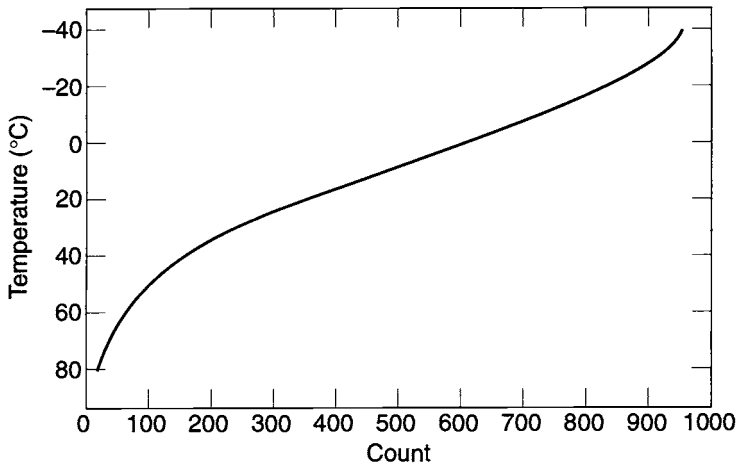
Fig. 7.20. Calibration curve for thermistor described in Table 7.2.

Table 7.2. Sample Thermistor Characteristics

Temperature (°C)	Resistance (Ω)	Nominal Telemetry Count
−40	168,300 ± 1.33	956
−30	88,530 ± 0.80	903
−20	48,560 ± 0.70	823
−10	27,670 ± 0.65	716
0	16,330 ± 0.52	589
10	9951 ± 0.48	457
20	6247 ± 0.45	336
30	4029 ± 0.43	235
40	2663 ± 0.40	157
50	1801 ± 0.38	98
60	1244 ± 0.36	57
70	875.7 ± 0.34	27
80	628.1 ± 0.39	6
90	458.2 ± 0.50	Saturates
100	339.6 ± 0.60	at 0 counts
−54	1580[a]	82
−31	90,900[a]	906

[a]Precision reference resistor

of the thermistor resistance (temperature) readings, and stores the corrected values as counts in the heater and thermistor data table.

Heater Switching

Once calibrated temperature measurements have been made, the distributed processor units compare the measured temperatures to the set points for each of the heaters that is stored in the heater set-point table. When the measured temperature drops to the set point, the processor uses the address found in the heater-switch-unit address table to send a digital signal to the appropriate controller to turn on the heater. The controller unit then sends an analog +15 Vdc drive signal to the HSU, which activates the heater. (The power is supplied to the heater from the 28 Vdc heater power bus, not the 15 Vdc drive signal.) When the temperature rises 2.8°C above the set point, the processor sends a digital signal to the controller to turn the heater off. The controller then changes the HSU analog drive from +15 to −15 Vdc, disconnecting the heater from the power bus. The 2.8°C dead band is achieved by storing the temperatures in the processor unit's set-point table with a granularity of 2.8°C. Figure 7.21 shows the resulting heater temperature cycling.

To ensure that a failed thermistor does not cause a heater to stick on or off, the distributed processor unit actually reads both the primary and redundant temperature sensors associated with each heater. If both thermistors' counts are all zeros or all ones (off scale high or low), the processor switches to the redundant heater-control circuit. If one thermistor's count is all zeros or ones, it is rejected as being too hot or cold to be a valid reading and the other thermistor is used for heater control. If both thermistors' values are within the valid range, the lesser (warmer) value is used to control the heater.

Spacecraft Modes

Different spacecraft operating modes often require different temperatures for the same thermal zone. To support this requirement, the distributed processor units change the set points that are used during the different mission phases. The processors accomplish this change using different look-up tables for different operating modes. Table 7.3 lists the various heater modes used during different phases of the mission. Set-point tables for all of these modes are stored in the spacecraft's mass memory unit and can be downloaded to the distributed processor units via the Milstar satellite processor.
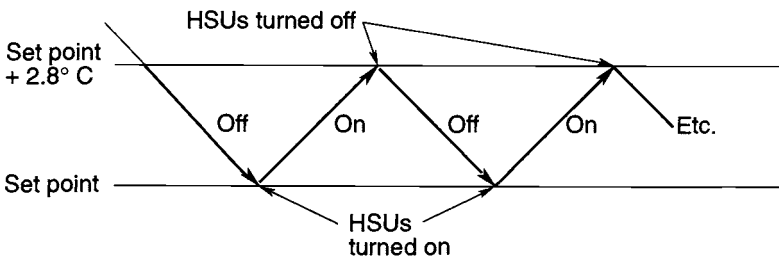

Fig. 7.21. Heater cycling.

Table 7.3. Correspondences between Heater Control Modes and Spacecraft Operational Modes

Heater Mode	Description
Initialization/ascent	Most zones control at survival temperature. Some zones preheat to survival +6°C.
Centaur discrete 5	Most zones control at survival temperature. Some zones control at survival +8°C.
Centaur discrete 7	All zones control at survival temperature.
First eclipse	Most zones control at survival temperature. Some zones preheat to 17°C via MSP command.
Equipment heat-up	Some zones control at minimum operating temperature. Some zones at minimum operating temperature +17°C.
Functional temperatures	All zones control at minimum operating temperature.
Orbit eclipse	Most zones control at minimum operating temperature. Some zones preheat to 17°C via MSP command.
Safe mode	Some zones control at minimum operating temperature. Some zones control at survival temperature.
Load shed	Some zones control at minimum operating temperature. Some zones control at survival temperature.

Radioisotope Heater Units

Spacecraft traveling to the outer planets (Jupiter and beyond) face a fundamental power/thermal challenge because the very low levels of solar radiances at such great distances from the sun create a cold environment and make solar power generation unattractive. Traditionally, the solution to the power challenge has been the use of radioisotope thermoelectric generators (RTGs). Their low efficiency and high cost, however, still make power a precious commodity. A particularly clever response to this challenge has been JPL's development of radioisotope heater units (RHUs), devices that place the heat of radioactive decay directly where it is needed, thereby bypassing the inefficiency of converting the heat in the RTG to electricity and then back into heat in an electrical-resistance heater.

At the center of each RHU, shown in Fig. 7.22, is a plutonium-dioxide ceramic fuel pellet. A single RHU weighs 42 g and fits snugly in a cylindrical enclosure 26 mm in diameter and 32 mm long. Each unit delivers 1.04 ± 0.3 W of heat at the time of encapsulation by means of radioactive decay of its plutonium fuel. From that point on, however, the heat-generation rate decreases with time. Figure 7.23 shows the decay curves for the Cassini/Huygens mission, for both primary and backup launch dates. Cassini/Huygens used a total of 117 RHUs.

While the application of a nearly constant heat source to a spacecraft component can be accomplished by attaching one or more RHUs, the ability to control the application of heat at a particular temperature, as a thermostatically controlled heater does, would provide much more flexibility. The variable radioisotope heater unit (VRHU) was developed to provide just such a capability. It consists of a cylindrical RHU holder that contains up to five RHUs and rotates on bearings
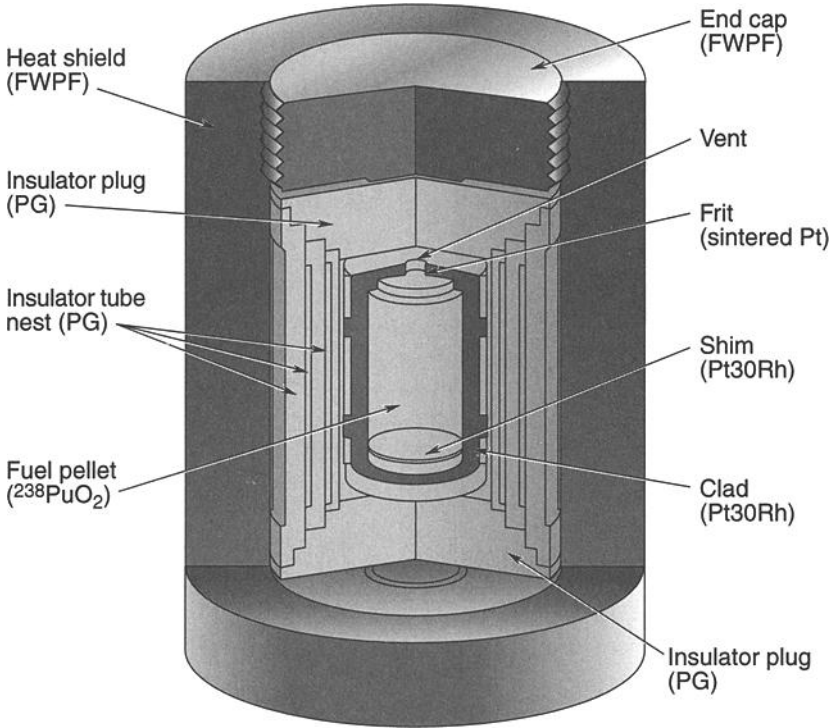
Fig. 7.22. Radioisotope Heater Unit (RHU). (Provided courtesy of the Jet Propulsion Laboratory.)

when driven by two temperature-sensitive bimetal springs. As illustrated in Figure 7.24, one side of the cylindrical RHU holder is painted white while the other side is covered with a 22-layer, all-Kapton (high-temperature) multilayer insulation (MLI) blanket. The RHU holder is thermally isolated from the bimetal actuator, which is thermally coupled to the hardware that is being temperature-controlled. When the hardware temperature goes below the set-point temperature of the bimetal springs, the holder is rotated so that the high-emittance surface (the side painted white) faces the hardware and the blanketed side faces space. When the hardware temperature goes above the set point, the holder rotates to expose the high-emittance side to space and the blanketed side to the hardware. The bimetal springs can be calibrated for any desired open-point temperature between –20 and +50°C with the fully open condition occurring 28°C above the open-point temperature. Figure 7.25 shows a VRHU. Without RHUs, the unit weighs 390 g.

RHU heat dissipation decreases with time, and that condition affects VRHU performance. Figure 7.26 shows the VRHU performance for the Cassini/Huygens mission for both the primary and backup launch dates. The upper curve represents the maximum VRHU performance that occurs at the beginning of the mission for
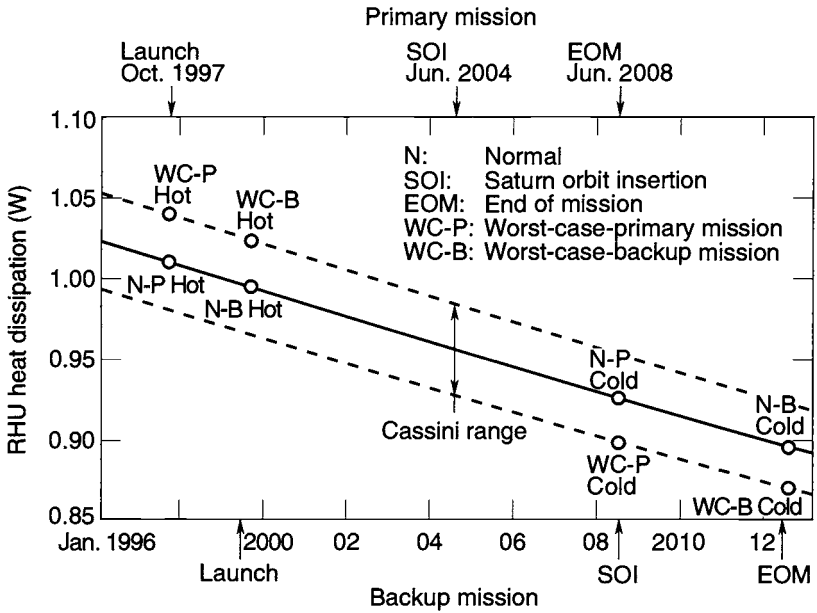
Fig. 7.23. RHU heat dissipation for the Cassini/Huygens mission. (Reprinted with permission from SAE Paper No. 941268 ©1994 Society of Automotive Engineers, Inc.)
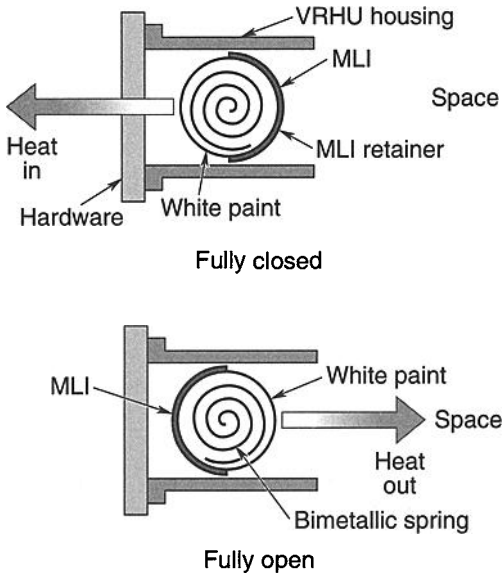

Fig. 7.24. The Variable Radioisotope Heater Unit (VRHU) concept. (Reprinted with permission from SAE Paper No. 941268 ©1994 Society of Automotive Engineers, Inc.)
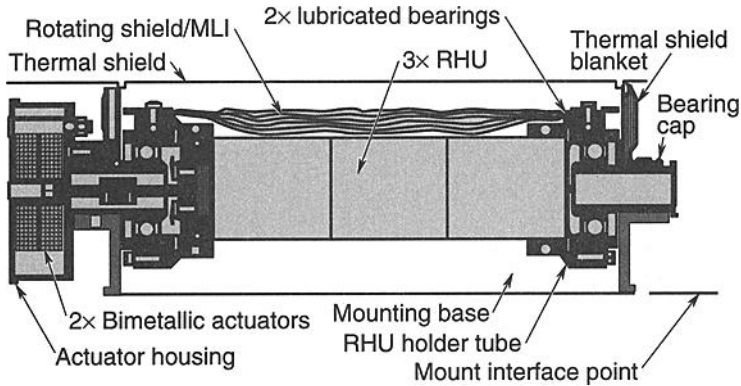
Fig. 7.25. Variable Radioisotope Heater Unit (Reprinted with permission from SAE Paper No. 941268 ©1994 Society of Automotive Engineers, Inc.)
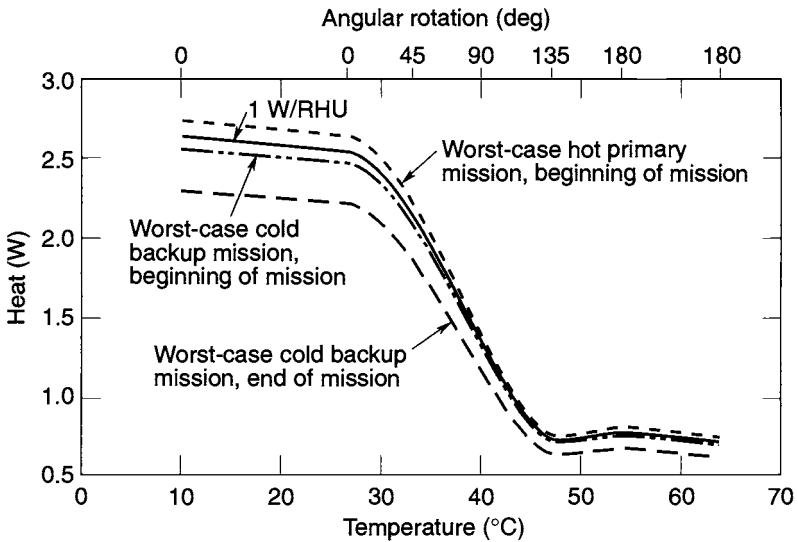
Fig. 7.26. VRHU Cassini/Huygens mission characterization. (Reprinted with permission from SAE Paper No. 941268 ©1994 Society of Automotive Engineers, Inc.)

the primary (earliest) launch, when the individual RHUs have their highest heat output. The bottom curve corresponds to the end of the mission and is based on data that assumes the backup (latest) launch date has a longer total flight time. This lower curve represents minimum VRHU performance resulting from the reduction in heat output that occurs almost 13 years after the RHU was loaded

with plutonium. The performance for a given VRHU decreases 8% and 10% over the course of the 11- and 13-year primary and backup missions, respectively.

Since VRHUs may also be exposed to sunlight, testing was performed to characterize the effect of solar illumination on their performance. Steady-state results for the worst-case condition of sun normal to the opening, at varying irradiances, are shown in Table 7.4, which also shows performance characteristics without sun for comparison. As can be seen in the data, the absorbed solar backload increases with mounting-plate temperature. This occurs because more of the paint (as opposed to MLI) is directly exposed to the sun when mounting-plate temperatures are higher. This change in exposed surface, coupled with cavity effects, causes more sunlight to be absorbed and conducted to the mounting plate. The solar load is large and may be significant in steady-state applications. It may be reduced by design changes that lessen the cavity effect and modify the thermal-shield height, although such changes lower efficiency somewhat.

While RHUs and VRHUs are very useful for government-sponsored deep space missions, the presence of plutonium precludes their use on most other projects. Even if control of the nuclear material were not an issue, the cost of RHUs makes them less attractive than electrical-resistance heaters for most missions where solar electric power is practical.

Table 7.4. VRHU Performance with and without Solar Illumination[a]

	Solar Irradiance (suns)					
	1.0	1.0	0	2.7	2.7	0
Performance (W)						
Solar load	1.60	2.14	0	4.64	6.28	0
RHU heat	2.54	1.95	1.95	2.54	1.35	1.35
Total	4.14	4.09	1.95	7.18	7.63	1.35
Temperature (°C)						
Mounting plate	26	36	36	26	43	43
RHU holder	91	101	78	110	146	74
Actuator housing	27	37	36	29	45	43
Mounting base	29	38	37	30	47	44
Thermal shield	52	52	31	89	114	37

[a]Reprinted with permission from SAE Paper No. 941268 ©1994 Society of Automotive Engineers, Inc.

8 Mountings and Interfaces

D. F. Gluck[*] and V. Baturkin[†]

Introduction

This chapter deals with the thermal design, analysis, and performance of a wide variety of spacecraft mechanical interfaces, as well as thermal predictive methods for use with those interfaces. Heat removal from electronic units is a foremost spacecraft concern, and thus the problem of developing an optimal conductive interface between unit baseplate and spacecraft mounting is critical. The elements of this very difficult problem must be addressed sequentially at increasingly higher levels of complexity: the engineer needs to consider the effects of uniform pressure between plates in vacuum, the use of bolts or screws to join plates, the effects of fluid in the gap between plates, and the use of interface fillers. The interface problem is compounded by structural and thermal hardware, including honeycomb mounting panels, heat pipes, and thermal doublers. For problems such as this, combined thermal and structural analysis is an important design and evaluation tool. Some thermal interfaces must be compliant rather than rigid; others must reduce and minimize rather than enhance heat transfer. Still others involve composite or polymer materials. In addition, some interfaces must transfer heat across mobile bearings. All of these issues are addressed in this chapter, with the object of providing practical design and analysis aids, performance predictions, and guidance to the practicing spacecraft thermal engineer. Chapter 16 contains a more detailed discussion of the theoretical models of thermal contact resistance and supporting experimental work.

Unit Conduction Cooling

Unit Mounting

In most cases, an electronic unit is designed so that the power dissipated within it is transported as heat to the unit's mounting surface (baseplate). This heat is transferred by conduction to a section of the spacecraft structure (here called the mounting plate) and thence by a variety of methods and paths to the space sink. A smaller number of units are cooled partially (sometimes largely) by radiation. Such units are designed so that heat can be radiated from various unit surfaces, but usually not the mounting surface, to the surrounding space-vehicle enclosure or directly to space. The spacecraft's mounting plate is dealt with here, as is the predominant heat-transport method, conduction cooling from the unit's baseplate to the spacecraft's mounting plate.

The temperature rise across the mounting interface should be small; this requirement is important, because each part and device within the unit is subject to this

---

*DFG Engineering, Albuquerque, New Mexico.
†National Technical University of Ukraine (formerly Kyiv Polytechnic Institute), Kyiv, Ukraine.

temperature rise. Reliability and, possibly, functional performance are adversely affected by high temperature.

Most space-vehicle electronics boxes have baseplates ranging in size from 100 by 150 mm to 450 by 600 mm, with power levels sometimes exceeding 1000 W. Mounting is typically done by bolts set in a pattern along the baseplate perimeter, as shown schematically in Fig. 8.1. Flange mounting is convenient, because it makes bolts or screws accessible and enables the application of torque from above. When electronics boxes are built up from "slices" or modules (Fig. 8.2), the bolts are arranged along two opposed sides of the baseplate. Where power dissipation or local power per unit area is large, additional screws in the inboard regions of the unit are used. These secure from below, extending from the spacecraft mounting plate to the unit baseplate (Figs. 8.3 and 8.4). Because these screws must be inserted from below, their use complicates the assembly process. However, they increase the conductance from baseplate to mounting surface.

Conductance for Surfaces under Uniform Pressure

Possible modes of heat transfer from the unit baseplate to the space-vehicle mounting surface are convection, radiation, and conduction. However, because of the vacuum condition of space, essentially no convection occurs at the interface.
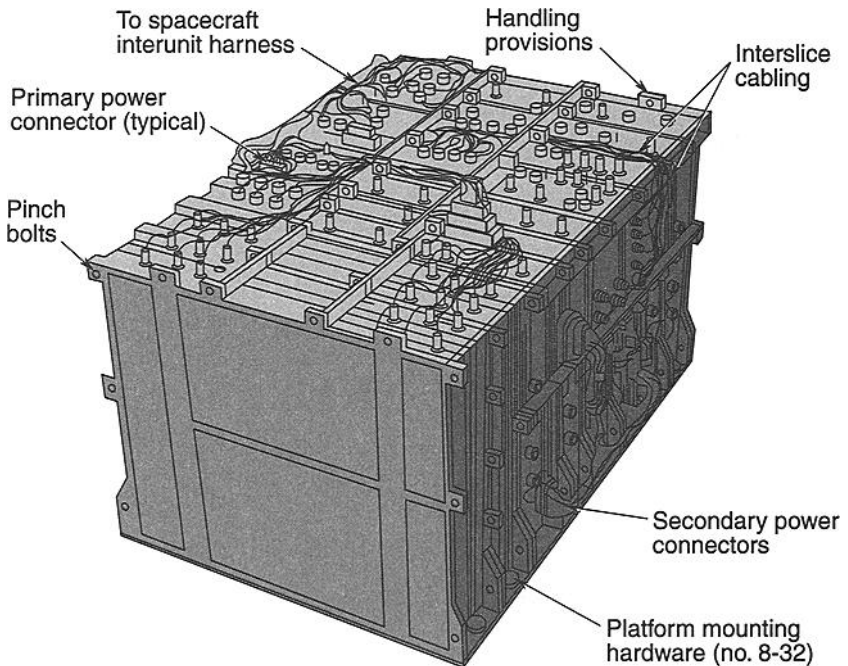

**Fig. 8.1. Mounting of electronics box by a bolt pattern along perimeter of baseplate.**
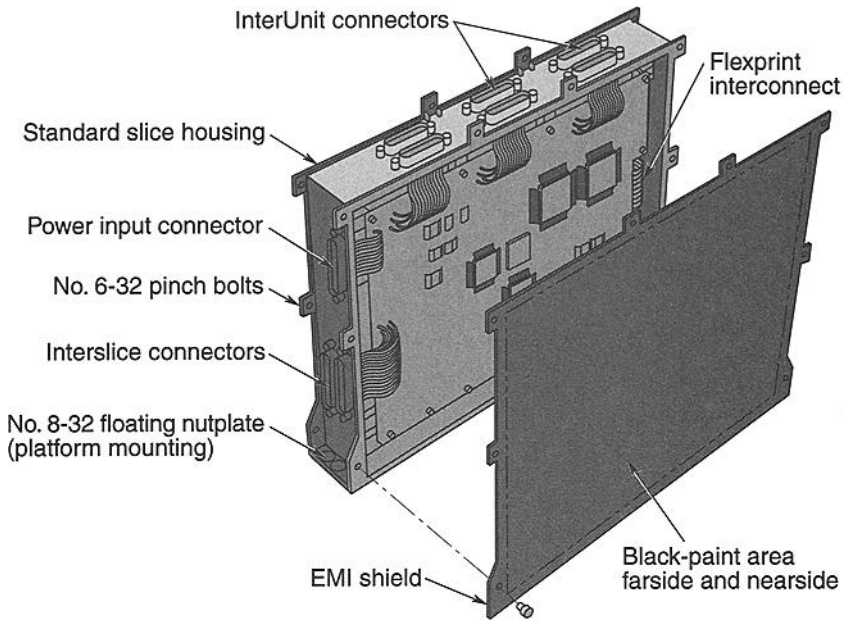
Fig. 8.2. Electronics boxes built up from modules.

Moreover, for the relevant temperature range, −50 to 110°C, the amount of heat transferred via radiation is generally very small compared to the amount transferred by conduction.
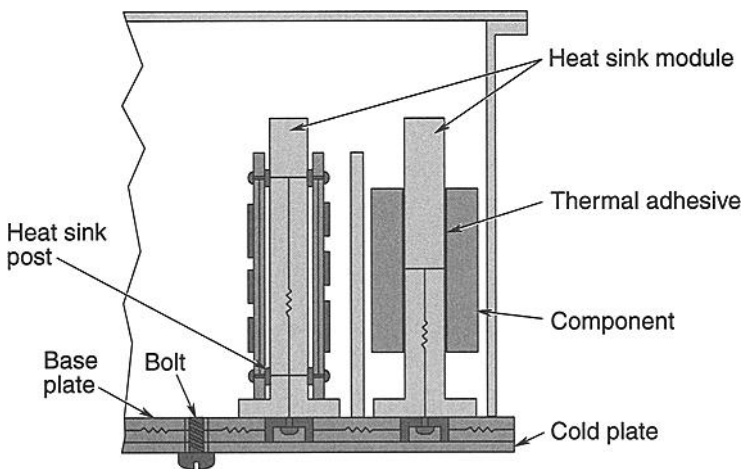

Fig. 8.3. Schematic showing bolt inserted from mounting-plate side.
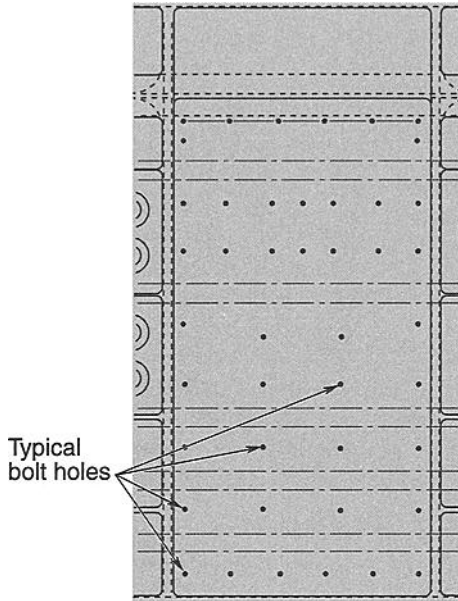
Fig. 8.4. Unit mounting footprint showing bolt holes.

Conduction taking place from one surface to another is called contact conductance. The problem of how to predict heat transfer in contact conductance has been studied widely for the case of two surfaces pressed together under uniform pressure. The corresponding problem for two surfaces that are bolted together and therefore experience a nonuniform pressure profile is considerably more complex; it is discussed in a subsequent section. In what follows here, the measurement of contact-conductance heat flow is characterized by the "heat-transfer coefficient," h, expressed in units of $W/m^2 \cdot K$. In keeping with spacecraft thermal-control usage, the term "conductance," denoted by C, will be reserved for the product of the heat-transfer coefficient and the area, hA, expressed in units of W/K.

Introduction

Figure 8.5[8.1] shows small- and large-scale imperfections of machined surfaces: roughness and waviness. Roughness typically results from the action of the cutting tool, extrusion die, casting mold, or grinding abrasive.[8.2] Contact resulting from roughness is small-scale contact (microcontact). Waviness can result from vibration or gaps in the machining equipment, or heat treatment.[8.3] Contact resulting from waviness is larger-scale contact (macrocontact).

Flat, Rough Surfaces in Vacuum

Rough-surface contact actually occurs over only a small fraction of the apparent contact area. At each microcontact, heat flow constricts (Fig. 8.6).[8.3] Mikic and coworkers[8.4–8.6] have made some important contributions to the theory of contact
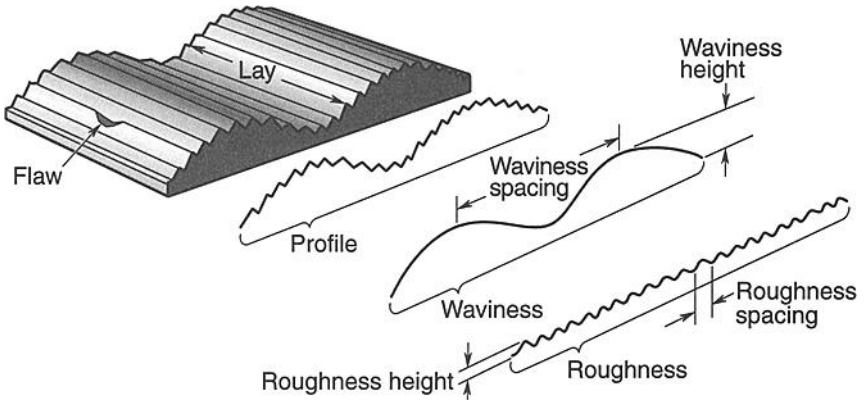
Fig. 8.5. Surface profile showing waviness and roughness.

conductance of flat, rough surfaces. They assumed that the asperity heights can be characterized by a random process that is stationary and for which the distribution of heights is Gaussian above a mean plane. The surfaces' combined profile can then be characterized by the standard deviation of profile height, σ, and the mean of the absolute value of the slope, m. Here $\sigma = (\sigma_1^2 + \sigma_2^2)^{1/2}$, where the subscripts denote the two surfaces. The variable σ is also the root-mean-square (rms) roughness. Typical values of σ_1 and σ_2 are 0.2 to 3.5 μm, although much larger and smaller values are possible (Table 8.1, from *Machinery's Handbook*). If both slopes are normally distributed, then $m = (m_1^2 + m_2^2)^{1/2}$. Slope has been correlated to roughness[8.7] by the equation $m_{1 \text{ or } 2} = 0.076(\sigma_{1 \text{ or } 2} \times 10^6)^{0.52}$ with m sometimes assumed to be in the range 0.10 to 0.15.

The uniform or apparent pressure applied to the surfaces results in much higher pressure on the asperities in contact. When this pressure is sufficiently great that the yield strength is exceeded, elastic deformation transitions to plastic deformation. Because both types of deformation are possible, Mikic developed predictive equations for heat-transfer coefficients for both of them:

$$h_e = 1.55(k_h m/\sigma)(2^{1/2}P/E'm)^{0.94} \qquad \text{(elastic)} \qquad (8.1)$$

and

$$h_p = 1.13(k_h m/\sigma)(P/H_C)^{0.94} \qquad \text{(plastic).} \qquad (8.1)$$

According to Mikic, deformation is predominantly plastic or elastic if the group $\gamma = H_C/(E'm)$ is less than 0.33 or greater than 3.0, respectively. Here k_h is the harmonic-mean thermal conductivity, P is the apparent loading pressure (i.e., the pressure calculated by dividing force by nominal flat surface area), H_C is the contact microhardness of the softer of the two surface materials, and E' is determined by the following equation:

Table 8.1. Surface Roughness Produced by Common Production Methods[a]

Process	Roughness Average R_a [μm (μin)][b]												
	50 (2000)	25 (1000)	12.5 (500)	6.3 (250)	3.2 (125)	1.6 (63)	0.8 (32)	0.4 (16)	0.2 (8)	0.1 (4)	0.05 (2)	0.025 (1)	0.012 (0.5)
Flame cutting	███	███	███										
Snagging	███	███	███	███									
Sawing	███	███	███	███	███								
Planing, shaping		███	███	███	███	███							
Drilling			███	███	███	███							
Chemical milling			███	███	███								
Elect. discharge mach			███	███	███								
Milling		███	███	███	███	███	███						
Broaching				███	███	███							
Reaming				███	███	███							
Electron beam				███	███	███	███						
Laser				███	███	███	███						
Electrochemical			███	███	███	███	███	███					
Boring, turning		███	███	███	███	███	███	███	███				
Barrel finishing					███	███	███	███	███				
Electrolytic grinding						███	███	███					
Roller burnishing						███	███	███					
Grinding				███	███	███	███	███	███				
Honing						███	███	███	███				
Electro polish						███	███	███	███	███	███	███	███
Polishing							███	███	███	███	███	███	
Lapping							███	███	███	███	███	███	
Super finishing							███	███	███	███	███	███	
Sand casting	███	███	███										
Hot rolling	███	███	███										
Forging		███	███	███	███								
Perm mold casting				███	███								
Investment casting				███	███	███							
Extruding			███	███	███	███							
Cold rolling, drawing				███	███	███							
Die casting					███	███							

[a]*Machinery's Handbook*, Industrial Press
[b]The ranges shown are typical of the processes listed. Higher or lower values may be obtained under special conditions.

a) Contact spot   b) Elementary flux tube

Fig. 8.6. Microcontacts and constricted heat flow. (Courtesy F. Milanez)

$$E' = \{[(1 - v_1^2)/E_1] + [(1 - v_2^2)/E_2]\}^{-1}. \tag{8.2}$$

Lambert and Fletcher[8.7] and Mantelli and Yovanovich[8.3] point out that contact microhardness is significantly greater than bulk hardness, H, or macrohardness, H_L. This difference is the result of the work-hardening of metallic surfaces during machining and further the result of indentor penetration during hardness measurement. Formulas for contact microhardness developed by Hegazy[8.8] and Song and Yovanovich[8.9] are reported to be essentially the same[8.7] and are provided in review papers[8.3,8.7] that discuss deviations from Eqs. (8.1) and (8.2) resulting from anisotropy and heat-flux direction.[8.7] More recently, Sridhas and Yovanovich[8.10] have developed a single elastoplastic model for flat, rough plates. It models and specifies bounds for three regimes: elastic, elastoplastic, and plastic. This model predicts heat-transfer coefficients through an iterative process.[8.3]

Wavy, Rough Surfaces in Vacuum

Clausing and Chao[8.11] modeled surface waviness with spherical crowns (Fig. 8.7). They determined the macrocontact radius a_L from the Hertz model[8.12] for elastic, smooth spheres. From the ratio a_L/b_L the macroconstriction and macrothermal resistance were determined in a manner analogous to that used by Mikic for the determination of microconstriction and microthermal resistance for flat, rough surfaces. This determination assumes that the waviness length, $d_1 + d_2$, is much greater than the roughness, σ, and therefore the asperities do not increase a_L and affect contact pressure distribution. The predictive equations developed by Clausing and Chao for micro and macro heat-transfer coefficients are reported by Mantelli and Yovanovich.[8.3] Total thermal resistance is the series sum of the macro and micro resistances. Lambert and Fletcher[8.7] review numerous expansions of and improvements to the Clausing and Chao theory.

A typical flatness specification for mounting plates calls for flatness less than 0.001 cm/cm and total included reading (TIR) less than 0.5 mm for the footprint. Significant waviness or bowing can be analyzed only with difficulty[8.13,8.14] and must be avoided in practice.
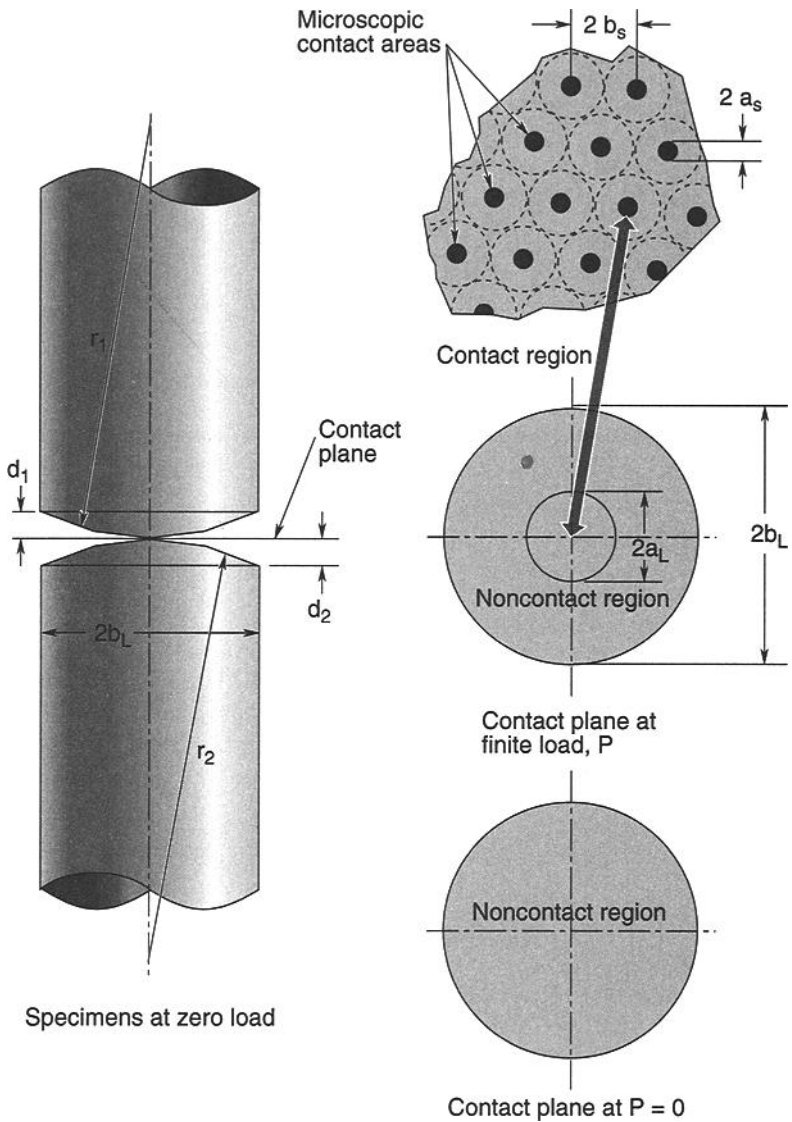
Fig. 8.7. Clausing and Chao[8.11] model for spherical contact.

Effect of Gap Fluid

Before on-orbit use, electronic units are often subjected to thermal tests at ambient pressure. To characterize heat transfer in such ground testing, comparing temperatures reached with those expected in space, is a useful, sometimes necessary, practice. For plates in contact, such heat transfer involves gap conductance in combination with contact conductance.

The initial stage of the analysis considers two noncontacting smooth plates in parallel separated by a gas-filled gap with a width of distance d. Conductive heat transfer through such a gas layer is commonly classified into four heat-flow regimes with distinct ranges of the Knudsen (Kn) number: continuum ($Kn < 0.01$), temperature-jump ($0.01 < Kn < 0.1$), transition ($0.1 < Kn < 1.0$), and free-molecular ($Kn > 10$).[8.15] The Knudsen number is defined as:

$$Kn = (\Lambda/d), \tag{8.3}$$

where Λ is the molecular mean free path and d is the distance separating the plates. In the temperature-jump regime the energy exchange between gas molecules and the plate is incomplete, resulting in a temperature discontinuity at the gas-plate interface.

For the continuum regime the gap heat-transfer coefficient is given by:

$$h_g = k_g/d, \tag{8.4}$$

where k_g is the thermal conductivity of the gas filling the gap. For the temperature-jump, transition, and free-molecular regimes, gas conduction is retarded by rarefaction effects. This retardation is often modeled as a distance serially added to the heat-flow path, with Eq. (8.5) becoming:

$$h_g = k_g/(d + M), \tag{8.5}$$

where $M = [(2 - TAC_1)/TAC_1 + (2 - TAC_2)/TAC_2] \times [2\gamma/(\gamma + 1)](1/Pr)\Lambda$; TAC_1 and TAC_2 are thermal-accommodation coefficients corresponding to the gas-solid combination of surface 1 and 2, respectively; γ is the ratio of specific heats; and Pr is the Prandtl number.

In the more complex case of two plates in contact under pressure, plate separation, d, is replaced by Y, the effective gap thickness. The value of Y depends on plate material(s), pressure, and roughness—and is generally unknown. For the limiting case of low contact pressure, Song et al.[8.16] take Y to be R_p, the maximum peak height of the rougher surface of the plates in contact. Further, for very low contact pressure Song and Yovanovich[8.17] provide a semi-empirical, dimensionless equation for predicting h_g:

$$G = f + M^*, \tag{8.6}$$

where $G = k_g/h_g R_p$; $f = 1 + 0.304/[(R_P/\sigma)(1 + M/R_p)] - 2.29/[(R_P/\sigma)(1 + M/R_p)]^2$; $M^* = M/R_p$; and $TAC = 0.55$ (helium), 0.90 (argon), or 0.78 (nitrogen).

Over a fairly wide range of parameters (Table 8.2), for the case of low contact pressure (0.38 to 0.60 MPa), predicted values for the gap heat-transfer coefficient agreed well with experimental results (e.g., Fig. 8.8). More generally, at increased contact pressure, the effective gap thickness is reduced. Prediction of the gap heat-transfer coefficient for this more general case is difficult. While no general predictive method or correlation is available, Song et al.[8.18] can provide useful guidance.

Table 8.2. Range of Parameters for Light-Load Gas-Gap Experiments[a]

Parameters	Experiment 1	Experiment 2	Experiment 3	Experiment 4
Specimens	SS 304	SS 304	Ni 200	Ni 200
Gap gases	He, Ar, N_2	He, Ar, N_2	He, Ar, N_2	He, Ar, N_2
$\sigma(\mu m)$	1.53	4.83	2.32	11.8
R_p (μm)	5.55	14.7	8.61	30.6
R_p/σ	3.63	3.04	3.71	2.59
h_c (W/m^2·°C)	452 ± 25	241 ± 3	1130 ± 30	725 ± 30
h_g (W/m^2·°C)	711 to 9660	460 to 5150	625 to 17,900	417 to 7830
h_c/h_g	1.57 to 21.4	1.91 to 21.4	0.553 to 15.8	0.575 to 10.8
P_g (torr)	9.4 to 711	9.5 to 665	9.6 to 698	9.4 to 700
Kn	0.019 to 4.2	0.0078 to 1.6	0.013 to 2.6	0.0034 to 0.76
P (MPa)	0.60 ± 0.02	0.47 ± 0.02	0.52 ± 0.02	0.38 ± 0.01
T_c (°C)	172 ± 4	168 ± 4	170 ± 3	172 ± 4
ΔT (°C)	5.8 to 85.5	6.7 to 105.9	5.5 to 39.9	12.2 to 63.8
q (kW/m^2)	27.7 to 58.7	34.4 to 55.5	52.7 to 104.9	55.9 to 104.1

[a]Song and Yovanovich
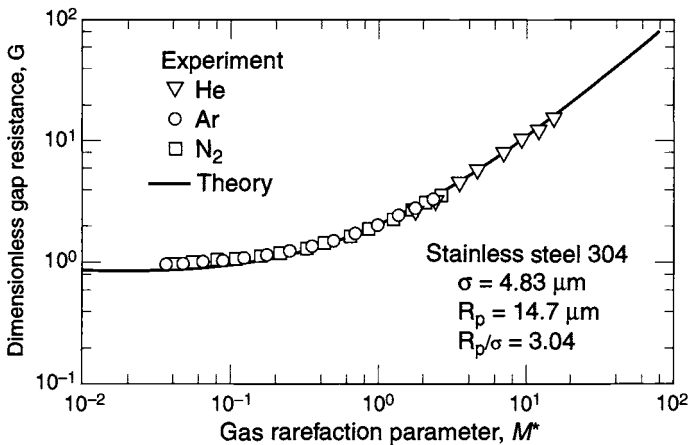
Fig. 8.8. Gap resistance for lightly loaded plates: Comparison of theory and experiments.[8.17]

Data and Correlations

Schneider[8.19] presented heat-transfer coefficient/contact pressure data (Fig. 8.9, Table 8.3) from four sources.[8.20–8.23] These data apply to both vacuum and ambient-pressure cases, and in some cases they include the use of interface fillers. At low contact pressure the curve representing data in air flattens, showing that gap conductance is the primary mode of heat transfer. Swartz[8.24] replotted aluminum-plate data of Fried and Costello,[8.20] Fried and Kelley,[8.25] and Fried and Atkin[8.26] (Fig. 8.10) to obtain continuous curves of heat-transfer coefficient versus apparent contact pressure in vacuum (Fig. 8.11).

Real data are often not well represented by either the early Mikic models [Eqs. (8.1) and (8.2)], the Sridhas and Yovanovich[8.10] elastoplastic model, or the Clausing and Chao[8.11] spherical-crown model. These models represent geometric extremes: Eqs. (8.1) and (8.2) and the Sridhas and Yovanovich model are for flat, rough surfaces, while the Clausing and Chao model is for wavy (nonflat) surfaces where roughness is not accounted for in determining pressure distribution and macrocontact area. Lambert and Fletcher[8.7] point out that the models for flat, rough surfaces usually predict the slope of the line in the graph of heat-transfer coefficient versus apparent pressure to be 0.94 to 0.99, whereas the slope predicted by the Hertz[8.12] theory for smooth spheres is 0.333. Moreover, the correlations for four independent investigations for nominally flat surfaces had slopes that varied from 0.56 to 0.74.[8.7] Thus it appears that many surfaces considered to be flat are indeed not so.
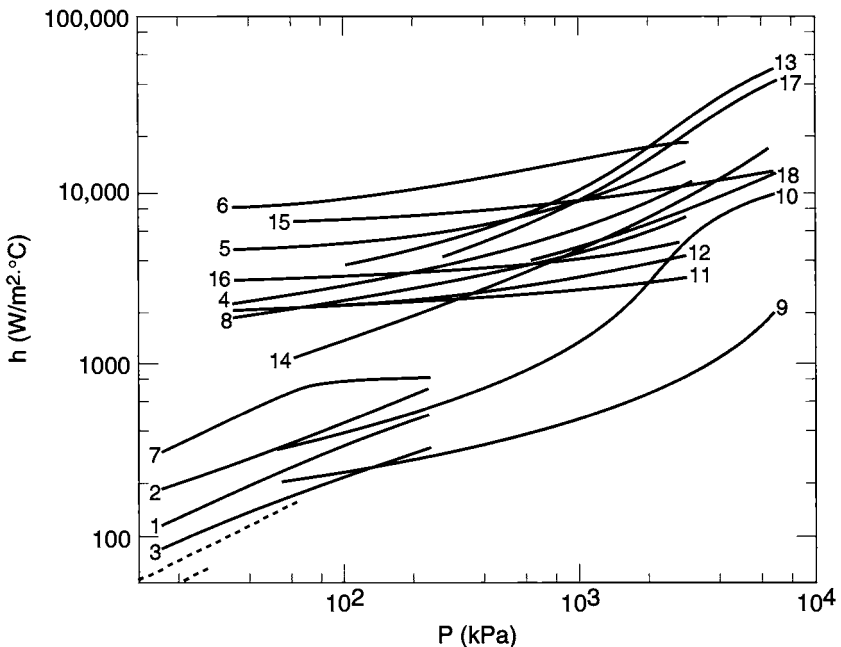

Fig. 8.9. Interface heat-transfer coefficients.[8.19]

Table 8.3. Interface Conditions for Conductance Data in Fig. 8.9

Curve	Material Pair	RMS Surface Finish (μm)	Gap Material	Mean Contact Temp. (°C)
1	Aluminum (2024-T3)	1.2–1.6	Vacuum (10^{-4} mm Hg)	43
2	Aluminum (2024-T3)	0.2–0.5	Vacuum (10^{-4} mm Hg)	43
3	Aluminum (2024-T3)	0.2–0.5 (wavy)	Vacuum (10^{-4} mm Hg)	43
4	Aluminum (75S-T6)	3.0	Air	93
5	Aluminum (75S-T6)	1.6	Air	93
6	Aluminum (75S-T6)	0.3	Air	93
7	Aluminum (2024-T3)	0.2 (wavy)	Lead foil (8 mil)	43
8	Aluminum (75S-T6)	3.0	Brass foil (1 mil)	93
9	Stainless (304)	1.1–1.5	Vacuum (10^{-4} mm Hg)	29
10	Stainless (304)	0.3–0.4	Vacuum (10^{-4} mm Hg)	29
11	Stainless (416)	2.5	Air	93
12	Stainless (416)	2.5	Brass foil (1 mil)	93
13	Magnesium (AZ-31B)	1.3–1.5 (oxidized)	Vacuum (10^{-4} mm Hg)	29
14	Magnesium (AZ-31B)	0.2–0.4 (oxidized)	Vacuum (10^{-4} mm Hg)	29
15	Copper (OFHC)	0.2	Vacuum (10^{-4} mm Hg)	46
16	Stainless/Aluminum	0.8/1.6	Air	93
17	Iron/Aluminum	—	Air	27
18	Tungsten/Graphite	—	Air	132

Lambert and Fletcher[8.7] review models for the thermal contact conductance of metals and provide a methodology for calculating the heat-transfer coefficients.[8.13,8.14] They show that the models of Mikic and Yovanovich overpredict heat-transfer coefficients not only for nonflat surfaces (as is expected for these models, whose basic premise requires flat, rough surfaces), but also for flat surfaces with very small roughness (0.14 to 0.16 μm).[8.13] On the other hand, the Clausing and Chao model generally underpredicts heat-transfer coefficients, perhaps because it does not account for the increased macrocontact area resulting from roughness. The Lambert and Fletcher methodology is the only one known that appears to accurately predict heat-transfer coefficients for nonflat surfaces of any radius of curvature and roughness. It requires the use of several equations and five design charts. It uses the concept of TIR to characterize the flatness deviation
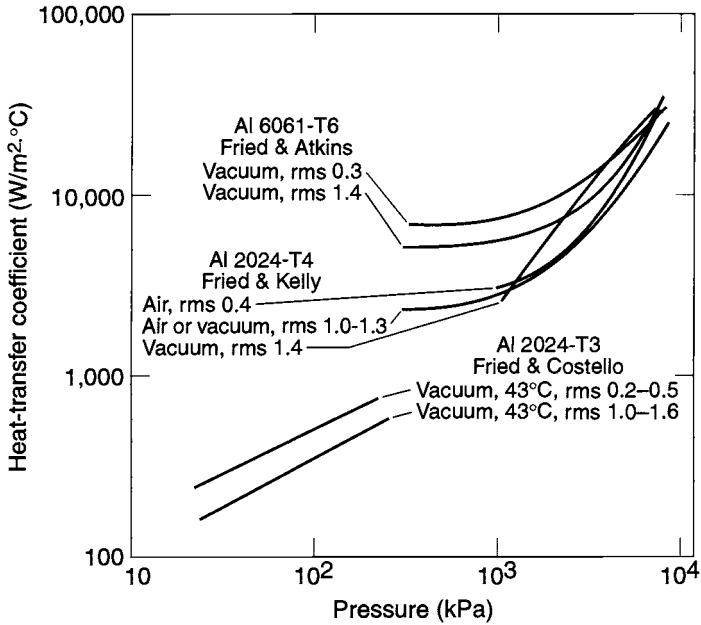
Fig. 8.10. Heat-transfer coefficient vs. pressure for aluminum in vacuum (rms in μm).[8.24]

of two components in contact. It is self-sufficient in that it provides all of the needed relationships or curves, save for the theoretical Hertz radius for smooth spheres, which can be found in the source manuscript[8.12] or in Timoshenko and Goodier.[8.27]
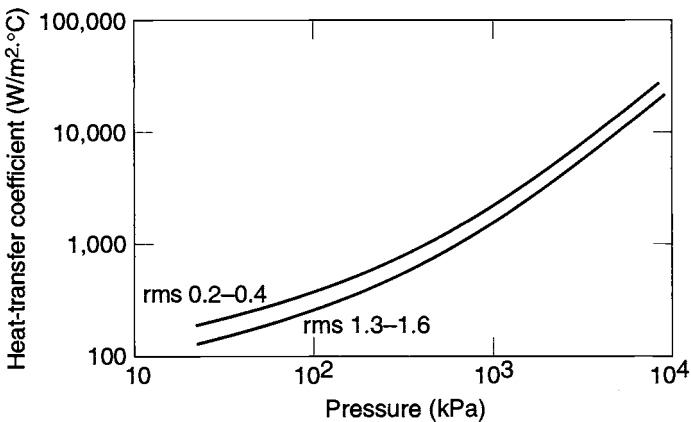

Fig. 8.11. Generalized heat-transfer coefficient vs. pressure for aluminum in vacuum.[8.24]

Bolted-Joint Conductance without Interface Filler

Theory

At the macroscopic level, bolted plates deform elastically, as in Fig. 8.12. Separation of plates, though exaggerated in the figure, does occur, and at relatively small distances from the bolt. In its most basic statement, the bolted-joint problem can be considered the contact-conductance problem for a nonuniform interface pressure. Figure 8.13(a) shows schematics of an interfacial pressure profile with ($\sigma > 0$) and without ($\sigma = 0$) roughness.

An excellent theoretical treatment of this subject has been provided by Roca and Mikic[8.28,8.29] for plates that are nominally flat when unstressed. Roca and Mikic extended the theory beyond the single-plate midplane work of Fernlund[8.30] and others to two plates with surface roughness. The biharmonic equation was used to characterize the elastic deformation of the plates. Their method assumed that deformation of the plates is elastic, asperity height above a mean plane is Gaussian, and asperity contact is normal with no tangential component. Both plastic and elastic asperity deformation were treated. The structural model used is shown in Fig. 8.13(b), and typical calculated results obtained using an iterative method are shown in Fig. 8.13(c).

The thermal model used by Roca and Mikic is shown in Fig. 8.14(a) for the upper plate. Heat enters around the perimeter, flows radially inward, and then passes from one plate to the other in the contact region. Boundary conditions are:

$$k\frac{\partial T}{\partial Z} = h_C(r)(T - T_i) \qquad \text{at } Z = 0,$$

$$k\frac{\partial T}{\partial Z} = 0 \qquad Z = t,$$

$$k\frac{\partial T}{\partial Z} = 0 \qquad r = D_S/2,$$

and

$$k\frac{\partial T}{\partial r} = q/A \qquad r = R.$$
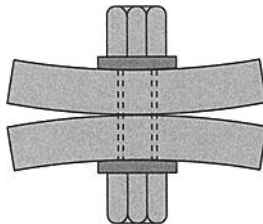

Fig. 8.12. Bolted interface.
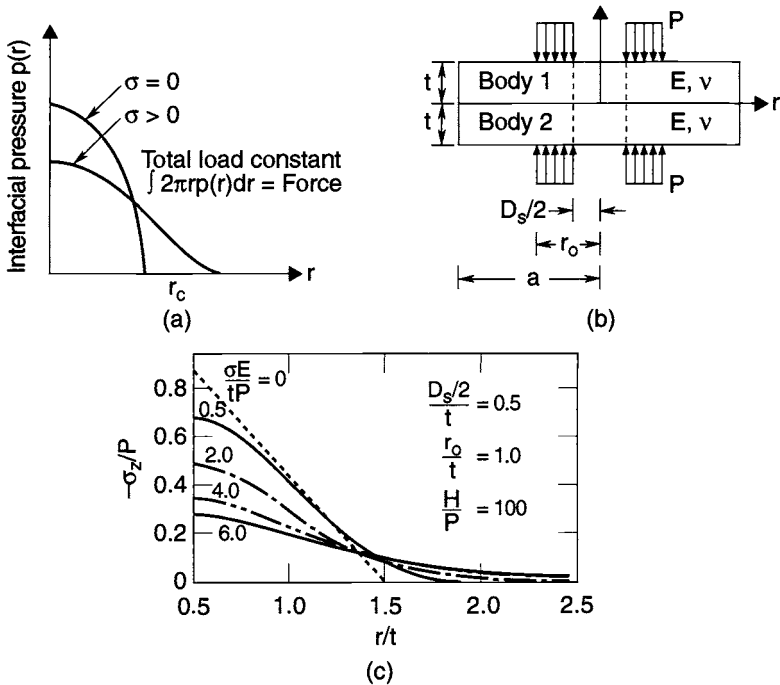
Fig. 8.13. (a) Schematic showing interfacial pressure profiles with and without roughness.[8.28,8.29] **(b)** Model used by Roca and Mikic[8.28,8.29] for bolted joint. **(c)** Typical interfacial pressure profiles predicted by Roca and Mikic.[8.28,8.29]

The heat-transfer coefficient in the contact region, h_c, is a function of local pressure, $P(r)$, and is given by

$$h_C = 1.45(km/\sigma)[P(r)/H_C]^{0.985}, \qquad (8.7)$$

which is similar to Eq. (8.2). Here, H_C is the lesser of $H_{C,1}$ and $H_{C,2}$.

Roca and Mikic define an overall resistance from the perimeter to a constant-temperature (T_i) region on the other side of the interface:

$$R = [T(r=R,Z=t/2) - T_i]/q/A. \qquad (8.8)$$

Their results are shown in Figs. 8.14(b), (c), and (d). Overall thermal resistances vary with roughness (with the group $\sigma E/tP$) in a complex way. The greater the roughness, s, the longer the constricted conduction path from surface to surface, and hence the greater contact resistance. However, as roughness increases, the contact radius increases by virtue of increased interference. This condition tends
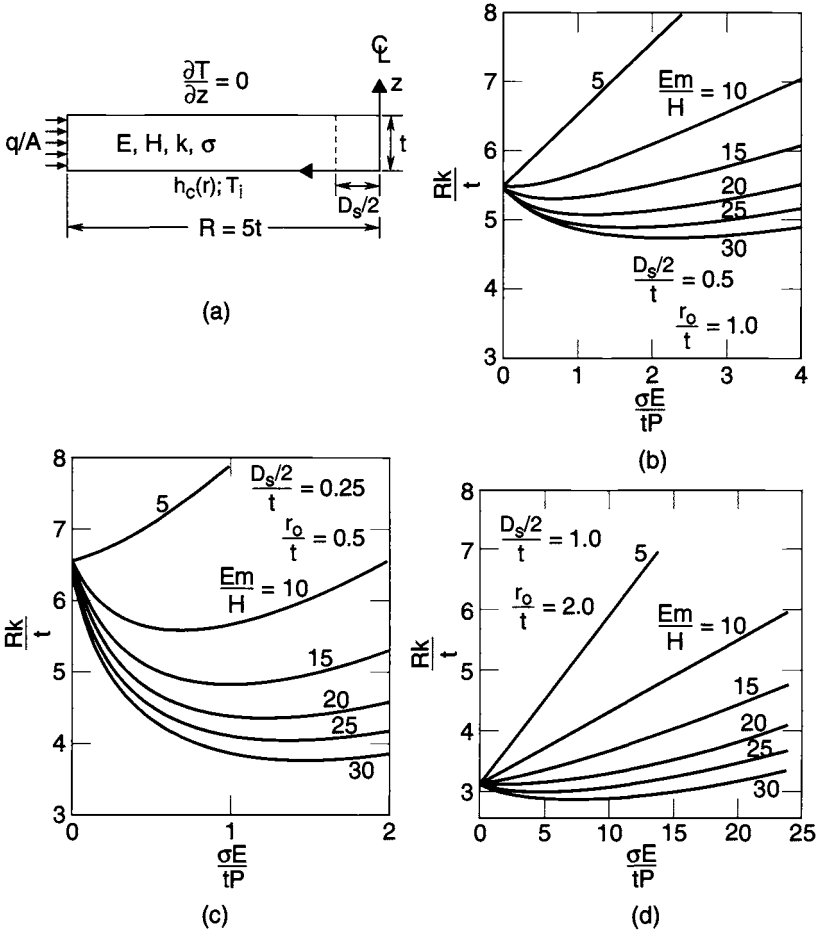
Fig. 8.14. Overall interface resistance from Roca and Mikic.[8.28,8.29] **(a) Model used in heat-transfer example. (b), (c), (d) Changes in thermal resistance with roughness.**

to decrease the overall thermal resistance by allowing the radial heat inflow to turn downward toward the other plate at a greater radius, decreasing the average heat flux in the contact region. The group Em/H in Fig. 8.14 is the inverse of the group γ previously encountered for surfaces under uniform pressure, and it characterizes the propensity for deformation of the asperities to be plastic or elastic.

Roca and Mikic show that, with region size increasing as roughness increases, no simple representation for contact region is possible. Yet rules of thumb have come into use. These rules are generally consistent with elastic analysis of loaded plates with no roughness and with experimental measurements. A popular form is:

$$r_C/t = r_O/t + N. \tag{8.9}$$

The value of N is given by, or can be extracted from, various sources as follows: 1.05 (Fernlund),[8.30] 1.0 (Greenwood),[8.31] 1.3 (Coker and Filon),[8.32] 1.7 (Aron and Columbo),[8.33] and 0.5 (Gould and Mikic).[8.34] For bolted joints, in engineering practice r_C is sometimes taken as $1.5D_S$.

Although it facilitates understanding, the theoretical treatment of Roca and Mikic is not particularly practical. Use of overall resistance commingles contact resistance and plate-constriction resistance, providing many pages of graphical results but few design and analysis aids for the engineer. Bevans et al.[8.35] use a simpler model (Fig. 8.15). In it, two plates are bolted together with a contact region A_b with radius R_o. A uniform heat flux, F, is incident on the top plate and exits the bottom plate. Heat flows radially inward in the top plate (the constriction flow) until the contact region is reached. Heat flows from the top plate to the bottom plate in this region. Heat flow in the bottom plate is the reverse of that in the top plate. (Resistors are shown by jagged lines.)

The steady-state heat-conduction equation for a differential element in the region between R and R_o for the top plate can be written

$$q_{out} - q_{in} = q_{absorbed} \tag{8.10}$$

or

$$2\pi krt(dT/dr) - \{2\pi krt(dT/dr) + 2\pi krt[d/dr(rdT/dr)dr]\} = F2\pi rdr \tag{8.11}$$

with the following boundary conditions:

$$\text{At } r = R, \, dT/dr = 0.$$

$$\text{At } r = R_O, \, T = T_O.$$
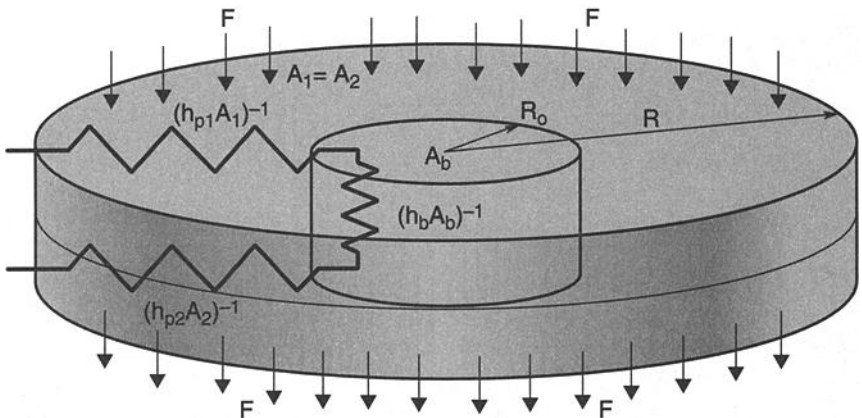
Fig. 8.15. Bolted interface model from Bevans et al.[8.35]

Equation (8.12) can be integrated and solved for the temperature distribution across the plate in the region between the edge and the outer radius of bolt contact, yielding

$$T_O - T = (FR^2/kt)\{1/4(\eta^2 - \eta_O^2) + 1/2[\ln(\eta_O/\eta)]\}. \tag{8.12}$$

In accord with the work of Bevans, the conduction equation can be recast in integral form as

$$Q = h_P \int_{Ro}^{R} (T - T_O)dA, \tag{8.13}$$

where h_p can be considered a "heat-transfer coefficient" for the region between R and R_o. Noting that $Q = F\pi(R^2 - R_o^2)$, one obtains

$$h_P = F\pi(R^2 - R_O^2)/[\int_{Ro}^{R} (T - T_O)2\pi r dr]. \tag{8.14}$$

Substituting Eq. (8.8) into Eq. (8.10) and integrating, one finds that the heat-transfer coefficient in the plate region from R to R_o becomes

$$h_P = [2k(R^2 - R_O^2)]/\{R^4[\eta_O^2 - (\eta_O^4/4) - \ln(\eta_O) - 3/4]\}. \tag{8.15}$$

This heat-transfer coefficient is fictitious, as heat does not flow from the top to bottom plate in the region $R > R_o$. More properly, this is the coefficient that would exist if the uniform heat flux F flowed from the top to bottom plate by virtue of the temperature profile of Eq. (8.13).

The overall resistance of the configuration in Fig. 8.15 is given by the equation

$$1/(hA) = 1/(h_{P,1}A_1) + 1/(h_b A_b) + 1/(h_{P,2}A_2), \tag{8.16}$$

where the subscripts 1 and 2 refer to the top and bottom plates, respectively. After replacing $h_{p,1}$ and $h_{p,2}$ with Eq. (8.16), and noting that $A_1 = A_2$, one finds that the overall heat-transfer coefficient of the approximated bolted joint becomes

$$h = 1/\{\{A R^4[\eta_O^2 - (\eta_O^4/4) - (ln(\eta_O)) - 3/4]/[2A_1(R^2 - R_O^2)]\} \tag{8.17}$$
$$\times [1/(k_1 t_1) + (1/(k_2 t_2))] + A/(h_b A_b)\}.$$

If both plates are of the same material, $k_1 = k_2$; using $A = \pi R^2$, one finds

$$A_1 = \pi(R^2 - R_o^2),\ A_b = \pi R_o^2,\ \text{and}\ I = \eta_o^2 - 0.25(\eta_o^4) - ln(\eta_o) - 0.75;$$

results in:

$$h = 1/\{[R^6 I(t_1 + t_2)]/[2(R^2 - R_O^2)^2(kt_1 t_2)] + R^2/(h_b R_O^2)\}. \tag{8.18}$$

The terms in this equation that are not known are R_o and h_b.

Application of Theory: Contact Region

TRW Inc.[8.36] has provided nominal values of thermal resistance across screwed/bolted joints (Table 8.4). The company allows that these values can be increased or decreased depending on such parameters as screw torque, materials, surface finish, and flatness. Recommendations for bolt maximum thermal resistance have been obtained from Lockheed-Martin Inc. (Table 8.5).[8.37] The TRW and Lockheed-Martin results are presented in terms of resistance in consistent units in Table 8.6.

These results are useful for many engineering purposes; however, such results often combine the contact region with a small constriction region near the bolt. This small constriction region, as it is near the centerline, towards which heat fluxes are converging, can have a resistance that is large compared to that of the contact region. A study was therefore conducted to obtain conductances of the contact region per se. Existing data in the literature was reviewed to find studies that contained credible contact-region data. Among other requirements, either the thermocouples had to be located very close to the bolt or, if they were located at some distance, the plate thickness and thermal conductivity had to be sufficiently great that constriction resistance was small compared to contact resistance.

A few suitable studies were found.[8.33,8.35,8.38-8.41] In these, both plates of the surface pair were aluminum alloy save for one test where the surface pair was telluride copper and aluminum alloy. The alloys were not specified in every case; where specified they were usually Al 6061-T6, with Al 6063-T6 used by one investigator. The bolts were all of stainless steel. The range of test parameters is given in Table 8.7. Flatness deviation in terms of TIR is included in the table, although it was not given in all the investigations. From these studies both a dimensional and a dimensionless correlation were developed. The former is shown in Fig. 8.16. Here contact region or bolted-joint conductance in units of W/K is plotted against a corrected torque parameter with units of N·m. Correlation is achieved by the dimensional equation as

$$C_b = 503[\tau(\alpha_{al} - \alpha_{ss})(T_p - 200)]^{0.775} \qquad (8.19)$$

Table 8.4. Thermal Conductance Design Guideline from TRW

Screw Size	Conductances (W/K)	
	Small Stiff Surfaces	Large Thin Surfaces
2–56	0.21	0.105
4–40	0.26	0.132
6–32	0.42	0.176
8–32	0.80	0.264
10–32	1.32	0.527
1/4–28	3.51	1.054

Table 8.5. Bolt Thermal Resistance Estimate

Maximum Resistance versus Bolt Size and Plate Thickness (°C/W bolt)[a]

| Steel Bolt | | 1.57 mm | 3.18 mm | 6.35 mm | 9.53 mm |
Size	Shaft Diam (mm)	Aluminum	Aluminum	Aluminum	Aluminum
NC 4-40	2.84	12.6	—	—	—
NC 6-32	3.51	6.6	2.2	—	—
NC 8-32	4.17	4.5	1.5	0.75	—
NF 10-32	4.83	3.0	1.0	0.50	0.30
NF 1/4-28	6.35	2.1	0.7	0.19	0.23
NF 5/16-24	7.92	1.5	0.5	0.25	0.17
NF 3/8-24	9.53	—	0.4	0.19	0.13
NF 7/16-20	11.10	—	—	0.16	0.11
NF 1/2-20	12.70	—	—	—	0.09

[a]Assumptions:
• Typical spacecraft bolted aluminum interface in vacuum
• Bare clean mill rolled surface finish
• Standard steel bolts torqued to specification
• Primary heat transfer through compressed area near bolt
Note: Confirmation measurements suggested for thermal-design purposes
Reference: NASA CR119933 June 1971 and other limited measurements

Table 8.6. TRW and Lockheed Martin Bolted-Joint Resistance Data

| Bolt | Diam (mm) | Resistance Values from Several Sources (°C/W)[a] | | | | | |
| | | TRW Large Thin Surfaces[b] | LM Plate Thickness (mm)[c] | | | | TRW Small Stiff Surfaces[b] |
			(1.57)	(3.18)	(6.35)	(9.53)	
2-56	—	9.48	—	—	—	—	4.74
NC 4-40	2.8	7.59	12.6	—	—	—	3.79
NC 6-32	3.5	5.69	6.61	2.2	—	—	2.37
NC 8-32	4.2	3.79	4.5	1.5	0.75	—	1.25
NF 10-32	4.8	1.90	3.0	1.0	0.5	0.333	0.76
NF 1/4-28	6.4	0.95	2.1	0.7	0.35	0.233	0.28
NF 5/16-24	7.9	—	1.5	0.5	0.25	0.167	—
NF 3/8-24	9.5	—	—	0.39	0.194	0.128	—
NF 7/16-20	11.1	—	—	—	0.16	0.106	—
NF 1/2-20	12.7	—	—	—	—	0.089	—

[a]Bolted aluminum interface in vacuum, bare clean mill rolled surface finish (LM), standard steel bolts torque to specification (LM), primary heat transfer through compressed area near bolt (LM).
[b]TRW, March 1984.
[c]LM, George D. Rhoads, 20 July 1988.

Table 8.7. Bolted-Joint Correlation: Range of Test Parameters

Range	Bolt Size	Bolt Shaft Diam (mm)	Torque (N·m)	Plate Thick-ness (mm)	Roughness σ (m/m/K)	Flatness TIR (m)	Plate Temp. (°C)	Conduc-tance (W/K)
Minimum	6–32	3.51	0.34	1.02	6.26×10^{-7}	1.02×10^{-5}	19.3	0.41
Maximum	1/4–20	6.35	9.39	12.70	2.26×10^{-6}	1.27×10^{-4}	127.3	13.8

$$C_b = 503[\tau(\alpha_{al}-\alpha_{ss})(T_p - 200)]^{0.775}$$
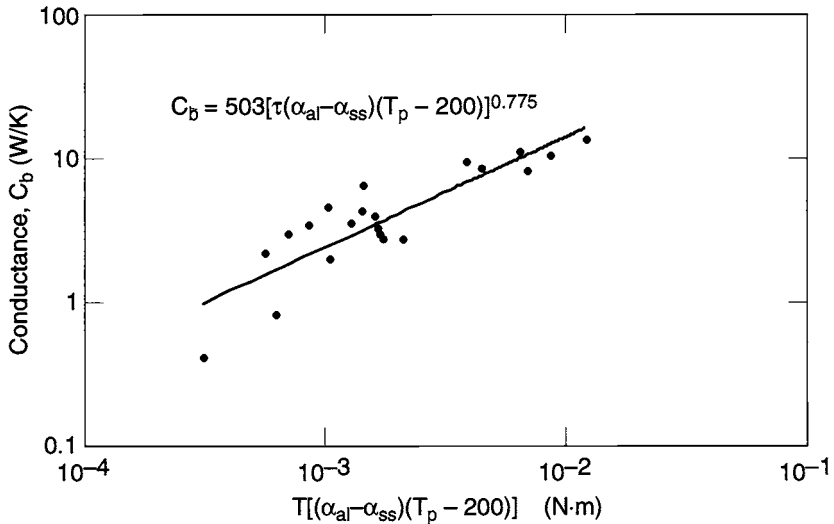
Fig. 8.16. Dimensional correlation of bolted-joint conductance.

with an R^2 value of 0.75. Observation has shown, for the aluminum plate–stainless steel bolt combination, that differential expansion and contraction affect the torque.[8.42,8.43] Hence the applied torque, τ, is multiplied by the correction factor $(\alpha_{al} - \alpha_{ss})(T_p - 200)$. The first term in parentheses is the difference in the coefficients of thermal expansion for aluminum and stainless steel. The second term is the plate temperature minus a lower-limit temperature, 200 K. Observation has shown that as temperature is reduced, at some point torque decreases rapidly.[8.43] That lower limit is taken here as 200 K.

The dimensionless correlation obtained is shown in Fig. 8.17. The resulting equation is

$$C_b/(k_h\sigma) = 1.06 \times 10^9 \{[\tau(\alpha_{al} - \alpha_{ss})(T_p - 200)]/(E'\sigma^{2.5}D_S^{0.5})\}^{0.652} \quad (8.20)$$

with an R^2 value of 0.76. The conductance, C_b, is normalized by dividing by the harmonic-mean thermal conductivity, k_h, and the combined rms roughness, σ. The

$$C_b/(k_h\sigma) = 1.06 \times 10^9\{[\tau(\alpha_{al}-\alpha_{ss})(T_p - 200)]/[E'\sigma^{2.5}D_s^{0.5}]\}^{0.652}$$

Axis labels: vertical axis $C_b/k_h\sigma$; horizontal axis $[T(\alpha_{al}-\alpha_{ss})(T_p - 200)]/[E'(\sigma^{2.5})(D_s^{0.5})]$
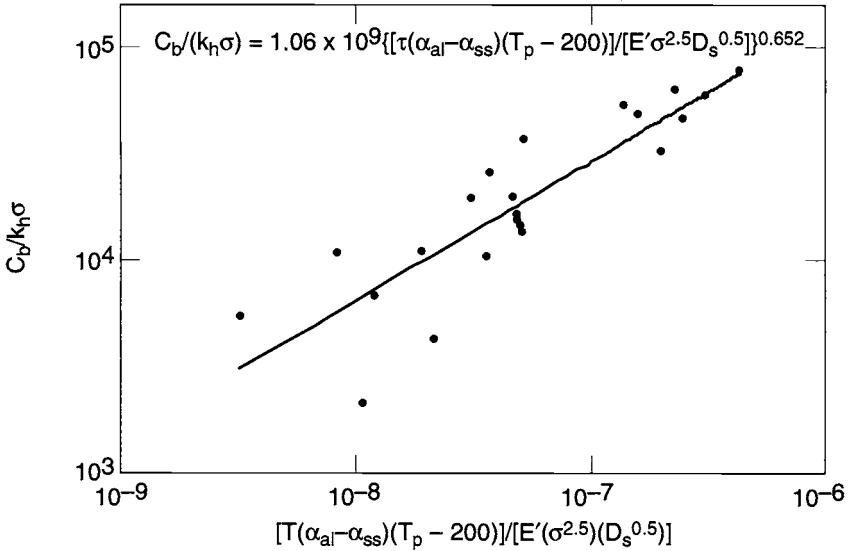
Fig. 8.17. Dimensionless correlation of bolted-joint conductance.

numerator of the ordinate of Eq. (8.21) is the ordinate of Eq. (8.20). The denominator is the product $E'\sigma^{2.5}D_S^{0.5}$. The term E', the effective modulus as defined by Eq. (8.3), was used in the correlation rather than microhardness, H_C, as the latter is a more complex term, itself a function of the unknown applied pressure. The term D_S is the diameter of the bolt shaft. Flatness deviation, TIR, could not be included in the correlation as it was not provided by all the investigators. Roughness, σ, while provided by all the investigators, was not always measured in a consistent manner, and slope, m, was not measured by any investigator. Plate thickness was found to be a poor correlation parameter. The slopes of Eqs. (8.20) and (8.21) are lower than that of Eq. (8.1) for flat surfaces subjected to uniformly applied pressure. This may be a characteristic of torque-applied pressure as well as a result of the (largely unknown) flatness deviation of the surfaces tested. The conductances given by Eqs. (8.20) and (8.21) are a few times greater than those recommended in Tables 8.4 through 8.6. This is believed a consequence of near elimination of constriction effects in the selected tests. To convert these conductances to heat-transfer coefficients, h_b, as used in Eqs. (8.17) through (8.19), the relations $h_b = C_b/\pi\, r_C^2$ and $r_C = 1.5D_S$ should be used.

Application of Theory: Overall Conductances

The correlations of Eq. (8.20) and (8.21) apply only to the bolt or screw contact region and do not characterize the constriction conductances within the two plates. Overall conductances include both the bolt and the constriction terms. For axisymmetric heat flow to the bolt region, overall conductance is given by Eq. (8.18) or (8.19).

Perimeter Bolt Pattern

For configurations where a perimeter bolt pattern is used, the analysis method of Bevans *et al.*[8.35] is recommended. The plate is divided into sectors (Fig. 8.18) with Eqs. (8.10) to (8.19) applicable. As an example Fig. 8.19 shows a 90-deg segment where radius R_o is equal to r_C of Eq. (8.10). For more complex shapes or for cases where thickness is not constant, the overall thermal network can be modeled using finite-difference or finite-element methods. Bolt-region conductances from Tables 8.4 through 8.6 or Eqs. (8.20) and (8.21) can be used in such models.

Where the perimeter bolt pattern employs bolts on two opposed flanges, a rectangular version of Bevans's equation can be used. In this case a strip between two bolts is subjected to a uniform flux, F (Fig. 8.20). Following Bevans for a half-slice leads to

$$T - T_O = (F/2kt)(L^2 - x^2) \tag{8.21}$$

$$h_P = FWL/[\int_0^L (T - T_O)w\,dx]. \tag{8.22}$$

Substituting Eq. (8.22) into Eq. (8.23) and integrating, one finds

$$h_P = 3kt/L^2. \tag{8.23}$$

Plate conductance is

$$C_P = h_P A_P = (3kt/L^2)WL = 3ktW/L. \tag{8.24}$$
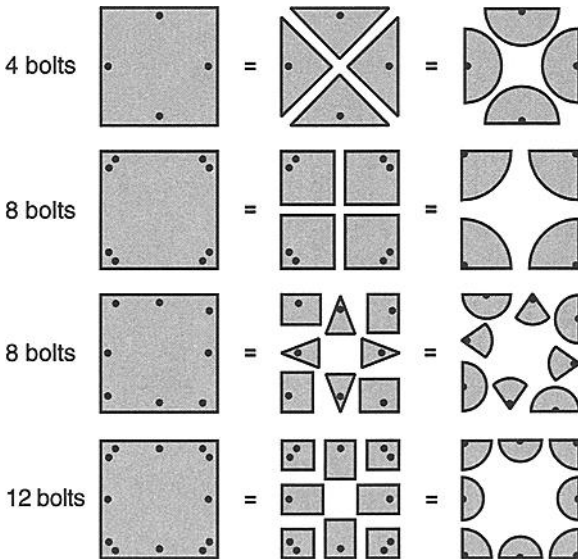
Fig. 8.18. Division of plates with perimeter bolt mounting from Bevans *et al.*[8.35]
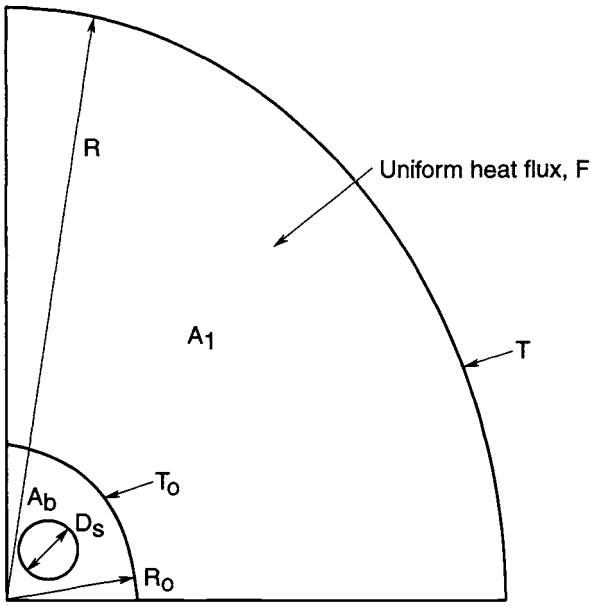
Fig. 8.19. Elementary conduction element, four bolts, perimeter-mounted.
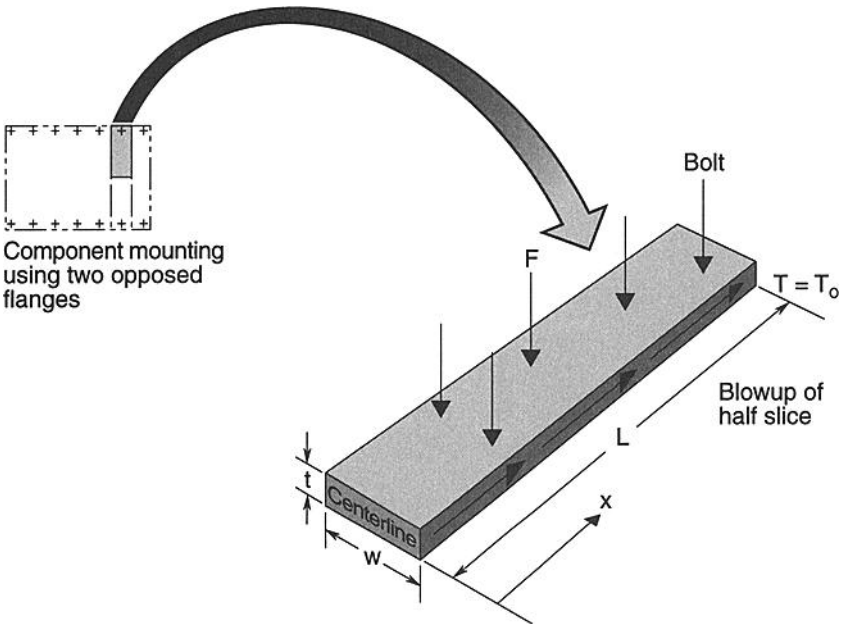
Fig. 8.20. Model of conduction heat flowing in a slice.

If heat entered the half-slice entirely at the centerline end, the conductance would be

$$C_P = ktW/L,\qquad(8.25)$$

which is one-third the conductance for the uniform-heat-flux case. Equation (8.24) or (8.25) can be used with the bolt-region heat-transfer coefficient or conductance to obtain the overall heat-transfer coefficient [Eqs. (8.17) through (8.19)] or overall conductance.

A design recommendation is available from TRW Inc.[8.36] for average overall heat-transfer coefficients for perimeter bolt patterns (Fig. 8.21). This recommendation derives from the work of Bevans *et al.*[8.35] for the configurations of Fig. 8.22. Plates are relatively thin, with $t_m = (1.59 + 3.17)/2 = 2.38$ mm. Results are characterized by inverse screw density (in cm^2 per screw). Heat-transfer coefficients for the bare interface are small, generally below 115 W/m^2·K; this condition is a consequence of the constriction-plate resistances for the long spans between bolts, i.e., bolt-contact-region conductances are relatively high compared to the constriction-plate conductances.

This information is verified and supplemented by the work of Welch and Ruttner.[8.41] The configuration they studied is shown in Fig. 8.23 with Al 6063-T6 plates that were each 7.94 mm thick. The 279-mm-by-152-mm plates were fastened by 16 No. 8-32 stainless-steel screws. Torques were 1.13 and 2.26 N·m. Average heat-transfer coefficients for the entire plate, provided by the authors, are given in Table 8.8.

The Welch and Ruttner screw-spacing results in 26.6 cm^2/screw, which for the Bevans configuration yields a heat-transfer coefficient of about 90.8 W/m^2·K. The Welch coefficients are a factor of three to four greater than those of Bevans. This difference is explained to a large degree by the ratio of the arithmetic-mean plate thicknesses for the two investigators:

$$\frac{t_{m,\text{Welch}}}{t_{m,\text{Bevans}}} = \frac{7.94}{0.5(1.59 + 3.17)} = 3.34\qquad(8.26)$$
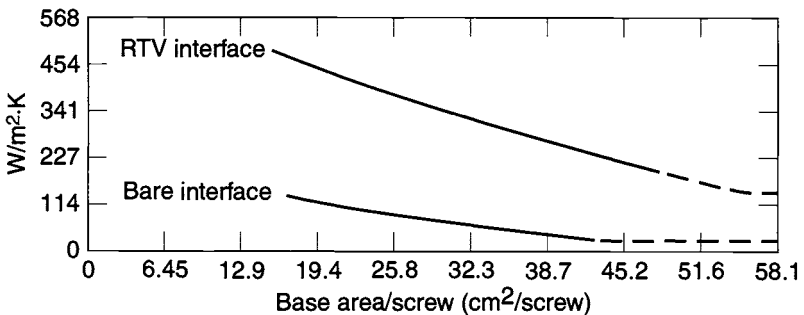
Fig. 8.21. Recommended overall heat-transfer coefficients for perimeter bolt pattern from TRW Inc.[8.36]
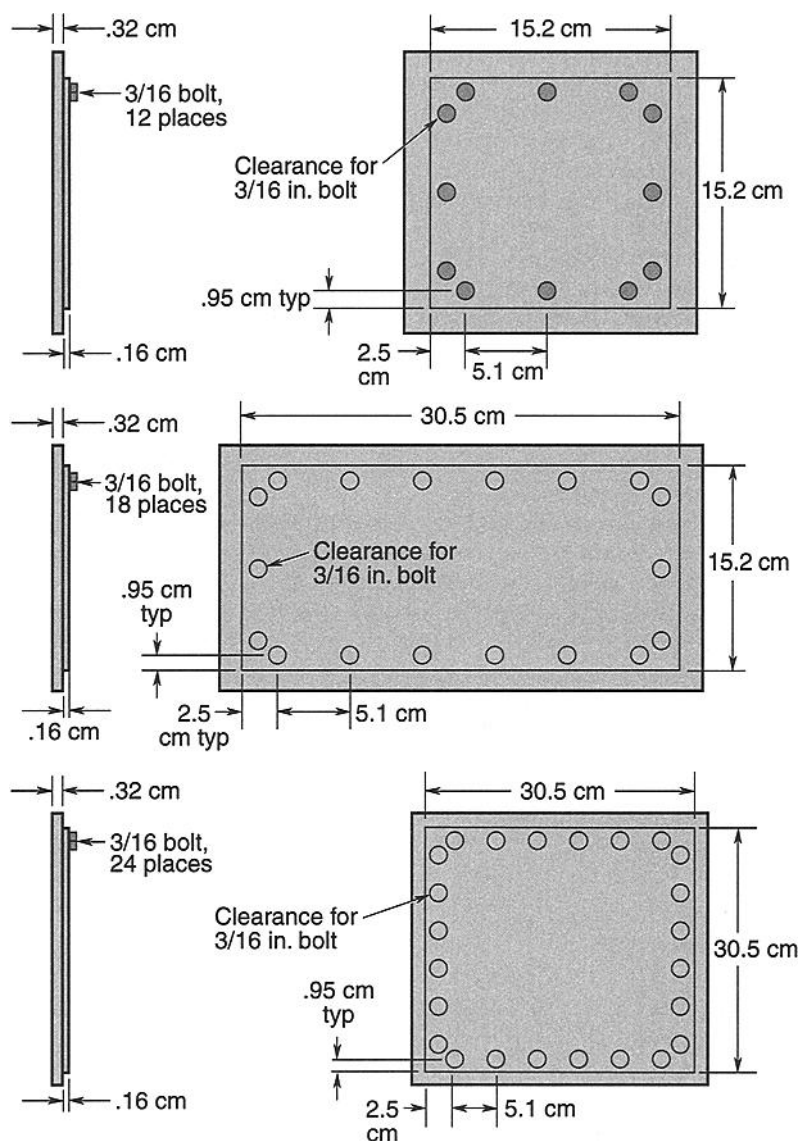
Fig. 8.22. Bolted-joint configurations tested by Bevans *et al.*[8.35]

Therefore, for perimeter-bolt-pattern fastening of an electronics unit to a mounting plate, the bare interface curve of Fig. 8.21 should be used for mean plate thickness of about 2.5 mm. Table 8.8 should be used for plates with thickness closer to 7.5 mm. Results obtained this way can be cross-checked by computing overall heat-transfer coefficients using one of the geometries of Fig. 8.18 and Eqs. (8.18) or (8.19), or by using a finite-difference or finite-element thermal model. Contact
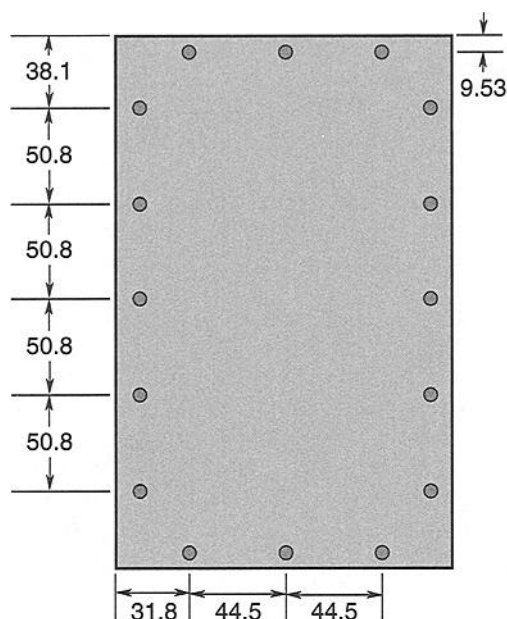
Fig. 8.23. Bolted-joint configuration tested by Welch and Ruttner (dimensions in mm).[8.41]

Table 8.8. Welch and Ruttner Bare Interface Results Summary

Torque (N·m)	Temperature (°C)	Average Heat-Transfer Coefficients (W/m²·K)
1.13	−34	284
1.13	71	369
2.26	−34	329
2.26	71	397

(bolt) region conductances are to be obtained for either approach from the "Application of Theory: Contact Region" section.

Nonperimeter Bolt Patterns

Figure 8.4 shows a bolt pattern that combines perimeter and inboard bolts as described in the "Conduction Cooling" section. For the configuration of this figure and other configurations encountered in practice, a number of the bolts are in a uniform or near-uniform pattern. These bolts could be analyzed individually using the plate-division method of Fig. 8.18 and the analytic techniques given above. However, such analysis can be time-consuming and, moreover, heat flows through parallel bolts were found not to be independent for at least one case with $d* = 5.$[8.44] Here $d* = d/(2r_O)$, where d is the distance between bolt centers and r_O

is the radius of the applied load. Therefore a simpler, approximate method was developed to predict an overall heat-transfer coefficient for uniform bolt spacing. The result, a dimensional correlation,

$$ht_t/k_h = 54.7[A_N/(t_t^3 \tau^{0.5})]^{-0.764}, \tag{8.27}$$

is shown in Fig. 8.24. Here ht_t/k is dimensionless; h is the overall heat-transfer coefficient, t_t is the thinnest of the two plates in contact, and k_h is the harmonic-mean thermal conductivity. The term $A_N/(t_t^3 \tau^{0.5})$ has dimensions $[m(m - N)^{0.5}]^{-1}$, where A_N is the area per bolt or screw, t_t is the thickness of the thinnest of the two plates in contact, and τ is the torque. Data came from General Electric Inc. reports and from six TRW Inc. reports (the latter supplied by H. A. Pudewa). The correlation has an R^2 value of 0.93 and includes data with the following ranges: plate thickness from 1.59 to 25.4 mm, torque from 0.037 to 9.48 N·m, bolts from 0-80 to 1/4-20, bolt area per screw of 0.272 to 19.4 cm², with screw patterns ranging from a single screw to 5 by 2. The screws were all stainless steel, and all the plates were aluminum alloys save for a set where one plate was copper.

Honeycomb Mounting Plates

Often the spacecraft side of the interface is of honeycomb/facesheet construction (Fig. 8.25). Threaded inserts must be embedded in the honeycomb to receive the screws. Such construction provides high ratios of stiffness and strength to weight. However, facesheet thickness for practical applications can be well below 1.0 cm, typically 0.4 to 1.2 mm. Honeycomb facesheets tend to be less flat, but stiffer, than thin metal plates—resulting in counterbalancing effects on overall conductance.
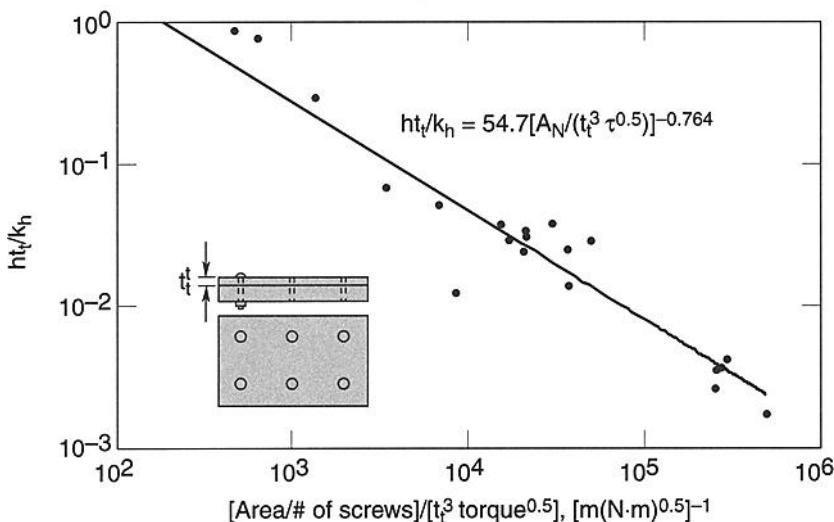

Fig. 8.24. Dimensional correlation for overall heat-transfer coefficient for a uniform bolt pattern.
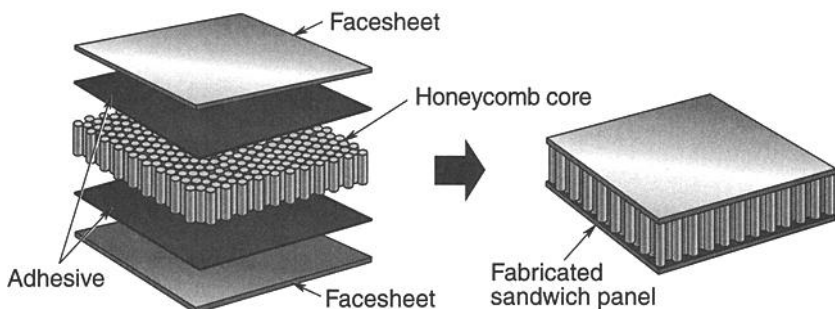
Fig. 8.25. Honeycomb/facesheet mounting panel.

Because the facesheets are thin, constriction resistance is relatively high. Few experimental data are available on conductances where honeycomb-mounting-panel construction is used, either in the contact region or for the entire mounting region. Unless data are available, overall conductance values no higher than those for the bare interface in Fig. 8.21 should be used.

If heat pipes are embedded in the honeycomb below the unit, overall conductance tends to increase. This is especially so if the heat pipes bridge from facesheet to facesheet. General results are not available. However, the problem can be treated by developing thermal math models (TMMs) that account for the various conduction paths.

Bolted-Joint Conductance with Interface Filler

Contact conductance can be improved through the use of appropriate filler materials between the two plates. Such materials fill the microscale voids present because of surface roughness, and some materials can also fill the macroscale voids resulting from flatness deviation. For the microscale voids, because the dimensions are small, even a low-conductivity material, if thin enough, may provide an improvement over the radiative heat transfer that existed before filling. However, care must be exercised in the use of fillers. Fletcher *et al.*[8.45] show in Fig. 8.26 that a wide variety of fillers have a lower heat-transfer coefficient than an unfilled bare aluminum joint. Such fillers are thermal insulators and may be useful for applications where thermal isolation is required. As a rule of thumb, for a given thickness, filler thermal performance is proportional to thermal conductivity divided by hardness. For convenience, fillers can be divided into three classes: greases, gaskets, and cured-in-place room-temperature-vulcanized (RTV) silicone compounds. Greases and gaskets are available from many suppliers in a wide variety of materials, and the offerings are summarized in Appendix C, "Summary of Thermally Conductive Filler Materials and Suppliers."

Use of fillers can create problems not present with bare interfaces. These include interference with unit grounding, inability to remove a unit for rework (or difficulty in doing so), structural loads, contamination, and outgassing—the last two problems being particularly important in spacecraft applications. Other considerations in the use of fillers are: electrical isolation as evidenced by high dielectric strength and breakdown voltage; mechanical properties such as compressive
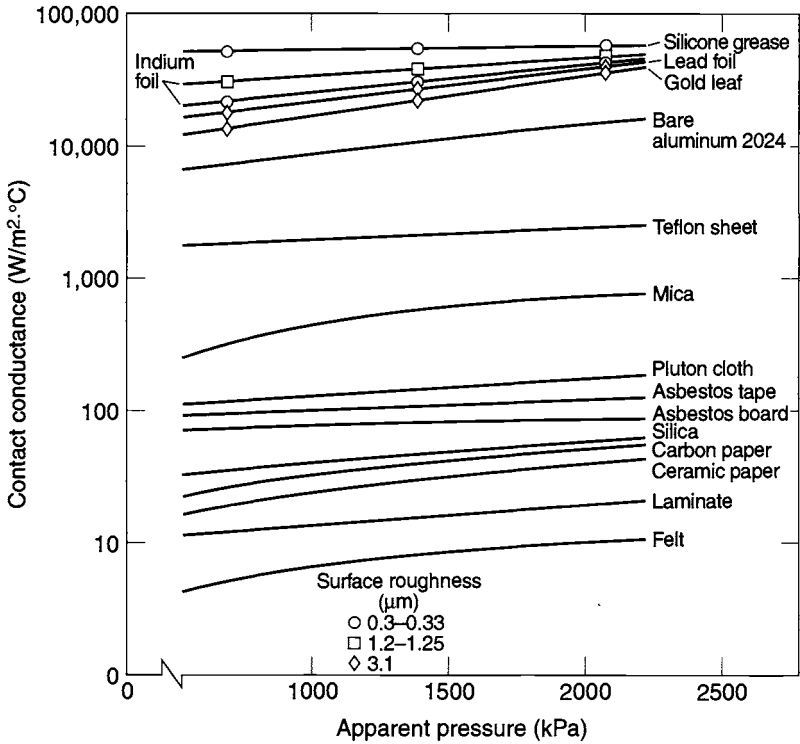
Fig. 8.26. Heat-transfer coefficients of selected interstitial materials.[8.45]

deflection, stress relaxation, and compressive set; and chemical and heat resistance. Silicone grease has superior thermal performance (Fig. 8.26) but may be a source of contamination. Greases without silicone mitigate this problem and are seeing some usage in small, less-expensive spacecraft. However, for the vast majority of spacecraft applications, thermal gaskets and cured-in-place RTV silicone compounds are the fillers of choice.

Thermal Gaskets

A variety of thermal gaskets are available for use with bolted joints. Application of such gaskets is shown in Fig. 8.27. To provide the desired thermal performance, some of these gaskets must be subjected to high pressure (Fig. 8.28). This creates structural loads and can cause bowing of the mounting panel. Moreover, separation (zero pressure) may occur at some distance from the bolt (Fig. 8.29). These conditions typically limit use of thermal gaskets to applications where the span between bolt centerlines is not large.

The Chomerics Division of Parker Hannifin Corporation provides a variety of thermal gaskets under the trade name CHO-THERM (Table 8.9). They are often thermally conductive but electrically isolating materials loaded with thermally conductive particles (aluminum oxide, magnesium oxide, boron nitride) within an
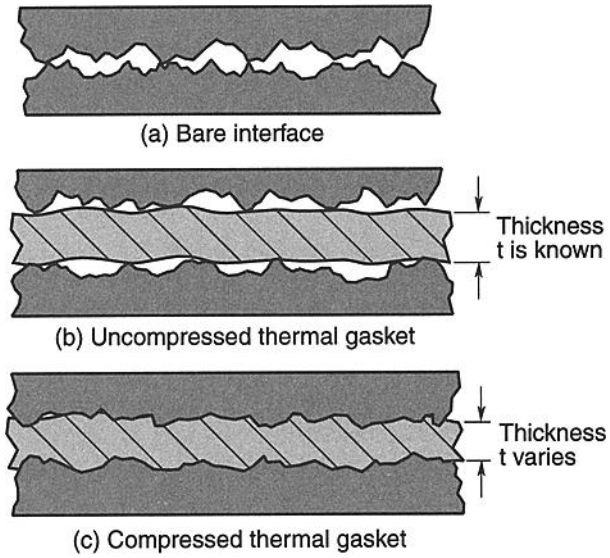
Fig. 8.27. Use of thermal gaskets as an interface filler.
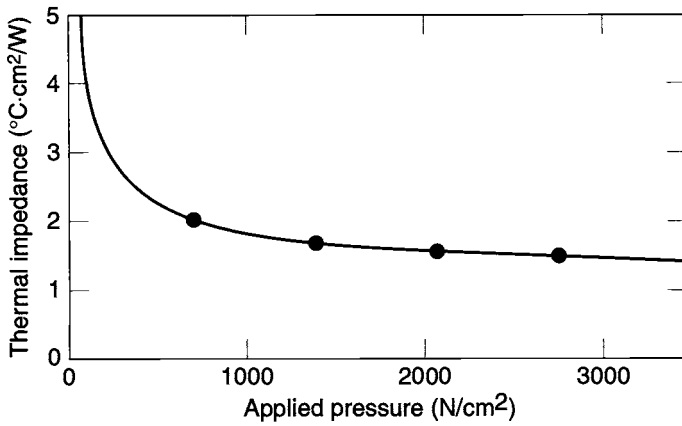
Fig. 8.28. Thermal impedance vs. pressure for CHO-THERM 1671 material.
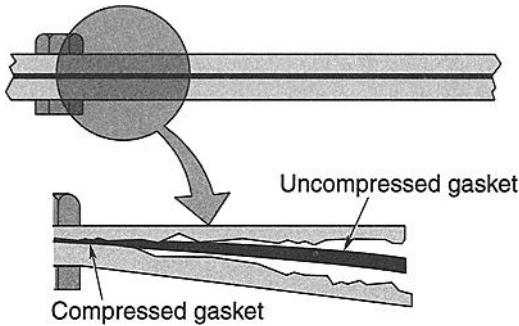
Fig. 8.29. Bolted-joint configuration with gasket.

elastomeric binder (silicone, fluorosilicone, urethane). These gaskets are tailored to provide a variety of special capabilities: dielectric strength; EMI shielding; ability to conform well to surface irregularities; solvent, temperature, and cut-through resistance. Table 8.10 provides properties for a number of CHO-THERMs.

While suitable for many applications, CHO-THERM has a limitation when used as a thermal gasket for unit mounting: It has an extremely high electrical resistivity, on the order of 10^{14} to 10^{15} Ω cm. The use of a continuous sheet may preclude meeting unit electrical-grounding requirements. A typical requirement is that the electrical resistance from unit to mounting be less than 2.5 mOhm. Therefore, if CHO-THERM is used, an auxiliary grounding method should be considered. This could be the use of gasket cutouts in the bolt region where compressible wire-grounding mesh is installed, or it could be the use of grounding straps.

Polycarbon, Inc., a member of the SIGRI Group, provides a flexible graphite gasket, Calgraph. Its typical properties are given in Table 8.11. Comparing this information with the CHO-THERM information in Table 8.10, one finds the Calgraph thermal conductivity normal to the surface two or three times greater than that for CHO-THERM, and the thermal conductivity parallel to the surface 59 to 150 times greater. Electrical resistivity is 15 to 18 orders of magnitude less. That is, Calgraph is a sufficiently good electrical conductor that it can, perhaps, be used as a continuous gasket and still meet unit-grounding requirements. Alfatec GmbH offers KERATHERM graphite gaskets in either a blank version or in electrically insulated versions laminated with wax or filled adhesive. The wax laminate incorporates a phase-change material. Unlaminated graphite gaskets should be used with caution in joints that may be disassembled, because electrically conductive carbon fibers and particles can be generated as the material shreds when the surfaces are separated. Processes must be in place to ensure that all conductive particles are contained so that they cannot find their way into electrical connectors or moving mechanical assemblies and cause shorts or jamming.

Table 8.9. CHO-THERM Properties and Features[a]

Compound	Properties						Features						
	Thermal Impedance[a]	Dielectric Strength[a]	Fiberglass-Reinforced	Polyimide-Reinforced	Polyester-Reinforced	Aluminum-Reinforced	No Mounting Pressure Required	Contains No Silicone	Continuous Rolls for Automation	Custom-Molded Pads	Thermal Adhesive	Resists Petrochemicals and Hydrocarbons	NASA Outgassing Approved
1679 Boron nitride, silicone	L	M	•										•
1671 Boron nitride, silicone	L	M	•										•
1661 Boron nitride, silicone	L	M											•
1678 Boron nitride, silicone	L	M	•										
1674 Aluminum oxide, silicone	M	M	•						•				
1677 Boron nitride, fluorosilicone	M	M	•									•	•
1682 Magnesium oxide, urethane	M	M			•			•	•				
1684 Magnesium oxide, urethane	M	H						•	•				
1688 Boron nitride, urethane	L	H		•				•	•				
1694 Magnesium oxide, silicone	M	H		•					•				
1698 Boron nitride, silicone	L	H		•					•				
1680 Boron nitride, Kapton,[b] silicone	M	H		•			•		•				
1646 Boron nitride, silicone	L	None		•		•			•				
T274 Aluminum oxide, silicone	M	H	•							•			
1641 Aluminum oxide, silicone	M	M									•		
1642 Aluminum oxide, silicone	M	M									•		

[a]L = Low; M = Moderate; H = High.
[b]Trade name

Table 8.10. CHO-THERM Typical Properties

Typical Properties	1679	1671	1677	1674	1678	1661	Test Method
Binder	Silicone	Silicone	Fluorosilicone	Silicone	Silicone	Silicone	—
Filler	Boron nitride	Boron nitride	Boron nitride	Aluminum oxide	Boron nitride	Boron nitride	—
Color	Yellow	White	White	Blue	Red	White	—
Thermal conductivity (W/m·°C)	2.7	2.4	2.1	1.2	1.9	3.8	Chomerics Test Method No. 28
Thermal impedance $\left(\frac{°C·cm^2}{W}\right)$	.97–1.16	1.16–1.42	2.45–2.71	1.94–2.19	1.42–1.55	1.55–1.81	Typical flat plate test values
Voltage breakdown rating (VAC)	4000	4000	4000	2500	2500	4000	ASTM D149
Outgassing (% TML) (% CVCM[a])	0.40 0.10	0.76 0.07	0.57 0.01	0.45 0.20	0.55 0.12	0.76 0.08	ASTM E 595-77
Thickness (mils)	10±2	15±2[b]	20±4	10±2	10±2	20±3[c]	—
Tensile strength (kPa)	6900	6900	2800	10,300	6900	1400	ASTM D412
Tear strength (kg/cm)	18	18	11	18	18	1.8	ASTM D624
Elongation (%)	10	2	10	2	10	2	ASTM D412
Hardness (Shore A)	95	90	85	90	90	90	ASTM D2240
Specific gravity	1.55	1.55	1.70	2.20	1.60	1.60	ASTM D792
Maximum use temperature (°C)	–60 to 200	–60 to 200	–60 to 200	–60 to 200	–60 to 200	–60 to 200	—
Volume resistivity (Ωcm)	10×10^{14}	10×10^{14}	10×10^{14}	2×10^{14}	10×10^{14}	10×10^{14}	ASTM D257

[a]Collected volatile condensable materials (0–10% acceptable).
[b]CHO-THERM 1671 is available up to 35 mils on custom orders.
[c]CHO-THERM 1661 is available up to 100 mils on custom orders.

Table 8.11. Calgraph Properties

Property	Units	Value
Electrical Resistivity		
"a" direction (parallel to surface)	Ohm-cm	0.0010
"c" direction (normal to surface)	Ohm-cm	0.064
Bulk Density	g/cm^3	1.1
Thermal Conductivity		
"a" direction (parallel to surface)	W/m·K	220
"c" direction (normal to surface)	W/m·K	6.9
Thermal Expansion 21–980 °C		
(bulk density 1.7–1.9 g/cm^3)	$10^{-6}/°C$	5.0–7.9
Hardness (Shore Scleroscope)		
At 1.0 g/cm^3	—	30
At 1.3 g/cm^3	—	40
Tensile Strength		
At 1.0 g/cc and 0.015-in. foil	kPa	4800
Permeability		
Air	cm^2/g	<0.00001
Emissivity		
At 500°C	—	0.4
Sublimation Temperature		
(does not melt)	°C	3600
Temperature limit (in air)	°C	540

Welch and Ruttner[8.41] conducted a study to determine if Calgraph was a suitable interface filler for perimeter-mounted electronic units as large as 279 mm by 152 mm (Fig. 8.23). They divided the test plate into four regions as shown in Fig. 8.30. Using a TMM of the test setup and correlating test results to math-model predictions, they determined local heat fluxes and heat-transfer coefficients. A comparison of local heat-transfer coefficients so calculated for bare and Calgraph-filled interfaces at a torque of 2.26 N·m is shown in Table 8.12. Results are shown for cold plates at –34 and 71°C. Use of Calgraph improved heat-transfer coefficients in all regions except the center region. In that region, separation clearly has occurred, and pressure is essentially zero with or without the Calgraph. The largest improvement is seen in the screw region, where enhancement of a factor of 2.8 to 3.1 was observed. In the region between the screws and in the center-loop
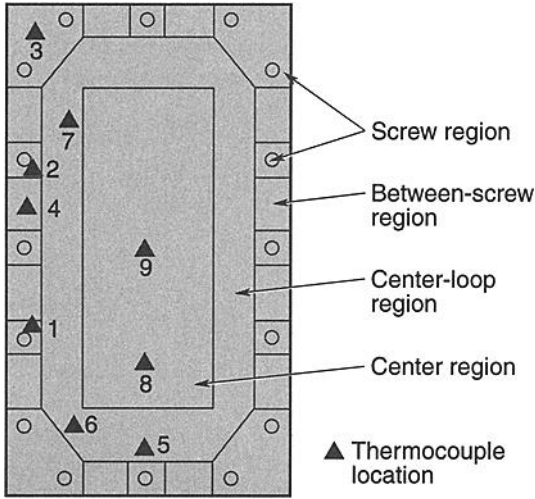
Fig. 8.30. Test plate showing thermocouple and region locations.[8.41]

Table 8.12. Local Heat-Flux Heat-Transfer Coefficients (W/m^2·K) that Match Experimental Data for the 2.26 N·m Test

	Interface			
	Bare		Calgraph	
	Temperature (°C)		Temperature (°C)	
Region	−34	71	−34	71
Screw region	1420	2560	3980	7960
Between screws	850	850	1420	1135
Center loop	570	570	1135	1135
Center region	0.6	5.7	2.8	34

region, enhancement varied from 1.33 to 2.0, and in the large center region no enhancement was observed. Most investigators do not use TMMs, and they present their results as average heat-transfer coefficients based on an assumed uniform heat flux from top to bottom plate (e.g., Bevans *et al.*[8.35]). Therefore, Welch and Ruttner presented results in this form (Table 8.13). On this basis, enhancement by a factor of 1.5 to 1.9 was observed. Calgraph was also tested by Taylor on a small, stiff configuration.[8.40] An aluminum block 51 by 192 by 38 mm high was mounted to a 12.7-mm-thick aluminum plate by four No. 8-32 screws. Average heat-transfer coefficients reported were 14,800 W/m^2·K and 4980 W/m^2·K, with and without Calgraph, an improvement by a factor of three. This is the magnitude of improvement seen by Welch and Ruttner in the screw region.

Table 8.13. Area-Averaged Heat-Transfer Coefficients (W/m²·K) Based on Uniform Heat-Flux Assumption

Region	Screw Torque (N·m)			
	1.13		2.26	
	Temperature (°C)		Temperature (°C)	
	−34	71	−34	71
Bare	284	369	330	398
Calgraph	511	705	506	705

Cured-in-Place RTV Silicone Compounds

Thermal gaskets provide a factor of 1.5 to 1.9 improvement on an overall basis for 7.94-mm-thick plates for a typical perimeter-mounting configuration, with the largest improvement in the region of the bolts. No improvement is found in the center region, a consequence of bowing of the plates. To avoid this problem and provide near-continuous contact between the two plates, cured-in-place RTV silicone compounds are widely used in the industry. A process specification kindly provided by TRW Inc. calls for surface cleaning and drying, use of primer (on both surfaces) or mold-release compound (on at least one surface), installation of a stainless-steel mesh screen with gold-plate finish (for grounding) to be engaged by the mounting hardware, application of torque, extrusion of filler material from at least 75% of the periphery of the mating surfaces (for coverage), and cure-in-place. Belleville washers can be used at each screw instead of the wire mesh to achieve grounding. Some contractors forgo the use of a primer to allow easy removal of the electronic unit.

Use of RTV compounds creates a mold that conforms to the profile of the cavity created between unit baseplate and mounting plate resulting from the action of bolt torque. Centerline gap caused by bowing can be on the order of 10 to 20 mils. A variety of RTV compounds are used. Choice depends on properties such as cure time, viscosity (low viscosity aids filler extrusion from between mating surfaces), and low volatility. A typical material is an RTV566 kit consisting of RTV566A and RTV566B, supplied by General Electric. Some contractors in their spacecraft applications use RTV compounds filled with thermally conductive particles.

For a small stiff configuration, Taylor[8.40] reported an average heat-transfer coefficient with RTV filler of 15,250 W/m²·K, a factor of three greater than that for a bare interface. Bevans et al.[8.35] reported factors of four to six improvement for an average heat-transfer coefficient using RTV-11 for the configurations of Fig. 8.22. These results have been used by TRW in establishing the upper curve of Fig. 8.21. Overall, heat-transfer coefficients are in the range of 150 to 480 W/m²·K.

Usage Recommendation for Filled Interfaces

For filled interfaces, a practice similar to that used for bare interfaces is recommended. Separate treatment should be used for the region near the bolt and for the plate. Near the bolt or for small stiff plates, as studied by Taylor, a factor of 2.5 to 3 improvement in heat-transfer coefficient over bare-interface values is justified

for thermal gasket[8.40,8.41] and RTV filler[8.40] interfaces. Overall heat-transfer coefficients for large, thin plates with a perimeter-bolt pattern are considerably less for thermal-gasket filler than for RTV filler. This is a consequence of bowing and lack of gasket contact in the center region. For thin plates or honeycomb panels with thin facesheets, use of RTV filler is recommended—with the upper curve of Fig. 8.21 recommended for predictive purposes.

For thick plates with a perimeter bolt pattern, the data of Welch and Ruttner[8.41] can be used to determine heat-transfer coefficients for bare interfaces and those with a flexible graphite thermal gasket. On an overall basis the values in Table 8.13 can be used. In conjunction with a TMM analysis, the local values from Table 8.12 can be used. For thick plates employing RTV filler, a TMM analysis should be conducted using the Welch and Ruttner[8.41] Calgraph data of Table 8.12, except the center-region coefficients should be between 250 and 400 $W/m^2 \cdot K$.

Complex Configurations and Special Topics

Heat-Pipe Interfaces

Heat pipes are fluid-filled, wicked heat-transport components often used in spacecraft thermal control. They utilize capillary forces and latent heat in their operation, and their mechanical and thermal interfaces are an important input to the thermal design. They are discussed in more detail in Chapter 14.

Typical Interfaces

Typical heat pipe–payload integrations are shown in Figs. 8.31 through 8.33. Figs. 8.31 and 8.32 show schematics of heat pipes embedded into honeycomb panels. Such panels are constructed of high-thermal-conductivity facesheets and stiff honeycomb core. They can be utilized in the spacecraft interior or as direct radiators on the exterior. The facesheets withstand the bending loads and act as lateral conductance fins for the mounted unit (Fig. 8.31), while the core resists shear loads, provides stiffness, retains the component fastener, and provides low-level transverse conductance. The heat pipes are bonded to the interior surfaces of the
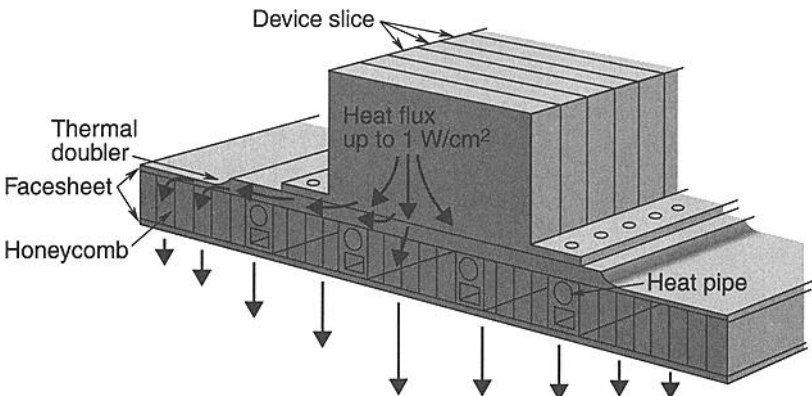

**Fig. 8.31. Electronic unit mounted to honeycomb/facesheet panel with embedded heat pipes.**
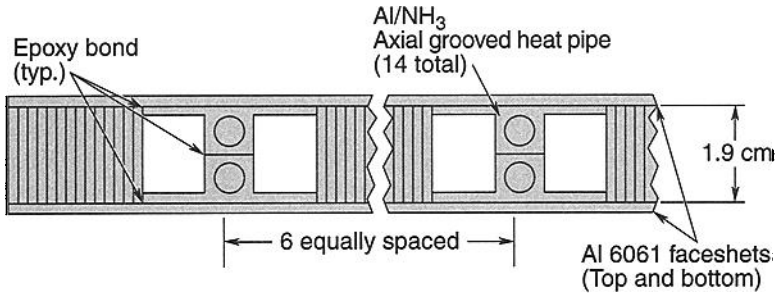
**Fig. 8.32. Honeycomb/facesheet panel with embedded heat pipes.**
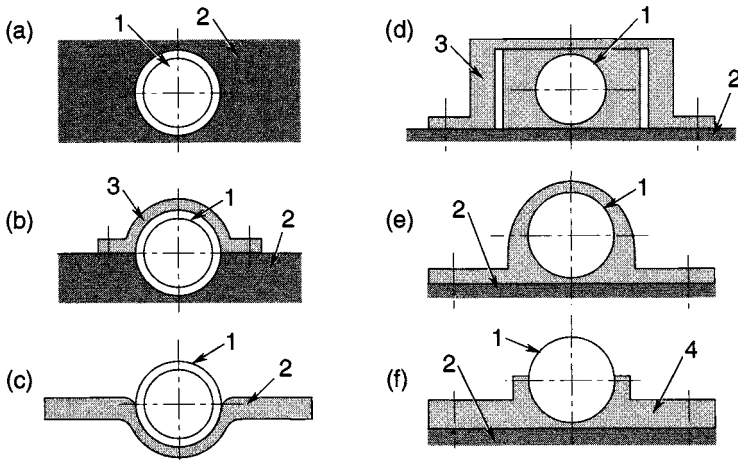
Fig. 8.33. Heat-pipe integration. 1: heat-pipe casing; 2: mounting surface of payload device; 3: saddles; 4: thick flange.[8.46]

facesheets; they provide lateral thermal conductance and, in some configurations (Fig. 8.32), transverse conductance by virtue of the casing. The heat pipes of Fig. 8.32 are bonded together and provide one-for-one redundancy.

Figure 8.33 shows six heat-pipe integration configurations. Configuration (a) is "buried" within the mounting. Mechanically the heat pipe is attached by threading or by virtue of a tapered casing (in detachable designs), glue, or low-temperature solder (in nondetachable designs). Configuration (b) uses a bolted saddle, while in configuration (c) the mounting is shaped to allow heat-pipe bonding. Configuration (d) shows an extruded rectangular-section heat pipe affixed by a saddle. Saddles for configurations (b) and (d) may be one continuous piece or multiple interrupted segments. Configuration (e) shows an aluminum heat-pipe extrusion with two integral flange ribs for mounting. Configuration (f) shows a stainless-steel or copper-casing heat pipe joined by low-temperature solder to a thick aluminum (sometimes copper) flange.

Design Guidelines

Each of the proposed heat-pipe interfaces of Fig 8.33 has its own thermal efficiency, which depends on flange thickness and layout of screws. Flange design may include thin flange ribs (thickness 1 to 2 mm) with M2.5 to M4 screws spaced from 12 to 40 mm, or thick ones (thickness 4 to 8 mm) with M4 to M8 screws or bolts spaced from 40 to 90 mm. Here European/metric screws are designated where, for example, M2.5 denotes a nominal 2.5-mm shaft diameter. The average area per bolt varies—for the first case 2 to 15 cm^2, for the second 10 to 40 cm^2. Sometimes the screw layout is nonuniform; screws can be allocated in groups of two or three with the closest possible spacing. The distance between such groups is two to four times greater than when uniform screw spacing is used. The thin-ribs flange design is more attractive for low heat density (up to ~0.5 to 1 W/cm^2), especially where such sources are distributed and nonuniform. The thick-ribs flange design is more reasonable for high-heat-density components (more than 1 W/cm^2) with linear extent greater than 10 cm. Stainless-steel bolts or screws are used as a rule for flange and payload-device connection. Contact conductance between flange and device can be estimated from recommendations made in the "Application of Theory: Contact Region" section.

Some Hardware Configurations

Examples of heat-pipe flange design are presented in Figs. 8.34 to 8.36. Figure 8.34 shows an extruded aluminum heat-pipe attachment to a spacecraft payload platform. The length of the flange is 325 mm, width 30 mm, and thickness 1.2 mm, with 42 M3 screws used. Maximum power transferred is 90 W.[8.47,8.48] Figure 8.35 shows a heat-pipe condenser-zone attachment to a device mounting plate. The heat pipe is made of copper with the device housing made of nickel-coated aluminum. The flange thickness is 10 mm with M8 bolts used. Nominal power transferred is 160 W.[8.49] Figure 8.36 shows two heat-pipe flanges for attachment to a device mounting plate. The heat pipes are made of stainless steel, the flange aluminum, coated with nickel. Flange lengths are 85 and 120 mm, and thicknesses are 2.2 and 3 mm, respectively. M3 screws are used and nominal power is 10 W.[8.50]

The heat pipe transports heat from the device, and a device heat-collecting zone must be part of the design as well. The most common way to collect and transport distributed heat is to exploit the thermal conductance of the device's structural elements. A heat-pipe variant that realizes this is presented in Fig. 8.37, a heat-pipe-device/spacecraft interface using a carbon-fiber, carbon-matrix (carbon-carbon, or

Fig. 8.34. Extruded aluminum heat-pipe attachment to payload platform.[8.47,8.48] (Courtesy of National Technical University of Ukraine NTUU, formerly Kyiv Polytechnic Institute)
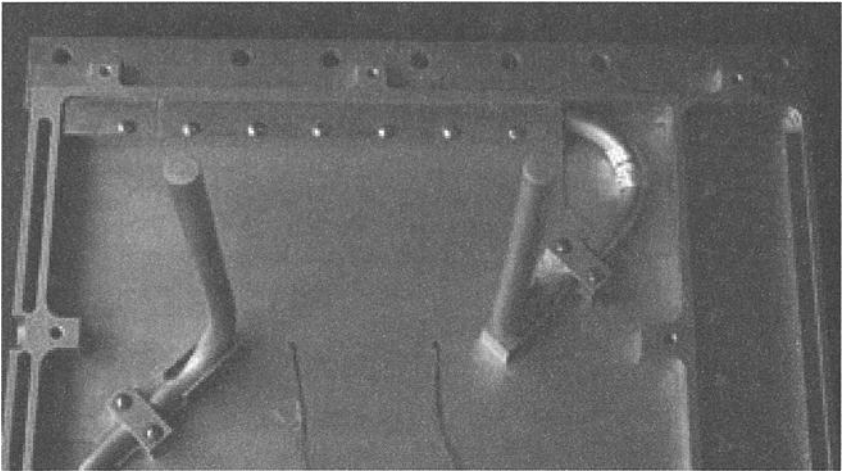
Fig. 8.35. Heat-pipe condenser zone attachment to device mounting plate.[8.49] (Courtesy of National Technical University of Ukraine NTUU, formerly Kyiv Polytechnic Institute)
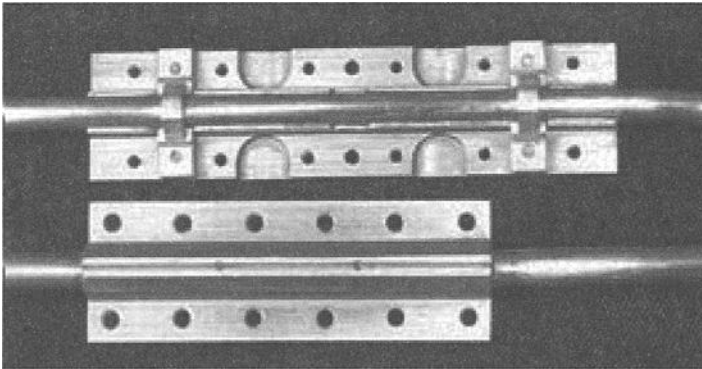

Fig. 8.36. Heat-pipe condenser zone attachment to device mounting plate.[8.50] (Courtesy of National Technical University of Ukraine NTUU, formerly Kyiv Polytechnic Institute)

CC) high-conductance layer as well as carbon-fiber/honeycomb (CF/HC) panels. Its size in-plane is 500 mm.[8.51]

Thermal Modeling Example

Temperature gradients and nonuniform heat flow are seen at the heat-pipe flange because of the discrete increments between heat pipes and the heat-flow processes in the heat-pipe casing. The influence of this temperature nonuniformity should be estimated beforehand numerically or analytically.[8.46,8.52,8.53] Finite-element software has been used for analysis of temperature gradients and heat flows for heat
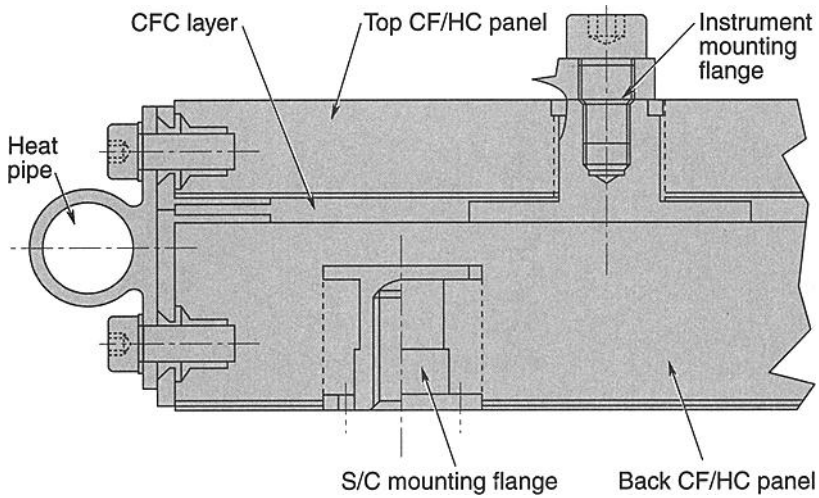
Fig. 8.37. Heat pipe–device interface showing usage of carbon-fiber, carbon-matrix (CFC) high-conductance layer.[8.51] (Reprinted with permission from SAE Paper No. 981639 ©1998 Society of Automotive Engineers, Inc.)

pipe–flange designs, and for heat-pipe integration into honeycomb panels.[8.53] As an example, the assembly shown in Fig. 8.38 was analyzed. A constant heat flux was applied to the aluminum doubler. Contact interfaces are located between the
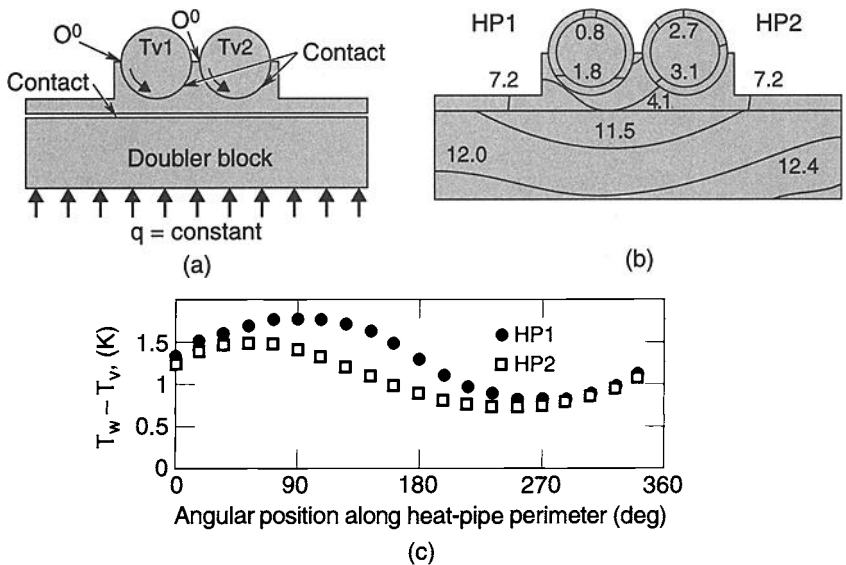

Fig. 8.38. Example of heat-pipe-assembly thermal prediction by finite-element method: (a) configuration and boundary condition; (b) temperature profiles; (c) wall-vapor temperature difference along heat-pipe perimeter.

doubler and the aluminum flange, and between the flange and the two copper heat pipes. The leftmost heat pipe, HP1, has an inner heat-transfer coefficient of 10,000 $W/m^2 \cdot K$ and vapor temperature of 0°C compared with 7000 $W/m^2 \cdot K$ and +2°C for HP2. Figure 8.38 shows temperature profiles in the heat-pipe assembly as determined by the finite-element analysis. In the figure the difference "wall temperature minus vapor temperature" is plotted as a function of angle along the perimeter of each heat pipe; here the angle is measured counterclockwise from the 0-deg locations shown in Fig. 8.38. Maximum temperature occurs along the bottom of the heat pipes in the region centered over the flange. The locations of minimal and maximal values are nonsymmetrical, as the heat flow to the pipes is unequal. Heat accepted by each heat pipe can be calculated by integration of temperature difference "heat pipe wall minus vapor" with respect to individual transfer coefficient. By dividing total heat to the bottom surface of the doubler by the difference in average temperature between this surface and that of the heat-pipe vapor, the conductance of the assembly as a whole is determined.

Special Configuration: Saddle with Two-Step Assembly

A novel saddle design by C. Gerhart[8.54] is shown in Fig. 8.39. This design allows independent assembly of the saddle to the heat pipe and then the saddle/heat-pipe assembly to the mounting plate. The two-step bolting/assembly process, intrinsic to this design, provides the potential for better fit, and higher and more uniform clamping pressure.

Compound-Cylinder Interface

In some engineering applications, the requirement for a cylindrical interface as in Fig. 8.40 may arise. For example, an annular heat exchanger could be mounted concentrically to the condenser section of a heat pipe. Contact pressure, which was a key determinant of contact conductance for flat interfaces, can no longer be explicitly determined. This pressure depends on a number of parameters including
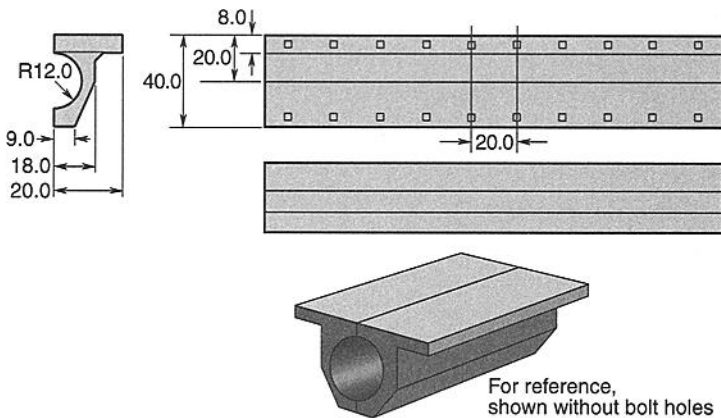

Fig. 8.39. Saddle with independent bolting to heat pipe and mounting (dimensions in mm).[8.54]

Direction of heat flow
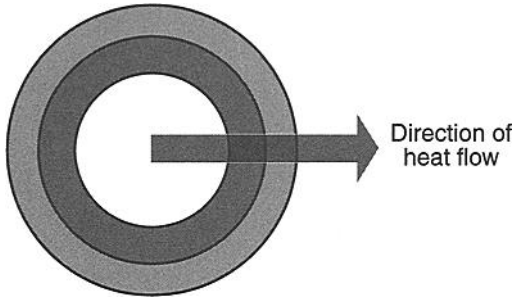
Fig. 8.40. Heat flow through a compound cylinder.

initial fit, differential expansion of the cylinders, and heat flux. In addition to these parameters, contact conductance depends on geometry, surface characteristics, interface medium, and thermomechanical properties of the cylindrical materials. Ayers et al.[8.55] have reviewed studies on this subject; they find the field to be in need of additional work. They provide an empirical correlation for eight different material/medium groupings—five in air and three in vacuum, including two where the inner cylinder is aluminum and the outer stainless steel:

$$h^* = 81.8(F^*)^{0.685} \tag{8.28}$$

where

$$h^* = h\sigma_E/k_E m_E \tag{8.29}$$

and

$$F^* = (F\alpha_E R_E/k_E)(E_E/H_E)(\alpha_i/\alpha_o)^3[0.5(1 + P_{amb}/P_{atm})]^2. \tag{8.30}$$

Ambiguity was present in the definition of mean or effective value as used by Ayers et al.[8.55] The roughness, σ_E, elasticity, E_E, and hardness, H_E, were called the "effective" value, but not explicitly defined. The asperity slope, m_E, thermal conductivity, k_E, and the coefficient of thermal expansion, α_E, were called the "effective (geometric mean)" value. The most likely meaning of the various terms is believed to be as follows: $\sigma_E = \sigma = (\sigma_i^2 + \sigma_o^2)^{1/2}$, where the subscripts denote the inner and outer surfaces; E_E is given by E' of Eq. (8.3); $H_E = H_C$, the microhardness of the softer of the two surfaces; $m = (m_i^2 + m_o^2)^{1/2}$; and $\alpha_E = (\alpha_i^2 + \alpha_o^2)^{1/2}$. While most probably $k_E = (k_i^2 + k_o^2)^{1/2}$, k_E is usually defined as the harmonic mean, i.e., $k_E = 2k_i k_o/(k_i + k_o)$. The term P_{atm} is sea-level atmospheric pressure, and P_{amb} is local ambient (e.g., vacuum) pressure.

Thermal Doublers

Introduction

For electronic units where power dissipation per unit surface area is large, excessive temperatures can occur if heat is directly conducted from the baseplate to the spacecraft mounting plate. This is especially likely if the thermal resistance between

baseplate and mounting plate is large. Temperatures can be reduced if a high-conductivity heat spreader is used between the unit and the heat sink. Such spreaders, or thermal doublers, function by conducting heat laterally from high-power dissipation regions before final transport to the spacecraft mounting plate.

Analysis

Bobco and Starkovs[8.56] analyzed a rectangular doubler of uniform thickness (Fig. 8.41). Starkovs[8.57] expanded the analysis to include two heated footprints on a rectangular doubler (Fig. 8.42), while Bobco[8.58] analyzed various types of terraced doublers (Fig. 8.43). Bobco and Starkovs[8.56] developed and solved the equation

$$k\delta_O(\partial^2 T/\partial^2 x + \partial^2 T/\partial^2 y) - h(T - T_\infty) = -q(x, y), \tag{8.31}$$

which accompanies Fig. 8.41. The term T_∞ is the equivalent sink temperature of the environment about the baseplate, and h is the overall heat-transfer coefficient from the baseplate to the sink. In this formulation, the doubler is assumed to be sufficiently thin so that no temperature gradient exists in the z direction. Not included in the above three analyses is the additional contact interface associated with use of a doubler.
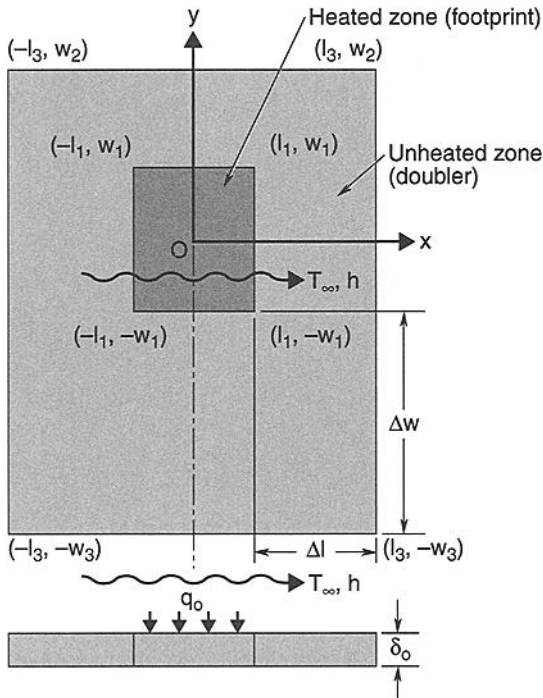

Fig. 8.41. Schematic of thermal doubler with single symmetry.[8.56]
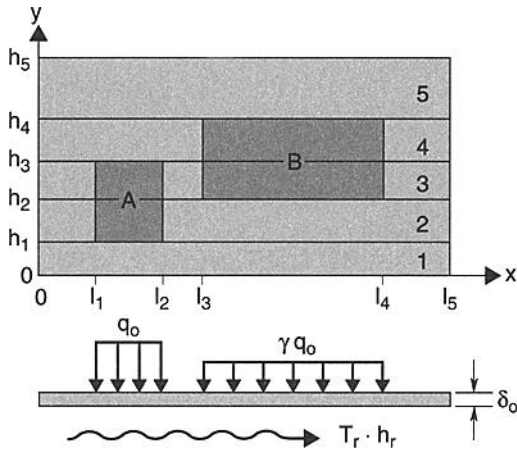
Fig. 8.42. Schematic of a rectangular doubler with two heated footprints.[8.57]

(a) η-terrace

(b) ξ-terrace

(c) Two-dimensional single terrace

(d) Two-dimensional partial double terrace
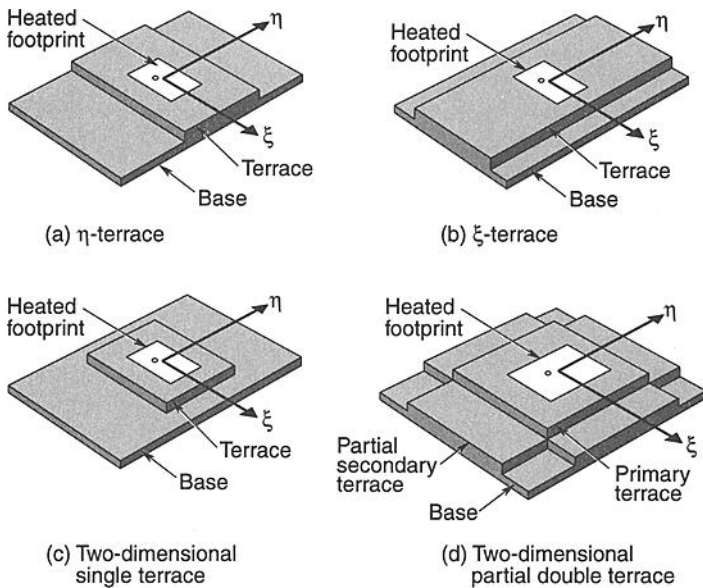
Fig. 8.43. Four terraced-doubler configurations that allow closed-form, separable solutions.[8.58]

Considerable analytic results were obtained in these three investigations. Typical results are shown in Figs. 8.44[8.56] and 8.45.[8.57] Bobco and Starkovs[8.56] point out that thermal-doubler design is an intricate task involving constraints of unit baseplate area, available mounting-plate area, and the surrounding environment.

Max temperature = 63.89°C $\lambda_1 = 4$
Location T_{max} = 0.00 cm $\lambda_3 = 4$

(a) Footprint location at $v = 1$

Max temperature = 67.27°C $\lambda_1 = 4$
Location T_{max} = 1.020 cm $\lambda_3 = 4$

(b) Footprint location at $v = 0.5$

Max temperature = 86.61°C $\lambda_1 = 4$
Location T_{max} = 7.18 cm $\lambda_3 = 4$
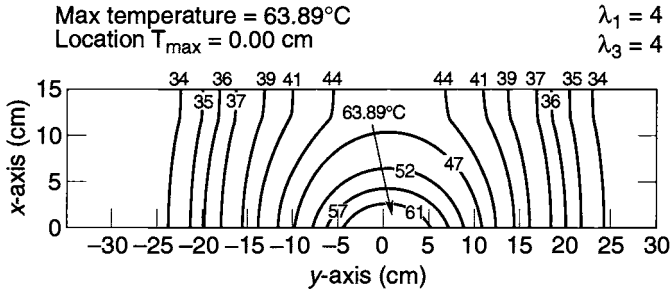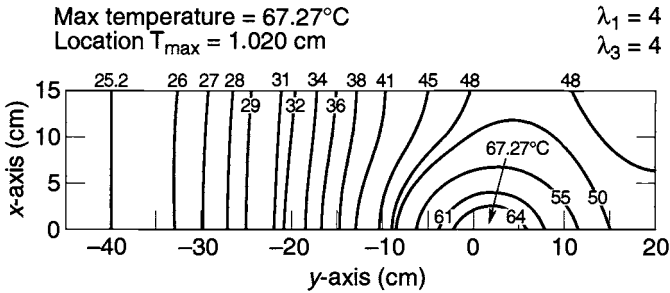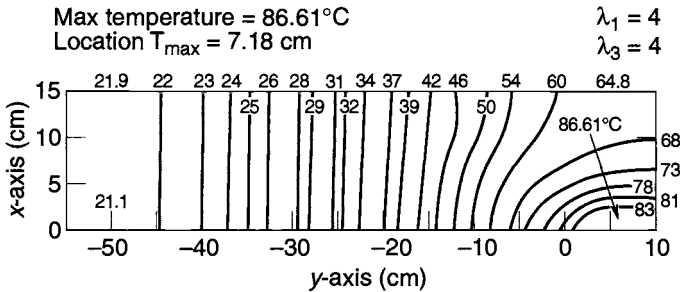
(c) Footprint location at $v = 0$
Isotherm maps

Fig. 8.44. Typical results for a single footprint.[8.56]

The intent is to provide the lightest-weight practical doubler design consistent with these constraints that satisfies the maximum-allowable unit-temperature requirement. Analytic solutions should be confirmed by finite-difference or finite-element TMM results.

For an axisymmetric doubler (Fig. 8.46), Gluck and Young[8.59] relieved the assumptions of no vertical temperature gradient in the doubler and no contact resistance between the doubler and baseplate. Here k is thermal conductivity, h is the contact heat-transfer coefficient, $f = T - T_o$, T is temperature within the doubler,

$T_r = 10°C$ $l_1 = 10$ cm $h_1 = 5$ cm $l_S = 1$
$h_r = 10$ W/m^2·°C $l_2 = 15$ cm $h_2 = 10$ cm
$\delta_0 = 0.02$ cm $l_3 = 20$ cm $h_3 = 15$ cm
$k = 220$ W/m·°C $l_4 = 40$ cm $h_4 = 20$ cm
$Q_A = 30$ W $l_5 = 50$ cm $h_5 = 25$ cm
$Q_B = 40$ W
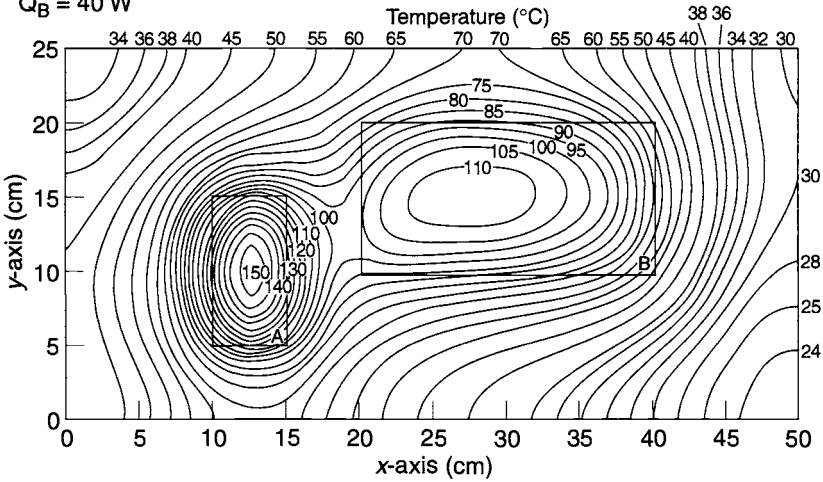
Rectangular doubler with two heated footprints: $l_3 = 20$ cm, $l_4 = 40$ cm

Fig. 8.45. Typical results for two footprints on a rectangular doubler.[8.57]
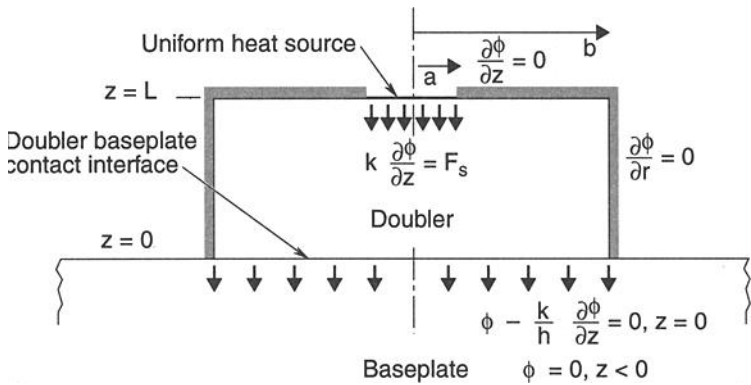

Fig. 8.46. Axisymmetric doubler model from Gluck and Young.[8.59]

and T_o is the baseplate (sink) temperature. For this problem, formulation of an optimum doubler thickness results, beyond which unit temperature increases (Fig. 8.47), where $\psi = k\phi/(2aF_S)$. This is a consequence of the combined effects of increased spreading (which reduces the temperature rise across contact interface)
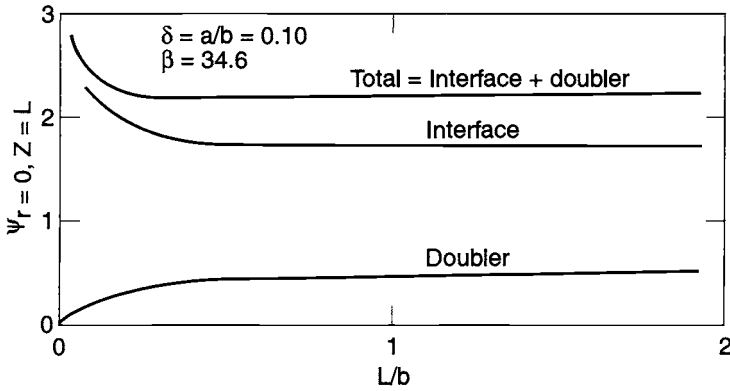
Fig. 8.47. Dimensionless centerline temperature rise at top of doubler vs. doubler height.[8.59]

and increased doubler thermal resistance with doubler thickness. Results are governed by an inverse Biot-like group, $\beta = k/hb$, as shown in Fig. 8.48(a). Here δ is a/b, the ratio of the heat-source radius to the doubler radius. For small values of β heat flow tends to be columnar (no spreading), and for large values heat flow diffuses radially (perfect spreading). The term F_0 is the average heat flux across the cross section. Performance results are presented in Fig. 8.48(b), (c), and (d), where ϕ and ψ are the centerline values at $z = L$. For $L/b = 0.01$, columniation is noted for $\beta < 10^{-2}$, and nearly perfect diffusion is noted for $\beta > 10^2$. As L/b increases, the columnar region diminishes. At $L/b = 1.0$ columniation and diffusion are of the same order for $\beta < 10^{-2}$. Figure 8.48(e) and (f) present optimization results. The former presents a plot of the minimum value of $\psi_{r=0,\,z=L}$ versus β for eight values of δ. The latter presents the values of L/b that correspond to these minimum values.

Materials

Technological breakthroughs in the last decade have resulted in new composite materials with thermal conductivities several times higher than that of copper, together with low densities and coefficients of thermal expansion (CTEs) close to those of semiconductor electronic materials. These new materials can be divided into four classes:[8.60-8.63]

- polymer matrix composites (PMCs)
- metal matrix composites (MMCs)
- ceramic matrix composites (CMCs)
- carbon/carbon composites (CCCs)

Properties of some new composites are presented in Table 8.14 together with properties of commonly used materials. Because composite properties are usually anisotropic, values are given for the x, y (in the plane of the material), and z (through the thickness) directions. One figure of merit for these materials is the conductivity divided by the density, which gives an indication of relative weights of doublers that are made of different materials but provide the same overall
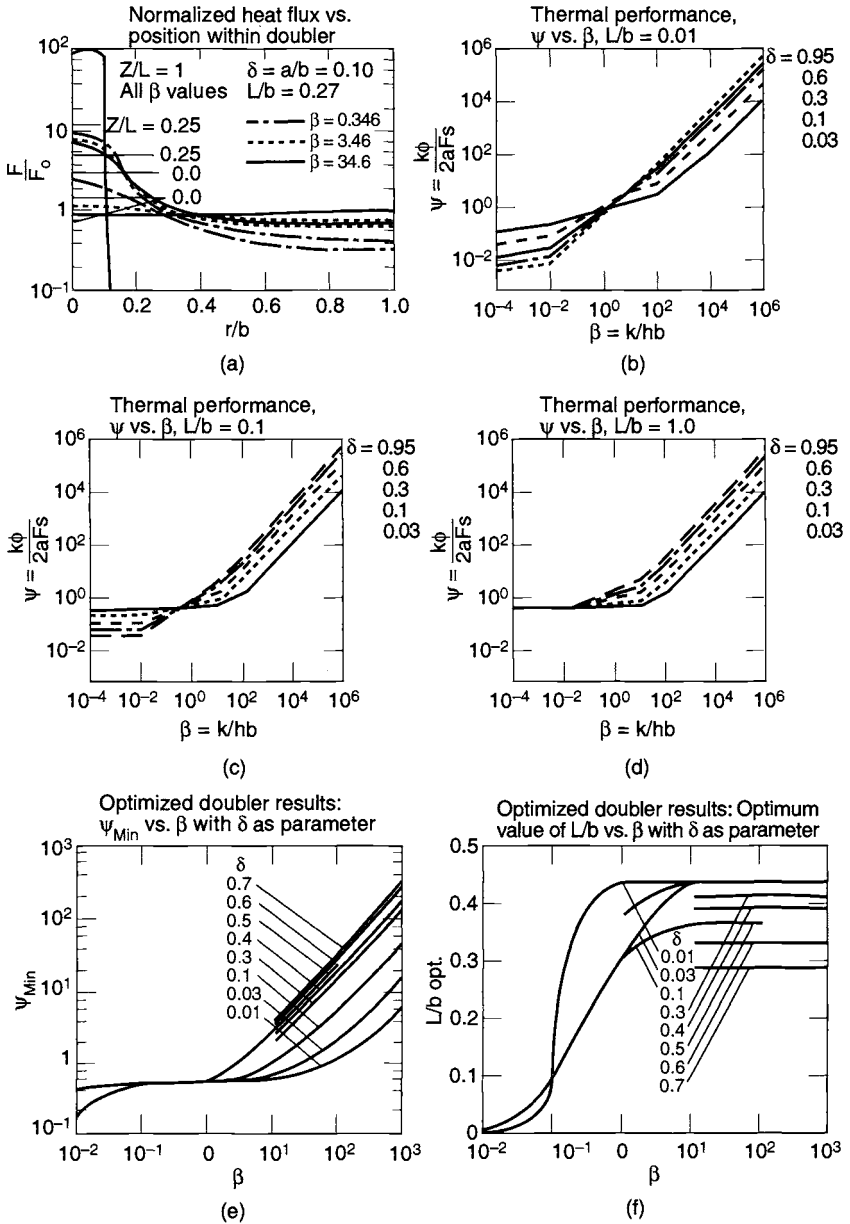
Fig. 8.48. Doubler performance.[8-59]

**Table 8.14. Properties of Materials Used as Doublers
and Heat Spreaders**

Matrix	Reinforcement†	Thermal Conductivity	Density	Relative Performance[a]	CTE	Ref.
		Basic Materials				
Aluminum	none	230 (W/m·K)	2.9 (g/cm³)	1.0	23 (ppm/K)	8.60
AlN	none	140–220	3.3	0.5–0.8	4.5	8.60
AlSiC	none	180		—		8.64
BeO	none	250	2.9	1.1	7.6	8.60
Silicon	none	150	2.3	0.8	4.1	8.61
Epoxy	none	1.7	1.2	0.02	54	8.61
Kovar	none	17	8.3	0.03	5.9	8.61
Copper	none	400	8.9	0.6	17	8.60
W-10Cu	none	167	16.6	0.1	6.5	8.60
Woven carbon fiber 1D 2D	none	350 (x) 175 (x/y)	<1.85	2.4 (x) 1.2 (x,y)		8.62
Pyrolytic graphite (material has minimal structural integrity)	none	1200 (x/y),10(z)	2.2	6.9 (x,y), 0.06 (z)	−1.0(x/y); 20(z)	8.62
Annealed pyrolytic graphite	none	1700 (x,y), 10(z)		—		8.64
		Polymer Matrix Composites				
Epoxy	K1100 Carbon Fiber	300 (x/y)	1.8	2.1	−1.1	8.61
Polymer	K1100 Discontinuous Carbon Fiber	20 (x/y)	1.6	0.2	4–7	8.61
Polymer Matrix Composite (PMC) 1D 2D		600 (x) 300 (x/y)	1.65	4.6 2.3		8.62
		Metal Matrix Composites				
Aluminum	2D Fabric1	280 (x/y)	2.3	1.5	2.8	8.60
Aluminum	3D Fiber Mat1[b,c]	187 (x/y), 74 (z)	2.5	0.9 (x/y), 0.4 (z)	10.4	8.60

**Table 8.14. Properties of Materials Used as Doublers
and Heat Spreaders** *(Continued)*

Matrix	Reinforcement†	Thermal Conductivity	Density	Relative Performance[a]	CTE	Ref.
Aluminum	3D Fiber Mat2[b,c]	226 (x/y), 178 (z)	2.3	1.2 (x/y), 1.0 (z)	5.5	8.60
Aluminum	MMCC 3D-2[b,c]	222 (x/y), 100 (z)	2.3	1.2 (x/y), 0.5 (z)	5.0	8.60
Aluminum	MMCC 3D-1[b,c]	189 (x/y), 136 (z)	3.1	0.8 (x/y), 0.6 (z)	6.0	8.60
Aluminum	K1100 Carbon Fiber	290 (x/y)	2.5	1.5 (x/y)	6.5	8.61
Aluminum	Si Particle	126-160(x,y,z)	1.9	0.8–1.1	6.5–13	8.61
Aluminum	SiC Particle	120-170(x,y,z)	3.0	0.5–0.7	6.2–7.3	8.61
Beryllium	Beryllia Particle	240(x,y,z)	2.6	3.0	6.1	8.61
Copper	+/–2⁰SRG[b]	840(x), 96(y), 49(z)	3.1	3.4 (x), 0.4 (y), 0.2 (z)	–1.1(x) 15.5(y)	8.60
Copper	+/–11⁰ SRG[b]	703(x), 91(y), 70(z)	3.1	2.9 (x), 0.4 (y), 0.3 (z)	-1.3(x) 15.5(y)	8.60
Copper	+/–45⁰ SRG[b]	420(x), 373(y), 87(z)	3.1	1.7 (x), 1.5 (y), 0.4 (z)	1.2(x) 3.6(y)	8.60
Copper	0⁰, 90, 0⁰ [b]	415(x), 404(y), 37(z)	3.1	1.7 (x), 1.6 (y), 0.2 (z)	5.3(x) 5.4(y)	8.60
Copper	2D Fabric2	342(x), 335(y), 84(z)	5.6	0.8 (x), 0.8 (y), 0.2 (z)	2.7(x) 3.3(y)	8.60
Copper	K1100 Carbon Fiber	400 (x/y)	7.2	0.7 (x,y)	6.5	8.61
Tungsten	Copper	167 (x/y/z)	16.6	0.1	6.5	8.61
Molybdenum	Copper	184 (x/y/z)	10.0	0.2	7.0	8.61
Aluminum	Beryllium	210 (x/y/z)	2.1	1.3	13.9	8.61
Silver	Invar	153 (x/y/z)	8.8	0.2	6.5	8.61
Carbon-Carbon Composites						
Carbon	K1100 Carbon Fiber	350 (x/y)	1.9	2.3 (x,y)	–1.0	8.61

Table 8.14. Properties of Materials Used as Doublers
and Heat Spreaders *(Continued)*

Matrix	Reinforcement†	Thermal Conductivity	Density	Relative Performance[a]	CTE	Ref.
Carbon	Carbon Fibers (in x direction)	800 (x), 50(y/z)	1.85	5.5 (x), 0.3 (y/z)	−0.05 (x/y),	8.62
	Carbon Fiber (in x and y directions)	350 (x/y), 40(z)		2.4 (x,y), 0.3 (z)	5–7 (z)	
Carbon	Carbon Fibers (in x direction)	800(x), 50(z)	1.8	5.5 (x), 0.3 (z)	−1.5 (x/y),	8.62
	Carbon Fiber (in x and y directions)	550(x/y), 40(z)		3.9 (x/y), 0.3 (z)	5–7(z)	

[a]Conductivity/density, relative to aluminum.
[b]Metal infiltration performed by Metal Matrix Cast Composites (MMCC) Inc.
[c]CTEs for reinforced composite with continuous fibers are in-plane isotropic values.

heat-transport capability. Such a figure of merit, normalized to that of aluminum, is given in Table 8.14.

Doublers for use under electronics boxes or as heat-conduction planes behind circuit cards can be made of composite materials having conductivities greater than that of copper, with a density of 2–3 g/cm³ and a CTE value near to that of silicon. These characteristics allow the design of doublers with mass, size, and performance resulting in effective technical solutions to some heat-spreading problems. Of course, some effort is required to match mounting interfaces between the doubler and heat source to account for the layout of holes and insets, contact-conductance adjustment, and so on.

A different kind of composite, pyrolytic graphite encased in aluminum, copper, graphite epoxy, or AlSiC, is available under the trade name TC1050. This material, properties of which are shown in Table 8.15, has been used in aircraft applications. It provides an in-plane conductivity of 1700 W/m·K and a through-thickness conductivity of 10 W/m·K. Additional experimental work has been done with pyrolytic graphite encased in AlSiC.[8.64] In an application with two heat sources of 128 W mounted on a square (15 × 15 cm) spreader of such a composite, an effective conductivity of 860 W/m·K, a CTE of 8.1 ppm/K, and an effective density of 2.6 g/cm³ were achieved. A similar disk-shaped doubler (diameter about 10 cm) had effective conductivities of 740 W/m·K (x/y) and 360 W/m·K (z) with a CTE of 8.1 ppm/K and an effective density of 2.6 g/cm³. Some spacecraft programs have been hesitant to use encased pyrolytic graphite because of concerns that in-plane cleavage of the graphite could reduce through-thickness conductivity. Proper design, however, can minimize this risk.

Thermal Doubler/Heat-Pipe Synergy

Another way to further improve the efficiency of a doubler is to exploit the very high conductance of a heat pipe to spread heat over the doubler's surface. The heat pipe can be manufactured as a "flat plate,"[8.65,8.66] replacing the doubler structure

Table 8.15. Encapsulated Graphite Properties

Case Material	Core Material	Thermal Conductivity	Density	Relative Performance[a]	CTE	Ref.
AlSiC	Annealed pyrolytic graphite	$740(x,y)$ W/ m·K	2.6 g/cm^3	3.6 (x,y)	6.8 ppm/K	8.64
Aluminum 6061, OFHC copper, graphite fiber/Polymer, or AlSiC	Pyrolytic graphite	$1700(x,y)$, $10(z)$	< 2.8 (unless copper casing used)	7.7 (x,y), 0.05 (z)	−1 to 24, depending on encapsulant	8.63

[a]Conductivity/density, relative to aluminum.

entirely, or as a conventional cylindrical pipe that can supplement the doubler by virtue of very high longitudinal conductance along the heat pipe's axis. To illustrate the synergy of heat-pipe/doubler combinations, parametric studies were performed using the configuration and boundary conditions of Fig. 8.45 as the baseline case. The four configurations studied were (Fig. 8.49): (1) the baseline case with a doubler conductivity of 220 W/m·K; (2) a case in which the conductivity of the doubler was increased to 1000 W/m·K; (3) a case where the doubler is a flat-plate heat pipe (inner heat-transfer coefficient is 2000W/m^2·K); and (4) a study where a heat pipe with a 1-cm width was embedded in the doubler material. Temperatures on the doubler external side, predicted by finite-element analysis, are plotted against x-axis position in Fig. 8.49. The figure shows that configurations (2), (3), and (4) reduce the maximum temperature by more than 40°C. The most effective configuration is the flat-plate heat pipe, case (3), which produces a nearly uniform temperature over the doubler surface.

Combined Thermal and Structural Analysis

An example of a combined thermal and structural analysis was previously discussed with regard to the work of Roca and Mikic.[8.28,8.29] More recently, finite-element codes have been used to conduct such analyses. Layton[8.68] conducted a thermal/structural study of a traveling wave tube (TWT) using ABACUS and NASTRAN, with PATRAN used for graphical display. As part of that analysis, local heat-transfer coefficients were determined between the TWT baseplate and the cold plate to which it was mounted. Fastening was accomplished by the use of two screws through a flange on one side of the TWT. Both surfaces were assumed to be perfectly flat and smooth. Computed pressure profiles and heat-transfer coefficients (W/cm^2·K) are shown in Figs. 8.50(a) and (b). The highest pressures are observed nearest each of the bolts, while pressure decreases to nearly zero at some
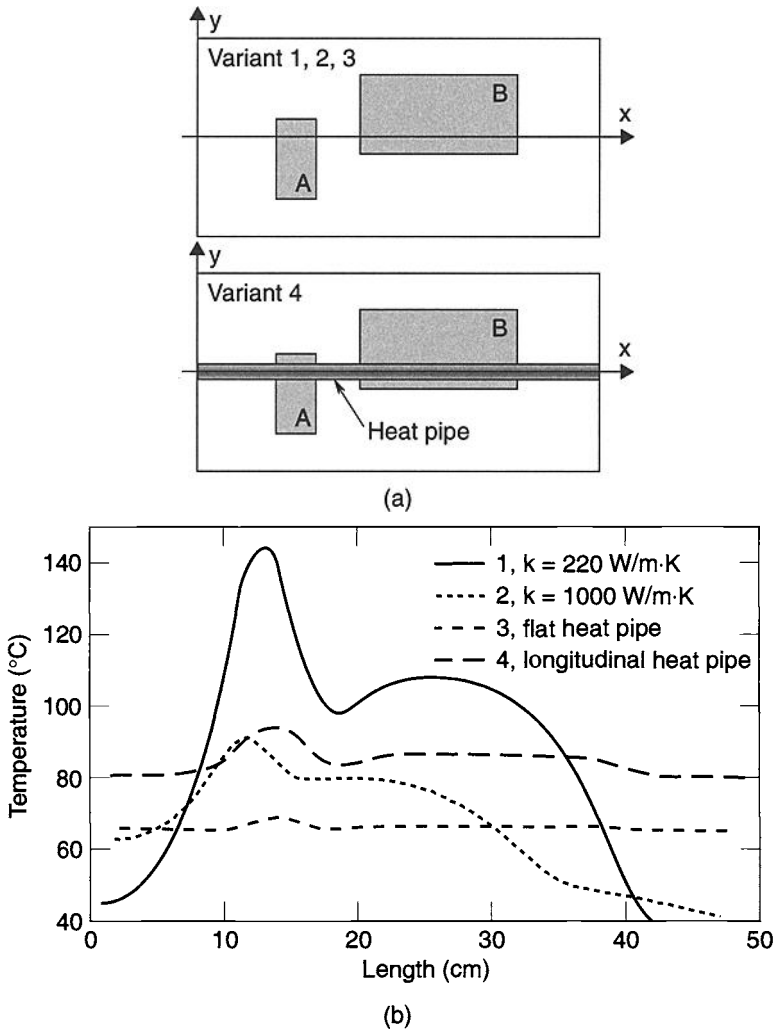
Fig. 8.49. Comparison of several doubler–heat pipe configurations/technologies: (a) schematics of doubler–heat pipe with two heat sources, A and B; (b) temperature profiles along x-axis for design variants 1, 2, 3, 4.

distance away. Layton characterized the local heat-transfer coefficient as a function of pressure from the work of Swartz[8.24] (Fig. 8.11) and others. He used the integration method of Goit[8.69] and a multivariable interpolation routine to determine from the pressure profile average heat-transfer coefficients for each element. Welch and Hamada[8.70] have compared heat-transfer coefficients using ABACUS finite-element analysis with those determined from finite-difference analysis and from experimental results. The basis for the comparison was the study by Welch
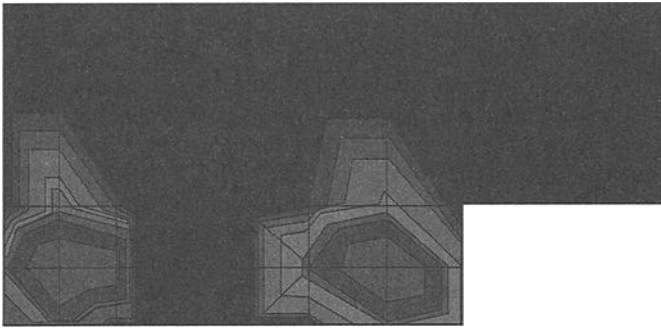
(a) Pressure profiles

0.073	0.071	0.074	0.070	0.067	0.070	0.074	0.070	0.069	0.065	0.065
0.149	0.159	0.076	0.078	0.076	0.070	0.143	0.137	0.070	0.070	0.065
0.84	1.12					0.79	0.66			
		0.47	0.082	0.083	0.22					
1.00	1.17					0.80	0.64			

(b) Local heat-transfer coefficients (W/cm^2·K)

Fig. 8.50. Finite-element thermal/structural analysis result from Layton.[8.68]

and Ruttner[8.41] as reported here (Figs. 8.23 and 8.30; Tables 8.8, 8.12, and 8.13). Figure 8.51 shows pressure profiles for a preloaded (torque applied to screws) plate at ambient temperature. Welch and Hamada analytically confirmed the previously noted[8.42,8.43] effect of plate temperature on a bolted-joint heat-transfer coefficient. As expected, the different CTEs of the aluminum alloy plates and stainless-steel screws increased or decreased contact pressure as plate temperature was, respectively, above or below ambient temperature. At the lowest torque used, 1.13 N·m, the predicted contact pressure was 393, 1965, and 3378 kN/m^2 for temperatures of –34°C, ambient, and 71°C.

Heat-transfer coefficients in the screw region differed greatly depending upon whether they were determined from finite-element analysis, finite-difference analysis, or test data. They were greatest from finite-element analysis and least from test data, with the difference as much as a factor of 15. However, these differences were largely a result of the different contact-region area used in the three methods. The finite-element analysis, which arguably uses the most correct contact area (because the area is determined from pressure profiles), used the smallest contact area—roughly three times the screw diameter. The test data was reduced using "region" areas—relatively large (and unverifiable) contact areas. A fairer comparison of the finite-element and finite-difference analyses is based on conductance (heat-transfer coefficient multiplied by the applicable area for each analytic or data-reduction method). The conductances so obtained showed relatively good agreement.

Scale in kN/m²

A =   41   F = 2234   K = 4426
B =   483   G = 2675   L = 4868
C =   917   H = 3109   M = 5309
D = 1358   I = 3551   N = 6088
E = 1800   J = 3985
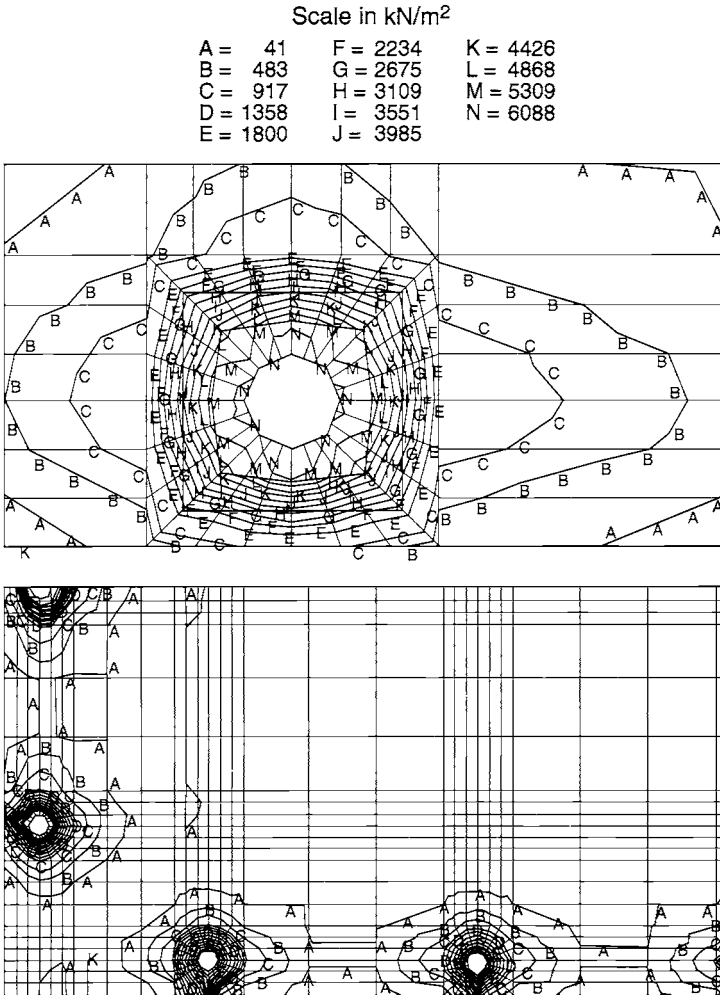
Fig. 8.51. Pressure profiles in kN/m² (kPa) for preloaded plates at ambient pressure.[8.70] (Reprinted with permission from SAE Paper No. 961504 © 1996 Society of Automotive Engineers, Inc.)

Mechanically Compliant Joints

In general, joints provide a mechanical attachment and a thermal path with specific heat-flow and temperature requirements. In many cases the thermal path must have mechanical flexibility to connect in three dimensions to coupling points or surfaces; such thermal paths may also require high thermal conductance with minimal mechanical loads and torque on the device. Such flexible or compliant joints

are often used to provide vibration isolation, relieve stress caused by CTE mismatches, or accommodate sliding applications. They are often found in CCD modules, heat-storage modules, and sensors and focal-plane assemblies for optical cameras and telescopes. These compliant thermal paths can be manufactured from a variety of high-conductivity materials such as copper, aluminum, beryllium, silver, or carbon fibers. The choice of material is dictated by thermal conductivity, geometrical flexibility, and workability of the soldering/welding/gluing process. Properties of candidate materials are presented in Table 8.16.

Flexible Straps

A typical flexible thermal strap consists of flexible strips, cable braid, or several braids in parallel, with lugs at each end for attachment. One of these attachments can be to a device sensitive to mechanical loads. In Fig. 8.52 is the flexible strap used in the VEGA Project[8.50,8.75] (Soviet Union, 1986), which connected a CCD matrix cooling finger with a heat pipe. This thermal strap conducted 0.5 to 1.0 W with an overall resistance of 14°C/W. It had a mass of 40 g, a length of 120 mm (the length of the flexible part was 80 mm), an external-braid diameter of 8 mm, a 180-deg bend capability, a force to bend 90 deg of 2 N, and a twist range along longitudinal axes of 20 deg.

Figure 8.53 presents two variants of flexible interfaces having an overall thermal resistance of 0.7°C/W and intended for heat transfer at higher power (up to 10 W). The heat-absorbing flange is attached to the device being cooled, and the heat-removal flange is connected to the cooling system. The variant on the right is characterized by

Table 8.16. [a] **Typical Properties of Materials for Fabrication of Flexible Thermal Straps**[8.71–8.74]

Material	Density (kg/m^3 at 20°C)	Conductivity (W/m·K at −100 and 20°C)	Heat Capacity (J/kg·K at −100 and 20°C)	Typical Forms	Enlongation/ narrowing (%)	Strap Resistance/ mass[b] [(K/W)/g]
Copper	8920	413/398	340/385	fibers, strands, strips	53/46 74/65	2.5/90
Aluminum, >99.75% pure	2700	220/218	500/885	strips	43/44 84/90	4.5/27
Beryllium	1840	—/157	—/1674	strips	–	6.5/19
Silver	10,493	389/376	219/230	strips	–	2.4/100
Amoco P100 carbon fiber	2160	—/550	—/—	strands, strips		1.8/22

[a]© 1999 American Institute of Aeronautics and Astronautics, Inc. Reprinted with permission.

[b]Calculated values for a 10-cm-long strap with an effective cross section 1 cm^2, without end clamps.
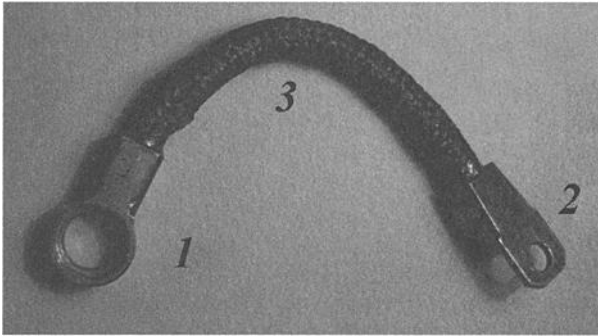
Fig. 8.52. Photo of flexible strap: (1), (2) connectors; (3) flexible copper braid.[8.50,8.75]

brazing of the braid strap to the cooling-system heat pipe to minimize the overall thermal resistance.[8.76] This design, which has a mass of about 60 g and distance between heat-exchanging surfaces of 25 mm, consists of 32 braids, each with a 3-mm diameter. The movement of the heat-absorbing flange is ±5 mm, and the allowable rotation along the longitudinal axis is about 20 deg. An important note is that the seepage of liquid solder into the gaps between fibers must be prevented during manufacture in order to assure flexibility.

The thermal resistance, R, of a flexible strap can be estimated based on the one-dimension conduction equation:

$$R = \Delta L^* \eta / (A^* k), \tag{8.32}$$

where ΔL is the measured length of the braid, η is a coefficient relating the real heat-transfer length of threads with ΔL, A is the area, and k is the thermal conductivity. The coefficient, η, should be defined experimentally.
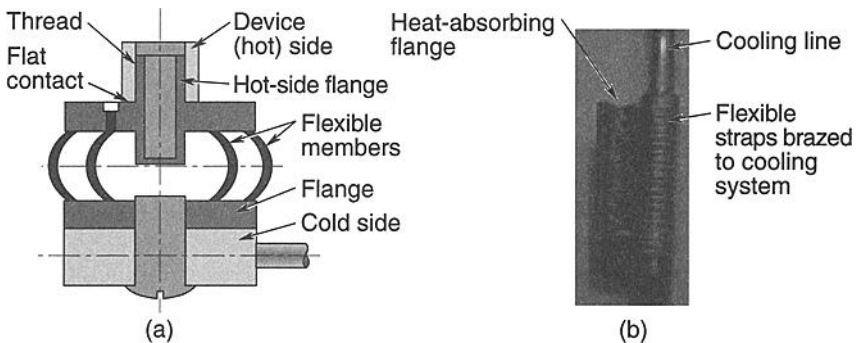
Fig. 8.53. Two variants of flexible interfaces.[8.76] (Courtesy of National Technical University of Ukraine NTUU, formerly Kyiv Polytechnic Institute).

Figure 8.54 shows two examples of cascaded flexible heat-transfer straps[8.77] with a thermal resistance of about 3°C/W. The schematic drawing shows the two flexible straps in series fabricated as copper braids and copper strips, while in the photo only the copper braids can be seen. With these straps, the optical device is controlled over the narrow temperature band of 7 to 17°C. The use of a solid stiff thermal interface in this case was unacceptable because of the inability to adjust the focal-plane location relative to the optics.

Some other thermal-strap variants, developed by Dornier GmbH (Germany) for the Mars 94/96 mission, are presented in Fig. 8.55.[8.78] Variant (a) enabled easy joining of the front-end focal-plane electronics with a heat sink over a distance of about 100 mm. This variant had a heat-transport capacity of several watts. Variant (b) was intended for higher-power heat transfer over a distance of 120 mm.

Gap Fillers

The mounting of some electronic devices results in large gaps. A special class of interface fillers has been developed for such mountings (Fig. 8.56). Known as gap fillers, they are very soft and compressible. Alfatec GmbH provides gap fillers made of ceramically loaded elastomers in their KERATHERM Softtherm product line. A generic analysis[8.79] has shown that thermal resistance of such elastomers reaches minimal values at pressures of 2.1 to 3.4 MPa. At lower pressures, 0.07 to 0.35 MPa, the thermal resistance is three times as much. The Bergquest Company[8.80] gives the range of gap-filler thicknesses as 0.51 to 4.1 mm, conductivity as 0.8 W/m·K, and thermal resistance of a 2.5-mm-thick pad as 0.0032 $K·m^2/W$ at a pressure of 0.069 MPa.

Flexible straps welded as copper interface braids

Flexible straps as copper strips

Welded interface to heat pipe
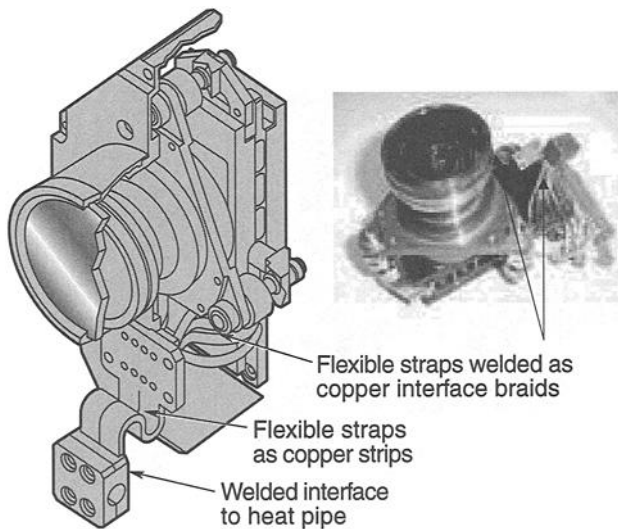
Fig. 8.54. Cascaded flexible thermal interfaces in WAOSS camera.[8.77] (Courtesy of DLR)
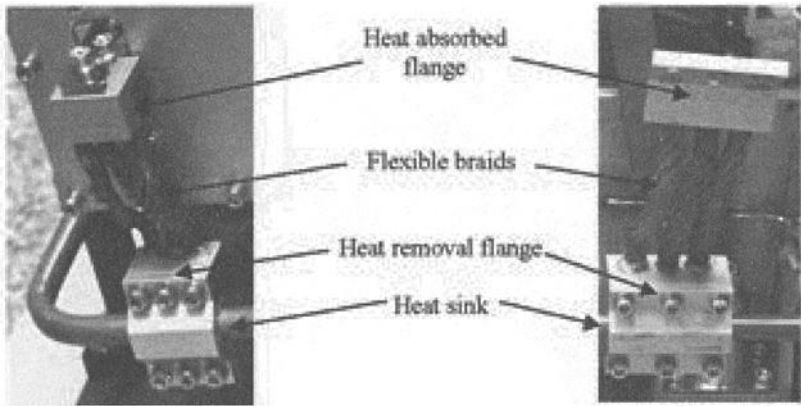
Fig. 8.55. Variant of extremely flexible strap, DLR/Dornier GmbH (now part of Astrium).[8.78] (Courtesy of DLR)
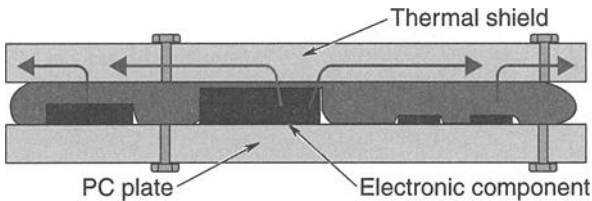

Fig. 8.56. Schematic of conformable pad application for cooling of microelectronics.

Carbon-Velvet Gaskets

Another type of flexible joint is provided by the carbon-velvet thermal-interface gaskets under development by Energy Science Laboratories, Inc. (ESLI)[8.81] These gaskets have not yet been used in space applications. They are made of a soft velvet consisting of numerous carbon fibers aligned perpendicularly to the substrate and anchored in a thin layer of adhesive (Fig. 8.57). The velvets are fabricated by precision-cutting continuous tows of carbon fiber and electrostatically "flocking" the fibers into uncured adhesive. Fiber diameter, length, and packing fraction typically vary from 5 to 12 μm, 0.25 to 3 mm, and 0.1 to 24%, respectively. Two velvets can be meshed together (like the surfaces in Velcro) to create a compliant joint between planar or curved surfaces. Various types of tailoring can improve this gasket's range of applicability.

Engineers must trade off the thermal and mechanical performance of the ESLI gasket. Highest thermal conductivity occurs with short, stiff velvets, while greatest compliance occurs with long, low-modulus velvets of low thermal conductivity. Table 8.17 shows the properties of three velvets as given by ESLI, with the most conductive, least compliant specimen in the top row, and the least conductive, most compliant specimen in the bottom row.
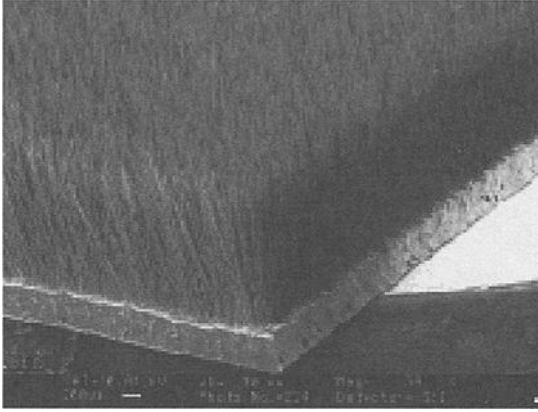
Fig. 8.57. SEM of ESLI[8.81] carbon-fiber velvet in vinyl substrate. Fibers are ~1 mm long. (© 2001 American Institute of Aeronautics and Astronautics, Inc. Reprinted with permission.)

Figure 8.58 shows the overall conductance of the intermediate specimen of Table 8.17 as measured in air by ESLI. The maximum value of 700 $W/m^2 \cdot K$ is a factor of two less than that given in the table. In vacuum, the overall conductance is expected to be less than 300 $W/m^2 \cdot K$.
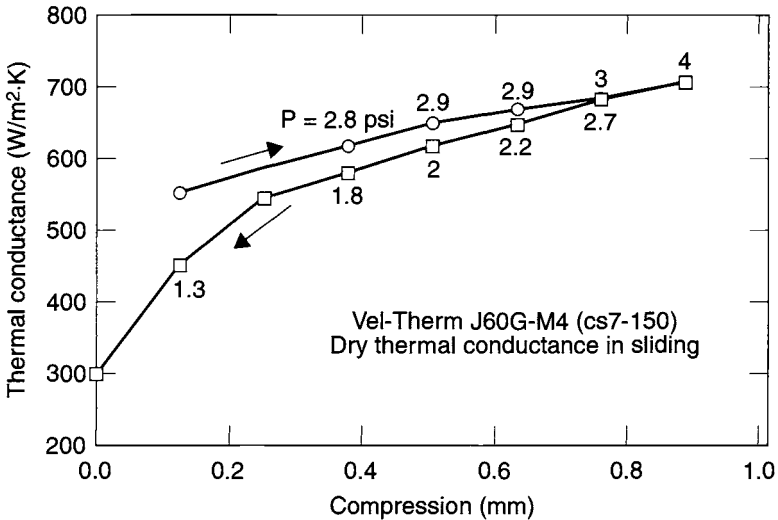

Fig. 8.58. Heat-transfer coefficient of intermediate test specimen of Table 8.16, as a function of compression and decompression.[8.81] (© 2001 American Institute of Aeronautics and Astronautics, Inc. Reprinted with permission.)

Table 8.17. Properties of Selected Carbon-Fiber Velvets[8.81]

Fiber	Fiber Length (mm)	Fiber Diam (μm)	Packing Fraction (%)	Fiber Conductivity (W/m·K)	Fiber Modulus (GPa)	Velvet Critical Buckling Stress (Pa)	Velvet Thermal Conductivity (W/m·K)	Velvet Thermal Conductance (W/m²·K)
A20	0.5	10	10	1000	896	5.52×10^6	100	15,500
J60	1.5	7	3	100 to 200	434	34,500	3 to 6	1550
F100	2.5	6	2	20	234	4140	0.4	155

Figure 8.59 shows the overall thermal conductance for three pitch fiber velvets as measured in air by ESLI. The fibers were applied directly into the thermally loaded adhesive spread onto the lower aluminum bar. Much of the heat is conducted from the fiber to aluminum through air, which has a low thermal conductivity. Conductance improves with pressure and by biasing the fibers at an angle or by lapping the fiber tips so they are all the same height. Overall conductance values approaching 12,000 W/m²·K can be achieved in air by encapsulating the fibers in silicone gel.

While high thermal conductance can be achieved in some configurations by special measures, the most compelling applications of the carbon-velvet thermal-interface gaskets are expected to involve low-to-moderate conductance with the ability to accommodate sliding interfaces, applications with large or uneven gaps,
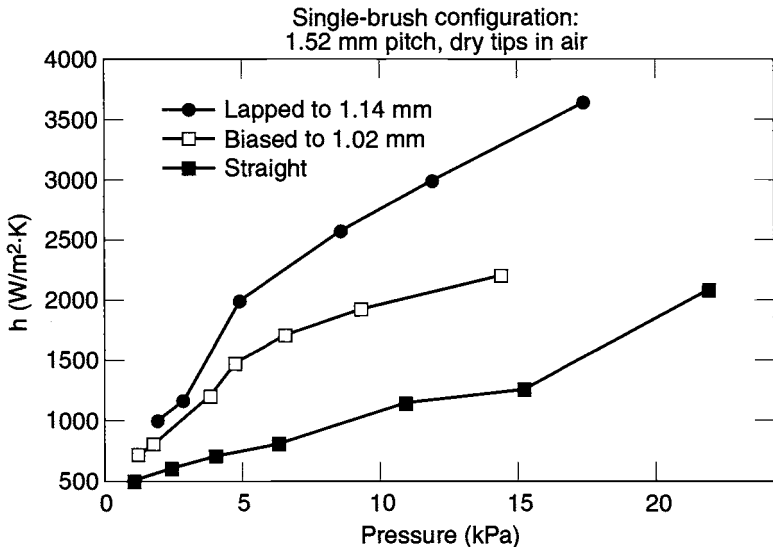

Fig. 8.59. Heat-transfer coefficient plotted against pressure for three pitch carbon-fiber velvets.[8.81] (© 2001 American Institute of Aeronautics and Astronautics, Inc., Reprinted with permission.)

and vibration isolation. An extremely important note is that this material can shed electrically conductive carbon fibers and should therefore be used only in applications where the fibers can be contained. Stray fibers in electrical connectors, electronics boxes, or moving mechanical assemblies can cause electrical shorts or mechanical jamming.

Thermal Isolation

Thermal isolators limit conductive heat transfer through a mechanical connection and provide temperature gradients between elements of a component. Typical applications include solar-panel and propellant-line supports, isolation under the mounting feet of instruments, coolant transport line and radiator isolation, battery mounting, and hydrazine-thruster catalyst-bed supports. Isolators can also be used to thermally decouple the spacecraft body from heat-storage units and optical devices, such as baffles and lenses.

These isolators can be made of a wide variety of low-conductivity materials, including fiberglass, stainless steel, titanium, and plastics. The choice of material is dictated by the conductivity, temperature range, thermal expansion, and mechanical properties required for the particular application. Properties of candidate isolator materials are presented in Table 8.18.

Table 8.18.[a] Typical Properties of Materials for Isolating Supports[8.82–8.85]

Material	Density (kg/m^3)	Young's Modulus (GPa)	Strength (MPa)	Coeff. of Thermal Expansion $(\mu m/m/K)$	Thermal Conductivity $(W/m \cdot K)$	Thermal Resistance of Column[b] (K/W)
Titanium alloy Ti-6A1-4V	4400	110	825[c]	9.4	6–8	125–170
Stainless steel 304L	7800	193	170[c]	17.2	12–16	60–80
Graphite epoxy (Generic)	1580	190[d] 8[e]	525[d,f] 60[e,f]	−0.5[d] 29[e]	53[d] 2[e]	18.9[d] 500[e]
Polyether-etherketone (PEEK)	1320	3.6	92[c]	47	0.25	4000
Fiberglass-epoxy (CCO-BL)	2000	—	900[f]	—	< 1–2	> 500–1000
S-glass epoxy	1860	54	1450[f]	10.8[d] 36[e]	0.42	2380

[a]© 2001 American Institute of Aeronautics and Astronautics. Reprinted with permission.
[b]Calculated value for sample column with height 10 cm and cross section 1 cm^2
[c]Yield strength
[d]Longitudinal
[e]Transverse
[f]Ultimate strength

In the design of a thermal isolator that supports a significant mass, the efforts of thermal engineers should be coordinated with those of mechanical and structural designers. The idealized thermal requirements of minimum cross-sectional area and maximum length are generally the opposite of what is needed for structural stability. A typical simple isolator, shown in Fig. 8.60, includes isolation both between the components being bolted together and under the bolt head and nut to avoid a thermal "short" through the bolt. Contact resistances at the interfaces are generally ignored because they are small compared to the resistance through the isolator material itself. The resistance down the bolt can be increased by using titanium or, for very small devices, plastic bolts. In addition, the isolators should have a "lip" to prevent the bolt from shifting under launch vibration and contacting the isolated component. This type of isolator requires careful control of tolerances on hole diameters and locations so that all the pieces come together without interference for all of the "feet" on the device.

Additional thermal-isolator designs, verified in spaceflight applications, are presented in Fig. 8.61. The straightforward approach to realizing high thermal resistance via fiberglass rods is illustrated in Fig. 8.61(a).[8.50,8.85] By proper choice of rod height and diameter, a 2-kg mass was supported by four rod assemblies having an overall resistance greater than 400 K/W in this particular design. For heavier devices, with masses between 5 and 20 kg, rods long enough to meet thermal-isolation requirements will often not have sufficient structural strength to withstand launch vibration loads. In such cases, solid rods may be replaced with larger-diameter hollow tubes that have the same conductive cross-sectional area but are much stronger. Figure 8.61(b) shows an example of an instrument supported on six fiberglass tubes that achieved a thermal isolation of 218 K/W. Another alternative means of achieving thermal isolation is to use a conical tube to reduce the effective cross section and required standoff height. In one application,[8.86] illustrated in Fig. 8.61(c), four fiberglass/epoxy conical standoffs (total mass 0.1 kg) supported a mass of 8.4 kg; thermal resistance greater than 300 K/W was achieved.
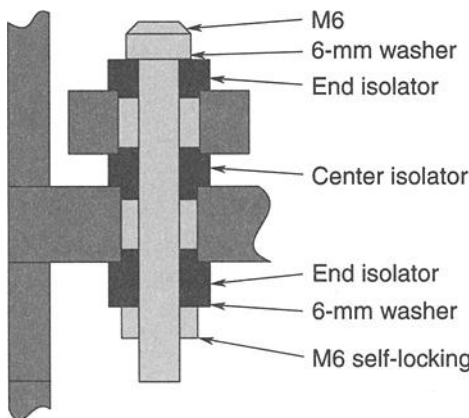

**Fig. 8.60. Thermal isolation at bolted-joint interface.**
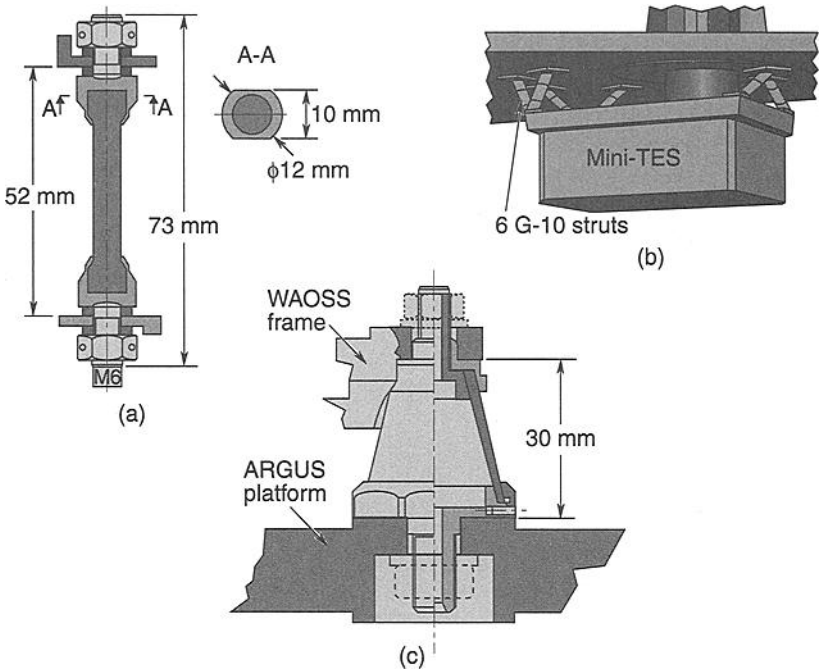
Fig. 8.61. Designs of thermal isolating standoffs. (a) Fiberglass rod. Courtesy of NTUU (KPI); (b) Courtesy NASA/JPL; (c) Courtesy of DLR.

The design can resist static loads of 3.5 kN in tension and 10 kN in compression. Devices heavier than 20 kg often do not require supports with very high thermal resistance because heat leaks through MLI and cables may dominate the thermal balance. In this regime, diverse support designs, having typical values of thermal resistance of 50 to 400 K/W, can be applied. One such design, presented in Fig. 8.62, increases the heat-transfer length between closely spaced plates through the use of
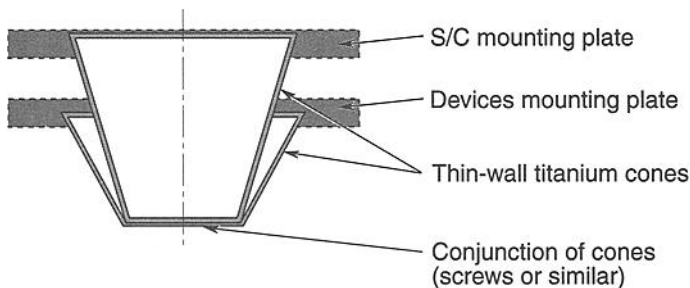

Fig. 8.62. Low-conductance support design using embedded titanium cones.

embedded cones. This design was used by DLR/Dornier GmbH for the high-resolution stereo camera flown on the Russian Mars 94/96 mission.[8.87]

Low-conductance mechanical attachment of large-area units such as solar arrays can be accomplished without the use of local standoffs like those discussed above. A schematic of a solar array attached to the Champ spacecraft with an open-cell Kapton foam[8.88] is presented in Fig. 8.63. In this design, the Kapton foam is glued to the honeycomb-panel satellite structure and covered with a graphite-epoxy facesheet to which the solar cells are attached. The thermal resistance of this isolation was not reported, although the response of the inner honeycomb panel to a solar-cell temperature range of −120 to +120°C was only 20°C.

Composite and Polymeric Interfaces

Modern spacecraft are making greater use of composite and nonmetallic materials for weight saving and CTE reduction, and in some cases for thermal conductivity and strength enhancement. Not much information has been published on joints made of these materials. What is available concerns uniformly applied pressure, not joints that use bolts or screws.

Rhoads and Moses[8.89] studied carbon fiber/epoxy resin composites in air. Samples had unidirectional continuous fibers oriented at 0 and 90 deg to the heat flow, with 0/0, 90/90, and 0/90 pairs investigated. Pressure was varied from 200 to 500 kPa. Best conductance was obtained with the 0/0 deg pair, although heat-transfer coefficients changed greatly (from 1000 to 3200 W/m^2·K) as the samples were rotated 15 deg with respect to each other between tests. Results were poor with the 90/90 and 0/90 pairs with heat-transfer coefficient varying from 200 to 800 W/m^2·K. The effect of pressure was very small for the 90/90 and 0/90 pairs, the 0/0 pair showing a slight increase with pressure. The authors attribute the better performance of the 0/0 pair, where the fibers are perpendicular to the contact surface, to the proximity of fiber ends at the contact surface. They attribute the variability to the change in relative fiber position at the contact surface resulting from the differential rotation of the samples between tests. They believe the poor performance of the 90/90 and 0/90 pairs was a result of the insulating effect of the resin, and the low transverse thermal conductivity of the carbon fibers that are parallel to the contact surface for the 90-deg samples.

The other relevant studies are all by the group at Texas A&M University led by L. S. Fletcher.[8.90–8.93] These studies all had mixed interfaces—a metal in contact with a composite or a polymer. Mirmira et al.[8.90] studied contact conductance of discontinuous and misoriented graphite fiber-reinforced composites at temperatures of 20 and 60°C over pressures from 172 to 1720 kPa. Three different fiber types
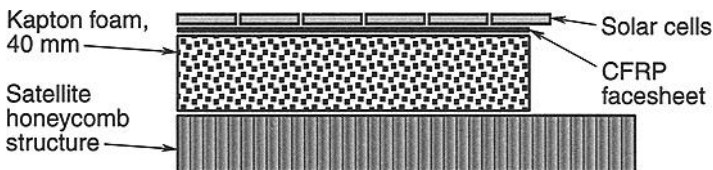

Fig. 8.63. Mechanical/thermal interface for spacecraft solar arrays.[8.88]

(Amoco supplied DKEX and DKAX, and Mitsubishi supplied K22XX) and three fiber-volume fractions (55, 65, and 75%) in a cyanate-ester matrix were studied. Composites so formed were in contact with an aluminum 6061-T6 surface. Heat-transfer coefficients varied from 100 to 1150 W/m²·K, with temperature having little influence. Results were correlated by the empirical equation

$$(h t V_f / k_h)^{1/3} = 3.03 (P/H_{C,h})^{0.0703}, \qquad (8.33)$$

which, when solved directly for heat-transfer coefficient, yields

$$h = 28.0 (k_h / t V_f)(P/H_{C,h})^{0.211}. \qquad (8.34)$$

The harmonic-mean thermal conductivity and hardness are based on fiber and matrix. The properties of the aluminum surface do not enter into the correlation.

Mirmira and Fletcher[8.91] tested a variety of fiber-resin formulations and configurations as described in Tables 8.19 and 8.20. The mating surface in this case was that of an electrolytic iron heat-flux meter. Heat-transfer coefficients as a function of pressure are shown in Fig. 8.64. The three neat (pure) resins have the lowest

Table 8.19. Characteristics of Cured Carbon and Glass Fiber-Reinforced Composites[a]

Sample Number, Resin	Fiber	Weave	Orientation	Fiber Volume (%)
Resin 1 (amine-cured epoxy)	none	none	Neat resin	0
Resin 2 (amine-cured epoxy)	none	none	Neat resin	0
1, resin 1	IM7	Plain weave	[0]	51.3
2, resin 1	E-glass	Style 7781	[(0/90)]	50.5
3, resin 1	AS4	Plain weave	[0]	58.0
4, resin 1	Carbon	Uniweave	[0]	50.7
5, resin 1	AS4	5 harness satin	[0]	51.1
6, resin 1	E-glass	Style 7781	[(0/90)]	49.7
7, resin 1	AS4	5 harness satin	[(0/90)]	48.5
8, resin 2	E-glass	Style 7781	[(0/90)]	50.5
9, resin 2	Carbon	Uniweave	[0]	47.3
10, resin 2	IM7	Uniweave	[0]	52.1
11, resin 2	AS4	Uniweave	[0]	57.1
12, resin 2	IM7	Uniweave	[0]	62.1
13, resin 2	AS4	Plain weave	[(0/90)]	52.3
14, resin 2	E-glass	Uniweave	[(0/90)]	47.0

[a]© 1996 American Institute of Aeronautics and Astronautics, Inc. Reprinted by permission.

Table 8.20. Characteristics of Cured Pitch Graphite Fiber-Reinforced Composites

Sample Number, Resin	Fiber	Manufacturer of Fiber	Thermal Conductivity, Parallel to Axis (W/m·K)	Fiber Volume (%)
Resin 3 (cyanate ester)	none	—	—	0
15, resin 3	DKAX	Amoco	900	55
15, resin 3	DKAX	—	—	65
15, resin 3	DKEX	—	617	55
15, resin 3	DKEX	—	—	65
15, resin 3	K22XX	Mitsubishi	600	55
15, resin 3	K22XX	—	—	65
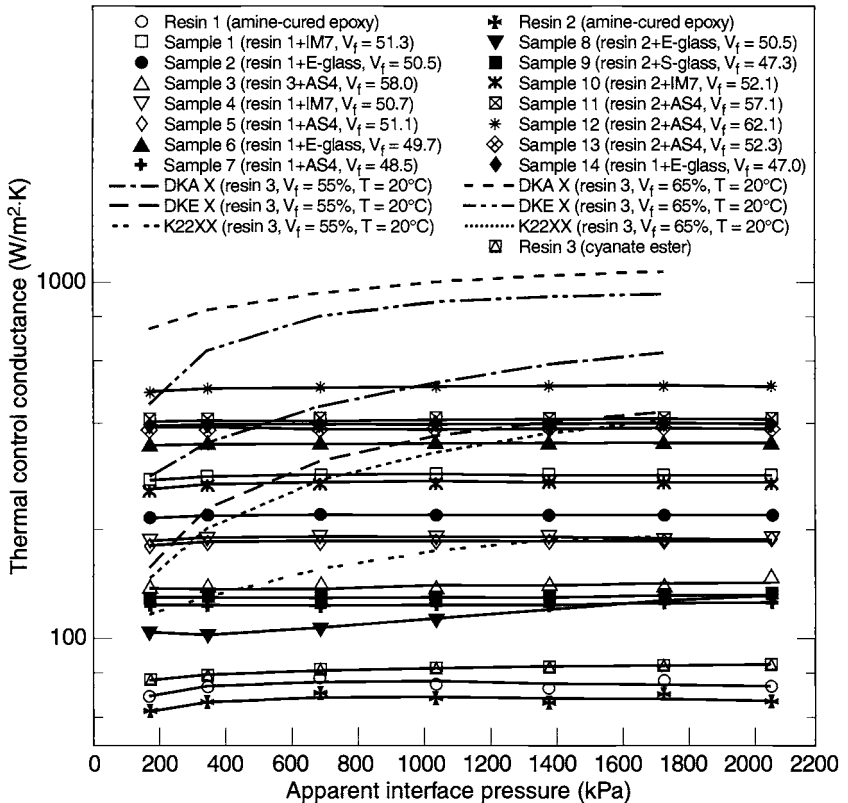
Fig. 8.64. Heat-transfer coefficient of composites as a function of apparent interface pressure.[8.91] (© 1999 American Institute of Aeronautics and Astronautics. Reprinted with permission.)

coefficients (30 to 75 W/m^2·K), each independent of pressure. The heat-transfer coefficients for the composites of the amine-cured epoxy resins (resins 1 and 2) are invariant with pressure. The authors attribute this to absence of sample thinning with pressure. The pitch graphite resin composites have moderately high coefficients (110 to 710 W/m^2·K) at 180 kPa pressure, with coefficients increasing to 200–1050 W/m^2·K as pressure increases to 1700 kPa. Mirmira and Fletcher attribute this to the observed sample thinning and reduction in interface resistance between fiber and matrix with pressure.

Marotta and Fletcher[8.92] studied the contact conductance of thermosetting and thermoplastic polymers: ABS, Delrin, Teflon, Nylon 6,6, LE phenolic, polycarbonate, UHMW polyethylene, polypropylene, and polyvinyl chloride. The mating surface was aluminum 6061-T6. Results are shown in Fig. 8.65. UHMW polyethylene showed the highest heat-transfer coefficients; both UHMW polyethylene and polycarbonate showed an increase in coefficient with temperature. Results were compared to the Cooper-Mikic-Yovanovich (CMY) plastic model[8.4] in Fig. 8.66. Here k_S is the harmonic-mean thermal conductivity of the polymer and Al 6061, H is the microcontact hardness of the softer of the mating materials, and s/m
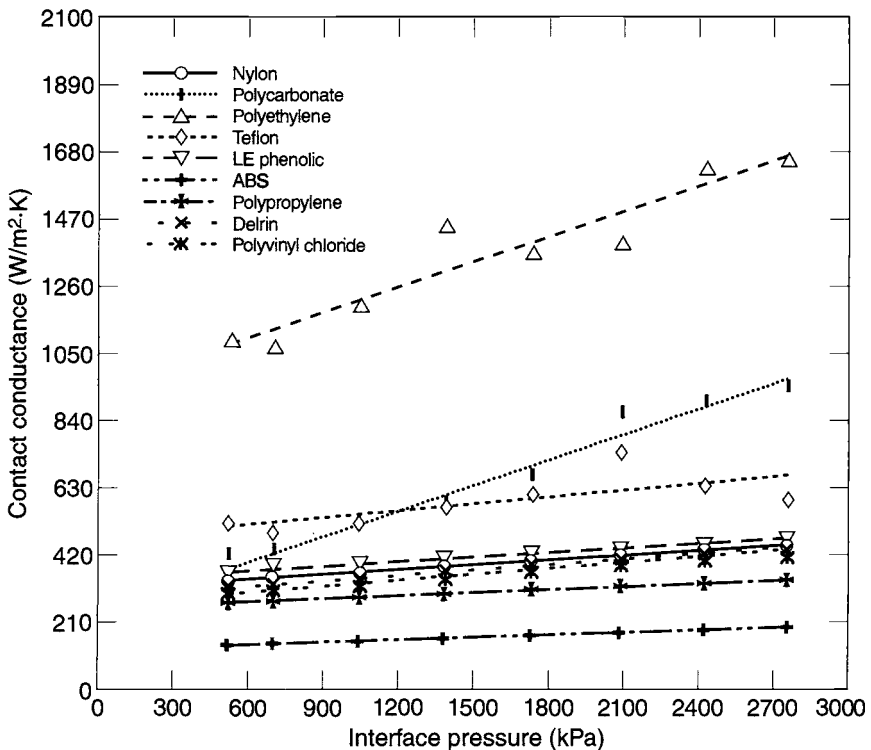

Fig. 8.65. Heat-transfer coefficient of polymers as a function of apparent interface pressure.[8.92]
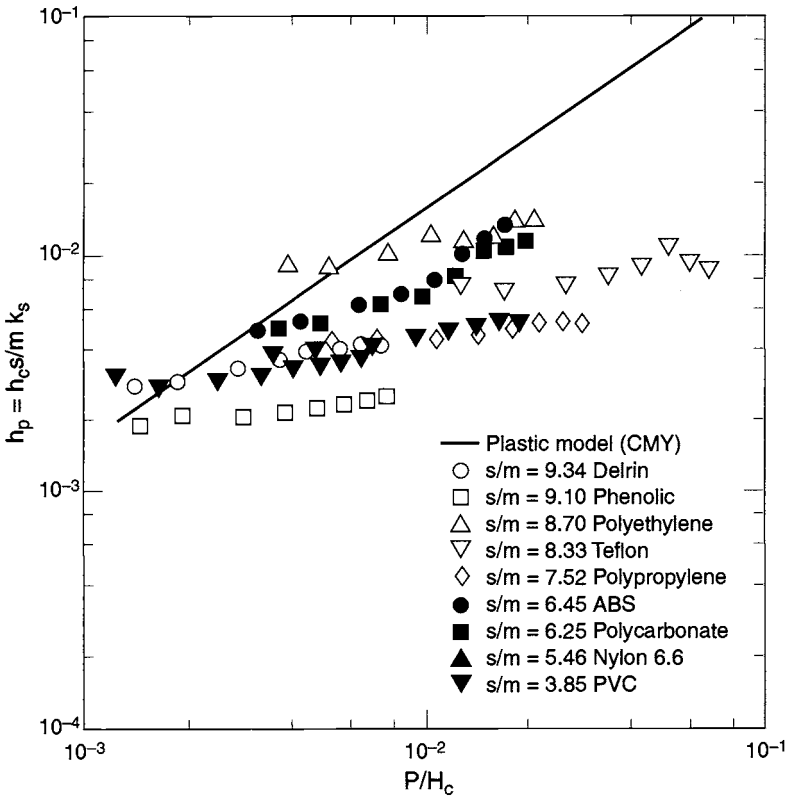
Fig. 8.66. Comparison of dimensionless contact heat-transfer coefficient for various polymers with CMY[8.4] plastic model.[8.92] (©1996 American Institute of Aeronautics and Astronautics, Inc. Reprinted by permission.)

in the legend is rms roughness divided by asperity slope with units μm. For the various polymers the plot of dimensionless heat-transfer coefficient against dimensionless pressure shows slopes much lower than that of the CMY model. Marotta and Fletcher attribute this difference to the softness of the polymers.

Lambert and Fletcher[8.93] determined heat-transfer coefficients for bare and electroplated silver-coated continuous-K1100-graphite reinforced aluminum 6063 in contact with aluminum A356-T61 at 20, 60, and 100°C. The silver coating is needed in marine or corrosive environments to prevent galvanic corrosion. For a pressure at 180 to 3000 kPa, heat-transfer coefficients for the former pair varied from 750 to 23,000 W/m·K, and for the latter pair they varied from 1000 to 4400 W/m·K.

Bearing Conduction

Conductance across bearings is one of the most uncertain parameters in spacecraft thermal analysis. The large dependence of the conductivity upon factors such as bearing design, speed, lubricant type and quantity, load, and temperature gradients from inner to outer race make identifying "generic" conductivities for bearings impossible.

The bearing cross section shown in Fig. 8.67 illustrates the conduction mechanisms for a ball bearing in vacuum. A conduction path runs through the ball/race contact regions as well as through the lubricant. The contact conductance is affected by lubrication and the load, which is itself driven by preload, gravity effects, speeds, and temperature differences between the races. The conduction through the lubricant is complex and highly dependent upon the type and amount of lubricant and the rotational speed. Figures 8.68 through 8.70 contain measured
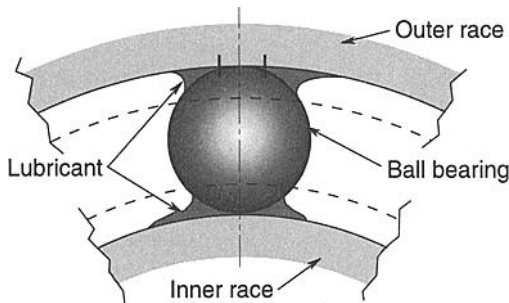


Fig. 8.67. Bearing cross section.
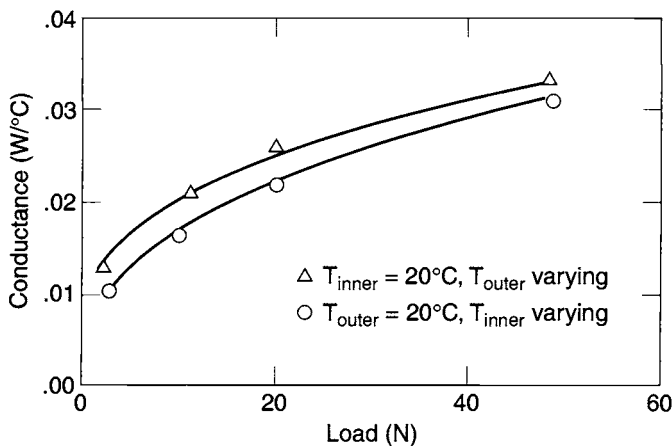
**Fig. 8.68. Mean conductance as a function of load for lead-lubricated, nonrotating 42-mm O/D bearing.**[8.94]
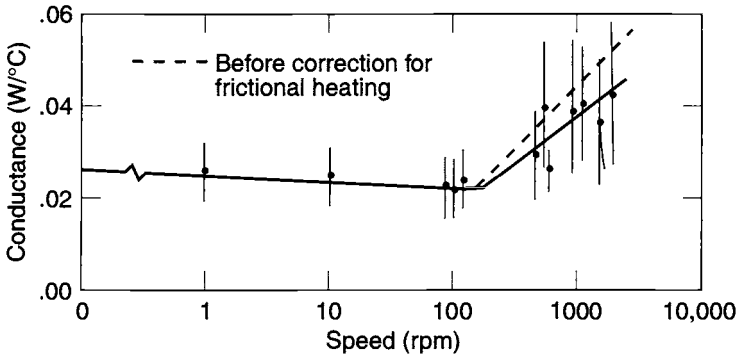
Fig. 8.69. Conductance versus speed for 42-mm O/D lead-lubricated bearing.[8.94]
**Load = 20 N; T_i = 40°C; T_o = 20°C.**
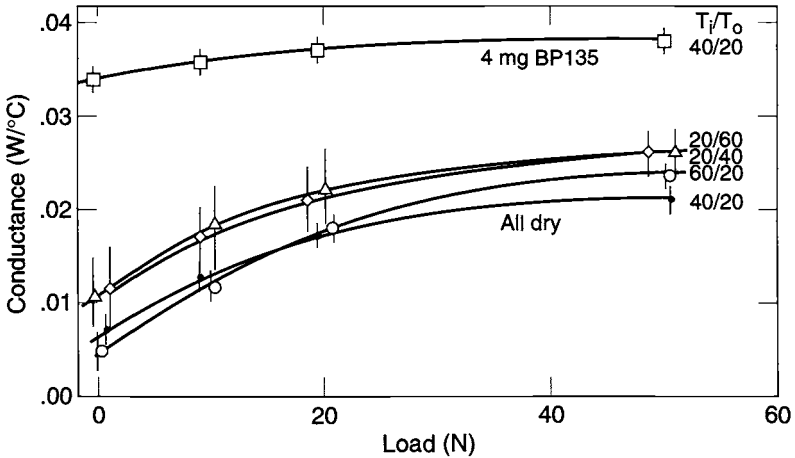
Fig. 8.70. Conductance as a function of load for nonrotating 16-mm O/D bearing.[8.94]

data for a particular set of bearings,[8.94] which illustrate the considerable effect of some of these factors on bearing conductance. The reader may wish to consult Yovanovich[8.94] for additional discussions on this subject. Other reports and papers[8.95,8.96] have discussed the theoretical and experimental evaluation of the factors affecting bearing conduction.

Despite the considerable research done in this area, a generalized set of conduction values for thermal analysis involving bearings cannot be provided. The analyst has the options of performing tests[8.94–8.96] to measure the conductivities of the bearings in question, or bounding the problem by looking at a wide range of conductance values. Any test must accurately simulate the lubrication, load, speed, vacuum-temperature ranges, and gradients expected in flight, while ensuring that

any gravity effects are accounted for. If a bounding analysis is conducted, a suitably wide range of conductances must be considered, e.g., from zero to a fairly high contact conductance across the entire area of the races. If the analysis shows a considerable sensitivity to bearing conductance, test measurements on the bearings early in the program are recommended. Do not rely on system-level thermal tests that may not provide the right conditions and that will usually occur too late in the program for practical design changes.

Classical Contact-Conductance References from the Former USSR

Considerable work was performed in the former USSR in the field of contact-conductance heat transfer. Two references are particularly useful.[8.97,8.98] Popov[8.97] presents a survey of experimental and theoretical work on contact heat exchange, with description of physical and mechanical interaction in the contacting zone of solid bodies. A special chapter of the work is devoted to analysis of contact heat exchange for flat surfaces, for surfaces with waviness and macroroughness, and for surfaces in contact at high static pressure loading (109 literature sources). The author depicts methods of experimental study of thermal contact and includes a section with original data. The essential part of the book is devoted to analysis of experimental data for contact of flat surfaces under initial and sequent loading; nonsteady heat transfer; and the influences of waviness, roughness, time of loading, and oxide layer. Also contained within are recommendations for regulating contact conductance (in particular, with the use of glues) and practical examples of technical solutions.

Shlykov *et al.*[8.98] analyze steady and unsteady methods of thermal-contact experimentation. They present a vast survey of experimental and theoretical works on contact heat exchange (175 sources) including heat contact transfer in nuclear technology, energy converters, cryogenic technology, and electronics. One chapter of this work presents a theoretical model of contact conductance with different boundary conditions. The correlations obtained have been adapted to conditions of real contact: contact of rough bodies, conductivity via gas gap, and conductivity in the contact zone. The authors have proposed a generalized equation for contact heat exchange that complies well with experiments.

Nomenclature

a	contact radius; outer radius in Roca and Mikic mechanical model; heat-flux radius at top of doubler, Gluck and Young (m)
A	area (m^2)
A_b	area of contact region near bolt or screw (m^2)
A_N	area divided by number of bolts or screws (m^2)
b	component radius; doubler radius, Gluck and Young (m)
C	conductance (W/K)
C_b	bolt region conductance (W/K)
CCD	charge-coupled device
CTE	coefficient of thermal expansion (K^{-1})

d	height of waviness represented as spherical crown; gas gap between parallel plates; distance between bolt centers (m)
d^*	normalized distance between bolt centers, $d^* = d/(2r_O)$
D_s	bolt-shaft diameter (m)
DLR	Deutsches Zentrum für Luft- und Raumfahrt e.V. /German Aerospace Center
E	elastic modulus; effective elastic modulus, Roca and Mikic (N/m^2)
E'	effective elastic modulus (N/m^2), $E' = [(1-\upsilon_1^2)/E_1 + (1-\upsilon_2^2)/E_2]^{-1}$
f	factor from Song representing Integral model of Yovanovich, $f = 0.304/[(R_p/\sigma)(1+M/R_p)] - 2.29/[(R_p/\sigma)(1+M/R_p)]^2$
F	heat flux (W/m^2)
F_O	average heat flux through doubler, Gluck and Young (W/m^2)
F_S	heat flux over radius, a, at top of doubler, Gluck and Young (W/m^2)
F^*	dimensionless heat flux, Ayres et al., $F^* = (F\beta_E R_E/k_E) (E_E/H_E) (\beta_i/\beta_o)^3 [0.5(1 + P_{amb}/P_{atm})]^2$
G	dimensionless gap resistance, $G = k_g/h_g R_p$
h	heat-transfer coefficient (W/m^2·K)
h_b	bolt region heat-transfer coefficient, Bevans et al. (W/m^2·K)
h_C	contact region heat-transfer coefficient, Roca and Mikic (W/m^2·K)
h_p	plate region heat-transfer coefficient, Bevans et al. (W/m^2·K)
h_r	linear radiation heat-transfer coefficient, Bobco and Starkovs (W/m^2·K)
h^*	dimensionless heat-transfer coefficient, Ayres et al., $h^* = h\sigma_E/k_E m_E$
H	bulk hardness (N/m^2)
H_C	microcontact hardness (N/m^2)
$H_{C,h}$	microcontact hardness, harmonic mean of fiber and matrix, Mirmira et al. (N/m^2)
H_L	macrocontact hardness (N/m^2)
I	geometric term, Bevans et al., $I = \eta_O^2 - \eta_O^4/4 - ln(\eta_O) - 3/4$
k	thermal conductivity; harmonic-mean thermal conductivity, Roca and Mikic (W/m·K)
k_h	harmonic-mean thermal conductivity (W/m·K), $k_h = 2k_1k_2/(1/k_1 + 1/k_2)$
k_S	harmonic-mean thermal conductivity, Cooper-Mikic-Yovanovich model (W/m·K)
Kn	Knudsen number, $Kn = \Lambda/d$
KPI	Kyiv Polytechnic Institute, Ukraine
l	length in x direction, Bobco and Starkovs (m)
L	length; doubler height, Gluck and Young (m)
m	combined mean absolute profile slope (m/m), $m = (m_1^2 + m_2^2)^{1/2}$
M	gas parameter (m), $M = [(2 - TAC_1)/TAC_1 + (2 - TAC_2)/TAC_2] \times [2\gamma/(\gamma + 1)][1/Pr]$
M^*	gas rarefaction parameter, $M^* = M/Rp$
N	bolted plate contact parameter
NTUU	National Technical University of Ukraine
p	pressure (N/m^2)
P	uniform or apparent pressure; applied pressure, Roca and Mikic (N/m^2)

P_{amb}	local pressure, e.g., vacuum, Ayres *et al.* (N/m^2)
P_{atm}	atmospheric pressure at sea level, Ayres *et al.* (N/m^2)
PSA	pressure-sensitive adhesive
Pr	Prandtl number
q, Q	heat flow rate (W)
q	heat flux, Bobco and Starkovs (W/m^2)
q_o	thermal doubler heat flux, Bobco and Starkovs (W/m^2)
r	radial coordinate (m)
r_C	radius of contact region (m)
r_O	radius of applied load (m)
R	outer radius, Roca and Mikic, Bevans *et al.* (m)
R	thermal resistance, Roca and Mikic (Km^2/W)
R	thermal resistance, Compliant Interfaces-flexible braid (K/W)
R_o	radius of contact region near bolt, Bevans *et al.* (m)
R_P	maximum peak height of the rougher surface of the plate pair in contact, Song (m)
RTV	room-temperature vulcanized
s	rms roughness, Cooper-Mikic-Yovanovich model (m)
s/m	rms roughness divided by asperity slope, Cooper-Mikic-Yovanovich model (μm)
t	thickness; thickness of plate (m)
t_t	thickness of thinnest of two plates in contact (m)
T	temperature (K)
T_i	boundary-condition sink temperature, Roca and Mikic (K)
TAC	thermal-accommodation coefficient
TIR	total included reading, i.e., flatness deviation (m), $TIR = TIR_1 + TIR_2$
T_o	baseplate temperature, Gluck and Young (K)
T_∞	equivalent sink temperature, Bobco and Starkovs (K)
V_f	volume fraction of fiber
w, W	width (m)
x	coordinate (m)
y	coordinate (m)
Y	effective gap thickness (m)
z, Z	vertical coordinate (m)
a	coefficient of thermal expansion
b	Biot-like group, $\beta = k/hb$, Gluck and Young
g	deformation mode parameter, $\gamma = H_c/(E'm)$; ratio of specific heats
d	ratio of heat-source radius to doubler radius, $\delta = a/b$, Gluck and Young
δ_O	thermal doubler thickness, Bobco and Starkovs, (m)
h	dimensionless radius, Bevans *et al.*, $\eta = r/R$
η	coefficient relating the real heat-transfer length of threads with *L*, Compliant Interfaces section
η_O	dimensionless radius at end of contact region, Bevans *et al.*, $\eta_O = R_O/R$
L	molecular mean free path (m)

u	Poisson ratio
σ	combined root mean square (rms) roughness (m), $\sigma = (\sigma_1{}^2 + \sigma_2{}^2)^{1/2}$
σ_z	normal stress, Roca and Mikic (N/m^2)
t	torque (N·m)
f	temperature difference, $T - T_o$, Gluck and Young (K)
y	dimensionless temperature difference, $k\phi/(2aF_s)$, Gluck and Young

Superscripts

| ' | effective |

Subscripts

al	aluminum
b	bolt
C	contact
e	elastic
E	effective, Ayres *et al.*
g	gas
h	harmonic mean
i	inside
L	large-scale, macroscopic
m	arithmetic mean
o	outside
p	plastic, plate
ss	stainless steel
S	small-scale, microscopic
1	surface or plate 1
2	surface or plate 2

References

8.1. A. N. Tabenkin, "Use Surface Finish to Get Optimum Production," *Modern Machine Shop* **62**, 52–62 (February 1990).

8.2. M. A. Lambert and L. S. Fletcher, "A Correlation for the Thermal Contact Conductance of Metallic Coated Metals," AIAA 93-2778, presented at the *AIAA 28th Thermophysics Conference* (July 1993).

8.3. M. B. H. Mantelli and M. M. Yovanovich, "Thermal Contact Resistance," Chapter 16 in *Spacecraft Thermal Control Handbook*, 2nd ed., edited by D. G. Gilmore (The Aerospace Press, El Segundo, California, 2002).

8.4. M. G. Cooper, B. B. Mikic, and M. M. Yovanovich, "Thermal Contact Conductance," *Int. J. Heat Mass Transfer* **12**, 279–300 (1969).

8.5. B. B. Mikic, "Analytic Studies of Contact of Nominally Flat Surfaces; Effect of Previous Loading," ASME Paper 71-Lub-M, 1971.

8.6. B. B. Mikic, "Thermal Contact Conductance: Theoretical Considerations," *Int. J. Heat Mass Transfer* **17**, 205–214 (1974).

8.7. M. A. Lambert and L. S. Fletcher, "Review of Models for Thermal Contact Conductance of Metals," *AIAA Journal of Thermophysics and Heat Transfer* **11** (2), 129–140 (April–June 1997).

8.8. A. A. Hegazy, "Thermal Joint Conductance of Conforming Rough Surfaces," Ph. D. thesis, University of Waterloo, Waterloo, ON, Canada, 1985.

8.9. S. Song and M. M. Yovanovich, "Relative Contact Pressure: Dependence on Surface Roughness and Vickers Microhardness," *AIAA Journal of Thermophysics and Heat Transfer* **2** (1), 43–47 (January 1988).

8.10. M. R. Sridhar and M. M. Yovanovich, "Elastoplastic Contact Conductance Model for Isotropic Conforming Rough Surfaces and Comparison with Experiments," Thermal Phenomena at Molecular and Microscales and in Cryogenic Infrared Detectors, *ASME HTD* **277**, 43–56 (1994).

8.11. A. M. Clausing and B. T. Chao, "Thermal Contact Resistance in a Vacuum Environment," *Journal of Heat Transfer* **87** (3), 243–251 (May 1965).

8.12. H. R. Hertz, *Miscellaneous Papers*, English translation (MacMillan and Co., London, 1896).

8.13. M. A. Lambert and L. S. Fletcher, "Thermal Contact Conductance of Spherical, Rough Metals," HTD-Vol. 327, *National Heat Transfer Conference*, Vol. 5, ASME (1996), pp. 169–175.

8.14. M. A. Lambert and L. S. Fletcher, "Thermal Contact Conductance of Spherical, Rough Metals," ASME Transactions, *Journal of Heat Transfer* **119** (4), 684–690 (November 1997).

8.15. G. S. Springer, "Heat Transfer in Rarefied Gases," in *Advances in Heat Transfer*, Vol. 7, edited by T. F. Irvine and J. P. Hartnett (Academic Press, New York, 1971) pp. 163–218.

8.16. S. Song, M. M. Yovanovich, and F. O. Goodman, "Thermal Gap Conductance of Conforming Surfaces in Contact, Part I: Theory," *10th Symposium on Thermophysical Properties* (Gaithersburg, MD, 20–23 June 1988).

8.17. S. Song and M. M. Yovanovich, "Thermal Gap Conductance of Conforming Surfaces in Contact, Part II: Experimental Results," *10th Symposium on Thermophysical Properties* (Gaithersburg, MD, 20–23 June 1988).

8.18. S. Song, M. M. Yovanovich, and K. Nho, "Thermal Gap Conductance: Effect of Gas Pressure and Mechanical Load," AIAA-89-0429, 1989.

8.19. P. J. Schneider, "Conduction" in *Handbook of Heat Transfer*, edited by W. M. Rohsenow and J. P. Hartnett (McGraw-Hill, New York, 1973).

8.20. E. Fried and F. A. Costello, "Interface Thermal Contact Resistance Problem in Space Vehicles," *ARS Journal* **32**, 237–24 (1962).

8.21. M. E. Barzelay *et al.*, "Effect of Pressure on Thermal Conductance of Contact Joints," NACA TN 3295, Washington, D. C., 1955.

8.22. E. Fried, "Study of Interface Thermal Contact Conductance," General Electric Co. 64SD652, May 1964 (also ARS Paper No. 1690-61, April 1961).

8.23. H. Fenech and W. H. Rohsenow, "Prediction of Thermal Conductance of Metallic Surfaces in Contact," *J. Heat Transfer, Trans. ASME* **85,** 15–24 (1963).

8.24. C. Swartz, "Thermal Conductance in Aluminum Bolted Joints," The Aerospace Corporation ATM 82(9975)-29, 19 January 1982.

8.25. E. Fried and M. J. Kelley, "Thermal Conductance of Metallic Contacts in a Vacuum" in *Thermophysics and Temperature Control*, edited by G. Heller (Academic Press, New York, 1966).

8.26. E. Fried and H. L. Atkins, "Thermal Joint Conductance in Vacuum," ASME Paper 63-AHGT-18, 1963.

8.27. S. Timoshenko and J. N. Goodier, *Theory of Elasticity*, 2nd ed. (McGraw-Hill, New York, 1951).

8.28. R. T. Roca and R. E. Mikic, "Thermal Contact Resistance in a Non-Ideal Joint," Massachusetts Institute of Technology, Report No. DSR 71821-77, Nov. 1971.

8.29. R. T. Roca and R. E. Mikic, "Thermal Conductance in a Bolted Joint," AIAA Paper No. 72-282, April 1972.

8.30. I. Fernlund, "A Method to Calculate the Pressure Between Bolted or Riveted Plates," Report No. 17, Chalmers University of Technology, Gothenberg, Sweden, 1961.

8.31. J. A. Greenwood, "The Elastic Stresses Produced in the Mid-Plane of a Slab by Pressures Applied Symmetrically at its Surface," *Proc. Camb. Phil. Soc.* **60**, 159–169 (1964).

8.32. E. H. Coker and L. N. G. Filon, *A Treatise on Photo-Elasticity*, 2nd ed. (Cambridge University Press, Cambridge, 1957).

8.33. W. Aron and G. Colombo, "Controlling Factors of Thermal Conductance across Bolted Joints in a Vacuum Environment," ASME Paper 63-WA-196, 1963.

8.34. H. H. Gould and B. B. Mikic, "Areas of Contact and Pressure Distribution in Bolted Joints," M.I.T. Heat Transfer Report DSR 71821-68, June 1970.

8.35. J. T. Bevans, T. Ishimoto, B. R. Loya, and E. E. Luedke, "Prediction of Space Vehicle Thermal Characteristics," Air Force Flight Dynamic Laboratory Technical Report AFFDL-TR-65-139, August 1965.

8.36. Anon., "Thermal Environments," in TRW, Inc. Project MILSTAR Engineering Design Standards, Section 2.2, March 1984.

8.37. G. D. Rhoads, informal data transmittal, 1990.

8.38. E. Veilleux and M. Mark, "Thermal Resistance of Bolted of Screwed Metal Joints in Vacuum," *J. Spacecraft* **6** (3) (March 1969).

8.39. C. A. Baumgartner to R. L. MacGregor, "Interface Resistance—Aluminum to Aluminum Test Report Project ROARS," TRW Inc. interoffice correspondence 7415.1-467, June 1969.

8.40. P. F. Taylor to W. A. Hagemeyer, Jr., "TWT Collector Thermal Interface Test," Hughes Inc. interdepartmental correspondence 72261/0042, December 1985.

8.41. J. W. Welch and L. E. Ruttner, "An Experimental and Computational Analysis of the Thermal Interface Filler Material Calgraph," Paper AIAA-89-1658 presented at the *AIAA 24th Thermophysics Conference* (June 1989).

8.42. T. F. Bratkovich, "Correlations for Contact Region Bolted Joint Conductance in Vacuum," The Aerospace Corporation, ATM No. 91(9975)-15, 10 April 1991.

8.43. M. B. H. Mantelli and M. M. Yovanovich, "Experimental Determination of the Overall Thermal Resistance of Satellite Bolted Joints," Paper AIAA 94-0123 presented at *32nd Aerospace Sciences Meeting and Exhibit* (January 1994).

8.44. M. B. H. Mantelli and C. J. Goncalves, "Thermal Resistance of Parallel Plate-Washer Bolted Joints: Model and Experimental Verification" Paper AIAA 99-3489 presented at *33rd Thermophysics Conference* (June–July 1999).

8.45. L. S. Fletcher, P. A. Smuda, and D. A. Gyorog, "Thermal Contact Resistance of Selected Low-Conductance Interstitial Materials," *AIAA Journal* **7** (7), 1302–1309 (1969).

8.46. P. Brennan and E. Kroliczek, NASA Report N81-70113, Heat Pipe Design Handbook, National Aeronautics and Space Administration, Goddard Space Flight Center, June 1979.

8.47. F. Lura, B. Biering, and V. Baturkin, "Heat Pipe Application for Thermal Stable Bench Arrangement in Small Satellite Design," Rep. No. 2000-01-2460, *Proceedings of the 30th Int. Conference on Environmental Systems (ICES)* and *7th European Symposium on Space Environmental Control Systems* (Toulouse, France, 10–13 July 2000).

8.48. V. Baturkin and D. Olefirenko, "Research on Axially Grooved Heat Pipe Heat Transfer Characteristics in Ground Tests," Rep. No. 2001-01-2237, *Proceedings of the 31th Int. Conference on Environmental Systems (ICES)* (Orlando, 9–12 July 2001).

8.49. B. Lehmann, B. Biering, V. Baturkin, *et al.*, "Cooling of Electronic Unit Elements with Application of Heat Pipes," *Proceedings of the Int. Symposium on Heat Pipe Research and Application*, Japan Association for Heat Pipes (Shanghai, China, 24–27 April 1991), pp.192–197.

8.50. M. G. Semena., V. M. Baturkin, N. K. Gretchina, *et al.*, "Working Out of the Cryogenic Cooling System on the Base of Heat Pipes for VEGA Television Camera," Paper N 1072 presented at Space Research Institute of USSR AS, 1986.

8.51. F. Lura, B. Biering, *et al.*, "TCS Design of the Microsatellite BIRD for Infrared Earth Observation," Rep. No. 981639, *Proceedings of the 28th Int. Conference on Environmental Systems* (Danvers, MA, 13–16 July 1998).

8.52. V. Baturkin and K. Shkoda, "Heat Transfer in Zones of Heat Supply and Removal of Heat Pipes," *Proceedings of the Int. Symposium on Heat Pipe Research and Application*, Japan Association for Heat Pipes (Shanghai, China, 24–27 April 1991), pp. 89–95.

8.53. V. Baturkin V., L. Bondar, and K. Shkoda, "Thermal Regimes Simulation of Ramified Heat Pipes Communications by Finite Element Method," Rep. No. 951553, *Proc. of 25th International Conference on Environmental Systems* (San Diego, CA, 10–13 July 1995).

8.54. D. Gluck, C. Gerhart, and S. Stanley, "Characterization of a High Capacity, Dual Compensation Chamber Loop Heat Pipe," presented at *Space Tech. & Applications International Forum (STAIF-99)* (Albuquerque, NM, Jan.–Feb., 1999).

8.55. G. H. Ayers, L. S. Fletcher, and C. V. Madhusudana, "Thermal Contact Conductance of Composite Cylinders," *Journal of Thermophysics and Heat Transfer* **11** (1), 72–81 (January–March 1997).

8.56. R. P. Bobco and R. P. Starkovs, "Rectangular Thermal Doublers of Uniform Thickness," *AIAA Journal* **23** (12), 1970–1977 (December 1985).

8.57. R. P. Starkovs, "Rectangular Thermal Doublers with Two Heated Footprints," AIAA-87-1612, June 1987.

8.58. R. P. Bobco, "Thermal Doublers: Closed Form Solution for Three Single Terrace Categories and a Partial Double Terrace," Hughes Aircraft, Space and Communications Report 4132.15/2594, 25 January 1984.

8.59. D. F. Gluck and P. H. Young, "Performance and Optimization of an Axisymetric Thermal Doubler," *Proceedings, 1988 Summer Computer Simulation Conference* (Seattle, WA, 25–28 July 1988).

8.60. M. Ryals, technical brief: "Graphite Fiber Reinforced Al and Cu Alloys for Thermal Management Application," *Electronic Cooling* 5 (1), 42 (January 1999).

8.61. C. Zweben, "High Performance Thermal Management Materials," *Electronic Cooling* 5 (3), 36–42 (September 1999).

8.62. Carbon Base Heat Spreaders, On website: http://www.enertron-inc.com (2001).

8.63. Thermal Management Materials, On website: http://www.advceramics.com (2001).

8.64. M. Montesano. "Thermal Management for Advance 3D Packaging of Payload Electronics," *11th Spacecraft Thermal Control Technology Workshop*, The Aerospace Corporation (El Segundo, CA, 1–3 March 2000).

8.65. V. Baturkin, K. Shkoda, N. Gudkova, *et al.*, "Study of Thermal Performance of Isothermal Electronic Plate with Regulated Temperature," In *Digest: Design and Technology of Manufacture of Space Apparatus* (Nauka Publisher, Moscow, 1988), pp. 92–105.

8.66. Integrated Plate Heat Pipe. Technical note by Showa Aluminum Corp., Japan, 1999.

8.67. V. Baturkin, S. Zhuik, N. Grechina, *et al.*, Rep. No. 961603, "Working out of Heat Pipes for Low Temperature Radiative Cooling Systems for Space Optic Sensors," *Proc. of 26th International Conference on Environmental Systems* (Monterey, CA, 8–11 July 1996).

8.68. W. C. Layton, "Traveling Wave Tube Thermal/Structural Study," Report No. TOR-0088(9975)-1, The Aerospace Corporation, 1 August 1988.

8.69. E. H. Goit, "Third Degree Integration Formulas with Four Points in Two Dimensions," M. S. thesis, State University of New York at Buffalo, February 1969.

8.70. J. W. Welch and B. T. Hamada, "Calculation of Heat Transfer Coefficients Across an Electronic Box Bare Interface Using a Finite Element Approach," presented at *26th Int. Conf. on Envir. Sys.* (Monterey, CA, July 1996).

8.71. S. Bogdanov, O. Ivanov, A. Kuprianova, "Material Properties," in *Refrigeration Engineering Handbook*, 3rd ed. (Agropromizdat, Moscow, 1985), p. 208.

8.72. *Satellite Thermal Control Handbook*, 1st ed., edited by D. G. Gilmore (The Aerospace Press, El Segundo, California, 1994).

8.73. L. Novitskiy and I. Kozhevnikov, *Thermal Properties of Materials at Low Temperatures Handbook* (Mashinostroenie, Moscow, 1975) 216 pages.

8.74. K. Buesking and B. Sullivan (MSNW, Inc.) "Composite Properties for Thermal-Structural Materials Solutions for Spacecraft," Prepared for Lockheed-Martin Missiles and Space Division, Feb. 1996.

8.75. G. Avanesov, Y. Ziman, V. Tarnopolsky, *et al.*, TV Survey of Comet Halley (Nauka, Moscow, 1989).

8.76. V. M. Baturkin and N. K. Gretchina, "Investigation of Thermocontrol Behavior of the Cooling System Based on Heat Pipes with Thermodiode Properties," Report N 922-Uk-89, 31.03, Deposited in Ukrainian Scientific Information Institute, Kyiv (1989).

8.77. I. Walter, F. Schrandt, and U. Grote, "Konstruktion und Technologie eines Optoelektronischen Weitwinkelscanners fur den Tiefraumeinsatz – WAOSS," Report Jt98_117 in Jahrbuch der Deutschen Gesellschaft für Luft- und Raumfahrt (Lilienthal-Oberth e.V., DGLR, 1998).

8.78. G. Neucum, R. Jaumann, H. Hoffmann, *et al.*, "A High Resolution Space Camera (HRSC) for Earth Observation in Regional Scales," *Proceedings of ESA Symposium on Space Station Utilization*, SP-385 (Darmstadt, Germany, December 1996), pp. 609–614.

8.79. M. de Sorga, "Thermal Interface Materials," *Electronic Cooling* **2** (3) (September 1996).

8.80. Sil-Pad Design Guide, Rev.030397, The Bergquest Company, 1997–1998.

8.81. C. L. Seaman and T. R. Knowles, "Carbon Velvet Thermal Interface Gaskets," Paper AIAA-2001-0217, presented at the *AIAA Aerospace Sciences Meeting* (Reno, NV, 8–11 January 2001).

8.82. *Spacecraft System Engineering*, P. Fortescue and J. Stark, eds. (John Wiley & Sons Ltd., 1995), p. 242.

8.83. Technical information on http://www.ensinger-online.com, 2001.

8.84. ASM Committee, "High-Strength Medium-Temperature Thermoset Matrix Composite," in *Composites, Engineered Materials Handbook*, Vol. 1 (ASM International, Metals Park, OH, 1987), pp. 399-415.

8.85. V. M. Baturkin, N. K. Grechina, V. I. Kostenko, *et al.*, "Cryogenic System for the Videospectrometric Complex (VSC) Cooling in Project 'FOBOS'," Paper Pr-1409 presented at Space Research Institute AS USSR, 1988.

8.86. Anon., "Weitwinkel Stereoscanner WAOSS fur die Mission Mars 96," Deutsche Hochschulschriften 1146, Deutsches Zentrum fur Luft- und Raumfahrt e.V., 1998, pp. 222–223.

8.87. G. Neukum, U. Carsenty, K. Eichentopf, *et al.*, "The Experiments HRSC and WAOSS on the Russian MARS 94/96 Missions," *Acta Astronautica* **38** (9), 713–720 (1996).

8.88. A. Zaglauer, W. Pitz, "Champ—the First Flexbus in Orbit," Digest of the 3rd Int. Symposium (Small Satellite for Earth Observation) of the Int. Academy of Astronautics, Berlin, 2–6 April 2001, edited by H. P. Roser, R. Sandau, A. Valenzuella (Wissenschaft und Technic Verl., Berlin, 2001) pp.105–109.

8.89. M. Rhoads and W. Moses, "Thermal Contact Conductance between Aligned Unidirectional Carbon/Epoxy Resin Composites," Paper AIAA 90-0540, presented at the *28th Aerospace Sciences Meeting* (January 1990).

8.90. S. R. Mirmira, M. C. Jackson, and L. S. Fletcher, "Effective Thermal Conductivity and Thermal Contact Conductance of Graphite Fiber Composites," *J. Thermophysics* **15** (1), 18–26 (2001).

8.91. S. R. Mirmira and L. S. Fletcher, "Comparison of Effective Thermal Conductivity and Contact Conductance of Fibrous Composites," *J. Thermophysics* **13** (2), 272–276 (1999).

8.92. E. E. Marotta and L. S. Fletcher, "Thermal Contact Conductance of Selected Polymeric Materials," *J. Thermophysics* **10** (2), 334–342 (1996).

8.93. M. A. Lambert and L. S. Fletcher, "Experimental Thermal Contact Conductance of Continuous Fiber Metal Matrix Composites," Paper AIAA 94-0122, presented at the *32nd Aerospace Sciences Meeting* (January 1994).

8.94. M. Yovanovich, "Analytical and Experimental Investigation on the Thermal Resistance of Angular Contact Instrument Bearings," Report No. E-2215, MIT Instrumentation Laboratory, December 1967.

8.95. H. J. Deacon, "Thermal Conductance of ASAT Bearing," The Aerospace Corporation, ATM 87(2426-02)-3, 20 November 1986.

8.96. K. T. Stevens and M. J. Todd, "Thermal Conductance Across Ball Bearings in Vacuum," European Space Tribology Laboratory, Report No. ESA (ESTL), 25 February 1977.

8.97. V. Popov, *Heat Exchange in Zone of Contact of Split and Nondetachable Connections* (ENERGIYA, Moscow, 1971).

8.98. Y. Shlykov, E. Ganin, and S. Zarevsky, *Contact Thermal Resistance* (ENERGIYA, Moscow, 1977).

9 Louvers

B. E. Hardt,[*] R. D. Karam,[†] and R. J. Eby[†]

Introduction

Louvers are active thermal-control elements that have been used in different forms on numerous spacecraft. While most commonly placed over external radiators, louvers may also be used to modulate heat transfer between internal spacecraft surfaces, or from internal surfaces directly to space through openings in the spacecraft wall.

In general, a louver in its fully open state can reject six times as much heat as it does in its fully closed state, with no power being required to operate it. Thus louvers find application where internal power dissipation varies rather widely as a result of equipment duty cycles. The most commonly used louver assembly is the bimetallic, spring-actuated, rectangular-blade (venetian-blind) type. Hydraulically activated louvers and pinwheel louvers are used less often today than in the past.

Louver reliability can be improved at the design stage by making each louver blade independently actuated by a bimetallic clock spring. Thus a single-point failure is associated with one blade, not the entire assembly. The spring can be integrated with a heater/controller to decrease the passive closed-to-open temperature range of 10–17°C to as little as 1°C.

Louver radiator assemblies (illustrated in Fig. 9.1) consist of five main elements: baseplate, blades, actuators, sensing elements, and structural elements. The baseplate is a surface of low absorptance-to-emittance ratio that covers the critical set of components whose temperature is being controlled. Blades, which are driven by the actuators, are the louver elements that give variable-radiation characteristics to the baseplate. While closed, louvers shield and decouple the baseplate from the surroundings, but while open, they allow a radiative coupling between the baseplate and the surroundings. The radiation characteristics of the baseplate can be varied over the range defined by these two extreme positions.

The actuators drive the blades according to the perceived baseplate temperature. Actuators of louvers flown on satellites have been bimetallic spirals or bellows, although other types of actuators could be used, such as Bourdon spirals and electrical devices. In a single-actuation system, all the blades are driven by a single actuator. In a multiple-actuation system, several actuators are required. Generally, bimetallic devices are used as actuators in multiple-actuation systems, and bellows in single-actuation systems.

The actuator drives the blade angle as determined by the baseplate temperature. A strong conductive path between the actuator and baseplate is therefore sought to minimize the temperature gradient between them. The thermal coupling between a bimetallic actuator and baseplate is composed of both radiative and conductive paths. Bellows and Bourdon actuators use a tank or tube containing liquid or both

---

*The Aerospace Corporation, El Segundo, California.
†Orbital Sciences Corporation, Dulles, Virginia.
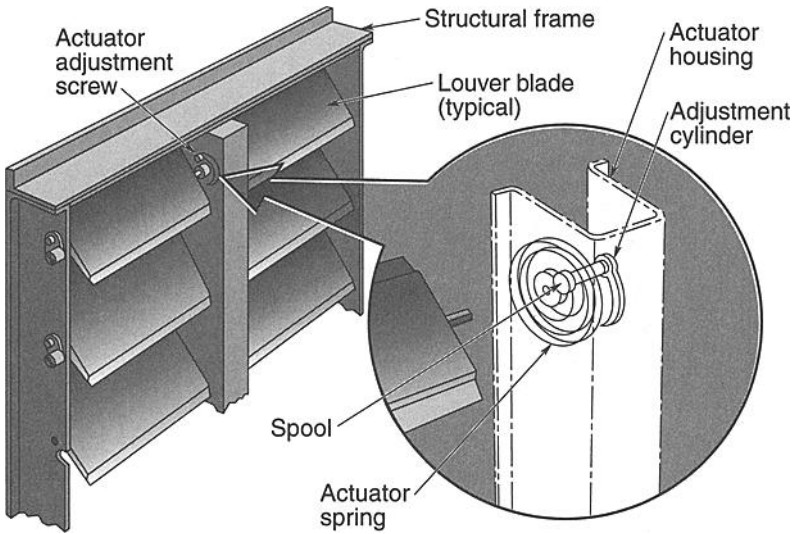
Fig. 9.1. Orbital Sciences louver assembly schematic.

liquid and vapor to actuate the blades. The tank or tube is typically soldered to the baseplate to ensure a strong conductive coupling.

Louver assemblies have been designed for operation in both shadow and sunlight. Two design approaches that have been followed for operation in sunlight are the use of a sun shield and the modification of the louver assembly for high temperature operation.

Vane Louvers

As noted earlier, the most widely used louver assembly is the bimetallic, spring-actuated, rectangular-blade type, known as "venetian-blind" or "vane" louvers. The arrangement of actuators, housing, blades, and structure for a vane louver assembly is shown schematically in Fig. 9.1. Design features vary depending on whether the assembly is to be exposed to solar illumination and whether actuation is to be provided by a bimetallic spring alone or by a bimetallic spring in conjunction with a heater/controller, as well as according to supplier-specific differences. Current principal suppliers are Orbital Sciences Corporation, Swales Aerospace, and Starsys. Characteristics of flight-qualified rectangular-blade louver assemblies are listed in Table 9.1.

In most designs, blade rotation is effected by the expansion or contraction of a spiral bimetallic actuator, by virtue of heat gained or lost in exchange with the equipment-mounting plate (Fig. 9.2). One end of the actuator is attached to the frame structure and the other to the Teflon spool. A square cutout in the spool supports the inboard louver-blade end. The actuator is coated black in order to enhance radiative interchange. The conduction path is through the aluminum housing. The actuator is adjusted relative to the frame to obtain the desired temperature

Table 9.1. Characteristics of Flight-Qualified Rectangular-Blade Louver Assemblies[a]

	OSC	Swales	Starsys
Blades	3 to 42		1 to 16
Open set points (°C)		0 to 40	–20 to 50
Open/close differential (°C)	10 or 18	10 or 18	14
Dimensions (cm)			
Length	20 to 110	27 to 80	8 to 43
Width	36 to 61	30 to 60	22 to 40
Height		6.4	6.4
Area (m^2)	0.07 to 0.6	0.08 to 0.5	0.02 to 0.2
Weight/area (kg/m^2)[b]	3.2 to 5.4	~ 4.5	5.2 to 11.6
Flight history	Nimbus, Landsat, OAO, ATS-6, Viking, GPS, SolarMax, AMPTE, SPARTAN, Hubble, Magellan, GRO, UARS, EUVE, TOPEX, GOES, MGS, MSP	XTE, Stardust	Rosetta[c], Quickbird[c] JPL:[d] Mariner, Viking, Voyager, Galileo, MLS, Magellan, TOPEX, NSCAT, Cassini, Seawinds

[a]This table contains representative values from past louver designs. Contact manufacturer for additional design possibilities or values for specific designs.
[b]Weight without sunshield.
[c]Launch to occur after date of handbook publication.
[d]The Starsys design is a slightly modified version of a JPL louver design that has flown on the indicated spacecraft.
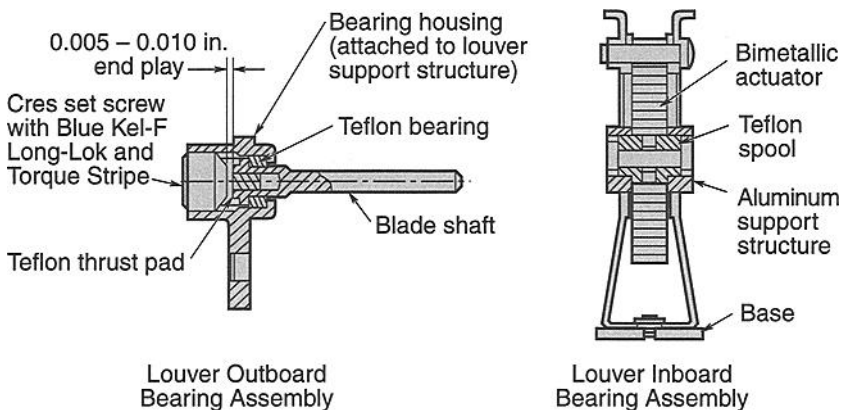
Fig. 9.2. Louver bearing assemblies.

range between fully closed and fully open positions. Each blade is supported inboard and outboard by a bearing assembly (see Fig. 9.2). Inboard, the Teflon spool bears against and rotates with respect to the aluminum support structure. The outboard end of the louver-blade shaft rotates within and is supported by a Teflon bearing, with end play established by the distance between the Teflon thrust pad and the set screw. Each louver blade consists of a central torque tube bonded to flanges. The louver-blade cross section forms a hollow, thin-walled rectangle of high aspect ratio. The blades are highly polished to reduce emittance.

Louver assemblies of the type described above have been used in satellite applications where direct solar illumination is generally avoided, such as Pegasus, the Orbiting Astronomical Observatory, NIMBUS, the Earth Resources Technology Satellite, Voyager, Seasat, and the Global Positioning System (GPS). Each louver assembly contains several independently actuated blades, so a degree of redundancy is inherent in this design approach.

An old RCA design approach employs active control of blade position though a bimetal/heater assembly (Fig. 9.3). Frame structures are used for the larger louver
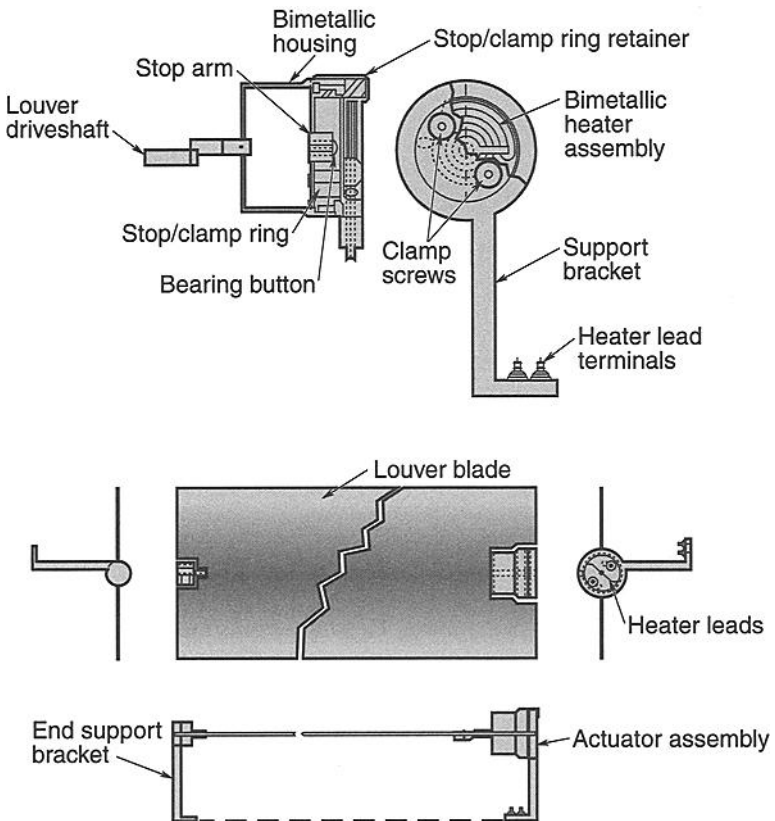
Fig. 9.3. Lockheed Martin louver assembly.

assemblies, while the smaller assemblies are frameless. In the latter case, the actu-ator and the end-support bracket are aligned and then attached to the equipment mounting plate with a foamed closeout used at the edges. The blades are sup-ported and centered inboard by the bimetal/heater assembly. The fiberglass shaft with bonded-on, ball-end pivot is supported outboard by a Delrin AF bushing in the end-support bracket. The blades, composed of a foam sandwich about the fiberglass quill, have a 1-mil, first-surface-aluminized Kapton film on each side.

The bimetal/heater assembly drives the blade from fully closed to fully open over only a 1°C temperature change. The louver begins to open passively (by con-duction from the mounting plate to the bimetallic spring) at about 10°C. This pas-sive opening provides backup if the active controller fails off. The failed-on case can be corrected by ground disabling of the heater circuit. The bearing/support system provides a load-carrying capability during ground testing and, if alignment is true, the absence of friction on-orbit.

Analysis of Vane Louvers

Heat-Transfer Characteristics

Radiation through louvers is characterized by an effective emissivity ε_{eff} and an effective absorptivity α_{eff} that satisfy the steady-state energy equation for an iso-thermal body in a solar-space environment:

$$\frac{\dot{Q}}{A} = \varepsilon_{eff}\sigma T^4 - \alpha_{eff}S, \tag{9.1}$$

where $\dot{Q}$ (W) is the net heat transfer from louvered area A (m^2), σ is the Stefan-Boltzmann constant (5.668 x 10^{-8} W/m^2·K^4), T (K) is the absolute temperature, and S (W/m^2) is the solar constant.

Effective Emissivity

Effective emissivity is the ratio of net heat transfer from a louvered surface to the radiation from an equivalent black area ($\varepsilon = 1.0$) at the same temperature but with-out louvers. When no external heat sources are present, the definition reduces to

$$\varepsilon_{eff} = \frac{\dot{Q}}{A\sigma T^4}. \tag{9.2}$$

Equation (9.2) is written in this form to express a simplified equivalence to gray-body radiation. Actual heat transfer in louvered systems involves conduction along the frame and actuator housing cover, heat loss through actuator insulation and blade shafts, and variable feedback from reflections off the specular blades. In addition, friction effects are inconsistent and generally result in nonuniformity in the blades' angular positions. Effective-emissivity test values obtained by Eq. (9.2) will inherently contain these distortions and other deviations from the values associated with a purely radiative system.

Effective-emissivity tests are conducted in a cryogenic vacuum chamber.[9.1,9.2] A louvered panel is instrumented with heaters and thermocouples; its unlouvered

back side is covered by multilayer insulation (MLI) and guard heaters. This setup practically eliminates radiation from the back and provides more accurate estimates of the amount of energy escaping through the louvers. The assembly is suspended in the chamber by low-conducting wires, and a series of steady-state temperatures are recorded corresponding to various heater power levels. Effective emissivity is calculated from the data via Eq. (9.2).

Some test results are shown in Fig. 9.4, with additional data in Table 9.2. All panels in the tests were uniformly heated and maintained nearly isothermal. The data were adjusted to account for a vacuum-chamber wall temperature higher than absolute zero (usually −190°C).

Friction effects are thought to account for the discrepancy between the values of effective emissivity obtained as equilibrium is approached from above versus the values obtained when it is approached from below, but the test points in these graphs can generally be contained within two straight lines that bound the louver's performance. A linear variation between closed and open positions is commonly assumed in thermal analysis, thus

$$\varepsilon_{\text{eff}} = \varepsilon_c (\text{constant}), T \leq T_c \tag{9.3}$$

$$\varepsilon_{\text{eff}} = \varepsilon_o - \frac{\varepsilon_o - \varepsilon_c}{1 - T_c/T_o} (1 - T_c/T_o), \, T_c \leq T \leq T_o \tag{9.4}$$

$$\varepsilon_{\text{eff}} = \varepsilon_o (\text{constant}), T \geq T_o \,, \tag{9.5}$$

Table 9.2. Louver Effective Emissivity (Test Data)

Program Louver Size (cm)	Radiator Hemispherical Emittance	ε_{eff} Open	ε_{eff} Closed	Radiator[a] ΔT (K)
ATS-6[b] 45.7 × 58.2	OSR $\varepsilon = 0.77$	0.62	0.114	18.0
ATS-6 45.7 × 58.2	Z-306 $\varepsilon = 0.88$	0.71	0.115	18.6
GPS 40.6 × 40.5	Z-306 $\varepsilon = 0.88$	0.70	0.090	18.0
Intelsat CRL[c] 62.2 × 60.5	AgTEF $\varepsilon = 0.76$	0.67	0.080	10.0
MMS Landsat-4[d] 55.6 × 108.1	Z-306 $\varepsilon = 0.88$	0.39	0.100	17.0

[a]$\Delta T = T(\text{open}) − T(\text{closed})$. In vacuum there is usually about a 2°C lag between radiator temperature and bimetallic temperature.

[b]ATS-6 has white stripes on the louver blades and a fiberglass actuator housing treated with aluminized Kapton tape (Kapton out).

[c]Counterrotating blades ATS-6 housing and blades and enlarged springs.

[d]Aluminum shield with AgTEF exterior and Z-306 painted interior.

where the subscripts o and c refer to fully open and fully closed positions. A quadratic form of this equation sometimes more accurately represents temperature dependence in the active region:

$$\varepsilon_{eff} = \varepsilon_o - \frac{\varepsilon_o - \varepsilon_c}{(1 - T_c/T_o)^2} (1 - T/T_o)^2, \, T_c \leq T \leq T_o \qquad (9.6)$$

Analysis shows variations that can be represented by segments of sine or cosine curves.[9.3,9.4] This variation is an expected result of the idealized mathematical models that incorporate assumptions of infinite blade length and heat transfer only by radiation. Under those assumptions, effective emissivity varies almost linearly with projected open area, which is a trigonometric function of blade angle.

Equation (9.2) is also used to calculate from test data the effective emissivity of a shielded louver, F_ε. Theoretically, F_ε is related to ε_{eff} (effective emissivity of a louver without a shield) by the equation

$$F_\varepsilon = \frac{\varepsilon_i \varepsilon_{eff}}{1 + \frac{\varepsilon_{eff} \varepsilon_i}{\varepsilon_e}} \qquad (9.7)$$

where ε_i and ε_e are internal (facing the louver) and external emissivities of the shield. Since test values include conduction and other forms of heat loss, they are found to be slightly higher than the theoretical values obtained via Eq. (9.5).
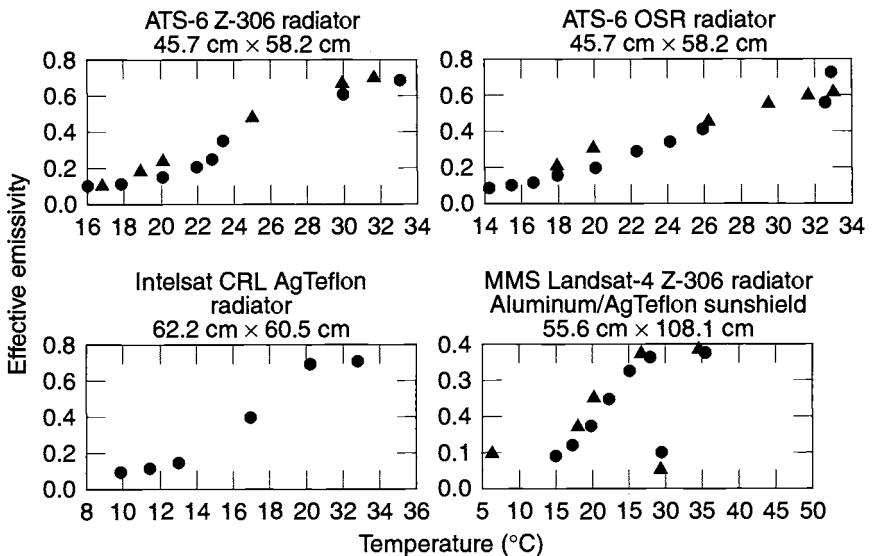
Fig. 9.4. The variation of louvers' effective emissivity with temperature (test data).

Effective Absorptivity

Effective solar absorptivity of a louvered panel may be defined as the fraction of incident solar energy absorbed per unit area of a louvered surface. The definition appears in Eq. (9.1) as

$$\alpha_{eff} = \frac{\varepsilon_{eff}\sigma T^4 - \dot{Q}/A}{S} \tag{9.8}$$

where, again, $\dot{Q}$ is actual net heat loss by a louvered surface having area A. The impinging solar flux S (nominally 1350 W/m^2 in Earth orbit) is not modified by the direction cosines, so the values of α_{eff} inherently contain the effects of solar multireflection off specular components.

Equation (9.6) is used to obtain the effective absorptivity by testing. The test configuration used for finding ε_{eff} is modified to include a sun simulator and a means of varying the angle of incidence. A detailed description of a typical facility is given in Michalek, Stipandic, and Coyle.[9.1]

Few solar-simulation tests have been performed on louvers to date, and published data remain scanty. The results of tests on two early versions of the type eventually used in the ATS-6 program are reported in Michalek, Stipandic, and Coyle.[9.1] These units, however, did not have many of the design features later added to enhance thermal performance, and the results differ somewhat from those obtained with later louvers. Data from two sets of louvers that represent current designs are given in Fig. 9.5. The effective absorptivity was calculated using Eq. (9.6), with effective emissivity (as a function of fixed-blade angle) already known from tests without solar input. The tests were conducted in solar-simulation chambers using xenon compact-arc-type lamps with a beam half-angle collimation of less than 1.5 deg. The mounting radiators were uniformly heated and
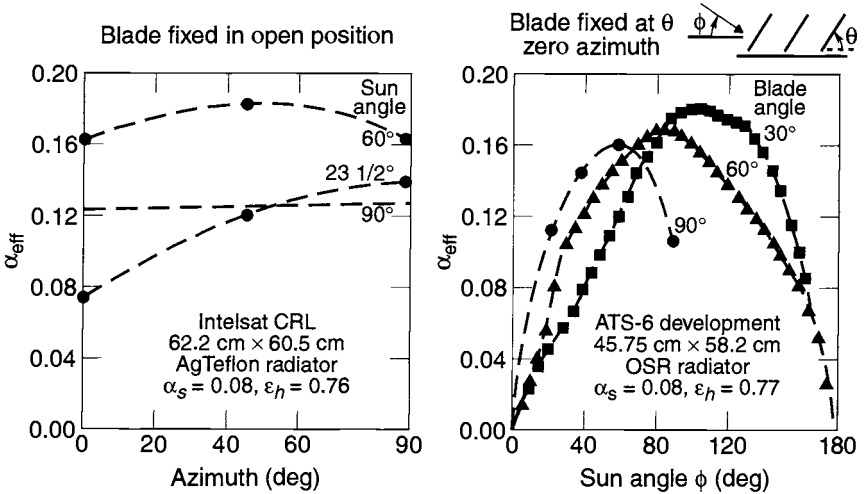
Fig. 9.5. Louver effective solar absorptivity variation with azimuth and blade angle (test data).

were sufficiently conductive (1.27-cm-thick aluminum) to limit lateral gradients to less than 2°C. All data were obtained shortly after application of radiator coating and hence are undegraded values. For long-term performance evaluation, and at least for fully open louvers, the practice has been to increase the values of ε_{eff} by the ratio of the radiator's estimated degraded absorptivity to the as-applied value.

Experimental data on the trend of variation of effective absorptivity with blade angle at zero azimuth agree reasonably well with analysis.[9.3,9.1] Correlation with the predicted values is also good when the mathematical models incorporate the gap between the blade louver edge and the mounting panel.[9.5] However, for azimuths other than zero, correlation becomes erratic, particularly at blade angles less than fully open. The major reasons for this irregularity probably lie in falsely assuming during analysis that the blades are infinitely long (length-to-width ratio of a blade is generally less than 5.0) and in ignoring the presence of the frame and the actuator assembly.

Effective absorptivity is not defined for shielded, louvered radiators. An efficient sun-shield design requires a low-solar-absorptance, high-emittance coating on the exterior. The interior surface should have high emittance to enhance heat exchange with the radiator when the blades are open. In cases where spacecraft envelopes permit, an oversized shield of potentially very low temperature should be considered.

Performance Curves

Performance curves of louvered radiators relate the heat-rejection rate to the radiator temperature. The curves are usually generated for steady-state, isothermal conditions in order to reflect maximum and minimum heat-rejection capabilities. This information is used in the initial phase of development of a thermal design to determine a louver size that will accommodate the required heat-rejection rates at specified temperatures and environment.

Equation (9.1) can be modified to include heat inputs from infrared (IR) sources (such as Earth) and reflected solar energy (albedo):

$$\frac{\dot{Q}}{A} = \varepsilon_{eff}(\sigma T^4 - I) + \alpha_r fS - \alpha_{eff}S \tag{9.9}$$

Here I is infrared and $\alpha_r fS$ (f is the albedo factor) is reflected solar energy (usually diffuse), which filters through the louver and is absorbed by the radiator with solar absorptance α_r. In practice, a lack of experimental and flight data results in uncertainty in including this effect. One approach is to modify incident albedo by the effective emissivity before multiplying by α_r. This technique adjusts the diffuse input, in a sense, by a view factor prior to impingement on the radiator. A more conventional but conservative approach is to replace α_r by α_{eff}.

The effective emissivity, ε_{eff}, in Eq. (9.7) implicitly contains the radiator emissivity and is a predetermined function of radiator temperature. Effective absorptivity is assumed to be a known function of blade angle (which is linearly related to temperature) and sun angle. IR radiation, as it appears in Eq. (9.7), is the value adjusted by view factors to an imaginary louver plane parallel to the radiator. Incident

solar flux, S, is not modified by the angle of incidence, in conformity with the definition of α_{eff}.

Net heat rejected from a shielded louvered surface is obtained from the equation

$$\frac{\dot{Q}}{A} = F_e \left\{ \sigma T^4 - \left[\frac{\alpha_e}{\varepsilon_e} S(\sin\theta + f) + I \right] \right\}, \tag{9.10}$$

where θ is the sun incident angle and the subscript e refers to the exterior of the shield. IR flux is adjusted by script-F from sources to shield.

For many satellite systems, the performance of louvered radiators may be evaluated by considering net heat rejection averaged over an orbital period. In this approach Eqs. (9.7) and (9.8) become very useful. This averaging technique has been found valid for many thermal designs in which massive electronic components are mounted to a louvered honeycomb tray.[9.6,9.7]

Shielded vs. Unshielded Louvers: Special Cases

In a louvered design, maximum heat rejection must occur in the open-blade position, while only negligible heat should be transferred when the blades are closed. While the mere presence of louvers will inevitably lead to some radiation blockage with open blades, the situation can be improved by making the thicknesses of blades and frame and the width of the actuator housing as small as is practical, and by providing a highly reflective finish on the surfaces viewed by the radiator. But, as noted earlier, the specularity of louver parts leads to sun-ray entrapment and a reduction in heat rejection. Shielding will eliminate this effect, at the expense of introducing an additional resistance to radiation to space.

In the following special cases, a comparison is made between the hot-case operations (open louvers) of shielded and unshielded louvers based on orbital average performance under various environments. The shielded system is assumed to be a configuration of the Multimission Modular Spacecraft (MMS) type, with the following characteristics:

- Sun shield $\alpha_e = 0.14$
- Sun shield $\varepsilon_e = 0.76$
- Sun shield $\varepsilon_i = 0.88$
- Radiator $\varepsilon_r = 0.88$
- Effective emissivity without shield $\varepsilon_{eff} = 0.71$
- Effective emissivity with shield (Eq. [9.5]) $F_e = 0.34$

The properties of the unshielded system are assumed to be those of the Intelsat counterrotating louver (CRL), with effective emissivity of 0.67 and effective absorptivity as described in Fig. 9.5. In the calculations, the solar constant was taken as 1350 W/m^2, albedo factor 0.35, and Earth radiation 200 W/m^2.

Solar and Albedo Equal Zero

For satellites where louvers are mounted on shadowed or antisun sides having negligible albedo input, heat rejection is

$$\left(\frac{\dot{Q}}{A}\right)_{\text{unshielded}} = \varepsilon_{\text{eff}}(\sigma T^4 - I) \qquad (9.11)$$

$$\left(\frac{\dot{Q}}{A}\right)_{\text{shielded}} = F_e(\sigma T^4 - I) . \qquad (9.12)$$

Since for the given data ε_{eff} is nearly twice F_e in the open position ($\varepsilon_{\text{eff}} \sim F_e$ in the closed position), unshielded louvers are much preferred in a purely IR environment. The orbital average-heat rejection as a function of radiator temperature is given in Fig. 9.6. An I value of 200 W/m^2 corresponds to Earth-flux input in a low-altitude orbit. The case $I = 0$ corresponds to a geosynchronous orbit with perfectly aligned north and south faces.

Sun-Oriented Low Earth Orbit

A similar comparison can be made for a spacecraft that is sun-oriented in a 370-km, 30-deg-inclined orbit. Two orientations are considered: the first, shown in Fig. 9.7, is such that the sun vector is parallel to the open louver blades during the sunlight portion of the orbit; in the second, shown in Fig. 9.8, the sun vector is inclined 30 deg off the normal to the plane of the louver. The second orientation represents the maximum solar input to an open louver array as indicated in Fig. 9.5. The graphs in Figs. 9.7 and 9.8 illustrate that the orbital average heat rejection is greater for unshielded louvers in both cases.

Earth-Oriented Low Earth Orbit

A condition in which the combined absorbed solar and Earth flux is maximum during a near-Earth polar orbit is given in Fig. 9.9. In this case, the sum of the Earth- and solar-flux inputs to exposed louvered radiators is relatively large and remains nearly constant when the angle between the sun and the plane of the louvers varies between 30 deg and 60 deg. At smaller angles, close to 30 deg, heating
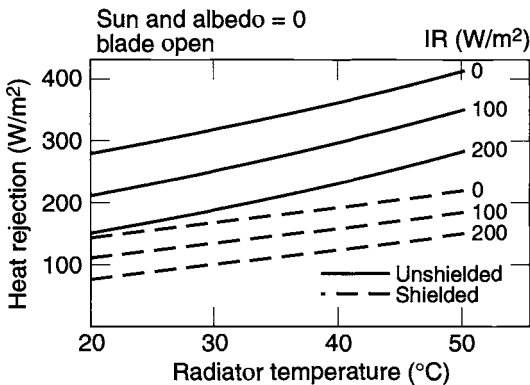
Fig. 9.6. Louver heat rejection in IR environment.
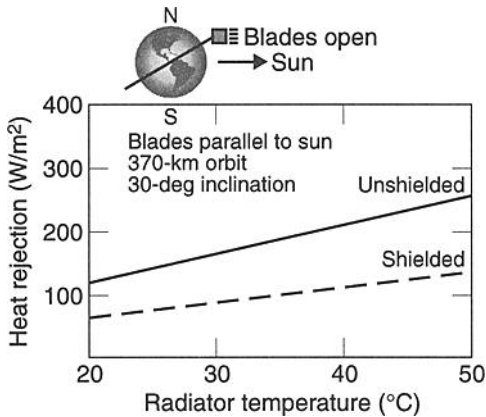
Fig. 9.7. Shielded vs. unshielded louvers in sun-oriented near Earth orbit, sun parallel to blades.
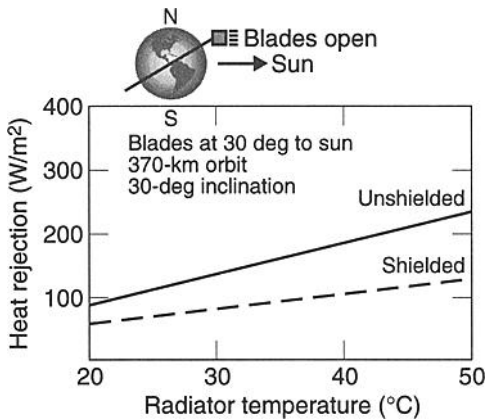
Fig. 9.8. Shielded vs. unshielded louvers in sun-oriented near Earth orbit, sun at 30 deg to blades.

from the Earth represents about 50% of the total absorbed input. At larger angles, although Earth flux diminishes, solar flux increases. In this particular orbit, the exposed louver system can exhibit less heat rejection capability than a shielded configuration. A change in the orbit hour, however, equivalent to a rotation of the plane of the orbit, introduces a shadow period that reduces the net solar input so that, even for short shadow time, exposed louvers are more efficient on an orbital average basis. The crossover point depends on radiator temperature. For 30°C it is shortly after 8 hours.
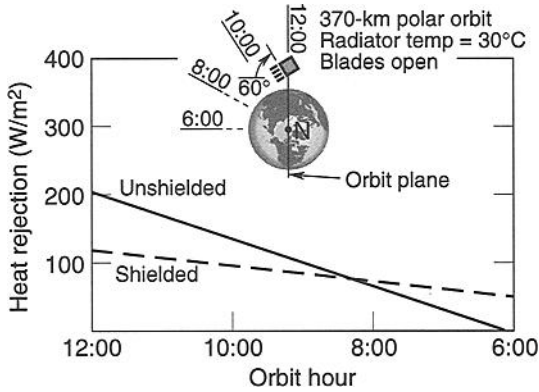
Fig. 9.9. Shielded vs. unshielded louvers in near-Earth polar orbit, louver blades at 60 deg to orbit plane.

Earth-Oriented Geosynchronous Orbit (No Shadow)

Consider an Earth-oriented geosynchronous orbit during which the solar vector moves at various angles inclined to the plane of the louver. The effective absorptivity for exposed louvers varies continuously with azimuth, as shown in Fig. 9.5. The orbital average value of α_{eff} for open blades (Table 9.3) at a given sun angle can be calculated from CRL test data.

Figure 9.10 shows heat rejection plotted as a function of radiator temperature for no-shadow periods. Even under the worst heating angles, unshielded louvers are more efficient than shielded ones at the radiator temperatures usually encountered in spacecraft temperature control.

This study shows that an exposed louver system offers greater heat rejection in most practical cases. An exception is a near-Earth orbit in which the louver continuously views the sun 30-deg to 60-deg off normal. Of course, other orbits and trajectories are possible, and comparison studies must include orbital transient variations. But with the introduction of even small shadow periods, most systems exhibit greater heat-rejection rates when the louvers are exposed.

Table 9.3. Orbital Average Value of Effective Absorptivity for Exposed Louvers

Sun Angle (deg)	Orbit Average α_{eff}
0.0	≈0.0
23.5	0.109
60.0	0.178
90.0	0.124
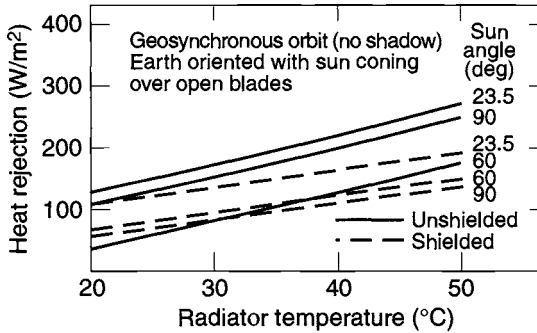
Fig. 9.10. Shielded vs. unshielded louvers in Earth-oriented geosynchronous orbit.

Louver Transient Response

In most applications, louvers are mounted to equipment baseplates with large thermal masses. Hence the orbital temperature change of radiators is generally not radical, and bimetallic response follows closely.

Actuator response time may be quantified by considering hypothetical cases in which an instantaneous step change in radiator temperature occurs. Response time can then be characterized by the time required for a louver to complete a half cycle, from fully closed to fully open or vice versa.

The transient problem is usually treated by constructing a small nodal model with conduction coupling between the radiator and the actuator housing and radiation couplings between the radiator, the actuator, and the external environment. There is significant sensitivity of response time to the values of conductances, and it may become necessary to conduct simulation tests if response time is a critical factor in predicting performance.

Typical profiles are given in Figs. 9.11 and 9.12. These graphs represent the results of analysis of shielded louvers in a near-Earth high-noon orbit. The mounting flange of the actuator housing was assumed to contact the radiator with an interface conductance of 140 $W/m^2 \cdot K$. The actuators were radiatively coupled to the inner structure of the housing, which is coupled to the exterior structure through the surrounding MLI. The effective emissivity of the louver was assumed to vary linearly between 0.115 (at 10°C) and 0.70 (at 28°C). The actuator temperature reaches the value for which the louver opens or closes in approximately 24 minutes.

Nonisothermal Transient Analysis

Thermal analysis of nonisothermal and transient radiators is performed by resorting to nodal computer models.[9.7] A typical arrangement is shown in Fig. 9.13. The nodes labeled 1 through 6 are located immediately facing the actuators and are thermally coupled to them. The temperatures of nodes 1 through 6 are used to determine the emissivity values of the other louver nodes with respect to their location within blade pairs or within a blade and an end frame. For example, the temperature of nodal point 1 sets the emissivity value of 7 and 8 in accordance
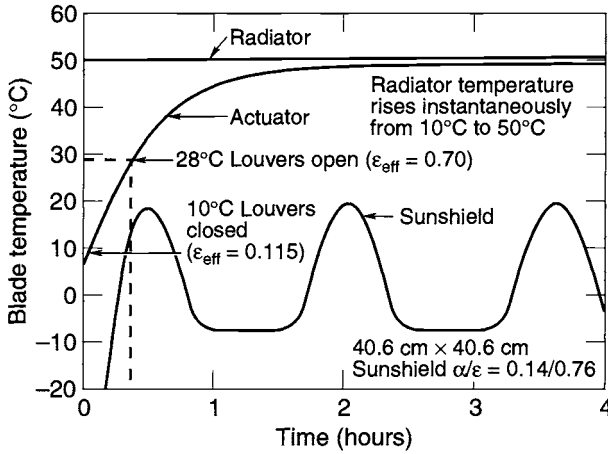
Fig. 9.11. Louver heat-up response (450-km noon orbit).

with a given temperature-emissivity matrix. The input data file may also contain the effective absorptivity as a function of sun angle (in plane ψ and azimuth ϕ) and blade angle θ, or temperature.

For exposed louvers, the quasi-steady-state equation

$$\frac{\dot{Q}}{A} = \varepsilon_{\text{eff}}(\theta)[\sigma T^4 - I] - \alpha_r(\theta)fS - \alpha_{\text{eff}}(\psi, \phi, \theta)S \qquad (9.13)$$
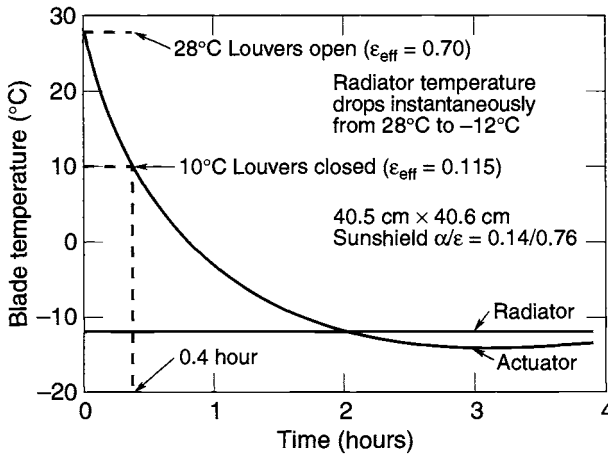
Fig. 9.12. Louver cool-down response (450-km noon orbit).
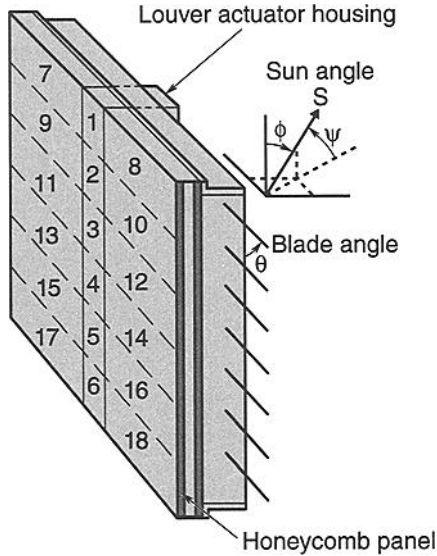
Fig. 9.13. Nodal model of a louvered panel.

is used with applicable orbital parameters to generate values of Q as a function of T (or θ) and (ψ,ϕ). The values are tabulated as bivariate arrays and input to the transient thermal model (usually in SINDA format). The computer program performs a first interpolation using orbit position (time) to select for each θ the appropriate T and Q array. A second interpolation, made using the value of sun angles, calculates heat rejected at a particular nodal point. The double interpolation for each node can require lengthy computer time, and consideration may be given to generating orbital average (steady-state) data for approximate representation of actual behavior.

Shielded louvered radiators are similarly modeled with nodes on the shield corresponding, in a one-to-one radiation coupling, to opposing nodes on the radiator. Cross-viewing among nodes does not generally exist, because of the close proximity of louver blades and shield.

An analytical treatment of nonisothermal louvered radiators is presented in Karam.[9.8] An important conclusion from that study is that the usual profiles of effective emissivity vs. temperature, generated for isothermal panels, apply in nonisothermal systems, provided that the distance between centers of adjacent blades is not too large. Another conclusion is that the use of louvers leads to significant reduction in potential lateral gradients.

Designing Louvers for Operation in Sunlight

As shown earlier, trapping of sunlight between louver blades can reduce the efficiency of louvered radiators by increasing their effective solar absorptance. While pinwheel louvers and sun-shielded vane-type louvers eliminate solar trapping,

they have inherently lower heat-rejection capability per unit area. Therefore, in some circumstances, a louver designed to operate with direct solar illumination proves to be the best alternative. Successful operation in a solar environment requires isolation of the actuator from solar heating, avoidance of material or bond degradation from overheating, and an increase in radiator area to compensate for the trapped solar heat load. Swales and Orbital Sciences make louvers designed for unshielded operation under solar loads in Earth orbit, and JPL has designed (and licensed to Starsys) a louver capable of solar exposure at up to 2.7 solar constants.

Available test data on louvers in sunlight confirm the prediction that high temperatures can be reached on the blades.[9.4] This condition presents problems of outgassing and delamination in designs where adhesives are used to bond plate sections. In addition, conduction-heat transfer from heated blades can reduce the long-term reliability of the bearings and actuator spool.

The temperature may be lowered by introducing strips of white paint (low absorptivity and high emissivity) on the blade surfaces. The equivalent absorptance-to-emittance ratio is thus reduced, leading to cooler temperatures. This effect is apparent in Fig. 9.14, a graph that depicts the results obtained in research at NASA Goddard Space Flight Center. The graph in Fig. 9.15 shows how blade temperature can relate to the percentage of blade surface area (one side) that is painted. Standard applications limit the amount to about 15%, and the stripes are usually located near the blade edge that is farthest from the radiator with the white exposed when the blades are closed. The effect of increased blade emissivity on effective emissivity is shown in Fig. 9.16.

Orbital Sciences' high-temperature louver assembly employs an insulated housing, blade white-striping to reduce blade temperature, a Vespel shaft to isolate the actuators from blades having a maximum predicted temperature of 220°C, and a silvered Teflon second-surface tape over the base. The JPL/Starsys design (Fig. 9.17) uses spot-welded blades riveted to the shaft for high-temperature mechanical integrity, a titanium shaft for high-temperature strength and low conductance,
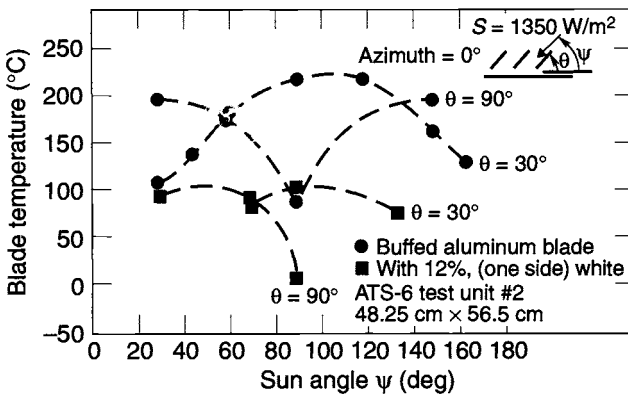

**Fig. 9.14. Louver-blade temperature in the sun (test data).**
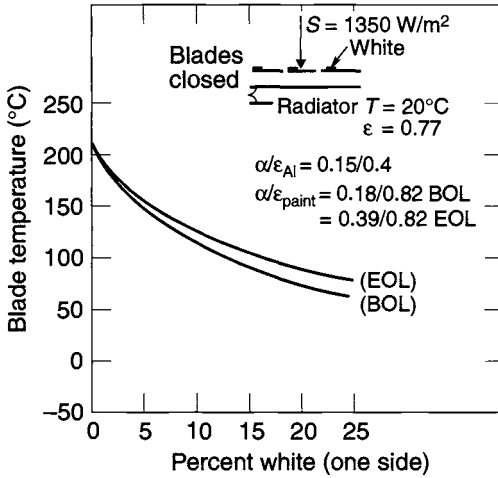
Fig. 9.15. Effect of white paint on blade temperature.

and a steel stop lever keyed to the main shaft that prevents deformation of the blade as a result of mechanical loads induced when the blades are driven open against the stop-pin at high temperature. This design can withstand the 370°C temperatures expected for partially opened blades and the 350°C expected for fully opened blades under the 2.7 solar constant illumination at 0.61 AU from the sun. One of the most important lessons learned in the development of this louver was that the bearing assembly had to accommodate the 1.5 mm of blade expansion that occurs at high temperature.
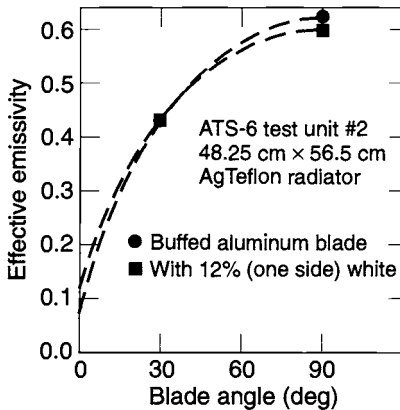
Fig. 9.16. Effect of painted blades on effective emissivity (test data).
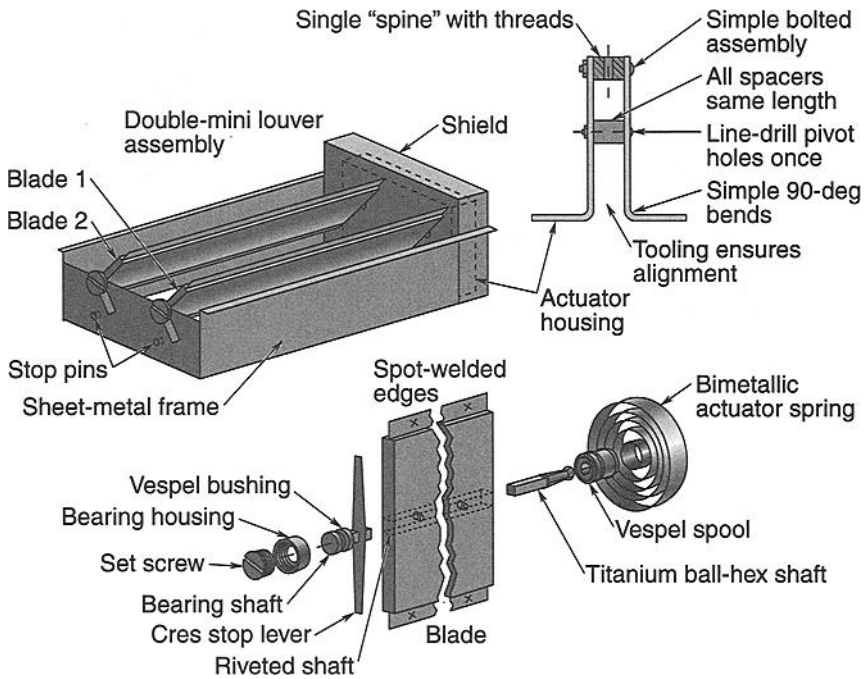
Fig. 9.17. JPL high-temperature louver.

Pinwheel Louvers

The pinwheel louver consists of a lobed louver blade, an actuator assembly, a guard ring, and a special radiator pattern, as shown in Fig. 9.18. This type of louver may be selected because of its low mechanical profile (it is less than 1.28 cm tall) or its tolerance of solar loads. The louver opens passively through the action of a bimetallic spring or is driven open by an electronic controller and a small heater on the spring. When fully open, however, the radiator surface constitutes only 5% of the circular area. An old RCA pinwheel louver-blade design, shown in detail in Fig. 9.19, consists of a fiberglass hub, foam sandwich blades, a fiberglass support framework, and a single aluminized-Kapton-film outer shield. The latter shields the hub and blades from most of the external environment. This protection is necessary to prevent wide variations in hub and blade temperatures, which would affect the bimetal temperature and thus its response.

The pinwheel actuator assembly is shown in detail in Fig. 9.20. It consists of a bimetallic element, bimetallic heater strip, driveshaft assembly, bimetallic housing, outer housing, clamp ring, stop element, and two Delrin AF bushings. The bimetallic heater strip is bonded directly to the bimetallic element, which in turn is bonded into the bimetallic housing.

The driveshaft assembly is attached to the inner coil of the bimetallic element and carries the stop arm and two bearing surfaces that ride in the Delrin AF bushings, one of which is mounted in the bimetallic housing. The bimetallic housing

Closed

Rotation

Fully open

Partially open

I

I

I

I

I

R

R

R

R

R

R

I

R

R

I

I

R

I

Louver blade

Rotating vane

Actuator

Honeycomb structure

Heater leads

I: Kapton insulation
R: Teflon radiator
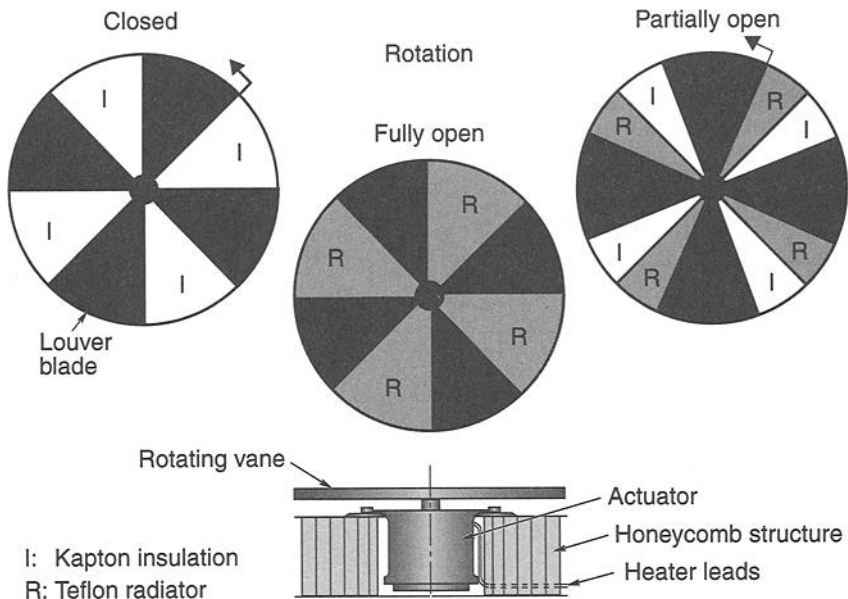
Fig. 9.18. Pinwheel thermal louver.

Fiberglass frame (edge closure)

Foam sandwich material

10-mil fiberglass aluminized inside

10-mil fiberglass aluminized both sides

1-mil single-sided aluminized Kapton (bare side out)

10-mil fiberglass

1-mil aluminized Kapton

1-mil single-sided aluminized Kapton (bare side out)

0.12 Thick open cell urethane foam

Fiberglass frame (ribs)

Section B – B

B

B

A

A

1-mil single-sided aluminized Kapton

1-mil single-sided aluminized Kapton

Aluminum reinforcing ring

Fiberglass hub aluminized top side only

Section A – A

Fig. 9.19. Pinwheel louver blade.
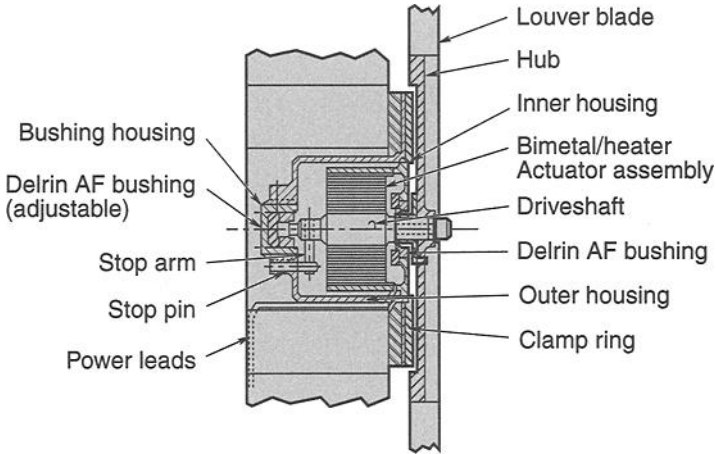
Fig. 9.20. Pinwheel louver actuator.

mounts inside the outer housing, which contains the stop element and an adjustable Delrin AF bushing. The whole assembly mounts in a hole in the spacecraft honeycomb-panel external wall and is held in place with a clamp ring. The actuator passive set point is adjusted by loosening the clamp ring, rotating the bimetallic housing, then retightening the clamp ring.

The stop elements limit the blade rotation at the fully closed and fully open positions (45 deg of angular rotation). The actuator operation is the same as for a vane louver actuator. A temperature change of 15°C is required to drive the louver from the fully closed position to fully open.

The Delrin AF bushings are adjusted at assembly to limit the driveshaft axial movement to 10 mils. They also provide low-torque louver-blade support during 1-g testing; this support minimizes the 1-g testing error.

The radiator/guard-ring assembly is shown in detail in Fig. 9.21. The radiator consists of a guard ring for louver-blade protection and alternating radiator segments of second-surface aluminized Teflon and aluminized Kapton. The Teflon areas are the radiating areas and have a low solar-absorptance value ($\alpha < 0.2$). The aluminized Kapton areas are the low emittance areas, which act as insulation when the louvers are closed. The louver blade covers the Teflon areas when in the closed position and the Kapton areas when in the open position.

Each RCA pinwheel louver had a heat-rejection capacity of approximately 25 to 30 W when open and a heat leakage of approximately 5 to 7 W when closed. The heat-rejection rate is linearly proportional to the louver-blade position.

Mounting hole for actuator

10-mil aluminized Teflon bonded to spacecraft panel on sections 2, 4, 6, and 8

1-mil aluminized Kapton fiberglass reinforced on sections 1, 3, 5, and 7

Polished aluminum guard ring

Spacecraft panel (covered with insulation)
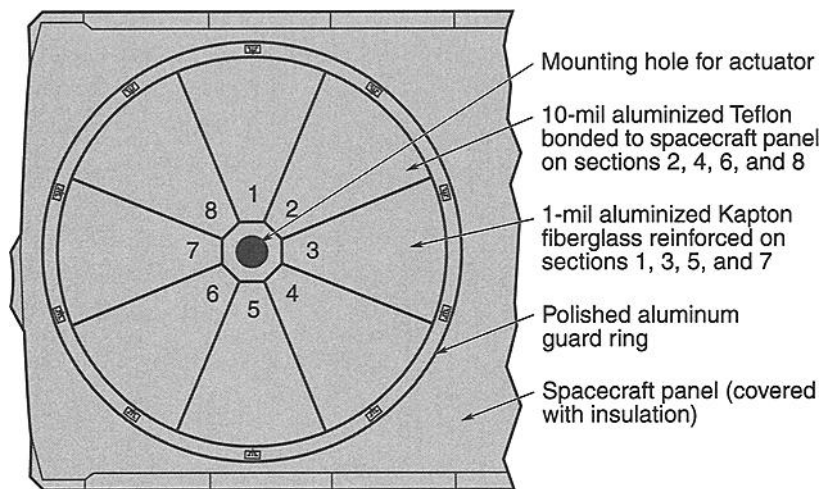
Fig. 9.21. Pinwheel louver radiator/guard ring assembly.

References

9.1. T. J. Michalek, E. A. Stipandic, and M. J. Coyle, "Analytical and Experimental Studies of an All Specular Thermal Control Louver System in a Solar Thermal Vacuum Environment," AIAA Paper 72-268 (1972).

9.2. W. H. Kelly, J. H. Reisenweber, and H. W. Flieger, "High Performance Thermal Louver Development," AIAA Paper 76-460 (1976).

9.3. M. Furukawa, "Analytical Studies on Design Optimization of Movable Louvers for Space Use," *Journal of Spacecraft and Rockets* **16**, 412–425 (Nov.–Dec. 1979).

9.4. J. A. Plamondon, "Analysis of Movable Louvers for Temperature Control," *Journal of Spacecraft and Rockets* **1**, 492–497 (Sept.–Oct. 1964).

9.5. COMSAT Louver Thermal Analysis for INTELSAT, Fairchild Space Company Report No. 310-SR-2001 (with appendix) (May 1975).

9.6. R. O. Wales, ed., "ATS-6 Final Engineering Performance Report," Vol. I, NASA Reference Publication 1080 (Nov. 1981).

9.7. H. Hwangbo, J. H. Hunter, and W. H. Kelly, "Analytical Modeling of Spacecraft with Heat Pipes and Louvers," AIAA Paper 73-773 (1973).

9.8. R. D. Karam, "Temperature Distribution in Louvered Panels," *Journal of Spacecraft and Rockets* **16**, 92–97 (March–April 1979).

9.9. H. Frankel and R. Eby, "SMM Hardware Evaluation," Proceedings of the SMRM Degradation Study Workshop, NASA Document 408-SMRM-79-0001 (May 9–10, 1985), pp. 105–123.

9.10. A. J. Boscia, "A Laboratory Method for the Determination of Effective Emittance of Spacecraft Thermal Control Louvers," Joint National Meeting of American Astronautical Society (15th Annual) and Operations Research Society (35th National), (Denver, CO, June 17–20, 1969) Paper No. VIC. 3.

9.11. Design Catalog, Chase Thermostatic Metals, GTE Metal Laminates Division, 1704 Barnes Street, Reidsville, NC 27320.

10 Heat Switches

K. Lankford[*]

Introduction

Heat switches, known also as thermal switches, are devices that switch as needed between roles as good thermal conductors and good thermal insulators. When one is installed in the heat-conduction path between a warm, heat-producing component and a heat sink, the change in thermal conductance it affords can control the temperature of the component. Heat switches can passively control the temperature of warm electronics or instrumentation without the use of thermostats and heaters, thereby reducing power requirements as well as the need for heater control circuitry and software.

Cryogenic applications use heat switches to minimize heat loads on cooling systems by disconnecting components when cooling is not required or disconnecting redundant refrigerators that are not providing cooling because they have failed or have been turned off. In general, cryogenic systems include different types of heat switches than the ones found in applications closer to room temperature.

Heat switches differ from thermostats; the latter control heaters by opening or closing electrical circuits at a given temperature, while heat switches open, close, or vary heat-conduction paths. Heat switches thus function similarly to diode or variable-conductance heat pipes; however, they achieve temperature control by modulating a conduction path rather than a two-phase flow process.

Most heat switches that operate in normal spacecraft temperature ranges are passive devices that automatically self-regulate their conductance rather than react to signals received from a controller. The control they exercise is characterized by a variable adjustment of conductance between "on" and "off" values. The time constant of heat switches is usually short enough to handle rapid fluctuations in power, yet well enough damped by thermal capacitance and mechanical characteristics to avoid overshooting desired temperatures. The name "heat switch" is therefore somewhat misleading because these devices afford a more complex control than the simple on/off function provided by a switch.

This chapter provides an overview of several types of heat switch, including paraffin heat switches and cryogenic heat switches. Other heat-switch designs have been proposed and/or prototyped, including designs for magnetostrictive, electrolytic, and electrostatic switches, as well as mechanical switches actuated by electric motor or liquid-to-gas phase change.

Although the concept of heat switches was first devised in the early 1960s for use on the Mariner mission to the moon, their practical development is still relatively new. Switches based on more recent paraffin-based technology will fly on the Propulsive Small Expendable Deployer System (ProSEDS) tether experiment mission in late 2002, and some additional heat switches are currently in the baseline design for the Jet Propulsion Laboratory (JPL) Mars '03 Rovers. Recent

*Starsys Research Corporation, Boulder, Colorado.

353

development efforts have focused on reducing mass and increasing reliability to make switches more attractive to spacecraft programs. As heritage and experience are gained, heat switches may find increased use. Until a larger experience base is established, however, analysts must consider the risks associated with such a new technology.

Heat-Switch Applications

Thermal Control of Individual Components

A typical application of a heat switch to control the temperature of an individual component is shown in Fig. 10.1. Here, a heat switch is mounted between an instrument or electronics box and a cold sink, such as a spacecraft structural panel or radiator. The heat switch controls the temperature to a set point selected when the switch is manufactured. When the temperature of the electronics box rises above the set-point temperature, the switch conductance increases, allowing the excess heat to be transferred through the switch to the radiator and out to space. As the box cools, its temperature drops below the set-point temperature, causing the switch conductance to decrease. At the lower conductance level, the instrument is kept warm by its own heat or a low level of heater power. A heat switch can thus maintain the temperature of electronics or instrumentation within a comfortable range despite fluctuations in component heat load or variations in cold-sink temperature.

System Applications

Heat switches could serve as the basis for an entire spacecraft thermal-control system, but such an application would require a shift in philosophy beginning in the early stages of the design process. In many cases, compelling reasons might justify this shift, but designers could find the lack of an extensive flight history a difficult barrier to overcome in making the transition to this new technology.

Examination of a typical conventional thermal design reveals why heat switches could be desirable as the basis for a spacecraft thermal-control system. As shown in the design examples of Chapter 3, the industry standard for spacecraft thermal control involves connecting internal heat-producing components to external radiator surfaces through either heat pipes or spacecraft structure. Radiators are then sized so that, in the worst-case hot mission environment and worst-case heat dissipation of the components, they still run cold enough to keep all components below
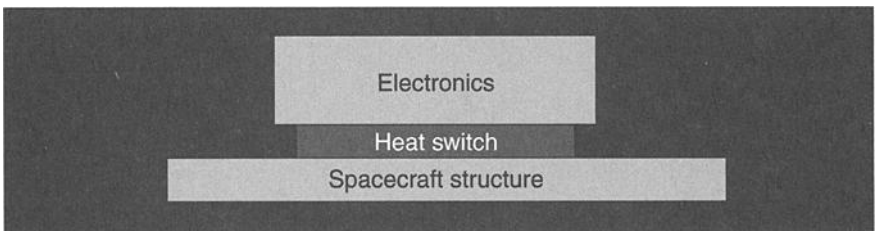

Fig. 10.1. Heat-switch application.

their upper temperature limits. Heaters keep the hardware above lower temperature limits when the system is in a low-power state or when it experiences worst-case cold mission environments.

The biggest advantage of the conventional approach to spacecraft thermal design is that it efficiently tailors the thermal-control system to specific hardware characteristics and mission environments of a particular spacecraft. However, this advantage also highlights a weakness, because the conventional approach is not very robust and entails a great deal of analysis, one-of-a-kind manufacturing, and testing. Thermal switches, on the other hand (along with other emerging technologies, such as electrochromic surface finishes and capillary pumped loops), open the possibility of a new approach that could dramatically reduce the amount of analysis and testing required to produce a thermal-control system for a particular satellite. Such an approach would use the tremendous control range of heat switches, capillary pumped loops, and electrochromics to produce a generic thermal control system capable of maintaining acceptable temperatures for a wide range of equipment complements in a wide range of thermal environments.

As an example, standard north and south heat-pipe panels for geosynchronous communication satellites could be sized to reject 3000 W of heat at a maximum temperature of 30°C. Payload and bus electronics boxes could be mounted to this standard heat sink with thermal switches that couple the boxes to the radiator only when box temperature exceeds a particular value, such as 40°C. The boxes themselves would have a low-emittance finish and low-emittance cable wraps so that the only significant heat-transfer path would be the connection between the thermal switch and the radiator panel. Even if the payload were turned off entirely, only a small amount of heater power would be required to keep each of the electronics boxes warm, since the switches would decouple the boxes from the radiator when the former were cold. For each new satellite, bus and payload electronics boxes could be mounted to the panel according to simple design rules that specify parameters such as maximum allowable box power per square centimeter, maximum total power per panel, and maximum power per heat switch. In cases where the thermal switch or radiator system provides enough "dynamic range," detailed thermal analyses and some thermal balance testing might be eliminated.

Heat-Switch Integration

In general, heat switches can control spacecraft component temperatures either from a location between an insulated spacecraft structure and an external radiator or from between the components themselves and the structure of the spacecraft. These two options lead to somewhat different switch operating modes.

Heat Switches Mounted between Structure and Radiator

Figure 10.2 shows a heat switch mounted between the spacecraft structure and an external radiating panel. Here, the switch maintains the entire structure of the spacecraft near the desired temperature. Meanwhile, the temperature of the external radiator varies according to the amount of power dissipated through it. When power dissipation is low, the radiator temperature drops, while the structure and internal components remain warm. This type of spacecraft thermal control differs
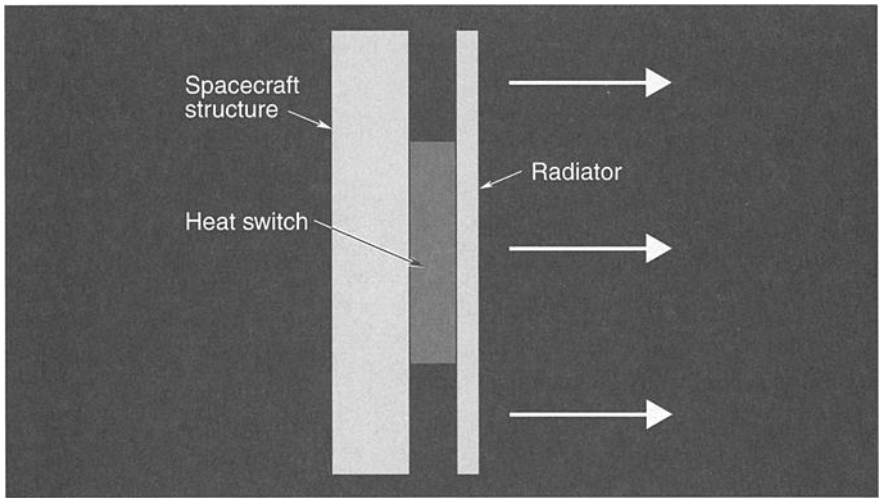
Fig. 10.2. Heat switch between spacecraft structure and radiator.

substantially from the more traditional type, where radiator temperatures follow the bulk temperature of the spacecraft structure. The heat switch passively controls the temperature of the structure and therefore the internal components (electronics, batteries, and instrument packages) by self-regulating the thermal conductance through the switch. When a large amount of heat is produced, the switch adjusts itself to a high conductance. When little or no heat is produced, the switch adjusts itself to a lower conductance. Similarly, when the spacecraft goes into eclipse or changes its orientation, the heat switch adjusts itself to maintain the level of conductance needed to keep the structure at the desired temperature.

One important advantage to this approach over conventional thermal control is that radiator area can be oversized without affecting the spacecraft temperature. Excess radiator area reduces the temperature of the radiator itself but has no effect on the temperature of internal components. Radiators can be designed quickly and easily with robust margins to cover degradation of surface coatings, eclipses, changes in orientation, varying distances to the sun, changing view factors as a result of deployment of nearby solar panels or antennas, and other considerations.

Heat Switches Mounted between Components and Structure

Figure 10.3 shows heat switches positioned between individual components and the spacecraft structure. Here, the temperature of the spacecraft structure is allowed to vary with that of the radiators. When power dissipation is low, the temperatures of both the structure and radiators will drop to a relatively low level. When power dissipation is high, the structure and radiators will warm up. The temperatures of components, however, are controlled individually. This approach provides more flexibility than the option of mounting heat switches between the spacecraft structure and an external radiator, in that it allows maintenance of different components at different temperatures by the selection of switches with different set points. Thermal control is completely passive and is applied only to those individual
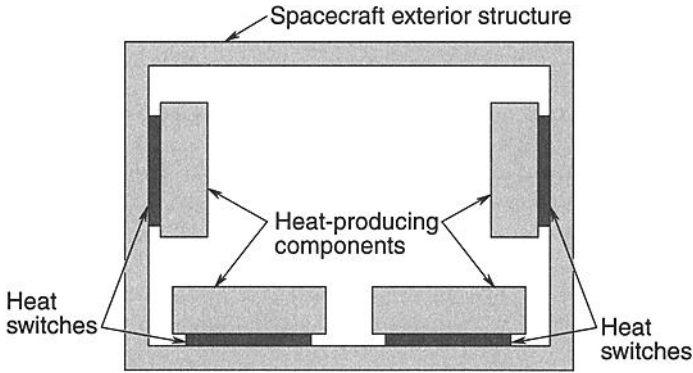
Fig. 10.3. Multiple heat switches between components and spacecraft structure.

components that require it, not to the entire structure. The design philosophy behind this technique is both efficient and effective. Very little energy is wasted.

One important advantage of this approach is that it allows the external surfaces of the spacecraft to be utilized as radiator area. Since excess radiator area does not affect the temperature of the internal components, the need for multilayer insulation (MLI) blankets around the spacecraft is reduced or eliminated (unless blankets are necessary for micrometeoroid protection). External surfaces can simply be coated with low α/ε surface coatings (white paint or silver Teflon) rather than covered in MLI. For this approach to work, the spacecraft must have enough radiator area to dissipate the worst-case maximum power (the size of this area must take into account the additional temperature rise across the heat switches and account for degradation of external radiating surface properties during the life of the mission). Fortunately, most low- and medium-power spacecraft have plenty of available external surface area.

Although it has important advantages, this approach has never been used, and its adoption may be slow, since it represents a large departure from conventional satellite thermal-control philosophy. Ambient-temperature heat switches will probably initially be used on risk-tolerant, small, or microsatellite projects that require a simple, low-cost, passive thermal-control system.

Paraffin Heat Switches

A variety of paraffin-based heat switches have been developed for the temperature ranges associated with most spacecraft components. (The principal supplier of paraffin heat switches is Starsys Research in Boulder, Colorado.) Paraffin use in heat switches is an extension of the technology in spacecraft mechanical systems; high-output paraffin actuators are widely employed in powered hinges, latch releases, launch-caging mechanisms, and a number of other spacecraft mechanical components. Operation of these devices is enabled by the phase-change properties of specially formulated paraffin compounds. When paraffin melts, it expands approximately 15%. This volume change creates hydraulic force, which translates

into movement. In a paraffin heat switch, this movement brings two thermally conductive surfaces in contact, creating a path through which heat readily flows.

A significant amount of heat is associated with the phase change of paraffin from solid to liquid. This property gives paraffin heat switches a thermal capacitance that enhances their thermal-control capabilities. Typically, when the switch is controlling the temperature near its set point, the paraffin is partially frozen and partially melted. In this state, a large spike in energy is required to move the temperature away from the paraffin melting point because a sharp rise in heat output is first absorbed in the melting of the paraffin (see Chapter 11, "Phase-Change Materials"). This behavior has the effect of damping the response, allowing the switch to respond in a smooth, controlled fashion, with no cycling in response to a change in heat load because the system is overdamped. The resulting control is therefore gentle and robust. Paraffin heat switches typically respond to a step change in power on the order of a minute.

The paraffin must be refined and synthesized to meet specific requirements. Different types melt at different temperatures, depending on the number of carbon atoms in the paraffin chain (see the items *n*-undecane through *n*-octacosane listed in Table 1 of Chapter 11). This variety of melting points allows the analyst to tailor the switch set-point temperature to the application. The range of available temperatures is –95 to +86°C with increments approximately every 10°C.

Pedestal Heat Switch

One of the earliest paraffin designs is the Starsys Pedestal Switch, shown in Fig. 10.4. This is a robust medium-capacity heat switch that can handle significant structural loads. Its operating characteristics are summarized in Table 10.1.
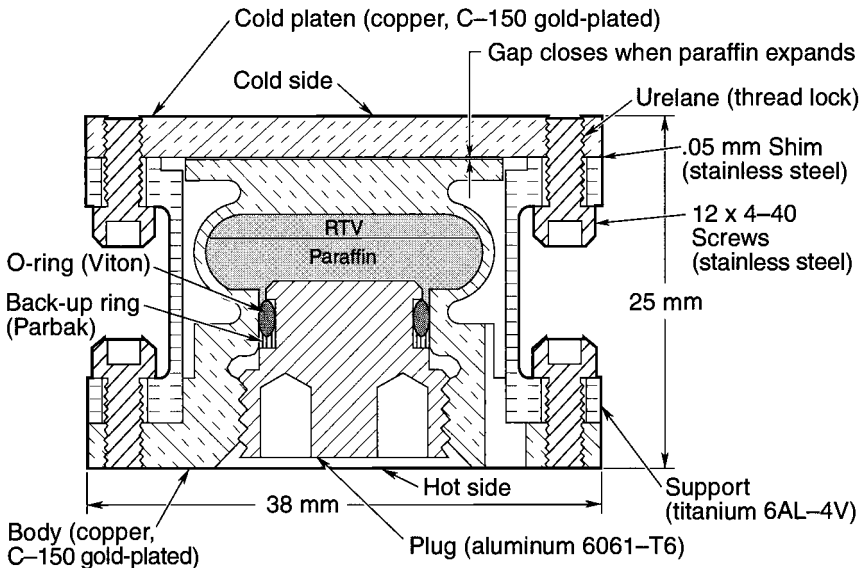

Fig. 10.4. Pedestal Heat Switch.

<div align="center">

Table 10.1. Starsys Pedestal Switch Characteristics

</div>

Characteristic	Value
Conductance ratio	100:1
Maximum conductance	0.73 W/°C
Minimum conductance	0.0075 W/°C
Mass	100 g
Diameter	38.1 mm
Height	25.4 mm

In the Pedestal switch, a central bellows chamber contains paraffin. When the switch is "open," a small gap (nominally 0.05 mm) separates the central bellows chamber and a cold platen above it. In space, a high vacuum is present in the gap; when the paraffin is cool and the gap is open, the only path for a heat-conduction leak is one that goes through the switch's outer support structure, which is made from an effective insulating material. Radiation also "leaks" heat across the gap, but this effect is small compared to conduction through the support. When the hot side of the switch is heated (by heat dissipation from the electronics), the paraffin melts and expands the bellows, closing the gap between the cold platen and the bellows chamber. This action creates a good conduction path through the copper bellows and across the contact interface.

The switch provides self-regulating variable conductance. Higher temperatures lead to a larger percentage of melted paraffin and higher pressure at the interface. Contact conductance at the interface is dependent on the pressure applied. Thus when the heat load increases, the contact conductance increases, which tends to bring the temperature back down.

Diaphragm Thin Plate Heat Switch

Figure 10.5 depicts the Starsys Research Diaphragm Thin Plate design. The top image is an enlarged cross section of a single cell from one such switch, and the bottom half is a schematic diagram of a full multicell plate. The multicell approach provides a high level of redundancy, allowing each cell to operate independently. If the performance of one cell degrades, the others adjust to pick up the slack.

The operating principle of the Thin Plate heat switch is similar to the principle of the Pedestal heat switch. When the switch is open, a narrow (0.13 mm) gap separates the cold side from the hot side. Conduction from side to side takes place only through the fasteners and insulating standoffs that are designed to provide very low heat loss. A thin layer of paraffin contained in each switch cell expands when heated, deflecting the metal diaphragm of the charge plate and closing the gap, creating a thermally conductive contact with the colder top sheet. An O-ring at the outside diameter of each cell seals in the paraffin.

Plotted on the graph in Fig. 10.6 are data from thermal vacuum testing of a 12.7-by-12.7-cm Diaphragm Thin Plate heat switch consisting of an array of nine cells. The area-normalized thermal conductance across the switch plate is plotted against the hot-side temperature. (Note: this is the thermal conductance across the
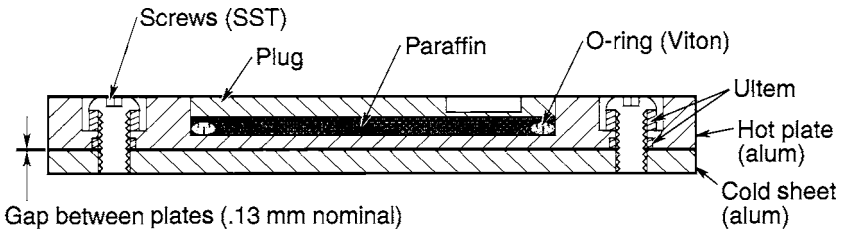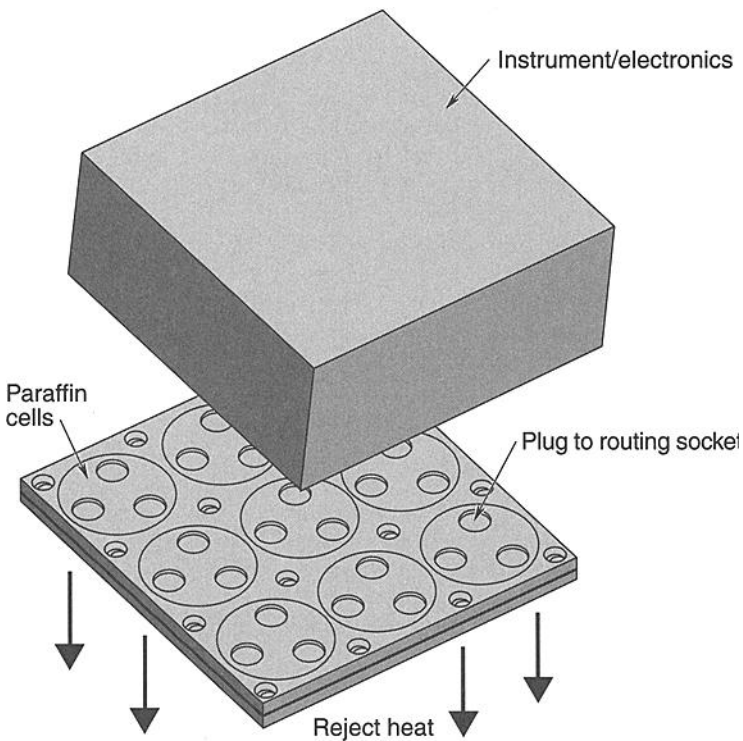
Fig. 10.5. Starsys Diaphragm Thin Plate heat switch.

switch plate itself and does not include the thermal resistance at the mounting interfaces to adjacent components or spacecraft structure.

Heat-Switch Fasteners

The Starsys Research High Performance Heat Switch Fastener is shown in Fig. 10.7. The concept for this switch was proposed by the Naval Research Laboratory
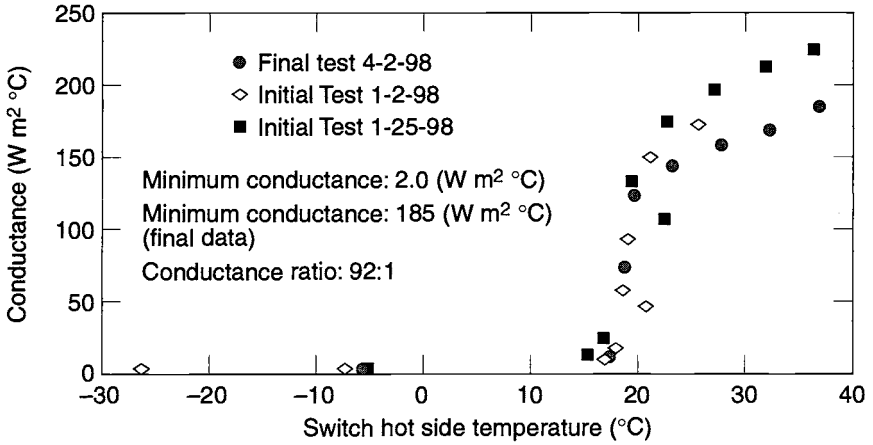
**Fig. 10.6. Diaphragm Thin Plate heat switch vacuum test data.**
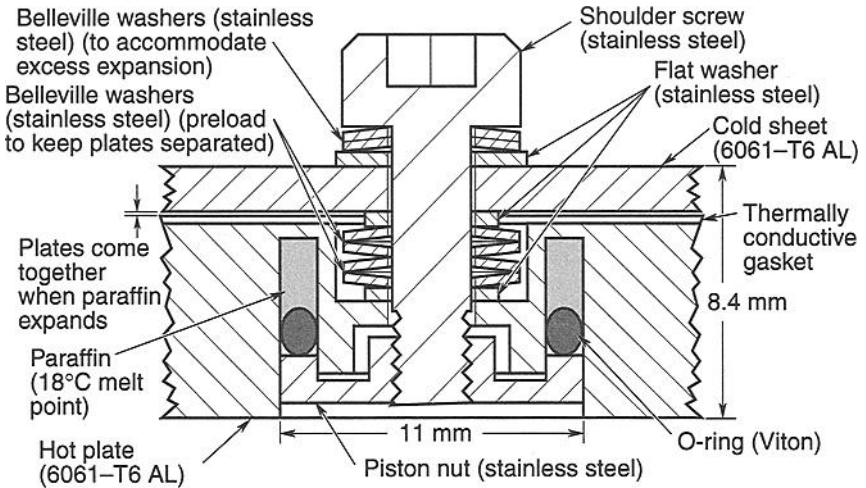
Fig. 10.7. Heat Switch Fastener.

and developed by Starsys Research in conjunction with JPL. A more advanced version, called a Heat Switch Washer, is shown in Fig. 10.8. These "washers" are used together with standard off-the-shelf screws to mount an electronics box to a cold plate or spacecraft structure by fastening the perimeter flange of the box to the cold plate. A countersink must be provided in the underside of the electronics box flange to accept the two-part washers. Standard screws are then installed from the box side through the washer into the cold plate.
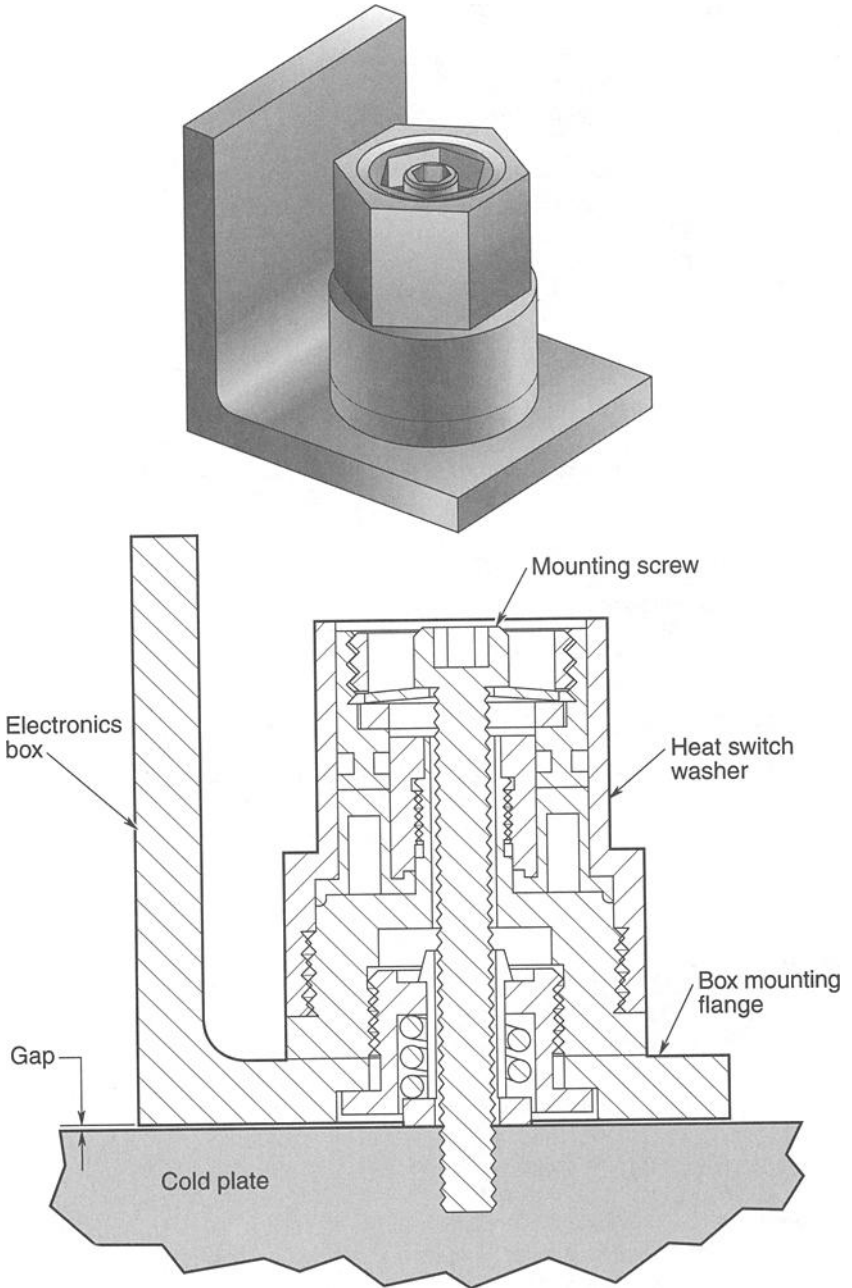
Fig. 10.8. Heat Switch Washer.

Each washer is a miniature actuator. When the electronics get too warm, the washers actuate to physically bring the electronics box in contact with the cold sink. When the electronics are too cool, the spring-loaded washers push the box away from the cold plate, creating a small gap. The gap creates good thermal isolation, which keeps the electronics from becoming too cold. The maximum relative movement is small, on the order of 0.2 mm. The concept is different from the principle behind the Pedestal Heat Switch and the Diaphragm Thin Plate Heat Switch, where there is no relative movement between the heat source and heat sink. The Heat Switch Washer approach has an advantage in that it can provide better maximum conductance with less mass and is very easy to integrate with a typical electronics box.

As in other designs, the paraffin can modulate the amount of force it generates to pull the box onto the cold plate. With this ability to adjust contact pressure, the washer serves as a variable-conductance device that self-adjusts the level of conductance to maintain the warm-side temperature of the box near the set-point temperature of the switch. This modulation of contact pressure also means that no "on/off cycling" is required to maintain temperatures. Instead, the box is always in contact with the cold plate, and the switch continuously makes very minute adjustments to regulate the contact pressure. Actually, if the switch is ever in full open mode with a true gap between surfaces, it is operating outside its intended range, and the electronics are likely too cold.

The total contact surface area can be tailored to achieve desired results. For example, with high-power electronics, the box can be designed for full face contact to achieve better conductance rather than contact only around the perimeter flange. The spacing of fasteners also has an effect on conductance. Close spacing results in better closed-switch conductance but poorer open-switch isolation. More generous spacing results in better open-switch isolation but poorer closed-switch conductance.

The mass penalty associated with Heat Switch Washers is relatively small. Each will typically add 3–5 g over a standard fastener. However, the number of fasteners required and stiffness of the mounting surfaces play an important role in the thermal performance of the design. Many applications will need a larger number of fasteners and a stiffer mounting flange than would otherwise be necessary for purely structural support. Applications must be evaluated on a case-by-case basis.

Radiator Module with Integral Heat Switch

A radiator panel module that mounts to a spacecraft exterior via a heat switch is shown in Fig. 10.9. The top portion of the figure shows a front view of the 21.6-by-21.6-cm radiator and a cross section of the 3.2-by-3.2-cm heat switch. The lower part of the figure shows a three-dimensional cross section of the heat switch. In the latter image, the radiating surface points downward and the uppermost surface of the switch itself is the heat-transfer interface with the spacecraft. (This mounting interface is also the warm side of the switch during normal operation.) The capacity of this particular module is about 10 W, which would be suitable for thermal control of a microsat or small instrument. Using a large number of such modules to reject the waste heat from a larger satellite would provide massive redundancy and high system reliability.

.05 - to - .23 mm gap closes when paraffin expands

Radiation to space

Paraffin

Annular hat seal

Insulator (4x)

Radiation to space

View A-A

Compression springs (4x) keep plates separated

21.6 cm

3.2 cm

3.2 cm

21.6 cm

Radiator panel

Gap

Paraffin
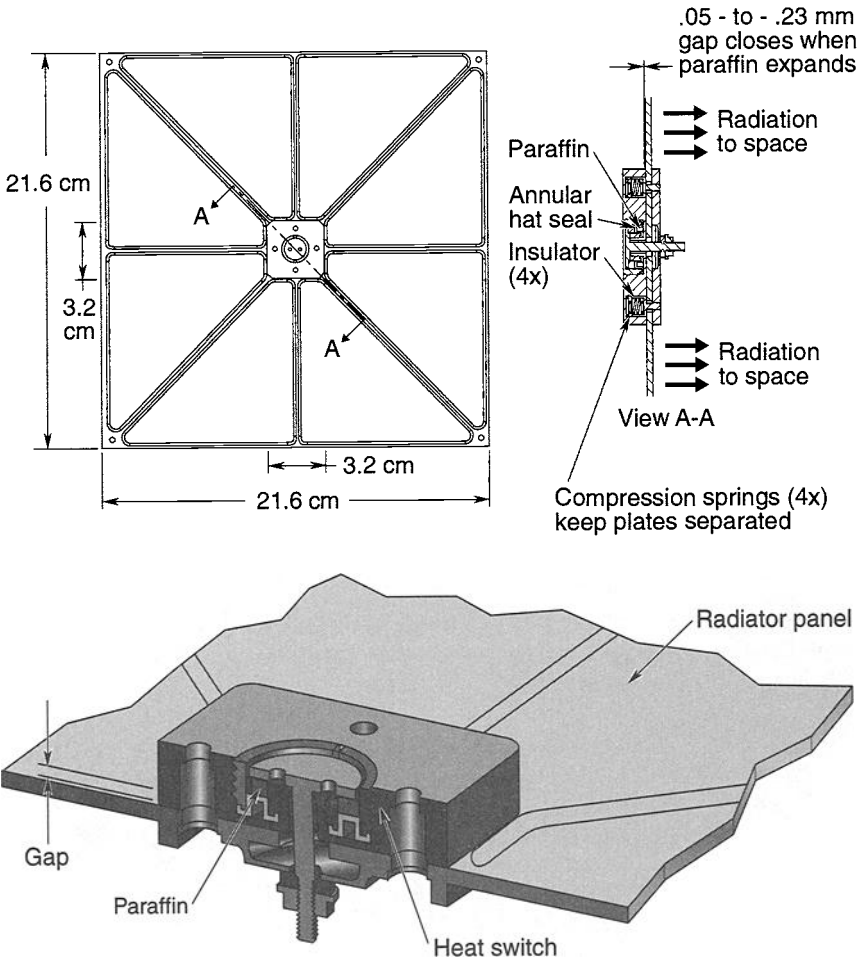
Heat switch

Fig. 10.9. Radiator heat switch.

The heat switch in the radiator module is based on a single-cell paraffin design similar to the design of the heat-switch washer discussed above. When the switch is cold, a small (0.10 mm) gap separates the heat-switch plate and the radiator panel. When the heat switch is warmed by power dissipated from instruments in the satellite, this gap closes, creating good thermal contact between the heat switch and the radiator panel.

As with the other paraffin-based heat switches, expansion of heated paraffin results in thermal contact between surfaces. In this case, paraffin is contained in an annular cavity surrounding the center bolt; the cavity is sealed with a hat-shaped, annular, elastomer seal. The edges of the seal are captured with threaded rings. When the paraffin expands, it pushes this seal upward. This upward movement

pushes on a bushing ring, which in turn pushes on the flanged portion of the center screw. The center screw is attached through a nut to the opposite side of the heat switch. The expanding paraffin pulls the two sides together, closing the gap and creating good thermal contact at the interface between the heat switch and the radiator panel. As the paraffin continues to expand into the liquid region, it creates more pressure at the interface, improving the thermal conductance.

Under most normal operating conditions, and also during launch, the heat switch is in the closed position and no gap separates the heat-switch plate and the radiator panel. When the switch is cold, the gap is maintained in the open position by springs at the corners of the heat switch (see cross section in upper half of Fig. 10.9). An insulator material thermally isolates the springs from the heat switch.

As with any radiator design, high radiative heat loads from the environment may cause the temperature of the radiator to rise above the desired control level. The conventional solutions of using low α/ε coatings or placing radiators on different sides of the spacecraft are equally effective here. With the heat-switch radiator module, however, it is also possible to place an additional reverse switch in series that decouples the radiator from the spacecraft if the radiator gets too warm.

Louvers and heat-switch radiators are competing technologies. Louvers, an established technology developed over 25 years, have flown on many spacecraft. Both louvers and heat switches are passive devices, but louvers regulate the radiative thermal coupling to space while heat switches regulate the conductive thermal coupling between heat-producing components and radiators.

The data in Table 10.2 compare a 16-blade, 50-W louver with five heat-switch radiators in parallel. The comparison assumes no solar illumination, a premise that actually favors the louver because it eliminates the reduced louver effectiveness caused by a sun shield or solar trapping between the louver blades (see Chapter 9). Even given this handicap, heat-switch radiators compare favorably in terms of overall power turndown ratio and mass, as the table illustrates. For a spacecraft in Earth orbit with a radiator receiving illumination, heat-rejection capability will be degraded much more severely for the louver than the heat-switch radiator, giving the heat-switch design a significant mass advantage.

However, because louvers and heat-switch radiators operate differently, a complete comparison is not as straightforward as the basic parameters in the table might suggest. These technologies differ in response time, set point, and thermal-control band. Also, heat-switch radiators require the heat flow to be necked down and funneled through a small cross section. This may lead to the need for greater structural mass to conduct the heat to the heat switch or the use of additional, closely spaced heat switches to avoid temperature gradients in the equipment panel from which the heat is being taken.

Shape Memory Heat Switches

Besides paraffin, shape memory alloys are another class of substance that could serve as the basis for heat switches. These are metallic materials that can return to a previous shape or size when they are subject to the right thermal conditions. Shape memory alloys undergo a solid phase change from martensitic to austenitic crystal structure at a prescribed temperature that can be selected within the range of roughly −200 to +100°C. Their physical properties change as the alloys undergo

Table 10.2. Comparison of Heat-Switch Radiators and Louver (no solar illumination)

Characteristics	Louver (16-blade)	Heat-switch radiators (five in parallel)
Maximum power dissipation (W)	47	50
Heat-switch conductance ratio	NA	107:1
Louver effective emittance ratio[a]	7.1:1	NA
Overall power turndown ratio[b]	7:1	20:1
Radiating area (cm^2)	1425	2330
Mass (g)	875[c]	733
Mass of heat switches only (g)	NA	90

[a]Louver maximum effective emittance 0.78, minimum effective emittance 0.11.
[b]Power turndown ratio based on 0 to 20°C acceptable temperature band.
[c]Louver mass does not include radiator (assumes existing structure used for radiator).

phase transition. Utilizing this change, one can "train" the alloys to either shrink or grow 3–6% during the phase transition. Shape memory alloys are typically formed into wire, springs, tubes, or cylinders and are used to actuate mechanisms; an example is the shape memory actuators currently used in aircraft applications. The Naval Research Laboratory has proposed development of a shape-memory-actuated heat switch for small-satellite thermal control. If properly developed, this approach could provide a reliable, low-cost heat switch. To date, however, no prototype testing of this concept has been reported.

Cryogenic Heat Switches

The operation of a number of important space instruments (typically infrared sensors) requires cryogenic temperatures. Maintenance of these temperatures depends on complex, heavy cooling systems, many of which utilize mechanical cryocoolers that must be redundant for high reliability. Unfortunately, when a redundant cryocooler is connected to a system but not used, it introduces a large parasitic heat load possibly several times the size of the baseline load. The resulting system, with cryocoolers significantly oversized for the task, is inefficient.

A heat switch can significantly improve this situation by thermally disconnecting the backup cryocooler from the system when it is not in use. This disconnect is accomplished by the insertion of a heat switch between each cryocooler and the cold load (see Fig. 10.10). Under normal operation, the primary cryocooler is thermally connected to the load and the backup cooler is isolated. If the primary cryocooler fails, the states of the heat switches are reversed, thermally connecting the backup cooler and disconnecting the primary cooler. This application requires an actively controlled heat switch with excellent isolation in the open switch state, a large conductance ratio, and very low power dissipation to the cold side. Gas-gap and differential thermal-expansion heat switches are designed specifically for these applications. A heat switch can reduce parasitic heat losses by 80% or more.

In similar applications, heat switches selectively couple or decouple loads as needed. One example is the use of intermediate cryoradiators. At certain times a spacecraft
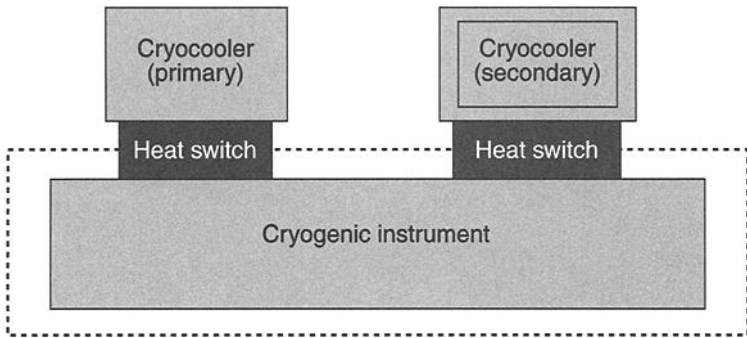
Fig. 10.10. Cryocooler application.

must be oriented so the radiator is exposed to sunlight or another radiant heat load. When this happens, disconnecting the radiator from the cryogenic load can help prevent a large influx of heat. Other similar cryogenic applications are discussed in more detail in Volume II of this handbook.

Gas-Gap Heat Switches

The gas-gap heat switch, originally developed at JPL for cryogenic applications, was actually the first heat switch to see significant development effort. Its history began in the early 1960s, when heat switches were first proposed for spacecraft. Cryogenic applications continue to be its primary use.

Figure 10.11 is a cross section of a gas-gap heat switch design developed recently at JPL for a cryocooler application with a cold-end temperature of 60 K and heat flow of up to 8 W. Heat flows from end to end across the narrow conical gap. When the gap is evacuated, only a small amount of heat is transferred by radiation across the gap or by conduction through the thin bellows support structure and center tie rod. When the gap is filled with hydrogen gas, however, a large amount of heat is transferred by conduction through the gas. To turn the switch on and off, the gas is either absorbed or released from a reservoir containing zirconium nickel hydride, activated charcoal, or other sorbent material, the choice of which depends on the application temperature. These materials absorb gases at low temperatures and expel them at higher temperatures. When the sorbent bed is actively heated, typically with an electrical resistance heater bonded to the outside shell of the sorbent bed reservoir, gas is released to pressurize the gap and turn the switch on. When the heater is turned off, the sorbent bed cools, absorbing the gas and evacuating the gap. Switching time for this design was approximately 5 min.

Figure 10.12 is a similar design developed at the NASA Ames Research Center for operation with a 0.05 W adiabatic demagnetization refrigerator operating between 2 and 10 K. The gas used in this design was helium, and the sorbent material was activated charcoal. The turn-on time for this design was approximately 1 min, and the turn-off time was approximately 10 min.

By designing the gap to be very narrow with a large surface area, the engineer can achieve very high conductance ratios in a gas-gap heat switch. The conductance ratio of the JPL design shown in Fig. 10.11 is approximately 700:1, while that
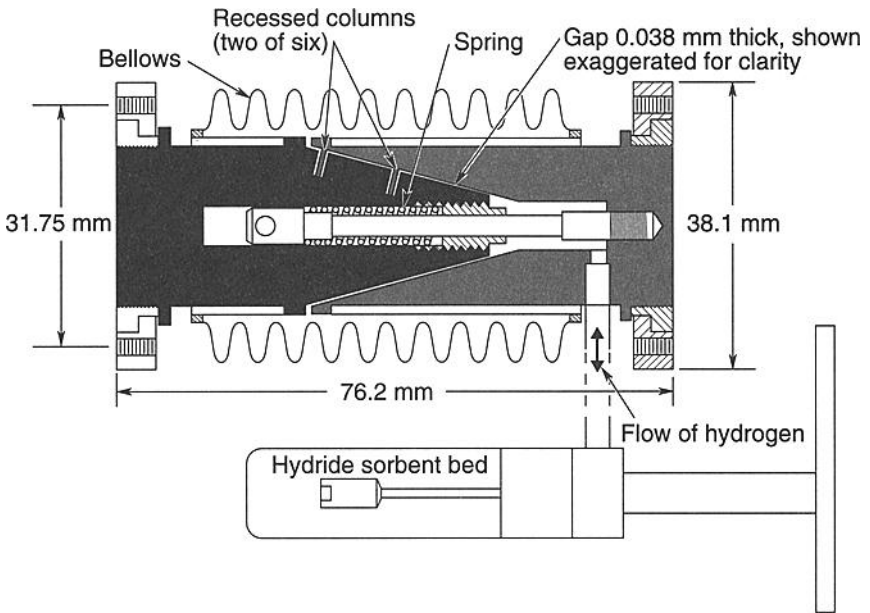
**Fig. 10.11. JPL gas-gap heat switch.** (Courtesy of JPL)
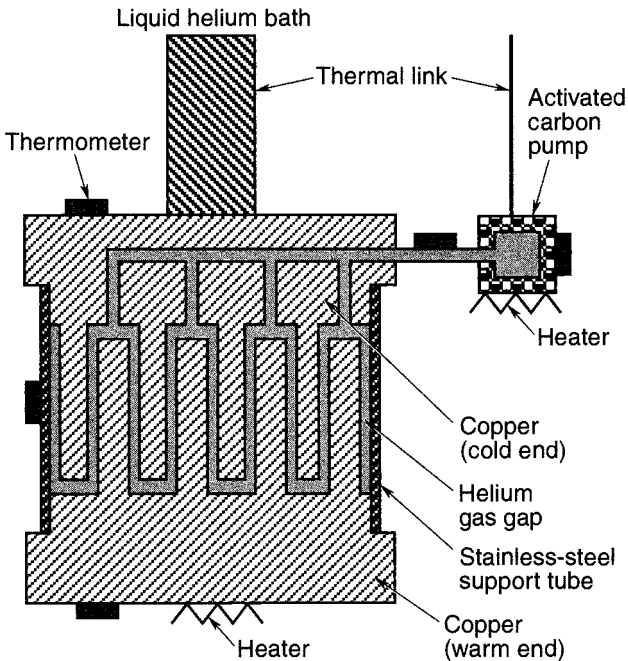
Fig. 10.12. NASA Ames gas-gap heat switch. (Courtesy of NASA)

of the Ames design (Fig. 10.12) is 1300:1. Ratios of up to 2500:1 have been reported for more elaborate designs that utilize greater surface area. A variation of this design, also developed at Ames, used liquid helium (He II) in the gap instead of gas. This design showed a conductance ratio of 6900:1 with the cold-end temperature near 2 K.

Disadvantages of the gas-gap approach include slow switching times (5 min to 1 h), high cost, reliability concerns, and high mass requirements. Some concerns are related to manufacturing: obtaining the very narrow gaps needed for high performance requires very tight machining tolerances, and the hermetic seal requires a weld of high integrity. These factors lead to a high construction cost and reliability concerns. Another concern is the life of the sorbent materials and the ability to reuse them.

Differential Thermal Expansion Heat Switches

Differential thermal expansion heat switches utilize the difference in coefficient of thermal expansion (CTE) of two different materials to make or break physical contact at an interface. One part essentially shrinks more than the other as a result of a change in temperature. This is a simple, straightforward approach that can produce a very reliable and robust design.

One difficulty with this approach is that CTE of most materials is very small, typically measured in millionths of a unit length per degree. Consequently, either the temperature difference creating the actuation or the physical size of the parts must be large in order to achieve actuation distances that are significantly greater than the machining and assembly tolerances encountered in manufacturing the switch. Fortunately, cryogenically cooled components typically use a switch to decouple themselves from much warmer components on the spacecraft. Because of the large temperature differences encountered, the use of differential CTE heat switches in cryogenic applications makes good sense.

Figure 10.13 shows a relatively unique design from Swales Aerospace. This device will passively switch between "on" and "off" operating modes. With the addition of the heater to the center tube, the switch may be actively turned off, which greatly reduces the transition time from on to off (without the heater, the cryogenic component is warmed to open the gap and turn the switch off). Application of power to the heater results in the development of a large temperature gradient in the center tube. The tube expands as it heats up, creating a gap between the beryllium cylinder and beryllium endplate. In a vacuum, conduction across this gap is virtually eliminated, and the switch provides excellent thermal isolation (i.e., the "off" mode). Once the beryllium endplate reaches a predetermined temperature (one that is between the spacecraft and the cryogenic component operating temperatures and is adjustable based on the gap dimensions at assembly), the center tube is expanded sufficiently so that the switch will remain in the off condition with no added heater power. To transition the switch from off to on, the beryllium endplate is cooled with the cryocooler (heater off). This causes the center tube to contract more than the beryllium endplate and cylinder, bringing the cylinder and endplate into contact, closing the gap, and putting the switch into the "on" (i.e., thermally conducting) mode. This design has a good conductance ratio, a high open switch resistance, and a fairly short transition time from the on state to the off state, as shown in Table 10.3.
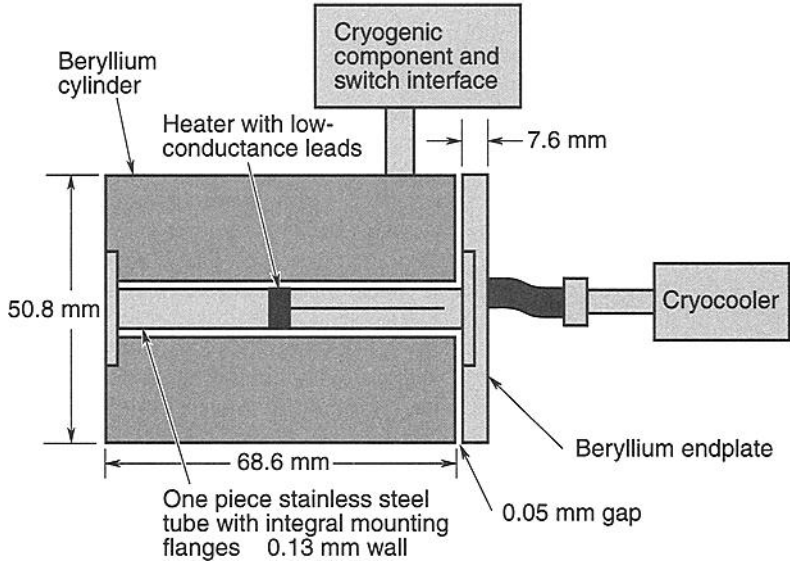
Fig. 10.13. Swales differential CTE heat switch. (Courtesy of Swales Aerospace)

Table 10.3. Swales Differential CTE Heat Switch Characteristics

Characteristic	Value
"Open" thermal resistance	1400 K/W
Conductance ratio	700:1
On-to-Off transition time	5 min
Mass	250 g[a]

[a]A smaller (< 60 g) version is under development.

References

10.1. J. Bascunan, T. Nixon, and J. Maguire, "Development of a Flight Qualified Heat Switch for LN2 Temperatures," *Advances in Cryogenic Engineering, Vol. 37B—Proceedings of the 1991 Cryogenic Engineering Conference* (Univ. of Alabama, Huntsville, AL, 11–14 June 1991).

10.2. C. K. Chan and R. G. Ross, *Design and Application of Gas Gap Heat Switches*, Final Report of Phase I, NASA-CR-187339, JPL publication 90-38 (15 March 1990).

10.3. R. Chave, J. Dooley, C. Lindensmith, and R. Ottocan, "Heat Switches for Cryogenic Application and Polycrystalline Magnetostrictive and Superconducting Flux Tube Actuation," Cryogenic Engineering and Materials (Montreal, PQ, Canada, 12 July 1999).

10.4. D. J. Frank and T. C. Nast, "Getter-Activated Cryogenic Thermal Switch," *Advances in Cryogenic Engineering, Vol. 31—Proceedings of the 1991 Cryogenic Engineering Conference* (Cambridge, MA, 12–16 August 1985) (A87-50751 22-31). New York, Plenum Press, 1986, pp. 933–940.

10.5. D. S. Glaister, D. G. T. Curran, V. N. Mahagen, and M. Steyanof, "Application of Cryogenic Thermal Switch Technology to Dual Focal Plane Concept for Brilliant Eyes Sensor Payload," Aerospace Applications Conference (Aspen, CO, 3–10 February 1996).

10.6. N. L. Hyman, "An Alternative to Deployed Thermal Radiators: Deployed Equipment Modules with Individual Package Temperature Control," *11th AIAA/USU Conference on Small Satellites*, SSC97-II-1 (Logan, UT, 1997).

10.7. D. L. Johnson and J. J. Wu, "Feasibility Demonstration of a Thermal Switch for Dual Temperature IR Focal Plane Cooling," (Waterville, NH, 25–26 June 1996).

10.8. A. Kashani, B. P. M. Helvensteijn, F. J. McCormack, and A. L. Spivak, "Helium Liquid and Gas-Gap Heat Switches for Applications at 2 K," *Proc. of 1993 CEC*, 39:1657 (1994).

10.9. K. Lankford, "Thin Plate Heat Switches—Development Performance and Applications," 10th Spacecraft Thermal Control Technology Workshop (March 1999).

10.10. T. Nast, G. Bell, and C. Barnes, "Development of Gas Gap Cryogenic Thermal Switch," *Advances in Cryogenic Engineering, Vol. 27—Proceedings of the 1991 Cryogenic Engineering Conference* (San Diego, CA, August 11–14, 1981) (A83-43220 20-31). New York, Plenum Press, 1982, pp. 1117–1124.

10.11. P. R. Roach, "A (He-3)-Gap Heat Switch for Use below 2 K in Zero G," Advances in Cryogenic Engineering, Vol. 37, pt. B, pp. 923–930 (1 January 1992).

10.12. M. T. G. Van Der Laan, R. Tax, H. H. J. Ten Kate, and L. J. M. Van De Klundert, "A Mechanically Driven Switch for Decoupling Cryocoolers," *Advances in Cryogenic Engineering, Vol. 35B, Proceedings of the 1989 Cryogenic Engineering Conference* (Los Angeles, CA, 24–28 July 1989). New York, Plenum Press, 1990, pp. 1457–1463.

10.13. L. D. Wing, *Automatic Thermal Control Switches*, AIAA paper 82-1764 (1 January 1982).

10.14. H. Ziad, T. Slater, P. vanGerwen, E. Masure, F. Preudhomme, and K. Baert, *Thermal Switch for Satellite Temperature Control*, NASA Technical Report Doc ID 19960054141 N (96N36387) (1 January 1995).

11 Phase-Change Materials

L. Bledjian,[*] D. V. Hale,[†] M. J. Hoover,[†] and M. J. O'Neill[†]

Phase-Change-Material Applications

The use of phase-change materials (PCMs) for thermal control is not new; consider the use of the icebox to store perishable foods before the development of efficient, inexpensive, active refrigeration systems. Recently, however, research and development in PCM technology has resulted in novel applications for both terrestrial and space environments.

The numerous electrical components on a spacecraft present thermal-control challenges. High-power-dissipating components must be prevented from overheating, without the earthbound benefits of free convection to the air or conduction to a cold plate. Conversely, components that are only activated occasionally must be prevented from cooling to temperatures below operational level, and the lack of atmosphere precludes normal convective methods of thermal control. Such components present an ideal application for PCM thermal control.

The simplest form of PCM thermal control for electronic components is the one that is used for short-duty-cycle components in launch or reentry vehicles. Although such components are used only once, they generate large quantities of heat that must be removed so that they will not overheat and subsequently fail. A PCM can thermally protect such a component, as shown in Fig. 11.1. The generated heat is absorbed via latent heat of fusion by the PCM without an appreciable temperature rise of the component. This kind of system is totally passive and very reliable.
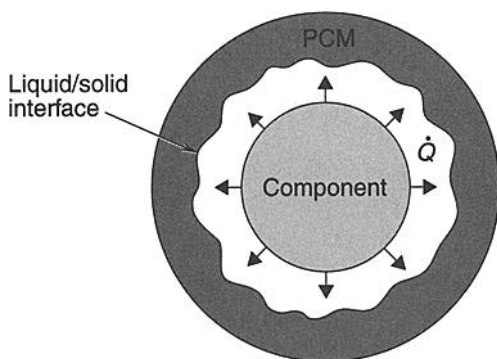
Fig. 11.1. PCM thermal-control system for one-duty-cycle electronic component on launch or reentry vehicle. (Courtesy of NASA[11.1])

A more general application of PCM thermal control for electronic components is for cyclically operating components (i.e., ones that operate in on-off cycles). Such a system is shown in Fig. 11.2. In this arrangement, when the component generates heat during the "on" portion of its cycle, the energy is stored via phase change in the PCM. During the "off" portion, the heat-of-fusion energy is removed via radiator, heat pipe, thermal strap, or other means, to refreeze the PCM in preparation for the next "on" portion. The alternate melting and freezing of the PCM enables the component to operate very nearly isothermally at all times.

Three PCM thermal-control systems were used on the Lunar Roving Vehicle (LRV) during the Apollo 15 mission. The first was attached to the Signal Processing Unit (SPU) and to batteries via thermal straps. During each LRV sortie, the heat produced by the SPU was absorbed through phase change in the PCM package. The thermal mass of the batteries offered additional heat-storage capability. After the sorties, louvers were opened on a radiator that was also connected to the PCM package via thermal straps. The PCM was thus refrozen by dumping the latent heat of fusion to space via radiation, thereby preparing the PCM package for the next sortie. The second PCM system was integrally bonded to the Drive Control Electronics (DCE). During a sortie, the heat dissipated within the DCE was absorbed by the PCM. After the sortie, the PCM was refrozen via a thermal-strap louvered radiator system. The third PCM system was integrally bonded to the Lunar Communications Relay Unit (LCRU). During a sortie, heat generated by the LCRU was stored within the PCM. After the sortie, insulation pads covering radiator surfaces on the LCRU were manually removed to allow heat radiation to escape to space, to refreeze the PCM.

This concept of storing and releasing energy via phase change can be extended to a larger scale for space missions that will present varying spacecraft thermal
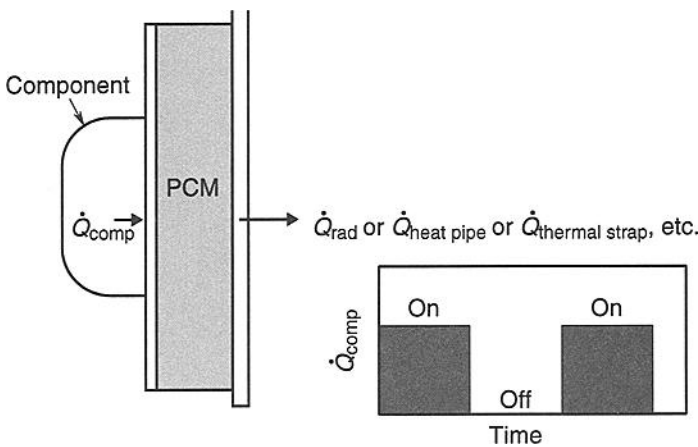

Fig. 11.2. PCM thermal-control system for cyclically operating components. (Courtesy of NASA[11.1])

environments. For example, a satellite orbiting Earth encounters drastically different thermal environments cyclically as it passes in and out of Earth's shadow. During such a mission, a PCM package can store and release solar energy to damp the otherwise large temperature changes that a spacecraft would experience during the orbit cycle. This strategy could enable a crew compartment or refrigeration compartment to remain nearly isothermal throughout the orbit. The compartment could be enveloped by a layer of PCM that would absorb and release solar energy during the orbit to provide isothermal conditions at the melting-point temperature of the PCM.

Another example of variable spacecraft thermal environment is encountered by landing vehicles on planets or moons that do not have an atmosphere. The day/night cycle on those bodies presents a thermal environment that changes radically. If the landing craft is enshrouded in PCM, solar energy can be conserved from the day for use during the night, thus ensuring a stable inner thermal environment for crew and/or components.

Another sample PCM thermal-energy storage (TES) device is shown in Fig. 11.3, in schematic form. Energy from electronic components lost through dissipation, which generally is treated as wasted energy, can be heat-piped to a central PCM TES device for later use in thermal control or energy production. This recovery of usually wasted energy for conversion into reusable energy should be beneficial for long space voyages.

PCMs with high melting-point temperatures can be used in conjunction with electronic power-producing systems. Radiators for collecting solar energy can be packed with PCM to store the energy via phase change at the melt temperature. This stored energy can then be converted into electrical power by using the large temperature difference between the radiator and deep space to drive either thermionic or thermoelectric devices. If the power-producing devices are sized for the mean solar power received during the planetary orbit, production of electrical power can continue during the shadow portion of the orbit because of the capability of the PCM to store heat and maintain the radiator at a constant temperature. With conventional photoelectric radiators, the power production ceases during the shadow portion of the orbit, and energy is stored in cells or batteries for use during
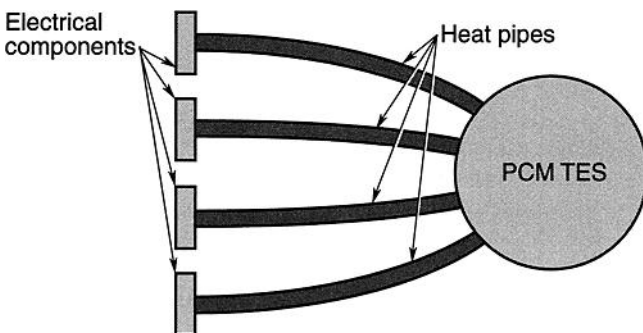

Fig. 11.3. Central PCM thermal-energy storage system. (Courtesy of NASA[11.1])

the "off" portion of the cycle. When fully developed, the thermionic or thermo-electric concept may offer significant increases in efficiency over the conventional concepts. Preliminary analytical and experimental studies reported by Humphries and Griggs[11.2] indicate the feasibility of this PCM application, and researchers have identified materials with suitable properties for such PCM systems.

PCM systems can be used in conjunction with space-flight experiments. Many delicate experiments rely upon precisely calibrated instruments. PCM packages can be integrated into these instruments (see Fig. 11.4) to maintain thermal stability or ensure isothermal conditions during the experiment.

PCMs can be used to great advantage in fluid-loop/radiator systems because of their unique isothermal heat-storage capacity. One such application was used on Skylab. The coolant fluid returning from the external radiators experienced sizable temperature variations during the course of an orbit cycle. For efficient operation of the heat exchangers, through which the fluid passed, these temperature variations were too large. A thermal capacitor utilizing PCM damped these temperature variations by alternate melting and freezing, as illustrated in Fig. 11.5. Thus the thermal capacitor maintained the fluid entering the heat exchanger within an allowable temperature range.

Another thermal capacitance application for PCM is in the radiator itself. Ordinarily, if a radiator is to be subject to cyclical heat-removal requirements during a mission, it must be sized for the peak load for successful operation. If PCM is integrated into the radiator, the radiator can be sized for the mean heat-removal requirement, since it can store the energy at peak load via phase change for later
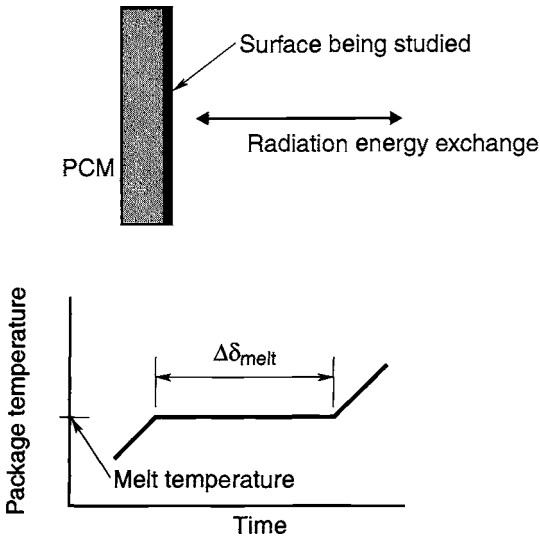

Fig. 11.4. PCM storage for radiometric property device. (Courtesy of NASA[11.1])
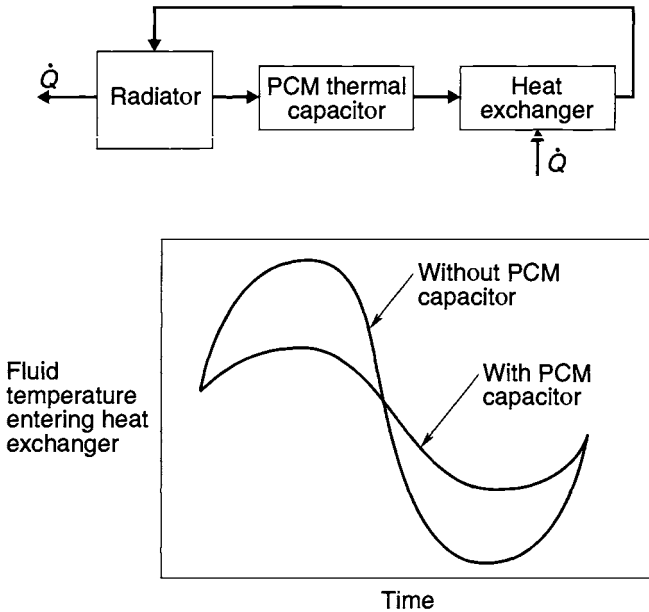
Fig. 11.5. PCM thermal capacitor in fluid loop. (Courtesy of NASA[11.1])

dumping to space by radiation. Significant savings in area and mass can be obtained with such a PCM radiator.

Phase-Change Materials

The most common phase-change transformations are solid-liquid (melting and freezing), liquid-to-gas (vaporization), solid-to-gas (sublimation), and anhydrous salt transformations. Because of the very large volumetric changes involved in vaporization and sublimation, consideration of these two phase-change transformations for reversible heat storage is impractical. One could, however, design a device, such as a heat pipe, that would act as a reversible heat-storage unit. Usually vaporization and sublimation are used in an open-loop fashion, where the vaporized or sublimed vapor is vented overboard (expendable cooler). Water is a very effective expendable coolant and has been used in several space applications, including Gemini, Apollo, and the space shuttle. Water melts at 0°C, absorbing 333 kJ/kg. The amount of heat required to raise the temperature of water from 0°C to 100°C (sensible heat) is 418 kJ/kg. The amount of heat required to vaporize water at 1 atm of pressure is 2253 kJ/kg. The total energy required to vaporize ice is the sum of the sensible and phase-change heats involved, which is 3004 kJ/kg. Most other expendable coolants absorb considerably less heat, ammonia (NH_3) being the second-best expendable coolant that is used extensively. The design and fabrication of expendable cooling devices for aerospace and military uses is a specialized field.

A number of classes of materials have been investigated for use in phase-change devices. Some of the more important are:

- inorganic salt hydrates, e.g., $Na_2SO_4 \cdot 10H_2O$ (Glauber's salt) and $CaCl_2 \cdot 6H_2O$
- organic compounds, e.g., paraffins (C_nH_{2n+2}), alcohols, phenols, aldehydes, and organic acids
- eutectics of organic materials, e.g., 88-mole% acetic acid + 12-mole% benzoic acid
- natural inorganic elements, e.g., sulphur (S).

Table 11.1 gives a representative list of candidate PCMs in the temperature range of −25 to +62°C; the melting-point temperature of most materials listed is

Table 11.1. Typical PCMs in the Range of −25 to +62°C

Material	Melting Point (°C)	Heat of Fusion (kJ/kg)
n-Eicosane ($C_{20}H_{42}$)	37	246
Polyethylene glycol 600 [$HO(CH_2CH_2O)_nH$]	20–25	146
Nitrogen pentoxide (N_2O_5)	30	320
Phosphonium chloride (PH_4Cl)	28	752
Dibasic sodium phosphate ($Na_2HPO_6 \cdot 12H_2O$)	37	279
Sodium sulfate ($Na_2O_4 \cdot 10H_2O$)	31	215
Glycerol [$C_3H_5(OH)_2$]	18	199
Calcium chloride ($CaCl_2 \cdot 6H_2O$)	29	170
p-Xylene [$C_6H_4(CH_3)_2$]	16	164
Sodium chromate ($Na_2CrO_4 \cdot H_2O$)	23	164
n-Undecane ($C_{11}H_{24}$)	−25	141
n-Dodecane ($C_{12}H_{26}$)	−12	211
n-Tridecane ($C_{13}H_{28}$)	−6	155
n-Tetradecane ($C_{14}H_{30}$)	6	228
n-Hexadecane ($C_{16}H_{34}$)	17	237
n-Heptadecane ($C_{17}H_{36}$)	22	213
n-Octadecane ($C_{18}H_{38}$)	28	244
n-Nonadecane ($C_{19}H_{40}$)	32	187
n-Octacosane ($C_{28}H_{58}$)	62	253
1-Tetradecanol [$CH_3(CH_2)_{12} \cdot (CH_2)OH$]	38	230
Acetic acid (CH_3COOH)	17	187
Water	0	333

near room temperature. This temperature range is pertinent to temperature control of electronic equipment and to environmental control of crewed spacecraft.

Table 11.2 gives a representative list of candidate PCMs for lower-temperature applications, such as infrared detectors and other solid-state electronic devices. Modern material databases can quickly provide lists of several candidate organic or inorganic PCMs for any given melting-temperature range. Keville,[11.3] Bledjian et al.,[11.4] and Grodzka[11.5] provide information useful for preparing and conducting a PCM heat-storage development program.

Solid Heat Sinks

Thermal-energy storage may also be accomplished with solid materials. For sensible heat storage the figure of merit is the specific heat of the material, c_p (kJ/kg·°C), when weight is critical, or the product of density and specific heat, ρc_p (kJ/cm^3·°C), when volume is critical. To avoid large and objectionable temperature

Table 11.2. Typical PCMs for Lower Temperatures

Material	Melting Point (°C)	Heat of Fusion (kJ/kg)
Methyl propyl ketone (C_5H_{10})O	−78	104
Amyl alcohol ($C_5H_{12}O$)	−79	112
1-Methyl-1,2 ethylbenzene (C_9H_{12})	−81	88
Ethyl acetate ($C_4H_8O_2$)	−82	118
Methyl ethyl ketone (C_4H_8O)	−86	111
n-Butylbenzene ($C_{10}H_{14}$)	−89	82
Isopropyl alcohol (C_3H_8O)	−89	88
Butyl alcohol ($C_4H_{10}O$)	−89	125
n-Heptane (C_7H_{16})	−91	140
Toluene (C_7H_8)	−94	72
Ethyl benzene (C_8H_{10})	−95	86
n-Hexane (C_6H_{14})	−95	151
Isopropylbenzene (C_9H_{12})	−96	81
n-propylcyclopentane (C_8H_{16})	−117	88
1-Neptune (C_7H_{14})	−119	126
2,4-Dimethyl pentane (C_7H_{16})	−119	67
Chloropropane (C_3H_7Cl)	−123	84
Butane (C_4H_{10})	−135	76
Ethane (C_2H_6)	−172	93
Methane (CH_4)	−183	59

gradients, a heat sink should have a relatively high thermal conductivity. Some of the best-known heat-sink materials for spacecraft applications are beryllium and its alloys, with c_p = 1.88 kJ/kg·°C and ρc_p = 0.0035 kJ/cm³·°C. Typical aluminum and magnesium alloys, used often in spacecraft designs, have c_p = 0.837 kJ/kg·°C and ρc_p = .0019 to approximately .0023 kJ/cm³·°C. Beryllia and alumina ceramics have been used as sensible heat-storage materials for electronic parts. Sensible heat storage is a well-documented engineering concept, and many handbooks provide values of density, specific heat, and thermal conductivity. At very low temperatures (less than 30 K), the specific heat of most solid materials becomes very low; thus lead and its alloys have been used for heat storage at low temperatures.

When To Use a PCM

As mentioned earlier, PCMs are generally useful for providing stable temperatures or for allowing radiators to be sized for average, rather than peak, heat-load conditions. In either case, the PCM is one of several potential thermal-design approaches. In most spacecraft applications, criteria for design selection boil down to which one has the lowest mass and power requirements, with further programmatic factors such as cost and development complexity also playing substantial roles. Competing thermal-control approaches include using a solid heat sink made from a high-specific-heat material such as beryllium, relaxing temperature-stability requirements, and using a conventional radiator/heater system. In the trade-off with a solid heat sink, an efficiently packaged PCM will usually show a mass advantage over the solid heat sink, but the cost and complexity of developing the PCM design may make it unattractive to the program if the mass savings are not substantial. For designs where the goal is to reduce temperature cycle ranges, the trade between temperature stability and thermal-design mass and cost must also be made on a case-by-case basis according to the value system of the particular program.

A direct comparison of the mass for a PCM radiator design with mass for a non-PCM design can be made, because the PCM design is not affected by subjective programmatic values. For a given application, we can safely say that the radiator size and mass may be reduced through the use of thermal storage if the peak heat-dissipation rate is larger than the average heat-dissipation rate. The first question that the thermal engineer must answer, however, is whether the added mass of the thermal-storage system is less than the mass saved by reducing the radiator size, i.e., is there a net benefit? With launch costs sometimes exceeding $20,000/kg, a substantial mass savings could pay any additional development cost for the PCM system. In some cases, a spacecraft program may have to reduce mass to meet launch vehicle mass limits, making any mass savings even more valuable.

The first step in the trade-off is to bound the limits of thermal-storage benefits by determining the maximum potential mass savings of a thermal system with a PCM versus one without. To control a payload component to its desired temperature requires sizing the radiator for peak dissipation if thermal storage is not considered and somewhere between the peak and average dissipation if thermal storage is included. A bound can be derived for the benefit of thermal storage if we

compare the peak-power-sized thermal system mass with the average-power-sized system mass including storage.

Busby and Mertesdorf[11.6] have outlined an analytical technique to identify the duty cycle at which a PCM becomes attractive in a design. Using their approach, consider the general case of a payload having a periodic heat dissipation pulse of magnitude $\dot{Q}_{pulse}$ and a duty cycle of β, as shown in Fig. 11.6. (The duty cycle is the fraction of the total cycle time, Δt_{cycle}, that the payload is "on.") If we use a radiator weighing m_{rad} kg/m^2 that can reject a net $\dot{Q}_{rad}$ W/m^2 and a PCM system that can store Q_{PCM} W·hr/kg (including the mass of packaging), we can calculate the masses of the competing systems as

$M_{w/oPCM}$ = mass of radiator sized for peak component dissipation rate.

$$M_{w/oPCM} = \frac{(\dot{Q}_{pulse} m_{rad})}{\dot{Q}_{rad}} \tag{11.1}$$

$M_{w/PCM}$ = mass of radiator sized for average heat rate plus weight of PCM system.

$$M_{w/PCM} = \frac{\beta*(\dot{Q}_{pulse}\, m_{rad})}{\dot{Q}_{rad}} + \frac{\beta*\Delta t_{cycle}\,(\dot{Q}_{pulse} - \beta\dot{Q}_{pulse})}{Q_{PCM}} \tag{11.2}$$

Setting these two equations equal to one another, we can solve for the heat-pulse duty cycle, β', at which the PCM design becomes attractive from a mass perspective (Ref. 11.33):

$$\beta' = \frac{m_{rad}Q_{PCM}}{\dot{Q}_{rad}\Delta t_{cycle}} \tag{11.3}$$
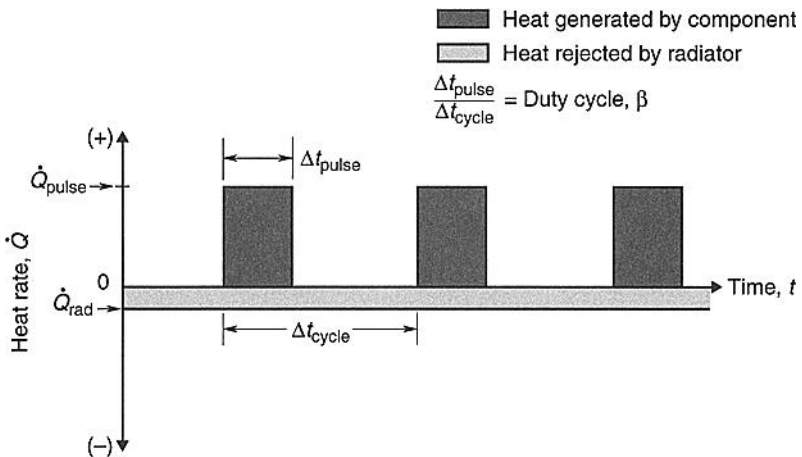
Fig. 11.6. Periodically operating component.

This equation clearly shows that the physical constants describing the characteristics of the thermal system set an upper bound on the maximum pulse duration for which thermal storage makes sense. Duty cycles greater than β' do not benefit from thermal storage because the mass penalty associated with the PCM and its packaging is greater than the mass saved as the result of using a smaller radiator.

This upper limit for the usefulness of thermal storage is illustrated by the example shown in Fig. 11.7, in which the masses of designs with and without PCMs are shown as a function of component heat-pulse duration. This example assumes a component dissipating 1000 W for a portion of the 1.5-hour orbital period is mounted to a wall of a spacecraft that can be used as a radiator surface. Because an existing structural panel is used, radiator mass is assumed to be limited to the mass of the heat pipes needed to spread the heat from the component plus the mass of thermal surface finishes, or about 5 kg/m^2. Furthermore, the radiator is assumed to be capable of rejecting a net 300 W/m^2 to the external environment and a PCM with high-performance packaging is assumed to be available to give a net specific storage capacity of 35 W-hr/kg. As can be seen in Fig. 11.7, PCMs show a net advantage for a pulse duration less than 35 min for a 39% duty cycle in this particular application. The results of this calculation are, of course, highly dependent on the parameters assumed, and the critical duty cycle will vary from application to application. In the case of very small duty cycles, the mass of the equipment being cooled (which was not included in the preceding example) may be large enough to directly absorb the heat pulse with an acceptably small rise in temperature, making a PCM unnecessary. In other cases, benefits such as heater power reduction or smaller heat-transport loops to connect the component to a remote radiator may also need to be considered. In such cases, the above preliminary assessment approach would still apply but would require modification to account for any mass savings in the power subsystem or heat-transport loop.
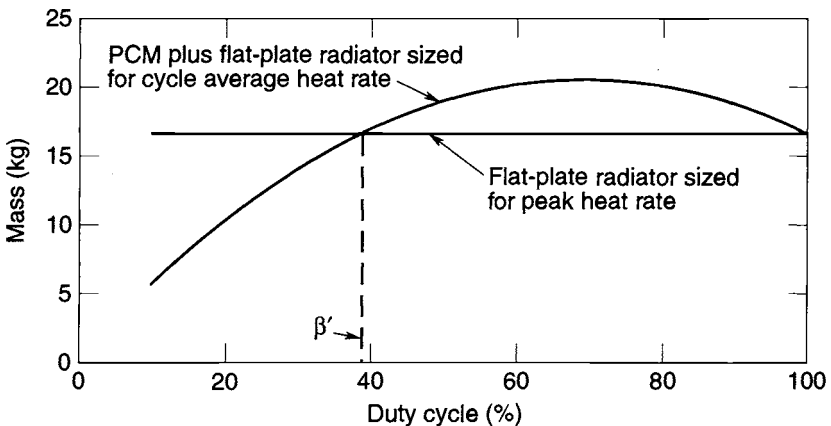

Fig. 11.7. Thermal-control mass with and without PCM.

PCM Design Details

In designing PCM thermal-control systems for specific applications, a number of factors other than heat of fusion must be considered. These include thermodynamics, heat transfer, combined thermodynamics and heat transfer, the function of fillers, containment, and an engineering approach that yields the proper design of a PCM thermal-control system from the initial requirements. The design guidelines presented in this section were developed during a study conducted by Lockheed (now Lockheed Martin) for NASA's Marshall Space Flight Center in 1971.[11.1]

Choice of PCM

In selection of a PCM for a specific application, the most important criterion is the operational temperature range of the component to be protected. The PCM must have a melting-point temperature well within this range to ensure that unintentional undercooling or overheating will not damage the component. Tables 11.1 and 11.2 give the melting-point temperatures of some representative PCMs, and extensive data on these and many others can be found in Humphries and Griggs[11.2] and Hale and Hoover.[11.1]

Designing and fabricating thermal-storage devices for solid-liquid transformation is considerably simpler than selecting a PCM because of the absence of a large volumetric change in melting or freezing. The selection of a suitable PCM, however, is often a project of considerable size and complexity. A good PCM should possess the following characteristics: high heat of fusion per unit mass; proper melting-point temperature (or temperature range); noncorrosiveness; nontoxicity; reversible solid-to-liquid transition; high flash point; low coefficient of expansion; stability; high thermal conductivity in both phases; little or no supercooling; and low vapor pressure at room temperature. A realistic figure of merit should take all these desirable characteristics into consideration. One should not assume that once a good match on melting-point temperature is found, high heat of fusion per unit mass is the controlling characteristic. However, an effort should be made to select a PCM with a heat of fusion greater than 150 kJ/kg for room-temperature applications, and greater than 40 kJ/kg for cryogenic applications.

If more than one PCM is found with suitable melting-point temperatures, comparisons of other characteristics should be made to eliminate all but the best PCM. The secondary characteristics that should be considered are summarized in Table 11.3. None of the PCM candidates may be superior in all characteristics, so engineering trade-offs may be necessary in selecting the best PCM for a specific application. In general, the prime candidates should cause fewer design problems than their nonprime counterparts.

Thermodynamic Considerations

To design a PCM thermal-control system properly, the analyst generates thermodynamic conservation equations for the system. These simple thermodynamic relationships allow estimation of the energy-storage requirements of the PCM, the required mass of PCM, and the size of the radiator. While these relationships will vary from application to application, the following example illustrates the general method for quantifying the thermodynamic relations for a specific application.

Table 11.3. Secondary Characteristics of PCMs

Property or Characteristic	Desirable Value or Tendency
Heat of fusion	High
Thermal conductivity	High
Specific heat	High
Density	High
Volume change during melting	Low
Vapor pressure	Low
Melting and freezing behavior	Dependable and reversible
Availability	Readily available
Cost	Low
Compatibility	Compatible with container and filler materials
Toxicity	Nontoxic
Hazardous behavior	Not exhibited
Property data	Readily available and well documented
Surface tension	Low

Consider a component with the cyclical heat-generation profile shown in Fig. 11.6. Its temperature is to be controlled by the PCM package/radiator system in Fig. 11.8. Since the component is to be controlled to a specific temperature, the ideal radiator will operate very close to the PCM melting-point temperature at all times and have nearly constant radiant-heat rejection to the external environment. If the component heat generation and radiation to space are the only energy exchanges to which the package is subject, the radiator is sized so the total energy dissipated by the component during one cycle equals the total energy radiated by the radiator over that same time period. This is expressed mathematically as

$$\varepsilon A_{\text{rad}} \sigma T_{\text{melt}}^4 \Delta t_{\text{cycle}} = \dot{Q}_{\text{pulse}} \Delta t_{\text{pulse}}, \qquad (11.4)$$

assuming an absolute-zero thermal-radiation sink and no solar or planetary radiation incident upon the radiator surface. (For applications in which incident radiation is appreciable, the above equation must be adjusted by subtracting the radiant energy absorbed from the surroundings from the energy emitted by the radiator.) Since T_{melt}, ε, Δt_{cycle}, $\dot{Q}_{\text{pulse}}$, and Δt_{pulse} are fixed quantities for any particular application, the required radiator size may be calculated as follows:

$$A_{\text{rad}} = \frac{\dot{Q}_{\text{pulse}} \Delta t_{\text{pulse}}}{\sigma \varepsilon T_{\text{melt}}^4 \Delta t_{\text{cycle}}} = \dot{Q}_{\text{gen}_{\text{avg}}} \left(\frac{1}{\sigma \varepsilon T_{\text{melt}}^4} \right) \qquad (11.5)$$
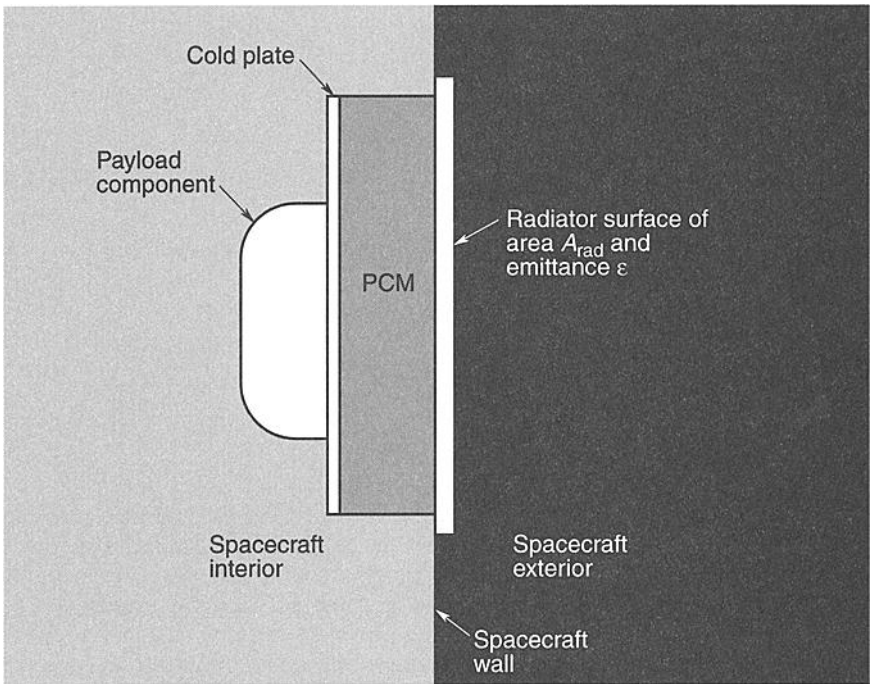
Fig. 11.8. PCM/radiator thermal-control system.

Notice that the PCM allows the radiator to be sized for the average power being dissipated by the component over the entire cycle. If a PCM were not used, the radiator would have to be sized for the peak heat rate encountered during the pulse, making such a radiator larger by the ratio $\dot{Q}_{pulse}/\dot{Q}_{avg}$. Reduction of radiator size and mass is therefore one of the advantages of a PCM system.

The net energy stored in the PCM as the component goes through its on/off cycles is shown as a function of time in Fig. 11.9. To store and release the $\dot{Q}_{pulse}$ energy as heat of fusion, the quantity of PCM must be:

$$m_{PCM} = \frac{E_{max}}{h_f} \tag{11.6}$$

where E_{max} is as shown in Fig. 11.9.

Heat-Transfer Considerations

Although the thermodynamic considerations are simple and straightforward, the heat-transfer problems are perhaps the largest obstacles in the design of PCM systems. As a general rule, materials with relatively large heats of fusion have relatively low thermal conductivities. Therefore, for significant heat fluxes, a very large temperature difference may be required to transfer the heat from component to PCM. This temperature gradient can result in a large temperature rise of the component during the melting process.
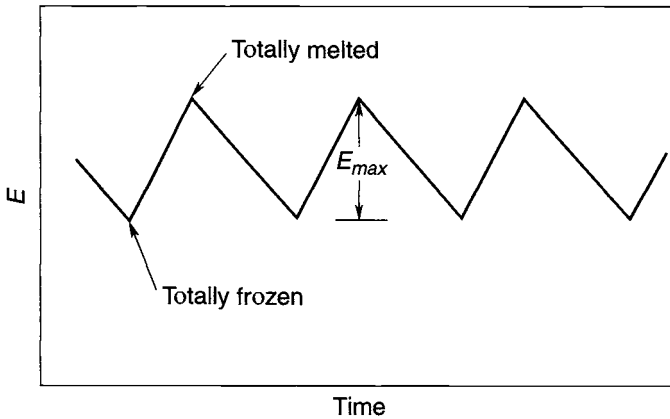
Fig. 11.9. Net energy in PCM.

In the PCM/radiator example discussed previously, the heat fluxes at the cold plate and radiator can be used to determine the temperature distribution within the package as a function of time. An assumption that will be used in determining the temperature distributions is that the time to achieve a linear quasi-steady-state temperature distribution will be shorter than the time required for the liquid/solid interface to move an appreciable distance. The transient period can be neglected principally because c_p/h_f is such a small ratio that the transient period is negligible compared to the time required for appreciable interface movement. The validity of this assumption has been confirmed by computer thermal analysis of representative PCM systems. (Deviations from this assumption would actually result in improved performance, making this a conservative analytical approach.)

At the point during the cycle when total solidification has just occurred, all the heat stored in the PCM will have been rejected to space by the radiator, the surface temperature of which is slightly below the melt temperature of the PCM. The temperature distribution through the system will therefore be as shown in Fig. 11.10.

If the quantity of PCM has been chosen correctly, heat will be conducted from the PCM to the radiator at a constant rate throughout the cycle. Therefore, the slope of the temperature distribution through the PCM's solid portion must equal:

$$\left(\frac{\partial T}{\partial X}\right)_s = \frac{\sigma A_{rad} \varepsilon T^4_{melt}}{k_s A_{cp}} \tag{11.7}$$

If the thermal-control system has been properly designed, the next component heat pulse should start just as the solid boundary reaches the cold plate and the PCM near the component should begin to melt. After approximately 50% of the PCM has melted, the temperature distribution will be as shown in Fig. 11.11. The slope of the temperature distribution in the solid region remains the same as before, but the liquid phase now has a linear temperature distribution with the slope, and the rate of melting can be easily calculated as
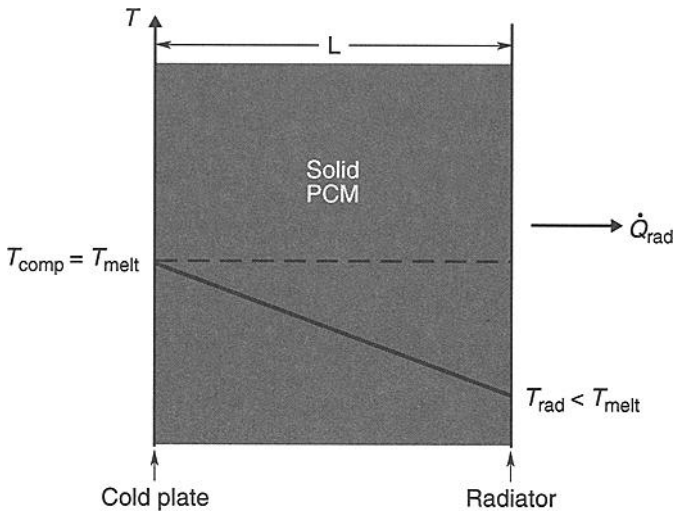
Fig. 11.10. Temperature distribution at total solidification.
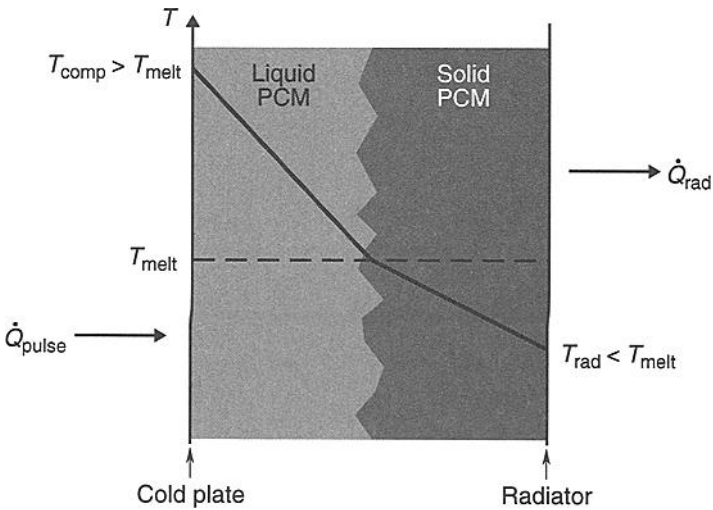
Fig. 11.11. Temperature distribution at 50% melt.

$$\left(\frac{\partial T}{\partial X}\right)_l = \frac{\dot{Q}_{pulse}}{k_l A_{cp}} \tag{11.8}$$

$$\dot{m} = \frac{\dot{Q}_{pulse} - \dot{Q}_{rad}}{h_f} \tag{11.9}$$

When all of the PCM has melted, the distribution will assume the shape shown in Fig. 11.12, and the slope remains the value cited in Eq. (11.7).

Because the liquid phase thickness is maximum at total melt, the component temperature will be at its maximum value at this point, namely,

$$T_{comp_{max}} = T_{melt} + (L)\left(\frac{\partial T}{\partial X}\right)_l. \tag{11.1}$$

If the system is optimally designed, the component heat generation will cease just as the liquid boundary reaches the radiator. Freezing will begin at the radiator surface, and the freeze boundary will move toward the cold plate. After 50% of the PCM has frozen, temperature distribution will assume the shape in Fig. 11.13.

The liquid will be near the melt temperature, and the solid will have the slope $(\partial T/\partial X)_s$ described earlier. After the solidification has completed, the distribution will return to that given in Fig. 11.10 and the cycle will then repeat itself.

Of primary importance to the design engineer is the maximum temperature the component will reach during the cycle. Recall the relation developed previously,

$$T_{comp_{max}} = T_{melt} + (L)\left(\frac{\partial T}{\partial X}\right)_l, \tag{11.10}$$

$$\left(\frac{\partial T}{\partial X}\right)_l = \frac{\dot{Q}_{pulse}}{k_l A_{cp}}. \tag{11.11}$$

where substitution yields:

$$T_{comp_{max}} = T_{melt} + \frac{\dot{Q}_{pulse}L}{k_l A_{cp}}. \tag{11.12}$$
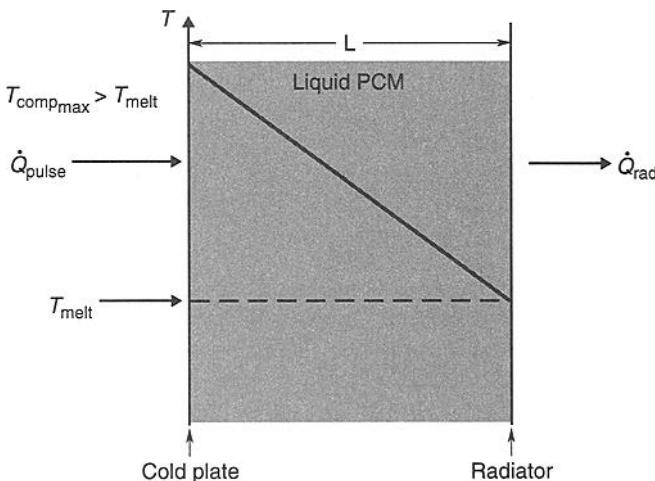

Fig. 11.12. Temperature distribution at total melt.
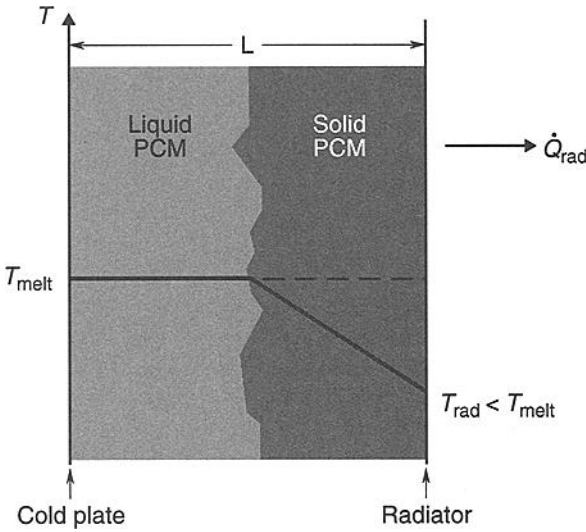
Fig. 11.13. Temperature distribution at 50% solidification.

$$T_{\text{comp}_{\max}} = T_{\text{melt}} + \frac{\dot{Q}_{\text{pulse}}L}{k_l A_{cp}} . \tag{11.13}$$

If the component is to operate properly, this $T_{\text{comp}_{\max}}$ must be less than the maximum allowable operating temperature of the component. However, if the best PCM for this operational temperature range has a relatively low thermal conductivity (as is usually the case), the following design barrier presents itself. From the thermodynamic discussions presented earlier,

$$m_{\text{PCM}} = \frac{E_{\max}}{h_f} = \rho_{\text{PCM}} A_{cp} L . \tag{11.14}$$

Solving for L yields:

$$L = \frac{E_{\max}}{h_f \rho_{\text{PCM}} A_{cp}} \tag{11.15}$$

Substituting for t in our relation for $T_{\text{comp}_{\max}}$ yields:

$$T_{\text{comp}_{\max}} = T_{\text{melt}} + \frac{\dot{Q}_{\text{pulse}} E_{\max}}{k_l A_{cp}^2 h_f \rho_{\text{PCM}}} . \tag{11.16}$$

For a given application and given PCM for the desired temperature range, T_{melt}, Q_{pulse}, E_{max}, k_l, A_{cp}, h_f, ρ_{PCM} are all fixed quantities. Therefore, $T_{\text{comp}_{\text{max}}}$ is fixed, and if it exceeds the maximum allowable operating temperature of the component, it presents an apparent roadblock to the designer. High-conductivity filler materials allow the designer to overcome this obstacle.

The Function of Fillers

When the component temperature rise for a particular application exceeds the maximum operational temperature of the component, filler materials must be integrated into the PCM package to improve the thermal conductivity of the PCM. The function of filler materials is to provide low-thermal-resistance paths through the PCM, thus raising its equivalent thermal conductivity and reducing the temperature gradient necessary to transfer the imposed heat load into the PCM. The reduced temperature gradient thereby reduces the maximum temperature of the component.

A number of different fillers have been tested for use in PCMs, including carbon fibers, copper foam, alumina foam and powder, and aluminum powder, foam, honeycomb, and fins. Aluminum or alumina powder-PCM composites were found to produce no noticeable improvement in the thermal conductivity of lithium nitrate according to Grodzka.[11.7] Aluminum wool has been found to produce some improvement in system performance, but significantly less than that predicted by the pretest analysis.[11.8] The same was generally true of the copper and aluminum foams tested. Various test results reported with different PCMs indicate that aluminum honeycomb, aluminum fins, and carbon fibers offer the most system improvement.[11.7–11.9]

Combined Thermodynamic and Heat-Transfer Relations

This section is devoted to the development of the combined thermodynamic and heat-transfer relations for a PCM package with filler materials uniformly distributed within. For the purposes of this discussion, we assume that the contact resistance between the filler material and the cold plate is negligible, and that three-dimensional heat-transfer effects between the filler and PCM can be neglected. (The errors introduced by these assumptions are discussed later.)

A conceptual illustration of a PCM thermal-control system using filler materials is shown in Fig. 11.14. Five equations in five unknowns can be derived to describe such a system. These equations represent conservation of energy and mass, additive conductance and area relations, and temperature-range constraints.

Conservation of Energy

After the maximum energy that must be stored by the PCM package E_{max} is determined, the heat balance shown in Eq. (11.17) will hold. This equation includes both the energy stored through latent heat of fusion and sensible heat stored within the liquid PCM and the filler material.

$$E_{\text{max}} = \rho_{\text{PCM}} A_{\text{PCM}} L h_f + \left[\rho_F A_F C_{p_F} + \rho_{\text{PCM}} A_{\text{PCM}} C_{p_{\text{PCM}}} \right] \frac{L}{2} (T_{\text{comp}_{\text{max}}} - T_{\text{melt}}) \quad (11.17)$$

PCM

Filler

A – A

Filler cross-sectional area = A_F
PCM cross-sectional area = A_{PCM}
$A_F + A_{PCM} = A_T$ = total cross-sectional area
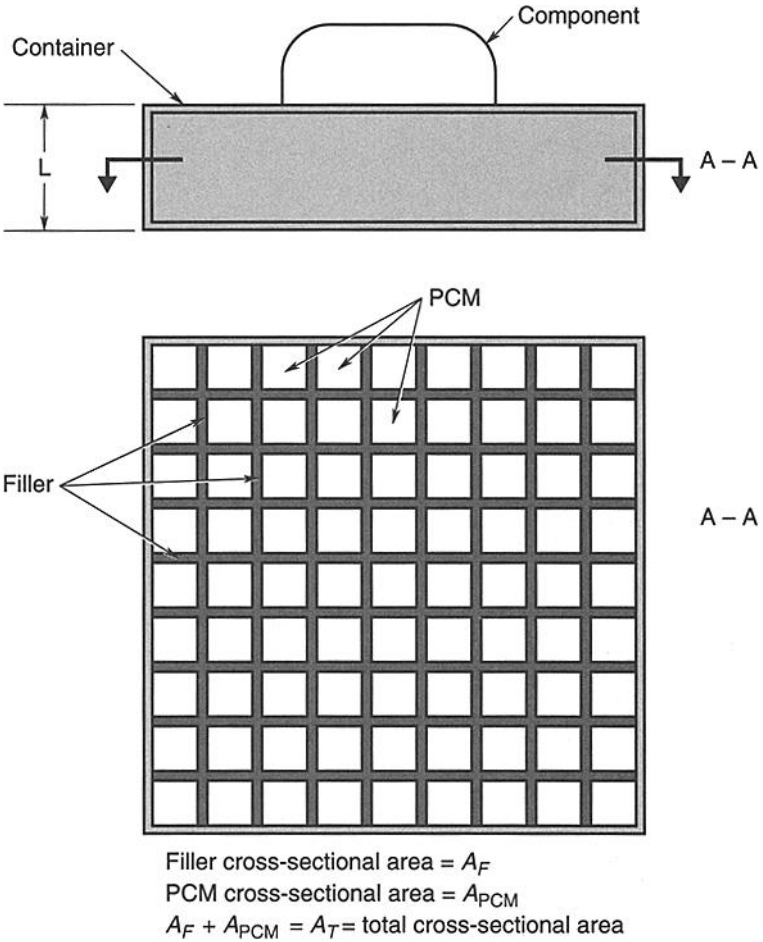
Fig. 11.14. PCM package with filler.

(Note: $E = 0$ when filler and PCM are at T_{melt} throughout, and PCM is solid throughout.)

Temperature Range Constraint

As discussed earlier, any resistance in the heat-transfer path between the component and the PCM will cause the component temperature to rise above the PCM melt temperature. This temperature rise must be limited so that the component does not exceed its maximum allowable operating temperature. This constraint may be expressed as

$$\dot{Q}_{pulse} = \frac{k_T A_T (T_{comp_{max}} - T_{melt})}{L} . \tag{11.18}$$

This equation establishes a relation between the total conductivity, area, thickness, and temperature rise of the component, $(T_{comp_{max}} - T_{melt})$.

Additive Conductance Relation

For parallel conductance paths through the PCM and filler, the total equivalent conductance can be described as:

$$k_T A_T = K_{PCM} A_{PCM} + k_F A_F \tag{11.19}$$

This relation neglects three-dimensional effects and contact resistances. (The errors imposed by neglecting these factors are discussed later.)

Conservation of Mass

The design engineer will want to know the mass of the PCM, container, and filler. The mass balance shown in Eq. (11.20) will hold.

$$W_T = (\rho_{PCM} A_{PCM} + \rho_F A_F)L + \rho_c[2A_T + (4\sqrt{A_T})L]L_C. \tag{11.20}$$

The radiator mass is neglected here because the outer surface of the container could be coated to serve as a radiator or another method of heat removal might be used for other applications. Neglecting the thermal mass of the radiator is conservative.

Additive Area Relation

The total area is the sum of the cross-sectional areas of the PCM and filler. Thus,

$$A_{PCM} + A_F = A_T. \tag{11.21}$$

Solution of Simultaneous Equations

For a given application, PCM, filler material, and container material, these five simultaneous equations can be solved to yield W_T, L, k_T, A_{PCM}, and $\Delta T_{excursion} = T_{comp_{max}} - T_{melt}$ as functions of filler area, A_F. By conducting a parametric study, the thermal engineer can gain insight into the functional relationships between these variables that will lead to an optimal design solution.

As an example, consider a component that dissipates 100 W for 1 h and is mounted on a 0.093-m² (1 ft²) PCM heat sink that uses aluminum as the container and filler material and a fictitious PCM having the properties shown in Table 11.4.

Using the above equations, we can calculate the total mass and thickness of the PCM heat sink and the temperature rise of the component as a function of filler area-fraction, as shown in Fig. 11.15. These curves illustrate several interesting

Table 11.4. Properties of a Fictitious PCM

| Property	Variable	Value
Density	ρ_{PCM}	1602 kg/m³
Thermal conductivity	K_{PCM}	0.519 W/m-K
Specific heat	C_{pPCM}	1673.6 J/kg-K
Heat of fusion	h_f	232,400 J/kg
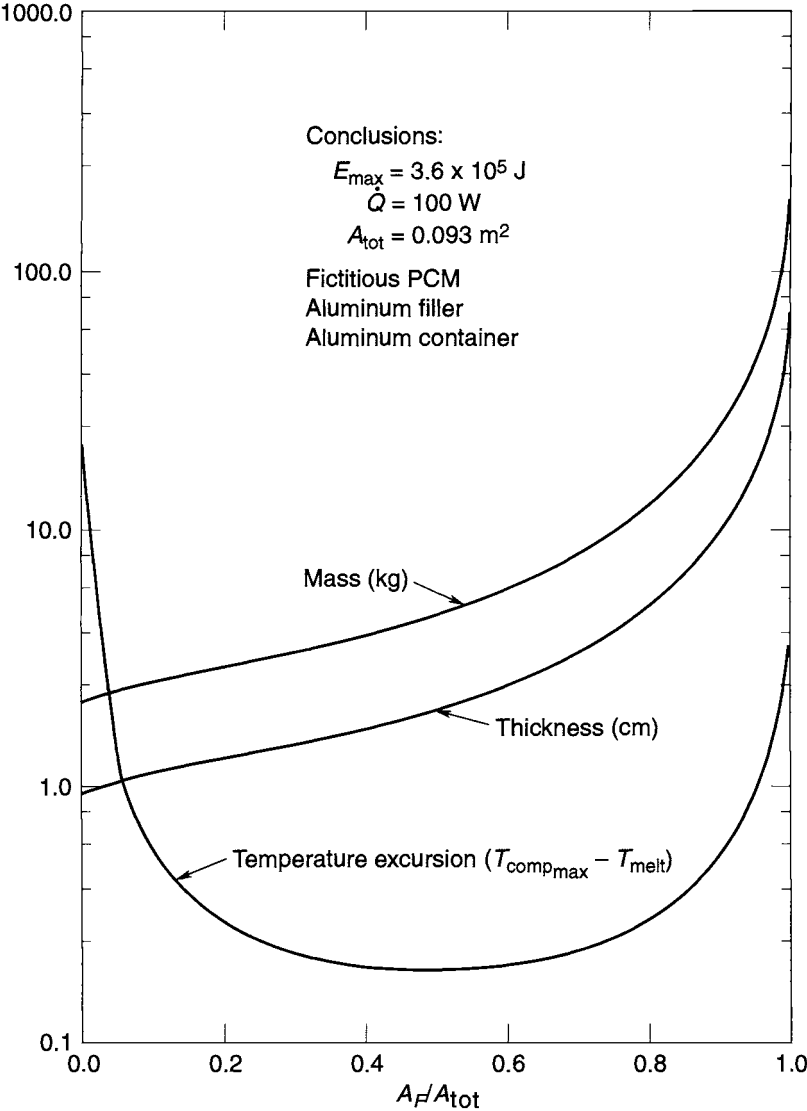
Fig. 11.15. PCM design optimization.

facts. The intersections of the three curves with the y-axis represent the mass, thickness, and temperature excursion for a PCM package without filler. The thickness and mass are least for this condition, and addition of filler causes an increase in both quantities. However, the component temperature rise is highest at this condition, and it decreases drastically with small additions of filler until a minimum point is reached at around 50% filler fraction. The minimum temperature will

occur at the 50% point whenever the sensible heat storage of the package and the thermal conductivity of the PCM have negligible effects upon total energy storage and total heat transfer, respectively. Since most designs will try to maximize the effectiveness of the PCM, the minimum temperature will tend to occur near this $0.5 A_T$ point. However, for applications in which sensible heat storage and/or PCM thermal conductivity become significant, the minimum value may occur at some other filler fraction. Similarly, the intersections of the three curves with the A_F/A_{tot} = 1.0 vertical line represent the mass, thickness, and temperature excursion for a solid aluminum heat sink. At this condition, the mass and thickness reach their maximum values, showing the inferiority of a solid heat sink compared to a PCM package.

Curves of this type can easily be generated for a particular application, PCM, container, filler, and cold-plate area. Knowing the maximum temperature excursion the component can sustain, the designer can consult the curve for temperature excursion and find the minimum filler area required to maintain the excursion below the maximum. From the other curves, the required minimum mass and thickness can be obtained. If the mass represents a savings over other thermal-control techniques, then more sophisticated analytical and experimental design studies should be considered. If either the mass or the thickness is not competitive with other thermal-control techniques, then the PCM technique can be eliminated from further consideration.

Contact Resistance and Three-Dimensional Effects

Errors introduced by contact resistance and three-dimensional conduction effects were neglected in the preceding analysis. These errors can be significant, as the following discussion indicates.

Consider a filler material of aluminum honeycomb in a container 1 cm thick. The thermal conductivity of the PCM is so much less than that of aluminum that the total equivalent conductance through the PCM/honeycomb composite is approximately $k_{Al}A_{Al}/L$. If a relatively high-conductivity metal-filled adhesive is used to bond the honeycomb to the cold plate, the thickness of adhesive between the honeycomb and cold plate will represent a thermal resistance between the honeycomb and cold plate. The resistance of the adhesive will be $L_{adh}/k_{adh}A_{adh}$ ~ $L_{adh}/k_{adh}A_{Al}$. The total resistance through the package now becomes the sum of the two series resistances, namely

$$R_{eq} = \left(\frac{L_{adh}}{k_{adh}} + \frac{L}{k_{Al}}\right)\frac{1}{A_{Al}} . \tag{11.22}$$

Since k_{adh} will at best be only a few percent of k_{Al}, perhaps 3%, an adhesive thickness of 3% L or 0.03 (1 cm) = 0.3 mm will cause the resistance R_{eq} to be double the value obtained by neglecting the adhesive resistance. Since the heat entering the package must pass through both resistances, $Q = \Delta T/R_{eq}$, doubling the R_{eq} will double the ΔT through the package, and consequently the temperature excursion of the component will be doubled. In addition, bubbles can form in the adhesive upon curing, reducing the effective cross-sectional area of the heat path through the adhesive and thereby increasing the resistance further. These resistances

can obviously cause the component temperature to rise appreciably above the value predicted by the idealized one-dimensional analysis presented earlier. These effects indicate the need for a metal-to-metal contact that could be accomplished by some form of welding, soldering, or integral fabrication of filler and cold plate.

The simplified one-dimensional analysis presented earlier is the first step in determining if a PCM approach offers potential advantages for a particular design problem. However, because the one-dimensional analysis does not account for three-dimensional heat-spreading effects in the plate and PCM, one must still perform a detailed computer analysis. Such an analysis is likely to show that the PCM, while still advantageous, is not quite as good as the simplified analysis had suggested.

Containment Considerations

The design of the container for a PCM package must take into account both structural and thermal considerations. Structural considerations include the need for the package to be leakproof (for a liquid PCM) and to withstand all imposed static and dynamic loads. A primary thermal consideration is the requirement for the container to be integrated into the thermal-protection package without degrading system performance.

A major problem in the design of PCM containers is the need to accommodate the volume change that occurs when the contents melt or freeze. Several methods have been developed to deal with the phase-transition volume change; one is shown in Fig. 11.16. An elastic bellows between the cold plate and the opposite wall is prestressed in tension during the fill process. After filling is complete, the bellows exerts a compressive load on the liquid PCM. When solidification occurs, the bellows further contracts and still maintains a compressive load on the PCM. A bellows container using stainless steel as the bellows material was built and tested.[11.10] No filler material was used in the bellows container, but a filler could be attached to the cold plate in such a container. The major advantage of a bellows container is that no void or gas volume must be left in it to provide room for PCM expansion upon melting. Since void or gas volume could cause a decrease in heat transfer within the container, use of the bellows container does have a distinct
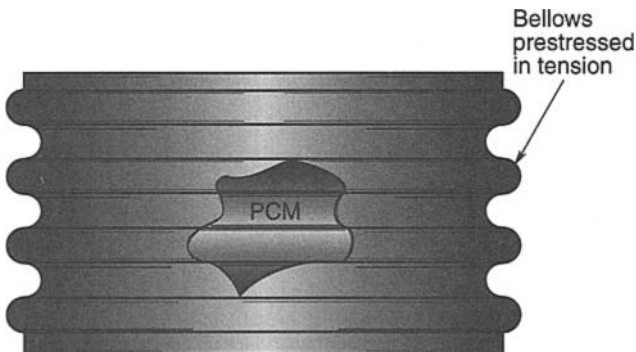

Fig. 11.16. Elastic bellows container.

thermal advantage over other techniques. However, the nonrigidity of the container and the cyclical change in loading could cause structural or leakage problems. The design engineer should consider these risks. The more commonly used container is the rigid container that has void or gas volume for expansion of the PCM during melting. Rigid containers have been used on the Lunar Roving Vehicle and on the Skylab Cluster. Such a container is shown in Fig. 11.17. In this figure, the void region is shown at the top, where it would be under terrestrial gravitation, but in a "0-g" environment the void volume would occupy different regions of the container.

A significant problem in designing the rigid container is the sizing of the void volume. If the container were totally vacuum-tight and evacuated prior to flight, theoretically the void volume required would merely be the volume change upon expansion of the PCM, namely,

$$\text{Void volume} = V_L - V_S = m_{\text{PCM}}\left(\frac{1}{\rho_L} - \frac{1}{\rho_S}\right) \tag{11.23}$$

However, gas will be in the void volume while the solid phase exists in the container, as a result of equilibrium vapor-pressure formation above the solid phase and prelaunch molecular diffusion through the minute holes that will exist in joints and seams of the container. Regardless of the pressure of this gas above the solid phase, when complete liquefaction occurs, a large pressure will be set up within the container since no volume exists for the gas phase to occupy. Therefore, sufficient volume must be added to the container to maintain trapped gases at a reasonable pressure.

Some designers of rigid containers[11.11] take the most conservative view that the pressure above the solid phase has reached atmospheric pressure because of leaks before launch. With the aid of Fig. 11.18, one sees from the ideal gas law at constant temperature that the relation between maximum pressure and total volume is

$$P_{\text{max}} = P_{\text{atm}}\left(\frac{V_T - V_S}{V_T - V_L}\right) = \left[\frac{V_T - \dfrac{m_{\text{PCM}}}{\rho_s}}{V_T - \dfrac{m_{\text{PCM}}}{\rho_s}}\right](p_{\text{atm}}) . \tag{11.24}$$
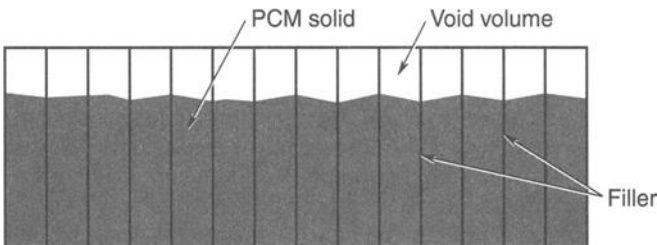

Fig. 11.17. Rigid PCM container.
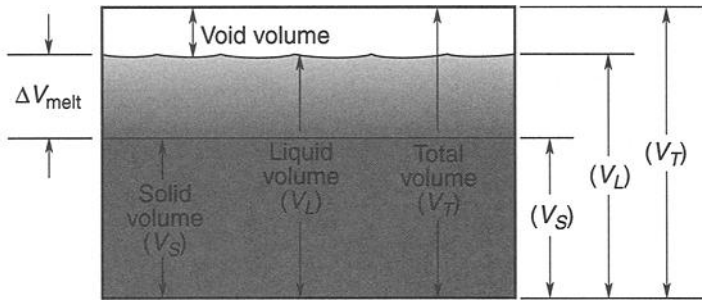
Fig. 11.18. Volume relationships for rigid containers.

The container should therefore be designed to withstand the P_{max} structural maximum loading associated with the final choice of V_T. If the PCM liquid will rise appreciably above the melt point at any time during planned operation, the thermal expansion of the liquid should also be considered in determining the total container volume.

The effects of the void or gas volumes within the container on heat transfer are hard to estimate quantitatively. However, such void spaces will decrease the conduction heat transfer below that for the idealized void-free models currently assumed for analysis, especially if voids were to form between the cold plate and PCM or between the filler and PCM. In general, degradation as a result of voids should be least for materials with high wetting tendencies, i.e., those that cling to the solid metallic surfaces within the package. The previous discussion demonstrated that materials with very small percentage volume changes during phase transition cause fewest thermal and structural problems for the design engineer.

The bonding between any filler material present and the cold-plate portion of the container is a problem area previously discussed. To prevent thermal resistance at the bond, use metal-to-metal bonding. Soldering and brazing techniques can be used for a particular application if welding is not possible.

A slightly different packaging technique can improve thermal performance of PCM systems that are to be used for one-duty-cycle components. Such components generate high amounts of heat for a period of time and then cease operation, never again to be activated. Such a component can be placed in thermal contact with a PCM package to keep it relatively isothermal for its short life. The PCM package essentially absorbs, via phase change, all the energy generated by the component, and refreezing after the cycle is unnecessary. The container technique shown in Fig. 11.19 could be used for such an application.

The spring initially could be compressed so that throughout the melt process it would hold the solid firmly in contact with the cold plate. The liquid would pass to the bottom and the cold plate would remain virtually isothermal at the melting-point temperature without the addition of filler materials to the package. In a similar technique presented by Fabian and Vaccari,[11.10] a pressurized bladder performs the same function as the spring.
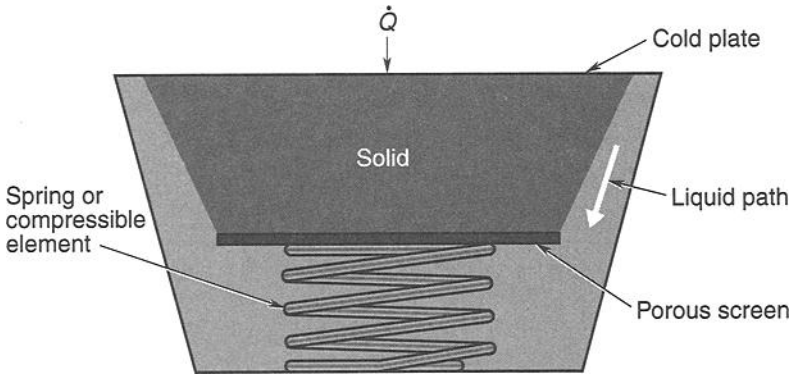
Fig. 11.19. One-duty-cycle PCM container.

Material Properties and Compatibility

In selecting container and filler materials, the engineer must consider their thermal and mechanical properties as well as the compatibility of PCM materials with their containers. Metals have been the universal choice for PCM containers and for fillers because of their high thermal conductivity, yet none of the PCM candidate materials have been rigorously tested for long-term compatibility with these aerospace metals. Generally the concern is corrosion of the container metal by the PCM itself or by some impurity in the PCM. Of course, some impurities have no effect on the compatibility of the basic materials, and a few types of impurities even inhibit corrosion.

Material Corrosion

The primary mode of material corrosion of concern in PCM technology is chemical corrosion. Generally, PCMs of the salt-hydrate-metallics and fused-salt categories are the most corrosive. Corrosion by PCM impurities can occur when the contaminant is a metal ion such as Pb^{+2} and the base PCM material, such as water, acts as an electrolyte between the ion and the container metal.[11.12] The result is that ionization removes the aluminum from the container. This form of corrosion can occur for a large variety of combinations of container metals and contaminants. None of the combinations are documented with regard to severity of corrosion in a PCM application. Furthermore, the concentration of the contaminants along with several other variables influences the extent of corrosion. For these reasons, specific combinations to avoid are not presented. Bregmon[11.13] and Bosick[11.14] present the limited information that is available. A general guideline, however, can be found in Table 11.5, where any metal listed will react with any ion listed below it. For example, iron (Fe) will dissolve in a nickel (Ni) solution, plating out nickel metal. There are exceptions to the general trend indicated in the table, so design decisions regarding contaminants should not be based solely on this data.

Table 11.5. Potentials of Electrochemical Reactions

Element	Reaction
Beryllium	$Be^{2+} + 2e^- = Be$
Aluminum	$Al^{3+} + 3e^- = Al$
Titanium	$Ti^{2+} + 2e^- = Ti$
Manganese	$Mn^{2+} + 2e^- = Mn$
Vanadium	$V^{2+} + 2e^- = V$
Zinc	$Zn^{2+} + 2e^- = Zn$
Chromium	$Cr^{3+} + 3e^- = Cr$
Gallium	$Ga^{3+} + 3e^- = Ga$
Iron	$Fe^{2+} + 2e^- = Fe$
Chromium	$Cr^{3+} + e^- = Cr^{2+}$
Titanium	$Ti^{3+} + e^- = Ti^{2+}$
Thallium	$Tl^+ e^- = Tl$
Vanadium	$V^{3+} + e^- = V^{2+}$
Nickel	$Ni^{2+} + 2e^- = Ni$
Tin	$Sn^{2+} + 2e^- = Sn$
Lead	$Pb^{2+} + 2e^- = Pb$
Hydrogen	$2H^+ + 2e^- = H^2$
Tin	$Sn^{4+} + 2e^- = Sn^{2+}$
Copper	$Cu^{2+} + e^- = Cu^+$
Copper	$Cu^{2+} + 2e^- = Cu$

Corrosion Inhibitors

A corrosion inhibitor is a substance used to reduce the corrosion rate of metals by materials. The first step for selecting a corrosion inhibitor for a specific system is a thorough study of the system itself. Inhibitors that are valuable for some applications can be harmful in others. Extrapolation from one system to another has caused considerable damage to many industrial systems. Although inhibitors for some corrosion problems can be similar to inhibitors for others, this similarity should be regarded as coincidence. The lengthy procedures required for the development of a good corrosion inhibitor explain why most inhibitors are developed by specialists.[11.13]

There are two basic categories of inhibitors.

- **Oxide films,** such as those formed on aluminum, titanium, and stainless steel, form a protective layer that is inert to many PCMs. When corrosion resistance needs to be increased, the oxide coating is treated to make it thicker.

- **Additives** form protective coatings on the metal surface to provide physical protection against corrosive attack. These include long-chain aliphatic acids and aqueous solutions of sodium bicarbonate and sodium phosphate. These inhibitors can be added in small amounts to the PCM to decrease corrosion. (A common use of this type of additive is rust inhibition for radiators, steam boilers, etc.) Although added to the bulk of the PCM, they adsorb onto the metal surface to form a continuous layer.

There are many possibilities for effective applications of inhibitors. Suggested inhibitors for specific PCM/metal combinations are listed in following paragraphs, and Bregmon[11.13] provides additional information.

PCM Container and Filler Materials

Three metals are currently used for PCM containers: aluminum, titanium, and stainless steel. They have high strength-to-mass ratios and are corrosion-resistant. All have been widely used in aerospace technology.[11.15] Although stainless steel is heaviest, it is more elastic and can thus accommodate PCM volume changes. Each of these metals has its own advantages and special characteristics. A designer must choose the metal or metal combination most suitable for a particular application. Other metals or metal alloys may also be highly desirable and merit consideration.

Aluminum

Because of aluminum's low density, high thermal conductivity, and corrosion resistance, many PCM designers use it for containers and fillers. Aluminum is amphoteric: it can form compounds with PCMs that are either strong acids or strong bases (alkali hydroxides). It forms salts with strong acids (chlorides, nitrates, and sulfates) and aluminates (AlO_2^{-1}) with bases.[11.16] PCM materials that are compatible with aluminum are shown in Table 11.6.[11.12,11.7] Inhibitors that may be useful for reducing corrosion of aluminum with various PCMs are shown in Table 11.7, and further information can be obtained from Van Horn[11.17] and Dambal and Rama Char.[11.18]

Table 11.6. PCMs Compatible with Aluminum

Category	PCMs
Acids	Acetic, elaidic, myristic, stearic, benzoic
Alcohols	Ethylene glycol
Dry inorganic salts (except salt hydrates)	Most fused salt eutectics
Miscellaneous organics	Acetamide, methyl fumarate, paraffins, polyethylene glycol, tristearin, oxazoline waxes, silicates
Oxidizing PCMs	(Only if protective aluminum oxide film is present)
Sulfur compounds	Most PCMs that are inorganic sulfides or organic sulfides
Water	High-purity: distilled or deionized water

Table 11.7. Corrosion Inhibitors for PCMs in Aluminum Containers

PCM Category	Corrosion Inhibitor
Acids	Soluble oils, alkyl arylsulforates, and amines
Alkaline compounds	Silicates with a high ratio of silicate to soda
Water	Borates, silicates, nitrates, phosphates, soluble oils

Aluminum can be soldered, brazed, and welded. Soldering aluminum differs from soldering other common metals in several ways. The refractory oxide coating on aluminum requires special fluxes. With aluminum, resistance to corrosion depends much more on solder composition than it does for most other metals. Aluminum-to-aluminum joints are generally superior in strength to joints between aluminum and dissimilar metals.[11.19] Silver solders commonly used for joining other metals cannot be used for joining aluminum because none of them has a low enough melting range. The various types of solders and fluxes are described in Reference 11.19.

Titanium

Titanium is superior to all other metals on a strength-to-mass basis[11.20,11.21] and has outstanding corrosion resistance. It is one of the few metals that would be suitable for use with gallium and alloys of gallium, since these PCMs are very destructive to most metals, especially aluminum. This resistance is a result of the formation of a protective film, promoted by oxygen or oxidizing agents.[11.22] Titanium's thermal conductivity, however, is about 1/16 that of aluminum. Table 11.8 lists PCMs that are compatible with titanium under ordinary service conditions.

Stainless Steel

In PCM technology, stainless steels have been used for containers or parts of containers. Stainless-steel bellows were used in containers because of their elasticity in adjusting to continual volume changes caused by PCM melting and freezing. The advantages of great strength, elasticity, and corrosion resistance have qualified this metal for some PCM applications.[11.12,11.23,11.24]

Table 11.8. PCMs Compatible with Titanium

Category	PCMs
Acids	Acetic, chloroacetic, stearic, lactic, salicylic, succinic
Salts	Most inorganic and organic salts, magnesium sulfate, sodium chloride, sodium sulfate, potassium chloride
Miscellaneous	Water, gallium, hydrogen sulfide

Stainless steels can be soft-soldered and silver-soldered. No problems such as sensitization, hardening, or tempering arise at the low temperatures involved in soldering. All stainless steels can be brazed, and no fluxes are required. Welding with few problems is common. Corrosion resistance is a major consideration in the selection of a stainless-steel alloy. Basically, corrosion resistance of all stainless steel depends upon its chromium content. Chromium as a pure metal is very active, but it occurs as an oxide in stainless steel, usually $FeO\cdot Cr_2O_3$. Stainless steel is inert to many environments as a result of the formation of this oxide.[11.24] Since the alloys vary so widely in corrosion resistance, researching specific alloys is advisable. Generalizations about their corrosion resistance are difficult to make, but all stainless steels are moderate to excellent in this area.

The PCM Design Process

To proceed quickly and efficiently in the design of a PCM thermal-protection system, the designer should follow a process similar to the following.

1. Choose the PCM with the best properties, as described previously, whose temperature range matches the temperature range of the component.
2. Perform thermodynamic analysis to: define thermal flux and storage requirements; determine most efficient heat dump for cyclical components; size radiators, thermal straps, heat pipes, or other heat dump methods; and determine initial estimate of PCM quantity required.
3. Perform combined thermodynamic and heat-transfer analysis to obtain mass, thickness, and temperature excursion as functions of filler amount. Pick the minimum mass and thickness that will meet temperature-excursion requirements.
4. Select a compatible container material and design container according to guidelines given earlier.
5. Conduct necessary detailed thermal analysis to verify the performance of the PCM system.
6. Conduct necessary experimentation to prove the performance and reliability of the PCM system.

References

11.1. D. V. Hale, M. J. Hoover, and M. J. O'Neill, "Phase Change Materials Handbook," NASA Contractor Report CR-61363 (September 1971).

11.2. W. R. Humphries and E. I. Griggs, "A Design Handbook for Phase Change Thermal Control and Energy Storage Devices," NASA Technical Paper 1074 (November 1977).

11.3. J. F. Keville, "Development of Phase-Change Systems and Flight Experience on an Operational Satellite," *Progress in Astronautics and Aeronautics*, **56** (1977).

11.4. L. Bledjian, J. R. Burden, and W. H. Hanna, "Development of a Low-Temperature Phase Change Thermal Capacitor," *Progress in Astronautics and Aeronautics*, **65** (1979).

11.5. P. G. Grodzka, E. Picklesimer, and L. E. Conner, "Cryogenic Temperature Control by Means of Energy Storage Materials," AIAA-77-763 (1977).

11.6. M. S. Busby and S. J. Mertesdorf, "The Benefit of Phase Change Thermal Storage for Spacecraft Thermal Management," AIAA-87-1482 (1987).

11.7. P. G. Grodzka, "Space Thermal Control by Freezing and Melting, Second Interim Report," LMSC-HREC D148619, NAS8-25183, Lockheed Missiles & Space Co., Huntsville, Ala. (May 1969).

11.8. E. W. Bentilla et al., Research and Development Study on Thermal Control by Use of Fusible Materials, Final Report of Contract NAS8-11163, Northrup Space Laboratories, NSL 65-16-1, Hawthorne, Calif. (April 1966).

11.9. A. P. Shlosinger and E. W. Bentilla, "Research and Development Study on Thermal Control by Use of Fusible Materials," Northrop Space Laboratories, Interim Report NAS8-11163 (February 1965).

11.10. E. W. Bentilla, K. F. Sterrett, and L. E. Karre, "Research and Development Study on Thermal Control by Use of Fusible Materials," Northrop Space Laboratories Final Report, Contract No. NAS8-11163 (April 1966).

11.11. W. R. Humphries, Communication, NASA-MSFC, S&E-ASTN-PLA, March 1971.

11.12. R. J. Fabian and J. A. Vaccari, "How Materials Stand Up to Corrosion and Chemical Attack," Materials Engineering **73** (2) (February 1971).

11.13. J. I. Bregmon, Corrosion Inhibitors (Macmillan Co., New York, 1963).

11.14. J. F. Bosick, Corrosion Prevention for Practicing Engineers (Barnes and Noble, Inc., New York, 1970).

11.15. J. B. Rittenhouse and J. B. Singletary, Space Materials Handbook, 3rd ed., Lockheed Palo Alto Research Laboratory, AFML-TR-68-205 (July 1968).

11.16. The Aluminum Data Book (Reynolds Metals Co., Richmond, Va., 1961).

11.17. K. R. Van Horn, Aluminum, Vol. I (American Society for Metals, Metals Park, Ohio, 1967).

11.18. R. P. Dambal and T. L. Rama Char, "Corrosion Prevention of Aluminum by Cathodic Protection," Corrosion Prevention and Control (February 1971).

11.19. K. R. Van Horn, Aluminum, Vol. III (American Society for Metals, Metals Park, Ohio, 1967).

11.20. J. L. Everhart, Titanium and Titanium Alloys (Reinhold Corp., New York, 1954).

11.21. Titanium Reference Guide, Titanium Metals Corp. of America, New York.

11.22. Materials Selector, Materials Engineering, Vol. 72, No. 6 (Reinhold Corp., New York, 1970).

11.23. J. G. Parr and A. Hanson, An Introduction to Stainless Steel (American Society for Metals, Metals Park, Ohio, 1965).

11.24. T. Lyman and C. H. Gerlach, Metals Handbook (American Society for Metals, Cleveland, Ohio, 1954).

11.25. T. R. Knowles and G. W. Webb, "Metal/Phase-Change Material Composite Heat Sinks," Air Force document AFWAL-TR-88-3069 (October 1988).

12   Pumped Fluid Loops

T. T. Lam,[*] G. C. Birur,[†] and P. Bhandari[†]

Introduction

Spacecraft thermal control techniques can be categorized as passive thermal control (PTC) or active thermal control (ATC). PTC can be achieved by control of conductive and radiative heat paths through selection of the proper geometrical configurations, insulation blankets, sun shields, radiating fins, surface thermo-optical properties, thermal coatings, heat sinks, and phase-change materials. A PTC system does not involve moving parts or fluids. The spacecraft component temperatures are maintained within the desired range by proper control of the dissipated energy between all spacecraft elements through the conductive and radiative heat paths. However, to execute a design in which the PTC techniques cannot deal with environmental extremes or to accommodate equipment dissipating high power, employment of ATC techniques may be more efficient. In such cases, designs can be executed by the use of heaters, louvers, heat pipes, thermoelectric coolers, cryogenic coolers, and pumped fluid loops (PFLs).

PFLs are devices that provide efficient transfer of a large amount of thermal energy between two points by means of forced liquid convective cooling. PFLs for space applications are the subject of this chapter. A simplified PFL, as shown in Fig. 12.1, consists of a pumping device, a heat exchanger, and a space radiator. The cooling can be accomplished by the use of a coolant as the thermal energy transport agent. The coolant absorbs the dissipated thermal energy from a component and transfers it to a heat sink. The final heat-rejection process depends on whether the coolant is expendable or nonexpendable. With expendable coolant,
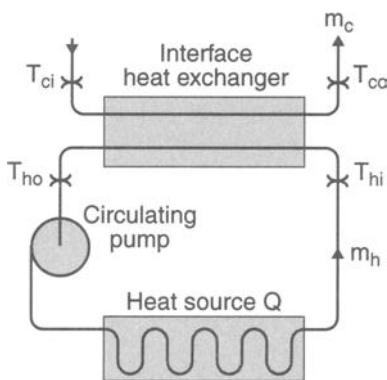

Fig. 12.1. Schematic of a simplified PFL system.

*The Aerospace Corporation, El Segundo, California.
†Jet Propulsion Laboratory, California Institute of Technology, Pasadena, California.

the working fluid is rejected from the space vehicle once it has accomplished its mission. In the case of nonexpendable coolant, the working fluid is recirculated within the system once its thermal energy has been radiated to space via a radiator.

Space vehicles of recent years, such as the Defense Satellite Program and the space shuttle orbiter, have used PFLs in their ATC subsystems. The schematic orbiter ATC subsystem is depicted in Fig. 12.2. The subsystem collects excess heat from the cabin interchanger, the fuel-cell heat exchanger, the hydraulics heat exchanger, the GSE (ground support equipment) heat exchanger, and the payload heat exchanger, and it ejects heat from the orbiter to space. The ATC payload-cooling elements consist of the radiator panels, the flash evaporator, the aft cold plates, and the ammonia boiler. The radiators provide cooling for the payload while the payload-bay doors are open on orbit. As the flow diagram suggests, the thermal control design of an ATC subsystem with PFLs is normally more difficult than that of a PTC subsystem. Subsequent sections of this chapter explain the PFL design in detail.

In what follows, basic fluid-flow equations and friction analysis of pipes and tubes are presented first, followed by the forced-convection heat-transfer process, PFL hardware, working fluids, engineering design guidelines, computer-analysis tools, and the application of a PFL on the Mars Pathfinder spacecraft. Providing all applicable details and analytical equations for PFL design would be impossible; therefore, numerous references are listed at the end of this chapter.
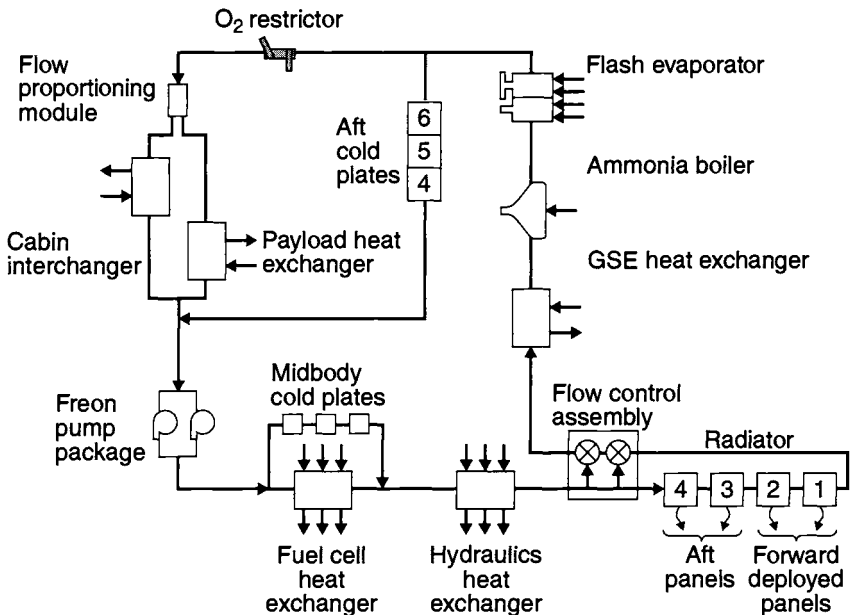

Fig. 12.2. Orbiter ATC system.

Fluid-Flow Concepts and Basic Equations

General

The various components (pump, heat exchanger, radiator, etc.) within a PFL system are connected mainly by conduits. The flows through pipes or tubes may be laminar or turbulent. The pipe-flow regime is primarily a function of the Reynolds number, $Re = \rho VD/\mu$, where ρ is the density of the fluid, V the average flow velocity, D the pipe diameter, and μ the dynamic viscosity of the fluid. A critical Reynolds number distinguishes the flow regimes between laminar or turbulent flow in pipes. The flow becomes turbulent when $Re > 2300$. However, a range of Reynolds numbers for transition flow has been observed experimentally. Depending on the pipe roughness and smoothness, the flow changes from laminar to turbulent in the range of the Reynolds numbers from 2000 to 4000.

In the study of fluid flow in a piping system, the conservation principles are used to set up the governing equations. These principles are the conservation of mass, the conservation of momentum, and the conservation of energy. The following sections briefly present some basic equations used in pipe-flow analysis.

Fundamentals of Pipe Flow

Continuity Equation

Consider steady flow through a portion of the stream pipe; the principle of conservation of mass states that the net mass outflow from section 1 to 2 of the control volume must be zero. Since no flow occurs through the wall of the stream pipe, the continuity equation for one-dimensional flow in a pipe can be written as

$$\dot{m} = \rho_1 V_1 A_1 = \rho_2 V_2 A_2 \,, \tag{12.1}$$

where the subscripts 1 and 2 refer to the flow parameters at the inlet and the outlet, respectively; $\dot{m}$ is the mass flow rate; V the mean velocity; and A the cross-sectional area.

Bernoulli's Equation

Steady-state one-dimensional internal flow is generally known as internal pipe flow, and the equation that governs it is called Bernoulli's equation. A flow network is simulated by specifying flow-passage connections, which can include pipes, pumps, and valves. Associated with a flow passage are the upstream and downstream pressures, and the characteristics that govern the pressure drop.

The pressure drop across a pipe is given by Bernoulli's equation. The general form of this equation, including head loss resulting from irreversibilities for pipe flow along a streamline, is

$$\left(\frac{P_1}{\rho} + \frac{V_1^2}{2} + gZ_1\right) - \left(\frac{P_2}{\rho} + \frac{V_2^2}{2} + gZ_2\right) = h_{l_t} \,, \tag{12.2}$$

where subscripts 1 and 2 refer to the flow parameters at the inlet and outlet; P is pressure; V is average fluid velocity; ρ is density; g is the gravitational constant; Z

is elevation; and h_{l_t} is total head loss. This equation shows that the total head loss is the difference in potential energy, flow energy, and kinetic energy. The importance of the total head loss will be discussed in detail in the next section.

Head Loss

The main purpose of analysis of flow in pipes and tubes is to evaluate the pressure changes that result from incompressible flow in the system. The pressure changes in a flow system result from friction and changes in elevation and flow velocity. In a frictionless flow, the Bernoulli equation could account for the effects of changes in elevation and flow velocity. In a real flow, analysis must also include the effect of friction. This effect acts to decrease the pressure, causing such a case, unlike the frictionless flow case, to exhibit a pressure "loss." This pressure loss, h_{l_t} (total head loss) in Eq. (12.2), contains two constituents: the major head loss, h_l (resulting from friction in fully developed flow in constant-area portions of the system), and the minor head loss, h_{l_m} (resulting from frictional effects in flow-through valves, tees, elbows, and other nonconstant-area parts of the system). Thus, the total head loss h_{l_t} in a piping system can be defined as

$$h_{l_t} = h_l + h_{l_m}, \tag{12.3}$$

where h_l is the major head loss and h_{l_m} is the minor head loss.

The details of the major and minor losses in fluid flow are discussed in the following section.

Major Losses

Flow through a piping system causes a reduction in static head, which may be expressed in terms of velocity head $V^2/2$. The major head loss is given by

$$h_l = f\frac{L}{D} \cdot \frac{V^2}{2}, \tag{12.4}$$

where L and D are the length and diameter of the pipe, respectively. The friction factors are

$$f = \frac{64}{Re} \tag{12.5}$$

for laminar flow, and for turbulent flow in smooth pipes:[12.1–12.3]

$$f = \frac{0.079}{Re^{0.25}} \qquad\qquad 4 \times 10^3 < Re < 2 \times 10^4 \tag{12.6}$$

$$f = \frac{0.184}{Re^{0.2}} \qquad\qquad 2 \times 10^4 < Re < 3 \times 10^5 \tag{12.7}$$

$$f = \frac{0.046}{Re^{0.2}} \qquad 2 \times 10^4 < Re < 10^6 \qquad (12.8)$$

$$f = \frac{1}{[1.581 ln(Re) - 3.28]^2} \qquad 10^4 < Re < 10^7 \qquad (12.9)$$

In laminar flow, the friction factor is a function of the Reynolds number only; it is independent of roughness. The widely used frictional factor f is determined from empirical correlation of the Moody diagram,[12.4] shown in Fig. 12.3 as

$$f = \frac{0.25}{\left[log\left(\dfrac{\dfrac{\varepsilon}{D}}{3.7} + \dfrac{5.74}{Re^{0.9}} \right) \right]^2}, \qquad (12.10)$$

where Re ($= \rho VD/\mu$) is the Reynolds number, μ is the dynamic viscosity, and ε/D is the relative roughness. The choice of the cutoff Reynolds number between the two regimes (laminar and turbulent) is somewhat arbitrary.
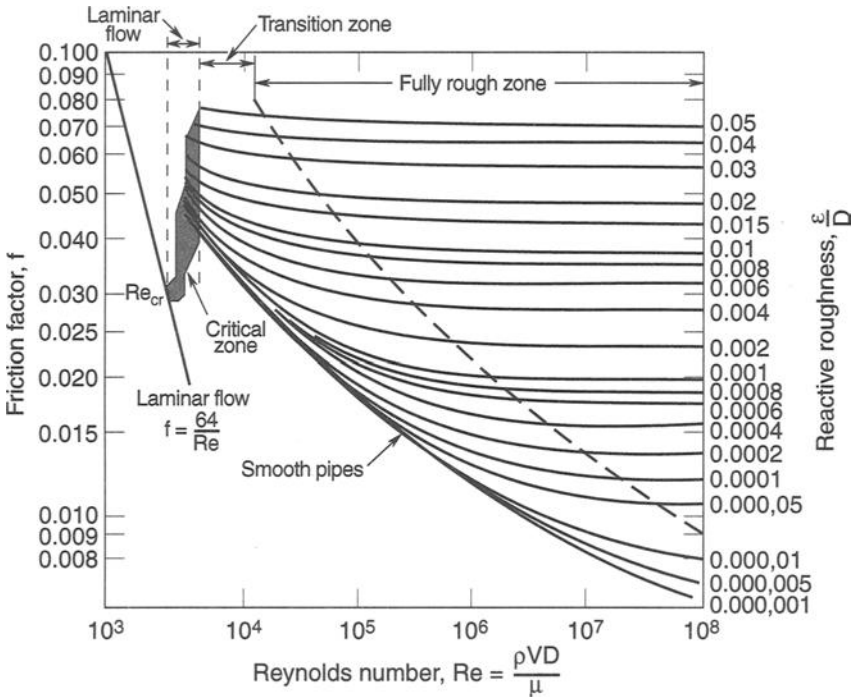
Fig. 12.3. Friction factor for fully developed flow in circular pipes.

Minor Losses

Flow in a piping system may be required to pass through a variety of fittings, bends, or abrupt changes in area, which usually results in flow separation. Energy in the fluid is dissipated by the mixing of fluid in the separated zones. This results in additional head losses, which are primarily the results of flow separation. These losses are small compared to the frictional losses and are, therefore, called minor losses. The minor head loss may be expressed by either

$$h_{l_m} = K \frac{V^2}{2} \qquad (12.11)$$

or

$$h_{l_m} = f \frac{L_e}{D} \cdot \frac{V^2}{2}, \qquad (12.12)$$

where L_e is the equivalent length, and K, the loss coefficient, must be determined experimentally for each situation. Loss coefficients for various types of entrances and exits are shown in Tables 12.1 and 12.2. Minor loss coefficients for sudden area changes (enlargements and contractions) are given in Table 12.3 and Figs. 12.4 and 12.5.

Table 12.1. Loss Coefficients for Pipe Exits[a]

Exit Type	Diagram	Loss Coefficient (K)
Projecting pipe		1.0
Square-edged		1.0
Rounded		1.0
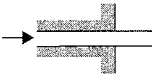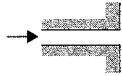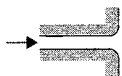
[a]Based on $h_{l_m} = K(\overline{V}^2/2)$, calculation of head loss.

Table 12.2. Loss Coefficients for Pipe Entrances

Entrance Type	Diagram	Loss Coefficient (K)[a]
Re-entrant		0.78
Square-edged		0.34
Slightly rounded		0.2–0.25
Well rounded[b]		0.04
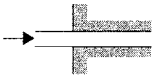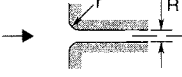
[a]Based on $h_{l_m} = K(\bar{V}^2/2)$, where $\bar{V}$ is the mean velocity in the pipe.

[b]$r/R = 0.35$.

Table 12.3. Loss Coefficients for Gradual Contractions

Diagram	Included Angle, θ (deg)	Loss Coefficient, K[a]
	30	0.02
	45	0.04
	60	0.07
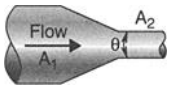
[a]Based on $h_{l_m} = K(\bar{V}^2/2)$.
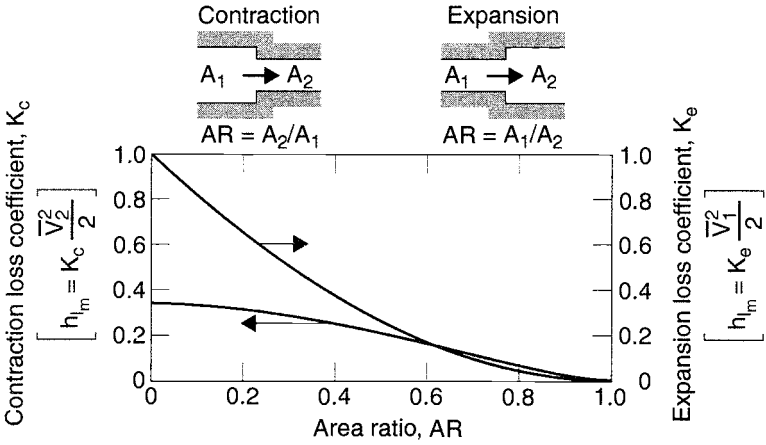
Fig. 12.4. Loss coefficients for flow through sudden area changes.
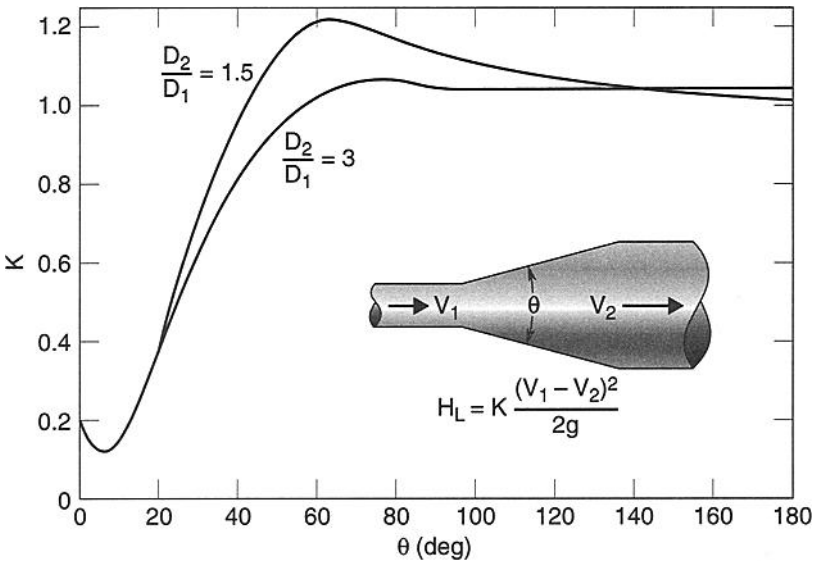
Fig. 12.5. Loss coefficients for conical expansions.

The minor loss of a pipe bend is normally expressed by an equivalent length of straight pipe. The equivalent lengths of a 90-deg pipe bend and miter bend are shown in Figs. 12.6 and 12.7. The representative equivalent lengths for valves and fittings are also given in Table 12.4.
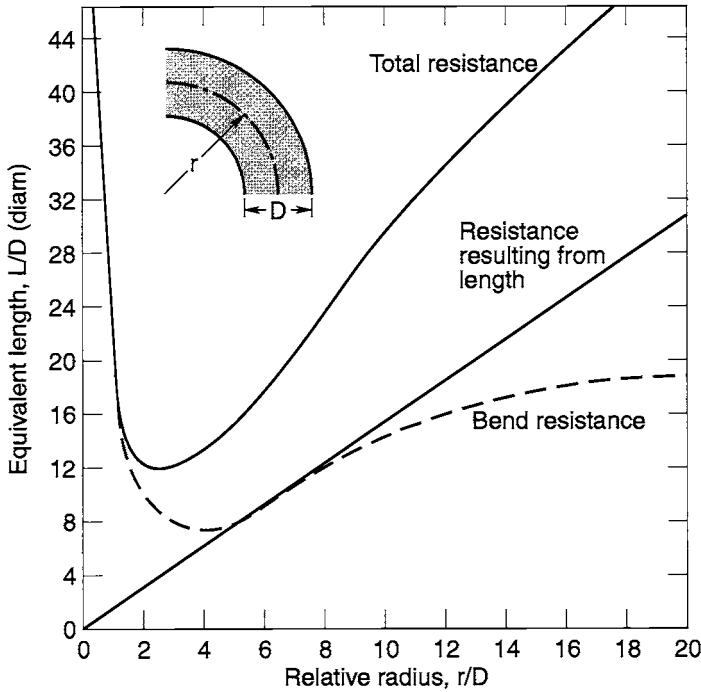
Fig. 12.6. Design chart resistance of 90-deg bends in circular pipe with fully developed turbulent flow.

Friction Factor and Pressure Drop

The Bernoulli equation can be interpreted as the difference of energy per unit weight between two points on a streamline. The change of kinetic energy is usually small compared to the total head loss. Hence, it will be neglected in the evaluation of the pressure drop. Using Eq. (12.2), one can state the pressure drop across a pipe as

$$P_2 - P_1 = \frac{\rho h_{l_t}}{g_c} - \frac{\rho g}{g_c}(Z_2 - Z_1). \qquad (12.13)$$

By using Eqs. (12.3), (12.4), and (12.11) in Eq. (12.13), one finds that the pressure drop across a pipe becomes

$$P_2 - P_1 = -\frac{\rho V^2}{2g_c}\left(f\frac{L}{D} + K\right) - \frac{\rho g}{g_c}(Z_2 - Z_1), \qquad (12.14)$$

where g_c is a conversion factor. The value of g_c is 32.2 ft·lbm/lbf·sec^2 in the British Gravitational System, 1 kg·m/N·sec^2 in the *Systeme Internationale d'Unites* (SI) System, and 1 gm·cm/dyne·sec^2 in the Absolute Metric System.
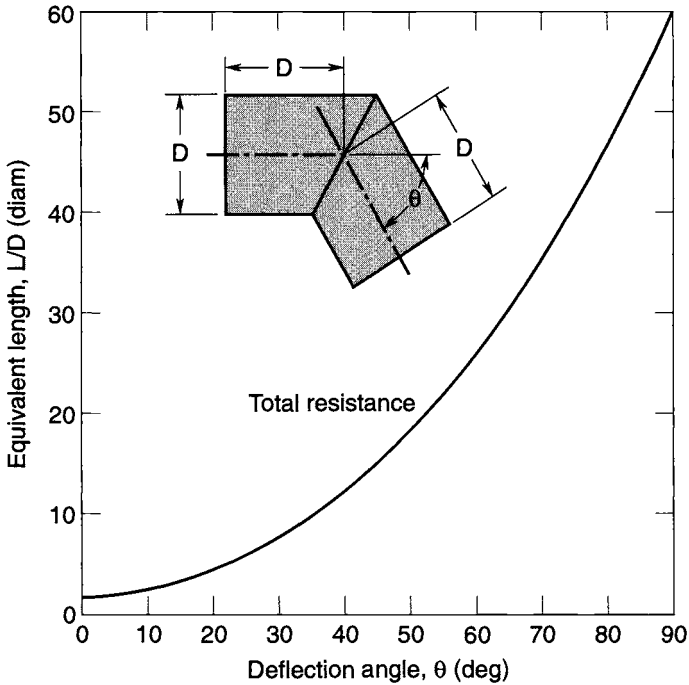
Fig. 12.7. Design chart resistance of miter bends in circular pipe with fully developed turbulent flow.

Table 12.4. Representative Equivalent Lengths in Pipe Diameters (L_e/D)
for Valves and Fittings

Fitting Type	Description	Equivalent Length (L_e/D)[a]
Globe valve	Fully open	350
Gate valve	Fully open	13
	3/4 open	35
	1/2 open	160
	1/4 open	900
Check valve		50–100
90-deg std. elbow		30
45-deg std. elbow		16
90-deg elbow	Long radius	20
90-deg elbow		50
45-deg street elbow		26
Tee	Flow-through run	20
	Flow-through branch	60
Return bend	Close pattern	50

[a]Based on $h_{l_m} = f \dfrac{L_e}{D} \cdot \dfrac{\bar{V}^2}{2}$.

Incorporating the continuity equation, Eq. (12.1), one can rewrite Eq. (12.14) as

$$P_2 - P_1 = -\frac{\dot{m}^2}{2\rho A^2 g_c}\left(f\frac{L}{D} + K\right) - \frac{\rho g}{g_c}(Z_2 - Z_1).$$ (12.15)

The equation shows that the pressure drop across a piping system is the sum of the elevation difference of the two points under consideration and the total head loss. In the case of neglecting the elevation change and the minor loss, Eq. (12.14) can be rewritten as

$$\Delta P = P_2 - P_1 = -\frac{\rho V^2}{2g_c}f\frac{L}{D}.$$ (12.16)

Forced Convection in Pipes and Tubes

General

In convective heat transfer in internal flow in pipes or tubes, an axially local heat-transfer coefficient h_x is customarily defined as

$$q_x = h_x(T_w - T_b),$$ (12.17)

where T_w and T_b are the mean pipe-wall temperature and the fluid-bulk mean temperature, respectively. The flow-length average heat-transfer coefficient $\bar{h}$ is the integrated average of h_x for the total of the pipe from $x = 0$ to $x = L$,

$$\bar{h} = \frac{1}{L}\int_o^L h_x dx.$$ (12.18)

For convenience, the heat-transfer coefficient is commonly related to the dimensionless Nusselt number in convective heat transfer. The Nusselt number, by definition, is the ratio of the convective conductance, h, to the molecular thermal conductance, k/D. The local Nusselt number, Nu_x, is then expressed by

$$Nu_x = \frac{h_x D}{k}.$$ (12.19)

The mean flow-length-average Nusselt number based on $\bar{h}$ is defined as

$$Nu_D = \frac{\bar{h}D}{k} = \frac{1}{L}\int_o^L Nu_x dx.$$ (12.20)

When the effects of axial heat conduction, viscous dissipation, and flow work are neglected within the fluid, the heat transfer within the system can be evaluated by Eq. (12.21).

$$q = \bar{h}(T_w - T_b) = \left(\frac{Nu_D k}{D}\right)(T_w - T_b). \tag{12.21}$$

Heat Transfer in Laminar Tube Flow

Let $T(r,z)$ be the temperature distribution in the fluid, where r and z are the radial and axial coordinates, respectively. The heat flux from the fluid to the tube wall is governed by Fourier's law of heat conduction,

$$q(z) = -k\left[\frac{\partial T(r, z)}{\partial r}\right]_{\text{wall}}, \tag{12.22}$$

where k is the thermal conductivity of fluid. Combining Eq. (12.22) with Newton's law of cooling, Eq. (12.17), one can write the heat-transfer coefficient in terms of the dimensionless temperature gradient as

$$h = -k\left[\frac{\partial q(r)}{\partial r}\right]_{\text{wall}}. \tag{12.23}$$

The temperature profile for flow inside a circular tube can be obtained by performing an energy analysis on a fluid element.[12.8–12.10] From knowledge of the temperature profile, the heat-transfer coefficient may be shown to be of the form[12.11]

$$Nu_D = \frac{hD}{k} = 4.364 \quad \text{for uniform heat flux at the tube wall,} \tag{12.24}$$

and

$$Nu_D = \frac{hD}{k} = 3.66 \quad \text{for constant tube-wall temperature.} \tag{12.25}$$

The Nusselt number for laminar flow inside a circular tube was given above for two different boundary conditions, namely, the constant wall temperature and the constant wall heat flux. Shah and London[12.12] have compiled a list of Nusselt numbers and the quantities $f \cdot Re$ (i.e., the product of the friction factor and the Reynolds number) for geometries other than the circular tube and parallel plates for the above boundary conditions. The results are listed in Table 12.5.

The Nusselt number and the friction factor for laminar flow in ducts of various cross sections have been determined in the region where velocity and temperature profiles are fully developed. If the duct cross section for flow is not circular, then the heat transfer and friction factor, for many cases of practical interest, can be based on the hydraulic diameter, D_h, defined as

$$D_h = \frac{4A_c}{P}, \tag{12.26}$$

Table 12.5. Nusselt Number and Friction Factor for Fully Developed Laminar Flow in Ducts of Various Cross Sections (Ref. 12.9)

Geometry ($L/D_h > 100$)		Nu_T[a]	Nu_H[b]	Nu_H[c]	fRe
⬤		3.657	4.364	4.364	64.00
$2a$ ▲ $60°$ $2b$	$\dfrac{2b}{2a} = \dfrac{\sqrt{3}}{2}$	2.470	3.111	1.892	53.33
⬣		3.340	4.002	3.862	60.22
$2b$ ▪ $2a$	$\dfrac{2b}{2a} = 1$	2.976	3.608	3.091	56.91
$2b$ ▬ $2a$	$\dfrac{2b}{2a} = \dfrac{1}{2}$	3.391	4.123	3.017	62.20
$2b$ ▬ $2a$	$\dfrac{2b}{2a} = \dfrac{1}{4}$	3.660	5.099	4.35	74.80
$2b$ ⬬ $2a$	$\dfrac{2b}{2a} = 0.9$	4.439	5.331	2.930	72.93
$2b$ ▬ $2a$	$\dfrac{2b}{2a} = \dfrac{1}{8}$	5.597	6.490	2.904	82.34
▬	$\dfrac{2b}{2a} = 0$	7.541	8.235	8.235	96.00
▬ Insulated	$\dfrac{b}{a} = 0$	4.861	5.385	—	96.00
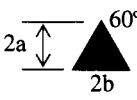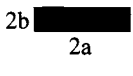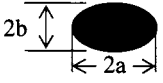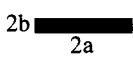
[a]Nusselt number for uniform wall temperature.
[b]Nusselt number for uniform wall heat flux in the flow direction while the wall temperature remains uniform around the periphery.
[c]Nusselt number for uniform wall heat flux both in the flow direction and around the periphery.

where A_c and P are the cross-sectional flow area and the wetted perimeter, respectively. This diameter is the one that should be used in the calculation of the Nusselt and Reynolds numbers.

Heat Transfer in Turbulent Tube Flow

A classical expression for computing the local Nusselt number for fully developed turbulent flow in a smooth circular tube can be obtained from the Chilton-Colburn analogy. The analogy relates the local drag coefficient C_f to the local Stanton number St ($= Nu/Re \cdot Pr$) in the form

$$StPr^{2/3} = \frac{C_f}{2} = \frac{f}{8}, \qquad (12.27)$$

where Pr ($= \upsilon/\alpha$) is the Prandtl number, the ratio of kinematic viscosity and thermal diffusivity of a fluid, which represents the relative magnitudes of diffusion and heat conduction in the fluid medium. Substituting the friction factor from Eq. (12.7) into Eq. (12.27) yields the Colburn equation for turbulent flow inside a smooth tube:

$$Nu = 0.023 Re^{0.8} Pr^{1/3}. \qquad (12.28)$$

Eq. (12.28) is applicable for $0.7 < Pr < 160$, $Re > 10{,}000$, and $L_e/D > 60$ for smooth tubes. A large number of empirical correlations have been developed by many investigators in the past to determine the heat-transfer coefficient; some are presented in Table 12.6.

System Hardware

Pumps

General

A pump is a machine that adds energy to liquid. It converts kinetic energy into pressure potential. A pump consumes more power than it gives off because of internal friction losses. Some major losses include hydraulic losses (flow friction and turbulence) and mechanical losses (friction in bearings and other internal mechanical parts). Depending on their design and mechanical action, most pumps used in space applications can be classified into one of the following categories:[12.21]

- **Rotodynamic.** These pumps add energy to a liquid medium through the work done by a rapidly rotating vaned impeller. The radial-flow centrifugal pumps, mixed-flow pumps, axial-flow pumps, and propellers can be classified as rotodynamic pumps. Some typical rotodynamic pumps are shown in Table 12.7.
- **Displacement.** This category includes the reciprocating (Table 12.8) and rotary (Table 12.9) pumps. These pumps impart energy by a positive displacement action.

Table 12.6. Summary of Correlations for Forced-Convection Turbulent Flow inside Duct[a]

Correlation	Remarks
$f = (1.82 \log Re - 1.64)^{-2}$	Smooth tubes, $Re > 10^4$
$f = 0.316 Re^{-0.25}$	Smooth tubes, $Re < 2 \times 10^4$
$f = 0.184 Re^{-0.2}$	Smooth tubes, $2 \times 10^4 < Re < 3 \times 10^5$
$Nu = 0.023 Re^{0.8} Pr^{1/3}$	$0.7 < Pr < 160$; $Re > 10{,}000$; $L/D > 60$; smooth pipes
$Nu = 0.023 Re^{0.8} Pr^n$ $n = 0.4$ for heating $n = 0.3$ for cooling	$0.7 < Pr < 160$; $Re > 10{,}000$; $L/D > 60$; smooth pipes
$Nu = 0.027 Re^{0.8} Pr^{1/3} \left(\dfrac{\mu_b}{\mu_w}\right)^{0.14}$	$0.7 < Pr < 16{,}700$; $Re > 10{,}000$; $L/D > 60$; smooth pipes
$Nu = \dfrac{RePr}{X}\left(\dfrac{f}{8}\right)\left(\dfrac{\mu_b}{\mu_w}\right)^n$ where: $X = 1.07 + 12.7\,(Pr^{2/3} - 1)(f/8)^{1/2}$ $n = 0.11$ heating with uniform T_w $n = 0.2$ cooling with uniform T_w $n = 0$ uniform wall heat flux or gases	Smooth or rough pipes $10^4 < Re < 5 \times 10^6$ $0.5 < Pr < 200$ with 5 to 6% error $0.5 < Pr < 2000$ with 10% error Properties, except m_w, are evaluated at bulk mean temperature.
$Nu = 0.036 Re^{0.8} Pr^{1/3}\left(\dfrac{D}{L}\right)^{0.055}$	$10 < \dfrac{L}{D} < 400$
$Nu = 5 + 0.016 Re^c Pr^d$ where: $c = 0.88 - \dfrac{0.24}{4 + Pr}$ $d = 0.33 + 0.5 e^{-0.6Pr}$	$0.1 < Pr < 10^4$ $10^4 < Re < 10^6$ $\dfrac{L}{D} > 25$

[a]Subscript b indicates fluid properties evaluated at the bulk mean temperature; subscript w indicates fluid properties evaluated at the wall temperature.

The European Space Agency[12.21] has compiled a list of some important features of the rotodynamic and displacement pumps; the information is contained in Table 12.10. The following requirements are normally imposed on pumps for space-application fluid loops:

- high efficiency
- low mass
- relatively low mass-to-output-power ratio
- hermetically sealed structure
- minimum operational noise level
- ability to withstand mission vibration and shock loads
- compatibility with onboard electrical system
- applicability to aerospace-environment usage
- ability to handle typical liquid coolants as working fluids
- high operational reliability

Table 12.7. Rotodynamic Pumps

Class	Typical Model
Radial flow	℄ shaft
Mixed flow	℄ shaft
Axial flow or propeller	℄ shaft
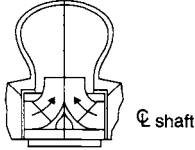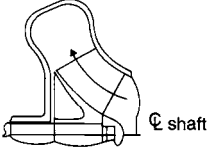
Table 12.8. Reciprocating Displacement Pumps

Class	Typical Model
Piston	
Diaphragm	
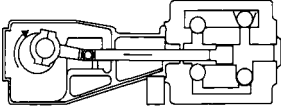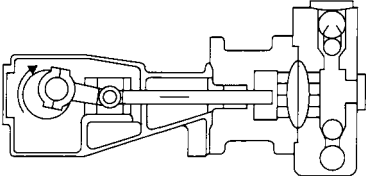
Table 12.9. Rotary Displacement Pumps

Class	Typical Models
Vane	Sliding vane External vane
Piston	Axial piston
Flexible member	Flexible tube Flexible vane Flexible liner
Gear	External gear Internal gear
Lobe	Single lobe Treble lobe
Circumferential piston	Circumferential piston
Screw	Single screw Screw and wheel Double screw
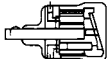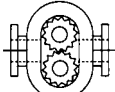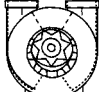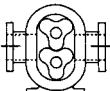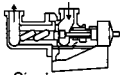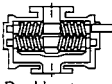
Table 12.10. Main Features of Typical Pumps[a]

Rotodynamic Pumps	Positive-Displacement Pumps
Very efficient when operating at speeds from 1200 to 3600 rpm, within the usual range of alternating-current electric motors.	Operate at very low rotating speed (220 to 500 rpm).
Cannot be run efficiently at low speeds to pump small quantities.	Efficiencies, although they can be high, are below those of rotodynamic pumps.
Overall efficiency usually ranges from 0.7 to 0.85.	Efficiency decreases when wear increases leakage.
Not easily regulated. Regulation by throttling is simple but wasteful. Regulation by running speed adjustment more or less maintains the efficiency but requires auxiliary equipment that is expensive, complicated, and unreliable. Multiple winding motors and invertors are used to control motor speed considerations.	The discharge characteristic is a pulsating one. A smoother discharge is obtained in double- or treble-acting units. Rotary pumps exhibit greater uniformity of delivery than reciprocating pumps.
Cannot deliver at high pressure unless a large and heavy type is used. Pressure rise increases as peripheral speed is increased.	The delivery is substantially constant, regardless of the pressure rise developed.
Cannot handle viscous liquids.	Can be used with very viscous liquids. This feature applies especially to the case of rotary pumps. The pressure rise drops with increasing viscosity.
Not self-priming, although that limitation can be overcome in various ways.	Self-priming and capable of coping with high-suction lifts.
No relief valves are to be used. Even complete throttling does not present any danger to the pump or loop, as no further pressure rise develops.	Relief or bypass valves are to be used. Unable to operate against a closed discharge. Even a slight decrease in delivery may cause a substantial pressure rise.
Limited by cavitation and power.	Able to handle large proportions of vapor. Enough liquid must be present to provide a liquid sealing file for the clearances. Suitable for pumping hot liquid. Limited by pressure and power.
Leak through the shaft seal. Submerged pumps can be used to prevent this drawback.	Problems of leakage are minimized, particularly with diaphragm pumps.
Smaller in size than other types with equal capacity.	Much bigger than rotodynamic pumps because of low rotating speed.
Low-cost, rugged, and reliable in operation.	Complicated construction. Unlike rotary pumps, they require the use of inlet and outlet valves. Very sensitive to wear because comparatively large surface areas move in close contact. Diaphragm pumps do not present friction, but diaphragm materials are of limited use at elevated temperatures.

[a]Arranged by the compiler (Ref. 12.21) after: Nekrasov (1969), London (1974), Pollak & Cruger (1974), Scoble (1974), Settles *et al.* (1977).

Characteristic Curves

The performance parameters for a typical pump include the pressure head (H), the input power (P), and the machine efficiency (η) under some specific operating conditions. These parameters are the pump-dependent variables. The volumetric flow rate (Q), angular speed (ω), impeller diameter (D), and fluid properties (e.g., density, ρ) are the independent variables. Pump-characteristic curves are generated by plotting a dependent variable as a function of one of the independent variables. Pump performance is difficult to predict analytically except at the design point of the specific machine; hence, it is measured experimentally. Some typical characteristic curves showing head, efficiency, and horsepower as a function of the discharge for a typical centrifugal pump are shown in Fig. 12.8. These curves are shown for a centrifugal pump tested at constant speed. When a pump with performance curves like these is installed in a pumping system, its design operating point is controlled by the so-called system-components (e.g., piping, valves, and fittings) resistance. The system resistance, as defined in Eq. (12.16), is proportional to the square of the velocity. The friction factor and equivalent length vary somewhat with flow rate, accounting for the deviation from a parabolic velocity distribution. The head-capacity curve of a typical pump with the system-resistance curve superimposed is shown in Fig. 12.9 as a function of the volume flow rate. The only possible system operating point is the intersection of these two curves where the head developed by the pump just balances the head loss resulting from friction in the system.

Pump Laws

The basic pump laws are derived using the principles of dynamic similarity and dimensional analysis. "Similarity" in pump design refers to the case of two machines operating under identical flow conditions. The results from the basic pump laws[12.22] are presented in Eqs. (12.29–12.31).
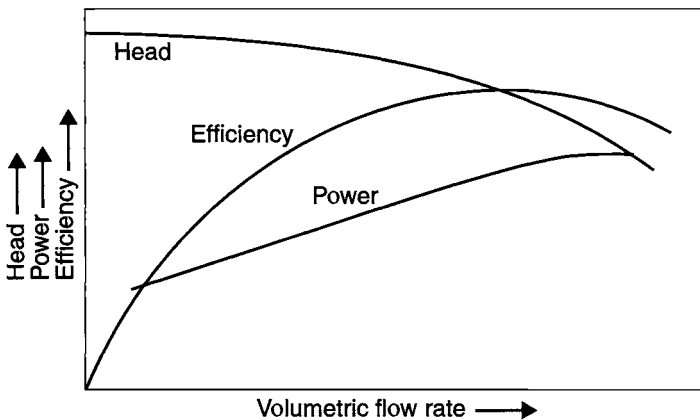
Fig. 12.8. Characteristic curves for a typical centrifugal pump.
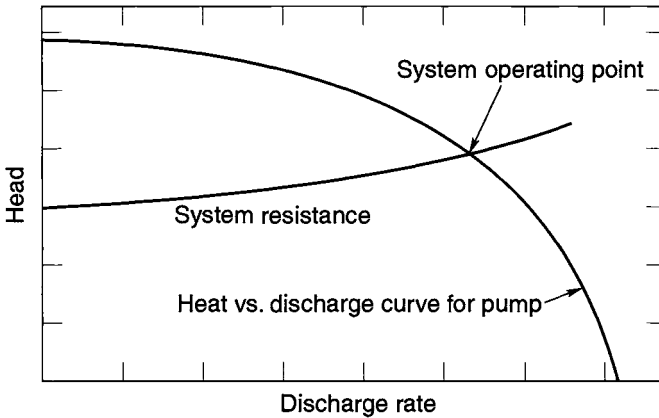
Fig. 12.9. Pump and system curves.

$$\frac{Q_1}{\omega_1 D_1^3} = \frac{Q_2}{\omega_1 D_2^3},$$ (12.29)

$$\frac{H_1}{\omega_1^2 D_1^2} = \frac{H_2}{\omega_2^2 D_2^2},$$ (12.30)

and

$$\frac{P_1}{\rho_1 \omega_1^3 D_1^5} = \frac{P_2}{\rho_2 \omega_2^3 D_2^5},$$

and the specific speed is defined by

$$N_s = \frac{\omega Q^{1/2}}{H^{3/4}}.$$ (12.31)

These laws only hold true at different operating conditions as long as the pump efficiency is constant.

Heat Exchangers

Types of Heat Exchangers

The most common heat exchangers fall into three categories:
- **Flat-plate**.
- **Shell-and-tube.** The simplest form is the double-pipe exchanger shown in Fig. 12.10(a). If the hot and cold fluids both flow in the same direction, it is referred to as a parallel-flow type; otherwise, it is a counterflow type. Some common types of shell-and-tube heat exchangers are shown in Fig. 12.10(b).
- **Crossflow.** In this type of exchanger, the two fluids flow at right angles to each other, as shown in Fig. 12.10(c). The flow may be called mixed or unmixed within the crossflow arrangement.
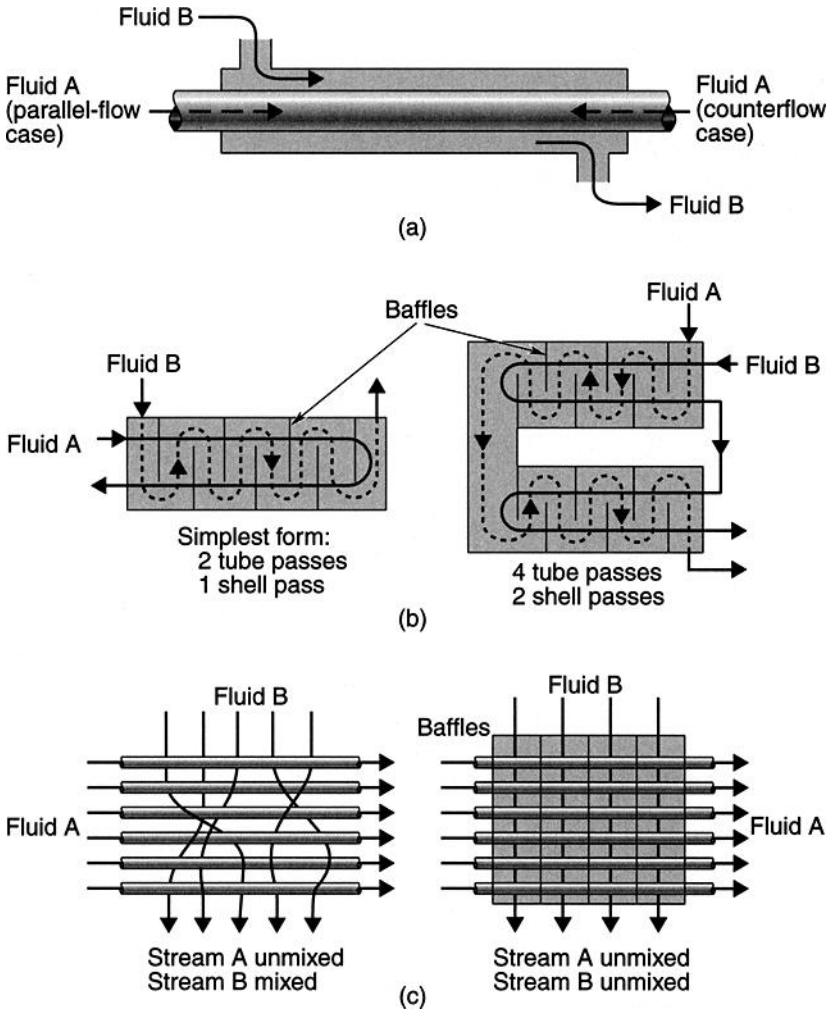
Fig. 12.10. Basic types of heat exchanger. (a) Parallel and counterflow heat exchangers, (b) two kinds of shell-and-tube exchanger, and (c) two kinds of crossflow exchanger.

Heat-Transfer Calculations

The main objective in the thermal design of heat exchangers is to determine the necessary surface area required to transfer heat at a given rate for given fluid temperatures and flow rates. One important factor is the knowledge of the overall heat-transfer coefficient, U, which can be related in the fundamental heat-transfer relation in Eq. (12.32).

$$Q = UA(\Delta T_m),\tag{12.32}$$

where A represents surface area for heat transfer consistent with the definition of U, and ΔT_m is the mean temperature difference across the heat exchanger.

Overall Heat-Transfer Coefficient. The overall heat-transfer coefficient, U, is proportional to the reciprocal of the sum of the thermal resistances. Consider a wall exposed to a hot fluid A on one side and cooler fluid B on the other side. Some common configurations include a plane wall:

$$U = \cfrac{1}{\cfrac{1}{h_o} + \cfrac{L}{K} + \cfrac{1}{h_i}},$$

and a cylindrical wall:

$$U_o = \cfrac{1}{\cfrac{r_o}{r_i h_i} + \cfrac{r_o}{k}ln\!\left(\cfrac{r_o}{r_i}\right) + \cfrac{1}{h_o}}, \qquad U_i = \cfrac{1}{\cfrac{1}{h_i} + \cfrac{r_i}{k}ln\!\left(\cfrac{r_o}{r_i}\right) + \cfrac{r_i}{r_o h_o}},$$

here subscripts i and o represent the inside and outside surfaces of the wall.

Log-Mean Temperature Difference (LMTD). The mathematical expression for the LMTD can be derived by considering a parallel-flow flat-plate exchanger, the temperature profiles of which are shown in Fig. 12.11. From an energy balance on a differential fluid element with length dx for each fluid, the mean temperature ΔT_m for either parallel or counterflow can be determined from the expression in Eq. (12.33).
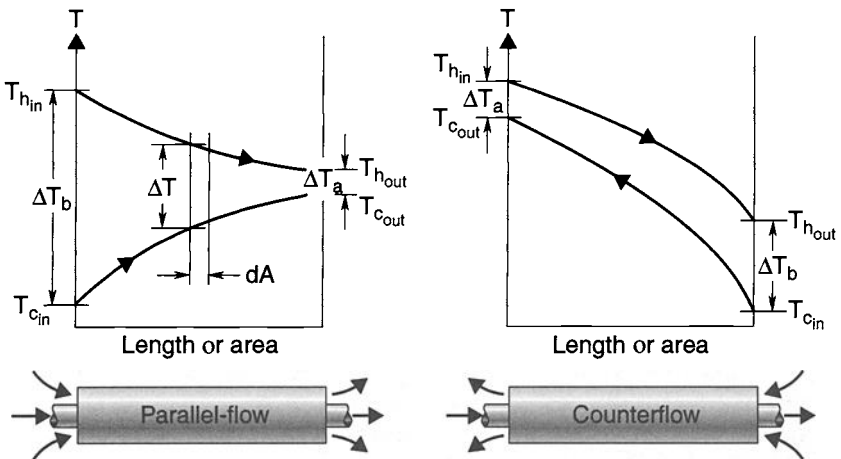
Fig. 12.11. The temperature variation through single-pass heat exchangers.

$$Q = UA\Delta T_m = UA\left[\frac{\Delta T_a - \Delta T_b}{ln\left(\frac{\Delta T_a}{\Delta T_b}\right)}\right]. \qquad (12.33)$$

Thus, the average effective temperature difference ΔT_m in Eq. (12.33) can be written as

$$\Delta T_m = LMTD = \frac{\Delta T_a - \Delta T_b}{ln\left(\frac{\Delta T_a}{\Delta T_b}\right)}. \qquad (12.34)$$

The expression defined by Eq. (12.34) is called the LMTD.

Correction Factors for Complex Heat Exchangers. For more complex heat exchangers, such as those involving multiple tubes, several shell passes, or cross-flow, determination of the average effective-temperature difference is so difficult that the usual practice is to modify Eq. (12.33) by a correction factor, F. Correction factors for several common configurations are given in Fig. 12.12. In these figures the notation (T,t) to denote the temperatures of the two fluid streams has been introduced, since it is immaterial whether the hot fluid flows through the shell or the tubes.

Heat-Exchanger Effectiveness (NTU Method)

The performance of a heat exchanger can be determined once its configuration and the imposed temperature difference are known. However, either the inlet or outlet temperature of the heat exchanger may not be known until the design is complete. An iterative process requiring a trial-and-error approach to finding the heat-transfer rate and the exit temperature is necessary. The so-called effectiveness method developed in full detail by Kays and London in the book *Compact Heat Exchangers* is useful in heat-exchanger design. Heat-exchanger effectiveness is defined as

$$\varepsilon = \frac{\text{actual heat transfer}}{\text{maximum possible heat transfer}} = \frac{Q_{\text{actual}}}{Q_{\text{max}}}. \qquad (12.35)$$

The maximum possible heat transfer occurs if one fluid has undergone a temperature change equal to the maximum temperature difference available within the system. This difference is equal to the temperature of the entering hot fluid minus the temperature of the entering cold fluid. The procedure uses the effectiveness ε to eliminate the unknown discharge temperature. As a result, the solution for the heat-exchanger effectiveness becomes a function of the other known system parameters. These include the mass flow rate of the fluid ($\dot{m}$), heat capacity (c_p), heat-transfer area (A), and the overall heat-transfer coefficient (U). Letting the heat capacitance $C = \dot{m}c_p$, one finds that

$$Q_{\text{actual}} = C_h(T_{hi} - T_{ho}) = C_c(T_{co} - T_{ci}). \qquad (12.36)$$
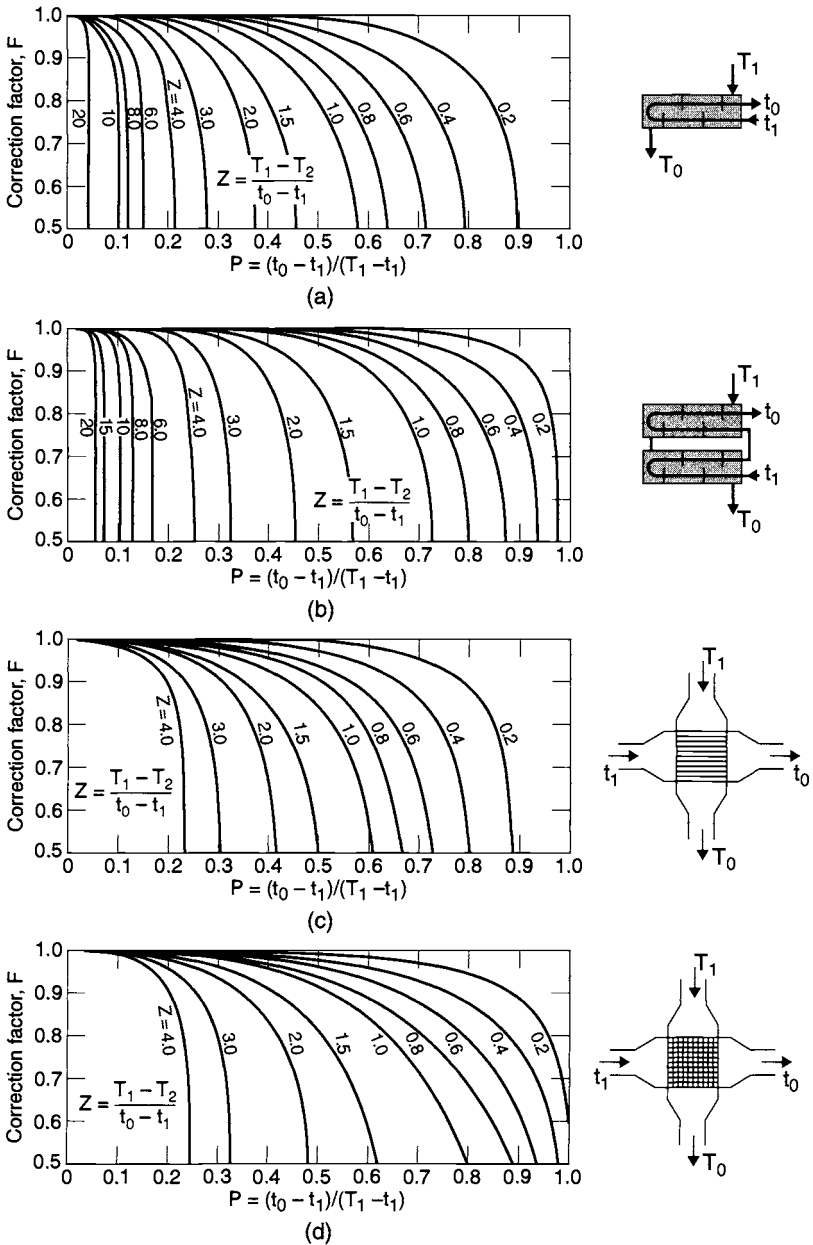
Fig. 12.12. Correction factors for some common heat-exchanger configurations: (a) one shell pass and an even number of tube passes, (b) two shell passes and twice an even number of tube passes, (c) crossflow with one fluid mixed, and (d) crossflow with both fluids unmixed.

Equation (12.36) is an energy balance of both the hot and cold fluids. The maximum possible heat transfer occurs when the fluid of smaller heat capacitance undergoes the maximum temperature variation. This can be stated as

$$Q_{max} = C_{min}(T_{hi} - T_{ci}). \qquad (12.37)$$

Combining Eqs. (12.36) and (12.37), one determines that in terms of the heat-exchanger effectiveness, actual heat transfer is governed by the equation

$$Q_{actual} = \varepsilon C_{min}(T_{hi} - T_{ci}). \qquad (12.38)$$

The heat-transfer rate can be determined once the specific value of the heat-exchanger effectiveness is known. The effectiveness (ε) for the parallel single-pass heat exchanger is

$$\varepsilon = \frac{1 - \exp[-(1 + C_{min}/C_{max})NTU]}{1 + C_{min}/C_{max}}, \qquad (12.39)$$

and the corresponding expression for the counterflow case is

$$\varepsilon = \frac{1 - \exp[-(1 - C_{min}/C_{max})NTU]}{1 - C_{min}/C_{max}\exp[-(1 - C_{min}/C_{max})NTU]}, \qquad (12.40)$$

where C_{max} and C_{min} are the maximum and minimum values of the C ($= \dot{m}\, c_p$) for the hot or the cold fluid. Expressions for the effectiveness of other configurations are given in Table 12.11 and Fig. 12.13, where $C = C_{min}/C_{max}$. Note that for an evaporator or condenser $C = 0$, because one fluid remains at a constant temperature, making its effective specific heat infinite. The NTU appearing in the last two expressions is the so-called number of heat-transfer units, defined as

$$NTU = \frac{UA}{C_{min}}. \qquad (12.41)$$

The NTU may be considered as a heat-exchanger size-factor.

Heat-Exchanger Design

The preceding sections have provided means for predicting heat-exchanger performance. Other considerations in designing heat exchangers are important in addition to the prediction of heat transfer. The primary ones are the minimization of pumping power and the minimization of weight. The weight and size of heat exchangers used in space or aeronautical applications are very important parameters.

Table 12.11. Effectiveness for Various Heat Exchanger Configurations

Exchanger Type	Effectiveness	Graph
Parallel-flow: single-pass	$$e = \frac{1 - \exp[-NTU(1 + C)]}{1 + C}$$	Fig. 12.13(a)
Counterflow: single-pass	$$e = \frac{1 - \exp[-NTU(1 - C)]}{1 - C\exp[-NTU(1 - C)]}$$	Fig. 12.13(b)
Shell-and-tube (one shell pass; 2, 4, 6, etc., tube passes)	$$e_1 = 2\left[1 + C + \frac{1 + \exp[-NTU(1 + C^2)^{1/2}]}{1 - \exp[-NTU(1 + C^2)^{1/2}]}(1 + C^2)^{1/2}\right]^{-1}$$	Fig. 12.13(c)
Shell-and-tube (n shell passes; $2n$, $4n$, $6n$, etc., tube passes)	$$e_n = \left[\left(\frac{1 - e_1 C}{1 - e_1}\right)^3 - 1\right]\left[\left(\frac{1 - e_1 C}{j - e_1}\right)^3 - C^{-1}\right]$$	Fig. 12.13(d) for $n = 2$
Crossflow (both streams unmixed)	$$1 - \exp\{C(NTU)^{0.22}[\exp[-C(NTU)^{0.78}] - 1]\}$$	Fig. 12.13(e)
Crossflow (both streams mixed)	$$e = NTU\left[\frac{NTU}{1 - \exp(-NTU)} + \frac{(NTU)(C)}{1 - \exp[-(NTU)(C)]} - 1\right]^{-1}$$	
Crossflow (stream C_{min} unmixed)	$$e = C\{1 - \exp[-C[1 - \exp(-NTU)]]\}$$	Fig. 12.13(f) (dashed curves)
Crossflow (system C_{max} unmixed)	$$e = 1 - \exp\{-C[1 - \exp[-(NTU)(C)]]\}$$	Fig. 12.13(f) (solid curves)
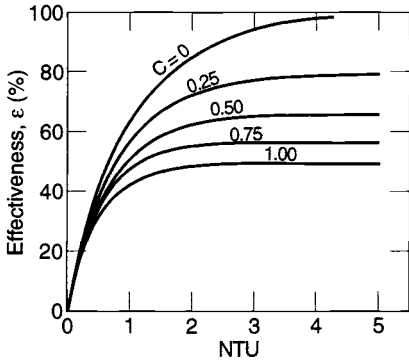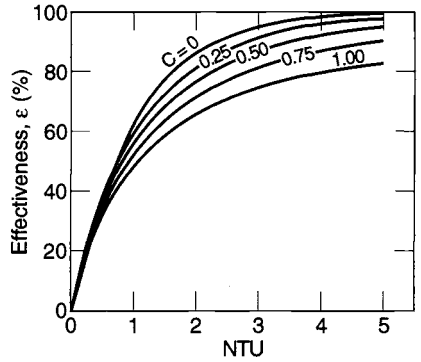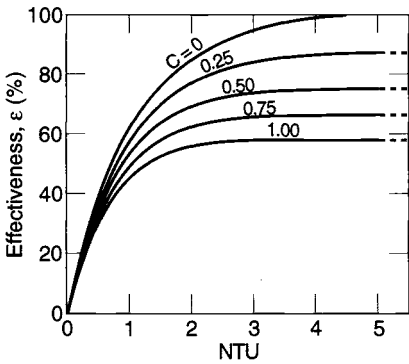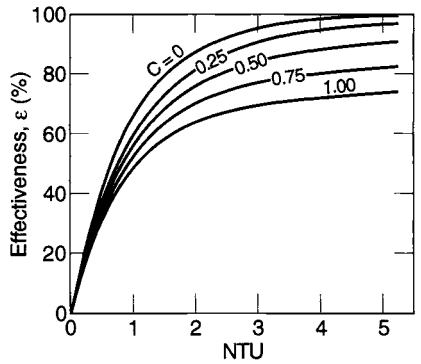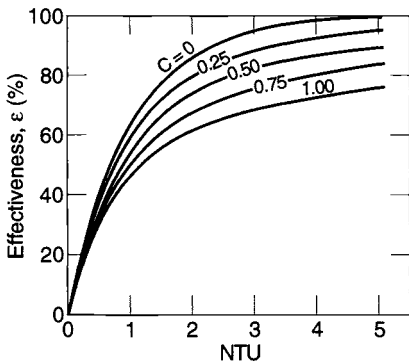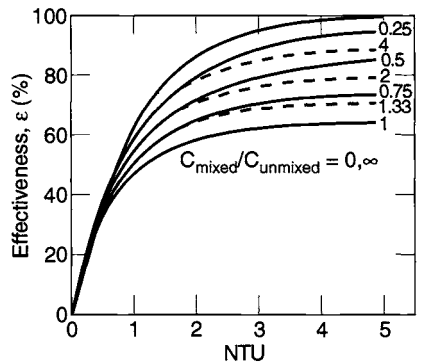
Fig. 12.13. Heat-exchanger effectiveness.

Working Fluids

The graphs that follow in Figs. 12.14–12.24 show physical properties of some of the most commonly used coolants in heat exchangers. Properties such as vapor pressure (P_{sat}), density (ρ), specific heat (C_p), dynamic viscosity (μ), and thermal conductivity (k) are given. The coolants include:

- Monsanto OS 59 (Fig. 12.14)
- FC 75 (Fig. 12.15)
- Freon E1, E2, E3, E4, E5 (Fig. 12.16)
- Freon 11, 12, 13, 21, 22, 113, 114, 142 (Fig. 12.17)
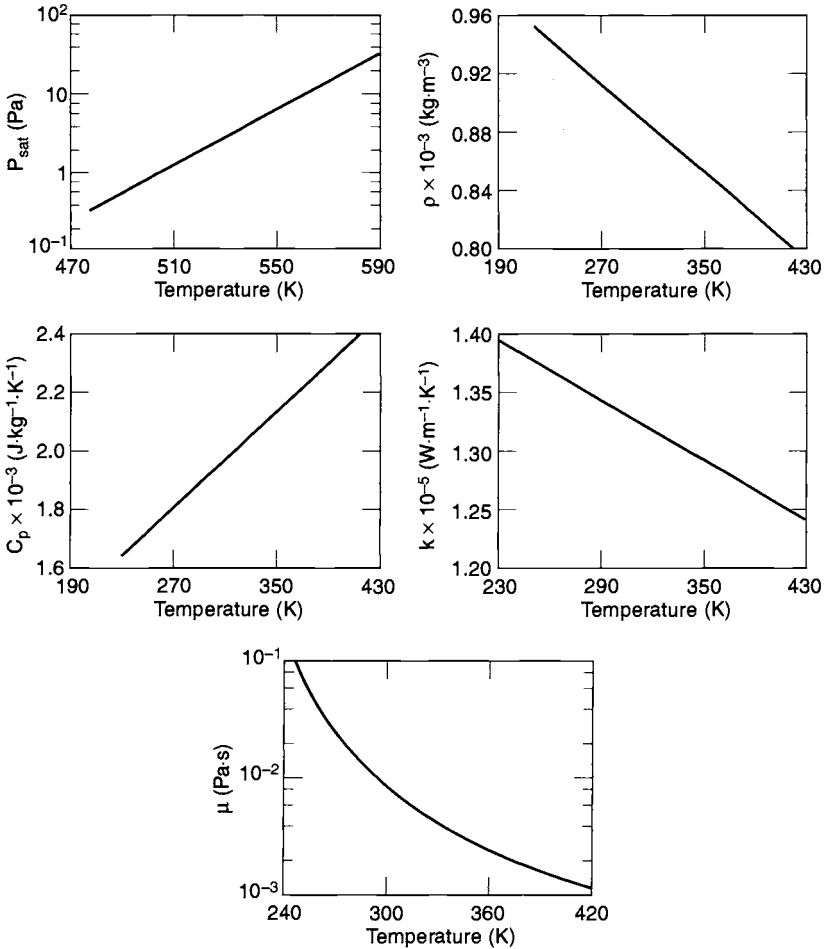
Fig. 12.14. Physical properties of Monsanto OS 59.

- Flutec PP-2, PP-9, PP-50 (Fig. 12.18)
- water/glycol solutions (Fig. 12.19)
- Coolanol 15, 25, 35, 45 (Fig. 12.20)
- carbon tetrachloride (Fig. 12.21)
- water (Fig. 12.22)
- methanol/water solution, DC-200 (Fig. 12.23)
- air (Fig. 12.24)

References 12.49 and 12.59 contain information on other coolants.
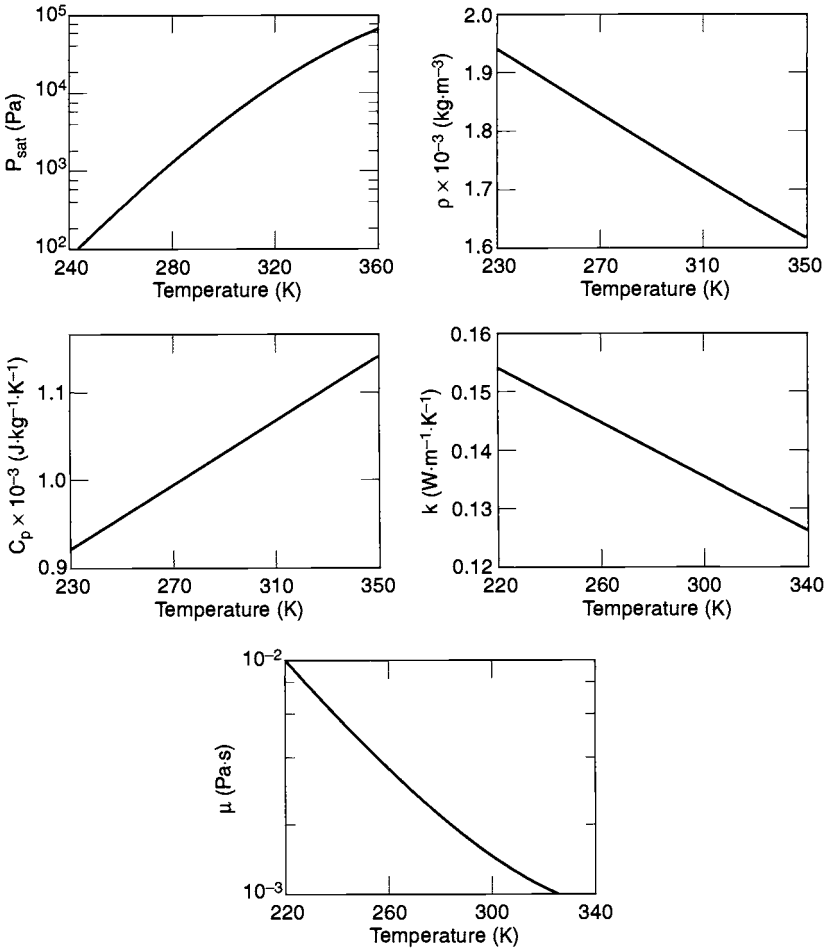
Fig. 12.15. Physical properties of FC 75.
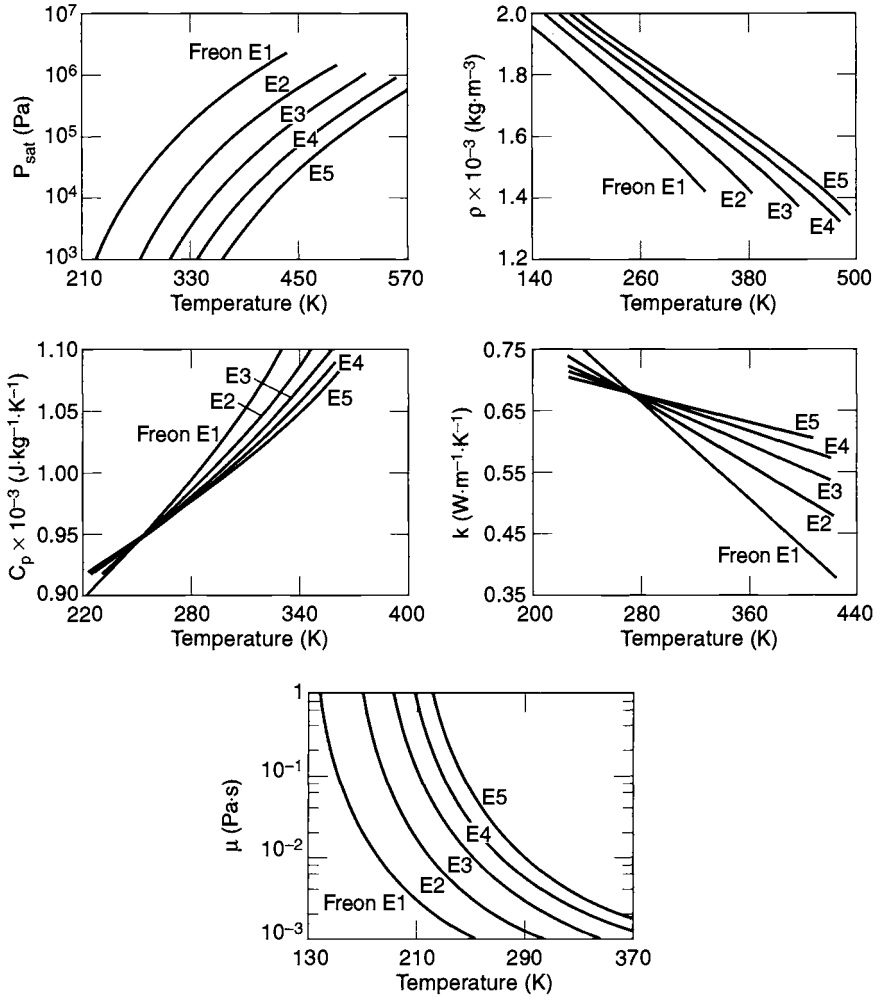
Fig. 12.16. Physical properties of Freon E1, E2, E3, E4, E5.
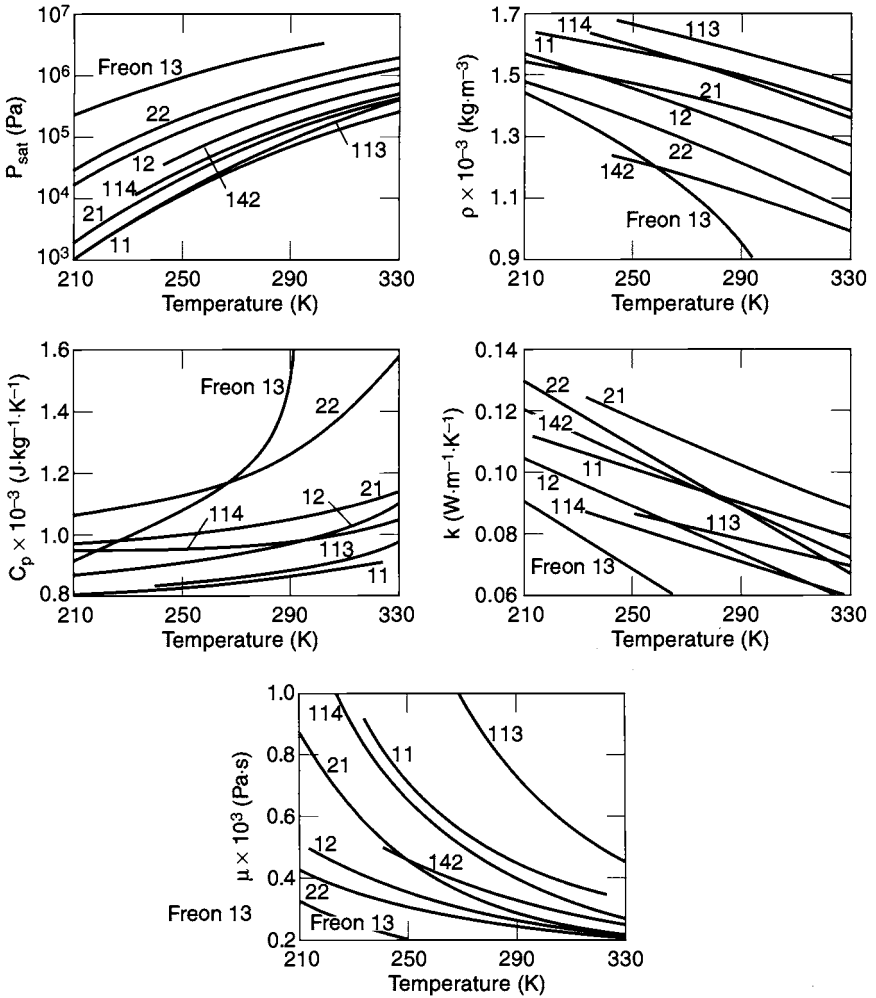
Fig. 12.17. Physical properties of Freon 11, 12, 13, 21, 22, 113, 114, 142.
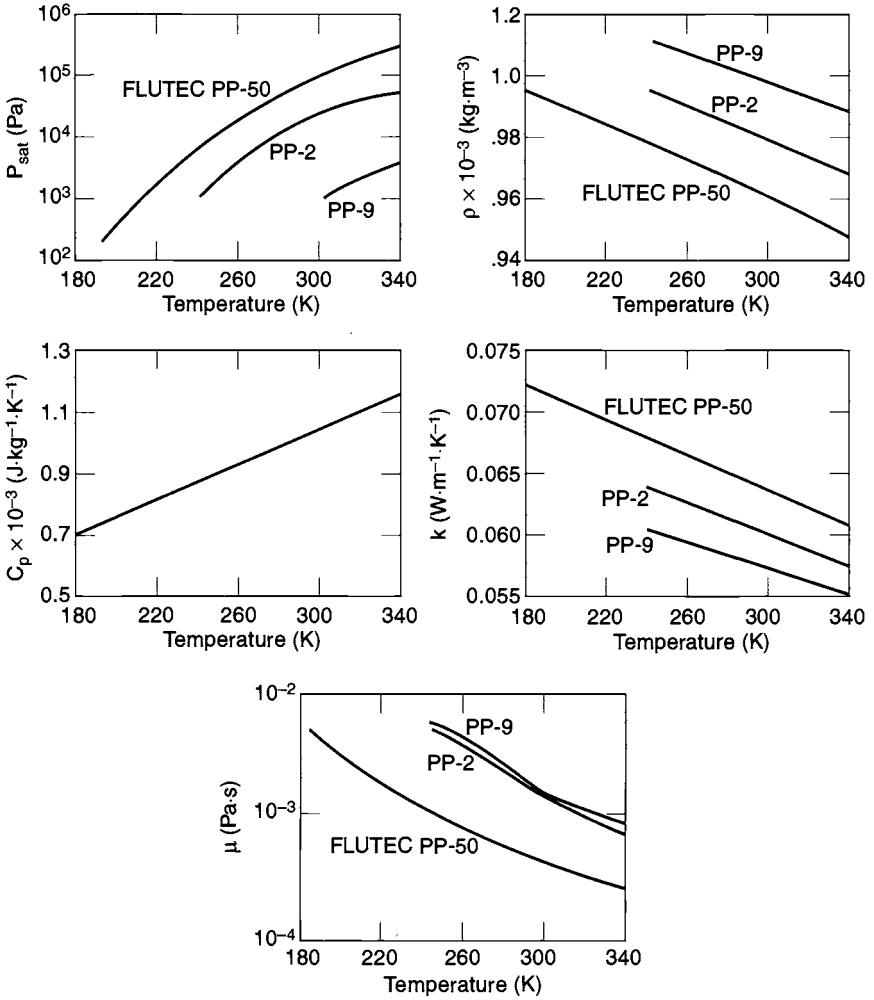
Fig. 12.18. Physical properties of Flutec PP-2, PP-9, PP-50.
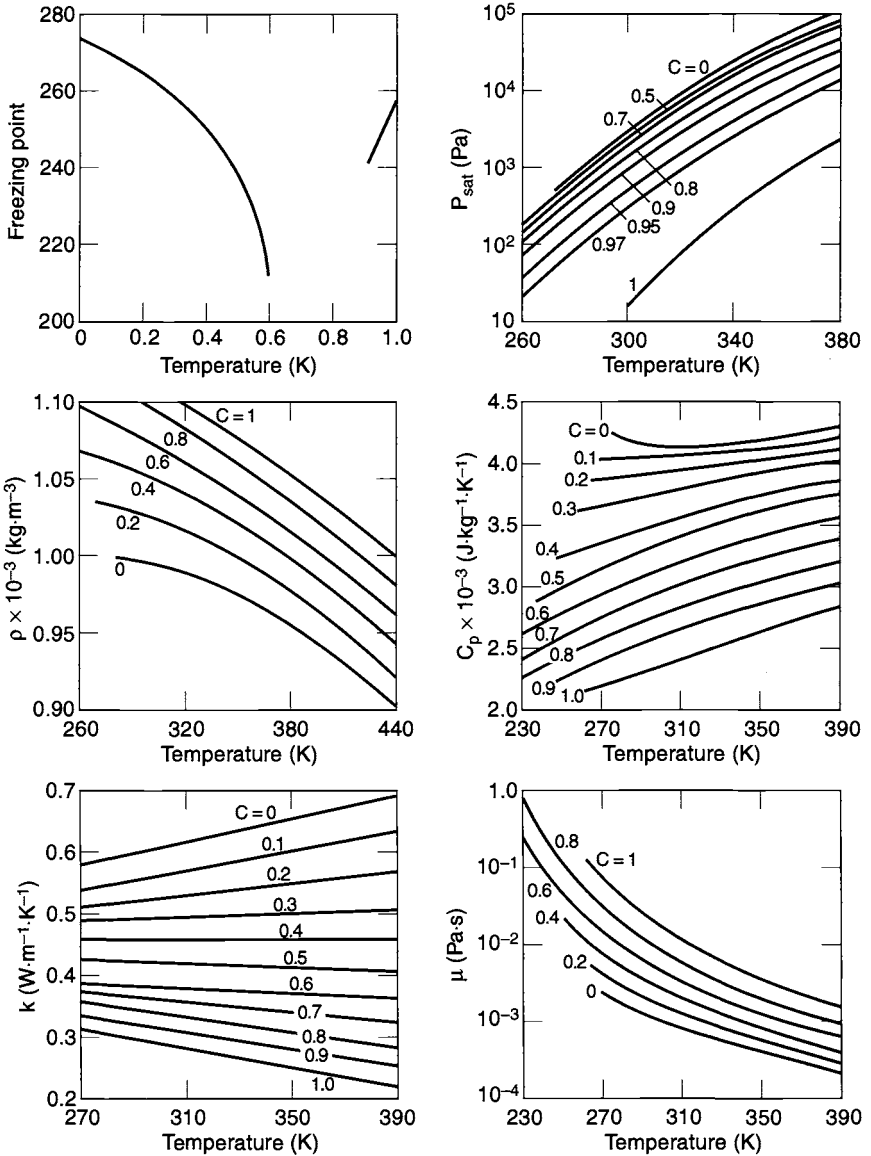
Fig. 12.19. Physical properties of water/glycol solutions.
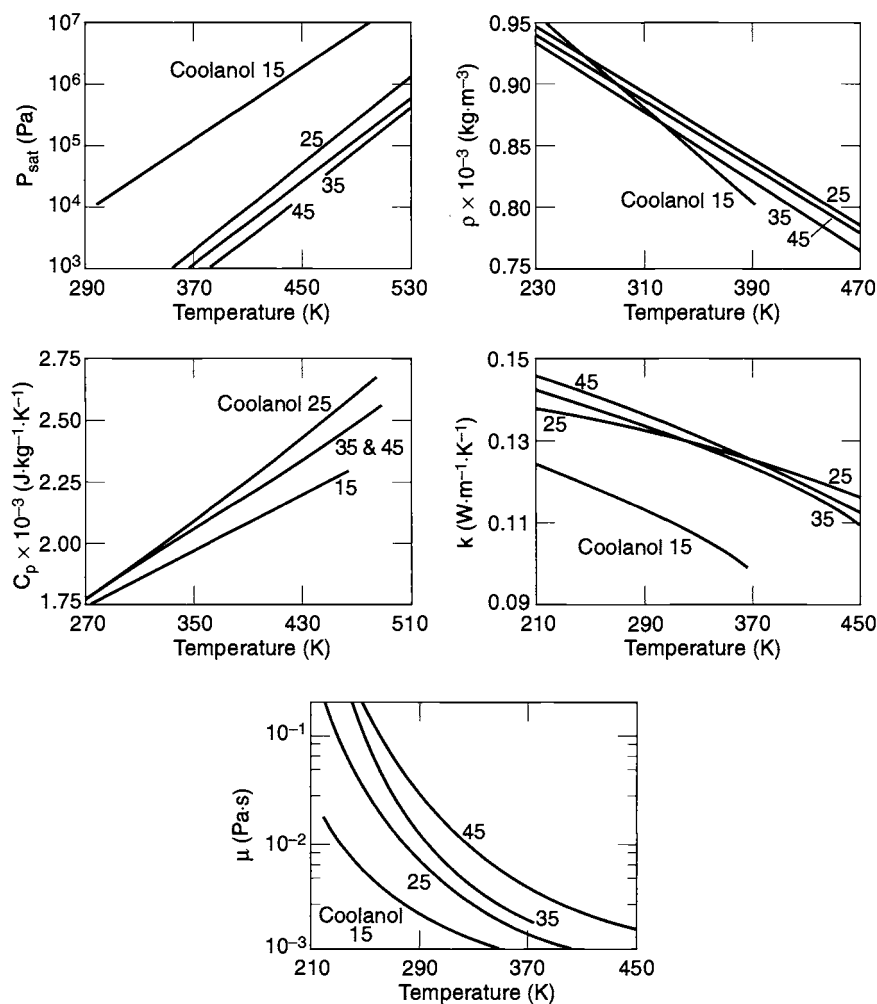
Fig. 12.20. Physical properties of Coolanol 15, 25, 35, 45.
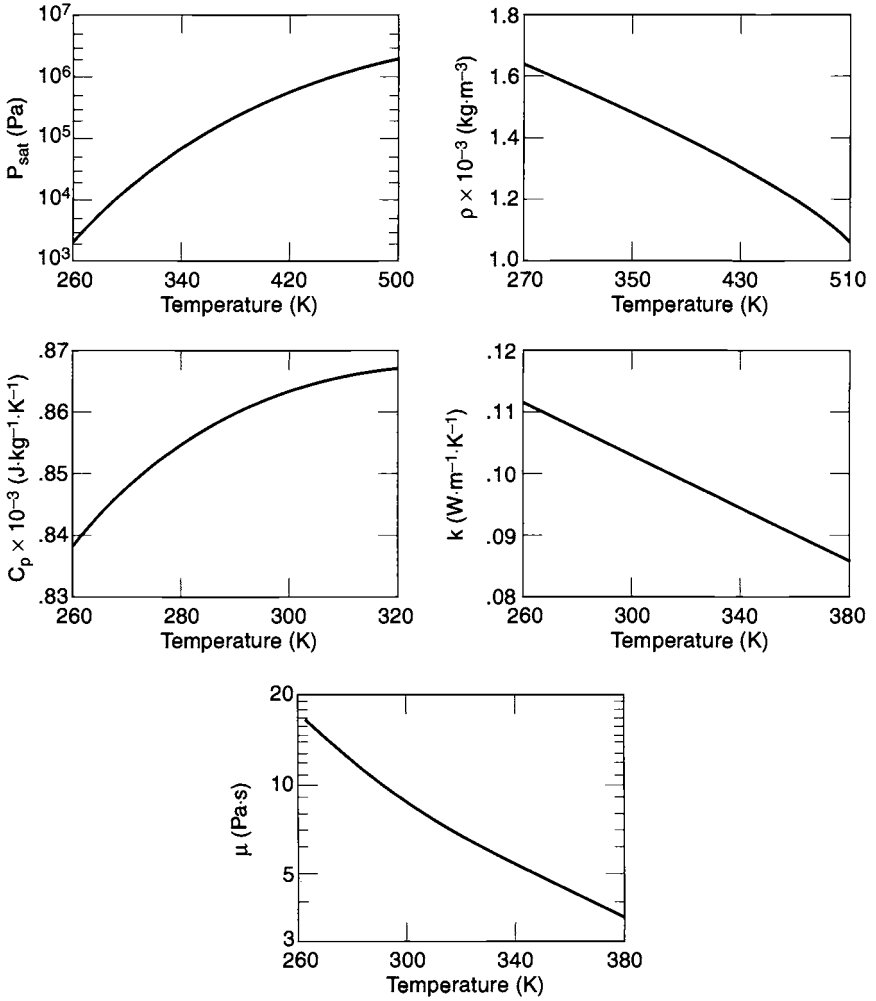
Fig. 12.21. Physical properties of carbon tetrachloride.
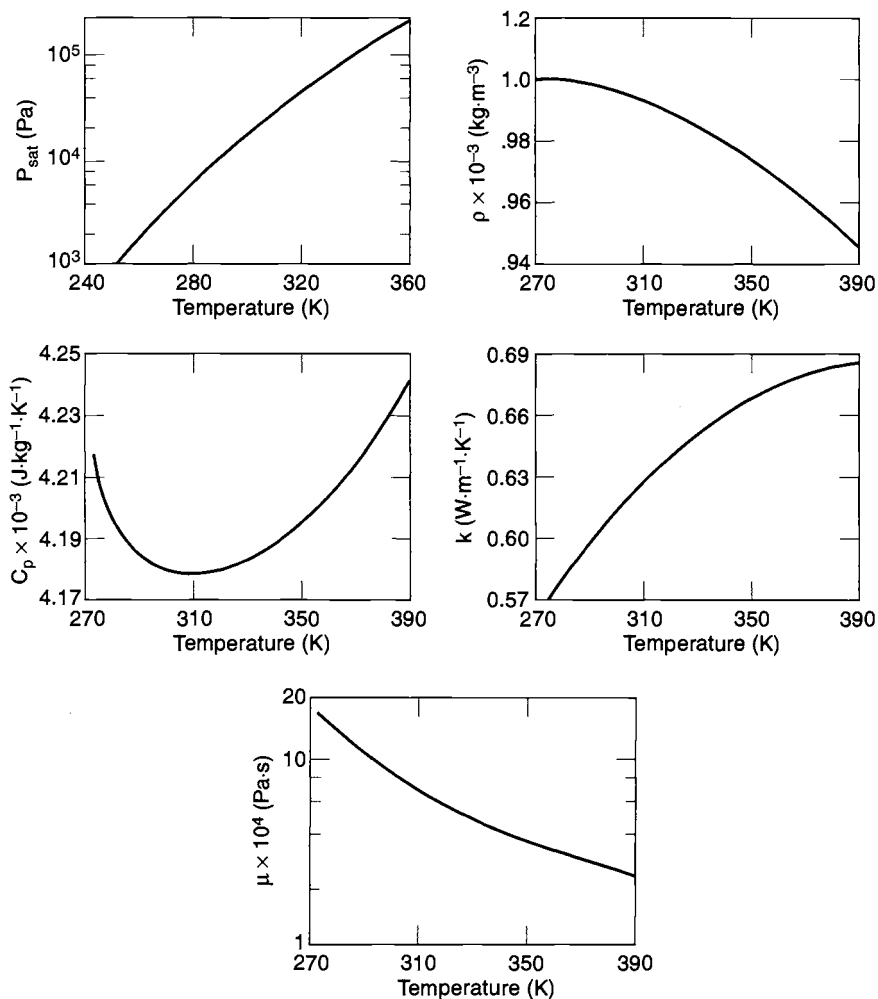
Fig. 12.22. Physical properties of water.
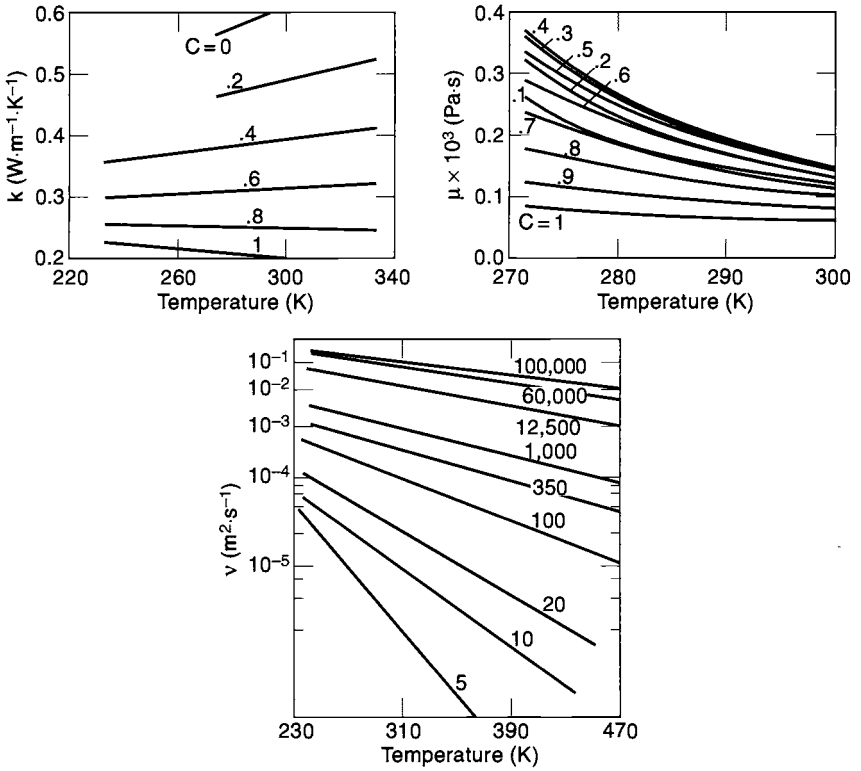
Fig. 12.23. Physical properties of methanol/water solution, DC-200.
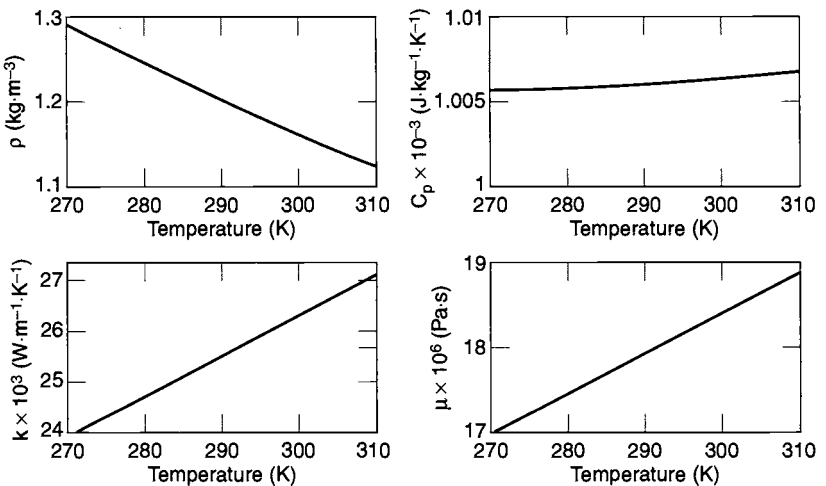
Fig. 12.24. Physical properties of air.

Analysis of a Fluid Loop

The engineering background presented in the previous sections is adequate for analyzing the fluid loop in Fig. 12.1. The design procedure in this section follows closely the analysis provided in Ref. 12.60. The following engineering data are assumed to be known for the system.

- general layout of the fluid loop, including system geometry and dimensions
- thermal properties of the coolant (k, c_p, ρ, μ)
- total heat-flow rate to be removed, Q
- mass flow rates in each loop and heat exchanger (m_h, m_c)
- inlet temperature of the cold fluid in the heat exchanger (T_{ci})

The temperatures throughout the loop and the pumping-power requirements can be determined by performing an energy balance on the system. To compute the temperatures in the loop, the heat-exchanger effectiveness must be calculated. The following steps are needed.

1. Compute the required heat-exchanger heat-transfer surface areas.
2. Compute fluid properties such as density (ρ), specific heat (c_p), thermal conductivity (k), dynamic viscosity (μ), and Prandtl number (Pr).
3. Compute the Reynolds number (Re) for each section of the loop.
4. Compute the Nusselt number (Nu) and the convective heat-transfer coefficient (h).
5. Compute the temperature effectiveness (η) of all the extended surfaces.
6. Compute the overall heat-exchanger thermal conductance (U).
7. Compute the number of heat-transfer units (NTU).
8. Compute the heat-exchanger effectiveness (ε).

Once all of the above engineering data are available, the temperatures throughout the loop can be calculated from these equations:

$$T_{co} = T_{ci} + \frac{Q}{C_c}, \tag{12.42}$$

$$T_{hi} = T_{ci} + \frac{Q}{\varepsilon C_1}, \tag{12.43}$$

and

$$T_{ho} = T_{ci} + Q\left(\frac{1}{\varepsilon C_1} - \frac{1}{C_h}\right), \tag{12.44}$$

where C_1 is the smallest of C_h and C_c.

The pumping power, P_p, required to operate the fluid system against the pressure drop, ΔP, can be calculated from the relation

$$P_p = \Delta P \frac{\dot{m}}{\rho} \cdot \frac{1}{\eta_p}, \tag{12.45}$$

where η_p is the overall pump efficiency, ΔP is the pressure loss through the system, $\dot{m}$ is the fluid-mass flow rate, and ρ is the fluid density at the location of the pump. Thus, the term $\dot{m}/\rho$ represents the fluid-volume flow rate through the pump. The following procedure can be used as a general guideline to compute the pressure losses within the system:

1. Compute the Reynolds number (Re) in all flow conduits.
2. Compute the friction factor (f) for the straight parts of the tubes.
3. Compute pressure loss resulting from friction along the tube walls.
4. Compute pressure loss for all pipe bends.
5. Compute pressure loss in all the fittings (e.g., valves, manifolds, entrances).
6. Compute pressure loss in heat source and heat sink.

Computer Software for System Analysis

Two of the more commonly used thermal fluid network analyzers, SINDA (Systems Improved Numerical Differencing Analyzer)/FLUINT and ESATAN-FHTS (European Space Agency Thermal Analysis Network-Fluid Heat Transfer System), are presented in this section along with a description of The Aerospace Corporation's version of SINDA. This discussion is not intended to cover all available codes, but to provide a brief overview of representative code capabilities. The interested reader should consult the reference list[12.61,12.62] for more detail.

SINDA/FLUINT[12.63]

Under a NASA contract, Martin Marietta Corporation undertook the task of developing an advanced SINDA thermal analysis computer program in 1983.[12.64] The final product of the contract was SINDA '85. This version of SINDA has been improved by a series of enhancements that include the fluid-flow network capability known as the fluid integrator (FLUINT). The combined new computer code SINDA/FLUINT has both thermal and fluid network capabilities. It can perform the pressure/flow analysis of a system containing an arbitrary tube network simultaneously with the thermal analysis of the entire system being cooled, permitting the mutual influences of thermal and fluid problems to be included in the analysis. Companion codes Thermal Desktop and FloCAD provide a graphical user interface for building one-dimensional flow models within a 3-D thermal model.

FLUINT is intended to provide a general analysis framework for internal one-dimensional fluid systems. The computer code can be applied to any arbitrary fluid system; it is not restricted to specific geometries or configurations. Users can select from 20 refrigerants that are immediately available as working fluids, or they can specify their own fluid properties for any specific applications. The code can handle both single- and two-phase flow as well as transitions between these states. FLUINT also includes some common fluid-system components (pumps, valves, and ducts). Inputs are parameterized within spreadsheet-like variables, allowing complex models to be rapidly manipulated, and routines are available for automated model correlation to test data.

ESATAN-FHTS[12.65]

FHTS was developed by GEC Engineering Research Centre in the United Kingdom as an extension of the European Space Agency's principal thermal analysis package, ESATAN. The FHTS computer code can solve both steady-state and transient fluid-flow problems. It can obtain thermal hydraulic solutions to single- or two-phase fluid-flow systems. With it, users are able to construct PFLs from basic node and conductance data to simulate hardware such as pumps and heat exchangers. By defining fluid nodes, fluid conductances, and mass flow links within the framework of ESATAN, one can perform engineering simulations for all-fluid, all-thermal, or combined fluid and thermal systems simultaneously. A variety of predefined models commonly used in fluid systems, known as fluid elements (e.g., pumps, heat exchangers, tee fittings, valves), have been included within the software to reduce the users' input effort. The FHTS has an internal library of fluid-property correlations that can simulate various types of coolant. These include water, ammonia, R11, R12, R22, R114, R502, and air. The user can specify any of these fluids by assigning the appropriate one to the nodal entity. The final system solution gives pressure and temperature (or enthalpy) at each fluid node, and mass flow rate on each fluid link. Reference 12.65 contains more detail on the FHTS.

The Aerospace Corporation's SINDA[12.66]

A flow-network solution scheme has been implemented in The Aerospace Corporation's version of the SINDA thermal analyzer. The computer code can be used for standalone fluid flow and coupled heat-transfer/fluid-flow networks. For standalone flow problems, the flow-network solution capability can be used as a design tool to size the various flow elements such as the pipes, valves, and pump. In coupled thermal/fluid problems the coupling arises from the temperature dependence of the fluid properties. The fluid is assumed to be single-phase, viscous, and incompressible. In addition, the flow is one-dimensional and completely bounded by solid boundaries. Another major assumption in the flow solution is that the flow is always at quasi steady state. Hence, the transient pressure fluctuation is assumed to be negligible. However, the validity of this assumption breaks down for high-speed flows when shock waves are formed or when the flow becomes choked. The solution to a flow network includes the pressure distribution and the mass flow rate across each flow passage.

PFL Application

General

A mechanically pumped single-phase cooling loop was successfully flown on the Mars Pathfinder (MPF) spacecraft, which safely landed on the Martian surface on July 4, 1997, after a seven-month cruise in space. One of the key technologies that enabled the mission to succeed was an active heat-rejection system (HRS) that cooled the electronics. This HRS consisted of a mechanically pumped single-phase cooling system for cooling the electronics and other spacecraft components on the MPF spacecraft. This was the first time in U.S. space history that an active

pumped-liquid cooling system was used in an uncrewed Earth-orbiting or deep-space-mission spacecraft.

The mechanically pumped loop was developed for the MPF mission because of the unique requirements and constraints posed by the mission.[12.67,12.68] Several thermal control design concepts, employing hardware elements such as variable-conductance heat pipes, constant-conductance heat pipes, and detachable thermal/mechanical links, were evaluated before the selection of the pumped cooling loop.

A schematic of the spacecraft and a picture of the assembled spacecraft are shown in Fig. 12.25. The same communications and data-analysis electronics were used during both cruise and landed operations. This equipment was located

Fig. 12.25. MPF thermal control configuration. *Top:* **MPF spacecraft completely assembled;** *bottom:* **spacecraft schematic showing the thermal control system configuration.**

on the base petal of the lander and was completely enclosed in very high-performance insulation to conserve heat during the Martian nights, which can be as cold as –80°C. During cruise, the same equipment was operated continuously at about 90 W of power to communicate with ground. Passive dissipation of this heat is very difficult because of: (1) high power level, (2) high temperature outside the insulated enclosure (15°C near Earth), and (3) additional insulation from the stowed airbags. These conditions in the spacecraft configuration necessitated an HRS for Pathfinder. The main functions of the HRS were to transfer heat from the lander during cruise and minimize heat leak from the enclosure during Martian nights.

Several new approaches were used for the design, qualification, and verification of the HRS because of the short time available for its implementation on the spacecraft. The engineering and flight development were done in parallel; the whole cooling system was designed, built, tested, and installed on the spacecraft in less than two years. A description of this design, fabrication, and testing is given in Refs. 12.69, 12.70, and 12.71.

Active HRS Design

The MPF active HRS was designed to keep the key spacecraft components within the allowable temperature range. This objective was accomplished by using a mechanically pumped single-phase liquid loop to transfer excess heat from the components inside the spacecraft to an external radiator. After the mechanically pumped cooling loop was chosen to serve as the HRS for MPF, a system-level design study was performed on the spacecraft and the following requirements were developed for the HRS.

Performance Requirements

These performance requirements for the HRS were developed based on the Pathfinder mission requirements:

Physical:
1. Mass of the HRS system: < 18 kg
2. Input electrical power: < 10 W

Thermal:
1. Cooling power: 90–180 W
2. Allowable temperature range of equipment: –60 to –20°C (low limit), 5 to 70°C (high limit)
3. Freon liquid operating temperature of –20 to +30°C
4. < 3 W parasitic heat loss on Martian surface (from any remnants of the cooling loop)

Integrated Pump Assembly (IPA):
1. 0.76 l/min Freon flow rate @ > 27.6 kPa pressure rise
2. < 10 W total power consumption during cruise

3. < 8 kg weight

4. > 2 years of continuous operation without failure

Leakage:

1. Meet specified (very low) leak rate (liquid and gas) to maintain liquid pressure well above saturation pressure—at least 206 kPa higher

Venting:

1. Freon to be vented from HRS prior to lander entering Martian atmosphere to prevent contamination of Martian surface (Freon would interfere with chemical experiments to be performed by Pathfinder on Mars)

2. Freon lines from lander to cruise stage to be cut by pyro cutter after Freon has been vented to allow separation of cruise stage from the lander

3. Negligible nutation torque of spacecraft resulting from venting process

4. Negligible contamination of spacecraft components during Freon venting

HRS Design Description and Trade-Offs

The HRS consisted of six distinct parts. A schematic of this system is shown in Fig. 12.26. The key components are the following:
- IPA (integrated pump assembly)
- Freon-11 working fluid (also known as Refrigerant 11)
- HRS tubing
- electronics assembly
- Freon vent system
- radiator

The primary spacecraft electronics (the key heat source) was located in the lander base petal in a highly insulated enclosure. The IPA circulated the Freon through the HRS tubing from the electronics-equipment shelf to the cruise-stage radiator. The vent system was used to vent the Freon prior to Martian entry.

IPA

The IPA had two centrifugal pumps; one was primary, whereas the second one served as backup in case the primary one failed. Only one pump was on at any time. Each pump (powered by its own motor) produced more than 27.6 kPa pressure differential at 0.76 l/min. The pump/motor assembly had hydrodynamically lubricated journal bearings to minimize bearing wear and frictional power loss, and to maximize the life of the system. Each pump/motor assembly was powered by its own individual radiation-hardened electronics.

Two wax-actuated thermal control valves automatically and continuously split the main Freon flow between the radiator and a bypass to the radiator to provide a fixed (mixed) temperature fluid to the inlet of the electronics shelf—this was to account for the continuously decreasing environmental temperature of the radiator on its journey from Earth to Mars and the constantly changing heat load on the electronics. The thermal control valves used an enclosed wax pellet with bellows to open and close two ports leading up to the radiator and its bypass depending on
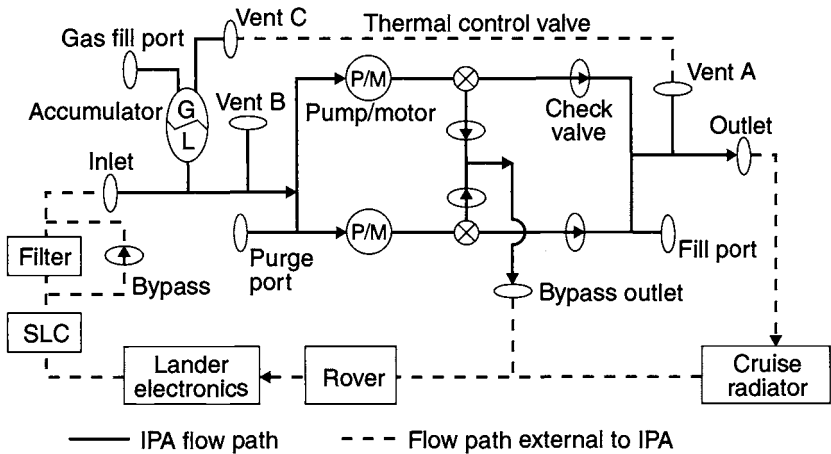
Fig. 12.26. Mars Pathfinder HRS.

the temperature of the Freon entering the valves. The set point of the valves was 0 to –7°C, a range that was chosen because it is approximately in the middle of the operating temperature limits of the electronics being cooled by the HRS. When Freon entered the thermal control valves, if the temperature was higher than 0°C, all the flow was allowed to go through the radiator, whereas when the temperature fell below –7°C, all the flow bypassed the radiator. For intermediate temperature values, the valves opened partially in each direction.

Four check valves in the IPA prevented the flow from recirculating from the primary (active) pump to the backup (inactive) pump, and they prevented bypassing of either the electronics or the radiator whenever only one pump was on and the thermal control valves were either diverting the flow fully or partially to the radiator. Because of the changing environment temperature, the bulk of the Freon liquid experienced a temperature change (–40 to +50°C) during the flight and ground testing. To accommodate this, the IPA employed a bellows accumulator to maintain the liquid pressure at least 2×10^5 N/m^2 (30 psi) above its saturation pressure throughout the flight to prevent cavitation of the centrifugal pumps. The accumulator bellows has a stroke volume of 393 cm^3 and is sized to account for a liquid volume change of 229 cm^3 because of temperature changes and liquid leaks as large as 164 cm^3 during the flight (7 months or 5100 hours). A detailed design description of the IPA is provided in Ref. 12.69.

Freon-11 Working Fluid

About 15 fluids (Ref. 12.68) were traded off as candidate working fluids before the selection of Freon-11 (CCl$_3$F, trichlorofluoromethane), a refrigerant commonly used for building air conditioners. The working fluid was designed to remain in the liquid phase under all conditions, to allow the mechanical pumps to work satisfactorily; this and other considerations led to the selection of several criteria used to trade off these liquids. The liquids included various Freons, methanol, ethanol, glycols, Dowtherms, and trichloroethylene. The selection criteria were:

- freezing point (should be less than about −90°C because during the radiator bypass the Freon in the radiator could get as cold as −80°C)
- boiling point (should be as high as possible to ensure that the operating pressure required to maintain the liquid state is low; also should be higher than room temperature for ease of handling during ground operations)
- specific heat and thermal conductivity (should be high); viscosity (should be low, for high heat-transfer rates and low pressure drops)
- compatibility with commonly used materials like aluminum and stainless steel (should be excellent for long-term corrosion proof performance)

The important properties of Freon-11 are:

- freezing point = −111°C
- normal boiling point = 24°C
- vapor pressure at 50°C (highest operating temperature) = 138 kPa
- specific heat = 900 J/kg·K
- thermal conductivity = 0.084 W/m·K
- viscosity = 5×10^{-4} N·s/m^2
- density = 1459 kg/m^3
- Prandtl number = 4
- very compatible with stainless steels
- very compatible with aluminum at low moisture levels (~10 ppm)
- quite corrosive at high moisture levels (~100 ppm)
- compatible with some elastomers, such as Viton, and materials like Teflon

Tube Diameters and Materials

Tube diameters of 12.7, 9.53, and 6.35 mm (1/2 in., 3/8 in., and 1/4 in.) were traded off for heat transfer, pressure drop, pumping power, and weight. Tubing with a 6.35-mm (1/4 in.) diameter was used for the electronics shelf for high heat transfer and the fact that the length was short enough (1 m) that the consequent pressure drop was not excessive. Tubing with a 9.53-mm (3/8 in.) diameter was used for the radiator because the heat-transfer coefficient was not critical in the radiator (large available area, about 8.22 m long); 9.53-mm (3/8 in.) tubing was also used for the transfer lines. The radiator and the transfer lines had long lengths of tubing; this also minimized the pressure drop in the loop. Freon flow rates were traded off in terms of heat transfer and pressure drops to come up with an optimum value of 0.76 l/min.

The electronics shelf and radiator used aluminum tubing because the tubing in these zones was brazed to aluminum surfaces that were used to ensure high heat-transfer rates with minimum weight. The transfer lines were made of stainless steel for ease of welding, better compatibility with Freon, shorter lengths, and lack of heat-transfer requirements.

Electronics-Shelf Tubing Layout

Several tubing layouts were investigated to minimize component temperatures, Freon pressure drop, and pumping power. The key constraints were the temperature limits of the solid-state power amplifier (SSPA; 40°C) and the battery (−20 to +25°C), and the highly localized heating in the SSPA (43 W in a relatively small area). The cooling-loop tubing was strategically routed and wrapped near the

high-power-dissipation area of the SSPA to minimize its temperature rise; the other electronics boxes had a relatively uniform power dissipation and did not require strategic routing of the cooling-loop tubing to pick up their heat.

The shelf's facesheet thickness was varied to trade off heat transfer and mass. Local thickening of facesheet near hot spots was also investigated. A basic thickness of 1.5 mm for the facesheet (no local thickening) was chosen, which satisfied all the thermal requirements. After MPF's entry into the Martian atmosphere and landing, the HRS was no longer functional, and the electronics in the lander relied on its thermal mass to manage its temperatures within its limits. Since the SSPA power density was so high, the facesheet was thickened near the SSPA to 4.5 mm to satisfy the entry and Martian surface requirements (coupling the high-power, low-mass SSPA to the low-power, high-mass IEM (integrated electronic module) box to improve the transient response).

In addition to the lander electronics shelf, two other components were cooled by the cooling loop: the shunt limit controller (SLC) and the Rover cold finger. The Rover cold finger is coupled to a split clamshell, which grabs onto the HRS tubing to reject its heat (2 W). The SLC had a heat dissipation varying from 0 to 60 W (depending on the shunted power), and its cooling was achieved by bonding a cold plate to its interface—two feet of the cooling-loop tubing were brazed to the cold plate for Freon flow.

Venting

Before MPF entered the Martian environment, the Freon had to be removed from the lander (to minimize contamination of the Martian surface) by either venting all of it to space or repositioning it to the cruise stage (which was separated from the lander before entry). Several schemes to vent the Freon were investigated before engineers came up with one that minimized the resultant torque on the spacecraft. One method proposed the use of high-pressure gas (N_2) in the accumulator to "piston out" Freon from the HRS by opening a pyro valve that connects the gas side of the accumulator to the liquid; the liquid in turn would be vented to space via a nozzle that is opened to space via another pyro valve. Another method proposed discharging the Freon from opposing (T-shaped) nozzles to cancel the torques, or, through a single nozzle with the nozzle axis passing through the spacecraft center of gravity (c.g.), with the nozzle outlet pointed in a direction opposite to the c.g.

The main reason for the torque on the spacecraft is the reaction from the momentum of the venting Freon; hence the rationale for entertaining the possibility of repositioning the Freon, because until the spacecraft is intact (with the cruise stage connected to the lander), repositioning the Freon within the spacecraft should minimize the reactional torque. The proposed scheme was to use the accumulator gas to push the Freon into a separate (extra) thin-walled and lightweight "holding" tank in the cruise stage (sized to hold the entire volume of liquid Freon). An extra check valve would prevent backflow from the holding tank to the HRS.

Venting Freon to space through a single nozzle with its axis passing through the spacecraft c.g. was the venting method that was chosen and implemented, a simple scheme to implement with minimum contamination and minimum hardware changes to the spacecraft. The diameter of the nozzle was 1 mm, which met the attitude-control system's requirements for the disturbing torque—the time to vent

all the Freon was predicted to be about three minutes. The initial thrust from the nozzle was estimated to be about 0.5 N with an initial exit speed of 21 m/s. The thrust, of course, decays very rapidly (exponentially) and is less than 0.05 N at the end of the vent process.

Radiator

The radiator used to reject the 180 W of heat (maximum) is 8.22 m long by 0.2 m wide. It is a circumferential strip of aluminum (0.75 mm thick and thermally attached to the 9.53-mm-diameter HRS tubing) located at the circumference of the cruise stage. It is mechanically attached to the cruise-stage ribs and thermally (conductively) decoupled by isolators. Both sides are painted white (NS43G on the outside surface, Dexter Crown Metro gloss white on the inside surface; high α, low ϵ) to maximize the radiator's heat-loss potential. The inside surface is radiatively coupled to the warm cruise stage underside and the backshell to preclude freezing of the Freon in the radiator when the radiator faces a cold environment and most of the Freon bypasses the radiator (94% bypass).

The reason for relying on the radiative coupling instead of the conductive coupling to pick up some heat from the cruise stage is that the radiative coupling (and heat input) is much easier to predict and implement than the conductive coupling. This is the case because the conductive coupling is achieved via a very convoluted and complex thermal path that also involves contact conductances. For the coldest conditions the cruise stage is at $-30°C$ while the backshell is at $-65°C$—these surfaces provide enough heat to the radiator in the coldest conditions to maintain the temperature of the coldest portion of the radiator above $-80°C$, which is well above the freezing point of the Freon-11 ($-111°C$). The radiator temperature would not fall below $-80°C$ even if there were no Freon flow through the radiator.

IPA Design, Fabrication, and Test

The IPA, which is a major element of the HRS, circulates and controls the flow of Freon-11 in the mechanical cooling loop. It consists of mechanical centrifugal pumps, an accumulator, thermal control valves, and control electronics. The specifications, design, and implementation of the IPA in the Pathfinder HRS are described in Ref. 12.69. The key new technologies developed and implemented in the system are the use of Freon-11 as a single-phase working fluid and a wax-actuated thermal control valve to control the fluid temperature in the loop. A description of the thermal control valve is given in Ref. 12.69.

IPA Specifications

The IPA design specifications were based not only on the spacecraft thermal control considerations but also on the spacecraft system-level considerations of reliability, mass, power, and cost. As a consequence, the overall system consisted of redundant pump systems: each unit had its own pump/motor, motor-control electronics, check valves, and thermal control valve to bypass the flow. The only non-redundant component in the IPA was the accumulator. The specified arrangement of the components in the IPA is shown in Fig. 12.26.

The specifications developed for the IPA covered hydraulic and electrical performance, component descriptions, mechanical and electrical design, electronic

and mechanical parts, electromagnetic compatibility, operating and nonoperating environments, fabrication and assembly requirements, and quality-assurance provisions. The key specifications are listed in Table 12.12.

Design and Fabrication

The detailed mechanical and electrical design of the IPA was developed by the vendor based on the specification provided by JPL. The mechanical design consisted of four major components mounted on a baseplate: the accumulator, the

Table 12.12. Key IPA Specifications

Section	Specification Detail
Thermal and hydraulic	
Flow rate and pressure rise	Freon flow rate of 0.76 l/min, at 27.6 kPa in the operating temperature range of −20 to 30°C
Maximum operating pressure	690 kPa
Operating temperature range	−30°C to 40°C
Bypass ratio	Above 0°C, 100% radiator flow; below −7°C, 100% bypass flow
Leak rate	Helium leak rate of 10^{-7} scc/sec for the gas and 10^{-4} scc/sec for the liquid side
Storage temperature	−40°C to 50°C
Physical	
Mass	Maximum of 8 kg dry
Size	$25.4 \times 25.4 \times 16.5$ cm
Service valves	One for gas charge and two for liquid fill and purge
Mounting	Mounted on a base plate
Operation	
Life	10,000 hours continuous, 3 calendar years
Starts/stops	1000
Electrical	
Input voltage	To operate in 27 Vdc to 36 Vdc
Power	10.6 W maximum
Isolation	One MΩ electrical isolation
Electronics parts	MIL-STD-975 Grade 2; MIL-STD-883C Grade B for microcircuits; withstand a radiation environment of 500 rads (SI); CMOS and MOSFETs meet single-event effect parameters
Acceptance tests	IPA hydraulic performance, sinusoidal and random vibration, thermal vacuum test, proof pressure, and leak-rate tests

pump/thermal control manifold, an electronics box housing all the motor-control electronics, and a front panel housing the service valves. The materials used for the IPA were 304L stainless steel, Inconel 718, and aluminum. Stainless steel was used for all the wetted paths of the IPA except the accumulator bellows, for which Inconel 718 was used, whereas aluminum was used for the baseplate and the electronics box. The electronics box was designed as a modular unit so that it could be removed from the pump assembly during welding of the pump assembly to tubing that would circulate Freon in the spacecraft.

The accumulator featured a welded Inconel 718 double-walled bellows to contain the Freon liquid with the pressurant gas (nitrogen) on the outside of the bellows. The stroke volume of the bellows was 393 cm^3. A service valve was mounted on the housing to provide access to charge the accumulator with gas to the required pressure. A strain-gauge-type pressure transducer was welded to the accumulator housing to measure the gas pressure during ground operations and testing. The pump manifold was machined from wrought stainless steel, which housed the check valves, thermal control valves, pump/motors, and the inlet and exit ports.

A centrifugal pump was chosen over other types of pumps on the basis of life and reliability data on pumps and the suitability for the current application. The hydraulic performance and electrical-power requirements of the Pathfinder HRS favored the centrifugal-type pump. The Pathfinder HRS required a small pressure rise at a large flow rate, and it had very little power available for the pumps. At the required performance point of 0.76 l/min at 27.6 kPa, the specific speed of 1267 predicted a pump head efficiency of 10% for a centrifugal pump, meeting power requirements. The concept of using a positive-displacement pump was rejected because of a lower service life and material restrictions. The selected pump featured a radial vane Barsky-type impeller, driven by a brushless DC motor with Hall effects sensors embedded in the stator. The impeller was a four-vane design without side shrouds to minimize viscous losses, and it was attached directly to the motor shaft. The motor rotor, which rotates at about 12,000 rpm, was supported by two carbon graphite journal bearings, lubricated by the working fluid. The rotor consisted of permanent magnet poles made of Samarium Cobalt. A stainless-steel sleeve isolated both the rotor and stator from the working fluid. This wet design negated the need for a shaft seal, improving the pump life.

The vendor had used this design a few years earlier for a developmental unit for another program. This unit was ground-tested and had run for about 3000 hours and experienced more than 300,000 starts and stops. The clearances in the pump varied from about 6 μm in the journal bearings to 125 μm in the bypass loop for wetting the journals. Two developmental pumps were first built for the Pathfinder program as life test unit pumps. These pumps went through thermal cycles and random vibration tests, and one of the units, shown in Fig. 12.27, was life tested. This pump had operated for more than 14,000 hours as of August 1997. Details of these tests are given in Ref. 12.71.
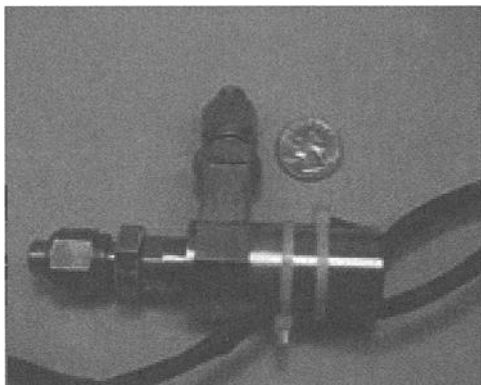
Fig. 12.27. Engineering model of the centrifugal pump used in the IPA life tests at JPL.

The check valves used were made of stainless steel with a cracking pressure of 1.4 kPa. These valves used Teflon O-rings as seals. The thermal control valve used a wax actuator that provided an actuation of 0.5 mm within a temperature range of −7 to 0°C. The actuator moved a spool in the valve that opened or closed the bypass port depending on the temperature of the Freon flowing through the valve. The wax was hermetically sealed from the working fluid by a stainless-steel bellows, preventing wax loss through a dynamic seal, as is common to most wax actuator designs. The original design consisted of stacked bimetallic discs. However, some developmental tests revealed that the disc material was not compatible with Freon and that the discs did not produce smooth linear motion because of stiction. Therefore, a new development effort was undertaken to build a wax actuator that would meet the Pathfinder needs.

The motor-control electronics was enclosed in a wrought-aluminum box housing the circuit-card assemblies of both the pump/motors. A connector was mounted on one end of the box for the input power, and another connector on the bottom box connected the motor controller to the pump/motors. The circuit cards were multilayer boards with lead-in components soldered to the boards. The circuits were designed to meet the Pathfinder fault-tolerance requirements for radiation susceptibility. The parts used met the reliability requirements (MIL-STD-975 Grade 2 and MIL-STD-883C Grade B). The single-event effect-sensitive parts used were JPL-approved radiation-hardened parts. EMI filters were included to meet the conducted and radiated emissions and susceptibility requirements of the Pathfinder spacecraft.

The fabrication was done in three major subassemblies before the whole unit was put together: the accumulator assembly, the pump manifold assembly, and the motor-controller electronics subassembly. The accumulator and the pump manifold were all welded stainless-steel units, whereas the controller electronics housing was in a hogged-out aluminum box with a bolted-on lid. The welds were made to qualify weld schedules by MIL-STD-1595 certified weld operators. The sample welds were made on the day of the flight weld and inspected under high magnification for sound weld quality (depth of penetration, porosity, cracks, etc.) before

the actual hardware was welded. The unit was leak-tested before the next series of welds was undertaken.

The accumulator assembly consisted of the machined housing, the bellows, service valve, pressure transducer, and purge tubing. All the parts were cleaned thoroughly to remove the particulates above 25 µm in size before the parts were assembled, tested, and welded. The unit was tested for leak rate and bellows performance between each series of welds. Electron-beam welds were used for all the welds in the accumulator subassembly. After the assembly was completed, the pressure transducer output was calibrated against pressure-gauge readings.

All the motor assemblies, valves, and inlet and outlet tubing were assembled into the wrought-stainless-steel pump manifold. All these parts were welded into the block using laser welding. Because of the magnetic properties of the motors, electron-beam welds could not be used for this assembly. As in the case of the accumulator fabrication, the pump manifold parts were cleaned and the unit tested between each series of welds. The tests consisted of checking the performance of each pump and thermal control valve, and the check valves, before the next series of welds was made.

The motor controller was designed using discrete electronic components. Two reasons led to the selection of this option rather than an integrated-circuit-based design. The first was the tight schedule for the design and fabrication of the controller. The second reason was the flexibility the discrete-component design allowed in the use of the available electronic parts. The motor-controller electronics-box fabrication consisted of fabricating the circuit cards and populating them with parts. The multilayer circuit cards were fabricated to MIL-P-55110. All the lead-in components were soldered to the boards per the MIL-STD-2000. The boards were conformally coated before they were installed in the box.

The final dry mass of the IPA before it was installed on the spacecraft was 8.3 kg. The IPA in its final assembled state is shown in Fig. 12.28.

Performance Tests

Three types of performance tests were done on the IPA: hydraulic, electrical, and system proof-pressure and leak. The hydraulic performance tests were conducted to verify that IPA met the specification requirements. These requirements related to the flow rate and pressure rise at various temperatures. The IPA flow rate at various pressure rises is shown in Fig. 12.29 for the IPA with one pump operating.

Fig. 12.28. Pathfinder IPA.

Pressure vs. flow rate at 25°C
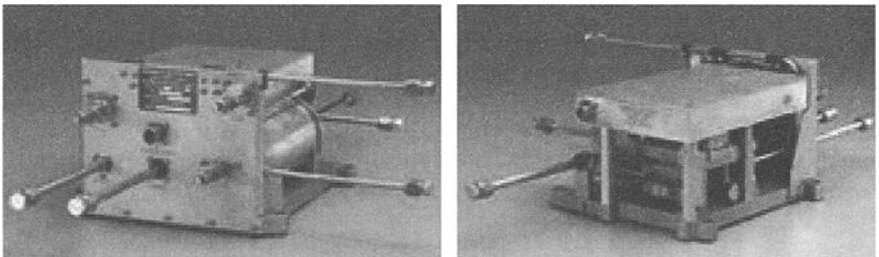
Pressure vs. flow rate at −10°C
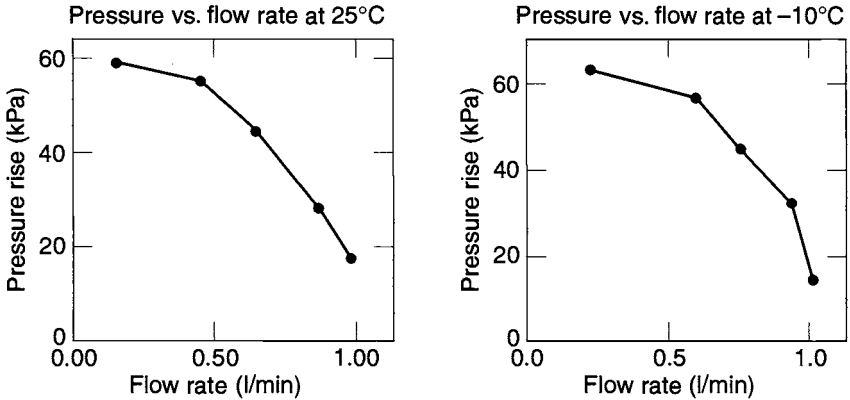
Fig. 12.29. Pressure rise vs. flow rate performance tests on IPA.

In the electrical performance tests, the current draw of the IPA at various flow rates was measured. The input voltage to the IPA was varied between 27 Vdc and 36 Vdc, and the IPA current draw was measured. The IPA electrical performance is shown in Fig. 12.30.

To verify the integrity of the IPA fabrication, the unit was proof tested and leak checked. The unit was successfully tested to a proof pressure of 1275 kPa. Two leak rates were specified for the IPA—one for the gas side of the accumulator and a second for the rest of the unit, which is the liquid side. For the gas side, the maximum leak rate was specified at 2×10^{-7} scc/sec of helium, whereas for the liquid side, it was specified as 1×10^{-4} scc/sec helium. The leak rates for each weld and valve were computed based on these total leak rates and were tested to the computed levels during the leak check of the assembly.

Pressure vs. flow rate at 25°C

Pressure vs. flow rate at −10°C
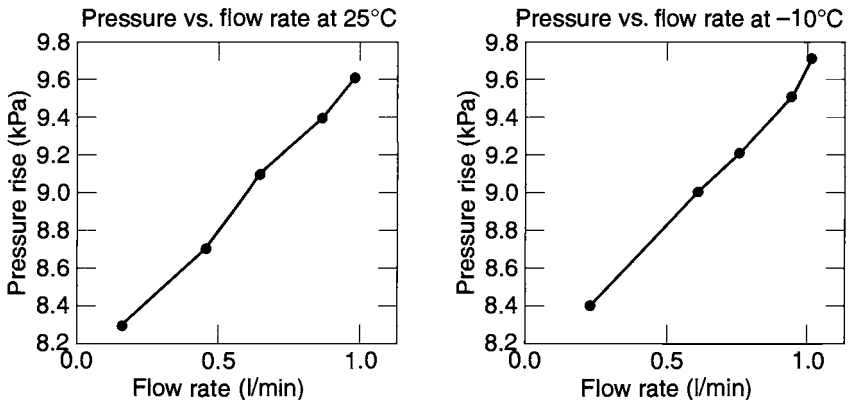
Fig. 12.30. Power vs. flow rate performance tests on IPA.

Qualification Tests

Three types of qualification tests were done on the IPA besides the performance tests: vibration tests, thermal vacuum tests, and electromagnetic compatibility and susceptibility tests. The unit was tested to protoflight levels because the flight unit was used instead of an engineering model to flight-qualify the IPA. The order of the acceptance tests is given in Table 12.13.

The test requirements for the sine and random vibration tests are given in Table 12.14. The IPA successfully underwent these tests while both the pumps were operating. The performance was monitored during the actual vibration. The sine vibration test consisted of sweeping at the specified sinusoidal amplitude levels from the lowest frequency to the highest frequency and back to the lowest frequency at a rate of 2 octaves/minute in each of the three orthogonal axes. The random vibration tests were conducted for one minute per axis. Accelerometers were used to monitor the responses during both the tests.

The thermal vacuum test on the IPA consisted of two types of tests. The first was done on the motor-controller electronics separately. The electronics box was mounted on a baseplate that was maintained at 70°C while both pumps were continuously on for a seven-day period. Electrically simulated loads were used for the pumps in this test. The second thermal vacuum test was conducted on the whole IPA and consisted of a one-day cold and two-day hot soak.

Table 12.13. IPA Acceptance Tests

Type of Test	Verification Purpose
Performance	Performance of the IPA before the start of the qualification tests
Sine vibration	Design for the protoflight launch loads
Random vibration	Design for the protoflight launch loads
Functional	Functionality of the unit after acceptance test
thermal vacuum	Design for the protoflight temperature range
Functional	Functionality of the unit after acceptance test
Proof pressure	Design for the operating pressure
Leak-detection	Leak rates of the IPA
Performance	Performance of the IPA at the completion of qualification tests

Table 12.14. Sine and Random Vibration Specifications for IPA

Axis	Protoflight Test Level	Frequency Band
Sine vibration—All	1.27 cm double amplitude 10.0 g (acceleration 0-to-peak)	5–20 Hz
Random vibration—All	+ 6dB/octave 0.2g2/Hz −12 dB/octave 13.2 g_{rms}	20–80 Hz 80–700 Hz 700–2000 Hz Overall

The flight cooling system was tested at two levels, the assembly level and the spacecraft level. At the assembly level, tests were done to verify the performance of the subassemblies, such as the IPA. Here the hydraulic, electrical, and thermal performance of the IPA was tested. In addition, the IPA was subjected to the thermal vacuum, random and sinusoidal vibration, and electromagnetic interference and compatibility (EMI and EMC) tests to qualify it for the flight.

The EMI qualification tests for conducted emissions and susceptibility were done on a separate life test pump/motor unit that was of the same design as the flight pump/motor unit and the flight electronics. The EMI tests were performed for the power-line ripple and power-line transients for both emissions and susceptibility. The EMI qualification tests for radiated emissions and susceptibility were performed at the spacecraft level. The IPA went through the tests and satisfactorily met the spacecraft requirements.

The IPA was bolted and welded onto a support structure before being installed on the spacecraft. Apart from the IPA, the support structure housed the HRS filter, pyro/vent system, and a heat exchanger for the shunt electronics box. Two views of the support structure are shown in Fig. 12.31. Figure 12.32 shows the IPA installed on the cruise stage of the assembled spacecraft.
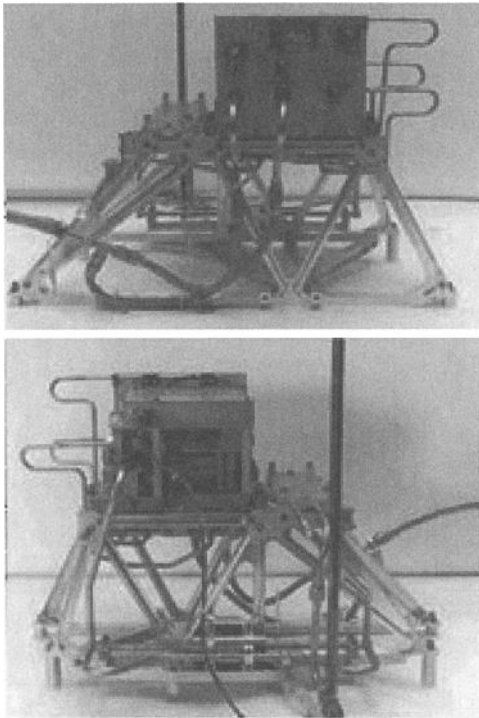
Fig. 12.31. Support structure with the IPA installed.
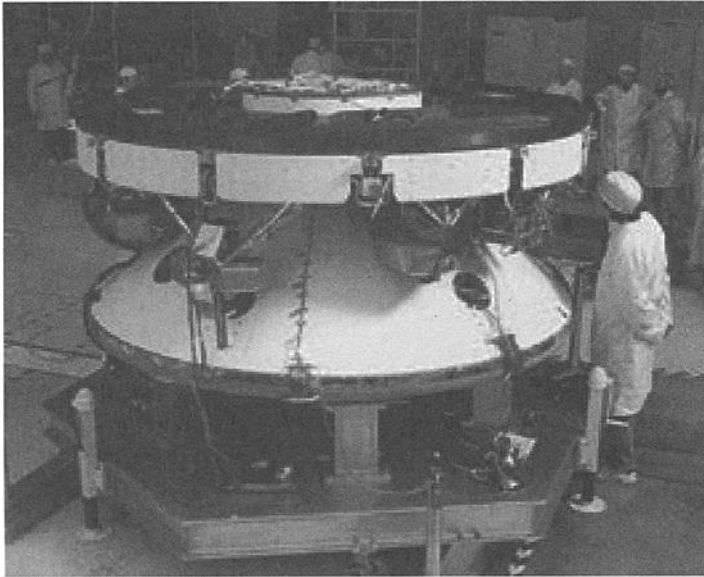
Fig. 12.32. Assembled spacecraft with the IPA installed on the cruise stage.

At the spacecraft system level, the whole system went through a series of system-level tests. These tests consisted of vibration, EMI and EMC, and system thermal vacuum tests. The end-to-end performance of the HRS was tested during the thermal vacuum test.

HRS Development Tests

Several development tests were conducted to characterize the performance of the cooling loop. These tests, performed in parallel with the design effort, were very helpful in ensuring that the final design would meet its requirements.

Thermal and Hydraulic

A development test was performed to simulate the electronics shelf and the radiator to validate the thermal and hydraulic performance models used in predicting the performance of the cooling loop. Details of these tests are given in Ref. 12.68.

Leaks

Because of integration constraints, 17 mechanical joints (B-nuts or AN fittings) were used to complete the assembly; the rest of the assembly is welded. Any large leaks from the HRS during the seven-month flight to Mars would seriously jeopardize the mission. Welded joints were not deemed to leak any significant amount of Freon. The B-nuts, however, being mechanical in nature, could potentially leak, so conducting tests on them was considered highly desirable, to ascertain that they would not leak at rates substantial enough to deplete the flight accumulator during the mission. Also desired were better schemes for providing extra insurance against potential leaks (such as epoxying the joints).

An extensive test was conducted for assessing the Freon leak rate through the mechanical joints (B-nuts or AN fittings) in the MPF HRS. All the combinations of materials (aluminum, stainless steel) and sizes (1/4 in., 3/8 in.) used in the flight HRS were simulated. Teflon flex lines identical to the flight ones were also tested for leaks through their joints. Use of epoxies to provide insurance against leaks was also assessed. Twenty-four B-nut joints were examined; they were subjected to cyclic mechanical flexing and torsion to simulate the experiences encountered by the worst joint in the flight system during launch. This testing was followed by thermal cycling to simulate the excursions during ground testing and flight.

Helium leak tests were conducted on each joint under vacuum and under internal pressure of 690 kPa. In addition, all the joints were pressurized with liquid Freon-11 (used in flight system) and tested for Freon leaks. All the tested joints exhibited leak rates that were much lower than those used to size the flight accumulator—it was sized to accommodate a leak of 164 cm^3 of liquid Freon in the seven-month flight, whereas tests showed that the total leak should be much less than half of this value even under the worst conditions. Use of soft cone seals and retorquing was recommended, as well as the use of an epoxy on the exterior surfaces of the joints' leak paths.

Material Compatibility

Within the HRS, Freon-11 was in constant contact with materials like aluminum, stainless steel, and some elastomers. Concerns for potential corrosion of aluminum, particularly in contact with moist Freon, were alleviated by conducting tests to investigate the compatibility of Freon-11 with aluminum and stainless steel. Several test samples of aluminum and stainless steel were inserted in Freon-11 with different levels of moisture. (Freon is supplied in drums at a moisture level of about 10 parts per million, and it saturates at 100 ppm.) These samples were examined chemically, visually, and under electron microscopes to measure the levels of corrosion as a function of time. For aluminum, no evidence of corrosion was observed for low moisture levels (close to 10 ppm) but a very strong evidence of corrosion was observed at the high moisture levels (those much higher than 10 ppm and close to 100 ppm). This test showed the extreme importance of minimizing moisture to prevent corrosion of aluminum, and elaborate safeguards were taken in the Freon storage and loading process to minimize the moisture levels (to levels not much more than the 10-ppm level, as in the manufacturer-supplied Freon drums).

No evidence of corrosion was observed for stainless steel for all the moisture levels tested. Viton (used in the check valves) was found to swell significantly when inserted in Freon-11; however, subsequent leak tests performed on the check valves demonstrated that the leaks through them in the check direction were very small and well within acceptable limits. All other materials in contact with the Freon underwent long-term compatibility tests and were found acceptable.

Performance of the Pumped Loop during Life Tests

A life test cooling loop was built and subjected to long-term operation to verify the reliability of the various components of the flight HRS. A schematic of the setup is shown in Fig. 12.33. The life test simulated the long-term operation of the
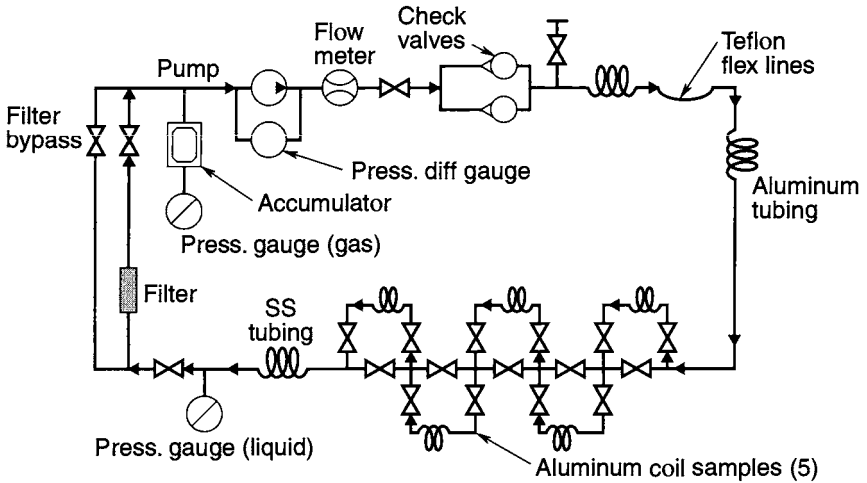
Fig. 12.33. MPF HRS life test schematic.

pump assembly, particle filter, and the rest of the HRS (aluminum and stainless-steel tubes, Teflon tubing, accumulator, check valves, etc.). A detailed description of this setup is given in Ref. 12.69.

The life test was also used to investigate and measure the long-term corrosion of the HRS tubing materials (aluminum and stainless steel) in a flowing environment with all the materials and components used in the flight system. Samples of tubing and the working fluid were taken out and tested periodically. Further, the long-term leak rates of the HRS were monitored during the life test.

Life Test Cooling Loop

Because the cooling loop was used throughout the flight for seven months (5100 hours), and its reliable functioning throughout this duration was critical to guarantee mission success, a life test setup was built and is undergoing long-term testing. The schematic of this test is shown in Fig. 12.33. It simulated the long-term operation (> 5100 hours flight duration) of pump assembly and particle filter, in conjunction with the rest of the HRS (aluminum, stainless steel, Teflon tubing, accumulator, check valves, etc.). This system clocked about 18 months (14,000 hours) of uninterrupted operation with no pump failures, exceeding the 5100 hours required for flight by more than a factor of two.

In addition to the compatibility tests described earlier (performed on small sections of tubing materials in a nonflowing environment of Freon), this life test was also used to investigate and measure the long-term synergistic corrosion of the HRS tubing (aluminum, stainless steel) in a flowing environment with simulation of all the materials and components used in the flight system. Samples of aluminum tubing and Freon liquid were taken out periodically for analysis; no evidence of corrosion was found in the first seven months. The sampling was not followed up after this period because of the severe budgetary constraints.

This life test was also used to measure long-term leaks from the HRS, particularly those resulting from mechanical joints (AN fittings, B-nuts). Relatively large leaks were observed in the beginning of the test, and they were corrected. They prompted a more elaborate leak test that was conducted separately (this test was discussed earlier).

Fig. 12.34 shows the variation in the flow rate, pressure drop, and pump input power as a function of time for this life test. During the first five months of the test the filter was slowly getting clogged (at the end of this period the filter got so clogged that it was bypassed; this situation is discussed below), the flow rate dropped to about half its value at the start of the test, the pressure drop across the system increased by 20%, and the pump input power decreased slightly.

As soon as the filter was bypassed, the flow rate increased to a value even larger than at the beginning of the test (25% larger because of the lack of the pressure drop associated with even a virgin filter); the pressure drop in the system was lower than at the beginning of the test by 15%, and the power level was about the same. These changes make sense, because the bypassing of the clogged filter reduced the overall resistance of the loop and allowed a greater flow rate at smaller pressure differences. Since even a virgin filter has a nonzero resistance, the flow rate without the filter was even larger than it was at the beginning of the test, when an unclogged filter was in the flowing loop.

The flow rate and the pressure drop across the system remained essentially constant after the filter bypass; however, the power level did fluctuate as a result of leaving the pump idle because of inadvertent power outages. A more detailed description of these effects is presented next.
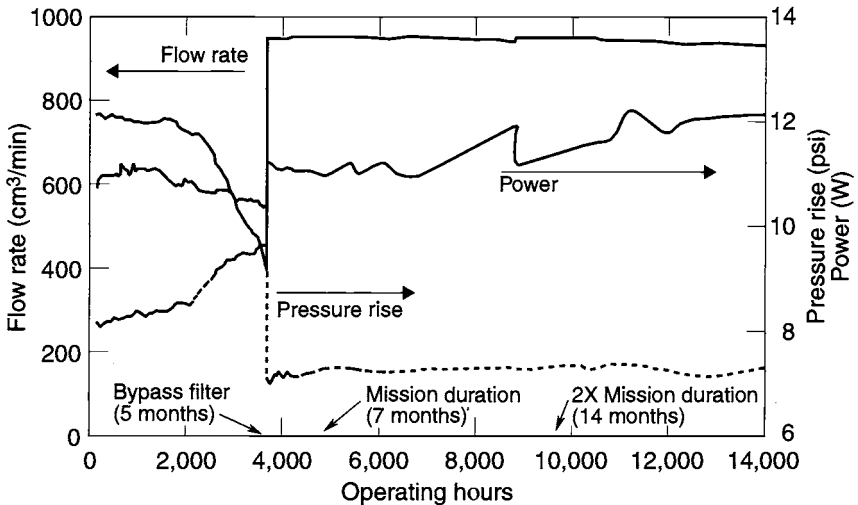
Fig. 12.34. Life test performance.

Filter Clogging

The filter used in this mock-up had inadequate capacity and was bypassed after 3600 hours or 5 months. (The flight filter had a capacity for particles at least six times higher.) To avoid the potential for significantly reduced flow rate resulting from a clogged filter, the flight filter used a check valve to bypass it when the filter's pressure drop was higher than 17.2 kPa. Since the IPA produces a pressure rise of more than 41.3 kPa at the required flow rate of 0.76 l/min, and the pressure drop in the cooling-loop system was expected to be only 13.8 kPa, this additional pressure drop from a clogged filter was not anticipated to pose a problem in providing the required flow rate of Freon throughout the flight.

The exact reason for the clogging of the filter is still not known, because the cooling loop has not yet been disassembled. Even though the cooling loop was thoroughly cleaned and tested before the beginning of the life test, the clogging of this filter was surprising. Some speculate that a possible reason for the clogging was the presence of particles generated by the graphite within the Teflon flex line. The Teflon line was impregnated with graphite on its inside surface to prevent electrostatic discharge (ESD) caused by the flowing Freon from creating micro-holes in the Teflon that could lead to a leak within the cooling loop. A more definitive reasoning will be found after disassembly of the test loop. Since the flight filter has at least six times the capacity of the life test filter, engineers hope the flight filter will be less prone to clog. In addition, the flight filter's automatic bypass upon clogging provides further insurance.

High Current Draw of Stalled Pump

The flight-system primary pump was programmed to be on for the entire duration of the flight, with the secondary pump idle. The secondary was to be turned on automatically only if the primary failed. The main reason for leaving the secondary pump idle was to maximize its available life to serve as a full backup in case the primary failed. The power supply for the life test loop pump was connected to a relay preventing the pump from restarting automatically after a power outage; a manual switch for the relay would be used to restart the pump after a shutdown. This programming was done to prevent an unattended turn-on of the pump (and the possible consequent damage) during power surges typical during outages.

After almost one year of uninterrupted flawless operation of the life test loop, a power outage occurred, and the pump did not restart automatically, as designed. Following this outage, the pump was idle for about a month because of its unattended status. However, when an attempt was made to restart the pump manually, the 500-mA fuse was seen to be blown (normal current draw is 400 mA). Replacements of the fuse with those rated for as much as 1.5 A were unsuccessful in restarting the idle pump. Following these attempts, the pump was gently tapped twice and it restarted—the current draw was about 450 mA immediately after restarting and dropped down to its nominal value of about 400 mA in a few minutes.

During the period between this manual restart and the time when nominal steady-state performance was reached (a duration of less than 15 minutes), the current draw was also observed to momentarily rise to as much as 475 mA a few times. Simultaneous with these momentary peaks, an audible change in the pitch

of the pump would be heard when one could "observe" a flock of particles traveling through the loop via the pump.

Following this outage the pump was allowed to run for a few days and was deliberately turned off for two- to three-week periods to attempt repeating its failure to restart. Five such attempts to repeat this failure were unsuccessful. After these attempts, five more inadvertent power outages occurred, and in most instances the pump was off for about two or more weeks. In all cases the starting current required was higher than 500 mA. Also, in all cases except one, the pump started satisfactorily with a current draw larger than 500 mA, without any tapping of its body. In one instance, restarting the pump required a few gentle taps.

One theory that could explain all these effects is that the clogging of the filter followed by its bypass allowed the generated particles to collect within the loop without being removed from the flowing fluid. As long as the fluid was flowing, it would not allow particles to collect in one zone. However, upon stoppage of fluid flow after a power outage, the particles could settle in local "valleys" such as the gaps between the pump's bearings. Since these bearings are hydrodynamically lubricated, the gaps are very tiny (6 to 18 μm wide), which implies that the particles could create enough friction to increase the starting current significantly.

Implications for the Flight System

The results of this long-term life test were used in the design and operation of the flight system. On the basis of recommendations made according to those results, the following steps were taken:

- The primary pump was maintained on and was not allowed to be turned off under any circumstance under the control of the mission operators.
- The secondary or backup pump, which was normally idle, was turned on for an hour once every two to four weeks to remove any settled particles, even though one would not expect any settling in zero gravity (during the life test power outages, the pump could always restart without any tapping as long as the idle period was less than two weeks, and two- to four-week frequency was practical for the mission).
- A filter much larger (6×) than that used for the long-term development-test loop was implemented for the flight system.
- The mechanical fittings (B-nuts) used for assembling the loop, which used soft-cone (aluminum) seals, were retorqued after a few days of the initial torquing, and epoxy was used on the exterior surfaces of the joints' leak paths to provide as much insurance against leaks as possible.

The life test setup had operated continuously for 8000 hours before the actual launching of the MPF spacecraft in December 1996. The results from the operation of the life test are described in Ref. 12.72. The performance of the life test loop was continuously monitored and is shown in Fig. 12.34. This graph shows flow rate, pressure rise, and electric-power consumption of the pump. The test results showed no evidence of the corrosion after seven-month operation of the loop. The leak rate of the fluid from the system was minimal; it was much lower than the leak rate that was allowed in the flight system.

One lesson learned from the life test loop was that the backup pump needed to be turned on regularly to flush any particles that might settle in the pump bearings.

During the life test operation, the particles were observed to settle in the bearings and impeller area if the pump were stopped for an extended period of over four weeks. Based on this information, engineers decided to turn on the backup pump in the flight system for an hour once every month.

After the successful landing of the MPF on Mars in July 1997, the life test system was stopped. By this time the life test pump had continuously operated for more than 14,000 hours. The tubing and the fluid were investigated for corrosion and other particulate material. Of particular importance was the particulate that had clogged the filter during the life test.

The chemical analysis showed no evidence of corrosion in the aluminum tubing. The particulate in the fluid sample was found to consist of particles with sizes in the 1-to-40-µm range. The large particles were mostly silica, fibers, and some metallic particles. The smaller particles were mostly chromium, iron, and aluminum. The moisture levels were less than 5 ppm, whereas levels were about 17 ppm in samples taken at 5-month period. The organic residue found in the Refrigerant 11 was similar to the material used in the thread of the in-line filter. Most of the particles generated in the life test loop were found to be present because of the materials used in the life test setup. Except for the Teflon tubing and the chromium used in the pump, none of the other materials were used in the flight system.

The scanning electron microscopy done on the aluminum tubing indicated that the prominent mode of corrosion of the aluminum tubing was physical erosion by the chromium particles formed at the pump.

Performance of the Loop during Flight

The HRS performance was continuously monitored during the entire cruise to Mars. The HRS was first activated on the launchpad about two hours before launch. Both pumps were turned on, and the functioning of the system was verified by the current draw of the pumps. The temperature of the electronic equipment shelf and the radiator were also monitored to make sure the working fluid was flowing freely. About four hours after launch, the backup pump was turned off and only the primary pump remained on during the rest of the seven-month cruise. The backup pump was turned on once a month for an hour to ensure that no particulate accumulated in the idle pump.

The performance of the HRS during the initial periods was very close to the performance predicted and verified during the system-level thermal vacuum test. The equipment-shelf temperature was maintained at around +5°C, whereas the radiator temperature was around –4°C. At these radiator temperatures, all the cooling fluid coming out of the equipment shelf was above 0°C, and the thermal control valve was completely open. All the fluid flowed through the radiator without any bypass. A temperature profile of the equipment shelf and the radiator for a one-hour duration on January 28, 1997, is shown in Fig. 12.35.

The radiator temperature was a function of the distance from the sun and the solar angle on the spacecraft. This temperature dropped as the spacecraft cruised away from Earth toward Mars. The temperature dropped from –4°C immediately after launch to below –12°C after 45 days into the cruise. At this time, the fluid
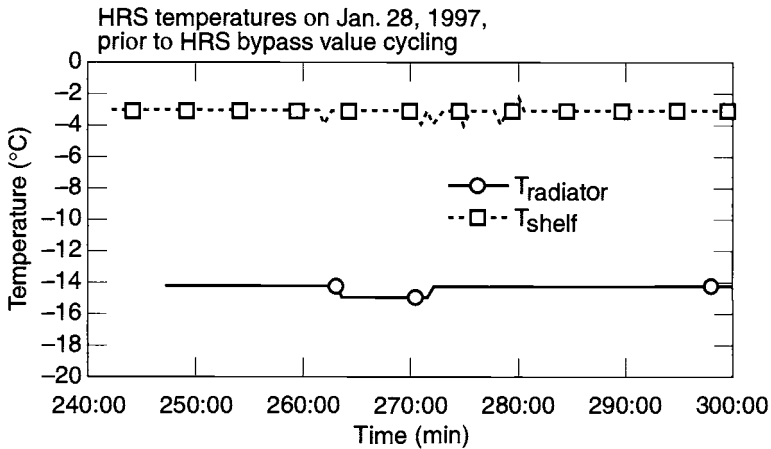
Fig. 12.35. HRS temperature during initial part of the cruise.

temperature coming out of the shelf was below 0°C. As this fluid entered the IPA, the wax-actuated thermal valve would open the bypass port, and part of the fluid would bypass the radiator. This bypass was designed to keep the electronics shelf above –7°C irrespective of the radiator temperature.

In Fig. 12.36, the temperatures of the equipment shelf and the radiator are shown for the day when the radiator bypass had just started. During this period, the shelf temperature was maintained between –4 and –2°C, while the radiator temperature varied between –16 and –14°C. The small fluctuations in the radiator and shelf temperatures were a result of the valve actuator's continuous attempts to adjust to the fluid temperature. This condition was observed and investigated during
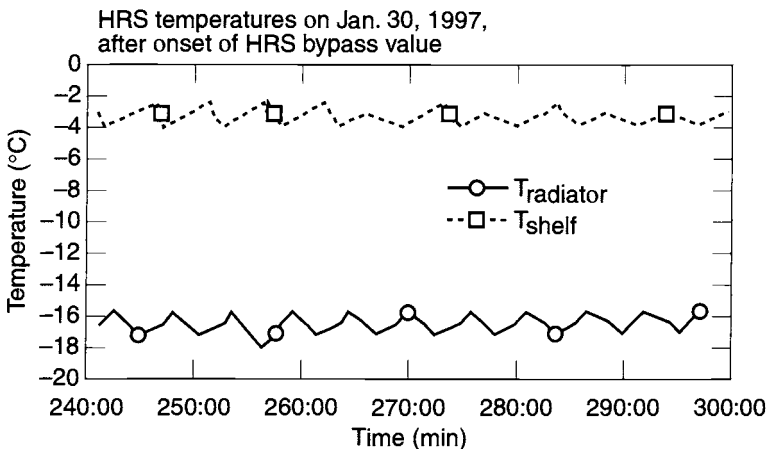
Fig. 12.36. HRS temperatures during latter part of the cruise.

the system thermal vacuum test. The fluctuation was attributed to an underdamped flow system and was considered harmless to the system.

While the spacecraft neared Mars, the radiator temperature gradually dropped to –70°C. However, the equipment shelf maintained its temperature at around –4 °C. The radiator and the electronics-shelf temperatures during the complete mission are shown in Fig. 12.37.

The HRS was designed to vent all working fluid just prior to entering the Martian environment. About 90 minutes before the entry, the vent system was activated by the opening of a pyro valve that connects the high-pressure gas side of the accumulator to the liquid. The liquid was in turn vented to space via a nozzle, which is opened to space via another pyro valve.[12.68] This event occurred on July 4, 1997, around 8 A.M. Pacific Standard Time. The spacecraft navigational data received by the ground controllers indicated that the nutation resulting from venting was less than two degrees and did not affect the spacecraft's course to the Martian landing site.

Mars Pathfinder PFL Summary

An active HRS consisting of a mechanically pumped single-phase liquid was designed and developed for the MPF mission. The unique requirements of the mission necessitated the use of the pumped-loop system for the thermal control of the spacecraft during its cruise to Mars. Because this was the first time that such a system was designed and flown, several new technologies were developed to make the loop successful, including the use of Refrigerant 11 (Freon-11) as a cooling fluid and a wax-actuated thermal control valve to bypass the flow. The Refrigerant 11 system allows the operation of the system at temperatures as low as –110°C.

MPF was the first U.S. deep-space mission to use a mechanically pumped cooling loop, and its successful flight demonstration showed that an active cooling system can be reliably used in deep-space missions. The data from the life test pump, combined with the flight data, show that the mechanical pumps can be reliably operated
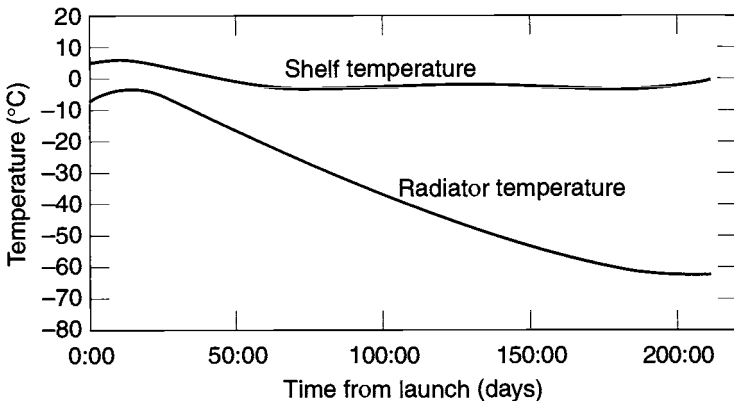
Fig. 12.37. Radiator and electronics-shelf temperatures during the entire cruise to Mars.

for missions lasting more than two years. The flexibility provided by the mechanically pumped cooling loop systems in the design, integration, test, and flight operation of spacecraft makes this cooling system ideal not only for faster, better, and cheaper missions but also for other missions.

References

Fluid-Flow Concepts and Basic Equations

12.1. W. M. Kays and M. E. Crawford, *Convective Heat and Mass Transfer*, 2nd ed. (McGraw-Hill, New York, 1972).

12.2. B. S. Petukhov, "Heat Transfer and Friction in Turbulent Pipe Flow with Variable Physical Properties," in *Advances in Heat Transfer*, Vol. 6, T. F. Irvine and J. P. Hartnett, eds. (Academic Press, New York, 1970), pp. 504–564.

12.3. M. N. Ozisik, *Heat Transfer—A Basic Approach* (McGraw-Hill Book Company, New York, 1985).

12.4. L. F. Moody, "Friction Factors for Pipe Flow," *Trans. Am. Soc. Mech. Eng.* **66**, 671–684 (1944).

12.5. "Flow of Fluids through Valves, Fittings, and Pipe," Crane Company, New York, N.Y., Technical Paper No. 410 (1982).

12.6. R. W. Fox and A. T. McDonald, *Introduction to Fluid Mechanics*, 3rd ed. (John Wiley & Sons, Inc., New York, 1985).

12.7. P. K. Swamee and A. K. Jain, "Explicit Equations for Pipe-Flow Problems," *Proceedings of the ASCE, Journal of the Hydraulics Division* **102**, HY 5, 657–664 (1976).

Forced Convection in Pipes and Tubes

12.8. J. P. Holman, *Heat Transfer*, 6th ed. (McGraw-Hill Book Company, New York, 1986).

12.9. M. N. Ozisik, *Heat Transfer—A Basic Approach* (McGraw-Hill Book Company, New York, 1985).

12.10. F. P. Incropera and D. P. DeWitt, *Fundamentals of Heat and Mass Transfer*, 2nd ed. (John Wiley & Son, Inc., New York, 1985).

12.11. S. R. Sellars, M. Tribus, and J. S. Klein, "Heat Transfer to Laminar Flow in a Round Tube or Flat Plate—The Graetz Problem Extended," *Trans. Am. Soc. Mech. Eng.* **78**, 441–448 (1956).

12.12. R. K. Shah and A. L. London, *Laminar Flow: Forced Convection in Ducts* (Academic Press, New York, 1978).

12.13. R. W. Allen and E. R. G. Eckert, "Friction and Heat-Transfer Measurements to Turbulent Pipe Flow of Water (Pr=7 and 8) at Uniform Wall Heat Flux," *Journal of Heat Transfer* **86**, 301–310 (1964).

12.14. A. P. Colburn, "A Method of Correlating Forced Convection Heat Transfer Data and a Comparison with Fluid Friction," AIChE J. **29**, 174 (1933).

12.15. F. W. Dittus and L. M. K. Boelter, *University of California (Berkeley) Publications in Engineering* **2**, 443 (1930).

12.16. J. P. Hartnett, "Experimental Determination of the Thermal Entrance Length for the Flow of Water and of Oil in Circular Pipes," *Trans. Am. Soc. Mech. Eng.* **77**, 1211 (1955).

12.17. R. H. Norris and D. D. Streid, "Laminar-Flow Heat-Transfer Coefficient for Ducts," *Trans. Am. Soc. Mech. Eng.* **62**, 525–533 (1940).

12.18. W. Nusselt, "Der Warmeaustausch zwischen Wand und Wasser im Rohr," Forsch. Geb. Ingenieurwes., 2, pp. 309 (1931).

12.19. B. S. Petukhov, "Heat Transfer and Friction in Turbulent Pipe Flow with Variable Physical Properties," in J. P. Hartnett and T. F. Irvine, (eds.), *Advances in Heat Transfer*, Vol. 6 (Academic Press, Inc., New York, 1970), pp. 504–564.

12.20. E. N. Sieder and C. E. Tate, "Heat Transfer and Pressure Drop of Liquids in Tubes," *Industrial and Engineering Chemistry* **28**, 1429 (1936).

System Hardware

12.21. "Spacecraft Thermal Control Design Data," Vol. 2, Section Q, European Space Agency, (1981).

12.22. R. W. Fox and A. T. McDonald, *Introduction to Fluid Mechanics*, 3rd ed. (John Wiley & Sons, Inc., New York, 1985).

12.23. N. H. Afgan and E. U. Schlunder, *Heat Exchangers: Design and Theory* (McGraw-Hill, New York, 1974).

12.24. R. A. Bowman, A. C. Mueller, and W. M. Nagle, "Mean Temperature Difference in Design," *Trans. Am. Soc. Mech. Eng.* **62**, 283–294 (1940).

12.25. D. H. Fax and R. R. Mills, Jr., "General Optimal Heat Exchanger Design," *Trans. Am. Soc. Mech. Eng.* **79**, 653–661 (1957).

12.26. A. P. Fraas and M. N. Ozisik, *Heat Exchanger Design* (John Wiley & Sons Inc., New York, 1965).

12.27. K. Gardner and J. Taborek, "Mean Temperature Difference: A Reappraisal," *AIChE J.* **23**, 770–786 (1977).

12.28. J. P. Gupta, *Working with Heat Exchangers* (Hemisphere Publishing Corporation, Washington, 1990).

12.29. G. F. Hewitt (ed.), *Hemisphere Handbook of Heat Exchanger Design* (Hemisphere Publishing Corporation, Washington, 1989).

12.30. Hydraulic Institute, Hydraulic Institute Standards for Centrifugal, Rotary and Reciprocating Pumps, latest edition, Cleveland, OH.

12.31. W. Hyrnisak, *Heat Exchangers* (Academic Press, New York, 1958).

12.32. S. Kakac, R. K. Shah, and A. E. Bergles (eds.), *Heat Exchangers: Thermal-Hydraulic Fundamentals and Design* (Hemisphere Publishing Corporation, Washington, 1982).

12.33. W. M. Kays and A. L. London, *Compact Heat Exchangers*, 2nd ed. (McGraw-Hill Book Company, New York, 1964).

12.34. D. Q. Kern, *Process Heat Transfer* (McGraw-Hill Book Company, New York, 1950).

12.35. J. H. Lienhard, *A Heat Transfer Textbook* (Prentice-Hall Inc., New Jersey, 1981).

12.36. A.V. London, "Factors in the Selection of Pumps for Process and Chemical Duties," Pumps-Pompes-Pumpen, No. 88, pp. 25–31, 1974.

12.37. B. Nekrasov, *Hydraulic for Aeronautical Engineers*, translated from the Russian by V. Talmy, 1st ed. (MIR Publishers, Moscow, 1969) Chapter VI, pp. 80-87, Chapter XII, pp. 182–221.

12.38. D. R. Pitts and L. E. Sissom, *Heat Transfer, Schaum's Outline Series* (McGraw-Hill Book Company, New York, 1977).

12.39. F. Pollak and C. O. Cruger, "Comparison of Applications and Characteristic of Positive Displacement and Centrifugal Pumps," Pumps-Pompes-Pumpen, No. 96, pp. 400–407, 1974.

12.40. E. U. Schlunder (ed.), *Heat Exchanger Design Handbook* (Hemisphere Publishing Corporation, Washington, 1983).

12.41. G. Scobie, "Select the Pump that Meets Your Needs," *Chart. Mech. Eng.* **21** (51), 59–63 (1974).

12.42. G. S. Settles, J. T. Hamick, W. J. Barr, M. Summerfield, and M. Gunn, "Energy-Efficient Pumps Utilization," *J. Energy* **1** (1), 65–72 (1977).

12.43. R. K. Shah, A. D. Kraus, and D. Metzger (eds.), *Compact Heat Exchangers—A Festschrift for A. L. London* (Hemisphere Publishing Corporation, Washington, 1990).

12.44. K. P. Singh and A. I. Soler, *Mechanical Design of Heat Exchangers and Pressure Vessel Components* (Arcturus Publishing, Inc., Cherry Hill, NJ, 1984).

12.45. Standards of the Tubular Exchanger Manufacturers Association, Tubular Exchanger Manufacturers Association, New York (latest edition).

12.46. J. Taborek, "Evolution of Heat Exchanger Design Techniques," *Heat Transfer Engineering* **1**, 15–29 (1979).

12.47. G. Walker, *Industrial Heat Exchangers—A Basic Guide*, 2nd ed. (Hemisphere Publishing Corporation, Washington, 1990).

Working Fluids

12.48. *ASHRAE Handbook—Fundamentals* (American Society of Heating, Refrigerating and Air-Conditioning Engineers, Inc., Atlanta, latest edition).

12.49. R. C. Downing, "Refrigerant Equations," ASHRAE Paper 2313, Transaction of the American Society of Heating, Refrigerating and Air-Conditioning Engineers, 80, Part II, pp. 158 (1974).

12.50. E.I . DuPont de Nemours & Co., Bulletin T-11 (1972).

12.51. E. I. DuPont de Nemours & Co., Bulletin T-22 (1972).

12.52. E. I. DuPont de Nemours & Co., Bulletin T-502 (1969).

12.53. E. I. DuPont de Nemours & Co., Bulletin T-503 (1968).

12.54. L. Haar and J. S. Gallagher, "Thermodynamic Properties of Ammonia," *J. Phys. Chem. Ref. Data* **7**, 635–792 (1978).

12.55. J. J. Martin, "Thermodynamic Properties of Dichlortetrafluoromethane," *Journal of Chemical and Engineering Data* **5**, 334–336 (1960).

12.56. J. J. Martin, "Thermodynamic Properties of Perfluorocyclobutane," *Journal of Chemical and Engineering Data* **7**, 68–72 (1962).

12.57. "Spacecraft Thermal Control Design Data," Vol. 2, Section Q, European Space Agency, (1981).

12.58. *Thermodynamic Properties of Refrigerants* (American Society of Heating, Refrigerating and Air-Conditioning Engineers, Atlanta, 1969).

12.59. N. B. Vargaftik, *Tables of the Thermophysical Properties of Liquids and Gases*, 2nd ed. (Hemisphere Publishing Co., Washington, 1975).

Analysis of a Fluid Loop

12.60. "Spacecraft Thermal Control Design Data," Vol. 2, Section Q, European Space Agency, (1981).

Computer Software for System Analysis

12.61. "RETRAN 02—A Program for Transient Thermal Hydraulic Analysis of Complex Fluid Flow Systems," Vol. 1: Theory and Numerics (Ref. 2), EPRI NP 1850 CCMA (1984).

12.62. T. M. Porsching, J. H. Murphy, and J. Redfield, "Stable Numerical Integration of Conservation Equations for Hydraulic Networks," *Nuclear Science and Engineering* **43**, 218–225 (1971).

12.63. "SINDA/FLUINT: Systems Improved Numerical Differencing Analyzer and Fluid Integrator," Cullimore and Ring Technologies, Inc. (1996).

12.64. "SINDA '85/FLUINT—Systems Improved Numerical Differencing Analyzer and Fluid Integrator," User's Manual, Version 2.3, Martin Marietta Denver Aerospace, Denver, CO (1990).

12.65. J. R. Turner, T. J. Swift, T. M. Andrews, and A. Lebru, "ESATAN FHTS—A Piped Fluid Network Capacity," *Proceedings of the 3rd European Symposium on Space Thermal Control and Life Support Systems, Noordwijk, The Netherlands, 3–6 Oct. 1988* (ESA SP-283, December 1988).

12.66. "SINDA/1987/ANSI Code," User's Manual, The Aerospace Corporation, El Segundo, CA (1990).

PFL Application

12.67. J. Lyra and K. Novak, "The Mars Pathfinder System Level Solar Thermal Vacuum Test," Paper No. AIAA-97-2454, *32nd Thermophysics Conference* (Atlanta, 23–25 June 1997).

12.68. P. Bhandari, G. Birur, and M. Gram, "Mechanical Pumped Cooling Loop for Spacecraft Thermal Control," Paper No. 961488, *26th International Conference on Environmental Systems* (Monterey, CA, 8–11 July 1996).

12.69. G. Birur, P. Bhandari, M. Gram, and J. Durkee, "Integrated Pump Assembly—An Active Cooling System for Mars Pathfinder Thermal Control," Paper No. 961489, *26th International Conference on Environmental Systems* (Monterey, CA, 8–11 July 1996).

12.70. G. Birur and P. Bhandari, "Mars Pathfinder Active Thermal Control System: Ground and Flight Performance of a Mechanically Pumped Loop," Paper No. AIAA-97-2469, *32nd Thermophysics Conference* (Atlanta, 23–25 June 1997).

12.71. G. Birur and P. Bhandari, "Mars Pathfinder Active Heat Rejection System: Successful Flight Demonstration of a Mechanically Pumped Cooling Loop," SAE Paper Num-

ber 981684, *28th International Conference on Environmental Systems* (Danvers, MA, 13–16 July 1998).

12.72. P. Bhandari and G. Birur, "Long Term Life Testing of a Mechanically Pumped Loop for Spacecraft Thermal Control," Paper No. AIAA-97-2470, *32nd Thermophysics Conference* (Atlanta, 23–25 June 1997).

13   Thermoelectric Coolers

A. Chuchra[*] and T. Stevenson[†]

Introduction

Thermoelectric coolers (TECs) are miniature solid-state heat pumps capable of providing localized cooling to devices that require cold temperatures for proper operation. Before 1990, their use was confined to unique situations, generally in laboratories or other engineered environments. Throughout the 1990s, however, thermoelectrically cooled devices became somewhat common in everyday terrestrial and commercial applications. Notable examples include six-pack-sized minirefrigerators for automotive and marine use and night-vision devices. TECs in space have also become relatively common; they cool low noise amplifiers (LNAs), star trackers, and IR (infrared) sensors. Table 13.1 lists spaceborne TECs.

Background

TECs provide cooling via the Peltier effect, which is the cooling that results from the passage of an electric current through a junction formed by dissimilar metals. (Note: The Peltier effect is the inverse of the Seebeck effect, the basis for common thermocouples—in the Seebeck effect, a [temperature-varying] voltage results from the junction of dissimilar metals.) The simplest TEC consists of two semiconductors, one p-type and one n-type (one "couple"), connected by a metallic conductor, as depicted schematically in Fig. 13.1. Heat is pumped from the cold junction to the hot junction. The net cooling is diminished by the effects of Joulean losses generated by the current, and heat conduction through semiconductor material from the hot to the cold junction. Semiconductors, principally bismuth telluride (Bi_2Te_3), have made these devices practical. Prior to the advent of such semiconductors, parasitic conduction through metal elements largely negated any useful cooling.
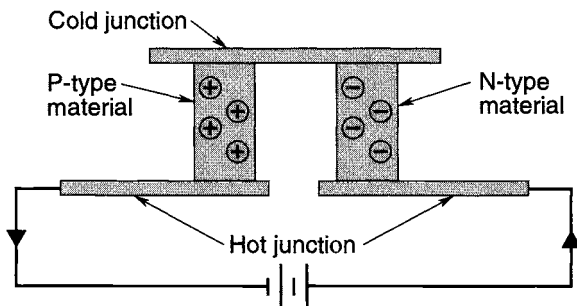
Fig. 13.1. Peltier thermoelectric couple.

*Swales Aerospace, Beltsville, Maryland.
†University of Leicester, Leicester, United Kingdom.

Table 13.1. Survey of Spaceborne TECs

Spacecraft or Mission	Instrument/ Component	Institution	Launch	No. of Stages	Parallel TECs	Cold Temp. (°C)	Rejection Temp. (°C)	Net Cooling (Tot.) (W)	Input Power (Tot.) (W)
Satcom K	CLNA	RCA Astro	1985	4	Single	−50	15	0.79	8.0
Various	Star tracker	Ball	Many for 2 decades	1	Single	0	20	1.8	1.7
Hubble Space Telescope	STIS	Ball, GSFC	1997	4	Single	−80	20	0.3	17.7
Hubble Space Telescope	NICMOS	Ball, UAZ, GSFC	1997	3	Dual	−73	10	0.25	10.75
				3	Dual	−47	5	0.6	2.4
FUSE	Fine error sensor (star sensor)	ComDev, CSA, JHU-APL	1999	2	Single	−32	−10 to 0		2 (typ) 5 (max)
Future missions									
Hubble Space Telescope	Advanced camera	Ball, JHU-APL	2003	2	Quad	−35	24	1.0	9
				4	Single	−77	24	0.4	16.6
				4	Single	−81	24	0.3	15.5
Swift	XRT	Univ. of Leicester	2003	5	Single	−95 to 105	< −38	~0.1	4 to 5
Hubble Space Telescope	Wide field camera III	Ball, GSFC	2004	1	TBD	TBD	TBD	TBD	TBD
				2	Quad	−55	−5	0.8	9
				4	Dual	−83	−5	0.2	8.8
				6	Single	−123	−35	0.028	12
Mercury Messenger	MLA	GSFC, APL	2004	1	Single	10 to 25	10 to 25	0.6	0.6

Vendors supply TEC modules as single-stage or multistage assemblies. A stage generally contains many elements electrically joined in series, with all cold junctions soldered to metallization on one ceramic plate and all hot junctions soldered to the opposite ceramic plate. Vendors can select the number of stages, the number of couples, and the geometry of the p or n post to optimize the coefficient of performance (COP). The COP is the useful cooling divided by the input power to the TEC. TECs with low COPs consume more power than is optimal and produce excessive waste heat. The exact temperature difference at which use of multistage TECs becomes more efficient than use of single-stage devices is not generally agreed upon. However, space applications have favored multistage TECs where the desired temperature difference exceeded the 25–40°C range. The shape of a multistage TEC resembles that of a multitiered wedding cake, with the upper layer representing the cold stage and the base layer representing the hot stage. Each stage needs to be larger than the one above it, to handle progressively larger amounts of waste heat; hence the cascading shape. This geometry also stems from the need to minimize the parasitic thermal coupling between stages.

For space application, TECs have the advantages of simplicity, reliability, compactness, low mass, and noiseless, vibrationless operation. Unlike common heat pumps (compression/expansion-based and Stirling cycle), these devices have no moving parts. Their use in spacecraft is limited by their relatively low COP, particularly with large temperature differences. Because of their limited efficiency, they are best suited to situations with modest heat loads, cold temperatures not below 150 K, and hot-to-cold-side differences not exceeding 100°C. Other cooling methodologies are generally better suited (more efficient) for applications with greater heat loads or larger temperature-difference requirements. Figure 13.2 compares the useful temperature range and heat-load capacity of TECs to the corresponding values for other cooling methodologies. TECs are not recommended for use below 130 K because of their prohibitively low efficiencies. This recommendation is not a hard rule; it indicates that operation below 130 K is likely to be impractical but not necessarily implausible.

A major TEC issue is the structural integrity of bismuth telluride and soldered joints when subjected to differential thermal expansion stresses. Externally imposed stresses are commonly resolved through the inclusion of a compliant conductive strap on the cold side of the device. Compliant straps are generally fabricated of multiple layers of thin copper foil (2 mil is a common thickness); these straps typically are quite compliant along two axes and somewhat less so along the third. Another potential issue is redundancy, which can lead to increased complexity, larger heat loads, greater radiator area, and/or warmer rejection temperatures. TECs are fairly reliable; therefore, space applications have generally not flown redundant TECs.

Characteristics

Figure 13.3 depicts actual and theoretical TEC performance characteristics and compares the performance of some TECs built for terrestrial in-vacuo applications. Some of the listed manufacturers are no longer actively producing and marketing TECs; still, this figure has been included to demonstrate general TEC performance
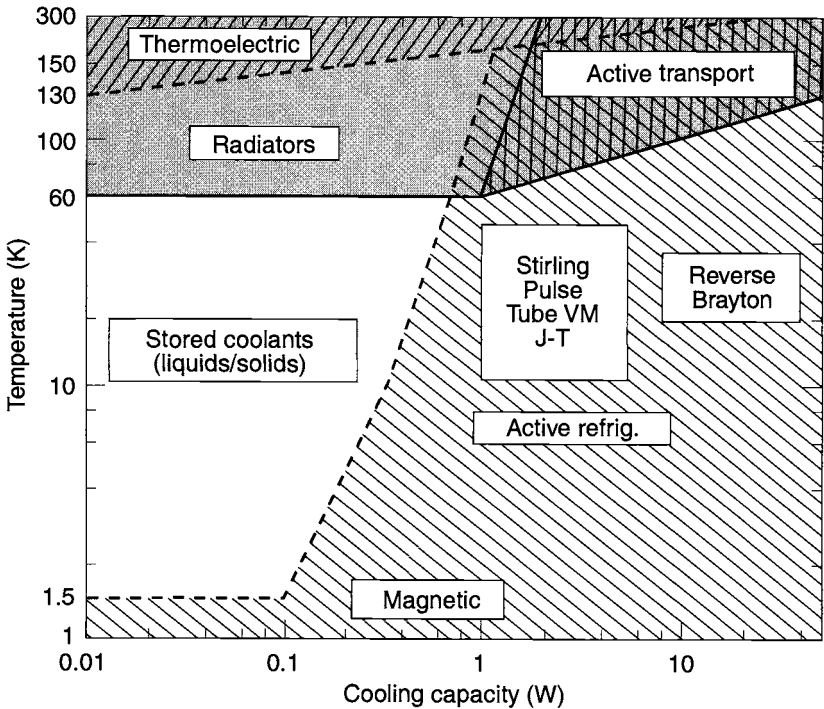
Fig. 13.2. TECs versus other cooling methodologies.

characteristics. The theoretical curve for 300 K shows that specific-power consumption increases very rapidly for colder cold-junction temperatures (typically doubling with each 10°C drop)—and this pattern does not factor in the increased parasitic cooling load. The performance of several of the units does not approach the theoretical performance limit (to the left of the 300 K curve). One point of reference shown by this chart is that at the theoretical performance limit, a TEC with a −54°C cold side and a 27°C hot side needs 10 W of input power to produce 1 W of cooling.

Two other sources of readily available TEC performance information are the Web sites www.marlow.com and www.melcor.com. These sites have a wealth of practical TEC information, as well as free downloadable cooler-sizing software. However, this information is generally limited to one- and two-stage TECs. Also, some advice on these sites may not necessarily be applicable to space systems.

Optimizations

For space applications, the use of customized TECs is appropriate for optimizing the COP for the expected hot- and cold-side temperatures and heat flow. Not using an optimized TEC could increase power consumption as well as heat-rejection area, both generally valuable resources in spacecraft. Also, vendors can add robustness to custom TECs by physically enlarging the footprint of the upper
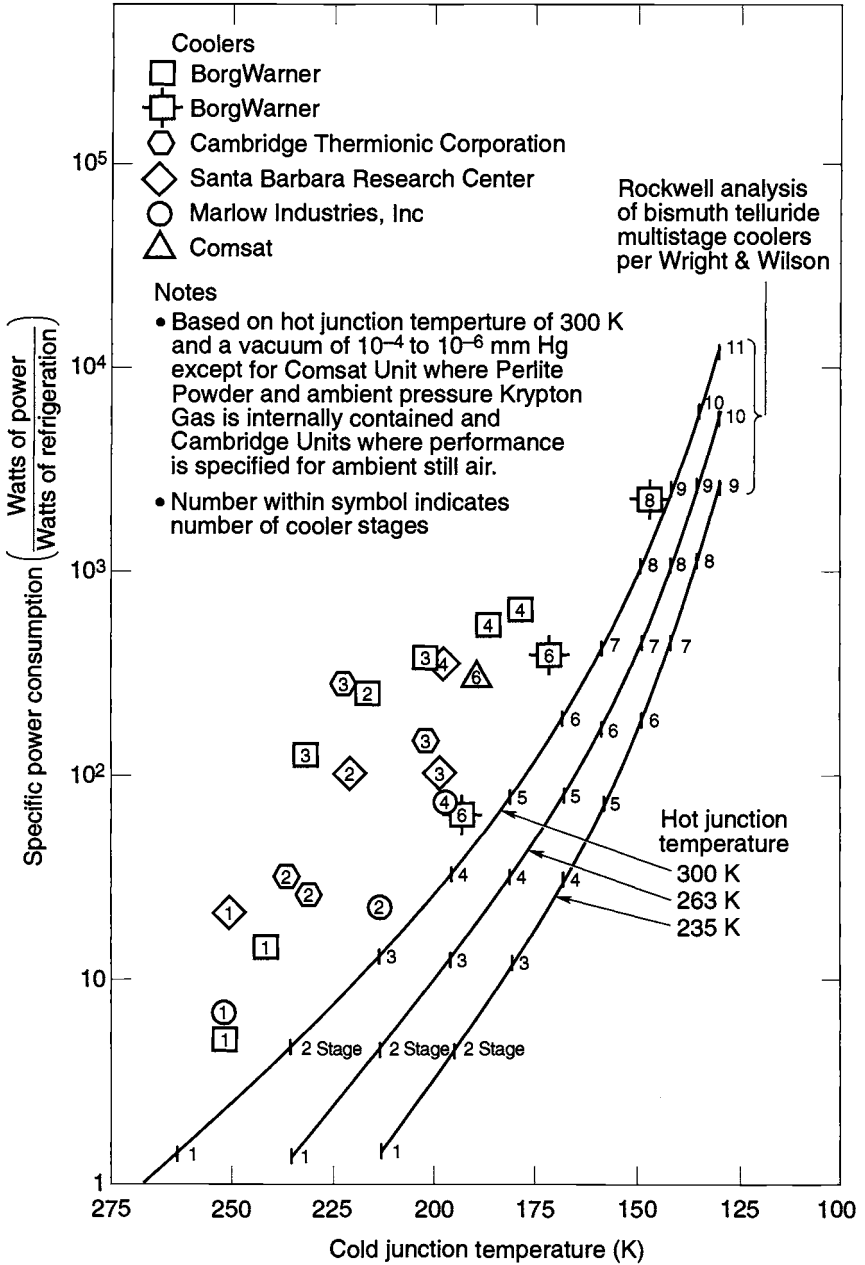
Fig. 13.3. Performance of TECs.

stage(s) and locating the majority of elements around the upper-stage periphery. Per the wedding-cake analogy, making a larger top layer with a hollow center can make the TEC stronger. In addition, a custom TEC can take advantage of an available spacecraft bus voltage, thereby avoiding any additional power conversion.

The ability to readily tailor the rejection temperature (by manipulating radiator parameters) offers control of a variable used in the overall system optimization. The system can be designed to optimize power, mass, and area according to spacecraft allocations and resource priorities. The hot-side temperature selection can trade the use of a larger radiator (i.e., a case in which the radiator operates at a lower temperature) for a more capable cooler (i.e., a case where the radiator handles higher dissipation at a higher temperature) for obtaining an efficient system.

Heat Load Testing

In installations with significant uncertainty about the parasitic heat load, heat load testing is recommended. The test-article configuration can be simplified as long as it is thermally representative. An oversized "off the shelf" (but calibrated) cooler can be employed in determining heat loads. Such tests can use an oversized radiator and heater with dedicated power supply for independent hot-side temperature control. Alternatively a temperature-controlled heat sink can be used.

The potential for a "thermal runaway" condition, which may arise from constrained applications such as limited radiator area, may be staved off by reducing the thermal resistance between the TEC hot side and the heat sink. Thermal runaway, explored in the application example below, is a condition in which temperature rise at the radiator necessitates an increase in drive power to the TEC, thus causing a further rise in temperature at the radiator, and so on.

Interfaces

A paramount design detail for TEC integration is an efficient heat-transfer path at the cooler interfaces that does not induce mechanical failures. Differences in coefficient of thermal expansion (CTE) between the TEC substrate and mating surfaces can cause internal stresses, fatigue, and failure. The construction of TECs and their associated fragile nature make their mounting extremely difficult. Traditionally, they are bonded or clamped. In the first case, a controlled and effective bondline may have a high inherent resistance, and in the second, the clamping may give rise to high local mechanical loads, variable resistance from assembly to assembly over time, and the need for coupling compound. Certain low-heat-load and low-watt-density installations can effectively employ a pliable interface material to minimize stress resulting from the temperature-induced differential expansion. However, pliable interface compounds are low-conductance phenolics that can yield significant gradients, which then would need to be overcome, hence further taxing the TEC. Often, both approaches prove impossible to use in a contamination-sensitive context, such as a location close to optical detectors.

However, for a ceramic-substrate TEC to be manufactured, the substrates are metallized. This process can also be productively utilized on the hot and cold interfaces to provide a surface receptive to a solder joint. This joint must, of necessity, be made after the TEC itself has been manufactured and tested; in addition

the soldering temperature must be lower than that used in the TEC assembly process itself. TEC manufacturers commonly anticipate this approach and use the highest-temperature solder possible consistent with their manufacturing process. Nevertheless the purchaser of a high-performance, high-cost TEC is advised to engage the manufacturer in the mounting process to avoid accidental internal damage or degradation during TEC soldering into the mounts.

Mounts should be of a relatively close match in terms of CTE to the TEC substrate. Alumina, a common TEC substrate, has a CTE of 7×10^{-6} K^{-1}, which is considerably lower than that of conventional spacecraft materials (e.g., aluminum) downstream from the TEC hot side. One potential CTE mismatch solution involves an intermediary beryllium sink, which better matches the TEC substrate CTE. Again, hard materials may cause thermal-resistance problems at joints, and further metallurgical (soldering or brazing) joining techniques may be indicated.

XRT Focal-Plane TEC Mounting

In accordance with this design philosophy, the TEC for the Swift X-Ray Telescope (XRT) focal-plane camera assembly employed two metallurgical joints (copper/beryllium solder and beryllium/aluminum alloy braze) resulting in a tenfold thermal-conductance improvement over a bonded system. This improvement reduced the peak ΔT requirement on the TEC by 10 K. The corresponding reduction of power dissipated may be estimated from the TEC power characteristic shown in Fig. 13.4.

Figure 13.5 is a photo of the flight model Swift XRT focal-plane camera-assembly CCD mounted on the cold side of the TEC. The hot-side mounting details may be discerned, along with the provision for strain-relieved electrical wiring (note the gauge of the wire). The aluminum alloy base is 40 mm on a side; this measurement conveys the scale of the image. Also, note the appearance of the upper stages of the TEC in the highly reflective baseplate.

TEC power for 168 K cold side and 50 mW cooler load
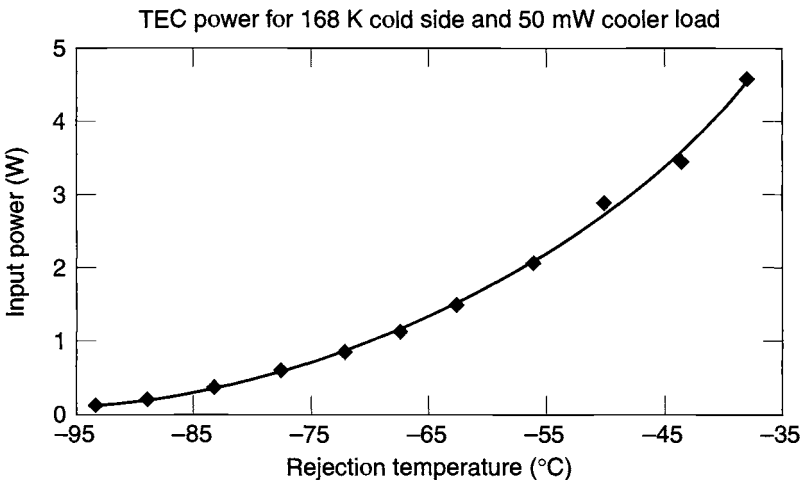
Fig. 13.4. TEC performance data from XRT development program (courtesy of University of Leicester, United Kingdom).
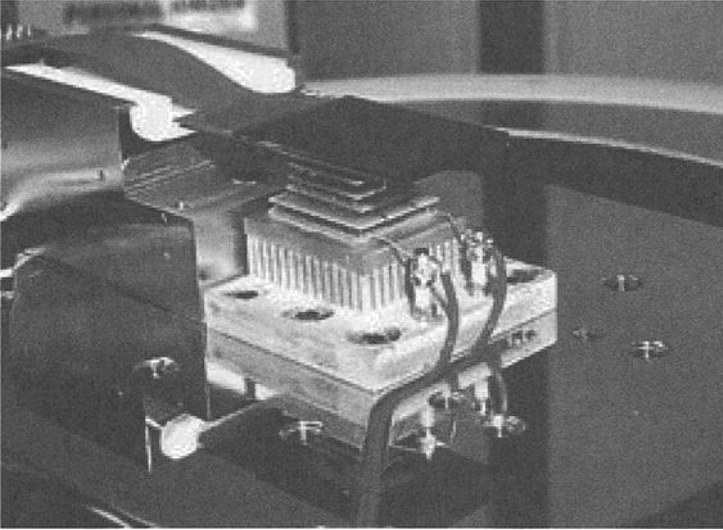
Fig. 13.5. Swift XRT CCD integrated with TEC and heat sink (photo courtesy University of Leicester).

Design Development

Decisions regarding the number of stages, the number of junctions per stage, and the like should be left to the TEC vendor. The TEC end user, however, needs to be aware of how such decisions can affect performance and margins. Adding more stages than are optimal will generally depress efficiency. Demanding a cooling load that is greater than optimal can make a TEC operate in an inefficient regime. As a general rule, TECs with fewer stages offer the potential for greater cooling-load margin while TECs with more stages offer the potential for greater temperature margin. Sharing uncertainties and margin preferences with the TEC vendor could result in a better-suited TEC—particularly in regimes where discretion can be exercised with respect to number of stages.

Clearly, prediction of TEC performance is critical to early design decisions. Prediction invariably requires the involvement of the TEC vendor, because the thermoelectrical coefficients are a function of materials and construction, and they are often proprietary. This modeling effort is a standard service that is part of the custom device development, and it gives some confidence that what is being offered is optimal for the application. Despite the apparent precision of TEC mathematical modeling, procurement of a prototype early in the design process for the heat-rejection system is strongly advised. Testing this prototype will allow subsequent steps to take place in a timely fashion—more precise sizing of other thermal components, trials on jointing techniques and their qualification, and development of the electrical control system (a step that is crucial to avoiding thermal runaway).

Power Supply

Stable dc voltages with pulse-width modulated power supplies are recommended for TECs. Particularly in optical systems, where outgassing constituents are most likely to collect on the coldest local object, it may be appropriate for the TEC power supply to have a reverse-power mode for heating and driving contaminants from the optical sensor. A smart power supply may be employed in situations where limiting thermal runaway is warranted.

Application Example

In 1986, the RCA Satcom Ku-band spacecraft was launched into geosynchronous orbit with a cooled low noise amplifier (CLNA) operating at –50°C for improved uplink receiver performance. Uplink signals reaching geosynchronous satellites are very weak because of the long transmission distance and the fading that results from atmospheric effects. Receiver signal quality is improved by operating the initial amplifier stages at this cold temperature, where the largest source of noise, "thermal noise," is suppressed.

Figure 13.6 depicts the heat flow and energy balance for the heat pump and amplifier. The TEC uses the Peltier effect to pump heat from the cold side (amplifier) to the hot side (radiator). The TEC pumps amplifier dissipation and any parasitic heat through a compliant conductive strap; this heat, as well as the TEC input power, is conducted to the local radiator, where the heat is rejected to space. The conductive strap provides a mechanically compliant heat path that relieves stresses from induced differential thermal expansion. The cooler's remote power-supply unit, the TEC controller (TECC), monitors the amplifier's temperature and modulates cooling power, thus maintaining the amplifier temperature at –50±1°C.

Environmental heat
$Q_E = 0.740$ W

Amplifier dissipation

$Q_A = 0.050$ W

Amplifier

Heat load $Q_L = 0.790$ W
$Q_L = Q_E + Q_A$

Heat pump
electrical power
$E = 8.0$ W

LNA heat pump

North panel
radiator

Heat rejected
to space
$Q_R = 8.790$ W
$Q_R = Q_L + E$
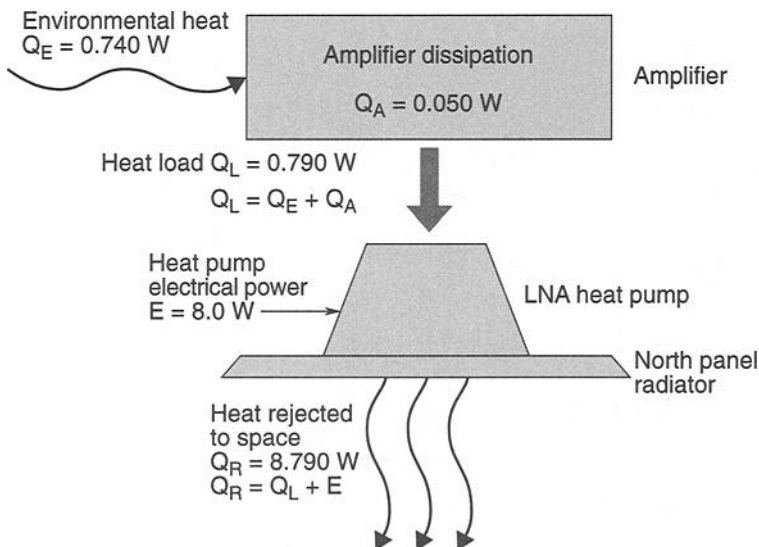
Fig. 13.6. TEC and amplifier energy balance and heat flow.

General Configuration

Figure 13.7 depicts the general configuration and thermal features of the CLNA assembly. The waveguides, which serve as the input and output RF (radio-frequency) path, suspend and thermally isolate the LNA within the enclosure. The LNA is conductively coupled via the compliant strap to the TEC's cold side. The CLNA enclosure is formed of a low-emittance aluminum foil bonded with a conductive adhesive to the CLNA assembly spreader plate and top plate. The foil also serves to attenuate noise. The aluminum legs form the primary conductive coupling from the top plate to the spreader plate; they typically keep gradients between the top plate and spreader plate less than 2°C. For heat rejection, the CLNA assembly is mounted onto, and is in intimate thermal contact with, the satellite's north radiator panel.

Thermal Design Development

The thermal design goal was to produce a stable −50°C operating environment for the LNA without substantial increase in system weight, power consumption, or risk. To meet this goal, development efforts concentrated on reducing the LNA parasitic heat loads, quantifying the cooling requirement, specifying an optimum TEC, and sizing its radiator.

Plastic Waveguide

The largest initial amplifier heat load was via the waveguide. Conventional satellite waveguides are fabricated of 30-mil (or thicker) aluminum, a highly conductive material. It became obvious that the waveguide conductive path needed to be nearly eliminated. Conduction through polymer is typically three orders of magnitude lower than that through aluminum. A competing requirement was that this waveguide also be electrically conductive, to channel RF signals. So a highly insulating polymer waveguide with a vapor-deposited thin metal was developed. A
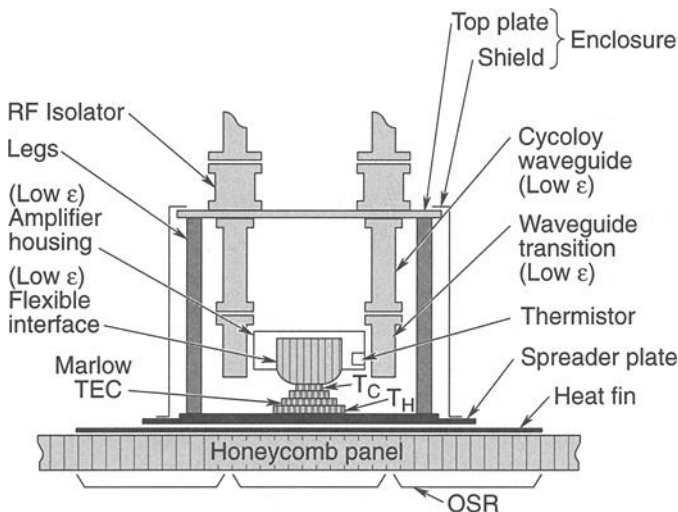
Fig. 13.7. LNA and enclosure.

polycarbonate, Cycoloy, was selected for its combination of mechanical and thermal properties—low outgassing, machinability, and affinity for thin plating (the last an especially desirable property). The Cycoloy waveguides have a vapor-deposited thin metal coating on the interior and flange surfaces that renders the waveguide electrically conductive without substantially affecting its ability to serve as a thermal isolator.

Miscellaneous Details

To minimize radiative heat absorbed by the amplifier, the LNA used surfaces of low emittance throughout. The amplifier's 32-gauge electrical leads were chosen to minimize heat leak down the lead without compromising structural integrity.

Compliant Conductive Strap

The purpose of the compliant strap was to provide mechanically compliant heat transport between the TEC and LNA with a modest temperature gradient. The strap was similar in concept to other mechanically compliant thermal links, with stacked layers of metal curved to provide virtually no resistance to small displacements in two planes. The strap departed from the usual mechanically compliant thermal links in three ways. First, it was constructed of silver rather than copper. Silver is lighter and imparts lower loads to the TEC during vibration. Second, to eliminate interlayer gradients, the silver layers were fused to each other, but only in the vicinity of the cooler and LNA interfaces. Third, to reduce the TEC-to-strap gradient, the strap was permanently bonded to the TEC with a conductively loaded adhesive.

Aluminum Enclosure

The decision to set the local radiator operating temperature to a maximum of 15°C (as discussed below) clarified the advantage of creating an enclosure around the CLNA assembly. The initial thought was to use multilayer insulation (MLI) to form an effective barrier to radiation from the satellite's interior environment (which can be as warm as 30°C). With an outer enclosure conductively tied to the local radiator, LNA radiative parasitic heat loads from the surrounding spacecraft would be further reduced. The low-emittance aluminum-foil enclosure therefore would shunt spacecraft ambient radiation energy directly to the radiator and would surround the LNA in a 15°C cavity.

Radiator Sizing Criticality

The primary parasitic heat flow path into the LNA is radiation from the enclosure and conduction down the leads and waveguides. Because the enclosure temperature is quite close to that of the radiator, the heat flow (and therefore the cooling requirement) is directly proportional to the radiator temperature. If the enclosure (or radiator) temperature increases, the cooler has to work harder, thereby raising the radiator temperature. With this radiator-cooler relationship, the sizing of the radiator is critical, and undersizing it could lead to a thermal runaway condition in which additional power supplied to the cooler causes the cold area to be warmer.

Cooler Heat Load Determination

To size and specify the cooler, we first determined the cooler heat load. Initial analysis predicted 525 mW. Because of the low efficiency of TECs, even small errors in estimating this value would translate into significant errors in the cooler waste heat and necessary radiator size. Therefore, the cold-side heat load was determined experimentally, as a function of the cooler's hot-side temperature. A series of calorimetric tests was conducted with a thermally representative CLNA assembly and a calibrated oversized TEC rejecting heat to a temperature-controlled heat exchanger. These tests established the cooling requirement to maintain the LNA at −50°C for a range of baseplate temperatures (27, 15, and 0°C). The net cooling was deduced from the measured power and the calibrated cooler performance curves. Sensitivity of the amplifier heat load to hot-side temperature is shown in Fig. 13.8. Because experimental values were more conservative than the analytical values, they were used for cooler selection and radiator sizing.

Selection of Rejection Temperature

Rejection temperature was the final parameter needed to design and build an optimized cooler. This temperature affects both the specification (and therefore the optimization) of the TEC and the local radiator sizing. Selecting an excessively cold rejection temperature would result in a large and heavy radiator, while an excessively warm rejection temperature would cause the TEC to consume excessive power, resulting in inappropriate use of radiator area. The selection needed to be a compromise between radiator area (a warmer rejection temperature would be needed for a smaller area) and power consumption (a colder temperature would be needed for lower power). Optimal rejection temperature would balance TEC power consumption against radiator area.
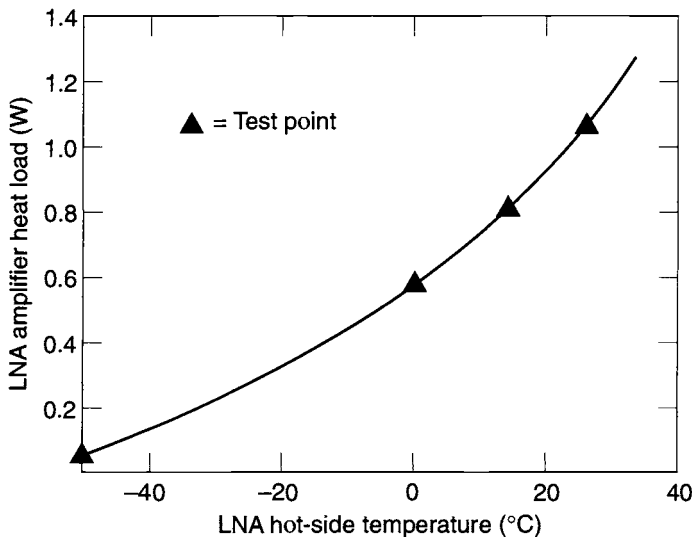
Fig. 13.8. LNA amplifier heat-load dependence on hot-side temperature.

We first looked to establish the minimum possible range of radiator temperatures by determining the effect of external equivalent sink temperature and the internal environment on the radiator. The external equivalent sink temperature is a single sink temperature that is equivalent to the environmental flux (solar flux), radiative interchange with other bodies (13% worst-case view to solar array at 50°C) and surface-finish parameters (absorptance and emittance). In calculations or in IR testing, using an equivalent sink causes the object in question to run at the same temperature as it would with all those external fluxes and parameters imposed. The external equivalent sink temperature was calculated to be −16°C using Eq. (13.1):

$$T_{\text{ext eq sink}} = [(\alpha/\varepsilon \cdot S \sin(\theta) + F_{\text{array}}\sigma T^4_{\text{array}})/\sigma]^{1/4}. \qquad (13.1)$$

This calculation assumes an OSR solar absorptance (α) of 0.25, emittance (ε) of 0.80, solar constant (S) of 0.135 W/cm^2, incident solar angle (θ) of 23.5 deg, worst-case view factor to the solar array (F_{array}) of 13%, and solar array temperature (T_{array}) of 50°C. The Stefan-Boltzmann constant (σ) is 5.67×10^{-8} W/m^2·K^4.

The local internal temperature (T_{int}) can be as warm as 30°C. The sum of the internal and external equivalent sinks (per Eq. [13.2]) represents the net equivalent sink for the CLNA radiator. The low-emittance irridite surface finish ($\varepsilon_{\text{int}} = 0.11$) was selected for the radiator interior surface to minimize radiant heat absorbed from the spacecraft interior, thereby allowing the CLNA radiator to achieve colder temperatures. The net effective sink (considering both internal and external environments) is −9°C:

$$T_{\text{net eq sink}} = [(\varepsilon T^4_{\text{ext eq sink}} + \varepsilon_{\text{int}} T^4_{\text{int}})/(\varepsilon + \varepsilon_{\text{int}})]^{1/4}. \qquad (13.2)$$
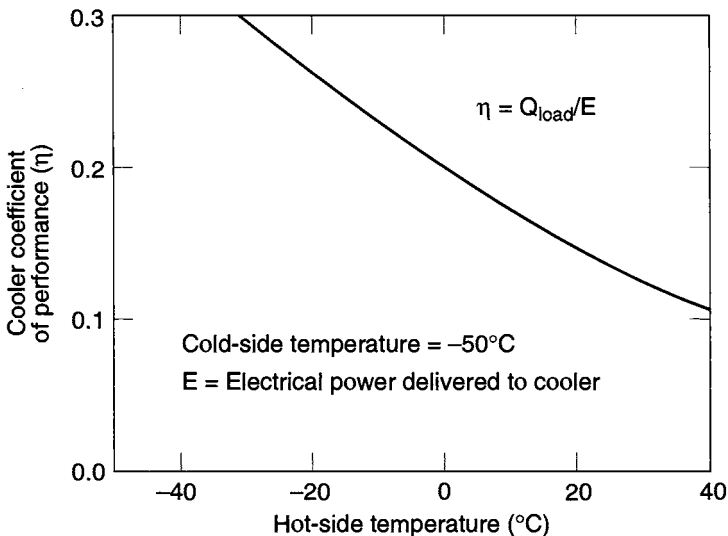
Fig. 13.9. Estimated theoretical limit of cooler performance.

This calculation indicates that even with an infinitely efficient TEC, the CLNA radiator could not operate at a temperature of –9°C or below. Thus the cold bound of plausible rejection temperatures was established.

To compare various rejection temperatures, we needed heat-pump performance for various hot-side temperatures and –50°C for the cold side, but this data was not directly available. TEC manufacturers typically evaluate and publish performance data with the cooler hot side at 27°C. We estimated this performance curve using published TEC performance curves and a performance-equivalence transform suggested in the cooler-sizing guide published by Marlow Industries, Inc.[13.1] The transform indicates that for a given power, reducing the hot-side temperature by 3°C reduces cold-side temperature by 1°C. The resulting transformation and interpolation yielded Fig. 13.9, which represents the estimated theoretical limit of cooler performance for the cold side at –50°C. Each incremental point on the curve represents an optimized cooler for that particular hot-side temperature. Hence this curve represents an optimistic bound on performance.

Using a spreadsheet is a straightforward means to establish TEC power consumption and radiator area required over the range of plausible rejection temperatures. The TEC cooling load (Fig. 13.8) and COP (Fig. 13.9) can be represented by equation or table. Dividing the heat load by the COP gives the TEC power consumption. Table 13.2 indicates that the power continues to increase with temperature. The area is calculated using radiation heat-transfer equations and appropriate couplings to both space and the spacecraft interior. For this application, the spreadsheet indicated a range of reasonable solutions with the radiator temperature between 5°C and 30°C. A design hot-side temperature of 15°C was selected as a compromise between low input power and radiator area.

The TEC vendor was given the following parameters: 790 mW cooling requirement, –52°C cold-side temperature (allowing for a 2°C gradient in the strap), and +15°C hot-side (rejection) temperature. The vendor's optimization indicated that a four-stage cooler would consume 8 W of power.

Table 13.2. Radiator Sizing Summary

$T_{radiator}$ (°C)	Theoretical Input Power (W)	Area (cm^2)
–5	2.5	2023
0	3.0	1005
5	3.5	732
10	4.1	610
15	**4.9**	**545**
20	5.7	509
25	6.7	491
30	7.9	485
35	9.4	490
40	11.2	506

Radiator Sizing

The final design step was to size the CLNA radiator, using the 8 W input power plus the 0.79 W heat pumped, and an assumed 0.80 fin effectiveness. Radiated heat from internal and external sources was covered by virtue of using the equivalent sinks. Heat conduction along the waveguide external to the CLNA assembly was erroneously neglected, but that condition was probably more than offset by improvements to the surface finishes and enclosure. The required radiator area was 0.106 m^2.

Test Results and Flight Data

A test of the final CLNA configuration was performed with an engineering model CLNA bolted to an equivalent aluminum plate representing the radiator panel. This test demonstrated adequate cooling and radiator-area margin. The CLNA operation was as expected during spacecraft thermal-balance testing, which simulated the worst hot expected flight environment. Initial flight data also indicated that the CLNA was properly maintaining the LNA at –50°C.

Reference

13.1. Marlow Industries, Inc., "A Guide to Thermoelectric Heat Pumps," Catalogue No. 98-002.

14 Heat Pipes

R. C. Prager,[*] M. Nikitkin,[†] and B. Cullimore[‡]

Overview

Heat pipes use a closed two-phase liquid-flow cycle with an evaporator and a condenser to transport relatively large quantities of heat from one location to another without electrical power. A heat pipe can create isothermal surfaces; as a thermal "transformer," it can change the flux density of a heat flow; and it can function in various ways as a thermal-control device. One-way (diode) heat pipes have been tested and flown, as have variable-conductance heat pipes (VCHPs), which maintain a constant-temperature evaporator surface under varying load conditions. Because the driving mechanism in a heat pipe is capillary pumping, a relatively weak force that is provided by a wick, the pipe may be susceptible to severe performance degradation when operating in a gravitational field. Planning is therefore needed to facilitate the ground testing of systems that include heat pipes.

How a Heat Pipe Works

Consider a simple horizontal heat pipe in equilibrium with an isothermal environment. The liquid in the wick and the vapor in the vapor space are at saturation. If heat is applied to the evaporator, raising its temperature, liquid in the wick evaporates (removing some of the added heat), which depresses the meniscus in the evaporator because less liquid remains there. This process also raises the local vapor pressure, because that pressure must be in saturation with the heated liquid in the wick.

The difference between the increased curvature of the meniscus in the evaporator wick and the unchanged meniscus in the condenser wick causes a difference in capillary pressure sufficient to pull liquid from the condenser wick toward the evaporator wick. This action replenishes the liquid in the evaporator wick. At the same time, heated vapor flows from the evaporator to the condenser, which is at a lower pressure. When this vapor comes in contact with the cooler surfaces of the condenser, it condenses. This cycle of evaporation and condensation is shown schematically in Fig. 14.1.
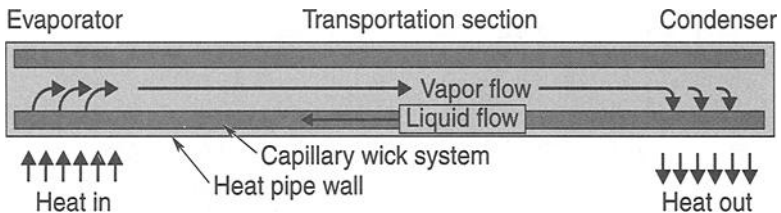
Fig. 14.1. Heat-pipe schematic.

*The Aerospace Corporation, El Segundo, California.
†Swales Aerospace, Beltsville, Maryland.
‡C&R Technologies, Littleton, Colorado.

Because the latent heat of vaporization of most heat-pipe working fluids is high, only small amounts of fluid need to flow to transport significant quantities of heat. The driving mechanism, the temperature difference between the evaporator wall and the condenser wall, is also small.

Types of Heat Pipe

Constant-Conductance Heat Pipe

This most basic heat pipe consists of a working fluid, a wick structure, and an envelope. This pipe is used to move heat from one location to another (possibly changing the flux density in the process) or to isothermalize a surface. It need not be shaped like a conventional cylindrical pipe—flat plates several feet across have been built and tested as heat pipes for special applications. Constant-conductance heat pipes are often categorized according to the type of wick structure they use.

Groove Wicks

The simplest heat-pipe wick design consists of axial grooves in the wall of extruded aluminum tubing. Grooves can be formed in tubes of other materials, such as copper (by swaging) or even refractory metals (by deposition), but they are formed most often in tubes of aluminum. This class of wick is very susceptible to gravitational effects during ground testing, but it is relatively inexpensive to produce and it performs very consistently. Its moderate heat-transfer capability is sufficient for many applications. Most grooves are rectangular or trapezoidal, but some have more complex shapes, such as the "teardrop" or "keyhole," which can be extruded with difficulty (Fig. 14.2).

"Monogroove" Design

The monogroove design, a high-capacity design consisting typically of a wick in one large, teardrop-shaped groove connected to a vapor space (Fig. 14.3), can be considered an extension of the basic groove concept. Unlike a heat pipe with many
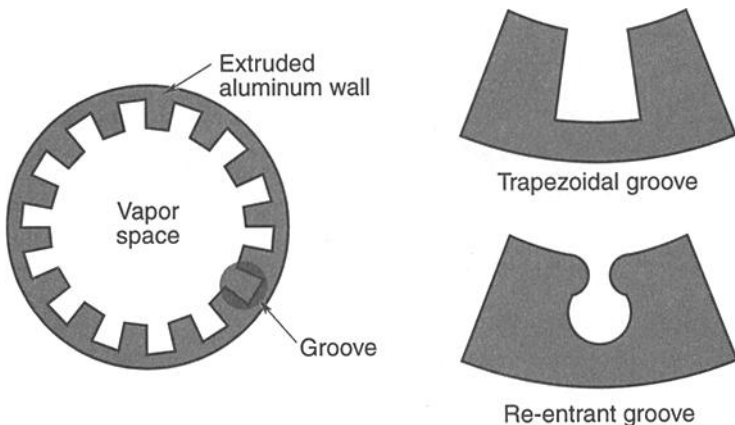
Fig. 14.2. Grooved heat pipe.
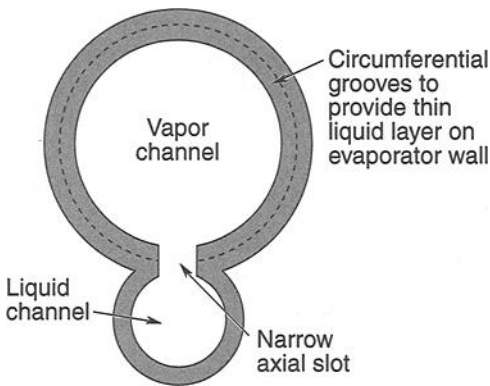
Fig. 14.3. Monogroove heat pipe.

smaller grooves of the same total area, the monogroove heat pipe has a large single groove that provides relatively unrestricted longitudinal flow. Liquid is distributed on the evaporator wall by means of a secondary wick consisting of small circumferential grooves or screen. This design has shown very high capacity during ground testing, but it encountered difficulties during early shuttle testing. Later experiments were more successful. As of this writing, no monogroove heat pipe has been used on a production spacecraft.

Composite Wicks

Among composite wicks, the simplest (and the oldest heat-pipe wick) consists of several layers of screen fastened to the inside wall of a heat pipe. More capacity can be obtained by using more layers of screen, to increase the wick flow area—at the cost of increasing the heat-pipe temperature difference resulting from the temperature drop needed to conduct heat through the thick saturated wick. To overcome this penalty, some heat-pipe manufacturers separate the wick into two parts, the portion that spreads the fluid circumferentially about the wall of the evaporator, and the portion that carries the fluid down the length of the heat pipe. The former, kept as thin as possible, can consist of circumferential grooves cut in the wall of the heat pipe or of a single layer of screen or metal mesh bonded to the wall. The latter is held off the wall by means of legs or straps, or makes contact with the wall in only a few places. This type of wick has capacities similar to the axially grooved heat pipe, but has much more capability when tilted. Because the wick must be assembled of relatively fragile materials, care is required in building such a pipe, and no two supposedly identical pipes will perform in exactly the same manner. Sample wick designs of this type are shown in Fig. 14.4.

Artery and Tunnel Wicks

This class of heat pipe is based on the composite wick, but provides one or more relatively unrestricted liquid-flow paths in parallel with the longitudinal wick. These paths will fill with fluid in space, because of minimum surface-energy considerations, and will greatly reduce the viscous pressure drop in the heat pipe, thereby increasing capacity. When properly designed, these arteries will fill as the
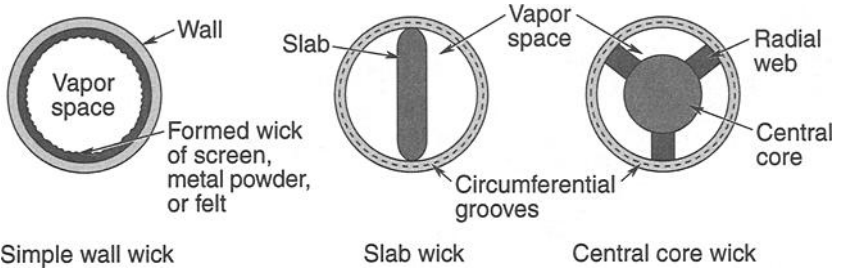
Fig. 14.4. Composite wicks.

heat pipes operate in a gravitational field. Wicks in this class can be blocked by bubbles of noncondensable gas in the arteries (see Abhat *et al.*[14.1] and Saaski[14.2]), but they are attractive because of their large heat-transfer capability in a small envelope. If the liquid in the artery remains subcooled when it reaches the evaporator, bubble formation can be avoided. A number of mechanical schemes have been proposed and tested to prevent bubbles from blocking the arteries of VCHPs (see Eninger[14.3]). These pipes are particularly prone to bubble formation because the liquid in the artery contains dissolved control gas, which tends to come out of solution as the liquid warms during its transit of the pipe from condenser to evaporator. Cross sections of some of these wick structures are shown in Fig. 14.5.

Diode Heat Pipes

A constant-conductance heat pipe can be modified so that operation occurs normally in one direction but ceases when an attempt is made to transfer heat in the other, "wrong" direction, resulting in a diode action. Even when blocked, however, the pipe transfers some heat, if only by conduction down the pipe wick and
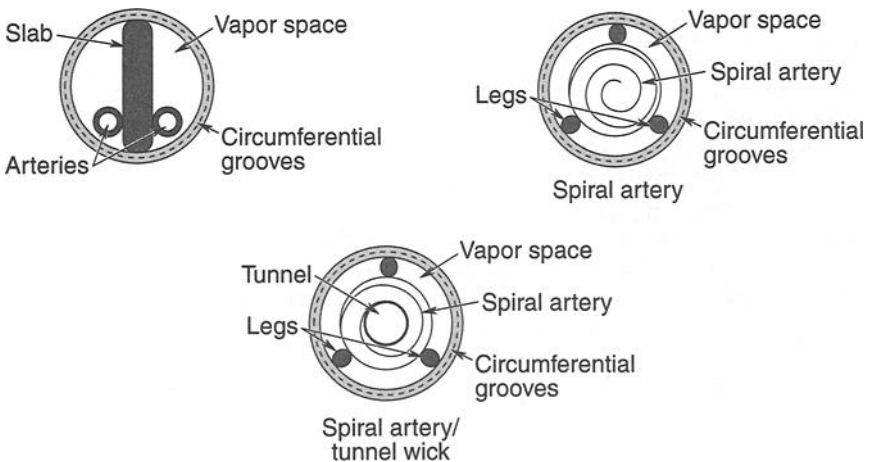
Fig. 14.5. Artery and tunnel wicks.

wall. This type of heat leak is particularly significant in cryogenic systems. Common diode heat pipes are the liquid-trap, liquid-blockage, and gas-blockage diodes.

Liquid-Trap Diode

The most common type of heat-pipe diode, the liquid-trap diode has a wicked reservoir at the evaporator end designed so that it is heated by the same environment that heats the evaporator. Although the envelopes are connected, the reservoir wick is not connected to the rest of the heat pipe. When, during normal operation, heat is applied to the evaporator and reservoir, heat is transferred from the evaporator to the condenser as in the constant-conductance heat pipe, and any fluid in the reservoir wick evaporates and joins the vapor flow to the condenser. (The reservoir wick should be dry during normal operation.) When ends of this pipe are reversed, and the evaporator and reservoir become cooler than the condenser, some of the hot vapor coming from the condenser condenses in the reservoir and is lost to the rest of the heat pipe. Sufficient liquid is tied up in the reservoir to cause the pipe to dry out. "Shutoff" is neither instantaneous nor complete. A schematic of the operation of this type of diode is shown in Fig. 14.6.

Liquid-Blockage Diode

At its condenser end, the liquid-blockage diode (Fig. 14.7) has a wicked reservoir cooled by the same environment that cools the condenser. The reservoir's wick is not in contact with that of the remainder of the heat pipe, and it is normally full of

Liquid trap diode—normal operation

Liquid trap diode—reverse (shutoff) operation
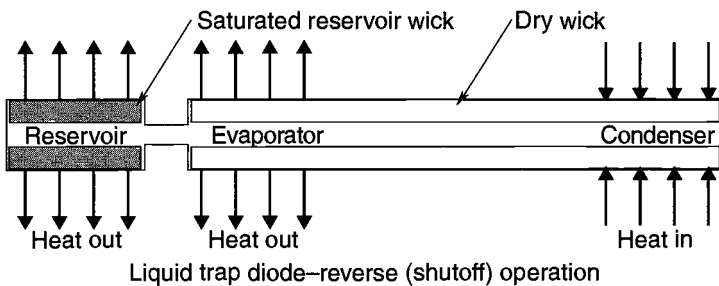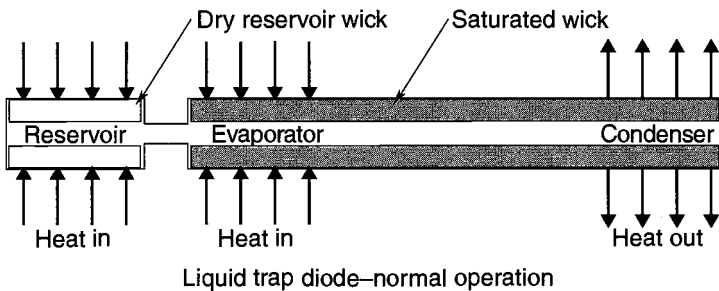
Fig. 14.6. Liquid-trap diode.
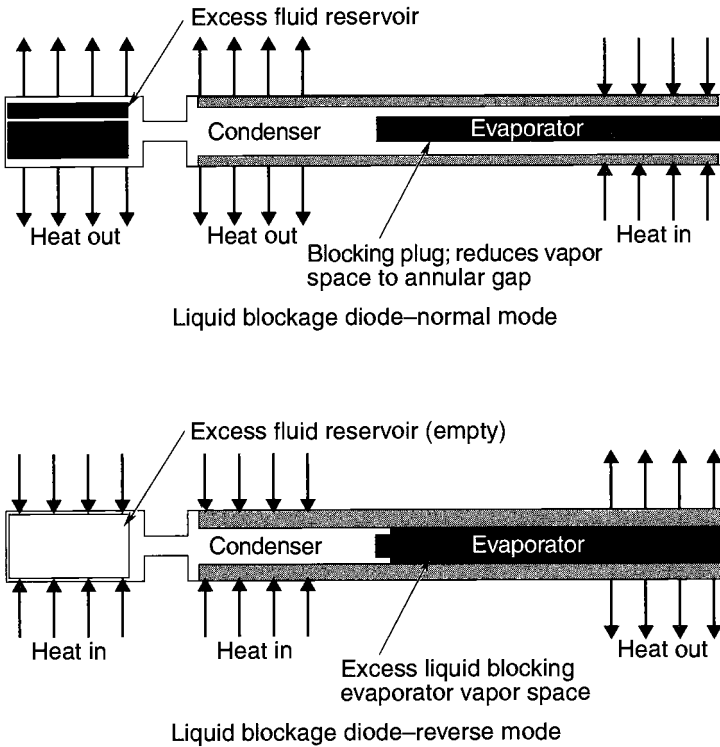
Fig. 14.7. Liquid-blockage diode.

working fluid—in effect, it traps a large fluid slug. When the ends of the pipe are reversed, the fluid slug travels to the normal evaporator end, where it completely fills the evaporator vapor space (and that of a large portion of the transport section), preventing condensation. Optimum design of the wick structure and vapor space must be compromised to control the liquid slug during shutoff, and such control requires maintaining close tolerances during the manufacturing process. Proper control of the fluid (and therefore operation of the diode) in a gravitational field requires maintaining the gap between the evaporator wall and the blocking plug at a size that enables the gap to fill with liquid if it is available.

Gas-Blockage Diode

The gas-blockage diode is similar in design to the liquid-blockage diode, except the reservoir, which can be unwicked, contains a noncondensable gas. When the ends of the pipe are reversed, the gas flows to the evaporator and, as above, completely fills the vapor space, preventing condensation. However, as the temperature rises, the gas slug can be compressed to the point where the heat pipe will start working again. Furthermore, convection within the gas slug may be a significant heat-leak component. A schematic of the operation of this type of diode is shown in Fig. 14.8.
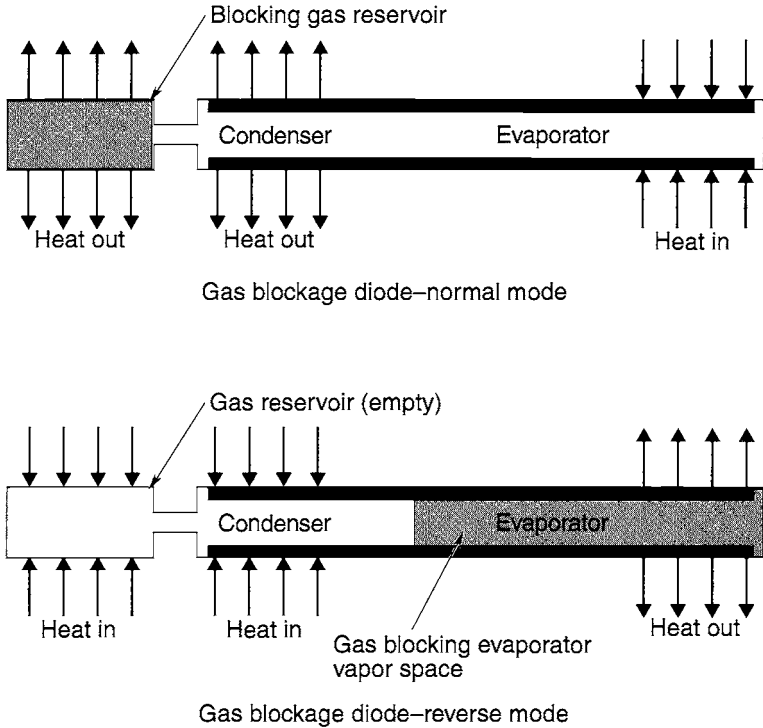
Fig. 14.8. Gas-blockage diode.

Other Diodes

Any heat pipe that has a wick with a finer pore size in the evaporator than in the condenser or the adiabatic section will show some signs of diode operation, and its capacity will differ depending upon the direction in which it is trying to move heat. The most extreme case is that of a heat pipe with no wick in the condenser (see the capillary pumped loop [CPL], below), as the pipe will dry out quickly and shut off if heat is applied there.

VCHPs

VCHPs use a gas reservoir connected to the end of the condenser. The reservoir is filled with a noncondensable gas to control the operating area of the condenser based on the evaporator temperature. (In effect, in a typical spacecraft application, the active radiator area becomes a function of the electronics-box cold-plate temperature, with increasing box temperatures leading to increased radiator areas.) Although complicated models of the gas front exist, the gas front may be considered an impermeable floating piston. If the temperature at the cold plate rises, the vapor in the evaporator (at the saturation pressure of the liquid in the evaporator) rises rapidly. The pressure of the mixture of control gas and vapor in the reservoir must rise to compensate, so the "gas-front-as-piston" will move further into the

condenser, decreasing the volume of control gas. This process, shown schematically in Fig. 14.9, opens up more of the condenser area to heat-pipe operation. A number of VCHP schemes have been flown; they have differed mainly in how they treat the reservoir. Some have wicks, some are kept hot or cold by exposure to different environments, and some become elements of what is arguably an active thermal-control system by means of heaters connected via feedback control to sensors at the evaporator or payload. Sufficient control gas is usually present in the reservoir to enable these pipes to function as gas diodes if the ends of the heat pipe are reversed. The VCHP operation temperature profile in Fig. 14.10 shows temperature as a function of position along the pipe.

Hybrid (Mechanically Assisted) Systems

Hybrid systems are essentially extensions of the CPL. They cannot be considered passive thermal control systems, because of the addition of small pumps to force liquid flow. Because they are two-phase systems, only small quantities of the working fluid need to be carried to the evaporation site in the liquid phase to transport large amounts of heat energy. Several such systems had been proposed for use on the Space Station, and a number of prototypes have been built and tested.

Analysis

Heat-Pipe Capacity (Capillary Pumping Limit)

Return flow of liquid from the condenser to the evaporator is caused by differences in the capillary pressure between the evaporator and condenser. The capillary

VCHP at high power

VCHP at low power
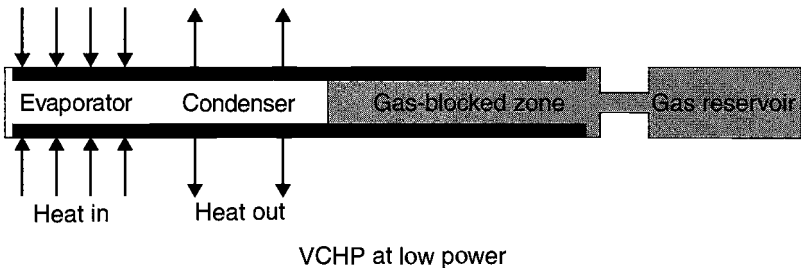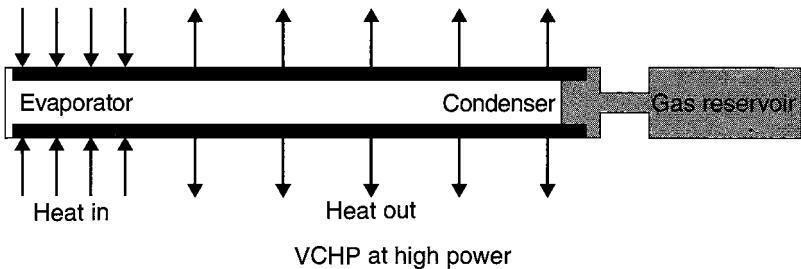
Fig. 14.9. VCHP operation schematic.

Temperature profile
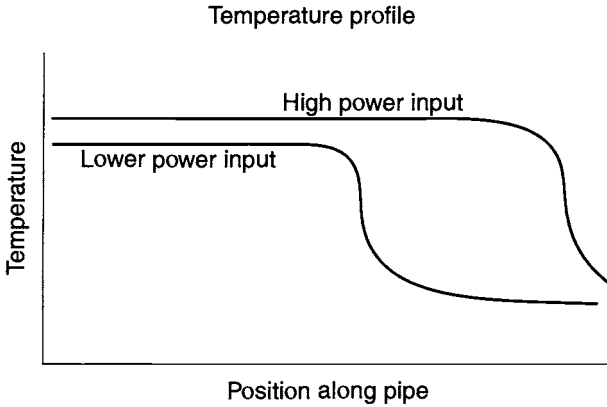
Fig. 14.10. VCHP operation temperature profile

pressure acting on the liquid surface is inversely proportional to the radius of cur-
vature of the fluid surface at the liquid/vapor interface in the wick. For purposes of
the analysis, the liquid surface in the condenser is usually assumed to be flat, so
that the radius of curvature (and hence the capillary force) is zero. As liquid evap-
orates, the meniscus in the evaporator depresses, causing a difference in capillary
pressure between the evaporator and condenser surfaces (Fig. 14.11). This differ-
ence in pressure pulls liquid through the wick from the condenser to the evapora-
tor in an attempt to restore equilibrium.

A heat pipe "dries out" when the flow of working fluid through the wick caused
by this pressure difference is insufficient to supply liquid at the same rate at which
working fluid is being vaporized in the evaporator. This point is illustrated in the
Eq. (14.1), which balances the pressure drops in the system:
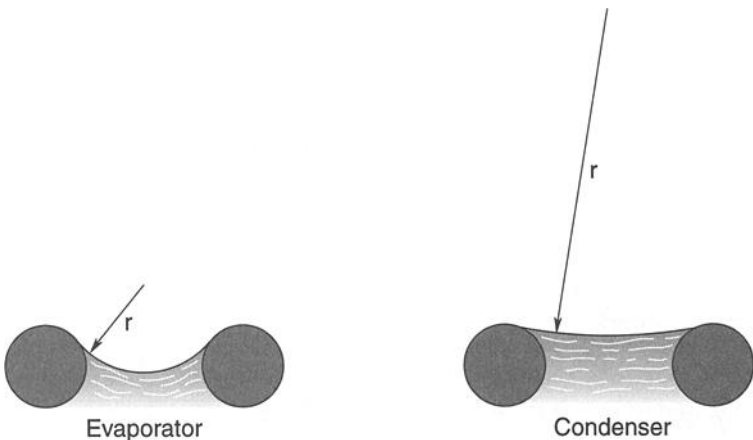
Fig. 14.11. Depression of the meniscus.

$$\Delta P_{\text{CAPILLARY}} - \Delta P_{\text{GRAVITY}} = \Delta P_{\text{LIQUID}} + \Delta P_{\text{VAPOR}}. \tag{14.1}$$

In this equation, $\Delta P_{\text{CAPILLARY}}$ (capillary pressure rise) is the maximum possible difference in capillary pressure between the evaporator and the condenser. This term is a function of the surface tension (which depends on the choice of working fluid and the temperature) and the wick pore size (which depends upon the wick material and type of wick).

$\Delta P_{\text{GRAVITY}}$ (gravity head loss) is the "head loss" that must be overcome by capillary pressure to sustain fluid in the evaporator. In addition to gravity, other accelerations, such as those on a spinning spacecraft, affect the value of this term.

ΔP_{LIQUID} (liquid pressure drop) is the pressure loss resulting from viscous flow through the wick. This term is simple for an axial-groove wick, but it can become extremely complicated for a composite-artery wick, where viscous pressure losses in liquid flowing through complicated structures of layered screens, metal felt, or sintered powder must be modeled. Expressions for these losses usually contain empirical constants, which is one of the reasons why performance testing of each pipe is usually necessary.

ΔP_{VAPOR} (vapor pressure drop) is the pressure loss resulting from vapor flow from the evaporator to the condenser. This term is usually small unless the vapor density is very low or the vapor velocity is high because of constricted vapor space.

The exact equation will depend upon the wick design used. Many formulations are given in the references.

Thermodynamic Considerations

If operation near the freezing point is needed—as would be the case for water at typical room temperatures, for almost any cryogenic liquid, or for liquid metals at start-up—high vapor velocities and large vapor-pressure drops will be encountered, because in these situations the vapor density and pressure are very low. These large pressure drops cause their own temperature drops in the pipe (because saturation temperature is a function of pressure). In some cases, the pressure drop in the vapor required to support the calculated heat-pipe capacity would result in a negative vapor pressure in the condenser, an obvious impossibility. Under similar low-density conditions, choked flow (the "sonic limit") has been observed in liquid-metal heat pipes. Although not a true limit, the operating temperature of the heat pipe rises so thermal equilibrium can be established, which may cause the temperature to rise beyond the desired range. In short, do not design a heat pipe that must run in a temperature regime where its working fluid has a very low vapor pressure.

If the relative velocity of liquid and vapor is high enough (as measured by the Weber number), liquid can be pulled out of the wick and returned to the condenser in the form of droplets entrained in the vapor. This phenomenon (the "entrainment limit") was first observed in liquid-metal heat pipes where the droplets could be heard to "ping" against the end cap. It is an operating limit in that, to support a given rate of heat transfer from the evaporator, an excess of liquid must be pulled through the wick, because not all of the liquid will reach the evaporator.

The "boiling limit" or "heat-flux limit" is concerned with the flux density of the thermal load on the evaporator. Even if the heat-pipe wick could theoretically return the liquid from the condenser required by the heat load, if the load is concentrated in too small an area, nucleate boiling can occur in the evaporator wick. The creation of bubbles in an otherwise filled wick reduces the area of the wick available for fluid flow, and hence reduces the capacity of the wick.

Working Fluids

The choice of working fluid is usually governed by the temperatures of the desired operating range. A heat-pipe working fluid can be used effectively between a temperature somewhat above its triple point and another that is below its critical temperature. If the triple point is approached too closely, temperature drops in the vapor flow increase (see the discussion above, "Thermodynamic Considerations"). As the critical point is approached, the distinction between liquid and vapor blurs, and the surface tension drops to zero. (The pressure that must be contained by the envelope also increases significantly.) The triple points and critical temperatures of several heat-pipe working fluids are given in Table 14.1.

Table 14.1. Heat-Pipe Working Fluids[a]

Fluid	Melting Point (K)	Melting Point (°F)	Boiling Point (K)	Boiling Point (°F)	Critical Temp. (K)	Critical Temp. (°F)
Hydrogen	14.0	−434.4	20.4	−423.0	33.0	−400.3
Neon	24.5	−415.6	27.1	−410.9	44.4	−379.8
Oxygen	54.3	−361.8	90.2	−297.3	154.8	−181.1
Nitrogen	63.1	−346.0	77.3	−320.4	126.2	−232.4
Ethane	89.9	−297.8	184.5	−127.6	305.5	90.2
Methane	90.7	−296.4	111.4	−259.2	190.5	−116.8
Methanol	175.2	−144.3	337.9	148.5	513.2	464.1
Acetone	180.0	−135.7	329.4	133.2	508.2	455.1
Ammonia	195.5	−107.8	239.8	−28.0	405.6	270.4
Water	273.2	32.0	373.2	212.0	647.3	705.4
Potassium	336.4	145.8	1032.2	1398.3	2250.0	3590.0
Sodium	371.0	208.1	1152.2	1614.3	2500.0	4040.0
Lithium	453.7	357.0	1615.0	2447.0	3800.0	6380.0

[a]Data from Brennan and Kroliczek, *Heat Pipe Design Handbook*.[14.4]

Two parameters have been developed to aid in comparing the relative performance of heat-pipe working fluids. The first, the "zero-g figure of merit," is given by $\frac{\sigma\rho\lambda}{\mu}$, where σ is the surface tension, ρ is the liquid density, λ is the latent heat of vaporization, and μ is the dynamic viscosity. This parameter neglects vapor flow entirely, but for most applications, vapor flow is not the limiting factor. The group of fluid properties included in the parameter definition appears in the heat-pipe capacity equation. A second parameter, the "one-g figure of merit" or "wicking height factor," compares the relative sensitivity to gravity effects of working fluids: $\frac{\sigma}{\rho}$, where the properties are as defined above. It is a relative measure of how high a given wick structure will be able to pump a working fluid in a gravitational field (or as a result of inertia effects, as in a spinning spacecraft).

Material Compatibility

Because a heat pipe is a completely sealed container, any chemical reactions between the working fluid and the wall or wick material can be disastrous. None of the reaction products can escape, and any material that is consumed cannot be replaced. Certain combinations of materials, such as ammonia and copper, are known to react quickly with one another, and hence are not likely to be chosen, even by a novice.

However, combinations of materials that are traditional and acceptable in the chemical-process industry (such as water and stainless steel, or water and nickel) have been demonstrated to react with one another, generating noncondensable gas. In general, the cryogenic working fluids up through ammonia can be used with either stainless steel or aluminum (although some evidence indicates that ammonia reacts slowly with aluminum, and the combination of ammonia, aluminum [as is found in a wall material], and stainless steel [such as would be found in a typical wick material] can react more quickly with one another).

Methanol works well with stainless steel but reacts with aluminum. Water seems to work well with copper, and possibly monel, but not with 304 or 316 stainless steel or nickel. Some short-term success has been achieved with carbon steel, but pipes using it appear to be generating hydrogen gas, which diffuses through the pipe wall; this observation indicates an internal reaction is taking place.

Materials available for higher-temperature (liquid-metal) heat pipes must hold together at those higher temperatures and be inert to some very corrosive working fluids. This area is still under investigation.

Testing

During Fabrication

The heat-pipe envelope will be checked for leaks during the fabrication process, usually with a helium mass-spectrometer leak detector. However, once the pipe is sealed at the fill tube, the integrity of this seal is open to question. Although some chemical tests have been used (see Edelstein[14.5]), the most thorough seems to be checking for the presence of working fluid outside the heat pipe when it is placed in an evacuated chamber.

Performance of each heat pipe as a function of tilt should be measured at some typical operating temperature(s) to determine whether the wick functions properly. Testing at a low temperature will show whether noncondensable gas is present. (At high temperatures, the noncondensable gas can be compressed into a thin plug so that it isn't detectable using thermocouples mounted on the heat pipe.)

If the heat pipe is to be installed in a spacecraft in a position where it will be tested vertically (with gravity assist) during system-level testing, such as a thermal-vacuum or thermal-balance test, then it must be tested in the same orientation with a similar heat load before installation. In this way, the performance of the heat pipe that will be seen in the vacuum chamber will be known before the test is performed. This data will help to avoid unpleasant surprises and scrambling for logical explanations at a time when the heat pipe can't be reached without breaking vacuum and tearing open the spacecraft.

In the case of a heat pipe that is to be curved in three dimensions and can't be tested in a single plane, some manufacturers build a test pipe with the same number of curves in the wick, but with all of the curves in a single plane. In this way, the wick performance to be expected in space can be characterized.

After Integration into the System

After integration of a heat pipe into a system, the heat pipe should be verified to determine whether any deterioration took place during the integration procedure, and also to verify the performance of the integrated thermal control system.

Heat-Pipe Applications and Performance

The most obvious application of a heat pipe is one requiring physical separation of the heat source and sink. If a heat pipe is used, all hardware to be cooled need not be mounted directly on radiator panels, and relatively inefficient conductive couplings need not be used. (Requirements for this type of coupling are usually found in cases where boxes must be cooled and kept close to each other for more efficient electrical or microwave design.) By the same token, heaters need not be mounted directly on hardware to be heated if a heat pipe is employed.

A closely related class of applications is that of the thermal transformer. In this scenario, a small high-powered box is mounted on one side of a radiator with integral heat pipes; the heat generated is spread and dissipated at a much lower flux density over the entire surface of the radiator. This approach also permits more efficient use of available "real estate"—the area available for a radiator is seldom centered symmetrically about the heat source, facing the optimal direction.

Heat pipes have been used to reduce temperature gradients in structures to minimize thermal distortion. The telescope tube of the NASA Orbiting Astronomical Observatory (OAO) had three ring-shaped heat pipes to minimize circumferential temperature gradients. The ammonia heat pipes worked throughout the eight years of mission life.

The diode heat pipe was first proposed as a means of connecting a device to two radiator panels on opposite sides of a spacecraft, with the understanding that at least one of the radiators would be free of any direct solar load at all times during the orbit. The diodes would couple the device to the cold radiator, while preventing heat from leaking back into the system from the radiator in the sun. This type

of thermal-design problem, in which heat from a temporarily warm radiator or from a failed refrigerator must be kept from leaking back into the system, is an obvious application for a diode heat pipe.

The VCHP can control the amount of active radiator area, providing reasonably good temperature control without the use of heaters. This capability is particularly attractive if electrical power is limited, and this type of design has been flown on a number of satellite experiments. However, if the application requires maintaining a box or baseplate at a virtually constant temperature, feedback control (at the expense of some heater power) may be employed. A sensor on the baseplate of the device to be controlled can be routed to an onboard computer, and whenever the temperature drops below the desirable range, heaters on the VCHP reservoirs are activated, causing the control gas to expand and block off more of the radiator area. If the temperature rises above the range desired, power to the reservoir heaters is reduced, increasing the active radiator area. This concept usually requires less power than the direct use of heaters on the box or system to be controlled.

The use of flexible heat pipes or rotatable joints in heat pipes to cool devices on rotating or gimbaled platforms has been proposed, but flexible heat pipes tend to have too much resistance to motion, and rotating joints in heat-pipe walls leak under extreme conditions. These areas are still under active investigation.

Heat-Pipe References

More detailed discussions of a broad range of topics concerning heat-pipe design and applications can be found in Refs. 14.1 through 14.17. In addition, papers concerning new developments in heat-pipe design and analysis and discussing new applications, or the results of tests or experiments, are usually presented at the AIAA Thermophysics Conference. Volumes of proceedings from the International Heat Pipe Conference, which is held every four years, can be found in technical libraries.

LHPs and CPLs

Because of performance advantages, unique operational features, and recent successful flight experiments, the Western-heritage capillary pumped loops (CPLs) and the Russian-heritage loop heat pipes (LHPs) are rapidly gaining acceptance in the aerospace community. They are used as baseline thermal-control technology for a number of missions, including NASA's EOS-AM, GLAS, SWIFT, and GOES; ESA's ATLID; CNES's STENTOR; a retrofit mission for the Hubble Space Telescope (HST); and various commercial geosynchronous communication satellites.

Despite wide use of the emerging CPL and LHP technologies, fundamental confusion persists about their operation, limitations, and even their similarities and differences. This discussion, by engineers who have participated in CPL and LHP development on both sides of the Atlantic, explains the concepts behind them for potential users.

Initially many perceived CPLs and LHPs as alternatives to conventional heat pipes at high transport powers (> 500 W, with up to 24 kW demonstrated), but in recent years the intrinsic advantages of a small-diameter piping system without distributed wick structures have been exploited at low powers (20 to 100 W).

Many advantages of CPLs and LHPs are only truly exploited when these devices are considered early in the design phase, rather than treated as replacements for existing heat-pipe–based designs. Their advantages include:

- tolerance of large adverse tilts (a heat source up to 5 m above a heat sink, facilitating ground testing and even enabling many terrestrial applications)
- tolerance of complicated layouts and tortuous transport paths
- easy accommodation of flexible sections, make/break joints, and vibration isolation
- fast and strong diode action
- straightforward application in either fixed-conductance or variable-conductance (active-temperature-control) mode
- separation of heat-acquisition and -rejection components for independent optimization of heat transfer footprints and even integral independent bonding of those components into larger structures
- accommodation of mechanical pumps
- apparent tolerance of large amounts of noncondensable gases, which means an extended lifetime
- no vapor/liquid entrainment concerns or boiling limits

For this discussion, only single-evaporator systems such as those currently being baselined will be described. Multiple-evaporator as well as multicondenser systems are under active development by many parties, and they already have flight heritage in a flight experiment. However, to introduce the plethora of design options possible in those systems would cause unnecessary confusion in this basic discussion of LHPs, CPLs, and their advantages and disadvantages. Likewise, complications that can arise when multiple LHPs are networked together will not be addressed here.

CPL Overview

CPLs were invented in the United States in the 1960s, but active development on them did not begin until around 1980. Through most of the 1980s, NASA Goddard Space Flight Center (GSFC) sponsored the majority of CPL development with OAO Thermal Systems and Dynatherm (both now part of Swales Thermal Systems) performing a large part of the development and test effort. A typical single-evaporator CPL system, such as that used for several instruments on the EOS-AM spacecraft, is depicted in Fig. 14.12.

In this system, vapor generated by the evaporator flows to the condenser, where not only is it condensed, but also a certain amount of subcooling (5 to 10°C minimum) is generated. The liquid flows back toward the evaporator, whereupon it enters the core (the inner diameter) via an optional bayonet. One purpose of the bayonet is to position any gas or vapor voids nearest the coldest (incoming) liquid such that they are minimized. Often secondary wicks or arteries are positioned within the liquid core in an attempt to prevent any bubbles from axially blocking off portions of the wick, especially in microgravity environments. The liquid is pulled radially through the primary wick, and it is vaporized on the surface of that wick, where the meniscus exists, returning as vapor to the condenser.

A key problem for CPLs is vaporization within the liquid core of the evaporator. This vaporization can be caused by the back-conduction or so-called heat leak through the primary wick. The vapor can block the liquid core; this will prevent
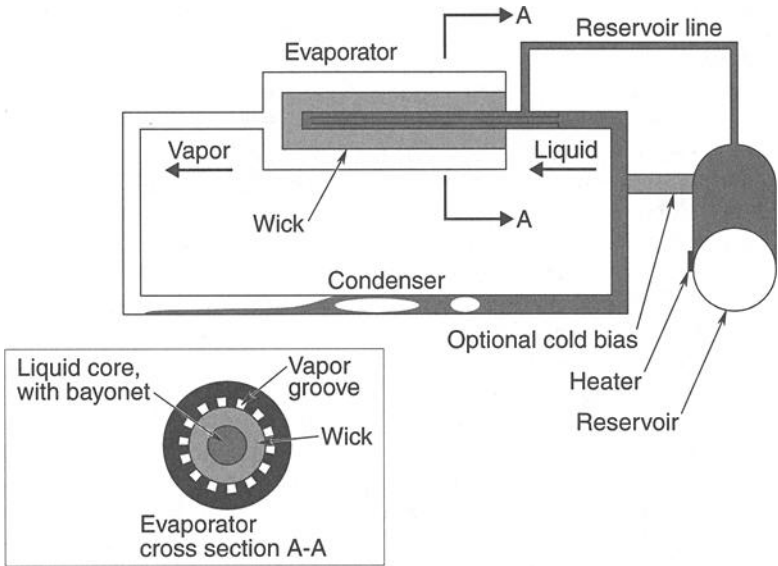
Fig. 14.12. Typical single-evaporator CPL.

proper supply of the evaporator with liquid, which in turn may result in evaporator dryout and CPL deprime (cessation of circulation).

Because this vaporization is possible, the traditional CPL employs an evaporator with a wick of polyethylene. Although the low conductivity of that material greatly reduces back-conduction, and although it is very easy to work with, its pore sizes are relatively large (15–20 μm), and consistent, inexpensive suppliers of the material are scarce. Polyethylene wicks are used in the EOS-AM, MSP, and HST missions, but future CPL wicks will probably use alternate materials such as titanium or ceramics.

CPLs feature a reservoir plumbed into the liquid line of the loop, and perhaps thermally connected to that line for temperature-control purposes, although other relatively weak sources of cold-biasing also suffice. The EOS-AM and HST CPLs, for example, use externally mounted reservoirs for mission-specific reasons, whereas in other CPL designs the reservoir is internal and cold-biased via a thermal connection to the liquid line.

In modern CPLs, the reservoir is plumbed into the evaporator itself using a very thin line, making the evaporator a "flow-through," "three-port," or "starter-pump" (a historical misnomer) design. No capillary connection links the reservoir and the evaporator, as is the case with LHPs, although additional wicks or baffles are almost always used within the CPL reservoir, to manage the two phases in that device.

The CPL reservoir is heated above the evaporator's temperature before start-up to ensure that liquid is in the wick and that bubbles in the evaporator core have been collapsed. Thus, the only void in the system exists within the reservoir before start-up. As the reservoir cools and/or the evaporator warms, boiling eventually

takes place on the vapor side of the evaporator (perhaps even violently if the evaporator superheats); vapor fills the vapor line and condenser, which pushes liquid into the reservoir. Advantage is taken of this rapid liquid displacement to flush the evaporator core of bubbles that may have been created during the initial boiling or during the stressful clearing of the vapor line (the "purge surge").

The reservoir is oversized such that a void always exists within it. This makes the devices operate in a variable-conductance mode, wherein the temperature of the thermally remote reservoir controls the evaporator temperature, and the condenser floods (i.e., is thermally "blocked" with liquid, with little energy exchange occurring in the liquid region compared to the two-phase region) as needed such that the overall conductance of the device is controlled by this reservoir temperature. The EOS-AM unit is such a variable-conductance design, as were the COMET CPLs (which were never flown, because of an unrelated mission failure) and the HST design.

In the late 1980s, the fixed-conductance mode of operation was invented to deal with the problems associated with multiple CPLs operating in parallel. If too much heat is added to a variable-conductance CPL and the reservoir is oversized, then the condenser will open up too much and either lose too much subcooling or, worse, let vapor pass to the evaporator. "Fixed-conductance mode" simply means that the reservoir and charge have been sized such that the reservoir becomes hard-filled with liquid before this "overdrive" failure mode is encountered. When excessive heat is added to a CPL that operates in a fixed-conductance mode, the temperature of the loop simply rises as the reservoir ceases to control the saturation temperature of the loop. In many ways, a fixed-conductance CPL regulates its own subcooling just as an LHP does.

Unfortunately, the fixed-conductance CPL is susceptible to start-up failures when the evaporator is thermally attached to a significant mass and/or enough noncondensable gas is present. For these reasons, the fixed-conductance CPL concept was abandoned. Because LHPs can experience start-up difficulties for similar reasons, however, the lessons learned from the fixed-conductance CPL should not be lost. Fortunately, in LHPs an alternative is available that has no counterpart in CPLs—compensation-chamber (CC) cooling. Start-up of LHPs is described in more detail below.

An alternative design measure that also avoids loss of subcooling at high powers and/or warm environments was employed successfully in the HST CPL. That design relies on a control system to heat the reservoir as needed to maintain subcooling, in effect simulating the fixed-conductance mode while maintaining a void in the reservoir. The substantial length and large diameter of the liquid line in this system yielded a long time constant of approximately 20 minutes, which provided considerable latitude in the design of the reservoir heater-control system. Application of this heater-control technique to smaller CPLs remains to be demonstrated.

As with LHPs, many variations of single-evaporator CPLs are possible; this makes the technology confusing to the outsider accustomed to working within the constraints of heat pipes, which have constant cross sections and few if any plumbing or arrangement options. One would perhaps not even recognize as the same device the CPLs used on the EOS-AM, HST, and COMET missions—each was highly customized.

An even more dramatic variation was achieved in 1993 with the creation of the first cryogenic (80 K) CPL, which used nitrogen (and later was recharged and retested with neon) as a working fluid. These miniature (0.5–5.0 W) devices, which introduced new components such as the "hot" (room temperature) reservoir, are able to start with a room-temperature evaporator in an unflooded (indeed, superheated and perhaps even supercritical) loop. Flight tests of this device in 1998 proved its zero-g performance and reliable startup in microgravity.

LHP Overview

LHPs were invented in Sverdlovsk (now Ekaterinburg), Russia, by scientists from the Institute of Thermal Physics of the Ural branch of the Russian Academy of Sciences. In the early 1980s the first Russian and U.S. patents, as well as some European patents, were issued. Originally the LHP was called the antigravitational heat pipe, but in the late 1980s it was renamed loop heat pipe. A large role in LHP evolution and the adaptation of preliminary concepts to practical design applications was played by the Lavochkin Association (Khimky, Russia) of RKA (Russian Space Agency) and HPO PM Krasnoyarsk (Russia).

The traditional schematic of an LHP is presented in Fig. 14.13. A classical LHP consists of evaporator and CC assembly, condenser, and transport lines. The specific configuration of an LHP is determined by the application.

As mentioned above, both an LHP and a CPL theoretically only require wick material in the active evaporator zone; the remainder of the LHP is wickless tubing (condensers can use various designs, but they need not contain any wicks). As with a CPL's reservoir, the LHP's analogous CC normally also contains some wick structure with properties different from evaporator wick structure, but such "secondary wicks" are not strictly necessary; they merely enhance performance and robustness and help adapt an LHP to zero-g applications.
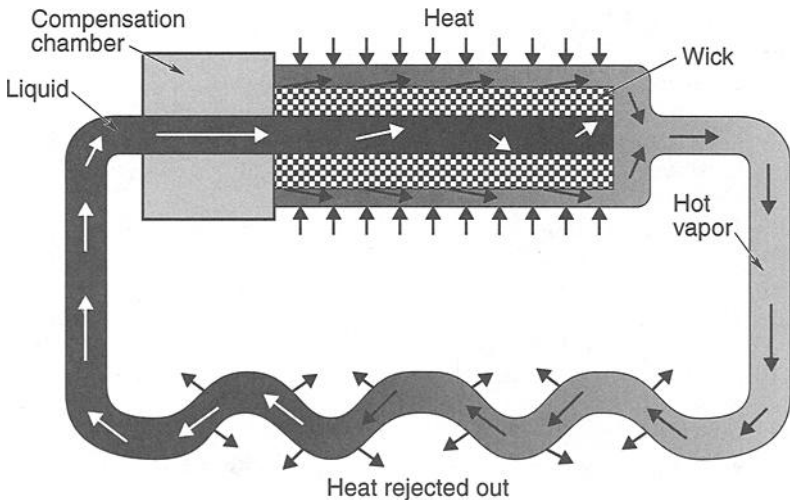
Fig. 14.13. Classical LHP with direct-condensation condenser.

Traditionally, the evaporator consists of a cylindrical metallic case with the wick inserted into it. The case then either is attached to the heat-acquisition surface or actually forms the surface itself. Several successful attempts were made to create a "flat" evaporator with platelike case; however in most cases the internal pressure of the LHP system is so high that pressure-containment considerations dominate the evaporator design, and walls of such an evaporator case would be too thick.

A network of vapor-removing channels is formed at the area of contact between body and the wick. This area is considered the active evaporator area.

The CC shares liquid with the inside of the primary wick in the evaporator (i.e., the liquid core). This sharing is accomplished either by gravitational forces or via the use of a secondary distribution wick. Vapor and liquid lines enter and exit the evaporator and CC assembly. The liquid return in an LHP flows either into or through the CC (unlike the return in a CPL, which does not flow into or through the reservoir), with intimate thermal contact with the CC's contents. The CC is a critical component: Its design has to be considered very carefully, because its sizing affects the performance of the LHP (conductance, maximum power, minimum start-up power, etc.).

The condenser of an LHP plays the same role as the condenser of a CPL: It condenses the vapor that was generated in the evaporator and transfers heat to the sink (by any means: conduction, radiation, or convection). ESA has performed a detailed study of different types of condensers for space application.[14.18] For modern space applications two types are usually considered in trade-off studies: direct and indirect. Direct condensation assumes that the condenser has been designed as tubing network (parallel or series) attached directly to the radiator facesheet (or another heat-rejecting device). Indirect condensation assumes that an additional interface is interposed between the surface of condensation and the heat sink, which in most cases is a heat exchanger to the evaporator of a heat pipe. Both approaches have advantages and disadvantages, as detailed in Ref. 14.18.

Transport lines are simply smooth tubing without capillary structure.

The selection of materials for LHP components as well as the working fluid is the subject of detailed study during the design phase. The most studied and reliable combination of LHP materials includes stainless steel, aluminum, nickel, and ammonia. This combination was experimentally proven compatible, and the compatibility minimizes noncondensable gas generation. (Noncondensable gases and physical leakage are the two most important factors that can reduce LHP lifetime.) A detailed experimental study[14.19] of LHPs with this combination of materials showed that even the most conservative predictions of the noncondensable gas volume generated at the end of life in such an LHP does not cause much distortion in LHP behavior and performance. Alternate LHP materials include nickel for the evaporator body, porous titanium for the wick, and propylene for the working fluid.

To simplify consideration of LHP operation, an LHP with a very simple, classical point design will be discussed: a single evaporator combined with CC, serial direct-condensation condenser, and semiflexible transport lines. The working fluid is ammonia.

LHP designers consider three cases of LHP operation:

- **Cold case.** In the cold case, zero power is applied to the evaporator, and condenser and transport lines are exposed to coldest environment conditions. The

most conservative assumption in this case is that the entire loop (other than most of the CC) is liquid filled, including the primary wick and the evaporator's vapor exhaust grooves.

- **Hot case.** In the hot case, maximum power is applied, and the rest of the loop is exposed to the hottest environmental conditions. The assumed fluid distribution in a hot case is as follows: The vapor exhaust grooves in the primary wick, the vapor line, and the condenser are filled with vapor, while the primary wick, the liquid line, and most of the CC are filled with liquid.
- **Maximum nonoperating temperature.** In the third case, which is often a driver in LHP design, the exposure is to the maximum temperature under non-operating conditions (storage, transportation, perhaps some manufacturing process like bonding) after the loop has been charged with the working fluid. The concern with this case is that enough void must remain in the loop to avoid bursting as a result of hydrostatic pressures.

The hot case is used to size the radiator to allow rejection of the heat without overheating the payload, and without hard-filling the CC with warm (low-density) liquid (such a condition would lead to condenser blockage). In the cold case the designer must worry about the potential freezing of the system along with the requirement that some liquid must exist within the CC despite the high density of the cold fluid. The name "compensation chamber" ("hydroaccumulator" and "reservoir" are frequently used as synonyms) derives from the main purpose of that volume, to compensate for the thermal expansion of the working fluid at different operating temperatures. In other words, the main idea of the LHP is to have the CC and the fluid charge sized in a manner that provides enough liquid in the cold case to keep the evaporator wetted before start-up, yet prevent condenser blockage in the hot case.

The typical performance curve (temperature vs. power) of a classical LHP design is presented in Fig. 14.14. The shapes of the hot- and cold-case curves are
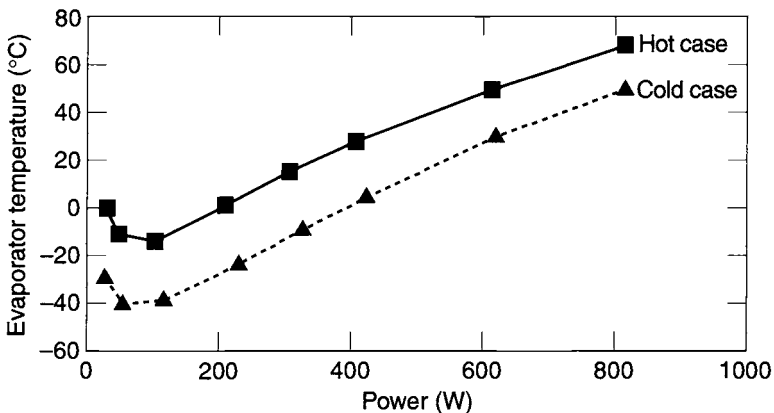
Fig. 14.14. Typical performance curves of an LHP hot case (T_{sink} = 233 K) and cold case (T_{sink} = 153 K).

identical. The only difference between the cases—operating temperature—results from different sink conditions. The performance curve of a classical LHP consists of two parts: the variable-conductance mode (the curved line at lower powers), and the constant-conductance mode (the straight line at higher powers).

The curves in Fig. 14.14 show the evaporator-case temperature as a function of heat input. This type of curve is common whenever the sink temperature is lower than the ambient temperature. In the figure, the evaporator temperature at low powers (up to about 100 W for this particular loop in this particular environment) drops with increasing power (the drop corresponds to a decrease in the overall resistance), until a minimum temperature is reached. As power continues to increase, the curve of T versus Q has a positive slope and its shape approaches a straight line; the overall resistance is nearly constant in this regime. There is a difference between evaporator and vapor temperatures as a result of the finite evaporator resistance. This difference is zero at low powers and increases linearly with power.

This particular behavior is directly related to the location of the CC and its coupling to the evaporator. When power is applied to the evaporator, a capillary pressure difference across the wick develops to sustain the pressure drop created by the hydraulic resistance of the transport lines and condenser. This capillary pressure must also sustain the gravity head of the liquid column in the return line (if the evaporator is located higher than the condenser). The pressure difference across the wick, which is the driving force of the working fluid in any LHP, also creates a corresponding temperature difference across this wick as a result of the Clausius-Clapeyron relationship. The resulting heat leak can eventually increase the CC temperature (and pressure) to the point where the driving potential of the pressure difference will not be able to move working fluid through the loop. In a real LHP system, such a heat leak is compensated by the subcooling of the liquid that enters the CC from the condenser. This subcooling is generated in the condenser by its partial "blockage." When powers applied to the LHP are low, the small flow rate in the loop means very little liquid is flowing into the CC. In such low-power cases, the CC temperature is dominated by its heat exchange with the evaporator and with the environment.

This effect can be illustrated by a simple model of the CC thermal balance. The required subcooling (Q_{subcool}) that needs to be generated in the condenser must equal the sum of the heat leaks to the CC: heat leaked through the environment (Q_{CC}), heat leaked through the wick and evaporator structure and environment (Q_{wick}), and heat applied to the liquid line ($Q_{\text{liq-line}}$):

$$Q_{\text{subcool}} \approx Q_{\text{CC}} + Q_{\text{wick}} + Q_{\text{liq-line}}. \tag{14.2}$$

The generated subcooling brought into the evaporator can be determined using the following simple equation, where m is the mass flow rate determined by the applied power and the latent heat of the working fluid ($m \approx Q_{\text{loop}}/H_{fg}$) and $\Delta T_{\text{subcool}}$ is the difference between the saturation temperature of the loop and the temperature of the liquid exiting the condenser:

$$m \cdot C_p \cdot \Delta T_{\text{subcool}} = Q_{\text{subcool}}. \tag{14.3}$$

At low powers the flow rate m is small and $\Delta T_{\text{subcool}}$ is limited by the sink temperature. Therefore the required and actual subcooling are not equal, and the thermal balance of the CC will be dominated by the parasitic heat leaks (from the wick and the environment), which will increase the system temperature to the point where $\Delta T_{\text{subcool}}$ will be high enough to satisfy the balance between the required and generated subcooling.

At zero flow there is no capillary pressure difference across the wick of a horizontal (or microgravity-based) LHP and, because saturation conditions exist on both sides of the wick, no temperature gradient. Consequently, the only heat input to the CC is from the environment, and the CC's temperature will equal the ambient temperature. As the heat is applied to the evaporator, some degree of subcooled liquid starts to enter the CC. As the heat input increases, more (and cooler) liquid from the condenser gradually lowers the temperature of the CC. The saturation temperature follows the downward trend because the subcooling production increases while the parasitic heat leaks into the CC remain approximately unchanged.

If the sink temperature is constant, the decrease in evaporator temperature is synonymous with increasing heat-pipe conductance. As with any heat pipe, the overall conductance of an LHP is determined by the evaporator and condenser conductances:

$$1/C_{\text{overall}} = 1/C_{\text{evap}} + 1/C_{\text{con}}. \tag{14.4}$$

The evaporator conductance is normally assumed to be constant; thus the increase in overall conductance with increasing power must be the result of increasing condenser conductance. This is explained by gradual displacement of liquid from the condenser (i.e., movement of the last two-phase point within the condenser) and the subsequent exposure of more condenser length for two-phase heat exchange.

At zero or very small power levels, only a short section of the condenser is active, and the remainder is filled with liquid, producing as much subcooling as possible in an attempt to compensate parasitic heat leaks into the CC, but being limited by the low flow rate.

As the power is increased, more and more condenser area becomes active and the overall conductance of the LHP continues to increase. In this mode of operation, the LHP behaves like a variable-conductance heat pipe (VCHP). The range of power over which the VCHP behavior applies and the exact nature of the accompanying temperature changes depend on the design of the LHP as well as on the current temperatures of the sink and the environment.

At a certain power the condenser is completely active, reserving only a very small percentage of its length to produce the required subcooling. Further increase in the condenser conductance is no longer possible. To reject additional power, the driving potential between condenser and sink must increase, resulting in an increased saturation temperature. From this point, the LHP behaves like a fixed-conductance heat pipe (FCHP): The temperature difference between evaporator and condenser increases linearly with power.

The physics of LHP operation were well studied in the former Soviet Union, the device's country of origin. One of the most detailed publications on LHP fundamentals is Ref 14.20.

CPLs vs. LHPs

The distinction between CPLs and LHPs is historical and controversial. Coming from different heritages, they were associated with different design philosophies. Each approach has some basic pros and cons. Because both CPLs and LHPs are relatively new to many users, difficulties associated with their application to modern spacecraft are described in this section along with their relative merits.

The approaches share many similarities;[*] one can even build devices that are somewhere between a traditional CPL approach and a traditional LHP approach; these have their own advantages and disadvantages. Therefore, although the following sections concentrate on the distinctions between the traditional CPL and LHP approaches from the standpoint of a potential user, remember that extensive design flexibility exists for customizing these devices, and that the distinctions are given only to help explain the fundamentals of their operation, not to replace critical consultations that should be sought when making procurement decisions.

Distinguishing the Two Traditional Loops

The basic distinction between a traditional CPL and a traditional LHP lies in the fluidic and thermal attachment of the reservoir or CC. This seemingly simple distinction has a large impact on the design and operation of the loop.

In a traditional CPL, the circulating fluid does not pass through the reservoir. Instead, the reservoir is attached to the liquid side of the loop by a small-diameter line whose time-averaged flow rate is zero under steady conditions. Although not strictly necessary, the returning subcooled liquid is usually thermally (but not fluidically) connected to the reservoir, providing a cold bias for control purposes instead of (or in addition to) any cold bias afforded by heat losses to the reservoir's thermal environment. The CPL reservoir may therefore be located anyplace. Although wicks are located within the reservoir for phase-management purposes, no wick connections are between the reservoir and the evaporator, much less any other part of the loop. The loop is sized such that liquid with adequate subcooling is always supplied to the evaporator, perhaps via the use of a feedback-controlled heater on the reservoir, as with the HST CPL.

In a traditional LHP, on the other hand, the CC (the LHP equivalent of the CPL reservoir) must have a good flow path between the liquid within it and the main evaporator wick to provide reliable operation in transient modes. Unless gravity is available to maintain this path, a secondary wick is used. Because the liquid return flow often flows into or through the CC, the thermal connection between the liquid line and the CC can be essentially infinite. The evaporator liquid core is normally considered to be part of the CC. The loop is sized and charged with working fluid such that the CC can never be completely filled with liquid nor completely void of liquid.

Start-Up

In addition to advantages that CPLs and LHPs offer over mechanically pumped systems and conventional heat pipes, these systems introduce a particularly

---

[*]For example, a fixed-conductance CPL with a void in the evaporator core is thermodynamically identical to an LHP. Although this is an "off design" condition for a CPL, it is a normal operating point for an LHP.

important feature: start-up assurance. Two-phase systems require some degree of preconditioning to achieve a proper and reliable start-up.

From the very early days of two-phase loop development, an understanding of the start-up phenomena was the focus of technology developers on both sides of the Atlantic. This attention was warranted because the ideal LHP starts without any concern for orientation, history, or preconditioning. An LHP does not require such extensive preconditioning and in most cases does not require any at all. As soon as the temperature gradient between the CC and the evaporator (i.e., the temperature gradient across the wick) is big enough to build up the pressure difference required to initiate circulation, the LHP starts. The only problem with LHP start-up is achieving this threshold gradient. CPLs, on the other hand, cannot start without intentional preconditioning of the system. This preconditioning consists of flooding the capillary pump and the vapor line with liquid by heating the reservoir a few degrees (perhaps 5 to 15°C) above the evaporator for a period lasting from 30 minutes to 3 hours.[14.21–14.25]

The start-up process for two-phase systems is very complicated: Many random and design-specific factors can prevent successful start-up. Both CPLs and LHPs can experience problems starting with very low powers (heat flux is a very important parameter), or in the presence of heavy masses attached to the evaporator (the thermal mass affects the evaporator heating rate, and the rate at which heat penetrates into the CC). However, the LHP is especially susceptible to these problems when the low-power start-up is experienced following diode operation or very cold conditions, when large amounts of gas are present, or when the evaporator is elevated above the condenser.

A successful start-up is characterized by the generation and maintenance of an adequate temperature difference across the evaporator. This threshold temperature difference is evaporator design-specific and is also affected by application requirements, environmental conditions, and even prior usage history. Because of the unknown state of the wick core, start-up can occur in a number of ways, and the exact scenario is unpredictable without knowledge of the recent history of the loop. (This does not mean that computational predictions cannot be used as a design tool, only that conservatisms and enveloping are required to accommodate uncertainties.) Some LHP designs, especially those operating at mid and high powers, do not require any additional start-up precautions.

One of the first publications that summarized the basic understanding of the processes that occur in the LHP evaporator before, during, and after the start-up event was the referenced paper by Maidanik *et al.*[14.26] Maidanik *et al.* presented another paper on this subject at the following ICES conference.[14.27] These two publications were the first to describe the basic physics of the LHP start-up process. Subsequently, a number of studies were performed to investigate the transient behavior of LHPs and to create a better understanding of the start-up phenomena.

As mentioned above, LHPs were always intended as devices that would neither cause start-up problems nor require special treatment. They were therefore initially represented as self-starting, worry-free heat-transfer devices that (when compared to CPLs) do not require complicated start-up procedures. This declaration was repeated in presentations and papers for several years: "An LHP does not require any in-orbit operation approach because it is a passive, self-starting device

that does not require external power or any preconditioning. An LHP starts when the heat load is applied and operates until the heat load is removed or the sink conditions cannot maintain the operating temperature range." This statement contrasted strongly with descriptions of CPLs, some of which at the time were suffering from start-up difficulties despite the care given to preconditioning.

Unfortunately, recent investigations have demonstrated that LHP start-up is not so simple, and its requirements must be considered more carefully. In recent years, basic understanding of the start-up behavior was further developed. This research has provided LHP designers and users with more confidence, trust, and flexibility in utilizing LHPs in realistic applications.

In a nutshell, start-up is not to be treated lightly for either device: Both can exhibit anomalous behavior, as is described below along with possible solutions. One of the key distinctions of the LHP in this regard, however, is the availability of certain success-enhancing design measures not applicable to CPLs, giving LHPs an edge.

The dynamics and design solutions associated with LHP start-up are described in more detail below. Start-up is a greater concern with LHPs than with CPLs, but although it is an area of concern for both devices, it is more frequently overlooked by engineers considering LHP solutions. It is important to note that many of the same physical processes that occur in LHPs during start-up occur as well in CPLs.

Assisted Startup: Active Design Measures

The wide range of LHP and CPL applications includes design cases in which these loops may require start-up assistance. The assistance may be necessary because of an insufficient level of evaporator heat flux, an excessively high "heat leak" through the wick into the liquid core or, in case of an LHP, an unfavorably warm CC (the liquid core of the evaporator is usually considered to be an integral part of the CC). The heat flux applied to the evaporator should be sufficient to generate the required superheat on the outer surface of the primary wick. However, in some cases, the heat flux applied is insufficient to superheat the liquid on the outer surface of the evaporator or to overcome gas or adverse tilt without also heating the liquid core of the evaporator. This lack of sufficient heat flux can result from insufficient power being applied to an evaporator with a large evaporation surface, or to a large mass attached to the evaporator, or to an attached redundant system (i.e., another LHP, CPL, or other heat-transfer device attached to the same heat source for redundancy).

Certain combinations of initial conditions and mission scenarios can be dangerous because they can, in some cases, lead to start-up problems. Fortunately, these potential problems are related to the difficulties associated with creating the minimum required temperature gradient across the wick, so active design measures can be implemented to assist the two-phase system in establishing this gradient—either by heating the outside of the wick or by cooling the inside of the wick (effectively, by cooling the CC).

The first method, heating the outside of the wick, is the simplest and most popular. A starter heater is mounted onto the evaporator surface. This starter heater need not be of high wattage; the main requirement for this heater is to add a concentrated local heat flux to the normal distributed heat load on the evaporator, at

least when superheat for nucleation is the concern. This concentrated flux heats the local area under the heater much faster than it creates heat leaks into the wick. As a result, local superheat is created, and as soon as it exceeds the critical value, the vaporization will start. The initial vapor bubble will grow explosively if the liquid has been superheated, expanding into the rest of the vapor space of the evaporator. In an LHP or in a three-port CPL evaporator system, this expansion and extensive vaporization will force the colder liquid from the condenser and liquid line to enter the evaporator core (and in the case of an LHP, the CC as well), initiating loop circulation.

Starter heaters for specific applications can have different designs, but the main requirement is to maximize the heat flux over a localized area. A number of different types of starter heaters, from a bulky cartridge resistance heater to a very light but fragile ceramic heater, were proven to be sufficient aid for various designs. Normally, film heaters cannot provide the desired heat flux and can be used only with some design restrictions. Starter heaters can be defeated by thick, highly conductive evaporator cases and by tight thermal connections to massive plates and payloads (or even to redundant LHPs and traditional heat pipes), so careful design is required.

Unfortunately, because they must necessarily be small, starter heaters (though they may be effective at overcoming incipient superheat thresholds) are less effective at establishing gradients across the wick as needed to overcome gas and adverse tilt conditions. In those cases, the alternate strategy may be applicable: cooling the CC. This second design measure is neither as simple nor as common as the first and can only be applied to LHPs. In the early 1990s this method was proposed by Russian authors to enhance the start-up performance of LHPs designed for applications with special requirements.[14.28]

The use of thermoelectric coolers (TECs, also called Peltier coolers) to cool the CC became well known. This method was even "baselined" by a few companies as a solution for their LHP start-up problems. The cold side of the thermoelectric element is attached to the CC surface, and the TEC's hot side is attached to the evaporator via a thermal shunt. The electric energy applied to the TEC will not only cool the CC but will heat the evaporator as well, enhancing the positive effects of CC cooling.

This active design measure has two disadvantages. The major disadvantage is the need for a special high-current, low-voltage power supply. The other one can be major without proper design: The TEC can become a very effective condenser for vapor generated on the internal surface of the primary wick. If a vapor bubble is present in the wick core, the TEC will assist an internal "heat-pipe effect" that can hinder the creation of the required temperature difference. If established, this internal heat-pipe effect eliminates all advantages of the TEC approach because it extracts heat from the evaporator.

Subcooling and Overall Conductance

CPLs and LHPs require different degrees of subcooling, because of their different thermodynamic processes. An LHP requires some subcooling to compensate the heat leak from the evaporator and environment to the CC, which is usually very small (less than a watt). However, because flow rates are so low and so little

energy is available via the sensible cooling that subcooling represents, these fractions of a watt can translate into several degrees of required subcooling. This same sensitivity applies to CPLs, although their requirements for subcooling are even larger.

Theoretically, a CPL should require no subcooling, and because it normally has no void in the liquid side of the wick, it can even operate with superheated liquid (this has, in fact, been demonstrated). However, in practice a CPL requires subcooling both (like an LHP) to compensate for the heat leaks into the liquid part of the system, including back-conduction through the wick, and (unlike an LHP) to guarantee that any vapor bubbles that occasionally appear in the liquid core will be collapsed or at least will not grow without bound. In other words, under ideal conditions a CPL requires less subcooling than an LHP. However, in practice a CPL's sensitivity to vapor blockage means that, to operate robustly, more subcooling must be designed into the system than is theoretically required. Given the same wicks, a CPL will require more subcooling and therefore have a lower overall loop conductance. (However, recall that CPLs traditionally have been made with lower conductivity and lower-pore-size plastic wicks, so the above generalization has not always been evident.)

To appreciate basic differences between a CPL and an LHP, consider the addition of a small amount of heat to the liquid line in both systems. The extra heat appears to have no effect on a CPL; temperatures do not change. This makes the performance of CPLs relatively easy to predict. In essence, some of the "overdesign" in subcooling is used to compensate for this heat addition. However, if the amount of heat is raised sufficiently (on the order of perhaps 10 W), the CPL will deprime (i.e., fluid will cease to circulate), and the evaporator temperature will increase without bound unless a reprime cycle (heating of the reservoir) is initiated. In other words, once the liquid-line heating either generates bubbles in the liquid line or causes a preexisting bubble in the evaporator core to grow excessively, the evaporator wick will be starved of liquid and will deprime.

An LHP acts very differently. Even small amounts of energy (e.g., tenths of a watt) added to the liquid line cause a noticeable change in temperatures and overall conductance, especially at low powers. However, continuing to add energy does not result in an abrupt deprime of the LHP as it does the CPL: The temperature of the evaporator will simply continue to grow relative to the condenser. In effect, the LHP autonomously changes its state as needed to generate enough subcooling to counterbalance the applied heating, a feat that cannot be matched by a CPL except by addition of a reservoir heater controller. If a large enough heat rate is applied to the liquid line, however, an LHP will eventually deprime, but it will be a more graceful shutdown than would be the case with a CPL.

The performance of a CPL is like a step function: Either it continues with no change, or it fails. An LHP's performance is more like a ramp function: It changes in response to environmental (thermal or gravitational) changes, but it does not so much fail as degrade gracefully in response to adverse conditions.

Robustness

The LHP is arguably the more robust device of the two. If a CPL does not have adequate subcooling on average, perhaps because of a design or implementation

problem, it will deprime. On the other hand, if an LHP does not have adequate subcooling, its operating temperature will simply rise to create sufficient subcooling. To oversimplify, minimum subcooling graphically represents a "cliff" to a CPL, a point beyond which the device cannot operate, whereas an LHP (in its so-called "autoregulating" mode) will always adjust itself to maintain the required subcooling.

Ultimately, the CPL is sensitive to bubbles within the evaporator core, lacking a good mechanism for removing or collapsing them other than subcooling. The LHP responds more gracefully to bubbles. The loop conductance decreases, but does not abruptly shut down.

Reservoir Location

A disadvantage of the LHP as compared to the CPL is that the CC of an LHP must be physically very close to the evaporator because they share fluid either directly or via a relatively weak capillary link. This requirement can cause integration difficulties, because the CC is often relatively large. Worse, it is sensitive to heat gains: Packaging the evaporator and CC assembly next to a heat source can be difficult in some applications, because real estate near the source is often scarce. For example, embedding the evaporator and CC assembly within honeycomb panels is difficult because a strong thermal connection must be made with the evaporator, while the CC must be thermally isolated from the source.

The CPL's reservoir, on the other hand, is connected to the evaporator via a very-small-diameter line that can be arbitrarily long. Also, the reservoir in a CPL is not as sensitive to heat leaks. The evaporator is a separate unit that is amenable to integration into planar baseplates. Therefore, in some applications CPLs can be easier to integrate than LHPs.

Controllability

Both CPLs and LHPs can be controlled to maintain set-point temperatures. Because subcooled liquid flows directly through its CC, an LHP usually requires somewhat greater heater power to maintain a set point in cold modes of operation,[*] but in both cases only a very small fraction of the loop power is needed to control the set point. The ease with which such control can be added to these loops may confuse engineers familiar with traditional heat pipes. In those devices, temperature control is achieved not simply by adding a thermostatic heater, but by effecting a complete change in design (from fixed to variable conductance) with a corresponding jump in cost and complexity. With CPLs and LHPs, control is rather easily added to the design if required (Fig. 14.15).

It is useful to note differences in the process by which control is achieved. The heating of the CPL reservoir causes the additional thermal blockage of the condenser, and accordingly affects the maintenance of the system temperature level. (That level changes as a result of the reduction of the effective condensation area.) The amount of heat required on the reservoir to maintain a set point is therefore a

---

[*]On the other hand, in an LHP the heat for such control can be extracted in part from the payload dissipation itself by a thermal connection between the vapor and liquid lines, or even via the introduction of a three-way valve.
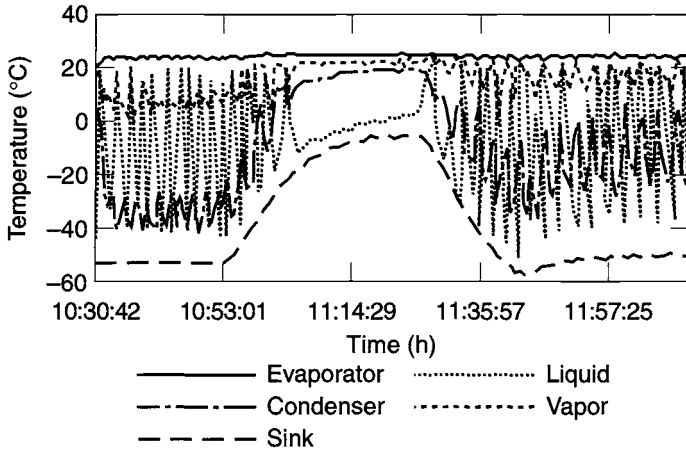
Fig. 14.15. Typical LHP behavior in case of active regulation (maintain the evaporator set point, 21°C, at 100 W and sink transient –60°C to +5°C to –60°C).

function of its local thermal environment and is unrelated to the loop operation. The heating of the LHP CC also causes condenser blockage but by a somewhat different mechanism: the need to generate sufficient subcooling to offset the heat added to the CC. This statement is illustrated in Fig. 14.16.
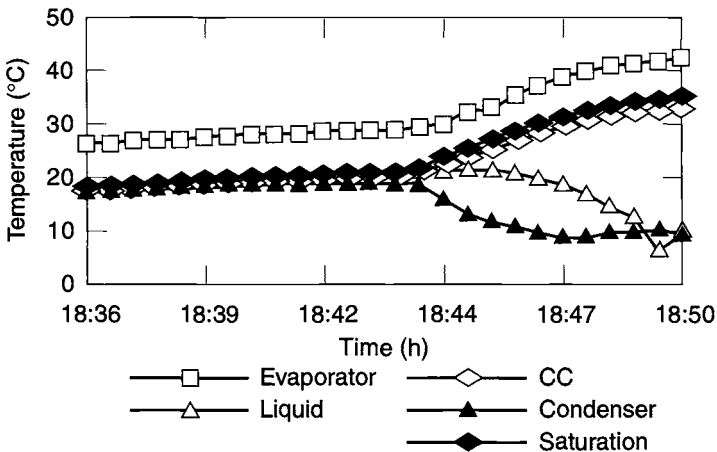
Fig. 14.16. Typical LHP temperature history with the heating of the CC, 30 W, applied (the LHP was running at 400 W).

Selecting a Design

The thermal engineer is responsible for selecting the simplest and safest system that will suffice; therefore, simple fixed-conductance heat pipes should be chosen if possible. However, given the occasional disadvantages of heat-pipe systems (many of which are apparent only upon producing a complete design from scratch that takes advantage of the unique features of LHPs and CPLs), a loop design may be compelling if not enabling.

The top-level selection of an LHP or CPL architecture should be made with care. Remember that certain mission-specific requirements may dictate the choice, and that these devices both have tremendous design flexibility to accommodate specific requirements. This flexibility includes the creation of devices that are not easily classified but exhibit both CPL and LHP characteristics. At the risk of over-generalizing, however, the following ideas should serve as guidelines.

LHPs are simpler and usually more robust than CPLs. They exhibit turnkey start-up, tolerance of inadvertent liquid-line heat leaks or loss of condensation, etc. Somewhat like a thermal analogy to electrical extension cords, they are excellent choices for retrofits or cases where any improvement is helpful though the path between the source and the sink may be tortuous. Just as simple heat pipes should be attempted before using loop designs, LHPs should be attempted before using CPLs.

CPLs find application in cases where more mission involvement is either tolerated or desired, such as missions demanding active reprime contingencies, and of course missions that are tolerant of preconditioning requirements before the initial start-up. The remoteness of a CPL's reservoir may cause start-up disadvantages but can also be the source of some of the CPL's advantages. The reservoir of a CPL can be attached remotely in almost any convenient location and can thus enable the design to avoid LHP difficulties caused by the need to locate a CC (that is rather sensitive to heat additions) with an evaporator in areas where real estate is usually limited.

For example, in the case of a start-up cryogenic loop, the ability to collocate the reservoir near the condenser instead of the evaporator (thus avoiding the need for a separate cryocooler to precool the CC of a cryogenic LHP[*]) provides CPLs with a design advantage at those temperature ranges.

Analysis Tools

The original developers of LHP technology, working at the Russian company TAIS, created a single-evaporator LHP model using a Pascal interpreter more than 10 years ago. Since then, this model has been upgraded several times. Swales Aerospace developed several versions of a mathematical model in spreadsheet format. Other companies develop their own software in-house.

C&R makes available a free SinapsPlus "prebuilt" model with graphical spreadsheet-like access to an underlying SINDA/FLUINT thermal/ hydraulic model of a generic LHP that allows users to estimate the performance of an LHP in

---

[*]A competing LHP concept is to use two or more loops in parallel with different working fluids: One (perhaps using propylene) is used at high temperatures to bring the temperature of the other loop's CC down to where it can begin to operate.

steady-state and transient modes. This prebuilt is intended both as a demonstration of LHP modeling techniques and as template for trade-study and system-integration models.[*] It can be used with or without SinapsPlus, and requires no software purchases.

These models take into account both the energy balance of the CC and the pressure drop along the fluid paths in the loop. It is impossible to achieve good analytical correlation of the predicted thermal performance of an LHP to test data without tracking minor heat leaks and boundary conditions (especially of the liquid line and the CC) and accurately modeling the pressure drops in the system, which affect the back-conduction term in the CC. Short time-scale thermal/hydraulic transients (such as start-up phenomena, noncondensable gas effects, condenser quenching, etc.) have been analyzed using SINDA/FLUINT (Refs. 14.29 and 14.30, for example), but often this level of detail is needed by CPL/LHP developers and researchers, not users.

SINDA/FLUINT is similarly used for steady-state and transient CPL analyses, although no starting-point CPL prebuilt is yet available, in part because much more variation is available in CPL designs. Models built for various publicly funded systems (EOS-AM, CAPL II, CAPL III, HST) are available, however. C&R provides free training notes for use in modeling capillary systems such as LHPs and CPLs using SINDA/FLUINT.

In modeling CPLs, one need not track pressure losses and heat leaks to predict thermal performance, provided that adequate margin is applied to the design in the first place. However, some analysis cases for CPLs are not normally applied to LHPs. These include start-up from a hard-filled state (a case that is often adequately analyzed using pseudosteady bracketing studies) and pressure oscillations. (The latter phenomena may also occur in an LHP, but they are usually less of a concern.)

In both CPLs and LHPs, rather simple models suffice to characterize the transport lines, evaporators, and reservoirs for steady states or thermally dominated transients. More detail is often needed, however, in modeling condensers, where thermal performance is a function of layout (which can be quite varied and customized), bonding and integration options, orbital environment, etc. Accurate predictions of subcooling production are important for both systems, but especially for LHPs. Fortunately, the challenges associated with detailed condenser modeling are more related to the size of the model than to the complexity of concepts and modeling options. For such detailed condenser/radiator analyses, it is convenient to use a traditional thermal tool such as SINDA combined with the 1D line layout options in Thermal Desktop, with FloCAD. Figure 14.17 depicts an LHP with a 1D serpentine condenser on a 2D discretized plate (finite-difference in this case, although finite elements may also be used). Parallel, manifolded condensers may also be used, along with flow-control devices that assure even distributions in parallel-condenser designs.

More detailed information on simulation is provided in Ref. 14.31.

---

*For example, it was used as a template by Aerospatiale to create a model of the STENTOR multi-evaporator LHP.
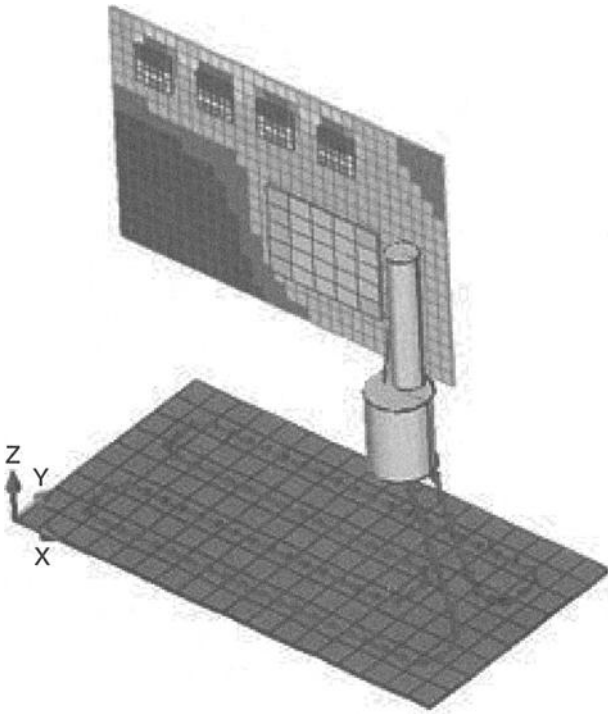
Fig. 14.17. Geometric (CAD-based) LHP thermal/fluid model, including serpentine condenser.

Conclusions

As a result of their growing acceptance, CPLs and LHPs continue to be active subjects of research and development. Current areas of research include:
- reliable lightweight low-pressure-drop parallel condensers
- freeze-tolerant radiators
- advanced high-performance, low-conductivity wicks
- evaporators of different aspect ratios (long, thin, flat, miniaturized, etc.)
- heat-transfer performance improvements
- miniature systems
- simplification of the technology, for adaptation to mass production
- multi-evaporator and multicondenser systems, including reversible loops and large-scale isothermalizers
- cryogenic systems
- high-temperature systems

CPLs and LHPs offer tremendous advantages to many thermal-control applications, especially when trained designers consider these loop transport systems early in the design process, and not just as replacements for traditional heat-pipe technology.

CPLs and LHPs are very similar devices, and they in fact represent two extremes in a spectrum of design possibilities. However, each device type has specific advantages and disadvantages, and both will continue to find application in future missions because of the broad range of mission requirements and constraints.

References

14.1. A. Abhat, M. Groll, and M. Hage, "Investigation of Bubble Formation in Arteries of Gas-Controlled Heat Pipes," AIAA Paper 75-655, May 1975.

14.2. E. W. Saaski, "Arterial Gas Occlusions in Operating Heat Pipes," AIAA Paper 75-657, May 1975.

14.3. J. E. Eninger, "Menisci Coalescence as a Mechanism for Venting Noncondensable Gas from Heat-Pipe Arteries," AIAA Paper 74-748, July 1974.

14.4. P. Brennan and E. J. Kroliczek, *Heat Pipe Design Handbook* (B&K Engineering, Towson, MD, 1979).

14.5. F. Edelstein, "Heat Pipe Manufacturing Study," Grumman Aerospace Corp., Final Report to NASA, NAS5-23156, August 1974.

14.6. S. W. Chi, *Heat Pipe Theory and Practice: A Source Book* (Hemisphere Publishing Co., McGraw-Hill, New York, 1976).

14.7. P. Dunn and D. A. Reay, *Heat Pipes*, 2nd ed. (Pergamon Press, Oxford, United Kingdom, 1978).

14.8. R. S. Gaugler, U.S. Patent Application (21 December 1942). Published U.S. Patent No. 2,350,348 (6 June 6 1944).

14.9. G. M. Grover, T. P. Cotter, and G. F. Erickson, "Structures of Very High Thermal Conductance," *J. Appl. Phys.* 35, 1990 (1964).

14.10. T. P. Cotter, "Theory of Heat Pipes," Los Alamos Scientific Laboratory Report LA-3246-MS, February 1965.

14.11. B. D. Marcus, "Theory and Design of Variable Conductance Heat Pipes," TRW, NASA Contractor Report CR-2018, April 1972.

14.12. A. Basiulis, "Unidirectional Heat Pipes to Control TWT Temperature in Synchronous Orbit," *Symposium on Thermodynamics and Thermophysics of Space Flight*, Palo Alto, March 1970.

14.13. B. Swerdling, R. Kosson, M. Urkowitz, and J. Kirkpatrick, "Development of a Thermal Diode Heat Pipe for the Advanced Thermal Control Flight Experiment (ATFE)," AIAA Paper 72-260, April 1972.

14.14. P. J. Brennan, E. J. Kroliczek, H. Jen, and R. MacIntosh, "Axially Grooved Heat Pipes—1976," AIAA Paper 77-747, June 1977.

14.15. J. Alario, R. Haslett, and R. Kosson, "The Monogroove High Performance Heat Pipe," AIAA Paper 81-1156, June 1981.

14.16. E. J. Kroliczek, J. Ku, and S. Ollendorf, "Design, Development, and Test of a Capillary Pump Loop Heat Pipe," AIAA Paper 84-1720, June 1984.

14.17. G. P. Peterson, "Analytical Comparison of Three External Artery Heat Pipes," AIAA Paper 87-1616, June 1987.

14.18. A. A. Delil *et al.*, "High Efficiency, Low Pressure Drop Two-Phase Condenser," Final Report NLR CR 96002 L, 1986.

14.19. W. Bienert *et al.*, "Experimental Study of Loop Heat Pipe Behavior in the Presence of Noncondensible Gas," *10th International Heat Pipe Conference*, Stuttgart, Germany, 1997.

14.20. Y. Maidanik *et al.*, "Theoretical Basis and Classification of Loop Heat Pipes and Capillary Pumped Loops," *10th International Heat Pipe Conference*, Stuttgart, Germany, 1997.

14.21. EOS CPHTS Reliability Analysis, Lockheed Martin, 1999.

14.22. Reliability Analysis, EOS-AM Spacecraft Thermal Control Subsystem, Lockheed Martin Astro Space, Design Note EOS-DN-REL-15A, Rev. A, 1 November 1995.

14.23. Failure Modes and Effects Analysis (FMEA), EOS-AM Spacecraft Thermal Control Subsystem, Lockheed Martin Astro Space, Design Note EOS-DN-REL-16A, Rev. A, 1 November 1995.

14.24. W. J. Krotiuk and J. E. Fredley, "EOS-AM Spacecraft Capillary Pumped Loops," presented at *Spacecraft Thermal Technology Workshop, The Aerospace Corporation*, March 1996.

14.25. J. E. Fredley and C. E. Braun, "A Low Pressure Drop Heat Exchanger with Integral Heat Pipe," *1988 ASME National Heat Transfer Conference*, Houston Texas, 24–27 July 1988.

14.26. Y. Maidanik, Y. Fershtater, V. Pastukhov, and M. Chernysheva, "Experimental and Theoretical Investigation of Startup Regimes of Two-Phase Capillary Pumped Loops," Paper 932305, *23rd International Conference on Environmental Systems, Society of Automotive Engineers*, 12–15 July 1993.

14.27. Y. Maidanik, N. Solodovnik, and Y. Fershtater, "Investigation of Dynamic and Stationary Characteristics of a Loop Heat Pipe," *ICES Conference*, 1994.

14.28. E. Y. Kotlyarov and G. P. Serov, "Methods of Increase of the Evaporators Reliability for Loop Heat Pipes and Capillary Pumped Loops," Paper 941578, *24th International Conference on Environmental Systems, Society of Automotive Engineers*, June 1994.

14.29. J. Baumann *et al.*, "Noncondensible Gas, Mass, and Adverse Tilt Effects on the Start-up of Loop Heat Pipes," SAE 1999-01-2048.

14.30. J. Baumann *et al.*, "An Analytical Methodology for Evaluating Start-Up of Loop Heat Pipes," AIAA 2000-2285.

14.31. J. Baumann *et al.*, "Steady State and Transient Loop Heat Pipe Modeling," SAE 2000-ICES-105, July 2000.

15 Thermal Design Analysis

D. G. Gilmore[*] and R. L. Collins[*]

Introduction

This chapter introduces the thermal analysis and design process as it applies to spacecraft projects. After an overview that includes the phases in a typical spacecraft program and the type of thermal-engineering support they require, the chapter provides a detailed discussion of how the analysis is performed, what computer programs are used, and why they are used. A description of the thermal analysis performed for a real program is included.

Spacecraft Project Phases

The phases in a spacecraft project are concept definition, validation, full-scale development, and operation. The actual activities for each vary from program to program, but the following discussion gives a general idea of the thermal engineer's role as a program matures. Throughout the design or program-development process, formal reviews are conducted to verify that the design has reached a particular level of maturity and meets technical requirements. In this discussion, the various reviews are referenced by names that are common in the industry; however, they may also be known by other names.

The Concept Definition Phase

The concept definition phase is normally the first phase of a program for which engineering support is called upon. This phase usually consists of a customer-sponsored trade study examining the feasibility of various approaches to meet the intent of a concept. At this point, the intent may be little more than a qualitative description of a mission or capability that planners would like to see filled. The concept normally changes during these studies in response to technical and fiscal realities, or competition from alternative systems. Usually the only constraint given to the various specialists is the cutoff year for state-of-the-art technology projections (the date at which all required technologies are projected to be at a flight-ready level of maturity). The basic end products of these concept definition studies are a parametric analysis of viable approaches, a subsystem state-of-the-art assessment, and the definition of a baseline spacecraft-configuration concept.

The thermal engineer's effort in this phase consists of defining and analyzing, parametrically, one or more alternative approaches to thermal control of the spacecraft. The engineer must consider the thermal requirements of all vehicle elements —housekeeping electronics, payload electronics, batteries, sensors, propulsion, antennas, etc.—for all mission phases from prelaunch testing through on-orbit operations. For many of these elements the engineer will quickly see that standard thermal-control techniques involving finishes, small heaters, or multilayer insulation (MLI) will suffice. These elements are of little concern at this point, and a

---

*The Aerospace Corporation, El Segundo, California.

very rough estimate of the types of finishes, weights, and heater powers based on the engineer's experience with other programs is usually quite sufficient.

The real effort in the concept phase centers around elements of the thermal-control system that have significant system-level impacts resulting from size, weight, power requirements, or development complexity. Examples include heat-pipe systems for high-capacity batteries, deployable radiators for rejecting unusually large amounts of waste heat, devices for cooling high-power-density electronics, cryogenic coolers, etc. For each significant element a possible thermal-design approach may be identified, and each approach analyzed parametrically to determine its relative merits in terms of performance, weight, volume, radiator area, heater power, etc. For example, an infrared (IR)-sensor design operating at cryogenic temperatures might be analyzed as a function of focal-plane temperature or parasitic heat-leak rates. The bottom line for these analyses is usually thermal-subsystem weight, volume, and power requirements.

The engineer is often tempted at this stage to jump directly to a point design rather than perform parametric analyses. Doing so is generally unwise, however, because the input parameters upon which the thermal design is based usually change quickly, and more important, the parametric analyses allow the design team greater insight into the impact of system requirements on the weight and complexity of the thermal-control subsystem.

From the parametric analyses performed by each of the subsystem engineers, a baseline spacecraft design is synthesized by the study team. Ideally, this design represents an optimum balance between the competing requirements of different subsystems and overall system constraints such as weight, volume, reliability, and cost. The thermal engineer is responsible for specifying a baseline thermal-control system design and providing a preliminary assessment of its performance capabilities and characteristics, weight, power requirements, and any relevant issues or areas of concern.

The final task during this phase is to assess the subsystem state of the art through a review of all required thermal-control technologies. Most of these technologies will be mature and flight-demonstrated. Others, however, may require significant development before they are flight-ready. A critical input at the concept definition phase is identification of any research and development required to bring needed technologies to maturity, along with an assessment of what work is currently in progress in the industry or required in the future to meet program needs. Useful sources of information on the current state of the art for various technologies include The Aerospace Corporation, the Air Force Research Laboratory, NASA, recent conference papers, and the on-line databases available through the Internet and many libraries. A particularly useful tool for characterizing the maturity of a given technology or design is the NASA nine-point scale of technical maturity (Table 15.1).

At the onset of a concept definition study, the technical specialist must plan the depth and breadth of support to be consistent with the study schedule, the amount of funding available, and the level of effort of the other technical disciplines. Understand the overall study milestones and gear your effort accordingly. Be careful that your projected effort does not drive the study schedule. If you anticipate that it may, advise the study leader. If available funding is not sufficient to provide

Table 15.1. NASA Civil Space Technology Development Stages and Corresponding Readiness Levels

Development Stage	Corresp. Readiness Levels	Readiness Level Definitions
Basic technology research	1, 2	1. Basic principles observed and reported
Research to prove feasibility	2, 3	2. Technology concept and/or application formulated
Technology development	3–5	3. Analytical & experimental critical function and/or characteristic proof-of-concept
Technology demonstration	5, 6	4. Component and/or breadboard validation in laboratory environment
System/subsystem development	6–8	5. Component and/or breadboard validation in relevant environment
System test, launch, and operations	8, 9	6. System/subsystem model or prototype demonstration in a relevant environment (ground or space)
		7. System prototype demonstration in a space environment
		8. Actual system completed and "flight qualified" through test and demonstration (ground or space)
		9. Actual system "flight proven" through successful mission operations

meaningful support to the study, raise this issue with the leader. Any issues that cannot be adequately addressed because of funding or schedule limitations must be documented.

The scope and detail of supporting thermal analyses should be tailored to fit the schedule and available funding. In general, many parametric analysis cases with a small model are of greater value to a concept study than are detailed analyses with large models. Scaling existing designs from other programs can also be an efficient way of answering study needs without conducting time-consuming analyses and "reinventing the wheel." In other cases, back-of-the-envelope calculations using Earth heating and view-factor tables and/or very simple thermal mathematical models (TMMs) are sufficient to parametrically characterize a design. If, however, more-extensive analyses are absolutely necessary, be sure to budget adequate time to account for machine turnaround time and reanalysis needed because of inadvertent errors.

The type of documentation required will vary. Some team leaders may expect formal weekly presentations to the study team, while others may ask for periodic written reports. You should have a clear understanding of what inputs are expected and the format in which they should be presented.

Finally, be sure to convey to the leader your commitments and their priorities before you join the team. Because many engineers work in matrix organizations

and support more than one program, complete or dedicated support during key phases of the study may be out prioritized. Nothing frustrates a program office more than a change in support personnel in the middle of a study, and one way to preclude this is to keep supervisors updated.

The Validation Phase

Once the concept definition studies have been completed, the design concept, supporting trade studies, and predicted system performance are reviewed by officials, and a decision is made on whether to proceed. If a go-ahead is given, the program enters a validation phase, in which the customer team generates a description of the system that they will ask a contractor (or contractors) to build. This is done by refining the concept-phase studies and determining what technologies and capabilities can realistically be achieved, given the cost and schedule constraints of the program. A System Requirements Review (SRR) is then held to reach agreement between customer and contractor personnel as to what the top-level requirements will be. Once these are established, special studies and tests are performed to address any critical technology questions. In many cases, as an effort matures, a System Design Review (SDR) is held to complete the validation of the system design. The end result of this phase will be a Request For Proposal (RFP), which the customer issues to industry.

Contractors who wish to bid on the program will be given an RFP package that includes basic information such as schedules, instructions for submitting a proposal, and government points of contact. Of greater interest to the technical specialists, however, are the Statement of Work (SOW), system and subsystem design specifications, applicable specifications and compliance documents, and the Contract Data Requirements List (CDRL).

For all practical purposes, the SOW is the top-level technical document from the proposal phase onward. The basic contract that is awarded to the winning contractor at the completion of the source-selection phase (to be discussed in the next section) actually takes legal precedence over the SOW, but because it usually contains little technical information it is not of much interest to the technical specialist.

The SOW core document contains numbered paragraphs that define what the contractor shall do and what ground rules and assumptions will be in effect. The SOW is a list of tasks to be performed, such as thermal analyses, trade studies, tests, etc. (Specifications for the design, on the other hand, are usually contained in ancillary SOW documents, which will be discussed later.) Because the SOW is part of the legal contract, wording is extremely important, and all tasks are identified and clearly specified as actions the contractor must perform.

Included in various SOW attachments and appendixes will be the CDRL, a list of applicable specifications and compliance documents, and system/subsystem design specifications, if any.

The CDRL is a list of reports, meeting minutes, Interface Control Documents (ICDs), drawings, and documentation that the contractor must deliver to the customer. The list includes only major items of documentation, not the memos and small reports that are informally transmitted.

Other common specifications and applicable documents that may be cited as requirements or provided as recommendations include:

- MIL-STD-1540D, "Product Verification Requirements for Launch, Upper Stage, and Space Vehicles"
- MIL-HDBK-340A, "Test Requirements for Launch, Upper Stage, and Space Vehicles"
- MIL-STD-24236 (Rev. C), "General Specification for Metallic and Bimetallic Thermostat Switches"

The final area of the SOW is the system/subsystem design specification. Specifications for the design of each subsystem, including thermal control, may or may not be included depending upon the degree of control that the customer wishes to exercise over the contractor's design. In the event that a thermal-control subsystem specification is included, the key items that the engineer should expect to find are:

- A requirement to keep all component temperatures within allowable limits during all mission phases from prelaunch to end of life (EOL), considering worst-case variations in power dissipations, environments, operating modes, and contamination/degradation.
- Emphasis on the simplest, most reliable flight-demonstrated technology with no single-point failures.
- For military programs, guidance on analysis margins and test verification derived from MIL-STD-1540D and MIL-HDBK-340A. For NASA and commercial communication-satellite programs, compliance with the customer's analysis margin and test requirements philosophies, which may not be engendered in a formal specification like those used by the military.
- A design that is predictable by thermal analyses and verifiable by ground test.
- Identification of key trade-off studies required.
- Identification of key development and final verification tests.

Proposal Evaluation

Usually, once an RFP has been issued, any interested contractor may submit a proposal. A typical proposal consists of an executive summary, a technical proposal, a management proposal, and a cost proposal, all limited to a certain length, as specified in the RFP.

To evaluate the technical proposal(s), a team of customer personnel is assembled, representing a wide range of technical disciplines. If you serve on such a team, you will find that the source selection takes priority over all other assignments. Because of the competitive, and sometimes contentious, nature of the contract-award process, no information, notes, or documentation concerning the evaluations or the content of any of the proposals may be taken outside of the proposal-evaluation office area or discussed with anyone who is not a member of the source-selection team. Furthermore, evaluators are expected to provide their own technical evaluations of the proposals free from management concurrence. Your findings are not reported to your managers, even if they are members of the same source-selection team. The objective is to provide a fair, unbiased evaluation.

The proposal-evaluation process usually begins with an overview briefing to all of the evaluators by the customer program managers. From attending this briefing and from reading the actual RFP, each evaluator must become thoroughly familiar with the RFP requirements, the evaluation criteria, and the evaluation procedures.

This familiarity is critical because each proposal must be evaluated against the RFP requirements and evaluation criteria and not against the other proposals. At no time can Contractor A's proposal be compared to Contractor B's; all proposals are evaluated separately for compliance with RFP requirements only.

The actual review of the proposal documents will occur in an office area set aside for that activity, and it will be accessible only to members of the evaluation team. Although you will be asked to evaluate only these areas of the proposals related to your area of expertise (thermal control), you should read the entire technical proposal, and sometimes the executive summary, to ensure that thermal issues affecting other subsystems are properly addressed. If the spacecraft requires large deployable radiators, for example, the impact of that need on vehicle dynamics, sensor fields of view, and launch packaging should be covered in other areas of the proposal. Similarly, the need for large heaters may affect the sizing of the electrical-power subsystem.

Any thermal-control issue affecting other spacecraft subsystems should be discussed with the team members evaluating these subsystems to make sure that they are aware of the impacts. Unfortunately, to maintain propriety and document the evaluation process, a large amount of paperwork is required.

Evaluation of proposals must be conducted in light of the specialists' knowledge of what is required to analyze, design, test, and build a spacecraft thermal-control system. Neither the SOW nor the proposal attempt to specify every detailed task that must be performed by the contractor, but the reviewer must ensure that what the contractor has written demonstrates a sound understanding of what is required to develop the thermal-control system and ensure successful completion of the project, on time and within budget. An overly vague proposal that does not reflect a sound grasp of the requirements and does not commit to specific tasks should be viewed with much concern.

The proposal should discuss the proposed thermal-design approach and testing that the contractor will do to verify the thermal-control system. The proposal should also show that the contractor understands and has made a preliminary evaluation of all environments, operating modes, unusual thermal requirements, and potential areas of concern. Analysis and test schedules and estimated staffing levels should also be presented in enough detail to show that the contractor has made a realistic estimate of the thermal-subsystem cost and development schedule. Particular attention should be paid to any newer or exotic technology items that may require extensive development effort.

The reviewer should also verify that all values presented by the contractor are reasonable and consistent. For instance, if the power subsystem puts out 10,000 W and the thermal design is based on 2000 W of heat dissipation, clearly something is wrong. Similarly, simple hand calculations can determine if estimated radiator sizes are approximately correct. "Sanity checks" like these are useful at this stage to ensure that the contractor understands the thermal-control task.

All findings are documented and are used to create a final briefing that summarizes for customer management the strong and weak points and risk assessment of the entire team. Proposal-evaluation team leaders will return to you for further explanation of significant issues that you have raised. Several conversations with a team leader may be necessary before that person completely understands your

concerns, especially if the leader does not have a thermal background. An accurate understanding of this situation must be passed along to ensure a fair and accurate evaluation.

At the conclusion of the source selection, one or more contractors are selected to continue into the full-scale development phase. There may be one prime contractor, two or more prime contractors who will compete until a final selection of one prime contractor is made, or two or more associate contractors developing different parts of the satellite. Generally, the larger the program, the greater the number of contractors.

The Full-Scale Development Phase

Contract Award through PDR

During the period from contract award through Preliminary Design Review (PDR), customer personnel establish working relationships with the contractor and begin engineering development of the spacecraft and related ground systems. The emphasis during this phase is at the system level, and the type of effort is similar to the effort made during the concept definition phase, only with a greater level of detail. The spacecraft design is still fairly flexible at this point, and significant changes in configuration, payloads, and subsystem designs (including thermal) should be expected—hence the importance of continuing the types of trade-off studies and parametric analyses that were conducted during the concept definition phase. Doing so assists the systems-engineering staff and program management in defining an optimal baseline spacecraft design before the PDR.

At this stage, another important action is identifying potential technical or development problems with the thermal or system designs under consideration. Thinking ahead is crucial, because changing a design now is far easier than later, when program "inertia" makes fundamental changes nearly impossible. You will have the greatest possible leverage on a program at this stage, and forward thinking here can save much frustration later. Don't postpone dealing with any possible problems.

Meetings with specialists in other spacecraft subsystem areas, program managers, and the customer will increase significantly. They may seem like time-consuming affairs that take you away from your "real" work, but they are the medium through which the results of studies and analyses are funneled into the program. You may perform many analyses, but if you do not present your results and press for changes that you think are required, your work may be ignored by program managers and customer personnel who are preoccupied with their own priorities. Sometimes much persistence is required to get your point of view recognized and to effect substantive changes, so don't give up. Walking away and writing a "Pearl Harbor" memo doesn't do much to bring a program to a successful completion.

During this phase, key requirements must be identified and a preliminary thermal design selected and documented. Among the requirements that should be addressed are the following.

- range of mission orbits
- normal attitude(s) of satellite
- launch-phase configurations and attitudes
- ground cooling needs

- autonomy requirements
- attitudes during stressed/failure modes
- temperature limits and reliability requirements
- equipment power dissipations and operating modes
- thermal-distortion budgets
- launch-system interfaces
- interfaces with other subsystems, such as
  --payloads
  --propulsion
  --attitude control
  --electrical power
  --structures
  --telemetry, tracking, and command
  --computer and data handling
- contamination control
- special thermal-control requirements for batteries, crystal oscillators, sensors, etc.

To support the selection of a preliminary thermal design, the contractor is expected to provide results of trade-off studies addressing issues such as the degree of active versus passive control, solid-state heater controllers versus thermostats, deployable versus fixed radiators, refrigerators versus stored cryogenics versus cryogenic radiators, hardware or material trades to minimize weight, etc. Clearly not all of these trades are applicable to any given spacecraft, but they are representative of the types of trades that are expected.

Once a preliminary thermal design is established it should be well documented prior to PDR. This documentation should provide a complete description of the design, including key assumptions, radiator areas, insulation requirements, thermal finishes and their assumed optical properties, heater sizes and locations, heat sinks, heat-pipe types, sizes, and locations, a flight instrumentation list, refrigerator descriptions and power requirements, etc. In addition, any thermal development and acceptance/qualification test plans should be addressed, a schedule for all thermal analysis and testing should be presented, and any potential problem areas should be discussed. By the time a preliminary design is identified, analysis should exist to back up the design choices. This analysis, although preliminary, should address all of the issues listed earlier, and it should be well documented.

The PDR itself is usually a large meeting involving many of the contractor's technical specialists, systems engineers, and program managers, as well as a sizable contingent of customer personnel and their technical advisors. During the review, the design is critiqued in a process that may leave uninitiated technical specialists feeling like they are being hounded by an angry mob! Bear in mind that the objective of this process is to identify any weakness in the design early enough to easily correct it. Critiques of the thermal-control subsystem design are not a criticism of the skill or judgment of the thermal engineer and should not be taken personally. Concerns, recommendations, and action items generated in the PDR should be carefully considered so that the designers can take full advantage of the experience and lessons learned that may be embodied in the reviewer's comments.

Some comments, of course, will reflect a simple misunderstanding of a design that may be difficult to fully appreciate after seeing only a few hours of presentation material. No concern or recommendation, however, should be dismissed without fully considering the implications of the potential problem that has motivated the reviewer's comments.

PDR to CDR

The period from PDR to Critical Design Review (CDR) is the time when most of the design and analysis work takes place. Starting with the PDR itself, the design and supporting analysis and development efforts should be paced against the standards to which they will be judged at program completion. Although a greater deal of work remains to be done and substantial uncertainties may exist, contractor staff members should at all times be able to demonstrate that they are on the right track to deliver a high-quality product. Table 15.2 shows an extensive list of evaluation criteria that the contractor should eventually be able to meet. Progress against this list should be closely monitored during the period from PDR to CDR, with the goal of being able to answer all items by CDR.

During this period, close contact should be maintained between the customer and the contractor's thermal people. Regular Technical Interchange Meetings (TIMs), formal or informal, should be scheduled to discuss progress and any thermal-engineering concerns. Face-to-face meetings at the contractor's office, where data and reports are readily available, are far superior to telephone discussions and should be scheduled on a regular basis, even if the program is going smoothly.

Extensive detailed thermal analysis of the spacecraft and all of its components under worst-case hot and cold conditions must be performed during this period. The description of the Hubble Space Telescope thermal design in Chapter 3 illustrates the number of components that must be analyzed. The report that summarized the results of the thermal analyses conducted for that program is more than 500 pages long—a figure that suggests how much analysis may be required. By CDR, a thermal design must be firmly established and all supporting analyses and development tests of critical components completed.

CDR to Launch

The period following CDR is generally devoted to making any design changes dictated by the outcome of the CDR, conducting subsystem development tests, building the satellite, and testing it. The work during this period becomes less oriented to concepts, more to hardware. Final drawings must be made by the designer and signed off by the technical specialists; thermal-control system hardware must be specified in detail and manufactured or purchased; and thermal-balance and thermal-vacuum tests must be planned and executed (see Chapter 19). Although the level of effort for the thermal engineer is generally less than during the PDR-to-CDR period, a great deal of work remains to be done. Attending to all the low-level details and completing all required documentation and test planning can seem like endless tasks.

The most important activity in this phase, and perhaps the most important single event in the entire program for the thermal engineer, is the thermal-balance test.

Table 15.2. Thermal-Control Subsystem (TCS) Evaluation

TCS Evaluation Criteria

Design Features
- No single-point failures possible
- Reliable
- Flight-proven
- Predictable by thermal analyses
- Verifiable by ground test
- Provides adequate thermal margin
  - Passively controlled components: 11°C beyond worst-case predictions made by a test-correlated thermal model
  - Passively controlled components where a temperature margin is not feasible: a rational, well-documented equivalent of 11°C
  - Actively controlled components: control authority of at least 25%, which can be shown to be equivalent to the 11°C margin specified for passively controlled components
- Meets satellite life requirement
- Insensitive to the space environment
  - Vacuum
  - Natural and ultraviolet radiation
  - Contamination
  - Temperature cycling
  - Micrometeoroids and manmade debris
  - Electrostatic charge accumulation
- Insensitive to the ground and launch environment
  - Vibration
  - Acoustic noise
  - Venting
  - Handling and storage
  - Contamination
- Takes into account the maximum range of component power dissipations
- Considers the maximum range of orbital thermal environments
  - Operational hot orbit
  - Operational cold orbit
  - Eclipsing orbit (if different than cold)
  - On-orbit maneuvering
  - Interplanetary cruise (if applicable)
  - Failure mode and recovery
  - Initial outgassing orbit attitude
- Takes into account maximum range of other important mission environments, such as:
  - Prelaunch
  - Launch
  - Transfer orbit
- Elements of TCS hardware, including MLI, paints, coatings, adhesives, conductive thermal compounds, thermal straps, isolators, thermal doublers, heat pipes, fasteners, tapes, etc., meet or exceed the NASA outgassing criteria.
  - Weight loss no greater than 1.0%
  - CVCM (collected volatile condensable materials) less than 0.1%
- Autonomous
- Fault tolerant
- Allows for proper venting and outgassing by well-defined paths for all spacecraft parts, subsystems, and payloads
- Can be readily integrated
- Imposes minimum amount of operational restrictions on the satellite and launch vehicle
- Allows for growth

Table 15.2. Thermal-Control Subsystem (TCS) Evaluation—*Continued*

TCS Evaluation Criteria

Hardware Development Programs
- Of sufficient depth and breadth to reduce the risk of not having flight-qualified hardware when needed
- Heat pipes
- Phase-change materials (PCMs)
- High-capacity constant-conductance heat pipes (CCHPs)
- Loop heat pipes or capillary pumped loops
- High-capacity variable-conductance heat pipes (VCHPs)
- High-fin-effectiveness composite radiators
- Heat plane materials and heat pipes for electronic equipment

Completion of Key Trade-Offs
- Extent of passive versus active thermal control
- Distributed versus centralized thermal control using an onboard computer
- Solid-state temperature control versus bimetallic thermostats
- Selection of location and configuration of radiators
- Selection of heat pipes
- Extent of ground cooling required
- Transfer-orbit battery requirements from upper stage

Demonstration that TCS Design Meets Requirements (Analyses)
- Geometric model of selected configuration
- TMMs
- Thermal analysis results for orbital worst-case hot and cold environments
- Thermal analysis results showing sensitivity to assumed beginning-of-life (BOL) and EOL thermal properties
- Analysis results showing adequate margin for both hot and cold cases
- Documentation and substantiation of key assumptions
- Thermal analysis results for worst-case hot and cold environments corresponding to prelaunch, launch, and transfer orbit

System-, Subsystem-, and Component-Level Testing
- Plans and commitment to perform thermal balance (T/B) testing to validate the proposed design
- Development tests
- Heat-pipe performance tests
- System-level qualification T/B test

Despite the sophistication of today's analytical techniques and the maturity of satellite thermal technology, errors occur frequently in the analysis and design of spacecraft thermal-control subsystems. The thermal-balance test is the one chance the designer has to catch these errors before it is too late. In one sense, the test is even more important than all of the work that came before it, in that it may uncover a problem that would have caused the loss of a mission costing hundreds of millions of dollars if the satellite had been launched "as is." Errors large enough to represent fatal flaws in the design of satellites do occur in thermal-control

subsystems, although they are not common. A more likely outcome of the test is finding that some adjustments must be made to the design or to the mathematical models. In any event, the thermal-balance test is the critical verification of the thermal design, and a conclusive test is considered mandatory to program success.

The Operation Phase

Once the satellite has been built and successfully tested, it is delivered to the customer for launch and operation. During this phase, the thermal engineer supports launch rehearsals as well as the actual launch, and typically provides an assessment of the performance of the thermal-control subsystem on orbit. If any anomalous performances or failures in the thermal subsystem occur, the thermal engineer typically performs analyses, assessments, or tests to determine what caused the problems and what corrective actions should be taken. If additional spacecraft are to be built in the future, then design changes may need to be investigated.

Assuming that the thermal subsystem performs as expected, the primary activity during this phase will be launch support. The level of support expected from thermal engineers during launch varies tremendously from program to program. Some small programs may have no thermal support, while other programs may have 24-hour coverage by several thermal engineers for up to two weeks. Most programs will require a launch-site inspection of the satellite configuration and functional verification of commandable thermal components, such as heaters. Technical assistance is also generally required of the thermal engineer at the satellite control room from launch until the satellite is stabilized in its operational orbit or interplanetary trajectory and initial deployments of solar arrays, antennas, and other appendages are complete. This period generally lasts from a couple of days to a week, and it may involve one thermal engineer who comes in for critical events or several engineers on shifts providing around-the-clock coverage. The principal activities are monitoring temperatures, heater status, and other telemetry to ensure that the thermal design is functioning normally, and also providing recommendations for corrective action if the thermal subsystem or another vehicle subsystem malfunctions.

Thermal Design/Analysis Process Overview

The thermal-design process is a combination of design selection and supporting analysis. The selection of a viable thermal-design approach may become almost intuitive for a thermal engineer who has worked a number of programs. Detailed thermal analyses are, however, always required to verify and refine the design. Experience minimizes the number of time-consuming analysis iterations required to close in on a final design.

A wide range of thermal-control hardware and techniques is available, from simple surface finishes to complex refrigeration systems (Chapters 4 through 14). The spacecraft system requirements to minimize weight, cost, and test complexity while maximizing reliability are usually served best by keeping the thermal design as simple as possible and by avoiding the use of active components. A design that relies only on surface finishes and insulation blankets will be lighter, far less expensive to build, more reliable, and easier to test than a design involving heat

pipes, louvers, or refrigerators. Therefore, although active or semi-active components will sometimes be required, they should be avoided wherever possible.

Before starting the design/analysis process, the engineer must plan the overall effort. Remember that the goal is to provide a reliable thermal-control system at minimum cost for the spacecraft or component in question. All of the analysis, design, and testing activities are only tools to be used to reach that goal, and any unnecessary expenditure of time or money should be avoided. Thus the design should be no more complex than is required to do the job, the TMMs should have the minimum number of nodes needed to verify the design, and, if any difficulties are encountered in analysis, design, or testing, the engineer should ask if a simpler route is available. It is easy to get bogged down in an overly complex design, and some experience is required to know the optimum trade between detail/complexity and practicality.

The first step in the thermal-design process is to clearly understand the objective(s) and any ground rules or constraints. The objective might be to develop a complete thermal-control system for a new spacecraft, to predict temperatures for an existing satellite in a new attitude, to modify the thermal design of a component in response to changes in component design, etc. Understanding the objective and its requirements may require meetings with program managers and other subsystem specialists. Once an objective is established, project ground rules and constraints must also be considered, since these will affect the thermal-design effort. These factors—such issues as how much staffing is available and what this project's priority is relative to other considerations—will play a major role in structuring the effort.

Once the objectives and ground rules are understood, an approach to problem resolution must be selected. The approach may be to do an analysis, perform tests, do hand calculations, adapt the thermal design from a thermally similar device, or a combination of these activities. Each potential approach must be evaluated to determine whether its elements are meaningful to the solution of the problem. Some problems, for instance, may not lend themselves to detailed analysis, but may find a more meaningful solution in simple hand calculations followed by a good test. To identify the approach, one must also consider schedule, budget, and any risks, such as reliance on new or unproven technologies or analysis software.

Once a technically sound approach to the design effort is established, a preliminary schedule and cost estimate should be made. The engineer develops an outline of tasks required to support the job, which should include major milestones, criteria for determining if objectives are met, staffing levels, and a clear definition of what is expected from whom and when. While this outline may adequately be handled mentally for a simple task, it will quickly grow to memo size for even a small thermal-design effort. This top-level plan is invaluable in keeping the effort

- identify development-test requirements
- form matrix of required computer runs
- define math model (number and location of nodes)
- obtain thermal property data
- construct math model(s)
- debug model
- make production runs (number of runs, cost)
- conduct development tests
- reduce/review data
- finalize design
- document/present design analysis
- plan, support, and document testing
- evaluate test data and modify design accordingly

If the estimated time and cost for the effort is not consistent with program requirements, the thermal engineer must either find a simpler, lower-cost approach to the thermal design, or renegotiate funding or schedule. Planning up front and negotiating with program management early will avoid headaches later. As the effort unfolds, cost and schedule should be monitored regularly for measuring performance, and any program slips or changes should be incorporated into the thermal plan.

Once a plan that meets technical and program requirements is established, the design analysis begins. The first step is to establish working relationships with all individuals who provide needed inputs or receive results—typically the lead engineers responsible for the other spacecraft subsystems and payloads, such as propulsion, battery, payloads, or attitude control. Coordinating with these individuals to establish objectives, understand requirements of their subsystems, determine impacts on the thermal design, etc., is important. Failure to communicate regularly may result in wasted time analyzing an out-of-date design.

To prepare for the design effort, you must gather a fair amount of data and information about the system. This data typically includes drawings and sketches of the hardware, estimated heat dissipation and weights of components, definition of orbit and attitude, information about thermal environments from prelaunch through EOL, operating modes of the spacecraft, and thermal property data for materials that may be used. This information is needed to identify a preliminary thermal-design approach and to construct the TMMs.

Before the thermal analysis can begin, a thermal-design approach must be identified. This is usually done by a combination of experience and simple hand calculations to determine if a given approach is viable (this process will be discussed in more detail later). Consideration of all factors—including cost, practicality, analyzability, reliability, and testability—is important at this point.

Using the data and design approach discussed above, the analyst constructs the thermal models: a geometric math model (GMM) for calculating radiation interchange factors and a TMM for predicting temperatures. The GMM is a mathematical representation of the physical surfaces of the satellite or component and is used to calculate the radiation couplings between all surfaces in the model, as well as heating rates to each surface from external flux sources such as solar, Earth IR, and albedo radiation. The TMM is usually a lumped-parameter representation of

the thermal capacitance of each node and thermal conduction terms between nodes, and it is directly analogous to an electrical RC (resistance-capacitance) network. These models are constructed using a combination of computer-aided design (CAD) technologies and hand calculations, and later they will be discussed in detail.

The completed (and debugged) thermal model is run to predict hardware temperatures under worst-case hot and cold conditions. A number of runs may be required to determine what exactly is the worst-case combination of factors, such as orbit beta angle, operating mode, vehicle attitude, surface properties, etc., and a number of parametric runs may be required to close in on optimum sizing of radiators, heaters, and so on. In addition, many analyses will have to be rerun to reflect design changes or updates to analysis inputs, such as box power dissipations, that will occur as the vehicle design matures. Periodic reviews with management and other program personnel are required to ensure that the analysis reflects the current system design and will provide the results needed for other subsystem design efforts. Peer review is also a good way of uncovering the errors that inevitably occur in any analysis before they can do any harm.

The final and sometimes most-tedious step is documentation. The thermal design analysis report(s) should include a complete description of the final thermal design, an in-depth discussion of all the significant math-model inputs and assumptions, an attachment containing a listing of the thermal models, predicted temperatures and margins for all components and heater powers for worst-case conditions and operating modes, and a discussion of any significant concerns or recommendations. In preparing such a report, one must first review and understand all work performed. A critical appraisal must be made of all results to ensure that they are valid, complete, and consistent. The report itself must be written to meet the needs of those to whom it is addressed, as well as to provide a record for the future reference of the analyst. It should conclude with a concise summary of why each task was done, how it was done, what was found, and what should be done as a result.

Fundamentals of Thermal Modeling[*]

Thermal Math Modeling as a Cognitive Process

The body of thermal math modeling concepts, principles, and techniques constitutes a valid tool that can be applied to real engineering problems. A brief introduction to the rudimentary techniques of thermal modeling, coupled with a simple understanding of the various basic heat-transfer mechanisms, is the prerequisite for learning thermal math modeling. Succeeding sections of this chapter present the basic principles and techniques of this discipline.

Developing a good lumped-parameter representation of a thermal system requires—in addition to learning the basic concepts, principles, and techniques— an elusive mixture of experience (with real systems, both physical and model) and

---

*This section is taken from the "Thermal Network Modeling Handbook" prepared by TRW under NASA contract 9-10435.

engineering judgment to transfer the end product into an accurate, versatile, and cost-effective TMM. Experience, of course, can only be acquired from hands-on work with real thermal systems and participation in the modeling and analysis thereof. Engineering judgment is a capability gained by abstracting, from the discipline's body of unique, familiar information, a general understanding that can guide the investigation and comprehension of unfamiliar areas. As such, engineering judgment cannot be captured in written form.

Generally, the problems encountered in developing a TMM reduce to an overall object of achieving the greatest accuracy for the least cost. Cost factors are rather well defined and fall into two classes, development and use. Development costs can be based almost solely on the actual engineering staff-hours required to do the job within the constraints of time and budget; however, the potential costs involved in using a model are often not as obvious nor as linear.

The problem of achieving accuracy, while subject to cost constraints, varies greatly from one TMM to another. For example, general accuracy requirements might be stated as straightforwardly as this: "Temperature accuracy shall be compatible with thermocouple A/D converter quantization error." On the other hand, accuracy levels might be indirectly indicated by requiring that a model "be sufficiently detailed to permit meaningful parametric analyses with respect to insulation thickness variations in increments of 0.5 cm." Clearly, a great deal of engineering judgment will be involved in developing a model that is "sufficiently detailed" to be "meaningful."

Network Solution

Two systems are analogous when they are represented by similar equations and boundary conditions, and the equations describing the behavior of one system can be transformed into the equations for the other by simply changing symbols of the variables. Thermal and electrical systems are two such analogous systems, as shown in Table 15.3.

Table 15.3. Thermal-Electrical System Analogy

Quantity	Thermal System	Electrical System
Potential	T	E
Flow	$\dot{Q}$	I
Resistance	R	R
Conductance	G	$1/R$
Capacitance	C	C
Ohm's Law	$\dot{Q} = GT$	$I = E/R$

The analogy between thermal and electrical systems allows the thermal engineer to utilize widely known basic electrical laws such as Ohm's Law and Kirchhoff's Laws, which are used for balancing networks. Numerical techniques used to solve the partial differential equations describing such electrical systems have been conveniently adapted to computer solutions of thermal networks, thus enabling the thermal engineer to readily compute temperature distributions and gradients of complex physical thermal networks.

Thermal-analysis computer programs have been developed that require the user to define a system thermal network analogous to an electrical circuit. Once data describing the network components are input, preprogrammed routines calculate the transient or steady-state solutions. This section discusses the development of a thermal network and the numerical techniques for solving it.

Nodes

To develop a thermal network and apply numerical techniques to its solution, one subdivides the thermal system into finite subvolumes called nodes. The thermal properties of each node are considered to be concentrated at the central nodal point of each subvolume. Each node represents two thermal-network elements, a temperature (potential) and a thermal mass (capacitance), as shown in Fig. 15.1.

The temperature, T, assigned to a node represents the average mass temperature of the subvolume. The capacitance, C, assigned to a node is computed from the thermophysical properties of the subvolume material evaluated at the temperature of the node, and it is assumed to be concentrated at the nodal center of the subvolume. Because a node represents a "lumping" or concentration of parameters at a single point in space, the temperature distribution through the subvolume implied by the nodal temperature is linear, as shown in Fig. 15.2(c), and not a step function, as illustrated in Fig. 15.2(b).

In a homogeneous material, the temperature at a point other than the nodal point may be approximated by interpolation between adjacent nodal points where the temperatures are known.

The error introduced by dividing a system into finite-sized nodes, rather than volume dx^3 where dx approaches zero, is dependent on numerous considerations: material thermal properties, boundary conditions, node size, node-center placement, and time increment of transient calculations. The techniques for proper nodalization to minimize the error will be discussed in a later section.
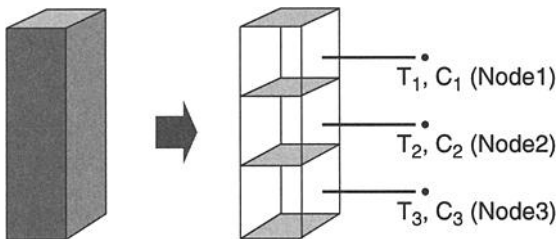

Fig. 15.1. Nodalization.
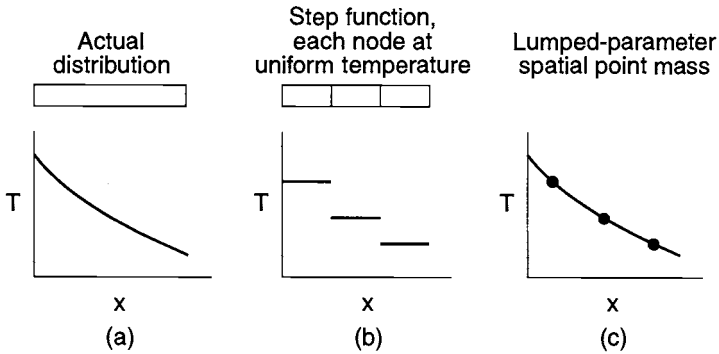
Fig. 15.2. Temperature distributions.

Up to this point, only nodes that represent subvolumes with a finite thermal mass (capacitance) have been discussed. In many instances, two other types of nodes are required to define a thermal network. They are nodes having a zero capacitance or an infinite capacitance. Thermal analyzers such as the program SINDA (Systems Improved Numerical Differencing Analyzer) usually name the three types of nodes as follows:

- diffusion (finite thermal mass)
- arithmetic (zero thermal mass)
- boundary (infinite thermal mass)

The diffusion node (finite capacitance) is used to represent normal material, the temperature of which can change as a result of heat flow into or out of the nodes. It is characterized by a gain or loss of potential energy, which depends on the capacitance value, the net heat flow into the node, and the time during which the heat is flowing. Mathematically, a diffusion node is defined by this expression:

$$\Sigma \dot{Q} - \frac{C\Delta T}{t} = 0. \tag{15.1}$$

The arithmetic node (zero capacitance) is a physically unreal quantity; however, its effective use with numerical solutions can often be helpful in interpreting results in such applications as surface temperatures, bondline temperatures, and node-coupling temperatures. It also finds use in representing thermal-system elements that have small capacitance values in comparison to the large majority of the other nodes in the system, which results in computer run-time reduction with minor changes in overall accuracy. These elements could include small components such as bolts, films, or fillets; gaseous contents of small ducts or tubes; and low-mass insulations. The number of arithmetic nodes should be small compared to the total number of nodes in the network. The temperature of an arithmetic node responds instantaneously to its surroundings. Mathematically, an arithmetic node is defined by this expression:

$$\Sigma \dot{Q} = 0. \tag{15.2}$$

The boundary node (infinite capacitance) is used to represent a boundary or sink whose temperature is set and will not change no matter how much heat flows into or out of it from other nodes in the model. Common uses are representation of deep-space sink temperature, recovery temperature, and planet-surface temperature. In addition, boundary nodes may represent thermal-system components that have a very large thermal mass (capacitance) relative to the other nodes, such as the bulk propellant in a large tank. Mathematically, a boundary node is defined as:

$$T = \text{constant.}$$

The placement of the diffusion-node centers and the choice of node shapes depend on several factors: the points where temperatures are desired, the expected temperature distribution, physical reasonableness, and the ease of computation. The actual size of the node is dependent on other considerations: accuracy desired, structural design, computer storage capabilities, and computer time required. Each factor, however, embodies other considerations. For example, to anticipate the expected temperature distribution, one must draw heavily on engineering judgment as to the effects of the expected boundary conditions and associated material properties.

In general, the shape of a diffusion node is chosen to be a simple geometric figure having areas and volumes that can be easily calculated. Irregularly shaped structural members may be approximated with simple shapes by employing assumptions that are consistent with the desired results. In some cases, nodal divisions are decided first, with the node-center locations thus defined as a consequence. In these cases, nodal edges will usually lie along structural edges, and structural members will be divided in a symmetric and equal fashion. In other cases, output requirements will dictate the locations of node centers, with the nodal edges assigned as a consequence. These two approaches are illustrated in Fig. 15.3. In case (a), the objective is to prepare a general model of the structure, but in (b), the objective is to model the response of two thermocouples located on the bondline between the two members.

The above example suggests that rectangularly shaped nodes are generally desirable. This is true simply because with such nodes, the areas and volumes

(a) General node boundaries

(b) Node centers at thermocouple locations
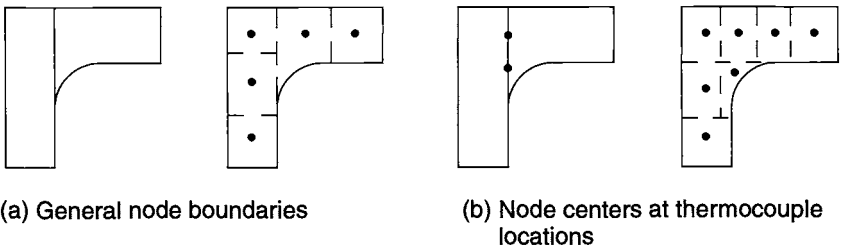
Fig. 15.3. Alternate nodalization methods.

required for the input calculations are easy to compute. The use of such simple nodal shapes is in keeping with current engineering practice. By contrast, Dusinberre[15.1] suggested that nodalization be performed in such a manner that the paths of heat flow assume a triangular pattern, as shown in Fig. 15.4(a). The only drawback to this theoretically sound approach is that the engineer must compute the volumes of the irregular polygonal nodes that are the consequence of such a tack, as shown in Fig. 15.4(b).

Note how much simpler the rectangular nodalization approach is, as indicated in Fig. 15.4(c). As might be expected, to achieve the same simplicity of calculation, circular structures are nodalized in pie-wedge shapes, annular shapes, or a combination of the two, as shown in Fig. 15.5.

Boundary nodes are used to define points, lines, or surfaces of constant temperature in one-, two-, or three-dimensional models, respectively. The physical location of a boundary node is determined solely by the conduction paths connected to it. A single boundary node may be used to model all boundaries at the same temperature. This point is illustrated in Fig. 15.6, which shows that the indicated boundary node will suffice as a model of the entire constant-temperature edge of the structure (in this case, 30°C).


(a) Triangular heat-flow paths

(b) Nodes shapes resulting from paths in (a)

(c) Simple rectangular nodalization
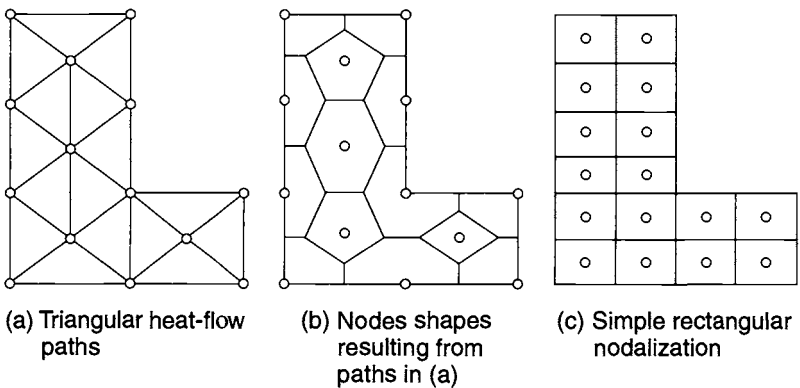
Fig. 15.4. Polygonal nodalization vs. rectangular nodalization.

(a)

(b)

(c)
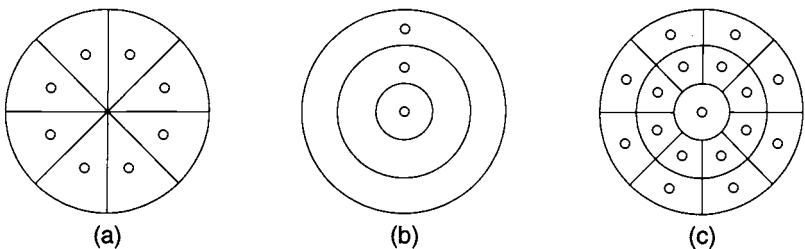
Fig. 15.5. Nodalization of circular elements.
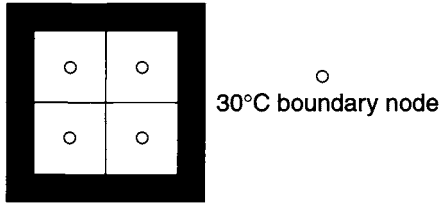
Fig. 15.6. Sample boundary node.

Arithmetic nodes have a number of uses that are consequences of the fact that such nodes serve as an engineering model of the proverbial "wafer of thickness dx, where dx approaches zero." A typical application lies in the modeling of exterior surfaces of reentry vehicles, which are often subjected to severe, rapidly changing boundary conditions. In the physical system, the surface temperature remains very close to radiation equilibrium with the surface heating rate, indicating that this system can be accurately simulated by the use of a surface arithmetic node. This application is illustrated in Fig. 15.7.

The case where heat flows from a surface by conduction is usually one in which two structures are bonded together and a bondline temperature is sought. When the structures are homogeneous, a bondline temperature may be established by simple linear interpolation between the nearest node centers. When the materials are dissimilar, a more appropriate technique is to use an arithmetic node at the bondline, leaving to the computer the process of performing a conductance-weighted averaging of the adjoining diffusion-node temperatures, which, in essence, is the result of finding the steady-state (heat in = heat out) temperature for an arithmetic node.

Arithmetic nodes may also be used advantageously in place of diffusion nodes that have a capacitance that is small when compared to the great majority of nodes in the system. This usage often occurs when modeling a small quantity of gas in a tube or other enclosure, or when modeling small structural parts, such as wires,
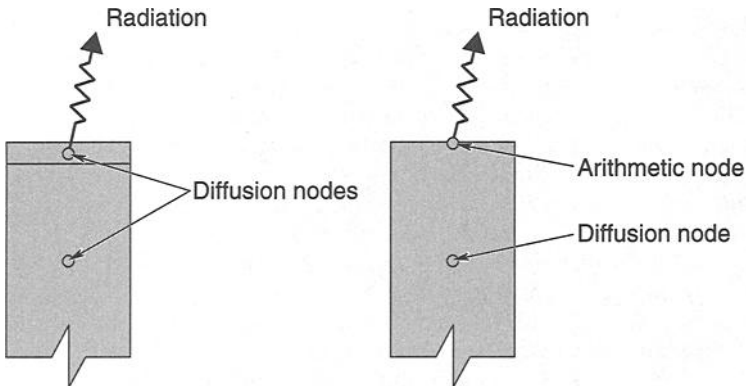

Fig. 15.7. Use of arithmetic nodes to model surfaces.

bolts, fillets, films, and sheets, where detailed temperatures are desired (which precludes lumping such items along with larger nearby nodes). The correct use of arithmetic nodes in these cases generally results in a considerable saving of computer time when the model is processed.

In the development of a thermal network, computations with respect to nodes are generally limited to calculating the capacitance of diffusion nodes. The following formula is used:

$$C = \rho \cdot V \cdot C_p, \tag{15.3}$$

where C is thermal capacitance (J/°C), ρ is density (kg/cm^3), V is volume (cm^3), and C_p is specific heat (J/kg·°C).

The specific heat (C_p) and the density (ρ) of materials may vary with temperature. The necessity to utilize temperature-dependent properties for analysis depends on the degree to which the properties vary and the temperature range over which the capacitance of the material will be calculated. Most thermal-analysis computer codes can accommodate temperature-varying thermal properties.

The use of arithmetic nodes may also require some computations. Replacement of small-capacitance diffusion nodes with an arithmetic node must be preceded by computations to verify that the capacitance-conductor effects are such that the node in question will essentially reach steady-state temperatures during the time step required by the larger nodes. The use of an arithmetic node to predict surface temperatures where surface radiation or very high heating rates are involved requires careful analysis to ensure the stability of the arithmetic node. Stability criteria and solution techniques are discussed later. This section shows that solution techniques using linearized "last-pass" temperature values may require the use of analyzer control constants to restrict the maximum node temperature change or computation time step. The engineer must further be cautioned against using coupled arithmetic nodes without a complete understanding of the implications and required analyzer control constants used to ensure a valid solution.

Conductors

Conductors are the thermal math modeling network elements that represent the heat-flow paths through which energy is transferred from one node to another. Figure 15.8 illustrates the element node temperatures (T), capacitances (C), and conductors (G) that comprise a thermal network.

The three processes by which heat flows from a region of higher temperature to a region of lower temperature are conduction, convection, and radiation. Conduction is the process by which heat flows within a medium or between different mediums in direct physical contact. The energy is transmitted by molecular communication. Figure 15.9 illustrates the conduction conductor.

Convection is the process of energy transport by combined action of heat conduction, energy storage, and mixing motion. Heat will flow by conduction from a surface to adjacent particles of fluid; then the fluid particles will move to a region of lower temperature, where they will mix with, and transfer a part of their energy to, other fluid particles. The energy is actually stored in the fluid particles and is carried as a result of their mass motion. Figure 15.10 illustrates the convection conductor.
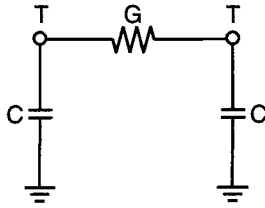
Fig. 15.8. Thermal network elements.
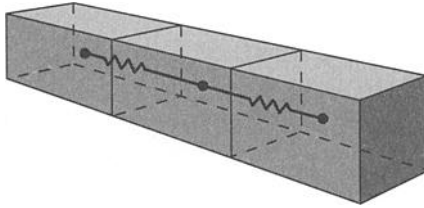
Fig. 15.9. Conduction conductor.
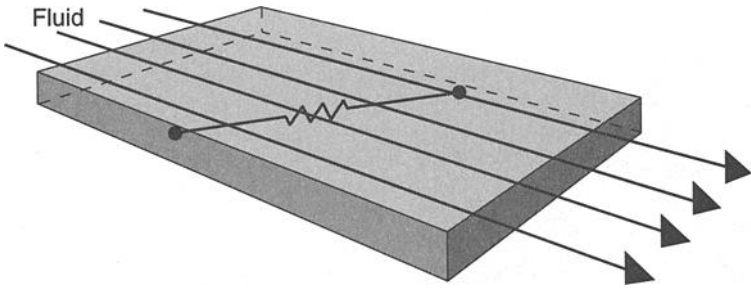
Fig. 15.10. Convection conductor.

Conductors that represent conduction or convection paths are referred to as linear conductors, because for those paths, the heat-flow rate is a function of the temperature difference between nodal temperatures to the first power.

$$\dot{Q} = G_{ij}(T_i - T_j). \tag{15.4}$$

Radiation is the process by which heat flows between two bodies separated in space. Energy is transferred through electromagnetic wave phenomena. Radiation conductors (illustrated in Fig. 15.ll) are termed nonlinear, because the heat flow between two surfaces by radiation is a function of the difference of the fourth powers of the surface temperatures:

$$\dot{Q} = G_{ij}(T_i^4 - T_j^4). \tag{15.5}$$
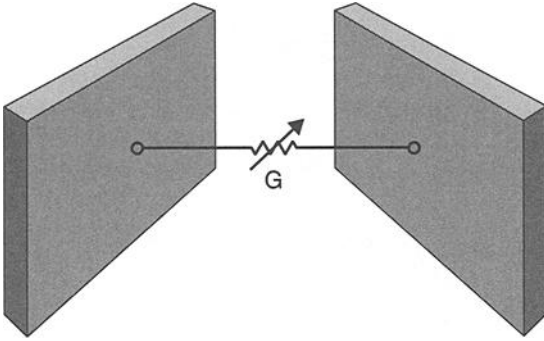
Fig. 15.11. Radiation conductor.

Fluid-flow thermal systems may also be simulated by thermal modeling. Energy stored in the thermal mass (capacitance) of a fluid lump (node) is transferred from one point to another by the movement of the fluid mass. This type of conductor is generally referred to as a one-way or mass-flow conductor, and it is illustrated in Fig. 15.12. The mass-flow conductor is linear and actually asymmetric, because upstream nodes are unaffected by what happens downstream.

$$\dot{Q} = G_{ij}(T_i - T_j) \tag{15.6}$$

Conduction

Conduction conductors for rectangular nodes are computed from this equation:

$$G = \frac{kA}{L}, \tag{15.7}$$

where G is thermal conductance (W/°C), k is thermal conductivity (W/m·°C), A is cross-sectional area through which heat flows (m^2), and L is the distance between adjoining nodes (m). (SI units are shown, but other consistent units could be used.)

The thermal conductivity (k) of materials may vary with temperature or other influencing factors within the system; the cross-sectional area through which the heat flows (A) and distance between node centers (L) are determined by the size and shape of the adjoining nodes. As with the capacitance calculations, necessity
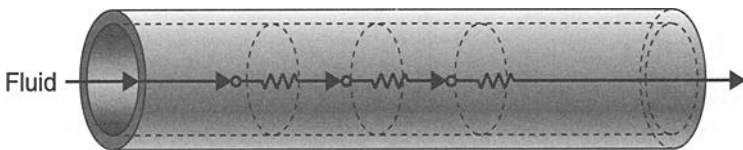
Fig. 15.12. Mass-flow conductors.

to use temperature-dependent properties depends on the degree to which the conductivity changes over the temperature range expected during the analysis.

Rectangular Sections

The length, L, of the heat-flow path, used for conduction-conductance calculations for rectangular nodes, is the distance between node centers, and the area, A, to be used is the area of a node cross-section perpendicular to the line joining the node centers. The convention is depicted in Fig. 15.13.

Cylindrical Nodes

For conductors between nodes that are cylindrical, the conventions shown in Fig. 15.14 should be used.

Parallel Paths

Two or more parallel conduction paths between nodes may be summed to create one conductor value by the following equation:

$$G_T = G_1 + G_2 + ...G_n. \tag{15.8}$$
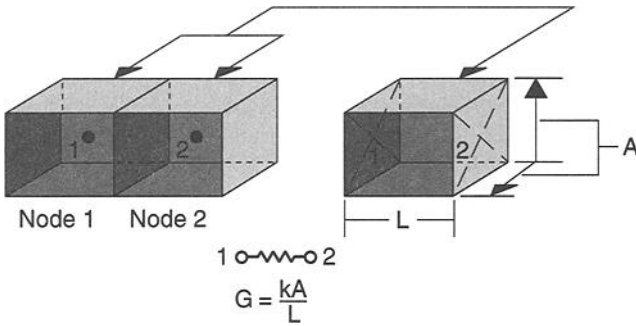
Fig. 15.13. Simple conductor representing a heat-flow path through material.
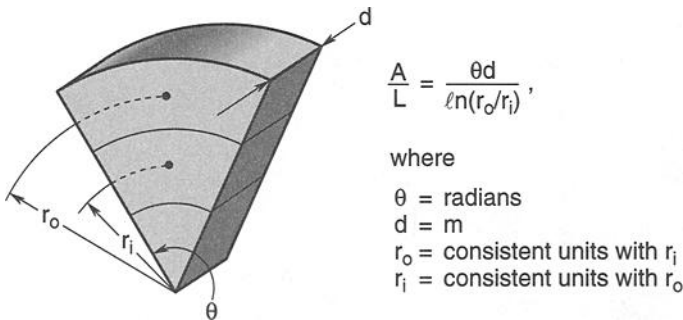
Fig. 15.14. Area and length equivalents for cylindrical nodes.

Equation (15.8) may be helpful in computing an equivalent conductor between two nodes, as illustrated in Fig. 15.15.

Series Paths

Two or more series conduction paths between nodes may be combined to create one conductor value by the following equations:

$$\frac{1}{G_T} = \frac{1}{G_1} + \frac{1}{G_2} + \dots \qquad G_T = \frac{1}{\dfrac{1}{G_1} + \dfrac{1}{G_2} + \dots \dfrac{1}{G_n}}. \qquad (15.9)$$

These equations may be helpful in computing the conductors between two dissimilarly shaped nodes or two nodes of dissimilar materials, as shown in Fig. 15.16.

Convection

Convection conductors are computed from the expression

$$G = hA,$$

where G is thermal conductance (W/°C), h is the convective heat-transfer coefficient (W/m^2·°C), and A is surface area in contact with the fluid (m^2). (Again, SI units are used as an example.)

G is the product of the average-unit thermal convective conductance h (convective heat-transfer or film coefficient) and the nodal surface area A in contact with the fluid. However, h is a complicated function of fluid flow, the thermal properties of the fluid medium, and the geometry of the system.

Because the convective process of heat transfer is so closely linked to fluid motion, the first requirement is to establish whether the fluid flow is laminar or turbulent. In laminar flow, the fluid moves in layers and the fluid particles follow a smooth and continuous path. Heat is transferred only by molecular conduction within the fluid as well as at the interface between the fluid and the surface. In turbulent flow, the path of the fluid particles is irregular, and although the general trend of the motion is in one direction, eddies or mixing currents exist. Not only is the conduction mechanism modified, but increased heat transfer also occurs in turbulent flow when energy is carried by fluid particles across flow streamlines and mixes with other fluid particles.

In addition to knowing whether the fluid motion is laminar or turbulent, one must know the process by which the motion was induced. When the heat flows
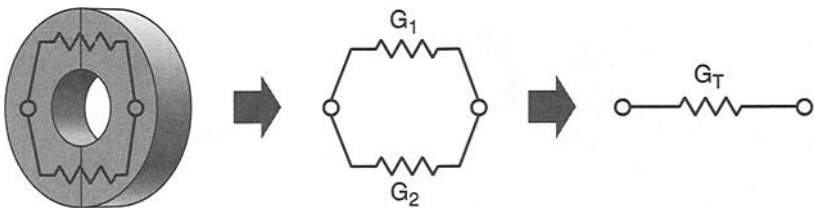
Fig. 15.15. Parallel conductor flow paths.

$$G_T = \frac{1}{\frac{1}{G_1} + \frac{1}{G_2}} = \frac{G_1 G_2}{G_1 + G_2}$$
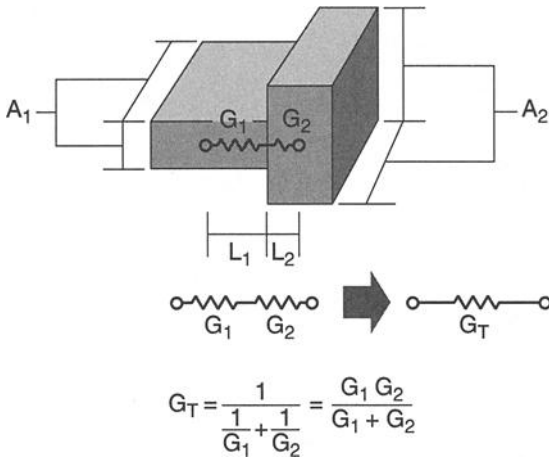
Fig. 15.16. Series conductor paths.

between the fluid and the surface as a result of fluid motion caused by differences in fluid density resulting from temperature gradients in the fluid, the heat-transfer mechanism is called free or natural convection. When the motion is caused by some external agent, such as a pump or blower, the heat-transfer mechanism is called forced convection.

Table 15.4 illustrates typical values of average heat-transfer coefficients encountered in engineering practice. The predicted values for h are only approximate. The accuracy of the heat-transfer coefficient calculated from any available equation or graph may be no better than 30%.

Radiation

Most thermal-analysis computer programs linearize the radiation term prior to performing the heat balance at each time-step. This operation simply amounts to the following. First, $(T_i^4 - T_j^4)$ is factored into $(T_i^3 + T_i T_j^2 + T_i^2 T_j + T_j^3)$ and $(T_i - T_j)$. Then the term $(T_i^3 + T_i T_j^2 + T_i^2 T_j + T_j^3)$ is evaluated by the computer each

Table 15.4. Order of Magnitude of Convective Heat-Transfer Coefficients

Convective Medium	Convective Heat-Transfer Coefficient $h(\text{W}/\text{m}^2 \cdot {}^\circ\text{C})$
Air, free convection	1–10
Air, forced convection	25–300
Oil, forced convection	50–200
Water, forced convection	300–12,000
Water, boiling	3000–60,000
Steam, condensing	5000–12,000

time-step using the current values of T_i and T_j. The quantity thus obtained is then multiplied by the input value of the radiation conductor, thus reducing the radiation equation to a linear form. The thermal engineer need only be concerned with the input value of the radiation conductor, which takes the following form:

$$G_{ij} = \sigma \varepsilon_i F_{i\text{-}j} A_i \text{ for radiation to a blackbody, and}$$
$$G_{ij} = \sigma \Im_{i\text{-}j} A_i \text{ for radiation between gray surfaces,}$$

where G_{ij} is the input value for radiation conductors (W/K^4); σ is the Stefan-Boltzmann constant, 5.669×10^{-8} (W/m^2·K^4); ε_i is the emittance of surface i (dimensionless); $F_{i\text{-}j}$ is the geometric (configuration) factor from surface i to surface j (dimensionless); A_i is the area of surface i (m^2); and $\Im_{i\text{-}j}$ is the gray-body radiation factor (dimensionless).

The emittance, ε, is a measure of how well a body can radiate energy as compared with a blackbody. Emittance is the ratio of the total emissive power of a real surface at temperature T to the total emissive power of a black surface at the same temperature. The emittance of a surface is a function of the material, the surface condition, and the temperature of the body. The surface of a body, and therefore the emittance, may be altered by polishing, roughing, painting, etc. The values of ε for many common materials and surface conditions have been measured at various temperatures and are presented in Chapter 4, Appendix A, and in many reference manuals. The engineer must determine the value of emittance to be used and whether the variation of ε with temperature is significant over the temperature range expected for the surface.

The geometric (configuration) factor from surface i to surface j, $F_{i\text{-}j}$, is the fraction of total radiated energy from surface i that is directly incident on surface j; surface i is assumed to be emitting energy diffusely. $F_{j\text{-}i}$ would be the fraction of total radiant energy from surface j that is intercepted by surface i. The configuration factors for finite regions of diffuse areas are related by the equation

$$A_i F_{i-j} = A_j F_{j-i} . \tag{15.10}$$

The configuration factor, $F_{i\text{-}j}$, is a function of the geometry of the system only. Several computer programs have been developed to compute the shape factors between surfaces with complex geometries, and they will be discussed later. Form factors between some surfaces with simple geometries can be hand-computed. Hand-calculated view factors can be used for preliminary analysis or to check the results of view factors generated by computer programs.

Reference 15.2 presents configuration factors for various simple geometries. The use of these figures and configuration-factor algebra will allow the engineer to determine form factors for many simple radiation problems.

The gray-body shape factor $\Im_{i\text{-}j}$ is the product of the geometric shape factor $F_{i\text{-}j}$ and a factor that allows for the departure of the surface from blackbody conditions. For radiation enclosures, the $\Im_{i\text{-}j}$ factors are generally evaluated with a computer program. The inputs for the program are the $A_i F_{i\text{-}j}$ values from every surface of the enclosure to every other surface and the emittance and area for each surface. Simplified equations for $\Im_{i\text{-}j}$ exist for two-component gray enclosures.

Infinite parallel flat plates: $F_{1\text{-}2} = F_{2\text{-}1} = 1$.

$$\Im_{i-j} = \frac{1}{\left(\dfrac{1}{\varepsilon_1} + \dfrac{1}{\varepsilon_2} - 1\right)} . \tag{15.11}$$

Concentric cylinders of infinite height or concentric spheres:

$$F_{1-2} = 1, F_{2-1} \neq 0 \tag{15.12}$$

$$\Im_{1-2} = \frac{1}{\dfrac{1}{\varepsilon_1} + \dfrac{A_1}{A_2}\left(\dfrac{1}{\varepsilon_2} - 1\right)} \tag{15.13}$$

For nonenclosed surfaces, an effective emittance, ε_{eff}, between the surfaces may be used to compute the gray-body form factor with the following equation:

$$\Im_{i-j} = \varepsilon_{\text{eff}i}F_{i-j} . \tag{15.14}$$

The effective emittance is a function of the emittances of the two surfaces and the configuration factors (F) between them. The error induced with use of ε_{eff} is the result of neglecting secondary reflections from surfaces other than the two for which the effective emittance was determined. By reducing Hottel's method for two flat surfaces with emissivities of ε_1 and ε_2 in a black enclosure, one can construct the following equation:

$$\varepsilon_{\text{eff}} = \frac{\varepsilon_1\varepsilon_2}{1 - F_{1-2}F_{2-1}(1-\varepsilon_1)(1-\varepsilon_2)} . \tag{15.15}$$

The examples of configuration-factor algebra in Fig. 15.17 should be helpful.

Energy Sources and Sinks

Energy sources and sinks, designated by Q, are modeling elements that allow the impression of positive or negative heating rates on the nodes of a thermal network, independent of conductor paths to the nodes.

$A_1F_{1\text{-}3} = A_3F_{3\text{-}1}$

$A_1F_{1\text{-}34} = A_1F_{1\text{-}13} + A_1F_{1\text{-}4}$

$A_{12}F_{12\text{-}34} = A_1F_{1\text{-}34} + A_2F_{2\text{-}34}$

$A_{12}F_{12\text{-}34} = A_1F_{1\text{-}3} + A_1F_{1\text{-}4} + A_2F_{2\text{-}3} + A_2F_{2\text{-}4}$

$A_1F_{1\text{-}4} = A_3F_{3\text{-}2}$ (symmetrically positioned)
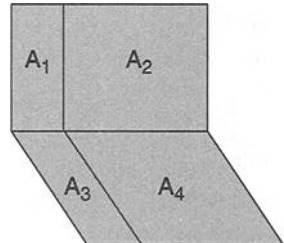
Fig. 15.17. Configuration-factor algebra.

Common engineering applications of heat sources in thermal models are:
- solar and planetary heating
- aerodynamic heating
- avionic cold-plate heat loads
- change-of-state latent energy
- thermal-control heaters
  Common applications for heat sinks are:
- change-of-state latent energy
- radiator heat rejection
- aerodynamic cooling

Heating rates may be impressed on diffusion (finite-capacitance) or arithmetic (zero-capacitance) nodes. Most thermal analyzers provide a separate entry block for entering heating or cooling rates. For example, the SINDA computer program uses the SOURCE data block for such entries. In the usual case, heating rates are not considered when computing the time steps for transient analysis, and large heating rates on low-capacitance nodes may create instability in the network solution. Also, the impression of large heat sources on arithmetic nodes with radiation (nonlinear) conductors attached often causes large erroneous temperature oscillations in the arithmetic and adjoining nodes. Both of these difficulties can be avoided with the use of the program-control constants incorporated in most thermal-network analyzers. These control constants are the time-step multiplication factor and the maximum temperature change allowed.

Thermal Design Analysis Example: POAM

The Polar Ozone and Aerosol Monitor (POAM) sensor will be used as an example of a thermal design analysis. This sensor measures the concentrations of ozone and aerosols in the upper atmosphere of Earth's polar regions. The experiment was funded by the U.S. Strategic Defense Initiative Office, administered by the Office of Naval Research, and flown on the French SPOT Earth resources satellite.

The sensor measures the concentrations of ozone and aerosols by observing the attenuation of sunlight as it passes through the atmosphere during sunrise and sunset events while the satellite circles Earth in a polar, sun-synchronous orbit, as shown in Fig. 15.18. The sensor actually contains nine small telescopes, each of which has a filter and a sensor. These telescopes measure the intensity of sunlight in nine very narrow wavebands. Observing the intensity of sunlight as the sun sets or rises enables the measurement of concentrations at different heights in the atmosphere to a resolution of about 1 km. These measurements support research into the depletion of the protective ozone layer in the upper atmosphere, as well as other atmospheric studies.

Physical Configuration

The POAM sensor (Fig. 15.19) consists of a rectangular base with four mounting feet, called the azimuth housing, and a dome-shaped enclosure containing the telescope assembly. The dome is attached to a short shaft that rides on a pair of bearings in the azimuth housing. The only physical connections between these two assemblies are the bearings and a small cable bundle that runs down the center of the
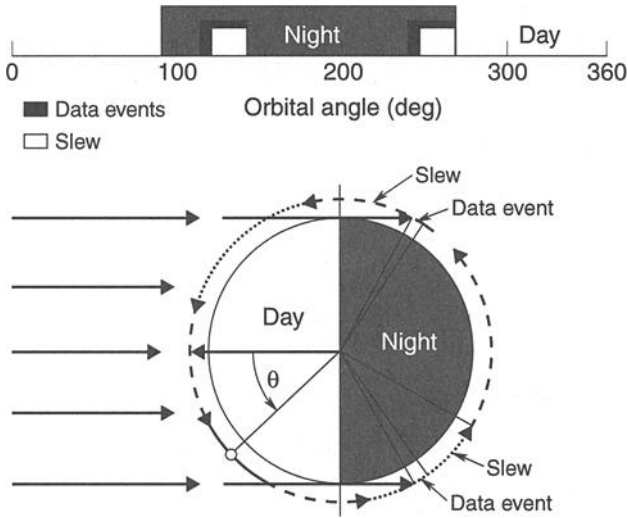
Fig. 15.18. POAM data events.

hollow shaft, which is not shown in the figure. The telescope assembly is similarly connected to the dome only through a pair of bearings and a few small wires. Because heat conduction across ball bearings and along fine wires is relatively weak, the telescope, dome, and azimuth housing are only rather weakly coupled together thermally.

The entire sensor assembly is mounted to an exterior face of the host SPOT satellite (Fig. 15.20). The mounting is accomplished by a bracket, as shown in the figure. The satellite itself is placed in a 822-km, 98.738-deg inclined, circular sun-synchronous orbit with a period of 100 min and a range of beta angles from 14.5
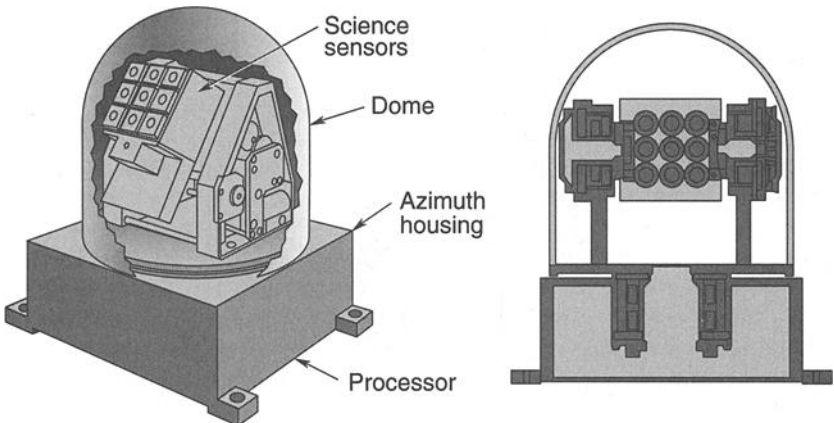
Fig. 15.19. POAM sensor (TTC).
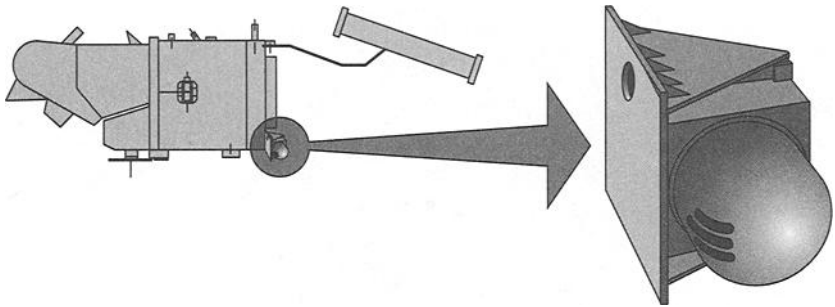
Fig. 15.20. POAM on SPOT spacecraft (TTC, Astrium).

to 29.8 deg. At the sunrise event, the sensor makes one minute of observations and then rotates the dome about 130 deg in azimuth to be in the proper position for the sunset event that occurs about 40 min later. Only small rotations of the telescope on its elevation bearings are required to track the sun during each observation. A typical observation sequence is illustrated in Fig. 15.21.

Thermal-Design Requirements

The thermal-design requirements for POAM, driven by both the instrument and the host spacecraft, are listed in Table 15.5. From the sensor's point of view, the
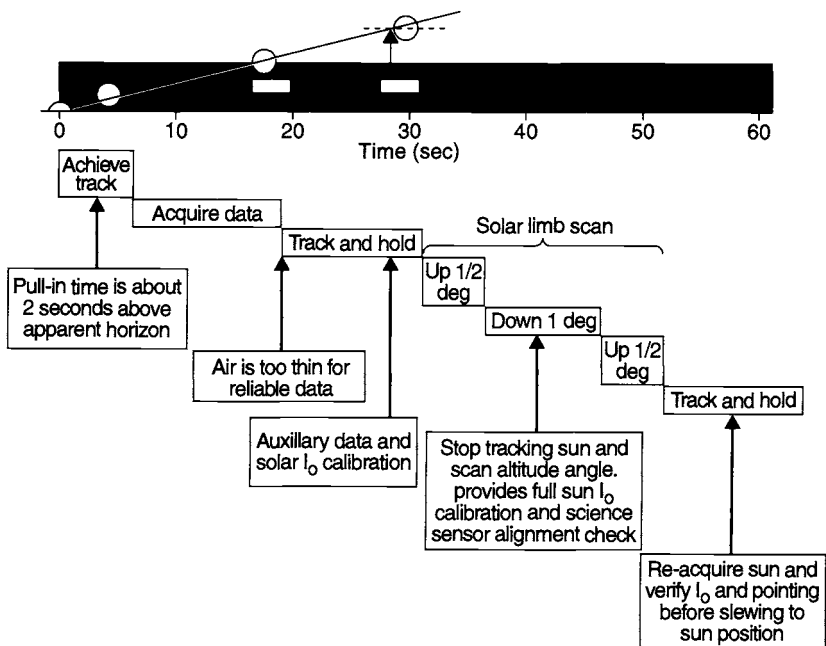
Fig. 15.21. POAM observation sequence.

Table 15.5. POAM Thermal-Design Requirements

- Optical head case temperature ranges from −10 to 50°C.
- Survival/turn-on limit equals −30°C.
- Spacecraft must survive without power for 3-1/2 hours after launch.
- Spacecraft must survive without power for two orbits returning from safe to nominal operating mode.
- Uncertainty margin of 10°C applied to predicted temperatures, 25% margin on heater power.
- Conduction between optical head and bracket limited to less than 0.07 W/K.

instrument must be maintained between −10 and +50°C while operating, and between −30 and +50°C while not operating or at turn-on. From the spacecraft's point of view, certain mission-related requirements must be met, including: the ability to go for 3-1/2 hours after launch with no power supplied to the instrument; the ability to survive the spacecraft safe-mode condition in which only survival-heater power is available to the instrument; the ability to withstand a two-orbit (approximately 3-1/2 hour) transition from safe mode to normal operating mode, during which time neither electronics nor survival-heater power will be available; and the ability to limit conduction between the instrument and the spacecraft mounting bracket to less than 0.07 W/K. Furthermore, all organizations involved agreed that an uncertainty margin of 10°C would be applied to all temperature predictions and any heaters would be sized to provide either a 10°C margin to lower temperature limits or a 25% excess capacity at the lower temperature limit.

Conceptual Design

The first step in the design process is to identify the factors that will drive the design. Such factors include the previously discussed design requirements levied by the instrument designers and the satellite, as well as the instrument heat dissipation and range of external environments.

The instrument heat dissipation varies around the orbit because of the operation of motors during telescope slewing. At the conceptual design phase of this program, the electrical-power draw for the instrument (which is all converted to heat because no significant amount of energy is output) was estimated to be no greater than that shown in Fig. 15.22. Because periods could also occur of several orbits or longer during which no observations would take place and the drive motors would not be in operation, the minimum power draw was assumed to be a constant 4.4 W. Most of this heat is dissipated in the azimuth housing, with only a small portion dissipated in the telescope.

The instrument is also exposed to solar, Earth IR, and albedo environmental heating fluxes. Because the satellite is Earth-facing in a sun-synchronous orbit, the sun position relative to the vehicle forms a cone as the satellite goes around Earth, as shown in Fig. 15.23. This cone has an elevation angle that equals the orbit beta angle, 14.5 to 29.8 deg. Eclipse time ranges from 32.5 to 34.6 min, as can be calculated from the equations in Chapter 2. Because the spacecraft is Earth-facing, the
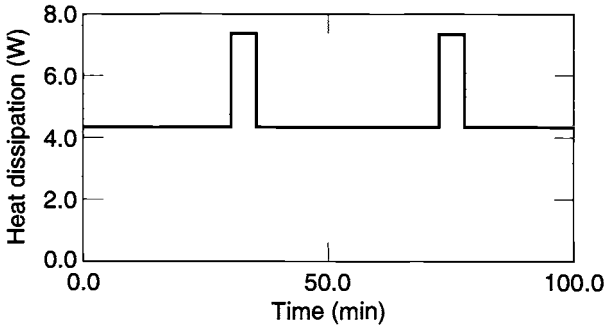
Fig. 15.22. Instrument heat dissipation.
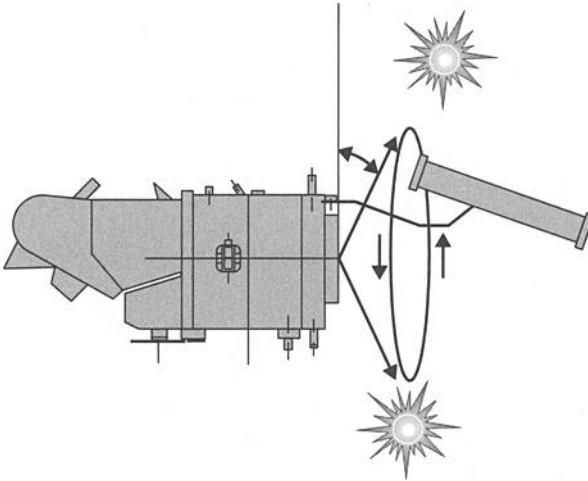
Fig. 15.23. Solar illumination angles.

instrument is always pointing with the dome facing straight down at Earth, and Earth IR loads can therefore be assumed to be constant around the orbit. Albedo loads will, of course, vary around the orbit, but the narrow range of beta angle ensures that orbit-average albedo loads will not change a great deal over time.

Given the estimated heat dissipation, and the requirement that the instrument be conductively isolated from the satellite, some amount of radiator area will be required to reject the instrument waste heat to space. Most of this heat dissipation is in the base, which is largely covered on three sides by its mounting bracket. The side facing away from the spacecraft is the only one with a fairly clear view to

space, although it does have a small view to the spacecraft solar array. To determine if this side would have sufficient area to reject the waste heat, a simple calculation can be performed. The maximum orbit-average internal heat plus the maximum orbit-average environmental heat flux must not exceed the energy radiated from the surface at the maximum allowable temperature;

$$\dot{Q}_{\text{ELECTRONIC}} + \dot{Q}_{\text{ENVIRONMENTAL}} = A\varepsilon\sigma T^4 . \tag{15.16}$$

(The small amount of heat backload from the spacecraft solar array may be neglected for this preliminary evaluation. Also, the mass of the instrument, 11 kg, gives it a large heat capacity relative to the heat pulses during motor operations. This ensures that the temperature will not vary too much from the orbit average, making these orbit-average calculations reasonably accurate.)

The maximum orbit-average internal heat dissipation can be calculated in a straightforward manner from Fig. 15.22 to be 4.7 W. The worst-case solar heating for this surface would occur when the sun is at its maximum elevation angle above the surface, 29.8 deg, as shown in Fig. 15.23. The orbit-average solar load is given by:

$$\dot{Q}_{\text{solar}} = (\sin 29.8°)S\alpha(\% \text{ of orbit in sunlight}), \tag{15.17}$$

where S is the solar constant and α is the absorptance of the surface.

With a 5-mil silvered Teflon radiator-surface finish, the EOL absorptance would be approximately .18 after 3 years in low Earth orbit. This figure is based on a BOL α of .05, and a degradation of .09. The maximum solar constant is 1414 W/m^2 (Chapter 2), and the percent sunlight time is

$$\frac{\text{orbit period} - \text{eclipse time}}{\text{orbit period}} = \frac{100 \text{ min} - 32.5 \text{ min}}{100 \text{ min}} = 67.5\%. \tag{15.18}$$

Substituting these values in Eq. (15.17) gives a maximum orbit-average absorbed solar load of 84.6 W/m^2.

The orbit-average Earth IR load can be calculated using Fig. 15.24, which is applicable to flat, unblocked surfaces. Because the satellite's orientation is Earth-pointing, the instrument radiator surface remains perpendicular to Earth all around the orbit, so Earth IR heating will not change. The ρ angle for Fig. 15.23 is therefore 90 deg, and the altitude is 822 km. At the intersection of ρ = 90 deg and h = 822 km, find F_E = .22, project F_E = .22 to the line labeled q_E, then project this point horizontally to the q_E (Earthshine) scale to read q_E = 47.8 W/m^2. The heat absorbed is the incident value times the emissivity of the surface, or (47.8)(.78) = 37.3 W/m^2 for 5-mil silvered Teflon.

Albedo loads can be calculated in a similar fashion using Fig. 15.25; however, one must calculate the value for several points because albedo changes as the satellite travels the orbit. Using Fig. 15.25, begin with the same altitude and ρ angle as in the Earth-IR calculation, i.e., 822 km and 90 deg. At the intersection of ρ = 90 deg and h = 822 km, find F_R = .22. Because the satellite is in an orbit with a beta angle of almost 30 deg, shift down to the scale labeled β = 30 deg and draw a
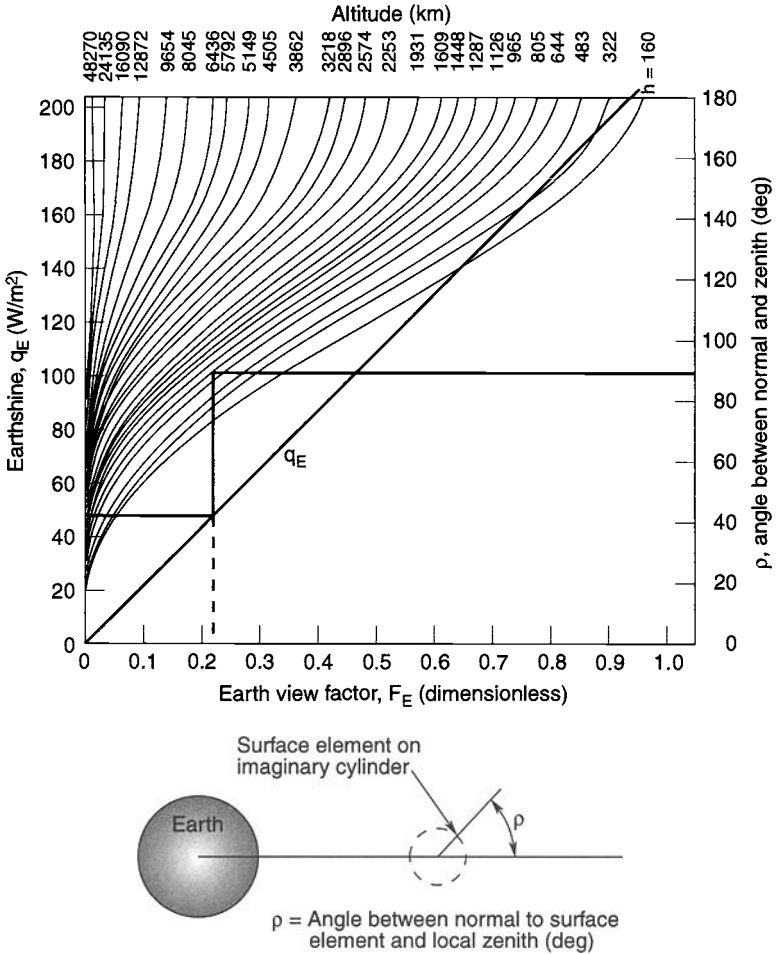
Fig. 15.24. Incident Earthshine irradiation on a surface element in an Earth orbit (courtesy of Lockheed Martin).

vertical line at $F_R = .22$. The intersections of this line with the family of lines labeled $\theta = x$ deg gives the incident albedo flux for various points around the orbit at position angles of θ deg, measured from the closest approach to the subsolar point. Figure 15.25 gives the values for the half of an orbit, on the sunlit side of Earth. If these values are averaged and then divided by two to account for the dark half of the orbit, which experiences no albedo load, the resulting value is the orbit-average incident albedo of 33.8 W/m². Multiplying this by the silvered Teflon solar absorptivity of .18 gives an orbit-average absorbed-albedo load of 6.1 W/m². The albedo load is therefore a fairly small contributor compared to the solar (84.6 W/m²) and Earth IR (37.3 W/m²) heat loads.
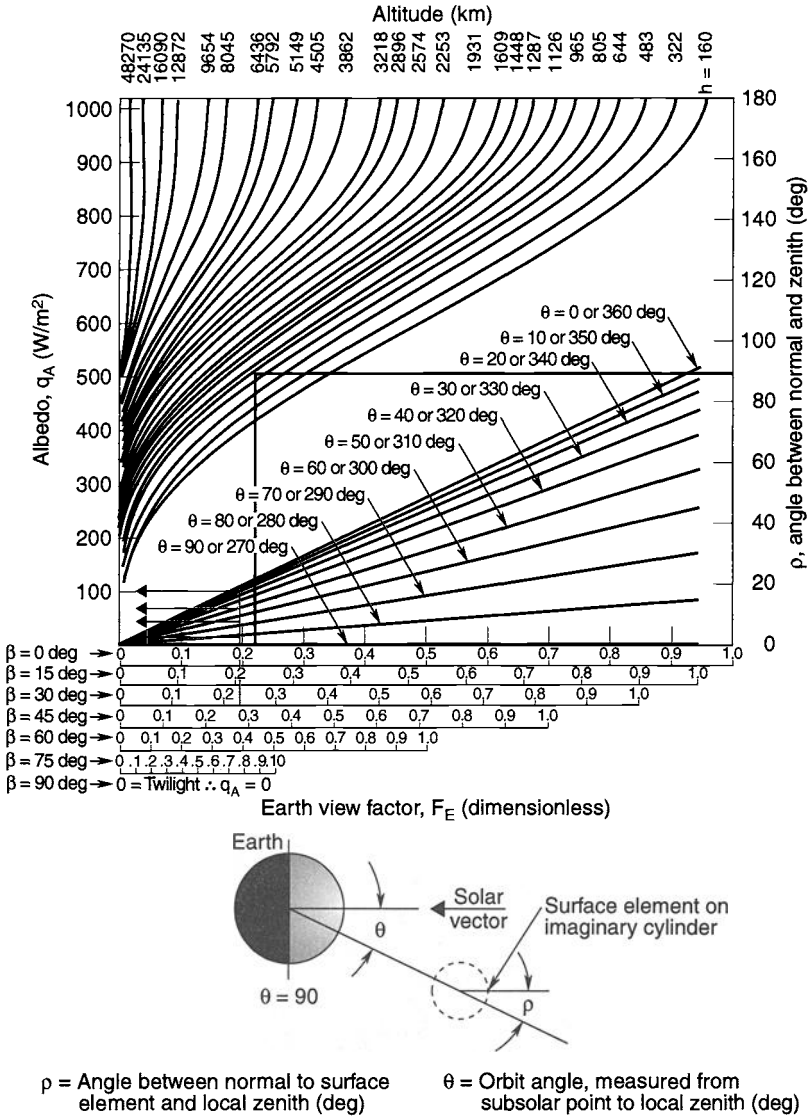
Fig. 15.25. Incident albedo irradiation on a surface element in an Earth orbit. (Note: Earth reflectance is assumed to be 0.38. Albedo plotted is an approximation, with the largest error near the terminator [θ = 90].) (Courtesy of Lockheed Martin.)

Substituting the orbit-average electronics heat, solar IR, and albedo loads into Eq. (15.19) and solving for the radiator area at a temperature of 40°C (313 K) gives:

$$\dot{Q}_{ELECT} + \dot{Q}_{ENVIR} = A\varepsilon\sigma T^4 \tag{15.19}$$

$$16.0 + [84.6 + 37.3 + 6.1]A = A(0.78)(5.669 \times 10^{-8})(313)^4 \tag{15.20}$$

$$A = 0.01571 \text{ m}^2 = 157 \text{ cm}^2. \tag{15.21}$$

Because the face of the azimuth housing has an area of 203 cm^2, adequate area for a radiator is available. (Note: A radiating temperature of 40°C was selected to allow for the required 10°C margin between analysis and the maximum allowable instrument temperature limit of 50°C.)

The minimum temperature of the instrument under cold-case conditions using the radiator size calculated above was determined in the same manner. Solar, albedo, and Earth IR heating for the cold-case orbit (β = 14.5 deg, summer) and electronics waste heat without motor operations were summed and, with an area of 157 cm^2, Eq. (15.19) was solved for T. This gave a cold-case temperature of 22°C. These preliminary hot- and cold-case calculations indicated that the entire side of the azimuth housing (203 cm^2), rather than the 157 cm^2 calculated above, could be used as a radiator to bring the average temperature down a little. Lower operating temperatures generally increase the life and reliability of electronic components.

Based on the preliminary radiator sizing and the requirements listed in Table 15.5, the thermal-design concept shown in Fig. 15.26 was identified. The side of the azimuth housing facing away from the spacecraft would be covered with 5-mil silvered Teflon, and it would serve as the primary radiator. All other surfaces of the azimuth housing and dome would be covered with MLI blankets to minimize loss of heat through these surfaces and to essentially eliminate radiative thermal
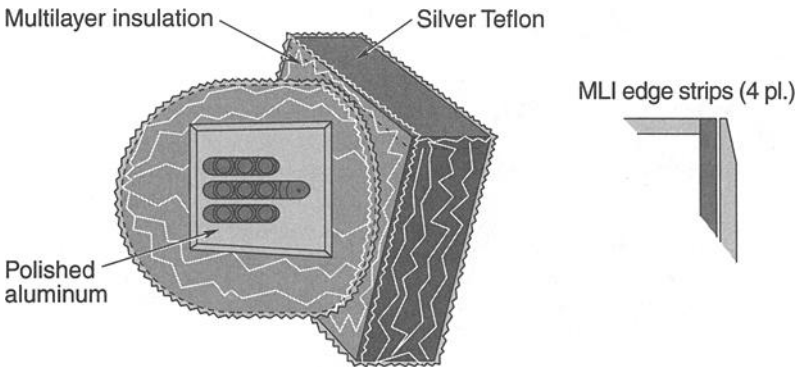
Fig. 15.26. POAM thermal design.

interactions between the instrument and the spacecraft. A small "window" would be made in the MLI covering the dome to allow the telescopes a view out. The surface of the aluminum dome exposed in the window area, however, would be polished to provide a low absorptance and emittance to minimize both radiative heat loss and energy absorbed from incident environmental heat fluxes. Because of their poor conductive-heat transfer, the bearings between the telescope and the dome and between dome and azimuth housing tend to thermally isolate these components. Therefore, to tie them together radiatively as much as possible, the telescope external surface and the dome internal surface would be given a black high-emittance finish. The bottom of the dome and the top of the azimuth housing would also be painted black to maximize the radiative coupling in the interface. Plastic isolators would be placed under each of the mounting feet to meet the requirement of limiting conductive-heat transfer between the instrument and the spacecraft-supplied support bracket.

Detailed Design Analysis

Once a design concept is identified, a detailed analysis must be conducted to fine-tune the design and predict instrument temperatures under the entire range of flight conditions. This involves identifying analysis cases to be run and constructing a GMM and a TMM of the instrument. For the POAM program, a thermal analysis of the overall instrument was conducted, with separate additional analyses performed of the individual circuit cards and telescope photo detectors. This discussion will be limited to the instrument-level analysis.

The GMM and TMM serve different purposes. The GMM, a mathematical representation of the physical surfaces of the instrument, is used to calculate greybody radiation couplings between surfaces as well as heating rates resulting from environmental fluxes. The TMM, most often a lumped-parameter network representation of the thermal mass and conduction and radiation couplings of the instrument, is used to predict instrument temperatures. The radiation interchange couplings and environmental heat fluxes calculated by the GMM are used in constructing the TMM. Both the GMM and TMM are constructed and executed using industry-standard computer programs. The most common GMM codes are TRASYS[15.3] and NEVADA,[15.4] and the most common TMM code is SINDA.[15.5,15.6] Other commercially available codes do exist, however, and some large companies use their own internally developed codes. The codes mentioned above will be discussed in detail in later sections of this chapter.

Analysis Cases

Based on the instrument operating modes and thermal-design requirements discussed earlier, four significant thermal-design analysis cases were identified, as shown in Table 15.6. Normal on-orbit operations are bounded by the hot and cold operating cases. The responses of the instrument to launch and a potential spacecraft "safe mode" condition were also analyzed.

The hot operating-case conditions include maximum solar heating, which occurs at the highest beta angle with the winter solar constant, maximum Earth IR and albedo, maximum (EOL) solar absorptance on the external surface finishes, good insulation-blanket performance, maximum motor operations, telescopes

Table 15.6. Design Environments/Assumptions

Hot Operating	Cold Operating	Safe Mode	Launch/Ascent
$\beta = 29.8°C$, winter	$\beta = 14.5°C$, summer	NA	$\beta = 14.5°C$, summer
EOL $\alpha = 0.17$	BOL $\alpha = 0.08$	NA	BOL $\alpha = 0.08$
MLI $\varepsilon^* = 0.01$	MLI $\varepsilon^* = 0.05$	MLI $\varepsilon^* = 0.05$	MLI $\varepsilon^* = 0.05$
Telescope sees sun twice per revolution	Telescope does not see sun	Telescope does not see sun	Telescope does not see sun
10 min/rev motor operations (3 W)	No motor operations	No motor operations	No motor operations
Hot spacecraft	Cold spacecraft	Cold spacecraft	Cold spacecraft
Radiator to solar-array view varies around revolution	Radiator to solar-array view varies around revolution	Fixed radiator view to solar array	Radiator to solar-array view varies around revolution
4.4-W electronics heat	4.4-W electronics heat	No power, heaters only	No power, no heaters
Earth IR = 234 W/m^2	Earth IR = 208	No Earth IR	Earth IR = 208
Albedo = 0.42	Albedo = 0.34	No albedo	Albedo = 0.34

looking at the sun twice per orbit, maximum spacecraft temperatures, and maximum electronics waste heat. Cold operating-case conditions include minimum solar loads, minimum (BOL) solar absorptances, poor insulation-blanket performance, no motor operations, telescope stopped in a position where it does not see the sun, cold spacecraft temperatures, minimum Earth IR and albedo, and minimum electronics waste heat (which happens to be the same as the maximum heat because it is constant for this instrument).

During safe mode, the spacecraft turns and points constantly at the sun instead of Earth and the POAM instrument is turned off, although some power is available to run heaters, if required. Because the instrument is off and shadowed from the sun by the spacecraft, this is a cold-case condition. It is therefore also assumed that there is no Earth IR or albedo heating for conservatism.

During the launch phase, POAM is turned off. While sitting on the launchpad, the instrument will be at approximately the same temperature as the purge gas inside the booster fairing (15°C), because it has no internal heat dissipation. For the first three minutes after liftoff the booster fairing is in place and experiences a large temperature rise. Because of the large thermal mass of POAM and the brief duration of this phase, the thermal effect on the instrument is negligible. This is followed, however, by a 1/2-hour period during which the spacecraft attitude is not controlled and the POAM radiator may see the sun, Earth, and/or deep space. Because the instrument is not powered, this is a cold case, and the assumption was therefore made that the radiator was facing deep space with no environmental heat

fluxes incident on any surface. After 1/2 hour the spacecraft is stabilized in its normal attitude, but POAM is still not powered. The point of this analysis case is to determine how long the instrument can go after launch with no power without violating its lower survival temperature limit of –30°C.

GMM Construction

The GMM of the POAM mounted on the host spacecraft was constructed using the NEVADA code. The model, shown in Fig. 15.27, consists of a simple representation of the spacecraft, POAM, and the support bracket. It was constructed on a CAD-like system using rectangular, circular, hemispherical, and cylindrical surface elements available in the NEVADA package, and each surface was assigned the appropriate absorptance, emittance, and specularity. Details about how these models are constructed using NEVADA can be found in Ref. 15.4.

The GMM was then run using NEVADA to calculate the radiation interchange factors between all surfaces. NEVADA also outputs a radiation-conductor block that may be merged directly into the SINDA TMM. This block of conductors will be discussed later.

The GMM was then placed mathematically into the proper orbit and attitude using another section of the NEVADA software. Solar, Earth IR, and albedo heat loads absorbed on each surface were calculated for a dozen points around the orbit for both the hot-case (maximum beta angle, winter, maximum absorptance) and the cold-case (minimum beta angle, summer, minimum absorptance) orbits. These heat rates are also output by NEVADA in arrays that can be merged directly into the TMM.

TMM Construction

The TMM consists of nodes representing parts of the instrument, diffusion and radiation conductors between nodes, blocks of arrays and constants for storing inputs such as environmental heating rates calculated by NEVADA, and logic blocks for controlling the execution of the program. A listing of the POAM TMM in SINDA format is shown in Table 15.7.
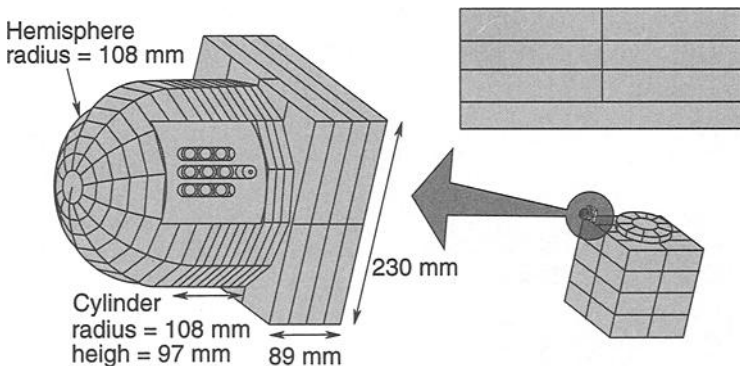

Fig. 15.27. POAM geometry.

Table 15.7. POAM TMM Listing

```
BCD 3THERMAL LPCS
END
BCD 3NODE DATA
    101,50.,.085        AZIMUTH HOUSING NODES
    3,50.,.13
    4,50.,.13
    5,50.,.13
    6,50.,.13
    7,50.,.13
    8,50.,.13
    9,50.,.54
    10,50.,.54
    11,50.,.089
    12,50.,1.6          DOME NODE
    112,50.,0.61        TELESCOPE NODE
    22,50.,-1.          DOME MLI NODE
    23,50.,-1.          AZIMUTH HOUSING NODE
    -997,150.,0.        SPACECRAFT SOLAR ARRAY BOUNDARY NODE
    -998,80.,0.         SUPPORT BRACKET BOUNDARY NODE
    -999,-460.,0.       SPACE BOUNDARY NODE (TEMPERATURE=ABSOLUTE ZERO)
END
BCD 3CONDUCTOR DATA
    1,3,101,1.04        DIFFUSION CONDUCTORS IN AZIMUTH HOUSING
    2,8,101,1.04
    3,101,9,3.13
    4,3,4,1.
    5,4,5,1.
    6,5,6,1.
    7,6,7,1.
    8,7,8,1.
    9,9,10,3.48
    10,9,8,1.15
    11,9,3,1.15
    12,10,4,1.15
    13,10,5,1.15
    14,10,6,1.15
    15,10,7,1.15
    16,11,101,.12
    17,11,3,.063
    18,11,4,.063
    19,11,5,.063
    20,11,6,.063
    21,11,7,.063
    22,11,8,.063
    23,3,998,.033       CONDUCTION ACROSS ISOLATORS TO SPACECRAFT
    24,4,998,.033
    25,7,998,.033
    26,8,998,.033

                            RADIATION CONDUCTORS
    -101,101,999,1.61E-10   FROM RADIATOR TO SPACE
    -102,101,997,4.14E-11   FROM RADIATOR TO SOLAR ARRAY
    -103,12,999,7.48E-11    FROM DOME WINDOW TO SPACE
    -104,12,997,8.31E-12    FROM DOME WINDOW TO SOLAR ARRAY
    -105,112,999,4.97E-12   FROM TELESCOPE TO SPACE
    -106,112,12,1.23E-9     FROM TELESCOPE TO DOME (INTERNAL)
    -107,22,999,1.49E-9     FROM DOME MLI OUTER LAYER TO SPACE
    -108,22,997,0.166E-9    FROM DOME MLI OUTER LAYER TO SOLAR ARRAY
    -109,22,12,1.34E-11     FROM DOME THROUGH MLI TO OUTER LAYER
    -110,12,9,1.42E-10      FROM BOTOM OF DOME TO AZIMUTH HOUSING
    -111,12,10,1.42E-10      "      "     "      "       "
    -112,23,9,0.72E-12      FROM AZIMUTH HOUSING THROUGH MLI TO OUTER LAYER
    -113,23,10,0.72E-12      "       "       "      "    "     "
    -114,3,998,9.37E-13     FROM AZIMUTH HOUSING THROUGH MLI TO OUTER LAYER
    -115,4,998,9.37E-13
    -116,5,998,9.37E-13
    -117,6,998,9.37E-13
    -118,7,998,9.37E-13
    -119,8,998,9.37E-13
    -120,11,998,0.45E-11
    -123,23,22,1.13E-10     FROM DOME MLI TO AZIMUTH HOUSING MLI (EXTERNAL)
    -124,23,999,3.6E-10     FROM AZIMUTH HOUSING MLI OUTER LAYER TO SPACE
END
```

Table 15.7. POAM TMM Listing *(Continued)*

```
BCD 3CONSTANTS DATA
    TIMEO=0.,ARLXCA=.1,DRLXCA=.1,NLOOP=5000       PROGRAM CONTROL CONSTANTS
    NDIM=5000,BALENG=.05,CSGFAC=1.                 "      "      "
    1,0.,2,0.,3,0.,4,0.,5,0.                      CONSTANT STORAGE LOCATIONS
    6,0.,7,0.,8,0.,9,0.,10,0.
    11,0.,12,0.,13,0.,14,0.,15,0.
    16,0.,17,0.,18,0.,19,0.
END
BCD 3ARRAY DATA
C   AZIMUTH HOUSING RADIATOR AREA*VIEW TO SPACE VS. TIME FOR ONE ORBIT
    1,0.,.0945,.21,.0917,.42,.116,.63,.108,.84,.111
    1.05,.111,1.26,.0917,1.47,.0945,1.68,.0945,END
C   AZIMUTH HOUSING RADIATOR AREA*VIEW TO SOLAR ARRAY VS. TIME FOR ONE ORBIT
    2,0.,.0245,.21,.0273,.42,.0027,.63,.0105,.84,.0105,1.05,.008
    1.26,.0273,1.47,.0245,1.68,.0245,END
C   SOLAR ARRAY TEMPERATURE VS. TIME FOR ONE ORBIT
    3,0.,176.,.653,133.,.822,-112.,1.212,-126.,1.213,133.
    1.68,176.,END
C   ENVIRONMENTAL HEATING ON TELESCOPE BODY VS. TIME FOR ONE ORBIT
    4,0.,1.17,.047,.79,.377,.56,.374,.19,.512,.19,.513,5.26
    .56,5.34,.606,5.44,.653,5.88,.654,.19,1.212,.19
    1.213,5.85,1.4,5.02,1.54,3.74,1.68,1.17,END
C   ENVIRONMENTAL HEATING ON DOME IN WINDOW AREA VS. TIME FOR ONE ORBIT
    5,0.,2.5,.04,2.5,.186,4.82,.42,5.9,.513,6.3
    .653,4.8,.654,1.5,1.212,1.5,1.213,4.8,1.245,5.
    1.32,2.0,1.58,2.5,END
C   ENVIRONMENTAL HEATING IN GAP BETWEEN DOME AND AZIMUTH HOUSING VS. TIME
    6,0.,1.6,.467,1.4,.56,4.3,.653,4.2,.654,1.,1.212,1.
    1.213,4.2,1.307,4.3,1.4,1.4,1.68,1.6,END
C   ENVIRONMENTAL HEATING ON OUTER LAYER OF DOME VLT
    7,0.,58.,.09,48.,.19,48.,.28,58.,.37,70.,.47,83.
    .56,89.,.653,95.,.654,24.,1.212,24.,1.213,96.
    1.26,96.,1.44,83.,1.68,58.,END
C   AZIMUTH HOUSING ELECTRONICS WASTE HEAT
    8,0.,15.,1.68,15.,END
C   AZIMUTH MOTOR WASTE HEAT
    9,0.,0.,.652,0.,.653,10.23,.736,10.23,.737,0.,1.244,0.,1.245,10.23
    1.32,10.23,1.321,0.,1.68,0.,END
C   SOLAR HEAT FLUX PER SQ. IN. INCIDENT ON AZIMUTH HOUSING RADIATOR VS. TIME
    11,0.,1.53,.653,1.53,.654,0.,1.212,0.,1.213,1.53,1.68,1.53,END
C   ALBEDO HEAT FLUX PER SQ. IN. INCIDENT ON AZIMUTH HOUSING RADIATOR VS. TIME
    12,0.,.19,.187,.15,.373,0.,1.307,0.,1.493,.15,1.68,.19,END
C   EARTH IR FLUX PER SQ. IN. INCIDENT ON AZIMUTH HOUSING RADIATOR VS. TIME
    13,0.,.107,1.68,.107,END
END
BCD 3EXECUTION
M   TIMEND=100.            PROGRAM CONTROL CONSTANTS
M   OUTPUT=10.                 "        "        "
    ATSDUF                     "        "        "
END
BCD 3VARIABLES 1
M   IF(TIMEO.GT.98.3) OUTPUT=1./60.
    D11CYL(1.68,TIMEO,A1,XK1)          INTERPOLATES ARRAYS AND PLACES CURRENT
    D11CYL(1.68,TIMEO,A2,XK2)              VALUES IN CONSTANT LOCATIONS
    D11CYL(1.68,TIMEO,A3,XK3)
    D11CYL(1.68,TIMEO,A4,XK4)
    D11CYL(1.68,TIMEO,A5,XK5)
    D11CYL(1.68,TIMEO,A6,XK6)
    D11CYL(1.68,TIMEO,A7,XK7)
    D11CYL(1.68,TIMEO,A8,XK8)
    D11CYL(1.68,TIMEO,A9,XK9)
    D11CYL(1.68,TIMEO,A11,XK11)
    D11CYL(1.68,TIMEO,A12,XK12)
    D11CYL(1.68,TIMEO,A13,XK13)
```

Table 15.7. POAM TMM Listing *(Continued)*

```
M       T997=XK3                              SETS CURRENT SOLAR ARRAY TEMPERATURE

M       G101=(XK1*8.4)*(30.6*.78)*(.1714E-8)/144. ADJUSTS RADIATOR RELATIVE VIEW TO
M       G102=(XK2*8.4)*(30.6*.78)*(.1714E-8)/144. SPACE AND SOLAR ARRAY AS ARRAY TURNS

M          Q23=32.            ENVIRONMENTAL HEATING ON AZIMUTH HOUSING MLI OUTER LAYER
V          Q22=XK7                  "          "      "   DOME MLI OUTER LAYER
M          Q101=30.6*(.15*(XK11+XK12)+.78*XK13) "  "   AZIMUTH HOUSING RADIATOR
V          Q3=XK8/4.          AZIMUTH HOUSING ELECTRONICS WASTE HEAT
M          Q4=Q3                  "          "      "      "
M          Q7=Q3                  "          "      "      "
M          Q8=Q3                  "          "      "      "
V          Q112=XK4        ENVIRONMENTAL HEAT ON TELESCOPE
M          Q12=XK5+XK6/2.      ENVIRONMENTAL HEATING ON DOME
M          Q9=XK9/2.+XK6/4.   ENVIRONMENTAL AND AZIMUTH DRIVE MOTOR WASTE HEAT
M          Q10=Q9                 "          "      "      "
        END
        BCD 3VARIABLES 2
        END
        BCD 3OUTPUT CALLS
            TPRINT
        END
        BCD 3END OF DATA
```

The nodalization scheme chosen for the TMM is shown in Fig. 15.28. Because the base, dome, and telescope are all constructed of thick (2.5–5.0 mm) aluminum, they can each be assumed to be fairly isothermal, and a minimum number of nodes are required to model them. The entire telescope is therefore modeled as one node, as is the dome assembly. The location of the radiator on one side of the azimuth housing, however, means that some temperature gradient could exist between it and heat-dissipating elements on the opposite face. The azimuth housing was therefore modeled using ten nodes, as shown in Fig. 15.28. The MLI covering the dome and azimuth housing were represented by one node each. Temperatures of the spacecraft solar array, the mounting bracket, and the outer layer of the


Fig. 15.28. POAM TMM nodes.

spacecraft MLI were all supplied by the spacecraft engineers and were therefore put in the POAM TMM as boundary-driver nodes.

Capacitances of each node were hand-calculated either by using a weight found in a mass-properties report for the instrument and multiplying by the specific heat, or by calculating the volume of material and multiplying by the density and specific heat. Arithmetic (zero-capacitance) nodes were used to represent MLI blankets because the blankets are extremely light and respond almost as if they had zero mass. The boundary nodes do not require a capacitance because they are treated by the program as constant-temperature (infinite-capacitance) sinks.

Diffusion conductors were calculated in a straightforward manner using the $k\frac{A}{l}$ relationship as discussed in the "Fundamentals of Thermal Modeling" section. One exception to this was the conduction between the azimuth housing and its rear cover, which is held in place with screws. The contact conduction between these nodes was based on screw-conduction terms found in Chapter 8. Another exception was the conduction across the azimuth and elevation bearings. Because bearing conduction is so uncertain, two cases were run to bound the problem: zero conductivity at one extreme, and a conduction equal to 315 W/m^2 over the entire area of the bearing race at the other extreme. Both values were used for each of the four design analysis cases for POAM, and the value that resulted in the most extreme temperatures was chosen.

Conductive heat transfer between the instrument and its mounting bracket had to be limited to less than .07 W/°C per spacecraft requirements. To accomplish this, the fiberglass isolators shown in Fig. 15.29 were designed for installation

$$G_{\text{through bolt}} = \frac{1}{\dfrac{1}{G_2} + \dfrac{1}{G_3} + \dfrac{1}{G_4}}$$

$$G_{\text{total}} = G_{\text{through bolt}} + G_1$$
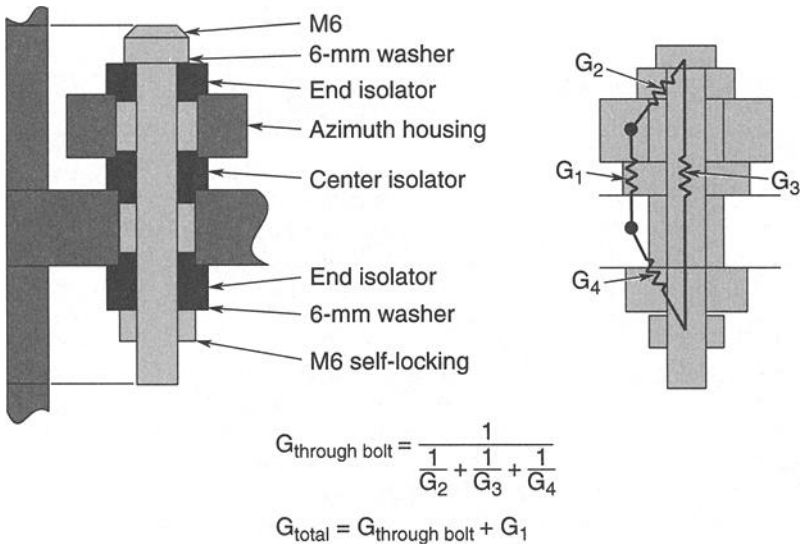
Fig. 15.29. POAM mounting isolator.

under the four mounting feet. The calculations of the conductance across these isolators are shown in the figure.

Radiation conductors generated by NEVADA were merged into the TMM. The conductors through the MLI blankets, however, were calculated manually. The heat leak through MLI can be modeled as an effective emittance, ε^*, as discussed in Chapter 5. A range of effective emittances was used for this analysis, because predicting the exact performance of an insulation blanket before it is built and tested is difficult. For the hot case, a value of .01 was chosen, while .05 was used in the cold case. An ε^* of .05 is rather high, but it is justified in this case because the blankets are small and therefore more susceptible to the heat-leak effects of edges and attachments. For each node covered with MLI, a radiation conductor was calculated as (Area)(ε^*)(σ) between the instrument node and the node representing the outer layer of the MLI blanket. The radiation couplings from the outside face of the MLI blanket to space and to the spacecraft were previously calculated by the NEVADA model and were already merged into the TMM.

The complete hot-case TMM is shown in Table 15.7. The first block contains the node data. Each node is given an integer number, initial temperature, and capacitance. Arithmetic (zero-capacitance) nodes are represented in SINDA by negative capacitance values, and boundary (infinite-capacitance) nodes are represented by negative node numbers, as can be seen in the table. The next block contains the conductor data. Each conductor input contains an integer conductor number, the nodes that the conductor connects together, and a conductor value. Radiation conductors are given negative conductor numbers in SINDA. The next block contains the user and SINDA data constants. In this case, a number of program-control constants are present, as well as ten constant-storage locations, which will be discussed later. The next block contains array data. In this case arrays are here giving time-varying environmental-heat fluxes previously calculated by NEVADA, time-varying electronics-waste-heat rates, and time-varying radiation conductors between the POAM radiator node and the rotating spacecraft solar array (this was also previously calculated by NEVADA and input manually into the TMM).

The next three blocks control the execution of the program. The second of these, "VARIABLES 1," specifies how much heat is on each node as well as what the radiation coupling is from the POAM radiator to the solar array at any given time. This block is accessed before the start of each time step as the program calculates the change of POAM temperatures with time. The final block specifies the data to be output by the program. In this case, temperatures and impressed heat rates for each node are requested.

Predicted Temperatures

The file in Table 15.7 was executed by the SINDA program, and temperatures were calculated. Similar files were constructed for the cold-operating, safe-mode, and launch-ascent cases. Predicted temperatures for these conditions are shown in Figs. 15.30 through 15.32. Comparison of these results to the requirements of Table 15.5 shows that all requirements are met with adequate (10°C or greater) margin. For the safe-mode case a heater was required to maintain the instrument above its lower survival temperature.
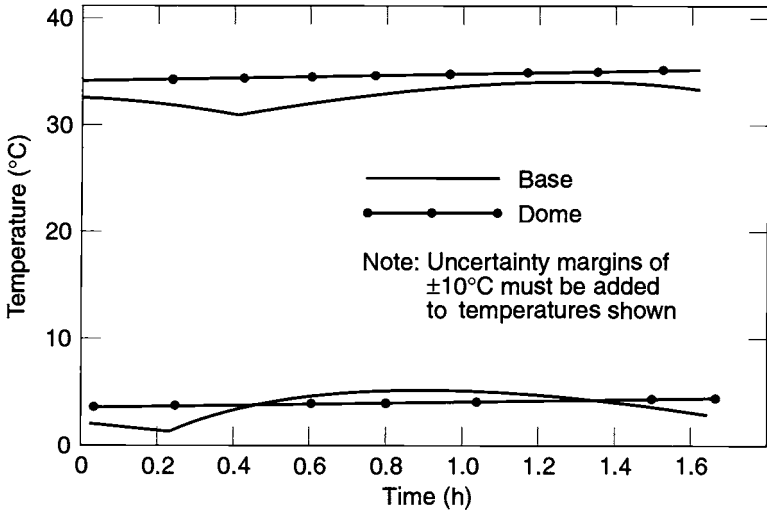
Fig. 15.30. Hot and cold operating temperatures
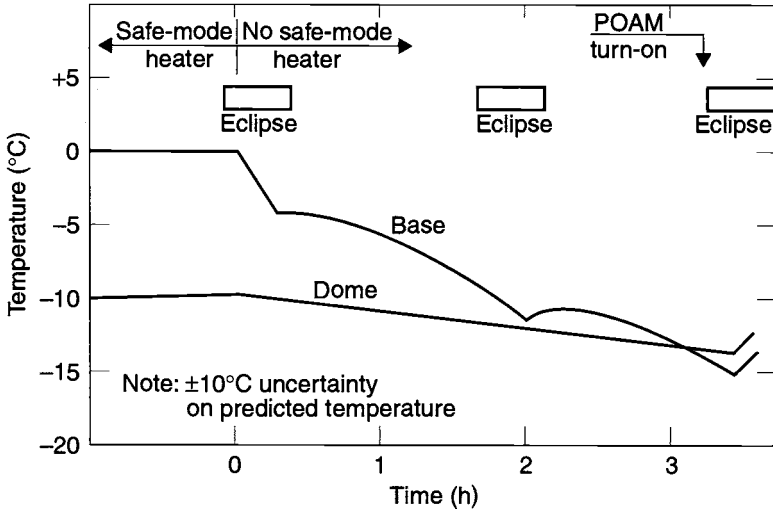
Fig. 15.31. Safe-mode temperatures.
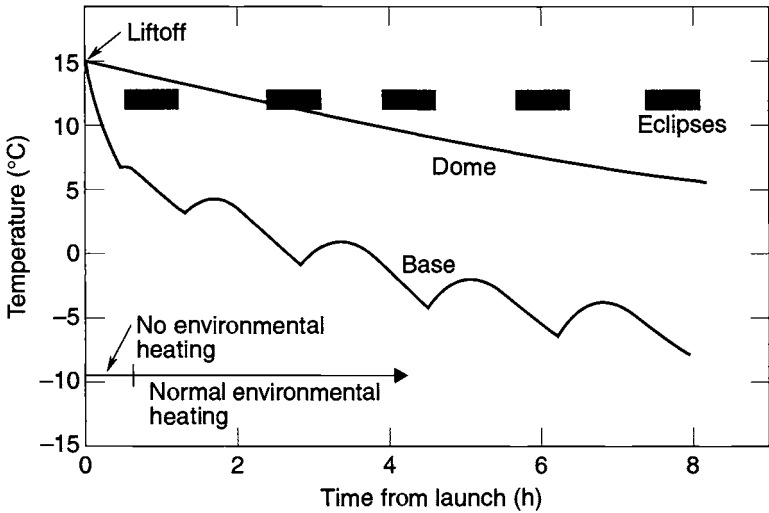
Fig. 15.32. Launch/ascent temperatures.

Thermal-Balance Test

The thermal analysis described above was verified by a thermal-balance test. This was conducted during spacecraft-level thermal-vacuum testing in Toulouse, France. The POAM instrument was installed on the spacecraft in the flight configuration. Hot- and cold-case test phases were planned. Because of limitations associated with the spacecraft, these were not precise representations of the flight hot and cold cases, but they were close, and they provided two good conditions with which the TMMs could be checked and correlated.

The temperature instrumentation used is shown in Fig. 15.33, and the hot- and cold-case steady-state temperatures are shown in Fig. 15.34. As can be seen from this data, the azimuth housing is nearly isothermal with only a 2 to 3°C variation around the box. The dome assembly, however, ran approximately 15°C cooler than the azimuth housing. This temperature difference indicates that little conductive coupling exists between the dome and azimuth housing, as was assumed in the design analysis for conservatism. The dome runs cooler because no electronics
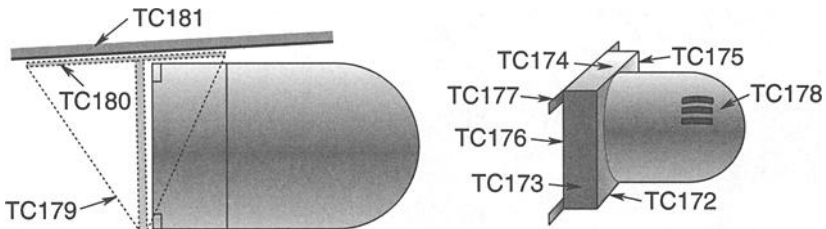
Fig. 15.33. Test thermocouples.
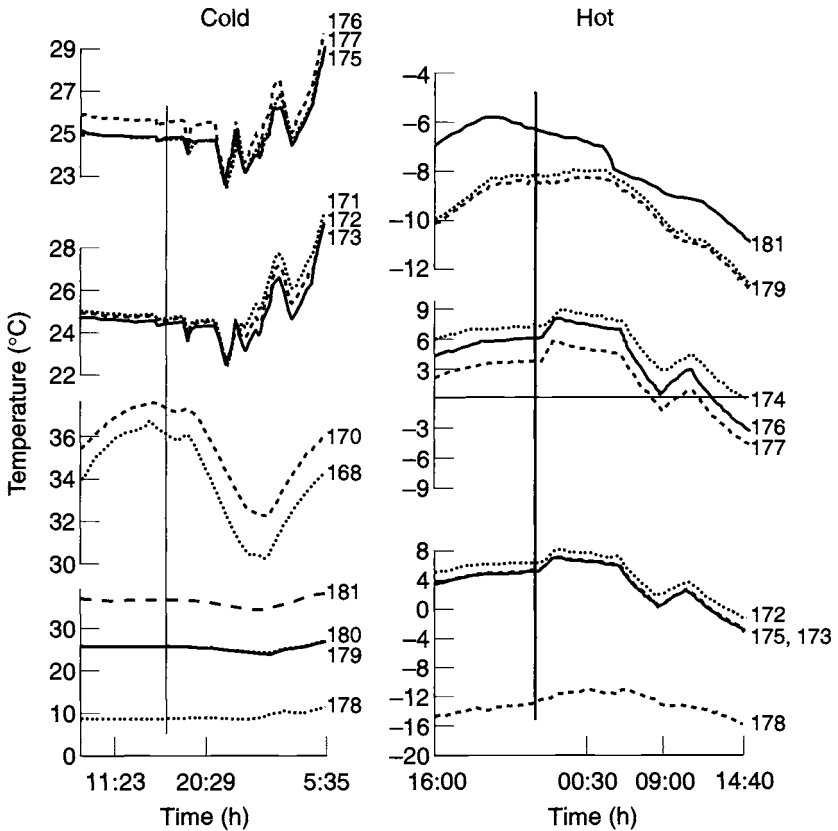
Fig. 15.34. Thermal-balance test temperatures.

waste heat is dissipated in the telescopes and no sunlight is shining into the telescope aperture in the test chamber. Looking at the sun twice per rev on orbit will cause the dome temperature to rise closer to that of the base during flight operations.

The optical-head thermal model was run using the as-run test environment. Comparison of the model predictions to test data showed that the conductance value through the thermal isolators between the optical head and its support bracket was low by approximately 40%. The lower conductance value reflected an earlier isolator design that used titanium rather than stainless-steel bolts. Further comparisons also revealed that heat losses through the gap between the dome and azimuth housing, which had been neglected in the analysis, had a noticeable impact on both the optical-head temperature and the temperature difference between the dome and azimuth housing. After corrections for these two effects, the TMM and test data agreed within ±3°C, as shown in Table 15.8.

Table 15.8. TMM Correlation to Test Data

	Cold Case (°C)			Hot Case (°C)		
	Test	Model	D	Test	Model	D
Dome	−11	−8	+3	9	8	−1
Azimuth housing	6	8	+2	25	23	−2
Fin	7	9	+2	24	24	0

Margins

Even the best thermal analyses are subject to uncertainties. Despite our best efforts and the sophistication of today's analytical codes and computer workstations, flight experience teaches that predicted temperatures are not always precisely accurate. Some inaccuracies result from factors that are known to be uncertain, such as contact conductances and the performance of insulation blankets. Some uncertainties are just the results of the simplifications that are inherent in the analytical techniques. Some are caused by errors. In any event, our understanding of these uncertainties is not yet sufficient to eliminate them from the analysis process.

When one compares temperatures predicted by analysis with those that actually occur in flight, one notes significant dispersions. Figure 15.35 shows such a comparison for two satellites, FLTSATCOM and DSCS II. A study of a number of satellite programs conducted by Stark (Ref. 6 of Chapter 19) concluded that an 11°C margin was required to provide 2-σ (95%) confidence that flight temperatures would be within limits (Table 15.9). This study is the basis of the MIL-STD-1540 analytical uncertainty margin of 11°C. It is important to note that this margin is applied to predictions made by analytical models that have been correlated to thermal-balance test data. For an uncorrelated model, the uncertainty jumps to 17°C. In addition, very large discrepancies (40 or 50°C) do occur now and then. A thermal-balance test is needed to catch these large, potentially mission-threatening, errors before the satellite is launched. Simply using the 17°C margin and forgoing a thermal-balance test could be a costly mistake.

Table 15.9. Temperature Uncertainty Margin Based on Spaceflight Database

		Temperature Uncertainty (°C)	
Standard Deviation	Percent of Confidence	Unverified Analytical Predictions	Predictions Verified by Testing
1.0	68	8.3	5.6
1.4	85	12.2	7.8
2.0	95	16.7	11.8
3.0	99	25.0	16.7
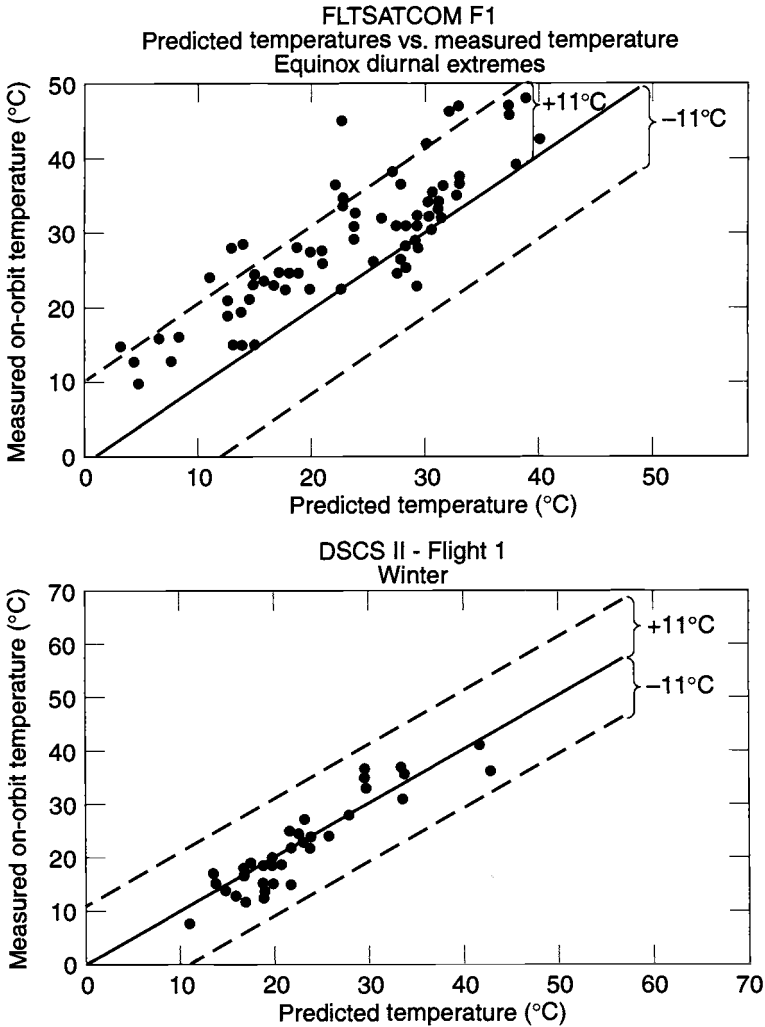
Fig. 15.35. Thermal-model accuracy assessment.

Unlike military programs, NASA and commercial-satellite procurement agencies do not have a specification on uncertainty margins for thermal analysis. An informal survey of NASA and commercial-satellite programs showed that 5°C was the most common margin used, although significantly different margins were used on some programs. A summary of margins typically used on commercial programs is shown in Table 15.10.

Table 15.10. Commercial Satellite Component Temperature Ranges[a]

	Thermal Analysis Range (°C)	Acceptance Range (°C)	Qualification Range (°C)
Boeing	+5 to 55	0 to 60	−5 to 65
Lockheed Martin	−5 to +50	−10 to +55	−15 to 60
Space Systems Loral	+5 to 55	0 to 60	−5 to 65

[a]Temperature ranges for many commercial programs are self-imposed by the contractor and not contractually required by the customer.

Recommended Margins

For components that have no thermal control or have passive thermal control (PTC) only, an uncertainty margin of at least 11°C should be included in all cases in determining the maximum or minimum expected flight temperature. This 11°C thermal margin is applied to the temperature predictions made by the TMMs after correlation to the thermal-balance test. This usage implies that even larger thermal margins are required at the beginning of a program to accommodate changes that typically evolve from preliminary design to final product. The suggested margin during the design phase is 17°C, which can be reduced to 11°C after the thermal-balance test.

For cryogenic systems operating below approximately −70°C, the heat-load margins shown in Table 15.11 are recommended in lieu of the 11°C temperature margin.

A constant-conductance heat pipe is are considered a PTC element and should use the 11°C margin discussed above. In addition, the heat-transport capability of the pipe should be at least 50% greater than that required for the maximum heat load at the maximum expected flight temperature.

Self-regulating heaters that use resistance elements that exhibit a large variation in resistance with temperature (such as "auto trace" or positive-temperature-coefficient thermistors) are considered passive devices, and they require a margin of 11°C.

For thermal designs in which temperatures are actively controlled by variable-conductance heat pipes, louvers, heat pumps, expendable coolant systems, or refrigerators, a heat-load margin of 25% may be used in lieu of the 11°C specified above at the worst-case hot and/or cold extreme design conditions. Similarly, for thermostatically or proportionally controlled heaters, a 25% heater-capacity margin

Table 15.11. Thermal Uncertainty Margins for Cryogenic Systems

Milestone	Heat-Load Margin (%)
Program go-ahead	50
PDR	45
CDR	35
Qualification	30
FDR/Flight acceptance	25

may be used in lieu of the 11°C at the cold end, which translates into a duty cycle of no more than 80% at the minimum expected flight temperature under worst-case cold conditions.

Chapter 19 contains a discussion of how these margins relate to test temperatures of spacecraft components.

TMM Computer Codes

Solving the general heat-transfer equation is the objective of all thermal-analysis codes in the spacecraft industry. The general partial differential equation of heat conduction with source term for a stationary heterogeneous, anisotropic solid is

$$\rho C_p \frac{\partial T}{\partial t} = \nabla \cdot (K \cdot \nabla T) + Q(T, t) \text{ (Energy rate per unit volume)} , \qquad (15.22)$$

where ρ is density (kg/m^3), C_p is specific heat (J/kg·°C), ∇ is gradient operator (1/m), K is conductivity tensor (W/m·°C), T is temperature (°C), t is time (sec), and Q is the source term (W/m^3). Equation (15.22) is a parabolic differential equation in which the Fourier conduction law ($q = -K \cdot \Delta T$) is used. Although temperature (T) is a scalar that can vary with position, i.e., $T = (x, y, z, t)$, the heat flow depends on the temperature gradient in a particular direction and is therefore a vector quantity.

The intent of this section is not to derive heat-transfer equations or provide a detailed discussion of SINDA applications, but to serve as an overview of heat-transfer theory and available software for developing TMMs. For more information on these subjects, consult the textbooks by F. Kreith,[15.7] J. P. Holman,[15.8] and M. S. Carslaw and J. C. Jaeger,[15.9] which provide a good review of heat-transfer theory, and the SINDA manuals, [15.5,15.6] which contain more detail about building thermal models.

Most aerospace companies in the spacecraft industry use finite-difference numerical techniques to solve Eq. (15.22) for various heat-transfer problems with appropriate boundary conditions. For this purpose, these companies generally have either SINDA/1987, written by J. Gaski,[15.5] or SINDA85/FLUINT,[15.6] developed by Martin Marietta for NASA Johnson Space Center (JSC). Some companies still use the original version of SINDA, developed by Gaski in 1966, known as CINDA (Chrysler Improved Numerical Differencing Analyzer).

SINDA consists of a preprocessor and an execution library. The preprocessor reads a SINDA input file and, following certain rules, constructs a FORTRAN executable. The analyst selects subroutines from the SINDA library to obtain temperatures. SINDA allows the user to include the necessary FORTRAN logic to solve a specific heat-transfer problem. FORTRAN code can be added into any of the SINDA operation blocks. The Gaski SINDA has a one-dimensional incompressible-fluid thermal-analysis capability for evaluating pumped-fluid heat-transfer networks.

SINDA85 represents a significant evolution from the previous SINDA-type codes. It has fluid-network analysis capability for evaluating various types of thermal networks, including incompressible, compressible, two-phase flow, and others, and it also allows the analyst to build a thermal model from separate submodels. Both features are very powerful.

The Finite-Difference Method (FDM)

These codes determine the solution to a finite-difference model that approximates the physical object. The nodes or subvolumes are assumed to be isothermal, and physical properties are assumed to be constant within a node. Some heat-transfer books refer to finite-difference-node meshes as lumped-parameter representations. The nodes are interconnected by conduction and/or radiation. The governing partial differential equation is converted into a system of finite-difference equations by constructing an FDM mesh. The basis for this step is the Taylor series approximation. A three-dimensional Cartesian coordinate system is assumed for this discussion. From Fig. 15.36, which shows typical one- and two-dimensional FDM meshes, the Taylor series about x_0 for $T(x)$ is written for the one-dimensional mesh:

$$T(x_o + \Delta_x) = T(x_o) + \frac{\partial T}{\partial x}\bigg|_{x = x_o} \cdot \Delta x + \frac{\partial^2 T}{\partial x^2}\bigg|_{x = x_o} \cdot \Delta x^2/2! + \frac{\partial^3 T}{\partial x^3}\bigg|_{x = x_o} \cdot \Delta x^3/3! + - - \quad (15.23)$$

From this approximation, the first and second derivatives can be derived:

$$\frac{\partial T}{\partial x}\bigg|_{x = x_o} = \frac{T(x_o + \Delta x) - T(x_o)}{\Delta x} + 0(\Delta x) \quad (15.24)$$

$$\frac{\partial^2 T}{\partial x^2}\bigg|_{x = x_o} = \frac{\dfrac{T(x_o + \Delta x) - T(x_o)}{\Delta x} - \dfrac{T(x_o) - T(x_o - \Delta x)}{\Delta x}}{\Delta x} + 0(\Delta x^2) \,,$$

where $0(\Delta x)$ and $0(\Delta x^2)$ are a means of expressing the order of the truncation error associated with the approximation. Equation (15.22) can be written for a

$$x_0 - \Delta x \qquad x_0 \qquad x_0 + \Delta x$$

One-dimensional mesh uniform spacing

$$x_0, y_0 + \Delta y$$

$$x_0 - \Delta x, y_0 \qquad x_0, y_0 \qquad x_0 + \Delta x, y_0$$

$$x_0, y_0 - \Delta y$$

$\bullet \, \Delta x = \Delta y$

Two-dimensional mesh uniform spacing
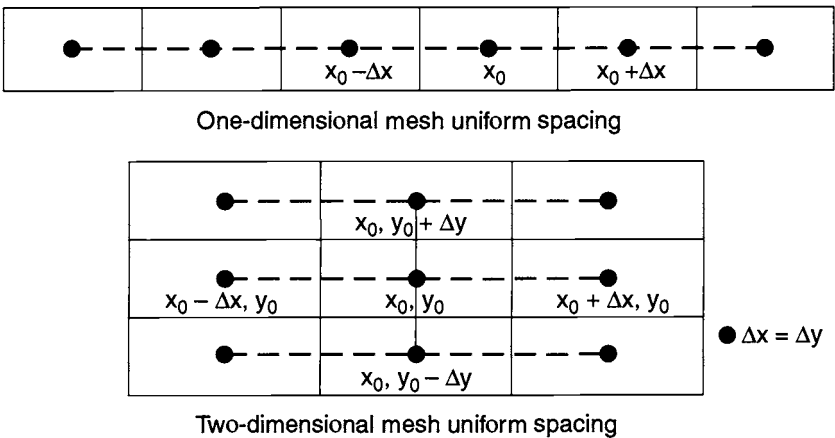
Fig. 15.36. Finite-difference method.

heterogeneous, anisotropic solid, the conductivity of which in each of the three principal directions is a function of temperature:

$$\rho C_p \frac{\partial T}{\partial t} = \frac{\partial}{\partial x}\left[k_x(T)\frac{\partial T}{\partial x}\right] + \frac{\partial}{\partial y}\left[k_y(T)\frac{\partial T}{\partial y}\right] + \frac{\partial}{\partial z}\left[k_z(T)\frac{\partial T}{\partial z}\right] + Q(T, t). \qquad (15.25)$$

The x-partial derivative, $\frac{\partial}{\partial x}\left[k_x(T)\frac{\partial T}{\partial x}\right]$, can be written as

$$\left[k_x(\delta^+) \bullet \left(\frac{T_{n+1}(x+\Delta x, y, z, t) - T_n(x, y, z, t)}{\Delta x}\right)\right. \qquad (15.26)$$
$$\left. - k_x(\delta^-) \bullet \left(\frac{T_n(x, y, z, t) - T_{n-1}(x-\Delta x, y, z, t)}{\Delta x}\right)\right]/\Delta x,$$

where n is the node number about which the Taylor series is applied, and

$$\delta^\pm = \frac{[T_n(x, y, z, t) + T_j(x \pm \Delta x, y, z, t)]}{2}, j = n+1 \text{ or } n-1 \qquad (15.27)$$

$$\text{or} \qquad \delta = T_n(x, y, z, t), \qquad (15.28)$$

where j is the adjacent node, x, y, and z are the spatial coordinates of n, and t is time. Multiplying Eq. (15.26) by the volume $\Delta x \cdot A$, where $A = \Delta y \cdot \Delta z$, one obtains

$$A \cdot k_x(\delta^+) \cdot \frac{(T_{n+1} - T_n)}{\Delta x} - A \cdot k_x(\delta^-) \cdot \frac{(T_n - T_{n-1})}{\Delta x}, \qquad (15.29)$$

where T_i is shorthand for $T_i(x, y, z, t)$ and $i = n$.

Let the coefficient $A \cdot k_x(\delta^+) / \Delta x$ be defined as the parameter G, the conductance. Hence, Eq. (15.29) becomes

$$G_{n+1} \cdot (T_{n+1} - T_n) - G_{n, n-1} \cdot (T_n - T_{n-1}), \qquad (15.30)$$

where $G_{n+1, n} = \dfrac{k(\delta^+) \cdot A}{\Delta x}$ and $G_{(n, n-1)} = \dfrac{k(\delta^-) \cdot A}{\Delta x}$. Similar expressions can be written for the other terms, $\frac{\partial}{\partial y}\left[k_y(T)\frac{\partial T}{\partial y}\right]$ and $\frac{\partial}{\partial z}\left[k_z(T)\frac{\partial T}{\partial z}\right]$, in Eq. (15.25).

The conductance, G, is placed in the conduction block of SINDA. Hence, through the Taylor series approximation, a partial differential equation has been converted into a set of finite-difference equations that can now be solved numerically. The source term in Eq. (15.25), $Q(t)$, is the means by which external and internal radiation, convection, and heat sources are added to the difference equation. The radiation term is typically written as

$$\sigma A \Im_{n, n+1}(T_n^4 - T_{n+1}^4), \qquad (15.31)$$

where σ is the Stefan-Boltzmann constant, A is the surface area of the radiating surface, and $\Im_{n,n+1}$ represents the net radiation exchanged between two real surfaces, including all possible reflection paths. From the SINDA perspective $A\Im_{n,n+1}$ is just another conductance, except it is a radiation coefficient. In SINDA, radiation conductances are distinguished from convection and conduction coefficients by a minus sign; e.g., $-G$ denotes a radiation conductor and G indicates a normal (conduction or convection) conductor.

In building a thermal model the analyst decides how many nodes to use, how to distribute them, and how to connect them by radiation, conduction, or convection. The resulting model network produces a system of finite-difference equations with either constant or variable coefficients. The number of equations to be solved depends on the number of nodes selected by the user in the thermal model minus any boundary nodes, which have a prescribed temperature history. For example, space is considered a boundary node and is set at 0 K ($-273°$C).

To convert the finite-difference equations to a set of algebraic equations that are then solved within SINDA, you must approximate the time derivative, just as the spatial derivatives are approximated. The $\frac{\partial T}{\partial t}$ in Eq. (15.25) can be approximated as follows :

$$T(t^* + \Delta t) = T(t^*) + \theta \cdot \frac{\partial T}{\partial t}\bigg|_{t^* + \Delta t} \cdot \Delta t + (1-\theta) \cdot \frac{\partial T}{\partial t}\bigg|_{t^*} \cdot \Delta t , \qquad (15.32)$$

where θ is a variable-weighted implicit factor. Multiplying Eq. (15.25) by the volume $(\Delta x \cdot A)$, one observes that the coefficient for $\frac{\partial T}{\partial t}$ becomes

$$C_n = \rho \cdot C_p \cdot \Delta x \cdot A , \qquad (15.33)$$

where C_n denotes the capacitance of node n and A is the cross-sectional area $\Delta y \cdot \Delta z$. Combining Eqs. (15.30), (15.31), and (15.32), one finds that Eq. (15.26) becomes

$$C_n \frac{[T_n(t + \Delta t) - T_n(t)]}{\Delta t} \qquad (15.34)$$

$$= \theta \cdot \left[\sum_{j=1}^{N} G_{jn}(T_j - T_n) + \sigma \cdot \sum_{j=1}^{N} \Im_{jn} A_n (T_j^4 - T_n^4) + Q_n(T_n, t) \right]_{t^* + \Delta t}$$

$$+ (1-\theta) \cdot \left[\sum_{j=1}^{N} G_{jn}(T_j - T_n) + \sigma \cdot \sum_{j=1}^{N} \Im_{jn} A_n (T_j^4 - T_n^4) + Q_n(T_n, t) \right]_{t^*} .$$

This equation contains the parameter θ, which can be adjusted along with the FDM mesh size and time step to yield various finite-difference approximations with different local truncation errors. The values $\theta = 0$, 1/2, and 1 yield the forward-explicit, Crank-Nicolson, and backward-implicit approximations.

Selecting a particular FDM mesh scheme and evaluating the coefficients in Eq. (15.34) yields a system of n algebraic equations where n is the number of finite-difference nodes. Note that n does not include boundary nodes. If $\theta = 0$, each equation is explicit and has only one unknown temperature, T_n. If $\theta > 0$, a system of algebraic equations exists and must be solved by either iterative techniques, matrix-inversion schemes, or decomposition procedures. Typically the system of equations is written as

$$T_{new} = [A] \cdot T_{old}, \tag{15.35}$$

where $[A]$ is an $n \times n$ matrix and T is an $n \times 1$ or column matrix. For thermal models of ten or more finite-difference nodes, $[A]$ is typically a sparse matrix because each node is normally connected to a small subset of the total number of nodes in the model. For most heat-transfer problems, $[A]$ is not banded because of radiation interchange between the nodes. Consequently the efficient solvers for tridiagonal matrices are not generally useful.

FDM Errors

Three types of errors can occur with the application of the FDM to heat-transfer problems. The first is the truncation error, which is the difference between the differential equation and the approximating difference equations.[15.10–15.12] This type of error can be illustrated for the one-dimensional heat-transfer equation with constant conductivity. Let

$$F_{pde}(T) = \left(\frac{\partial T}{\partial t} - k \cdot \frac{\partial^2 T}{\partial x^2}\right) \text{ (partial differential equation)} \tag{15.36}$$

and

$$F_{fd}(T_i) = \left(\frac{T_{t^* + \Delta t, x^*} - T_{t^*, x^*}}{\Delta t}\right) \tag{15.37}$$
$$- k\left(\frac{T_{x^* + \Delta x, t^*} - 2T_{x^*, t^*} + T_{x^* - \Delta x, t^*}}{\Delta x^2}\right) \text{ (finite-difference equation)},$$

then $[F_{fd}(T_i) - F_{pde}(T)]$ represents the truncation error at each node. T_i refers to the temperature at three successive nodes, $x^* + \Delta x$, x^*, and $x^* - \Delta x$, and t^* designates a discrete time. The temperature T in the analytical solution is a continuous function. The truncation error is determined from the finite-difference node spacing (mesh size) and the size of the time step. As the number of finite-difference nodes is increased and the time step decreased, the error associated with the Taylor series approximation (truncation) decreases and approaches zero in the limit. In this case the truncation errors approach zero and the difference equation is said to be consistent with the partial differential equation. However, as the number of nodes in the network expands, the corresponding number of difference equations to be solved increases. This, in turn, increases execution time.

From the viewpoint of algebraic simplicity, an analyst prefers the coarsest network possible. The best thermal model is a compromise between node size and

computational cost. No specific rules are available for selecting the optimal network size; one must rely on insight and experience. One way to judge the truncation errors introduced by too coarse a network is to estimate the truncation error as the calculation proceeds.

The second type of error is related to the stability of the numerical solution. If the effect of errors tends to diminish as the numerical solution progresses, then the solution is stable and converges. However, if the errors tend to grow with time, then the solution becomes unstable and diverges.

The third type of error is the computer rounding error made during numerical calculations. This is the difference between the exact numerical answer and the actual numerical answer (i.e., the truncated numerical answer generated by the computer). Rounding error is a significant problem with 16-bit computers, somewhat of a problem with 32-bit machines, and generally not a problem with 64-bit computers. Hence, the numerical temperature, T_{num}, is given as

$$T_{num} = T_{ex} + (T_{num} - T_{exn}) + (T_{exn} - T_{ex}), \qquad (15.38)$$

where T_{ex} is the analytical solution and T_{exn} is the exact numerical solution. The discrete error is the combination of the truncation and stability errors. As discussed previously, these errors are directly coupled to the mesh size and time step assumed by the analyst. The truncation error for a uniform mesh (Fig. 15.36) is typically $O(\Delta x^2)$, i.e., second-order. However, for a nonuniform mesh (see Fig. 15.37), the truncation error becomes $O(\Delta x)$, i.e., first-order. Hence, a nonuniform FDM mesh reduces the order of the truncation error and decreases the accuracy of the approximation. Most spacecraft thermal models are not uniform; however, if sufficient thermal nodes are used, the numerical answers will be reasonably accurate.
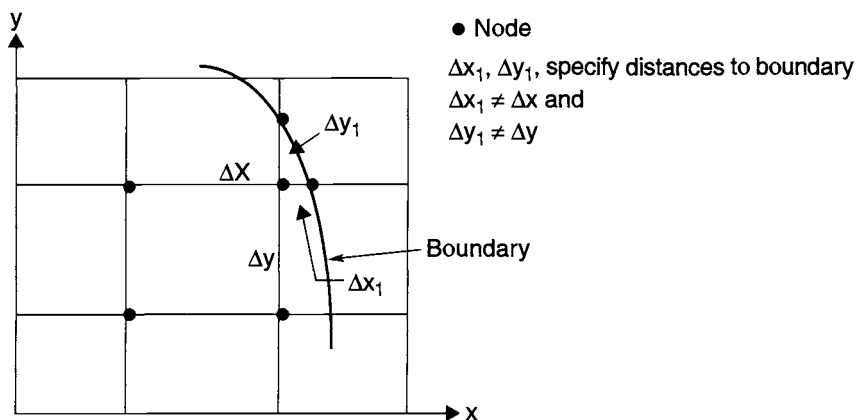

Fig. 15.37. FDM two-dimensional nonuniform mesh.

Forward-Differencing Approach to Heat-Transfer Equations

The forward-differencing expression is obtained from Eq. (15.32) by setting $\theta = 0$; hence,

$$T(t^* + \Delta t) = T(t^*) + \frac{\partial T}{\partial t}\bigg|_{t^*} \cdot \Delta t \quad , \tag{15.39}$$

and the expression is shown in Fig. 15.38. This method requires that the calculation of T_i at $t^* + \Delta t$ be based on values of T_i that are known at t^*, the previous time. This is illustrated by setting $\theta = 0$ in Eq. (15.34). The forward-differencing assumption is explicit, and the solution can be unstable if the time step, Δt, is too large. The criteria for stability are determined by calculating the minimum value

$$\tau_n = \frac{C_n}{\sum_j G_{nj}} \tag{15.40}$$

for each finite-difference node, where τ is the stability factor and j is the sum of all conductors connecting other nodes to n by conduction or radiation. (Convection would be included in a prelaunch environment.) The thermal capacitance of the node is C_n, and the values of G_{nj} are the conductance values between adjacent nodes. If radiation occurs between two nodes, the value is linearized to obtain

$$G_{nj} = \sigma \Im_{nj} A_j (T_n^2 - T_j^2)(T_n + T_j) \ . \tag{15.41}$$

In SINDA, τ is called CSGMIN. CSGMIN represents the smallest time constant in the thermal network at each time step. It can change from time step to time step. CSGMIN includes the effect of boundary conditions if the node that has the smallest τ is connected to any boundary nodes. The solution process will remain stable if the time step, Δt, is always less than CSGMIN. In SINDA $\Delta t = 0.95^*$ CSGMIN/ CSGFAC is always used, with CSGFAC defaulted to 1.0.
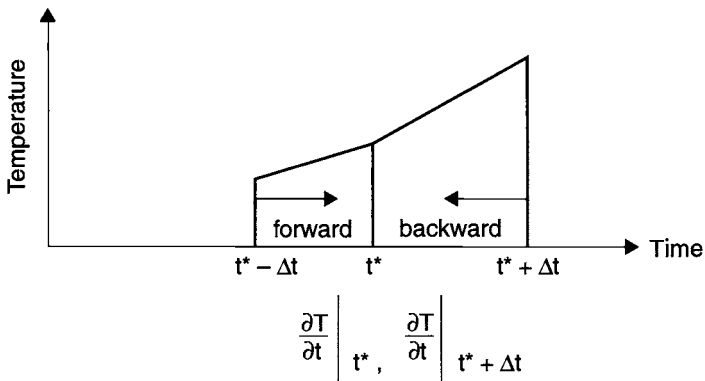

Fig. 15.38. Explicit and implicit derivatives.

The forward-differencing equation has one unknown node temperature at $t^* + \Delta t$, with all the other temperatures known at t^* (see Eq. [15.34] with $\theta = 0$). Any radiation terms are approximated by Eq. (15.41). Although this explicit equation is simple to solve, the time step, Δt, is limited by the stability criteria for the node with the smallest time constant. Hence, in using this technique the analyst is trading simplicity for potentially many small time steps, a situation that can cause excessive execution time and completely consume the CPU on a local workstation. In applying the forward-differencing equations, the analyst does not have to specify the convergence criteria and a time step, since these can be conveniently computed from the specified thermal data.

Backward-Differencing Approach to Heat-Transfer Equations

Another technique used to solve heat-transfer equations is backward differencing. In this case the heat balance is written in terms of the unknown temperatures at $t^* + \Delta t$,

$$T(t^* + \Delta t) = T(t^*) + \frac{\partial T}{\partial t}\bigg|_{t^* + \Delta t} \cdot \Delta t \quad . \tag{15.42}$$

This equation is obtained by setting $\theta = 1$ in Eq. (15.32). Figure 15.38 illustrates the backward slope $\frac{\partial T}{\partial t}$. This approach yields a system of n equations, where n is the total number of finite-difference nodes whose temperatures are calculated at each time step. Boundary nodes are excluded. This formulation is called implicit. The minimum time constant CSGMIN is still calculated in SINDA for implicit methods. Since implicit methods are unconditionally stable, the time step Δt can exceed CSGMIN. However, if the time step selected is too large, although stable, the truncation error can become significant. When using an implicit method, the analyst must specify the time step. The user should always compare the specific time step to CSGMIN. If the selected time step is five to ten times CSGMIN, it is probably too large. Obviously, this judgment depends on the problem being solved.

Iterative schemes are typically used to solve systems of equations. Such techniques require a convergence criterion. For transient problems, the SINDA constants DRLXCA and ARLXCA must be specified to use the implicit schemes. Two constants are required because SINDA allows both diffusion and arithmetic nodes. Diffusion nodes have mass, whereas arithmetic nodes do not. DRLXCA is the convergence criterion for diffusion nodes, and ARLXCA is the convergence criterion for arithmetic nodes.

The advantage of backward differencing rests with the ability to vary the time step. During periods of rapidly varying boundary conditions, the time step can be reduced. Similarly, during periods of slowly changing boundary conditions, the time step can be increased. Typically, implicit numerical schemes are faster than the explicit-forward method because of the large time steps allowed. However, the larger the time step, the more iterations required to achieve a solution. Each iteration is essentially equivalent to a time step. Hence, the actual implicit time step is approximately the specified Δt divided by the number of iterations required to achieve a solution. The user needs to compare this modified time step to CSGMIN

to verify that the specified time step is providing the increased computational speed expected over the explicit method. For some problems the implicit scheme may not be any faster than the explicit method.

The following stability criteria are associated with Eq. (15.34):

$$\theta = 0, \qquad \Delta t < \text{CSGMIN}. \tag{15.43}$$

$\theta < 1/2,$ conditionally stable, i.e., $\text{CSGMIN} < \Delta t < \text{CSGMIN} (1+\Delta)$
where $\Delta \rightarrow \infty$ as $\theta \rightarrow 1/2$.

$1/2 \leq \theta \leq 1,$ unconditionally stable for any Δt.

All the SINDA codes allow three types of nodes: diffusion (with mass), arithmetic (no mass), and boundary (specified temperature). These definitions are particularly useful when solving equations whose time constants vary by several orders of magnitude or higher values. If arithmetic nodes were not allowed, the algebraic system of equations would be very stiff. This class of problem (stiff equations) can only be solved with implicit techniques. However, when CSGMIN is very small for some diffusion nodes, they can be converted to arithmetic nodes. This helps make the equations less stiff and improves the computational efficiency without sacrificing accuracy. The temperature of an arithmetic node is obtained by noting that the total heat flow into the node is zero. An example of the use of arithmetic nodes is the inclusion of MLI blankets in a design; typically, they are modeled as arithmetic nodes because they are light and respond instantaneously to the environment. Another example is the analyst's placement of arithmetic nodes at the interface of two surfaces to obtain the interface temperature.

Limiting ΔV and Δt

In summary, the finite-difference approximations to the partial differential heat-transfer equation discussed in the preceding sections require that continuous variables be quantized. Spatial variables are quantized as nodes and connected by conductors, while time is divided into discrete steps, denoted by Δt. For finite-difference nodes of size $\Delta V = \Delta x \cdot \Delta y \cdot \Delta z$, the time step and spatial dimensions are related in SINDA through the CSGMIN definition.

Since the finite-difference solution approaches the exact solution as ΔV and Δt approach zero, the logical question is, what limits ΔV or Δt? The answer is cost and computer storage (model size). Together these constraints limit ΔV to a non-zero minimum value. A small ΔV means a large number of nodes and conductors, and the computer memory must contain enough space to hold all parameters (capacitance, temperature, conductance, etc.) associated with the model. A large model takes a long time to execute on a computer and many engineering staff-hours to develop. The analyst has to use engineering judgment to decide how much detail is sufficient to determine the thermal response of the physical system being analyzed.

The time step is chosen consistent with CSGMIN for the forward-explicit method. An excessively small value of CSGMIN can greatly increase the computation time. The implicit methods allow time steps greater than CSGMIN. In these cases the analyst needs to determine the largest acceptable Δt that will not impact the accuracy of the calculated temperatures. For each thermal problem the analyst is faced with the task of developing a model and selecting a technique for solving it that will yield the most accurate, stable temperatures for the least cost.

Other Approaches to Finite-Difference Equations

Numerous other approaches to formulating and solving finite-difference equations are available. The Gaski SINDA/1987 has several transient and steady-state solutions. This approach provides the analyst with the flexibility to select a solution subroutine that will work. As noted previously, the forward-explicit method is limited to time steps less than CSGMIN. However, two other explicit schemes, one by Saul'yev and the other by Dufort-Frankel, allow time steps greater than CSGMIN because these methods are unconditionally stable. The Saul'yev alternating-direction explicit method is implemented in the Gaski SINDA/1987 as the execution subroutine SNADE, and the modified Dufort-Frankel technique is called SNDUFR in the Gaski SINDA/1987.[15.4] The original Dufort-Frankel method used the following approximations:
in time,

$$\frac{\partial T}{\partial t} = \frac{1}{2}(T_n|_{t^*+\Delta t} - T_n|_{t^*-\Delta t}),$$ (15.44)

and in space,

$$T_n|t^* = \frac{1}{2}\left(T_{n+1}|_{t^*} - T_{n-1}|_{t^*}\right).$$ (15.45)

These approximations produced a finite-difference technique whose truncation error was $0(\Delta t^2, \Delta x^2)$ accurate as compared to the forward-differencing scheme, which is $0(\Delta t + \Delta x^2)$ accurate. The central-difference approximation in Eq. (15.44), which is $0(\Delta t^2)$ accurate, causes a term

$$\frac{\partial^2 T}{\partial t^2} \cdot \frac{\Delta t^2}{\Delta x^2}$$ (15.46)

to appear in the truncation error. Depending on the relationship between the spacing of the nodes and the time step, the resulting equation can be hyperbolic instead of parabolic. The old SINDA codes used the original Dufort-Frankel approximation, which generated temperatures that were off by 5 to 10°C. This was a direct result of the term

$$\frac{\partial^2 T}{\partial t^2} \cdot \frac{\Delta t^2}{\Delta x^2}.$$ (15.47)

By using the Euler approximation in time, which is normally used, we have

$$\frac{\partial T}{\partial^2} = T_n|_{t^*+\Delta t} - T_n|_{t^*}.$$ (15.48)

The modified Dufort-Frankel method uses Eqs. (15.45) and (15.48), and it produces accurate solutions for time steps greater than CSGMIN. The truncation

error is $0(\Delta t, \Delta x^2)$. The $\dfrac{\partial^2 T}{\partial t^2} \cdot \dfrac{\Delta t^2}{\Delta x^2}$ term is higher-order and is not a factor with this approximation. One final note; the Richardson explicit method used the time approximation in Eq. (15.44) with the standard approximation in the spatial derivative. This method was unconditionally unstable. The application of Eq. (15.44) as an approximation in time has generally not been successful.

The most common implicit scheme is the Crank-Nicolson (CN) method. Its approximation is obtained from Eq. (15.34) with $\theta = 1/2$. The Crank-Nicolson technique is simply an application of the trapezoid rule. The method has a truncation error $0(\Delta t^2, \Delta x^2)$. The basic CN equation for one dimension can be derived from adding:

$$\frac{T_{t^* + \Delta t/2} - T_{t^*}}{\Delta t/2} = \left[\frac{T_{n+1} - 2T_n + T_{n-1}}{(\Delta x^2)} \right]_{t^*} \text{Explicit forward,} \tag{15.49}$$

and

$$\frac{T_{t^* + \Delta t} - T_{t^* + \Delta t/2}}{\Delta t/2} = \left[\frac{T_{n+1} - 2T_n + T_{n-1}}{(\Delta x)^2} \right]_{t^* + \Delta t} \text{Implicit backward,} \tag{15.50}$$

to yield

$$T_{t^* + \Delta t} - T_{t^*} = \frac{\Delta t}{2\Delta x^2} \cdot \left[[T_{n+1} - 2T_n + T_{n-1}]_{t^* + \Delta t} \right. \tag{15.51}$$
$$\left. + [T_{n+1} - 2T_n + T_{n-1}]_{t^*} \right].$$

This approximation is not limited to one dimension, which was selected to illustrate the method. The CN approximation can also be obtained by simply adding the classic explicit and implicit methods. Centering the approximation about $t^* + \Delta t/2$ accounts for the increased accuracy in time over the classic-explicit and backward-implicit methods, which are centered at t^* and $t^* + \Delta t$, respectively. FWD-BCK in the Gaski SINDA/1987 uses the CN method. The SNTSM method in SINDA/1987[15.5] is a Taylor series method with the weighted average approximation [Eq. (15.33)] and automatic time-step selection. Table 15.12 lists the various transient and steady-state execution subroutines used in SINDA/1987. SINDA/FLUINT uses only four execution subroutines.

Several steady-state subroutines are used in SINDA/1987. Table 15.12 contains the available subroutines. For most reasonably sized thermal models, SCROUT, which is based on the Choleski method, is the best selection for steady-state solutions. The steady-state convergence criterion for the iterative methods is based on first meeting a global-temperature relaxation error, next a system-energy balance criterion, and finally a nodal-energy balance error. The user specifies the minimum acceptable criteria. Typically, a $T_{i+1} - T_i$ difference of less than .005°C (if °C is the unit being used), a system-energy balance error of 1% and a nodal energy balance error of .5% are used. Note i is the iteration count. The analyst can adjust the error

Table 15.12. Typical SINDA Execution Subroutines for FDM

Subroutine		Description
Transient		
SNFRDL		Explicit forward differencing
FWDBKL (FWDBCK, FDBKCD)		Quadratic or linear equation, implicit finite differencing, successive point iteration
SNADE		Alternating direction explicit finite differencing
SNDUFR		Modified Dufort-Frankel explicit finite differencing
ATSDUF		Automatic time-step selection, like SNDUFR otherwise
ATSFBK		Automatic time-step selection, like FWDBCK otherwise
SNTSM	(SNTSM1) (SNTSM3) (SNTSM4)	Taylor series with weighted average, automatic time-step selection
Steady-state		
STDSTL		Quadratic or linear equation with successive point iteration
SNHOS	(SNHOSD)	Taylor series, explicit
SNSOSS		Taylor series, implicit
SNDSNR		Newton-Rhapson with Gauss-Jordan reduction
SCROUT		Matrix decomposition, elimination method
SNSOR	(SNSOR1)	Successive over-relaxation

constants in SINDA by specifying values for specific user constants. Three steady-state criteria are used because temperature relaxation can signal false convergence for some problems; thus, by specifying system- and nodal-energy balance criteria, convergence to the correct answer is assured even if the temperature relaxation is misleading.

The Finite-Element Method (FEM)

The FEM provides a second approach to the numerical solution of heat-transfer problems.[15.13] The FEM-mesh schemes are the real strength of this technique. Each finite-element model normally has hundreds of elements. Two approaches are used to develop a solution with the FEM: the methods of weighted residuals (MWR) and the Ritz variational method. The most widely used finite-element technique is the Galerkin approach, which is one of four MWRs. The FEM seeks an explicit expression for the temperatures, $\tilde{T}$, in terms of known functions that, on average, satisfy the governing differential equations and the boundary conditions

exactly on an element. The $\tilde{T}$ is the finite-element approximation to the actual temperature, T. The form used for $\tilde{T}$ is

$$\tilde{T}(t, a_i) = \sum_{i=o}^{N} a_i \varnothing_i(t) , \qquad (15.52)$$

where the a_i are referred to as degrees of freedom (DOF), N is the total number of DOF, and the $\varnothing_i$ (t) are called by various authors as trial, basis, shape, interpolation, or coordinate functions. Typically the $\varnothing_i$ are assumed to be powers of x, sine, cosine, etc., on the element. This approach parallels the analytical technique of finding a function or set of functions that solves the differential equation and also satisfies the prescribed boundary conditions. An example of a basis function is

$$\varnothing_i = 0, t = a \qquad (15.53)$$

$$\varnothing_i = \frac{a-t}{a-b}, a < t < b$$

$$\varnothing_i = 1, t = b .$$

Hence $\varnothing_i$ is a linear function whose value varies from 0 to 1. A bar element has an element node at each end, and a triangle element has a node at each corner (Fig. 15.39). The a_i are specified at each element node. For a thermal problem, a_i equals T_i, where the T_i are the element-node temperatures. The essence of the method is to obtain a set of algebraic equations for the element-node temperatures T_i that form a column vector called $\tilde{T}$. The temperatures between element nodes are found by applying the basis function between those nodes. For example Eq. (15.53) for $\varnothing_i$ would be used to find the temperature between element nodes a and b. For a reasonable FEM mesh, $\tilde{T}$ should approach T, the exact temperature solution. Basis functions used in Eq. (15.52) can be linear [Eq. (15.53)], quadratic, cubic, or quartic. Examples of element shapes are:
- bar (one-dimensional)
- triangular, rectangular, quadrilateral (two-dimensional)
- hexahedral, pentahedral, tetrahedral (three-dimensional)

To improve the accuracy of the finite-element method, either a smaller mesh (more elements) is used or higher-order basis functions (increased DOF) on the elements are needed. This FEM-mesh technique does not provide the analyst with an error estimate like finite-difference, which is based on Taylor series expansions. Hence, the analyst either repeats the problem with a smaller mesh or, based on experience, develops an FEM mesh that appears to provide an acceptable solution. This process leads to detailed-mesh structures, since the associated errors are not easily calculated and the analyst does not want to solve the same problem twice for two different mesh sizes to establish a convergence criterion.

Many finite-element codes that can be used for thermal analysis are available in the aerospace industry. These include NASTRAN, ADINAT, ABAQUS, ANSYS, COSMOS, and TOPAZ. All were developed to perform structural analysis. Every major aerospace company has at least one.

One-dimensional bar elements

One-dimensional element

Assume unit depth

Two-dimensional triangular elements

= Triangular element

Assume unit depth

Two-dimensional rectangular elements

= Triangular element

Assume unit depth
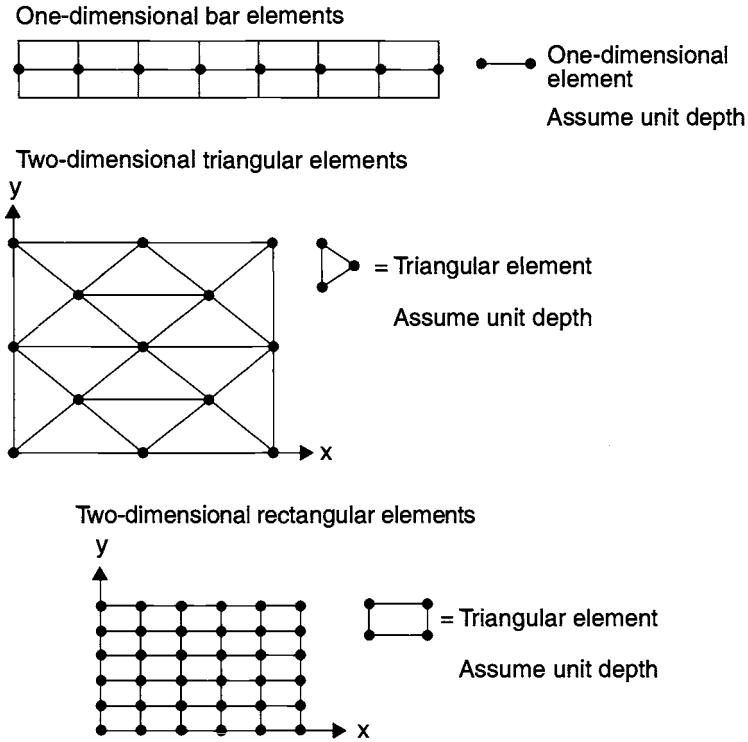
Fig. 15.39. FEM-mesh subdivision.

Finite-Difference vs. Finite-Element

In summary, either method, finite-difference or finite-element, can be used to solve heat-transfer problems. The FDM is based on Taylor series approximations to develop the algebraic equations that are solved numerically to find a set of temperatures. Each finite-difference node is located at the center of mass and is assumed isothermal throughout the volume occupied. The error associated with the calculation can be estimated. The finite-element method is based on using elements that are one-, two-, or three-dimensional, depending on the problem being solved. Combinations of elements can also be used. Each element has element nodes at its corners. Parameter values, for example temperatures, are usually specified or calculated at element nodes. Variations within the element are calculated by using interpolation (basis) functions within the element. Hence the properties and temperature can vary across the element. The Galerkin MWR is normally used to develop the algebraic equations that determine the element-node temperatures.

The FDM is excellent for building spacecraft-system models. It is compatible with the basic surface primitives (e.g., cones, cylinders, spheres) used to describe spacecraft surfaces in the radiation codes. Heat-transfer problems that are primarily driven by radiation can be easily solved with this method. The FDM mesh does not have to be uniform; however, the truncation error decreases from $0(\Delta x^2)$

to $O(\Delta x)$. The accuracy of the method is judged by the truncation error from the Taylor series expansions. This assumes that the analyst is using an inherently stable integration scheme and that rounding error is small, which may not always be the case. The truncation error can be reduced with a smaller FDM mesh and smaller time steps.

Comparing the accuracy of finite-difference and finite-element methods is very difficult unless an exact solution is available. This is never the case for nonlinear problems, which is typical for radiation-dominated thermal analyses; the dominant mode of heat transfer for spacecraft is radiation. Thermal models developed with this method can have three types of isothermal nodes: diffusion, arithmetic, and boundary. The arithmetic node, which is a zero-mass node, can be used to avoid stiff equations that always have a large spread in the time constants. In many spacecraft models one thermal node represents an electronics box. This is easily accommodated by finite-difference schemes, but not by finite-element schemes. To overcome the mesh-generation problem for finite-difference techniques, several aerospace companies have used FEM-mesh generators like PATRAN to build a mesh and then convert it to finite-difference for the finite-difference analysis codes like SINDA. The resulting temperatures are then returned to the finite-element mesh-generation code for display. Without a finite-difference pre- and postprocessor, FDM has a serious disadvantage in building thermal models and displaying the results.

The FEM is extensively used in structural analysis. The method is excellent for solving thermal/stress problems. Normally the structural model requires significantly more detail than the equivalent thermal model. Hence the structural characteristics will typically drive the size of the thermal analysis for a combined thermal-stress analysis. Applications of finite-element techniques to the thermal analysis of circuit boards, traveling wave tubes, and rocket nozzles are common. The real strengths of finite-element techniques are the mesh-generation schemes. These techniques can easily handle irregular surface shapes and the interface between two different mesh schemes.

Because of the longtime application of FEMs to structural problems, several excellent commercial mesh-generation packages are available. These include PATRAN from MSC, GEOMOD (IDEAS-SDRC), and ANVIL from MCS. The pre- and postprocessing capabilities of these codes are excellent. Currently, some commercial FDM-mesh-generation/postprocessing packages of comparable capability are also available.

FEM-mesh-generating schemes are still used in most thermal software packages to develop and postprocess finite-difference temperature results. The finite-element codes have the equivalent to diffusion (nodes with mass) and boundary nodes. They do not allow arithmetic (zero-mass) nodes. Because of this the resulting algebraic equations can be very stiff and lead to excessive computational costs. Also, the finite-element codes cannot use just one node for an electronics-box simulation, as finite-difference codes can. For typical thermal analysis, finite-element models will always be larger than necessary. This condition is driven by the requirement that each element face must share a complete interface with another element, and it is also driven by the lack of information about the error associated with the calculations. Hence, the analyst tends to construct smaller

meshes than may be necessary. Typically, curved surfaces like cones and cylinders require far more finite-element surfaces to describe the shape than are needed for finite-difference codes. One node of 360 deg may be all the analyst really needs. Such a representation is not possible with finite-element codes. The Monte Carlo radiation codes recognize and use the actual surface description for a cone and cylinder. This provides radiation-interchange factors that are correct. Approximation of these surfaces by flat surfaces or polynomial fits can impact the accuracy of the interchange factors and unnecessarily increase the cost and complexity of obtaining them. The combination of increased surface numbers and resulting interchange factors can significantly impact the execution time of the thermal model. This increased detail forced by the method of solution will normally not add any additional real information.

Most finite-difference codes, such as SINDA, allow the analyst to include extensive user logic (e.g., FORTRAN subroutines) in the thermal model. Finite-element codes, like NASTRAN, are far more restrictive in this area.

Implicit-solution schemes are best for transient finite-element analysis. This is mainly driven by the fact that the algebraic equations being solved can be very stiff. Many finite-element solution schemes are most efficient with banded matrices; however, with radiation the matrices are not conveniently banded.

The only way to check the accuracy of the finite-element codes is to run the problem again with a smaller mesh size or high-order elements. This is obviously not an inexpensive procedure for determining the error. Typically, error calculations are not made within the finite-element codes.

An approach used to construct a spacecraft thermal model is shown in Fig. 15.40. The various codes used to complete this process at The Aerospace Corporation are listed in Table 15.13. This software was first developed between 1981 and 1985. Whereas in the 1960s and 1970s most analysts developed thermal models by hand with the time-consuming use of punch-cards, in the 1980s, with the development of minicomputers (e.g., the DEC VAX) and workstations (e.g., those from companies such as Sun Microsystems, Inc., and Hewlett-Packard Co.), the time required to build a thermal model could be greatly reduced through the interactive use of software codes that aid the analyst in model construction, debugging, and execution.

In the 1990s several integrated thermal-analysis programs were developed that were similar to the Aerospace software. These programs allow the analyst to generate complete TMMs and GMMs, execute them, and display the results in a user-friendly, menu-driven environment on a workstation or PC. These newer systems typically have a model builder, an orbital display capability, a radiation analyzer, a thermal analyzer, and postprocessing software to display temperature distributions and temperature heat-flux plots. Most have a limited capability to read in models built in other CAD systems. For example, a NASTRAN model can be read into IDEAS. The NASTRAN model could have been built by PATRAN. Another example is a TRASYS geometric model that can be read into TSS. The thermal analyzers are mostly finite-difference (e.g., SINDA). The radiation codes are based either on the Monte Carlo technique or the gray-diffuse assumption (these are discussed in the next section).

External Interfaces TIDES (surfaces)	Model Builder Defines geometry SURTRAN (surfaces) SOTRAN (solid mesh)	Orbit Definition and Display SOAP ORBITDEF

SURTRAN	Radiation interchange factors	
ATRIUM	Environmental heat fluxes	SINDA
SOAP	SOTRAN	Temperatures

EXCEL Generates temperature and heat-flux plots	CASCADE Displays temperature contours
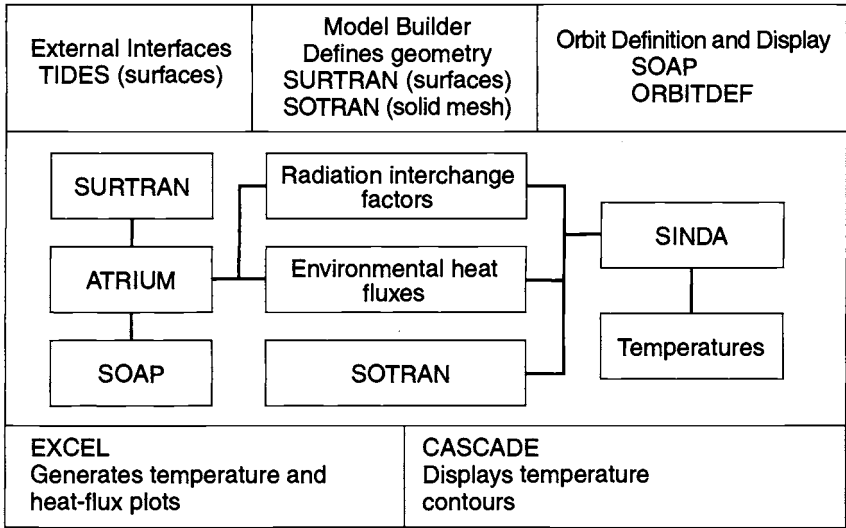
Fig. 15.40. Thermal-analysis system flow used by the integrated thermal analysis platform (ITAP) at The Aerospace Corporation.

Table 15.13. Software Used by ITAP at The Aerospace Corporation

Component	Function/Type of Software
TIDES	Converts surface geometric models between radiation codes
SURTRAN	Constructs, verifies surface geometric radiation model
SOAP	Verifies surface model orientation for specified orbit parameters
SOTRAN	Constructs solid-conduction model
SOSURF	Converts solid model to surface model
ORBITDEF	Defines orbit parameters
ATRIUM	Calculates radiation interchange factors and absorbed fluxes
SINTAB	Formulates ATRIUM output to SINDA tables
SINDA	Finite-difference thermal-analysis code
THERMODATA	Database containing thermophysical properties
CASCADE	Graphical postprocessing for temperatures
EXCEL	Spreadsheet program

The commercially available thermal-analysis software packages are the following.

- Thermal Synthesizer System (TSS) by SPACEDESIGN under license to NASA/JSC
- Thermal Desktop (TD) by Cullimore and Ring Technologies; TD uses AUTOCAD
- THERMICA by Network Analysis Inc. under license to ASTRIUM
- FEMAP/SINDAG Modeling System by Network Analysis Inc.
- IDEAS TMG Thermal Modeling System by MAYA; FEMAP can also be used instead of IDEAS
- ITAS by Analytix Corporation
- Thermal Analysis System by Harvard Thermal

The model builders for these systems are based on either surface primitives (shapes) or elements, e.g., patches. The commercially available shape-based systems are TSS, THERMICA, and ITAS. TD can be shape or element based. The others are element-based systems. ITAP, used by The Aerospace Corporation, is based on shapes. The thrust of these systems is to facilitate the analyst's ability to build thermal models in a fast, efficient manner. The goal is to let the computer perform as many of the calculations as possible, so that the analyst can think more about the physics of the problem. The workstations and PCs presently available allow the incorporation of all aspects of the thermal-model building process (Fig. 15.41). This relieves the user of the need to interface with different computer systems to build, analyze, and postprocess the results of a thermal model. These workstations and PCs provide the analyst with enough computer power to support graphics, analysis packages, and window-display systems, all integrated into powerful analysis platforms. Because platforms are constantly being improved, the software systems developed for specific workstation applications need to be portable to reduce redevelopment costs because of hardware obsolescence.

In addition to these commercially available thermal-analysis systems, several useful commercial codes can assist an analyst in either building a thermal model or analyzing results:

- SINAPS (Cullimore and Ring Technologies, Inc.)
- Pre-SINDA (VERIDIAN)
- SSPTA (Swales and Associates, Inc.)

Radiation Analysis Codes

Radiation interchange factors between surfaces and energy absorbed on surfaces of spacecraft are calculated by radiation codes. The book *Thermal Radiation Heat Transfer* by Siegel and Howell[15.14] provides an excellent summary of assumptions made by these radiation codes and the techniques that they use. The codes use either the gray-diffuse assumption or the Monte Carlo approach.

The Gray-Diffuse Assumption

Codes like TRASYS,[15.3] an industry standard for many years, assume a gray-diffuse surface to calculate the emission and absorption of radiation on a surface. This assumption implies:

1. The temperature is uniform over that surface.
2. The emittance, absorbance, and transmittance of a surface are independent of wavelength and direction.
3. All energy from a surface is emitted and reflected diffusely.
4. The incident and reflected energy flux is uniform over each surface.

With these assumptions a set of blackbody geometric configuration factors or view factors are calculated. A blackbody is a surface that completely absorbs all incident radiation of all wavelengths and from all directions. The view factor, F_{ij}, is simply the fraction of energy leaving black surface i that arrives at black surface j. The view factor can be calculated from a double integral sum, the unit-sphere method, or the contour integration method. TRASYS uses one of the first two techniques.

The energy per unit time transferred from black element dA_1 to dA_2 over the distance S is given as:

$$dQ_{dA1 \rightarrow dA2} = F_{12}\sigma T_1^4 dA_1, \qquad (15.54)$$

where

$$F_{12} = \frac{\cos G_1 \cos G_2}{\Pi S^2} dA_2 \qquad (15.55)$$

is the configuration or view factor (Fig. 15.41). This assumes the blackbody total intensity, i_b, is related to the blackbody total hemispherical emissive power, e_b, by the equation

$$i_{b_1} = \frac{e_{b_1}}{\Pi} = \frac{\sigma T_1^4}{\Pi}, \qquad (15.56)$$

where σ is the Stefan-Boltzmann constant, π is 3.14159265, and T is the temperature of the surface.

Once the values of F_{ij} are known, the values of B_{ij} can be calculated. B_{ij} is the fraction of energy emitted by black surface i that is absorbed by real surface j, including all intervening reflections from other real surfaces, including i. For the assumptions in TRASYS the real surface is assumed to be gray, a diffuse emitter and a diffuse reflector. A gray surface has radiative properties that do not vary with wavelength. A gray surface emits and absorbs a fraction of what a black surface does. For these assumptions, the Gebhart Method[15.14] can be used to calculate the B_{ij} values from the F_{ij} values and the specified surface emittances.

TRASYS can also calculate energy absorbed by a surface. To perform this calculation TRASYS determines the shadow factors, i.e., how one surface shadows another. This information is obviously dependent on the direction of the incident solar energy. The accuracy of the shadow factor depends on how a surface is subdivided into a mesh. The shadow factor requires each small mesh element to be either illuminated or shadowed.
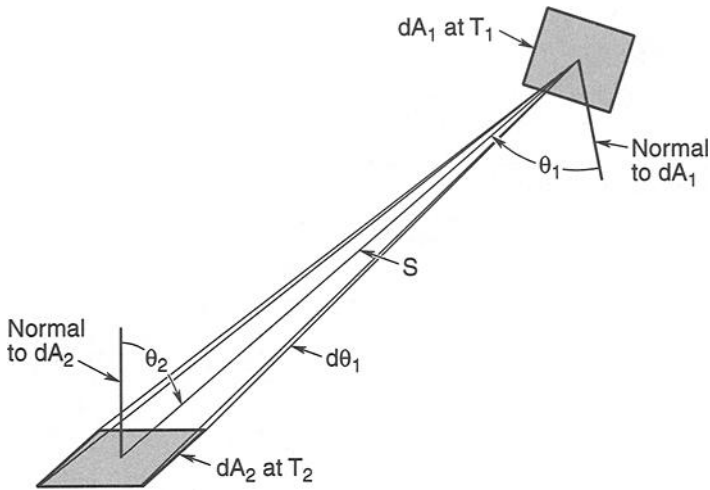
Fig. 15.41. Radiative interchange between two black differential area elements.

To calculate absorbed energy on a surface, whether shadowed or not, the code must be able to specify the orientation of a surface in an orbit with respect to the sun and Earth (these are the external-environment sources of heat for a spacecraft surface). The parameters to specify an orbit are discussed in Chapter 2. After defining the orbit, the code specifies a set of reference axes, e.g., solar-inertial, planet-centered (one axis always pointed at the center of Earth), etc. The coordinate system for each surface is then specified in relation to the spacecraft reference axes. This reference axis is then oriented with respect to the orbital reference axes. Hence, the orientation of any surface with respect to the sun or Earth can be specified and its illumination calculated.

TRASYS[15.3] was developed in the 1960s by Lockheed Martin and is still used by many aerospace companies. A limited ray-tracing capability was added to TRASYS in the early 1980s.

The Monte Carlo Approach

The Monte Carlo method was first used in the aerospace industry in the 1970s. In the late 1970s NEVADA,[15.4] a Monte Carlo code, became commercially available. Eventually most aerospace companies licensed and used this stand-alone software despite the limitations of its very basic two-dimensional graphics display package. Most of the commercially available thermal-analysis systems that proliferated in the late 1990s included a Monte Carlo radiation code. TSS, TD, THERMICA, IDEAS, and ITAS provide examples. NEVADA is used with the SINDA/G system.

Most of the Monte Carlo codes use surface primitives, i.e., they are shape based. Those thermal-analysis systems that use finite-element mesh-generating schemes (e.g., IDEAS/MAYA) cannot construct surface primitives with one element. For example, several elements are needed to create a cylinder or cone. This requirement can add unnecessary surfaces to a geometric model. As noted previously,

those extra surfaces can impact the execution time of a Monte Carlo code if many curved surfaces have to be constructed from smaller elements.

With the tendency to build large detailed thermal models of subsystems and spacecraft, the geometric models can become very large. This can greatly increase the execution time of the Monte Carlo software.

The amount of time spent in finding a ray/surface interaction can be excessive in Monte Carlo codes. Techniques for speeding up the ray tracing within the code by reducing the number of time-consuming ray/surface intersection calculations have been developed. One of these techniques, the OCTREE method, subdivides a three-dimensional surface geometric model into cells or compartments. Typically only a small number of surfaces are in each cell. Some surfaces may be split between cells. When a ray is emitted from a surface in one cell, the code checks to determine if any surface in that cell is hit. If not, the code moves to the next or adjacent cell in the direction the ray is moving. The method greatly reduces the search time to find the surface the emitted ray intersects or hits. The key to this method is breaking the surface geometric model into a reasonable number of three-dimensional cells. If too many cells are used, then the Monte Carlo calculation time can become excessive.

The Monte Carlo codes, like TRASYS, can calculate the energy absorbed on a surface. The shadowing of a surface by another surface automatically falls out from the ray/intersection calculations, i.e., a ray either hits the targeted surface or the shadowing surface. To calculate energy absorbed on a surface whether shadowed or not, the code, like TRASYS, must be able to specify the orientation of a surface in an orbit with respect to the sun or Earth. As with TRASYS, after a set of reference axes is specified in the orbit, e.g., solar-inertial, planet-centered (one axis always pointed at the center of Earth), etc., the coordinate system for each surface is then specified in relationship to the spacecraft's reference axes. These reference axes are then oriented with respect to the orbital reference axes. Hence, the orientation of any surface with respect to the sun or Earth can be specified, and its illumination can be calculated.

All the radiation codes use the semigray approximation, a solution method that assumes that radiant interchange can be treated in two independent spectral regions, one solar and the other IR.

As noted previously, TRASYS assumes all surfaces are gray diffuse.

The Monte Carlo codes are not limited to this assumption. The surfaces can be gray diffuse, specular, or some combination of the two reflectances. In addition, transmittance can be allowed. Direction-dependent surface properties can also be used. For example, the NEVADA software allows the analyst to enter the directional dependence in the form of tables. The directionally dependent data would come from bidirectional surface-property measurements made at certain wavelengths and at certain angles. The Aerospace Corporation has an in-house project to analytically calculate directional properties using surface fractals. Directional dependence could impact Monte Carlo code execution time. The conservation of energy yields, for incident energy on a surface,

$$\alpha \text{ or } (\varepsilon) + \rho + \tau = 1 \qquad (15.57)$$

where α is the absorptance of the surface at solar wavelengths, ε is the fraction of energy emitted or absorbed by a surface in the IR wavelengths, ρ is the fraction of energy reflected by a surface at solar or IR wavelengths (the reflectance could be diffuse, specular, or directional), and τ is the fraction of incident energy transmitted through a surface. (IR refers to that part of the electromagnetic spectrum in the wavelength region of 0.7–1000 μm. The solar part of the electromagnetic spectrum encompasses 0.3–0.7 μm.)

As discussed previously, the OCTREE method is useful for speeding up the determination of a ray/surface intersection in a single processor. Another powerful method is to develop a distributed-processing system for a Monte Carlo code. In this case tens of processors can be used. Such a system can significantly reduce execution times for problems with hundreds of surfaces. The efficiency of any of the commercially available Monte Carlo codes on a single processor is important. However, running a Monte Carlo code on multiple processors and on numerous computers has a significantly greater impact on reducing execution times for a given problem.

The Aerospace Corporation's ATRIUM and one commercially available thermal-analysis system, TSS by SpaceDesign, are the only codes that have a distributed-processing capability at this time.

Nomenclature

A	area
C	thermal capacitance
C_p	specific heat
D	diameter
D_H	hydraulic diameter
E	voltage
F	radiation configuration (form) factor
G	thermal conductance
h	convective heat-transfer coefficient
K	conductivity tensor
L	length or running length
I	current
k	thermal conductivity
$\dot{m}$	mass flow rate
n	arbitrary exponent
N	number of iterations
$\dot{Q}$	heat rate
r	radius
R	resistance

Nomenclature—*Continued*

t	time
T	temperature
T_∞	surrounding media or free stream temperature
U	velocity
U_∞	free stream velocity
V	volume
$\dot{w}$	flow rate
ws	sampling frequency
wc	maximum frequency
x	arbitrary distance
dT	temperature difference
$\mathfrak{F}$	radiation interchange factor for real surfaces (script "F")
α	thermal diffusivity
β	coefficient of volumetric expansion
δ	convergence criterion (relaxation criterion)
ε	emittance
ζ	damping factor
θ	angle
λ	radiation linearization factor
ρ	density
σ	Stefan-Boltzmann constant
τ	stability factor

Symbols, subscripts, and units not specifically mentioned in the nomenclature are explained at the point of usage within the text.

References

15.1. G. M. Dusinberre, *Heat Transfer Calculations by Finite Differences* (International Textbook Company, Scranton, PA, 1961).

15.2. D. C. Hamilton and W. R. Morgan, "Radiant Interchange Configuration Factors," National Advisory Committee for Aeronautics Technical Note 2836 (December 1952).

15.3. TRASYS User's Manual, Lockheed-Martin in support of JSC, April 1988, Houston Texas.

15.4. NEVADA User's Manual, TAC Technologies, Incline Village, NV.

15.5. J. D. Gaski (R. Behee), computer code SINDA 1987/ANSI (Network Analysis Associates, Inc., ASU Research Park, Tempe, AZ).

15.6. B. A. Cullimore, computer code SINDA '85/FLUINT System Improved Numerical Differencing Analyzer and Fluid Integrator, Version 2.3 (Martin Marietta, 1990).

15.7. F. Kreith, *Principles of Heat Transfer,* 3rd ed. (Intext Educational Publishers, New York, 1976).

15.8. J. P. Holman, *Heat Transfer,* 4th ed. (McGraw-Hill Inc., New York, 1976).

15.9. H. S. Carslaw and J. C. Jaeger, *Conduction of Heat in Solids,* 2nd ed. (Oxford University Press, 1959).

15.10. L. Lapidus and G. F. Pinder, *Numerical Solution of Partial Differential Equations in Science and Engineering* (John Wiley and Sons, New York, 1982).

15.11. J. H. Ferziger, *Numerical Methods for Engineering Applications* (John Wiley and Sons, New York, 1981).

15.12. G. D. Smith, *Numerical Solution of Partial Differential Equations* (Oxford University Press, Oxford, United Kingdom, 1978).

15.13. D. S. Burnett, *Finite Element Analysis* (Addison-Wesley Publishing Co., 1987).

15.14. R. Siegel and J. R. Howell, *Thermal Radiation Heat Transfer* (Hemisphere Publishing Corp., New York, 1981).

16 Thermal Contact Resistance

M. B. H. Mantelli* and M. M. Yovanovich†

Introduction

In vacuum environments on spacecraft, convective heat transfer is absent and conduction becomes a more important heat-transfer mechanism than it is for most terrestrial hardware. The heat generated by piece parts within a spacecraft electronics box must flow, by conduction, to the box surface, where it is either radiated away or conducted to a heat sink. Included in this conductive path are a number of joints where heat must be transferred by contact between surfaces. These joints include screws or Wedglock guides that attach circuit boards to an electronics-box chassis, and bolts used to attach the electronics box to a spacecraft shelf or heat-pipe network. Hence the thermal conductance of contacting surfaces is an important parameter for spacecraft thermal design.

This chapter presents analytical tools for modeling thermal joint resistance (or its inverse, conductance) between contacting surfaces. Many different analytical models have been developed over the last 40 years that take into account the different physical phenomena involved in contact heat transfer. What follows is not a complete survey of these models, but a look at some that can be of practical use in spacecraft thermal design.

Unfortunately, no universal model exists that can enable one to predict the joint resistance between any two surfaces. To determine which of the available analytical models is appropriate for a situation, the thermal engineer must assess the surface conditions, addressing questions such as: Are the surfaces flat and/or rough? Are oxides on the surfaces? What is the pressure distribution within the contact? What is the real contact area? For surfaces where these questions can be answered with a high degree of certainty, some of the analytical models validated by extensive lab tests can be reliably used to predict overall thermal joint resistance.

In situations where values of the parameters required by the contact-resistance models are not well known, the designer might guess about the surface conditions and select a model to use, or try more than one model to get a feeling for the range of thermal behavior that a particular joint might exhibit. In these situations, however, spacecraft thermal engineers more commonly choose approximate contact-resistance values that have been used successfully in past design efforts. Such generic design values and their use in the thermal-design process are addressed in Chapters 8 and 15. When none of the available models or approximate design values fit the engineer's needs, experimentation is the best choice.

In the material that follows, a list of the parameters influencing thermal contact resistance is presented, followed by a discussion of the various thermal joint-resistance models. Since a complete joint-resistance model should include a thermal-constriction model, a surface-geometry model, and a surface-deformation model,

*Federal University of Santa Catarina, Florianopolis, Brazil.
†University of Waterloo, Waterloo, Canada.

sections will be devoted to each of those topics. Flat, wavy-smooth, and wavy-rough contacting surfaces are treated, and the relevant models are discussed. The effects of oxides or coatings on the contacting surfaces and thermal-interface filler materials on overall joint resistance are also explored. At the end of each subsection, practical, easy-to-apply, and extensively used correlations are presented along with some experimental data. A typical experimental setup used to generate data for model correlation is also presented.

Contact Heat-Transfer Background

Analysis from the microscopic point of view reveals that all machined surfaces have imperfections or deviations from their idealized geometry. These imperfections are usually categorized according to their roughness and waviness. Roughness is a low-scale imperfection and is the result of tool shape, machining process, casting mold, etc. Waviness is a larger-scale imperfection, a consequence of the heat treatment or vibrations and gaps in a vise or other machining equipment.

Because these surface geometrical imperfections are present, only at a few discrete points do flat surfaces actually touch when two bodies are in contact. As pressure between the bodies increases, the highest surface asperities deform, creating regions where the heat flux can flow by conduction. In the regions where the physical contact is not effective, the heat is transferred by conduction, through the gas that fills the gaps, or by radiation. If the bodies are under vacuum conditions, the heat is transferred through the gaps only by radiation.

The heat flux close to the interface is constricted in the microcontact regions, generating a microconstriction resistance, as shown schematically in Fig. 16.1.
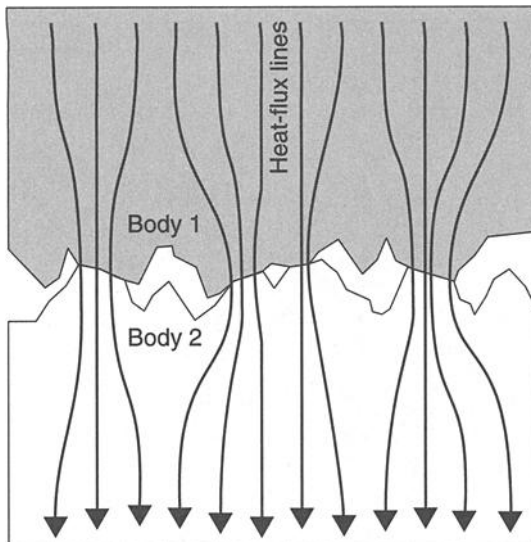

Fig. 16.1. Heat conduction through contacting points (not to scale). (Courtesy F. Milanez)

Macroscopically, the thermal resistance effect can be obtained by measuring the temperature profile of the contacting bodies along their centerline, and extrapolating the resulting one-dimensional line to the contact interface, as illustrated in Fig. 16.2. The contact resistance, R_j, is then defined as the ratio between the temperature drop, T_j, and the heat transferred, or:

$$R_j = \frac{\Delta T_j}{q A_a} \tag{16.1}$$

where q (in W/m^2) is the heat flux that crosses the joint and A_a (in m^2) is the apparent cross-section area.

In the literature, the contact-conductance concept is many times employed instead of the contact-resistance concept and is defined as follows:

$$h_j = \frac{1}{R_j A_a} \tag{16.2}$$

This joint conductance is equal to the sum of three heat conductances in series: the conduction through the contacting points, the radiation through the gaps between the surfaces, and the gas conduction through the gas that fills these gaps, or

$$h_j = h_c + h_r + h_g \tag{16.3}$$

The radiative heat transfer can be modeled as the heat exchange between two gray infinite parallel surfaces, as presented by McWaid.[16.1] For most space applications, this heat-transfer mode can be neglected. Similarly, the gaps between the surfaces are also modeled as two parallel plates separated by a distance equivalent to the average thickness of the gaps. Heat transfer through the gas that fills the gaps is mainly a result of conduction, because the small dimensions of the gaps do not allow convective heat transfer to occur (Song and Yovanovich,[16.2] Hegazy[16.3]). For most space applications, surface contact is in a vacuum environment, and the amount of gas present in the gaps is negligible and so is the conductive
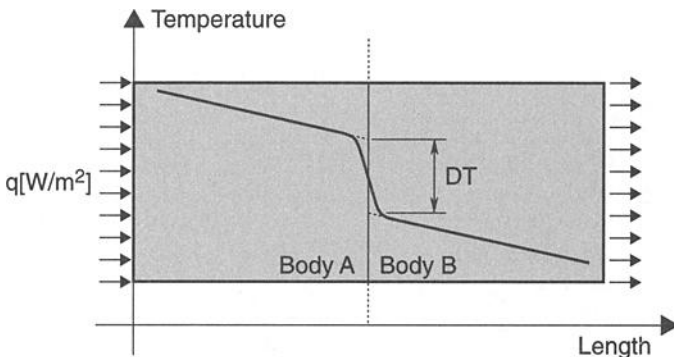

Fig. 16.2. Temperature drop in the joint. (Courtesy F. Milanez)

heat transfer through the gaps. Therefore, for the purpose of discussion in this chapter, the joint conductance is related only to the heat conduction through the contacting points, i.e., $h_j = h_c$.

The contact resistance (or conductance) can be divided into two resistances (or conductances) in series, according to the scale of the surface imperfections. When at least one of the contacting surfaces has large-scale imperfections such as waviness, the contact points are not uniformly distributed over the apparent contact region. They are concentrated in well-defined areas within the apparent contact area. Therefore the heat crossing the interface is first constricted to the macrocontact area (macrocontact resistance) and then through the contact points (microcontact resistance). When both contacting surfaces are specially machined to the point at which they can be considered to be flat, only the microcontact resistance is encountered.

Parameters Influencing Thermal Joint Resistance

Whenever two real surfaces are placed in contact, intimate solid-to-solid contact occurs only at discrete parts of the interface, and the real contact area represents a small fraction (less than 2%) of the nominal contact area. Therefore the pressure at the real contact area is much greater than the apparent contact pressure, and it is related to the flow pressure of the contacting asperity peaks. The interface is idealized as a plane, but the actual thickness of the joint ranges from 0.5 μm for smooth surfaces to about 60 μm for very rough surfaces.

The process of heat transfer across a joint is complex because the thermal resistance can depend upon many geometric, thermal, and mechanical parameters, of which the following are very important.

- geometry of the contacting solids (surface roughness, asperity slope, and waviness)
- gap thickness
- type of interstitial fluid or material (vacuum, grease, foil, etc.)
- thermal conductivities of the contacting solids and the interstitial substance
- hardness or yield pressure of the contacting asperities (which affects the plastic deformation of the highest peaks of the softer solid)
- modulus of elasticity of the contacting solids (which affects the elastic deformation of the wavy parts of the interface)
- average temperature of the interface (which affects material physical properties)

Because thermal contact resistance is such a complex concept, some simplifications are necessary for the development of analytical models and correlations. The following assumptions are made in the development of several contact-resistance models to be discussed later.

- Contacting solids have isotropic thermal and physical properties.
- Contacting solids are thick relative to their surface roughness or waviness.
- Contact is static, so no vibration effect is present.
- Only the first loading cycle is considered, so no hysteresis is present.

- Relative apparent contact pressure (P/H) is neither too small nor too large (between 10^{-6} and 10^{-1}).
- Heat flux is not too large (less than 10^8 W/m^2).

Thermal Joint Resistance Models

As mentioned earlier, a complete contact-resistance model should include a thermal-constriction model, a surface-geometry model, and a surface-deformation model. Several models have been published in the literature covering each of these three main components. Combining these models, one should be able to predict, under some conditions, the thermal contact resistance for the following types of metallic surfaces in contact in a vacuum environment.

- nominally flat, rough surfaces
- smooth wavy surfaces
- rough wavy surfaces

The main objective of this section is not to present a complete survey of the models in the literature; only those considered useful for spacecraft thermal control are discussed here. First, a thermal-constriction model used in most of the thermal contact-resistance studies will be presented, followed by a surface-geometry model and a surface-deformation model. These models are then combined, resulting in complete models that sometimes can be presented in the form of correlations. Before selecting the model to be used in a spacecraft thermal-design calculation, the engineer should analyze the hypotheses adopted in the various models so that the most appropriate model can be applied to the problem.

Thermal-Constriction Models

The conductive heat transfer that occurs through the actual contact points resulting from the physical interaction between two surfaces has been studied extensively in the last four decades. The heat-transfer models developed for this purpose can be divided into two main groups: microconstriction models that are usually used for conforming surfaces and macroconstriction models used for interactions where at least one surface has considerable waviness.

Microconstriction Thermal Resistance Models

Figure 16.3(a) shows a schematic of the points resulting from the contact between two rough, nominally flat surfaces. Cooper et al.[16.4] demonstrated that if the surfaces do not have waviness, the contact spots are randomly distributed over the apparent contact area. Furthermore, if the geometry and the thermal properties of the contacting surfaces are isotropic, all the contact points are approximately circular, isothermal, and at about the same temperature level. Under such circumstances, an elemental heat-flux tube can be associated with each contact spot, as shown in Fig. 16.3(b).

The elemental heat-flux tube, of radius b, defines the influence region of the contact spot, of radius a, located at its center. Far from the interface, the heat-flux lines are considered parallel, and they converge to the contact spot as the heat flux approaches the interface. The temperature distribution within the tube, of conductivity k_1, is axisymmetric. The following boundary conditions are applied:

a) Contact spot   b) Elemental flux tube
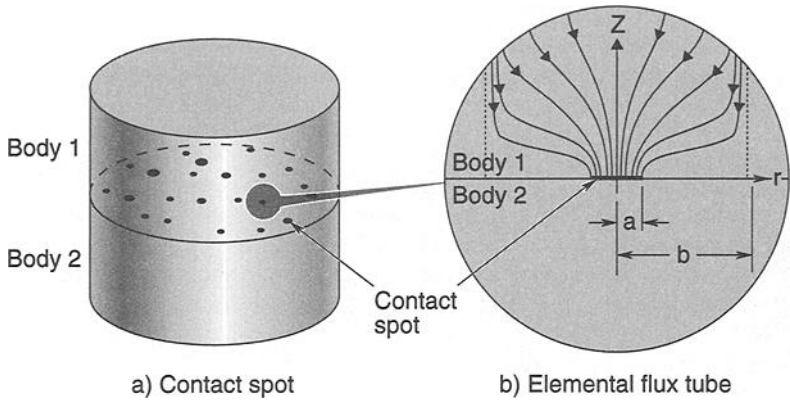
Fig. 16.3. *(Fig. 8.6, reproduced here for your convenience.)* **Microcontacts and constricted heat flow.** (Courtesy F. Milanez)

$$\left. \begin{array}{ll} T = T_0 = \text{constant} & 0 \le r < a \\[2mm] k_1 \dfrac{\partial T}{\partial z} = 0 & a < r < b \end{array} \right\} \quad \text{at} \quad z = 0 \qquad (16.4)$$

$$k_1 \frac{\partial T}{\partial z} \to \frac{Q}{\pi b^2} \qquad z \to \infty \qquad (16.5)$$

$$k_1 \frac{\partial T}{\partial r} = 0 \qquad r = b \qquad (16.6)$$

The main difficulty in solving this problem is the mixed boundary condition at $z = 0$. Many different approaches were employed to obtain the analytical solution, and different expressions were obtained. These solutions actually led to similar temperature-distribution results, as presented by Mikic and Rohsenow.[16.5] Based on this work, Cooper *et al.*[16.4] proposed the substitution of the isothermal contact at $0 < r < a$ by a heat-flux condition, where the resulting temperature distribution is nearly constant over that area. This new condition is:

$$\left. \begin{array}{ll} k_1 \dfrac{\partial T}{\partial z} = \dfrac{Q}{2\pi a \sqrt{a^2 - r^2}} & 0 < r < a \\[3mm] k_1 \dfrac{\partial T}{\partial z} = 0 & a < r < b \end{array} \right\} \quad \text{at} \quad z = 0 \qquad (16.7)$$

The resulting expression for the microconstriction resistance for the heat-flux tube is:

$$R_s = \frac{\psi}{4k_1 a} \tag{16.8}$$

where the constriction parameter ψ can be approximated by the following expression, valid for $0 < a/b < 0.4$:

$$\psi = \left[1 - \left(\frac{a}{b}\right)\right]^{1.5} \tag{16.9}$$

Adding in series the microconstriction resistances of the two elemental tubes that form the contact, one gets the contact resistance of the ith contact spot:

$$R_{si} = \frac{\left(1 - \frac{a_i}{b_i}\right)^{1.5}}{4k_1 a_i} + \frac{\left(1 - \frac{a_i}{b_i}\right)^{1.5}}{4k_2 a_i} \tag{16.10}$$

The contact resistance is the sum of the microconstriction resistances of N contact spots in parallel. It is given by:

$$\frac{1}{R_c} = 2k_s \sum_{i=1}^{N} \frac{a_i}{\left(1 - \frac{a_i}{b_i}\right)^{1.5}} \tag{16.11}$$

where $k_s = \frac{2k_1 k_2}{k_1 + k_2}$ is the harmonic mean of the conductivities of the two bodies (1 and 2) in contact.

The challenge now is to quantify the number and size of the contact spots and the radius of the elemental heat-flux tubes. The problem is simplified if the contact radius a_i and the tube radius b_i are approximated by their mean values a and b.

Actually, the ratio $\frac{a}{b}$ can be expressed as a function of the ratio between the real contact area, A_r, and the apparent contact area, A_a, by the expression (Yovanovich, 1982):

$$\frac{a}{b} = \sqrt{\frac{A_r}{A_a}} \tag{16.12}$$

For N contact spots, the contact resistance can be expressed as

$$R_c = \frac{1}{\displaystyle\sum_{i=1}^{N} \frac{1}{R_{si}}} = \frac{\psi}{2k_s a N} \tag{16.13}$$

and the contact conductance as

$$h_c = \frac{1}{A_a R_c} = \frac{2k_s}{A_a} \frac{Na}{\left(1 - \sqrt{\frac{A_r}{A_a}}\right)^{1.5}} = 2k_s \frac{na}{\left(1 - \sqrt{\frac{A_r}{A_a}}\right)^{1.5}} \qquad (16.14)$$

where $n = \dfrac{N}{A_a}$ is the contact-spot density per unit apparent area.

In a study based on the Roess[16.6] analysis, Clausing and Chao[16.7] obtained an expression similar to Eq. (16.13) for determining the microconstriction resistance. They used a different constriction parameter, ψ, given by:

$$\psi\left(\frac{a}{b}\right) = 1 - 1.40925\left(\frac{a}{b}\right) + 0.29591\left(\frac{a}{b}\right)^3 + 0.05254\left(\frac{a}{b}\right)^5 + 0.02105\left(\frac{a}{b}\right)^7 + \dots \qquad (16.15)$$

This ψ expression is in close agreement to the results of Eq. (16.9) for $0 < a/b < 0.4$ and differs by a few percent for $a/b = 0.6$.

Macroconstriction Thermal Resistance Models

Clausing[16.8] observed that flat surfaces are difficult to produce. As a result of the fabrication process, many surfaces have waviness, and when they are put into contact, the actual microcontact spots are concentrated in well-defined regions. Therefore, the heat flux crossing the joint experiences two constrictions: the micro, as described in the last section, and the macro, where the heat-flux lines are constricted to the region where the contact spots are located. Clausing considered the thermal contact resistance as composed of three resistances in series: macroconstriction, microconstriction, and oxide-film resistance. Clausing and Chao[16.7] modeled the surface waviness by means of spherical crowns on the tops of cylinders. The macroscopic contact area was determined by means of the Hertz elastic theory for two spherical surfaces subjected to a mechanical load. The microcontact spots were considered uniformly distributed over the macrocontact areas.

Figure 16.4 shows a schematic of the apparent contact region between two cylinders of identical radius b_L. The waviness of the contacting surfaces is represented by spherical crowns of radius r_1 and r_2. The distances d_1 and d_2 represent the waviness height. For determining the macrocontact resistance, Clausing and Chao[16.7] assumed that:

- the length of the cylinder is large in comparison to b_L
- the contact is perfect over the macrocontact area
- the heat is transferred only by conduction across the macrocontact area
- the cylinder temperature is uniform far from the contact plane
- the material properties of the contacting solids are isotropic, homogeneous, and constant with temperature
- $d_i \ll r_i$ ($i = 1$ and 2).

The macroconstriction and microconstriction resistance problems are very similar, and the left side of Fig. 16.4 is also representative of the microconstriction resistance. The actual contact spots are considered uniformly distributed inside the contour area, according to the surface waviness. Therefore Eqs. (16.13) and (16.15)
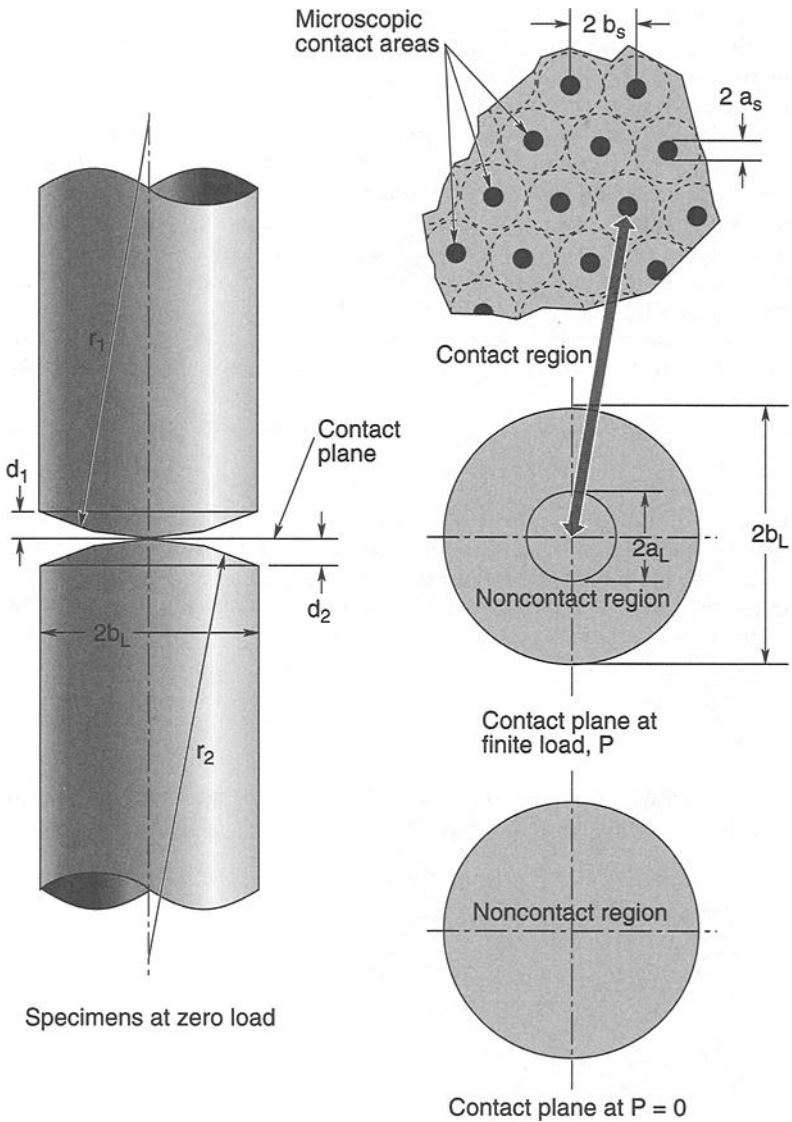
Fig. 16.4. (Fig. 8.7, reproduced here for your convenience.) Schematic of the apparent contact area, according to Clausing and Chao.[16.7]

can be applied to determine the macroconstriction resistance, where a/b is replaced by a_L/b_L. In the next section, a model to determine a_L/b_L, the ratio of the apparent contact-area radius to the cylinder radius, will be discussed. The model of Clausing and Chao[16.7] is applicable when the flatness deviation is several times greater than the roughness. Actually, the Hertz theory was developed for smooth

spherical contacting surfaces, and a correction factor should be applied because the roughness increases the contact area. Clausing and Chao[16.7] did not account for the roughness effect, which is negligible for very wavy surfaces.

Mikic and Rohsenow[16.5] developed a mathematical model for a physical model similar to the mathematical model developed by Clausing and Chao. The expression they obtained is similar. They also concluded that the macro- and microconstriction resistances are similar phenomena that can be described by the same analytical formulation, if the appropriate characteristic dimensions are used. The macrocontact area is estimated using the Hertz theory. Again, Eq. (16.13) can be used for calculation of the macroscopic thermal contact resistance, R_L, with the ψ parameter given by Eq. (16.9), where a/b is replaced by a_L/b_L or D/L, where D represents the diameter of the contour area, L is the wavelength of the spherical waviness (Fig. 16.5), and $N = 1$. This results in the following expression, valid for $0 < D/L < 0.4$:

$$R_L = \frac{\psi}{2k_s a_L} = \frac{\psi}{k_s D} \tag{16.16}$$

Mikic and Rohsenow[16.5] also conducted analytical studies of the heat flow through the macroscopic heat channel, where the contour area is in the form of a strip. This geometry may appear as a result of some machining process. When the contour area is kept at a constant temperature, the constriction resistance of one half of the heat channel is:

$$R_L = \frac{1}{k\pi^2} \frac{b}{a} \sum_{i=1}^{\infty} \frac{1}{i^2} J_0\left(i\pi\frac{a}{b}\right)\sin\left(i\pi\frac{a}{b}\right) \tag{16.17}$$

When the heat flux over the contour area is taken to be uniform, the constriction resistance can be expressed as in Eq. (16.18).

Contour area (for case of spherical waviness)
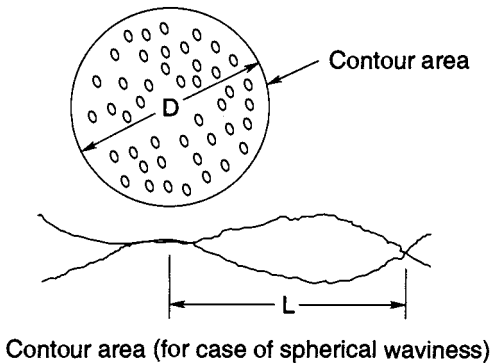
Fig. 16.5. Schematic of rough wavy contacting surfaces. (Mikic and Rohsenow[16.5])

$$R_L = \frac{1}{k\pi^3}\left(\frac{b}{a}\right)^2 \sum_{i=1}^{\infty} \frac{1}{i^3} \sin^2\left(i\pi\frac{a}{b}\right) \tag{16.18}$$

In the last two equations, a represents the half width of the strip and b the half width of the macroscopic heat channel (see Fig. 16.6a).

Mikic and Rohsenow[16.5] also developed the macroconstriction resistance of two surfaces in contact where the contour area forms a rectangle. For the case of a uniform heat flux over the contour area, the constriction resistance is

$$R_L = \frac{4bc}{k_s\pi^3}\left[\frac{b^2}{ca^2}\sum_{i=1}^{\infty}\frac{\sin\left(\frac{i\pi a}{b}\right)}{i^3} + \frac{c^2}{bd^2}\sum_{j=1}^{\infty}\frac{\sin^2\left(\frac{j\pi d}{c}\right)}{j^3}\right] \tag{16.19}$$

$$+ \frac{8b^2c^2}{k_s\pi^2 a^2 d^2}\sum_{i=1}^{\infty}\sum_{j=1}^{\infty}\frac{\sin^2\left(\frac{i\pi a}{b}\right)\sin^2\left(\frac{j\pi d}{c}\right)}{i^2 j^2\sqrt{\left(\frac{i\pi}{b}\right)^2 + \left(\frac{j\pi}{c}\right)^2}}$$

where a, b, c, and d are as shown in Fig. 16.6b.

Macro/Microcontact Thermal Resistance Models

When heat crosses an interface between two contacting surfaces, the flow is first constricted to the large-scale contact areas, and then it is further constricted to the microscopic contact spots within this macroscopic area. The thermal contact resistance of this joint, in the absence of a conducting fluid, can be represented by two resistances in series: the large-scale or macroscopic resistance, R_L, and the small-scale or microscopic resistance, R_s:

$$R_c = R_s + R_L \tag{16.20}$$

Substituting the appropriate expressions for R_L and R_s, one gets an analytical model that takes into account both the macro- and microcontact resistances. According to Clausing and Chao,[16.7] Yovanovich,[16.9] and Mikic and Rohsenow,[16.5] this resistance can be determined by:

$$R_c = \frac{\psi\left(\frac{a}{b}\right)}{2k_s aN} + \frac{\psi\left(\frac{D}{L}\right)}{k_s D} \tag{16.21}$$

where the parameter D/L may be replaced by D_{eff}/L, to account for the influence of the roughness over the contacting area, using the model developed by Mikic and Rohsenow,[16.5] which will be presented in the next section.

a) Macroscopic heat channel for cylindrical waviness in one direction

b) Macroscopic heat channel for cylindrical waviness in two directions
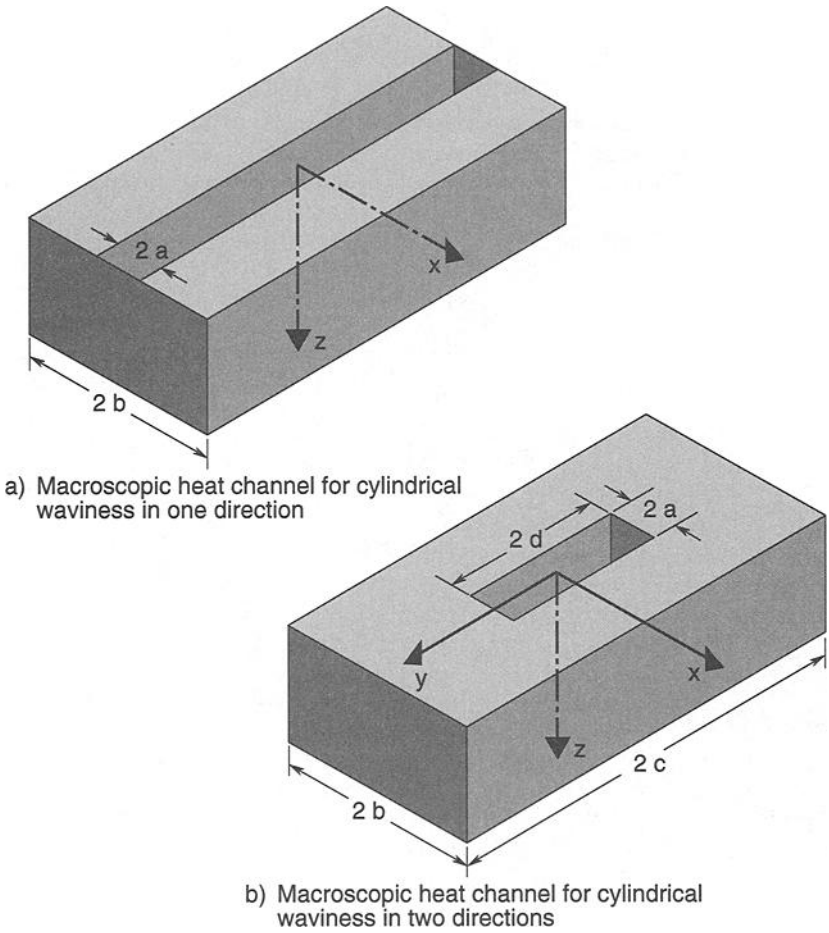
Fig. 16.6. Special macroscopic heat channels. (Mikic and Rohsenow[16.5])

An alternative expression for overall thermal contact resistance is presented by Mikic and Rohsenow:[16.5]

$$R_c A_a = \frac{1}{h_c} = \frac{\psi\left(\frac{a}{b}\right)}{2k_s\left(\frac{a}{b}\right)\sqrt{\frac{n}{\pi}}} + \frac{\psi\left(\frac{D}{L}\right)}{\frac{4}{\pi}k_s\left(\frac{D}{L}\right)}L \tag{16.22}$$

One should note in this case that n is obtained from the macrocontact area

$$A_L = N_L \frac{\pi D^2}{4} = n\pi b^2 \tag{16.23}$$

where:

$$N_L = \frac{A_a}{\pi \frac{L^2}{4}} \tag{16.24}$$

Then, the number of microcontacts per unit apparent area is

$$n = \frac{\left(\frac{D}{L}\right)^2}{\pi b^2} \tag{16.25}$$

Again, in Eqs. (16.22) and (16.25) D/L may be replaced by D_{eff}/L.

Other studies in macro/microcontact thermal resistance can be found in the literature. Burde and Yovanovich[16.10] studied the theoretical thermal resistance of rough wavy contacts. They considered a contact between a flat rough surface and a smooth sphere. The equivalent roughness of the contacting surfaces is considered concentrated on the flat surface and the equivalent waviness on the sphere. The authors obtained an expression for the contact resistance, but their results were only compared with data obtained from idealized smooth spherical/rough flat contacts. Lambert and Fletcher[16.11] (1997) also studied the thermal contact resistance of spherical rough metals. They considered that the pressure within the contacting surfaces is not uniform and used an expression, developed by Mikic,[16.12] to represent the pressure as a function of the radius. They showed that their model is in good agreement with the literature data, but they did not obtain an analytical expression for the thermal resistance.

Geometric and Deformation Models for Flat Rough Surfaces

The thermal-constriction models presented above demonstrate that the number of contacts per unit of contour area and the ratio between the apparent area and real contact area are important parameters. The ratio A_r/A_a is expected to be very small when conforming flat rough surfaces are in contact under typical pressures, and therefore the mean pressure applied in the real contact area is much higher than the nominal applied pressure. The question that arises is whether the behavior of the contacting asperities, subjected to this high stress, is elastic or plastic. Cooper et al.[16.4] (1969) state that if the surfaces are imagined to be moving normally toward each other under increasing pressure, successive contacts are made, which are deformed elastically and then may flow plastically as the nominal interface pressure increases.

A critical review of the elastic and plastic thermal contact resistance models available in the literature is presented by Sridhar and Yovanovich,[16.13] who compared several plastic models and concluded that they generally present the same trends and results. Because the model developed by Cooper et al.[16.4] requires fewer parameters, they selected this model. A similar study was conducted for elastic deformation, and Mikic's[16.14] model was selected. Sridhar[16.15] also developed an elastoplastic model, which takes into account both the elastic and plastic deformation of the asperities. In this section, these three models are briefly described.

Plastic-Deformation Model

Independent studies by Mikic *et al.*[16.16] and Greenwood and Williamson[16.17] assumed that the asperities can be represented by spherical surfaces in contact and that the heights of the asperities on the surfaces form a Gaussian distribution. They suggested that even at moderate nominal pressures, very few contact points are each subjected to only light pressure, so the asperities are deformed elastically.

Mikic *et al.*,[16.16] Cooper *et al.*,[16.4] and Yovanovich[16.18] employed a Hertzian elastic analysis to determine the stresses as a function of the interference and deduce the interference at which elastic stress is exceeded and behavior becomes plastic. They assumed that the contacts are all plastic and that, at each contact, the pressure is equal to the maximum that can be sustained by the softer of the two materials when plastically deformed.

Each surface in contact can be characterized by several sample profiles taken from the surface, from which statistical properties can be deduced. The surface profile $y(x)$, illustrated in Fig. 16.7, can be considered a random stationary process, meaning that the group of profiles is invariant. Furthermore, the probability density of height and slope are assumed to be independent, and the surface height is assumed to be normally distributed, with the probability density function

$$p(y) = \frac{e^{-\frac{y^2}{2\sigma^2}}}{\sigma\sqrt{2\pi}} \tag{16.26}$$

where σ represents the standard deviation for height (or root mean square deviation), specified by the relation

$$\sigma = \left[\frac{1}{L}\int_0^L y^2 dx\right]^{1/2} = \left[\int_{-\infty}^{\infty} y^2 p(y)\,dy\right]^{1/2} \tag{16.27}$$

and readily obtained from the profilometer.

In analysis of the geometry, the conforming surface contact is modeled as the interaction between two surfaces—a rough, rigid, nominally flat surface, which is pressed against the other one, a perfectly flat and smooth surface that is Y distance away from the mean plane of the rough surface. As the surfaces are pressed
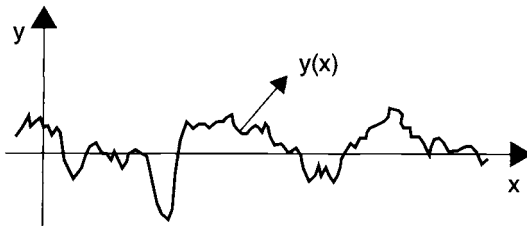

Fig. 16.7. Contacting surface profile. (Courtesy F. Milanez)

against each other, the asperity peaks penetrate into the smooth surface, which experiences a plastic deformation. This physical model is represented schematically in Fig. 16.8. The details of this geometric analysis are described by Mikic[16.5,16.14,16.19] and by Cooper et al.[16.4] These hypotheses lead the problem to a geometric analysis of the interference lengths, which are converted to areas, yielding the following important results.

The contact conductance parameter:

$$\frac{1}{A_a} \sum_{i=1}^{N} a_i = \frac{1}{4\sqrt{2\pi}} \frac{m}{\sigma} e^{-x^2} \qquad (16.28)$$

The relative real contact area:

$$\varepsilon^2 = \frac{A_r}{A_a} = \left(\frac{a}{b}\right)^2 = \frac{1}{2} erfc(x) \qquad (16.29)$$

The contact-spot density:

$$n = \frac{1}{16}\left(\frac{m}{\sigma}\right)^2 \frac{e^{-2x^2}}{erfc(x)} \qquad (16.30)$$

The mean contact-spot radius

$$a = \sqrt{\frac{8}{\pi}} \frac{\sigma}{m} e^{x^2} erfc(x) \qquad (16.31)$$

where $x = \dfrac{Y}{\sqrt{2}\sigma}$ and $\dfrac{Y}{\sigma}$ is called the relative mean plane separation. The surface parameter m is the effective absolute surface slope.

The hypothesis adopted when two rough surfaces are in contact is exactly the same as the one presented in Fig. 16.8, i.e., that a rough, rigid surface, with equivalent roughness and slope, penetrates a perfectly flat and smooth surface. Equations
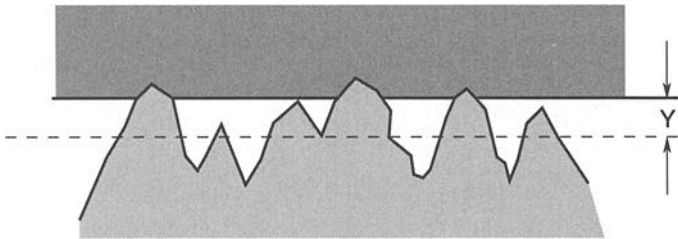
Fig. 16.8. Asperities-deformation model of a rough, rigid, nominally flat surface pressed against a smooth flat surface, Y distance away from the mean plane of the rough surface. (Courtesy F. Milanez)

(16.28) to (16.31) are valid, with the mean planes considered Y distance apart and with the roughness and slope given by

$$\sigma^2 = \sigma_1^2 + \sigma_2^2 \tag{16.32}$$

and

$$m^2 = m_1^2 + m_2^2 \tag{16.33}$$

where the indexes 1 and 2 refer to the contacting surfaces.

An important observation is that the only parameter left is the macrocontact area, whose determination is not made by means of a statistical treatment of the surfaces, but through a deformation analysis.

Yovanovich[16.18] proposed a correlation, which compared within ±1.5% with the complete theory, including the thermal, geometric, and deformation aspects, for $2 \le \dfrac{Y}{\sigma} \le 4.75$:

$$\frac{h_c \sigma}{k_s m} = 1.25 \left(\frac{P}{H_c} \right)^{0.95} \tag{16.34}$$

Hegazy[16.3] observed that the surface microhardness H_c is not constant with depth. The regions close to the surface are harder as a result of the work-hardening process. He proposed a method for determining the appropriate contact hardness, based on the Vickers microhardness measurement. This method was improved by Song and Yovanovich,[16.2] who proposed the following expression for the nondimensional contact pressure, where C_1 and C_2 are the Vickers correlation coefficients, given in Table 16.1, and σ/m is given in μm.

$$\frac{P}{H_c} = \left\{ P / \left[C_1 \left(1.62 \frac{\sigma}{m} \right) \right]^{C_2} \right\}^{\frac{1}{1 + 0.071 C_2}} \tag{16.35}$$

This expression can be inserted in Eq. (16.34) for any level of contacting pressure, improving the precision of the results.

Table 16.1. Vickers Microhardness Parameters (Hegazy[16.3])

Material	C_1 (MPa)	C_2
Ni 200	6.3	-0.264
SS 304	6.27	-0.229
Zr-Nb	5.88	-0.267
Zr-4	5.677	-0.278
Al-6061	1.11	-0.00487[a]

[a]Nho [16.21]

The experimental data obtained by Hegazy[16.3] provide ample evidence that the preceding conforming rough-surface contact-conductance model is accurate. Data were obtained under vacuum conditions for a variety of metals, including SS 304, Zr - 4, and Ni 200. Each interface consisted of a relatively smooth, lapped surface and a rough, bead-blasted surface of identical material. The surface roughness parameter σ/m was 8.2 μm to 12.4 μm for the smoothest interfaces and 38.3 μm to 59.8 μm for the very rough interfaces. The mean interface temperature ranged from 99°C to 178°C. For apparent contact pressures ranging between approximately 0.45 MPa to 890 MPa, the measured contact conductance obtained by the Eq. (16.34) correlation, where $\dfrac{P}{H_c}$ is determined by Eq. (16.35), shows very good agreement with data. In the plot shown in Fig. 16.9, the dimensionless contact conductance is shown as a function of the dimensionless contact pressure, and the correlation and data are compared.

The equation shown in the figure:

$$\frac{\sigma\, h_c}{m\, k_s} = 1.25 \left(\frac{P}{H_c}\right)^{0.95}$$

Pair	(μm)	m	Solid
1–□	1.21	0.139	Ni200
2–○	4.27	0.240	Ni200
3–●	4.29	0.239	Ni200
4–△	8.48	0.344	Ni200
5–■	4.77	0.126	SS304
6–▲	4.11	0.122	SS304
7–▽	3.20	0.103	Zr - 2.5 wt % Nb / Zr - 4
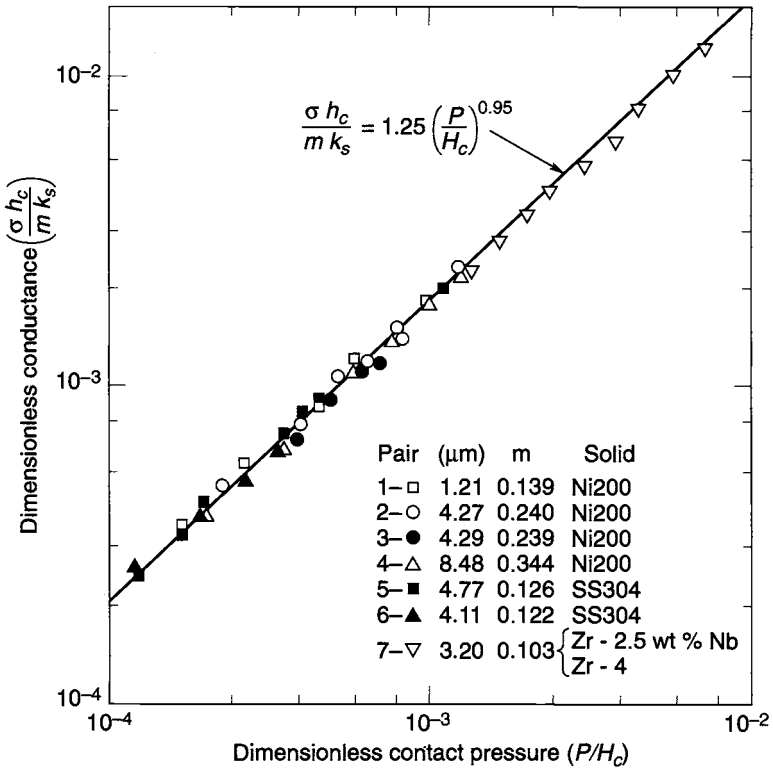
Fig. 16.9. Comparison of contact-conductance theory against test data for clean, bare surfaces in vacuum.

Elastic-Deformation Model

Mikic[16.14] derived an expression for an asperity in contact with a flat surface in elastic deformation. The asperity is considered to be hemispherical, and the contact area is related to the displacement using Hertzian theory. Mikic showed that, at the same separation of the mean contacting planes Y, the contact area for purely plastic deformation for any specific asperity is twice the contact area in elastic deformation, or:

$$\frac{A_{r,\,elastic}}{A_{r,\,plastic}} = \frac{1}{2} \tag{16.36}$$

Therefore, using the expressions obtained for plastic-deformation contacts, one obtains the following expressions.

Contact conductance parameter:

$$\frac{1}{A_a}\sum_{i=1}^{N} a_i = \frac{1}{8\sqrt{\pi}}\frac{m}{\sigma}e^{-x^2} \tag{16.37}$$

Relative real contact area:

$$\varepsilon^2 = \frac{A_{r_{elastic}}}{A_a} = \frac{1}{4}erfc(x) \tag{16.38}$$

Contact-spot density (same as plastic deformation):

$$n = \frac{1}{16}\left(\frac{m}{\sigma}\right)^2\frac{e^{-2x^2}}{erfc(x)} \tag{16.39}$$

Mean contact-spot radius:

$$a = \frac{2}{\sqrt{\pi}}\frac{\sigma}{m}e^{x^2}erfc(x) \tag{16.40}$$

Mikic[16.14] derived an expression for the ratio of real to apparent area for two isotropic rough surfaces undergoing elastic deformation:

$$\frac{A_r}{A_a} = \frac{\sqrt{2}P}{E'm} \tag{16.41}$$

where

$$E' = \frac{E_1 E_2}{E_2(1-v_1^2) + E_1(1-v_2^2)} \tag{16.42}$$

and where E is modulus of elasticity, v is Poisson's ratio, and m is given by Eq. (16.33).

This theory was correlated through the relation

$$\frac{h_c \sigma}{k_s m} = 1.55\left(\frac{P\sqrt{2}}{E' m}\right)^{0.94}$$

(16.43)

Mikic[16.14] observed that h_c is a very weak function of m. Taking $m = 0.1$, which is the average value for blasted surfaces, one gets the following expression, which can be used for most metallic contacts under elastic deformation:

$$h_{se} = 1.9\frac{k}{\sigma}\left(\frac{P}{E'}\right)^{0.94}$$

(16.44)

Sridhar and Yovanovich Elastoplastic Deformation Model
Sridhar and Yovanovich[16.20] developed a single deformation model for asperities of a flat rough surface experiencing partially elastic and partially plastic deformation. They combined the plastic model of Cooper *et al.*[16.4] (1969) and the elastic models of Mikic[16.14] and concluded that the ratio of the actual to the apparent area is equivalent to the ratio of the contact pressure to the elastoplastic hardness H_{ep} of the material. That is:

$$\frac{A_r}{A_a} = \frac{P}{H_{ep}}$$

(16.45)

They also obtained the following expressions.
Contact conductance parameter:

$$\frac{1}{A_a}\sum_{i=1}^{N} a_i = \frac{1}{4\sqrt{2\pi}}\frac{m}{\sigma}e^{-x^2}\sqrt{f_{ep}}$$

(16.46)

Relative real contact area:

$$\varepsilon^2 = \frac{A_r}{A_a} = \left(\frac{a}{b}\right)^2 = \frac{f_{ep}}{2}erfc(x)$$

(16.47)

Contact-spot density:

$$n = \frac{1}{16}\left(\frac{m}{\sigma}\right)^2\frac{e^{-2x^2}}{erfc(x)}$$

(16.48)

Mean contact-spot radius:

$$a = \sqrt{\frac{8}{\pi}}\sqrt{f_{ep}}\frac{\sigma}{m}e^{x^2}erfc(x)$$

(16.49)

where f_{ep} is obtained by the expression

$$f_{ep} = \frac{\left\{1 + \left[6.5/\left(4.61\sqrt{\left(\frac{E'm}{H_{ep}}\right)^2 - 2}\right)\right]^2\right\}^{1/2}}{\left\{1 + \left[13/\left(4.61\sqrt{\left(\frac{E'm}{H_{ep}}\right)^2 - 2}\right)\right]^{1.2}\right\}^{1/1.2}} \qquad (16.50)$$

and the nondimensional contact pressure is obtained by

$$\frac{P}{H_{ep}} = \left[\frac{0.9272P}{C_1\left(1.62\frac{\sigma}{m}f_{ep}^{0.429}\right)^{C_2}}\right]^{\frac{1}{1 + 0.071C_2}} \qquad (16.51)$$

The microhardness parameters C_1 and C_2, presented in Table 16.1, were obtained by Hegazy[16.3] and Nho,[16.21] for conforming rough surfaces. To determine P/H_{ep}, one must use an iterative procedure involving Eqs. (16.50) and (16.51).

With the objective of getting a correlation for their elastoplastic model, Sridhar and Yovanovich[16.20] proposed an index η, given by

$$\eta = 1.67\frac{E'}{S_f}m \qquad (16.52)$$

where S_f is the material yield or flow stress, given by

$$S_f = \frac{1}{2.76\sqrt{\frac{1}{H_{ep}^2} - \frac{2}{(E'm)^2}}} \qquad (16.53)$$

which specifies whether the asperities deformation is elastic ($0 < \eta < 5$), plastic ($400 < \eta < \infty$), or elastoplastic ($5 < \eta < 400$). For the elastic regime, their model reduces to the Mikic[16.14] correlation, which is given by Eq. (16.43). For the plastic regime, their model reduces to the Yovanovich plastic correlation, given by Eq. (16.34) with Eq. (16.35). For the elastoplastic regime, they proposed the following correlation:

$$\frac{h_{sep}}{k}\frac{\sigma}{m} = 1.245\left(1 + \frac{46690.2}{\eta^{2.48}}\right)^{1/30}\left(\frac{P}{H_{ep}}\right)^{0.948\left[1/\left(1 + \frac{2086.9}{\eta^{1.842}}\right)\right]^{1/600}} \qquad (16.54)$$

Equation (16.54) together with Eqs. (16.52), (16.53), (16.49), and (16.50) constitute the Sridhar and Yovanovich elastoplastic model. Its evaluation requires an iterative process, but the convergence is fast, because f_{ep} varies between 0.5 and 1.

Sridhar[16.15] used data from Hegazy[16.3] and Antonetti[16.22] in addition to his own to compare with his elastoplastic model, covering a wide range of thermal, material, and surface properties. The pressure ranged from 0.4 MPa to 8.9 MPa. The elastic modulus varied from 96 GPa for the zirconium alloys to 207 MPa for the

Ni 200 and SS 304. The data also covered a wide range of surface roughness (6 μm $< \sigma/m < 60$ μm), mean interface temperatures ($108 < T_c < 175°C$), and thermal properties ($10 < k_s < 77$ W/m·K). Figure 16.10 shows good agreement of all data with the two theoretical extremes, using the elastoplastic model: a full plastic and a full elastic asperity deformation. All the experimental data are expected to be within these two extreme curves.

Geometric and Deformation Models for Wavy Smooth Surfaces

Clausing and Chao[16.7] and Mikic and Rohsenow[16.5] modeled waviness as spherical caps of radii r_1 and r_2, as shown in Figs. 16.2 and 16.3. They assumed that the waviness is not too pronounced, i.e., $d/L \ll 1$. For the determination of the macrocontact area, they assumed that a perfect contact exists over the macroscopic contact area, i.e., $R_s \ll R_L$. They considered the deformation to be elastic and used the same Hertzian solution as before for the contact area of two spheres. The radius of the macrocontact area a_L is

$$a_L = \left[\frac{3P}{4} \left(\frac{1-\nu_1^2}{E_1} + \frac{1-\nu_2^2}{E_2} \right) \left(\frac{1}{r_1} + \frac{1}{r_2} \right)^{-1} \right]^{1/3} \qquad (16.55)$$
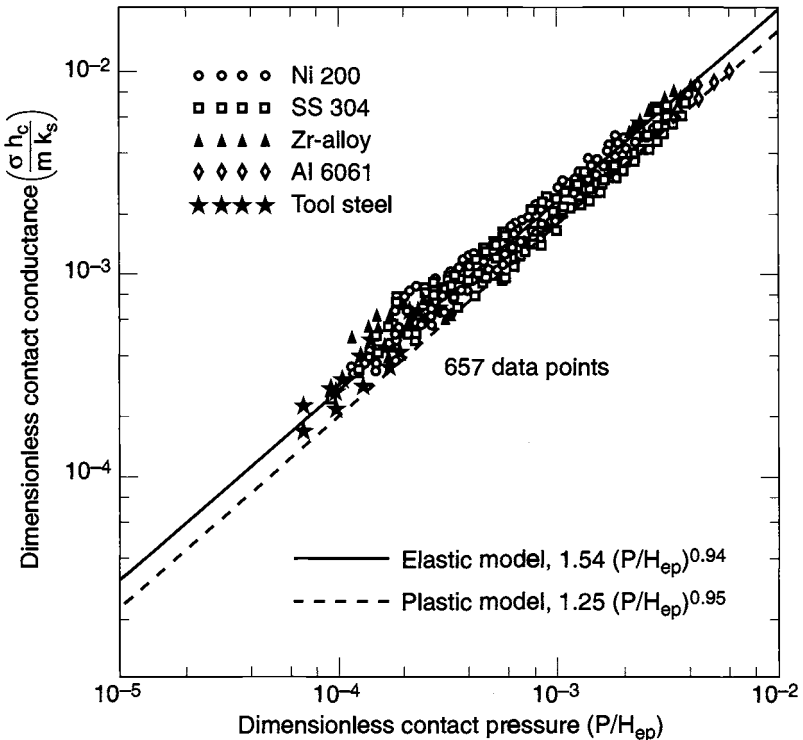
Fig. 16.10. Comparison of data with the elastoplastic model.

For most metals, where $v_1^2 = v_2^2 = (0.01)^2$, the ratio a_L/b_L, which is equivalent to the ratio of the macrocontact area diameter to the length of the waviness (D/L) (see Fig. 16.3), is shown to be

$$\frac{a_L}{b_L} = \frac{D}{L} = 1.285\left[\left(\frac{P_a}{E_s}\right)\left(\frac{b_L}{d_t}\right)\right]^{1/3} \tag{16.56}$$

where $d_t = d_1 + d_2$ and $E_s = \dfrac{2E_1 E_2}{E_1 + E_2}$ is the harmonic mean of the moduli of elasticity for the materials in contact.

Geometric and Deformation Models for Wavy Rough Surfaces in Contact

If the wavy surface in contact is also rough, one can anticipate that the contour area is larger than what is predicted by the Hertz theory and that the density of the contacting spots is not uniformly distributed, but decreases as the radius increases. Mikic[16.5] assumed a uniform distribution inside the contour area and obtained the following expression for the effective contact area, assuming that the mean surface deforms elastically:

$$\lambda_{\text{eff}} = \lambda^2 + 2\int_\lambda^1 \exp\left\{-\frac{d_t}{\sigma}\lambda^2 g\left(\frac{\lambda}{\lambda_H}\right)\left[2\sqrt{2}x + \frac{d_t}{\sigma}\lambda_H^2 g\left(\frac{\lambda}{\lambda_H}\right)\right]\right\}\lambda \, d\lambda \tag{16.57}$$

where $\lambda_{\text{eff}} = \dfrac{D_{\text{eff}}}{L}$, $\lambda_H = \dfrac{D}{L}$, $\lambda = \dfrac{2r}{L}$, r is the contact radius axis, and $g\left(\dfrac{\lambda}{\lambda_H}\right)$ is

$$g\left(\frac{\lambda}{\lambda_H}\right) = \left(\frac{\lambda}{\lambda_H}\right)^2 - 2\left\{1 - \frac{1}{\pi}\left[\left(2 - \frac{\lambda^2}{\lambda_H^2}\right)\sin^{-1}\left(\frac{\lambda}{\lambda_H}\right) + \left(\frac{\lambda^2}{\lambda_H^2} - 1\right)^{1/2}\right]\right\} \tag{16.58}$$

The parameter that appears in Eqs. (16.29), (16.38), or (16.47) is a function of λ, where

$$\varepsilon = \frac{1}{\lambda_{\text{eff}}}\left(\frac{P}{H}\right)^{1/2} \tag{16.59}$$

Obviously λ_{eff} is determined through an iterative process involving Eqs. (16.57) and (16.58), one that is expected to converge very quickly.

Clausing and Chao,[16.7] considering the contact resistance as consisting of the macro- and the microresistances in series, obtained the following correlations for the macro- and microconductances respectively:

$$h_L = \frac{k_s}{b_L}\frac{2\cdot 1.285\left[\left(\frac{P_a}{E_s}\right)\left(\frac{b_L}{d_t}\right)\right]^{1/3}}{\pi\psi\left\{1.285\left[\left(\frac{P_a}{E_s}\right)\left(\frac{b_L}{d_t}\right)\right]^{1/3}\right\}}, \text{ for } \frac{a_L}{b_L} < 0.65 \tag{16.60}$$

$$h_c = \frac{2P_a k_s}{\pi \xi H a \psi\left(\dfrac{a}{b}\right)} \tag{16.61}$$

where the factor ξ was suggested by Holm[16.23] to account for the elastic deformation of the asperities that is often assumed to be unity (plastic deformation). Figure 16.11, from Clausing and Chao,[16.7] compares the theoretical prediction with experimental data for brass, magnesium, stainless-steel, and rough aluminum surfaces, showing the good agreement obtained. Note that it is not an easy task to measure the parameter $\dfrac{b_L}{d_t}$ that is obtained from the study of the profile of the contacting surfaces from a profilometer reading.

Empirical Correlations

Two main types of correlations are found in the literature: those between the semiempirical correlations based on theory (presented previously) and experimental data, and the fully empirical correlations based only on experimental data. Usually, the expressions resulting from the correlations are simple and easy to use,
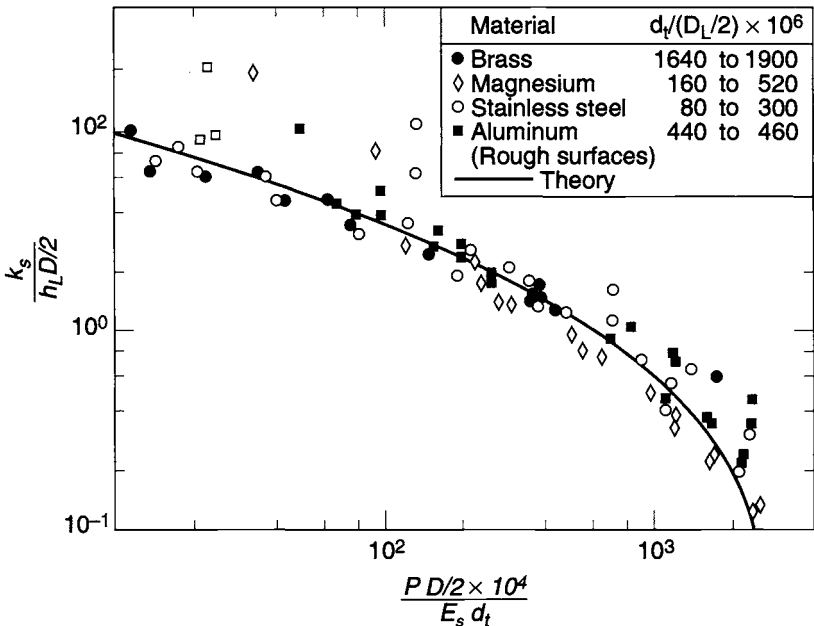
Fig. 16.11. Comparison between the Clausing and Chao[16.7] **wavy rough contact correlation and data.** (Courtesy of NASA)

as they require few input parameters. However, they are valid for a limited range of contacts. Fully empirical correlations can be applied only to contacts similar to those from which they were generated. Semiempirical ones can be applied to a larger range of contacts, especially when the user is aware of the theory behind the correlation.

Lambert and Fletcher[16.24] presented a review of the correlations available in the literature for thermal contact resistance. They made an interesting comparison of these correlations with the experimental data of Hegazy.[16.3] They concluded that the correlations that include gap conductance (which is negligible in vacuum conditions) do not compare well with vacuum data.

The authors also have shown that most of the Russian correlations are approximate to Hegazy's data only for very rough surfaces. Rough surfaces are relatively unworked, since they are not strain-hardened from machining processes. The Russian researchers assumed that the contact hardness is approximately equal to the bulk hardness. As explained earlier in this chapter, Mikic, Yovanovich, Hegazy, and many other investigators believe that the microhardness is a much more appropriate contact-deformation parameter. Lambert and Fletcher (1996) verified that, among the Russian correlations, Popov's correlations perform well for both smooth Ni 200 and rough SS 304. The Popov correlation expression was obtained for 80 data points for a variety of materials, for nominally flat rough surfaces where σ is assumed to be 30 μm. The relation is:

$$h_c = 2.7 \times 10^4 k_s \left(\frac{C_1 P}{3 S_U} \right)^{0.956}$$ (16.62)

$$C_1 = 12/(\sigma_{1,\,max} + \sigma_{2,\,max}) \ for \ 1 \mu m \le \sigma_{1,\,max} + \sigma_{2,\,max} < 5 \mu m$$ (16.63)

$$C_1 = [20/(\sigma_{1,\,max} + \sigma_{2,\,max})]^{0.63} for \ 5 \mu m \le \sigma_{1,\,max} + \sigma_{2,\,max} < 10 \mu m$$ (16.64)

$$C_1 = [30/(\sigma_{1,\,max} + \sigma_{2,\,max})]^{0.4} for \ 10 \mu m \le \sigma_{1,\,max} + \sigma_{2,\,max} < 30 \mu m$$ (16.65)

where S_U is the ultimate strength of the softer metal.

Lambert and Fletcher[16.24] also observed that the O'Callaghan and Probert (1974) empirical correlation agrees well with Hegazy's data for rough surfaces at low contact pressure. The O'Callaghan and Probert[16.25] expression, obtained for 344 aluminum data, for flat, rough surfaces, is:

$$h_c = 3.73 k_s \frac{\sigma}{A} \left(\frac{P \cdot A}{\sigma^2 H} \right)^{0.66}$$ (16.66)

Typical Experimental Setup

Experimental measurements of thermal contact resistance for use in spacecraft thermal analysis must be obtained in vacuum. Basically, all the data presented in this section were measured with an experimental setup very similar to the one described here and depicted in Fig. 16.12. A detailed description of a sample setup can be found in Nho.[16.21] In this case, the test column is enclosed within a Pyrex bell jar and a base plate. The test column consists of the heater block, the heat

meter, the upper and lower test specimens, the heat sink, and the load cell. The gas pressure within the bell jar is controlled by a vacuum system, which is a mechanical pump connected in series with an oil-diffusion pump. A vacuum level lower than 10^{-5} torr should be achieved. The heater may consist of two cartridge-type heaters embedded into a brass block. A closed-loop thermobath should be used to cool the aluminum cold plate. The load is applied to the test column with the aid of a diaphragm-type air cylinder. A calibrated load cell is used to measure the applied load. The mechanical loads, heater levels, and data acquisition can be controlled with a personal computer.

The Effect of Oxidation on Thermal Contact Resistance

Bare surfaces may oxidize when in contact with air, creating a very thin layer of low-conductivity material. The presence of oxides usually increases the thermal contact resistance because the oxides are harder and have lower conductivities than the substrate material.

Yip[16.26] studied, theoretically and experimentally, the effect of oxide films on thermal contact resistance. His model showed good agreement with his data and with another model, developed by Al-Astrabadi et al.[16.27] Only the latter model is presented here because it requires less computational effort. Figure 16.13 shows a schematic of the contact between nominally flat, randomly rough, and oxidized metallic surfaces.

The model of Al-Astrabadi et al.[16.27] uses a stochastic representation of the surface microtopography and assumes a uniform oxide film of thickness t. The
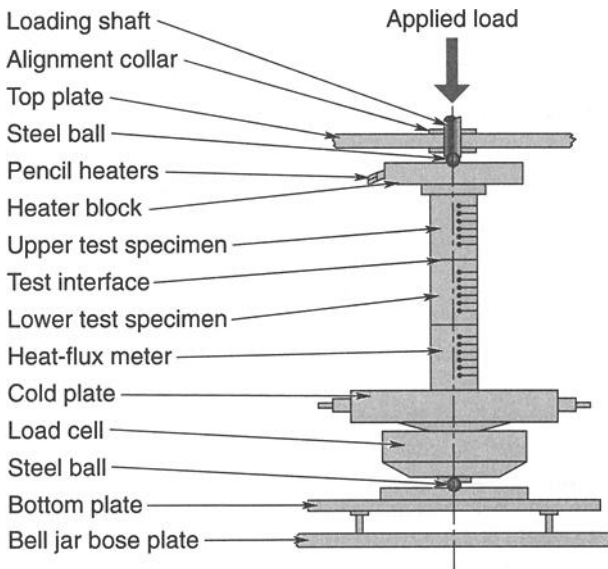
Fig. 16.12. Thermal contact conductance measurement experimental setup.
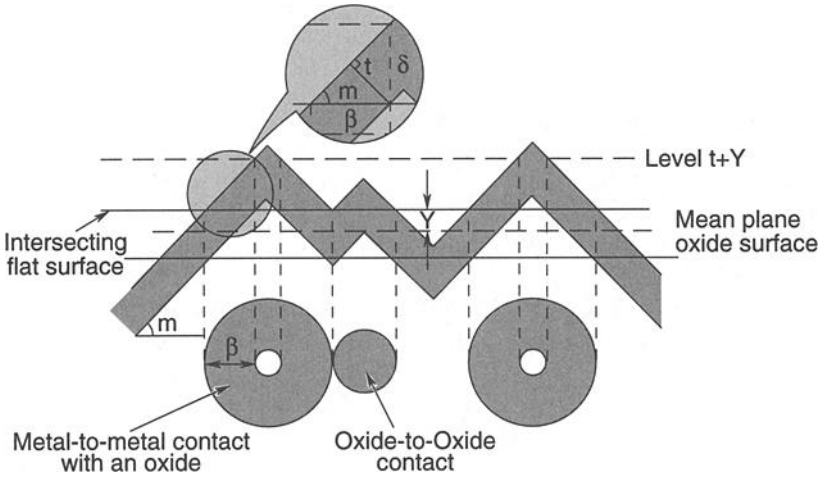
Fig. 16.13. Idealized contact of oxidized surfaces.

microcontacts are of two types—metal-to-metal bridges, surrounded by contacting annular oxide areas, and oxide-to-oxide bridges. All the microcontact regions are taken to be circular, and the asperities are assumed to be circular cones that deform plastically. The effective thermal conductivity of the oxide-to-oxide microcontact is given by the harmonic mean of the conductivities of the oxide and metal, $k_{co} = \dfrac{2k_m k_o}{k_m + k_o}$, while the effective thermal conductivity of the metal-to-metal contact surrounded by an annulus of oxide is given by the arithmetic mean of the conductivities of the oxide and metal, $k_{cm} = \dfrac{k_m + k_o}{2}$. In these equations, the subscript m refers to metal and o to oxide. The total resistance consists of two thermal resistances in parallel: the oxide-to-oxide resistance R_{co} and the metal-to-metal resistance R_{cm}, given respectively by

$$R_{co} = \frac{\psi}{2a_o n_o k_{co} A_a} \quad \text{and} \quad R_{cm} = \frac{\psi}{2a_m n_m k_{cm} A_a} \tag{16.67}$$

Then, the total contact resistance is

$$R_c = \left(\frac{1}{R_{co}} + \frac{1}{R_{cm}} \right)^{-1} \tag{16.68}$$

The value of the parameter ψ is given by Eq. (16.15), where a/b represents the ratio of the mean radii between the microcontact spot and the heat-flow channel to the parameter b, which is determined by Eq. (16.23). The total number of contacts per unit apparent area n_t, including oxide-to-oxide n_o and metal-to-metal n_m, is:

$$n_t a_t = n_m a_m + n_o a_o \tag{16.69}$$

On the other hand, the stochastic asperities-distribution model results in the following expression for the determination of the total number of contacts:

$$n_t = \left(\frac{1}{8}\sqrt{\frac{\pi}{2}}\frac{Y}{\sigma}m^2 e^{-\frac{1}{2}\left(\frac{Y}{\sigma}\right)^2} \right) \tag{16.70}$$

For the number of metal-to-metal contacts:

$$n_m = \frac{1}{8}\sqrt{\frac{\pi}{2}}\left(\frac{Y}{\sigma}+\delta\right)m^2 e^{-\frac{1}{2}\left(\frac{Y}{\sigma}+\delta\right)^2} \tag{16.71}$$

In Fig. 16.13, t is the oxide thickness in the slope direction of the surface, δ is its vertical projection, and β is the lateral spread of oxide surrounding each metal-to-metal contact spot. Values for δ and β are given by:

$$\delta = \frac{t}{\sigma\cos(|m|)} \quad \text{and} \quad \beta = \frac{t}{\sigma\sin(|m|)} \tag{16.72}$$

The number of oxide-to-oxide contacts per unit apparent area is:

$$n_o = n_t - n_m \tag{16.73}$$

The overall mean radius of the microcontact spot, a_t, is:

$$a_t = \frac{2\sigma}{\pi m \dfrac{Y}{\sigma}} \tag{16.74}$$

The metal-to-metal mean radius, a_m, is:

$$a_m = \frac{2\sigma}{\pi m \left(\dfrac{Y}{\sigma}+\delta\right)} + \beta\sigma \tag{16.75}$$

Finally, the normalized Y/σ and/or the mean plane separation Y are determined by the solution of this transcendental equation:

$$\left[\frac{1}{2}-\frac{1}{\sqrt{2\pi}}e^{-\frac{1}{2}\left(\frac{Y}{\sigma}+\delta\right)}\right] + \left[\frac{1}{\sqrt{2\pi}}e^{-\frac{1}{2}\left(\frac{Y}{\sigma}+\delta\right)^2} - \frac{1}{2}e^{-\frac{1}{2}\left(\frac{Y}{\sigma}\right)^2}\right]\frac{H_o}{H_m} = \frac{P}{H_m} \tag{16.76}$$

Al-Astrabadi et al.[16.27] conducted experiments to verify their theory using mild steel (EN3B) specimens with surface roughness ranging from approximately 0.12 to 2 μm, asperity slopes between 0.04 and 0.19 rad, and an oxide film thickness of 0.055 to 0.118 μm. The comparison between data and model was quite good. They noted that oxidation of the surfaces had a minimal effect on the surfaces' topography. They stated that the following three ratios influence the contact resistance: the ratio of coating to substrate hardness, the ratio of coating to substrate thermal conductivity, and the ratio of coating thickness to surface roughness. They

postulated that, if the coating is much thicker than the roughness, then the resistance increases with increasing coating thickness. Provided that the coating thickness is on the order of, or less than, the roughness, the resistance will decrease if the coating is much softer than the substrate.

Lambert *et al.* performed an experimental investigation of the thermal contact conductance of different anodized coatings. They concluded that the overall conductance of anodic coatings is greatly affected by coating thickness. They tested coatings with thickness greater than the average surface roughness of the underlying substrates, prior to anodization.

The Effect of Interstitial Materials on Thermal Contact Resistance

For space applications, low-resistance junctions are designed to provide a good thermal coupling between a heat source, such as an electronics box, and a heat sink, such as a shelf or radiator. Several techniques can be applied to decrease the thermal resistance of the contacting surfaces of these joints, including insertion of a soft foil between the contacting surfaces or application of a coating on one or both of the contacting surfaces. Several coating materials can be applied: vaporized metals, ceramics, diamondlike films, plastics, etc.

Modeling the contact resistance of such a junction is a difficult task, because the model must take into account the material of the coating and the substrate and their thermophysical and geometric properties. Some theoretical models can be found in the literature for the determination of the thermal contact resistance of these joints. They are not general; i.e., they are valid only for specific coatings and substrates. This section presents only the models that are easy to employ.

Foils

Any interstitial substance that is softer than the contacting surfaces will significantly increase the contact-spot density and also increase the contact-spot radius, thereby decreasing the joint resistance. The interstitial spaces are partially filled, and the result is an increased contact area. Yovanovich[16.28] has shown that the thermal performance of a foil depends primarily on the ratio of the foil's thermal conductivity to its microhardness. The higher this index, the better the foil's performance. The thickness of the foil is also critical to the performance, and for a given material an optimum foil thickness exists. Yovanovich tested Armco iron contacting-surface samples where lead, tin, aluminum, and copper were inserted in the joint. Figure 16.14, which is typical for all foil materials tested, shows the joint resistance of the tinfoil mounting as a function of the foil thickness for the joint subjected to five different levels of contact pressure. The joint resistance consists of two contact resistances and the foil material resistance in series. Chapter 8 discusses interstitial materials commonly used in spacecraft thermal control and provides general conductance values for such thermal joints.

Metallic Coating Model

Antonetti[16.22] and Antonetti and Yovanovich[16.29] provided a complete treatment of the thermal and mechanical problem associated with thermal contact resistance

of coated surfaces. The model presented in this subsection is valid for conforming rough surfaces.

Figure 16.15 shows a schematic of a contact between a flat smooth surface coated with a soft metallic layer of high conductivity and a flat rough surface. The prime parameters in the following equations are associated with the contact conductances for coated surfaces. The general expression for the contact conductance of this joint operating in vacuum is

$$h_c' = h_c \left(\frac{H}{H'} \right)^{0.93} \left[\frac{k_1 + k_2}{C k_1 + k_2} \right] \tag{16.77}$$
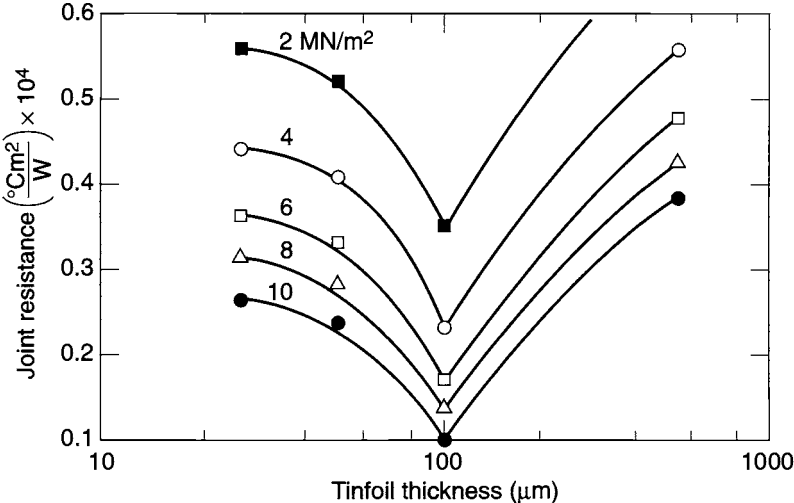
Fig. 16.14. Effect of the metallic foil thickness on joint resistance.
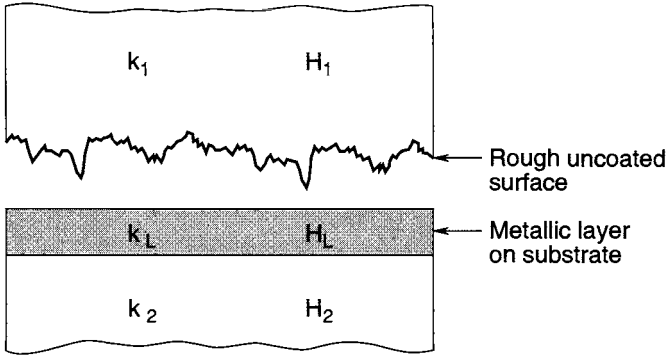
Fig. 16.15. Schematic of the coated joint.

where H' is the effective microhardness of the layer-substrate combination and C is a constriction-parameter correction factor that accounts for the heat spreading in the coated surface.

As can be seen from Eq. (16.77), the coated contact conductance is the product of three quantities: the uncoated contact conductance, h_c, a mechanical modification factor, $\left(\dfrac{H}{H'}\right)^{0.93}$, and the thermal modification factor, which is displayed in brackets. The uncoated conductance can be determined by evaluating Eq. (16.34). Therefore, for a given joint, the only unknowns are the effective microhardness, H', and the constriction-parameter correction factor, C. They are the key to solving contact problems with coated surfaces.

Mechanical Model

The best way to obtain the effective microhardness is to perform the Vickers measurement of the combination layer (coating)-substrate. This measurement will result in a plot of the effective microhardness as a function of the relative layer thickness (ratio between thickness of the layer and equivalent Vickers indentation depth, t/d), similar to that of the silver layer on a nickel substrate, as shown in Fig. 16.16.
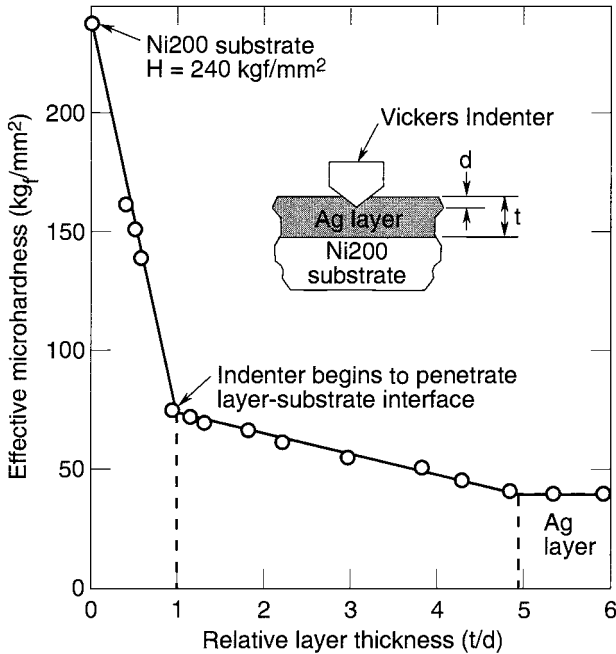
Fig. 16.16. Vickers microhardness measures for silver layer on Nickel 200 substrate.

When Vickers microhardness measurements are not available, for a first approximation, one assumes that the general form of the plot for the particular layer-substrate combination under consideration is similar to that shown in Fig. 16.16, and the following equations can be used to estimate the effective microhardness. For $t/d < 1.0$ (Antonetti[16.22]):

$$H' = H_2\left(1 - \frac{t}{d}\right) + 1.81 H_L\left(\frac{t}{d}\right) \tag{16.78}$$

where H_L is the microhardness of the layer and H_2 is the bulk microhardness of the substrate, both obtained from the Vickers microhardness test. For $1.0 \leq t/d \leq 4.90$:

$$H' = 1.81 H_L - 0.21 H_L\left(\frac{t}{d} - 1\right) \tag{16.79}$$

where the relative thickness t/d is determined from:

$$\frac{t}{d} = 1.04 \frac{t}{\sigma}\left(\frac{P}{H'}\right)^{-0.097} \tag{16.80}$$

When $t/d > 4.90$, the effective microhardness is equal to the layer microhardness H_L.

As t/d depends upon the effective microhardness and t/d must be known to determine the effective microhardness, an iterative approach is required. If the arithmetic average of the layer and substrate microhardness values is used as the initial guess, the convergence is rapid. If the substrate surface has been work-hardened, then use of the substrate bulk hardness is incorrect. Yovanovich, Hegazy, and De Vaal[16.30] proposed a method to determine a proper value of the effective microhardness.

Thermal Model

Antonetti[16.22] solved Laplace's equation for the temperature distributions within the layer and substrate subjected to the perfect contact boundary condition at their common interface. For the constriction resistance as defined in Eq. (16.8), the constriction parameter for a coated surface is shown to be:

$$\psi' = \frac{16}{\pi\varepsilon'} \sum_{n=1}^{\infty} \left[\frac{J_1^2(\lambda_n b'\varepsilon')}{(\lambda_n b')^3 J_0^2(\lambda_n b')}\right] \phi_n \gamma_n \rho_n \tag{16.81}$$

The first term to the right of the sigma in Eq. (16.81), the term in brackets, represents a dimensionless constriction parameter for an uncoated contact (considering uniform heat-flux conditions at the contact area); the second, ϕ_n, accounts for the influence of the layer; the third term, γ_n, accounts for the contact temperature basis used to determine the constriction resistance; and the fourth, ρ_n, accounts for the contact-spot heat-flux distribution. The eigenvalues λ_n are the roots of the equation $J_1(b'\lambda_n) = 0$. For adjoining surfaces, the contact spots are assumed to be isothermal. The modification factors in this case are $\gamma_n = 1$,

$$\phi_n = K\left[\frac{(1+K)+(1-K)e^{-2\lambda_n a'\tau}}{(1+K)-(1-K)e^{-2\lambda_n a'\tau}}\right], \tag{16.82}$$

and

$$\rho_n = \frac{\sin(\lambda_n b'\varepsilon)}{2J_1(\lambda_n b'\varepsilon)}, \tag{16.83}$$

where $\tau = \dfrac{t}{a'}$ is the relative layer thickness and K is the ratio of the substrate to layer conductivities. The constriction-parameter correction factor, C, is defined as the ratio of the constriction parameter with a layer [Eq. (16.81)] to that without a layer [Eq. (16.9) or (16.15)], for the same value of the relative contact-spot radius. For isothermal contact temperature, typical values are presented in Table 16.2. A more complete table for this factor can be found in Antonetti.[16.22]

Antonetti[16.22] also developed an alternative contact-conductance model, based on the Yovanovich[16.18] correlation [Eq. (16.34)]. Based on the expression on the left side of Eq. (16.81), considering that there are two constriction resistances in series (surfaces 1 and 2), for N contact spots in parallel, one finds the contact conductance for a coated contact:

$$h'_c = \frac{2a'k'}{\psi(\varepsilon')}\left(\frac{N}{A_a}\right) \tag{16.84}$$

where k' is based on Eq. (16.77) and is defined as

$$k' = \frac{2k_1 k_2}{C_2 k_1 + k_2}. \tag{16.85}$$

Equation (16.9) can also be used to determine the constriction parameter. The average contact-spot radius parameter can be determined from

$$a' = 0.77\left(\frac{\sigma}{m}\right)\left(\frac{P}{H'}\right)^{0.097}. \tag{16.86}$$

Table 16.2. Thermal Constriction Resistance Parameter Correction Factor

e	1/K	t/a	C
0.005	2	0.01	0.9842
0.200	2	0.50	0.6218
0.500	50	0.05	0.0260

By means of a force balance at the joint, the total number of contact spots per unit apparent area can be estimated by

$$\frac{N'}{A_a} = \frac{1}{\pi(a')^2}\left(\frac{P}{H'}\right). \tag{16.87}$$

Although Eqs. (16.77) and (16.84) differ algebraically, they yield the same numerical results. The advantage of Eq. (16.77) is that it permits the researcher to appreciate how the various parameters contribute to the coated contact conductance.

Antonetti[16.22] demonstrated that the bare conforming rough surface model of Cooper et al.[16.4] that was correlated by Yovanovich[16.18] can be used to correlate the contact with coated surfaces:

$$\frac{h'_c \sigma}{k'm} = 1.25\left(\frac{P}{H'}\right)^{0.95} \tag{16.88}$$

Antonetti[16.22] and Antonetti and Yovanovich[16.29] experimentally verified their model, performing thermal tests with Nickel 200 specimens. One of the specimens was coated with a thin layer of pure silver and the other was bead-blasted to different levels of roughness. The authors verified that the joint conductance was increased approximately by a factor of 10 when the layer is around 6 μm thick, for a surface having a roughness of 1.28 μm. The good agreement between the theory and data can be observed in the plot of the dimensionless thermal conductance, defined as $\dfrac{h_c'\sigma}{mk'}$ against the relative pressure $\dfrac{P}{H'}$ [H' is given by Eqs. (16.78) and (16.79)], presented in Fig. 16.17.

Experimental Data

Several publications deal with experimental measurements of the thermal resistance of contacting surfaces, where at least one of the surfaces is coated. In most cases, the coating is applied with the objective of enhancing the overall thermal conductance of the joint. Some of these experiments, which can be useful for satellite applications, are presented here.

Metallic Coatings

Kang et al.[16.31] studied the contact conductance of Aluminum 6061-T6 surfaces, where metallic coatings were vapor-deposited. Lead, tin, and indium were evaluated using four different coating thicknesses: 2.0 to 3.0 μm for indium, 1.5 to 2.5 μm for lead, and 0.2 to 0.5 μm for tin. The enhancement factors for the thermal contact conductance were found to be on the order of 700, 400, and 50%, respectively.

Chung et al.[16.32] (1993) studied the thermal contact conductance of a phase-mixed coating layer applied over metallic surfaces using a transitional technique that consists of a plasma-enhanced deposition onto a cold surface. Their experimental study was restricted to a relatively low ratio of the contact pressure to the
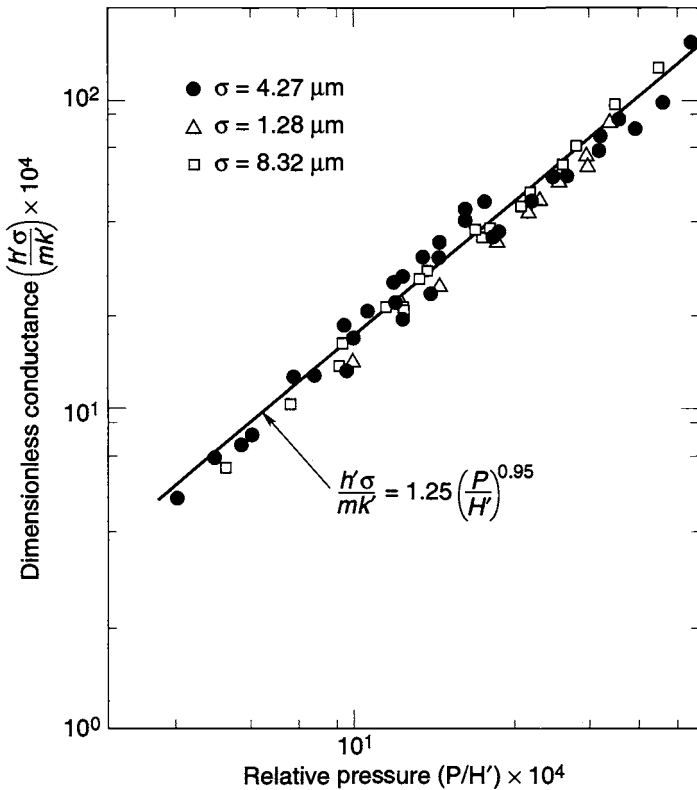
Fig. 16.17. Dimensionless contact conductance versus relative contact pressure for silver layer on nickel substrate.

microhardness $\left(10^{-4} < \dfrac{P}{H} < 6 \times 10^{-4}\right)$, where very few data exist. They coated Aluminum 6061-T6 surfaces with pure copper, pure silver, a phase mixture of copper and carbon, and another of silver and carbon. Actually, the pure layers yielded 10 to 30% higher values of the contact conductance when compared with the carbon mixtures. The researchers justified the use of phase-mixed coatings by the improvement of the mechanical properties of the coating.

Howard and Peterson[16.33] studied the effect of multiple layering on the thermal contact conductance of vapor-deposited metallic coatings. They concluded that oxidation and thermal cycling intrinsic to the mechanical coating process cause poor layer adhesion that resulted in a significantly smaller enhancement factor than that occurring from single-layer coatings with an equivalent thickness.

Lambert and Fletcher[16.34] observed that the literature models are valid for optically flat idealized surfaces, which are hard to find in engineering. They collected and correlated a large body of conductance data of contacts involving wavy and

rough engineering surfaces, obtained from different laboratories, resulting in the expression:

$$\frac{h'_c \sigma}{k'm} = 0.00503\left(\frac{P}{H'}\right)^{0.455} \tag{16.89}$$

This correlation presents a significantly smaller $\left(\frac{P}{H'}\right)$ exponent (0.455) than that predicted by Antonetti and Yovanovich[16.35] [0.95, Eq. (16.88)], indicating that nonflat wavy surfaces are less sensitive to contact pressure than the optically flat surfaces.

Li et al.[16.36] experimentally investigated four coating materials: tin, copper, aluminum, and silver. Two methods of coating were used, electroplating and filtered arc vapor deposition, and the experiments verified that optimum coating thickness varies according to the selected material. This thickness is determined by the hardness: the harder the coating material, the thicker the coating needs to be for better performance. Therefore, the authors suggested, the parameter k/H could be used to rank the coating material. They also concluded that the maximum enhancement of contact conductance is obtained when both contacting surfaces are coated. They observed that the enhancement factor, which ranges from 4 to 21, is a function of the contact pressure.

Other experimental conductance measurements of contacts where the surfaces are metal-coated can be found in the extensive literature review made by Lambert and Fletcher.[16.37] They also compared and ranked the thermal performance of the coating materials.

Nonmetallic Coatings

Marotta et al.[16.38] made a literature review of experimental data available for the thermal contact conductance of nonmetallic coatings, which they classified in four groups: oxides, carbon-based coatings, ceramics, and polymer-based coatings. The oxide films were already treated. Carbon-based coatings, such as polycrystalline diamondlike films, offer excellent thermophysical properties, which make them attractive coatings. The deposition temperatures of polycrystalline diamondlike films (770–900 K) limit the deposition of these films to metals that can withstand high temperatures without loss of mechanical properties. Ceramics generally exhibit good structural and thermal capabilities at high temperatures. They resist oxidation, erosion, and corrosion, and they wear more than most metals. Some of the ceramics tested are: titanium nitrite (TiN), titanium carbide (TiC), and silicon carbide (SiC). They can be applied to complex shapes. Impregnation coatings (synergistic) combine the properties of two or more materials to provide a surface with permanent dry lubricity, added wear, corrosion resistance, and high chemical inertness. Marotta and Fletcher[16.39] presented many experimental data obtained from their own experimental work on thermal contact conductance of a ceramic coating deposited on aluminum 6061-T6 and copper CC11000-H03. Marotta et al.[16.40] (1996) also conducted experiments on thermal contact conductance of diamondlike films deposited over these same materials (aluminum and

copper). Their studies confirmed and completed the information gathered from the literature.

The experimental work presented in this section for contact with nonmetallic coatings was intended for terrestrial applications. This technology is promising for space but should be tested accordingly before being applied.

Nomenclature

a	contact-spot radius
A	contact area
b	elemental heat-flux tube radius
c	geometry parameter as defined in Fig. 16.4(b)
C	ratio of the constriction parameter with a layer to that without a layer
C_1	Vickers correlation coefficient, correlation parameter
C_2	Vickers correlation coefficient
d	geometry parameter as defined in Fig. 16.4(b), height of the waviness represented by a spherical crown, Vickers indentation depth
D	diameter of the contour area
E	modulus of elasticity
f_{ep}	elastoplastic factor
g	contour area function
h	conductance
H	surface microhardness
J_o, J_1	Bessel functions
k	conductivity
K	ratio of the substrate to layer conductivities
L	wavelength of the spherical waviness
m	surface slope
n	number of microcontacts per unit apparent area
N	number of contact spots
p	probability density function
P	contact pressure
Q	heat flux
r	radius
R	thermal resistance
S_f	flow stress
S_U	ultimate strength
t	thickness
T	temperature
x	relative mean plane separation
$y(x)$	surface profile height
Y	mean plane separation height

Nomenclature—*Continued*

z	axial direction

Greek Letters

β	lateral spread of oxide
δ	oxide layer thickness vertical projection
ε	relative real contact area
Φ_n	uncoated contact dimensionless constriction parameter
γ_n	layer influence parameter
η	elastoplastic index
λ	contour area, eigenvalue
ρ_n	contact-spot heat-flux distribution
σ	standard mean height deviation (root mean square deviation)
τ	relative layer thickness
υ	Poisson's ratio
ξ	elastic deformation factor
Ψ	constriction parameter

Subscripts and Superscripts

a	apparent
c	contact
cm	metal-to-metal
co	oxide-to-oxide
e	elastic
eff	effective
ep	elastoplastic
g	gas
H	bulk
j	joint
L	large, layer
m	metal
max	maximum
o	oxide
r	radiation, real
s	microconstriction, harmonic mean
t	total
0	initial
$1,2$	surface coating

References

16.1. T. H. McWaid, "Thermal Contact Resistance Across Pressed Metal Contact in a Vacuum Environment," Ph. D. thesis, University of Waterloo, Canada, 1990, pp. 1–264.

16.2. S. Song and M. M. Yovanovich, "Relative Contact Pressure: Dependence on Surface Roughness and Vickers Hardness," *AIAA Journal of Thermophysics* **2** (1), 43–47 (January 1988).

16.3. A. A. Hegazy, "Thermal Joint Conductance of Conforming Rough Surfaces," Ph.D. thesis, University of Waterloo, Canada, 1985.

16.4. M. G. Cooper, B. B. Mikic, and M. M. Yovanovich, "Thermal Contact Conductance," *International Journal of Heat and Mass Transfer* **12**, 279–300 (1969).

16.5. B. B. Mikic and W. M. Rohsenow, "Thermal Contact Resistance," Technical Report No. 4541-41, Massachusetts Institute of Technology, Cambridge, MA, 1966, pp. 1–129.

16.6. L. C. Roess, "Theory of Spreading Conductance," appendix to N. D. Weills and E. A. Ryder, "Thermal Resistance Measurements on Joints Formed between Stationary Metal Surfaces," *Semi-Annual ASME Heat Transfer Divison Meeting* (Milwaukee, WI, 1948).

16.7. A. M. Clausing and B. T. Chao, "Thermal Contact Resistance in a Vacuum Environment," *Journal of Heat Transfer*, 243–251 (May 1965).

16.8. A. M. Clausing, "An Experimental and Theoretical Investigation of the Thermal Contact Resistance," Semi-Annual Status Report Number 8: Research Grant NASA NsG 242, University of Illinois, 1965, pp. 1–23.

16.9. M. M. Yovanovich, "Overall Thermal Resistance between Contacting Rough, Wavy Surfaces," *International Journal of Heat and Mass Transfer* **12**, 1517–1520 (1969).

16.10. S. S. Burde and M. M. Yovanovich, "Thermal Resistance at Smooth-Sphere / Rough-Flat Contacts: Theoretical Analysis," *Progress in Astronautics and Aeronautics: Thermophysics and Thermal Control* **65**, 83–102 (1978).

16.11. M. A. Lambert and L. S. Fletcher, "Thermal Contact Conductance of Spherical Rough Metals," *Journal of Heat Transfer* **119**, 684–690 (November 1997).

16.12. B. B. Mikic, "Thermal Constriction Resistance Due to Non-Uniform Surface Conditions: Contact Resistance at Non-Uniform Interface Pressure," *International Journal of Heat and Mass Transfer* **13**, 1497–1500 (1970).

16.13. M. Sridhar and M. Yovanovich, "Critical Review of Elastic and Plastic Thermal Contact Conductance Models and Comparison with Experiment" *AIAA 28th Thermophysics Conference* (Orlando, FL, July 1993), pp. 1–14.

16.14. B. B. Mikic, "Thermal Contact Conductance; Theoretical Considerations," *International Journal of Heat and Mass Transfer* **17**, 205–212 (1974).

16.15. M. R. Sridhar, "Elastoplastic Contact Models for Sphere—Flat and Conforming Rough Surface Applications," Ph. D. thesis, University of Waterloo, Canada, 1994, pp. 1–332.

16.16. B. B. Mikic, M. M. Yovanovich, and W. M. Rohsenow, "The Effect of Surface Roughness and Waviness Upon the Overall Thermal Contact Resistance," Technical Report No. 76361-43, Massachusetts Institute of Technology, Cambridge, MA, 1966, pp. 1–94.

16.17. J. A. Greenwood and J. B. P. Williamson, "Contact of Nominally Flat Surfaces," *Proceedings of the Royal Society, Vol. A-295* (The British Library—Photocopy Service, 1966), pp. 300–319.

16.18. M. M. Yovanovich, "Thermal Contact Correlations," *Spacecraft Radiative Transfer and Temperature Control, Astronautics and Aeronautics* **83**, 83–95 (1982).

16.19. B. B. Mikic, "Analytical Studies of Contact Nominally Flat Surfaces; Effect of Previous Loading" *Journal of Lubrication Technology*, 451–456 (October 1971).

16.20. M. R. Sridhar and M. M. Yovanovich, "Elastoplastic Contact Conductance Model for Isotropic Conforming Rough Surfaces and Comparison with Experiments," *Thermal Phenomena at Molecular and Microscales and in Cryogenic Infrared Detectors, ASME HTD* **277**, 43–56 (1994).

16.21. K. M. Nho, "Experimental Investigation of Heat Flow Rate and Directional Effect on Contact Conductance of Anisotropic Ground/Lapped Interfaces," Ph. D. thesis, University of Waterloo, Canada, 1990, pp. 1–291.

16.22. V. W. Antonetti, "On the Use of Metallic Coatings to Enhance Thermal Contact Conductance," Ph. D. thesis, University of Waterloo, Canada, 1983, pp. 1–198.

16.23. R. Holm, *Electrical Contacts Handbook*, 3rd ed. (Springer Handbook, Berlin, 1958).

16.24. M. A. Lambert and L. S. Fletcher, "A Review of Models for Thermal Contact Conductance of Metals," *34th Aerospace Sciences Meeting & Exhibit* (Reno, NV, 15–18 January, 1996).

16.25. P. W. O'Callaghan and S. D. Probert, "Effects of Static Loading on Surfaces Parameters," *Wear*, Elsevier Sequoia S. A., Netherland **24**, 133–145 (1973).

16.26. F. C. Yip, "The Effect of Oxide Films on Thermal Contact Resistance," *AIAA/ASME Thermophysics Specialist Conference* (Boston, MA, July 1974), pp. 1–8.

16.27. F. R. Al-Astrabadi, P. W. O'Callaghan, and S. D. Probert, "Thermal Resistance of Contacts: Influence of Oxide Films," *AIAA 15th Thermophysics Conference* (Snowmass, Aspen, CO, July 1980), pp. 267–283.

16.28. M. M. Yovanovich, "Effect of Foils upon Joint Resistance: Evidence of Optimum Thickness," *AIAA Progress in Astronautics and Aeronautics: Thermal Control and Radiation, Vol. 31*, edited by Chang-Lin Tien (New York, 1973).

16.29. V. W. Antonetti and M. M. Yovanovich, "Enhancement of Thermal Contact Conductance by Metallic Coatings: Theory and Experiments," *Journal of Heat Transfer* **107**, 513–519 (1985).

16.30. Yovanovich, Hegazy, and De Vaal (1982).

16.31. T. K. Kang, G. P. Peterson, and L. S. Fletcher, "Effect of Metallic Coatings on the Thermal Contact Conductance of Turned Surfaces," *Journal of Heat Transfer* **112**, 864–871 (November 1990).

16.32. K. C. Chung, J. W. Sheffield, H. J. Sauer Jr., and T. J. O'Keefe, "Thermal Contact Conductance of a Phase-Mixed Coating Layer by Transitional Buffering Interface," *Journal of Thermophysics and Heat Transfer* **7** (2), 326–333 (April–June 1993).

16.33. A. H. Howard and G. P. Peterson, "The Effect of Multiple Layering on the Thermal Contact Conductance of Vapor Deposited Metallic Coatings," *AIAA 31st Aerospace Sciences Meeting & Exhibit*, (Reno, NV, January 1993), pp. 1–7.

16.34. M. A. Lambert and L. S. Fletcher, "A Correlation for the Thermal Contact Conductance of Metallic Coated Metals," *AIAA 28th Thermophysics Conference*, (Orlando, FL, July 1993), pp. 1–8.

16.35. V. W. Antonetti and M. M. Yovanovich, "Thermal Contact Resistance in Microelectronic Equipments," *International Journal Hybrid Microelectronics* **7**, 44–50 (1984).

16.36. Y. Z. Li, C. V. Madhusudana, and E. Leonardi, "Enhancement of Thermal Contact Conductance: Effect of Metallic Coating," *Journal of Thermophysics and Heat Transfer* **14** (4), 540–547 (October–December 2000).

16.37. M. A. Lambert and L. S. Fletcher, "Review of the Thermal Contact Conductance of Junctions with Metallic Coatings and Films," *Journal of Thermophysics and Heat Transfer* **7** (4), 547–554 (October–December 1993).

16.38. E. E. Marotta, M. A. Lambert, and L. S. Fletcher, "A Review of the Thermal Contact Conductance of Non-Metallic Coating and Films," *AIAA 27th Thermophysics Conference*, (Nashville, TN, July 1992), pp. 1–17.

16.39. E. E. Marotta and L. S. Fletcher, "Thermal Contact Conductance of Refractory Ceramic Coatings," *Journal of Thermophysics and Heat Transfer* **10** (1), 10–18 (January–March 1996).

16.40. E. E. Marotta, L. S. Fletcher, and D. G. Blanchard, "Thermal Contact Conductance of Diamond-Like Films," *Journal of Thermophysics and Heat Transfer* **10** (1), 19–25 (January–March 1996).

17   Precision Temperature Control

J. Pecson,[*] D. A. Boyd,[†] A. Hashemi,[*] K. Aaron,[‡] J. Ambrose,[**]
J. F. Maddox,[†] E. M. Mattison,[†] and R. F. C. Vessot[†]

Introduction

Tight control of payload or component temperatures to values on the order of 1°C has been routinely accomplished on many programs during the past few decades. In recent years, however, some civilian and military payloads have been developed that demand much more stringent temperature stability for precision optical systems and high-accuracy clocks. For optical systems, even milliKelvin (mK) changes in temperature can result in thermal deformations in the range of nanometers and picometers that can translate into unacceptable errors in the pointing accuracy of optical elements. The Space Interferometry Mission (SIM), the Next Generation Space Telescope (NGST), and the Terrestrial Planet Finder (TPF) are examples of state-of-the-art programs with such strict deformation requirements on optical surfaces. Even tighter temperature control can be required for time-reference clocks where temperature changes of only tenths of a milliKelvin can cause unacceptable drift in time measurement. The hydrogen maser clock (HMC) program is an example of a time-reference system with such demanding thermal-control requirements.

Given that an aluminum atom has a diameter on the order of 0.3 nanometers, maintaining the relative position of the optical elements on a spacecraft structure to subnanometer accuracy is quite a feat. Either the coefficient of thermal expansion (CTE) of the structure and mirror material must be extremely low or the temperature field needs to remain nearly constant—or a combination of these requirements must be met. These are difficult requirements on the materials, and therefore thermal-stability issues are clearly at the heart of programs like SIM, NGST, and TPF. To achieve temperature stability, the thermal designers of these programs have chosen to thermally isolate the temperature-sensitive components from external heating variations and then rely on thermal capacitance and conductance effects to dampen residual temperature changes to values on the order of milliKelvins.

For other programs, like HMC, highly stable temperatures are achieved by isolating sensitive components from changes in the external environment and then actively controlling temperatures to the submilliKelvin level. In this type of design, the focus changes from passive to active control, from control of temperature to control of heat-flow paths and gradients, and from thermostats to detailed behavior of control loops and their compensation. Focus is also placed on limitations on control arising from heater-sensor placement. Calibration of and among

---

*Lockheed Martin, Palo Alto, California.
†Smithsonian Astrophysical Observatory, Cambridge, Massachusetts.
‡Jet Propulsion Laboratory, California Institute of Technology, Pasadena, California.
**Lockheed Martin, Sunnyvale, California.

nearly identical sensors, self-heating by measurement current, and resistance changes of lead wires become important. Electrical and thermal aspects of the control system become less separable, and local temperature sensitivity of the electronic control system can be critical. Long-term stability of sensors and electronics alike can limit design choices if control is required for months or years.

In this chapter, an overview of the SIM thermal-design philosophy and requirements is given to highlight the challenges of precision temperature control of optical systems. For this class of problem a methodology for multidisciplinary modeling is presented, and prediction and validation of a milliKelvin-level optical test bed are discussed. Similarly, the thermal design and test verification of the HMC are used to illustrate the thermal-design issues for active submilliKelvin-level temperature control at the component level.

The Space Interferometry Mission

To explore the issues of spacecraft-level precision temperature control, we begin with a description of SIM and its mission and thermal challenges. The SIM is an independent and essential stepping-stone within NASA's Origins Program. SIM will determine the positions and distances of stars several hundred times more accurately than any previous program. This accuracy will allow SIM to determine the distances from Earth to stars throughout the galaxy and to probe nearby stars for Earth-sized planets. SIM is a joint effort of the Jet Propulsion Laboratory (JPL), California Institute of Technology, Lockheed Martin Missiles and Space, and TRW.

The SIM flight system (Fig. 17.1) consists of the interferometer instrument system and the spacecraft system. The instrument system consists of the optics, actuators, sensors, and computers needed to make science observations. The spacecraft system provides the essential engineering functions for flight operations, including the structure, power subsystems, attitude control, propulsion, communication, and thermal control.
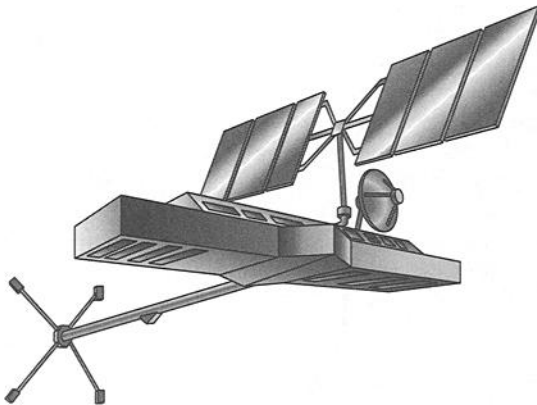
Fig. 17.1. The SIM flight system.

The SIM instrument (Fig. 17.2) operates by collecting starlight using pairs of small telescopes and combining the light onto sensitive CCD (charge-coupled device) detectors to create constructive interference. When all elements are carefully aligned, very precise measurements made using a laser interferometric metrology system, coupled with knowledge of guide star locations, can be used to establish the angular position of the target star or other celestial object.[17.1]

SIM performs astrometry (measurement of star locations) by using a white-light Michelson interferometer with a 10-m baseline. Groups of optical elements (similar to telescopes) are located 10 m apart on opposite ends of a precision support structure (PSS) to collect the starlight, as shown in Fig. 17.2. Light from these telescope-like assemblies is combined in an astrometric beam combiner (ABC) in the middle of this large instrument. Optical delay lines (ODLs) are used to adjust the path length followed by the starlight so that the wavefronts from both arms of the interferometer arrive at the detector at precisely the same time. The path lengths within the instrument are then measured to a precision (not accuracy) of a few tens of picometers using infrared laser metrology gauges. Based on these measurements and other laser gauge measurements of the baseline length, the angle between the target star and the baseline is determined. To find the orientation of the astrometric baseline, two other similar astrometric interferometers are used. The baselines for all the interferometers are kept as parallel as possible. The laser metrology system measures the small amount of deviation from parallelism to make corrections to the results.[17.2]

The SIM spacecraft will be launched from Cape Canaveral in 2009. In its orbit, the spacecraft will slowly drift away from Earth at a rate of approximately 0.1 AU
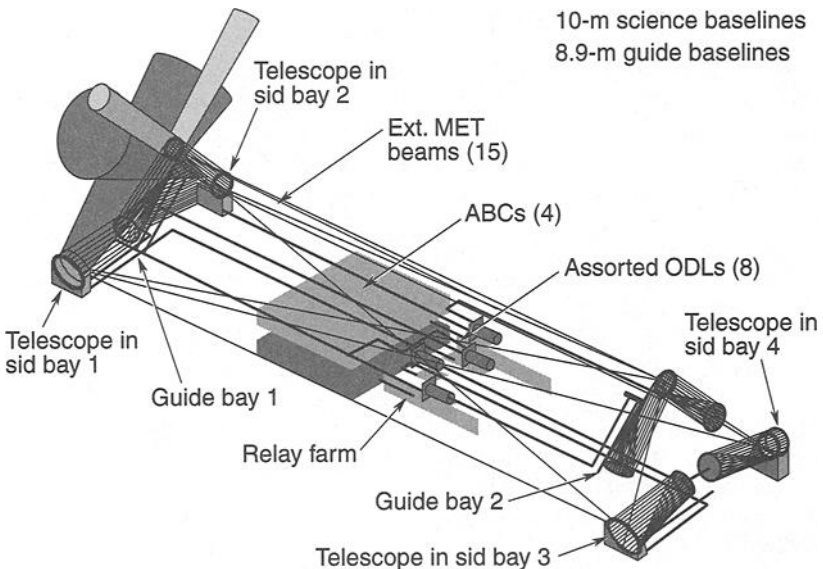
Fig. 17.2. The SIM instrument.

per year, reaching a maximum communication distance of about 95 million km after 5.5 years. In this Earth-trailing solar orbit the spacecraft will receive continuous solar illumination, avoiding the temperature swings caused by eclipses in an Earth orbit. This is one of the very few instances in which thermal-control requirements have actually dictated the choice of mission orbit!

Successful development of SIM requires that four "grand technological challenges" be overcome:

- nanometer-level control and stabilization of optical-element positions on a lightweight flexible structure
- subnanometer-level sensing of optical-element relative positions over meters of separation distance
- overall instrument complexity and the implications for interferometer integration and test and autonomous on-orbit operation
- picometer-level optical-deformation control and stabilization

Thermal Challenges and Design Approach

The challenging picometer-level optical requirements impose severe thermal and structural requirements on SIM. Its thermal-control subsystem technologies are designed to satisfy the stressing requirements on temperature stability and temperature gradients within the starlight-collecting optics and the instrument. Potential thermal disturbances to these subsystems include time-varying sun angles, on/off heater operation, optical-element position changes (slewing), heat pulses from cameras or actuators, and power variations in electronics units.

Thermally induced optical-path errors can arise from changes in the shape of the optics and changes in the shape of the structure that supports them. As an example, a 2.6-mK change in the front-to-back temperature difference of the compressor primary mirror during a 1-hr period will cause a 40-picometer error in the astrometric measurement.

Beam-walk errors occur because of the difference between the metrology and starlight optical paths. As long as this difference remains constant, the instrument can calibrate out the error. However, if the metrology-starlight difference varies as the instrument makes its observation, an error in the astrometric measurement will result. This difference can come from a number of sources. Thermally induced errors are a major source.

The overall design approach for the optics is to thermally isolate and minimize variations in the viewing temperature of the optics, as shown in Fig. 17.3. To meet this requirement, the view of exposed mirrors to space is maximized with each mirror having a heater plate radiating to its entire back and side surfaces to reduce and maintain stable gradients within the mirrors. The heater plate back and sides are enclosed in multilayer insulation (MLI). The enclosed optics are housed within 0.1-K-controlled bay walls and a precision support structure (PSS). Within this environment, the optics temperature can be stabilized to meet the milliKelvin stability required during data collection.

The thermal enclosures and the PSS employ multiple lightweight computer-controlled heaters and MLI blankets, as illustrated in Fig. 17.4. This thermal design cold-biases the PSS by using exterior surface components that are always colder than the desired operating temperature, even in direct sunlight. For the
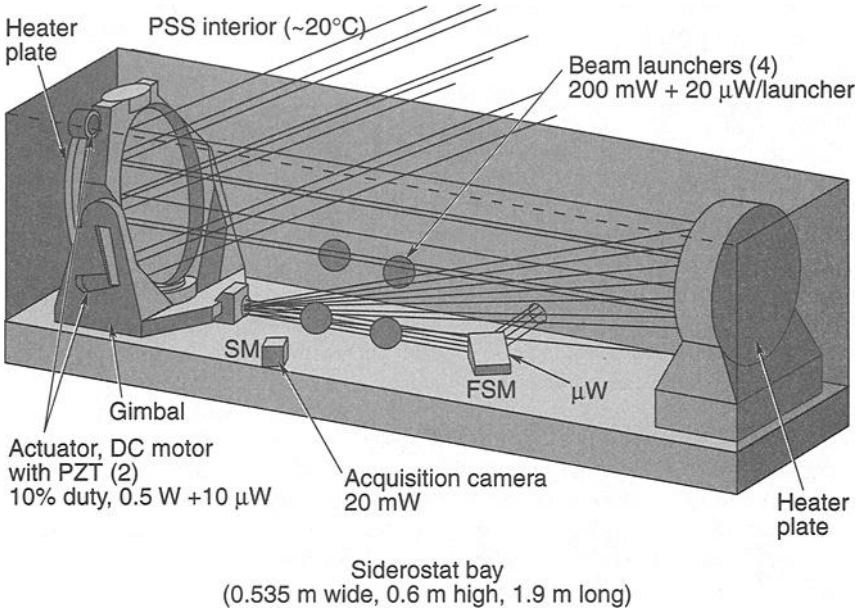
Fig. 17.3. Siderostat bay heat sources.
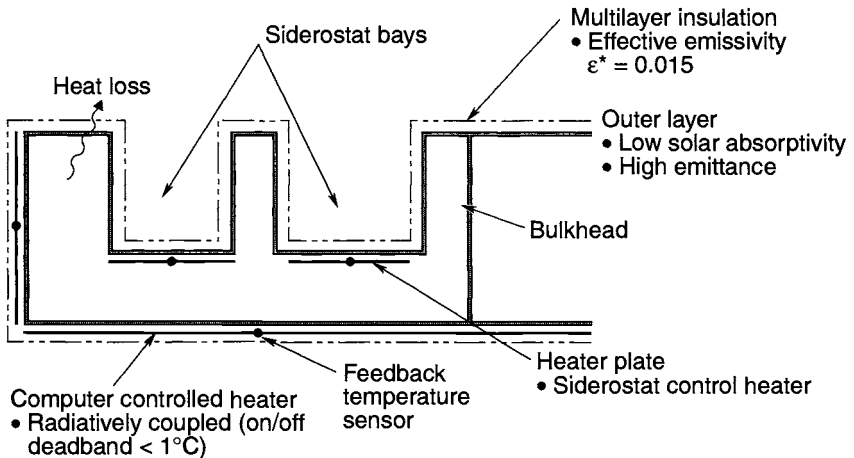
Fig. 17.4. PSS thermal control approach.

required five-year life, the cold-biasing objective would be achieved by using MLI with silvered-Teflon outer cover sheets. Heaters are controlled via the spacecraft computer, which sends on/off commands to the heater drive electronics.[17.1]

Analysis Approach

Optical design, with deformation requirements in the nanometer and picometer range, often requires testing and prediction capabilities beyond the state of the art. In this context, integrated thermal-optical-mechanical modeling is essential to aid the design process, predict system performance, and assign error budgets to various components and subsystems. This section describes a methodology for performing integrated design and analysis for space optical systems using OPTIMA, an optical analysis code, and I-DEAS/TMG, an integrated CAD/CAM/CAE software package. This approach was found to streamline the process for obtaining accurate and reliable design information and to enhance prediction capability.

The conventional design approach to modeling such systems is a lengthy and cyclic process involving geometric modeling and a series of analyses, each focusing on a different physical discipline. The performance and cost of the final design depend on how effectively and quickly the designer can accommodate the requirements imposed by each of these disciplines. Integrated multidisciplinary modeling is a cost-efficient way to substantially reduce design time, provide system optimization, and generate accurate predictions.

The design and analysis process described in this section involves multiple disciplines and assumes that an individual designer/analyst performs each role. In actual practice any number of engineering specialists could contribute to each function. The methodology starts with an optical designer, who develops the optics to meet the science requirements. A structural designer then specifies additional hardware to maintain the position of the optical components. Once the design is complete, a thermal analyst develops a thermal-control scheme and predicts the thermal response of the design to confirm that it satisfies the temperature requirements. Subsequently, a structural analyst calculates the thermal deformations induced by the temperature gradients. Finally, these deformations are used as input by the optical analyst in characterizing the impact of the displacements on the image quality. Figure 17.5 illustrates steps in the design methodology, which the following sections explain in greater detail.

Methodology

Optical Design

The first step in designing and evaluating a space optical system is to define the optical elements it comprises. Once a starting configuration is developed from a set of requirements, Lockheed Martin's optical design and analysis program, OPTIMA (or a similar commercial optical analysis tool, such as MACOS, Code V, or Optix) is used to optimize the design.

Many options are considered in designing optical systems to meet requirements. Material selection can have a significant impact on performance. The optical designer's choice of materials with near-zero CTE at operating temperature reduces thermal deformations. Also, thermal gradient effects are minimized by use of materials with a high thermal conductivity.
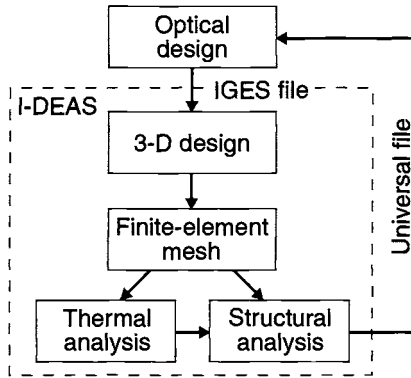
Fig. 17.5. Space optical-system design methodology.

Once the desired optical configuration is determined, the lens and mirror defini-tions with ray traces (light path) are translated by the optical designer into a series of Initial Graphics Exchange Specification (IGES) files for transfer to a structural designer.

Figure 17.6 shows a representative space optical system similar to that of one siderostat bay unit within the SIM spacecraft. The sequence of mirrors represents a beam collector (the siderostat mirror) and beam compressor (the primary mirror) with a focal point at 1.3 meters. The optical elements were created in OPTIMA and then imported into I-DEAS, via IGES files. The associated ray traces are also displayed in the figure. The light is collected by the siderostat mirror, which directs the starlight in a fixed outward direction toward the primary mirror and then through the remaining optical elements.
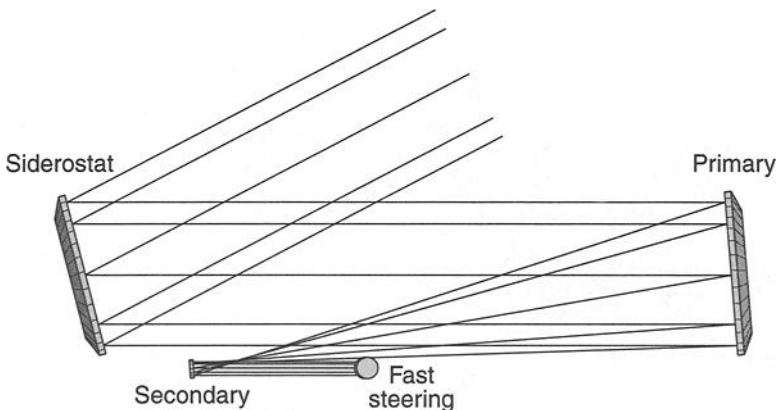
Fig. 17.6. Representative space optical system.

Structural Design

The IGES files from the optical designer are imported into I-DEAS, an integrated CAD/CAM/CAE software package for design and analysis of components and assemblies in a common environment. This commercial tool consists of various modules for design, drafting, assembly, meshing, and analysis. The graphical user interface and postprocessing module enable easy viewing of results, allowing rapid problem diagnosis and design evaluation.

The structural designer uses I-DEAS to create the support structure necessary to maintain the position of the components. This structure may include mirror mounts, an optical bench, and enclosure walls. Special care is given to the mirror mounts to ensure the force exerted on the optical components does not distort the optical surface. Designers strive to obtain high mounting stiffness to maintain optical element position. Other goals are ensuring mount size and weight are as small as possible and keeping costs low.

Once the support structure is created, various parts are grouped into logical levels of assembly, creating a hierarchy of all parts within a master assembly. For example, a mirror might belong to an instrument subassembly that (when coupled with the bus) comprises the satellite master assembly. A concrete example of the benefits this order creates will be presented in a subsequent section.

The materials for all parts, including optical components and support structure, are then incorporated into a material database within I-DEAS. Although the structural designer uses the software tool to apply material properties to each part, the optical designer is responsible for specifying the materials and surface coatings for all optical components.

Using the optics created in the previous step, the structural designer assembles a structure (Fig. 17.7) to precisely maintain the position of the optical components. The siderostat mirror gimbal is constructed to enable the mirror to rotate plus or minus several degrees to accommodate the science requirements. A mirror housing "wedge" and bipod flexure mount are created to support the primary mirror. Mirror mounts for the secondary and fast steering mirrors are also created. Finally, also shown in Fig. 17.7 is the optical bench. At this stage, material properties are associated with each part, and an assembly of the system is generated.

Thermal and structural analysts are able to take advantage of the data that has already been created by the structural designer, so the transition between analysis phases is easily made. Because of the common environment, information such as geometric dimensions, volumes, material properties, and assembly layout is automatically available to both thermal and structural analysts.

Finite-Element-Method (FEM) Mesh

Using the meshing module within I-DEAS, thermal and structural analysts generate FEM meshes depicting the optical system. Because the meshes are created in the same software environment in which the optical system was structurally designed, the analysts take full advantage of the geometry created in the previous step, eliminating redundancy. This significant process savings comes at a small cost. Typically some reduction to the solid model is necessary to ease the meshing process—not all features are required to perform an acceptable analysis. Features
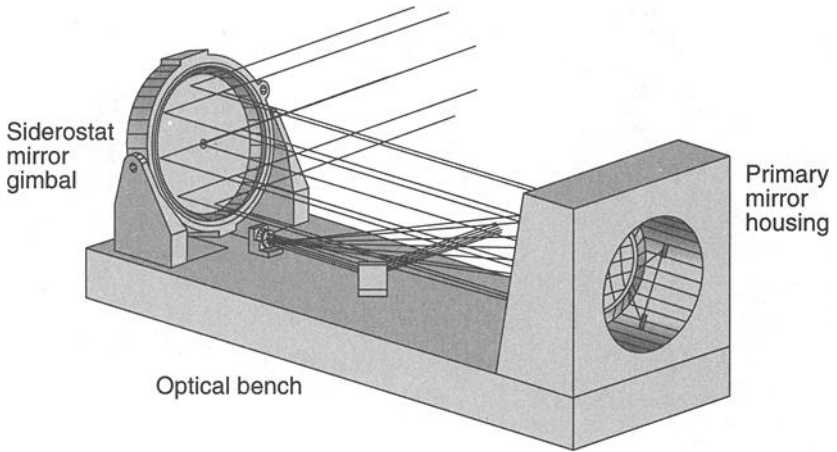
Fig. 17.7. Optics structure assembled to precisely maintain the position of the optical components.

such as fillets, bolt holes, and chamfers can be suppressed for the thermal or structural analysis, depending on the analysts' objectives. Suppressing such features is handled with utilities available in the software.

The mesh density of the model is related to the temperature resolution and deformation information required for the analysis. Each analyst is responsible for ensuring that the element types and mesh density used for a given component properly represent its thermal and structural behavior. Two meshes are typically created, one each for the thermal and structural analyses; however, in certain instances one is sufficient. If two are utilized, an automated temperature-mapping utility within I-DEAS maps temperatures from a thermal analysis onto a structural model using a local-element temperature function.

Another advantage of this integrated process is the ability to associate an FEM mesh with the solid geometry. This association enables the mesh to be updated when the geometry changes, which is particularly useful during early phases of design, when changes occur frequently. It also enables use of the assembly information generated by the structural designer. Parts occurring multiple times within an assembly are meshed once rather than repeatedly at each instance and correctly oriented into the proper locations. For example, an interferometer uses two identical telescopes to collect light. Using the solid geometry and taking advantage of the assembly information, the software meshes the first telescope's components, then automatically meshes the second telescope and orients it in the proper location.

Continuing with the example, we find an FEM mesh of the optical system is created (Fig. 17.8). Several of the parts are meshed individually and merged to form a system FEM mesh as shown in the figure. The assembly information created by the structural designer enables the correct placement of the parts in relationship to each other. Also, the material properties assigned to the 3-D solid geometry in the previous step are automatically associated to the mesh definitions for each part. (The mesh in Fig. 17.8 is not optimized to represent the mesh density
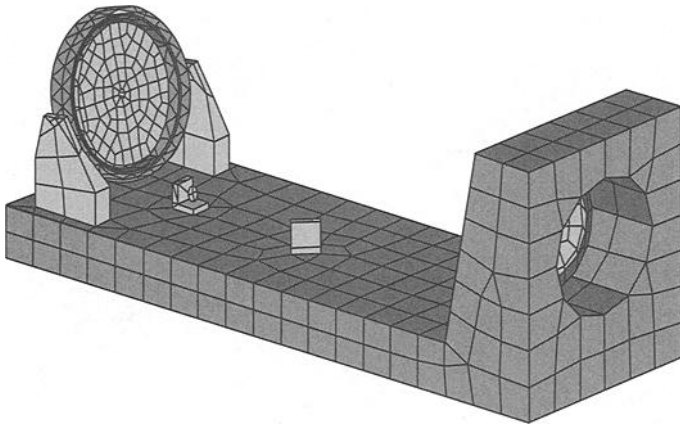
Fig. 17.8. FEM mesh of the optical system.

required to accurately capture milliKelvin-level deformation behavior required in the SIM mission. The figure is for demonstration purposes only.)

Thermal Analysis

Once the FEM mesh is completed, the thermal analyst defines the proper boundary conditions within the I-DEAS Thermal Model Generator (TMG). Thermal couplings, fixed-temperature boundary conditions, heat loads, heat fluxes, and orbital heating are candidate boundary conditions that the analyst considers.

Reliable operation of the optical system necessitates that thermal requirements are met throughout the mission; therefore a thermal-control scheme is devised. Passive and active thermal-control hardware ensures that the proper amount of heat transfer occurs. Examples of thermal-control methods include MLI, surface finishes, heaters, and radiators. MLI is an illustration of a passive method used to minimize heat absorption or rejection in certain areas. Heaters provide active thermal control to compensate for wide ranges of internal and external heat inputs. Because these components are typically not modeled by the structural designer, the thermal analyst may add FEM meshes or thermal couplings for such items.

Modeling the space environment to which the optical system is exposed is accomplished by specifying an orbit definition. Based on the altitude and orientation of the spacecraft, I-DEAS/TMG calculates the environmental thermal load generated by solar heating, Earth albedo, and Earth-emitted infrared (IR). Depending on whether results of steady-state or transient behavior are desired, solver parameters are set and temperatures are calculated using I-DEAS/TMG's finite-volume formulation.

For the representative space optical system, the thermal analyst begins by defining the environment to which such a system is exposed. For this system, the mirrors view deep space and the surrounding payload structure, which is covered with MLI. A radiation parameter is specified in I-DEAS/TMG to simulate the radiative heat transfer from the optical system to cold space. A temperature boundary condition and emissivity properties are established to represent the MLI on the

payload structure. The Zerodur mirrors must maintain room temperature to take advantage of the near-zero CTE. To achieve this condition, radiant heaters are placed behind the mirrors and a heat-load boundary condition is created, identifying the power required. The mirror sides and rear are then covered with MLI to reduce heat loss. A steady-state analysis is performed accounting for conductive and radiative heat transfer. Figure 17.9 shows the temperature distribution of the system. (Because the purpose of this section is to discuss methodology rather than specific results, no temperature values are shown.)

Structural Analysis

Using the thermal-analysis temperatures as boundary conditions, the analyst performs a thermal deformation on the system. As noted in the meshing section, a utility within I-DEAS/TMG is available to map temperatures from one mesh to another in cases where unique meshes are created by thermal and structural analysts. Care must be given to the global coordinate system of the two meshes—the target model must be oriented identically to the thermal model. Also, I-DEAS must be set to the same global measurement units in which the thermal model was solved.

Once the temperatures are associated with the structural mesh, additional mounting constraints are created using I-DEAS's Boundary Condition module. In high-precision optical systems, kinematic mounts are utilized to prevent additional distortion of the optical elements, which may occur because of changes in the mounting force resulting from thermal deformations. The advantages of kinematic mounts are increased stability, distortion-free optical mounting, simplicity, and low cost.[17.3,17.4] To model kinematic mounts, all six degrees of freedom (three translations and three rotations) of the optic are constrained in a manner that allows the optical element to freely deform without experiencing any external force (i.e., stress).

Given the temperature boundary conditions and the mounting restraints, the thermal-deformation model is solved using the I-DEAS Model Solution module.
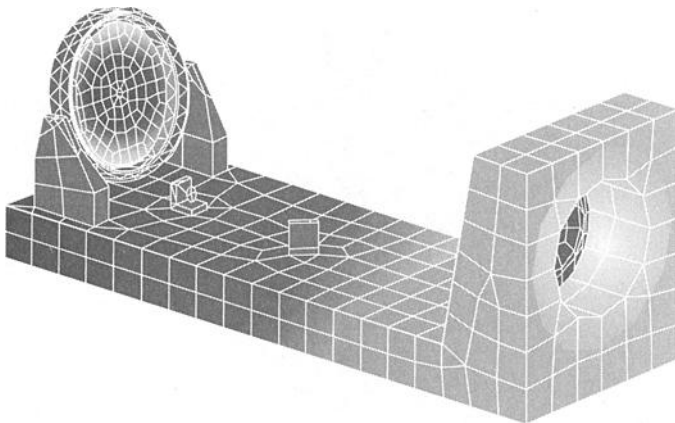
Fig. 17.9. Temperature distribution of a space optical system.

The surface nodes for each optical surface are then grouped, and their initial locations and displacements are exported to an I-DEAS Universal file format. This format is often used for transferring data between users of I-DEAS or other software programs such as OPTIMA.

To streamline demonstration of the methodology, the thermal-analysis FEM mesh is used for the deformation analysis. Using the computed temperatures and assuming a kinematic mount, Fig. 17.10 shows the resultant thermal deformation of the siderostat mirror. (Note: The deformation of the mirror is exaggerated to show detail; however, no actual results are displayed, because the focus is limited to the modeling process.) The surface nodes of the mirror with their original coordinates and displacements are then exported to an I-DEAS Universal file for transfer to the optical analyst.

Optical Analysis

Once the displacements are known, they are transferred to the optical designer, via Universal file, to characterize their impact on the image quality. No translation of coordinates is necessary, because the optical designer established the coordinate system in the first phase of the process. Utilizing OPTIMA, the optical analyst creates Zernike polynomials to represent the distorted surface and evaluates the optical performance. On the basis of the results from this process, the optical designer may propose design changes. If necessary, the process is repeated until a satisfactory design is established.

Several benefits are thus realized, including increased precision and prevention of duplication. These benefits are gained by taking advantage of a single material database for all analysis routines and sharing a common software environment for much of the analysis and design. Additionally, the methodology enables individuals
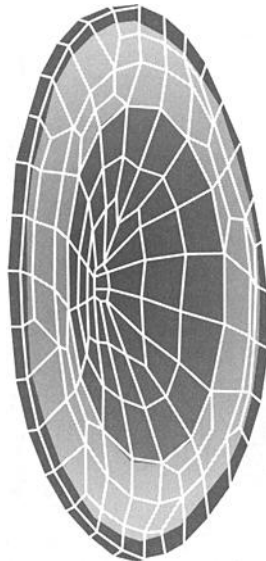
Fig. 17.10. Thermal deformation of siderostat mirror.

from various disciplines to work together, rather than in isolation, much earlier in the product-development process, reducing time to market.[17.5]

Test Verification

A thermal-vacuum test was conducted on a simulated SIM primary mirror to verify the ability to perform milliKelvin-resolution temperature measurements and to assess the measurement-system uncertainties. The thermal-modeling tools and approach were also validated by correlating the temperature-difference measurements in the mirror to predictions over a range of conditions, including small perturbations consistent with those allowable during flight science-observation periods.

The test was conducted on a 33.5-cm-diameter plano mirror under conditions of small thermal perturbations that induced steady-state temperature gradients of 10 to 100 mK. Tests were performed with small heat inputs to the back of the mirror, which was suspended in a thermally uniform shroud. Correlation of thermal models for both conductively and radiatively heated test configurations were performed, and results indicated very good agreement between the thermal-model predictions and the temperature measurements. After adjusting the model to match the known initial temperature indicated by the test data, the analytical uncertainty in predicting subsequent temperature changes from the initial condition was found to be on the order of ±3 mK.

Test Configuration

The test configuration used is shown in Fig. 17.11. A cylindrical copper shroud (91 cm long by 3.2 mm thick, with a 74-cm diam) sat on four fiberglass supports inside the vacuum chamber. The shroud was covered with a 20-layer blanket to radiatively isolate it from chamber-wall temperature fluctuations. It was painted black (Chemglaze polyurethane) on all interior surfaces to provide a high, uniform emittance and a uniform temperature. The test article was suspended in the copper shroud via 2.5-mm-diam Kevlar twine with end loops. Threaded eyes were used to
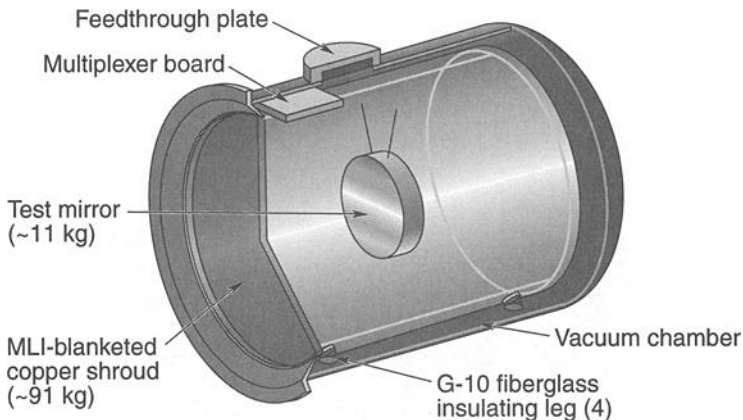
Fig. 17.11. Overall test configuration.

attach the lines to the shroud and the test article. The test article was heated to induce small temperature gradients that were measured using a high-accuracy sensor system.

The test article was a 33.5-cm-diam, 5-cm-thick Pyrex plano mirror, polished and coated with protected silver (Denton) on the front surface. The mirror had 22 small (1.1-mm diam, 8 mm deep) holes drilled into it for sensor installation, and two larger holes (9.5-mm diam, 31.8 mm deep) for installation of mounting hardware. The sensor hole locations are illustrated in Fig. 17.12. Note that the edge sensor holes are in a spiral pattern to allow axial and circumferential resolution. Small threaded invar plugs were epoxy-bonded into the mounting holes. The Kevlar support lines were attached to screws threaded into these plugs.

Two methods of heating the test article were used, conductive and radiative. Both used a 1-mm-thick, 33-cm-diam, 500-Ω nominal resistance, adhesive/foil-backed Kapton heater with embedded nichrome wire elements (7.2-mm spacing).

Calibrated miniature platinum resistance thermometers (PRTs) were installed at the 18 embedded locations on the mirror shown in Fig. 17.12. The locations were designed to show axial and radial temperature distributions in the mirror, while minimizing the impact of the sensor holes on the mirror temperature distribution. To obtain temperature measurements of sufficient accuracy for this project, a special measurement system was utilized to obtain measurements from the PRTs. The readout system consisted of a Linear Research KR-700 AC Resistance Bridge, a custom in-situ multiplexer to allow serial measurements, and a PC-based National Instruments data-acquisition system. The PRTs were specifically calibrated using this system in 5°C increments over the 15–40°C temperature range. The system attains relative accuracy (defined as the difference between different sensors when they are at the same true temperature) of ±1 mK, when sensors are undisturbed following calibration.[17.6]

Following instrumentation and heater attachment, the back and sides of the mirror were covered with MLI as shown in Fig. 17.12.

Test Results

Following establishment of a quasi-steady-state condition, the power input to the heater plate was incremented in steps of 10 or 20 mW. This case was intended to
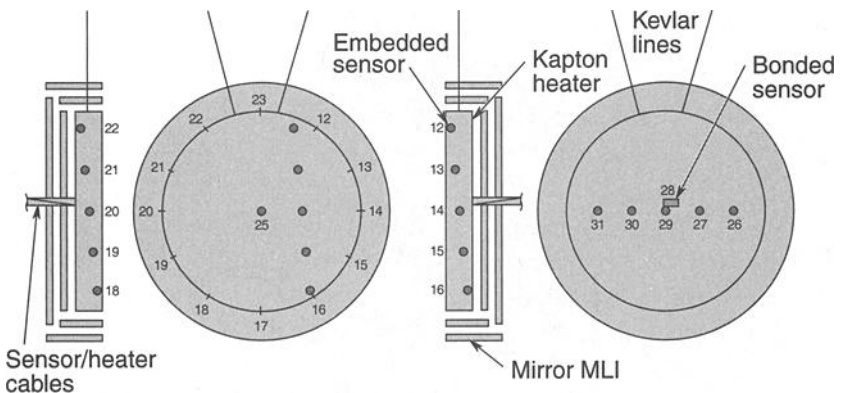
Fig. 17.12. Test mirror layout.

simulate the small thermal-environment perturbations predicted for the flight conditions. The changes in the centerline and edge gradients for the 20 mW transient step power change are shown in Figs. 17.13 and 17.14.
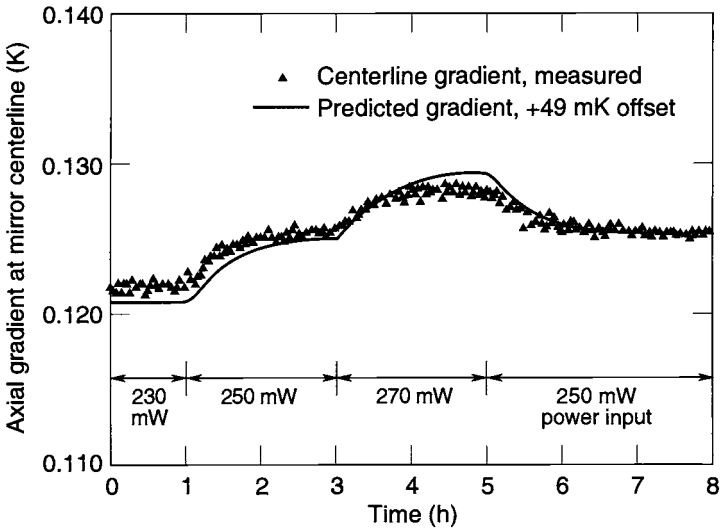
Fig. 17.13. Centerline gradient for 20 mW transient step power change.
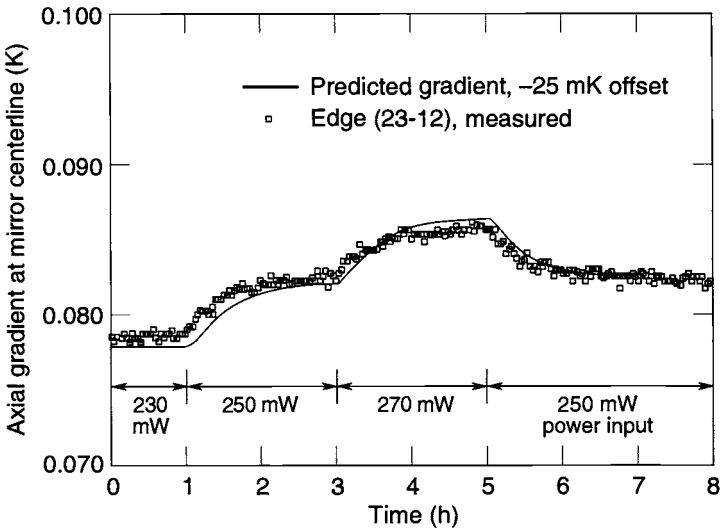
Fig. 17.14. Edge gradient for 20 mW transient step power change.

Thermal Model Description

The thermal model for test correlation was generated in I-DEAS/TMG.[17.7] The basic configuration is shown in Fig. 17.15; it consists of the mirror, heater or heater plate, mirror MLI, shroud, Kevlar lines, and cable bundle. The boundary conditions are:

- fixed, constant shroud temperature
- fixed temperature at Kevlar line ends (same as shroud)
- fixed temperature at cable bundle end (same as shroud)
- fixed heat load on heater or heater plate

The mirror submodel, shown in Fig. 17.16, consists of 3096 solid elements with 258 shell elements on the front and back faces and 624 shell elements on the cylindrical side surface. The mesh size was selected to provide a resolution consistent with the sensor spacing along the edges in the mirror axial direction (12 layers through-thickness). The size of the elements (average face-shell element of 342 mm^2) is substantially larger than that of the sensors (~2.5 mm^2 normal to the face). This contributes an uncertainty to the comparisons between specific element temperatures and sensor measurements.

The mirror MLI was modeled using zero-thickness elements with a much coarser mesh. There are 44 shell elements representing the MLI back surface and 40 shell elements for the edges and front-edge section. The cable bundle (2 elements) and Kevlar lines (4 elements each) were represented using beam elements.

Radiative view factors were calculated in I-DEAS/TMG for an enclosure consisting of the MLI external surfaces, the mirror front face, the shroud internal surface, and the cable bundle and Kevlar line beam elements. All surfaces were assumed diffuse for radiation calculations. The mirror shell elements beneath the MLI were thermally coupled to the MLI with radiation conductors. These are based on the primary element (mirror) area and a multiplying factor used to represent the MLI effective emittance.

Number of elements: 4888
Number of nodes: 4621
Mirror supports
Mirror MLI
Mirror
Copper shroud
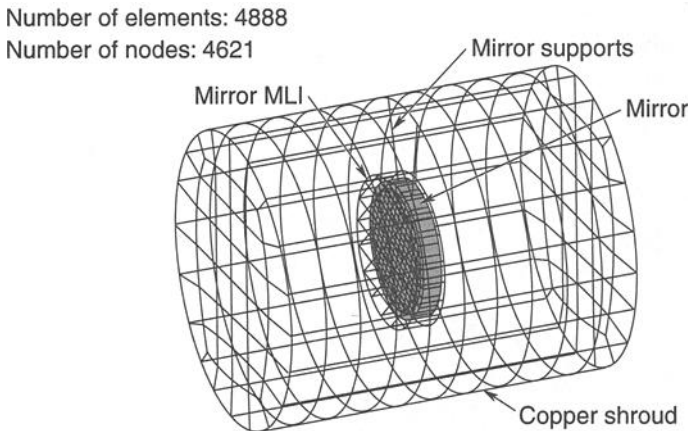
Fig. 17.15. Thermal model for test correlation.

Mirror face: 258 elements

12 layers solid elements through thickness
3 layers shell elements (front, back side faces)
Separate layer shell elements for heater
Separate layer shell elements for MLI
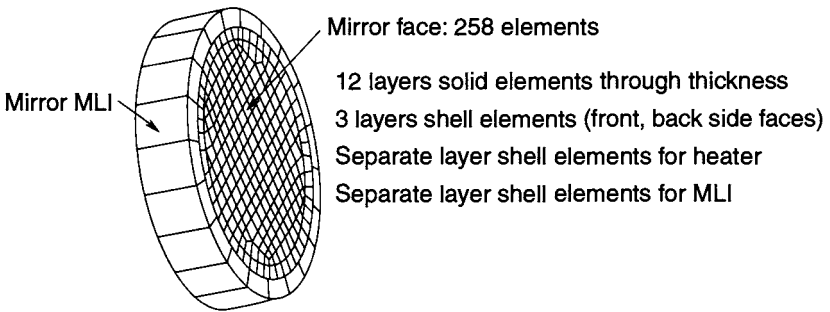
Fig. 17.16. Mirror submodel.

Results Comparison

Model correlation consisted of varying the thermal parameters to obtain the best match to the quasi-steady-state data. The model was then used to predict transient through-thickness gradient response. This value is considered to be of primary importance to meeting the SIM instrument-performance requirements. The MLI effective emittance is subject to much greater uncertainty than all other parameters. This is a result of both the large degree of uncertainty in the fabrication process and the empirical nature of the effective-emittance model used to predict performance. Uncertainties in MLI performance prediction of 50–100% are typical. Emittance of the mirror front surface is second in order of uncertainty, as shown by the measurements performed on the coating witness samples. Emittance of the MLI external surface is probably of an order similar to that of the mirror coating, but the results are less sensitive to this parameter. Other parameters considered to be less uncertain are the shroud internal coating emittance, mirror thermal conductivity, and mirror specific heat; the mirror temperature distributions are relatively insensitive to the range of values assumed.

The predictions for axial mirror temperature gradient were compared. The measured and predicted centerline axial temperature gradients for the 20-mW step power change are shown in Fig. 17.13. The measured and predicted edge axial temperature gradients for this same case are shown in Fig. 17.14. For convenience, these predictions assumed a constant shroud temperature. The measurements show that the shroud temperature varied by approximately ±150 mK during the period of interest. The transient behavior of the predicted gradients was found to match the measured values very well, with an agreement of approximately ±1 mK. The absolute gradient values differed by 25–50 mK. The predicted gradient values have been offset by the amounts shown to match the starting value of the gradient.

The Hydrogen Maser Clock

Frequency references—high-stability clocks—increasingly find applications in space missions. Atomic clocks of ever-increasing stability have present and potential uses as frequency references for Global Positioning System navigation satellites and for detection of gravitational radiation, local oscillators for space-based

Very Long Baseline Interferometry, "proper" clocks for tests of general relativity, and "traveling clocks" for worldwide time transfer.

An active atomic hydrogen maser for long-term use in space has been designed and built as part of the Smithsonian Astrophysical Observatory's HMC project. HMC is a NASA-sponsored program whose goal is to produce and demonstrate a space-qualified hydrogen maser with drift-removed fractional frequency stability of 10^{-15} or better in one day. Achieving such stability requires very precise temperature control. The HMC maser and its control electronics have been designed as an integrated system for use on a variety of spacecraft, requiring only an appropriate mechanical connection and electrical interface. It is an evolutionary outgrowth of a two-decade program of research and development of hydrogen masers for Earth and space use.

Mechanical and Structural Characteristics

The HMC maser's physics unit, shown in cross section in Figs. 17.17 and 17.18, takes the general form of a cylinder 84 cm long and 43 cm in diameter. The maser's main components are: a quartz storage bulb and low-expansion resonant cavity; the titanium vacuum tank that contains the cavity; vacuum manifold and source for producing a beam of hydrogen atoms; electrical heaters and thermistors for thermal control; and components for magnetic-field control. Separate electronics units contain analog and digital control and monitoring circuits and a microprocessor that controls the maser's electronics and acts as an interface with the spacecraft's data and command system.

The maser is supported structurally from a circular aluminum midplane plate, with its resonant cavity and vacuum tank on one side and its vacuum manifold and hydrogen source on the other. The midplane plate is the main structure for mounting the maser to the spacecraft. Two titanium tubes connect the vacuum tank to the midplane plate at the bottom end and to the maser's cylindrical outer aluminum housing at the top. The housing, in turn, transfers the upper tube's load to the midplane plate.

Thermal-Control System Design Features

Temperature changes of the maser's resonant cavity and storage bulb affect the maser's output frequency. To stabilize frequency the cavity temperature must be maintained constant to approximately 0.1 mK for more than a day. The HMC maser employs several strategies to achieve this level of temperature control. The integrated system is of particular interest because it embodies a large number of elements common to precision active thermal control for the space environment.

To control heat flow from the vacuum tank, the maser's structure is divided into three concentric isothermal control regions, or zones. Each region establishes the external environment of the next-inner region. If we assume the external environment varies roughly ±10°C, then each control zone must attenuate this variation by a factor of 50 to achieve the desired accuracy of maser thermal control. Thermal gradients are controlled by subdividing each isothermal region into multiple independently controlled zones, by mounting controlled guard heaters on heat-leakage paths, by separating heaters from the primary controlled structure (the vacuum tank), and by carefully calibrating and matching thermistors and set-point
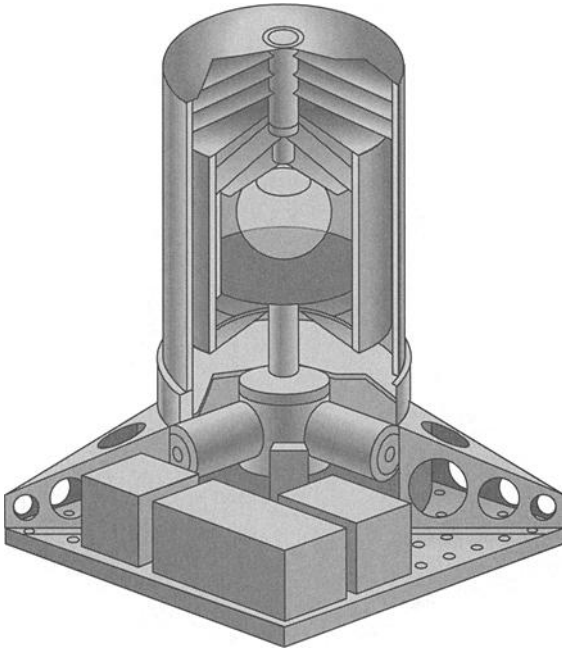
Fig. 17.17. The HMC.

resistors to ensure that all zones of an isothermal control region are at the same temperature. Radiative heat flow is controlled by surface emittances and selective use of MLI in the evacuated annular spaces between the regions, while conductive heat flow is controlled by design of the segmented nylon magnetic-shield support rings and interface materials and bolting pressures. The control-system configuration is entirely axial and radial; no side-to-side or circumferential control is used. External MLI was found to be adequate to isolate the package from typical satellite internal thermal environments.

As shown in Fig. 17.18, the innermost isothermal region, the titanium vacuum tank that surrounds the resonant cavity, is maintained at 50°C. The resolution of the tank control system is 0.1 mK. To reduce thermal gradients in the tank, the three tank heaters are separate from the tank itself, one located on the outside surface of the inner magnetic shield that is directly outside the tank and the others on the titanium tubes where they support either end of the tank.

The tank, in turn, is surrounded by a 40°C aluminum shell located directly over the third magnetic shield. This oven region acts as a guard to control heat that flows from the tank region both radiatively from the tank surface and conductively along the magnetic-shield supports and the titanium support necks. The oven region consists of three control zones located on the cylinder and two end surfaces of the oven, and two zones mounted on the outer ends of the support necks.

The third isothermal region consists of the midplane plate and an outer aluminum support shell that directly surrounds the fourth magnetic shield. This zone is
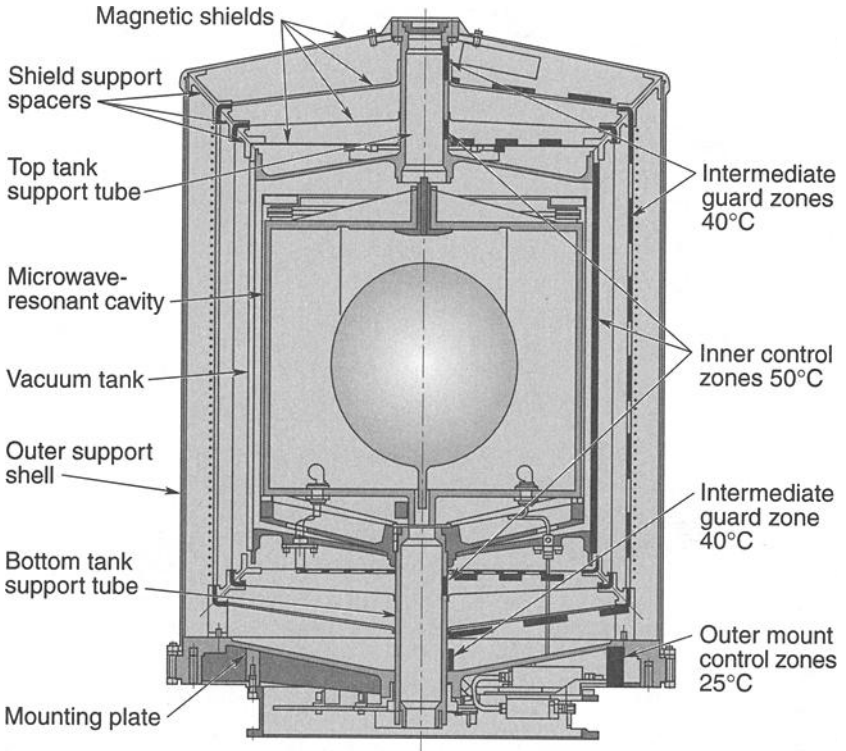
Fig. 17.18. Design elements and thermal zones of the HMC.

maintained at approximately 25°C by a control thermistor and heaters mounted on the midplane plate.

In addition to the thermal-control zones that are integral to the maser, the system includes a controlled-temperature guard station on the structure that mounts the maser to the spacecraft, to act as a first stage of isolation from the conductive environment. The entire instrument is surrounded with MLI to isolate it from the radiative environment.

Early trade-off studies established the major design choices in the thermal-control system. Highly stable thermistors were chosen over wire-wound thermal sensors to minimize effects of lead-wire resistance. Each zone has two identical thermistors, one for control and one for monitoring (which can replace the control unit if necessary). Proportional/integral control was selected to eliminate proportional-offset control error, and digital control was picked over the more conventional analog to decrease thermal effects on controller circuits and for ease in modifying loop gains and time constants. Kapton-insulated etched-foil heaters were chosen to reduce magnetic effects; in critical regions a specially designed "sandwich" of two identical elements with opposing currents was needed to ensure the lowest possible magnetic-field generation.

The thermal-control system incorporates several electronic and hardware features to achieve the required high degree of thermal stability. The digital electronic control system is based upon 68HC11 microcontrollers, each of which can control up to five thermal zones. Each 68HC11 includes a microprocessor, an 8-bit analog-to-digital converter (A-to-D) with eight-channel multiplexer, and timer registers that are used as pulse-width modulators driving a power stage for high-efficiency switched heater power control. The vacuum-tank heaters closest to the maser's resonant cavity are driven at high frequency (4 kHz) to avoid perturbation of the maser oscillation; the other heaters are switched at a 30-Hz rate. The thermal-control program provides for differential control as well, but this additional algorithm term is primarily useful in startup dynamics and has been found unnecessary. Temperature set-point resistors have low temperature coefficients, and are physically mounted on a temperature-controlled zone within the maser for minimum temperature perturbation.

High-Precision Control Considerations

Thermal control at milliKelvin stability levels requires integrated design of thermal, mechanical, and electronic hardware. Effects that are negligible in conventional thermal control must be addressed systematically and their impacts allocated and traded for performance. Figure 17.19 shows a schematic of the control system with the most important elements labeled. A discussion of some of the important system issues is useful, because they apply to a wider class of high-precision control systems, especially those under digital control.

Control Loop

The offset error can usually be controlled by integral compensation, except during transients. It is important to use an algorithm that does not increment the integral
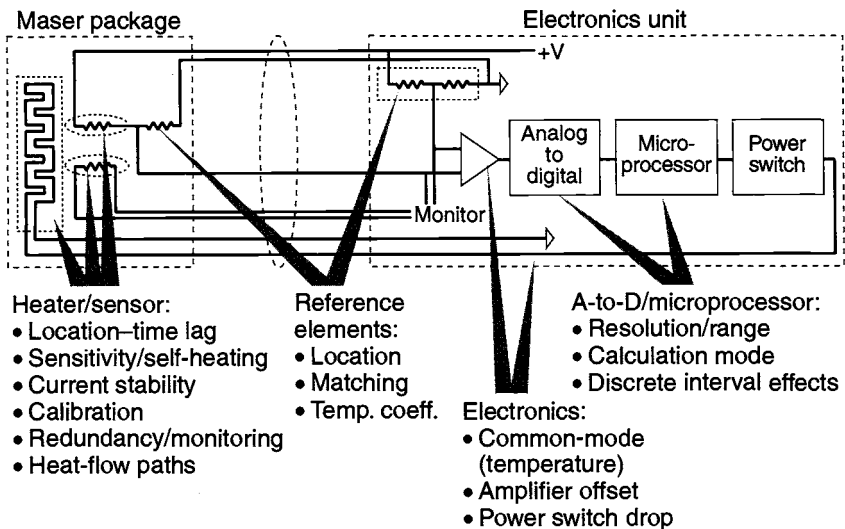
Fig. 17.19. HMC heater-control system.

when the temperature error is large, certainly not beyond the proportional band. The cycling period and heater/sensor time lag are closely related; the control sensor should be located as near the heater as possible, especially on poorly conducting substrates. Separating the natural cycling frequencies of adjacent zones is preferable, to prevent interaction.

Heater Power and Location

Good practice dictates that the heater should be well matched to the power requirement, and this is particularly true when the driving voltage is pulse-width modulated digitally. If, for example, the pulse width has 256 possible values, a heater operating at 50% duty cycle has a minimum power change of just under 1%. If the heater is oversized so that it operates at 8% duty cycle, the minimum power resolution is about 5%. This raises the effective system gain and can cause hunting or cycling. Heaters should be located so that power changes in response to the control loop do not induce thermal gradients in the most critical control zones; heat should flow primarily outward from each heater.

Sensors

Sensors were individually calibrated in an oven at the control temperature so that the set points could be corrected to minimize gradients in the vacuum-tank zones. If sensors are well matched, averaging more than one may be effective. On HMC two identical sensors were installed side-by-side for redundancy; one was used for independent monitoring of zone temperature, but it could be used for control in case of failure. Self-heating is significant—the self-heating constant of sensors cemented to the controlled surface was measured at about 150 mK/mW, and they are operated at about 0.3 mW. This yields a self-heating temperature rise of nearly 50 mK, which means that the current stability in the sensor must be good enough for the self-heating changes to be much smaller than the control resolution. In the future, consideration should be given to using narrow current pulses for sensors to reduce self-heating. Also, the sensor time constant was a significant contributor to the natural frequency in the HMC control loops.

Reference Elements

At the milliKelvin level, temperature effects on the fixed resistors in the control bridge can be significant. HMC located the set-point resistors in one of the controlled zones, and used a single-substrate matched resistor pair in the electronics unit for the other side of the bridge.

Cables can produce significant noise with microvolt-level signals. Noise is evident on the low-level error data and makes monitoring difficult. Shielding can be effective, but wiring in inner parts of the HMC left no space for it. Noise is not necessarily bad in the control loop as long as it averages to zero—but assurance of this is seldom available.

The instrumentation amplifier can have an input voltage/current offset that is temperature dependent, and that impresses electronics-unit temperature changes on the control circuit. Careful design is needed; using a pulse train on the temperature-sensing bridge may also eliminate the problem.

The A-to-D creates a basic trade-off in design: resolution versus range. HMC used an 8-bit A-to-D (256 values) in the control loop; for a minimum resolution of

0.1 mK, the total range was only 25 mK. This implies a very high gain; dynamic control is a potential problem, and control points must be set very carefully. A variable gain may be incorporated in future units: high near the set point for good resolution and lower elsewhere for increased range. The digital processor has a choice of integer vs. floating-point arithmetic. Integer arithmetic is faster and uses less memory, but control algorithms must be developed carefully to ensure that critical information is not lost in truncation.

The transistor power switch has a voltage drop that is temperature-sensitive. An increase in switch temperature decreases voltage to the zone heater and requires the control system to compensate. The same effect would occur with a variable bus voltage. Removing as many disturbances as possible is usually best, especially for high-gain loops. A secondary loop was considered (but not implemented) to compensate for heater voltage; this could be important for a system with wider voltage changes.

Thermal Analysis

A thermal mathematical model of about 100 nodes supported design and test of the HMC. This model's purpose was twofold: prediction of heater power requirements (rather than temperatures, which were controlled) for each of the zones, so that adequate control margins could be established, and study of some changes in design parameters (heater location, for example) to minimize critical gradients. The model, with the control-zone configuration, had only axial and radial detail. Each concentric shell—vacuum tank, magnetic shields, oven, and outer shell— was divided into six zones axially and three radially (each end). Individual surface emittances were maintained as independent parameters so that they could be used to "tune" the heat-flow paths.

Modeling the conductive paths was particularly difficult because of the large number of contact resistances with low interface pressures. The magnetic shields, for example, have end caps that are a slip-fit over the cylinders, and the surfaces have low measured emittance. These shields are held in place with padded nylon spacers because the strains induced by conventional fasteners would affect shielding properties. Interfaces between the titanium support tubes and the top and bottom structural supports, two primary heat-flow paths, have very small areas and insulating spacers. The top support-tube interface was in fact the primary area of "disagreement" between model and hardware. Thermal isolation in this path was considerably greater than expected, effectiveness of that guard heater was less than desirable, and the top oven-guard power was higher than expected.

Table 17.1 shows predicted and actual heater power and installed capacity for each zone. Control power predictions are acceptably close to measured values, indicating that use of the model to minimize heat flow and gradients in each zone was probably successful. Operating a control zone in the steady-state condition at about one-third to one-half its maximum range is desirable to allow upside and downside control margins and warm-up capability, and we achieved this goal for most control zones. The design provided for a choice of two voltage levels to drive the most critical zones in case predictions were greatly in error. Two zone-heater voltages were changed after initial test: the upper guard tube voltage was decreased

Table 17.1. Predicted, Actual, and Maximum Heater Power

	Heater Power (W)		
Control Zone	Predicted	Actual	Maximum
Support guard top	2.1	0.8	1.7 (was 6.6)[a]
Vacuum tank top	0.5	0.4	1.5
Vacuum tank radial	0.8	1.1	5.8 (was 1.3)[a]
Vacuum tank bottom	0.9	0.8	1.5
Oven guard top	0.2	0.6	2.5
Oven guard radial	1.4	2.9	4.2
Oven guard bottom	2.0	1.9	2.5
Support guard bottom	4.0	2.6	6.6

[a]Value was changed after testing, see text for explanation

because of the high thermal resistance path discussed above, and that of the tank radial zone was increased because measured power had little margin.

Tuning and Experimental Verification of the Thermal Design

The experimental portion of the HMC program had the dual goals of tuning the individual zones for best control performance and then evaluating both thermal performance and frequency of the clock under reasonable changes in external environments. Both tests were conducted in a vacuum tank, because gas-conduction effects would produce very different control results under ambient conditions. Changes in both the radiative environment on the outer-shell MLI and the conductive sink temperature were expected in the mission environment, so two fluid loops were incorporated in the test fixture, one surrounding the shell and the second at the mounting interface. In a near-Earth mission environment these environment changes would have a primary period of about 1.5 hours, which was difficult to simulate in the laboratory, so the primary focus was on the more severe case of measuring step response and inferring control performance from those measurements. This test was regarded as a reasonable simulation of a carrier vehicle maneuver that could significantly change solar exposure, for example.

The control loops were tuned using a classical method[17.8] that requires removing all integral/differential compensation and increasing linear loop gain until the temperature oscillates at a constant amplitude. Gain is then reduced and integral compensation added in a related amount to produce a slightly underdamped response to a step change. Control response was observed according to a classical rule of thumb that states that the primary oscillation is usually determined by the shortest lag or time constant in the system. Most of the high-gain loops oscillated with a 5–10-second period, which is likely related to the thermal lag between the heater mats and the adjacent control thermistors (measured at 1–3 seconds), and probably dominated by the 2-second thermistor time constant. In addition, the zones at either end of the vacuum tank, though locally identical mechanically and

in fabrication, were observed to have quite different control parameters when tuned properly. This emphasizes the need to retain flexibility in thermal-control system design to accommodate the effects of small but important variables in the as-built (versus design) configuration.

The similarity in natural frequency of adjacent control zones gave rise to concern about possible dynamic interaction between zones—the oscillatory response of a guard zone could induce a similar oscillation in an inner zone. This was tested by manually varying the set point of a guard zone at the observed frequency of the adjacent vacuum-tank zone, and no effect was observed. Evidently the combination of conductive damping and integral compensation is adequate to isolate the inner zone. Control system performance was tested by observing the amplified control-bridge null signal, the monitor thermistor resistance, and the heater output of critical control zones in response to environmental changes. Corresponding changes in maser frequency stability were also sought, although this was more difficult because of the known time lag and the presence of small perturbations in frequency from other sources. The approach to frequency-stability measurement was to make an environmental step change on one day and an offsetting change on the succeeding day, and look for a one-day offset response.

Sample Performance Results

Figure 17.20 illustrates an example of performance data recorded during a 2-1/2–day period of laboratory environment changes. The temperature of the surrounding environment was intentionally allowed to vary about 10°C. Temperature of the
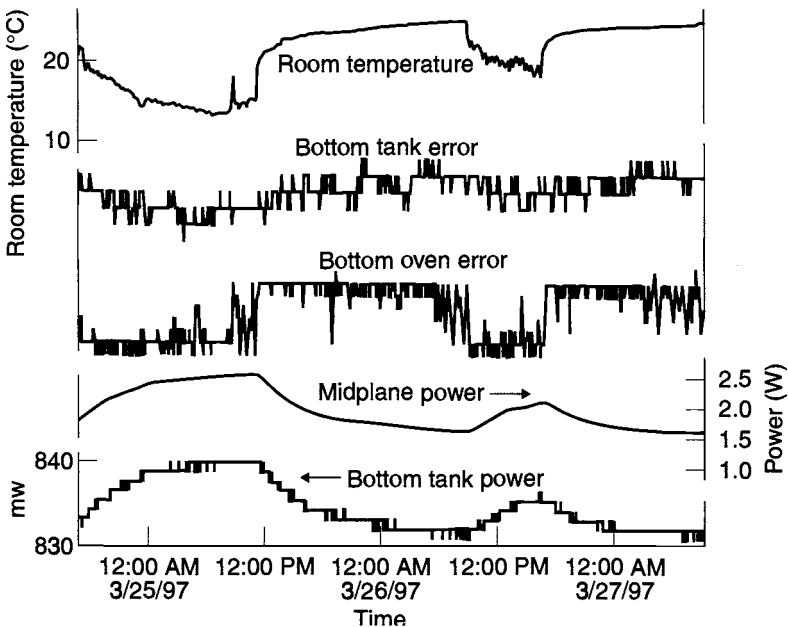
Fig. 17.20. Effect of external environment on control stability.

controlled zones is represented by the error signal from each sensor bridge. The midplane isolation zone sensor was held to less than a 10-mK variation with a power change of 60%. (With such a large power change, we certainly expected substantial gradients in the mounting plate, but we had no sensors with which to verify this expectation.) The bottom oven and neck guard zones, which control both conductive and radiative losses to the midplane zone, were stable to a fraction of a control resolution element (about 5 mK for the oven, below the threshold of measurement for the neck) with 7–9% power change. The adjacent inner tank zone was stable to a few parts in 0.01 mK with power variation a little more than 1% peak-to-peak. Relative power variations are an indirect measure of the degree to which the critical zones are isolated from the outside environment.

Figure 17.21 shows performance of an innermost zone when the adjacent guard zone is changed by a large amount. For this test the guard-zone control set point
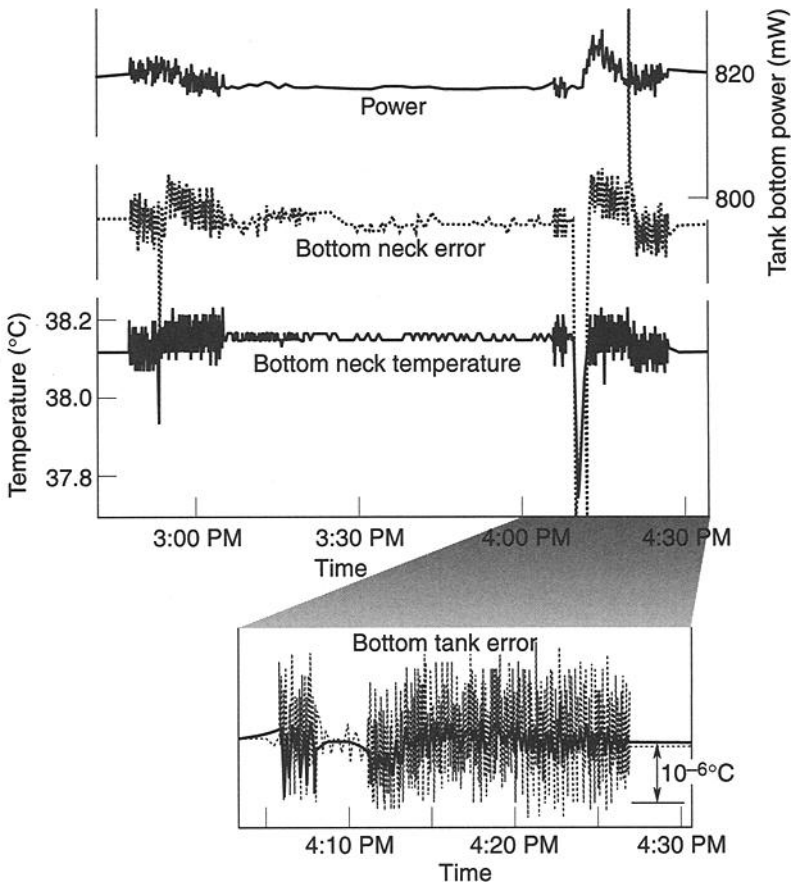
Fig. 17.21. Effect of guard zone on adjacent control-zone response.

on the bottom neck was increased by 30 mK (30 times its control band) for about an hour, then returned to its original setting (top trace; discontinuous data shows the digital measurement resolution, and the trace envelope indicates data noise that changes with sampling period). The bridge error of the guard zone (second trace) shows clearly the settling transients after each adjustment, with a peak-peak amplitude less than 10 mK. The critical zone is the vacuum-tank bottom; its power (third trace) decreases by about 0.3%, roughly the same as the temperature difference between its set point and that of the adjacent guard zone, and shows a 1% spike on resetting. The last trace expands the time scale of the control-zone error for the second (resetting) transient, and shows zero offset at 0.01-mK resolution across the transient. The peak-peak temperature error, noise included, lies within 0.3 mK even while the integral compensation drives the power transient, with a noise-corrected span (dark trace) within a 0.1-mK band.

Common-mode effects of electronics-unit temperature change are illustrated in Fig. 17.22. Electronics temperature was abruptly raised by about 10°C and decreased by 15°C two days later. The error signal from an internal tank zone barely shows change at the 0.01-mK level, but the indicated temperature measurement from an adjacent sensor appears to change by about 50 mK, well correlated in time with the electronics-unit changes. The monitor circuit is not designed for high-precision measurement but for telemetry over a wide range, and the relative response of the two measurements indicates the degree to which the control system is successfully isolated from common-mode effects.

HMC Test Program Conclusions

The laboratory test program of the HMC has confirmed the ability of the thermal-control system in the presence of varying environmental conditions both to maintain
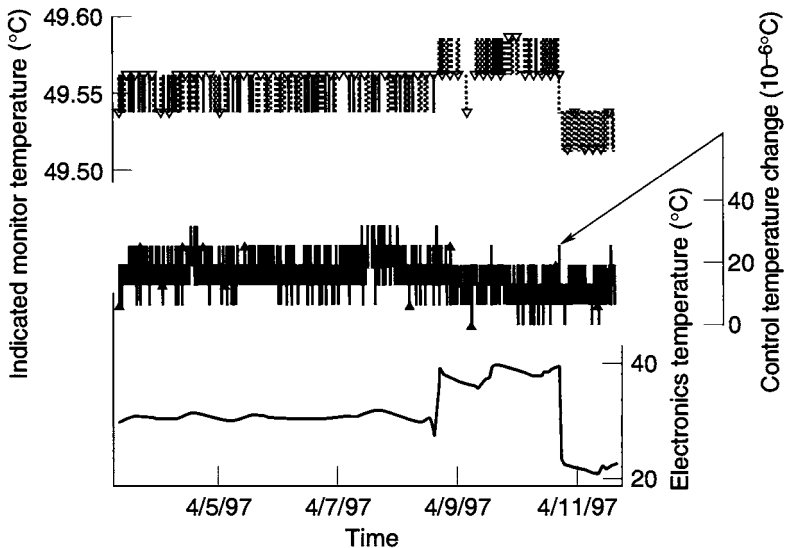
Fig. 17.22. Effect of electronics temperature on monitor and control.

internal-zone temperature stability to considerably better than 0.1 mK at the control sensors, and to attenuate control power changes. Of course, stability of control sensors must be distinguished from overall zone stability. A guard-zone power change of 7–9% surely induces some gradients, and a 1% inner-zone power change is a response to this guard-zone nonuniformity. Successful separation of dynamic response of zones was demonstrated.

The discrete nature of microprocessor-based control was not seen to degrade high-stability control performance, and its advantages in ease of optimizing system performance make it highly recommended for applications such as HMC.

While long-term stability at the submilliKelvin level was not a design issue for HMC, changes that would enhance long-term stability have been indicated. Other aging effects would need to receive the same design attention that has been illustrated here.

Summary

Despite the seemingly enormous challenges involved, maintaining temperature stability on the order of milliKelvins or better appears possible with the same basic techniques of heaters, MLI, low-emittance surfaces, and low-conductance mountings that are used in most other thermal designs. However, as the HMC experience illustrates, implementation of heaters for active control of temperature to the milliKelvin level is much more complex than for heaters in more conventional spacecraft applications. For instruments that must be exposed to the surrounding environment, such as the SIM payload, special orbits may also be required to eliminate variations in heat loads resulting from eclipses or changes in Earth-emitted IR or albedo.

References

17.1. K. Aaron, D. Stubbs, and K. Kroening, "Space Interferometry Mission Instrument Mechanical Layout," paper no. 319, IEEE Aerospace Conference, Big Sky, 2000.

17.2. K. Aaron, D. Stubbs, L. Ames, and T. Kvamme, "Space Interferometry Mission: Recent Instrument Configuration Developments," paper no. 020, IEEE Aerospace Conference, 2002.

17.3. D. Vukobratovich, "Introduction to Optomechanical Design," SPIE In-Company Customized Course in Optics and Potonics, Course Notes, May 1997.

17.4. D. Vukobratovich, D., "Advanced Topics in Opto-Mechanics," SPIE In-Company Customized Course in Optics and Potonics, Course Notes, October 1997.

17.5. J. Pecson and A. Hashemi, "Multidiscipline Analysis for Space Optical Systems," AIAA 2002-0358, 40th AIAA Aerospace Sciences Meeting & Exhibit, Reno, NV, January 2002.

17.6. J. Ambrose, A. Hashemi, J. Schneider, D. Stubbs, K. Aaron, M. Shao, and T. VanZandt, "Measurement and Prediction of Temperature Distributions in Optical Elements in the MK Regime," HTD-Vol.366-5, pp. 135–145, IMECE 2000, Orlando, FL, November 2000.

17.7. MAYA Heat Transfer Technologies, Ltd., I-DEAS Master Series 7 Course Guide, The Advanced TMG Course Manual, August 2000.

17.8. J. G. Ziegler and N. B. Nichols, "Optimum Settings for Automatic Controllers," *Trans. ASME* **64** (8), 1942.

18   Space Shuttle Integration

G. M. DeVault,[*] W. K. Smith,[*] B. P. Harris,[†] H. A. Rotter,[‡] R. Serna,[‡]
C. R. Miller,[‡] and G. E. Gurevich[**]

Introduction

The function of the flight- and cargo-integration effort is to ensure that elements of the total payload complement for a flight are compatible in form, fit, and function, and that all associated flight-design parameters and crew activities are within Space Shuttle Program (SSP) capabilities. This effort includes assessments by flight- and ground-systems engineering, safety, and all elements of SSP operations. Figure 18.1 illustrates the SSP/payload thermal-integration process in flowchart form. The
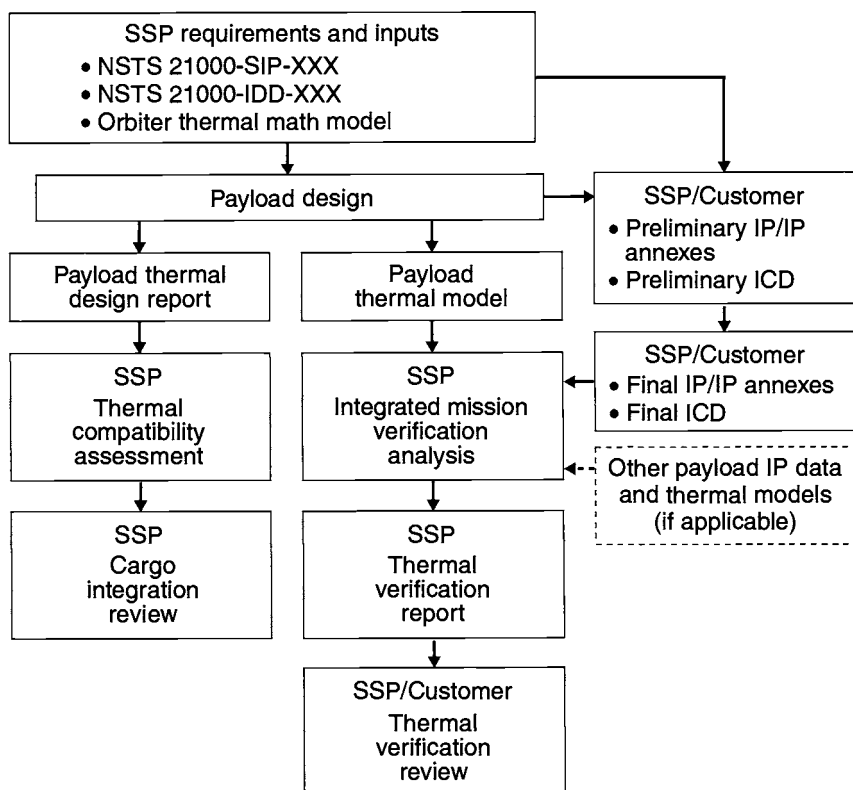
Fig. 18.1. SSP/payload thermal-integration process.

*The Boeing Company, Houston, Texas.
†United Space Alliance, Houston, Texas.
‡NASA/JSC, Houston, Texas.
**Microcosm Inc., El Segundo, California.

Cargo Integration Review (CIR) is the major cargo-related review of this assessment effort, and it occurs at the same time customer concurrence is obtained. A typical schedule of events leading to the CIR, subsequent reviews and, ultimately, flight is shown in Fig. 18.2.

The following assessments are required prior to formal reviews to ensure an adequate SSP understanding of the cargo and flight requirements and the ability to support such requirements.
- crew-activities assessment
- flight operations and support assessment
- payload operations control center/mission control center
- network assessment
- training assessment
- ground-operations assessment
- conceptual flight-profile assessment
- human use
- engineering-compatibility assessment
- interface-verification status
- safety assessment

*Initiation of this process can begin as early as the customer desires after Form 1628 submittal.

□ NSTS   ▽ Customer   O Joint
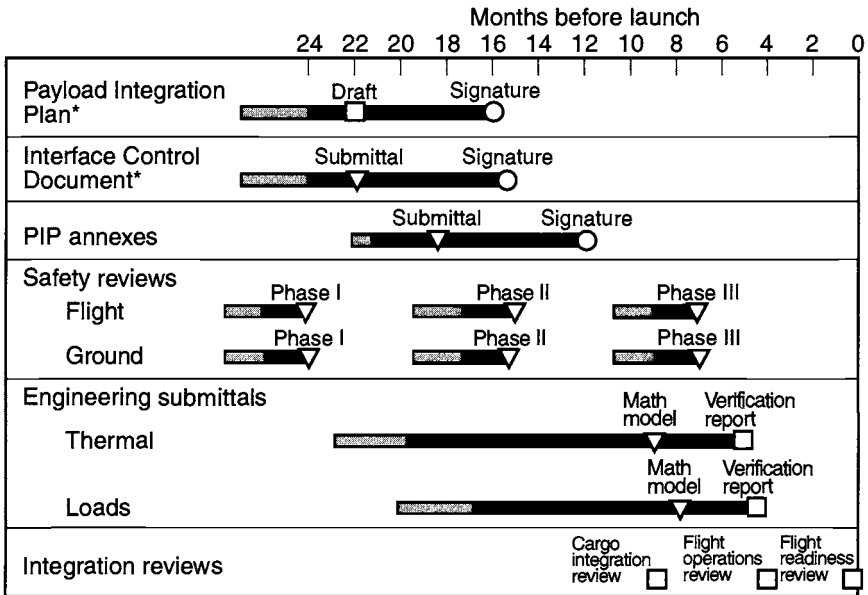
Fig. 18.2. SSP/payload integration timeline.

Most of these assessments do not require direct involvement of the payload thermal engineer; two that do, however, the engineering-compatibility assessment and the safety assessment, are examined in the sections that follow.

Engineering-Compatibility Assessment

One assessment that does require extensive support from the payload thermal engineer is the engineering-compatibility assessment. Its purpose is verification of the compatibility of the integrated SSP flight hardware, software, and engineering-flight products with current mission requirements, cargo requirements, and orbiter accommodations. This verification is accomplished by teams with specialization in thermal control, avionics, structures, electromagnetic compatibility, flight preparation, interface verification, reliability and certification, and cargo interfaces.

Because of the complexity of the space shuttle and its flight operations, much more documentation and analysis is required to control and verify the integration of payloads with the shuttle than with expendable launch vehicles. Figure 18.3 lists the standard STS (Space Transportation System) documents that describe the shuttle and its payload interfaces and ensure engineering compatibility between the shuttle and payloads. These documents are available in electronic form at the National Aeronautics and Space Administration/Johnson Space Center (NASA/ JSC) and United Space Alliance (USA) Web sites.

The individual payload compatibility assessment begins with the process of developing the payload Integration Plan (IP), the payload-unique Interface-Control Documents (ICDs) and drawings, the Command and Data Annex (Annex 4), the Orbiter Crew Compartment Annex (Annex 6), and the Extravehicular Activity (EVA) Annex (Annex 11). The individual payloads' physical and functional requirements are integrated by NASA into an engineering data package.

The thermal portion of the compatibility assessment includes a comparison of both the active and passive thermal-control requirements of the payload with the shuttle and cargo thermal capabilities and requirements, as defined in the Shuttle Orbiter/Cargo Standard Interfaces, ICD 2-19001. This document contains the orbiter vehicle attitude hold-time constraints, orbiter deorbit and entry-preparation constraints, typical temperature ranges for the cargo-bay wall/liner, entry-air inlet conditions, typical prelaunch and postlanding environments, typical Remote Manipulator System (RMS) thermal interfaces, orbiter surface materials and their optical properties, and the vent/purge and active cooling systems capabilities and parameters. This data should be reviewed and checked against payload requirements to ensure that no payload requirement conflicts with the orbiter's capability.

Not only is the payload-to-orbiter compatibility determined, but also the compatibility of the payload with stated mission objectives must be assessed. This is a more complicated task, as the mission objectives and companion payload's requirements and limitations may not be well defined. However, once payload thermal compatibility with the orbiter and mission is determined, a compatibility statement must be signed by both the contractor/payload thermal representative and the NASA/USA thermal-engineering team leader. This is typically done at the CIR. Sample active and passive thermal-compatibility statements are shown in Figs. 18.4 and 18.5.

NSTS 07700 Volume XIV
Space Shuttle System Payload Accomodations

NSTS 21492 Payload Bay
Payload User's Guide

Safety
• 45 SPW HB S-100/KHB 1700.7
• NSTS 1700.7B   • NSTS 16879
• NSTS/ISS 13830C • NSTS/ISS 18798
• NSTS 14046   • NSTS 22648

Shuttle/Payload
Standard Integration
Plans (SIPs)

*Annexes

Orbiter/Payload
Interfaces

Vol. XIV Appendixes:
System Description
and Design Data

NSTS 21000-SIP-ATT
Attached Payloads

NSTS 21000-SIP-DRP
Deployable/Retrivable
Payloads

NSTS 21000-SIP-GAS
Get Away Special
Payloads

NSTS 21000-SIP-MDK
Middeck Payloads

NSTS 21000-SIP-ISS
International Space
Station

ICD 2-19001:
Vol. XIV
Attachment 1 - Shuttle
Orbiter/Cargo
Standard Interfaces

NSTS 21000-IDD-SML
Small Payloads

NSTS 21000-IDD-ISS
International Space
Station

NSTS 21000-IDD-MDK
Middeck Payloads

Appendix 1
Contamination
Environment

Appendix 2
Thermal

Appendix 3
Electrical Power
and Avionics

Appendix 4
Structures and
Mechanics

Appendix 5
Ground Operations

Appendix 6
Mission Planning and
Flight Design

Appendix 7
Extravehicular
Activities

Appendix 8
Payload Deployment
and Retrieval System

Appendix 9
Intravehicular
Activities

Appendix 10
Integration Hardware

*Annexes
   (Note: appropriate annexes are outlined in the
   individual SIPs)
      Annex 1 Payload Data Package
      Annex 2 Flight Planning
      SIP Table 8.1 Data Submittals
      Annex 4 Command and Data
      Annex 5 POCC
      Interface Control Annex
      Annex 7 Training
      Annex 8 Launch Site Support Plan
      Operations and maintenance requirements
         Specifications Document (OMRSD)
      Annex 11 Extravehicular Activities (EVA)

Fig. 18.3. STS documentation for shuttle/payload compatibility.

STS _____ CARGO INTEGRATION REVIEW
COMPATIBILITY STATEMENT

The NASA/USA Team Leader and the contractor/payload representative have assessed the compatibility of the integrating hardware and software design against the STS and cargo requirements in the

TR/Thermal Systems Engineering - Passive _____ as of _____

(system or other)   (date)

The engineering assessments listed below, with the exception of (A) open items, and (B) open DNs/ECRs are found to be compatible.

☐   Verify compatibility of IH with cargo design

☐   Verify compatibility of IH with mission objectives

☐   Verify compatibility of IH with thermal constraints (max-min average temperatures,

    max-min entrapment temperatures, and predicted versus ICD temperatures)

☐   Status ICD TBDs, TBRs, and PIRNs

☐

☐

☐

(A)   Open Items

(B)   Open DNs/ECRs

_____   _____
Contractor/Payload Representative   Date   NASA/USA Team Leader   Date

Fig. 18.4. Passive thermal-control compatibility assessments.

STS _____ CARGO INTEGRATION REVIEW
COMPATIBILITY STATEMENT

The NASA/USA Team Leader and the contractor/payload representative have assessed the compatibility of the integrating hardware and software design against the STS and cargo requirements in the

TR/Thermal Active _____ as of _____

                          (system or other)   (date)

The engineering assessments listed below, with the exception of (A) open items, and (B) open DNs/ECRs are found to be compatible.

☐   Verify compatibility of Orbiter active thermal systems with payload heat loads

☐   Verify compatibility of Orbiter gas supply system with payload requirements

☐

☐

(A)   Open Items

(B)   Open DNs/ECRs

_____   _____

Contractor/Payload Representative   Date   NASA/USA Team Leader   Date

Fig. 18.5. Active thermal-control compatibility assessments.

The orbiter has, in general, greater attitude-hold capability than most payloads require. Although some payload capabilities exceed its capability, payload attitude-hold requirements may not exceed those defined for the orbiter, to ensure that there are no orbiter temperature-limit violations and that the heat-rejection requirements imposed by the orbiter systems, crew, and payloads are met.

Incorporated into the design of payloads that share flights with other payloads and utilize the standard accommodations must be a minimum thermal capability common to all users of a particular flight. To ensure this mixed-cargo compatibility, NASA has defined a set of on-orbit orbiter attitude requirements with which (as a minimum) all payloads sharing a flight must be compatible. All mixed payloads must be able to continuously accommodate a selected attitude, i.e., one that can be maintained without interruption. For missions with beta angles less than 60 deg, the selected attitude is one with the orbiter payload bay continuously facing Earth (+ZLV). For missions with beta angles greater than 60 deg, the selected attitude is specified as the one with the orbiter x-axis perpendicular to the solar vector within 20 deg and rolling about the x-axis at a rate of two to five revolutions per hour. (This attitude is called passive thermal control, or PTC.) The continuous attitude will be maintained during orbiter crew sleep periods as well as long-duration coast periods such as those between deployment opportunities for deployable spacecraft. Short-term deviations from the continuous attitude are required for the deployment of deployable spacecraft. As a minimum, all mixed payloads must be able to accommodate 30 min of orbiter $+z$-axis directed toward the sun, as well as 90 min of $+z$-axis directed toward deep space. Thermal recovery from the short-term solar or deep-space attitudes will be made in the applicable continuous attitudes; i.e., +ZLV or PTC.

Payloads that may be manifested on International Space Station (ISS) assembly or servicing missions must be compatible with a 51.6-deg-inclination orbit and with an extended duration in the ISS docked attitude. The docked duration during these missions is typically 6 to 8 days, and these durations may become longer in the future. The orbiter's primary orientation while docked is a local vertical, local horizontal (LVLH) attitude with the orbiter tail pointed toward Earth and the orbiter bottom in the velocity vector (VV); that is, +XLV, −ZVV.

As the following sections indicate, many analyses must be completed to adequately assess the payload's compatibility with the orbiter, other payloads, and the mission environment. Results of these analyses are used by NASA/USA to aid nominal and contingency mission planning. Analysis results defining the payload's thermal capabilities and limitations are placed in the payload IP. (Fig. 18.6 shows a sample form used for tailoring the IP.) Because these thermal assessments require accurate temperature predictions, payload thermal models should be verified by comparing model predictions to thermal-balance-test or flight data. Discrepancies should be worked so that precise temperatures can be predicted. Temperature margins, if required by the payload program, should also be added to predicted temperatures used to establish thermal limits to allow for analysis uncertainties. Documentation identifying and explaining payload thermal limits and margins should be developed and provided to NASA/USA.

MICB CHANGE REQUEST/ DIRECTIVE NASA-Johnson Space Center	Page: Date: 9/12/89
Number P17559-38	CHANGE TITLE Thermal Environment

4.2.3.1. Thermal Environment - (cont):

IS:

The payload design and operation shall be compatible with the following attitude conditions. The Orbiter will normally be oriented in one of the attitudes contained in Table 4-1. The payload will be designed to allow deep-space excursions that Include a 35-min inertial measurement unit (IMU) alignment occurring approximately every 12 hr. The table specifies the payload constraints and recovery times for these excursions, so that repeat of the attitudes can be planned.

Table 4-1.-Attitude Requirement/Capabilities

Attitudes	Time Constraint	Nominal recovery attitude	Time	Preferred operational recovery attitude	Time
+ZLV	Continuous	N/A	N/A		
PTC	Continuous	N/A	N/A		
+Z Solar	30 min	+ZLV	TBD		
+Z Space	TBD	TBD	TBD		
-XLV*	TBD	+ZLV	TBD	TBD	TBD
-XLV**	TBD	+ZLV	TBD	TBD	TBD
-XLV***	TBD	+ZLV	TBD	TBD	TBD
±XSI	TBD	+ZLV	TBD	TBD	TBD
+YLV, XPOP***	TBD	+ZLV	TBD	TBD	TBD

*	Nose down right wing velocity vector and rotated approximately 30°North of orbit plane.
**	Nose down left wing in velocity vector and rotated approximately 30°South of orbit plane.
***	Nose down wing perpendicular to orbit plane and bay on RAM.
****	Wing down, nose perpendicular to orbit plane and bay on RAM.

2. Revise 1st sentence of 3rd para as follows:

WAS:

In the event of an anomaly, the STS will observe the attitude constraints of either Table 4-1a or Table 4-1b, as appropriate, to the extent possible.

IS:

In the event of an anomaly, the STS will observe the attitude constraints of Table 4-1 to the extent possible.

3. Add the following paragraph to the end of section:

The payload must be designed to be safe with any cargo bay flood light failed on. (Reference para. 6.1.6 of ICD2-19001 for floodlight characteristics.) If floodlight operation impacts mission success, operational constraints and appropriate safeguards will be negotiated between the NSTS and customer and will be documented in the Flight Operations Support Annex, Annex 3.

Fig. 18.6. Instructions for tailoring the IP. The IP contains analysis results that define the payload's thermal capabilities and limitations.

Safety Assessment

In addition to the design and engineering-compatibility considerations associated with completion of payload mission objectives, STS safety requires special attention from the payload thermal engineer. The customer is responsible for investigating the potential effects of unplanned events that may occur to ensure that no payload thermal-limit violations exist that could endanger the crew or compromise the flight during any mission phase. This assessment has two aspects: verifying that the payload thermal design meets the minimum capability requirements for contingency operations, and defining the payload's ultimate safety constraints.

Minimum Design Requirements for Contingency Operations

Payloads must be designed to be thermally compatible with an abort return to Earth during any mission phase. During powered ascent, abort can occur as either a return to launch site (RTLS) or an abort to an alternate landing site, such as a transatlantic one. On-orbit aborts can occur prior to or subsequent to payload-bay door opening. Prior to door opening, abort-once-around (AOA) presents the minimum orbit time, while the maximum time depends on the orbit inclination. (AOA is an abort condition in which the orbiter lands after making one complete orbit around Earth.) The payload-bay doors are normally opened 1 to 1.25 h after liftoff; however, customers must design for a maximum door-opening time of 3 h. If the doors are not opened by 3 h, an abort will be declared and landing will occur by liftoff plus 6.5 h for 28.5-deg-inclination missions, or liftoff plus 11.5 h for 57-deg-inclination missions. Following the 3-h abort time, special orbiter contingency operations may be required necessitating curtailment of standard payload services (e.g., power, cooling). Following payload-bay door opening, aborts can occur at any time; therefore, payloads must be compatible with an abort from the worst hot or cold condition that could be encountered for that particular mission.

Payloads must also be designed so that they do not present a hazard to the orbiter for flights ending at contingency landing sites (i.e., those where ground services such as payload-bay purge or active cooling are not available). Payloads using orbiter-provided heat-rejection provisions must be designed so that they do not present a hazard to the orbiter if heat-rejection capabilities are reduced or lost. Payloads using orbiter-provided electrical energy for thermal control must also not present a hazard in the event of loss of power.

Definition of Ultimate Payload Safety Constraints

Thermal data must be provided to NASA/USA to support contingency planning. Payload temperature limits affecting safety must be identified, and long-term off-nominal exposure to worst hot or cold mission environments must be analyzed to determine how long the payload can tolerate those conditions before the identified safety limits are reached. For deployable payloads, limitations associated with delay in the deployment sequence or restow of erectable spacecraft (if applicable), and delayed deployment must be identified and thermal recovery periods defined.

Additional contingencies may exist as a result of payload-unique characteristics, and these contingencies, as well as those noted above, must be defined and documented in the applicable IP or IP annex. Also, payload operational constraints

associated with implementation of payload objectives should be established by conducting appropriate thermal analyses of the payload design.

Safety Assessment Activities

Safety assessments of the mission design and configuration for cargo are conducted in three activities.

- Payloads are assessed for compliance with requirements as specified in NSTS (National Space Transportation System) 1700.7B ("Safety Requirements for Payloads Using the NSTS").
- NSTS cargo-integration hardware is assessed for compliance with requirements as specified in NSTS 5300.4 ("Safety, Reliability, Maintainability, and Quality Provisions for the Space Shuttle Program").
- The plan for an Integrated Cargo Hazard Assessment (ICHA) is presented at the CIR for review and approval. A final report is presented to the Payload Safety Panel and to the Mission Integration Control Board (MICB), and is available prior to the Flight Readiness Review (FRR).

The status of these assessments is presented at the CIR. The final results of these assessments, along with the safety assessments of other NSTS elements, are used to develop an NSTS Mission Safety Assessment (MSA).

The Cargo Integration Review

The engineering-compatibility and safety work should be completed prior to the CIR. This review is a 4-day session held approximately 8.5 months prior to the subject flight. A CIR dry run (CIRD) of the briefings is completed one month prior to the CIR. A data package is then sent to the customer. The first two days of the CIR are devoted to team reviews of the engineering detailed in the package, and identification of discrepancies. The third day is a preboard review of all discrepancies, issues, and recommendations. This review includes Kennedy Space Center, orbiter, and payload-engineering members. The fourth day is a CIR board review of assessment summaries, unresolved discrepancies/issues, and recommendations. The board, chaired by the flight manager of the NSTS program, is responsible for the direction, conduct, and authorization of flight production. The following is a typical fourth-day agenda:

- Introduction
- Flight overview
- Flight planning
- Flight-design assessment
- Crew-activities overview and assessment
- Flight-operations support
- Ground data systems—Mission Control Center/Payload Operations Control Center (MCC/POCC) requirements/implementation
- Systems assessment
- Training
- Ground operations—payload processing
- Engineering-compatibility summary
- Safety (ground and flight)
- Summary/actions

Engineering-compatibility concerns and issues identified at the CIR should be worked and closed at subsequent status meetings, such as Mission Integrated Product Team (IPT) meetings and Payload Operation Working Group (POWG) meetings.

Orbiter Payload-Bay Thermal Environment

The thermal environment in the orbiter payload bay is considerably more diverse, and sometimes considerably more severe, than that on an expendable launch vehicle. The orbiter's tremendous attitude flexibility and multipayload manifesting have a downside for the thermal engineer in that they can expose the payload to a very wide range of environments, unless appropriate attitude restrictions are in place.

Payload-Bay Purge[*]

The payload-bay purge system supplies conditioned air or gaseous nitrogen (GN_2) to the payload bay during prelaunch operations with payload-bay doors closed, and it supplies conditioned air during the postlanding period at primary and alternate landing sites. The main function of the payload-bay purge system is to render the payload bay inert; the purge produces only limited thermal conditioning. Payloads that require close temperature control and/or large heat-rejection capacity may therefore benefit from the use of optional services, such as spigot cooling with purge gas or active cooling through the payload heat exchanger. The use of optional services, however, may increase the cost and complexity of the payload-integration process.

Purge air is normally provided to the payload bay after the payload-bay doors are closed, except during the following activities.

- mobile ground support equipment (GSE) facility/mobile GSE transfer
- towing of the orbiter
- orbiter mate/demate
- orbiter test- or purge-system line-replaceable-unit replacement or test
- GSE periodic maintenance at the Orbiter Processing Facility (OPF), Vertical Assembly Building (VAB), and pad

The purge gas that is used is conditioned air, except during cryogenic servicing of the orbiter power-reactant storage-and-distribution subsystem and during final launch countdown from just before external tank loading until launch (or through detanking, when necessary). During these periods, temperature-conditioned GN_2 is provided as the purge gas for inerting purposes. All gas used to purge the payload bay, whether air or GN_2, is filtered using high-efficiency particulate air (HEPA) filters (Class 5000). The resulting purge gas contains 15 or fewer parts per million of hydrocarbons based on methane equivalent.

The purge-gas inlet temperature can be set between 7 and 37°C at the pad, nominally controllable to within ±3°C. Under steady flow conditions, a tolerance of ±1.2°C with excursions to ±3°C for one hour over a period of 12 h is negotiable for temperature-sensitive payloads. The standard purge-gas inlet temperature is set

---

[*]The remainder of this chapter is derived from NSTS 07700, Volume XIV, Appendix 2, "System Description and Design Data—Thermal," courtesy of NASA.

at 18°C and can vary between 15 and 21°C. Payloads that require other than the standard purge temperature must negotiate a different purge temperature with any other payloads that are manifested on the same flight. Because the temperature control point is on the facility side (upstream of the orbiter T-0 umbilical), gas temperatures within the payload bay may vary from the set point, depending on ambient conditions. Orbiter payload-bay thermal analytical models (which will be discussed later) can predict purge-gas temperatures throughout the bay and account for the resultant influence on the payloads. Additional characteristics of the purge gas (including flow rates) are given in ICD 2-19001.

Payloads sharing a mission require special consideration of flow rate. The purge-gas flow enters the payload bay at the forward bulkhead location (X_0 576) and exits at the aft bulkhead (X_0 1307). Because of leakage through the payload-bay doors and flow to the lower midfuselage (the volume beneath the payload bay) through payload-bay vents, the local flow rate may be less than the inlet flow. Additionally, three spigots are available as an option to provide supplemental flow through special ducting to meet unique payload requirements. For analysis purposes, the supplemental spigot flow is introduced into the payload bay where it exits the using payload. Therefore, the local purge-flow rate may vary considerably for shared missions. Customers whose payloads share a flight must design for both the maximum and minimum flow rates specified in ICD 2-19001 because the location in the payload bay will be determined by NASA.

Payload-bay purge is normally provided at the planned primary and alternate landing sites, starting approximately 45 min after touchdown at the primary site and 90 min after touchdown at the alternate site. Payload-bay purge is provided within 72 h at any landing site. The payload-bay purge may not be used to satisfy payload safety requirements. Payload requirements for special postlanding services are negotiated with NASA and documented in the IP. Emergency-landing-site environmental conditions are documented in ICD 2-19001. Purge at ferry-flight stopover sites can be provided as an optional service.

Payload-Bay Wall Temperatures

During the prelaunch and ascent phases of the mission, when the payload-bay doors are closed, temperatures in the payload bay are relatively moderate. After the orbiter reaches orbit and the payload-bay doors are opened, however, temperatures can vary over a wide range, depending on flight attitudes and the payload/cargo configuration. Representative payload-bay wall temperature ranges for various mission phases are shown in Fig. 18.7. Actual temperatures are expected to fall within the ranges shown; they depend upon payload design, thermal characteristics, and flight conditions.

Significant solar entrapment may occur on orbit when direct solar radiation into the payload bay is present and the gap between the cargo and the payload-bay surface or adjacent payload is small. This phenomenon is illustrated in Fig. 18.8, which shows temperatures from an integrated thermal analysis of the Spacelab module and pallet cargo. Local temperatures can exceed the 93°C maximum reached if the payload bay is empty and can approach 162°C.

Another situation that can result in excessively high temperature is the "greenhouse effect" that can occur when a material that transmits solar energy (such as
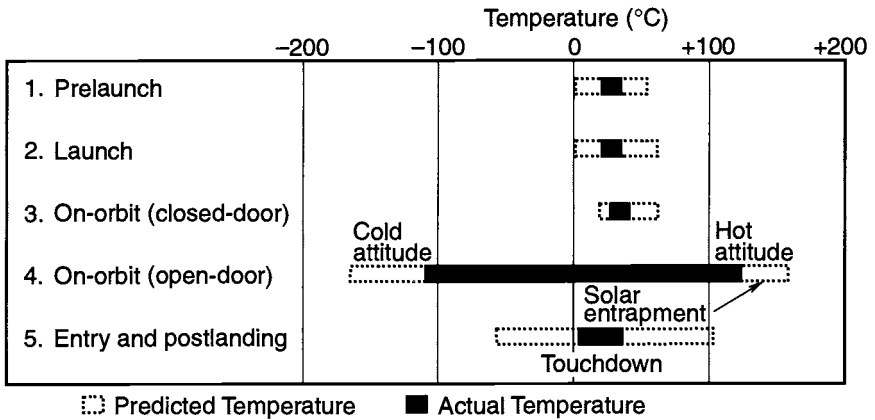
Fig. 18.7. Payload-bay wall temperatures.
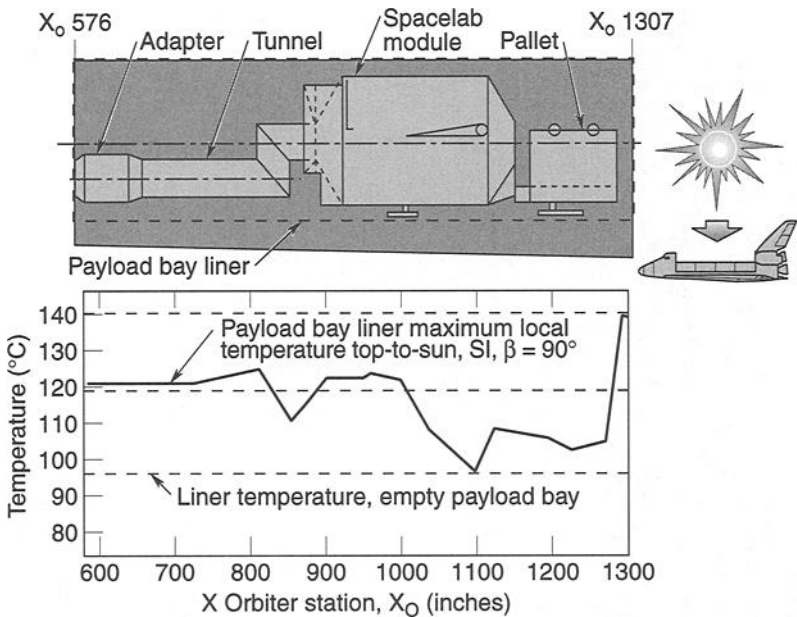
Fig. 18.8. Payload-bay liner temperature with solar entrapment.

Beta cloth) is used on the payload surface and is exposed to direct solar radiation. The portion of solar energy transmitted through the material becomes trapped under it, thereby creating relatively high temperatures on surfaces immediately below the material.

The payload-bay wall temperature ranges given in Fig. 18.7 can be used to estimate the thermal environment for use in initial payload thermal design. Table 18.1

Table 18.1. Steady-State Liner Temperature for Preliminary Design

Case Description	Empty Payload Bay Liner Temperature (°C)		Cylindrical Payload Liner Temperature (°C)	
	Maximum	Minimum	Maximum	Minimum
  −ZLV, XPOP, β = 90°	−107	−131	−43	−87
  +ZLV, XPOP, β = 90°	−15	−23	−14	−32
  −YLV, −XOV, β = 90°	−70	−81	−7	−32
  +YLV, −XOV, β = 90°	94	57	162	101
  +ZLV, −XOV, β = 90°	−14	−23	41	−5
  −ZLV, −XOV, β = 90°	−102	−129	−18	−70
  PTC (4 rev/h), β = 90°	—	−9	—	24
	For this case, liner temperature is for information only; orbiter temperature limits are exceeded under steady state conditions			
  +ZLV, −XOV, β = 0°	4	−1	16	4
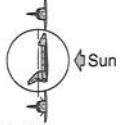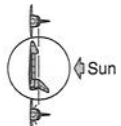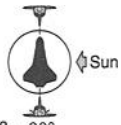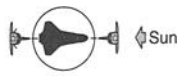
Table 18.1. Steady-State Liner Temperature for Preliminary Design—*Continued*

Case Description	Empty Payload Bay Liner Temperature (°C)		Cylindrical Payload Liner Temperature (°C)	
	Maximum	Minimum	Maximum	Minimum
  −XLV, +YOV, β = 0°	−18	−23	−11	−21
  PTC (4 rev/h), β = 0°	—	−15	—	16

Orbiter axis:
+X = Tail
−X = Nose
+Y = Right wing
−Y = Left wing
+Z = Top (up)
−Z = Bottom (down)

Direction of axis:
LH = Local horizontal
LV = Local vertical
OV = On velocity vector
POP = Left wing
SI = Solar inertial

Nomenclature:
Orbiter axis + direction of axis

Example:
+ZLV = Top local vertical
−YPOP = Left wing perpendicular to orbit plane

Definition of beta (β) angle

(a) Maximum negative β angle condition for a given orbit plane (ascending/descending nodes perpendicular to the sun vector.)

b) Maximum positive β angle condition for a given orbit plane (ascending/descending nodes perpendicular to the sun vector.)
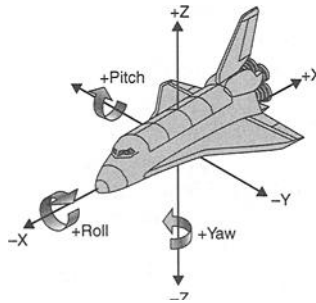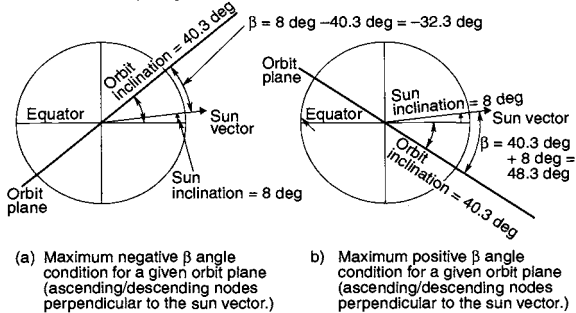
provides additional analytical predictions of steady-state liner temperatures for specific flight attitudes and beta angles when the payload-bay doors are open. The influence that a large payload has on payload-bay liner temperatures can be seen in the table data. Empty payload-bay liner temperatures can be used for the thermal design of payloads with diameters up to 230 cm if the payload centerline

coincides with the longitudinal axis of the payload bay. For payload diameters between 230 and 305 cm, liner temperatures can be estimated by interpolating between the empty payload-bay temperature and the temperature of the bay when it contains a cylindrical payload.

During entry and postlanding phases, the thermal environment is influenced by the initial pre-entry condition, entry heating and subsequent heat conduction inward, ground purge (if any), and weather conditions at the landing site. Generally, the maximum temperature is reached after landing as a result of heat soakback through the orbiter structure and air entering the payload bay through the vent doors.

Orbiter Attitude-Hold Capabilities

The maximum time that the orbiter can remain in a given attitude has been established, based on analyses, tests, and actual flight experience. The attitude-hold times (documented in ICD 2-19001) vary from 5 to 160 h, depending on the beta angle and the payload-bay orientation. These attitude-hold times are representative of orbiter maximum capability and are applicable to most payload missions.

The orbiter pre-entry thermal-conditioning attitude and duration are established during the mission and are based upon real-time temperature measurements. The thermal-conditioning duration may range from 0 to 12 h. For normal entry, the pre-entry thermal-conditioning attitude and duration are selected to be compatible with both orbiter and payload operational or refurbishment temperature limits. If mutually compatible requirements cannot be established, pre-entry conditioning will be accomplished by PTC.

In the event of an anomaly, NASA will observe the payload operational attitude constraints to the extent possible. If these constraints must be violated, payload safety constraints will be observed. Payload flight-safety constraints and operational or refurbishment attitude-hold constraints are established by the customer and documented in the payload-unique IP and IP annexes.

Payload-Bay Floodlights

Payload surfaces or elements that may be located near one or more payload-bay floodlights should be analyzed to determine if the heat flux from floodlight operation could cause overheating. If a temperature violation could occur and a suitable redesign is not feasible or practical, a floodlight operational constraint should be specified in the payload-unique IP and analysis results supplied to NASA/USA for evaluation and planning. Because floodlights can fail on, the payload must also be designed so as not to present a safety hazard if that should occur. The payload should not, however, be designed to utilize payload-bay floodlights for thermal control.To conduct a floodlight analysis, the engineer should use the payload-bay floodlight locations and thermal characteristics given in ICD 2-19001. In special situations that require a more detailed analysis, NASA/USA can provide a floodlight thermal math model (TMM).

Reflected Solar Energy

Cargo elements that extend above the payload-bay door-hinge line or that are deployed transversely over the orbiter radiators may be exposed to reflected solar radiation from the orbiter radiators. The radiators have moderately specular reflective surfaces.

The magnitude of the local fluxes and thermal effect is a function of cargo location, orbiter orientation relative to the sun, and duration of the exposure. In most cases, except for solar inertial attitude, if solar radiation is reflected onto a payload in the bay, the exposure is a brief, nearly instantaneous one resulting from the continuously changing solar angle. For payloads located in the bay, these reflected solar loads can only occur when the forward radiators are deployed, as shown in Fig. 18.9. (Normally, the forward radiators are not deployed unless maximum heat rejection is required.) For payloads that deploy from the bay, reflections from either stowed or deployed radiators are possible, unless attitude restrictions are specified by the customer. Reflection of solar energy from the radiators during payload-bay door opening is precluded by opening the doors with the payload bay facing Earth (+ZLV).

NASA and other organizations have conducted analytical studies of the solar focusing phenomenon from orbiter radiator panels. Solar ray tracing (plotting the path of light rays as they are reflected off surfaces) for various solar angles and radiator-panel geometries has been developed. Figure 18.10 illustrates ray tracing for various solar angles for a deployed forward radiator.

Air Inlet During Orbiter Re-entry

The temperature and mass flow rate of the air entering the payload bay during entry, and the resulting bay pressure (given in ICD 2-19001), are the maximum or worst conditions that occur at or near the payload-bay vents (Fig. 18.11). Thermally sensitive payload surfaces that may be located near a vent should be analyzed to determine the impact of exposure to hot entry air after the vent doors are opened. As given in the ICD, the entry-air temperature declines rapidly from approximately 205°C at vent-door opening (low-density air) to 38°C approximately 60 sec later. As the distance from a vent increases, the effect of entry air on a payload surface decreases rapidly.

Deployable radiators
(normally not deployed)

Fixed radiators
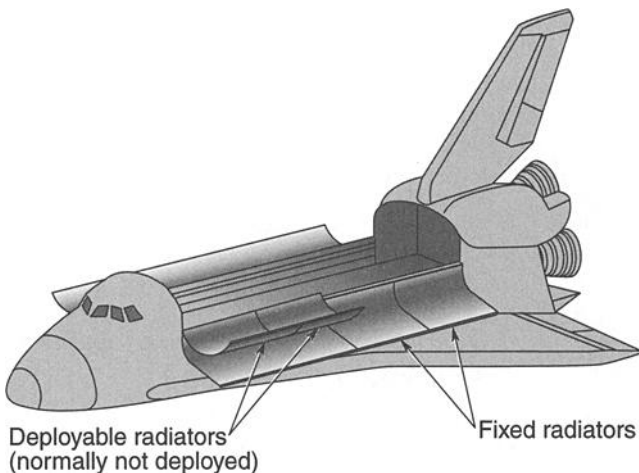
Fig. 18.9. Orbiter radiator configuration during on-orbit operations.
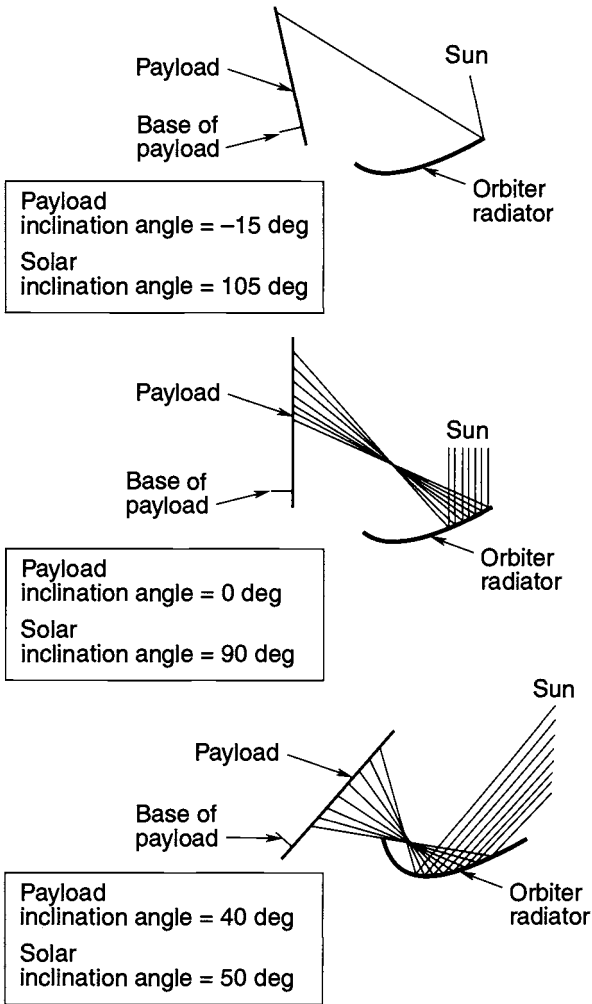
Fig. 18.10. Reflected solar-energy ray tracing from deployed orbiter radiator.

Normally, payload-bay vent doors are closed at the start of entry and do not open until after peak aerodynamic heating has occurred. However, customers must conduct thermal assessments to confirm that no safety hazards arise in either the payload or in its integration hardware if one or more vent doors fail in the open position and remain open during re-entry. The methodology for performing these assessments is presented in ICD 2-19001.

Integrated Thermal-Analysis Considerations

The payload thermal design and integration process must include an integrated payload/orbiter thermal analysis to ensure that the payload design meets expected
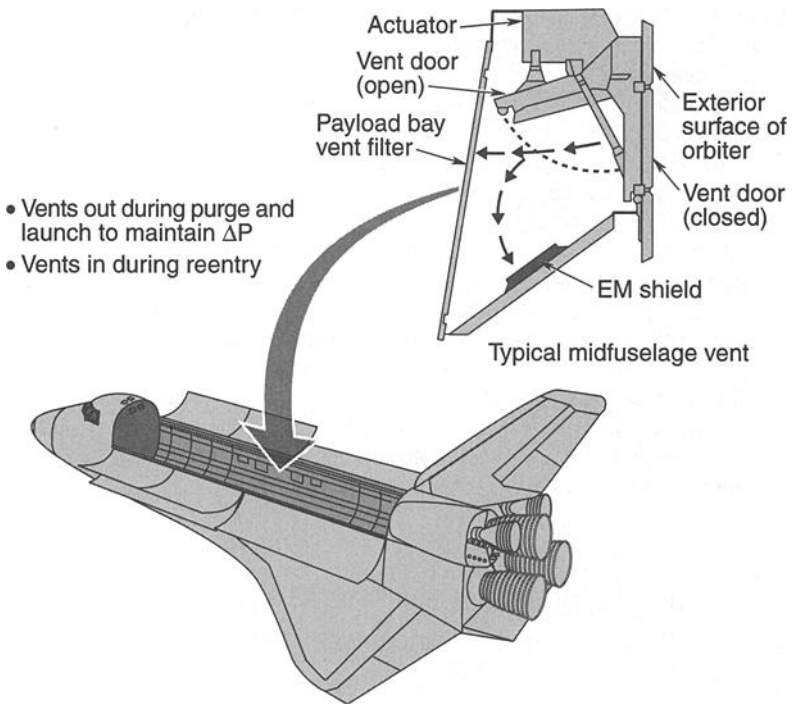
Fig. 18.11. Payload-bay vent ports.

mission objectives and to define payload-unique thermal requirements for inputs to the IP and ICD. Integrated thermal analysis can be an iterative process in which the initial effort is directed toward defining the payload thermal design and subsequent analyses, conducted after the payload design has matured, are directed toward establishing payload-unique requirements, particularly in orbit.

An integrated analysis may consist of several separate analyses, depending on the thermal interfaces involved with the particular payload. The following separate analyses should be performed:

- payload/orbiter analysis for payloads and Airborne Support Equipment (ASE) located in the payload bay
- payload-bay floodlight analysis for payloads in the payload bay (including failed-on floodlight analyses)
- failed payload-bay vent-door analysis
- heat-rejection analysis for payloads utilizing the payload heat exchanger
- heat-rejection analysis for payloads utilizing the spigot system
- ferry-flight analysis for payloads and ASE located in the payload bay, middeck, or aft flight deck
- payload/grapple fixture/end effector analysis for payloads utilizing the remote manipulator system (RMS). Grapple fixture thermal data are given in System Description and Design Data—Payload Deployment and Retrieval System, NSTS 07700, Volume XIV, Appendix 8.

The integrated thermal analysis for a payload and ASE, in the payload bay or deployed from the payload bay, is relatively complex. The process requires use of suitable payload and orbiter math models, development of relatively large integrated math models (with several hundred to thousands of nodes), and use of computer programs capable of analyzing them.

A flowchart of the integrated analysis task is presented in Fig. 18.12. Analysis cases should consist of the worst hot, worst cold, and design or nominal conditions. Design timelines for these conditions must be defined. The orbiter thermal and geometric math models to be used in the integrated analysis are available from NASA, as are the industry-standard thermal-analysis codes SINDA and TRASYS (see Chapter 15).

Generally, integrated TMMs (ITMMs) and analysis cases are tailored specifically for the payload, its mission conditions, and the objective of the analysis. For example, if the integrated analysis is performed primarily in support of payload thermal design, a detailed payload thermal model would be used in conjunction with the simplest models to represent the orbiter and adjoining payloads in the payload bay. These and other considerations that minimize the cost of integrated thermal analysis are discussed in subsequent sections.
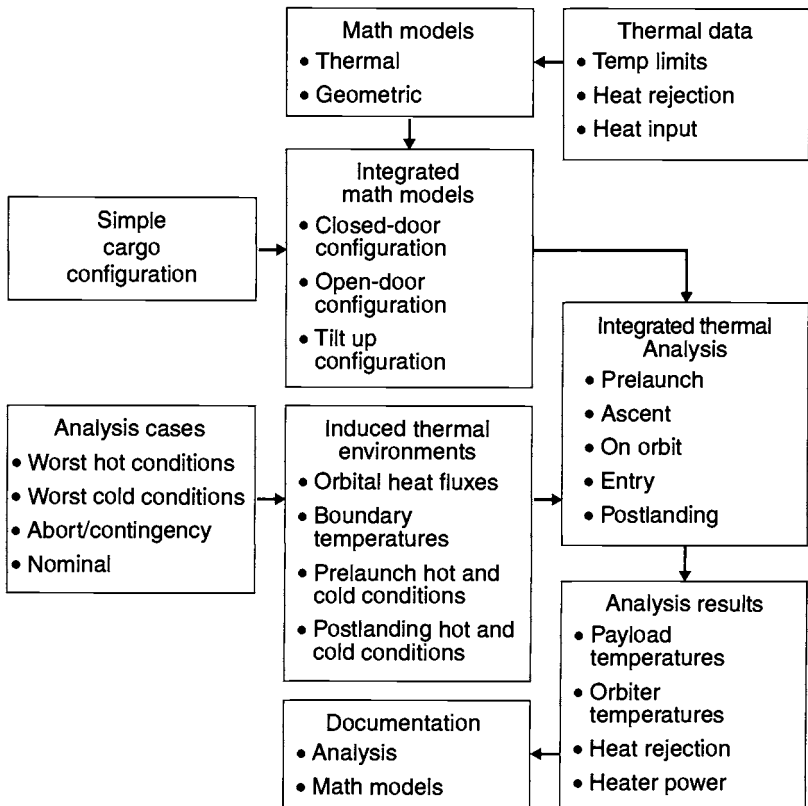
Fig. 18.12. Payload/orbiter integrated thermal-analysis flow diagram.

On-Orbit Attitudes and Constraints

The orbiter's attitude/duration constraints are identified in ICD 2-19001. Similar constraints for the payload must be determined by integrated analysis and documented in the payload-unique ICD. Worst hot and cold mission attitudes must be considered along with planned operational and nonoperational attitudes for all payloads. The standard worst hot and cold mission attitudes, +ZSI (bay toward the sun, inertial) and +XSI (tail toward the sun, inertial), are most often treated as limited-duration excursions from the nominal flight attitudes. Generally, the shortest time required to exceed the operating and nonoperating temperature limits of critical payload components in these worst-case attitudes is used to define constraints for the payload-unique ICD. Of course, if these constraints violate orbiter operational requirements, the needs of the orbiter prevail.

Some attitudes may be hotter or colder than the standard "worst" cases. These are the +X sun orbital rate (tail to sun, one revolution per orbit about the x-axis), which keeps the payload bay always facing deep space with little or no view toward Earth, or other specific attitudes that may represent extreme conditions resulting from special circumstances such as shadowing or reflection of sunlight, and unusual payload geometry or physical properties.In addition, the orbit beta angle influences the thermal severity of these and other attitudes. Identifying the true worst-case attitudes for a particular payload can require some analysis on the part of the thermal engineer.

In addition to the time required to exceed a temperature limit, the time to recover from a limiting temperature to a nominal condition (e.g., to +ZLV, payload bay facing Earth) is also of interest. This time establishes the waiting period before commencing another hot or cold attitude excursion. Depending on whether a hot or cold extreme has been reached, the recovery attitude is generally +ZLV, PTC, +XSI, or +ZSI. The designation PTC (passive thermal control) is assumed for analysis purposes to be rotation of the orbiter about its x-axis at two to five revolutions per hour with the x-axis within 20 deg of perpendicular to the sun vector. This type of rotation is sometimes called the barbecue mode.

The orbiter attitudes referred to above are depicted in Fig. 18.13. Note that other orbiter orientations could also satisfy these attitude designations. The direction of at least one other orbiter axis is needed to uniquely define the attitudes shown.

Prelaunch, Ascent, Entry, and Postlanding Mission Phases

These mission phases are of particular interest for AOA and contingency-landing-site conditions, and for cryogenic and high-heat-generating payload components, for which thermal compatibility with the closed-door orbiter must be determined. Launch and landing sites, time of year, time of day, and orbiter payload bay, purge-gas parameters and availability are variables that must be considered. Environmental and orbiter parameters required for analysis of these mission phases can be found in ICD 2-19001.

Analysis Approach

A typical approach to integrated thermal analysis is shown in Tables 18.2 and 18.3 for hot and cold cases, respectively. Figures 18.14 and 18.15 show sample hot- and
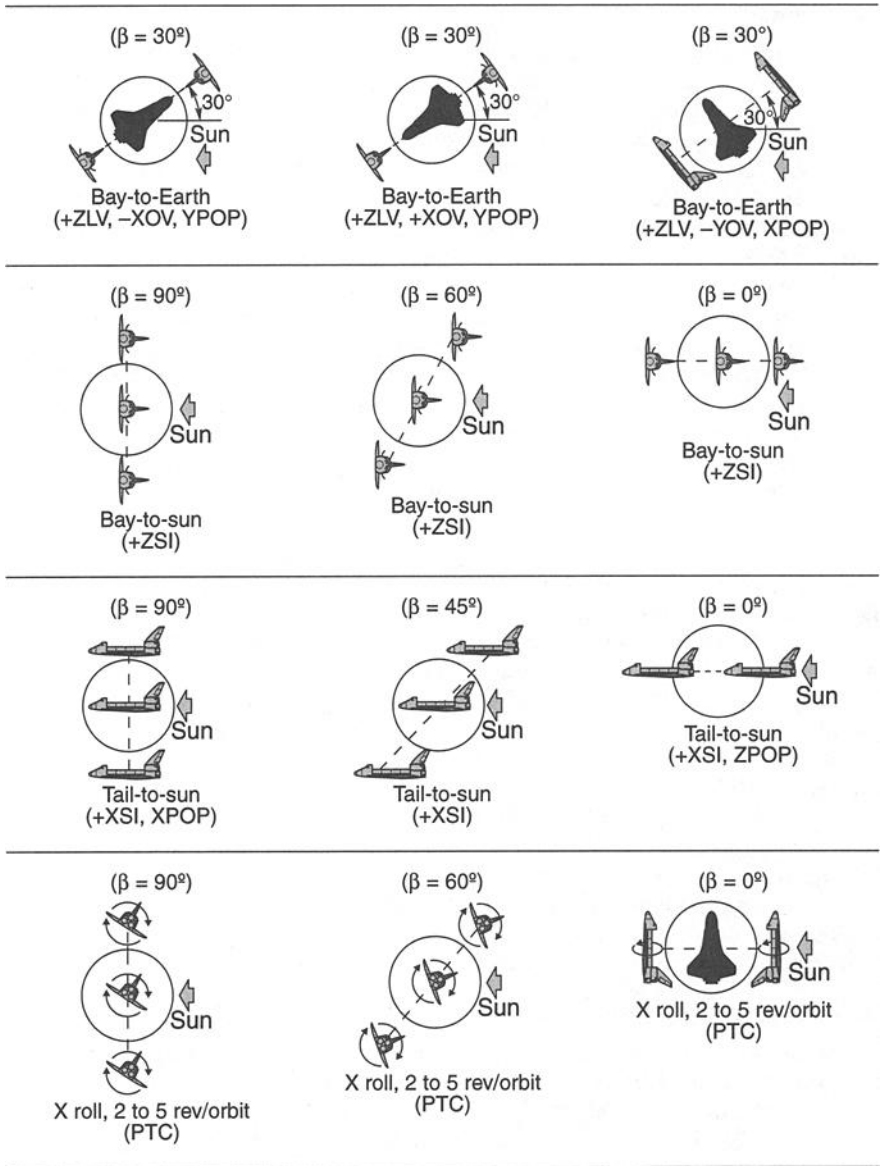
Fig. 18.13. Some standard orbiter attitudes.

Table 18.2. Typical Integrated Thermal Analysis Approach (Cold Case)

Analysis Task	Notes
Perform cold excursion/recovery analysis to satisfy IP TBDs	• Both SV/ASE and ASE alone (if required) • Use cold-biased mission timeline and environments to generate initial conditions
Perform cold entry/postlanding analysis to determine allowable exposure time to cold postlanding environment	• Both SV/ASE and ASE alone (if required) • Use coldest point in timeline for initial conditions • Assume no purge at landing site and continue analysis until cyclic steady state is reached • Cold safety limits eventually will be exceeded • Ground power or warm purge air is required • Establish length of time prior to power/warm air need

Table 18.3. Typical Integrated Thermal Analysis Approach (Hot Case)

Analysis Task	Notes
Perform hot excursion/recovery analysis to satisfy IP TBDs	• Both space vehicle (SV)/ASE and ASE alone • Use hot-biased mission timeline and environments to generate initial conditions
Perform hot entry/postlanding analysis to determine temperature rise for each component	• Both SV/ASE and ASE alone (if required) • Use hottest point in timeline for initial conditions • Assume no purge at landing site and continue analysis until all temperatures begin decreasing
Determine allowable excursion times prior to entry	• Both SV/ASE and ASE alone (if required) • Use temperature changes generated from excursion temperature curves to determine allowable times • Determine minimum allowable time for each excursion attitude
Run entry/postlanding to verify minimum allowable times	
Refurbishment limits can be similarly established	
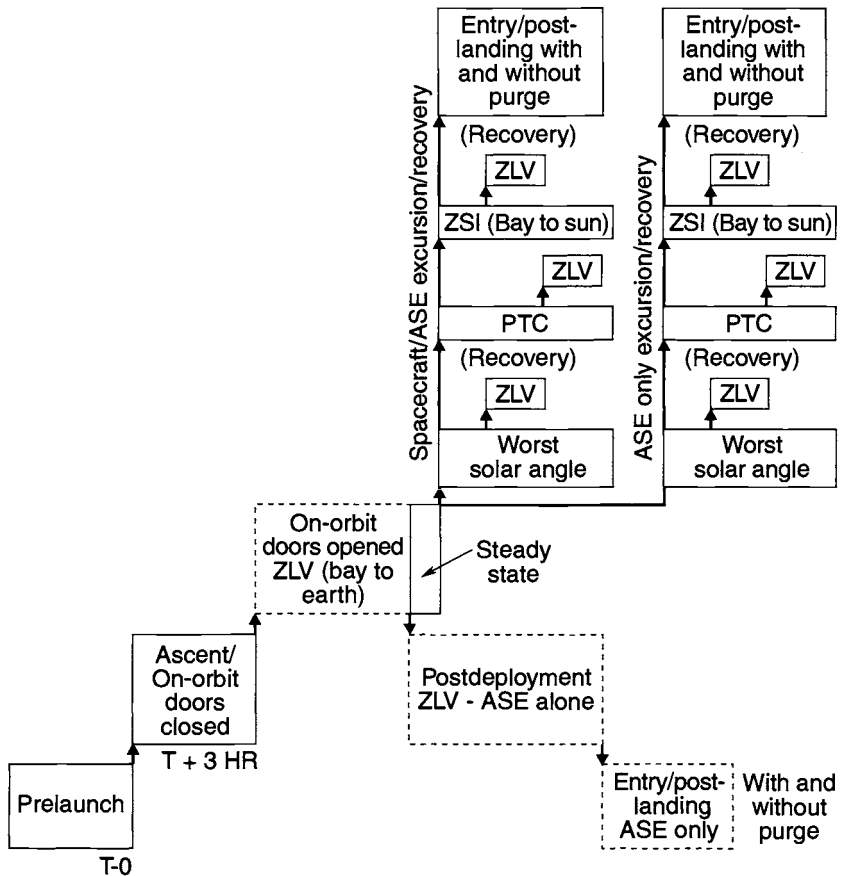
Fig. 18.14. Typical hot-case thermal design timeline.

cold-case timelines, and Figs. 18.16 and 18.17 illustrate temperature plots that can be used to determine on-orbit attitude hold and recovery times, attitude hold times prior to entry, times to reach entry/postlanding temperature extremes, and refurbishment times. Sample actual analysis timelines used for determining attitude thermal constraints and verifying mission thermal compatibility of a specific payload are presented in Fig. 18.18 for the hot condition, Fig. 18.19 for the cold condition, and Fig. 18.20 for the ASE-only configuration.

Payload TMMs

Among the first details a thermal analyst considers in preparing a payload TMM are those associated with its eventual inclusion in an orbiter TMM. An analysis with the resulting ITMM is required to confirm thermal compatibility of the payload with the orbiter and with its mission environment.
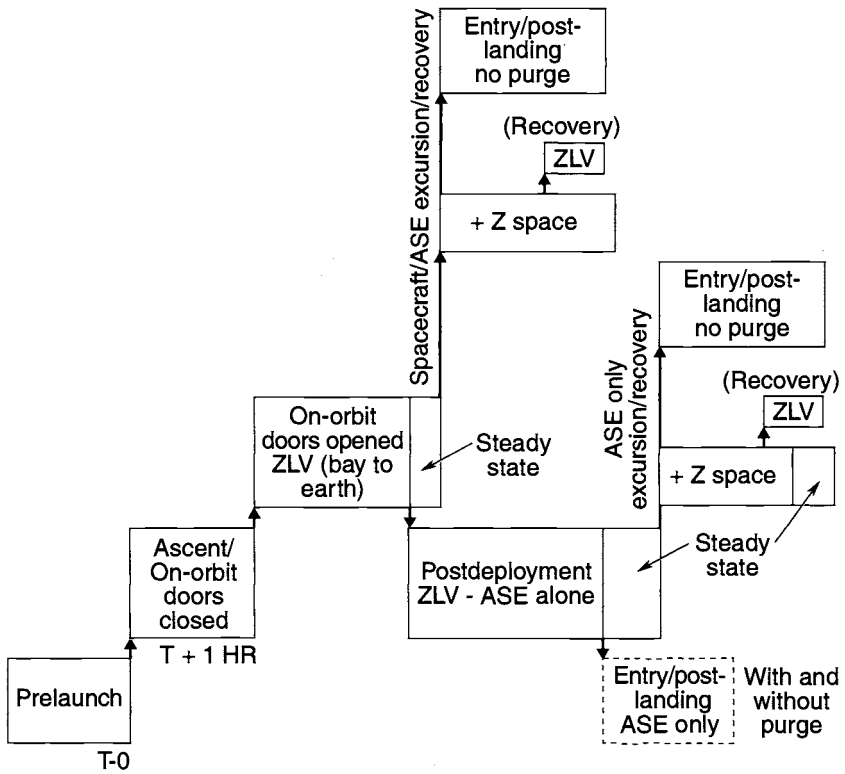
Fig. 18.15. Typical cold-case thermal design timeline.

Specific payload TMM criteria and guidelines have been established (Criteria/ Guidelines for Payload Thermal Math Models for Integration Analysis, JSC 14686) to assist the thermal analyst in TMM preparation. These criteria and guidelines ensure consistency of the TMM and supporting data, and adequacy of the TMM for economic and reliable analysis and compatibility with NASA standard services. Among these requirements are payload TMM size restrictions (i.e., number of nodes, conductors, external surfaces), minimum allowable stable-calculation time interval, payload/orbiter interface considerations, and adequate documentation.

A complementary payload geometric math model (GMM) is required for each TMM for combining with an orbiter GMM to produce an integrated GMM (IGMM) for use in calculating radiation interchange factors and orbital heat rates for external surfaces. Payload math-model documentation should be referenced in the payload-unique ICD.

Orbiter TMMs

Several orbiter-midsection/payload-bay TMMs are available for integrated thermal analyses and are authorized in the appropriate IDD or ICD. In Table 18.4 these are listed in order of decreasing detail, and major differences are noted.
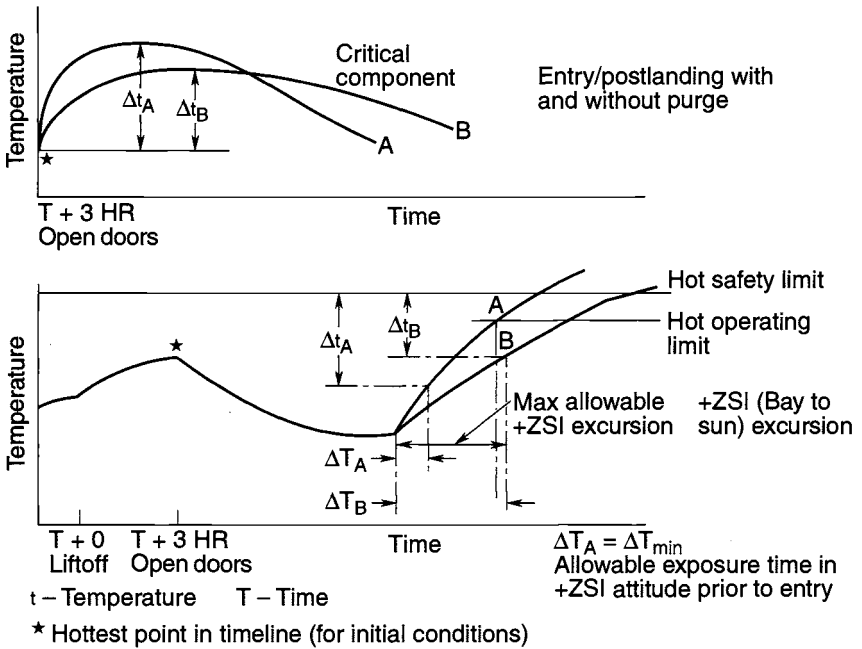
Fig. 18.16. Hot-case temperature profiles for determining safety and operating limits.

Table 18.4. Available Orbiter TMMs

Orbiter TMM Nodes	Modeling of Payload-Bay Liner and Outward through Orbiter	Wire Trays, Frames, and Aft Fuselage	External Orbiter Heat Loads and Radiation Interchange	References
390	Detailed	Included	Directly applied	ES3-76-1, ES3-77-3
136	Less detailed	May be added	Directly applied	ES3-76-7, ES3-77-1

Each orbiter TMM is constructed in a manner that allows for renodalization of its payload-bay liner and wire-tray nodes (or zones) to provide additional and/or better distribution of nodes to attain the desired degree of accuracy for both the liner/wire trays and an included payload TMM. Renodalization of the payload-bay liner should be considered when the sun's rays may shine directly into the payload bay parallel to the orbiter z-axis. (This process is discussed in more detail later.) The TMM references also describe how to add the optional payload-retention fittings and Remote Manipulator System (RMS).
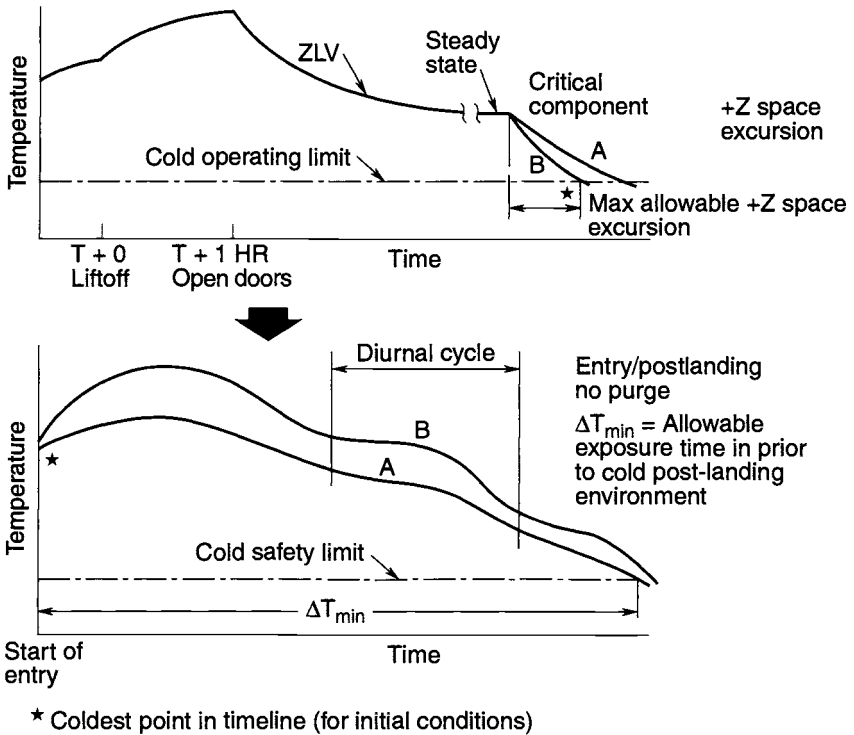
Fig. 18.17. Cold-case temperature profiles for determining safety and operating limits.

Input data for constant and diurnal prelaunch and postlanding environments, consisting of ambient air and surrounding boundary temperatures and solar heat rates for different conditions at the eastern test range (ETR), are included in the closed-door TMM documents, "390 Node" Atmospheric Orbiter Midsection/Payload Bay Thermal Math Model Description, ES3-77-3, ES3-76-7, and ES3-77-1.

Although simpler orbiter models may suffice for most applications, one should understand the capabilities and limitations of ES3-76-7 and ES3-77-1 before using them.

ITMMs

To keep analysis cost down, the size (number of nodes) of the ITMMs should be as small as practical and governed by the required accuracy of the results. Thus the ITMMs or models used primarily in support of payload design consist of a detailed payload TMM and the simplest orbiter-interface math model. The objective is to obtain accurate thermal results for the payload.

As the payload design matures, payload math models are finalized with emphasis on obtaining accurate temperatures at the payload and orbiter interfaces, so a more detailed orbiter-interface math model is needed, particularly in the payload bay.
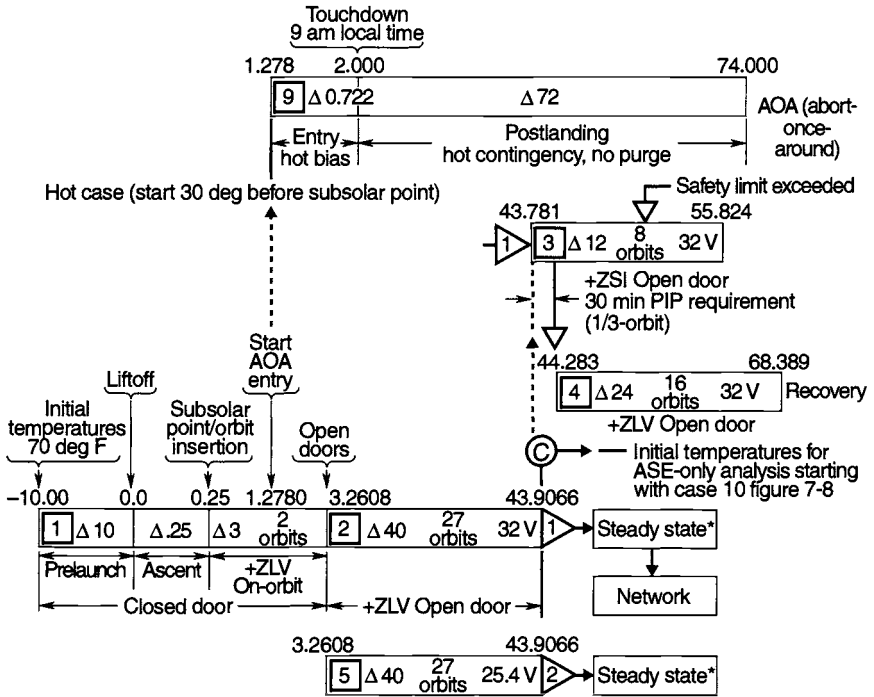
Fig. 18.18. Sample hot-case timeline for a specific payload.

To keep the overall integrated-model size within reasonable range and cost to run, the size of the payload math model may be reduced. The number of surface nodes has the maximum effect on the computer run time.

Generally, payload math-model simplification should aim to reduce the number of nodes "buried" within the payload or its components, because those nodes will have a small effect on the payload surfaces that constitute the interface with the orbiter. For example, a payload component that is covered with high-performance insulation could be represented by a single "lumped" node rather than several nodes, unless this element or component is sensitive to surface temperature or has

Fig. 18.19. Sample cold-case timeline for a specific payload.

a relatively strong influence on the surface temperature. The simplified payload TMM should be checked by comparing the temperature results with those derived from the detailed or original model to ensure that the payload surface temperatures, i.e., the interface temperatures, are in agreement.

Cold case —▷4▷ [13]Δ 40   27 orbits   28 V → Steady state*

|← +XSI open door →|
no limit
Recovery   exceedances 164.802   188.889
[14]Δ 24 16 28 V
orbits
+ZLV open door

84.093   124.822
Hot case —▷3▷ [11]Δ 40 27 + orbits 28 V → Steady state* ▷4▷

+ZSI open door
CDU upper limit exceeded

96.289   122.376
[12]Δ 24 16 28 V
orbits
Recovery
+ZLV open door

Touchdown
9am local time

84.552 85.274   157.274
▷3▷ [15] Δ   Δ 72
0.722

Entry hot bias |←—→|←— Postlanding —→|
hot contingency,
no purge

43.9066   84.552
© [10]Δ 40 27 28 V ▷3▷
orbits
+ZLV open door

Legend: One orbit = 1.5054 hours at 255 km altitude
voltage: 32 V maximum, 28 V nominal, 25.4 V minimum

*Using orbital average heat rates and constant
adjusted heater powers

[1] Case no. (typical)

▷1▷ Continue at   ASE only
times in hours unless
—▷1▷ With same or earlier temperatures (typical)   noted otherwise
(Δ times are nominal
MET is in hours   requested values)

Fig. 18.20. Sample timeline for ASE only.

Node and Conductor Identification Numbers

When adding a payload TMM to an orbiter TMM, do not assign duplicate node and conductor identification numbers. The preferred method is to use 5-digit node numbers greater than 20,000 and 6-digit conductor numbers when a payload TMM is first constructed. The payload GMM node or surface numbers should be treated similarly.

Convective Heat Transfer

When convection simulation is required, the orbiter TMM external surface convection code, which is built into the 390-node closed-door TMM (ES3-77-3), may be readily adapted to apply to the payload TMM external surfaces by making the

associated payload conductors adhere to the format and placement in the model of orbiter TMM convection conductors. Convection effects should be included in conductors across single-layer insulation blankets and multilayer insulation (MLI). For best results, these conductors should vary with pressure and temperature for ascent and entry mission phases. ES3-77-3 contains additional information regarding convection.

Other Effects

As noted, solar entrapment can present special problems. In a +ZSI (bay-to-sun inertial) attitude, the sun's rays are parallel to the orbiter z-axis. In this attitude, direct or reflected solar energy may make orbiter payload-bay bulkhead and payload surfaces significantly hotter than anticipated in local areas where the view factor to space is small. This solar entrapment can occur on payload surfaces that face the payload-bay liner and have no direct view of the sun. If a few relatively large payload-bay liner nodes are used in the analyses, this effect may not be discernible, especially if the payload shadow outline crosses a liner node. Therefore, to provide the needed accuracy, the payload-bay liner in the vicinity of the payload should be renodalized to more accurately simulate the trapping of local energy and the resulting temperatures.

Other nearby payloads can also cause solar entrapment by reducing the view factor to space. In determining payload-attitude thermal constraints, modeling this adjacent payload with a simulated blocking surface may suffice. For example, a large-diameter, insulated, adjacent payload can be simulated by employing two zero-capacitance back-to-back disks (or geometric shapes representing the projection of the adjacent payload on the orbiter y-z plane) located at the end of the adjacent payload nearest the payload of interest. A mission-verification integrated analysis, on the other hand, may require detailed modeling of both (all) payloads.

Middeck Payload Accommodations

Accommodations for payloads located in the orbiter middeck are provided by use of either standard orbiter lockers or adapter plates mounted to standard locker attachment provisions. Shuttle/Payload Interface Definition Document for Middeck Accommodations, NSTS 21000-IDD-MDK, specifies the standard thermal interfaces for middeck payloads. Standard middeck payloads are passively cooled; i.e., no active liquid or air cooling is provided as a standard service, although active cooling can be provided as a optional service. Payloads that generate waste heat and cannot reject it to the cabin air (using a fan or similar means) are limited to a continuous heat load of 60 W. Cooling requirements above this level must be negotiated with NASA. Figure 18.21 shows an overview of the middeck area and stowage locker locations. Figures 18.22 and 18.23 show an experiment apparatus container (EAC) payload and available mounting locations, while Fig. 18.24 depicts a fan-cooled payload. Inlet and outlet filtration are recommended if fans are used.
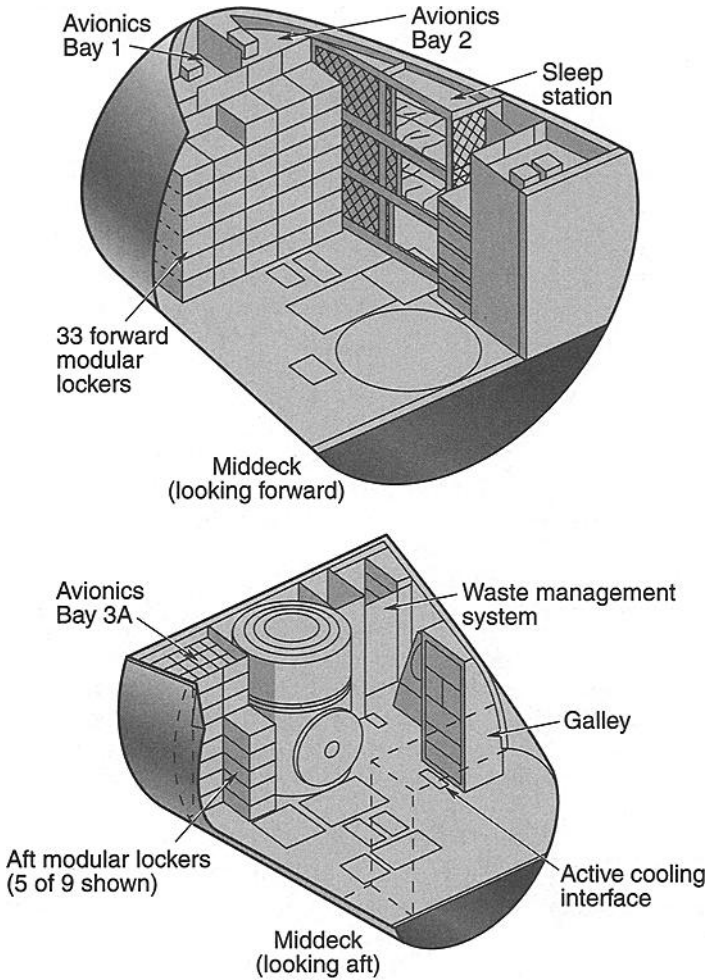
Fig. 18.21. Middeck stowage lockers

Maximum Temperature Limit

Middeck payloads should be designed so that external surface temperatures do not exceed 48°C. If the payload design incorporates a fan for enhanced heat rejection, the air outlet temperature should not exceed 48°C.

Middeck Environment

Heat generated by the payload is primarily rejected to the middeck air by means of convection resulting from the air movement in the middeck, or by enhanced forced-air convection from the use of an internal fan. During a nominal mission without any planned EVA, the cabin air temperature and pressure are at approximately 25°C and 10.1 N/cm^2. For missions with planned EVA, the cabin pressure
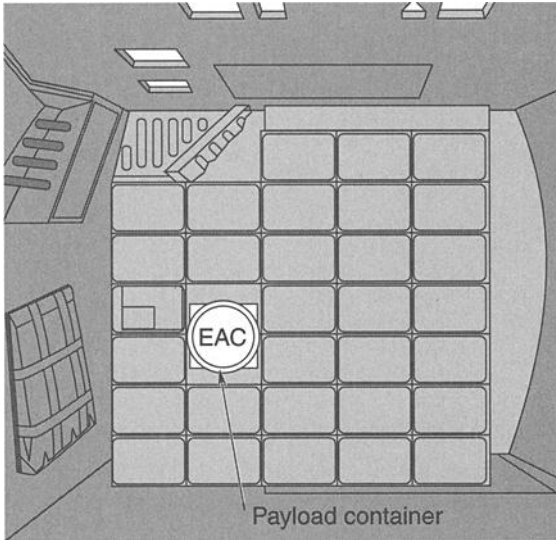
Fig. 18.22. Experiment apparatus container payload.
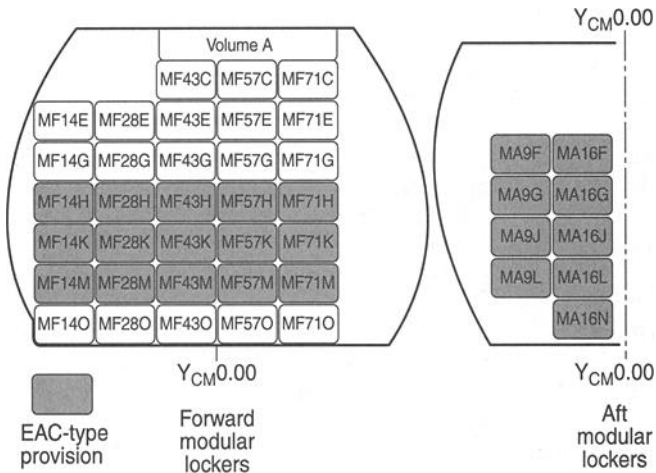
Fig. 18.23. Middeck locker locations for EAC-type provisions.

is normally reduced to 7.0 N/cm^2 during the EVA and EVA prebreathe periods. In both cases, the heat-removal capability is low because air flow in the middeck locker area is minimal. The natural heat-convection coefficient is normally low, approximately 1.4 W/m^{2}C for 10.1 N/cm^2 cabin pressure and 0.97 W/m^{2}C for a
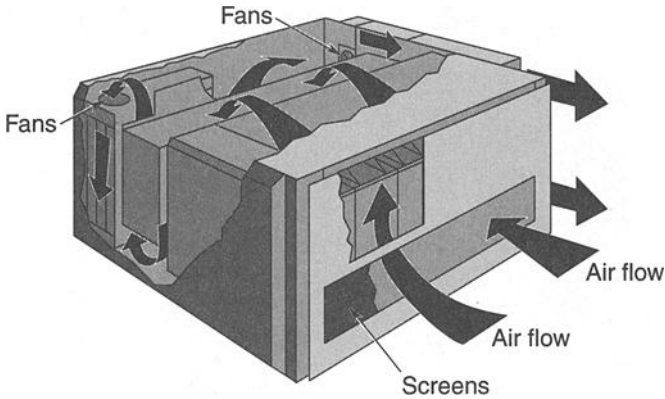
Fig. 18.24. Typical payload with internal fans.

7.0 N/cm^2 cabin. Additional heat generated by the payload is rejected by conduction and radiation to the adjacent structure, such as the avionics closeout panels and surrounding lockers. The maximum structure temperature is 48°C, as defined in NSTS 21000-IDD-MDK. However, it is normally lower, approximately 26 to 33°C, provided no heat generation is in the adjacent locker.

Thermal Analysis of Middeck Lockers

NASA performed a parametric study of middeck lockers for various heat loads, payload locations, and single and multiple lockers. Air temperature of 26°C in the cabin and avionics bays 1, 2, and 3 was assumed. The following general observations could be made:

- No single 60-W source will cause any exposed surface of any locker to exceed the 48°C limit.
- Within the range of heat sources of 30 to 60 W, the temperature increase in the surrounding lockers is proportional to the source power. For example, if 60 W heats an area to 32°C (6°C above cabin), then a 30-W source will heat the same area to 29°C (3°C above cabin).

Thermal-Analysis Requirements

Each payload should be analyzed by the payload designer to ensure that adequate cooling is provided. The analysis must consider the worst-case environment (defined in NSTS 21000-IDD-MDK). Where warranted, NASA/USA performs an integrated analysis based on a specific flight manifest. The manifest may include a combination of certain middeck payloads, not necessarily one single payload. The purpose of the integrated analysis is to determine if any external surfaces of the lockers or the payload containers exceed the touch temperature limit of 48°C and to ensure that adjacent lockers and equipment do not exceed temperature limits.

Ferry-Flight Accommodations

Usually when a shuttle flight ends at Edwards Air Force Base (EAFB) in California, the payload (cargo) remains aboard the orbiter, which is flown or ferried on

the shuttle carrier aircraft (SCA) from EAFB to the launch site in Florida. Payloads and ASE should be designed to be compatible with ferry-flight thermal environments.

During ferry-flight operations, payloads within the payload bay are exposed to ambient conditions that are not controlled or monitored. Payloads normally are not powered, heated, or cooled. Customers should specify any unique requirements in the IP, Annex 8, and the Operations and Maintenance Requirements and Specifications Document (OMRSD).

Flight Phase Thermal Environment

The maximum duration of any ferry-flight segment is limited to approximately 4 h, during which time the payload-bay environment is not controlled. According to measurements recorded during several ferry flights, the temperature in the payload bay could range from about 1 to 30°C. Although the payload-bay thermal environment is not controlled during ferry flight, the payload temperature range may be biased at takeoff, as an optional service, within a reasonable range by conditioned air supplied to the orbiter payload bay via the orbiter purge system while the orbiter and SCA are on the ground.

Ground Phase Thermal Environment

The interval on the ground at selected Air Force bases or NASA facilities varies from a few hours to 24 or more hours, and the payload-bay temperature may vary from about −12 to about +52°C as the result of diurnal and seasonal variations. During stops en route, conditioned air can be made available to the payload in the payload bay. If a payload requires conditioned air, the requirement must be specified in the IP, Annex 8, and in the OMRSD. The specific temperature range and flow rate are negotiated with NASA. When determining conditioned-air requirements, the customer should consider possible payload and payload-bay temperatures at touchdown, minimum duration of the ground service available between flights, and the influence of the ground environment and the payload-bay surface temperatures.

Payloads with Active Cooling Systems

For payloads that utilize water cooling, the water must be prevented from freezing in the cooling system during the ferry flight by employing a ground purge to precondition the payload bay before flight and at stopover sites. To prevent freezing for middeck payloads, NASA provides electrical power to the orbiter coolant pump so warm coolant can be circulated during the flight and during intervals on the ground.

Optional Services

NASA provides payload customers optional services that may significantly increase the cost and complexity of the thermal-integration process.

Active Liquid Cooling

Active liquid cooling is available to payloads located in either the payload bay or middeck. Cooling is accomplished by the payload heat exchanger, a component of

the orbiter active thermal-control system (ATCS). The payload heat load, together with loads from the various orbiter heat sources, are absorbed into the orbiter ATCS Freon-21 coolant loop as shown in Fig. 18.25. The ATCS, in turn, rejects the heat to one of the following sinks:

- GSE heat exchanger (during prelaunch and approximately 45 min after landing)
- flash evaporator (during ascent and deorbit)
- radiator supplemented by flash evaporator (on orbit)
- radiators and ammonia boiler operation (during descent and postlanding)

The payload heat exchanger has two passages available to payloads. One is normally provided to payloads in the middeck, and the other is provided to payloads in the payload bay. However, both passages can be made available to payloads in the payload bay. The supply temperature to the payload is a function of actual heat-exchanger performance and should be based upon the effectiveness curves defined in ICD 2-19001. Dual use of the payload heat exchanger will reduce performance, and the supply temperature will be determined by NASA/USA. The cooling capacity available at the payload heat exchanger varies as a function of mission phase. Cooling during the prelaunch, ascent, descent, and postlanding phases is limited to 1525 W. The on-orbit capacity is 8500 W after the payload-bay doors are opened. For checkout purposes, the 8500-W capacity is available for limited time periods during prelaunch; however, this availability requires special negotiation with NASA/USA, and the capacity is not available during the final hours of countdown. In addition, the cooling capacity for middeck payloads is limited to an amount that is not greater than the electrical power available to middeck payloads and that will not cause the cabin temperature limit to be exceeded during any mission phase.

The customer provides a pump package with an accumulator and controls coolant flow rate and pressure (123 N/cm^2 maximum) on the payload side of the heat exchanger. In addition, the customer is responsible for freeze protection, filtration, and instrumentation. Freon 114 or water may be used in the payload bay; however, Freon 114 is recommended to avoid potential freezing problems. The required coolant for middeck payloads is water, which is not expected to have freezing problems as long as at least two orbiter fuel cells are operating at a total of 11 kW. Water coolant is also required for habitable modules in the payload bay.

Although lines are insulated, stagnant sections of water lines may require heaters when water is used as a coolant for payloads in the payload bay. Failure modes that preclude proper water flow rates can cause water to freeze. When water is used as a coolant, a minimum flow rate of 4.6 kg/h is required during all on-orbit periods to prevent freezing. Water-line freezing can cause payload heat-exchanger over pressurization and present a catastrophic hazard to the orbiter if both orbiter Freon loops are lost.

In addition to having a maximum operating pressure of 123 N/cm^2, the payload must also withstand 123 N/cm^2 on the payload side of the heat exchanger if a leak develops in the heat exchanger between the payload side and the orbiter side.
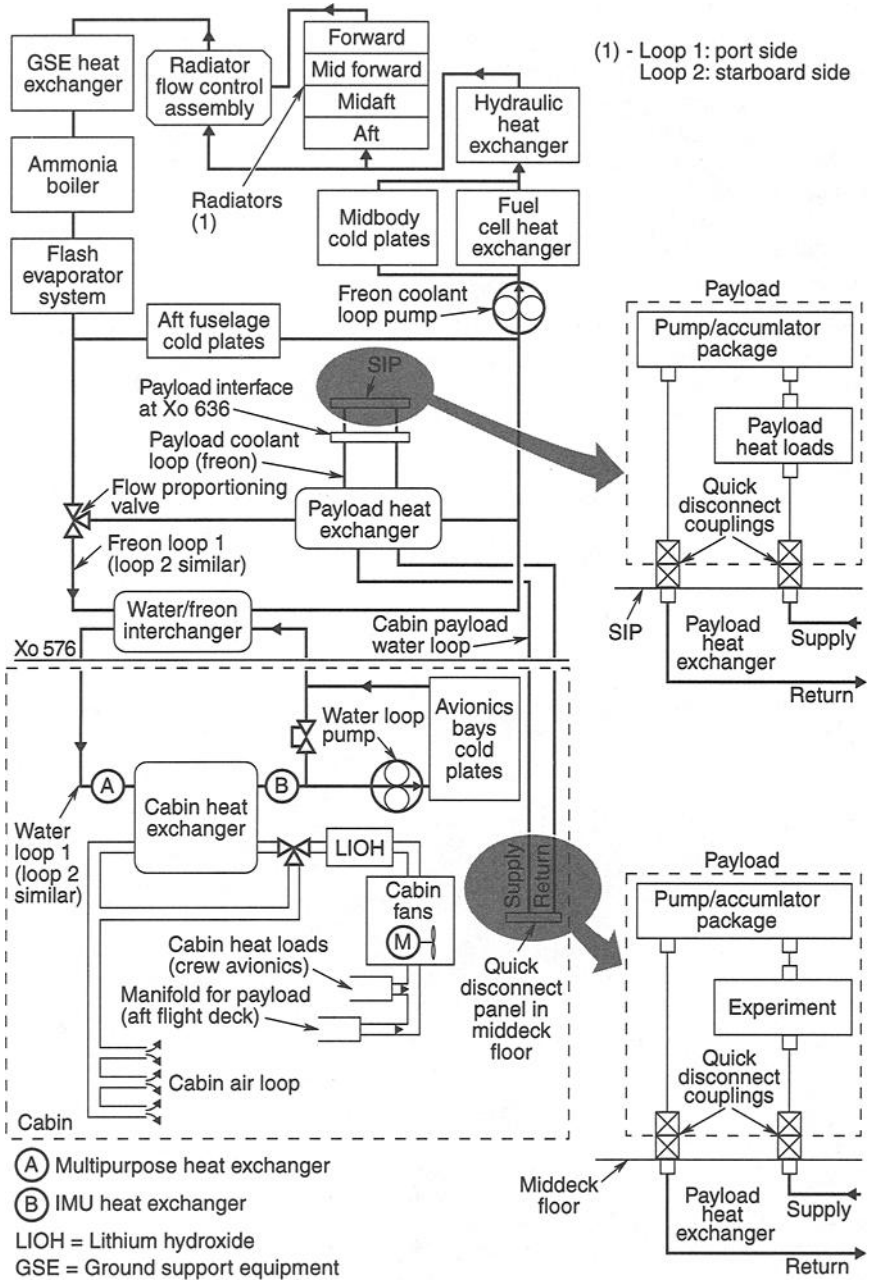
Fig. 18.25. Simplified orbiter active cooling system.

Payload Active Cooling Kit (PACK)

For a payload located in the payload bay, a PACK (Fig. 18.26) provides a connection to the orbiter ATCS. The plumbing interconnecting the PACK and the payload is furnished by the customer. The PACK interface is located on a standard interface panel on the port side of the orbiter at a longitudinal position specified in the payload-unique ICD. The PACK installation is designed for a wet mate (quick disconnect) interface and accommodates either horizontal installation of payloads in the Orbiter Processing Facility (OPF) or vertical installation at the launchpad. The quick disconnects are furnished by NASA/USA.

PACK Leakage Rates

For payload system analyses, the PACK leakage rates in Table 18.5 are used. The ground condition assumes an internal pressure of 41 N/cm^2 and an external pressure of 10.1 N/cm^2. The on-orbit condition assumes an internal pressure of 69.0 N/cm^2 and a vacuum outside the lines.

Cabin Middeck Payloads

The interface for liquid cooling in the middeck is via NASA-furnished quick disconnects located on the middeck floor as shown in Fig. 18.27. The system is designed for wet mate installation. The coolant plumbing located in the cabin
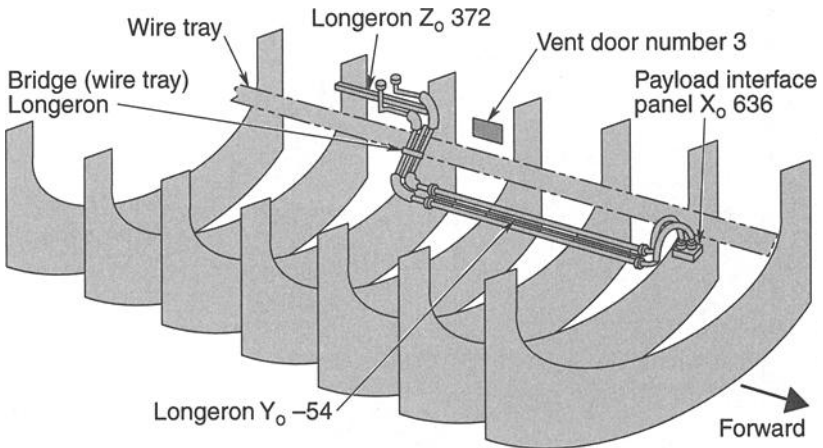
Fig. 18.26. Typical PACK installation.

Table 18.5. PACK Leakage Rates

	Ground (cm^3/h)	On-Orbit (cm^3/h)
Water	0.1	0.2
Freon 114	0.2	0.5
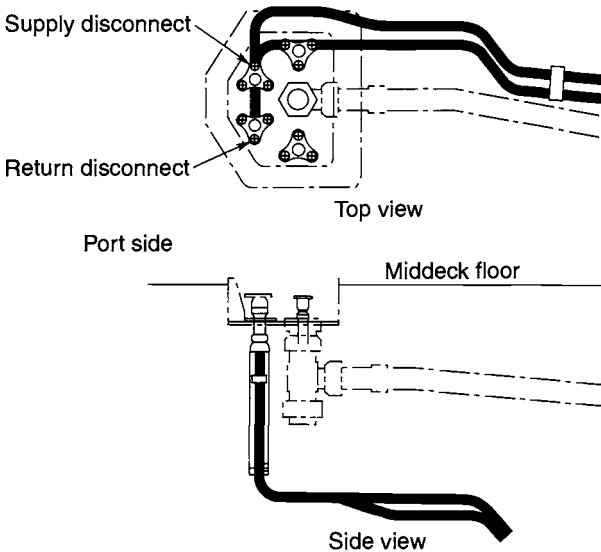
Fig. 18.27. Payload interface with the water loop in the orbiter middeck.

must be appropriately insulated to preclude condensation. Also, if the payload uses an air-to-water heat exchanger, the coolant water-temperature inlet should be controlled so that water does not condense at the heat exchanger. Maximum cabin dew point is defined in Shuttle/Payload Interface Definition Document for Middeck Payload Accommodations, NSTS 21000-IDD-MDK.

Prelaunch/Postlanding Spigot Cooling

Three gas-cooling spigots are available to supplement the standard payload-bay purge during prelaunch operations and the postlanding period at primary and alternate landing sites. If spigots are used, NASA designs and fabricates the ducting and support fixtures from the negotiated payload interface to one or more spigots, as required. The nominal flow of 22 kg/min is available from each spigot if all three spigots are utilized. If only one of them is used, the maximum flow rate is 45 kg/min for it. Since the spigot system is part of the payload-bay purge system, the conditioned gas is the same as the purge supply. Therefore, system designers must negotiate gas conditions and flow rates needed for compatibility with other payloads that are manifested for the flight.

Aft-Flight-Deck Air Cooling

Orbiter air ducting can provide air cooling for electronics boxes compatible with cooling by forced convection. Cabin air, at 35°C maximum, is drawn into the box and exits (via an orifice and interface duct) into the orbiter manifold duct. The orifice and interface duct are provided by NASA/USA. The combined pressure drop for the avionics box, the orifice, and the interface ducting is limited to 2.54 cm of water at the design air flow of 0.185 kg/h/W. Therefore, the payload-unique ICD must define the pressure-drop allocation for the payload. After the completion of

avionics-box pressure-drop testing (provided by the customer), the orifice is sized so that the total pressure drop is 2.54 cm of water. The payload-unique ICD is then updated, if necessary, to define the maximum pressure drop for the payload, as well as the other unique parameters (heat load, air-flow requirement, and geometric and connection interface definition).

Payload Station and Mission Station Support (10.1 N/cm^2 Cabin Pressure)

The orbiter can provide for the removal of a combined total of 725 W average from both stations during on-orbit operations. For prelaunch, ascent, descent, and postlanding, the air cooling is limited to 350 W. The above values include up to 100 W of cooling for aft-flight-deck payload equipment consuming small quantities of power (10 W each) by direct radiation or convection to the cabin. Specific forced-air cooling is not provided for these low-power boxes.

Total air flow available to the aft-flight-deck stations is approximately 135 kg/h but depends on the flow distribution requirement between the payload and mission stations as defined in the IDD. Air-cooled avionics air flow is provided at a rate of 0.185 kg/h/W of heat load, and therefore, cooling design is based on an air-temperature increase of 19°C across each avionics box.

Physical Location and Ducting Installation

Payload areas in the aft flight deck are shown in Fig. 18.28. Only compartments at L10, L11, L12, and R11 are dedicated for air-cooled payloads. Figure 18.29 depicts isometric views of the orbiter manifold duct at both the payload and mission stations. The available area for duct routing and connection accessibility is very limited because of wiring, connectors, and secondary structure, so NASA/USA provides interface ducting (between the manifold and avionics box) and installs the required orifice previously discussed.

Operation at Reduced Cabin Pressure

All air-cooled equipment may be subjected to reduced air flow because of the reduction of cabin pressure from 10.1 to 7.0 N/cm^2. The 7.0 N/cm^2 condition is implemented to accommodate on-orbit pre-EVA (prebreathe) operations, and it could last the entire on-orbit duration for some missions. The resulting air flow equals the 10.1 N/cm^2 air flow times the pressure ratio of the reduced cabin pressure (7.0 N/cm^2) to the normal cabin pressure (10.1 N/cm^2). The maximum air-inlet temperature for this condition is 27°C.

Another mode of reduced cabin pressure is the 5.5 N/cm^2 contingency mode. This mode, which occurs in the event of a puncture in the pressure walls of the cabin, is considered an abort mode. All payload equipment is powered off for this cabin condition so that maximum heat rejection is available for orbiter use.

Middeck Ducted Air Cooling

The ducted air-cooling interface is defined in NSTS 21000-IDD-MDK for middeck locker payloads that require active cooling. Each locker payload must provide its own circulation fan to draw air from the avionics-bay volume and dump hot (return) air into the orbiter return air duct. The avionics-bay volume (supply) air temperature is nominally 27°C, except during ascent, entry, and certain mission
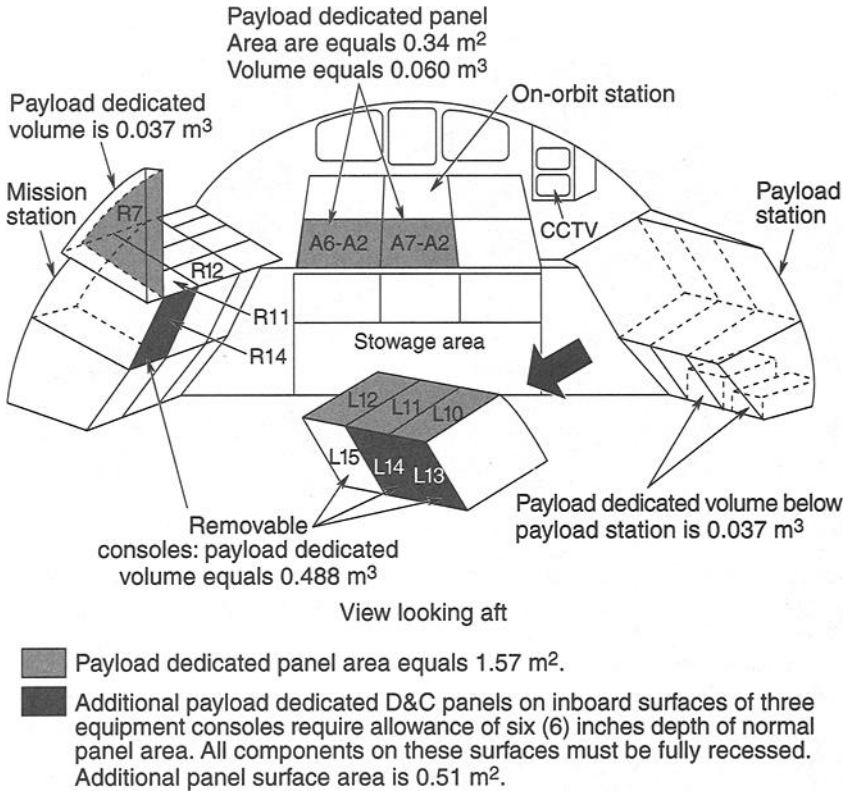
Fig. 18.28. Shuttle orbiter aft flight deck.

phases. The supply air for these mission phases is 29°C nominally with possible 10-min spikes up to 35°C. The services are available in avionics bays 1, 2, and 3A. The locker locations with the cooling interface in each bay are also identified in NSTS 21000-IDD-MDK. Each location has a dedicated air-cooling flow rate of either 51 or 102 liters/minute.

Middeck Accommodations Rack (MAR) Cooling

The MAR is designed to permit integration of small payloads and experiments into the middeck and supplement the middeck lockers. The payloads that use it must meet the requirements specified in NSTS 21000-IDD-MDK or those negotiated through the IP process. The amount of heat that can be dissipated into the cabin environment or into the orbiter coolant loop is limited to values dependent upon specific mission capabilities. The maximum heat loads that a payload is permitted to dissipate into the cabin atmosphere are specified in NSTS 21000-IDD-MDK or negotiated through the IP process.
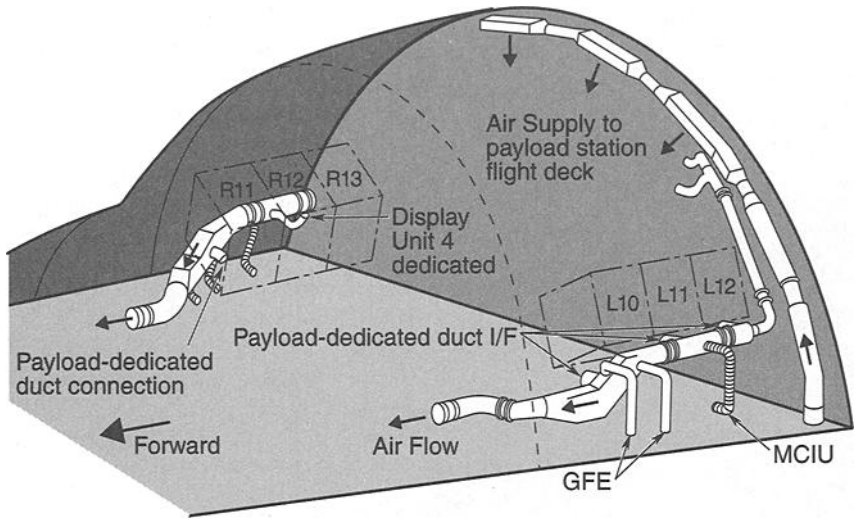
Fig. 18.29. Aft-flight-deck air-duct interface locations.

Thermal control for payloads or experiments installed in the MAR is obtained through one of the following methods, which must be approved through the IP negotiation with NASA:

- **Passive thermal control:** All payload-generated heat is conducted or radiated to the MAR structure for reradiation to the middeck cabin environment. Convective circulation of cabin air past the MAR dissipates the heat. A thermal-closeout panel is not installed when this method of thermal control is used.

- **Active thermal control:** A thermal-control module called the MAR cooling module, utilizing a water-to-air heat exchanger, is designed to dissipate heat loads of up to 1000 W of payload-generated heat with 28°C coolant temperature change. An integral fan and system of ducting create a closed system that circulates payload-heated air through the heat exchanger and back past the payload components. A payload-supplied thermal-closeout panel is installed when this method of thermal control is used.

- **Water-circulating pumps only:** The MAR cooling module is fabricated so that the circulating pumps and accumulator can be used alone. This is to accommodate users wanting water circulation through cold plates or a water jacket for thermal control. Using this system, a payload can get more than 1000 W of cooling if the orbiter payload cooling loop has enough reserve to allow it.

- **Payload-unique module:** When dictated by design of a payload or experiment, a payload-unique thermal-control module can be installed in the MAR for direct connection to the orbiter heat-exchange loop. All coolant lines and cold surfaces need insulation to prevent or minimize condensation. Installation of the thermal-closeout panel is optional when this method of thermal control is used.

19 Thermal Testing

J. W. Welch[*]

Introduction

To ensure successful vehicle and payload operation, space programs subject hardware to extensive ground testing. Thermal tests demonstrate the performance and operation of units, subsystems, payloads, and entire space vehicles in thermal environments that are, at minimum, realistic simulations of flight conditions. At the unit level, these tests include thermal cycling and thermal vacuum tests. At the space vehicle level, they include thermal cycling, thermal vacuum, and thermal balance tests. This chapter provides the objectives of each thermal test and describes the test parameters and procedures used to meet those objectives.

Over the past decades, a series of documents has specified and described military requirements for spacecraft thermal testing. The first, MIL-STD-1540A, was written in 1974 for Department of Defense space programs to standardize test requirements and establish a uniform set of definitions, environmental criteria, and test methods for military space vehicles, subsystems, and units. It introduced a common language defining test categories, levels, and sequences.

Published in 1982, MIL-STD-1540B was an update to MIL-STD-1540A and was oriented toward low-risk, long-life space vehicles. This document expanded testing provisions in that it disallowed flying qualification hardware, introduced the protoflight concept, reduced testing requirements for one-time or low-volume programs, separated the roles of workmanship verification and design demonstration, emphasized performance testing, and increased the role of thermal cycling. Three years later, MIL-HDBK-340 was published as an application guideline for MIL-STD-1540, providing much-needed explanations, guidance, and rationale to the users of MIL-STD-1540B.

MIL-STD-1540C, published in 1993, introduced test parameter flexibility and included test requirements for boosters and launch vehicles. It considered cost- and failure-effectiveness knowledge based upon statistical data and realigned definitions into a more standard terminology. To introduce industry practices related to the rapid expansion of commercial programs, MIL-STD-1540D was published in 1999. While it retained MIL-STD-1540C requirements as an attachment in MIL-HDBK-340A, MIL-STD-1540D was process oriented, providing "what to" and not "how to" guidelines. It aligned expected methodologies and acceptance testing requirements without specifically directing test practices and procedures.

The consequences of acquisition reform dramatically changed the process with which space hardware requirements are verified. In line with commercial practices, risk became a managed parameter, weighed against program cost and schedule. The industry response to MIL-STD-1540D has been mixed. Several companies whose prime customer remains the Air Force have developed internal

*The Aerospace Corporation, El Segundo, California.

environmental test documents based upon previous experiences with MIL-STD-1540 test requirements. Companies whose principal products are commercial spacecraft have adopted test practices that reflect commercial practices. These requirements tend to emphasize reduced cost and schedule testing with higher risk acceptance. Still other companies have proposed tailored versions of MIL-STD-1540C.

The reality of acquisition reform in the context of thermal testing is that non-commercial test requirements are moving toward equivalent commercial practices. For commercial spacecraft whose programs represent more than just a few vehicles, a higher level of risk may be acceptable. Military customers, however, are less willing to accept the level of risk associated with commercial vehicles, so the process of applying commercial practices to military programs is still in its infant stage. A primary observation is that without standard test requirements, such as those provided by MIL-STD-1540, the effectiveness of testing is a subject of debate. Acquisition reform should have resulted in "smarter testing"; instead the prevailing attitude favors test deletion.[19.1]

References to thermal test parameters in this chapter are keyed to requirements given in MIL-STD-1540B or MIL-STD-1540C. Present trends and current practices as they compare to MIL-STD-1540 recommendations are also discussed. Brief summaries of commercial and NASA space program thermal test practices are also provided.

Definitions

The following definitions have contributed to the establishment of a common terminology within the thermal testing community.

Item Levels

Unit

A unit is a functional item that is viewed as a complete and separate entity for purposes of manufacturing, maintenance, or record keeping. Examples include individual electronics box, battery, thruster, and electrical harness.

Subsystem

A subsystem is an assembly of functionally related units. It consists of two or more units and may include interconnection items, such as cables or tubing, and the supporting structure to which the units are mounted. Examples include electric power, attitude control, telemetry, thermal control, and propulsion subsystems.

Launch Vehicle

A launch vehicle is one or more of the lower stages of a flight vehicle capable of launching upper-stage vehicles and space vehicles, usually into a suborbital trajectory. A fairing to protect the space vehicle, and possibly the upper-stage vehicle, is typically considered to be part of the launch vehicle.

Upper-Stage Vehicle

An upper-stage vehicle is one or more stages of a flight vehicle capable of injecting a space vehicle or vehicles into orbit from a suborbital trajectory that resulted from operation of a launch vehicle.

Space Vehicle

A space vehicle is an integrated set of subsystems and units capable of supporting an operational role in space. A space vehicle may be an orbiting vehicle, a major portion of an orbiting vehicle, or a payload that performs its mission while attached to a launch or upper-stage vehicle. The space vehicle includes the payloads that constitute its mission.

Test Categories

Development Tests

Development tests, also known as engineering tests, are conducted to accomplish a number of objectives, including the validation of new design concepts and the reduction of risk in committing designs to hardware fabrication. A full list of development test objectives will be given in a subsequent section.

Requirements for a development test depend upon its objective, the maturity of the subsystem and units, and the operational requirements of the specific program or hardware. Development test requirements are necessarily unique to test objectives and are not specified in military or commercial standards. Development tests may be conducted on breadboard equipment, prototype hardware, or engineering models.

Qualification Tests

Formal qualification tests are conducted to demonstrate that the design, manufacturing process, and acceptance program produce mission items that meet specification requirements. Qualification tests also validate the planned acceptance program, including test techniques, procedures, equipment, instrumentation, and software.

Each type of flight item that is to be acceptance tested undergoes a corresponding qualification test, with the exception of some structural items. The test item is produced from the same drawings that are used for production of the flight hardware. Its production uses the same materials, tooling, manufacturing processes, and level of personnel competency as are used for production of the flight hardware.

To demonstrate design, the qualification environment exposes the qualification hardware to conditions more severe than expected during the operational life of the flight hardware. It considers not only the most extreme flight environments, but also the maximum number of cycles that can be accumulated in acceptance testing and retesting. Because of the severity of this environment, qualification hardware is not flown.

Acceptance Tests

Formal acceptance tests demonstrate the acceptability of a deliverable item. They verify conformance to specification requirements and provide quality-control

assurance against workmanship and material deficiencies. Acceptance tests act as an environmental stress screen to precipitate incipient failures resulting from latent defects in parts, materials, and workmanship. These tests, which are conducted after qualification testing, prove the flightworthiness of the article.

Alternative Test Strategies

Hardware items subjected to qualification tests are themselves not eligible for flight, because remaining life from the viewpoint of fatigue and wear has not been demonstrated. Yet programmatic realities of limited production, tight schedules, and budgetary constraints do not always provide for dedicated nonflight qualification items. In response, strategies have evolved to minimize the risk created by this situation. The concepts of spares, flightproofing, and protoqualification provide alternative test strategies for flight items that do not follow the qualification acceptance test sequence. These strategies, or a combination thereof, may be used at the vehicle, subsystem, and unit levels. They introduce a higher risk to the program than the standard acceptance test that follows qualification and design verification. The higher risk is sometimes mitigated by enhanced development testing and by increased design factors of safety.

Spares

In the spares concept, a qualification vehicle is refurbished with acceptance tested units. Qualification units are removed from the qualification vehicle, and the vehicle is refurbished as necessary. Usually a new set of critical units is installed that has only been acceptance tested. The vehicle is qualified for flight when it completes vehicle acceptance testing.

Flightproofing

With a flightproof strategy, all flight items are subjected to enhanced acceptance testing, and there is no qualification item. The risk is that reduced test margins allow possible design deficiencies to remain undetected, and formal demonstration of remaining life for the flight item does not exist. The risk is partially alleviated by acceptance testing the flight item to environmental stresses greater than those specified for acceptance tests (but less than qualification requirements).

Protoqualification

With a protoqualification strategy (also termed protoflight qualification, protoflight, or protoqual), a modified qualification (protoqualification) is conducted on a single item, and that test item is considered available for flight. The normal acceptance tests are then conducted on all other items. The primary difference between protoqualification and flightproof strategies centers on the number of items tested in the enhanced acceptance environment. Under flightproofing, all flight items are subjected to the enhanced acceptance environment, whereas under protoqualification, only one of a group of identical items is subjected to the enhanced acceptance environment.

Thermal Test Objectives

Environmental Stress Screening

Environmental stress screening is the process that subjects hardware to physical stresses and forces flaws that are not ordinarily apparent into observable failures. These flaws are latent defects that could cause premature component failure. The environment associated with environmental stress screening is more severe than the one expected in actual usage. In thermal testing, the test temperature, the number of test cycles, and the rate of temperature change are parameters that establish the efficiency of environmental stress screening.

Turn-On Capability

Turn-on capability demonstrates that a unit can be activated within a severe environment. For thermal verification, turn-on might be shown at hot and cold temperatures, in a rapidly changing temperature environment, or under severe thermal gradients.

Survival Demonstration

Survival temperatures represent the range over which a unit is expected to survive. The unit must demonstrate that it can be turned on at these temperatures, and although performance does not need to meet specification at these extreme temperatures, the unit must not show any performance degradation when the environment or unit temperature is returned to the unit's operational temperature range. The survival range is the most severe temperature range specification for a unit. Survival temperatures are sometimes given as operational survival and nonoperational survival. The cold turn-on temperature is often identical to, or nearly the same as, the cold survival temperature.

Thermal Tests

Thermal Cycle Tests

Thermal cycling subjects the test article to a number of cycles of hot and cold temperature plateaus in an ambient air or gaseous nitrogen environment. Convective heat transfer is enhanced such that the cycling can be relatively rapid. Cycling serves primarily as an environmental stress screen by revealing latent workmanship or material defects. Performance verification is a secondary objective accomplished through functional tests performed at hot and cold temperature plateaus.

Thermal Vacuum Tests

Thermal vacuum tests subject the test article to a number of cycles of hot and cold temperatures in a vacuum environment. Because it is conducted without convective heat transfer, this test is the most realistic ground simulation of the flight environment. Therefore its primary purpose is performance verification through functional testing. Temperature transition is slower than in the thermal cycling test, so stress screening is of secondary importance.

Thermal Balance Tests

Thermal balance tests, usually performed as part of subsystem or space vehicle thermal vacuum testing, have two purposes: verification of the thermal control

subsystem and correlation of thermal analytic models. Dedicated test phases that simulate flight conditions are used to gather steady-state temperature data that are compared to model predictions. Test phases also simulate cold and hot conditions to verify all aspects of the thermal hardware and software, including heater operation, radiator sizing, and critical heat transfer paths.

Burn-In Tests

Burn-in tests are typically part of unit thermal cycle tests in which additional test time is accrued to meet a set requirement. The unit is either cycled or held at an elevated hot temperature during the burn-in test, and the unit is operational, although functional tests are not performed.

Thermal Margins

Thermal Uncertainty Margin

The thermal uncertainty margin is a margin of safety applied to worst-case analytic temperature predictions (from all mission phases) to account for uncertainties inherent in parameters such as complex view factors, surface properties, radiation environment, joint and interface conduction, and ground simulation. For passive thermal control, the thermal uncertainty margin is a temperature added to worst-case temperature predictions. For active thermal control, the thermal uncertainty margin is a power margin to increase control authority. When the margin is added to worst-case temperature predictions, the resulting temperature forms the basis for the acceptance temperature range.

Protoqualification Thermal Margin

The protoqualification margin is the temperature margin added to acceptance temperatures for protoqualification testing. The margin is intended to increase the severity of the acceptance test environment, but not to the same extent that the qualification environment stresses the test hardware.

Qualification Thermal Margin

The qualification margin is the increase in an environmental condition over that expected during service life, including acceptance testing, to demonstrate that adequate ruggedness exists in the design and in its implementation. A margin may include an increase in level or range, or an increase in duration or cycles of exposure, as well as any other appropriate increase in severity. It is used to prove the design of the test hardware by exposing design defects, to demonstrate robustness, to show tolerance to degradation (fatigue and wear), and to prove test condition tolerances.

Additional Terminology

Temperature Stabilization

Temperature stabilization is a criterion that establishes the point at which the test hardware has reached a stable, or nearly steady, thermal equilibrium with the test environment and is within the test tolerance of the prescribed test temperature. For both thermal cycle and thermal vacuum testing, temperature stabilization for a unit is achieved when the unit baseplate is within the allowed test tolerance on the

specified test temperature, and the rate of temperature change has been less than 3°C per hour for 30 minutes. For steady-state thermal balance testing, temperature stabilization is achieved when the unit with the largest thermal time constant is within 3°C of its steady-state value, as determined by numerical extrapolation of test temperatures, and the rate of change is less than 1°C per hour.

Thermal Dwell

Thermal dwell of a unit at hot or cold extremes is the time required to ensure that internal parts and equipment have achieved thermal equilibrium or the test temperature. Thermal dwell begins at the onset of thermal stabilization and is followed by functional or performance testing of the unit.

Thermal Soak

The thermal soak duration of a unit at the hot or cold extreme of a thermal cycle is the time that the unit is operating and its baseplate is continuously maintained within the allowable tolerance of the specified test temperature.

Thermal Test Tolerance

The thermal test tolerance is the temperature tolerance accepted for thermal test parameters and conditions. Unless otherwise stated, thermal test parameters should be assumed to include the maximum allowable test tolerance of ±3°C over an applicable temperature range of −54 to +100°C. For conditions outside this range, the tolerance should be appropriate for the purpose of the test.

Design Environments

Thermal Environments

A thermal design environment includes the heat flowing into and out of a system, be that system a unit, a radiator surface, or a complete space vehicle. External heating from the sun, Earth, and other planets combines with internal heat generation to form the input to an energy balance. Radiation, conduction, and convection are modes of heat transfer that are used to assess heat flow throughout and across the boundaries of the system. These phenomena result in a representation of the thermal behavior of the system that allows heat flow and temperatures to be predicted for different environmental conditions.

In the design process, considerable time is spent analyzing realistic thermal environments to determine which conditions will be the most stressing. The selection of the worst-case environment considers all possible combinations of worst-case conditions that could occur during each operation mode. Factors include time of year, sun-orbit orientation, eclipse duration, operational mode, time of mission (beginning- or end-of-life), and surface degradation. These worst-case conditions are used to predict, using thermal analytic models, the hottest and coldest temperatures the unit or system may experience in its mission life. These values are computed unit by unit, as a worst-case combination of conditions for one unit may not prove to be worst case for another. The hottest and coldest temperatures establish a range called the nominal extreme temperature range (or analytic extreme temperature range), which is the basis for all test temperatures.

Process of Establishing Test Temperatures

The process of determining test temperatures will be described as applicable for military programs, and variations to this process will follow.

Unit Level Test Temperatures

Figure 19.1 illustrates how test temperatures are determined for units. To the nominal extreme temperatures, a thermal uncertainty margin is added. This margin, which can be quite large at the beginning of a program (e.g., 17 to 40°C), is reduced as the design and analysis process progresses. Following successful correlation of the thermal analysis with thermal balance test data, the thermal uncertainty margin can be reduced to ±11°C. If a unit is heater controlled at the cold extreme, 25% excess heater control authority is used in lieu of an 11°C temperature margin.

   The temperatures thus derived are named the maximum and minimum expected temperatures (maximum and minimum predicted temperatures in MIL-STD-1540B), and they establish the unit acceptance test levels, subject to the requirement that the mounting plate, shelf, or case temperature be at least as cold as −24°C and at least as hot as +61°C. If the minimum expected temperature is greater than −24°C, the cold acceptance temperature is lowered to −24°C; if the maximum is less than +61°C, the hot acceptance temperature is raised to +61°C. Testing beyond the nominal extreme temperature range at the unit level has proved successful for many years in reducing mission risk by (a) providing adequate environmental stress screening, (b) demonstrating unit survival capability, and (c) ensuring that temperature-insensitive and high-quality parts and materials are used in the design.
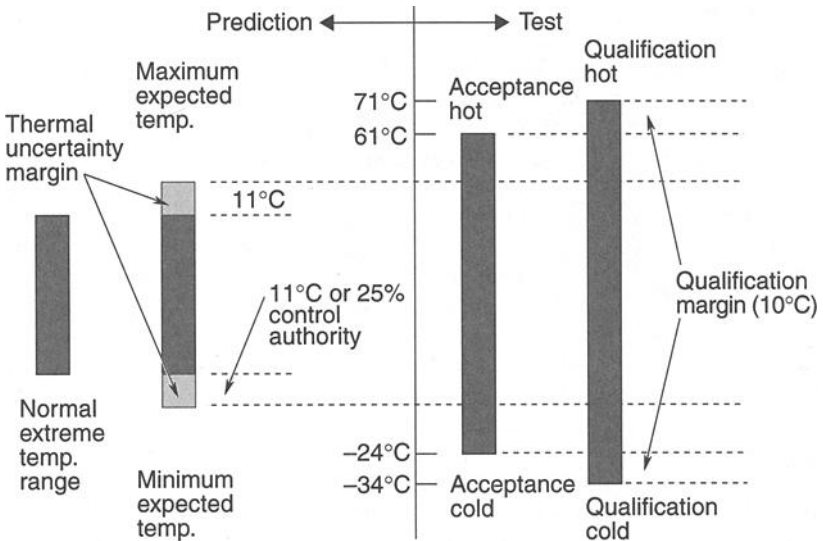
Fig. 19.1. Unit level predicted and test temperature ranges.

Unit qualification tests are conducted at temperatures 10°C colder (even if heaters are used for thermal control) and 10°C hotter than the acceptance test temperatures, subject to the constraint that the mounting plate or shelf be at least as cold as –34°C and at least as hot as +71°C.

With a protoqualification approach, a modified qualification test is performed on a single item, and that test item is then available for flight. The primary objective of qualification testing (verifying the design of the test article) is combined with the primary objective of acceptance testing (verifying the article's workmanship and flightworthiness) in this single test. Because this strategy eliminates the redundancy of building qualification hardware, it enables significant cost savings. At the unit level, protoqualification thermal testing is performed with the same test parameters as qualification testing, except the hot and cold temperatures are 5°C beyond the acceptance temperatures.

Certain temperature-sensitive units are sometimes exempt from the design margins described. Candidates for margin waiver are units that exhibit extremely tight operating temperature ranges (e.g., batteries, propellant valves, extremely accurate clocks, and some inertial reference units). Batteries are usually tightly controlled toward cold temperatures to increase life. Representative range values for NiCd batteries are: operating, 0 to +25°C; survival/turn-on, –10 to +40°C.

System Level Test Temperatures

At the system level, test temperature extremes are established for individual zones of the space vehicle. The zones represent logical groupings of similar equipment types and similar temperature ranges. Each is managed independently to achieve different temperature ranges. In each zone, as many units as are practical (but at least one) are driven to the zone's hot and cold temperature extremes, which include the appropriate thermal margins (acceptance or qualification). Care must be exercised and sufficient instrumentation installed to assure that no unit is exposed to temperature conditions beyond its unit test temperature.

System level temperature margins are the same as those used for unit level testing: the thermal uncertainty margin is 11°C, and the qualification margin is 10°C. Implementation of the thermal margin at the system level, however, depends upon the thermal test. Thermal vacuum testing applies both margins in a manner similar to unit level testing. Thermal cycle testing, on the other hand, specifies a total temperature range over which the satellite is tested. For acceptance testing, the minimum vehicle temperature range is 50°C; for qualification testing, 70°C.

Protoqualification testing at the system level is similar to protoqualification testing at the unit level. The thermal vacuum test has a 5°C margin beyond the acceptance temperature, and the thermal cycle test is performed over a 60°C range.

In practice, the approach described in establishing test temperatures is generally implemented as presented. The greatest deviation arises from using the standard acceptance temperature range of –24°C to +61°C for unit thermal testing. As in the case of batteries, some units have restricted thermal operation, such that these temperature ranges are not practical. In other cases, reliability concerns with operating equipment at elevated temperatures result in thermal designs that are biased in temperature to a worst-case hot value significantly colder than +61°C. Payload equipment is one such example where operational performance is sometimes not

possible at elevated hot temperatures. As a general rule, however, electronic equipment should be tested to as wide a temperature range as possible at the unit level to enhance the effectiveness of environmental stress screening.

Thermal Uncertainty Margin

As previously stated, the thermal uncertainty margin is a margin of safety used to account for uncertainties such as complex view factors, surface properties, radiation environment, joint and interface conduction, and ground simulation. The margin recognizes that many assumptions are used in the development of thermal analytic models that calculate temperature predictions. These assumptions have inherent uncertainties that can result in temperatures significantly different than those predicted with analytic thermal models. Units mounted internally are modeled with uncertainties associated with power dissipation, interface conduction, material conductivity, and boundary conditions. Units mounted externally typically have much higher uncertainties in thermal design parameters, such as view factors, environmental heating, and surface properties, as well as the uncertainties listed for internally mounted units. As a result, externally mounted equipment commonly carries thermal uncertainty margins greater than the minimum value.

Thermal uncertainty associated with temperature predictions is reduced during the design-analysis-test process as the hardware design becomes firm, as improved and more detailed analyses are conducted, and as development tests are completed. The thermal balance test substantially reduces temperature-prediction uncertainty. Deviation between on-orbit temperature measurements and preflight temperature predictions is a measure of the final uncertainty between the analytic and test processes.

The ±11°C thermal uncertainty margin is the result of extensive comparisons between preflight predictions and flight temperature measurements. In a report by Stark[19.2] that summarized much of the work, a study of 20 critical spacecraft units showed that the thermal balance test and subsequent model correlation reduced the standard deviation between prediction and on-orbit measurement from 9 to 5.5°C. As the intent of MIL-STD-1540 is to have a 95% (2-σ) confidence that design temperatures (maximum and minimum expected temperatures) are never exceeded in flight, the military practice is to use the 11°C thermal uncertainty margin for predictions verified by thermal balance test results and margins greater than this for unverified analytic predictions. Some have further proposed that the minimum thermal uncertainty margin be 17°C prior to the thermal balance test. As result of this work and the significant data accumulated since this report, the ±11°C uncertainty margin has been shown necessary to assure high confidence that flight temperatures will not exceed minimum and maximum expected unit temperatures.

Passive and Active Thermal Control Methods

The thermal uncertainty margin varies depending on whether passive or active thermal control techniques are used. The ±11°C margin is used for hardware controlled by passive methods and a 25% control authority margin is used for hardware controlled by active methods. Table 19.1 categorizes thermal control methods as active or passive and can be used for selecting the appropriate thermal uncertainty margin.

Table 19.1. Categorization of Passive and Active Thermal Control Methods

Passive	Active
Constant conductance or diode heat pipes	Variable conductance heat pipes, looped heat pipes, or capillary pumped loops
Hardwired heaters (fixed and variable-resistance, such as auto-trace or positive temperature-coefficient thermistors)	Resistance heaters with commandable mechanical or electronic controllers
Thermal storage devices (phase change or sensible heat)	Heat pumps and refrigerators
	Stored coolant systems
Thermal insulation (multilayer insulation, foams, or discrete shields)	Pumped fluid loops
Radiators (fixed, articulated, or deployable) (with louvers or pinwheels)	Thermoelectric coolers
Surface finishes (coatings, paints, treatments, second-surface mirrors)	

For designs that employ active thermal control techniques, a heat load margin of 25% may be used in lieu of the temperature margin. This margin is applicable at the condition that imposes the maximum and minimum expected temperatures. For example, for heaters regulated by a mechanical thermostat or an electronic controller, a 25% heater-capability margin may be used in lieu of the thermal margins at the minimum expected temperature and a minimum bus voltage. Like the thermal uncertainty temperature margin, the control authority uncertainty margin has been established based upon flight experience. The margin is demonstrated first in analysis, then in test, by monitoring the heater duty cycle. A maximum duty cycle of 80% demonstrates that the heater system has the required margin. Analysis may be necessary to show the equivalency of the 80% duty cycle when the heater temperature set point is greater than the minimum design requirement or when the input voltage is greater than the minimum design value. For example, a unit heater might be selected with a set point 6°C higher than the minimum expected temperature of 4°C. Because more heat is required to maintain the unit at 10°C than to maintain it at 4°C, the demonstrated duty cycle can be greater than 80%. In this case, a 92% duty cycle measured with the 10°C set point might be shown by analytic means to have capability equal to or greater than the 80% duty-cycle design requirement for a set point of 4°C.

A requirement for heater margin in excess of 25% (i.e., duty cycles of less than 80%) may apply where small capacity heaters are used or where an 11°C decrease in the minimum local environment may cause a heater with a 25% margin to lose control authority.

Additional guidance for specific devices listed in Table 19.1 is provided in the following sections.

Constant Conductance or Diode Heat Pipes

Constant conductance or diode heat pipes are categorized as passive devices because they require no power input and move heat from one location to another

with a minimal temperature difference. Thermal performance testing, which is conducted at the highest assembly level practical (subsystem or space vehicle level), should demonstrate the ±11°C margin and should also, if possible, provide data to show each heat pipe is functional at the system level acceptance test. The design is verified by demonstrating at the unit level the heat transport capability with at least 125% of that required for the nominal predicted heat under the temperature conditions providing the smallest capacity margin. The nominal heat load is defined as that predicted by the analytical model in its worst-case condition.

Variable Conductance Heat Pipes

Variable conductance heat pipes using noncondensable gas reservoirs for temperature control are categorized as active devices in Table 19.1. Although they work very similarly to constant conductance heat pipes, which are categorized as passive devices, variable conductance heat pipes almost always utilize heaters or another provision to control the gas-front radiator area. Thermal performance testing, which is also conducted at the highest assembly level practical, should demonstrate an acceptable heat rejection margin, variable conductance range, and heat pipe turnoff. The ability of the entire heat pipe system, not just the heat pipe, to reject heat should be verified. Therefore, the test must be performed at a high enough level to demonstrate performance parameters (with margin) that include the radiator area and environment. The heat rejection margin is shown when 125% of the nominal predicted heat load is applied to the evaporator mounting plate, under the worst-case hot simulated conditions, and the plate temperature is equal to or less than the maximum expected temperature. The variable conductance range is shown when 110% of the nominal predicted heat load is applied to the evaporator mounting plate, under the worst-case hot simulated environmental conditions, and the heat pipe still possesses variable conductance, as proven by the location of the gas or working fluid-vapor interface within the condenser portion of the pipe. Heat pipe turnoff requirements depend upon the type of reservoir in the system. For a heat pipe reservoir with active temperature control, the heat pipe is turned off, i.e., decoupled from the condenser by virtue of the gas (vapor) location, when the evaporator mounting plate temperature is at least 6°C or higher than the minimum expected temperature. For a heat pipe with a passively controlled reservoir, the turnoff points should be at least 11°C higher than the minimum expected temperature.

At the unit level, the heat pipe transport capability should be the same as defined for constant conductance heat pipes, at least 125% of that required for the nominal predicted heat load at the maximum expected temperature of the evaporator. The reservoir and evaporator temperatures may be adjusted as required to facilitate the simplest test procedure with the ambient environment available.

Heaters

Hardwired heaters or heaters using fixed or variable resistance elements that demonstrate a large variation in resistance with temperature are to be treated as passive devices. Resistance heaters with mechanical controllers (such as bimetallic thermostats), or commandable or electronic (solid-state) controllers, are active devices.

Cryogenic Thermal Uncertainty Margins

For passive cryogenic subsystems operating below −70°C, the thermal margin is a function of the operational temperature range. At temperatures significantly below room temperature, thermal uncertainties are managed at a higher level of scrutiny, and an 11°C margin represents an unrealistically high percentage of the operating range and the margin between this range and a temperature of absolute zero. Furthermore, the operating temperature range and the thermal design requirements typically are narrower. Table 19.2 provides specification of the appropriate margin, before and after thermal balance test validation. The decreased temperature margin attempts to retain a constant equivalent heat load margin.

In addition to the temperature margin, thermal uncertainty heat load margins have been recommended for hardware with active thermal control. For designs in which temperatures are actively controlled to less than −70°C by expendable coolants or refrigerators, the thermal uncertainty heat load margin of 25% should be increased in the early phases of development. For these cases, the following heat load margins have been recommended: 50% in the conceptual phase, 45% in the preliminary design, 35% for critical design review, and 30% for qualification.

Commercial Thermal-Margin Practices

Because of the proprietary nature of processes and practices held by contractors in the business of building commercial space vehicles, specific thermal test requirements cannot be disclosed. The following discussion therefore summarizes methodology, common practices, and risk management techniques noted at various commercial organizations.

Risk is managed very differently for commercial space vehicles than for military satellites. Operational capability is marketed as a commodity, so failures in performance rarely completely cripple the general mission. Insurance transfers the economic risk of the mission away from the customer and the contractor. Finally,

Table 19.2. Thermal Uncertainty Margins for Passive Cryogenic Subsystems

Predicted Temperature (°C)	Thermal Uncertainty Margin (°C)	
	Prevalidation	Postvalidation
Above −70	17	11
−70 to −87	16	10
−88 to −105	15	9
−106 to −123	14	8
−124 to −141	13	7
−142 to −159	11	6
−160 to −177	9	5
−178 to −195	8	4
−196 to −213	6	3
−214 to −232	4	2
Below −232	2	1

spacecraft are in some cases operational up to qualification limits, whereas on military programs, mission preservation is critical such that operation rarely exceeds acceptance limits.

Commercial contractors accept higher risk by adopting thermal margins smaller than those used on military vehicles. The basic method of achieving test temperatures, however, has remained unchanged. In some cases, even the margins themselves have not been dramatically compromised from military programs, given the operational practices of these programs. Commercial contractors still compute the minimum and maximum nominal extreme temperatures based upon the worst-case combination of environments and operational conditions. Care is still taken to predict temperatures analytically unit by unit in all mission environments, including launch, ascent, transfer-orbit, on-orbit, eclipse, and safe mode conditions.

Contractors have established the temperature margin between the nominal extreme temperature range and the acceptance test temperature range differently. Several have reduced the margin to 10°C and termed it the thermal uncertainty margin or the acceptance margin. Others have broken this margin into a thermal uncertainty margin and an acceptance margin. A 5°C thermal uncertainty margin and a 5°C acceptance margin are common. The uncertainty margin is maintained throughout the program, despite confidence gained from flight data that might reduce the uncertainty in the analytic predictions. However, contractors are willing to reduce the acceptance margin to 0°C following thermal model correlation. A third approach is to use a 5°C thermal uncertainty margin with no additional margin. Figure 19.2 compares these three approaches to the military practice.

The qualification margin has been nearly uniformly reduced from 10°C on military programs to 5°C for commercial programs, except in the case when the margin between model prediction and acceptance temperatures is only 5°C. If commercial space vehicles are operated to qualification temperatures, then these margins have arguably different roles. Furthermore, qualification units are typically more limited on commercial programs than on military programs, and the use of protoqualification or protoflight units is more common. Protoqualification margins on commercial programs have typically remained at 5°C, which is in agreement with the military program. Protoqualification test temperatures are therefore the same as qualification test temperatures for the first two commercial examples shown in Fig. 19.2.

In general, commercial thermal margins allow more risk than those in military programs, but the basic methodology for determining margins and the basic techniques for implementing them are similar in the two settings. The margins adopted by commercial contractors are in some cases very similar to military ones. For the most part, commercial contractors have experience with the military standards and understand how they were established.

NASA Thermal Margin and Unit Level Testing Practices

In the 1960s the NASA Jet Propulsion Laboratory (JPL) established a short-term allowable flight temperature range of +5 to +50°C for uncrewed lunar and planetary missions. The +5°C lower limit was just warmer than the freezing temperature of hydrazine, and the +50°C upper limit was based upon the temperature of a fully sunlit electronics bay after one hour of heating. A long-term stable
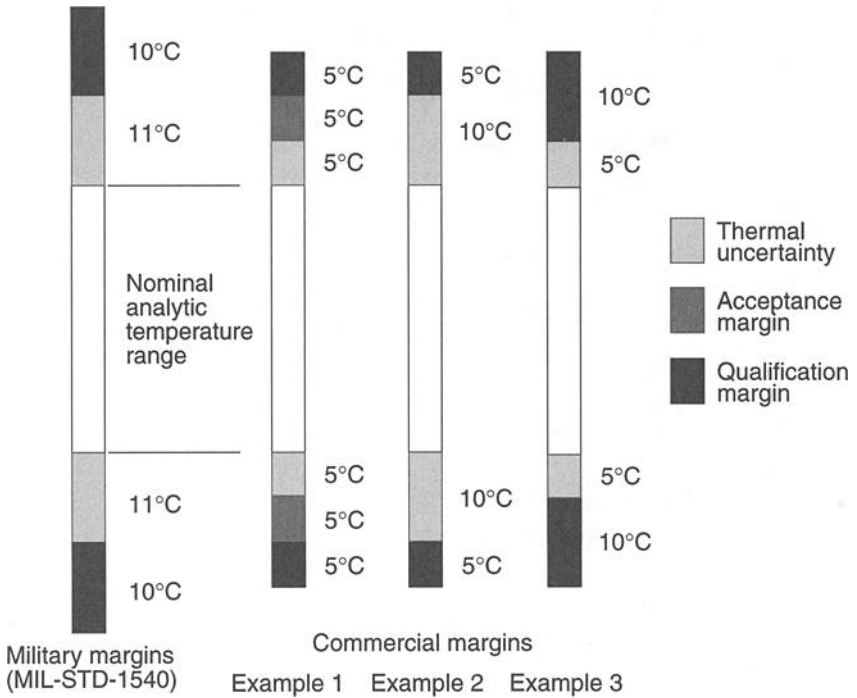
Fig. 19.2. Two typical commercial approaches to thermal margins.

temperature range of +25±5°C was desired, but for designing the thermal sub-system, the short-term range was used. A margin of ±25°C was then applied to the allowable flight range for qualification testing, resulting in the JPL standard minimum range of –20 to +75°C for testing of electronic assemblies.

Before 1980, JPL verified unit design and performance by using a "qualification/flight acceptance (FA)" verification program rather than a "protoflight" verification program. The qualification/FA program is similar to the military's proto-qualification program in that qualification testing is performed on the first unit to demonstrate design, and then FA testing is performed on subsequent units. In a protoflight program, all units are tested to protoflight levels. Currently, both qualification/FA and protoflight programs are used at JPL, depending on the number of units built.

The approach used by NASA and JPL to establish test temperatures is similar to that used by military and commercial programs. As shown in Fig. 19.3, the terminology may be different, but the methodology is nearly identical. To the worst-case hot and cold temperature range, a thermal design margin is added. This is the allowable flight temperature (AFT) range. The thermal design margin is similar to the military's thermal uncertainty margin, except its value may vary between programs. To the AFT range, an FA thermal reliability margin (±5°C) is added for
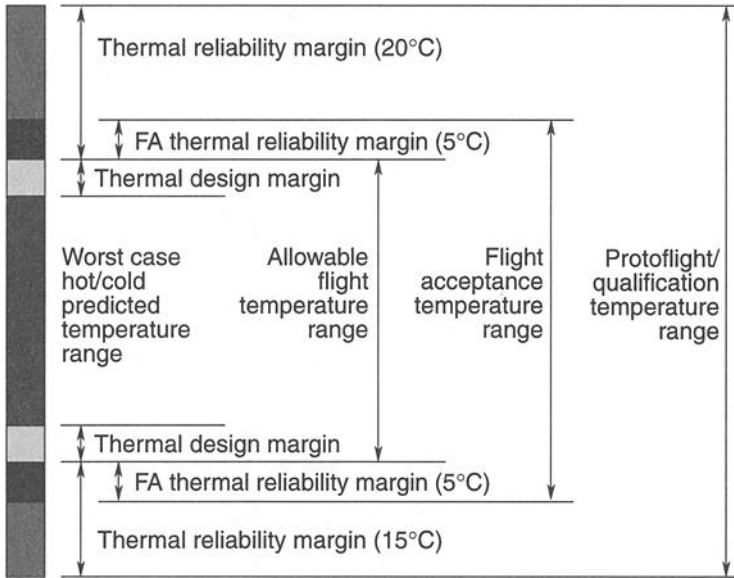
Fig. 19.3. Thermal margin terminology for JPL/NASA programs.

acceptance testing of FA units. To the AFT range, a thermal reliability margin
(–15°C, +20°C) is added for qualification or protoflight testing of qualification or
protoflight units. Qualification and protoflight requirements are at the same tem-
perature levels. Unlike military programs that rely on the thermal uncertainty and
qualification margin to establish test temperatures, JPL has used this test tempera-
ture range to guide thermal analysis efforts and ensure a positive thermal design
margin.

On many early NASA programs (Voyager, Galileo, Cassini, etc.), this approach
resulted in qualification testing over the –20 to +75°C temperature range. Wider
temperature ranges have been used in cases where a more severe environment was
anticipated. For example, temperature ranges of –55 to +70°C were used on the
Mars Pathfinder and the Mars Exploration Rover (AFT –40 to +50 with –15/+20
margins). In special cases, such as sensors with temperature-sensitive materials,
standard margins can be reduced. This change requires a trade-off between the
risks of damaging sensitive hardware during testing and the benefits of applying
standard margins.

Expanding the AFT from +5/+50 to –20/+55 allows a less costly thermal design
effort, but requires a thermally isolated propulsion system. Applying the –15°C,
+20°C thermal reliability margin to the expanded AFT results in a qualification/
protoflight temperature range of –35 to +75°C, which is typical of many current
NASA programs.

Testing requirements are also based on expected flight thermal cycling and pre-
ferred practices. For systems and units that do not cycle during their mission, such
as interplanetary missions, thermal dwell tests are performed on qualification or

protoflight hardware over the described temperature range in a one-cycle thermal vacuum test of extended duration. For units that cycle during their mission, practices similar to those in military programs are typically applied with an acceptance margin (±10°C) added to worst-case analytic temperature predictions. Also, at the unit level JPL typically requires thermal testing in a medium that simulates the mission environment (deep space vacuum or Mars pressure), whereas NASA has been more open to ambient thermal testing.

Development Thermal Testing

Development tests are performed as required to accomplish the following objectives:

- validation of new design concepts or application of proven concepts and techniques to a new configuration
- assistance in the evolution of designs from the conceptual phase to the operational phase
- reduction of the risk in committing designs to the fabrication of qualification and flight hardware
- validation of qualification and acceptance test procedures
- investigation of problems or concerns that arise after successful qualification

Development test requirements are necessarily unique to the test hardware and depend upon the objective of the test, the operational requirements of the specific program, and the maturity of the subsystems and units used. A common objective of development testing is to identify problems early in the design evolution so that any required corrective actions can be taken prior to starting formal qualification. Development tests verify design and performance margins, manufacturability, testability, maintainability, reliability, life expectancy, and compatibility with system safety. Where practical, development tests should be conducted over a range of operating conditions that exceed the design limits to identify marginal capabilities and marginal design features. The following sections describe objectives and processes for common thermal development tests.

Thermal Balance Test

The thermal balance test is typically part of the system thermal vacuum test, although it can be performed on units and subsystems at lower levels of assembly. The thermal balance test has two objectives: obtaining thermal data for analytic thermal model correlation and verifying the thermal control subsystem. To provide data for model correlation, individual conditions are simulated in the thermal vacuum chamber and thermal data are taken during temperature transition (for transient correlation) or at equilibrium (for steady-state correlation). A vehicle thermal balance test commonly includes simulations of hot operational phases, cold operational phases, cold nonoperational phases, transitions between conditions, and safe mode phases. Equilibrium temperatures or repeatable heater cycling profiles are typically the thermal data that are taken during the test. Verification of the thermal control subsystem includes performance verification of thermal hardware, including heaters, thermostats, flight thermistors, louvers, radiators, interface contact materials, heat pipes, and cryogenic systems. Temperature

and control authority margins are demonstrated from thermal data and hardware verification.

In nearly all cases, the thermal balance test is performed on flight hardware. Some testing at lower levels of assembly may require performing this test on non-flight hardware, such as a qualification unit or an engineering model. In such cases, the test hardware needs to consist of a thermal and structural equivalent of the flight equipment, to simulate that equipment's heat paths and thermal behavior. Further discussion of the thermal balance test is provided later in this chapter.

Thermal Mapping Test

For electronic units with high power levels or densities, a thermal mapping test is sometimes performed to verify their thermal characteristics. The test is basically a thermal balance test for a unit, slice, or printed wire board. It is performed in a thermal vacuum chamber possibly with an infrared (IR) camera. Objectives of the test are similar to those of the thermal balance test: obtain data for analytic thermal model correlation, verify the thermal control design, and establish confidence in the design and manufacturing processes. Specific concerns addressed in the thermal mapping are: (1) identification of hot spots on boards where power density is locally high, (2) assessment of deviations from accepted design techniques for subsystem interconnects, part mountings, board sizes and thicknesses, number of board copper layers, thermal coefficients of expansion, or installation methods, (3) verification of boundary conditions, and (4) confirmation of interface heat transport capability.

Thermal Conductance Tests

Thermal conductance tests are performed whenever confidence is needed in the heat transport capability through a material or across an interface. Common applications include an interface or material resistance, the directional conductivity in composite materials, the conductivity in vibration or thermal isolators, and the conductivity of cabling. Another is performance verification of thermal blankets, a test that is sometimes necessary when a highly resistive thermal blanket is specified for an application. It may be required because analytic predictions of thermal blanket performance have high uncertainties. Setup is difficult because of the small mass of the blanket layers. In some situations, instead of measuring the blanket temperature, one measures the temperature of an adjacent surface and deduces the blanket temperatures from the thermal interaction between these two surfaces.

Photometric Test

The photometric test is performed with nonflight hardware scaled to the dimensions of the flight hardware, with the objective of assessing optical properties of the vehicle and solar interaction. The test is performed by allowing solar-wavelength-collimated illumination to fall incident upon the test article. Locations are identified on the test article where solar heating or reflections are of interest. Handheld scopes are used to measure the sun equivalences at those locations. The results are used to verify environmental flux calculations predicted by geometric models. Careful attention must be paid in the planning and execution of this test to

ensure the accuracy of the scaled nonflight hardware, duplication of the surface finishes on the nonflight article, and use of identical procedures in the application of the surface finishes.

Deployment Mechanism Tests

Deployment mechanisms differ from other spacecraft units in that they are usually extremely critical to mission success and are mounted external to the vehicle, where thermal environments are severe. Deployment tests are commonly specified for these mechanisms to verify performance. In such tests, the simulation of harsh, but realistic, thermal environments is important. The tests are performed in hot and cold conditions as well as in an environment where the temperature is changing or a temperature differential is induced. The concerns that arise during these tests include: (1) differential expansion of materials causing deployment failure, (2) thermal gradients arising within the mechanism causing binding during deployment, (3) material, adhesive, or lubricant thermal degradation at extreme hot or cold temperatures, and (4) interaction between thermal blankets interfering with deployment.

Heat Pipe Tests

The high reliability of heat pipes is partially a result of the numerous development tests that they are subjected to for verifying workmanship and performance. Tests are performed to check for leaks, verify weld integrity, and demonstrate functional performance. A significant consideration for testing of heat pipes is the requirement that they be tested in a horizontal or level configuration for performance verification. A typical heat pipe development test program might include the tests listed in Table 19.3.

Unit Thermal Testing

As previously stated, the purpose of thermal testing is to verify a design and ensure its successful use in realistic thermal environments. This is accomplished

Table 19.3. Typical Heat Pipe Development Test Program

Test Category	Specific Examples
Heat pipe level testing	
Qualification	Burst pressure tests
Acceptance	Radiographic inspection of welds, proof pressure test, helium leak test, and functional performance test
Pallet level testing	
Qualification	Functional performance test, static load test, acoustic test, and thermal vacuum test
Acceptance	Gas charge verification, full tube leak test, functional performance tests, acoustic test, and thermal vacuum test
Further development testing	Aliveness test and in-gravity characterization test

by detecting flaws in the thermal design, materials, or manufacturing process, and by verifying that the unit tested performs within specifications during the test. Environmental stress screening is the process that subjects hardware to physical stresses and forces flaws that are not ordinarily apparent into observable failures. When these flaws are discovered, they are repaired, or problem equipment is replaced prior to flight. Ideally, qualification tests expose design defects, while acceptance tests uncover workmanship, part, material, and process defects. Performance verification is achieved when the item operates within specification when subjected to an extreme environment. These goals are generally accomplished most effectively at the unit level of testing.

To achieve effective ground testing, problems must be identified at the earliest practical point. Therefore, test levels and techniques are designed to maximize test rigor at the lowest levels of assembly and lessen in severity as the level of assembly increases. Problems are thus identified in time for orderly resolution and at a level of assembly that minimizes excessive teardown. For most spacecraft programs, a systems engineering perspective toward the test flow begins at the unit level. This discussion will adopt such an approach and assume that high-quality parts have been procured and that adequate part testing has been performed.

In a time of increasing pressure to reduce program cost and schedule, unit level testing has been scrutinized heavily. Despite reliable data on the effectiveness of unit tests, particularly the thermal cycle and thermal vacuum test, the current trend in spacecraft development is to shorten or completely eliminate these tests, deferring their objectives to a higher level of assembly. This trend conflicts with the basic philosophy of testing presented in the previous paragraph and increases risk to the unit's flightworthiness. Testing should be viewed over the complete build process, beginning at the unit level and ending after the system level. With this perspective, one can better manage system risk and more readily realize deficiencies in a unit's screening process.

Unit Thermal Tests

A unit is a functional item made up of modules and assemblies that are made up, in turn, of piece parts. Although tests and screens are conducted at lower levels of assembly, the lowest level addressed in most environmental specifications, test verification plans, and test practice manuals is the unit level. The three environmental thermal tests performed at the unit level are thermal vacuum, thermal cycling, and burn-in. Functional tests, which are not considered environmental tests, are performed at temperature extremes during thermal cycling and thermal vacuum.

For various units, Table 19.4 (MIL-STD-1540) specifies which unit tests should be considered required, optional, and not required at the qualification and acceptance levels. Regarding note (b) for unit thermal vacuum acceptance testing, most electronic units are unsealed, so this test would appear to be widely required. This note, however, also suggests that low power units do not require this test. Considerable effort has recently been devoted to understanding the implications of this note, and a more thorough explanation will be made later in this section.

Performance of moving mechanical assemblies can be extremely temperature-sensitive, as noted in the previous section. Binding of deployment mechanisms as the result of temperature or thermal gradients has occurred on orbit. Furthermore,

Table 19.4. Unit Test Baseline[a]

Unit	Unit Qualification and Protoqualification		Unit Acceptance	
	Thermal Cycle	Thermal Vacuum	Thermal Cycle	Thermal Vacuum
Electrical and electronic	R	R	R	R[b]
Antenna	–	R	–	O
Moving mechanical assembly	–	R	–	R[c]
Solar array	–	R	–	O
Battery	–	R	–	R[d]
Valve or propulsion unit	–	R	–	R
Pressure vessel or unit	–	O	–	O
Thruster	–	R	–	R
Thermal	–	R	–	R
Optical	–	R	–	R
Structural unit	–	O	–	O

[a]Recommended unit requirements: R = baseline requirement (high probability of being required); O = "other" (low probability of being required); – = not required (negligible probability of being required)
[b]Discretionary for sealed and low power units.
[c]Excluding hydraulic components for launch vehicles.
[d]Not required for batteries that cannot be recharged after testing.

temperature gradients can strongly influence friction in bearing assemblies. Tests on all of these units should be performed in a configuration that matches flight conditions, such as one that includes thermal blankets built to flight specifications and that properly simulates mounting surfaces and boundary conditions, to verify the proper motion of the mechanisms. Environmental simulation is also important for deployment testing, with proper simulation of boundary temperatures, thermal gradients, and transient conditions that could occur in flight.

Test planning for antennas is often given inadequate attention because they are commonly treated simply as part of the vehicle's structure. Test objectives to verify dish performance are typically deferred to payload level or system level tests. While in many instances this may be appropriate, proper design and workmanship must be verified. Knowledge of the antenna dish environment and performance requirements is crucial to accomplish this verification. Often, testing is conducted over wide temperature extremes to simulate predicted on-orbit temperatures. Sometimes, thermal gradients are imposed on the antenna to verify structural integrity. As most antenna dishes are made of composite materials, preparatory outgassing requirements must be considered.

Solar arrays experience wide temperature excursions in flight. Moreover, because of their low relative thermal mass, they respond rapidly to varying environments. The only required thermal test for solar arrays, according to Table 19.4, is thermal vacuum testing on the qualification unit, so workmanship issues on acceptance units are only detected in informal tests. Consideration should be

given to simulating thermal conditions, at least temperature, during solar-array verification, because solder-joint flaws in the array wiring have been detected, and on occasion these workmanship errors are exposed after repeated cycling at temperature extremes.

The performance and life of batteries can strongly depend on temperature. In battery testing, the thermal control design is verified by demonstrating temperatures are within limits, temperature gradients are minimized (within individual cells, between cells, and between batteries), and thermal resistances at critical interfaces are as expected.

Unit Thermal Test Objectives

Unit level thermal tests have three objectives: environmental stress screening, performance verification, and demonstration of survival and turn-on capability. The intent of environmental stress screening is to find faults in unit design, workmanship, materials, and processes. Ideally, the qualification test should uncover design defects, while the acceptance test should uncover defects in workmanship, parts, materials, and processes. Performance verification is accomplished through functional tests conducted prior to, during, and after environmental tests. A unit must perform within specification requirements before the functional test can be deemed successful. The intent of the survival and turn-on objective is to demonstrate that equipment can be soaked or dwelled in a specific thermal environment, then started and operated at cold and hot survival or turn-on temperature limits without experiencing performance damage or performance degradation when returned to the operational temperature range.

With regard to these objectives, the thermal cycle test and the thermal vacuum test have different roles. The thermal cycle test is best suited to accomplishing environmental stress screening; demonstrating performance, survival, and turn-on capabilities is secondary. The reverse is true for thermal vacuum testing.

Unit Thermal Cycle Testing

A unit's thermal cycle test demonstrates its ability to operate over the test temperature range. For qualification, the test demonstrates the unit's design and shows that the unit will endure the thermal cycle testing imposed during acceptance testing. At acceptance, the test detects material and workmanship defects prior to installation of the unit into a subsystem or vehicle. As shown in Table 19.4, thermal cycling should be performed on all electrical and electronic units. This is done primarily as an environmental stress screening. It is intended to enhance quality assurance by revealing latent defects in design, workmanship, and materials. Defects found in thermal cycling include loose connections, broken wire bonds, defective solder joints, inadequate stress relief, performance drift, bent connector pins, defective or contaminated parts, thermal-coefficient-of-expansion mismatches, and material deficiencies.

Unit Thermal Cycle Test Parameters

The important parameters in achieving effective thermal cycle testing of units are temperature range, number of cycles, dwell or soak duration, rate of temperature change during transitions, and operational conditions.

As discussed, unit level thermal cycle testing is performed at temperatures either based upon analytic predictions plus a thermal margin, or set at specific extremes, whichever values are more severe. At the acceptance level, either minimum to maximum expected temperatures (which includes the ±11°C thermal uncertainty margin) or cold and hot limits of –24 to +61°C are used. For example, if a unit has nominal expected temperature predictions of –18 to +42°C, the unit has minimum and maximum expected temperatures of –29 to +53°C. The hot temperature of +53°C is less severe than +61°C, so the acceptance test temperature range for this unit would be –29 to +61°C. At qualification, testing is performed at temperatures either 10°C colder than the minimum expected temperature and 10°C hotter than the maximum expected temperature, or at the specified extremes of –34 to +71°C. In the previous example, the qualification test temperatures would be –39 to +71°C.

The above discussion gives the general baseline procedure for establishing test temperatures at the unit level. If operational requirements prohibit testing over this temperature range, exception is made to the baseline procedure and testing is performed over the narrower operating temperature range. A risk assessment should be made on a unit-by-unit basis before the screening process is compromised.

Considerable work was performed in the 1970s and 1980s on the relationship between failure rates and number of cycles. Results showed that failures decreased with cycle count, sharply in the first few cycles and more gradually after a "knee in the curve" was achieved. Significant work was spent determining "knee" values and the appropriate number of cycles where infant mortality or a prescribed level of failures could be expected. Of particular note were studies performed by Martin Marietta in 1972[19.3] and the Institute of Environmental Sciences in 1984.[19.4] The research performed during these years aided in the establishment of test cycles for low-risk programs in the military standards.

For tailoring purposes, MIL-STD-1540C introduced the relationship between the number of cycles and the cycle temperature range:

$$C_2 = C_1 \left(\frac{\Delta T_1}{\Delta T_2} \right)^N, \tag{19.1}$$

where C_1 is the number of thermal cycles over temperature range ΔT_1, C_2 is the number of thermal cycles over temperature range ΔT_2, and N is a factor that depends on the stress level. Values of N have ranged from 1.4 for equivalent acceptance test programs (MIL-STD-1540C) to 2.6 for eutectic solder fatigue life demonstration. Typical values of N for electronics boxes are 2.0 to 2.6.

Recommendations for temperature rate of change are usually stated in maximal terms that take into account the chamber's capabilities. The location at which rate of change is measured is typically the same location at which the test temperature is recorded, such as the mounting point on the unit's baseplate for conductively cooled units or the unit's case for radiation-cooled units. Specific requirements for this parameter have been an average of 3 to 5°C per minute with a minimum of 1°C per minute. Few data are available on the effect of different rates of change. Generally, faster transitions, at least as great as those expected during ascent or re-entry, should be adopted as a practice. For a special type of units, such as digital

computers, one might consider a slow temperature transition on the final cycle to permit repetitious functional checkout over a narrow temperature range.

Engineers usually agree that units need to be operational during environmental testing. Experience has shown that failure rates significantly increase for operating, as compared to nonoperating, units. Beyond unit operation, performance should be monitored as much as possible throughout the test. In this manner, performance drift or anomalous readings can be detected. Hot and cold starts at operational and survival limits have also proven to be effective stress screens, in addition to demonstrating that the equipment is well designed and robust enough to survive mission-derived extreme environments and subsequently, to perform within specifications over the narrower operational temperature range. The process of performing hot and cold starts is discussed in the following section.

Finally, thermal dwell allows the unit to reach the test temperature. The requirement is necessary to ensure that the unit will be tested at the designated temperature extremes. Thermal dwell begins when the unit is within its test tolerance (typically 3°C) and concludes just prior to the start of the functional performance test. Thermal dwell should be a minimum of one hour at the hot and cold temperature extremes on the first and last cycle and is not required on intermediate cycles.

Thermal soak is a specification for the total time spent at the hot or cold temperature extreme, to ensure that adequate time is spent in the thermal environment. MIL-STD-1540 recommends a minimum of six hours on the first and last cycles and one hour on intermediate cycles.

The unit level thermal cycle test parameters are shown in Table 19.5. The source of this data is MIL-STD-1540B. These values represent typical unit testing parameters for current military programs.

Thermal Cycle Test Process

Prior to the test, a test plan must be available describing the procedures and the functional testing to be performed. Where practical, functional testing described in the test plan should be rehearsed with the unit at ambient temperature. The functional tests performed prior to (and following) the thermal cycle test should be identical to the functional tests that will be performed during the test.

Unit thermal cycling is typically performed in a thermal cycling chamber, where temperature-controlled dry air or gaseous nitrogen is used to heat or cool the unit. The nitrogen or dry air is used instead of ambient air to prevent moisture condensation on electronic parts or circuitry. During the heating cycle, the dry air or nitrogen is heated from the walls of the chamber. Usually direct heating need not be applied to the test article or to the mounting shelf. Cooling is accomplished by pumping liquid nitrogen through cooling tubes or coils mounted to the chamber baseplate. The baseplate is usually made of copper to provide good conduction over the interface with the test article. The environment is circulated with fans to prevent temperature gradients on the test article and to speed transitions in temperature. Baffles or flow directors are sometimes employed to better direct the circulating environment. When selecting a thermal chamber for a particular test, keep in mind that if relatively little room separates the internal walls of the chamber and the unit itself, air or gaseous nitrogen movement around the unit will be reduced. This may result in thermal gradients in the unit and a temperature-transition rate of change that is lower than desired.

Table 19.5. Unit Thermal Cycle Test Parameter Comparison

Thermal Cycle Test Parameter	Qualification	Protoqualification	Acceptance
Temperature	Minimum expected with −10°C margin to maximum expected with +10°C margin, or at least −34 to +71°C	Minimum expected with −5°C margin to maximum expected with +5°C margin, or at least −29 to +66°C	Minimum to maximum expected, or at least −24 to +61°C
Temperature range	105°C	95°C	85°C
Number of cycles	24 minimum	24 minimum	8 minimum
Thermal dwell	1 hr first and last cycles; not required on intermediate cycles	1 hr first and last cycles; not required on intermediate cycles	1 hr first and last cycles; not required on intermediate cycles
Thermal soak	6 hrs first and last cycles; 1 hr intermediate cycles	6 hrs first and last cycles; 1 hr intermediate cycles	6 hrs first and last cycles; 1 hr intermediate cycles
Transition	3–5°C/minute (1°C/minute minimum)	3–5°C/minute (1°C/minute minimum)	3–5°C/minute (1°C/minute minimum)
Failure-free cycles	Last 4 cycles	Last 4 cycles	Last 4 cycles

A typical thermal cycle test profile is shown in Fig. 19.4. Pictured is a history of a reference temperature, such as the temperature of the unit baseplate.

FF — Full functional performance test
AF — Abbreviated functional test
HS — Hot starts
CS — Cold starts
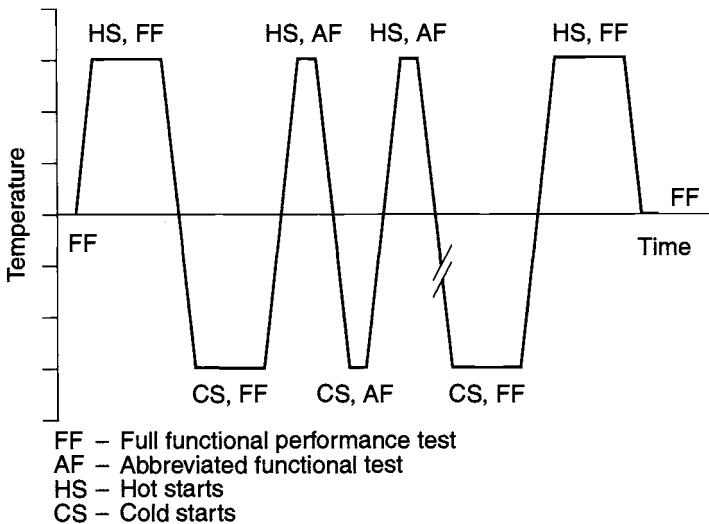
Fig. 19.4. Typical unit level thermal cycle profile.

For the majority of the thermal cycling test, the unit is operating with its performance monitored. Scrutiny of performance parameters during the test enables the identification of latent defects and is therefore considered critical in ensuring effective testing. Prior to the formal start of testing, steps are taken to preclude the unwarranted accumulation of moisture within the unsealed unit. This is accomplished by imposing a number of pretest cycles using dry air or nitrogen, where cold temperatures are not permitted to fall below the dew point of the air trapped within the unit. These pretest cycles purge moist air from internal spaces. To further reduce the risk of condensation, the test begins and ends with hot cycles or half-cycles. Prior to the test, a full functional performance test should be conducted to provide comparison data for results obtained during the test and to ensure that the unit is operating correctly before the environmental test begins.

The test begins with the unit operating and the chamber environmental control set to the hot temperature level. After the test temperature sensor reaches the test tolerance temperature, the thermal dwell period begins. As shown in Fig. 19.5, the thermal-stabilization period is the time between the test tolerance (typically the test temperature minus 3°C) and the test temperature. During this period, adjustments are made to the environmental control to bring the test article to the test temperature. The thermal dwell begins at the onset of thermal stabilization to allow internal locations in the test article to reach the test temperature. Following the thermal dwell, which is typically a minimum of one hour on the first and last cycle of the test, the unit should be hot started by turning it off and back on. To prevent the test item temperature from dropping below the test tolerance, reactivating the unit should be done shortly after turnoff. Following the hot start, full functional tests are performed to verify the unit's performance within specification. The requirements of the functional test depend upon the purpose of the unit. The testing should demonstrate that the unit meets its performance requirements within acceptable tolerances. Thermal soak is the duration with the unit operating between the start of the thermal dwell and the end of the functional test.

Following the hot functional test, the chamber environment is reconfigured to the cold temperature phase. This involves turning off the chamber heater system and activating the liquid nitrogen cooling. To assist in more rapidly reaching the cold temperature, test plans have specified that the unit be nonoperating. This specification is subject to debate, because performance parameters should be monitored during the transient period. Stresses that build during transient conditions can be quite different in their effects, so hardware should be carefully watched during the cooling period. However, the unit is commonly turned off just prior to reaching a specified cold temperature. For acceptance tests, the unit may be nonoperational once the nominal expected temperature is reached and for qualification testing, once the acceptance temperature is reached.

Thermal stabilization, thermal dwell, and thermal soak have similar definitions at cold and hot temperatures. Thermal stabilization and thermal dwell begin when the temperature sensor reaches the test tolerance temperature (typically 3°C warmer than the test temperature). Adjustments are made to the environmental control during the thermal stabilization period to bring the test article to the cold test temperature, and the thermal dwell period ensures internal locations are at the cold test temperature before functional testing. In some cases the unit is activated
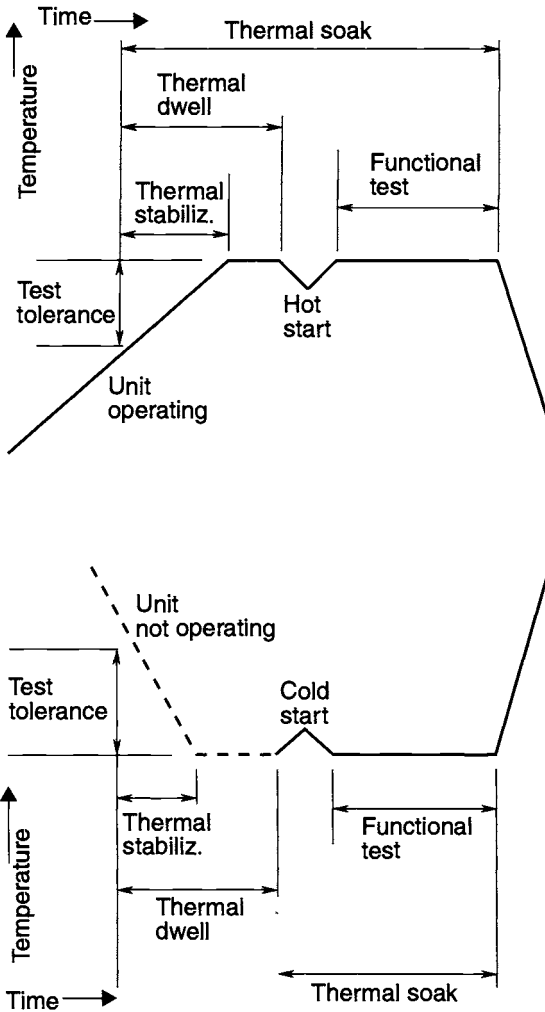
Fig. 19.5. *Top:* **thermal definitions at hot temperature plateau;** *bottom:* **thermal definitions at cold temperature plateau.**

during the dwell period to ensure that functional tests are performed at the test temperature. If the unit is inactive during the dwell, adjustments to environmental control may be necessary to keep the unit at the test temperature when it is turned on. Following the thermal dwell, a cold start is performed. If the unit was operating during the dwell, then the cold start will require turning the unit off and back on. If the unit was not operating during the thermal dwell, then the cold start will be simply turning the unit on. A full functional performance test follows the cold

start on the first and last cycles and should be nearly identical to the functional test performed at the hot temperature plateau.

Following the function test, the chamber environment is reconfigured to the hot environment, and as the temperature sensor passes through ambient, the first cycle is completed. The same procedure is repeated for the remaining cycles, with hot and cold starts performed at each temperature plateau. For intermediate cycles (those between first and last), abbreviated functional tests may be performed. These tests are subsets of the full functional performance test, and although they may be significantly shorter, they monitor key performance parameters and assess performance drift as the cycles accrue.

If a unit level thermal vacuum test is not being performed for a particular electronic unit, then survival demonstration should be accomplished during the unit thermal cycle test. One or two cycles of the thermal cycle test are modified to increase the hot test temperature to the survival hot value and decrease the cold test temperature to the survival cold value. At the hot survival temperature, the unit should be hot started by turning it off and back on. The temperature of the environment can then be reduced to the acceptance or qualification temperature for dwell and functional testing. At the cold survival temperature, the unit is probably off. Once that cold survival temperature is reached, the unit is cold-started. The environment can then be heated to the acceptance or qualification temperature, or the unit may be heated by its power dissipation, with control of the environment.

Unit Burn-In Testing

A necessary adjunct to the screening process is burn-in testing, during which the unit is operated for an extended period to precipitate failures. During burn-in, additional hours of operation beyond those accrued during unit thermal cycling and unit thermal vacuum testing are accumulated until a predetermined value is achieved. In this test, additional defects are precipitated, detected, and corrected, and failure-free performance is demonstrated. Because burn-in is a screen for workmanship errors, this test is only performed on acceptance units. According to MIL-STD-1540C, additional operation at the hot acceptance temperature is accumulated until the combined unit thermal cycling, thermal vacuum, and additional hot operation is at least 200 hours. The last 100 hours are to be failure-free, with 50 hours each on the primary and redundant sides.

Test plans have been proposed with burn-in testing at ambient temperature. These tests save considerable costs by not requiring a thermal chamber and by running units in parallel, but the stresses at ambient temperature are nearly negligible, so the screening effectiveness is extremely poor. Therefore, burn-in testing should only be performed in an environment that is, at minimum, the unit acceptance temperature. Table 19.6 lists burn-in test parameter requirements from the military guidelines.

Unit Thermal Vacuum Testing

The primary purpose of unit thermal vacuum testing is to verify the functional performance and design of the unit, although the test is still effective at stress screening. Without the convective environment, temperatures, thermal gradients,

Table 19.6. Unit Burn-In Test Parameter Comparison

Thermal Cycle Test Parameter	Thermal Cycle Test Parameter (MIL-STD-1540C)
Temperature	Maximum expected, or at least +61°C
Total operating time	200 hrs minimum, including thermal cycling and vacuum time
Failure-free hours	Last 100 hrs (50 hrs primary and 50 hrs redundant side)

and stresses will more closely simulate flight conditions than they do in the thermal cycle test. Thermal vacuum testing is vital in ensuring successful mission operation by demonstrating flightworthiness, workmanship, and design in the ground environment that best simulates on-orbit stresses. At the qualification level, the test verifies the unit design and demonstrates the ability of the unit to endure the thermal vacuum testing imposed on flight units during acceptance testing. At the acceptance level, the test detects material and workmanship defects and proves flightworthiness. In both tests, demonstration of operational performance is verified against specification requirements.

Unit Thermal Vacuum Test Parameters

The temperature range and extremes in the unit thermal vacuum test are identical to the thermal cycle test parameter requirements. Acceptance tests are performed at minimum and maximum expected temperatures, or at least –24 to +61°C, and qualification tests are performed at minimum and maximum expected temperature ±10°C, or at least –34 to +71°C. The number of cycles, however, is less, primarily because of the different objectives of the vacuum test and the fact that transitioning in vacuum takes significantly longer. A comparison of the thermal vacuum test parameters from the military standards is given in Table 19.7. The source of this data is MIL-STD-1540B. The one acceptance cycle for electronic units (if eight thermal cycles are performed) is commonly increased to either two or four cycles in actual spacecraft test programs. It is also typical for the number of protoqualification cycles to be the same as the number of qualification cycles because design verification is a high priority of unit protoqualification testing.

Vacuum environments may necessitate longer dwell times than necessary in the thermal cycle test, because without the convective heat transfer, bringing the internal part temperatures to the test level will take longer. Temperature sensors at locations away from the first sensor that reaches the test temperature should be monitored to estimate an appropriate dwell time. Furthermore, thermal analysis simulations can be performed to predict time required for internal parts to reach the test temperature after the unit's baseplate has reached the test temperature.

A pressure of 10^{-4} torr (13.3 mPa) has been recommended in the military guidelines. Low pressure is necessary to eliminate unrealistic effects of convective heat transfer in simulating thermal conditions encountered in space application, even at the molecular level. Achieving lower pressures where practical is highly desirable, especially for units that may require a longer-than-normal outgassing duration or

Table 19.7. Unit Thermal Vacuum Test Parameter Comparison

Thermal Cycle Test Parameter	Qualification	Protoqualification	Acceptance
Temperature	Minimum expected with −10°C margin to maximum expected with +10°C margin, or at least −34 to +71°C	Minimum expected with −5°C margin to maximum expected with +5°C margin, or at least −29 to +66°C	Minimum to maximum expected, or at least −24 to +61°C
Temperature range	105°C	95°C	85°C
Number of cycles (nonelectrical)	3 minimum	3 minimum	1 minimum
Number of cycles (electrical)	24 minimum if only TV performed; 3 if 24 TC cycles also performed	24 minimum if only TV performed; 3 if 24 TC cycles also performed	8 minimum if only TV performed; 1 if 8 TC cycles also performed
Thermal dwell	1 hr first and last cycles; not required on intermediate cycles	1 hr first and last cycles; not required on intermediate cycles	1 hr first and last cycles; not required on intermediate cycles
Thermal soak	6 hrs first and last cycles; 1 hr intermediate cycles	6 hrs first and last cycles; 1 hr intermediate cycles	6 hrs first and last cycles; 1 hr intermediate cycles
Pressure	10^{-4} torr or less	10^{-4} torr or less	10^{-4} torr or less

for units that include thermal blankets. An important feature of thermal vacuum testing is the monitoring of units that may exhibit anomalous behavior in certain ranges of reduced pressure. Electrical and radio-frequency (RF) equipment, which may operate during ascent, or which may be operated before trapped gases are able to fully escape, should be checked for corona arcing and multipacting. When multipacting is a possibility, a nuclear-radiation environment may be simulated to initiate possible multipacting.

Unit Thermal Vacuum Test Process

Performing a unit thermal vacuum test is similar to unit thermal cycle testing. The test profile in Fig. 19.2 can be used as a framework for thermal vacuum testing as well as thermal cycle testing. Furthermore, definitions given for thermal cycle testing apply similarly to the thermal vacuum test. Functional tests are performed to verify the operational performance of the unit at hot and cold temperature plateaus on each cycle. Full functional performance tests are performed on the first and last cycle, and abbreviated functional tests are performed on intermediate cycles. Full functional performance tests are also performed prior to and following the test, at ambient pressure. Throughout the test, electrical items, including all redundant circuits, are cycled through various operational modes, and perceptive parameters are monitored for drift, failures, and disconnections to the maximum extent. The unit is operational for the majority of the test, with nonoperation allowed at hot and cold starts on each cycle and on the cold transition after the minimum nominal expected temperature or minimum expected temperature is reached.

Survival and turn-on demonstration is particularly useful in the vacuum environment, because it best simulates the flight conditions. As recommended in the thermal cycle test, one or two cycles may have their temperature levels extended for turn-on verification with performance operation at the acceptance or qualification level.

Unit thermal vacuum tests are divided for convenience into two categories: (1) those where conduction to a heat sink is the dominant mode of cooling, and (2) those where appreciable radiation to surroundings is possible or included in thermal analysis. The former has been the more likely scenario for electronics boxes. Conduction cooling is usually accomplished by mounting the unit onto a nearly isothermal heat sink. This type of mounting may not be representative of actual unit installation, which may for example have inserts in an aluminum honeycomb with facesheets. It is usually acceptable, however, provided the differences between test mounting and flight mounting are accounted for by analysis and verified by testing at the system or the subsystem level. If the component is cooled primarily or appreciably by radiation or by both conduction and radiation, control of heat paths becomes very important. Radiation and conduction paths are simulated and controlled so that heat loss by these different modes occurs in approximately the same proportion as would be calculated for the flight environment. This simulation is necessary so that piece-part temperatures and unit thermal gradients duplicate those that occur in actual usage.

Waiving Thermal Vacuum Testing for Electronics Boxes

Testing provides confidence in the design and workmanship of the test article. Whenever a test is waived, engineers generally agree that either (1) the objectives of this test have already been met in a previous test or should be met in a subsequent test, or (2) the hardware is insensitive to the test environment. Where these deletions make sense, significant time can be saved and significant costs can be eliminated.

The objective in proposing a test waiver is to manage risk. Elimination of a low-level test defers risk to a higher level of assembly. Should a unit fail at the system level, the impact to cost and schedule to fix the failure increases dramatically. As a result, proposals to delete low-level testing must be reviewed carefully to ensure proper risk management. The difficulty is in the determination of how much design and workmanship risk is carried to the higher level of assembly with the elimination of a low-level test.

One test that can be extremely expensive is the thermal vacuum test. Military testing standards state that acceptance thermal vacuum testing of low power electronic units is discretionary. The rationale is that low power units have thermal characteristics that are more dependent on their environment than on their own power generation. A low power unit may be vacuum-insensitive in that internal piece part temperatures should be nearly the same in the thermal cycle test as they would be in the thermal vacuum test. Thermal cycles, however, cannot be simply substituted for thermal vacuum cycles. The tests have different objectives, and common purposes are accomplished by different means and with different efficiencies. As a result, careful consideration must be given to the objectives of these tests so that risks are reduced and not pushed to a higher level of assembly.

Despite a full array of unit level testing, experience shows that unit level failures still occur at the subsystem and system level. Therefore, where stress screens are most likely to uncover design or workmanship deficiencies, these tests should be maintained, not eliminated. Any deferment of a test screen must be done with adequate knowledge of the unit's design, performance, and heritage. For example, the performance of RF units is inherently temperature (and vacuum) sensitive, so thermal vacuum testing should not be waived for RF units. Furthermore, thermal vacuum and thermal cycle testing should be considered for all mission-critical units, regardless of power dissipation, to ensure operational success. Thermal vacuum testing should also be performed for units that:

- are or have parts that are pressure sensitive
- are temperature controlled to maintain performance within a narrow temperature range,
- have hermetically sealed items for which deflections under worst-case conditions could result in shorts with nearby items,
- have high voltages with corona or multipaction concerns
- have high localized power densities
- have case temperature predictions significantly hotter in vacuum than in air
- are of a new design with little or no flight heritage

The intent of these considerations is to enable a technical risk assessment for deferring the vacuum environment. In some instances thermal cycling in lieu of the thermal vacuum may be acceptable. When it can be shown that thermal vacuum effects are small and that heat paths are well understood, such as might occur for units with low power dissipation or with robust conductive heat transfer paths, the benefits of deferring the vacuum environment to a higher level of assembly may outweigh the associated risks. Unit assessment, however, is unique and must be handled on a unit-by-unit basis.

Commercial Practices for Unit Testing

Generally, commercial practices differ from military practices primarily in the number of cycles performed and the requirement for thermal vacuum and thermal cycle testing. Whereas military programs emphasize the need for unit level testing both in thermal vacuum and in ambient thermal cycling, commercial programs tend to perform either vacuum or cycling tests for units. The number of cycles in a commercial program is given as the total unit level thermal test cycle count and is less than the number recommended in the military standards. For example, instead of the 12 acceptance thermal cycles (8 thermal cycling plus 4 thermal vacuum) typical of a military program, a commercial program might perform 8 total cycles, either all in air or all in vacuum. Usually, the number of protoqual cycles is nearly the same as the number of acceptance cycles. The number of qualification cycles is typically higher than the number of acceptance cycles, but not greatly higher. Instead of 27 unit thermal cycles at qualification (24 thermal cycling plus 3 thermal vacuum), a commercial program would propose perhaps 10 to 12 total cycles.

Other commercial test parameters do not differ greatly from their military counterparts. Several commercial contractors continue to use standard acceptance

temperature ranges of –24 to +61°C. In some cases, payload electronics are tested within narrower temperature ranges as a result of performance constraints. Commercial practice regarding temperature margins was previously addressed.

Burn-in has been reduced by a number of commercial contractors. Differences vary greatly between contractors, but they include a lower number of hours in test, the elimination of redundant side operation, and an increased desire to perform the test at ambient temperature. Such compromises are not supported by published data on the subject of stress screening effectiveness. Depending on the power dissipation of the unit, ambient air burn-in testing can have almost negligible benefit to screening for failures.

On the whole, the level of stress screening is lower in commercial unit thermal testing than in military unit thermal testing. With the reduction in the number of cycles performed, the overall test effectiveness is lower. In theory, undetected failures at the unit level should result in an increased failure rate at higher levels of assembly (subsystem and system), but this has not generally been the case. One could conclude that the unit thermal testing performed on commercial satellites is therefore adequate and the military practices are excessive. Another argument, however, is that system level testing is not stressful or perceptive enough to catch these failures.

NASA Practices for Unit Testing

Of the many agencies in the aerospace community, NASA has promoted "better, faster, cheaper" practices more than any other. NASA and the Jet Propulsion Laboratory have performed considerable work to quantify test effectiveness and risk reduction for their space programs. Although risk trade-off guidelines and preferred practices have been written to provide test requirements for NASA programs, unit testing procedures vary between programs, so the follow paragraphs discuss typical practices.

As previously mentioned, unit testing is categorized between those that thermal cycle in flight (generally over a temperature range greater than 20°C, environmentally or power-cycling induced) and those that do not. For units that cycle in flight, thermal cycling includes two to ten thermal cycles (typically eight) over the appropriate temperature range. A distinction is not made between vacuum and air cycles, but rather the practices state that thermal cycling should be performed in a vacuum if the test item is designed to operate in a vacuum.

For units that do not cycle, thermal cycling includes one thermal cycle over the appropriate temperature range. The rationale for a single cycle test has commonly been that deep space NASA programs do not experience the same level of temperature cycling as compared to Earth-orbiting spacecraft. Thermal dwell tests are performed on protoflight hardware over the temperature range of –20 to +75°C. Performance demonstration is conducted at the cold temperature for 24 h and at the hot temperature for 144 h. Testing in vacuum is preferred to ambient air testing. Other test practices are very similar to military program procedures.

Subsystem and Payload Thermal Testing

Subsystem and payload level testing are performed after unit level testing, but before system level testing. These tests provide additional environmental stress screening, performance verification, and thermal balance. Generally, the objectives are more closely related to system level requirements than to unit level requirements. This alignment agrees with the philosophy that early detection of problems is desirable.

Many advantages may be gained by testing at the subsystem level as compared to the system level, including the following.

- Subsystem tests allow use of smaller test facilities and make it easier to tailor the thermal environment to the specific requirements of the test article.
- Configuration and heat pipe leveling requirements can be more readily met.
- The subsystem and its units are more accessible.
- Less interference with adjacent payloads, hardware, and test equipment is observed.
- Boundary conditions are better understood.
- Problems are easier to isolate.
- Data and instrumentation may be more thorough. For example, thermal balance model correlation may be easier because more thermocouples may be available for gathering thermal data.
- The retest time can be significantly shorter.
- Design and performance results are obtained in a more timely manner, and problems discovered at this level are significantly easier to correct.
- In some cases, the subsystem test suffices to demonstrate or prove some aspects of the design (e.g., thermal balance), when the test cannot be conducted in a meaningful way at the system level.
- Performance testing can be more thorough. Confidence is also gained, in that performance requirements are more easily demonstrated at the system level if they have been shown previously in the subsystem level.

In proposing a subsystem or payload test, one typically applies system level requirements, because the test's goals are usually system level objectives. Thermal testing parameters are therefore identical at the subsystem and system levels. In thermal tests, temperature ranges should be as wide as practical, possibly wider than what will be obtained at the system level.

System Thermal Testing

Also known as space vehicle level testing, system level testing has an emphasis very different from testing at the unit or subsystem level. As the final ground verification of system and unit performance in a realistic flight environment, system level testing focuses not on individual unit functionality, but rather on end-to-end performance verification of subsystems and mission requirements. Specifically, interfaces between units and subsystems are assessed, continuity of mission objectives is demonstrated, compatibility of different subsystem requirements is shown, and flightworthiness of the vehicle is proven.

At the qualification level, three thermal tests are common. Thermal vacuum testing demonstrates functional performance and the ability of the vehicle to meet design requirements under vacuum and at prescribed temperature extremes plus a margin. Thermal balance testing is part of the thermal vacuum test and is used for thermal model correlation and verification of the thermal control design and hardware. Thermal cycling accrues additional stress screening by detecting design defects and demonstrates performance prior to the thermal vacuum test.

At the acceptance level, the two typical tests are thermal vacuum and thermal cycling. Their primary goals are similar to those of the corresponding qualification level tests, but in the thermal vacuum test, functional performance tests are used to prove workmanship and flightworthiness, while in the thermal cycle test, additional environmental stress screening is accrued to expose workmanship and process defects, not design issues.

System Thermal Cycle Testing

Given its emphasis on performance verification, the thermal vacuum test is the focal thermal test at the system level. Its importance is a result of several factors: the vacuum environment provides the most realistic flight conditions in which to verify functional performance and thermal gradients. Temperature extremes are most accurately represented in this environment, and temperature signatures and transient responses in this environment represent flight results. The primary purpose of thermal cycling, environmental stress screening, should not be the emphasis of system level testing. Stress screening to detect problems should have been completed at the unit level, where problems are less costly to correct. Furthermore, the rapid rates of temperature change necessary for stress screening are difficult, if not impossible, to achieve at the system level.

Nevertheless, the system level thermal cycle test can provide programs with data that cannot be obtained in other tests, thus proving valuable. Besides providing environmental stress screening, the test has advantages over the thermal vacuum test. It can characterize temperature-related performance observations to be noted in the vacuum environment. Problems are easier to correct. Verification of test procedures that will be used in the vacuum test can be made. Finally, it can be significantly less expensive to perform and configure. This test, along with system thermal vacuum testing, has been beneficial in demonstrating flightworthiness.

Test parameters as specified in MIL-STD-1540C are given in Table 19.8. Instead of specific cold and hot test temperature requirements, as in unit testing, a temperature range is recommended for the system thermal cycle test. Protoqualification cycles are specified as half the number of qualification cycles in MIL-STD-1540C. The current trend in spacecraft test programs tends to reduce the number of cycles from those shown in Table 19.8 by approximately half.

Table 19.8. System Thermal Cycle Test Parameter Comparison

Thermal Cycle Test Parameter	Qualification	Protoqualification	Acceptance
Temperature range	70°C	60°C	50°C
Number of cycles	10	5	4

System Thermal Vacuum Testing

The thermal vacuum test consists primarily of functional performance tests between and at temperature extremes in a vacuum environment. Functional tests focus on unit and subsystem interaction and interfaces, and on end-to-end system performance in a vacuum environment at or near minimum and maximum predicted temperatures. These tests also detect material, process, and workmanship defects with an emphasis on mounting, cabling, connectors, and unit and subsystem interactions. Specific thermal balance test phases are used to demonstrate the thermal control subsystem. Thermal functions that are verified during this test include thermostat and heater activation, heater control authority, louver operation, heat pipe performance, and insulation effective emissivity.

Table 19.9 provides the military standard for system thermal vacuum testing. Temperature extremes for the test are based upon worst-case analytic predictions for at least one unit in each thermal zone. Temperature margins are the same ones used for unit level testing. Acceptance, protoqualification, and qualification tests are performed at 11°C, 16°C, and 20°C, respectively, beyond model predictions.

The test parameters given in Table 19.9 are based upon MIL-STD-1540B requirements. The number of cycles is given in terms of whether system level thermal cycle testing is also performed. At acceptance, a minimum of four thermal vacuum cycles are to be performed, but this number may be reduced to one, if thermal cycling is performed to the requirements given in the testing standard. In practice, thermal vacuum testing is typically performed with four cycles whether thermal cycling is conducted or not.

Typically, the space vehicle is divided into manageable zones based upon structural divisions, similar temperature predictions, or similar functions. Test temperatures are specified for individual zones based upon the most restrictive test temperature range for any unit in the zone. As a result, a variety of units, often tested to different temperature extremes in unit thermal testing, must be accommodated during system testing. For example, given three units in the same thermal zone with unit acceptance temperatures of −24 to +61°C for unit A, −18 to +71°C for unit B, and −35 to +45°C for unit C, the acceptance temperature range at the system

Table 19.9. System Thermal Vacuum Test Parameter Comparison

Thermal Vacuum Test Parameter	Qualification	Protoqualification	Acceptance
Temperature	Qualification	Protoqualification	Acceptance
Number of cycles	8 minimum if only thermal vacuum testing is performed	4 minimum if only thermal vacuum testing is performed; 1 if system thermal cycles are performed	4 minimum if only thermal vacuum testing is performed; 1 if system thermal cycles are performed
Thermal soak	8-hour first and last cycles; 4-hour intermediate cycles	8-hour first and last cycles; 4-hour intermediate cycles	8-hour first and last cycles; 4-hour intermediate cycles
Pressure	10^{-4} torr or less	10^{-4} torr or less	10^{-4} torr or less

level for this thermal zone would be −18 to +45°C. In this example, relatively wide unit temperature ranges of 85°C, 89°C, and 80°C were reduced to 63°C at the system level. This example illustrates the importance of unit testing to similar temperatures.

Another common approach is to base thermal-zone temperatures not on the acceptance temperatures of the units, but on their worst-case temperature predictions. In the above example, unit A may have been tested at the unit level to −24 to +61°C, but it may have a worst-case nominal temperature prediction range of 0 to +40°C. The thermal uncertainty margin would be added to this range, so for an 11°C margin, testing of this unit would at most be −11 to +51°C. This range would then be compared to the range of other units within the same thermal zone, so the 63°C range would likely be reduced even further.

The approach of the system thermal vacuum test with regard to achieving temperature is to drive as many units as possible, but at least one unit per vehicle thermal zone, to their qualification or acceptance temperature extreme, with the constraint that no unit should exceed its unit level test temperatures. Temperatures are continuously monitored to avoid overstressing or exceeding unit temperature levels. The system level test temperature approach (applying a margin to worst-case predictions) is identical to that at the unit level, except that the default values (−24 to +61°C for acceptance and −34 to +71°C for qualification) do not apply. To assist in not exceeding unit temperature limits, an additional test tolerance of typically 3 to 5°C is applied at both cold and hot temperatures. In the example given, functional testing would begin when the first thermistor or test thermocouple in that thermal zone reached a temperature below −13°C or above +40°C.

In this example, with test tolerances applied, the total test range has been reduced to only 53°C. System level test temperatures frequently are relatively benign as compared to the unit temperatures. In some cases, the hot test temperature for several thermal zones approaches room temperature levels. Thermal stresses over this temperature range are much smaller as compared to the stress levels that may have resulted over a wider temperature range at the unit level. This reduction in testing effectiveness must be remembered when considering the elimination of unit testing.

Another feature of system level testing that restricts the ability of the test to reach test temperature is chamber and vehicle limitations. In some cases, the chamber or heater lamps are not capable of driving a thermal zone to its test temperature. More commonly, interactions between thermal zones or restrictions of adjacent zones prevent the achievement of test temperatures. Table 19.10 compares test temperatures achieved during unit- and system level testing for an actual spacecraft. Payload panels 5–8 were tested to near-acceptance temperatures, but all other thermal zones had significantly smaller temperature ranges. These results are representative of results obtained on other programs.

The standards recommend an eight-hour thermal soak. For large spacecraft with extensive functional testing, the soak period will be perhaps a couple of weeks. No requirement is given for thermal dwell, but bringing the spacecraft to equilibrium prior to functional testing should be part of the test procedures.

Full functional performance tests are performed before and after the thermal vacuum test at ambient temperatures and pressure, and at cold and hot temperature

Table 19.10. System Level Actual Test Temperature Example

Unit/Panel	Unit Level Acceptance Test Temperatures (°C)		Actual System Level Test Temperatures (°C)	
	Min. to Max.	Range	Min. to Max.	Range
Computer	−34 to +60	94	+8 to +40	32
Battery regulator unit	−34 to +60	94	+4 to +52	48
Data handling panel	−34 to +60	94	+7 to +46	39
Electrical power panel	−34 to +60	94	−1 to +48	49
Reaction wheels	−12 to +63	75	+16 to +55	39
Batteries	−7 to +24	31	+1 to +13	12
Payload panel 1	−12 to +43	55	+9 to +42	33
Payload panel 2	−12 to +43	55	−5 to +39	44
Payload panel 3	−12 to +43	55	−1 to +31	32
Payload panel 4	−12 to +43	55	−1 to +34	35
Payload panel 5	−7 to +54	61	−7 to +51	58
Payload panel 6	−7 to +54	61	−7 to +49	56
Payload panel 7	−7 to +54	61	−6 to +51	57
Payload panel 8	−7 to +49	56	−3 to +52	55
Antenna enclosure 1	−15 to +60	75	−9 to +32	41
Antenna enclosure 2	−15 to +60	75	−8 to +33	41
Antenna 3 electronics	−40 to +60	100	+7 to +41	34

extremes on the first and last cycle. Abbreviated functional tests are performed on both temperature extremes on intermediate cycles. Throughout the test, equipment is active and functioning through different operational modes. Perceptive parameters are monitored continuously. The only exception to the operational status is during transitions from hot to cold temperatures and during the brief periods between hot and cold starts. Operating times are divided approximately equally between primary and redundant circuits. The test is performed in a similar fashion as outlined for unit level thermal cycle and thermal vacuum testing.

Thermal Balance Testing

The thermal balance test provides data necessary to verify the analytical thermal model and demonstrates the ability of the vehicle thermal control subsystem to maintain temperature limits. Almost always performed as part of the system thermal vacuum test, the thermal balance test consists of dedicated thermal phases that simulate specific flight conditions. A successful demonstration of the thermal control subsystem and subsequent model correlation establish the ability of the thermal design to maintain all payload and equipment thermal requirements for all mission phases. The test is classified as a qualification development test in that it is an aid to the thermal design and is only performed on the first vehicle of a particular build. Unlike strict qualification tests, the thermal balance test is rarely

performed on qualification hardware, but rather on flight hardware, namely on the lead vehicle of a series of spacecraft and on a block change in a series of vehicles.

The test involves simulating several mission phases with one or more vehicle configurations. On-orbit phase simulations may include several combinations of equipment operation and solar angle heating profiles. Unlike the thermal vacuum test, where equipment is driven to specific test temperatures, the thermal balance test uses a known environment (heater settings, chamber cold wall) and preset operational status to simulate the test phase. The vehicle is then allowed to achieve its equilibrium temperature for that environment. Other simulations may include transient conditions where the vehicle starts at an equilibrium condition and the environment and operational status are changed to reflect a flight condition, such as eclipse cooldown or ascent.

A baseline thermal balance test should consist of a set of phases that includes one or two hot operational phases, a cold operational phase, and a cold nonoperational phase. The hot phases will have high, but realistic, levels of equipment usage and absorbed environmental heating. The test frequently includes two hot phases, each with environmental heating on different sides of the spacecraft. The cold phases will involve minimal equipment usage, bus voltage, and environmental heating. The operational phases are intended to verify that unit operational temperature limits are maintained under different environmental conditions. The cold nonoperational phase is intended to demonstrate nonoperational temperature limits and verify heater operation. The test phases do not need to simulate the worst-case conditions expected on orbit, but they should stress the thermal control hardware so that confidence is gained in its flightworthiness. Using extreme conditions for thermal model correlation is important, so that flight predictions are not a significant extrapolation beyond the test simulation phases.

For higher-priority spacecraft, the baseline thermal balance test should be expanded to include such simulations as eclipse, ascent, transfer orbit, and safe mode. The test should also include a verification phase in which temperature data are taken at equilibrium and compared to analytic predictions after thermal model correlation has been completed. Temperature data from this phase are not used in the correlation, but rather as a check of the correlation.

Thermal Balance Test Process

Figure 19.6 illustrates a relatively simple thermal balance test profile. Thermal balance testing is almost always performed as part of the thermal vacuum test. It typically precedes the thermal vacuum test, so that if the thermal balance test must be halted and changes made to the thermal design, the integrity of the thermal vacuum verification is not compromised.

The test begins with closing the chamber door and evaluating the chamber air. Sometimes the pressure is reduced below 10^{-4} torr before the chamber walls are cooled to ensure that the door is sealed properly. Pressures lower than this are typical, especially if thermal blankets are in the chamber or if materials need to be outgassed. The walls are cooled with liquid nitrogen loops to simulate the space environment. In Fig. 19.6, the first thermal balance phase plotted is a cold operational phase. Some contractors prefer to begin the test with a cold phase, in order
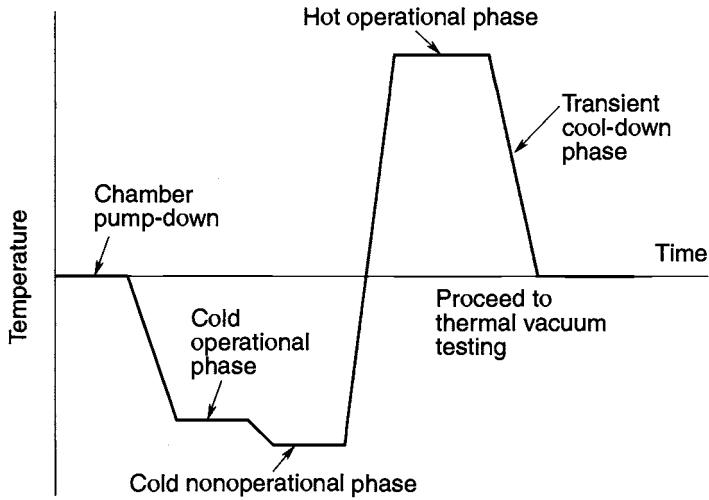
Fig. 19.6. Simple thermal balance test profile.

to simulate how the spacecraft will actually be flown, because temperatures usually decrease from launch into ascent. Others prefer to begin with a hot operational phase to increase outgassing of materials in the spacecraft.

The cold operational phase begins with the first environmental adjustment to heater banks and to the operational status of the vehicle. Prior to the test, computations are made to predict the heater lamp settings to simulate a desired environmental condition. The spacecraft electronics, bus equipment, and payload may be in a minimum power-dissipating mode. The settings for the environmental control and the operational status are made following chamber evacuation. No further changes are made to the operational status of the vehicle until the cold operational phases have completed. Environmental heating changes may be made if the controlling thermocouple on the vehicle indicates that adjustments are needed to better simulate the environmental conditions. These changes must be made well before the vehicle has reached steady-state conditions to facilitate acquiring equilibrium. All changes to equipment status and environmental control are documented and communicated through the test personnel.

The success criteria depend not only on demonstration of the thermal subsystem in operation and survival, but also on correlation of the test data with analytic thermal models. As a goal, correlation of test results to the thermal model predictions should be within ±3°C. Lack of correlation with the thermal model may indicate a deficiency in the model, test setup, or vehicle hardware. The correlated thermal math model will be used to make final temperature predictions for the various mission phases.

The correlation process begins prior to the test with thermal model predictions of the test article in the chamber configuration and environment. Modifications to the flight thermal model will include the following.

- the removal of hardware that will not be in the thermal chamber, such as solar arrays and propellant in tanks and lines
- the addition of thermal nodes for the representation of test hardware, including chamber walls, heater lamps, test stands, and equipment for payload testing
- the addition of thermal nodes for cabling with guard heater
- changes to power-dissipation levels and environments to reflect the test phase conditions
- changes to the radiation view factors to account for beginning-of-life surface properties and blockage resulting from test equipment and stowed hardware

In many cases, when the test configuration and test hardware do not resemble flight conditions, the geometric math model must be modified and run to compute view factors from the test article to the various test hardware surfaces. Test equipment may interfere with the view from the spacecraft to the chamber wall, so that its view factor is significantly reduced. The test condition view factors replace the flight view factors in the thermal model.

Once the thermal model is developed for the test conditions, temperature and heater power data are predicted for the various test phases in which correlation data are taken. These predictions are made prior to testing, so that during the test, an initial qualitative assessment can be made.

During the test, temperatures are allowed to stabilize during the correlation test phases so that reliable steady-state data are obtained. The thermal stability requirement for thermal balance testing is more stringent than it is for thermal cycle and thermal vacuum testing. The requirement commonly specifies that thermal stabilization should be achieved when the rate of temperature change is less than 1°C per hour, as measured over four hours. In addition to this criterion, engineering judgment is important. If a thermocouple is changing by 1°C per hour, but the rate of change appears constant, then the temperature has not stabilized. Verification that the rate of change is decreasing is also important, to ensure that the temperature is approaching a steady-state value.

For thermal zones cycling on heaters, the above criterion is not applicable, and yet verification of the repeatability of the heater duty cycle is important. A common criterion for heater activity is to demonstrate that the heater duty cycle is within 10% of its previous cycle. This goal is usually achieved by comparing cycle durations. In some cases, however, this criterion cannot be met. When heaters interfere with each other such that a clear, repeatable duty cycle does not occur, then engineering judgment must be used to assess whether the thermal zone has achieved equilibrium.

Because thermal vacuum testing can be extremely expensive, one tends to move to the next phase before all test thermocouples have completely stabilized. Furthermore, the time spent waiting for the final thermocouples to reach the criterion is usually a time of inactivity for all test-support personnel. However, long periods of inactivity are by nature part of thermal testing, and shortcuts will result in uncertainties in the correlation activity because they prevent proper achievement of the stabilized temperature. Experienced thermal engineers insist on soak durations after the criterion has been achieved to verify that temperatures are tending toward an equilibrium condition.

Once thermal data have been derived from a particular test phase, the thermal model correlation may begin. The thermal balance test need not be completed before correlation work is done. These activities can be performed in parallel, provided personnel are available. In fact, early model confirmation has advantages. Observations made during initial correlation activity can be checked during subsequent thermal balance test phases.

The first step in model correlation is running the thermal model with updated chamber conditions. Typically, the values of the bus voltage, lamp settings, chamber wall temperature, and operational status are slightly different than the values assumed for those parameters prior to the test. Rerunning the model will update temperature and heater power predictions for a better comparison.

The next step is to compare the model predictions with the test data. This should be done for a single test phase, typically a steady-state hot or cold phase without a majority of heaters operating. Thermal zones with large temperature discrepancies are worked first. Test conditions are reverified and obvious model omissions are checked. If these actions do not correct a problem, then the thermal model is adjusted in a direction chosen to make the temperature predictions agree with test data. Usually, heat transfer paths are altered with modifications to conductances and view factors. These changes should only be made on paths that have relatively high uncertainties, such as paths across interfaces or in complex geometries.

Changes should also be minor. Rarely are major changes made to a model. For example, a spacecraft thermal blanket should have an ϵ^* value between 0.015 and 0.060, and changing a value to something else suggests that other sources of error need to be investigated. Significant changes many times indicate a thermal model lacks sufficient detail. Changes also have to agree with the hardware design. Radiator areas and thermal mass must reflect the flight configuration. Material properties should be confirmed before they are altered.

After major discrepancies are resolved, the reconciliation process continues with other discrepancies greater than ±3°C. When the correlation is completed for the first test phase, the procedure is repeated for a second test phase. Care must be taken when changes are made in subsequent test phase correlations to ensure that the first-phase correlation is maintained. In many instances, the first-phase simulation will need to be repeated to ensure that subsequent changes to the model have not undone the correlation. When all temperature predictions have been brought to within ±3°C for all correlation phases, the thermal model is said to be correlated.

In practice, individual locations or regions of the thermal model may not correlate to within ±3°C. Inadequate knowledge of test conditions, uncertainty in how heater lamps may be interfering, and a lack of understanding of how payloads or equipment items interact are prevalent reasons as to why this may occur. In these cases, little can be done to improve correlation without guessing at conditions or adding larger uncertainties to the thermal model. The better practice is to keep the larger correlation errors and provide an explanation as to why the correlation cannot be brought to within ±3°C.

If the cause is insufficient detail or fidelity in the thermal model, then the model should be corrected to accurately reflect the heat transfer paths and physical geometry. Areas where detail is lacking typically have large temperature

differences between nodes or carry a relatively large percentage of power to be dissipated. A good understanding of the thermal model is crucial to correlation so that these observations can be made. Where practical, the developers of the thermal models should be the ones to lead their thermal correlation.

The thermal model should never be "forced" to match the test data, especially when there are few correlation test phases. Every model change should be documented with its effect, as illustrated by the temperature predictions before and after the change was made. Changes should be minimal, with a focus on those that more accurately reflect the test hardware and those that make noticeable improvements to the model correlation.

The goal of thermal model correction is bringing temperature predictions into agreement with test values (to within the criterion), but the purpose is to achieve a credible thermal model capable of making accurate flight temperature predictions and to gain a better understanding of the space vehicle's thermal performance.

The final step in the process, executed after the model is adequately correlated, is to make final flight temperature predictions. Temperature and heater power are predicted for the design conditions in worst-case operational modes, transfer orbit, ascent, safe hold, and so on. These predictions are compared to allowable limits for demonstration of uncertainty margins, both for temperature and heater power. In the case of military programs, the temperature difference between model predictions and thermal requirements would be 11°C for temperatures and 25% control authority for heater power. Correlation errors should not be used as biasing factors on these predictions. In other words, the correlation errors that result for the thermal model correlation activity should not be added to or subtracted from temperature predictions to increase thermal margins. At most, the correlation errors may be used to demonstrate that temperature predictions are qualitatively conservative with respect to the thermal balance test data, if this applies.

Commercial System Test Practices

While commercial programs perform thermal balance and thermal vacuum testing similarly to the way described in the previous paragraphs, the system thermal vacuum test has typically fewer cycles, and system thermal cycling is rarely performed. It is common for the qualification thermal vacuum test to consist of four cycles, but the same test at protoqualification and acceptance would be one or two cycles. Thermal balance testing would still be performed on the protoqualification vehicle, but the testing would generally be of shorter duration.

NASA System Test Practices

NASA and JPL system level testing is also similar to the system testing of military programs, with the emphasis on end-to-end performance verification. Test requirements are established based upon the intent of the mission (e.g., whether orbiting or deep-space). In general NASA programs are more commonly subjected to thermal vacuum tests with solar simulation heating than with heater elements. The differences between these techniques are discussed in the next section.

Thermal Vacuum Chambers

Thermal vacuum test facilities capable of handling space vehicles are classified as to whether they simulate solar heating and whether the test article is loaded from the top, bottom, or side of the chamber. All chambers must be relatively large, to accommodate space vehicles. A listing of solar simulation chambers and thermal vacuum chambers, with defining dimensions and parameters, is provided in the appendix. A representative nonsolar, end-loading chamber is shown in Fig. 19.7.

Mechanical pumps, roughing pumps, and diffusion pumps are used to accomplish pressure pump-down. Pressures as low as 10^{-3} to 10^{-4} torr are readily obtainable. Further depressurization can be achieved with cryopumps, sputter-ion pumps, or turbomolecular pumps.

Liquid nitrogen cooled internal walls typically simulate the cold environment of space. For large chambers, the walls are divided into zones capable of being independently controlled. Each zone has temperature monitors that are displayed in the test control center. Cold wall temperatures range from -196 to $-172°C$ (77 to 101 K). Although these temperatures are warmer than the absolute space temperature of $-273°C$, for nominal spacecraft temperatures, the difference in radiant-energy exchange between these two sink temperatures is less than one percent. The cold walls may also be used to warm the environment at the end or during a break in the test, with heated gaseous nitrogen circulated through the panels.

Pressurization of the chamber is accomplished with typically dry nitrogen. This allows the chamber to be returned to ambient pressure at any time that the cold wall and all major equipment in the chamber are above the minimum allowable temperature of the satellite. Moisture condensation is prevented with this method. Equipment must be above the dew point if ambient air is pumped into the chamber.

First-stage roughing pumps or diffusion pumps
Mechanical pumps capable of about 10^{-3} torr in about 4 hours

Second-stage cryo pumps or turbomolecular pumps
Capable of 10^{-6} torr in 1-2 hours after roughing

Interior of chamber: Simulates cold space LN_2-cooled cylindrical cold wall maintained at 77 K–90 K

Chamber body steel construction

Walkway and rails to transporting test article

Floor level

Fig. 19.7. Representative horizontal-loading thermal vacuum chamber (end view).

All equipment associated with the vacuum or cryogenic operations of the chamber should be redundant or able to have its function assumed by other equipment in the event of a failure. Safety measures are critical to the operation of a chamber, and keeping the vehicle in a known state is important, should supply power, cooling capability, or instrumentation monitoring be interrupted.

Methods of Heating and Cooling

The specific method used to simulate the thermal environment within a vacuum chamber depends on the chamber characteristics, size and power levels of the test article, and the experience base of the test personnel. Radiative or conductive heating is used. Cooling methods, for the most part, use the chamber cold wall as previously described, but special cooling capabilities are used in the different heating schemes. Table 19.11 summarizes the following information about the techniques.

Three radiative methods of heating are common: solar simulation, heating elements, and heater plates. Solar simulation heats the vehicle with solar-wavelength heaters that simulate the sun. A configuration such as that found in the JPL thermal chamber typifies the heating hardware. In this chamber, solar illumination is accomplished using an array of modules, each containing a 1-kW quartz-iodine lamp and a water-cooled collimator tube. The created spectrum approximates a 3000 K blackbody, so with the sun more nearly like a 5800 K blackbody, augmenting xenon short-arc lamps are used to improve spectral matching. Solar simulation is the preferred method of spacecraft heating, because it allows the natural blockage and cavity effects to occur, while imposing direct and reflected solar-wavelength radiant heating. Vehicle-handling provisions are necessary to illuminate different sides of the spacecraft. These usually enable pitch and roll capability that can put the vehicle in motion under test.

Heating elements (such as heater lamps) are perhaps the most common method of heating spacecraft in a thermal chamber. They are not necessarily within the IR wavelength band, so lamp settings must be determined prior to the test to achieve the desired heat flux. They consist of individual radiant-heating units or tubes with a half-cylinder reflector. In heater wires, a similar heating method, consisting of an array of wires through which a current runs, heating is the result of the losses within the wire. The test setup requires many lamps, but each is controlled independently, so good flexibility can be achieved.

Heater plates of a known temperature and optical property can be positioned near spacecraft surfaces and can effectively warm the test item. When the plates are placed within inches of a surface, they closely control the environment. Cooling loops on the plates are required because the heater plates block the surface's view to the chamber cold wall. The use of plates is especially well suited for payload level tests, and they have also been used at the spacecraft level.

Two conductive methods of heating are common: the use of heaters and heater plates. The heaters technique, in which resistive heaters are mounted directly to spacecraft surfaces, offers minimal test equipment blockage and in many cases is used with specific hardware heating, such as appendages (booms, antennas, etc.) that may be difficult to heat with other methods. When used with a thermal blanket, heaters are mounted to the blanket's outermost layer. This usage requires test blankets identical to the flight blankets.

Table 19.11. Advantages and Disadvantages of Heating and Cooling Methods

Method	Advantages	Disadvantages
Radiative Methods		
Solar simulation	Does not assume a prior known environment	Few solar simulation chambers sized for large spacecraft
	Minimal test equipment interference	Lamps provide parallel illumination, so some test scenarios may be impossible
	Accurately simulates solar environment	Cannot simulate nonsolar heat loads
	Can detect geometric model errors	Set can be complex
Heating elements	Lamps can be placed judiciously and operated independently, providing good flexibility	Lamps may interfere with view to chamber wall
		Many lamps required
		Heating from one zone can interfere with adjacent zones
Heater plates	Environment known accurately	Requires knowledge of absorbed fluxes for surfaces to establish lamp settings
	Provides good independent control of surfaces	
		Requires cooling in heater plates
Conductive Methods		
Heaters	Minimal test equipment interference	Requires knowledge of absorbed fluxes for surfaces to establish lamp settings
	Good for appendages such as booms, antennas, etc.	Test blankets are required if heaters are mounted to them
		Surfaces will require cleaning following heater removal
Heater plates	Direct heating of surface	Only applicable for small test articles
	Surfaces may be heated independently of others	Extremely limited test flexibility
		Cannot simulate complex environmental loads

The heater plate technique has limited application and is best suited for small test articles. The spacecraft sits upon a plate through which heat is conducted, either directly across the interface or through straps. Cooling is built into the plate because the surface cannot view the chamber wall. This technique has limited flexibility in that complex environments cannot be imposed and heat is directed from one side of the vehicle only. One disadvantage of using nonsolar-wavelength heating, inherent in all of these techniques except solar simulation, is that the incident flux is of a wavelength different from the surface treatment properties of the

space vehicle. As a result, prior to the test, the absorbed flux must be computed for each surface to establish lamp settings. Several techniques are used to account for this difference, such as direct computation of absorbed heating for the incident wavelength.

Another technique makes use of equivalent sink temperature calculations. Consider a surface shown in Fig. 19.8, such as a radiator, with an incident power dissipation from electronics, P, incident solar heating, Q_s, radiation away from the surface to other spacecraft surfaces, Q_i, and radiation to space, Q_r.

The energy balance for computing the temperature of the surface is given by

$$P + Q_s = Q_i + Q_r. \tag{19.2}$$

Expanding, one obtains

$$P + SA_1\alpha_1 = \sigma\varepsilon_1 A_1 (1 - F_{12}) T_1^4 + \sigma\varepsilon_1 A_1 F_{12} (T_1^4 - T_2^4) \tag{19.3}$$

and simplifying,

$$P + SA_1\alpha_1 = \sigma\varepsilon_1 A_1 (T_1^4 - F_{12} T_2^4). \tag{19.4}$$

If $P = 0$, then an equivalent sink temperature can be defined $T_1 = T_{ES}$ as given by

$$T_{ES} = \left(\frac{S\alpha_1}{\sigma\varepsilon_1} + F_{12} T_2^4\right)^{1/4}. \tag{19.5}$$

The conventional method of computing the equivalent sink temperature to account for absorbed heat is applied to all spacecraft surfaces that view the heating source. During the test phase, the source heating level is adjusted until the surface temperature equals the computed environmental sink temperature. This activity is performed for each test phase before the internal power dissipation is applied.

Surface 1 with absorptivity α_1, emissivity ε_1, temperature T_1, and area A_1

Surface 2 with temperature T_2

Radiative transfer, Q_r, to Surface 2 through view factor F_{12}

Radiative transfer, Q_r, to space

Power dissipation to be radiated, P

Solar heating with solar constant S
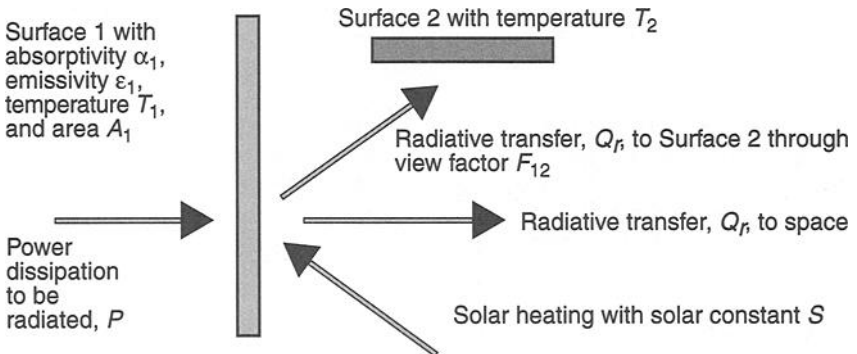
Fig. 19.8. Equivalent sink temperature schematic.

The surface temperature is monitored either with internal thermistors or, more commonly, heat flux calorimeters or radiometers.

Calorimeters and radiometers are thermocouples attached between two surfaces of controlled optical properties. Calorimeters attach to the spacecraft surface, and radiometers are typically suspended between the spacecraft surface and the heat source. In the case of a calorimeter, the control surface faces the heat source. The calorimeter is made of the same material as the spacecraft surface to which it attaches. The opposite side of the calorimeter consists of a small thermal blanket and a Velcro patch. The thermal blanket attaches to the thermocouple sensor plate on one side and supports the Velcro on the other. The Velcro mounts the calorimeter to the spacecraft and, along with the thermal blanket, minimizes conduction and radiation between the calorimeter and the spacecraft. With this insulation between sensor plate and spacecraft, the thermocouple approximates the temperature of the spacecraft surface, from which the absorbed heat can be computed.

Launch Site Thermal Testing

Just as checkout and functional tests are performed throughout the stages of the development and buildup of the space vehicle, so they are also required at the launch site. Such tests are often part of the formal development, qualification, and acceptance process, in that they verify the flight hardware has not been damaged or degraded during shipment and assembly. They consist mainly of functional tests to verify continuity and baseline performance. The tests are rarely dedicated to verifying thermal requirements; rather, to ensure that subsystems do not overheat in these tests, they include thermal control practices that typically involve gas or liquid cooling in an application such as maintaining battery temperatures.

Providing thermal control during tests may be difficult if adequate preparation has not been implemented with regard to the configuration of the subsystem or space vehicle in the launch configuration. Access to equipment panels or battery shelves is constrained by adjacent hardware (upper-stage vehicle, launch-vehicle payload fairing, acoustic blankets, etc.), such that making provisions for forced convection cooling may be difficult. The subsystem or space vehicle may be enveloped with contamination covers, shrouds, or the like, resulting in limited accessibility to forced convection cooling. Natural convection within the vehicle may result in heating of electronics in a manner different than expected in space. Finally, the subsystem or space vehicle may be oriented so that heat pipes are inoperative.

Early identification of launch site cooling requirements for checkout and functional tests is therefore imperative and is especially important for sensitive components such as batteries. Vehicle design accommodations and auxiliary ground equipment required to enable adequate cooling should be clearly specified. Items for this purpose may include ducting and fans, piping and pumps, and leveling hardware and instrumentation.

References

19.1. C. S. Tanner, "What's Happened to 1540?", Spacecraft Thermal Control Technology Workshop, The Aerospace Corporation (1 March 2000).

19.2. R. D. Stark, "Thermal Testing of Spacecraft," The Aerospace Corp. Report No. TOR-0172(2441-01)-4 (September 1971).

19.3. R. W. Burrows, "Special Long-Life Assurance Studies, Long Life Assurance Studies for Manned Spacecraft, Long Life Hardware," Martin Marietta Report No. MCR-72-169, Vol. IV (September 1972).

19.4. C. E. Mandel, Environmental Stress Screening Guidelines for Assemblies, Institute of Environmental Sciences, September 1984.

19.5. Application Guidelines for MIL-STD-1540C; Test Requirements for Launch, Upper Stage and Space Vehicles, MIL-HDBK-340, 1 July 1985.

19.6. Department of Defense Handbook, Test Requirements for Launch, Upper Stage, and Space Vehicles, Volumes 1 and 2, MIL-STD-340A (USAF), 1 April 1999.

19.7. Department of Defense Standard Practice, Product Verification Requirements for Launch, Upper Stage, and Space Vehicles, MIL-STD-1540D, 15 January 1999.

19.8. NASA Preferred Reliability Practices, Practice No. PT-TE-1402, Thermal Cycling, Lewis Research Center.

19.9. NASA Preferred Reliability Practices, Practice No. PT-TE-1404, Thermal Test Levels and Duration, Jet Propulsion Laboratory.

19.10. A. H. Quintero, J. W. Welch, and H. Wolf, "Perceptiveness of Thermal Vacuum Testing," 18th Aerospace Testing Seminar, 16–18 March 1999.

19.11. Risk/Requirements Trade-off Guidelines for Faster, Better, Cheaper Missions, Jet Propulsion Laboratory, JPL D-13277, Rev. E (February 1998).

19.12. Test Requirements for Launch, Upper-Stage, and Space Vehicles, Military Standard, MIL-STD-1540C, 15 September 1994.

19.13. J. W. Welch, "Unit Thermal Vacuum Test Consideration," Spacecraft Thermal Control Technology Workshop, The Aerospace Corporation (28 February 2001).

20   Technology Projections

T. T. Lam,[*] T. D. Swanson,[†] G. C. Birur,[‡] B. E. Hardt,[*]
J. G. Santiago,[**] and T. P. O'Donnell[‡]

Introduction

As the number of space vehicles increases, and those vehicles operate with greater power over longer life spans, their thermal management becomes ever more critical. Accompanying this trend is an unprecedented need for spacecraft size and weight reduction, and recurring launch costs are strongly tied to this need. However, reduced weight leads to higher power densities, and waste-heat dissipation densities have grown by orders of magnitude as smaller, more powerful electronics are continually flown, thanks to technology advances in semiconductor devices. In recent years, spacecraft power dissipation has increased relative to the weight of the thermal control subsystem as well as the spacecraft.

Thermal design problems that deal with these issues must be solved quickly, and, more important, the solutions must provide highly producible, cost-effective products required for all spacecraft and instruments. These trends drive development of advanced thermal control devices, materials, and techniques.[20.1] Accordingly, thermal control technologies must evolve over time.

The development effort is not, however, without its challenges. For example, one difficulty often encountered is the development of effective performance metrics for new thermal control technology. Many new thermal control technologies do not simply replace existing ones, but rather offer entirely new options for the design of the rest of the spacecraft and/or instrument. The ability of two-phase technology to separate a heat source from its eventual sink is a classical example of this capability. Hence, while the new thermal control hardware may actually be heavier or more expensive than the hardware associated with a conventional design, it may also allow mass/cost savings or performance upgrades in other subsystems. Such benefits are often indiscernible to nonspecialists, and thus the opportunity to employ new technology may be missed.

Garnering support for the development and use of new thermal control technology is often difficult. Part of this challenge is the classic "catch-22" problem: mission architecture and design are based on the projected capabilities of new technologies, but the development of technologies with broad, system-wide impacts (such as some thermal control technologies) is directly impacted by the definition of such mission architecture. Hence a trend has arisen to develop more-generic technologies that can be broadly applied to a variety of related mission concepts. This situation reflects the way technology innovations develop in other areas. Although often "necessity is the mother of invention," in actuality a great many

*The Aerospace Corporation, El Segundo, California.
†NASA Goddard Space Flight Center, Greenbelt, Maryland.
‡Jet Propulsion Laboratory, Pasadena, California.
**Stanford University, Palo Alto, California.

significant inventions either result from nondirected curiosity or find their greatest applicability in a purpose entirely different from that for which they were developed. While the steam engine, cotton gin, and atomic bomb resulted from directed-development efforts, the phonograph, gasoline engine, airplane, and transistor were initially inventions in search of a popular application. The same development patterns are found among thermal control innovations; hence the difficulty in anticipating both future performance capabilities and applications.

Technology Drivers

Clearly, the purpose of many new missions is to achieve new science or observational capabilities, and this goal inevitably requires more sensitive measurements, greater pointing accuracy, the ability to operate in more challenging environments, and other capabilities. To achieve these advanced capabilities the demands on the engineering subsystems will naturally increase. Conventional thermal control technologies, such as heaters, multilayer insulation (MLI), heat pipes, louvers, and specialized radiator coatings, are even now inadequate for many spacecraft. For example, numerous recently launched spacecraft (e.g., TERRA, Mars Pathfinder, high-power comsats) and others in the development stage (e.g., ICESAT, SWIFT, Mars Exploration Rover) use "new" technology, such as two-phase heat-transport devices and long-life mechanical pumps, simply to meet mission requirements. However, even these recent technology innovations will clearly be inadequate for future missions currently being envisioned. The future top-level system-level design drivers that will influence the development of thermal control subsystems include:[20.1]

- spacecraft functions and missions
- mission operational plan and specific requirements
- spacecraft orientation and orbital constraints
- spacecraft weight and size envelope (volume) constraints
- launch vehicle
- bus and payload configuration, equipment locations, deployments
- propulsion needs
- power and on-time percentage
- equipment operating-temperature ranges, power dissipations, power densities, and duty cycle
- requirement for temperature stability down to a few milliKelvin
- materials
- cryogenic cooling capacity
- integration and test
- manufacturability and cost

Thermal control subsystems must improve as spacecraft and instruments become increasingly sophisticated. The thermal subsystem is more and more intimately tied to other parts of the spacecraft, and it affects, and is affected by, other subsystems. These interrelationships greatly complicate the thermal design effort. Some of the current and emerging technical requirements pushing the development of new thermal control technology include:

- stringent temperature control (±1°C or less, as opposed to the much larger range, perhaps ±20°C, of earlier equipment)
- optics and instruments operating at increasingly deep cryogenic temperatures (40 K down to 4 K)
- components, such as lasers and microprocessors, with very high flux requirements (> 100 W/cm^2), possibly also coupled with tight temperature control
- small allowable temperature gradients over very large areas, included in designs to maintain dimensional stability for large mirrors, optical benches, antennas, or similar devices
- extremely challenging thermal environments (e.g., environments near the sun, planetary surfaces)
- minimal spacecraft resources (e.g., heater power, control circuitry, mass and volume allowances) with which to accomplish tight thermal control
- increasing interdependency of spacecraft/instrument subsystems that restrict use of conventional approaches to thermal design
- miniaturization of spacecraft, which may preclude the use of conventional devices because of space or resource issues
- fleets consisting of large numbers of spacecraft that must be designed nearly identically for cost reasons but that will be exposed to a wide variety of thermal environments
- radiator field-of-view constraints on complex spacecraft

Programmatic Concerns

In addition to the system and technical drivers discussed above, a variety of programmatic issues also impact the development of new technologies. These include: the shortening of spacecraft/mission development cycles, which compresses the technology-development effort; funding difficulties; perceived risk involving the introduction of new technology (e.g., performance, cost, schedule); the increasing use of "standardized spacecraft buses" that may not be ideally suited for scientific spacecraft; and the recurring push to minimize ground verification testing.

Future Technologies and Innovations

Despite programmatic and technical difficulties, to meet these new requirements and thus enable and enhance future missions, development of advanced thermal control technology is important. Accordingly, selected technology development efforts are currently underway. Many other technology thrusts are possible, but given the technical challenges and programmatic limitations addressed above, only some efforts are being pursued. What follows is a noninclusive discussion of such efforts.

Composite Materials

Composite packaging and structural materials have been used in the development of a variety of spacecraft components, including electronics packages, microwave components, heat sinks, chassis, and spacecraft structures.[20.2] Schmidt and

Zweben[20.3] and Zweben[20.4] discuss the large number of possible composite materials that can be achieved via combining various reinforcement materials (e.g., carbon/graphite fibers) with a large variety of matrix materials. Composites reduce weight and are excellent paths for the removal of excess heat from electronic devices. Kibler and Davis[20.5] identified possible applications for carbon-carbon (C-C) composites in spacecraft designs. They also predicted the possible range of properties for C-C composites and estimated the payoffs of using these composites over alternatives (typically aluminum). The four components considered to be appropriate candidate applications were

- thermal doublers
- electronic circuit-board heat sinks
- advanced battery components
- nonstructural radiators

The use of C-C composites in these applications should result in components with thermal conductivities greater than twice that of pure aluminum with a 20 to 40% decrease in weight. Glatz et al.[20.6] presented a succinct survey of possible electronic-component applications for advanced composites. Components and applications were divided into the following categories: power-generation devices, power-storage devices, electronic devices, heat-rejection devices, power signal/transmission devices, and structures. Glatz et al.[20.6] listed typical designs, suggested candidate materials, and discussed potential performance improvements.

Figure 20.1 shows the thermal conductivity of various carbon composite materials and conventional metals. K1100 fibers have been developed specifically for thermal management applications. This carbon fiber has a thermal conductivity three times that of copper (1100 W/m·K) and a density one-fourth that of copper,
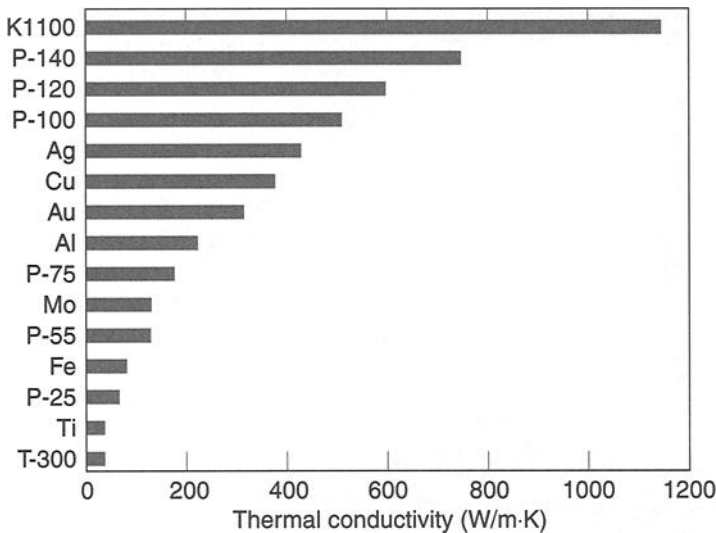
Fig. 20.1. Thermal conductivity of carbon composites.

and it is available commercially. This fiber has been successfully incorporated into organic and metal (e.g., copper, aluminum) matrices. Prototype substrate/heat sinks for electrical components on printed wiring assemblies and radiator panels have been successfully created utilizing these materials.

The carbon-composite conductivity values in Fig. 20.2 are for one-dimensional fibers only. Note that the theoretical value for a carbon fiber is 2400 W/m·K. The effective conductivity depends greatly on fiber orientation and processing techniques (carbon filled, epoxies, and metal matrix). It is very important to note that practical limitations prevent the achievement of such dramatic theoretical conductivity values. For example, while the carbon of a carbon fiber/resinous composite material may have conductivities on the order of 2400 W/m·K, the resin and/or other fill material can reduce such values by half or more. Additionally, such composite structures typically have high conductivity in one or at most two dimensions. In the other dimension they often function as thermal insulators. This can have a big impact on effective thermal conductance across joints.

Material properties desirable for satellite applications include tailorable and/or low coefficient of thermal expansion (CTE), extremely high thermal conductivity, high stiffness and strength, and low density. Other desirables include low cost and resistance to severe environments. As examples of recent advancements, Schmidt and Zweben[20.3] cited materials such as an experimental vapor-grown carbon fiber with a conductivity five times that of copper. A commercially available pitch-base carbon fiber combines a conductivity 50% greater than that of copper with an elastic modulus 12 times that of aluminum. In addition, materials with a CTE as low as 1.7×10^{-6} K^{-1} have been achieved.

Zweben[20.4] presented an excellent discussion of key trends in packaging and structure technology accompanied by a summary of material properties and applications.
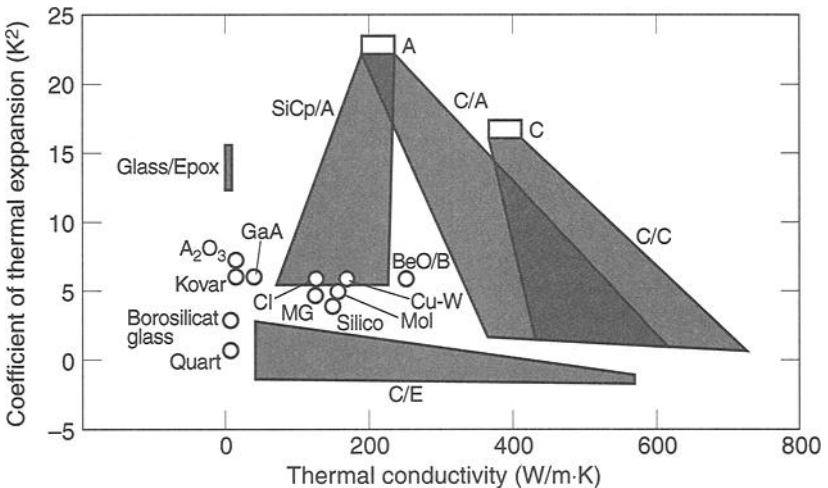
Fig. 20.2. Thermal conductivity and coefficient of thermal expansion.

The applications discussed include electronic and microwave packages, heat sinks for printed circuit boards (PCBs), and electronic enclosures. Furthermore, Zweben[20.4] discussed new and developing fabrication techniques such as pressure infiltration, pressureless infiltration, and investment casting. Also discussed were solder and brazer material technologies that would improve strength and creep resistance, and reduce CTE. Zweben[20.4] cited the potential of technologies such as diamond particles and fibers made using chemical-vapor deposition, two technologies that possess highly desirable properties but are, however, too costly to be practical.

C-C materials have been the subject of research and development efforts at the Air Force Phillips Laboratory, NASA, Amoco, Lockheed Martin, TRW, and the Naval Surface Warfare Center. The use of carbon as both the fiber and matrix material offers the advantage of much higher thermal conductivity through the thickness of the panel as well as the potential for high-temperature applications. Drawbacks, however, include much higher cost and a limited satellite-level manufacturing experience base compared to that of graphite-reinforced polymers.

As part of the C-C Spacecraft Radiator Partnership (CSRP), which consists of members from government and industry, a C-C radiator/structural panel (Fig. 20.3) was flown on EO-1 by NASA/GSFC (Goddard Space Flight Center) in November 2000, and the technology was successfully validated.[20.7,20.8] C-C radiator panels can reduce spacecraft weight and can be used as part of the spacecraft structure. The disadvantage of the C-C radiator is that it is easy to damage and is not very practical unless one is really pushing weight margins. Further development must take place on the C-C process to generate ways to reduce fabrication time and cost.

Aluminum matrix composites and C-C composites based on vapor-grown carbon fiber (VGCF) have been fabricated. Because of the highly graphitic nature of VGCF, the resulting composites exhibit high overall thermal conductivity. The new materials are useful for thermal management applications such as the packaging of high-power and high-density electronic devices. Figure 20.4 shows the thermal conductivity of VGCF in a carbon matrix (VGCF/C) composite as a function of temperature. A thermal conductivity of 1200 W/m·K at 160 K has been measured for VGCF/C composites (Applied Sciences, Inc.). NASA/Goddard has
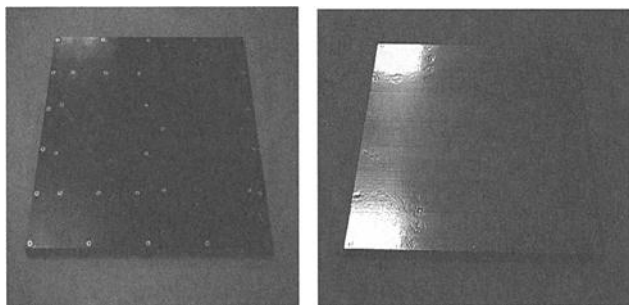
Fig. 20.3. EO-1 C-C radiator.
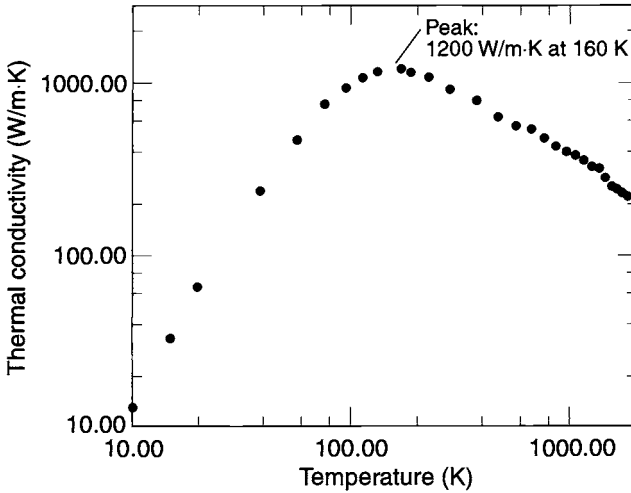
Fig. 20.4. Vapor-grown carbon-fiber/carbon-matrix composite thermal conductivity.

obtained similar test data that indicated the materials are suitable for midlevel cryo-type applications but not as good as Cu and others at very deep cryo.

Current Applications

Talley[20.9] presented a discussion of practical composite applications currently under development at Lockheed Martin Astro Space. Structures that combine highly thermally conductive carbon/cyanate-ester facesheets with more traditional aluminum components to provide low weight and high overall conductivity were presented. These structures use unidirectional and quasi-isotropic laminates, sandwich panels, and epoxy adhesives to provide thermal management and high strength. Solar panels in development that use carbon/cyanate-ester facesheets, film adhesives, and Kapton to provide lightweight construction were also discussed. Other applications presented included structural joints, transitional joints, and radiators.

Lockheed Martin[20.10] presented a forecast of its technological advancements over the next 10 years. In the area of high-conductivity composites, the following applications were cited: battery sleeves, thermal doublers, electronics substrates, thermostructures, and high-temperature applications (including aerobrakes and solar shields). Swales[20.11] presented a listing of advanced material applications that, for instance, use Kevlar-Epoxy and Graphite-Epoxy in the construction of solar panels, structural brackets, structural composite panels, tubes, and struts.

Most of the materials discussed in their presentation, such as pitch-based and pan carbon fibers, Aramid, and thermoplastic resins, are commercially available. Montesano and Cassin[20.12] presented a patented material that can be used in heatsink applications; it consists of graphite blocks encapsulated in aluminum. The material offers high thermal conductivity (more than four times that of pure aluminum) and low mass density (slightly lower than that of pure aluminum), and it has

been used successfully in specialized aircraft avionics. This "macrocomposite" can be manufactured using different encapsulates such as copper and aluminum/ beryllium alloy.

Material Property Measurements and Basic Research

In the last few years, significant research involving the basic study and measurement of the properties of composite materials has been conducted. Riley[20.13] discussed the properties of ThermalGraph (a C-C composite manufactured by Amoco), which has a conductivity 3.4 times that of pure aluminum and approximately 80% of its density. Ting and Corrigan[20.14] presented an investigation of the conductivity, density, strength, and CTE of vapor-grown carbon fibers.

Carbon fibers under study include Amoco's K1100, P-100, and P-120 and Nippon's XN-70A (see Crasto and Anderson,[20.15] Shih,[20.16] and Krumweide[20.17]). Crasto and Anderson[20.15] used X-ray diffraction and electron microscopy to examine the microstructure of high-modulus carbon fibers. They found that processing these fibers with lower degrees of graphitization produces fibers with better compressive strengths but with lower axial thermal conductivity (and higher electrical resistivity). Crasto and Anderson[20.15] cited this trade-off between compressive strength and thermal conductivity as an important consideration in the selection of a fiber for a thermal structure application. Users of these advanced carbon fibers have noted that obtaining quality fibers from American suppliers can be difficult and that raising the quality level of domestic fibers to that of Japanese competitors' fibers should be given some priority.

Silverman and Kagohara[20.18] presented the advantages of fabricating radiator-panel facesheets and doublers for use under electronics boxes made of K1100 C-C composite materials in lieu of the conventional aluminum. About 16% weight reduction was shown through the replacement of aluminum heat-pipe radiators with C-C radiators without heat pipes in one particular design. Note that the classic CTE mismatch issue needs to be resolved prior to use in real engineering applications. In addition, the authors suggested that up to 50% weight reduction can be achieved by the replacement of traditional aluminum facesheets and doublers with C-C, in some cases. More recently, Shih[20.16] presented properties of several carbon fibers that are good candidates for thermal doubler and radiator facesheet applications. Shih[20.16] discussed combining high-stiffness fiber composites with compliant adhesives in the construction of PCBs and avionic thermal plane attachments. Such materials would reduce both vibration amplitude and vibration-induced strain. Finally, Krumweide[20.17] presented an investigation of the properties and possible applications of Amoco's K1100X fiber. This investigation discussed K1100X's use in cardguides and cardcages, radiators, conductors, spacecraft bus structures, electronic packaging, and heat sinks.

Future Development Effort for Composite Materials

Composite materials have seen widespread use in structural applications. Loral is currently building GEO (geosynchronous orbit) comsats whose structures are almost entirely composite (the north and south radiator panels of these satellites hold most of the electronics and are not manufactured using composites). The principal impediment to use of composite radiators is the difficulty of attaching heat pipes to the composites because of widely different CTEs of the materials. To

date, bonds that are sufficiently compliant to accommodate the resulting relative displacements have had high thermal resistances. The higher resistance drives the use of panel facesheets that are much thicker and thereby eliminates the weight savings offered by the composite.

A second problem is the relatively poor thermal conductivity through the thickness of most composites. While the specific conductivity in the plane of a composite panel may be five times higher than that of aluminum, the conductivity through the thickness may be 300 times lower. For thin panels, the small conduction distance from the surface to the center of the material ensures a low temperature gradient. However, as the thickness increases, the resistance will become substantial, as in the case of thermal doublers.

Additional research efforts should be devoted to the development of technologies for joining low thermal resistance composites and heat pipes, as well as to the improvement of the through-thickness conductivity of composite panels. A possible solution to the joining problem may be development of space-qualified composite heat pipes. The emerging technologies of composite electronics boxes and circuit-card thermal planes present an opportunity for substantial weight savings through the use of stiff, high-conductivity, low-density materials.

Furthermore, materials need to be developed and demonstrated at low and high temperatures. This requirement is important because of the recent development of SiC electronics that can operate at high temperatures. The new materials can be used to decrease the temperature gradients between electronic parts.

Composite material that uses carbon for both the fiber and the matrix material has high thermal conductivity and good strength, and it is lighter than aluminum. It can be used in high-temperature applications (e.g., aircraft brakes, space-shuttle wing leading edges) but has been used with limited application elsewhere to date, primarily because of cost and production lead time. In an era when "faster, better, cheaper" is still a key focus for most space-related projects, the manufacturing process needs further development to obtain ways to reduce the fabrication time and cost.

Diamond Films

CVD (chemical vapor deposition) diamond films offer the potential for up to 3 to 4 times the conductivity of copper. Recent testing using a sample measuring $3 \times 0.5 \times 0.022$ inches has indicated values of 11 W/cm·K at room temperature. Additionally, other forms of advanced composite carbon devices (e.g., annealed pyrolytic graphite) have demonstrated (two-dimensional) conductivities of up to 13 W/cm·K at room temperature. In both cases the conductivity was very dependent on measurement technique (interface resistance, vacuum vs. air, temperature, etc.).

Ultrahigh-conductivity materials such as CVD diamond are also very promising for spreader-type applications where a large area needs to be cooled. Most typically these ultrahigh-conductivity materials could be used as films to collect energy and then could be connected to a more efficient heat-transport mechanism, such as a two-phase device, for transport over long distances.

CVD diamond is a unique substance, which can be used as a heat spreader. It is the hardest known material, with excellent mechanical strength; it is an excellent electrical isolator, and it may be used as a semiconductor. It also has the lowest

coefficient of friction and the highest thermal conductivity of any material, which is approximately 4 times that of copper, and it has diffusivity about 20 times that of copper. CVD diamond has a wide range of potential space applications. This material has been selected as a candidate for application as diode heat spreader.

Thermal Control Coatings

Thermal control coatings are used on a space vehicle for various purposes. Solar reflectors, such as second-surface mirrors and white paints or silver- or aluminum-backed Teflon, minimize absorbed solar energy, yet they emit energy as a black-body does. To minimize both the absorbed solar energy and infrared (IR) emission, polished metal such as aluminum foil or gold plating is used. On the interior of the vehicle, black paint is commonly used to exchange energy with the compartment and/or other equipment. Thus, today's space systems use a wide variety of wavelength-dependent coatings. In-space stability, outgassing, and mechanical adhesion to the substrate are common problems space systems encounter. Because many coatings have been fully qualified, development and qualification of a new coating for a new design has not typically been necessary until very recently. Now, new EPA requirements requiring the elimination of CFCs, electrostatic discharge (ESD) concerns for spacecraft in certain orbits, and other drivers have led to the need for new advanced coatings.

Factors that affect thermal control finishes are charged particles, atomic oxygen (AO), ultraviolet (UV) radiation, high vacuum, and contamination films that deposit on almost all spacecraft surfaces. The general result of these drivers is typically an increase in solar absorptivity with little effect on IR emittance. The degradation of these surfaces is undesirable from a thermal control standpoint because spacecraft radiators must be sized to account for the increase in absorbed solar radiation that occurs as a result of degradation over the mission. These radiators, which are oversized to handle the high solar loads at end-of-life (EOL), cause the spacecraft to operate much cooler in the early years of the mission, frequently necessitating the use of heaters to avoid undertemperature electronic components. The stability of the coating properties is therefore important to minimize radiator size, heater power, and weight.

Future thermal control requirements for space systems are projected to continue to become more demanding: tighter temperature control, higher power dissipation, smaller size and lighter weight, ability to endure longer missions, and more cost-effective designs. Projections suggest that advanced solar reflective coatings and variable-property coatings could provide significant benefits for future space systems. These benefits would lead directly to smaller radiators, lower heater-power requirements, and lighter systems.

One of the most common and critical spacecraft coatings is the solar reflective coating. These coatings are used on external surfaces to minimize absorbed solar radiation while maximizing the amount of energy emitted in the IR wavelengths. A number of these coatings are used in industry. Standard coatings include: OSR quartz mirrors, Silver Teflon FOSR, A276 Organic White Paint, and Z93 Inorganic White Paint.

A number of parameters drive selection of these materials, including protections against AO and ESD, UV/VUV (vacuum ultraviolet) radiation, protons, electrons,

manufacturing, cost, and environmental impacts. Primary consideration is given to solar absorptance and IR emittance. Solar absorptivity can significantly degrade in the space environments.

Silvered Quartz Mirrors

Silvered quartz mirrors are a very common type of optical solar reflector (OSR) with a long history in spacecraft thermal control. These OSRs are typically constructed by vapor-depositing a highly reflective metal, typically silver, on the underside of a piece of quartz. The thickness of the quartz (typically 5 to 10 mils) provides a high IR emittance while being transparent in the solar wavelengths. The major advantages are the high α/ε ratios and the stability. However, the mirrors are inherently rigid, brittle materials and are usually manufactured in units approximately 1 square inch in area. The small size necessitates time-consuming "tiling" of large radiator areas. The rigidity and brittleness of the quartz make it difficult to apply these mirrors to anything but nearly flat surfaces. A thin conductive coating is typically needed to meet the ESD requirements for today's space systems. This coating, typically indium tin oxide (ITO), is also a very brittle material. ITO is also very difficult to handle on the ground; it can be rubbed off very easily. Antimony tin oxide (ATO) and indium oxide (IO) are more-durable alternatives under development. Lastly, these mirrors are relatively heavy in comparison to white paints and flexible OSR (FOSR) materials.

OSRs continue to be used in spacecraft when the thermal design requires very high α/ε ratios and stability at the expense of weight, application, and handleability. However, recent advances in micro OSRs are replacing these materials.

Microsheets

Advances in the last few years have led to thinner OSR materials called microsheets. Although the sheet thickness of these materials has been reduced, their optical properties have been maintained. For instance, a 2-mil CMX mirror has approximately the same properties as an 8-mil quartz mirror. In addition, micro OSRs can be manufactured in larger areas than quartz mirrors, 4×4 inches rather than 1×1. The thin OSRs of yesteryear used to break very easily. Getting them to stick was also an issue.

Advanced Spray-On Thin Films

OSR materials offer excellent optical properties and stability in the space environment. However, drawbacks exist in terms of application, weight, brittleness, handleability, ESD protections, etc. Wright Patterson Laboratories is currently funding an SBIR (Small Business Innovative Research) Phase I program to investigate the potential of a novel spray-on OSR process. The concept is to first spray (in air) a silver undercoat directly on the desired surface to provide the solar reflective substrate. Then the high IR emittance and solar-transparent silica coating is sprayed onto the silver. The process is environmentally friendly. Small samples with thin silica layers (≈ 0.5 mils) have been produced as a proof of concept in the SBIR Phase I. The stability of these samples with respect to the space environment remains to be tested. Phase II will investigate the ability to produce films of acceptable thickness to achieve the acceptable optical properties.

Silvered Teflon FOSR

The most common type of FOSR is silvered Teflon. This material provides excellent beginning-of-life (BOL) properties with good application, cleanability, handleability, flexibility, etc. However, certain disadvantages accompany its use. First, it is known to degrade with high levels of electron and proton exposure. Second, Teflon acts as an excellent capacitor for storing electrostatic and bulk charge buildup, which can lead to catastrophic ESDs. At least one lead contractor in industry has internally prohibited using silvered Teflon on any system other than those traveling in low Earth orbit (LEO). The ESD problem has been addressed by using a conductive ITO coating. However, this coating is brittle and susceptible to cracking. Hence handling and cleaning concerns often are very time-consuming and costly. Much of the LEO problem with silver Teflon was found to be in how it was applied. Use of a transfer adhesive and vacuum bag is best and can give an EOL α of ~0.1.

Advanced Metalized Polymer-Based Film

Trident Systems and NASA Langley have been developing clear, oxygen-resistant polymer-based films. The films have been developed and tested for AO erosion. However, the susceptibilities of these films to electrons, protons, and UV/VUV radiation are of concern, based on experience with the parent material, Kapton.

Tedlar Film

Dupont has developed a film called Tedlar. Similar to Teflon, it comes in a number of colors. An oversimplified description of the product is that a Teflon-type clear binder is loaded with various pigments to obtain the desired color. Depending on the pigment loading and thickness of the film, the absorptivity and transmissivity of the film can vary significantly. These films have been shown to be susceptible to UV/VUV degradation. Electrostatic charging could also be of concern, depending on the conductivity of the pigment.

Advanced Coatings

A number of thin-film coatings are available that can be utilized in conjunction with the thin-film products to meet various requirements. OCLI has developed and qualified a proprietary AO/UV/VUV protective coating for white Tedlar films. This coating was developed and qualified for the NASA/Goddard Tropical Rainforest Measurement Mission (TRMM), which was launched in 1997. The coating provides very good AO resistance and good protection of the Tedlar from the UV/VUV degradation. However, this film does not provide a conductive path for protection against ESD events.

At least two coatings are used in industry to protect against ESDs: ITO and Germanium (Ge). Thin ITO films are relatively transparent in both the IR and solar wavelengths. Their application typically increases the solar absorptance by ~0.04 with little effect on the IR emittance. However, ITO can easily be removed from a surface through normal handling. IO and ATO do not appear to have this issue. Germanium, on the other hand, significantly changes both the solar absorptance and IR emittance of the material.

Organic White Coatings—Paints

When describing white paint used in industry, the term "organic" refers to the binder of the paint. In general, these paints tend to degrade very significantly with UV/VUV, electron, and proton exposure resulting from the darkening of the binder. They are also susceptible to charge build-up and AO erosion. The advantages of these coatings are the ease of application, durability, flexibility, and cost. In general, the degradation of the α/ε ratio and the ESD concerns hamper the widespread use of these paints, especially for systems with long mission requirements. Some work is being conducted to produce conductive organic paints to alleviate the ESD concerns. However, the basic degradation of the binder will continue to hinder the use of this paint for future systems. For LEO applications, ongoing research is taking place to utilize AO erosion of the binder material to "scrub" the surface clean and leave the pigment on the outer exposed surface, leading to a low α property.

Inorganic White Coatings—Paints

These inorganic binder paints, also used in industry, are more stable to the space environments than the organic binders. However, they tend to be hard to apply, nonflexible, and not very durable, and they require careful handling. Use of these paints has been very limited because of such issues. Some contractors have "unofficially" banned the use of inorganic paints. As with the organic binder paints, ESD issues remain unresolved.

Advanced Plasma Spray Coatings

A plasma spray process for depositing a ceramic coating on high-conductivity substrates is being funded by Wright Patterson. The advantages are: ease of application; good adhesion properties with C-C, aluminum, and polycyanate composites; possibly a tenth of the cost of traditional inorganic paints; and good AO resistance properties. The disadvantages and remaining concerns are: the ability of different substrates to withstand high-temperature application; the stability of the coating under UV/VUV and electron environments; and the ability to bleed off electrostatic charge build-up. The near-term goal is to optimize the process and identify the pigment powder size that would maximize the optical properties. Environmental testing will also be conducted to address the stability of the coating in the space environments.

Advanced Paints/Coatings

Limited funding is available for developing advanced white paints. The requalification of a number of white paints is being funded to meet new EPA (Environmental Protection Agency) requirements. ITTRI (ITT Research Institute) and Aztek have been able to reformulate a number of the paints to meet the EPA requirements while maintaining equivalent optical properties of the parent paints.

Concepts currently being explored on how to produce conductive paints include doping the paint with conductive pigments, encapsulating conductive pigments, and using conductive binders. All the approaches produce concerns involving the stability of the paint in space environments. The NASA SEE (Space Environments and Effects) Program is currently funding efforts to investigate this area.

The inorganic paints are more attractive than organic paints because of their better stability when exposed to UV/VUV radiation. However, adhesion, flaking, and handling concerns have significantly limited their use. A project has been funded to develop an inorganic white paint and a reliable process for coating any type of material. The preliminary samples have produced flexible inorganic white paints possessing good BOL properties ($\alpha < 0.15$, $\varepsilon > 0.85$). The process utilizes an intermediate conversion coating between the paint and the substrate. This conversion coating can be made conductive in an effort to reduce the ESD concerns. However, ESD concerns still exist with the paint itself.

Similarly, an effort has been funded to develop low-solar-absorptance coatings. Preliminary samples had measured BOL properties of $\alpha \approx 0.04$ and $\varepsilon \approx 0.90$. These types of coatings could offer a tremendous advantage to future space systems. However, ESD continues to be a major concern.

NASA/GSFC has been working with Aztek to develop Aztek White Low Alpha (AZW LA-II) paint (BOL: $\alpha = 0.07$ with $\varepsilon = 0.91$ for a 10-to-13-mil-thick coating). This paint is proving to be very difficult to apply in such thickness in a uniform manner, especially for nonflat surfaces. However, its properties are so good that NASA is compromising and going to an ~8 mil thickness, which is providing an α of 0.10. NASA/GSFC is currently applying this paint to the radiators for the BAT (Burst Alert Telescope) and XRT (X-ray telescope) instruments that will fly on the SWIFT mission in 2003.

Variable-Emittance Technologies

Minimizing heater power requirements and thermal control hardware weight in future space systems is highly desirable. The heater power and thermal control hardware weight can vary significantly depending on mission requirements. In the design of today's space systems, approximately 5–7% of the satellite power is typically allocated for heater power and 2–10% of the satellite dry weight is allotted for the weight of the thermal control subsystem.

An emerging technology that could significantly reduce these allocations is variance of the optical properties of the thermal radiator finishes. A number of types of surface treatments might produce variable properties: MEMS (microelectromechanical systems)-based minilouvers, electrochromic (EC) devices, and electrophoretic, electrostatic, and thermochromic devices. EC devices are polymer based and hence employ a "wet" chemistry. All previous attempts have demonstrated the difficulty of developing such EC devices that survive a vacuum. Ashwin-Ushas has very recently provided some samples that appear to have resolved this issue, but many questions remain. The same can be said of all the other candidate technologies. The electrophoretic concept didn't survive vacuum, and was dropped; a mechanical/electrostatic concept has replaced it. The other two are still in the infancy stage and have been assessed to have a number of significant concerns (contamination and stability, etc.) associated with their applicability to space systems.

Solid-state EC materials provide the capability to vary the optical properties of a surface by the application of a small voltage potential across the material. EC materials can behave thermally as mechanical louvers without complicated moving mechanical assemblies, bimetallic strips, solar trapping, or annoying hysteresis. This material characteristic would lead directly to more economical and reliable

space systems. However, these advantages have not been quantified. The information in the following sections is based on an article by Cogan[20.19] presented at The Aerospace Corporation's seventh Thermal Control Technology Workshop.

EC Principles

EC devices operate on the principle that an EC material changes its reflectance in IR wavelengths by the addition or removal of ions or electrons. When a small biased voltage (less than 2 Vdc) is applied, the charged ions are either collected or removed from the EC layer of the device, resulting in a change in the IR reflectance of the device. The EC process is a reversible, solid-state reduction-oxidation (redox) reaction. The prototypical EC materials are transition metal oxides that undergo reversible redox reactions. Two types of optical modulation are obtained depending on whether the EC material is crystalline or amorphous.

Crystalline EC materials develop a broad reflectance band in the IR (2–40 μm) and become increasingly reflective as the concentration of inserted alkali increases. The reflectance is the result of an increase in free-electron density, which causes the crystalline material to undergo a controlled transition between an IR-transparent wide-band gap semiconductor and an IR-reflective metal. In principle, crystalline EC materials exhibit a reflectance edge that moves to shorter wavelengths as the alkali concentration increases, and they are transparent at wavelengths shorter than the reflectance edge. In practice, the reflectance edge is broadened by free-electron scattering, and some absorption is observed at wavelengths shorter than the edge.

An amorphous EC material develops a broad absorption band from 0.4 to 2.0 μm upon alkali insertion. The absorption band is usually centered in the near-IR ($\approx$ 0.8–0.9 μm) and increases in intensity with increasing alkali insertion.

Thin-Film Devices for IR Modulation

An alternative approach is to use thin-film technology. In this approach, a thin film of tungsten oxide is used as the active material with lithium as the ion carrier. The materials offer potential advantages of a large number of switching cycles and increased IR-emittance modulation. A method for producing a low solar absorptance value is uncertain but may be possible using a dielectric mirror.

This technology is a spin-off of the development for terrestrial applications using variable solar-transmissive devices with amorphous tungsten oxide. A large number of cycles has been demonstrated on similar solar-transmissive materials used for terrestrial purposes. Thin-film devices to vary the transmissivity in the solar wavelengths are being actively pursued for terrestrial applications. This technology could provide devices that modulate the solar-absorptance property. The applicability of these devices in space systems would be much more specialized and not of general interest. However, this technology provides a good foundation for developing variable-emittance devices.

Polymer-Laminate Devices for IR Modulation

Dornier has actively been pursuing electrically controlled, low-absorptance, variable-emittance devices for spacecraft. The approach Dornier is taking is to develop a variable-emissivity, low-α, EC device. In this approach, conductive polymers are used as the active materials. However, of concern is the number of switching

cycles. The details of this work have not yet been obtained. A potential flight test of these materials aboard ASTRO-STAS has been rumored.

Some basic EC device requirements are:

- minimum high emittance (0.8) and maximum low emittance (0.2)
- time duration to switch states (60-sec goal but 300 acceptable)
- survival and qualification temperatures (−110 to 90°C)
- maximum power consumption (0.14 W·hr/m^2)
- maximum weight per unit area (1 kg/m^2)
- stability in electrons (1 MeV, 2×10^{15} electrons/cm^2) and protons (10 MeV, 1.0×10^{13} protons/cm^2)
- stability to UV radiation
- vacuum compatibility with low outgassing
- minimum number of thermal cycles (10,000)
- minimum number of switching cycles (10,000)
- ESD (must be unsusceptible to damage)

Variable-Emittance-Coating (VEC) Applications

Designs

A VEC design is composed of a variable-emittance coating that comprises a series of vacuum-deposited thin films with an overall thickness of ~1.5 mm. The emittance is modulated by application of a voltage between the electronic contacts. The magnitude and polarity of the applied voltage determine the reflectance of the crystalline EC layer. IR-emittance modulation is obtained by contrasting this reflectance against an emissive (IR-absorptive) substrate. The following schematic is EIC Laboratories' approach for developing a variable IR-emissive thin-film EC device. The variable transmissive device is somewhat similar but uses an amorphous WO$_3$ (tungsten trioxide) as the active layer.

Devices

In the area of variable-emittance devices and thermal switches, two specific technologies are being investigated. One is based on an inorganic material such as WO$_3$, and the other is an organic material based on conducting polymer (Chandrasekhar[20.20]). EC devices are being evaluated for their variable-emissivity property for replacing thermal control louvers on future spacecraft. The cost and mass of EC devices are an order of magnitude lower than those of the mechanical louvers currently used on spacecraft.

EC devices based on conducting polymers are currently undergoing tests at JPL and GSFC for their performance and also for their reliability in the space environment for long-term operation. (A sample of such an EC device fabricated by Ashwin-Ushas of New Jersey is shown in Fig. 20.5.) A change in the IR emissivity from 0.39 to 0.74 has been measured on these devices so far. Development and test efforts are currently underway to broaden this change to 0.3 to 0.8. This improvement will give an emissivity range of 0.5, which is similar to what is currently obtained from mechanical louvers. Further, these EC devices weigh less than 400 g/m^2, whereas the louvers weigh 5 kg/m^2.
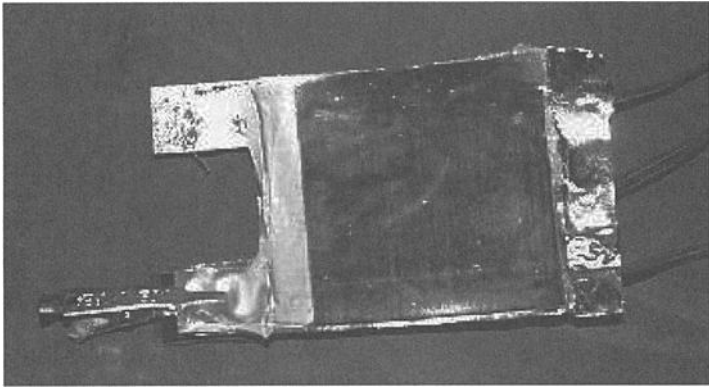
Fig. 20.5. Variable-emittance EC device (Ashwin-Ushas[20.21]).

Surface Treatments

Variable-emittance surface treatments (coatings) have been identified as perhaps the next major technological innovation in thermal control. Analytical system studies have demonstrated power savings of more than 90% and/or weight savings of more than 75% over conventional technologies for representative applications.[20.22] Three of these variable-emittance technologies are slated to be flight demonstrated on the ST-5 spacecraft that is to be launched in 2004. It is anticipated that one or more of these technologies will eventually demonstrate an emittance change of 0.6 to 0.8 and operate reliably in a space environment.

Current variable-emittance surface-treatment concepts under development include the use of MEMS-scale thermal louvers; thin flaps of insulation that can be held close to, or off of, a surface by utilizing an electrostatic effect; and polymer devices utilizing the EC effect. Thermochromic films have also been proposed. These treatments offer the potential to replace traditional techniques (mechanical louvers, variable-conductance heat-pipe arrays, or electrical heaters for make-up heat) that are used to shut down or reduce the effective capability of a radiator for a variety of safe-hold or operational modes. The MEMS microlouvers, electrostatic flaps, and EC polymer devices will be flight demonstrated on NASA Goddard's ST-5 spacecraft, now scheduled for launch in 2004.

The first of these three VEC concepts (microlouvers) has demonstrated, in a laboratory environment, a change in emissivity of approximately 0.3 to 0.4, with the potential of even greater changes. None of these concepts require more than a few tenths of a watt to operate, although they do need controllers. Survival in the space environment (with all of its difficulties, including UV, hard vacuum, wide temperature changes, AO, solar wind, micrometeroids, etc.) is expected to be the major technical challenge for these devices.

MEMS-Scale Thermal Louvers. Microscale mechanical louvers that function very similarly to conventional louvers have recently been developed. Current MEMS-based microlouvers contain shutters that measure 6 μm by 150 μm. A microphotograph is shown in Fig. 20.6.
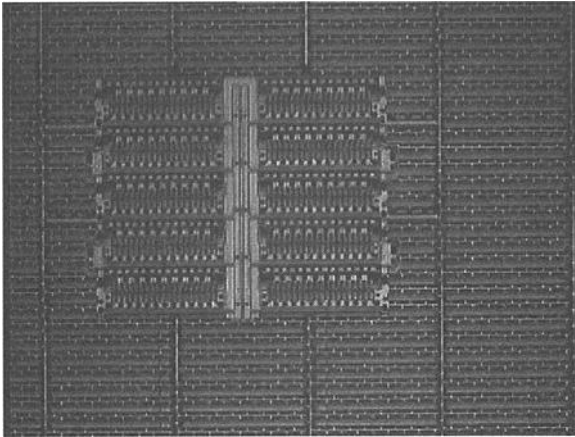
Fig. 20.6. MEMS microlouvers for variable emissivity.

These devices are currently under development and are at a NASA Technology Readiness Level (TRL) of about 5. Prototype devices have been fabricated by the DOE's Sandia National Laboratory for NASA Goddard/Johns Hopkins University Applied Physics Laboratory (JHU APL) and tested in a relevant environment, and they demonstrated an effective emittance change of about 0.4. Improved packaging designs should increase this change. Because these MEMS devices are made from solid silicon chips with a gold coating, they appear to be largely immune from space environmental effects. The major technical concern at this time appears to be contamination and ground handling.

Electrostatic Flap and EC Polymer Device. The electrostatic flap can be scaled to a wide variety of sizes and shapes. It is a very simple device but does require (in its current design) a few hundred volts dc potential to actuate. However, power consumption is negligible. The concept behind this device, currently being developed by Sensortex for GSFC, is illustrated in Fig. 20.7. The conducting polymer concept employs the EC effect that allows reflectance to be tuned over a broad IR wavelength (2 to 40 μm). The device may be considered a composite of several films bonded together. It is very flexible and can be applied over a curved surface.
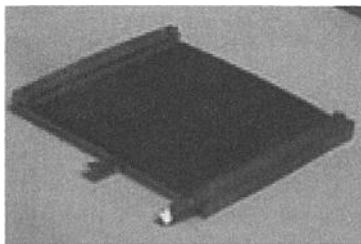
Fig. 20.7. Electrostatic flap.

Single-Phase Heat-Transport Devices

Mechanically Pumped Loop

The mechanically pumped cooling-loop technology that was successfully demonstrated on the Mars Pathfinder is being further developed for longer-life missions (Birur *et al.*,[20.23] Birur and Bhandari[20.24]). The pump used was a centrifugal pump driven by a brushless dc motor. The pump capacity was 0.75 liters per minute (l/min) of Refrigerant 11 with a 27 kPa differential head in the temperature range of −20 to 30°C. The pump consumed about 10 W of power. The pump assembly unit, which weighed about 8 kg, was installed into the cooling loop on the spacecraft. The cooling loop operated continuously for more than seven months on the Mars Pathfinder during its cruise. In a life-test setup, the pump has been successfully tested for a continuous operation of 14,000 hours.

A bearing- and seal-free pump is being developed under a NASA Small Business Innovative Research contract for space applications that require reliable long-life pumps. This pump technology was developed by Advanced Bionics Inc. for artificial heart applications. A prototype of this pump is currently being life-tested at JPL Thermal Technology Laboratory. The pump uses Refrigerant 11 as the working fluid and produces a pressure head of 27 kPa at a flow rate of 0.95 l/min. As of October 31, 2001, the pump had been operating for over 5000 hours without any change in performance.

Electrohydrodyamics (EHD) Devices

EHD devices contain cooling technologies embedded with sensors, electronic chips, or other devices. EHD is an emerging technology for pump single-phase fluids. It can be scaled to small sizes and directly integrated with sensors and other electronic components for spot cooling applications. While the EHD concept was originally demonstrated decades ago, it has only recently been developed to the point where significant pumping heads (in the thousands of Pascals) can be developed. Most recently an EHD system using liquid nitrogen was demonstrated. Although the power needed for pumping is negligible, for conventional-scale applications (e.g., 3-cm-diameter pumps) very high voltages (tens of thousands of volts) are needed. This requirement can be an issue, especially for space applications. However, at micro or MEMS scales the voltage level is reduced dramatically to hundreds or even tens of volts. This technology holds promise for spot electronic cooling, but significant development remains to be done.

MEMS-Based Pumped Cooling Loop

The current interest in micro- and nanospacecraft for future science missions by NASA has necessitated developing MEMS-based thermal control technologies for removing heat from very-high-power-density electronics, lasers, and sensors. The main reason for this is that even with the lower power levels of these spacecraft, the electronics-package power densities have increased because of the shrinking size of the spacecraft. Some of the future micro- and nanospacecraft that are being investigated have dimensions as small as 10 to 15 cm on the side and 5 to 10 cm in height. These systems, called systems-on-a-chip, could have power levels of 20 to 50 W and package avionics, propulsion, and thermal control all as a single unit. The power densities in future microspacecraft are expected to be as high as 25 W/cm^2.

A MEMS-based liquid-pumped cooling system is being investigated at JPL.[20.25] In this technology, a single-phase liquid removes heat from high-density electronics and rejects it at a heat exchanger. The liquid is pumped through microchannels etched in silicon substrate that is attached to the electronics package. The heat removed by the liquid is rejected at another heat exchanger, which is heat-sunk to the spacecraft cooling system. A schematic of this concept along with a picture of the actual microchannel device is shown in Fig. 20.8.

Two-Phase Heat-Transport Devices

Heat Pipes[20.26]

The earliest known description of a heat pipe (the Perkins tube) was published in 1892.[20.27] After the heat pipe was independently reinvented at Los Alamos National Laboratory, intensive development of the device began in the mid-1960s, with experiments continuing into the 1990s. Much of the research was funded by several NASA centers and performed by large aerospace firms.

Research is still being performed in optimization of grooved heat pipes, and in the performance penalties associated with single-sided heat input and removal. While the feedback-controlled heat pipe seems to be the leader in flight applications to spacecraft thermal control, the use of gas-controlled switches and diodes has recently been proposed.

The axial-groove heat pipe is the favored design because of its low cost and uniformity. Designs that can transport more heat over a given distance and withstand a larger adverse tilt are possible with composite or arterial wicks, but the additional capability has not been needed. As the power dissipated by components increases, thermal control systems no longer have the margin that they once did, and limitations (such as the reduction in performance resulting from single-sided input into a grooved pipe) are becoming a factor in design.

The heat-pipe operating-temperature ranges depend strongly on the working fluid. At $-32°C$, the vapor pressure of ammonia is about one atmosphere. As the saturation temperature decreases below this point, the pressure drop in the flowing vapor can become a significant percentage of the total pressure. A temperature drop exists corresponding to this pressure drop. In addition, any noncondensable gases present at the processing temperature have expanded significantly at this colder temperature, blocking off a noticeable part of the condenser. Above 90°C,
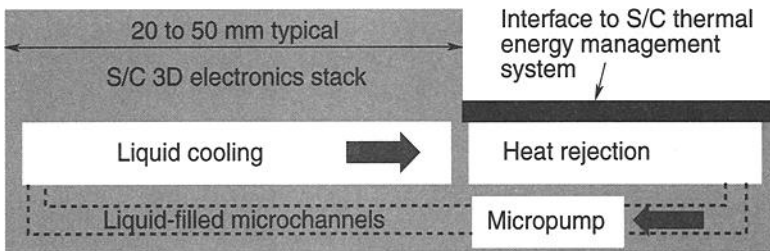
Fig. 20.8. MEMS-based pumped-liquid cooling system for micro/nano sciencecraft.

time-related failures that appear to be metallurgical in nature have been reported, although the ammonia pressure at this point is high.

A cryogenic heat pipe will reach a very high internal pressure if allowed to warm to room temperature. If the pipe walls are designed to be thick enough to withstand this pressure, the pipe is heavy and (if the pipe is to be a diode) conduction along the thick walls becomes significant, even when the pipe is shut off. If an expansion chamber is used to provide additional volume, some means of accommodating the additional volume must be found in the design.

The simplest variable-conductance heat pipe (VCHP) uses the difference in rate of change of pressure with temperature between a saturated vapor (high rate of change) and an ideal gas (low, linear rate of change) to provide temperature control. When a heat pipe that contains noncondensable gas starts up, the gas is swept toward the condenser and collects there. A VCHP has a reservoir to hold the gas at the end of the condenser. A VCHP can also be used as a thermal diode and a thermal switch. The thermal diode transports heat in one direction only, and shuts off if the "condenser" becomes warmer than the "evaporator." A conventional heat pipe would simply reverse—it transports heat as well in "reverse" as it does in the "forward" direction. A thermal switch is a heat path that can be turned on or off in response to an external signal. Because the noncondensable gas drifts in the heat pipe in the direction of vapor flow, if the heat flow is reversed (and if heat is applied to the reservoir as well as the condenser and if the reservoir has liquid in a wick on its wall), the gas will be swept back to the original evaporator, blocking it. However, since the volume of the evaporator is usually much smaller than the volume of the reservoir plus the condenser, a very long gas plug results, causing complete blockage quickly in the shutoff process.

The only heat-pipe envelope materials that have demonstrated long life are metallic. Unfortunately, metallic envelopes tend to have CTEs very different from those of composite structures. Because composite structures are generally cured at temperatures in excess of 90°C, and such structures (particularly radiator panels) can reach very cold temperatures (on the order of −73°C), the thermal stresses developed can crack the structure. One proposal is to allow a very thin metallic wall to flex.

In recent years, other new heat-pipe developments have included "flexible" and "inflatable" heat pipes. Flexible heat pipes generally have such stiff envelopes that they could more properly be considered bendable. Inflatable heat-pipe structures have been built for lunar applications with a single deployment and a small gravity assist in both deployment and operation, but they were not intended for long-term space operations. Some of the walls used were plastic, and flexing of the walls as the internal pressure changes and the generation of noncondensable gas remain potential problems.

The concept of a micro heat pipe was first proposed in 1984 by Cotter[20.28] to improve thermal control for semiconductor devices. A micro heat pipe was defined as one "so small that the mean curvature of the liquid-vapor interface is necessarily comparable in magnitude to the reciprocal of the hydraulic radius of the total blow channel." The sizes of micro heat pipes range from 1 mm in diameter and 60 mm in length to 30 mm in diameter and 10 mm in length. An overview of micro heat-pipe research and development is found in an article by Peterson.[20.29]

Other heat-pipe technology development efforts are still required for future thermal control applications. These include new control schemes, new wick designs, new materials, composite heat pipe, plastic heat pipe, and flat-plate heat pipe.

Loop Heat Pipes (LHPs)

LHPs are two-phase passive heat-transfer devices that use capillary action of a wick structure to pump liquid from a condenser to an evaporator. Unlike fixed-conductance heat pipes, in which the capillary grooves or wick are located along the entire length of the pipe, the LHPs have a main wick located only in the evaporator. The LHP consists of four major elements:

- the evaporator, where the working fluid, changing its phase from liquid to vapor, collects heat
- the condenser, where the vapor condenses and releases heat
- a compensation chamber (CC), where the excess working fluid is stored
- the transfer tubes that carry the vapor from the evaporator to the condenser and carry the condensed liquid back to the evaporator through the CC

LHPs are increasingly being used in Earth-orbiting spacecraft and communication satellites (Maidanik *et al.*,[20.30] Ku[20.31]). They were originally developed in the former Soviet Union and since have flown in several Russian spacecraft. A miniature variable-conductance LHP (VCLHP) is being investigated at JPL for the Mars Rover battery thermal control application. The VCLHP was designed and fabricated by the Dynatherm Corporation of Hunt Valley, Maryland, for JPL in June 1999 (Fig. 20.9). It is currently undergoing tests at JPL (Birur *et al.*[20.32]). The VCLHP has two condensers; one is on the battery and the other is on the external radiator. The variable-conductance function for the LHP is provided by a passive thermal valve integrated in the LHP. This valve allows the external radiator to be bypassed when the evaporator temperature drops below a certain level. The VCLHP is designed for heat-transfer applications with power levels of 60 W or below. The battery thermal application being investigated is for power levels less than 10 W.
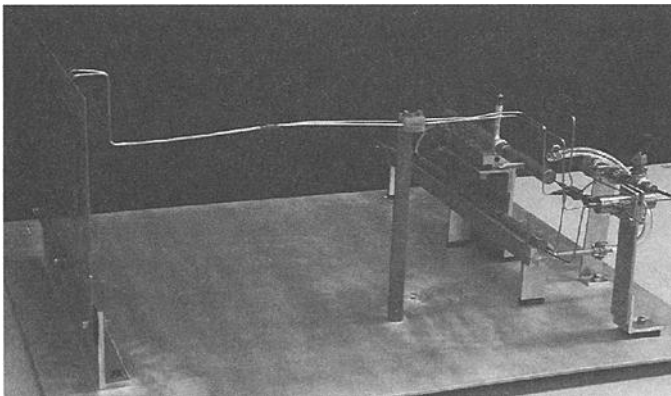
Fig. 20.9. Miniature variable-conductance loop heat pipe.

Capillary Pumped Loops (CPL)

CPLs are two-phase heat-transport devices capable of isothermalizing very large structures. Multi-evaporator CPL systems are now being developed that will allow multiple heat loads to be cooled simultaneously with the potential of heat-load sharing. In the heat-load sharing concept, waste heat from one or more loads is directed toward other loads that need make-up heat to stay warm. Implementation of this concept (which offers the potential of significant energy savings) is possible with multi-evaporator systems. A recent flight experiment, NASA/GSFC's CAPL-3, on STS-108 in December 2001, successfully demonstrated this idea.

Over the course of the flight, CAPL-3 (Fig. 20.10) was able to accomplish all of the minimum required tests, and most of the secondary tests also. The total operating time for CAPL-3 was more than 200 hours, and the longest period for continuous operation was 58 hours. Despite tight energy budgeting, numerous tests were performed, increasing our knowledge and understanding of CPL performance in a space environment. These tests included start-ups, low power operation under various conditions, steady power operation at various power levels, saturation temperature change tests, variable- and fixed-conductance transitions, heat-load sharing demonstrations, variable heat-load tests, single-pump and multiple-pump high-power tests, and pressure priming tests under heat loads. Many of these tests were performed at various operating temperatures and were repeated several times.

Mini-CPLs and -LHPs

Mini-CPLs and -LHPs (Fig. 20.11) are miniaturized thermal control devices suitable for microsats and nanosats. Current technology utilizes ~1.0-inch-diameter evaporators. Miniaturized two-phase heat-transport loops, with 0.5-inch-diameter evaporators and short transport lengths, have been demonstrated in the lab. The goal is to get down to ~0.25-inch diameters.
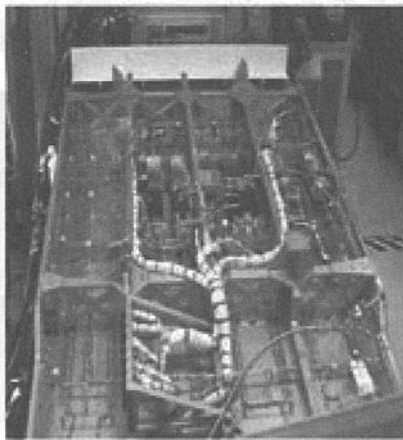
Fig. 20.10. CAPL-3 flight experiment.
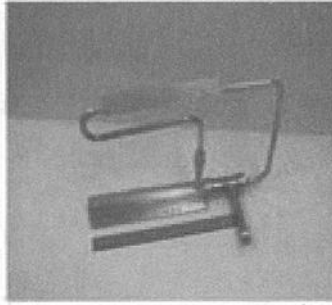
Fig. 20.11. Minicapillary pumped loop/loop heat pipe.

Cryogenic Two-Phase Heat-Transport Devices

Two-phase heat-transport devices capable of operating at deep cryogenic temperatures for sensors, optics, and electronic instruments, such as cryogenic, capillary pumped, two-phase devices (CPLs and LHPs) for heat transport, have been demonstrated both in the laboratory and in space.[20.32] These devices offer a major benefit by providing a greatly improved means of cooling sensors, optics, and electronics at cryogenic temperatures. Use of these devices enables engineers to locate the sensor/optics/electronics remotely from the cooling source (mechanical cryocooler, passive radiator, etc.), thus greatly reducing vibration and EMI and improving packaging design.

A CPL system using nitrogen as a heat-transfer fluid (operating in the 80–100 K range) flew on STS-95 in October 1998 as a flight experiment.[20.33] It successfully demonstrated reliable startup and operation with heat loads of 0.5 to 3.0 W. This CPL is depicted in Fig. 20.12.
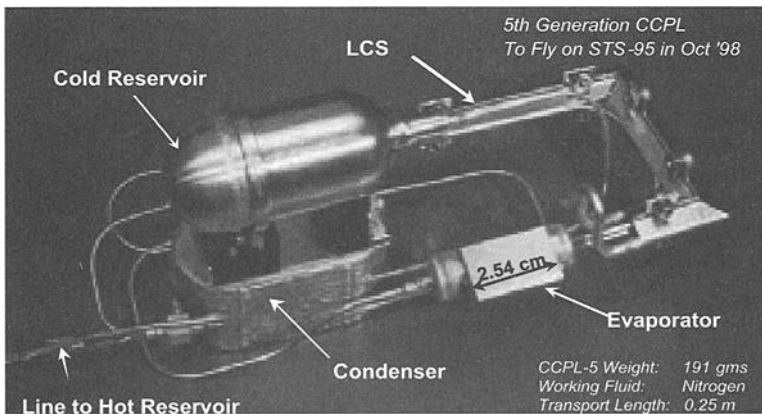
Fig. 20.12. CPL for sensor cooling.

A similar cryo-CPL was charged with neon and successfully operated in a laboratory environment at GSFC. It successfully demonstrated over 2 W of heat-transport capability in the vicinity of 30 K. Recently, a more advanced design demonstrated successful operation (start-up, temperature control, heat transport, etc.) using hydrogen as a heat-transfer fluid in the vicinity of 20 K.

Management of parasitics and effective startup are the major issues with this technology, but successful designs have been developed for devices that operate under temperatures as low as the vicinity of 20 K. Development of devices that operate in the 2–4 K range may also be possible by using helium as an operating fluid, but this technology has not yet been developed.

Heat-Storage Devices

Phase-Change-Material (PCM) Devices

PCM devices are heat-storage devices that utilize PCMs to greatly increase the effective "thermal capacitance" of a device, which will improve thermal stability under changing thermal loads/environments. PCMs absorb or discharge a great amount of energy when melting or solidifying. A PCM device for NASA's Vegetation Canopy Lidar mission is shown in Fig. 20.13.

PCM Storage Units

A PCM thermal storage unit was designed and fabricated for use with the VCLHP. The PCM is dodecane, which has a melting point of –9.6°C with a heat of fusion of 217 kJ/kg and a density of 720 kg/m^3. A thermal storage enclosure containing this PCM was designed so that the batteries can be housed inside. Energy Science Laboratories Inc. (ESLI) of San Diego, California, designed and built the unit in late 1998 to JPL's specifications. Typical challenges in using PCM thermal storage are the poor thermal conductivity of the PCM in its solid phase, containment of
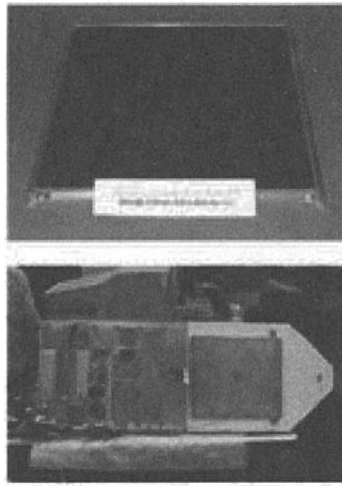
Fig. 20.13. PCM device for NASA's Vegetation Canopy Lidar mission.

the PCM in a leak-tight container that can handle expansion and contraction during the freeze-thaw process, and minimization of the PCM system mass. Several novel features were used in the design and fabrication of the PCM storage unit. A carbon-fiber core, used to provide the PCM with a good thermal conductivity in its solid phase, also provided structural strength to the module. Thin-walled aluminum sheets were used to build the container. In construction of the unit, structural epoxies were used to bond the various container parts. The PCM thermal storage unit is shown in Fig. 20.14. The PCM unit was 350 mm long and 95 mm in diameter. The various components of the unit and their masses are: carbon-fiber core, 80 g; dodecane PCM material, 530 g; and aluminum wall material, 175 g.

Spray Cooling Devices

Spray cooling devices are capable of absorbing very high heat fluxes (hundreds of W/cm^2) from lasers, electronic chips, power converters, and similar high-energy devices. Spray cooling is a relatively new concept now being investigated for ground applications. This technology involves impingement of a fine spray directly onto the surface to be cooled. Laboratory experiments have demonstrated the ability to cool fluxes in excess of 100 W/cm^2. While this concept offers considerable promise for cooling lasers and other high-flux situations, very little work has been done to address space applications of this technology. For example, the collection and condensation of the vapor could be a significant issue in zero gravity. Figure 20.15 is a schematic diagram for a spray cooling device.

Heat Rejection through Advanced Passive Radiators

Heat-rejection technology that makes use of advanced passive radiators is in need of rejuvenation. Many of the specialists who developed expertise in this area are no longer working, and existing designs are prohibitively expensive. A newer concept
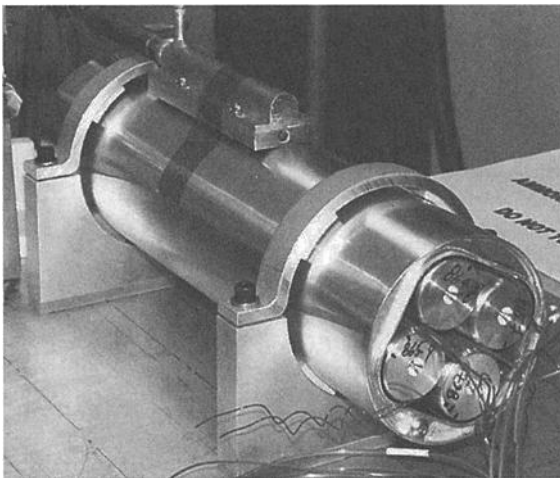
Fig. 20.14. PCM thermal storage system for battery thermal control.
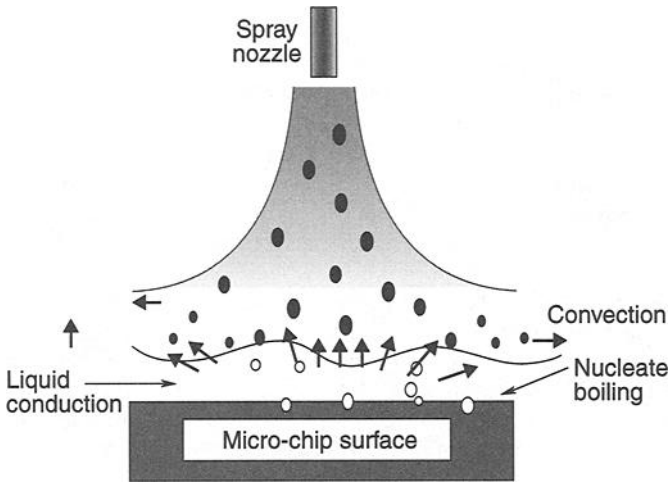
Fig. 20.15. Spray cooling device for thermal control.

currently being developed at GSFC involves the use of flat composite panels coated with a highly specular film and assembled in such a fashion so as to simulate a parabolic shape. This concept is modular and low cost, and it avoids the elaborate machining needed to fabricate a more conventional reflector.

Lightweight Thermal Insulation

High-performance lightweight thermal insulation is another technology that is very important for future spacecraft, especially for future Mars landing missions. New types of insulation, in which aerogel and carbon dioxide are the insulation media, are currently being examined (Tsuyuki *et al.*[20.34]). These new types reduce the mass by 50% compared to the battery thermal insulation currently used for Mars surface landers. In a thermal insulation concept using carbon dioxide as a thermal insulation medium, the insulation is fabricated using two layers of aluminized Kapton separated 4 cm by Mylar stand-offs. The gap between the two layers is filled with carbon dioxide. In the Martian surface operation, the gap is automatically filled by the 8-torr carbon dioxide that exists naturally in the environment. A thermal conductivity of 0.022 W/m·°C at –25°C, which is comparable to that of the batt insulation, has been measured in tests.

Mechanical Heat Switches

Mechanical heat switches have not been extensively used for spacecraft thermal control applications in the past, because of low performance (on/off heat-transfer ratio) and the large switch mass needed to conduct heat. Heat switches based on gas-gap technology are being investigated for situations where the heat-transfer rates are small. Heat switches based on bimetallic mechanisms have been occasionally used in the past but only for low heat-transfer rates. Wax-actuated heat switches are currently being investigated for spacecraft thermal control applications at JPL. Starsys of Boulder, Colorado, which has developed the wax-actuated

heat switch for space applications, is modifying a design created for JPL for application to Mars surface conditions. Those conditions, where an 8-torr carbon-dioxide atmosphere exists, require that the gap in the switch be substantially larger than that used in space. The current Starsys actuator, which weighs about 100 g, provides a heat-transfer rate of 0.7 W/°C and has a ratio of 100:1 for on/off operation (Lankford[20.35]). The heat switch for Mars application is expected to weigh about 60 g and have conductance of 0.45 W/°C and a closed-and-open-position heat-transfer ratio of 25:1.

A miniature heat switch is being developed for future microspacecraft applications under the NASA SBIR program. This technology, developed by ESLI, is expected to reduce the heat-switch mass by an order of magnitude compared to the switch mass in current state-of-the-art technology. The heat switch uses a PCM-based actuator to obtain high heat-transfer rates with low switch mass. A switch based on this technology has demonstrated a performance of 0.12 W/°C with an open/close ratio of 18:1, a weight under 8 g, and a contact area of less than 6 cm^2. The current development plan has goals for enhancing the performance by an order of magnitude.

Heat Pumps

Heat pumps allow radiative heat rejection when the temperature of the thermal sink is near or above the desired control temperature. This condition may occur in several situations, such as planetary/lunar applications, positions in which a radiator is forced to look at the sun, and very low orbits (possibly including balloon applications). Analytical studies[20.36] have demonstrated that a heat pump may be beneficial from a systems-level weight perspective if the effective thermal sink is within 50°C of the source. This assumes near-term technologies (with respect to efficiency and weight) that appear to be achievable; however, no funding has been available to effect the necessary improvements and system design. Some researchers have expressed a concern for the effects of zero gravity on existing designs, but others have suggested wicking schemes and forced convective flow to overcome those effects.

Summary

Advanced thermal control technologies are needed to meet the requirements of future space missions, and many are presently under development at various organizations. Thermal control applications include maintaining spacecraft equipment within allowable temperature limits, minimizing the spacecraft survival power, providing dimensional stability for large spacecraft structures, and providing thermal control for micro- and nanospacecraft. Some of these efforts are improvements on recently demonstrated technologies, such as mechanically pumped cooling loops and LHPs, whereas others are new technologies, such as EC devices for variable-emittance properties and MEMS-based devices for thermal control. At the current level of research and developmental efforts, some of these technologies are expected to be ready for flight applications in two to five years.

Improved thermal control technology is ultimately driven by need and created by the imaginations of thermal engineers. In addition to providing improved performance, many of the new technologies identified in this chapter are robust and

flexible in their applicability. These qualities can significantly enhance a designer's options in the development of a thermal control concept for a given spacecraft.

References

20.1. J. H. Ambrose, B. L. Drolen, and T. T. Lam, "Spacecraft Handle the Heat," *AIAA Aerospace America*, 35–40 (June 1995).

20.2. T. T. Lam, ed., "Study of Advanced Satellite Thermal Management Technology," The Aerospace Corporation, TOR-98(1057)-2, April 1998.

20.3. K. A. Schmidt and C. Zweben, "Advanced Composite Packaging Materials," in *Electronic Materials Handbook, Vol. 1* (ASM International, Materials Park, OH, 1990).

20.4. C. Zweben, "The Future of Advanced Composite Electronic Packaging," in *Materials for Electronic Packaging* (Butterworth-Heinemann, Boston, 1992).

20.5. J. Kibler and W. E. Davis, "Advanced Thermal Applications for Carbon-Carbon Composites," final report prepared for the Naval Surface Warfare Center under Contract No. N60921-91-D-0020/0004 (1992).

20.6. J. Glatz, F. Beavers, and D. Vrable, "Application of Advanced Composites for Electronic Component Thermal Management in Satellites" (written communication from SPARTA, Inc., San Diego, 1994).

20.7. N. M. Teti, "EO-1 Technology Validation Report for the Carbon-Carbon Radiators," Swales Aerospace, 27 July 2001.

20.8. D. Butler, "Carbon-Carbon Radiator," presented at the New Millennium Program's *Mission Technology Forum* (15–16 August 2001).

20.9. E. Talley, "R2100 Structure Development," presented at Lockheed Martin Astro Space (26 January 1996).

20.10. Lockheed Martin Astro Space, "Spacecraft Thermal Control Technology in 2005," presented at Lockheed Martin Astro Space (26 January 1996).

20.11. Swales Aerospace, "Thermal Systems and Composite Structures," presented at Swales Aerospace (January 1996).

20.12. M. J. Montesano and T. G. Cassin, "Demonstration of a High Conductivity, Low Mass Density Thermal Mass Management Material System with an Engineered Thermal Expansion," ASME HTD-Vol. 319/EEP-Vol. 15, 1995.

20.13. W. C. Riley, "'ThermalGraph'—A Carbon/Carbon Composite for Thermal Management" (written communication from Research Opportunities, Inc., Torrance, CA, 1994).

20.14. J. M. Ting and M. Corrigan, "Carbon/Carbon Composites for Space Thermal Management" (written communication from Applied Sciences, Inc., Cedarville, OH, 1994).

20.15. A. S. Crasto and D. P. Anderson, "A Microstructural Study of Carbon Fibers for Thermal Management and Space Applications," *American Institute of Physics Conference 960109* (1996).

20.16. W. Shih, "Carbon Composites for Thermal Management Applications," *American Institute of Physics Conference 960109* (1996).

20.17. G. C. Krumweide, "Applications of High Thermally Conductive K1100X/Resin Systems to Spacecraft Structure and Equipment," *American Institute of Physics Conference 960109* (1996).

20.18. E. M. Silverman and R. Kagohara, "Advanced Composites for Thermal Management Applications," report prepared for the NASA Langley Research Center under Contract No. NAS1-19291 (1994).

20.19. S. Cogan, "Solar Absorptance and Infrared Emittance Modulation with Thin-Film Electrochromic Coatings: Application to Thermal Control," *Seventh Annual Spacecraft Thermal Control Technology Workshop* (El Segundo, CA, The Aerospace Corporation, 6–8 March 1996).

20.20. P. Chandrasekhar, "Conducting Polymer Based Actively IR Modulating Electrochromics for Varied Spacecraft Applications," *Tenth Annual Spacecraft Thermal Control Technology Workshop* (El Segundo, CA, The Aerospace Corporation, 24–26 February 1999).

20.21. P. Chandrasekhar, C. Gerhart, G. Birur, T. Swanson, and L. Kauder, "Current Status of Variable-Emittance Panels Based on Conducting Polymer Electrochromics for Spacecraft Thermal Control," 12th Annual spacecraft Thermal Control Technology Workshop (El Segundo, CA, The Aerospace Corporation, 28 February–2 March 2001).

20.22. L. M. Grob and T. D. Swanson, "Parametric Study of Variable Emissivity Radiator Surfaces," *STAIF-2000 Proceedings* (January 2000).

20.23. G. C. Birur, P. Bhandari, M. B. Gram, and J. Durkee, "Integrated Pump Assembly—An Active Cooling System for Mars Pathfinder Thermal Control," SAE Technical Paper No. 961489, *26th International Conference on Environmental Systems* (Monterey, CA, 8–11 July 1996).

20.24. G. C. Birur and P. Bhandari, "Mars Pathfinder Active Heat Rejection System: Successful Flight Demonstration of a Mechanically Pumped Cooling Loop" SAE Technical Paper No. 981684, *28th International Conference on Environmental Systems* (Danvers, MA, 13–16 July 1998).

20.25. G. C. Birur, T. Sur, A. Paris, P. Shakkottai, A. Green, and S. Haapanen, "Microspacecraft Thermal Control Using a MEMS-based Pumped Liquid Cooling System," Paper no. 4560-28, *Microfluidics and BioMEMS Conference, SPIE Proceedings*, Vol. 4560 (October 2001).

20.26. R.C. Prager in T. T. Lam, ed., "Study of Advanced Satellite Thermal Management Technology," The Aerospace Corporation, TOR-98(1057)-2, April 1998.

20.27. L. P. Perkins and W. E. Buck, "Improvements in Devices for the Diffusion or Transference of Heat," UK Patent 22272, London, England (1892).

20.28. T. P. Cotter, "Principles and Prospects of Micro Heat Pipes," in *Proc. 5th International Heat Pipe Conference* (Tsukuba, Japan, 1984), pp. 328–335.

20.29. G. P. Peterson, "Overview of Micro Heat Pipe Research and Development," *Applied Mechanics Review* **45** (5), (1992).

20.30. Y. F. Maidanik, Y. G. Fershtater, and N. N. Soladovnik, "Loop Heat Pipes: Design, Investigation, Prospects of Use in Aerospace Technics," SAE Technical Paper No. 941185, *International Conference on Environmental Systems* (1994).

20.31. J. Ku, "Operating Characteristics of Loop Heat Pipes," Paper No. 1999-01-2007, *29th International Conference on Environmental Systems* (Denver, CO, 12–15 July 1999).

20.32. G. C. Birur, K. R. Johnson, K. S. Novak, and T. W. Sur, "Thermal Control of Mars Lander and Rover Batteries and Electronics Using Loop Heat Pipe and Phase Change Material Thermal Storage Technologies," SAE Technical Paper No 2000-01-2403, *International Conference on Environmental Systems* (Toulouse, France, 10–13 July 2000).

20.33. J. Ku, M. Kobel, D. Bugby, E. Kroliczek, J. Bauman, and B. Cullimore, "Flight Test of a Cryogenic Capillary Pumped Loop," SAE paper 1999-01-2627 (1999).

20.34. G. Tsuyuki, G. Birur, K. Novak, and J. Stultz, "Lightweight Thermal Insulation for Mars Surface Applications," *39th AIAA Aerospace Sciences Meeting and Exhibit* (8–11 January 2001).

20.35. K. Lankford, "Thin Plate Heat Switches—Development, Performance and Applications," *Tenth Annual Spacecraft Thermal Control Technology Workshop* (El Segundo, CA, 24–26 February 1999).

20.36. T. D. Swanson *et al.*, "Low-Temperature Thermal Control for a Lunar Base," 20th ICES, paper 901242 (July 1990).

Appendix A: Surface Optical Property Data

Most surface property values contained in this Appendix are courtesy of NASA/ GSFC.[*] Properties for materials marked with an asterisk*, however, are design values used by a particular program and are not from the NASA reference.

Unless otherwise noted, values are for beginning-of-life. For some surfaces, degraded values are shown for various periods of time on orbit. Because degradation rates are highly dependent on orbit altitude and the amount of contamination a surface experiences on a particular satellite, reported degraded values should be considered as rough estimates only. Chapter 4 contains extensive data on the degradation of optical solar reflectors and other materials.

Although all values shown are believed to be representative of those used for thermal design analyses in the industry, no guarantee of their validity is implied. In cases where a thermal design is sensitive to any of these parameters, surface optical property measurements and/or a solar-thermal balance test of the thermal design must be conducted to verify flight performance.

Material	α Solar	ε IR
Optical Solar Reflectors (OSR)		
Optical solar reflector (OSR), silvered fused silica (quartz)*	0.07	0.80
Optical solar reflector (OSR), diffuse*	0.10	0.80
Optical solar reflector, indium-tin-oxide (ITO) coated*	0.07	0.76
Optical solar reflector, silvered quartz, Helios program	0.07	0.79
Teflon, aluminized, 0.5 mil*	0.14	0.40
Teflon, aluminized, 1 mil*	0.14	0.48
Teflon, aluminized, 2 mil, sample 1*	0.14	0.60
Teflon, aluminized, 2 mil, sample 2*	0.08	0.66
Teflon, aluminized, tape, 2 mil*	0.17	0.76
Teflon, aluminized, sheet, 2 mil*	0.16	0.65
Teflon, aluminized, 5mil, sample 1*	0.22	0.81
Teflon, aluminized, 5 mil, sample 2*	0.13	0.81
Teflon, aluminized, 5 mil, sample 3*	0.17	0.77
Teflon, aluminized, 5 mil, sample 4*	0.14	0.75
Teflon, aluminized, 7.5 mil*	0.15	0.80
Teflon, aluminized, 10 mil, sample 1*	0.13	0.87

---

*J. H. Henninger, *Solar Absorptance and Thermal Emittance of Some Common Spacecraft Thermal Control Coatings*, NASA Reference Publication 1121 (1984).

Material	α Solar	ε IR
Teflon, aluminized, 10 mil, sample 2*	0.17	0.83
Teflon, aluminized, 10 mil, sample 3*	0.15	0.85
Teflon, silvered, 2 mil*	0.08	0.68
Teflon, silvered, 5 mil	0.08	0.81
Teflon, silvered, 10 mil*	0.09	0.88
<u>Black Coating</u>		
Black Z306 polyurethane paint, 3 mils thick, BOL*	0.95	0.87
Black Z306 polyurethane paint, 3 mils thick, 3 years GEO*	0.93	0.87
Black Z306 polyurethane paint, 3 mils thick, 5 years GEO*	0.92	0.87
Carbon black paint NS-7	0.96	0.88
Catalac black paint	0.96	0.88
Chemglaze Z306 black paint, BOL	0.96	0.91
Chemglaze Z306 black paint, EOL (time, orbit not specified)*	0.96	0.84
Delrin black plastic	0.96	0.87
Ebanol C black	0.97	0.73
Ebanol C black, 384 hours UV	0.97	0.75
GSFC black paint 313-1	0.96	0.86
GSFC black silicate MS-94	0.96	0.89
Hughson black paint H322	0.96	0.86
Hughson black paint L-300	0.95	0.84
Martin black paint N-150-1	0.94	0.94
Martin Black Velvet paint	0.91	0.94
Paladin black lacquer	0.95	0.75
Parsons black paint	0.98	0.91
Pyramil black on beryllium-copper	0.92	0.72
Rough black matte, black paint*	0.90	0.90
3M Black Velvet Paint, BOL	0.97	0.91
3M Black Velvet Paint, 2.5 years*	0.97	0.84
3M Black Velvet Paint, EOL*	0.97	0.84
Velvestat black plastic	0.96	0.85
Black anodize (see Anodize section)		

Material	α Solar	ε IR
Films and Tapes		
Aclar film, aluminized, 1 mil	0.12	0.45
Aclar film, aluminized, 2 mil	0.11	0.62
Aclar film, aluminized, 5 mil	0.11	0.73
Kapton, aluminized, aluminum side*	0.12	0.03
Kapton, aluminized, 0.08 mil	0.23	0.24
Kapton, aluminized, 0.15 mil	0.25	0.34
Kapton, aluminized, 0.25 mil	0.31	0.45
Kapton, aluminized, 0.50 mil	0.34	0.55
Kapton, aluminized, 0.50 mil, Dacron cloth reinforced*	0.35	0.53
Kapton, aluminized, 1 mil, sample 1	0.38	0.67
Kapton, aluminized, 1 mil, sample 2, BOL*	0.36	0.61
Kapton, aluminized, 1 mil, sample 2, 3 years GEO*	0.54	0.61
Kapton, aluminized, 1 mil, sample 2, 5 years GEO*	0.66	0.61
Kapton, aluminized, 1.5 mil	0.40	0.71
Kapton, aluminized, 2 mil, sample 1, BOL*	0.39	0.73
Kapton, aluminized, 2 mil, sample 1, 3 years (orbit not specified)*	0.55	0.73
Kapton, aluminized, 2 mil, sample 1, 5 years (orbit not specified)*	0.67	0.73
Kapton, aluminized, 2 mil, sample 2*	0.41	0.75
Kapton, aluminized, 2 mil, with indium-tin-oxide coating, BOL*	0.34	0.75
Kapton, aluminized, 2 mil, with indium-tin-oxide, 3 years (orbit not specified)*	0.47	0.75
Kapton, aluminized, 3 mil	0.45	0.82
Kapton, aluminized, 5 mil, sample 1, BOL*	0.49	0.83
Kapton, aluminized, 5 mil, sample 1, 2.5 years (orbit not specified)*	0.61	0.83
Kapton, aluminized, 5 mil, sample 1, EOL (time, orbit not specified)*	0. 70	0.83
Kapton, aluminized, 5 mil, sample 2	0.46	0.86
Kapton, aluminized, silicon oxide coated, 0.5 mil, BOL	0.12	0.18
Kapton, aluminized, silicon oxide coated, 0.5 mil, 4000 hours UV	0.28	0.24
Kapton, aluminized, chromium/silicon oxide coated (green), 1 mil	0.79	0.78

Material	α Solar	ε IR
Kapton, aluminized, aluminum-oxide coated, 1 mil	0.12	0.20
Kapton, aluminized, aluminum oxide coated, 1 mil, 1800 hours UV	0.12	0.20
Kapton, aluminized, silicon oxide coated, 1 mil	0.11	0.33
Kapton, aluminized, silicon oxide coated, 1 mil, 2400 hours UV	0.22	0.33
Kapton, silvered, aluminum oxide coated, 1 mil	0.08	0.19
Kapton, silvered, aluminum oxide coated, 1 mil, 2400 hours UV	0.08	0.21
Kapton, black (carbon loaded), 1 mil, BOL	0.92	0.88
Kapton, black (carbon loaded), 1 mil, 5 years GEO*	0.92	0.88
Kapton, black (carbon loaded), 1 mil, 10 years GEO*	0.89	0.88
Kimfoil polycarbonate film, aluminized, 0.8 mil	0.19	0.23
Kimfoil polycarbonate film, aluminized, 0.20 mil	0.20	0.30
Kimfoil polycarbonate film, aluminized, 0.24 mil	0.17	0.28
Mylar, aluminized, 0.15 mil (internal use only, disintegrates in sunlight)	–	0.28
Mylar, aluminized, 0.25 mil (internal use only, disintegrates in sunlight)	–	0.34
Mylar, aluminized, 3 mil (internal use only, disintegrates in sunlight)	–	0.76
Mylar, aluminized, 5 mil (internal use only, disintegrates in sunlight)	–	0.77
Silica cloth*	0.18	0.86
Skylab sail, initial	0.15	0.35
Skylab sail, 1900 hours UV	0.19	0.36
Skylab parasol fabric (orange), initial	0.51	0.86
Skylab parasol fabric (orange), 2400 hours UV	0.65	0.86
Tedlar, goldized, 0.5 mil	0.30	0.49
Tedlar, goldized, 1 mil	0.26	0.58
Tefzel, goldized, 0.5 mil	0.29	0.47
Tefzel, goldized, 1 mil	0.26	0.61
Teflon, goldized, 0.5 mil	0.24	0.43
Teflon, goldized, 1 mil	0.22	0.52
Teflon, goldized, 5 mil	0.22	0.81
Teflon, goldized, 10 mil	0.23	0.82

Material	α Solar	ε IR
Tape, 235-3M, black	0.95	0.90
Tape, aluminum*	0.10	0.04
Tape, 425-3M aluminum foil	0.20	0.03
Tape, aluminum, 2 mil, BOL*	0.15	0.04
Tape, 850-3M, aluminized Mylar	0.15	0.59
Tape, 7361 Mystic aluminized Kapton*	0.09	0.03
Tape, 7452 Mystic aluminum foil	0.14	0.03
Tape, 7800 Mystic aluminum foil	0.21	0.03
Tape, Y9360-3M, aluminized Mylar	0.19	0.03
White Coatings		
Skyspar, Andrew Brown Co.*	0.22	0.91
Barium sulphate with polyvinyl alcohol	0.06	0.88
Biphenyl (white solid)	0.23	0.86
Cat-a-lac white paint	0.24	0.90
Chemglaze A276 white paint*	0.23	0.88
Chemglaze A276, 15000 hrs UV in LEO, no atomic oxygen*	0.60	0.88
Chemglaze A276, 15000 hrs UV in LEO, atomic oxygen exposure*	0.35	0.88
DuPont Lucite acrylic lacquer	0.35	0.90
Dow Corning DC-007 white paint	0.19	0.88
Flamemaster Corp. STM K797 white paint, BOL*	0.22	0.85
Flamemaster Corp. STM K797 white paint, 4 years GEO*	0.60	0.85
NASA/GSFC NS43-C white paint	0.20	0.92
NASA/GSFC NS44-B white paint	0.34	0.91
NASA/GSFC NS74 white paint	0.17	0.92
NASA/GSFC NS-37 white paint	0.36	0.91
Hughson A-276 white paint	0.26	0.88
Hughson A-276 white paint, 1036 hours UV	0.44	0.88
Hughson V-200 white paint	0.26	0.89
Hughson Z-202 white paint	0.25	0.87
Hughson Z-202 white paint, 1000 hours UV	0.40	0.87
Hughson Z-255 white paint	0.25	0.89

Material	α Solar	ε IR
Magnesium oxide white paint	0.09	0.90
Magnesium oxide aluminum oxide paint	0.09	0.92
Opal glass	0.28	0.87
OSO-H 63W white paint	0.27	0.83
P764-1A white paint	0.23	0.92
Potassium fluorotitanate white paint	0.15	0.88
Sperex white paint	0.34	0.85
Dow Corning Thermatrol DC-92-007, BOL*	0.19	0.82
Dow Corning Thermatrol DC-92-007, 4 years GEO*	0.57	0.82
3M-401 white paint	0.25	0.91
Titanium oxide white paint with methyl silicone	0.20	0.90
Titanium oxide white paint with potassium silicate	0.17	0.92
Vita-var PV-100 white paint*	0.22	0.82
Z93 white paint*	0.19	0.89
S13 GLO white paint*	0.19	0.89
S13G white paint, BOL*	0.21	0.88
S13G white paint, 4 years GEO*	0.56	0.88
S-13G-LO white silicone paint, 10 mils thick, BOL*	0.22	0.88
S-13G-LO white silicone paint, 3 years GEO*	0.39	0.88
S-13G-LO white silicone paint, 10 mils thick, 5 years GEO*	0.47	0.88
Polyurethane white paint*	0.27	0.84
3M White Velvet 400 series white paint*	0.30	0.87
ZOT (IITRI YB-71) white paint, BOL*	0.20	0.91
ZOT (IITRI YB-71) white paint, 2.5 years (orbit not specified)*	0.45	0.91
ZOT (IITRI YB-71) white paint, EOL (time, orbit not specified)*	0.70	0.91
Zerlauts S-13G white paint, BOL	0.20	0.90
Zerlauts S-13G white paint, 2.5 years (orbit not specified)	0.52	0.85
Zerlauts S-13G white paint, EOL (time, orbit not specified)	0.70	0.85
Zerlauts Z-93 white paint	0.17	0.92
Z93 white paint, 10 years GEO*	0.55	0.92
ZOT (zinc orthotitanate) with potassium silicate	0.13	0.92

Material	α Solar	ε IR
Zinc oxide with sodium silicate	0.15	0.92
Zirconium oxide with 650 glass resin	0.23	0.88
Other Paints		
Brilliant aluminum paint	0.30	0.31
Chromacoat aluminum paint, BOL*	0.28	0.05
Chromacoat aluminum paint, 3 years (orbit not specified)*	0.33	0.05
Chromeric 586 silver paint	0.30	0.30
DuPont 4817 silver paint	0.43	0.49
Epoxy aluminum paint	0.77	0.81
Finch 643-1-1 aluminum paint	0.22	0.23
NASA/GSFC NS-43-G yellow paint	0.38	0.90
NASA/GSFC NS-53-B green paint	0.52	0.87
NASA/GSFC NS-43-E green paint	0.57	0.89
NASA/GSFC NS-43-C white paint	0.20	0.92
NASA/GSFC NS-55-F green paint	0.57	0.91
NASA/GSFC NS-79 green paint	0.57	0.91
Epon 828 leafing aluminum paint	0.37	0.36
80-U leafing aluminum paint	0.29	0.32
Naval Research Lab leafing aluminum paint	0.24	0.24
Naval Research Lab leafing aluminum paint	0.28	0.29
Silicone aluminum paint	0.29	0.30
Metals		
Aluminum, buffed*	0.16	0.03
Aluminum, heavily oxidized*	0.13	0.30
Aluminum, polished, BOL*	0.15	0.05
Aluminum, polished, EOL (time, orbit not specified)*	0.15	0.05
Aluminum, vapor deposited	0.08	0.02
Aluminum, vapor deposited, on fiberglass	0.15	0.07
Aluminum, vapor deposited, on stainless steel	0.08	0.02
Beryllium copper	0.31	0.03
Chromium, vapor deposited, on glass	0.56	0.17

Material	α Solar	ε IR
Chromium, vapor deposited, on 5 mil Kapton	0.57	0.24
Constantan-metal strip	0.37	0.09
Copper, buffed	0.30	0.03
Copper foil tape, plain	0.32	0.02
Copper foil tape, sanded	0.26	0.04
Copper foil tape, tarnished	0.55	0.04
Germanium, vapor deposited, on glass	0.52	0.09
Gold, vapor deposited, on glass	0.19	0.02
Gold, electroplated	0.23	0.03
Gold, polished, BOL*	0.30	0.05
Gold, polished, EOL (time, orbit not specified)*	0.30	0.05
Gold, sandblasted*	0.48	0.14
Inconel X foil, 1 mil	0.52	0.10
Iron oxide, vapor deposited, on glass	0.85	0.56
Molybdenum, vapor deposited, on glass	0.56	0.21
Nickel, vapor deposited, on glass	0.38	0.04
Nickel, electroless	0.39	0.07
Nickel, Kannigen alloy	0.45	0.08
Platinum foil	0.33	0.04
Rhodium, vapor deposited, on glass	0.18	0.03
Silver, vapor deposited, on glass, un-oxidized	0.04	0.02
Silver, polished, un-oxidized*	0.04	0.02
Silver, oxidized*	–	0.03
Silver, Denton vapor deposited, with protective overcoat*	0.06	0.03
Silver beryllium copper	0.19	0.03
Stainless steel, polished	0.42	0.11
Stainless steel, sandblasted	0.58	0.38
Stainless steel	0.47	0.14
Stainless steel, machine rolled	0.39	0.11
Stainless steel boom, polished	0.44	0.10
Stainless steel 304, 1 mil foil	0.40	0.05

Material	α Solar	ε IR
Tantalum foil	0.40	0.05
Titanium, vapor deposited on glass	0.52	0.12
Titanium*	0.40	0.55
Tungsten, polished	0.44	0.03
Tungsten, vapor deposited, on glass	0.60	0.27

Anodized Aluminum

The optical properties of anodized surfaces are highly dependent upon the anodizing process used. While the anodize properties shown below are representative, actual values may differ substantially from those shown here. Absorptance and emittance measurements of samples of the flight finish should therefore be made. A process for achieving controlled aluminum anodize properties is discussed in Chapter 4.

Material	α Solar	ε IR
Black anodize, sample 1	0.65	0.82
Black anodize, sample 2*	0.86	0.86
Black anodize, sample 3	0.76	0.88
Black anodize, sample 4	0.88	0.88
Blue anodize sample 1	0.67	0.87
Blue anodize sample 2	0.53	0.82
Brown anodize	0.73	0.86
Chromic anodize	0.44	0.56
Clear anodize sample 1	0.27	0.76
Clear anodize sample 2	0.35	0.84
Gold anodize	0.48	0.82
Green anodize	0.66	0.88
Plain anodize	0.26	0.04
Red anodize	0.57	0.88
Sulphuric anodize	0.42	0.87
Yellow anodize	0.47	0.87

Metal Conversion Coatings

The optical properties of conversion coatings are highly dependent upon the process used. While the properties shown below are representative, actual values may differ substantially from those shown here. Absorptance and emittance measurements of samples of the flight finish should therefore be made.

Material	α Solar	ε IR
Clad 7075 aluminum, BOL*	0.25	0.04

Material	α Solar	ε IR
Clad 7075 aluminum, 3 years GEO*	0.26	0.04
Clad 7075 aluminum, 5 years GEO*	0.27	0.04
Irridite aluminum	–	0.11
Alzac A-2	0.16	0.73
Alzac A-5	0.18	–
Black chrome	0.96	0.62
Black copper	0.98	0.63
Black irridite	0.62	0.17
Black nickel	0.91	0.66
Dow 7 on polished magnesium	–	0.49
Dow 7 on sanded magnesium	–	0.65
Dow 9 on magnesium	–	0.87
Dow 23 on magnesium	0.62	0.67
Ebanol C, black	0.97	0.77
TiNOX on copper*	0.95	0.05
Maxorb, nickel oxide or black chrome on nickel foil*	0.90	0.10
Blue anodize titanium foil*	0.70	0.13
Anodized titanium foil, 1 mil, BOL*	0.70	0.10
Anodized titanium foil c.p., 1 mil, 5 years GEO*	0.70	0.10
Composite Coatings		
Aluminum oxide, Al_2O_3, 12 $\lambda/4$, on buffed aluminum	0.13	0.23
Aluminum oxide, Al_2O_3, 12 $\lambda/4$, on buffed aluminum, 2560 hours UV	0.13	0.23
Aluminum oxide, Al_2O_3, 12 $\lambda/4$, on fused silica glass	0.12	0.24
NASA/GSFC dark mirror coating, SiO-Cr-Al	0.86	0.04
NASA/GSFC composite, SiO_x-Al_2-Ag	0.07	0.68
Inconel with Teflon overcoat, 1 mil	0.55	0.46
Silver beryllium copper with Kapton overcoat	0.31	0.57
Silver beryllium copper with Parylene C overcoat	0.22	0.34

Material	α Solar	ε IR
Silver beryllium copper with Teflon overcoat	0.12	0.38
Miscellaneous		
Vespel polyimide SP1*	0.89	0.90
Polyethylene, black *	0.93	0.92
Tedlar, black*	0.94	0.90
Tedlar, white*	0.39	0.87
Fiberglass epoxy (BOL and EOL are the same)*	0.72	0.89
Fiberglass polyimide, BOL*	0.75	0.89
Fiberglass polyimide, 2.5 years (orbit not specified)*	0.78	0.89
Fiberglass polymide, EOL (time, orbit not specified)*	0.80	0.89
Graphite epoxy (BOL and EOL are the same)*	0.93	0.85
Astroquartz fabric*	0.22	0.80
Beta cloth*	0.40	0.86
Grafoil BOL*	0.65	0.34
Grafoil EOL*	0.61	0.34

Appendix B: Material Thermal Properties

The room-temperature material property values contained in this appendix were obtained from a variety of sources. While the values shown are believed to be accurate, no guarantee of their validity is implied. In cases where a thermal design is sensitive to any of these parameters, material property tests and/or a design thermal balance test must be conducted to verify flight performance.

Solid Material Thermal Properties

Material	ρ (kg/cm^3)	k (W/cm°C)	c_p (W-hr/kg°C)
Aluminum			
208	0.00277	1.212	
222	0.00277	1.333	
242	0.00277	1.506	
295	0.00277	1.437	
B295.0	0.00277	1.610	
308	0.00277	1.419	
319	0.00277	1.142	
355	0.00277	1.506	
C355.0	0.00277	1.419	
356	0.00277	1.593	
A356.	0.00277	1.593	
A380.	0.00277	1.004	
A413.0	0.00277	1.212	
443	0.00277	1.454	
B443.0	0.00277	1.471	
514	0.00277	1.385	
518	0.00277	0.969	
520	0.00277	0.883	
D712.0	0.00277	1.385	
1060-0	0.00277	2.354	
1060-H18	0.00277	2.302	
1100-0	0.00277	2.216	0.256
1100-H18	0.00277	2.216	
1350-0	0.00277	2.337	
2011-0	0.00277	1.437	0.267
2011-T3	0.00277	1.506	
2011-T8	0.00277	1.714	

Solid Material Thermal Properties *(Continued)*

Material	ρ (kg/cm^3)	k (W/cm°C)	c_p (W-hr/kg°C)
2014-0	0.00277	1.887	0.256
2014-T4	0.00277	1.333	
2014-T6	0.00277	1.558	
2017-0	0.00277	1.921	0.256
2024-0	0.00277	1.887	0.256
2024-T3	0.00277	1.212	
2024-T36	0.00277	1.212	
2024-T4	0.00277	1.212	
2024-T6	0.00277	1.212	
2025-T6	0.00277	1.558	
2036-0	0.00277	1.593	
2219-0	0.00277	1.731	
3003-0	0.00277	1.766	0.256
3003-H18	0.00277	1.766	
3004-0	0.00277	1.627	0.256
3004-H38	0.00277	1.627	
4032-0	0.00277	1.558	
4032-T6	0.00277	1.385	
5005-0	0.00277	2.060	0.267
5005-H38	0.00277	2.060	
5050-0	0.00277	1.921	0.256
5050-H38	0.00277	1.921	
5052-0	0.00277	1.385	0.256
5052-H38	0.00277	1.385	
5056-0	0.00277	1.160	0.256
5056-H38	0.00277	1.160	
5083-0	0.00277	1.177	0.267
5083-H38	0.00277	1.177	
5083-H113	0.00277	1.177	
5086-0	0.00277	1.264	0.267
5086-H34	0.00277	1.264	
5154-0	0.00277	1.264	0.267
5154-H38	0.00277	1.264	
5252-0	0.00277	1.385	
5254-0	0.00277	1.264	
5254-H38	0.00277	1.264	
5356-0	0.00277	1.177	

Solid Material Thermal Properties *(Continued)*

Material	ρ (kg/cm^3)	k (W/cm°C)	c_p (W-hr/kg°C)
5356-H38	0.00277	1.177	
5357-0	0.00277	1.679	
5357-H38	0.00277	1.679	
5454-0	0.00277	1.350	
5454-H38	0.00277	1.350	
5456-0	0.00277	1.177	0.267
5456-H38	0.00277	1.177	
5457-0	0.00277	1.766	
5652	0.00277	1.385	
5652-H38	0.00277	1.385	
6009-0	0.00277	1.662	
6053-0	0.00277	1.714	
6053-T4	0.00277	1.558	
6053-T5	0.00277	1.714	
6053-T6	0.00277	1.558	
6061-0	0.00277	1.800	
6061-T4	0.00277	1.558	0.267
6061-T6	0.00277	1.679	0.267
6062-0	0.00277	1.714	
6062-T4	0.00277	1.558	
6062-T6	0.00277	1.558	
6063-0	0.00277	2.181	
6063-T42	0.00277	1.921	
6063-T5	0.00277	2.008	
6063-T6	0.00277	2.008	
6063-T42	0.00277	1.921	
6063-T5	0.00277	2.008	
6063-T6	0.00277	2.008	
6262-T9	0.00277	1.714	
6463-0	0.00277	2.181	
6463-T42	0.00277	1.887	
6463-T5	0.00277	2.095	
6463-T6	0.00277	2.008	
7075-T6-T7	0.00277	1.212	0.267
7079-T6	0.00277	1.264	
7178-T6	0.00277	1.264	

Solid Material Thermal Properties *(Continued)*

Material	ρ (kg/cm³)	k (W/cm°C)	c$_p$ (W-hr/kg°C)
Beryllium			
Beryllium	0.00185	1.506	0.523
Be-38 Al	0.00208	2.129	
Be-96A	0.00183	1.419	0.500
Beryllium oxide	0.00230	1.385	0.291
Beryllia	0.00304	2.718	0.291
Copper			
C10200	0.00886	3.912	0.107
C10400,CX	0.00886	3.877	0.107
C11000	0.00886	3.912	0.107
C11300,CXX	0.00886	3.877	0.107
C12200	0.00886	3.393	0.107
C14500	0.00886	3.549	0.107
C14700	0.00886	3.739	0.107
C15000	0.00886	3.670	0.107
C15500	0.00886	3.462	0.107
C17200	0.00886		0.116
C17400	0.00886		
C18200	0.00886	3.237	0.107
C19400	0.00886	2.597	0.107
C21000	0.00886		0.105
C22000	0.00886	1.887	
C22600	0.00886	1.731	
C23000	0.00886	1.593	
C24000	0.00858	1.402	
C26000	0.00858	1.212	0.105
C26800, C27000	0.00858	1.160	0.105
C28000	0.00830	1.229	0.105
C31400	0.00886	1.800	0.105
C33000, CX	0.00858	0.012	0.105
C34000	0.00858	1.160	0.105
C34200, CX	0.00858	1.160	0.105
C36000	0.00858	1.160	0.105
C36500, CX	0.00830	1.229	0.105
C37000	0.00830	1.194	0.105
C37700	0.00858	1.229	0.105

Solid Material Thermal Properties *(Continued)*

Material	ρ (kg/cm^3)	k (W/cm°C)	c_p (W-hr/kg°C)
C38500	0.00858	1.229	0.105
C40500, CX	0.00886		0.105
C44300, CX	0.00858	1.108	0.105
C46400, CX	0.00830	1.160	0.105
C48500	0.00858	1.160	0.105
C50500	0.00886	2.077	0.105
C51000	0.00886	0.692	0.105
C52100	0.00886	0.623	0.105
C52400	0.00886	0.502	0.105
C54400	0.00886	0.866	0.105
C61400	0.00803	0.675	0.105
C63800	0.00830	0.398	0.105
C64700	0.00886	1.766	0.105
C65100	0.00886	0.571	0.105
C65500	0.00858	0.364	0.105
C66700	0.00858	0.969	0.105
C67500	0.00830	1.056	0.105
C68700	0.00830	1.004	0.105
C68800	0.00830	0.398	0.105
C70600, CX	0.00886		0.105
C74500, CX	0.00858		0.105
C80100, CX	0.00886		0.105
C81400, CX	0.00886		0.105
C82000	0.00858	2.597	0.116
C82200	0.00886	1.835	0.116
C82400	0.00830	1.333	0.116
C82500	0.00830	1.298	0.116
C82600	0.00830	1.264	0.116
C82800	0.00830	1.229	0.116
C83600	0.00886	0.727	0.105
C84400, CX	0.00858		0.105
C86200, CX	0.00775	0.364	0.105
C87400	0.00830	0.277	0.105
C90300, Cx	0.00886	0.727	0.105
C92200, Cx	0.00858	0.727	0.105
C93200	0.00886	0.589	0.105
C93700	0.00886	0.467	0.105

Solid Material Thermal Properties *(Continued)*

Material	ρ (kg/cm³)	k (W/cm°C)	c_p (W-hr/kg°C)
C94700	0.00886	0.537	0.105
C94800	0.00886	0.381	0.105
C95200, Cx	0.00747		0.105
C96200, Cx	0.00886		0.105
C97300, Cx	0.00886		0.105
C99300	0.00775	0.433	0.116
Delrin	0.00130	0.004	0.407
Fiberglass			
Fiberglass properties are anisotropic and vary depending on lay-up. Manufacturer's data or testing recommended to establish values.			
Gallium arsenide			
Gallium arsenide	0.00526	0.329	0.093
Germanium			
Germanium	0.00526	0.606	0.090
Glass			
Fused quartz	0.00221	0.015	0.198
Hydrazine			
Liquid	0.00100	0.005	0.861
Solid	0.00116	0.017	0.558
Invar			
Invar	0.00803	0.133	0.140
Kapton			
Standard	0.00141	0.002	0.279
(Black)	0.00130	0.002	0.302
Kovar		0.164	
Magnesium			
AZ31B-F, A	0.00180	0.762	0.291
AZ61A-F	0.00180	0.589	0.291
AZ80A-T5	0.00180	0.502	0.291
ZK60A-T5	0.00180	1.194	0.291
HK31A-H24	0.00180	1.142	0.291
HM21A-T8	0.00180	1.367	0.291
HM31A-T5	0.00180	1.039	0.291
AZ63A	0.00180		0.291
AZ81A	0.00180	0.502	0.291
AZ91A, a	0.00180	0.537	0.291

Solid Material Thermal Properties *(Continued)*

Material	ρ (kg/cm³)	k (W/cm°C)	c_p (W-hr/kg°C)
AZ91C	0.00180		0.291
AZ92A	0.00180		0.291
AM100A	0.00180		0.291
EZ33A-T5	0.00180	1.004	0.291
HK31A-T6	0.00180	0.900	0.291
Molybdenum			
Molybdenum	0.01024	1.471	0.076
TZM	0.01024	1.471	0.076
Mycalex	0.00233		0.140
Nickel			
INCO Alloy	0.00803	0.123	0.128
Incol	0.00803	0.114	0.128
Inconel 825	0.00830	0.111	0.128
Inconel 600	0.00830	0.149	0.128
Inconel 601	0.00803	0.113	0.128
Inconel 625	0.00858	0.099	0.116
Berylm Nic	0.00803		0.140
Monel 400	0.00803	0.218	0.116
Monel 404	0.00886	0.211	0.116
Monel R-405	0.00886	0.218	0.116
Monel K-500	0.00858	0.175	0.116
Monel 502	0.00858	0.175	0.116
80 Ni	0.00830	0.004	0.128
75 Ni	0.00830	0.004	0.128
70 Ni	0.00830	0.004	0.128
60 Ni	0.00830	0.004	0.128
Hast	0.00913	0.134	0.105
Haste	0.00886	0.113	0.105
Alloy C-276	0.00886	0.130	0.116
Alloy G	0.00830	1.541	0.105
IN102	0.00858	0.113	
Inconel 600	0.00803	0.113	0.128
Inconel 617	0.00830	0.135	
Inconel 625	0.00803	0.118	0.128
Inconel 690	0.00830	0.114	
Inconel 700	0.00803	0.125	0.128
Inconel 706	0.00803	0.126	

Solid Material Thermal Properties *(Continued)*

Material	ρ (kg/cm³)	k (W/cm°C)	c_p (W-hr/kg°C)
Inconel 718	0.00830	0.113	
Inconel 722	0.00830	0.147	
Inc X-750	0.00830	0.119	
901	0.00830	0.133	
B-1900	0.00830	0.118	
D-979	0.00830	0.126	
MAR-M	0.00858	0.211	0.233
MAR-M-246	0.00858	0.251	
MAR-M	0.00803	0.270	
TD NI	0.00886	0.467	0.128
TD Ni Cr	0.00858	0.381	
Udimet 500	0.00803	0.244	0.116
Waspaloy	0.00830	0.168	
Nicrotung	0.00830	0.152	
Rene-41, R	0.00830	0.161	
GMR-235-D	0.00803	0.142	
Ha S	0.00886	0.142	
Has X	0.00830	0.158	0.128
Udimet HX	0.00830	0.158	0.128
Unite HX	0.00830	0.158	0.128
INCO HX	0.00830	0.158	0.128
RTV			
11	0.00111	0.003	
21, 41	0.00119	0.003	
31, 60	0.00133	0.003	
511	0.00108	0.003	
560, 577	0.00127	0.003	
615	0.00091	0.002	
616	0.00111	0.003	
630	0.00116	0.003	
632	0.00113	0.003	
634	0.00108	0.003	
619	0.00089	0.002	
627	0.00127	0.003	
655, 670	0.00097	0.002	
8111, 8112	0.00108	0.003	
8262	0.00136	0.003	

Solid Material Thermal Properties *(Continued)*

Material	ρ (kg/cm^3)	k (W/cm°C)	c_p (W-hr/kg°C)
Silicon	0.00233	1.489	0.198
Stainless steel			
201, 202	0.00803	0.163	0.140
203EX	0.00775	0.163	0.140
211	0.00775		
216	0.00803		
301	0.00803	0.163	0.140
302	0.00803	0.163	0.140
302B	0.00803	0.159	0.140
302HQ	0.00803	0.113	0.140
303, 303 Se	0.00803	0.163	0.140
303 PLUS-X	0.00803	0.163	0.140
304	0.00803	0.163	0.140
304L, 304LN	0.00803	0.163	0.140
305	0.00803	0.163	0.140
308	0.00803	0.152	0.140
309, 309S	0.00803	0.156	0.140
310, 310S	0.00803	0.142	0.140
316	0.00803	0.163	0.140
316L	0.00803	0.163	0.140
317	0.00803	0.163	0.140
321	0.00803	0.161	0.140
347-348	0.00803	0.161	0.140
384-385	0.00803	0.164	0.140
403	0.00775	0.249	0.128
405	0.00775	0.270	0.128
410, 410CB	0.00775	0.249	0.128
414	0.00775	0.249	0.128
416, 416SE	0.00775	0.249	0.128
420	0.00775	0.249	0.128
420F	0.00775	0.249	0.128
429	0.00775	0.256	0.128
430	0.00775	0.261	0.128
430F-430FSE	0.00775	0.261	0.128
431	0.00775	0.203	0.128
434	0.00775	0.263	0.128
436	0.00775	0.239	0.128

Solid Material Thermal Properties *(Continued)*

Material	ρ (kg/cm³)	k (W/cm°C)	c_p (W-hr/kg°C)
440A, B, C	0.00775	0.242	0.128
446	0.00747	0.209	0.140
501	0.00775	0.367	0.128
502	0.00775	0.367	0.128
Stainless W	0.00775	0.209	
17-4 PH	0.00775	0.180	
CB-7 Cu	0.00775	0.171	
17-7 PH	0.00775	0.168	
PH 15-7 MO	0.00775	0.161	
17-14 Cu Mo	0.00775	0.151	
AM-350	0.00775	0.154	
AM-355	0.00775	0.159	
JS700	0.00803	0.147	0.140
Uniloy 326	0.00775	0.196	0.116
Nitronic 40	0.00775	0.138	
Nitronic 50	0.00775	0.156	
CA-6NM	0.00775	0.251	0.128
CA-15	0.00775	0.251	0.128
CB-30	0.00747	0.222	0.128
CC-50	0.00747	0.218	0.140
CF-3M	0.00775	0.163	0.140
CD-4M Cu	0.00775	0.152	0.128
CE-30	0.00775	0.147	0.163
CF-3	0.00775	0.159	0.140
CF-8	0.00775	0.159	0.140
CF-20	0.00775	0.159	0.140
CF-8M, CF-12M	0.00775	0.163	0.140
CF-8C	0.00775	0.161	0.140
CF-16F	0.00775	0.163	0.140
CG-8M	0.00775	0.163	0.140
CH-20	0.00775	0.142	0.140
CK-20	0.00775	0.137	0.140
CN-7M	0.00775	0.209	0.128
HA	0.00775	0.260	0.128
HC	0.00775	0.218	0.140
HD	0.00775	0.218	0.140
HE	0.00775	0.147	0.163

Solid Material Thermal Properties *(Continued)*

Material	ρ (kg/cm^3)	k (W/cm°C)	c_p (W-hr/kg°C)
HF	0.00775	0.144	0.140
HH	0.00775	0.142	0.140
HI	0.00775	0.142	0.140
HK	0.00775	0.137	0.140
HL	0.00775	0.142	0.140
HN	0.00775	0.130	0.128
HP	0.00775	0.130	0.128
HT	0.00803	0.121	0.128
HU	0.00803	0.121	0.128
HW	0.00803	0.125	0.128
HX	0.00803	0.125	0.128
Tantalum	0.01661	0.545	0.042
Teflon			
FEP	0.00221	0.002	0.279
TFE	0.00221	0.002	0.267
Titanium			
Titanium	0.00443		0.145
Ti-0.15-0.2 Pd	0.00443	0.078	0.145
Ti-5Al-2.5 Sn	0.00443	0.078	0.145
Ti-5AL-6Sn-2Zr-1Mo	0.00443	0.066	0.145
Ti-8AL-1Mo-1V	0.00443	0.073	0.145
Ti-6Al-4V cast	0.00443	0.073	0.159
Ti-8Mn	0.00471	0.109	0.137
Ti-6Al-2Sn-4Zr-6Mo	0.00471	0.071	
Ti-6Al-6V-2Sn	0.00443	0.073	0.180
Ti-6Al-2Sn-4Zr-2Mo	0.00443	0.061	0.116
Ti-3Al-13V-11Cr		0.069	0.140
Tungsten	0.01938	1.679	0.040

Honeycomb Panel Thermal Properties

Honeycomb composites of various types are commonly used on spacecraft as equipment shelves, solar-array substrates, etc. The following equations for calculating the effective conductivity through honeycomb core material in different directions were developed by Lee Hennis of Boeing Satellite Systems.

Because of its construction, honeycomb has directionally dependent conductivities. These are presented for each of the three directions for a general hexagonal honeycomb structure, as well as the typical regular hexagonal structure. The final "k" and "C" equations given at the end of each section are expressed in terms of variables that can be obtained from the face of an engineering drawing. It should be noted that this section deals exclusively with the core material and does not in any way include the facesheets that will be bonded to the core. Also, radiation exchange between walls of hexagonal structure has been excluded from this discussion. (Note: radiation-heat transfer is small compared to conduction for aluminum honeycomb panels. –Editor)
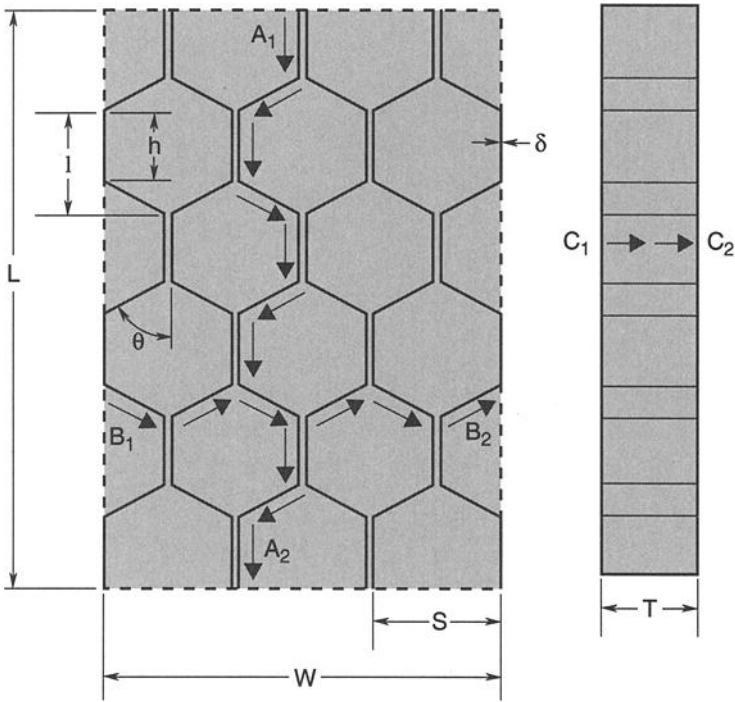
Nomenclature

L = Overall honeycomb length (in the ribbon direction)
W = Overall honeycomb width (perpendicular to ribbon direction)
T = Thickness of honeycomb
S = Cell size, face to face
δ = Ribbon thickness
h = Length of cell wall
θ = Cell angle

Conduction in the "L" direction

For one ribbon:

$$C_{A_1 - A_2} = KA/x$$

where k = conductivity of the ribbon material
A = cross-sectional area of the ribbon
x = total length of the ribbon
A = δT
x = σL
where σ = an extension factor
σ = $2h/l$
l = $h + h \cos \theta$
therefore s = 2/(+ cos θ)

Substituting:

$$C_{A_1 - A_2} = k\delta T/\sigma L$$

Now for n ribbons: (It is assumed that the net heat interchange between ribbons is negligible for this directional calculation.)

n = # of ribbons
n = 2W/S (W/S = # of cells in the W direction)
CL = kA/x
where k = conductivity of the honeycomb material
A = $\delta T(2W/S)$
x = σL

Substituting:

$CL = (2k\delta/\sigma S)(WT/L)$

or $\bar{k}_L$ = equivalent honeycomb conductivity in "L" direction

$\bar{k}_L = 2k\delta/\sigma S$

For the normal hexagonal honeycomb structure:

θ = 60°
σ = 2/(l + cos 60°)
σ = 2/1.5 = 4/3

Substituting:

$\bar{k}_L = 3k\delta/2S$

$$\boxed{CL = (3k\delta/2S)(WT/L)}$$

Conduction in the "W" direction

For one path $B_1 - B_2$: (It is assumed that the net heat interchange between paths is negligible for this directional calculation. It can be shown that the contact resistance at the ribbon interfaces along the path is also negligible compared to the material resistance.)
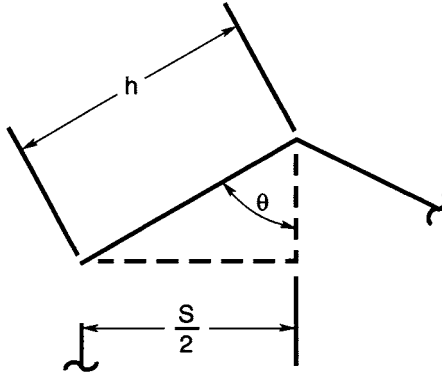
$$C_{B_1 - B_2} = kA/x$$

where k = path material conductivity
A = cross-sectional area of the path
x = total path length
A = δT
x = nh ($n = 2W/S$)
x = $2Wh/S$
$\sin \theta = S/2h$
$h = s/2 \sin \theta$
therefore $x = W/\sin \theta$

Substituting:
$$C_{B_1 - B_2} = k\delta T \sin \theta/W$$

Now for m paths:
m = # of paths
m = $L/l = L/(h + h \cos \theta) = \sigma L/2h = \sigma L \sin \theta/S$
$C_W = kA/x$
where k = conductivity of the honeycomb material
A = $m \, \delta T = \delta T(\sigma L \sin \theta/S)$
x = $W/\sin \theta$

Substituting:
$$C_W = (k \, \delta \sigma \sin^2 \theta/S)(LT/W)$$

or $\bar{k}_W$ = equivalent honeycomb conductivity in "W" direction

$$\bar{k}_W = k\,\delta\sigma\sin^2\theta/S$$

For the normal hexagonal honeycomb structure:
$$\theta = 60°$$
$$\sin^2\theta = 3/4$$
$$\sigma = 4/3$$

Substituting:
$$\bar{k}_W = k\,\delta/S$$

$$\boxed{C_W = (k\,\delta/S)(LT/W)}$$

Conduction in the "T" direction

For one ribbon:
$$C_{C_1-C_2} = kA/x$$
where k = conductivity of the ribbon material
A = cross-sectional area of the path
x = total path length
A = $\sigma L\delta$
x = T

Substituting:
$$C_{C_1-C_2} = k\sigma\delta\,L/T$$

Now for n ribbons: (It is assumed that the net heat interchange between ribbons is negligible for this directional calculation.)

$$C_T = kA/x$$
where k = conductivity of the honeycomb material
A = $n\,\sigma\delta L$
n = $2W/S$
A = $2\sigma\delta LW/S$
x = T

Substituting:
$$C_T = 2k\sigma\delta LW/ST$$
or $\bar{k}_T$ = equivalent honeycomb conductivity in "T" direction
$$\bar{k}_T = 2k\sigma\delta/S$$

For the normal hexagonal honeycomb structure:
$$\theta = 60°$$
$$\sigma = 4/3$$

Substituting:

$$\bar{k}_T = 8k\sigma\delta/3S$$

$$\boxed{C_T = (8k\sigma\delta/3S)\,(LW/T)}$$

Appendix C: Thermally Conductive Filler Materials and Suppliers

The following table contains detailed data for a wide variety of thermal interface enhancement materials. Not all of these have been qualified for spacecraft use. Verification of suitability for use in a space environment may therefore be required. Note: Content and volume of "Table of Typical Properties" depends on presented manufacturer information. In most cases the following data are included: density, color, thickness range, thermal impedance, thermal conductivity, operation temperature, dielectric strength, volume resistivity, adhesive characteristics, storage life, cleanability.

		Basic Characteristics					
Material	Advantages Application	Thick. (mm)	Cond. (W/mK)	Temp. (°C)	Available Technical Data	Structure	Manufacturer
Toptherm Red 86/82	High thermal conductivity, electrical isolation, best surface contact. Placed between hot devices (semiconductors) and heat sinks. Power, radio, TV, computer industries.	0.225	6.5	−40 to +250	Table of typical properties Breakdown voltage: >1 k V	Flexible foil based on elastomer with ceramic fillers	Alfatec Kerafol gmbh
Kera-therm Grafite 90/10	High thermal conductivity, electrically conductive. Mostly used in the CPU applications. 90/10-S version is combined with phase change material	0.2	55 in X and Y direction, 5.5 in Z direction	−40 to +500	Table of typical properties	100% pure graphite in blank version or laminated with wax, adhesive, or filled adhesive	Meckenloher Str.11 Rednitzhembach, Bayern 91126 Germany
Kera-therm Blue Soft-therm 86/200 G4	No outgassing, very soft and highly compressible. For RIMM—800 Mhz Modules between the small sensitive silicon-chips and the heat sink on top of them, http://www.rimm.com/; for flip chips	0.5 to 1.0	1.5	−40 to +120	Table of typical properties. Diagrams: deflection vs. pressure, thermal resistance vs. pressure. Dielectric breakdown of 15 kV/mm	Silicone free, ceramic filled; available in high mechanical strength or high thermal conductivity versions	Tel. +49 9122.9796.0 Fax +49 9122.9796.50 Email info@alfatec.de Web www.alfatec.de

| Material | Advantages Application | Basic Characteristics | | | | | | Manufacturer |
		Thick. (mm)	Cond. (W/mK)	Temp. (°C)	Available Technical Data	Structure		
Kera-therm Softtherm 86/260	Conformable and compressible polymer. PSA applications where enhanced stickiness required. Most suitable for heat-plate application.	0.5 to 5.0	1.5	−60 to +200	Table of typical properties. Diagram of compressibility. Dielectric breakdown of 10 kV/mm	Gap filler based on silicone polymer filled with ceramic powder		
Kera-therm Blue U23 (Polyure-thane)	Flexible foil, high electrical isolation, high mechanical strength. Power electronics, power supply	0.225	1.2	−40 to +90	Table of typical properties. Dielectric breakdown of 40kV/mm	Silicone free foil (based on polyure-thane)		
Kera-therm Copper 86/70	High flexibility. For EMC shielding, PC Boards.	0.25	1.7	−60 to +250	Table of typical properties. Dielectric breakdown of 1kV/mm	Copper lining on one side of foil		
Kera-therm Pink 86/50	High thermal conductivity, good electrical isolation. Especially suitable for power modules in which large quantities of heat needs to be conducted. Aerospace applications.	0.225	2.9	−60 to +250	Table of typical properties. Dielectric breakdown of 7 kV/mm	Standard foil filled with boron nitride. Available with PSA, fiberglass reinforced or combination		
Kera-therm Green 86/37	Especially suitable for use in industries requiring high electrical isolation. Automotive electronics, mechanical engineering, aviation.	0.225	1.8	−60 to +250	Table of typical properties. Dielectric breakdown of 26kV/mm	Available in basic version, or with one side PSA, fiberglass reinforced and com-bination		

Material	Advantages Application	Thick. (mm)	Cond. (W/mK)	Temp. (°C)	Available Technical Data	Structure	Manufacturer
					Basic Characteristics		
T-pli 200 Series™	Combination of very high thermal conductivity with soft compliant surface. Used as a mounting material between a solid state heat generating component and its heat sink. Micro heat pipe thermal solutions.	0.125 to 5	6	–40 to +200	Table of typical properties. Diagrams: thickness vs. thermal resistance, pressure vs. deflection. Dielectric strength: 3.2 to 6 kV	Boron nitride filled silicone elastomer	Thermagon, Inc. 4707 Detroit Ave., Cleveland, OH 44102 USA
T-gon 200 Series™	Thermally conductive insulator, good chemical resistance mechanical and physical performances. Used in interfaces where pressure is applied: diodes, resistors, micro-processors.	0.2 to 0.5	5	–60 to +200	Table of typical properties. High thermal stability to 200°C. Dielectric strength: >6 kV	Boron nitride filled silicone elastomer, fiberglass reinforced	Tel. 216.939.2300 Fax 216.939.2310
T-gon 800 Series™	Thermally and electrically conductive, conformable, good shock resistance. For cost-sensitive applications. Between heat sinks and semiconductor packages, most power devices	0.125 to 0.5	140 in X and Y direction, 5 in Z direction	–20 to +200	Table of typical properties	Grain-oriented, plate-like structure from graphitic composite—98% graphite without binders or additives	Email info@thermagon.com Web www.thermagon.com
T-flex 600 Series™	Ultimate blend of softness, compressibility and thermal conductivity. Used to blanket highly uneven surfaces; notebooks and automotive application, heat pipe thermal solutions	0.5 to 5	3	–45 to +200	Table of typical properties. Dielectric strength: >6 kV	Ultra soft polymer-based gap filler – boron nitride filled silicone elastomer	

| Material | Advantages Application | Basic Characteristics | | | | | |
		Thick. (mm)	Cond. (W/mK)	Temp. (°C)	Available Technical Data	Structure	Manufacturer
T-putty 502 Series™	Ultra soft thermally conductive putty. Used in applications where large tolerance differences can create the need for compression of the interface material beyond 50% of its original thickness, and to prevent cracking when interfacing ceramic modules to metal parts	0.5 to 5	3	−45 to +200	Table of typical properties. Dielectric strength: >6 kV	Boron nitride filled silicone elastomer, fiberglass reinforced	
T-form 400 series™	Combination of high thermal conductivity with elasticity and conformability of a soft gap filler, as well unprecedented strength. Used in semiconductor equipment, notebook manufacture. Micro heat pipe thermal solutions.	0.25 to 5	6	−45 to +200	Table of typical properties. Pressure—0.69 10^5 N/m^2. Diagram: thickness vs. thermal resistance. Elongation—up to 120%. Dielectric strength: >6 kV	Boron nitride filled, silicone elastomer	
Sil-less T-grease	Reduced contamination	–	0.8 to 2.5	−40 to +200	Table of typical properties	Silicone free joint compound (paste)	
Kool-pads K230	Thermally conductive, electric insulator. Used for high reliability equipment. Military, aerospace industries	0.23	1.1	−60 to +180	Table of typical properties, breakdown voltage: 4.5 kV, mounting pressures: 20.58 to 41.16 10^5 N/m^2	Low silicone content based interface material includes highly conductive fillers	Warth International LTD Birches Industrial Estate, East Grinstead, West Sussex RH19 1XH United Kingdom

Material	Advantages Application	Basic Characteristics					
		Thick. (mm)	Cond. (W/mK)	Temp. (°C)	Available Technical Data	Structure	Manufacturer
Kool-pads CM20	No outgassing, excellent heat transfer and electrical conductivity. Interfacing heat sinks, power modules.	0.2	3.9	−200 to +500	Table of typical properties. Diagram: torque per bolt vs. thermal resistance, recommended compression: $34.3\ 10^5\ N/m^2$	Dry carbon structure pads consisting of 98% graphite	Tel. +44 (0) 1342.315044 Fax +44(0) 1342.312969
Kool-pads PK17, PK23	Low cost, strong flexible and clean insulator, which will not crack, age, or permit contamination. Aerospace, telecommunication applications.	0.229	0.8 to 1.1	−20 to +150	Table of typical properties, breakdown voltage: 4.5 to 5.5 kV	Free of silicone polyester compound coated onto a layer of woven glass fibre	Email solutions@warth.co.uk Web www.warth.co.uk
KoolForm (KF)	Highly conformable thermally conductive air gap filler. Fills irregular gaps between hot electronic components and their adjoining heatsinks or mounting chassis. Electronics.	0.25 to 5	1.5 to 2.2	−60 to +200	Table of typical properties, breakdown voltage: >5 kV	Low modulus silicone polymer loaded with thermally conductive particles	
Kool-pads K381	High performance thermally conductive, electric isolator.	0.381	3.4	−60 to +180	Table of typical properties, breakdown voltage: 4 kV	Silicone elastomer specially loaded with boron nitride	

| Material | Advantages Application | Basic Characteristics | | | | | |
		Thick. (mm)	Cond. (W/mK)	Temp. (°C)	Available Technical Data	Structure	Manufacturer
Kool-pads HeatPath GTQ 1500	Combining softness and compressibility with good thermal performance and excellent surface wetting. Used in higher specification products.	0.25 to 1	1.1	−40 to +150	Table of typical properties. Dielectric breakdown voltage: 2 to 6 kV	Alumina-filled silicone gel incorporates a fiberglass carrier	
C695	Flexible, thermally and electrically conductive. Used in applications with multiple components on large heat sink	1.3	4.0	−30 to +150	Table of typical properties. Diagram: contact pressure vs. thermal resistance. Contact pressure: $<1.38 \ 10^5 \ \text{N/m}^2$	0.13 mm graphite film coated on one side with 0.025mm acrylic pressure sensitive adhesive (PSA)	Saint-Gobain Performance Plastics 14 McCaffrey St. Hoosick Falls, NY 12090-0320 USA
C675	Thermally conductive. Used in attaching microprocessors or isolated components to heat sink.	1.5	1.1	−30 to +150	Table of typical properties. Diagram: contact pressure vs. thermal resistance. Contact pressure: $<1.38 \ 10^5 \ \text{N/m}^2$	Material is constructed of 0.05 mm aluminum foil coated on both sides with 0.05mm acrylic PSA	Tel. 800.962.2666 518.686.7301 Fax 518.686.4840
Furon 400 Series	Soft, thermally conductive, good dielectric. Heat transfer gasket between power devices, heat generating devices and their mountings.	0.01 to 0.5	0.45 to 1	−27 to +204	Table of typical properties. Dielectric strength: 3.5 to 10 kV	Silicone coated fiberglass fabrics	Email Joanne.Brahan@ saint-gobain.com Web www.furon.com

		Basic Characteristics					
Material	Advantages Application	Thick. (mm)	Cond. (W/mK)	Temp. (°C)	Available Technical Data	Structure	Manufacturer
HTSP	High thermal conductance. Encapsulating, cable jointing, sealing and protection: manufacturing industries		2.9	−50 to +200	Table of typical properties	Silicone compound	Electrolube Wentworth House, Blakes Road Wargrave Berkshire PG108AW UK Tel.+44(0)118.940.4 031/3014 Fax +44 (0)118.940.3084
Cool-pad CPR 7156	Conformable thermal pad can be pre-applied onto heat sinks. Used inP C microprocessors, power supplies, between power devices and heat sinks		4	−55 to +150	Table of typical properties. Dielectric strength: > 20 kV/mm	Polymer interface pad	A.I.Technology, Inc. 70 Washington Rd. Princeton Junction, NJ 08550 USA
ME 8456-XT	Proven success for large area bonding. Electrically conductive. Electronics.		4 to 8	−55 to +150	Table of typical properties, outgassing data: TML = 0.25%, VCM = 0.05%	Flexible Ag-filled epoxy	Tel. 609.799.9388 Fax 609.799.9308 Email ait@aitechnology.com Web www.aitechnology.com
Polarchip CP7003	Soft, conformable, highly compressible material. Used for filling air gaps between heat generating devices on printed circuit boards and the heat sinks. Electronics.	0.5 to 2.0		−50 to +150	Table of typical properties. Diagrams: applied pressure vs. compression, initial clamping pressure vs. thermal impedance	Fluoropolymer composite consisting of an expanded polytetrafluoroethylene matrix filled with boron nitride particles	W. L. Gore & Associates, Inc. 2020 Prairie Lane Eau Claire, WI 54703 USA Tel. 800.445.4673

| Material | Advantages Application | Basic Characteristics | | | | | |
		Thick. (mm)	Cond. (W/mK)	Temp. (°C)	Available Technical Data	Structure	Manufacturer
Polarchip CP8000	Used for filling the air gaps between heat generating devices on printed circuit boards and the heat sinks, heat spreaders, and metal chassis that are used to dissipate the heat. Electronics.	0.5 to 2.0		−50 to +150	Table of typical properties. Diagrams: applied pressure vs. compression, initial clamping pressure vs. thermal impedance.	Fluoropolymer composite consisting of an expanded polytet-rafluoro-ethylene matrix filled with boron nitride particles	Fax 800.757.4673 Email bmahre@wgore.com Web www.gore.com/electronics
Sure-form	Highly conformable, soft, naturally tacky, for high compression loads. Used where surfaces textures vary and the space between surfaces is uneven. Electronics, optics.	2 and above	1.7	−40 to +150	Table of typical properties. Dielectric strength: 12.5 kV/mm	Gap filler formulated with non-silicone, dry-to-touch thermal grease	AOS Thermal Compounds 22 Meridian Road Suite 6 Eatontown, NJ 07724 USA
AOS Non-silicone HTC-60 (52031)	Superior thermal conductivity. Interfacing between a heat generating device and heat sink metal chassis		2.5	−40 to +200	Table of typical properties. Dielectric strength: 13.8 kV/mm	Non-silicone paste	Tel. 732.389.5514 Fax 732.389.6380
AOS Electrically Conductive Grease (57000)	Premium electrical and thermal conductivity, thermally stable and nonflammable. Low power electronic and high power electrical applications.		7.2	−40 to +200	Table of typical properties	Chemically inert heat sink compound—paste	Email sales@aosco.com Web www.aosco.com

| Material | Advantages Application | Basic Characteristics | | | | | |
		Thick. (mm)	Cond. (W/mK)	Temp. (°C)	Available Technical Data	Structure	Manufacturer
Poly-pads	Thermally conductive insulators for silicone-sensitive application. Aerospace applications	0.15; 0.23	0.9 to1.3	−20 to +150	Table of typical properties. Breakdown voltage: 2.5 to 6 kV	Ceramic filled polyester resins coating either side of a fiberglass carrier or a Kapton carrier	The Bergquist Company 18930 West 78th Street Chanhassen, MN 55317 USA
Sil-pad 1000	Thermally conductive electrical insulator. Used to electrically isolate power sources from heat sinks	0.23	1.2	−60 to +180	Table of typical properties, outgassing data: TML = 0.22%, CVCM = 0.08%. Breakdown voltage: 4.5 kV	Composite of silicone rubber and fiberglass special filled	Tel. 952.835.2322 Fax 952.835.0430 Email madeline@bergquist company.com
Sil-pad 2000	High thermal and dielectric performance. Military/aerospace, commercial applications	0.38 (0.25 to 1.5)	3.5	−60 to +200	Table of typical properties, outgassing data: TML = 0.07%, CVLM = 0.03%. Breakdown voltage: 4kV	Silicone elastomer specially filled	Web www.bergquistcompany.com
Sil-pad K-10	Highest thermal performance of the Bergquist film based insulators. Designed to replace brittle ceramic insulators	0.15	1.3	−60 to +180	Table of typical properties, outgassing data: TML= 0.36%, CVCM = 0.09%. Breakdown voltage: 6 kV	Combination of special Kapton MT polyamide film with a filled silicone rubber	

| Material | Advantages Application | Basic Characteristics | | | | | |
		Thick. (mm)	Cond. (W/mK)	Temp. (°C)	Available Technical Data	Structure	Manufacturer
Q-pad 3	Thermally/electrically conductive. Grease replacement material where electrical insulation is not required	0.15	2.0	−60 to +180	Table of typical properties	Graphite imbedded in a polymer matrix, fiber glass reinforced	
Therm-gap G974	Electrically nonconductive with high thermal performance. Power conversion, BGA packages, for applications with pressures from 0.03 to 0.69 Mpa	0.25 to 1.5	4.0	−60 to +150	Table of typical properties. Dielectric strength—6 kV/mm	Boron-nitride-filled silicone elastomer	Chomerics Division of Parker Hannifin Corp.
Cho-therm 1671	Low thermal impedance, high dielectric strength. Interfacing between power semiconductor devices and their heat sinks. Military application	0.38	2.6	−60 to +200	Table of typical properties, outgassing data: TML = 0.76%; CVCM = 0.07%. Contact pressure—$(2.07–3.55)10^6$ N/m^2. Breakdown voltage: 4 kV	Silicone elastomer filled with boron nitride particles	77 Dragon Court, Woburn, MA 01888 USA Tel. 781.935.4850 Fax 781.933.4318
Cho-therm 1678	Thermally conductive elastomer insulators. Electronics, power supplies	0.25	2	−60 to +200	Table of typical properties, outgassing data: TML = 0.55%; CVCM = 0.12%. Contact pressure $(2.07–3.55) 10^6$ N/m^2. Breakdown voltage: 2.5 kV	Boron nitride filled silicone reinforced with fiberglass	Email mailbox@ chomerics.com Web www.chomerics. com

| Material | Advantages Application | Basic Characteristics | | | | | Manufacturer |
		Thick. (mm)	Cond. (W/mK)	Temp. (°C)	Available Technical Data	Structure	
Cho-therm T500	Highly thermally conductive interface insulator. Replacing combination of beryllium oxide or mica wafers and silicone grease.	0.25	2.1	–60 to +200	Table of typical properties, outgassing data: TML = 0.4%; CV CM = 0.1%. Contact pressure—(2.07–3.55)10^6 N/m^2. Breakdown voltage: 5 kV	Combination of silicone binder with a boron nitride filler reinforced with fiberglass	
Sarcon GR-N Series	Highly conformable and high heat conducting electrically insulating materials, easily fit and adhere to most shapes and sizes of components. Used for filling air gaps and uneven surfaces.	1 to 5	7.9	–60 to +200	Table of typical properties	Advanced silicone rubber-gel materials	Fujipoly America Corp. 365 Camegie Ave. Kenilworth, NJ 07033-0679 USA Tel. 908.298.3850 Fax 908.298.1232 Email frank@fujipoly.com Web www.fujipoly.com
H74/ H77	Low outgassing dispensable pastes for hermetically sealing lids to packages, and general heat dissipation. Aerospace applications		1 to 1.1	150/ 160 max.	Table of typical properties	Two component, alumina filled epoxy	Epoxy Technology, Inc. 14 Fortune Dr. Billerica, MA 01821 USA Tel. 978.667.3805 Fax 978.663.9782 Email sales-info@epotek.com Web www.epotek.com

Index